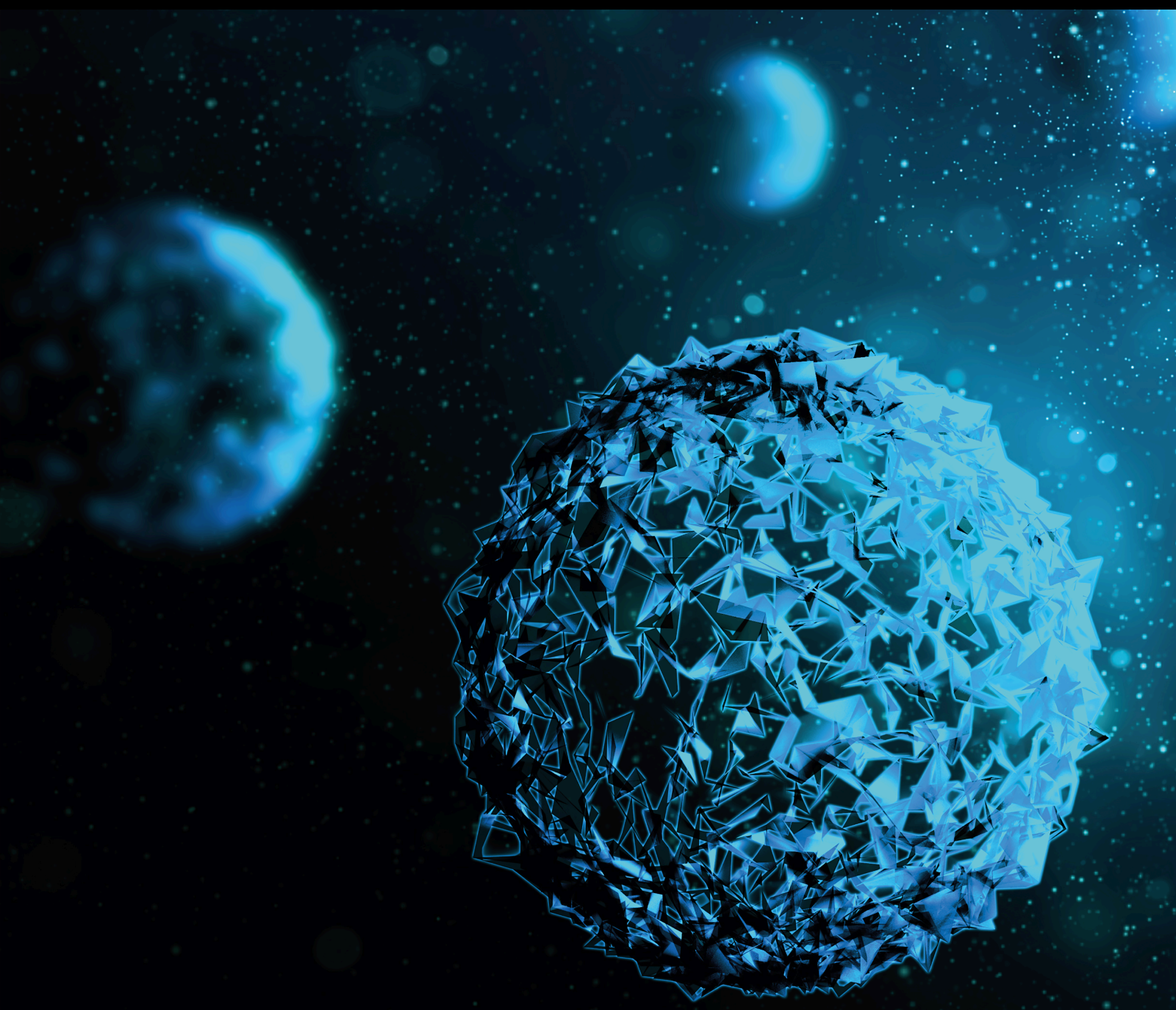


# Polymeric Platforms to Ameliorate Emerging Health Pathologies

Lead Guest Editor: Nauman Rahim Khan

Guest Editors: Hassan Albarqi, Abdul Wahab, and Barkat Khan





---

# **Polymeric Platforms to Ameliorate Emerging Health Pathologies**

BioMed Research International

---

## **Polymeric Platforms to Ameliorate Emerging Health Pathologies**

Lead Guest Editor: Nauman Rahim Khan

Guest Editors: Hassan Albarqi, Abdul Wahab, and  
Barkat Khan



---

Copyright © 2024 Hindawi Limited. All rights reserved.

This is a special issue published in "BioMed Research International." All articles are open access articles distributed under the Creative Commons Attribution License, which permits unrestricted use, distribution, and reproduction in any medium, provided the original work is properly cited.









## Section Editors

Penny A. Asbell, USA  
David Bernardo , Spain  
Gerald Brandacher, USA  
Kim Bridle , Australia  
Laura Chronopoulou , Italy  
Gerald A. Colvin , USA  
Aaron S. Dumont, USA  
Pierfrancesco Franco , Italy  
Raj P. Kandpal , USA  
Fabrizio Montecucco , Italy  
Mangesh S. Pednekar , India  
Letterio S. Politi , USA  
Jinsong Ren , China  
William B. Rodgers, USA  
Harry W. Schroeder , USA  
Andrea Scribante , Italy  
Germán Vicente-Rodríguez , Spain  
Momiao Xiong , USA  
Hui Zhang , China

## Academic Editors

### Pharmaceutics

Abdul Ahad , Saudi Arabia  
Raid Ghassan Alany, United Kingdom  
Javed Ali , India  
Sophia Antimisiaris, Greece  
Giulia Auriemma, Italy  
Sanjula Baboota , India  
Vikas Bali , India  
Mohammed Bourhia , Morocco  
Kun Cheng, USA  
Manish K. Chourasia , India  
Nahide Gulsah Deniz , Turkey  
Abdelfatteh El Omri , Japan  
Sanjay Garg , Australia  
Nabila Hassan, Egypt  
Nauman Rahim Khan, Pakistan  
Vesa-Pekka Lehto , Finland  
Wen-Wu Li , United Kingdom

Samuele Maramai , Italy  
Xin Ming , USA  
Ambikanandan Misra, India  
Narasimha Murthy, USA  
Sami M. Nazzal , USA  
Kamla Pathak , India  
Yunierkis Pérez-Castillo , Belgium  
Hugh D. Smyth , USA  
Fabio Sonvico , Australia  
Muhammad Taher , Malaysia  
Hu Wang , China  
Nilufer Yuksel , Turkey

## Contents

---

**Retracted: Downregulation of miR-221-3p by LncRNA TUG1 Promoting the Healing of Closed Tibial Fractures in Mice**

BioMed Research International

Retraction (1 page), Article ID 9823060, Volume 2024 (2024)

**Retracted: Identification of RPS7 as the Biomarker of Ferroptosis in Acute Kidney Injury**

BioMed Research International

Retraction (1 page), Article ID 9826969, Volume 2024 (2024)

**Retracted: Polyvinylpyrrolidone K-30-Based Crosslinked Fast Swelling Nanogels: An Impeccable Approach for Drug's Solubility Improvement**

BioMed Research International

Retraction (1 page), Article ID 9817465, Volume 2024 (2024)

**Retracted: Predicting Mental Health of Best Human Capital for Sustainable Organization through Psychological and Personality Health Issues: Shift from Traditional to Novel Machine Learning-Supervised Technique Approach**

BioMed Research International

Retraction (1 page), Article ID 9817085, Volume 2024 (2024)

**Retracted: The Anti-inflammatory Effect of Chitosan Oligosaccharide on Heart Failure in Mice**

BioMed Research International

Retraction (1 page), Article ID 9816307, Volume 2024 (2024)

**Retracted: Development and Optimization of a Prognostic Model Associated with Stemness Genes in Hepatocellular Carcinoma**

BioMed Research International

Retraction (1 page), Article ID 9815950, Volume 2024 (2024)

**Retracted: Glutathione, Cysteine, and D-Penicillamine Role in Exchange of Silver Metal from the Albumin Metal Complex**

BioMed Research International

Retraction (1 page), Article ID 9810690, Volume 2024 (2024)

**Retracted: The Disparity in the Management of Polycystic Ovary Syndrome between Obstetrician-Gynecologists in Different-Level Hospitals under the Hierarchical Medical System**

BioMed Research International

Retraction (1 page), Article ID 9809672, Volume 2024 (2024)

**Retracted: Serum Markers CA125, CA153, and CEA along with Inflammatory Cytokines in the Early Detection of Lung Cancer in High-Risk Populations**

BioMed Research International

Retraction (1 page), Article ID 9827549, Volume 2024 (2024)

**Retracted: Study on the Practice of Enterprise Financial Management System under the Epidemic Norm Based on Artificial Neural Network**

BioMed Research International

Retraction (1 page), Article ID 9893427, Volume 2024 (2024)

**Retracted: Meta-Analysis of the Comprehensive Efficacy of Intraocular Lens Implantation in Glaucoma Patients**

BioMed Research International

Retraction (1 page), Article ID 9891484, Volume 2024 (2024)

**Retracted: Influence of the Physical Inclusion of ZrO<sub>2</sub>/TiO<sub>2</sub> Nanoparticles on Physical, Mechanical, and Morphological Characteristics of PMMA-Based Interim Restorative Material**

BioMed Research International

Retraction (1 page), Article ID 9876827, Volume 2024 (2024)

**Retracted: Synthesis and Biomedical Applications of Zirconium Nanoparticles: Advanced Leaps and Bounds in the Recent Past**

BioMed Research International

Retraction (1 page), Article ID 9876192, Volume 2024 (2024)

**Retracted: Antihypertensive Activity in High Salt-Induced Hypertensive Rats and LC-MS/MS-Based Phytochemical Profiling of *Melia azedarach* L. (Meliaceae) Leaves**

BioMed Research International

Retraction (1 page), Article ID 9874053, Volume 2024 (2024)

**Retracted: Metabonomic Study of the Effect of Dingkundan Intervention Comparing with Oral Contraceptives on Primary Dysmenorrhea Using the UPLC-MS Technique**

BioMed Research International

Retraction (1 page), Article ID 9865214, Volume 2024 (2024)

**Retracted: HPV-16 Expression and Loss of Cell Differentiation in Primary Bladder Tumors**

BioMed Research International

Retraction (1 page), Article ID 9851042, Volume 2024 (2024)

**Retracted: Effect of Dihuang Yinzi on Inflammatory Response in Cerebral Ischemia-Reperfusion Model Rats by Regulating Gut Microbiota**

BioMed Research International

Retraction (1 page), Article ID 9849728, Volume 2024 (2024)

**Retracted: Synthesis and Evaluation of Finasteride-Loaded HPMC-Based Nanogels for Transdermal Delivery: A Versatile Nanoscopic Platform**

BioMed Research International

Retraction (1 page), Article ID 9846926, Volume 2024 (2024)

## Contents

**Retracted: Chemical Composition and Biological Evaluation of *Typha domingensis* Pers. to Ameliorate Health Pathologies: *In Vitro* and *In Silico* Approaches**

BioMed Research International

Retraction (1 page), Article ID 9840785, Volume 2024 (2024)

**Retracted: The Connection between High Myopia Patients and MiR-708a or MiR-148 Expression Levels in Aqueous Studies of Visual Acuity**

BioMed Research International

Retraction (1 page), Article ID 9831749, Volume 2024 (2024)

**Retracted: Phytochemical Analysis, Total Phenolic, Flavonoid Contents, and Anticancer Evaluations of Solvent Extracts and Saponins of *H. digitata***

BioMed Research International

Retraction (1 page), Article ID 9803470, Volume 2024 (2024)

**Retracted: Ameliorated Stomach Specific Floating Microspheres for Emerging Health Pathologies Using Polymeric Konjac Glucomannan-Based Domperidone**

BioMed Research International

Retraction (1 page), Article ID 9789506, Volume 2024 (2024)

**Retracted: Evaluation of the Antiasthmatic Activity of *Carissa opaca* in Animal Models**

BioMed Research International

Retraction (1 page), Article ID 9785928, Volume 2024 (2024)

**Retracted: Compound Shuganjieyu Capsule on CYP450 Enzyme Activity**

BioMed Research International



Retraction (1 page), Article ID 9785462, Volume 2024 (2024)



**Retracted: Effect of Previous Cancer History on Survival of Patients with Different Subtypes of Breast Cancer**

BioMed Research International

Retraction (1 page), Article ID 9760406, Volume 2024 (2024)


**Biodegradable Polymeric Pharmaceutical Nanoemulgel Coloaded with Eucalyptol-Lornoxicam: Fabrication and Characterizations for Possible Better Pain Management**

Muhammad Shafiq, Barkat Ali Khan , Sheikh Abdur Rashid , Muhammad Khalid Khan, Faiza

Naseem, Ali M. Alqahtani , Saad S. Alqahatni, Taha Alqahtani , and Ali Alamri

Research Article (16 pages), Article ID 4227242, Volume 2023 (2023)


**[Retracted] Serum Markers CA125, CA153, and CEA along with Inflammatory Cytokines in the Early Detection of Lung Cancer in High-Risk Populations**

Guangping Li, Hongxin Zhang, Lei Zhang, Huaqun Liu, Songlin Li, Yanan Wang, and Xiaoyun Deng 





Research Article (4 pages), Article ID 1394042, Volume 2022 (2022)



**[Retracted] HPV-16 Expression and Loss of Cell Differentiation in Primary Bladder Tumors**

Lei Pang , Zijun Ding, Fei Li, Hongqiang Chai, Ming Wu, and Jinkai Shao  
Research Article (6 pages), Article ID 6565620, Volume 2022 (2022)


**[Retracted] Identification of RPS7 as the Biomarker of Ferroptosis in Acute Kidney Injury**

Hao Zhang , Xuemei Liu, Lizhi Zhou , Zebin Deng , and Yinhuai Wang   
Research Article (14 pages), Article ID 3667339, Volume 2022 (2022)



**[Retracted] Compound Shuganjieyu Capsule on CYP450 Enzyme Activity**

Yunqiu Tang and Yunxia Li   
Research Article (8 pages), Article ID 3228738, Volume 2022 (2022)


**[Retracted] The Connection between High Myopia Patients and MiR-708a or MiR-148 Expression Levels in Aqueous Studies of Visual Acuity**

Jiang Shen , Hong Lou, Qihua Yu, Hongyan Yao, and Jianshu Yuan  
Research Article (7 pages), Article ID 3363830, Volume 2022 (2022)





**[Retracted] Development and Optimization of a Prognostic Model Associated with Stemness Genes in Hepatocellular Carcinoma**

Kefen Zhang, Kaisheng Xie, Xin Huo, Lianlian Liu, Jilin Liu, Chao Zhang , and Jun Wang   
Research Article (28 pages), Article ID 9168441, Volume 2022 (2022)




**[Retracted] The Anti-inflammatory Effect of Chitosan Oligosaccharide on Heart Failure in Mice**

Yubiao Zhang, Yu Wang, Yunen Liu, Tianxing Gong, and Mingxiao Hou   
Research Article (9 pages), Article ID 8746530, Volume 2022 (2022)


**[Retracted] Phytochemical Analysis, Total Phenolic, Flavonoid Contents, and Anticancer Evaluations of Solvent Extracts and Saponins of *H. digitata***

Osama M. Alshehri, Saleh Alshamrani, Mater H. Mahnashi , Mohammed Merae Alshahrani, Jalwa Ali Khan, Muhammad Shah, Mohammed Ali Alshehri, Rehman Zafar, Muhammad Zahoor , Muhammad Saeed Jan , Syed Shams ul Hassan, and Abdul Sadiq   
Research Article (12 pages), Article ID 9051678, Volume 2022 (2022)

**[Retracted] Predicting Mental Health of Best Human Capital for Sustainable Organization through Psychological and Personality Health Issues: Shift from Traditional to Novel Machine Learning-Supervised Technique Approach**


Muhammad Anees Khan , Sadique Ahmad , Mohammed A. El-Affendi , Rija Zaka, Saima Mahmood, and Muhammad Jehangir  
Research Article (9 pages), Article ID 5775640, Volume 2022 (2022)

**[Retracted] The Disparity in the Management of Polycystic Ovary Syndrome between Obstetrician-Gynecologists in Different-Level Hospitals under the Hierarchical Medical System**


Yue Wang, Jie Chen, Han Dong, Ruilin Ma, Ying Zou, Wei Wang, Qingmei Zheng, Ying Feng, Zhangyun Tan, Xiaoqin Zeng, Yinqing Zhao, Yan Deng, Yanfang Wang, Bei Gu, and Aijun Sun   
Research Article (12 pages), Article ID 9778678, Volume 2022 (2022)

## Contents







### **Novel Curcumin-Encapsulated $\alpha$ -Tocopherol Nanoemulsion System and Its Potential Application for Wound Healing in Diabetic Animals**

Muhammad Ali, Nauman Rahim Khan , Zakia Subhan, Saima Mehmood, Adnan Amin, Imran Rabbani, Fazal-ur -Rehman, Hafiz Muhammad Basit, Haroon Khalid Syed, Ikram Ullah Khan, Muhammad Shuaib Khan, and Sehrish Khattak  
Research Article (16 pages), Article ID 7669255, Volume 2022 (2022)


### **[Retracted] Synthesis and Biomedical Applications of Zirconium Nanoparticles: Advanced Leaps and Bounds in the Recent Past**

Hafiz Muhammad Arshad, Amir Shahzad, Sammia Shahid, Sadaqat Ali, Abdul Rauf, Shahzad Sharif, Muhammad Ehsan Ullah, Muhammad Inam Ullah, Muhammad Ali, and Hafiz Ishfaq Ahmad   
Review Article (9 pages), Article ID 4910777, Volume 2022 (2022)

### **[Retracted] Evaluation of the Antiasthmatic Activity of *Carissa opaca* in Animal Models**

Muddassar Ali, Umme Salma, Irfan Amir Khan, Taseer Ahmad, Kashif Bashir , Taous Khan , Mater H. Mahnashi , Abdulaziz H. Alhasaniah , Ahmed A. Al Awadh, Ibrahim A. Almazni, Mohammed M. Alshahrani , and Abdul Jabbar Shah   
Research Article (8 pages), Article ID 7011789, Volume 2022 (2022)





### **[Retracted] Study on the Practice of Enterprise Financial Management System under the Epidemic Norm Based on Artificial Neural Network**

Kaiheng Ji   
Research Article (10 pages), Article ID 7728596, Volume 2022 (2022)

### **[Retracted] Effect of Previous Cancer History on Survival of Patients with Different Subtypes of Breast Cancer**

Weixun Lin , Yaokun Chen , Zeqi Ji , Lingzhi Chen , Jinyao Wu , Yexi Chen , and Zhiyang Li   
Research Article (15 pages), Article ID 6116658, Volume 2022 (2022)





### **[Retracted] Polyvinylpyrrolidone K-30-Based Crosslinked Fast Swelling Nanogels: An Impeccable Approach for Drug's Solubility Improvement**

Muhammad Usman Minhas , Kifayat Ullah Khan , Muhammad Sarfraz , Syed Faisal Badshah, Abubakar Munir, Kashif Barkat, Abdul Basit , and Mosab Arafat  
Research Article (15 pages), Article ID 5883239, Volume 2022 (2022)

### **[Retracted] Downregulation of miR-221-3p by LncRNA TUG1 Promoting the Healing of Closed Tibial Fractures in Mice**

Laiyou Liu  and Yinpeng Yuan  
Research Article (11 pages), Article ID 1624446, Volume 2022 (2022)

### **[Retracted] Influence of the Physical Inclusion of $ZrO_2/TiO_2$ Nanoparticles on Physical, Mechanical, and Morphological Characteristics of PMMA-Based Interim Restorative Material**


Ali Alrahlah , Rawaz Khan, Fahim Vohra , Ibrahim M. Alqahtani, Adel A. Alruhaymi, Sajjad Haider, Abdel-Basit Al-Odayni, Waseem Sharaf Saeed , H. C. Ananda Murthy , and Leonel S. Bautista  
Research Article (11 pages), Article ID 1743019, Volume 2022 (2022)

**[Retracted] Effect of Dihuang Yinzi on Inflammatory Response in Cerebral Ischemia-Reperfusion Model Rats by Regulating Gut Microbiota**

Xinyu Wang , Lei Ye , Wanru Sun , Liya Li , Chaoyun Wang , Xiaoyan Xu , Zhaohai Pan , and Jianwei Gong 


Research Article (9 pages), Article ID 3768880, Volume 2022 (2022)

**[Retracted] Metabonomic Study of the Effect of Dingkundan Intervention Comparing with Oral Contraceptives on Primary Dysmenorrhea Using the UPLC-MS Technique**

Hong Cai, Yijing Zhang, Xiaoxia Ding, Shiyang Zhu, Xuesong Ding, Yan Deng, Xiao Ma, Jingwen Gan, Yanfang Wang, and Aijun Sun 

Research Article (9 pages), Article ID 6708200, Volume 2022 (2022)

**[Retracted] Meta-Analysis of the Comprehensive Efficacy of Intraocular Lens Implantation in Glaucoma Patients**

Qingyi Zhou 




Research Article (11 pages), Article ID 5130416, Volume 2022 (2022)

**[Retracted] Glutathione, Cysteine, and D-Penicillamine Role in Exchange of Silver Metal from the Albumin Metal Complex**

Nahed S. Alharthi , Haroon Khan , Fahad Jibrán Siyál , Zahid Ali Shaikh , Shumaila Parveen Arain , Lienda Bashier Eltayeb , and Altaf Ali Mangi 


Research Article (10 pages), Article ID 3619308, Volume 2022 (2022)

**Physicochemical Characterization of Chitosan-Decorated Finasteride Solid Lipid Nanoparticles for Skin Drug Delivery**

Muhammad Sohaib, Shefaat Ullah Shah , Kifayat Ullah Shah, Kifayat Ullah Shah, Nauman Rahim Khan , Malik Muhammad Irfan , Zahid Rasul Niazi, Abdulsalam A. Alqahtani, Ali Alasiri, Ismail A. Walbi, and Sajid Mahmood





Research Article (10 pages), Article ID 7792180, Volume 2022 (2022)

**[Retracted] Antihypertensive Activity in High Salt-Induced Hypertensive Rats and LC-MS/MS-Based Phytochemical Profiling of *Melia azedarach* L. (Meliaceae) Leaves**

Anam Saeed, Kashif Bashir, Abdul Jabbar Shah, Rahila Qayyum, and Taous Khan 

Research Article (17 pages), Article ID 2791874, Volume 2022 (2022)

**[Retracted] Synthesis and Evaluation of Finasteride-Loaded HPMC-Based Nanogels for Transdermal Delivery: A Versatile Nanoscopic Platform**




Aousaf Ahmad, Mahmood Ahmad , Muhammad Usman Minhas , Muhammad Sarfraz , Muhammad Sohail, Kifayat Ullah Khan, Sana Tanveer, and Shakeel Ijaz 

Research Article (22 pages), Article ID 2426960, Volume 2022 (2022)

## Contents





---

**[Retracted] Chemical Composition and Biological Evaluation of *Typha domingensis* Pers. to Ameliorate Health Pathologies: *In Vitro* and *In Silico* Approaches**

Rizwana Dilshad, Kashif-ur-Rehman Khan , Laiba Saeed, Asmaa E. Sherif , Saeed Ahmad, Chitchamai Ovatlarnporn, Jawad Nasim, Musaddique Hussain, Bilal Ahmad Ghalloo , Abdul Basit, and Imran Mukhtar

Research Article (16 pages), Article ID 8010395, Volume 2022 (2022)

**[Retracted] Ameliorated Stomach Specific Floating Microspheres for Emerging Health Pathologies Using Polymeric Konjac Glucomannan-Based Domperidone**

Jamal Moideen Muthu Mohamed , Nikita Mahajan, Mohamed El-Sherbiny , Shagufta Khan , Rasha Hamed Al-Serwi, Mohammed A. Attia, Qamar Alsayed Altriny, and Ahmed H. Arbab 

Research Article (12 pages), Article ID 3670946, Volume 2022 (2022)

## Retraction

# Retracted: Downregulation of miR-221-3p by LncRNA TUG1 Promoting the Healing of Closed Tibial Fractures in Mice

### BioMed Research International

Received 8 January 2024; Accepted 8 January 2024; Published 12 February 2024

Copyright © 2024 BioMed Research International. This is an open access article distributed under the Creative Commons Attribution License, which permits unrestricted use, distribution, and reproduction in any medium, provided the original work is properly cited.

This article has been retracted by Hindawi following an investigation undertaken by the publisher [1]. This investigation has uncovered evidence of one or more of the following indicators of systematic manipulation of the publication process:

- (1) Discrepancies in scope
- (2) Discrepancies in the description of the research reported
- (3) Discrepancies between the availability of data and the research described
- (4) Inappropriate citations
- (5) Incoherent, meaningless and/or irrelevant content included in the article
- (6) Manipulated or compromised peer review

The presence of these indicators undermines our confidence in the integrity of the article's content and we cannot, therefore, vouch for its reliability. Please note that this notice is intended solely to alert readers that the content of this article is unreliable. We have not investigated whether authors were aware of or involved in the systematic manipulation of the publication process.

Wiley and Hindawi regrets that the usual quality checks did not identify these issues before publication and have since put additional measures in place to safeguard research integrity.

We wish to credit our own Research Integrity and Research Publishing teams and anonymous and named external researchers and research integrity experts for contributing to this investigation.

The corresponding author, as the representative of all authors, has been given the opportunity to register their agreement or disagreement to this retraction. We have kept a record of any response received.

### References

- [1] L. Liu and Y. Yuan, "Downregulation of miR-221-3p by LncRNA TUG1 Promoting the Healing of Closed Tibial Fractures in Mice," *BioMed Research International*, vol. 2022, Article ID 1624446, 11 pages, 2022.

## Retraction

# Retracted: Identification of RPS7 as the Biomarker of Ferroptosis in Acute Kidney Injury

### BioMed Research International

Received 8 January 2024; Accepted 8 January 2024; Published 13 January 2024

Copyright © 2024 BioMed Research International. This is an open access article distributed under the Creative Commons Attribution License, which permits unrestricted use, distribution, and reproduction in any medium, provided the original work is properly cited.

This article has been retracted by Hindawi following an investigation undertaken by the publisher [1]. This investigation has uncovered evidence of one or more of the following indicators of systematic manipulation of the publication process:

- (1) Discrepancies in scope
- (2) Discrepancies in the description of the research reported
- (3) Discrepancies between the availability of data and the research described
- (4) Inappropriate citations
- (5) Incoherent, meaningless and/or irrelevant content included in the article
- (6) Manipulated or compromised peer review

The presence of these indicators undermines our confidence in the integrity of the article's content and we cannot, therefore, vouch for its reliability. Please note that this notice is intended solely to alert readers that the content of this article is unreliable. We have not investigated whether authors were aware of or involved in the systematic manipulation of the publication process.

Wiley and Hindawi regrets that the usual quality checks did not identify these issues before publication and have since put additional measures in place to safeguard research integrity.

We wish to credit our own Research Integrity and Research Publishing teams and anonymous and named external researchers and research integrity experts for contributing to this investigation.

The corresponding author, as the representative of all authors, has been given the opportunity to register their agreement or disagreement to this retraction. We have kept a record of any response received.

### References

- [1] H. Zhang, X. Liu, L. Zhou, Z. Deng, and Y. Wang, "Identification of RPS7 as the Biomarker of Ferroptosis in Acute Kidney Injury," *BioMed Research International*, vol. 2022, Article ID 3667339, 14 pages, 2022.

## *Retraction*

# **Retracted: Polyvinylpyrrolidone K-30-Based Crosslinked Fast Swelling Nanogels: An Impeccable Approach for Drug's Solubility Improvement**

### **BioMed Research International**

Received 8 January 2024; Accepted 8 January 2024; Published 9 January 2024

Copyright © 2024 BioMed Research International. This is an open access article distributed under the Creative Commons Attribution License, which permits unrestricted use, distribution, and reproduction in any medium, provided the original work is properly cited.

This article has been retracted by Hindawi, as publisher, following an investigation undertaken by the publisher [1]. This investigation has uncovered evidence of systematic manipulation of the publication and peer-review process. We cannot, therefore, vouch for the reliability or integrity of this article.

Please note that this notice is intended solely to alert readers that the peer-review process of this article has been compromised.

Wiley and Hindawi regret that the usual quality checks did not identify these issues before publication and have since put additional measures in place to safeguard research integrity.

We wish to credit our Research Integrity and Research Publishing teams and anonymous and named external researchers and research integrity experts for contributing to this investigation.

The corresponding author, as the representative of all authors, has been given the opportunity to register their agreement or disagreement to this retraction. We have kept a record of any response received.

## **References**

- [1] M. U. Minhas, K. U. Khan, M. Sarfraz et al., "Polyvinylpyrrolidone K-30-Based Crosslinked Fast Swelling Nanogels: An Impeccable Approach for Drug's Solubility Improvement," *BioMed Research International*, vol. 2022, Article ID 5883239, 15 pages, 2022.

## *Retraction*

# **Retracted: Predicting Mental Health of Best Human Capital for Sustainable Organization through Psychological and Personality Health Issues: Shift from Traditional to Novel Machine Learning-Supervised Technique Approach**

### **BioMed Research International**

Received 8 January 2024; Accepted 8 January 2024; Published 9 January 2024

Copyright © 2024 BioMed Research International. This is an open access article distributed under the Creative Commons Attribution License, which permits unrestricted use, distribution, and reproduction in any medium, provided the original work is properly cited.

This article has been retracted by Hindawi following an investigation undertaken by the publisher [1]. This investigation has uncovered evidence of one or more of the following indicators of systematic manipulation of the publication process:

- (1) Discrepancies in scope
- (2) Discrepancies in the description of the research reported
- (3) Discrepancies between the availability of data and the research described
- (4) Inappropriate citations
- (5) Incoherent, meaningless and/or irrelevant content included in the article
- (6) Manipulated or compromised peer review

The presence of these indicators undermines our confidence in the integrity of the article's content and we cannot, therefore, vouch for its reliability. Please note that this notice is intended solely to alert readers that the content of this article is unreliable. We have not investigated whether authors were aware of or involved in the systematic manipulation of the publication process.

Wiley and Hindawi regrets that the usual quality checks did not identify these issues before publication and have since put additional measures in place to safeguard research integrity.

We wish to credit our own Research Integrity and Research Publishing teams and anonymous and named external researchers and research integrity experts for contributing to this investigation.

The corresponding author, as the representative of all authors, has been given the opportunity to register their agreement or disagreement to this retraction. We have kept a record of any response received.

### **References**

- [1] M. A. Khan, S. Ahmad, M. A. El-Affendi, R. Zaka, S. Mahmood, and M. Jehangir, "Predicting Mental Health of Best Human Capital for Sustainable Organization through Psychological and Personality Health Issues: Shift from Traditional to Novel Machine Learning-Supervised Technique Approach," *BioMed Research International*, vol. 2022, Article ID 5775640, 9 pages, 2022.



## *Retraction*

# **Retracted: The Anti-inflammatory Effect of Chitosan Oligosaccharide on Heart Failure in Mice**

### **BioMed Research International**

Received 8 January 2024; Accepted 8 January 2024; Published 9 January 2024

Copyright © 2024 BioMed Research International. This is an open access article distributed under the Creative Commons Attribution License, which permits unrestricted use, distribution, and reproduction in any medium, provided the original work is properly cited.

This article has been retracted by Hindawi, as publisher, following an investigation undertaken by the publisher [1]. This investigation has uncovered evidence of systematic manipulation of the publication and peer-review process. We cannot, therefore, vouch for the reliability or integrity of this article.

Please note that this notice is intended solely to alert readers that the peer-review process of this article has been compromised.

Wiley and Hindawi regret that the usual quality checks did not identify these issues before publication and have since put additional measures in place to safeguard research integrity.

We wish to credit our Research Integrity and Research Publishing teams and anonymous and named external researchers and research integrity experts for contributing to this investigation.

The corresponding author, as the representative of all authors, has been given the opportunity to register their agreement or disagreement to this retraction. We have kept a record of any response received.

### **References**

- [1] Y. Zhang, Y. Wang, Y. Liu, T. Gong, and M. Hou, "The Anti-inflammatory Effect of Chitosan Oligosaccharide on Heart Failure in Mice," *BioMed Research International*, vol. 2022, Article ID 8746530, 9 pages, 2022.

## Retraction

# Retracted: Development and Optimization of a Prognostic Model Associated with Stemness Genes in Hepatocellular Carcinoma

### BioMed Research International

Received 8 January 2024; Accepted 8 January 2024; Published 9 January 2024

Copyright © 2024 BioMed Research International. This is an open access article distributed under the Creative Commons Attribution License, which permits unrestricted use, distribution, and reproduction in any medium, provided the original work is properly cited.

This article has been retracted by Hindawi following an investigation undertaken by the publisher [1]. This investigation has uncovered evidence of one or more of the following indicators of systematic manipulation of the publication process:

- (1) Discrepancies in scope
- (2) Discrepancies in the description of the research reported
- (3) Discrepancies between the availability of data and the research described
- (4) Inappropriate citations
- (5) Incoherent, meaningless and/or irrelevant content included in the article
- (6) Manipulated or compromised peer review

The presence of these indicators undermines our confidence in the integrity of the article's content and we cannot, therefore, vouch for its reliability. Please note that this notice is intended solely to alert readers that the content of this article is unreliable. We have not investigated whether authors were aware of or involved in the systematic manipulation of the publication process.

Wiley and Hindawi regrets that the usual quality checks did not identify these issues before publication and have since put additional measures in place to safeguard research integrity.

We wish to credit our own Research Integrity and Research Publishing teams and anonymous and named external researchers and research integrity experts for contributing to this investigation.

The corresponding author, as the representative of all authors, has been given the opportunity to register their agreement or disagreement to this retraction. We have kept a record of any response received.

### References

- [1] K. Zhang, K. Xie, X. Huo et al., "Development and Optimization of a Prognostic Model Associated with Stemness Genes in Hepatocellular Carcinoma," *BioMed Research International*, vol. 2022, Article ID 9168441, 28 pages, 2022.

## Retraction

# Retracted: Glutathione, Cysteine, and D-Penicillamine Role in Exchange of Silver Metal from the Albumin Metal Complex

### BioMed Research International

Received 8 January 2024; Accepted 8 January 2024; Published 9 January 2024

Copyright © 2024 BioMed Research International. This is an open access article distributed under the Creative Commons Attribution License, which permits unrestricted use, distribution, and reproduction in any medium, provided the original work is properly cited.

This article has been retracted by Hindawi following an investigation undertaken by the publisher [1]. This investigation has uncovered evidence of one or more of the following indicators of systematic manipulation of the publication process:

- (1) Discrepancies in scope
- (2) Discrepancies in the description of the research reported
- (3) Discrepancies between the availability of data and the research described
- (4) Inappropriate citations
- (5) Incoherent, meaningless and/or irrelevant content included in the article
- (6) Manipulated or compromised peer review

The presence of these indicators undermines our confidence in the integrity of the article's content and we cannot, therefore, vouch for its reliability. Please note that this notice is intended solely to alert readers that the content of this article is unreliable. We have not investigated whether authors were aware of or involved in the systematic manipulation of the publication process.

Wiley and Hindawi regrets that the usual quality checks did not identify these issues before publication and have since put additional measures in place to safeguard research integrity.

We wish to credit our own Research Integrity and Research Publishing teams and anonymous and named external researchers and research integrity experts for contributing to this investigation.

The corresponding author, as the representative of all authors, has been given the opportunity to register their agreement or disagreement to this retraction. We have kept a record of any response received.

### References

- [1] N. S. Alharthi, H. Khan, F. J. Siyal et al., "Glutathione, Cysteine, and D-Penicillamine Role in Exchange of Silver Metal from the Albumin Metal Complex," *BioMed Research International*, vol. 2022, Article ID 3619308, 10 pages, 2022.

## Retraction

# Retracted: The Disparity in the Management of Polycystic Ovary Syndrome between Obstetrician-Gynecologists in Different-Level Hospitals under the Hierarchical Medical System

### BioMed Research International

Received 8 January 2024; Accepted 8 January 2024; Published 9 January 2024

Copyright © 2024 BioMed Research International. This is an open access article distributed under the Creative Commons Attribution License, which permits unrestricted use, distribution, and reproduction in any medium, provided the original work is properly cited.

This article has been retracted by Hindawi following an investigation undertaken by the publisher [1]. This investigation has uncovered evidence of one or more of the following indicators of systematic manipulation of the publication process:

- (1) Discrepancies in scope
- (2) Discrepancies in the description of the research reported
- (3) Discrepancies between the availability of data and the research described
- (4) Inappropriate citations
- (5) Incoherent, meaningless and/or irrelevant content included in the article
- (6) Manipulated or compromised peer review

The presence of these indicators undermines our confidence in the integrity of the article's content and we cannot, therefore, vouch for its reliability. Please note that this notice is intended solely to alert readers that the content of this article is unreliable. We have not investigated whether authors were aware of or involved in the systematic manipulation of the publication process.

Wiley and Hindawi regrets that the usual quality checks did not identify these issues before publication and have since put additional measures in place to safeguard research integrity.

We wish to credit our own Research Integrity and Research Publishing teams and anonymous and named

external researchers and research integrity experts for contributing to this investigation.

The corresponding author, as the representative of all authors, has been given the opportunity to register their agreement or disagreement to this retraction. We have kept a record of any response received.

### References

- [1] Y. Wang, J. Chen, H. Dong et al., "The Disparity in the Management of Polycystic Ovary Syndrome between Obstetrician-Gynecologists in Different-Level Hospitals under the Hierarchical Medical System," *BioMed Research International*, vol. 2022, Article ID 9778678, 12 pages, 2022.

## Retraction

# Retracted: Serum Markers CA125, CA153, and CEA along with Inflammatory Cytokines in the Early Detection of Lung Cancer in High-Risk Populations

### BioMed Research International

Received 8 January 2024; Accepted 8 January 2024; Published 9 January 2024

Copyright © 2024 BioMed Research International. This is an open access article distributed under the Creative Commons Attribution License, which permits unrestricted use, distribution, and reproduction in any medium, provided the original work is properly cited.

This article has been retracted by Hindawi following an investigation undertaken by the publisher [1]. This investigation has uncovered evidence of one or more of the following indicators of systematic manipulation of the publication process:

- (1) Discrepancies in scope
- (2) Discrepancies in the description of the research reported
- (3) Discrepancies between the availability of data and the research described
- (4) Inappropriate citations
- (5) Incoherent, meaningless and/or irrelevant content included in the article
- (6) Manipulated or compromised peer review

The presence of these indicators undermines our confidence in the integrity of the article's content and we cannot, therefore, vouch for its reliability. Please note that this notice is intended solely to alert readers that the content of this article is unreliable. We have not investigated whether authors were aware of or involved in the systematic manipulation of the publication process.

Wiley and Hindawi regrets that the usual quality checks did not identify these issues before publication and have since put additional measures in place to safeguard research integrity.

We wish to credit our own Research Integrity and Research Publishing teams and anonymous and named external researchers and research integrity experts for contributing to this investigation.

The corresponding author, as the representative of all authors, has been given the opportunity to register their agreement or disagreement to this retraction. We have kept a record of any response received.

### References

- [1] G. Li, H. Zhang, L. Zhang et al., "Serum Markers CA125, CA153, and CEA along with Inflammatory Cytokines in the Early Detection of Lung Cancer in High-Risk Populations," *BioMed Research International*, vol. 2022, Article ID 1394042, 4 pages, 2022.

## *Retraction*

# **Retracted: Study on the Practice of Enterprise Financial Management System under the Epidemic Norm Based on Artificial Neural Network**

### **BioMed Research International**

Received 8 January 2024; Accepted 8 January 2024; Published 9 January 2024

Copyright © 2024 BioMed Research International. This is an open access article distributed under the Creative Commons Attribution License, which permits unrestricted use, distribution, and reproduction in any medium, provided the original work is properly cited.

This article has been retracted by Hindawi following an investigation undertaken by the publisher [1]. This investigation has uncovered evidence of one or more of the following indicators of systematic manipulation of the publication process:

- (1) Discrepancies in scope
- (2) Discrepancies in the description of the research reported
- (3) Discrepancies between the availability of data and the research described
- (4) Inappropriate citations
- (5) Incoherent, meaningless and/or irrelevant content included in the article
- (6) Manipulated or compromised peer review

The presence of these indicators undermines our confidence in the integrity of the article's content and we cannot, therefore, vouch for its reliability. Please note that this notice is intended solely to alert readers that the content of this article is unreliable. We have not investigated whether authors were aware of or involved in the systematic manipulation of the publication process.

Wiley and Hindawi regrets that the usual quality checks did not identify these issues before publication and have since put additional measures in place to safeguard research integrity.

We wish to credit our own Research Integrity and Research Publishing teams and anonymous and named

external researchers and research integrity experts for contributing to this investigation.

The corresponding author, as the representative of all authors, has been given the opportunity to register their agreement or disagreement to this retraction. We have kept a record of any response received.

### **References**

- [1] K. Ji, "Study on the Practice of Enterprise Financial Management System under the Epidemic Norm Based on Artificial Neural Network," *BioMed Research International*, vol. 2022, Article ID 7728596, 10 pages, 2022.

## Retraction

# Retracted: Meta-Analysis of the Comprehensive Efficacy of Intraocular Lens Implantation in Glaucoma Patients

### BioMed Research International

Received 8 January 2024; Accepted 8 January 2024; Published 9 January 2024

Copyright © 2024 BioMed Research International. This is an open access article distributed under the Creative Commons Attribution License, which permits unrestricted use, distribution, and reproduction in any medium, provided the original work is properly cited.

This article has been retracted by Hindawi following an investigation undertaken by the publisher [1]. This investigation has uncovered evidence of one or more of the following indicators of systematic manipulation of the publication process:

- (1) Discrepancies in scope
- (2) Discrepancies in the description of the research reported
- (3) Discrepancies between the availability of data and the research described
- (4) Inappropriate citations
- (5) Incoherent, meaningless and/or irrelevant content included in the article
- (6) Manipulated or compromised peer review

The presence of these indicators undermines our confidence in the integrity of the article's content and we cannot, therefore, vouch for its reliability. Please note that this notice is intended solely to alert readers that the content of this article is unreliable. We have not investigated whether authors were aware of or involved in the systematic manipulation of the publication process.

Wiley and Hindawi regrets that the usual quality checks did not identify these issues before publication and have since put additional measures in place to safeguard research integrity.

We wish to credit our own Research Integrity and Research Publishing teams and anonymous and named external researchers and research integrity experts for contributing to this investigation.

The corresponding author, as the representative of all authors, has been given the opportunity to register their agreement or disagreement to this retraction. We have kept a record of any response received.

### References

- [1] Q. Zhou, "Meta-Analysis of the Comprehensive Efficacy of Intraocular Lens Implantation in Glaucoma Patients," *BioMed Research International*, vol. 2022, Article ID 5130416, 11 pages, 2022.

## Retraction

# Retracted: Influence of the Physical Inclusion of ZrO<sub>2</sub>/TiO<sub>2</sub> Nanoparticles on Physical, Mechanical, and Morphological Characteristics of PMMA-Based Interim Restorative Material

### BioMed Research International

Received 8 January 2024; Accepted 8 January 2024; Published 9 January 2024

Copyright © 2024 BioMed Research International. This is an open access article distributed under the Creative Commons Attribution License, which permits unrestricted use, distribution, and reproduction in any medium, provided the original work is properly cited.

This article has been retracted by Hindawi following an investigation undertaken by the publisher [1]. This investigation has uncovered evidence of one or more of the following indicators of systematic manipulation of the publication process:

- (1) Discrepancies in scope
- (2) Discrepancies in the description of the research reported
- (3) Discrepancies between the availability of data and the research described
- (4) Inappropriate citations
- (5) Incoherent, meaningless and/or irrelevant content included in the article
- (6) Manipulated or compromised peer review

The presence of these indicators undermines our confidence in the integrity of the article's content and we cannot, therefore, vouch for its reliability. Please note that this notice is intended solely to alert readers that the content of this article is unreliable. We have not investigated whether authors were aware of or involved in the systematic manipulation of the publication process.

Wiley and Hindawi regrets that the usual quality checks did not identify these issues before publication and have since put additional measures in place to safeguard research integrity.

We wish to credit our own Research Integrity and Research Publishing teams and anonymous and named external researchers and research integrity experts for contributing to this investigation.

The corresponding author, as the representative of all authors, has been given the opportunity to register their agreement or disagreement to this retraction. We have kept a record of any response received.

### References

- [1] A. Alrahlah, R. Khan, F. Vohra et al., "Influence of the Physical Inclusion of ZrO<sub>2</sub>/TiO<sub>2</sub> Nanoparticles on Physical, Mechanical, and Morphological Characteristics of PMMA-Based Interim Restorative Material," *BioMed Research International*, vol. 2022, Article ID 1743019, 11 pages, 2022.



## Retraction

# Retracted: Synthesis and Biomedical Applications of Zirconium Nanoparticles: Advanced Leaps and Bounds in the Recent Past

### BioMed Research International

Received 8 January 2024; Accepted 8 January 2024; Published 9 January 2024

Copyright © 2024 BioMed Research International. This is an open access article distributed under the Creative Commons Attribution License, which permits unrestricted use, distribution, and reproduction in any medium, provided the original work is properly cited.

This article has been retracted by Hindawi following an investigation undertaken by the publisher [1]. This investigation has uncovered evidence of one or more of the following indicators of systematic manipulation of the publication process:

- (1) Discrepancies in scope
- (2) Discrepancies in the description of the research reported
- (3) Discrepancies between the availability of data and the research described
- (4) Inappropriate citations
- (5) Incoherent, meaningless and/or irrelevant content included in the article
- (6) Manipulated or compromised peer review

The presence of these indicators undermines our confidence in the integrity of the article's content and we cannot, therefore, vouch for its reliability. Please note that this notice is intended solely to alert readers that the content of this article is unreliable. We have not investigated whether authors were aware of or involved in the systematic manipulation of the publication process.

Wiley and Hindawi regrets that the usual quality checks did not identify these issues before publication and have since put additional measures in place to safeguard research integrity.

We wish to credit our own Research Integrity and Research Publishing teams and anonymous and named external researchers and research integrity experts for contributing to this investigation.

The corresponding author, as the representative of all authors, has been given the opportunity to register their agreement or disagreement to this retraction. We have kept a record of any response received.

### References

- [1] H. M. Arshad, A. Shahzad, S. Shahid et al., "Synthesis and Biomedical Applications of Zirconium Nanoparticles: Advanced Leaps and Bounds in the Recent Past," *BioMed Research International*, vol. 2022, Article ID 4910777, 9 pages, 2022.

## Retraction

# Retracted: Antihypertensive Activity in High Salt-Induced Hypertensive Rats and LC-MS/MS-Based Phytochemical Profiling of *Melia azedarach* L. (Meliaceae) Leaves

### BioMed Research International

Received 8 January 2024; Accepted 8 January 2024; Published 9 January 2024

Copyright © 2024 BioMed Research International. This is an open access article distributed under the Creative Commons Attribution License, which permits unrestricted use, distribution, and reproduction in any medium, provided the original work is properly cited.

This article has been retracted by Hindawi following an investigation undertaken by the publisher [1]. This investigation has uncovered evidence of one or more of the following indicators of systematic manipulation of the publication process:

- (1) Discrepancies in scope
- (2) Discrepancies in the description of the research reported
- (3) Discrepancies between the availability of data and the research described
- (4) Inappropriate citations
- (5) Incoherent, meaningless and/or irrelevant content included in the article
- (6) Manipulated or compromised peer review

The presence of these indicators undermines our confidence in the integrity of the article's content and we cannot, therefore, vouch for its reliability. Please note that this notice is intended solely to alert readers that the content of this article is unreliable. We have not investigated whether authors were aware of or involved in the systematic manipulation of the publication process.

Wiley and Hindawi regrets that the usual quality checks did not identify these issues before publication and have since put additional measures in place to safeguard research integrity.

We wish to credit our own Research Integrity and Research Publishing teams and anonymous and named external researchers and research integrity experts for contributing to this investigation.

The corresponding author, as the representative of all authors, has been given the opportunity to register their agreement or disagreement to this retraction. We have kept a record of any response received.

### References

- [1] A. Saeed, K. Bashir, A. J. Shah, R. Qayyum, and T. Khan, "Antihypertensive Activity in High Salt-Induced Hypertensive Rats and LC-MS/MS-Based Phytochemical Profiling of *Melia azedarach* L. (Meliaceae) Leaves," *BioMed Research International*, vol. 2022, Article ID 2791874, 17 pages, 2022.

## *Retraction*

# **Retracted: Metabonomic Study of the Effect of Dingkundan Intervention Comparing with Oral Contraceptives on Primary Dysmenorrhea Using the UPLC-MS Technique**

### **BioMed Research International**

Received 8 January 2024; Accepted 8 January 2024; Published 9 January 2024

Copyright © 2024 BioMed Research International. This is an open access article distributed under the Creative Commons Attribution License, which permits unrestricted use, distribution, and reproduction in any medium, provided the original work is properly cited.

This article has been retracted by Hindawi following an investigation undertaken by the publisher [1]. This investigation has uncovered evidence of one or more of the following indicators of systematic manipulation of the publication process:

- (1) Discrepancies in scope
- (2) Discrepancies in the description of the research reported
- (3) Discrepancies between the availability of data and the research described
- (4) Inappropriate citations
- (5) Incoherent, meaningless and/or irrelevant content included in the article
- (6) Manipulated or compromised peer review

The presence of these indicators undermines our confidence in the integrity of the article's content and we cannot, therefore, vouch for its reliability. Please note that this notice is intended solely to alert readers that the content of this article is unreliable. We have not investigated whether authors were aware of or involved in the systematic manipulation of the publication process.

Wiley and Hindawi regrets that the usual quality checks did not identify these issues before publication and have since put additional measures in place to safeguard research integrity.

We wish to credit our own Research Integrity and Research Publishing teams and anonymous and named external researchers and research integrity experts for contributing to this investigation.

The corresponding author, as the representative of all authors, has been given the opportunity to register their agreement or disagreement to this retraction. We have kept a record of any response received.

### **References**

- [1] H. Cai, Y. Zhang, X. Ding et al., "Metabonomic Study of the Effect of Dingkundan Intervention Comparing with Oral Contraceptives on Primary Dysmenorrhea Using the UPLC-MS Technique," *BioMed Research International*, vol. 2022, Article ID 6708200, 9 pages, 2022.

## Retraction

# Retracted: HPV-16 Expression and Loss of Cell Differentiation in Primary Bladder Tumors

### BioMed Research International

Received 8 January 2024; Accepted 8 January 2024; Published 9 January 2024

Copyright © 2024 BioMed Research International. This is an open access article distributed under the Creative Commons Attribution License, which permits unrestricted use, distribution, and reproduction in any medium, provided the original work is properly cited.

This article has been retracted by Hindawi following an investigation undertaken by the publisher [1]. This investigation has uncovered evidence of one or more of the following indicators of systematic manipulation of the publication process:

- (1) Discrepancies in scope
- (2) Discrepancies in the description of the research reported
- (3) Discrepancies between the availability of data and the research described
- (4) Inappropriate citations
- (5) Incoherent, meaningless and/or irrelevant content included in the article
- (6) Manipulated or compromised peer review

The presence of these indicators undermines our confidence in the integrity of the article's content and we cannot, therefore, vouch for its reliability. Please note that this notice is intended solely to alert readers that the content of this article is unreliable. We have not investigated whether authors were aware of or involved in the systematic manipulation of the publication process.

Wiley and Hindawi regrets that the usual quality checks did not identify these issues before publication and have since put additional measures in place to safeguard research integrity.

We wish to credit our own Research Integrity and Research Publishing teams and anonymous and named external researchers and research integrity experts for contributing to this investigation.

The corresponding author, as the representative of all authors, has been given the opportunity to register their agreement or disagreement to this retraction. We have kept a record of any response received.

### References

- [1] L. Pang, Z. Ding, F. Li, H. Chai, M. Wu, and J. Shao, "HPV-16 Expression and Loss of Cell Differentiation in Primary Bladder Tumors," *BioMed Research International*, vol. 2022, Article ID 6565620, 6 pages, 2022.

## Retraction

# Retracted: Effect of Dihuang Yinzi on Inflammatory Response in Cerebral Ischemia-Reperfusion Model Rats by Regulating Gut Microbiota

### BioMed Research International

Received 8 January 2024; Accepted 8 January 2024; Published 9 January 2024

Copyright © 2024 BioMed Research International. This is an open access article distributed under the Creative Commons Attribution License, which permits unrestricted use, distribution, and reproduction in any medium, provided the original work is properly cited.

This article has been retracted by Hindawi following an investigation undertaken by the publisher [1]. This investigation has uncovered evidence of one or more of the following indicators of systematic manipulation of the publication process:

- (1) Discrepancies in scope
- (2) Discrepancies in the description of the research reported
- (3) Discrepancies between the availability of data and the research described
- (4) Inappropriate citations
- (5) Incoherent, meaningless and/or irrelevant content included in the article
- (6) Manipulated or compromised peer review

The presence of these indicators undermines our confidence in the integrity of the article's content and we cannot, therefore, vouch for its reliability. Please note that this notice is intended solely to alert readers that the content of this article is unreliable. We have not investigated whether authors were aware of or involved in the systematic manipulation of the publication process.

Wiley and Hindawi regrets that the usual quality checks did not identify these issues before publication and have since put additional measures in place to safeguard research integrity.

We wish to credit our own Research Integrity and Research Publishing teams and anonymous and named external researchers and research integrity experts for contributing to this investigation.

The corresponding author, as the representative of all authors, has been given the opportunity to register their agreement or disagreement to this retraction. We have kept a record of any response received.

### References

- [1] X. Wang, L. Ye, W. Sun et al., "Effect of Dihuang Yinzi on Inflammatory Response in Cerebral Ischemia-Reperfusion Model Rats by Regulating Gut Microbiota," *BioMed Research International*, vol. 2022, Article ID 3768880, 9 pages, 2022.

## *Retraction*

# **Retracted: Synthesis and Evaluation of Finasteride-Loaded HPMC-Based Nanogels for Transdermal Delivery: A Versatile Nanoscopic Platform**

### **BioMed Research International**

Received 8 January 2024; Accepted 8 January 2024; Published 9 January 2024

Copyright © 2024 BioMed Research International. This is an open access article distributed under the Creative Commons Attribution License, which permits unrestricted use, distribution, and reproduction in any medium, provided the original work is properly cited.

This article has been retracted by Hindawi, as publisher, following an investigation undertaken by the publisher [1]. This investigation has uncovered evidence of systematic manipulation of the publication and peer-review process. We cannot, therefore, vouch for the reliability or integrity of this article.

Please note that this notice is intended solely to alert readers that the peer-review process of this article has been compromised.

Wiley and Hindawi regret that the usual quality checks did not identify these issues before publication and have since put additional measures in place to safeguard research integrity.

We wish to credit our Research Integrity and Research Publishing teams and anonymous and named external researchers and research integrity experts for contributing to this investigation.

The corresponding author, as the representative of all authors, has been given the opportunity to register their agreement or disagreement to this retraction. We have kept a record of any response received.

## **References**

- [1] A. Ahmad, M. Ahmad, M. U. Minhas et al., "Synthesis and Evaluation of Finasteride-Loaded HPMC-Based Nanogels for Transdermal Delivery: A Versatile Nanoscopic Platform," *BioMed Research International*, vol. 2022, Article ID 2426960, 22 pages, 2022.

## Retraction

# Retracted: Chemical Composition and Biological Evaluation of *Typha domingensis* Pers. to Ameliorate Health Pathologies: *In Vitro* and *In Silico* Approaches

### BioMed Research International

Received 8 January 2024; Accepted 8 January 2024; Published 9 January 2024

Copyright © 2024 BioMed Research International. This is an open access article distributed under the Creative Commons Attribution License, which permits unrestricted use, distribution, and reproduction in any medium, provided the original work is properly cited.

This article has been retracted by Hindawi following an investigation undertaken by the publisher [1]. This investigation has uncovered evidence of one or more of the following indicators of systematic manipulation of the publication process:

- (1) Discrepancies in scope
- (2) Discrepancies in the description of the research reported
- (3) Discrepancies between the availability of data and the research described
- (4) Inappropriate citations
- (5) Incoherent, meaningless and/or irrelevant content included in the article
- (6) Manipulated or compromised peer review

The presence of these indicators undermines our confidence in the integrity of the article's content and we cannot, therefore, vouch for its reliability. Please note that this notice is intended solely to alert readers that the content of this article is unreliable. We have not investigated whether authors were aware of or involved in the systematic manipulation of the publication process.

Wiley and Hindawi regrets that the usual quality checks did not identify these issues before publication and have since put additional measures in place to safeguard research integrity.

We wish to credit our own Research Integrity and Research Publishing teams and anonymous and named external researchers and research integrity experts for contributing to this investigation.

The corresponding author, as the representative of all authors, has been given the opportunity to register their agreement or disagreement to this retraction. We have kept a record of any response received.

### References

- [1] R. Dilshad, K. U. R. Khan, L. Saeed et al., "Chemical Composition and Biological Evaluation of *Typha domingensis* Pers. to Ameliorate Health Pathologies: *In Vitro* and *In Silico* Approaches," *BioMed Research International*, vol. 2022, Article ID 8010395, 16 pages, 2022.

## *Retraction*

# **Retracted: The Connection between High Myopia Patients and MiR-708a or MiR-148 Expression Levels in Aqueous Studies of Visual Acuity**

### **BioMed Research International**

Received 8 January 2024; Accepted 8 January 2024; Published 9 January 2024

Copyright © 2024 BioMed Research International. This is an open access article distributed under the Creative Commons Attribution License, which permits unrestricted use, distribution, and reproduction in any medium, provided the original work is properly cited.

This article has been retracted by Hindawi following an investigation undertaken by the publisher [1]. This investigation has uncovered evidence of one or more of the following indicators of systematic manipulation of the publication process:

- (1) Discrepancies in scope
- (2) Discrepancies in the description of the research reported
- (3) Discrepancies between the availability of data and the research described
- (4) Inappropriate citations
- (5) Incoherent, meaningless and/or irrelevant content included in the article
- (6) Manipulated or compromised peer review

The presence of these indicators undermines our confidence in the integrity of the article's content and we cannot, therefore, vouch for its reliability. Please note that this notice is intended solely to alert readers that the content of this article is unreliable. We have not investigated whether authors were aware of or involved in the systematic manipulation of the publication process.

Wiley and Hindawi regrets that the usual quality checks did not identify these issues before publication and have since put additional measures in place to safeguard research integrity.

We wish to credit our own Research Integrity and Research Publishing teams and anonymous and named external researchers and research integrity experts for contributing to this investigation.

The corresponding author, as the representative of all authors, has been given the opportunity to register their agreement or disagreement to this retraction. We have kept a record of any response received.

### **References**

- [1] J. Shen, H. Lou, Q. Yu, H. Yao, and J. Yuan, "The Connection between High Myopia Patients and MiR-708a or MiR-148 Expression Levels in Aqueous Studies of Visual Acuity," *BioMed Research International*, vol. 2022, Article ID 3363830, 7 pages, 2022.



## Retraction

# Retracted: Phytochemical Analysis, Total Phenolic, Flavonoid Contents, and Anticancer Evaluations of Solvent Extracts and Saponins of *H. digitata*

### BioMed Research International

Received 8 January 2024; Accepted 8 January 2024; Published 9 January 2024

Copyright © 2024 BioMed Research International. This is an open access article distributed under the Creative Commons Attribution License, which permits unrestricted use, distribution, and reproduction in any medium, provided the original work is properly cited.

This article has been retracted by Hindawi following an investigation undertaken by the publisher [1]. This investigation has uncovered evidence of one or more of the following indicators of systematic manipulation of the publication process:

- (1) Discrepancies in scope
- (2) Discrepancies in the description of the research reported
- (3) Discrepancies between the availability of data and the research described
- (4) Inappropriate citations
- (5) Incoherent, meaningless and/or irrelevant content included in the article
- (6) Manipulated or compromised peer review

The presence of these indicators undermines our confidence in the integrity of the article's content and we cannot, therefore, vouch for its reliability. Please note that this notice is intended solely to alert readers that the content of this article is unreliable. We have not investigated whether authors were aware of or involved in the systematic manipulation of the publication process.

Wiley and Hindawi regrets that the usual quality checks did not identify these issues before publication and have since put additional measures in place to safeguard research integrity.

We wish to credit our own Research Integrity and Research Publishing teams and anonymous and named

external researchers and research integrity experts for contributing to this investigation.

The corresponding author, as the representative of all authors, has been given the opportunity to register their agreement or disagreement to this retraction. We have kept a record of any response received.

### References

- [1] O. M. Alshehri, S. Alshamrani, M. H. Mahnashi et al., "Phytochemical Analysis, Total Phenolic, Flavonoid Contents, and Anticancer Evaluations of Solvent Extracts and Saponins of *H. digitata*," *BioMed Research International*, vol. 2022, Article ID 9051678, 12 pages, 2022.

## Retraction

# Retracted: Ameliorated Stomach Specific Floating Microspheres for Emerging Health Pathologies Using Polymeric Konjac Glucomannan-Based Domperidone

### BioMed Research International

Received 8 January 2024; Accepted 8 January 2024; Published 9 January 2024

Copyright © 2024 BioMed Research International. This is an open access article distributed under the Creative Commons Attribution License, which permits unrestricted use, distribution, and reproduction in any medium, provided the original work is properly cited.

This article has been retracted by Hindawi following an investigation undertaken by the publisher [1]. This investigation has uncovered evidence of one or more of the following indicators of systematic manipulation of the publication process:

- (1) Discrepancies in scope
- (2) Discrepancies in the description of the research reported
- (3) Discrepancies between the availability of data and the research described
- (4) Inappropriate citations
- (5) Incoherent, meaningless and/or irrelevant content included in the article
- (6) Manipulated or compromised peer review

The presence of these indicators undermines our confidence in the integrity of the article's content and we cannot, therefore, vouch for its reliability. Please note that this notice is intended solely to alert readers that the content of this article is unreliable. We have not investigated whether authors were aware of or involved in the systematic manipulation of the publication process.

Wiley and Hindawi regrets that the usual quality checks did not identify these issues before publication and have since put additional measures in place to safeguard research integrity.

We wish to credit our own Research Integrity and Research Publishing teams and anonymous and named external researchers and research integrity experts for contributing to this investigation.

The corresponding author, as the representative of all authors, has been given the opportunity to register their agreement or disagreement to this retraction. We have kept a record of any response received.

### References

- [1] J. M. M. Mohamed, N. Mahajan, M. El-Sherbiny et al., "Ameliorated Stomach Specific Floating Microspheres for Emerging Health Pathologies Using Polymeric Konjac Glucomannan-Based Domperidone," *BioMed Research International*, vol. 2022, Article ID 3670946, 12 pages, 2022.

## Retraction

# Retracted: Evaluation of the Antiasthmatic Activity of *Carissa opaca* in Animal Models

### BioMed Research International

Received 8 January 2024; Accepted 8 January 2024; Published 9 January 2024

Copyright © 2024 BioMed Research International. This is an open access article distributed under the Creative Commons Attribution License, which permits unrestricted use, distribution, and reproduction in any medium, provided the original work is properly cited.

This article has been retracted by Hindawi following an investigation undertaken by the publisher [1]. This investigation has uncovered evidence of one or more of the following indicators of systematic manipulation of the publication process:

- (1) Discrepancies in scope
- (2) Discrepancies in the description of the research reported
- (3) Discrepancies between the availability of data and the research described
- (4) Inappropriate citations
- (5) Incoherent, meaningless and/or irrelevant content included in the article
- (6) Manipulated or compromised peer review

The presence of these indicators undermines our confidence in the integrity of the article's content and we cannot, therefore, vouch for its reliability. Please note that this notice is intended solely to alert readers that the content of this article is unreliable. We have not investigated whether authors were aware of or involved in the systematic manipulation of the publication process.

Wiley and Hindawi regrets that the usual quality checks did not identify these issues before publication and have since put additional measures in place to safeguard research integrity.

We wish to credit our own Research Integrity and Research Publishing teams and anonymous and named external researchers and research integrity experts for contributing to this investigation.

The corresponding author, as the representative of all authors, has been given the opportunity to register their agreement or disagreement to this retraction. We have kept a record of any response received.

### References

- [1] M. Ali, U. Salma, I. A. Khan et al., "Evaluation of the Antiasthmatic Activity of *Carissa opaca* in Animal Models," *BioMed Research International*, vol. 2022, Article ID 7011789, 8 pages, 2022.

## Retraction

# Retracted: Compound Shuganjieyu Capsule on CYP450 Enzyme Activity

### BioMed Research International

Received 8 January 2024; Accepted 8 January 2024; Published 9 January 2024

Copyright © 2024 BioMed Research International. This is an open access article distributed under the Creative Commons Attribution License, which permits unrestricted use, distribution, and reproduction in any medium, provided the original work is properly cited.

This article has been retracted by Hindawi following an investigation undertaken by the publisher [1]. This investigation has uncovered evidence of one or more of the following indicators of systematic manipulation of the publication process:

- (1) Discrepancies in scope
- (2) Discrepancies in the description of the research reported
- (3) Discrepancies between the availability of data and the research described
- (4) Inappropriate citations
- (5) Incoherent, meaningless and/or irrelevant content included in the article
- (6) Manipulated or compromised peer review

The presence of these indicators undermines our confidence in the integrity of the article's content and we cannot, therefore, vouch for its reliability. Please note that this notice is intended solely to alert readers that the content of this article is unreliable. We have not investigated whether authors were aware of or involved in the systematic manipulation of the publication process.

Wiley and Hindawi regrets that the usual quality checks did not identify these issues before publication and have since put additional measures in place to safeguard research integrity.

We wish to credit our own Research Integrity and Research Publishing teams and anonymous and named external researchers and research integrity experts for contributing to this investigation.

The corresponding author, as the representative of all authors, has been given the opportunity to register their agreement or disagreement to this retraction. We have kept a record of any response received.

### References

- [1] Y. Tang and Y. Li, "Compound Shuganjieyu Capsule on CYP450 Enzyme Activity," *BioMed Research International*, vol. 2022, Article ID 3228738, 8 pages, 2022.

## Retraction

# Retracted: Effect of Previous Cancer History on Survival of Patients with Different Subtypes of Breast Cancer

### BioMed Research International

Received 8 January 2024; Accepted 8 January 2024; Published 9 January 2024

Copyright © 2024 BioMed Research International. This is an open access article distributed under the Creative Commons Attribution License, which permits unrestricted use, distribution, and reproduction in any medium, provided the original work is properly cited.

This article has been retracted by Hindawi following an investigation undertaken by the publisher [1]. This investigation has uncovered evidence of one or more of the following indicators of systematic manipulation of the publication process:

- (1) Discrepancies in scope
- (2) Discrepancies in the description of the research reported
- (3) Discrepancies between the availability of data and the research described
- (4) Inappropriate citations
- (5) Incoherent, meaningless and/or irrelevant content included in the article
- (6) Manipulated or compromised peer review

The presence of these indicators undermines our confidence in the integrity of the article's content and we cannot, therefore, vouch for its reliability. Please note that this notice is intended solely to alert readers that the content of this article is unreliable. We have not investigated whether authors were aware of or involved in the systematic manipulation of the publication process.

Wiley and Hindawi regrets that the usual quality checks did not identify these issues before publication and have since put additional measures in place to safeguard research integrity.

We wish to credit our own Research Integrity and Research Publishing teams and anonymous and named external researchers and research integrity experts for contributing to this investigation.





The corresponding author, as the representative of all authors, has been given the opportunity to register their agreement or disagreement to this retraction. We have kept a record of any response received.

### References

- [1] W. Lin, Y. Chen, Z. Ji et al., "Effect of Previous Cancer History on Survival of Patients with Different Subtypes of Breast Cancer," *BioMed Research International*, vol. 2022, Article ID 6116658, 15 pages, 2022.

## Research Article

# Biodegradable Polymeric Pharmaceutical Nanoemulgel Coloaded with Eucalyptol-Lornoxicam: Fabrication and Characterizations for Possible Better Pain Management

Muhammad Shafiq,<sup>1</sup> Barkat Ali Khan <sup>1</sup>, Sheikh Abdur Rashid <sup>1</sup>,  
Muhammad Khalid Khan,<sup>1</sup> Faiza Naseem,<sup>1</sup> Ali M. Alqahtani <sup>2</sup>, Saad S. Alqahatni,<sup>3,4</sup>  
Taha Alqahtani <sup>2</sup> and Ali Alamri<sup>2</sup>

<sup>1</sup>DDCL, Gomal Centre of Pharmaceutical Sciences, Faculty of Pharmacy, Gomal University, Dera Ismail Khan, Pakistan

<sup>2</sup>College of Pharmacy, King Khalid University, Abha, Saudi Arabia

<sup>3</sup>Department of Pharmacy Practice, College of Pharmacy, Jazan University, Jazan, Saudi Arabia

<sup>4</sup>Pharmacy Practice Research Unit, College of Pharmacy, Jazan University, Jazan, Saudi Arabia

Correspondence should be addressed to Barkat Ali Khan; [barki.gold@gmail.com](mailto:barki.gold@gmail.com)  
and Sheikh Abdur Rashid; [sheikhabdurrashid11@gmail.com](mailto:sheikhabdurrashid11@gmail.com)

Received 13 August 2022; Revised 21 September 2022; Accepted 10 October 2022; Published 13 May 2023

Academic Editor: Nikhil Agrawal

Copyright © 2023 Muhammad Shafiq et al. This is an open access article distributed under the Creative Commons Attribution License, which permits unrestricted use, distribution, and reproduction in any medium, provided the original work is properly cited.

Nanoemulgels are considered as potential and ideal drug delivery systems for the transdermal administration of poorly soluble drugs like lornoxicam. Their intrinsic characteristics, such as small globule size as well as excipient type, make transdermal passage of the drug easier. The current study was aimed at developing nanoemulgel based formulation of lornoxicam coloaded with eucalyptol to enhance drug skin permeation and bioavailability in order to promote therapeutic outcome in appropriate time. High shear homogenization technique was utilized to develop optimized lornoxicam encapsulated nanoemulsion followed by its conversion into nanoemulgel formulation by the addition of 1% Carbopol 940 as gelling agent. Different characterization tests were performed on optimized formulation such as surface charge, particle size and size distribution, viscosity, spreadability, pH, drug content determination, drug entrapment efficiency, in vitro drug release, and drug permeation analysis. The optimized formulation had globule size of  $143.7 \pm 2.18$  nm. The results of drug entrapment efficiency, in vitro drug release, and skin penetration experiments were found satisfactory. Based on the formulation type, permeability parameters such as permeability constant ( $K_p$ ), enhancement ratio (Er), and steady state flux ( $J_{ss}$ ) revealed greater values and satisfactory outcomes. When compared to other formulations (LRX nanoemulgel and EU nanoemulgel), the LRX-EU nanoemulgel formulation produced improved skin permeation profile (flux,  $189.63 \pm 7.68 \mu\text{g}/\text{cm}^2/\text{h}$ ; permeability coefficient,  $2.09 \pm 0.067$  cm/h; and ER, 4.274). This work clearly proved that lornoxicam coloaded with eucalyptol nanoemulgel formulations could be developed to generate stable drug delivery systems. Thus, LRX-EU NEG formulation seems promising in terms of physicochemical properties, enhanced bioavailability, and high skin penetration profile as compared to LRX NEG formulation.

## 1. Introduction

Nonsteroidal anti-inflammatory drugs (NSAIDs) have gained enormous popularity in the management of inflammatory conditions such as rheumatoid arthritis and osteoarthritis [1]. Inflammatory diseases can be effectively relieved

by taking NSAIDs orally. However, drug-associated side effects, such as gastrointestinal mucosal irritation and ulceration, have restricted its clinical usage. The administration of NSAIDs via transdermal route is one method to prevent toxicity and utilizing them for a longer period of time [2]. Transdermal systems, which carry medication via the skin

into the bloodstream, counteract changes in the rate of absorption and metabolism as well as gastrointestinal side effects brought on by oral drug delivery [3]. Chronic diseases are the perfect fit for it. It enables the delivery of potent drug moieties with the advantages of self-administration and improved therapeutic effectiveness [4]. Lornoxicam (LRX), member of oxamicam class, is quite an effective NSAID. It is frequently recommended for illnesses that are chronically inflammatory and painful in nature. Similar to other NSAIDs, oral administration of LRX has a number of negative renal, gastrointestinal, and hematological consequences. In addition to this, it requires repeated administration due to its short half-life of 3-4 h. Additionally, parenteral administration is not suggested for treating chronic diseases (R. U. [5]). Eucalyptol (1,8-cineole), a terpenoid oxide that is extracted from eucalyptus leaves, is found in high concentrations in a wide range of plants as essential oil. It improves drug permeation profile by disruption of skin intracellular lipids owing to its lipophilicity. It inhibits proinflammatory cytokines (TNF- and IL-1), as well as chemotactic cytokines, when evaluated on human monocytes and lymphocytes in vitro, making it an effective analgesic as well as anti-inflammatory drug. This inhibition results in its effectiveness in neurodegenerative illnesses [6].

An effective strategy to address all the issues with LRX administration is the controlled distribution of LRX via transdermal delivery [7]. In the current investigation, to increase the drug's bioavailability, LRX was developed as a nanoemulgel formulation coloaded with eucalyptol. Numerous studies have demonstrated that penetration enhancers can promote better skin permeation than isolated moieties when used in conjunction with cosolvents [8]. Cosolvents are often employed in transdermal formulations as penetration enhancers and carriers. These substances affect both drug release and permeation because they not only improve drug solubility but also change the skin topology and increase penetration rates [9]. In order to increase the transdermal permeability of LRX, the current study uses eucalyptol as a penetration enhancer and PEG 400 as a cosolvent. Taken altogether, Carbopol-decorated LRX nanoemulgel formulation coloaded with eucalyptol was produced by high shear homogenization method to portray constant drug release rate for a period of 24 h.

## 2. Materials and Methods

Lornoxicam was kindly gifted for research by Wilshire Pharma Pvt. Limited, Lahore, Pakistan; eucalyptol provided by DDCL was used as active ingredient as well as penetration enhancer; olive oil and almond oil (Marhaba Laboratories, Pakistan) were used as oil phase in nanoemulsion formulation; Carbopol 940 (BDH Industries) was employed as gelling agent in the formulation of nanoemulgel; Tween 80 and PEG 400 (Sigma-Aldrich, Germany) were used as surfactant and cosurfactant, respectively; triethanolamine (Merck, Germany) was employed as pH adjuster, and distilled water was used as vehicle. The chemicals used in this project were of analytical grade and purified.

**2.1. Lornoxicam Solubility Studies.** Solubility tests are used to screen surfactants, cosurfactants, and oils for nanoemulsion formulations that have a high rate of dissolution as well as possess high degree of skin penetration. In this study, first lornoxicam powder in excess amount was mixed with 10 ml olive oil, almond oil, PEG 400, Tween 80, propylene glycol, ethanol, phosphate buffer saline (pH 5.8, 6.8, and 7.4), and water in separate conical flasks. The flasks were subjected to continuous stirring by means of shaking water bath (1217.2E, Sheldon, USA) for 72 h time period. Finally, the separation of insoluble drug particles was made sure by subjecting the contents of the flasks to centrifugation process for 15 minutes at 5000 rpm. An aliquot was taken and subjected to filtration with the help of a Millipore filter (0.45  $\mu\text{m}$ ). The dilution was then subjected to UV-spectrophotometer (UV-1800, Shimadzu, Japan) by taking wavelength at 376 nm. Triplicate readings of concentration were determined [7].

**2.2. ATR-FTIR Studies.** The efficacy, stability, and success of solid dosage form are heavily dependent upon the rigorous excipient selection. The compatibility of the drug with excipients is critical for the efficacy, stability, and safety of the product [10]. ATR-FTIR spectra were produced by ATR-FTIR spectrometer (Spectrum 100, Perkin Elmer, USA) using MIRacle ATR accessory (PIKE Technologies, Madison, USA). The samples include pure lornoxicam, eucalyptol, Carbopol 940, Tween 80, PEG 400, lornoxicam nanoemulsion formulation, eucalyptol nanoemulsion formulation, lornoxicam cum eucalyptol (LRX-EU) nanoemulsion formulation, and their respective nanoemulgel formulations. Scans were recorded at a range of 4000  $\text{cm}^{-1}$  to 625  $\text{cm}^{-1}$ . The scan lasted 12 min, and the resulting spectra were examined for any spectral alterations [11].

**2.3. Nanoemulsion and Nanoemulgel Development.** Nanoemulsion formulations were prepared by high-speed homogenization technique [12]. An oily phase comprising olive oil, almond oil, PEG 400, and lornoxicam, either alone or in conjunction with eucalyptol, was subjected to stirring at 700 rpm for 1 h by hot plate magnetic stirrer (VELP Scientifica, Italy) at 70°C temperature as represented in Figure 1. Likewise, aqueous phase comprising Tween 80 and distilled water was subjected to constant stirring for 1 h at same temperature, i.e., 70°C. Drop by drop, the oil phase was injected into the aqueous phase to create the final formulation. Thermodynamic stability of the prepared nanoemulsion formulation was determined by centrifuging the optimized formulation. In this method, nanoemulsion formulation was centrifuged at 3500 rpm for 30 min. The process was carried out to investigate the chances of phase separation or formation of turbidity.

Numerous types of gel bases were employed for effective distribution of optimized nanoemulsion formulation in order to promote local drug accumulation in the skin while minimizing blood penetration. Carbopol 940 in different concentrations, i.e., 0.5, 1, 1.5, 2, and 2.5%, was used as gelling agent for the preparation of optimized nanoemulgel formulation. On the basis of physical appearance of a simple

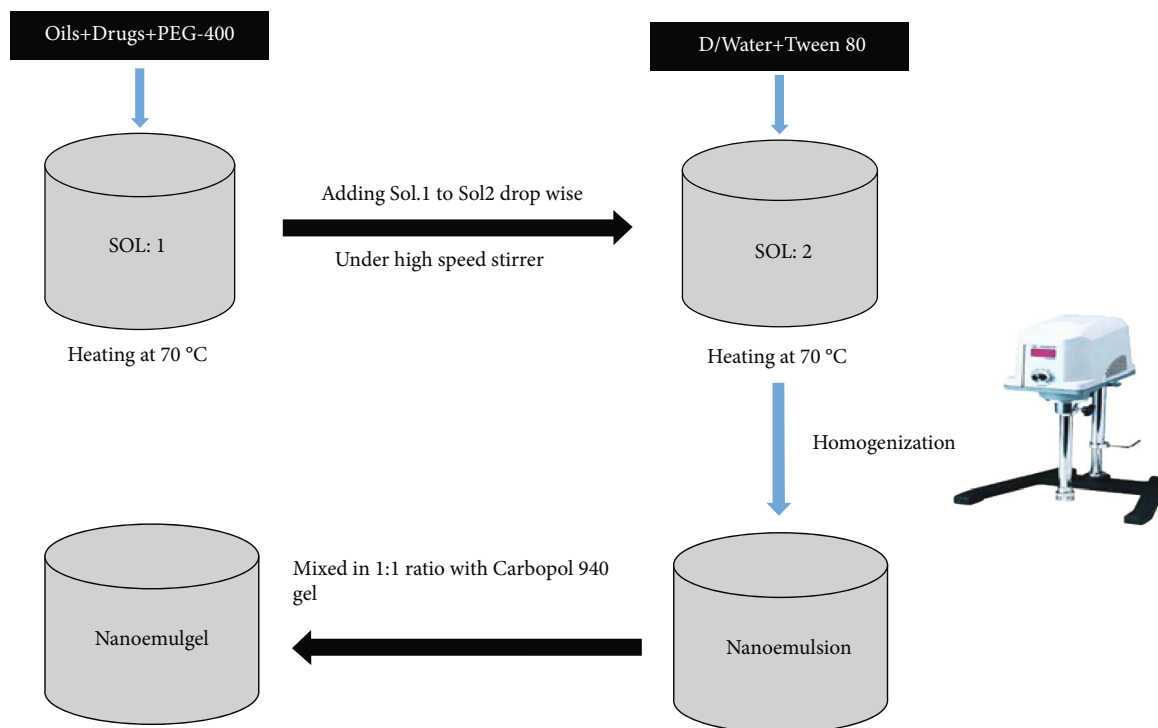


FIGURE 1: Schematic representation of preparation of nanoemulsion and nanoemulgel.

lornoxamic gel, Carbopol 940 having 1% concentration was selected for the development of lornoxamic/eucalyptol nanoemulgel. To develop a skin friendly formulation, the lornoxamic/eucalyptol-loaded nanoemulsion was mixed with Carbopol gel (1% *w/w*). Carbopol was gradually incorporated into distilled water by continuous stirring for 2-3 h time period at 700 rpm until the formation of a clear dispersion. The Carbopol dispersion was kept at room temperature for effective hydration and swelling for a time period of 3 h. The optimized lornoxamic/eucalyptol nanoemulsion formulation was mixed with Carbopol dispersion by means of gentle stirring. Finally, the mixture was made neutral ( $\text{pH } 7.0 \pm 0.5$ ) by the addition of 4-5 drops of triethanolamine in order to develop a transparent gel. The produced gel formulation was kept overnight to allow trapped air to escape [13]. A similar process was utilized to create lornoxamic nanoemulgel and eucalyptol nanoemulgel formulations. The composition of LRX NEG, EU NEG, and LRX-EU NEG are shown in Table 1 [14].

#### 2.4. Characterization of LRX-EU Nanoemulsion and Nanoemulgel Formulations

**2.4.1. pH Determination.** The optimized formulation of LRX-EU nanoemulsion and nanoemulgel was subjected to pH determination. The test was carried out at  $25 \pm 1^\circ\text{C}$  by means of pH meter (Denver, USA). Initially, the instrument was calibrated with the help of buffer solutions having different known concentrations (pH 3, 7, and 9). An average of three readings were taken, and the results were shown as mean  $\pm$  SD [15].

**2.4.2. Size and Size Distribution Analysis.** Particle size and particle size distribution of the optimized formulations were determined with the help of Zetasizer 90 (Malvern Instruments; Worcestershire, UK) by employing dynamic light scattering mechanisms. The Zetasizer is equipped with 6.34 version software having laser of wavelength 635 nm and a  $90^\circ$  detect angle. Mixtures of LRX-EU nanoemulsion as well as LRX-EU nanoemulgel ( $10 \mu\text{l}$ ) in deionized water were vortexed for a time period of 2 min in order to obtain a clear homogenous dispersion. The experiment was carried out in triplicates by maintaining the temperature at  $25 \pm 1^\circ\text{C}$ . The results were shown in the form of mean  $\pm$  SD [16].

**2.4.3. Determination of Polydispersity Index and Zeta Potential.** Polydispersity index (PDI) and zeta potential of LRX-EU nanoemulsion and LRX-EU nanoemulgel were investigated using Zetasizer 90 (Malvern Instruments; Worcestershire, UK). The test was executed by taking formulation ( $700 \mu\text{l}$ ) in a capillary tube, equipped with a gold electrode. The procedure was repeated three times at  $25 \pm 1^\circ\text{C}$ , with the results represented as mean  $\pm$  SD [17].

**2.4.4. Surface Morphology Analysis.** A simple light microscope (CX41RF, OLYMPUS, Japan) coupled with a 5 megapixel photographic camera was used to evaluate the surface morphology of the optimized nanoemulsion as well as nanoemulgel formulations of LRX-EU. A drop of the developed formulation was put on the slide and viewed under the microscope. After that, they were photographed.



TABLE 1: Composition of % w/w LRX-loaded nanoemulgel, EU-loaded nanoemulgel, and LRX-EU-loaded nanoemulgel formulations.

Components	LRX-loaded nanoemulgel	EU-loaded nanoemulgel	LRX-EU-loaded nanoemulgel
Carbopol 940	1	1	1
Triethanolamine	1	1	1
Optimized LRX-loaded nanoemulsion	50	—	—
Optimized EU-loaded nanoemulsion	—	50	—
LRX-EU nanoemulsion	25	25	1: 1
Distilled water	48	48	48

**2.4.5. Entrapment Efficiency.** Entrapment efficiency of optimized nanoemulsion and nanoemulgel formulations of LRX-EU was determined by indirect method. This involved centrifugation of formulations at a temperature of 20°C until the nanoemulsion formulation occupying filter unit and the aqueous phase relating to filtrate were completely separated. After the completion of separation process, the resultant filtrate was utilized in order to estimate the quantity of non-trapped lornoxicam using a UV-spectrophotometer (UV-1800, Shimadzu, Japan) set at maximum wavelength ( $\lambda_{\max}$ ) of 376 nm. Then, lornoxicam was quantified using a standard curve in PBS with a pH of 7.4, and the findings were represented as mean  $\pm$  SD ( $n = 3$ ). The findings were compared to a blank control formulation. By subtracting the free drug (lornoxicam) left in the filtrate from the drug initially incorporated into the nanoemulsion formulation, the following equation was used to calculate the quantity of incorporated drug in the nanoemulsion formulation and thus the entrapment efficiency [18]:

$$\text{Entrapment efficiency} = \frac{\text{added drug} - \text{free drug}}{\text{added drug}} * 100. \quad (1)$$

**2.4.6. Viscosity Determination.** The nanoemulsion and nanoemulgel formulations of LRX-EU were subjected to Brookfield viscometer (dv2t, Ametek Brookfield, USA) at room temperature for the determination of consistency [15]. By employing spindle no. 63 at different rotations, 0.5 ml of the sample was used for viscosity determination at  $25 \pm 0.5^\circ\text{C}$ . The experiment was repeated three times.

**2.4.7. Spreadability Determination.** The spreadability of optimized formulation of LRX-EU nanoemulgel was investigated by means of drag and slip assembly. The assembly is made up of a block of wood that is attached to the pulley. It also possesses two equal size glass slides, in which one is firmly attached to the wooden block while the other is moving. Between the two slides, sample is compressed, and a known weight is added onto it. About 2g of optimized LRX-EU nanoemulgel was added on static slide and then compressed by movable slide. On the upper surface of movable slide, approximately 50g weight was put. The time period in which upper slide move to 8 cm distance was calculated (M. K. [19]). The spreadability of nanoemulgel was

determined by the following equation:

$$S = M * \frac{L}{T}, \quad (2)$$

where  $S$  represents the spreadability of nanoemulgel,  $M$  represents the weight introduced on movable glass slide,  $L$  represents the glass slides length, and  $T$  represents the time in which slides cover the distance.

**2.4.8. Drug Content Determination.** The nanoemulsion and nanoemulgel formulations of LRX-EU were subjected to UV-spectrophotometer (UV-1800, Shimadzu, Japan) for analysis of drug content. In this test, the optimized nanoemulsion formulation of LRX-EU was taken in the Eppendorf tube (Cat no 037108; SCILOGEX, USA) and centrifuged at 13,000 rpm for a time frame of 15 min (D3024, SCILOGEX, USA). It was followed by subsequent collection of supernatant. Dilution of supernatant (0.5 ml) was done with phosphate buffer having pH 7.4. The solution was subjected to constant stirring by means of magnetic stirrer at 1,000 rpm for 10 min time period. By employing UV-spectrophotometer, absorbance of solution was taken at  $\lambda_{\max}$  376 nm.

For the extraction of entrapped drug in LRX-EU nanoemulsion formulation, mixture of methanol (1 ml) and sediment was vortexed for 5 min. Phosphate buffer, pH 7.4, was used to dilute the combination. After that, it was subjected to stirring for 10 min. Using a UV-spectrophotometer, the absorbance was estimated at a  $\lambda_{\max}$  376 nm. To determine the drug content, both sediment and supernatant drug loads were used [20].

$$\text{Drug content} = \text{Drug in supernatant} + \text{drug in sediment.} \quad (3)$$

**2.4.9. Drug Release Studies.** For the determination of drug release profiles of LRX-EU nanoemulsion and nanoemulgel formulations, the Franz diffusion cell (PermeGear, Inc. No. 4G-01-00-15-12; India) equipped with Tuffryn membrane was employed. The small pore size ( $0.45 \mu\text{m}$ ) of Tuffryn membrane plays the role of partitioning medium between the two compartments (donor and recipient) of the Franz diffusion cell. Approximately 7 ml of freshly prepared phosphate buffer, pH 5.5 (simulated skin fluid), was incorporated into receptor compartment, and the temperature was maintained at  $32 \pm 2^\circ\text{C}$ . After predetermined time intervals, 1 ml

samples were taken from the receptor compartment. The same amount of phosphate buffer was substituted. UV-spectrophotometer (UV-1800, Shimadzu, Japan) was employed for the analysis of the samples. An average of three readings were taken, and the results were represented as mean  $\pm$  SD. A plot of time versus concentration was obtained for the data. The responsible mechanism for drug release was modelled using a power law kinetic equation [12].

$$\frac{M_t}{M_\infty} = Ktn, \quad (4)$$

where  $M_t$  and  $M_\infty$  represent the drug fraction release after time  $t$ ,  $K$  represents the rate constant,  $n$  represents the value of exponential release.

When  $n$  value is 0.5, drug release occurs by Quasi Fickian diffusion mechanism; when  $n > 0.5$ , then drug release occurs by zero order or non-Fickian, or anomalous mechanism, and  $n$  value equal to 1 indicates zero order drug release.

#### 2.4.10. In Vitro Drug Permeation Analysis of LRX-EU Nanoemulsion and Nanoemulgel Formulations

(1) *Animal Skin Harvesting.* From *in vivo* research facility of Gomal Centre of Pharmaceutical Sciences, healthy male rabbits approximately weighing 2-2.5 kg were obtained. All operations involving the use of experimental animals were carried out in compliance with the Gomal University's ethics and regulations, which were adapted from the worldwide standards (OECD Environment, Health and Safety). For the goal of acclimatization, they were fed a regular diet for seven days. All of the animals were killed with an intravenous injection of sodium pentobarbital ketamine and cervical dislocation. Shaving blades were used to shave the abdomen, and the skin was gently excised. 0.9% NaCl solution (normal saline) was used to cleanse the skin. A knife was used to remove the attached fats. The skin was wrapped in aluminium foil and kept in a deep freezer at  $-20^\circ\text{C}$  until needed. Before usage, frozen skin was kept at room temperature for 3 hours.

(2) *Skin Permeation Determination.* For skin permeation tests, a Franz diffusion cell with a vertical diffusion cell (PermeGear, Inc. No: 4G-01-00-15-12; India) was used. Magnetic stirring and a heating circulation system with a programmable temperature control mechanism were included in the Franz diffusion cell assembly. The goal of the skin permeation investigation was to measure the drug transfer rate across the skin and forecast the quantity of localized drug in different skin layers. Skin hydration technique was utilized to precondition the rabbit skin before the experiment using PBS for 30 min. A magnetic stirrer was used to gently agitate the receptor fluid. The purpose of this stirring is to avoid boundary layer effects. 7 ml PBS, with pH 7.4, was added to the receptor compartment, which was then continuously stirred at 500 rpm. To keep the temperature at  $37 \pm 0.5^\circ\text{C}$ , a heating circulation system was used.

The rabbit skin was positioned between the donor and receptor compartments of the Franz diffusion cell with the epidermis facing the formulation and the dermis facing the receptor compartment. The upper surface of the mounted skin was allowed to dry and exposed for 1 hour. Both the receptor media and dermal side of the skin were in touch. The donor compartment was filled with about 1 ml formulation. At predefined time intervals, 1 ml of the samples was withdrawn from the sampling port. The receptor phase was immediately refilled with the same amount of freshly prepared solution and kept at the same temperature. Until the completion of the trial, the sink conditions were maintained. After samples dilution with PBS, pH 7.4, the obtained samples were analyzed for lornoxicam concentration using UV-spectrophotometer (UV-1800, Shimadzu, Japan). The data was presented in the form of mean  $\pm$  SD. The quantity of lornoxicam penetrated through rabbit skin as a function of time was shown. The following equation was used to compute the total quantity of lornoxicam penetrated per unit area:

$$Q_n = C_n V_r + \sum_{i=0}^{n-1} \frac{C_i V_s}{A}, \quad (5)$$

where  $Q_n$  represents the total quantity of drug penetrated per unit area relating to  $n$ th sample time,  $C_n$  represents the drug concentration in receptor fluid at  $n$ th sample,  $C_i$  represents the drug concentration in receptor fluid at  $i$ th sample ( $n - 1$ ),  $A$  represents the diffusion cell effective permeation area ( $1.767 \text{ cm}^2$ ),  $V_r$  represents the volume of receptor solution (7 ml), and  $V_s$  represents the volume of the sample withdrawn (0.5 ml).

The steady state flux, represented by  $J_{ss}$ , was shown as  $\mu\text{g}/\text{cm}^2/\text{h}$ . Permeability coefficient, represented by  $K_p$ , was calculated by dividing  $J_{ss}$  by initial drug concentration in the donor compartment. By dividing flux of test formulation by standard control formulation, enhancement ratio was estimated.

$$\begin{aligned} \text{Enhancement ratio} &= \frac{J_{ss} \text{ of LRX - EU NE}}{J_{ss} \text{ of LRX NE}}, \\ \text{Enhancement ratio} &= \frac{J_{ss} \text{ of LRX - EU NEG}}{J_{ss} \text{ of LRX NEG}}. \end{aligned} \quad (6)$$

A comparison was made between the results obtained from permeation study analysis to that of lornoxicam nanoemulsion as well as nanoemulgel [21].

2.5. *Stability Studies.* The optimized nanoemulgel formulation of LRX-EU was subjected to accelerated stability testing. This was done by storing the formulation at three different temperatures ( $4^\circ\text{C}$ ,  $25^\circ\text{C}$ , and  $45^\circ\text{C}$ ) [7]. The samples were examined for drug content, physical appearance, zeta potential, pH, PDI, and droplet size at regular intervals, i.e., 0, 30, 60, and 90 days. An average of three readings were taken.

**2.6. Statistical Analysis.** The variations between the two groups (control and treatment) in *in vivo* investigations were examined using a one-way ANOVA with Tukey's multiple comparison post hoc test. It was determined that a probability level of  $P < 0.05$  was statistically significant. SPSS was used to conduct statistical analysis (version 20).

### 3. Results and Discussion

**3.1. Lornoxicam Solubility Studies.** When it comes to achieving optimum bioavailability, a drug's solubility is crucial. Low water solubility is the most common obstacle in the formulation of novel drug moieties. The majority of the drugs exhibit either acidic or basic nature, with negligible water solubility. Lornoxicam also displays a low solubility in water. Olive oil, almond oil, PEG 400, Tween 80, propylene glycol, ethanol, phosphate buffer saline (pH 5.8, 6.8, and 7.4) and water were used to conduct solubility tests for the chosen drug. According to Table 2, lornoxicam exhibited least solubility in water and excellent solubility in phosphate buffer saline with pH 7.4. These findings matched those of Hashmat et al. [7], who found that highest drug solubility was exhibited in phosphate buffer, pH 7.4. Despite the fact that several oils have better lornoxicam solubility, olive oil was selected as the oil phase for nanoemulsion formulation. The optimum drug solubility and influence on skin permeability are two of the reasons [22]. An extensive literature review aided in the selection of the appropriate oil phase for producing the transdermal formulation. The choice of a good surfactant is difficult and needs careful consideration. Tween 80 was chosen as the surfactant in the nanoemulsion formulation. The optimal drug solubility and function in skin permeability are two of the reasons. Another reason is that it is a nonionic surfactant, which is less hazardous and more miscible with the components in the formulation. The solubility of the drug was also examined in cosurfactants, with PEG 400 being chosen as the cosurfactant molecule. It has been utilized as a cosurfactant in emulsion formulations, with the added benefit of acting as a cosolvent. The selection of an appropriate surfactant is difficult and necessitates extensive testing. For the formulation of nanoemulsions, Tween 80 was employed as surfactant because of optimum drug solubility as well as skin penetration profile [23]. Another advantage is that it is a nonionic surfactant, which is less toxic and has greater miscibility with other formulation components. The solubility of the drug was also examined in cosurfactants, and PEG 400 was selected as cosurfactant. It has been utilized in emulsion formulations as a cosurfactant with the added advantage of cosolvency. It not only prevents the formation of stiff structures such as precipitates, liquid crystals, and gels, but it also increases emulsion area [24].

**3.2. Nanoemulsion and Nanoemulgel Development.** In this work, a high-speed homogenizer was utilized to make various formulations of lornoxicam nanoemulsion as well as eucalyptol nanoemulsion. Lornoxicam coloaded with eucalyptol (LRX-EU) nanoemulsion was fabricated from optimized nanoemulsion formulations of lornoxicam and

eucalyptol by mixing equal volume of both nanoemulsion formulations, with Tween 80 acting as a surfactant. Tables 3 and 4 list the formulation components. Tween 80 is a nonionic surfactant, having HLB value 15 and exhibiting a lower CMC value than ionic surfactants. Surfactants reduce the tension between the aqueous and oily phases of emulsions. As a result, oil in water type of emulsions is formed very easily because of quicker and rapid oil dispersion in an aqueous medium. Tween 80 was chosen as an emulsifier because of a variety of reasons such as its nonionic nature, optimum HLB, capacity to reduce surface tension, steric ability of nanoemulsion formulations, and better permeation enhancer characteristics [25]. *In vivo* stability is also great for topical surfactants of nonionic nature. In this work, polyethylene glycol (PEG) was utilized as a cosurfactant to minimize interfacial stress and also provide flexibility to the interfacial layer. The droplets of nanoemulsion formulation undergo rapid and easy deformation due to the flexible nature of interfacial film. The responsible factor behind the deformation phenomenon is the decrease of polar groups between the surfactant molecules [26].

For additional research purpose, an optimized LRX-EU nanoemulsion was chosen on the basis of superior skin permeability characteristics. Many studies were conducted in order to find a suitable vehicle for applying LRX-EU nanoemulsion to the skin. Because of its nonirritant nature, great storage stability, high bioadhesive qualities, and capacity to produce translucent and pharmaceutically elegant gels, Carbopol (1% *w/w*) was chosen as a gelling agent [27]. Preliminary studies were carried out to identify the optimum concentration of Carbopol for required gel viscosity for topical application while avoiding the danger of the formulation being drained off (Table 1).

#### 3.3. Nanoemulsion and Nanoemulgel *In Vitro* Characterization

**3.3.1. Thermodynamic Stability.** Nanoemulsions should be stable at varied temperatures and be able to preserve their spontaneous emulsification nature when diluted. As a result, thermodynamic stability investigations were carried out. Optimized nanoemulsion formulations of lornoxicam, eucalyptol, and LRX-EU were subjected to numerous thermodynamically stressed environments. Any differences in color, odor, or overall appearance were observed and compared to a blank nanoemulsion formulation. Nanoemulsion formulation passed the required thermodynamic test, such as centrifugation. There were no signs of turbidity, creaming, or phase separation (Table 5). The phenomenon of centrifugation results in creaming or sediment formation. Because oil is less thick than aqueous phase, O/W emulsions are suitable choices. This approach is an indirect parameter that depicts emulsion stability against the force of gravitation. The developed nanoemulsion formulation of LRX-EU passed the centrifugation test, indicating that the overall system was more homogeneous and stable. Tween 80, when used as a surfactant and emulsifying agent, often prevents oil globules from moving due to centrifugal forces. Aggregation, creaming, and phase separation are all impeded as a result [15].

TABLE 2: Lornoxicam solubility studies at 25°C ( $n = 3$ ).

S. no.	Solvents	Solubility (mg/ml) Mean $\pm$ SD	Role
1.	Olive oil	0.385 $\pm$ 0.011	Oil phase
2.	Almond oil	0.032 $\pm$ 0.003	Oil phase
3.	PEG 400	1.354 $\pm$ 0.018	Cosolvent
4.	Tween 80	4.05 $\pm$ 0.047	Surfactant
5.	Propylene glycol	1.145 $\pm$ 0.021	Cosolvent
6.	Ethanol	0.073 $\pm$ 0.012	Cosurfactant
7.	Phosphate buffer saline (pH 5.8)	0.145 $\pm$ 0.008	Solvent/vehicle
8.	Phosphate buffer saline (pH 6.8)	0.298 $\pm$ 0.067	Solvent/vehicle
9.	Phosphate buffer saline (pH 7.4)	0.363 $\pm$ 0.003	Solvent/vehicle
10	Water	0.031 $\pm$ 0.001	Solvent/vehicle

TABLE 3: Composition of 1% *w/w* LRX O/W nanoemulsion formulation.

Formulation code	Lornoxicam	Olive oil	Tween 80	PEG 400	Water
LRX 1 (blank)	_____	7.5 g	7.5 g	5.5 g	q.s
LRX 2	1 g	7.5 g	7.5 g	5.5 g	q.s
LRX 3	1 g	6.5 g	6.25 g	6.25 g	q.s
LRX 4	1 g	5.5 g	7.75 g	7.75 g	q.s
LRX 5	1 g	7.5 g	8.50 g	7.50 g	q.s

LRX 2 = optimized nanoemulsion formulation.

TABLE 4: Composition of 1% *w/w* EU O/W nanoemulsion formulation.

Formulation code	Eucalyptol	Olive oil	Tween 80	PEG 400	Water
EU 1 (blank)	_____	7.5 g	7.5 g	5.5 g	q.s
EU 2	1 g	7.5 g	7.5 g	5.5 g	q.s
EU 3	1 g	6.5 g	6.25 g	6.25 g	q.s
EU 4	1 g	5.5 g	7.75 g	7.75 g	q.s
EU 5	1 g	7.5 g	8.50 g	7.50 g	q.s

EU 2 = optimized nanoemulsion formulation.

TABLE 5: Physical properties of blank and LRX-, EU-, and LRX-EU-loaded nanoemulsion at 4°C, 25°C, and 45°C.

Formulation codes	Temperature	Color	Odor change	Phase separation	Centrifugation stability	Thermodynamic test
Blank	4°C	White	No change	Nil	Stable	Passed
	25°C	White	No change	Nil	Stable	Passed
	45°C	White	No change	Nil	Stable	Passed
LRX NE	4°C	Pale yellow	No change	Nil	Stable	Passed
	25°C	Pale yellow	No change	Nil	Stable	Passed
	45°C	Pale yellow	No change	Nil	Stable	Passed
EU NE	4°C	White	No change	Nil	Stable	Passed
	25°C	White	No change	Nil	Stable	Passed
	45°C	White	No change	Nil	Stable	Passed
LRX-EU NE	4°C	Yellow	No change	Nil	Stable	Passed
	25°C	Yellow	No change	Nil	Stable	Passed
	45°C	Yellow	No change	Nil	Stable	Passed

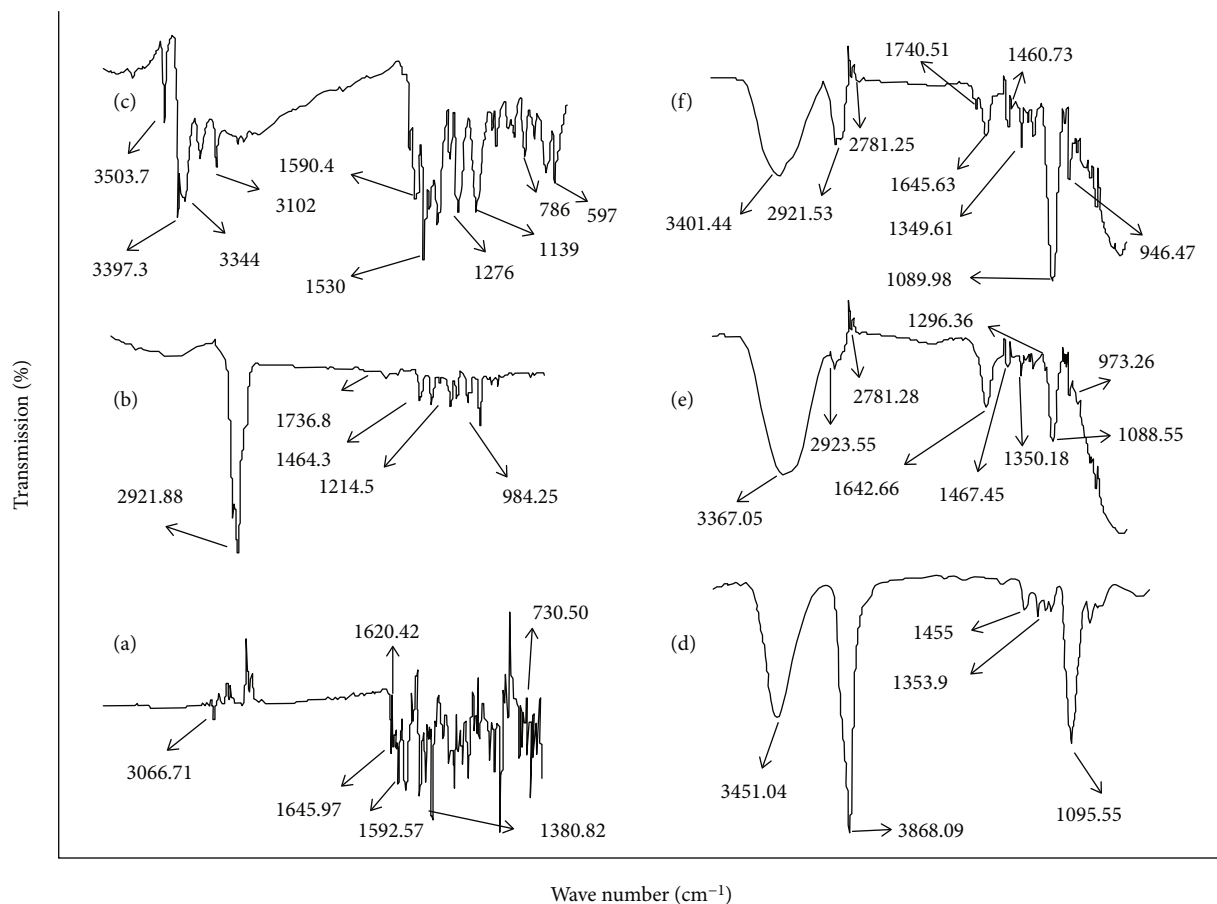


FIGURE 2: ATR-FTIR spectra of (a) lornoxicam, (b) eucalyptol, (c) Carbopol, (d) PEG 400, (e) LRX-EU NE, and (f) LRX-EU NEG.

**3.3.2. ATR-FTIR Studies.** The investigation of possible interactions taking place between lornoxicam, eucalyptol, and polymers in nanoemulsion and nanoemulgel formulations was carried out by means of ATR-FTIR spectrometer (Spectrum 100, Perkin Elmer, USA) using MIRacle ATR accessory (PIKE Technologies, Madison, USA). The ATR-FTIR spectra of lornoxicam, eucalyptol, and LRX-EU nanoemulsion and nanoemulgel formulations are presented in Figure 2. ATR-FTIR spectrum of lornoxicam exhibited characteristic band peaks at  $1644\text{ cm}^{-1}$  (primary amide stretching vibration),  $1618\text{ cm}^{-1}$  and  $1590\text{ cm}^{-1}$  (N-H group bending vibration),  $1143\text{ cm}^{-1}$ - $1380\text{ cm}^{-1}$  (O=S=O stretching vibration), and  $788\text{ cm}^{-1}$  (C-Cl stretching vibration) [28]. The presence of band peak at  $3064\text{ cm}^{-1}$  (C-H aromatic ring stretching vibration) was also exhibited. Similarly, ATR-FTIR spectra of eucalyptol exhibited characteristic band peaks at  $1464.3\text{ cm}^{-1}$  and  $1214.5\text{ cm}^{-1}$  (C-C band) and  $984.25\text{ cm}^{-1}$  (C-O-C stretching vibration), and the peak at  $1736.8\text{ cm}^{-1}$  corresponded to carbonyl group [29]. ATR-FTIR spectra of LRX-EU nanoemulsion and nanoemulgel formulations displayed characteristic band peaks of drug without the presence of blue or red shifts, but with accelerated intensities, confirming the absence of any possible interaction of drug (lornoxicam) with polymers. However, the drug peaks with less intensities confirmed the encapsulation of lornoxicam in nanoemulsion and nanoemulgel formulations.

**3.3.3. pH Determination.** The pH of lornoxicam, eucalyptol, and LRX-EU nanoemulsion and nanoemulgel formulations was found to be within the acceptable range of transdermal application as described in Table 6. The physiological skin pH of 4.9–5.9 clearly demonstrates that any change in this pH range might promote bacterial development, especially *Staphylococcus aureus*. The development of inflammation, irritation, and enzymatic abnormalities is possible [30]. Since the pH values of all formulations were within the defined range scale of physiological skin pH, as a result, it is envisaged that the composition would be skin friendly and cause no irritation when applied topically. Furthermore, it is predicted that the drug will be present in a more unionized form inside the formulation, with a pH comparable to that of the skin, resulting in increased drug absorption via the skin. As a result, the pH of the developed optimized formulations of LRX-EU nanoemulsion and nanoemulgel is suitable for transdermal administration. Compatibility profile with biological tissues and efficacy are other features of the formulation [31].

**3.3.4. Size and Size Distribution Analysis.** The values of both particle size and size distribution of blank as well as lornoxicam, eucalyptol, and LRX-EU nanoemulsions and nanoemulgels are shown in Table 7. Droplet size has a critical role in case of topical or transdermally delivered

TABLE 6: Physicochemical parameters of LRX, EU, and LRX-EU nanoemulsion and nanoemulgel formulations.

Formulations	pH	Viscosities (cps)	Drug content (%)
LRX NE	5.88 ± 0.03	6378 ± 3.6	94.75 ± 1.37
EU NE	5.91 ± 0.06	6280 ± 3.4	92.43 ± 0.56
LRX-EU NE	5.96 ± 0.05	6837 ± 11.7	98.29 ± 1.37
LRX NEG	6.52 ± 0.04	11860 ± 9.9	91.96 ± 2.41
EU NEG	6.36 ± 0.01	10250 ± 10.3	93.16 ± 1.88
LRX-EU NEG	6.71 ± 0.03	12384 ± 11.9	96.63 ± 0.64

TABLE 7: Physicochemical characterization tests of different formulations.

Formulations	Particle size (nm)	PDI	Zeta potential (mV)	Entrapment efficiency (%)
Blank NE	51.64 ± 0.2	0.195 ± 0.3	-3.69 ± 2.78	—
LRX NE	61.28 ± 1.3	0.389 ± 0.2	-3.94 ± 3.66	76.11 ± 1.8
EU NE	63.57 ± 1.04	0.267 ± 0.3	-4.18 ± 3.10	80.23 ± 2.1
LRX-EU NE	62.21 ± 2.11	0.351 ± 0.1	-11.6 ± 2.83	81.65 ± 1.7
Blank NEG	103.76 ± 0.3	0.242 ± 0.01	-7.82 ± 1.93	—
LRX NEG	136.65 ± 1.7	0.430 ± 0.21	-11.85 ± 2.19	75.32 ± 1.8
EU NEG	155.45 ± 1.17	0.361 ± 0.11	-16.9 ± 1.52	79.56 ± 1.9
LRX-EU NEG	143.7 ± 2.18	0.374 ± 0.12	-19.95 ± 4.78	81.67 ± 2.3

formulations. This parameter has a drastic impact on numerous prominent parameters like drug release, permeation, and biodistribution. The particle size of a nanoemulsion determines the drug's absorption and bioavailability. Because small particle size offers a large surface area, drug release into the aqueous media is increased, resulting in increased drug absorption. It has been claimed that integrated drug particles interact with the system's microstructure, lowering particle size, especially if the drug is amphiphilic in nature [32]. The blank nanoemulsion exhibited lowest droplet size ( $51.64 \pm 0.2$  nm) as compared to drug-loaded nanoemulsion formulations. Same trend was exhibited by blank nanoemulgel ( $103.76 \pm 0.3$  nm) formulation when compared to respective drug-loaded nanoemulgel formulations. It has been explored by Razzaq et al. [33] that drug loading can influence the size of droplet in the formulation as revealed in case of drug-loaded nanoemulsion as well as nanoemulgel formulations in comparison to their blank counterparts. Our results are in agreement with the previously published work that reported increased droplet size upon addition of curcumin to the blank formulation [34]. Carbopol 940 addition as gelling agent significantly increased formulation particle size. Our results are in accordance with the findings of other authors who described that polymer incorporation into the nanoemulsion systems resulted in larger droplet size owing to increased formulation viscosity caused by higher degree of cross-linking [35].

**3.3.5. Determination of Polydispersity Index and Zeta Potential.** The values of both PDI and zeta potential of blank, lornoxicam, eucalyptol, and LRX-EU nanoemulsion and nanoemulgel formulations are shown in Table 7. Within

the formulation, PDI provides globule size consistency. If PDI value of any formulation is  $<0.5$ , the formulation possesses homogenous and uniform size globules. Smaller size of globules is an important feature for topical administration of the formulation because it allows the drug to penetrate deeper into the skin. Our results of PDI values of both nanoemulsion as well as nanoemulgel formulations clearly reflect droplet size uniformity within each formulation [36]. The zeta potential values of blank, lornoxicam, eucalyptol, and LRX-EU nanoemulsion and nanoemulgel formulations are shown in Table 7, indicating that the system is stable physically. Electrostatic repulsion between the particles is represented by the zeta potential value. Zeta potential values of formulations larger than  $\pm 30$  mV are deemed stable without aggregation phenomenon [37]. The electrostatic repulsive interactions between oily globules were validated by higher values of zeta potential, avoiding coalescence and the formation of a dispersion with homogenous globule size as well as greater stability was resulted. The free fatty acids provide the oil globules a negative charge, and the  $\text{OH}^-$  adsorption from the water onto the interface of oil-water gives the system an overall net negative charge [38].

**3.3.6. Entrapment Efficiency.** The average entrapment efficiency of lornoxicam, eucalyptol, LRX-EU nanoemulsion and nanoemulgel formulations is presented in Table 7. The amount of drug entrapped within a nanoformulation in contrast to the original drug concentration in the formulation is known as entrapment efficiency. The entrapment efficiency and system's homogeneity are based upon higher drug solubility in conjunction with the specified oily phase and also drug compatibility with other constituents. The insoluble

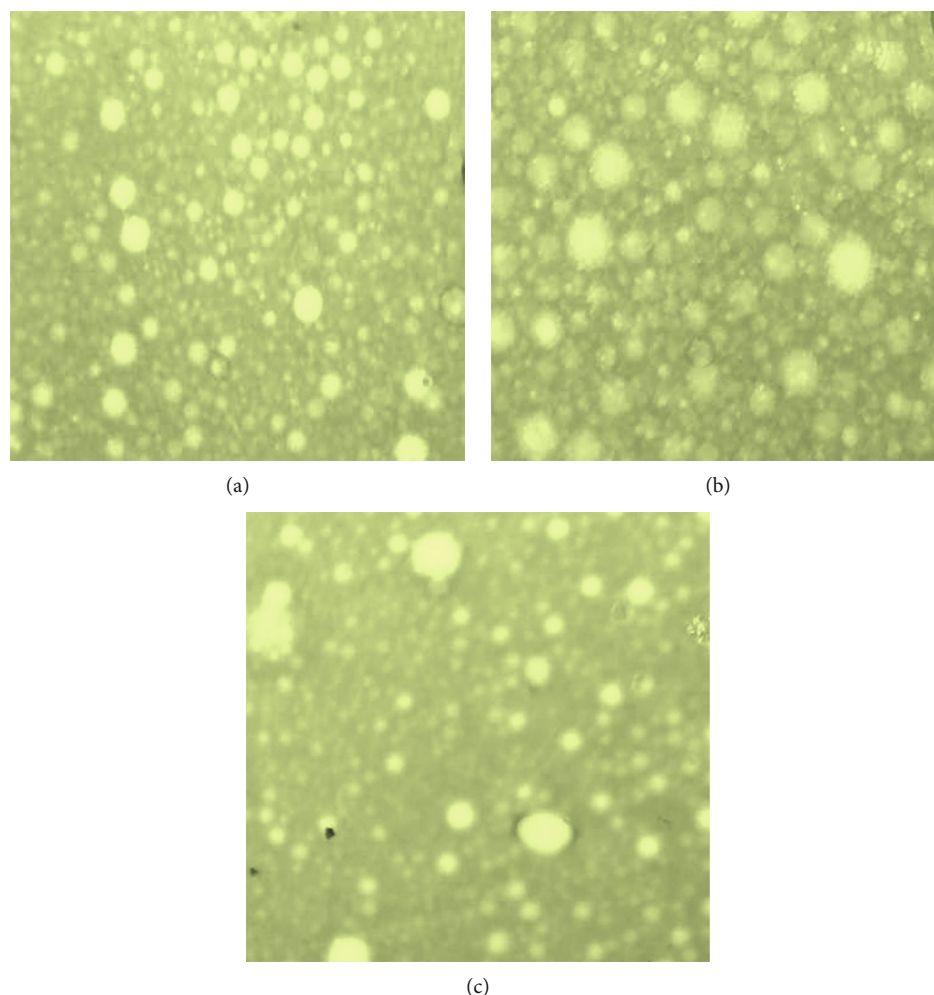


FIGURE 3: Microscopic images of (a) lornoxicam NE, (b) eucalyptol NE, and (c) LRX-EU NE.

nature of drug in water is responsible for its entrapment by oil globules, which can then be stabilized by means of employing surfactant and cosurfactant. The surfactant concentration, which has an inverse connection with encapsulation of drug, is also a highly important element that affects drug encapsulation. This might be because a higher surfactant concentration leads to smaller particle size, resulting in less entrapment of drug within nanoemulsion and nanoemulgel formulations [39]. Furthermore, drug partitioning resulted in increased solubilization of drug from the oily to the aqueous phase, resulting in a reduction in formulation viscosity, which improved the diffusion phenomenon during the process of self-assembly, demonstrating conclusive reason behind lesser entrapment efficiency of drug in the formulation.

**3.3.7. Surface Morphology Analysis.** The microscopic pictures presented in Figure 3 reveal the globules' homogeneity. The globules shape must be taken into account while formulating nanoemulsions since it has an impact on the formulation's performance [40]. A simple light microscope connected with a camera (5 MP) was used to investigate the surface morphology of the formulated nanoemulsion.

**3.3.8. Viscosity Determination.** The gels had viscosities ranging from  $10250 \pm 10.3$  to  $12384 \pm 11.9$  (Table 6). Viscosity signifies prominent role in topical or transdermal delivery of drugs. Literature revealed the direct impact of viscosity upon numerous formulation parameters such as spreadability, application ease, release data, and stability profile [41]. There is also a drastic impact of various gelling agents, emulsifiers, various oils, and cosurfactants present in the formulation upon viscosity. The spreadability of a formulation onto the skin is also determined by its viscosity. This is also necessary for proper skin penetration following its topical application [42]. Similar range of viscosity values has also been established by stable nanoemulgels [15], implying that produced nanoemulsion formulations possess the necessary viscosity for spreadability, stability, and transdermal absorption.

**3.3.9. Spreadability Determination.** Table 8 shows the average spreadability values for lornoxicam, eucalyptol, and LRX-EU nanoemulsion and nanoemulgel formulations. The spreadability of a topical formulation refers to how far it spreads across the skin. The therapeutic effectiveness of topical formulations is based on the spreadability of the

TABLE 8: Average spreadability values of nanoemulsion and nanoemulgel formulations at different temperatures (mean  $\pm$  SD,  $n = 3$ ).

Formulations	Spreadability (8°C)	Spreadability (25°C)	Spreadability (40°C)
LRX NE	15.93 $\pm$ 1.53	19.62 $\pm$ 1.11	24.56 $\pm$ 1.06
EU NE	16.10 $\pm$ 1.32	19.99 $\pm$ 1.17	25.35 $\pm$ 1.23
LRX-EU NE	16.59 $\pm$ 1.71	20.63 $\pm$ 1.12	26.11 $\pm$ 1.72
LRX NEG	11.71 $\pm$ 1.98	13.37 $\pm$ 1.09	14.84 $\pm$ 1.17
EU NEG	12.02 $\pm$ 1.31	13.93 $\pm$ 1.14	15.03 $\pm$ 1.07
LRX-EU NEG	12.46 $\pm$ 1.82	14.37 $\pm$ 1.39	16.09 $\pm$ 1.19

formulation [43]. For a formulation to expel from a container with optimal spreadability, a less amount of shear is necessary. The spreadability coefficient of a topical preparation is affected by a variety of factors, such as high and low temperatures. Generally, the viscosity of formulations increased at reduced temperatures. As a result, spreadability of formulation decreased. On the other hand, the viscosity of topical preparations reduced at high temperatures, resulting in greater spreadability [44]. When a comparison was made between the identical formulations stored at low temperatures, the formulations maintained at high temperatures demonstrated increased spreadability. Furthermore, as compared to nanoemulgel formulations, nanoemulsion formulations exhibited higher spreadability values, which can be attributed to the absence of the gelling agent and depicted statistically significant difference ( $P < 0.05$ ).

**3.3.10. Drug Content Determination.** Lornoxicam, eucalyptol, and LRX-EU nanoemulsion and nanoemulgel formulations with Tween 80 used as surfactant and PEG 400 employed as a cosurfactant produced by means of high shear homogenization process exhibited homogenous drug distribution within the formulations. The optimized nanoemulsion and nanoemulgel formulations of LRX-EU showed drug content values of  $98.29 \pm 1.37\%$  and  $96.63 \pm 0.64\%$ , respectively (Table 6). The findings of drug content experiment confirmed that % drug content was within United States Pharmacopoeia official limit, i.e.,  $100 \pm 10\%$  (M. K. [19]).

**3.3.11. Drug Release Studies.** Abdur Rashid et al. [14] found that nanocarrier systems incorporate the medicinal product in either dissolved or dispersed state. As a result, drug solubility in lipoidal matrix is a critical element in limiting drug release from nanocarriers. To achieve the criteria, in vitro drug release experiments were used to study the medication's release pattern. A UV-spectrophotometer with a wavelength of 376 nm and 556 nm was utilized for this purpose to estimate drug release as well as drug contents of lornoxicam and eucalyptol, respectively. To analyze in vitro drug release profiles of different formulations, the Franz diffusion cell was employed. To simulate physiological state of the skin, in vitro drug release profiles were evaluated. This experiment made use of a receptor medium with phosphate buffer solution (pH 5.5) at  $32 \pm 0.5^\circ\text{C}$ . LRX nanoemulsion, EU nanoemulsion, and LRX-EU nanoemulsion were studied in comparison, and the findings are presented in Figure 4. Sim-

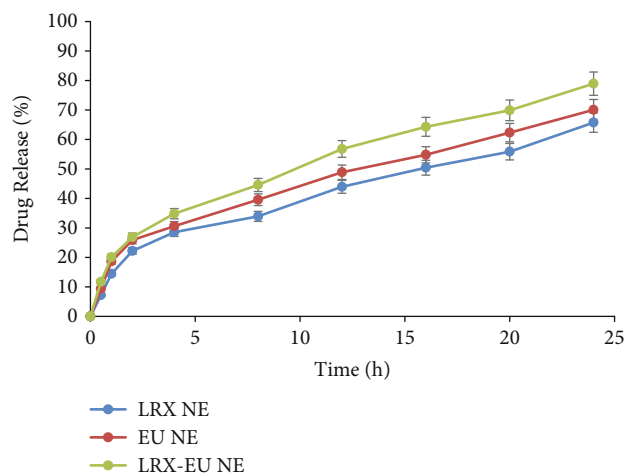


FIGURE 4: Percentage of drug release from optimized formulations LRX NE, EU NE, and LRX-EU NE. The data is presented as mean  $\pm$  SD and analyzed using one-way ANOVA.  $P < 0.03$  refers to LRX-EU NE which is statistically significant from LRX NE and EU NE.

ilarly, lornoxicam nanoemulgel and eucalyptol, nanoemulgel, and LRX-EU nanoemulgel were studied in comparison, and the findings are displayed in Figure 5. All nanoemulsion formulations had a quick initial drug release phase in the first 2 hours, followed by a 22-hour period of delayed release. Surface drug entrapment might be the cause of the initial burst release phenomenon from nanoemulsion formulations. This is aided by cooling caused by the shift from high to room temperature during the formation of nanoemulsion [12]. In nanodermatology, the proven sustained and prolonged drug release behavior is of tremendous interest. This type of drug release pattern may be assumed as the cornerstone of intended topical application. At pH 5.5, around 78.93% of the drug in LRX-EU nanoemulsion is released after 24 hours. In the order of LRX-EU nanoemulsion  $>$  EU nanoemulsion  $>$  LRX nanoemulsion, the drug release profiles improved producing statistically significant difference between the drug release of LRX-EU nanoemulsion versus LRX nanoemulsion ( $P < 0.05$ ). Similarly in case of nanoemulgels, the drug release pattern enhanced in the order of EU nanoemulgel  $>$  LRX nanoemulgel  $>$  LRX-EU nanoemulgel. There was statistically significant difference found between the drug release of LRX-EU nanoemulgel and LRX nanoemulgel formulations ( $P < 0.05$ ). Interactions between drug and surfactant molecules, as well as drug



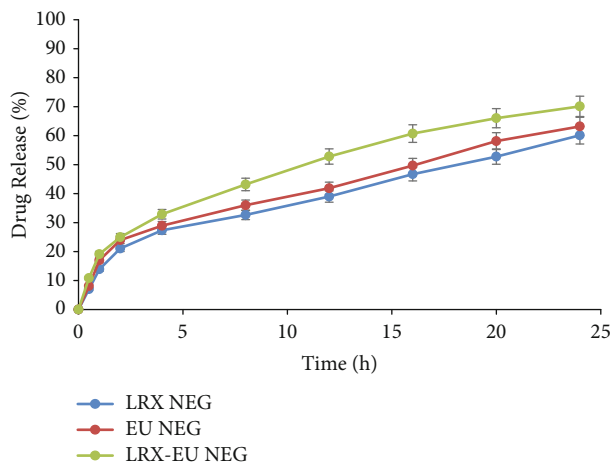


FIGURE 5: Percentage of drug release from optimized formulations LRX NEG, EU NEG, and LRX-EU NEG. The data is presented as mean  $\pm$  SD and analyzed using one-way ANOVA.  $P < 0.01$  refers to LRX-EU NEG which is statistically significant from LRX NEG and EU NEG.

partitioning between the oil and aqueous phases, are all regulating variables for drug release. The smaller globule size and larger surface area help to regulate optimal drug release from nanoemulsions. The nanosize of the formulation increases the rate of lornoxicam solubility into the aqueous phase. Dissolution rate and drug release are also improved. The release is done in a regulated manner. Slower drug release is advantageous in chronic painful and inflammatory disorders, but quick or burst release is not. Burst release is also responsible to cause toxicity since the medicine is released and is absorbed more quickly in inflamed regions [45]. In order to achieve gradual release of the active moiety as well as better drug retention parameters, the optimized nanoemulsion formulation was transformed into gel form. According to kinetic data analysis, the release mechanism and best fit  $R^2$  value for all nanoemulsion and nanoemulgel formulations are presented in Table 9.

**3.4. Ex Vivo Permeation Experiment.** The ultimate goal of this study was to investigate the potential of codelivery of lornoxicam and eucalyptol for enhanced bioavailability to attain optimum therapeutic efficacy for the management of painful inflammatory disorders. The Franz diffusion cell was used in this study to assess codelivery of lornoxicam and eucalyptol to evaluate their *in vitro* skin penetration capability. The skin of a rabbit was chosen as the model barrier. When nanoemulsion formulations of lornoxicam, eucalyptol, and coloaded formulation as well as their respective nanoemulgel formulations were compared, and the findings demonstrated a statistically significant difference ( $P < 0.05$ ). Table 10 summarizes the permeation experiment parameters, such as cumulative lornoxicam and eucalyptol penetrated after 24 hours, permeation flux, and enhancement ratio. It is easy to deduce from this that nanoemulsion formulations and nanoemulgel formulations of lornoxicam, eucalyptol, and combination of both play an important role in drug release and drug targeting to

the skin. Diffusion of epidermal drugs and aligned carriers is strongly reliant on interactions between formulation and components of this layer, which include enzymes, transporters, and a plethora of membrane components [46]. The diffusion rate is also controlled by the formulation's physicochemical properties. Hydrogen bonding, surface charge, drug loading ability, and drug application manner are among them [47]. The choice of surfactant is a critical component that influences drug flux rate. Surfactants with longer carbon chains allow for more medication penetration into the skin [48]. Surfactants interact with intercellular keratin to aid in the solubilization of lipophilic substances inside the stratum corneum. Due to stratum corneum fluidization, channels are formed, allowing for higher drug permeability [12]. In the formulations, Tween 80 is used as a surfactant. Lipid packing fluidization occurs as a result of Tween 80 incorporation. The skin lipid extraction process also raised the water content of the stratum corneum. The solvent polyethylene glycol has an effect on the drug penetration from nanoemulsion and nanoemulgel formulations. These cumulative effects cause the epidermis' barrier functions to be reduced, resulting in increased transdermal drug transfer. LRX-EU nanoemulsion > EU nanoemulsion > LRX nanoemulsion was the sequence of skin permeation parameters (Figure 6). Similarly, ex vivo permeation parameters also increased in the order of LRX-EU nanoemulgel > EU nanoemulgel > LRX nanoemulgel (Figure 7). Due to their capacity to squeeze themselves through the skin's comparatively smaller pores, nanoemulsion and nanoemulgel formulations of LRX-EU have superior skin penetration characteristics. When compared to LRX-EU nanoemulsion and LRX-EU nanoemulgel, however, LRX and EU nanoemulsion formulations and nanoemulgel formulations have a lesser penetration capacity. This might be due to inherent less permeation capability of lornoxicam [7]. After 24 hours, an average of 73.19% of lornoxicam was permeated from the LRX-EU nanoemulsion with an average flux of  $203.13 \pm 6.75 \mu\text{g}/\text{cm}^2/\text{h}$ , according to the permeation data. After 24 hours, the average quantity of drug penetrated from lornoxicam nanoemulsion was 56.16%, and the flux was  $44.36 \pm 2.95 \mu\text{g}/\text{cm}^2/\text{h}$ . The average quantity of drug penetrated and flux of LRX-EU nanoemulgel and lornoxicam nanoemulgel were determined to be 67.19%,  $189.63 \pm 7.68 \mu\text{g}/\text{cm}^2/\text{h}$  and 50.69%,  $41.25 \pm 3.13 \mu\text{g}/\text{cm}^2/\text{h}$ , respectively. The permeability of topical formulations is increased by systems based on nanoemulsion. The responsible mechanisms include adsorption onto the stratum corneum, vesicle fusion, oil or surfactant penetration across the skin, and targeted site [49]. Surfactant and oil-based nanoemulsions may readily permeate the stratum corneum's pores. Fusion or adsorption onto the stratum corneum occurs, followed by penetration across unbroken skin. The formulation's viscosity allows for homogeneous deposition on the skin and inhibits flocculation due to gravitational separation. Small droplet size improves penetration by increasing the overall surface area that is directly involved in the drug release, drug transfer, drug absorption, and droplets interaction on a given region of the stratum corneum. The introduction of nanoemulsion into the polar

TABLE 9: Kinetic profiling of drug release data from optimized nanoemulsion and nanoemulgel formulations.

Formulations	$K \pm SD$	$R^2$	Power law kinetic model	
			$n$	Release mechanism
LRX NE	$0.291 \pm 0.143$	0.8087	0.436	Fickian diffusion
EU NE	$0.011 \pm 0.0019$	0.9186	0.402	Fickian diffusion
LRX-EU NE	$0.045 \pm 0.021$	0.9765	0.553	Anomalous non-Fickian diffusion
LRX NEG	$0.186 \pm 0.002$	0.9615	0.513	Anomalous non-Fickian diffusion
EU NEG	$0.023 \pm 0.004$	0.9137	0.537	Anomalous non-Fickian diffusion
LRX-EU NEG	$0.051 \pm 0.131$	0.9867	0.568	Anomalous non-Fickian diffusion

TABLE 10: Permeation parameters of optimized nanoemulsion and nanoemulgel formulations (mean  $\pm$  SD,  $n = 3$ ).

Formulation codes	Permeation flux ( $\mu\text{g}/\text{cm}^2/\text{h}$ )	Permeability coefficient ( $\text{cm}/\text{h}$ ) $\times 10^{-2}$	Enhancement ratio
LRX NE	$44.36 \pm 2.95$	$0.34 \pm 0.014$	1
LRX-EU NE	$203.13 \pm 6.75$	$2.21 \pm 0.132$	4.579
LRX NEG	$41.25 \pm 3.13$	$0.31 \pm 0.018$	0.929
LRX-EU NEG	$189.63 \pm 7.68$	$2.09 \pm 0.067$	4.274

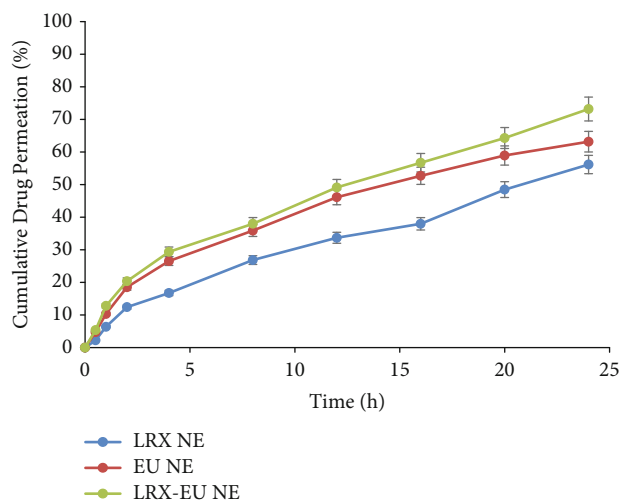


FIGURE 6: Percentage of drug permeated from optimized formulations LRX NE, EU NE, and LRX-EU NE. The data is presented as mean  $\pm$  SD and analyzed using one-way ANOVA.  $P < 0.05$  refers to LRX-EU NE which is statistically significant from LRX NE and EU NE.

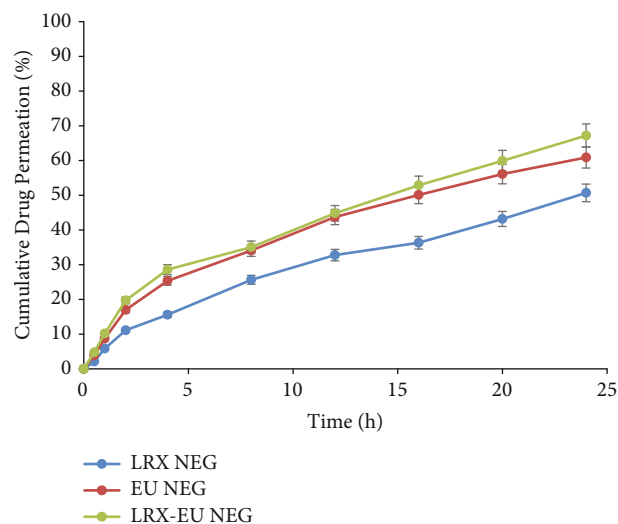


FIGURE 7: Percentage of drug permeated from optimized formulations LRX NEG, EU NEG, and LRX-EU NEG. The data is presented as mean  $\pm$  SD and analyzed using one-way ANOVA.  $P < 0.05$  refers to LRX-EU NEG which is statistically significant from LRX NEG and EU NEG.

route is predicted to increase the interlamellar volume of the stratum corneum’s lipid bilayers. This causes the interfacial structure to break down, increasing drug penetration.

**3.5. Stability Determination.** For three months, the developed formulation was monitored for changes in drug content, droplet size, pH, PDI, and surface charge under the storage conditions described in Table 11. Stability experiments were performed to assess the stability of the formulations over time under different environmental variables such as temperature, light, and humidity. As a result, determining the proper storage conditions for LRX-EU nanoemulgel is

an indirect method. There is no turbidity or phase separation after 3 months of storage at the stated conditions, indicating that the formulation is physically stable. The stored LRX-EU nanoemulgel and freshly manufactured formulations had similar surface charge and pH. Despite a nominal increase in globule size at accelerated and ambient conditions after 3 months, the globule size at selected specified conditions has not changed much, because globule kinetic energy is increased, resulting in collision and globule aggregation [45]. However, the globule size of the formulation

TABLE 11: Storage stability of LRX-EU NEG at various temperatures for 3 months.

Parameters	4°C	25°C	45°C
Zeta potential (mV)	-15.17 ± 3.87	-19.59 ± 3.93	-19.91 ± 4.41
Particle size (nm)	139.18 ± 3.54	145.88 ± 2.81	154.13 ± 4.76
PDI	0.253 ± 0.12	0.370 ± 0.04	0.461 ± 0.24
pH	6.01 ± 0.87	6.13 ± 0.04	5.97 ± 0.72
Drug content (%)	93.81 ± 2.13	93.92 ± 2.88	96.11 ± 1.83
Clarity	Clear	Clear	Clear
Color change	No change	No change	No change
Phase separation	Nil	Nil	Nil

and freshly developed LRX-EU NEG is almost identical (143.7 ± 2.18 nm), with a PDI of less than 0.3 at refrigerated temperatures over a three-month period, indicating overall formulation stability in line with the method utilized for its production. Because changes in particle size and other characteristics of the produced formulation and freshly synthesized formulation are fewer, these stability test findings represent the storage of LRX-EU NE and NEG at chilled settings [50].

#### 4. Conclusion

From the findings of this study, it can be concluded that the optimized LRX-EU nanoemulgel presented droplet size in nanorange with size uniformity. The formulation was found thermodynamically as well as physically stable. The *in vitro* drug release and drug permeation were found optimum. The optimized LRX-EU nanoemulgel exhibited controlled *in vitro* release behavior which may lead to enhanced bio-availability of lornoxicam as compared to single-loaded lornoxicam nanoemulgel. The use of eucalyptol and PEG as penetration enhancers was responsible for improved drug flux value through the skin. LRX-EU nanoemulgel can be best substituted to the oral administration of lornoxicam because of producing enhanced therapeutic effect with optimum patient compliance and reduced GIT side effects as well as frequency of drug administration for better pain management.

#### Data Availability

Data can be available on demand or request from the CA.

#### Conflicts of Interest

The authors declare that they have no conflicts of interest.

#### Acknowledgments

The authors are grateful to the Deanship of Scientific Research at King Khalid University for funding this study through large group project under grant number RGP2/3/43.

#### References

- [1] S. Bindu, S. Mazumder, and U. Bandyopadhyay, "Non-steroidal anti-inflammatory drugs (NSAIDs) and organ damage: a current perspective," *Biochemical Pharmacology*, vol. 180, p. 114147, 2020.
- [2] H. Al-Lawati, Z. Binkhathlan, and A. Lavasanifar, "Nanomedicine for the effective and safe delivery of non-steroidal anti-inflammatory drugs: a review of preclinical research," *European Journal of Pharmaceutics and Biopharmaceutics*, vol. 142, pp. 179–194, 2019.
- [3] L. Kumar, S. Verma, M. Singh, T. Chalotra, and P. Utreja, "Advanced drug delivery systems for transdermal delivery of non-steroidal anti-inflammatory drugs: a review," *Current Drug Delivery*, vol. 15, no. 8, pp. 1087–1099, 2018.
- [4] B. H. J. Gowda, M. G. Ahmed, A. Sahebkar, Y. Riadi, R. Shukla, and P. Kesharwani, "Stimuli-responsive microneedles as a transdermal drug delivery system: a demand-supply strategy," *Biomacromolecules*, vol. 23, no. 4, pp. 1519–1544, 2022.
- [5] R. U. Khan, S. U. Shah, S. A. Rashid et al., "Lornoxicam-loaded chitosan-decorated nanoemulsion: preparation and *in vitro* evaluation for enhanced transdermal delivery," *Polymers*, vol. 14, no. 9, p. 1922, 2022.
- [6] F. Islam, A. Khan, K. Vaibhav et al., "1,8-Cineole (eucalyptol) mitigates inflammation in amyloid beta toxicated PC12 cells: relevance to Alzheimer's disease," *Neurochemical Research*, vol. 39, no. 2, pp. 344–352, 2014.
- [7] D. Hashmat, M. H. Shoaib, F. R. Ali, and F. Siddiqui, "Lornoxicam controlled release transdermal gel patch: design, characterization and optimization using co-solvents as penetration enhancers," *PLoS One*, vol. 15, no. 2, p. e0228908, 2020.
- [8] S. Mahaparale and V. Gaware, "Formulation and evaluation of lornoxicam emulgel," *International Journal of Pharmaceutical Chemistry and Analysis*, vol. 4, no. 3, pp. 83–87, 2017.
- [9] R. Pereira, S. G. Silva, M. Pinheiro, S. Reis, and M. Luísa Do Vale, "Current status of amino acid-based permeation enhancers in transdermal drug delivery," *Membranes*, vol. 11, no. 5, p. 343, 2021.
- [10] P. K. Mohapatra, V. Tomer, and M. K. Gupta, "Design and Development of Losartan Potassium Floating Drug Delivery Systems," *International Journal of Applied Pharmaceutics*, vol. 10, no. 6, 2018.
- [11] L. H. Emara, A. R. Abdou, A. A. El-Ashmawy, and N. M. Mursi, "Preparation and evaluation of metronidazole sustained release floating tablets," *International Journal of Pharmacy and Pharmaceutical Sciences*, vol. 6, pp. 198–204, 2014.

- [12] S. A. Rashid, S. Bashir, H. Ullah et al., "Development, characterization and optimization of methotrexate-olive oil nanoemulsion for topical application," *Pakistan Journal of Pharmaceutical Sciences*, vol. 34, 1(Supplementary), pp. 205–215, 2021.
- [13] S. Singh, H. Vardhan, N. G. Kotla, B. Maddiboyina, D. Sharma, and T. J. Webster, "The role of surfactants in the formulation of elastic liposomal gels containing a synthetic opioid analgesic," *International Journal of Nanomedicine*, vol. 11, pp. 1475–1482, 2016.
- [14] S. Abdur Rashid, S. Bashir, F. Naseem et al., "Olive oil based methotrexate loaded topical nanoemulsion gel for the treatment of imiquimod induced psoriasis-like skin inflammation in an animal model," *Biology*, vol. 10, no. 11, p. 1121, 2021.
- [15] S. Dasgupta, S. Ghosh, S. Ray, S. Kaurav, and B. Mazumder, "In vitro & in vivo studies on lornoxicam loaded nanoemulsion gels for topical application," *Current Drug Delivery*, vol. 11, no. 1, pp. 132–138, 2014.
- [16] F. U. Din, W. Aman, I. Ullah et al., "Effective use of nanocarriers as drug delivery systems for the treatment of selected tumors," *International Journal of Nanomedicine*, vol. 12, pp. 7291–7309, 2017.
- [17] J. R. Madan, N. P. Ghuge, and K. Dua, "Formulation and evaluation of proniosomes containing lornoxicam," *Drug Delivery and Translational Research*, vol. 6, no. 5, pp. 511–518, 2016.
- [18] B. M. Altaani, A. M. Almaaytah, S. Dadou, K. Alkhamis, M. H. Daradka, and W. Hananeh, "Oral delivery of teriparatide using a nanoemulsion system: design, in vitro and in vivo evaluation," *Pharmaceutical Research*, vol. 37, no. 4, pp. 1–15, 2020.
- [19] M. K. Khan, B. A. Khan, B. Uzair et al., "Development of chitosan-based nanoemulsion gel containing microbial secondary metabolite with effective antifungal activity: in vitro and in vivo characterizations," *International Journal of Nanomedicine*, vol. 16, pp. 8203–8219, 2021.
- [20] A. Nawaz and T. W. Wong, "Microwave as skin permeation enhancer for transdermal drug delivery of chitosan-5-fluorouracil nanoparticles," *Carbohydrate Polymers*, vol. 157, pp. 906–919, 2017.
- [21] G. Ioele, L. Tavano, M. De Luca, G. Ragno, N. Picci, and R. Muzzalupo, "Photostability and ex-vivo permeation studies on diclofenac in topical niosomal formulations," *International Journal of Pharmaceutics*, vol. 494, no. 1, pp. 490–497, 2015.
- [22] M. N. Yukuyama, E. T. M. Kato, G. L. B. de Araujo et al., "Olive oil nanoemulsion preparation using high-pressure homogenization and d-phase emulsification - a design space approach," *Journal of Drug Delivery Science and Technology*, vol. 49, pp. 622–631, 2019.
- [23] A. Nawaz, S. U. Jan, N. R. Khan, A. Hussain, and G. M. Khan, "Formulation and in vitro evaluation of clotrimazole gel containing almond oil and Tween 80 as penetration enhancer for topical application," *Pakistan Journal of Pharmaceutical Sciences*, vol. 269, no. 3, pp. 617–622, 2013.
- [24] P. Tripura Sundari and P. Mounika India, "Formulation and evaluation of SMEDDS containing ebuxostat by employing coconut oil and labrasol as oil and surfactant system," *World Journal of Pharmaceutical Research*, vol. 7, no. 11, pp. 530–542, 2018.
- [25] C. Prieto and L. Calvo, "Performance of the biocompatible surfactant tween 80, for the formation of microemulsions suitable for new pharmaceutical processing," *Journal of Applied Chemistry*, vol. 2013, Article ID 930356, 10 pages, 2013.
- [26] A. Qadir, M. D. Faiyazuddin, M. D. Talib Hussain, T. M. Alshammari, and F. Shakeel, "Critical steps and energetics involved in a successful development of a stable nanoemulsion," *Journal of Molecular Liquids*, vol. 214, pp. 7–18, 2016.
- [27] N. Kaur, M. Kaur, M. Mahajan, and S. K. Jain, "Development, characterization and evaluation of nanocarrier based formulations of antipsoriatic drug "acitretin" for skin targeting," *Journal of Drug Delivery Science and Technology*, vol. 60, p. 102010, 2020.
- [28] J. Joseph, B. N. Vedha Hari, and D. Ramya Devi, "Experimental optimization of Lornoxicam liposomes for sustained topical delivery," *European Journal of Pharmaceutical Sciences*, vol. 112, pp. 38–51, 2018.
- [29] J. Olayinka Akolade, A. Mohammed Balogun, A. Swanepoel, R. Bolaji Ibrahim, A. Ahmed Yusuf, and P. Labuschagne, "Microencapsulation of eucalyptol in polyethylene glycol and polycaprolactone using particles from gas-saturated solutions," *RSC Advances*, vol. 9, no. 58, pp. 34039–34049, 2019.
- [30] H. Baurecht, M. C. Rühlemann, E. Rodríguez et al., "Epidermal lipid composition, barrier integrity, and eczematous inflammation are associated with skin microbiome configuration," *Journal of Allergy and Clinical Immunology*, vol. 141, no. 5, pp. 1668–1676.e16, 2018.
- [31] J. Lopes-de-Araújo, C. Pereira-Leite, I. M. Cuccovia, S. Reis, and C. Nunes, "Nanodelivery systems for NSAIDs: challenges and breakthroughs," in *Nanoparticles in Life Sciences and Biomedicine*, Jenny Stanford Publishing, 2018.
- [32] P. Pandey, N. Gulati, M. Makhija, D. Purohit, and H. Dureja, "Nanoemulsion: a novel drug delivery approach for enhancement of bioavailability," *Recent Patents on Nanotechnology*, vol. 14, no. 4, pp. 276–293, 2020.
- [33] F. A. Razzaq, M. Asif, S. Asghar et al., "Glimepiride-loaded nanoemulgel; development, in vitro characterization, ex vivo permeation and in vivo antidiabetic evaluation," *Cell*, vol. 10, no. 9, p. 2404, 2021.
- [34] T. P. Sari, B. Mann, R. Kumar et al., "Preparation and characterization of nanoemulsion encapsulating curcumin," *Food Hydrocolloids*, vol. 43, pp. 540–546, 2015.
- [35] R. Aziz, N. A. Elmarzugi, A. M. Eid, and H. A. El-Enshasy, "Preparation, characterization and anti-inflammatory activity of Swietenia macrophylla nanoemulgel," *Journal of Nanomedicine and Nanotechnology*, vol. 5, no. 2, pp. 1–10, 2014.
- [36] J. Ahmad, A. Gautam, S. Komath, M. Bano, A. Garg, and K. Jain, "Topical nano-emulgel for skin disorders: formulation approach and characterization," *Recent Patents on Anti-Infective Drug Discovery*, vol. 14, no. 1, pp. 36–48, 2018.
- [37] M. Sabitha, N. Sanoj Rejinold, A. Nair, V. K. Lakshmanan, S. V. Nair, and R. Jayakumar, "Development and evaluation of 5-fluorouracil loaded chitin nanogels for treatment of skin cancer," *Carbohydrate Polymers*, vol. 91, no. 1, pp. 48–57, 2013.
- [38] P. Rajitha, P. Shammika, S. Aiswarya, A. Gopikrishnan, R. Jayakumar, and M. Sabitha, "Chaulmoogra oil based methotrexate loaded topical nanoemulsion for the treatment of psoriasis," *Journal of Drug Delivery Science and Technology*, vol. 49, pp. 463–476, 2019.
- [39] S. Mokhtari, S. M. Jafari, and E. Assadpour, "Development of a nutraceutical nano-delivery system through emulsification/internal gelation of alginate," *Food Chemistry*, vol. 229, pp. 286–295, 2017.
- [40] H. Pool, S. Mendoza, H. Xiao, and D. J. McClements, "Encapsulation and release of hydrophobic bioactive components in nanoemulsion-based delivery systems: impact of physical form

- on quercetin bioaccessibility,” *Food & Function*, vol. 4, no. 1, pp. 162–174, 2012.
- [41] S. Kumar, M. Prasad, and R. Rao, “Topical delivery of clobetasol propionate loaded nanosponge hydrogel for effective treatment of psoriasis: formulation, physicochemical characterization, antipsoriatic potential and biochemical estimation,” *Materials Science and Engineering: C*, vol. 119, p. 111605, 2021.
- [42] D. Kumbhar, P. Wavikar, and P. Vavia, “Niosomal gel of lornoxicam for topical delivery: in vitro assessment and pharmacodynamic activity,” *AAPS PharmSciTech*, vol. 14, no. 3, pp. 1072–1082, 2013.
- [43] I. K. Burki, M. K. Khan, B. A. Khan, B. Uzair, V. A. Braga, and Q. A. Jamil, “Formulation development, characterization, and evaluation of a novel dexibuprofen-capsaicin skin emulgel with improved in vivo anti-inflammatory and analgesic effects,” *AAPS PharmSciTech*, vol. 21, no. 6, p. 211, 2020.
- [44] K. M. Hosny, H. M. Aldawsari, R. H. Bahmdan et al., “Preparation, optimization, and evaluation of hyaluronic acid-based hydrogel loaded with miconazole self-nanoemulsion for the treatment of oral thrush,” *AAPS PharmSciTech*, vol. 20, no. 7, p. 297, 2019.
- [45] G. Divya, R. Panonnummal, S. Gupta, R. Jayakumar, and M. Sabitha, “Acitretin and aloe-emodin loaded chitin nanogel for the treatment of psoriasis,” *European Journal of Pharmaceutics and Biopharmaceutics*, vol. 107, pp. 97–109, 2016.
- [46] M. Gupta, U. Agrawal, and S. P. Vyas, “Nanocarrier-based topical drug delivery for the treatment of skin diseases,” *Expert Opinion on Drug Delivery*, vol. 9, no. 7, pp. 783–804, 2012.
- [47] M. F. Pinto, C. C. Moura, C. Nunes, M. A. Segundo, S. A. Costa Lima, and S. Reis, “A new topical formulation for psoriasis: development of methotrexate-loaded nanostructured lipid carriers,” *International Journal of Pharmaceutics*, vol. 477, no. 1–2, pp. 519–526, 2014.
- [48] S. Mangalathillam, N. S. Rejinold, A. Nair, V. K. Lakshmanan, S. V. Nair, and R. Jayakumar, “Curcumin loaded chitin nanogels for skin cancer treatment via the transdermal route,” *Nanoscale*, vol. 4, no. 1, pp. 239–250, 2012.
- [49] V. Piazzini, E. Monteforte, C. Luceri, E. Bigagli, A. R. Bilia, and M. C. Bergonzi, “Nanoemulsion for improving solubility and permeability of Vitex agnus-castus extract: formulation and in vitro evaluation using PAMPA and Caco-2 approaches,” *Drug Delivery*, vol. 24, no. 1, pp. 380–390, 2017.
- [50] C. L. Ngan, M. Basri, M. Tripathy, R. A. Karjiban, and E. Abdul-malek, “Physicochemical characterization and thermodynamic studies of nanoemulsion-based transdermal delivery system for fullerene,” vol. 2014, Article ID 219035, 12 pages, 2014.

## *Retraction*

# **Retracted: Serum Markers CA125, CA153, and CEA along with Inflammatory Cytokines in the Early Detection of Lung Cancer in High-Risk Populations**

### **BioMed Research International**

Received 8 January 2024; Accepted 8 January 2024; Published 9 January 2024

Copyright © 2024 BioMed Research International. This is an open access article distributed under the Creative Commons Attribution License, which permits unrestricted use, distribution, and reproduction in any medium, provided the original work is properly cited.

This article has been retracted by Hindawi following an investigation undertaken by the publisher [1]. This investigation has uncovered evidence of one or more of the following indicators of systematic manipulation of the publication process:

- (1) Discrepancies in scope
- (2) Discrepancies in the description of the research reported
- (3) Discrepancies between the availability of data and the research described
- (4) Inappropriate citations
- (5) Incoherent, meaningless and/or irrelevant content included in the article
- (6) Manipulated or compromised peer review

The presence of these indicators undermines our confidence in the integrity of the article's content and we cannot, therefore, vouch for its reliability. Please note that this notice is intended solely to alert readers that the content of this article is unreliable. We have not investigated whether authors were aware of or involved in the systematic manipulation of the publication process.

Wiley and Hindawi regrets that the usual quality checks did not identify these issues before publication and have since put additional measures in place to safeguard research integrity.

We wish to credit our own Research Integrity and Research Publishing teams and anonymous and named external researchers and research integrity experts for contributing to this investigation.


The corresponding author, as the representative of all authors, has been given the opportunity to register their agreement or disagreement to this retraction. We have kept a record of any response received.

### **References**

- [1] G. Li, H. Zhang, L. Zhang et al., "Serum Markers CA125, CA153, and CEA along with Inflammatory Cytokines in the Early Detection of Lung Cancer in High-Risk Populations," *BioMed Research International*, vol. 2022, Article ID 1394042, 4 pages, 2022.

## Research Article

# Serum Markers CA125, CA153, and CEA along with Inflammatory Cytokines in the Early Detection of Lung Cancer in High-Risk Populations

Guangping Li,<sup>1</sup> Hongxin Zhang,<sup>2</sup> Lei Zhang,<sup>3</sup> Huaqun Liu,<sup>3</sup> Songlin Li,<sup>2</sup> Yanan Wang,<sup>3</sup> and Xiaoyun Deng<sup>1</sup> 

<sup>1</sup>Department of Clinical Laboratory, Tangshan Gongren Hospital, No. 27, Wenhua Road, Lubei District, Tangshan City, Hebei Province, China

<sup>2</sup>Department of Respiration, Tangshan Gongren Hospital, No. 27, Wenhua Road, Lubei District, Tangshan City, Hebei Province, China

<sup>3</sup>Department of Oncology, Tangshan Gongren Hospital, No. 27, Wenhua Road, Lubei District, Tangshan City, Hebei Province, China

Correspondence should be addressed to Xiaoyun Deng; mseifert@une.edu

Received 24 July 2022; Revised 13 August 2022; Accepted 20 August 2022; Published 17 October 2022

Academic Editor: Nauman Rahim Khan

Copyright © 2022 Guangping Li et al. This is an open access article distributed under the Creative Commons Attribution License, which permits unrestricted use, distribution, and reproduction in any medium, provided the original work is properly cited.

Lung cancer mortality and morbidity rates are the first among malignant tumors. It is extremely crucial to pay more attention to the early diagnosis and treatment of lung cancer and to grasp and judge the progress of the patient's condition promptly. In this study, lung cancer patients' early diagnosis with tumor markers and inflammatory variables is examined. The general surgery department of our hospital treated 98 patients with lung cancer and 100 patients with benign pulmonary hyperplasia from January 2017 to February 2018. Additionally, 100 healthy subjects who completed physical examinations during this time period were included. Based on the findings of the pathological examination, 100 patients with benign pulmonary hyperplasia were chosen as the benign group, 100 patients with lung cancer were chosen as the malignant group, and 100 healthy individuals were chosen as the healthy group. The tumor markers carbohydrate antigen 125 (CA125), CA153, and carcinoembryonic antigen (CEA), as well as inflammatory factors such as tumor necrosis factor- (TNF-) and high-sensitivity C-reactive protein, were measured in the venous blood of three groups of patients (hs-CRP). There was no discernible difference in tumor marker levels between the benign and healthy groups ( $P > 0.05$ ). In comparison to the benign and healthy groups, the malignant group had higher serum levels of CA153, CA125, and CEA ( $P < 0.05$ ). Between the benign and healthy groups, there was no discernible difference in the levels of inflammatory factors ( $P > 0.05$ ). TNF- and hs-CRP serum levels were observed to be higher in the malignant group compared to the benign and healthy groups ( $P < 0.05$ ). The combined detection of CA153 + CA125 + CEA + TNF- + hs-CRP showed the highest sensitivity and specificity, which were, respectively, 62.22 percent and 92.00 percent, when compared to single or mixed detection of tumor markers or inflammatory factors solely. Serum levels of inflammatory agents TNF- and hs-CRP may be related to the pathophysiology and other functions of patients with lung cancer, as well as to the development and metastasis of the disease. These markers include CA153, CA125, and CEA. For the early detection of lung cancer and the evaluation of the disease's severity, the detection of tumor markers in combination with inflammatory variables has a significant reference value.

## 1. Introduction

There has been significant progress in the diagnosis and therapy of lung cancer in the last ten years; however, the

mortality rate of lung cancer still ranks first in the world. Lung cancers are allocated into two subtypes of histological classification: nonsmall cell lung cancer and small cell lung cancer (SCLC). As a malignant tumor with high lethality,

the 5-year survival rate of lung cancer is only 4-17.7%. Radical resection with or without chemoradiotherapy is an effective treatment strategy for early-stage patients, including stages I, II, and a portion of stage III [1]. Unfortunately, because the early symptoms of lung cancer are insidious and the detection rate is low, most lung cancer patients are diagnosed at an advanced stage, which increases the difficulty of treatment and the risk of recurrence. Although molecular targeted therapy based on driver genes has gradually become the main force in the therapy of lung cancer, it has not fundamentally improved the high mortality rate of lung cancer, suggesting that the early diagnosis rate is a critical issue in improving the overall survival of lung cancer patients. In addition, there are many treatments for lung cancer, but the evaluation of cancer development and prognosis is limited owing to the tumor heterogeneity. Therefore, real-time monitoring of treating efficacy, quick, and precise recognition of drug resistance-related genes, the discovery of minimal residual disease, and the prognosis prediction are crucial to improve the therapeutic effect. At present, there are no clear measures for clinical diagnosis and treatment for lung cancer. In addition, the early symptoms are unknown, and most patients have missed the best treatment period when the disease is to be detected, resulting in continuous aggravation of the disease and missed treatment period. Tumor markers have the advantages of safety and noninvasiveness and have a certain guiding significance in cancer diagnosis. The early detection rate is low due to the lack of early signs. Most of them are in the middle and late stages when they are clinically diagnosed, and they lose the best chance of surgical treatment.

Therefore, early diagnosis and timely symptomatic treatment are the keys to improving the prognosis. In our study, we randomly choose a total of 98 patients with lung cancer and 100 patients with benign pulmonary hyperplasia from January 2017 to February 2018. We applied SPSS 20.0 to analyze data. We measured the tumor markers carbohydrate antigen 125 (CA125), CA153, and carcinoembryonic antigen (CEA), as well as inflammatory factors such as tumor necrosis factor- $\alpha$  (TNF- $\alpha$ ), and high-sensitivity C-reactive protein and compared results between benign and healthy groups. With the deepening of serum tumor markers in clinical research, carbohydrate antigen 15-3 (CA 15-3), CA 125, and carcinoembryonic antigen (CEA), as markers associated with lung cancer, have significant advantages in the diagnosis of lung cancer.

## 2. Materials and Methods

**2.1. Clinical Sample Collection.** A total of 98 patients with lung cancer and 100 patients with benign pulmonary hyperplasia who were treated at the general surgery department of our hospital from January 2017 to February 2018 were randomly selected, and 100 healthy subjects who received physical examination during this period were included. From the results of the pathological analysis, 98 lung cancer patients were included in the malignant group, 100 patients with benign pulmonary hyperplasia were included in the innocent group, and 100 healthy subjects were selected as the

healthy group. The mean age of patients in the malignant group was  $42.06 \pm 10.21$  years, and that in the benign and healthy groups was  $42.23 \pm 10.41$  and  $42.15 \pm 10.34$  year, respectively. No statistical difference was found in the general data among the three groups of respondents ( $P > 0.05$ ).

Inclusion criteria are (1) the pathological results meet the diagnostic criteria for lung cancer, (2) the first discovery of lung cancer, (3) unilateral lung cancer, and (4) sign the informed consent.

Exclusion criteria are (1) patients with a history of other malignant tumors, (2) pregnant or lactating women; (3) patients with inflammatory or metastatic lung cancer, (4) patients with cardiopulmonary insufficiency, and (5) the mentally ill.

**2.2. Check Metrics.** Fasting blood samples of subjects in the three groups were all collected in the morning, and 3 mL of venous blood was collected and centrifuged for use. (1) Tumor marker indicators: an automatic electrochemiluminescence immunoassay analyzer (Roche, model: RocheE601) was applied to detect serum CA125, CA153, and CEA levels. (2) Inflammatory factor indicators: an automatic immunoluminescence analyzer (Siemens, Germany, model: DPC IMMULTE2000) was applied to detect the level of tumor necrosis factor- $\alpha$  (TNF- $\alpha$ ), and an automatic specific protein analyzer (Spain BIOSTEC company, model: BiosystemsA15) was used to detect the level of hs-CRP.

**2.3. Statistical Methods.** All data were analyzed by SPSS 20.0, and the general information of researchers, tumor markers, and inflammatory factors were expressed as ( $x \pm s$ ) and analyzed by the  $t$  test.  $P < 0.05$  was set to the cut-off threshold for statistical significance.

## 3. Experimental Results

**3.1. Comparison of Tumor Marker Levels among Three Groups.** The levels of tumor markers showed no significant difference between the benign and healthy groups ( $P > 0.05$ ). However, the serum levels of CA153, CA125, and CEA were significantly higher in the malignant group than those in the benign and healthy groups ( $P < 0.05$ ). Table 1 shows the comparison of serum tumor marker levels in three groups of subjects.

**3.2. Comparison of Inflammatory Factors among Three Groups.** Serum levels of inflammatory factors presented no significant difference between the benign and healthy groups as well ( $P > 0.05$ ), but significantly higher levels of TNF- $\alpha$  and hs-CRP were found in the malignant group ( $P < 0.05$ ) (Tables 1 and 2).

**3.3. Single and Combined Detection of Tumor Markers and Inflammatory Factors.** Compared to detection of only tumor markers or inflammatory factors, combined detection of these biomarkers CA153 + CA125 + CEA + TNF- $\alpha$  + hs-CRP has the highest sensitivity and specificity, which were 62.22% and 92.00%, respectively, as shown in Table 3.



TABLE 1: Comparison of serum tumor marker levels in three groups of subjects.

Group	Number of cases	CA153 (U/mL)	CA125 (U/mL)	CEA (U/mL)
Malignant group	95	35.19 ± 17.03	21.51 ± 16.71	9.42 ± 4.29
Benign group	103	8.72 ± 4.02	13.09 ± 8.94	1.33 ± 1.63
Healthy group	106	8.22 ± 3.87	15.63 ± 9.52	1.09 ± 0.92
<i>F</i>		221.02	15.95	118.76
<i>P</i>		<0.001	<0.001	<0.001

TABLE 2: Comparison of serum inflammatory factor levels among three groups of subjects.

Group	Number of cases	TNF-alpha (pg/L)	hs-CRP (mg/L)
Malignant group	95	97.52 ± 16.39	16.85 ± 6.92
Benign group	103	79.25 ± 13.84	2.31 ± 1.09
Healthy group	106	68.33 ± 11.72	2.14 ± 1.18
<i>F</i>		101.97	263.81
<i>P</i>		<0.001	<0.001

TABLE 3: Single and combined detection of tumor markers and inflammatory factors.

Detection method	True positive	False positive	True negative	False negative	Sensitivity (%)	Specificity (%)
CA153 + CA125 + CEA	48	43	91	11	50.37	84.95
TNF – alpha + hs – CRP	39	45	81	15	43.29	82
CA153 + CA125 + CEA + TNF – alpha + hs – CRP	57	32	95	7	66.82	93.51

#### 4. Discussion

Tumor markers are formed by the interaction of the tumor, tumor tissue, and the patient's body. They can be detected by examining the patient's blood, tumor tissue, and tissue fluid and can reflect the tumor growth in the patient's body to a certain extent. It is reported that the process of tumor formation is long and complex. The error of a single tumor marker in detecting lung cancer is high, and the types of tumor diseases that different tumor markers can reflect are also different. Therefore, the combined detection of multiple tumor markers can be used to improve the lung cancer-diagnosis rate. NSE is an enolase isoenzyme produced in malignant tumors of peripheral nervous tissue, neuroectoderm, and central nervous system. NSE has been demonstrated to have a certain guiding significance in the diagnosis of SCLC and has high sensitivity and specificity for the detection of SCLC. CEA is produced in human embryonic tissue and is a nonorgan-specific tumor antigen, which can promote tumor metastasis to a certain extent. When healthy people have lung cancer, tumor cells can secrete a large amount of CEA and transfer it into the human blood circulatory system, resulting in a significant rise in the CEA level in the human body. Therefore, when diagnosing adenocarcinoma, the detection of CEA level has certain clinical guiding significance. CA125 is a glycoprotein complex and cannot enter the human blood circulatory system due to the influence of cell junctions and cell basement membranes in healthy humans. When human tumor cells

are necrotic or lysed, the protease is stimulated and activated, leading to the degradation of keratin, and CYFR A21-1 will enter the human blood circulatory system. CYFR A21-1 belongs to the cytokeratin 19 fragment antigen, which is usually distributed in the monolayer of epithelial cells. When human tumor cells are necrotic or lysed, the protease is stimulated and activated, which leads to the degradation of keratin, and CYFR A21-1 will enter the in the human blood circulatory system. After testing, it can be observed that the IYFRA21-1 level is elevated. SCCA, as a serine protease inhibitor, is a typical squamous cell carcinoma-related protein. The protein can be expressed in normal squamous epithelium, pseudostratified columnar epithelium, and malignant tumor tissues derived from multistratified squamous epithelium. The results in Table 2 showed that the positive detection rates of serum tumor markers in patients with different types of lung cancer in the observation group were different, but the combined detection of five indicators has higher sensitivity and specificity than each single indicator ( $P < 0.05$ ). It is further affirmed that the combined detection of multiple tumor markers in serum has a higher diagnostic accuracy.

#### 5. Conclusion

To sum up, the protein has certain clinical diagnostic significance for various types of squamous cell carcinoma. According to the results of this paper, the serum levels of several tumor markers were noticeably higher in the malignant group than those in the benign and healthy groups

## Retraction

# Retracted: HPV-16 Expression and Loss of Cell Differentiation in Primary Bladder Tumors

### BioMed Research International

Received 8 January 2024; Accepted 8 January 2024; Published 9 January 2024

Copyright © 2024 BioMed Research International. This is an open access article distributed under the Creative Commons Attribution License, which permits unrestricted use, distribution, and reproduction in any medium, provided the original work is properly cited.

This article has been retracted by Hindawi following an investigation undertaken by the publisher [1]. This investigation has uncovered evidence of one or more of the following indicators of systematic manipulation of the publication process:

- (1) Discrepancies in scope
- (2) Discrepancies in the description of the research reported
- (3) Discrepancies between the availability of data and the research described
- (4) Inappropriate citations
- (5) Incoherent, meaningless and/or irrelevant content included in the article
- (6) Manipulated or compromised peer review

The presence of these indicators undermines our confidence in the integrity of the article's content and we cannot, therefore, vouch for its reliability. Please note that this notice is intended solely to alert readers that the content of this article is unreliable. We have not investigated whether authors were aware of or involved in the systematic manipulation of the publication process.

Wiley and Hindawi regrets that the usual quality checks did not identify these issues before publication and have since put additional measures in place to safeguard research integrity.

We wish to credit our own Research Integrity and Research Publishing teams and anonymous and named external researchers and research integrity experts for contributing to this investigation.

The corresponding author, as the representative of all authors, has been given the opportunity to register their agreement or disagreement to this retraction. We have kept a record of any response received.

### References

- [1] L. Pang, Z. Ding, F. Li, H. Chai, M. Wu, and J. Shao, "HPV-16 Expression and Loss of Cell Differentiation in Primary Bladder Tumors," *BioMed Research International*, vol. 2022, Article ID 6565620, 6 pages, 2022.

## Research Article

# HPV-16 Expression and Loss of Cell Differentiation in Primary Bladder Tumors

Lei Pang<sup>1</sup>,<sup>ORCID</sup> Zijun Ding,<sup>2</sup> Fei Li,<sup>1</sup> Hongqiang Chai,<sup>1</sup> Ming Wu,<sup>1</sup> and Jinkai Shao<sup>1</sup>

<sup>1</sup>Department of Urology, The Fifth Hospital of Shanxi Medical University (Shanxi Provincial People's Hospital), No. 29 Shuangta East Street, Yingze District, Taiyuan, Shanxi 030012, China

<sup>2</sup>Department of Neonatology, Shanxi Children's Hospital, No. 13 North Xinmin Street, Xinghualing District, Taiyuan, Shanxi 030013, China

Correspondence should be addressed to Lei Pang; [panglei\\_3511@sina.com](mailto:panglei_3511@sina.com)

Received 26 August 2022; Accepted 3 October 2022; Published 15 October 2022

Academic Editor: Nauman Rahim Khan

Copyright © 2022 Lei Pang et al. This is an open access article distributed under the Creative Commons Attribution License, which permits unrestricted use, distribution, and reproduction in any medium, provided the original work is properly cited.

**Objective.** Primary bladder tumors have a high degree of malignancy. To investigate the expression of human papillomavirus type 16 (HPV-16) in primary bladder tumors and the loss of cell differentiation and to explore the significance of HPV-16 detection, it is expected to be a disease. Treatment provides a theoretical basis. **Methods.** Fifty-seven patients with primary bladder tumors admitted to our hospital from January 2019 to January 2022 were selected as the research subjects, and they were divided into HPV-related groups according to the human papillomavirus (HPV) infection status ( $n = 28$ ) and HPV unrelated group ( $n = 29$ ). The general data of patients were collected, the expression of HPV-16 in bladder tissue samples was detected, and the correlation between pathological parameters and HPV-16 expression was analyzed. **Results.** Among HPV subtypes, HPV 16 subtype accounted for the highest proportion, followed by HPV-18 and HPV-6 subtypes; there was no significant difference in tumor stage (stage 1, stage a, stage 2a) between the HPV-related group and the HPV-unrelated group (stage 1, stage a, and stage 2a).  $P > 0.05$ ; there was no significant difference in postoperative pathological expression (high expression and low expression) of patients ( $P > 0.05$ ); there was no statistical difference in age and gender between HPV-related and HPV-unrelated groups ( $P > 0.05$ ), HPV-related group and HPV-unrelated group compared daily regular drinking and smoking status, the difference was statistically significant ( $P < 0.05$ ); HPV-16 expression was not correlated with tumor differentiation degree and age of patients ( $P > 0.05$ ); the area under the curve (AUC) of HPV-16 for judging primary bladder tumor expression and cellular molecular deletion was 0.891, with a sensitivity of 83.94% and a specificity of 88.57%. **Conclusion.** HPV-16 is an upper, expressed in primary bladder tumors and will participate in the differentiation and loss of cells, which can provide effective guidance and basis for the diagnosis of primary bladder tumors, which is an important factor for judging the pathological stage and prognosis of patients and can provide a theoretical reference for the formulation of therapeutic measures.

## 1. Introduction

The latest reported data show that bladder tumor is a highly malignant tumor. In China, the incidence of bladder cancer ranks first in malignant tumors of the urinary system, and transitional cell carcinoma (TCC) accounts for about 90% of the pathological types of bladder tumors. However, the understanding of the pathogenesis of primary bladder tumors is low, and exposure to ionizing radiation, aromatic amines, and cyclophosphamide are currently identified as

risk factors [1]. HPV mainly appears after tumor invasion, HPV infection can indirectly or directly cause human tumor formation, and in particular, can have an impact on pathological grade [2]. Before, HPV-16 fragment in bladder tissue was often detected by specific primer Pcr. The results confirmed that there was a notable variation in the positive rate of HPV-16 fragment between normal bladder tissue and bladder tumor tissue. The expression of HPV-16 fragment in bladder tumor tissue was detected by Southern blot. The results showed that HPV-16 expression in bladder tumor

TABLE 1: Analysis of HPV subtypes in patients (situations, %).

Subtype	Number of detections (example)	Infection rate (%)
HPV-6	3	10.71
HPV-16	8	28.57
HPV-18	5	17.86
HPV-26	1	3.57
HPV-39	2	7.14
HPV-45	1	3.57
HPV-51	1	3.57
HPV-53	2	7.14
HPV-56	1	3.57
HPV-59	1	3.57
HPV-66	1	3.57
HPV-68	1	3.57
HPV-82	1	3.57

was notably correlated with the occurrence of primary bladder tumor [3, 4]. At present, it is mainly treated by comprehensive treatment methods such as chemotherapy, immunotherapy, and photodynamic therapy. Benign bladder tumors can be cured after treatment, but malignant tumors are prone to recurrence and metastasis after treatment. For bladder cancer, the presence or absence of invasion is one of the important prognostic factors for bladder cancer. However, the premise of treatment is to analyze the factors affecting the disease literature and the expression of HPV-16 in order to have a better reference for disease treatment.

Based on this, 57 patients with primary bladder tumors admitted to our hospital between January 2019 and January 2022 were opted as the study subjects to preliminarily investigate HPV-16 expression and analyze the relationship with patient prognosis, hoping to provide morphological evidence for disease healing, as reported below.

## 2. Materials and Methods

**2.1. General Data.** Fifty-seven patients with primary bladder tumors admitted to our hospital from January 2019 to January 2022 were opted as the study subjects and divided into two clusters according to human papillomavirus (HPV) infection. HPV-related cluster ( $n = 28$ ); 7 females; 21 males; aged 27-64 years; mean age ( $61.46 \pm 3.58$ ) years; HPV subtypes: HPV-6:3, HPV-16:8, HPV-18:5, HPV-26:1, HPV-39:2, HPV-45:1, HPV-51:1, HPV-53:2, HPV-56:1, HPV-59:1, HPV-66:1, HPV-68:1, and HPV-82:1; tumor stage: 9, stage a: 10, and stage 2a: 9; postoperative pathology: upper expression in 17 and bottom expression in 11. In the HPV-unrelated cluster ( $n = 29$ ), there were 8 females and 21 males, aged 27-64 years, with a mean age of ( $63.10 \pm 3.29$ ) years; tumor stage: 8 situations of stage 1, 10 situations of stage a, and 11 situations of stage 2a; postoperative pathology: 7 situations of upper expression and 21 situations of bottom expression. This study has been approved by the ethics department, and patients are aware of the study.

**Inclusion criteria:** (1) HPV positive; (2) older than 18 years old; (3) cervical biopsy or staining pathology diagnosis [5], diagnosed as primary bladder tumor; (4) did not receive antitumor hormone intervention before the study; (5) good spirit; (6) life cycle more than 12 months.

**Exclusion criteria:** (1) infectious diseases; (2) immune diseases; (3) combined with bladder cancer outside the tumor; (4) bottom compliance; (5) organ damage; (6) lactating or pregnant women.

### 2.2. Methods

**2.2.1. Specimen Source.** The specimens were opted from those who were pathologically diagnosed as primary bladder tumors. After the specimens were obtained, they were placed in EP tubes and then stored in  $-80^{\circ}\text{C}$  refrigerator. Various data were collected from the patients, including age, gender, alcohol consumption, and smoking status.

**2.2.2. DNA Preparation and PCR Detection.** *DNA sample extraction:* centrifuge the cell suspension, extract DNA, and perform various operations according to the kit instructions, then uniformly dilute the DNA concentration to  $100\text{ ng}/\mu\text{L}$  and store in  $-20^{\circ}\text{C}$  equipment.

*Amplification PCR:* PCR amplification is performed using primer nucleotide sequences.

*PCR product electrophoresis:* agarose gel electrophoresis of PCR products,  $10\ \mu\text{L}$  of PCR products were subjected to agarose gel electrophoresis (1.0%) and photographed by Tianneng gel imaging system.

*Judgment result:* if there is a bright band at the 217bp position, and the prejudgment result is loaded at the same time, it is confirmed that the HPV-16 test is a positive result, and the product is analyzed by electrophoresis to verify the sequencing result.

**2.3. Observation Indicators.** *HPV subtype analysis of patients:* including HPV-6, HPV-16, HPV-18, HPV-26, HPV-39, HPV-45, HPV-51, HPV-53, HPV-56, HPV-59, HPV-66, HPV-68, HPV-82 HPV subtypes.

*Tumor staging:* count the number of situations of stage 1, stage a, and stage 2a, and calculate the proportion.

*Postoperative pathological expression:* count the number of situations with upper expression and bottom expression, and calculate the proportion.

*General information:* including age, gender, alcohol consumption (regular daily drinking, occasional/never), and smoking (smoking, quit smoking, never).

*Logistic regression analysis:* the correlation between HPV-16 expression and the degree of tumor differentiation and age of patients.

*The value of HPV-16 in judging the expression of primary bladder tumor and the value of cell and molecular deletion:* calculate the diagnostic sensitivity and specificity of HPV-16.

*Analysis of the prognosis of patients:* count the number of situations of single tumor and multiple tumors, count the number of patients with tumor-free survival, recurrence, and death, and calculate the proportion.

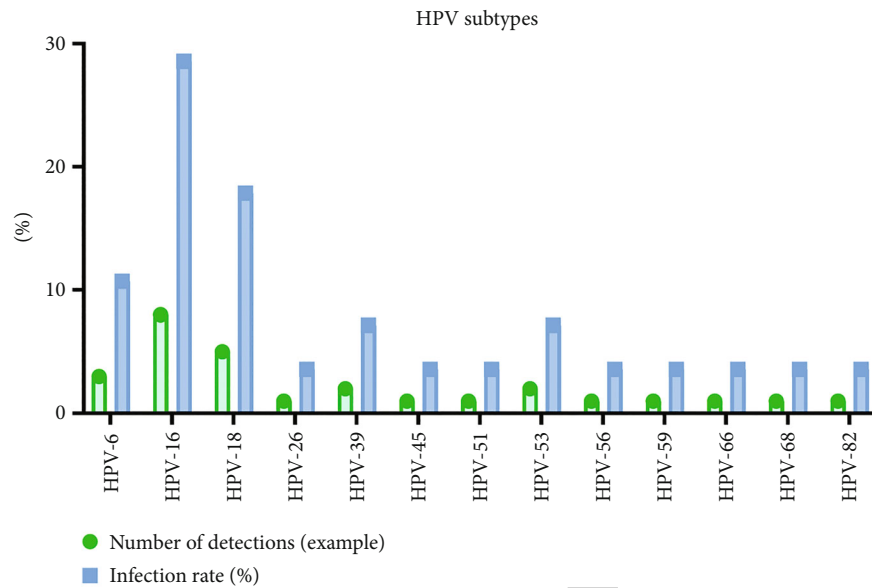


FIGURE 1: Analysis of HPV subtypes in patients. Note: HPV-6, HPV-16, HPV-18, HPV-26, HPV-39, HPV-45, HPV-51, HPV-53, HPV-56, HPV-59, HPV-66, and HPV-68. The proportions of HPV-82 subtypes were 10.71%, 28.57%, 17.86%, 3.57%, 7.14%, 3.57%, 3.57%, 3.57%, 3.57%, 3.57%, and 3.57%, respectively.

TABLE 2: Analysis of tumor stages in two clusters of patients (situations, %).

Tumor stage	HPV-related clusters (n = 28)	HPV-unrelated cluster (n = 29)	X <sup>2</sup>	P
Stage 1	9 (32.14)	8 (27.59)	0.024	0.886
Stage a	10 (35.71)	10 (34.48)		
Stage 2a	9 (32.14)	11 (37.93)		

2.4. *Statistical Methods.* The count data was expressed as *n* (%), and the contrastion between clusters was performed by the  $\chi^2$  test; the measurement data that obeyed the normal distribution was expressed as  $(\bar{x} \pm s)$ , and the contrastion between multiple clusters was performed by one-way variance and repeated measures. The data were contrasted using the analysis of variance of repeated measures data, and  $P < 0.05$  was regarded as a notable variation.

### 3. Results

3.1. *Analysis of HPV Subtypes in Patients.* Among HPV subtypes, HPV-16 subtypes accounted for the uppermost proportion, followed by HPV-18 and HPV-6 subtypes (Table 1 and Figure 1).

3.2. *Tumor Stage Analysis of Two Clusters of Patients.* None notable variation in tumor stage (stage 1, stage a, stage 2a) between the HPV-related cluster and the HPV-unrelated cluster ( $P > 0.05$ ) (Table 2 and Figure 2).

3.3. *Postoperative Pathological Expression Analysis of Two Clusters of Patients.* None notable variation in postoperative pathological expression (upper expression and bottom expression) of patients ( $P > 0.05$ ) (Table 3 and Figure 3).

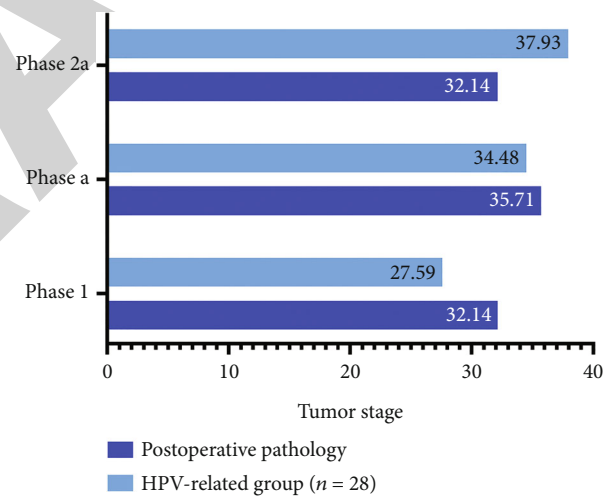


FIGURE 2: Analysis of tumor stage in two clusters of patients (situations, %). Note: the percentage of stage 1, a, and 2a staging in the HPV-related cluster was 32.14%, 35.71%, and 32.14%, respectively, and the percentage of stage 1, a, and 2a staging in the HPV-unrelated cluster was 27.59%, 34.48%, and 37.93%, respectively.

3.4. *General Data Analysis of Patients.* None notable variation in age and gender between the HPV-related cluster and the HPV-unrelated cluster ( $P > 0.05$ ). There was a notable variation between the HPV-related and HPV-unrelated clusters in daily regular drinking and smoking status ( $P < 0.05$ ) (Table 4).

3.5. *Correlation Analysis of HPV-16 Expression with Tumor Differentiation and Age in Patients.* None correlation between the expression of HPV-16 and the degree of tumor differentiation and age of the patients ( $P > 0.05$ ) (Table 5).

TABLE 3: Analysis of postoperative pathological expression in two clusters of patients (situations, %).

Postoperative pathology	HPV-related clusters (n = 28)	HPV unrelated cluster (n = 29)	$\chi^2$	P
Upper expression	17 (60.71)	11 (37.93)	0.889	0.346
Bottom expression	7 (25.00)	21 (72.41)		

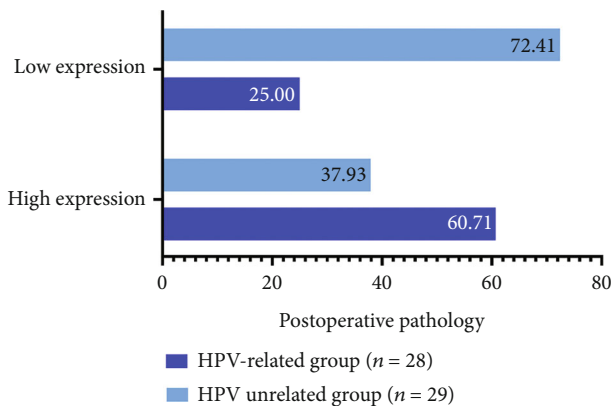


FIGURE 3: Analysis of postoperative pathological expression in two clusters of patients. Note: the postoperative pathological upper and bottom expression rates of the HPV-related cluster were 60.71% and 37.93%, respectively, and the postoperative pathological upper and bottom expression rates of the HPV-unrelated cluster were 37.93% and 72.41%, respectively.

3.6. *The Value of HPV-16 in Judging Primary Bladder Tumor Expression and Cell and Molecular Deletion.* The area under the curve (AUC) of HPV-16 for judging primary bladder tumor expression and cellular molecular deletion was 0.891, with a sensitivity of 83.94% and a specificity of 88.57% (Figure 4).

3.7. *Analysis of Patient Prognosis.* 57 patients, including 11 patients with single tumor and 46 patients with multiple tumors, were followed-up for 3 years. The follow-up found that 37 patients survived tumor-free, 17 patients recurred, and 3 patients died (Figure 5).

#### 4. Discussion

Males aged 40-70 are the main cluster of primary bladder tumors, with invasive growth and papillary growth as the main growth patterns, and the results are in good agreement with the results of most domestic studies [6]. Regarding the correlation between bladder cancer and HPV, the research conclusions are controversial. Shaker et al. showed that the positive rate of high-risk HPV-16/18 in BUCC was significantly higher than that in chronic cystitis and normal bladder tissue, and it was related to the clinical staging of bladder cancer patients. There is a certain correlation. Polesel et al. detected HPV in urine, and the results showed that there was no significant correlation between HPV and bladder

TABLE 4: Analysis of general data of patients.

General information	HPV-related clusters (n = 28)	HPV-unrelated cluster (n = 29)	$\chi^2$	P
Age (years)	61.46 ± 3.58	63.10 ± 3.29	1.802	0.077
Sex (male/female)	21/7	21/8	7.000	0.008
Alcohol consumption			1.636	0.201
Regular daily drinker	20 (71.73)	14 (48.28)		
Occasionally/never	8 (28.57)	15 (51.72)		
Smoke or not			2.643	0.267
Smoke	16 (57.14)	11 (37.93)		
Have quit smoking	7 (25.00)	8 (27.59)		
Never	5 (17.86)	10 (34.48)		

cancer. Schmid et al. conducted a prospective study on samples of Chinese and European populations, and the results showed that HPV infection was associated with the occurrence of bladder cancer. Not related to development. More and more studies have confirmed that patients with genitourinary tumors have a higher rate of HPV infection, especially HPV-16 infection [7, 8]. After the patient is infected, the P16 protein will be activated and overexpressed. It has a strong expression ability in the process of bladder tumor lesions and can judge the status of tumor lesions [9, 10].

Followed by HPV-18 and HPV-6 subtypes, no notable variation in tumor stage and pathological expression between the two clusters of patients, improving the comparability of the data between the two clusters [11, 12]. In addition, the study analyzed the correlation between HPV infection and primary bladder tumor disease, and the results showed that there is no correlation between the expression of HPV-16 and the degree of tumor differentiation and age of patients ( $P > 0.05$ ). The results of this study are consistent with other research results. Sex is not upper, which is related to the pathological composition and case conditions [13, 14]. However, HPV-16 has upper sensitivity and specificity for judging the expression and cell and molecular deletion of primary bladder tumors, and the results suggest that HPV-16 can be used as an important basis for judging disease progression [15, 16]. The analysis of the expression status of HPV-16 in primary bladder tumors can more accurately follow-up and grasp the prognosis of patients. The prognosis analysis showed that there were 57 patients, including 11 patients with single tumor and 46 patients with multiple tumors. After 3 years of continuous follow-up, 37 situations of tumor-free survival, 17 situations of recurrence, and 3 situations of death were found during follow-up. The results confirmed that HPV-16 can be used as an important reference for patient prognosis analysis [17, 18].

Research on the expression of HPV-16 in primary bladder tumors and the analysis of the loss of cell differentiation can provide theoretical reference value for the judgment of

TABLE 5: Correlation analysis of HPV-16 expression with tumor differentiation and age in patients.

General information	HPV positive (n = 28)	HPV negative (n = 29)	$\chi^2$	P
Age (years)			1.709	0.425
<65	28	9 (32.14)		
65~74	24	11 (45.83)		
≥75	5	1 (20.00)		
Degree of differentiation				
Upper differentiation	6	2 (33.33)	1.417	0.492
Moderately differentiated	24	6 (25.00)		
Bottom differentiation	27	11 (40.74)		

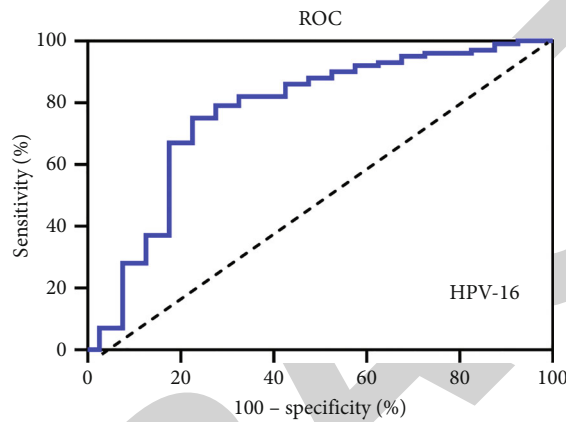


FIGURE 4: The value of HPV-16 in judging primary bladder tumor expression and cell and molecular deletion. Note: HPV-16 has upper sensitivity and specificity in judging the expression of primary bladder tumors and the deletion of cellular molecules. The results suggest that HPV-16 can be used as an important basis for judging disease progression.

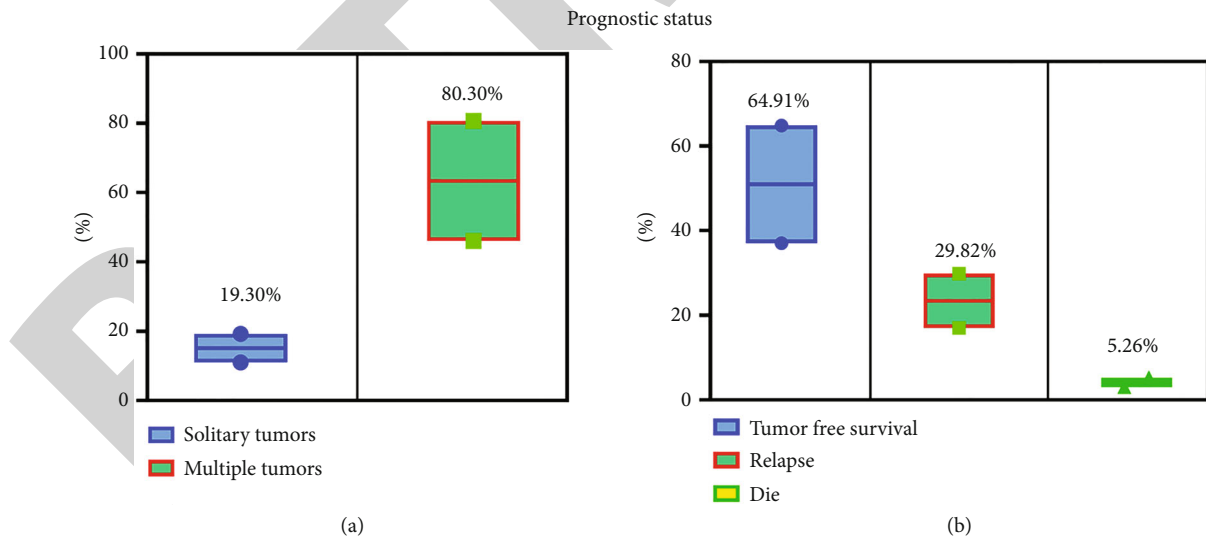


FIGURE 5: Analysis of patient prognosis. Note: the proportions of patients with single tumor and multiple tumors were 19.30% and 80.70%, respectively, and the tumor-free survival, recurrence, and mortality of patients were 64.91%, 29.82%, and 5.26%, respectively.

disease status [19, 20]. Even so, this study only analyzed the correlation of the expression of HPV-16. The lack of completeness of the research content will affect the accuracy and rationality of the research to a certain extent. Therefore, further analysis and exploration are required to ensure the feasibility of the study [21].

### 5. Conclusion

HPV-16 is an upper, expressed in primary bladder tumors and participates in cell differentiation and deletion. It may provide effective guidance and basis for the diagnosis of primary bladder tumors. It is an important factor in judging the

## Retraction

# Retracted: Identification of RPS7 as the Biomarker of Ferroptosis in Acute Kidney Injury

### BioMed Research International

Received 8 January 2024; Accepted 8 January 2024; Published 13 January 2024

Copyright © 2024 BioMed Research International. This is an open access article distributed under the Creative Commons Attribution License, which permits unrestricted use, distribution, and reproduction in any medium, provided the original work is properly cited.

This article has been retracted by Hindawi following an investigation undertaken by the publisher [1]. This investigation has uncovered evidence of one or more of the following indicators of systematic manipulation of the publication process:

- (1) Discrepancies in scope
- (2) Discrepancies in the description of the research reported
- (3) Discrepancies between the availability of data and the research described
- (4) Inappropriate citations
- (5) Incoherent, meaningless and/or irrelevant content included in the article
- (6) Manipulated or compromised peer review

The presence of these indicators undermines our confidence in the integrity of the article's content and we cannot, therefore, vouch for its reliability. Please note that this notice is intended solely to alert readers that the content of this article is unreliable. We have not investigated whether authors were aware of or involved in the systematic manipulation of the publication process.

Wiley and Hindawi regrets that the usual quality checks did not identify these issues before publication and have since put additional measures in place to safeguard research integrity.

We wish to credit our own Research Integrity and Research Publishing teams and anonymous and named external researchers and research integrity experts for contributing to this investigation.

The corresponding author, as the representative of all authors, has been given the opportunity to register their agreement or disagreement to this retraction. We have kept a record of any response received.

### References

- [1] H. Zhang, X. Liu, L. Zhou, Z. Deng, and Y. Wang, "Identification of RPS7 as the Biomarker of Ferroptosis in Acute Kidney Injury," *BioMed Research International*, vol. 2022, Article ID 3667339, 14 pages, 2022.



## Research Article

# Identification of RPS7 as the Biomarker of Ferroptosis in Acute Kidney Injury

Hao Zhang <sup>1</sup>, Xuemei Liu,<sup>2</sup> Lizhi Zhou <sup>1</sup>, Zebin Deng <sup>1</sup> and Yinhuai Wang <sup>1</sup>

<sup>1</sup>Department of Urology, The Second Xiangya Hospital at Central South University, Changsha, Hunan 410011, China

<sup>2</sup>Department of Functional Medicine, Hunan Provincial Maternal and Child Health Care Hospital, Changsha, Hunan, China

Correspondence should be addressed to Yinhuai Wang; wangyinhuai@csu.edu.cn

Received 26 August 2022; Accepted 17 September 2022; Published 13 October 2022

Academic Editor: Nauman Rahim Khan

Copyright © 2022 Hao Zhang et al. This is an open access article distributed under the Creative Commons Attribution License, which permits unrestricted use, distribution, and reproduction in any medium, provided the original work is properly cited.

**Objective.** This paper aims to explore novel ferroptosis-related biomarkers for acute kidney injury (AKI). **Methods.** Various bioinformatic methods, such as differential expression analysis, functional annotation analysis, machine learning, and chemical-gene network analysis, were used in this study. Furthermore, the expression and proferroptotic role of RPS7 were validated with further bioinformatics analysis and biochemical experiments. **Results.** GSE30718 dataset and GSE139061 dataset were used, and the differentially expressed genes (DEGs) were screened. The DEGs were overlapped with ferroptosis-related genes and genes associated with AKI, which led to the identification of four candidate genes. Machine learning and ROC curve analysis were conducted, and RPS7 and TRIB3 were selected for diagnostic model analysis and functional analysis. Finally, the upregulation of RPS7 in cisplatin-induced AKI was validated in cisplatin-induced AKI, and its proferroptotic role was confirmed in cisplatin-treated proximal tubular cells. **Conclusion.** Our results indicated that RPS7 might present as a novel ferroptosis-related biomarker for AKI, and it derived ferroptosis to accentuate cisplatin-induced AKI.

## 1. Introduction

Acute kidney injury (AKI) is characterized by a sudden decrease in renal functions, manifested by increased serum creatinine levels and decreased urine volume [1]. AKI is commonly observed in clinical practice, especially in patients in the intensive care unit [2]. The etiology of AKI is quite complicated, which incorporates ischemia-reperfusion injury, sepsis, cardiac surgery, and the medication of nephrotoxic drugs [3]. The molecular mechanisms of AKI have been investigated for decades, and various aspects of mechanisms have been reported in the occurrence of AKI. In clinical practice, the diagnosis of AKI relies on serum creatinine level and 24-hour urine output, which may cause a low earlier diagnosis rate [4]. The serum creatinine level usually takes 2-3 days to rise, and the volume of urine sometimes increases slightly in part of AKI patients [5, 6]. In this regard, identification of the novel markers for AKI is essential.

Ferroptosis is a type of nonapoptotic cell death denominated by Dixon in 2012 [7]. Unlike apoptosis, the bioprocess

of ferroptosis is absent of chromatin margination and caspase activation [8]. The reduction of mitochondria crista is commonly observed in cells undergoing ferroptosis [8]; however, no specific morphological alterations were reported. Mechanistically, the execution of ferroptosis relies on overwhelming lipid peroxidation, which can be generated via the iron-catalyzed Fenton reaction or the lipoxygenase pathway [9]. Noteworthy, lipoxygenases are a family of iron-containing oxidases, which further stress the role of iron in the pathogenesis of ferroptosis [10]. The process of ferroptosis can be accelerated by increased intracellular iron and ROS generation. The overwhelming lipid peroxidation is inclined to be detoxicated by the enzymatic activity of GPX4, leading to the termination of ferroptosis [9]. Recently, it was manifested that therapeutic medication targeting ferroptosis alleviated various types of AKI [10], but the modulation of ferroptosis in AKI has not been fully elucidated. Noteworthy, our previous publication indicated that the ferroptotic process was ignited in the very early stage of cisplatin-induced AKI [11], suggesting that

ferroptosis-related proteins may serve as early diagnostic markers for AKI.

In this study, several AKI-related datasets were incorporated for bioinformatics analysis to identify novel genes related to the pathogenesis of AKI. In addition, a ferroptosis-related gene set, acquired from FerrDb database and GeneCards database, was used to explore the relevance of the newly discovered genes with ferroptosis. Finally, cisplatin-induced AKI model was used, and the biochemical experiments indicated that RSP7 might present as a novel potential ferroptosis-related biomarker for the diagnosis and treatment of AKI.

## 2. Materials and Methods

**2.1. Datasets and Gene Collections.** Three AKI-related datasets, i.e., GSE30718, GSE139061, and GSE165100, were obtained from the GEO database. GSE30718 dataset contains the renal transcriptional expression profile (array) of 28 AKI patients and 11 control samples. GSE139061 dataset includes the high-throughput sequencing data of 9 AKI renal samples and 10 control samples (human). GSE165100 dataset incorporates the renal transcriptional expression profile (array) of 4 cisplatin-induced AKI mice and 4 control mice. Ferroptosis-associated genes were acquired from FerrDb database (<http://www.zhounan.org/ferrdb/current/>) and GeneCards database (<https://www.genecards.org/>), and 659 genes were selected after merging and deduplication of the two databases.

**2.2. Screening of the Candidate Genes for Ferroptosis in AKI.** Firstly, the differentially expressed genes (DEGs) were authenticated between AKI and control samples in GSE30718 dataset (Limma package, version 3.44.3,  $p < 0.05$ ) [12, 13]. Subsequently, the DEGs in GSE139061 dataset was also uncovered using the “limma” package based on  $p$  value  $< 0.05$ . WGCNA was used to filter AKI-associated genes in GSE30718 dataset. The R package “WGCNA” (version 1.70-3) was implemented to generate a coexpression network [14]. AKI samples were considered as trait data for WGCNA analysis, and turquoise module genes were retrieved as the ones highly associated with AKI. Finally, Venn diagram was applied to obtain the intersection DEGs, turquoise module genes, and ferroptosis-associated genes, followed by the identification of four candidate genes for ferroptosis and AKI.

**2.3. Functional Annotation Analysis.** R package “clusterProfiler” (version 4.0.2) [15] for Gene Ontology (GO) and Kyoto Encyclopedia of Genes and Genomes (KEGG) enrichment analysis was used in our studies. Noteworthy, GO was subdivided into cellular component (CC), molecular function (MF), and biological process (BP).  $p < 0.05$  was considered significantly different.

**2.4. Recognition of Ferroptosis-Associated Biomarkers in AKI.** Two machine learning methods, i.e., least absolute shrinkage and selection operator (LASSO) [16] and random forest (RF) [17], were applied to screen for disease characteristic genes. LASSO logistic regression in the R software package “glmnet” (version 4.0-2) was used, and the strong relevant

features were selected. The RF method was deployed to obtain the feature genes with 5-fold cross-validation. The overlapping genes certificated by LASSO and RF were defined as characteristic genes in AKI. ROC curves were generated by the “pROC” package (1.17.0.1). Genes with AUC values of the ROC curve greater than 0.7 in both GSE30718 and GSE139061 datasets were identified as the ferroptosis-associated biomarkers in AKI.

**2.5. Gene Set Enrichment Analysis (GSEA) Based on a Signal Gene.** The GO, KEGG, and Reactome gene sets were used as the reference gene sets, and the AKI samples in GSE30718 dataset were sorted according to the correlation coefficients between the expression of all genes and the expression of biomarkers. GSEA was executed using the R software “clusterProfiler” (version 4.0.2) package. Significance thresholds were  $|NES| > 1$  and  $p$  value  $< 0.05$ .

**2.6. Establishment of Cisplatin-Induced AKI Model.** For *in vitro* studies, BUMPT cells (a mouse proximal tubular cell line) were maintained in culture media with high glucose DMEM, 10% FBS, and antibiotics. Lentivirus (acquired from Vigene Biosciences) was used to interfere with the expression profile of RPS7 in BUMPT cells. The cells were treated with 20  $\mu$ M cisplatin for 16-24 hours to induce tubular injuries *in vitro*.

For *in vivo* studies, ethical approval was acquired from the Animal Ethical and Welfare Committee of the Second Xiangya hospital at Central South University (Approval number: 2022705). 8-12 weeks male C57BL/6J mice were divided into the control group and the AKI group (6 mice in each group). Mice in the AKI group received an intraperitoneal injection of 25 mg/kg cisplatin to induce tubular injuries, while PBS solution was applied to the control group. The kidneys and serum samples were harvested two days later for further investigation.

**2.7. H&E Staining.** Kidney tissues were embedded in paraffin wax, and 4- $\mu$ m paraffin sections were obtained. The sections were deparaffinized and rinsed. Then, they were sequentially stained with hematoxylin for 3 minutes and eosin for 30 seconds. Finally, the sections were evaluated by light microscopy.

**2.8. Immunoblotting.** Kidney tissues or BUMPT cells were lysed by RIPA buffer, and the protein concentration was qualified. 15-30  $\mu$ g protein samples were subjected to 10-12% SDS-PAGE gel, and the separated proteins were transferred to PVDG membranes (0.22  $\mu$ m). The membranes were blocked and sequentially incubated with primary antibody and secondary antibody before the evaluation by the ECL detector. The primary antibody used in our study includes anti-NCOA4 (Bethyl Laboratories, catalog A302-272A; 1:1000), anti-FTH1 (Cell Signaling Technology, catalog 3998S; 1:1000), anti-GPX4 (Abcam, catalog ab125066; 1:2000), anti-RPS7 (Proteintech, catalog 14491-1-AP; 1:2000), and anti- $\beta$ -actin (Proteintech, catalog 66009-1-Ig; 1:5000).

**2.9. qRT-PCR Analysis.** Total mRNA in kidney tissues or BUMPT cells was extracted with TRIzol (Invitrogen, catalog

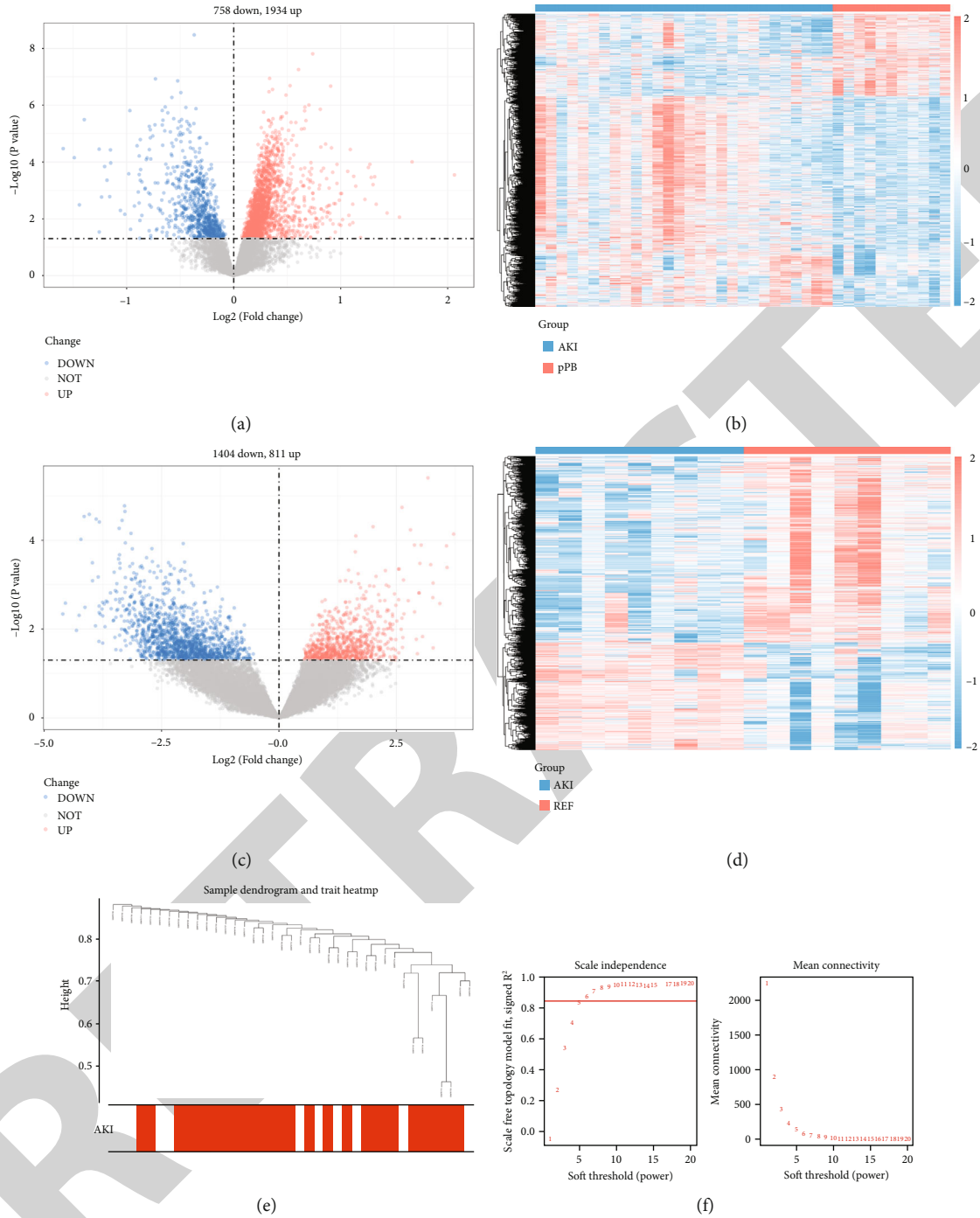


FIGURE 1: Continued.

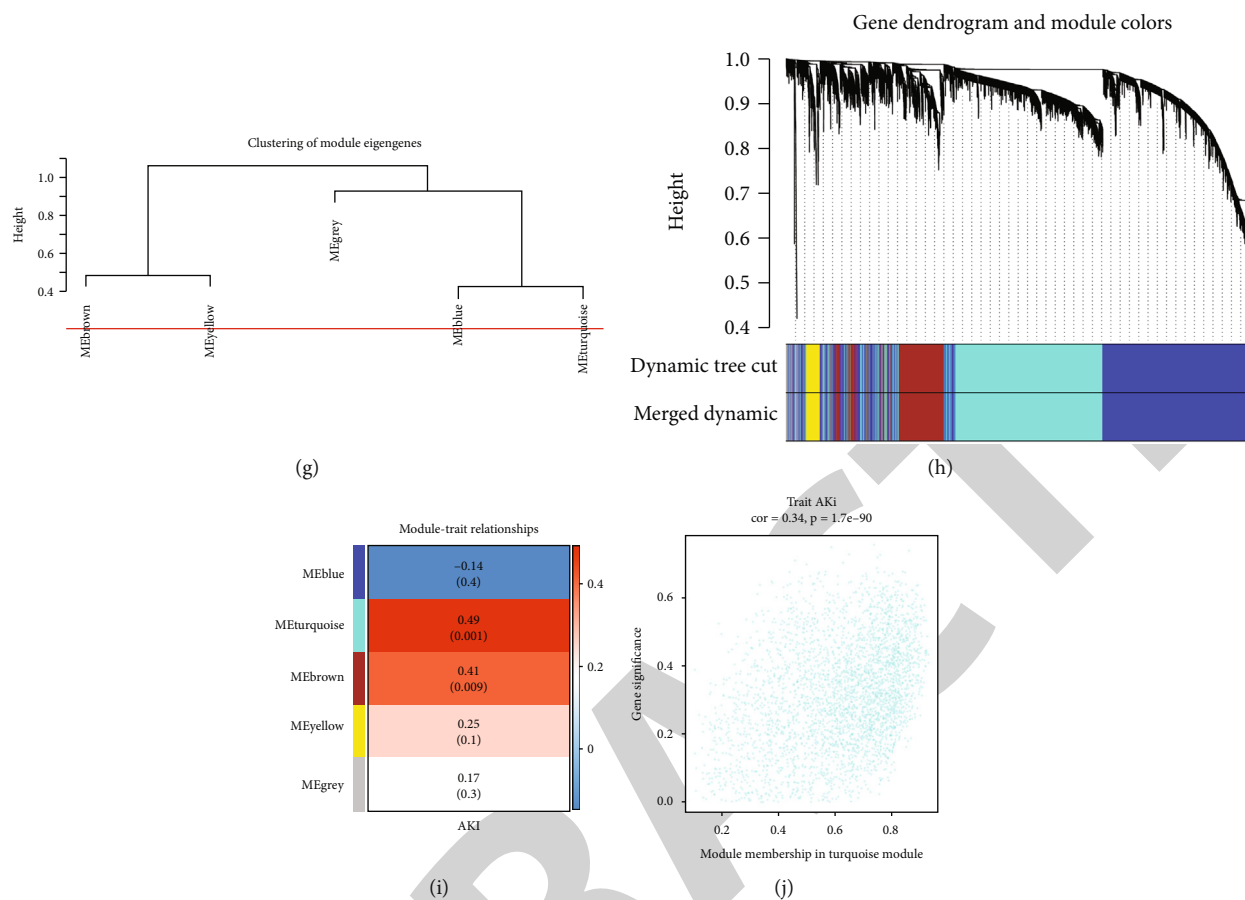


FIGURE 1: Screening of genes associated with AKI. (a and b) The DEGs in GSE30718 dataset. (c and d) The DEGs in GSE139061 dataset. (e and j) WGCNA analysis of GSE30718 dataset.

15-596-026). The mRNA was reverse-transcribed into cDNA with the PrimeScript™ RT reagent kit (Takara). Finally, the cDNA was subjected to an ABI PRISM 7900 Sequence Detector System (Applied Biosystems) with ChamQ™ Universal SYBR® qPCR Master Mix (Vazyme). The calculated values compared with  $\beta$ -actin were used for statistical analysis. The primers incorporated in our study were RPS7-F: TGCTCG AGCTGGAGATG AAC; RPS7-R: GCTGTCAGGGTACG GCTTC; TRIB3-F: AGCAACTGTGAGA GGACGAAG; TRIB3-R: TGGAAATGGGTATCTGCCAGC.

**2.10. Immunofluorescence Staining.** 4- $\mu$ m sections were deparaffinized and permeated before antigen retrieval. Subsequently, the sections were blocked and incubated with primary antibodies overnight. The sections were rinsed and incubated with secondary antibody for 1 hour. DAPI was used to stain the nuclei, and the sections were scanned by fluorescence microscopy. The primary antibodies used in our study were anti-Megalin (Abcam, catalog ab76969; 1:500) and anti-RPS7 (Proteintech, catalog 14491-1-AP; 1:500).

**2.11. Immunohistochemistry Staining.** 4- $\mu$ m paraffin sections were deparaffinized, permeated, rinsed, and antigen retrieved. Subsequently, the sections were suppressed by H<sub>2</sub>O<sub>2</sub> and blocked by goat serum. After that, the sections were sequentially incubated with anti-RPS7 antibody (Pro-

teintech, catalog 14491-1-AP; 1:500) and secondary antibody before the application of DAB solution. Finally, the sections were evaluated by light microscopy.

**2.12. MTT Assay.** The cellular survive rate was detected by MTT assay. Cells were seeded into 96-well plates for overnight attachment. Cisplatin was used to prime the cells, and MTT solution (1mg/ml Thiazolyl Blue Tetrazolium Bromide) were added for 4 hours after the treatment. The solutions were removed, and 150  $\mu$ l DMSO was added into each well. Finally, the plates were detected by a microplate reader (495 nm).

**2.13. Statistical Analysis.** The diagnostic model for ferroptosis-associated biomarkers was developed using the “lrm” function in R. All analyses were conducted using the R programming language, and the data from different groups were compared by the Wilcoxon test or Students’ *t*-test. If not specified above, *p* value less than 0.05 was considered statistically significant.

### 3. Results

**3.1. Screening of AKI-Related Genes.** The DEGs between AKI and control samples in GSE30718 and GSE139061 datasets were authenticated, respectively, to uncover the variably

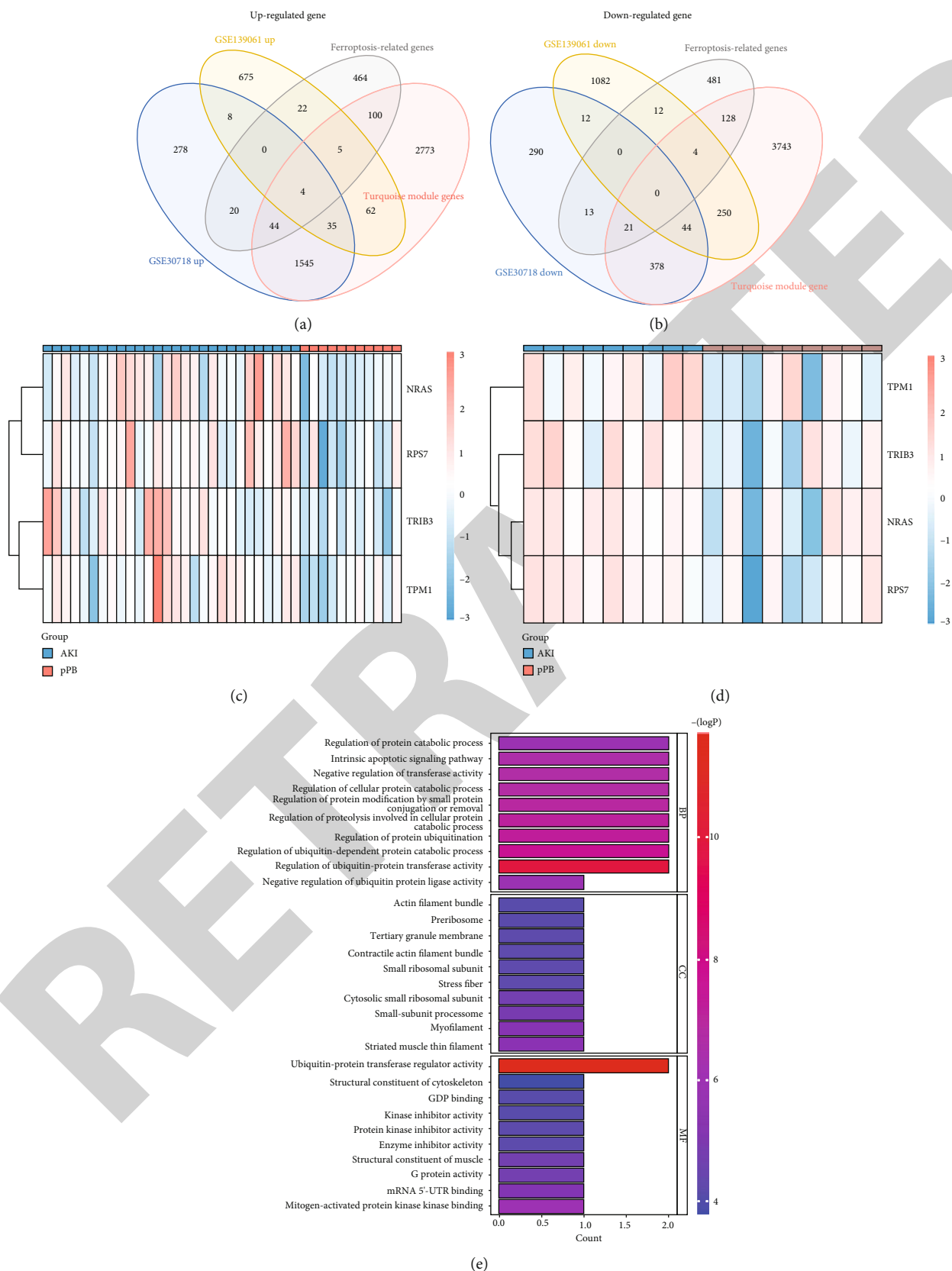


FIGURE 2: Continued.

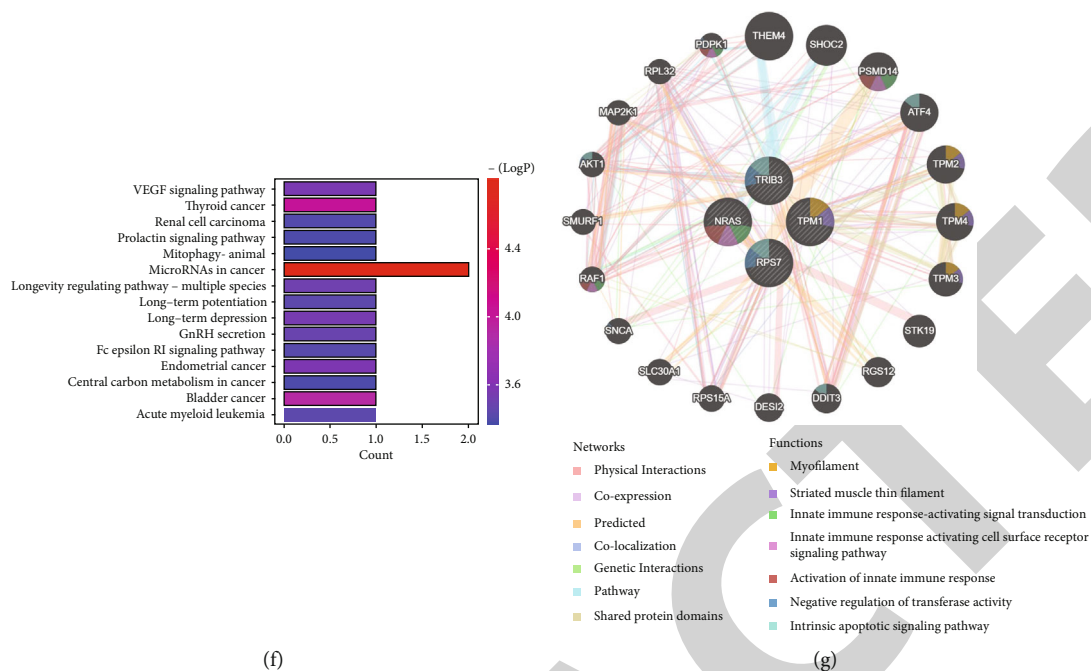


FIGURE 2: Identification of ferroptosis-related candidate genes in AKI. (a and b) The overlap of the DEGs, turquoise module genes, and ferroptosis-associated genes. (c and d) The expression of NRAS, TRIB3, TPM1, and RPS7 in GSE30718 and GSE139061 datasets. (e and f) Functional analysis of NRAS, TRIB3, TPM1, and RPS7. (g) GeneMANIA analysis of NRAS, TRIB3, TPM1, and RPS7.

expressed genes in AKI. 2692 DEGs (AKI vs. control), including 1934 upregulated genes and 758 downregulated genes in the AKI samples, were identified in GSE30718 dataset (Figures 1(a) and 1(b)). Meanwhile, a grand total of 2215 DEGs (AKI vs. control), including 811 upregulated and 1404 downregulated genes in the AKI samples, were determined in the GSE139061 dataset (Figures 1(c) and 1(d)). WGCNA analysis was applied to the data of GSE30718 dataset. Firstly, no outlier samples were excluded by sample cluster analysis (Figure 1(e)). Six were chosen as the optimal soft threshold ( $R^2 = 0.85$ ) to ensure that the interactions between genes maximally conformed to the scale-free distribution (Figure 1(f)). Next, a total of 5 modules were developed based on a gene clustering tree and dynamic tree cutting algorithm (setting the minimum number of genes per gene module at 100) (Figures 1(g) and 1(h)). The correlations between modules and AKI disease were computed, and turquoise module genes with the highest correlation were selected (Figures 1(i) and 1(j)). Hence, the 4568 genes in the turquoise module were regarded as genes closely associated with AKI. The DEGs and turquoise module genes were collected for further analysis.

**3.2. Identification of Potential Ferroptosis-Related Biomarkers in AKI.** In order to recognize ferroptosis-associated genes in AKI, 659 ferroptosis-related genes were selected from FerrDb database and GeneCards database, and they were overlapped with the DEGs and turquoise module genes. Four intersecting genes, i.e., NRAS, TRIB3, TPM1, and RPS7, were identified (Figures 2(a) and 2(b)). The expression of these four genes in GSE30718 and GSE139061 datasets was illustrated in the heat maps (Figures 2(c) and 2(d)). The role of these four genes was

explored by functional enrichment analysis. 185 GO items (146 BP items, 22 CC items, and 17 MF items) and 35 KEGG pathways were derived. The top 10 GO items under each classification and the top 15 KEGG pathways were showcased in bar charts (Figures 2(e) and 2(f)). The results revealed that these genes were involved in protein ubiquitination-related biological processes, vascular-associated smooth muscle cell migration, cellular response to reactive oxygen species, VEGF signaling pathway, Fc epsilon RI signaling pathway, EGFR tyrosine kinase inhibitor resistance, B cell receptor signaling pathway, ErbB signaling pathway, and Gap junction. In addition, the interactions between the four proteins and 20 other proteins were illustrated by GeneMANIA, and their functions were also characterized (Figure 2(g)).

Machine learning analysis was applied to the four candidate genes to further confirm their relevance with ferroptosis in AKI. As shown in Figures 3(a) and 3(b), three genes (NRAS, TRIB3, and RPS7) were picked out by LASSO logistic regression when  $\lambda_{\min}$  was 0.0241. Meanwhile, the same three genes (NRAS, TRIB3, and RPS7) were selected by RF model when the predicting accuracy of disease samples and normal samples was 0.8 (Figure 3(c)). Hence, three overlapping genes (NRAS, TRIB3, and RPS7) were obtained by crossing the genes filtered by two machine learning methods (Figure 3(d)). Subsequently, the ROC curves of the three genes were mapped in GSE30718 and GSE139061 datasets. As indicated in Figures 3(e) and 3(f), the AUC values of TRIB3 and RPS7 exceeded 0.7, suggesting that their expression profile could effectively distinguish AKI samples from control samples. Taken together, we reckoned that RPS7 and TRIB3 are highly potential ferroptosis-related biomarkers in AKI.

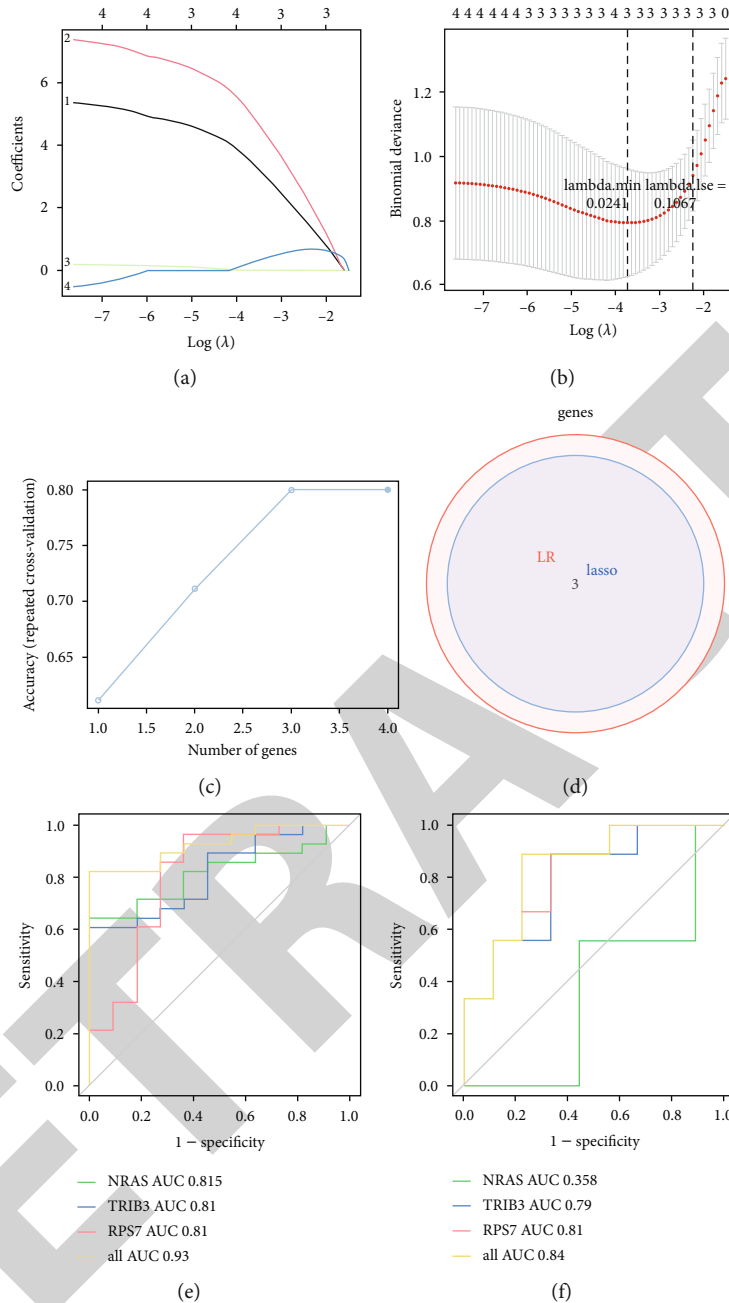


FIGURE 3: Machine learning of ferroptosis-related candidate genes. (a and b) The analysis of LASSO logistic regression. (c) The analysis of RF model. (d) Overlap of the two machine learning methods. (e and f) The ROC curve analysis of NRAS, TRIB3, and RPS7 in GSE30718 and GSE139061 datasets.

3.3. *The Diagnostic Model and Functional Analysis of RPS7 and TRIB3.* To verify the diagnostic value of TRIB3 and RPS7 in AKI, PCA analysis was conducted. The analysis of GSE30718 and GSE139061 datasets revealed that AKI samples and normal samples were largely in two different regions based on the expression of TRIB3 and RPS7, indicative of their diagnostic potency (Figures 4(a) and 4(b)). Subsequently, a diagnostic nomogram model based on the two ferroptosis-associated biomarkers was developed, which can predict an individual's risk and probability of suffering from AKI based on their expression profile (Figure 4(c)). In addition, the corresponding calibration curves were plot-

ted to assess the validity of the diagnostic model. Our data revealed that the gap between the predicted probability and the actual probability was puny, suggesting that the model was reliable in predicting the risk of AKI (Figure 4(d)).

Single-gene GSEA was performed based on the correlation coefficient between the expression of all genes and the expression of each biomarker (RPS7 and TRIB3, respectively) as a ranking criterion. Top 10 items under each gene set were displayed in Figure 5. RPS7 was associated with Ribosome, Proteasome, PI3K-Akt signaling pathway, Cytokine-cytokine receptor interaction, Natural killer cell-mediated cytotoxicity, and Hippo signaling pathway. TRIB3

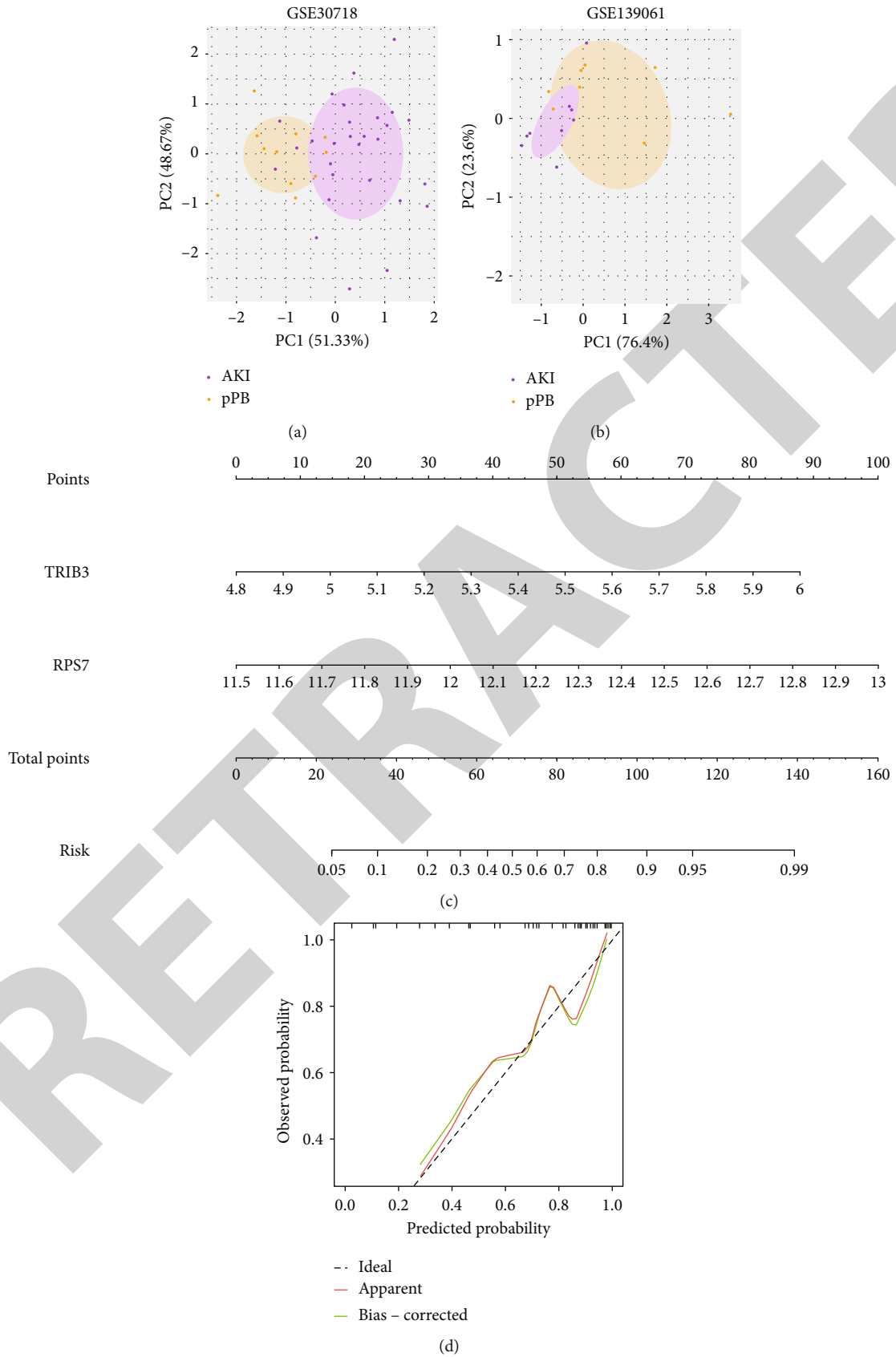


FIGURE 4: The diagnostic model of RPS7 and TRIB3 in AKI. (a and b) PCA analysis of RPS7 and TRIB3 in GSE30718 and GSE139061 datasets. (c) The diagnostic nomogram model of RPS7 and TRIB3. (d) The calibration curves of the diagnostic model.



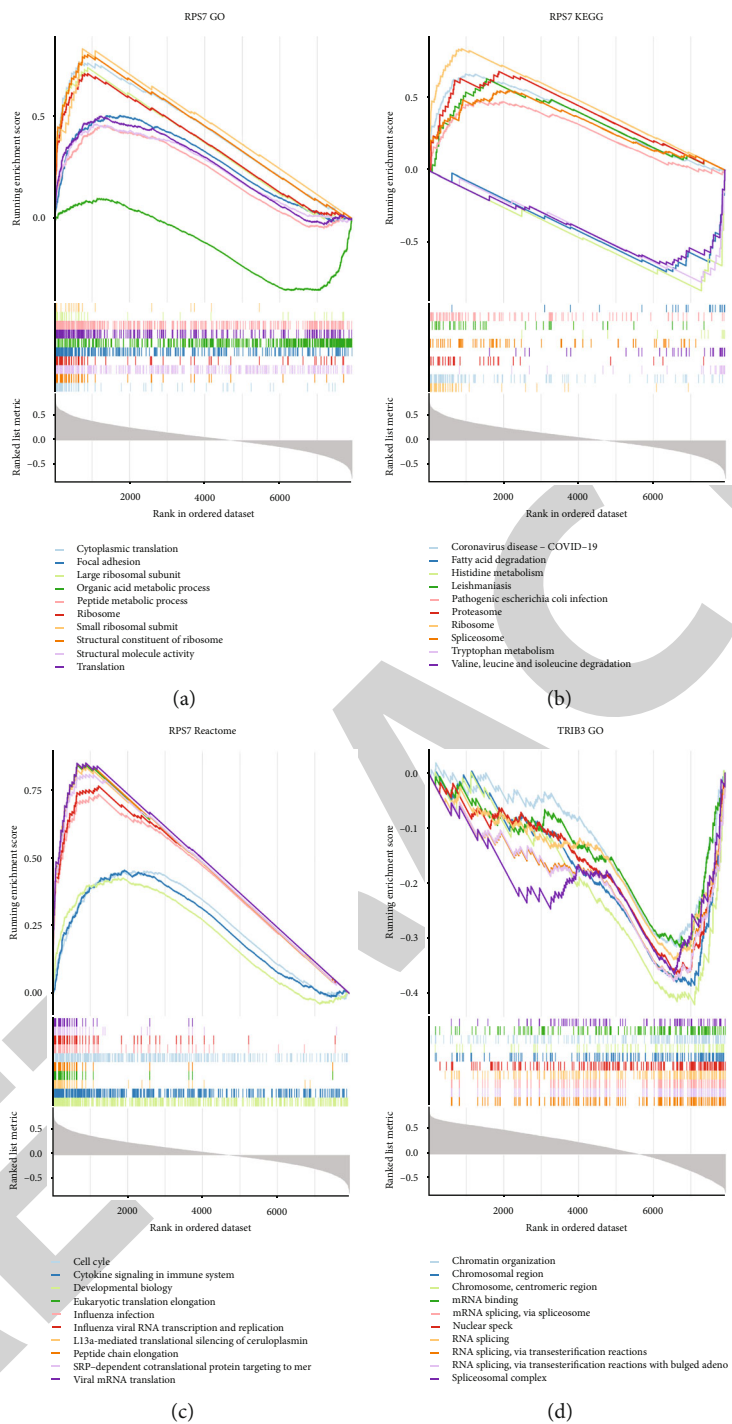


FIGURE 5: Continued.

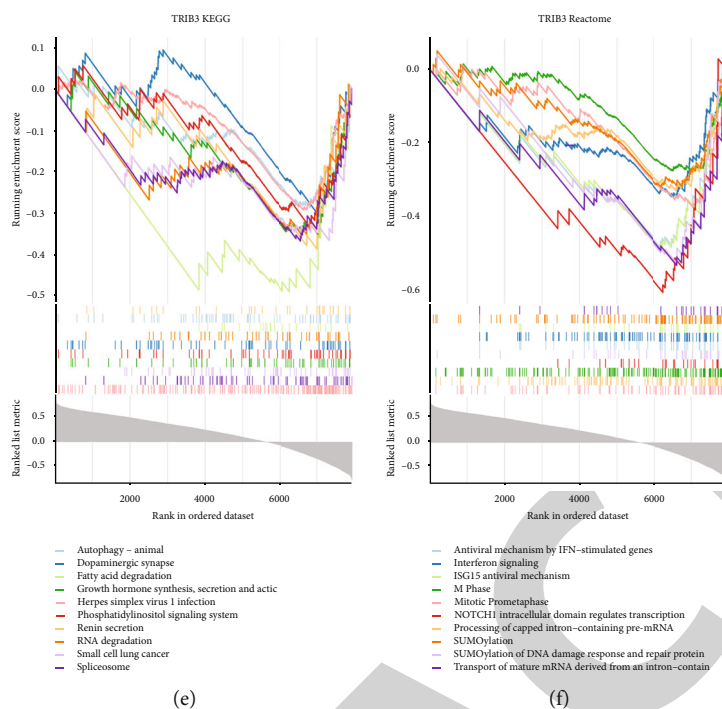


FIGURE 5: Single-gene GSEA of RPS7 and TRIB3. (a–c) Functional analysis of RPS7 based on GO, KEGG, and Reactome gene sets. (d–f) Functional analysis of TRIB3 based on GO, KEGG, and Reactome gene sets.

was relevant to RNA splicing, NF- $\kappa$ B binding, T cell chemotaxis, positive regulation of T cell migration, B cell homeostasis, and cell death in response to oxidative stress.

**3.4. The Expression Profile of Ferroptosis-Associated Biomarkers in AKI.** The expressions of RPS7 and TRIB3 were explored in multiple ways. As illustrated in Figures 6(a) and 6(b), RPS7 and TRIB3 were upregulated in AKI samples, as compared to control samples in GSE30718 and GSE139061 datasets. Similarly, the expressions of RPS7 and TRIB3 were conceivably increased in AKI samples in GSE165100 dataset (mouse) (Figure 6(c)). The expression profiles of RPS7 and TRIB3 were also investigated in *in vivo* and *in vitro* studies. Our qRT-PCR data showed that the mRNA level of RPS7 was very high in renal tubules, while the expression of TRIB3 was quite limited (Figure 6(d)). In this regard, RPS7 was selected for further investigations. Immunofluorescence staining demonstrated that RPS7 was extensively expressed in renal proximal tubular cells (marked by megalin) (Figure 6(e)). Cisplatin was used to induce AKI in BUMPT cells and mice. Within expectation, the expression of RPS7 was conceivably increased in cisplatin-treated BUMPT cells and mice kidneys, as validated by qRT-PCR analysis, immunoblotting, and immunohistochemistry staining (Figures 6(g)–6(j)).

**3.5. RPS7 Promoted Ferroptosis in Cisplatin-Treated BUMPT Cells.** Lentivirus was used to intervene in the expression of RPS7 in BUMPT cells. The overexpression or knockdown of RPS7 in BUMPT cells was initially validated by qRT-PCR studies and immunoblot analysis (Figures 7(a), 7(b), 7(e), and 7(f)). Our previous publication revealed that fer-

roptosis is an integral process in cisplatin-induced AKI, and we proceeded to explore the regulation of ferroptosis by RPS7 in cisplatin-related nephropathy. MTT assay revealed that RPS7 overexpression accentuated, while its gene disruption attenuated, cisplatin-induced BUMPT cell death (Figures 7(c) and 7(d)). The expressions of three ferroptosis markers, i.e., FTH1, GPX4, and NCOA4, were detected by immunoblotting. With expectation, a simultaneous decrease of the three markers was observed in cisplatin-treated BUMPT cells, which was accelerated by RPS7 overexpression but decelerated by RPS7 knockdown (Figures 7(g) and 7(h)).

## 4. Discussion

In this study, bioinformatics methods were employed to analyze the online AKI datasets and ferroptosis-related gene sets, which uncovered four candidate genes for ferroptosis in AKI. Further investigations with machine learning and ROC curve analysis revealed that TRIB3 and RPS7 might be the potential ferroptosis markers in AKI, and their diagnostic values and functions were preliminarily explored. Subsequently, the expression of TRIB3 and RPS7 was validated in AKI datasets and laboratory investigations, which revealed that RPS7 might present as the ideal ferroptosis marker for AKI. Finally, the regulatory role of RPS7 on the ferroptotic process was validated in cisplatin-induced AKI.

AKI is characterized by high morbidity and mortality, and its molecular mechanism has not been fully elucidated. Traditional diagnosis methods with serum creatinine levels and urine output failed to meet the demand for early diagnosis [2]. Thus, it is urgently needed to identify novel potential

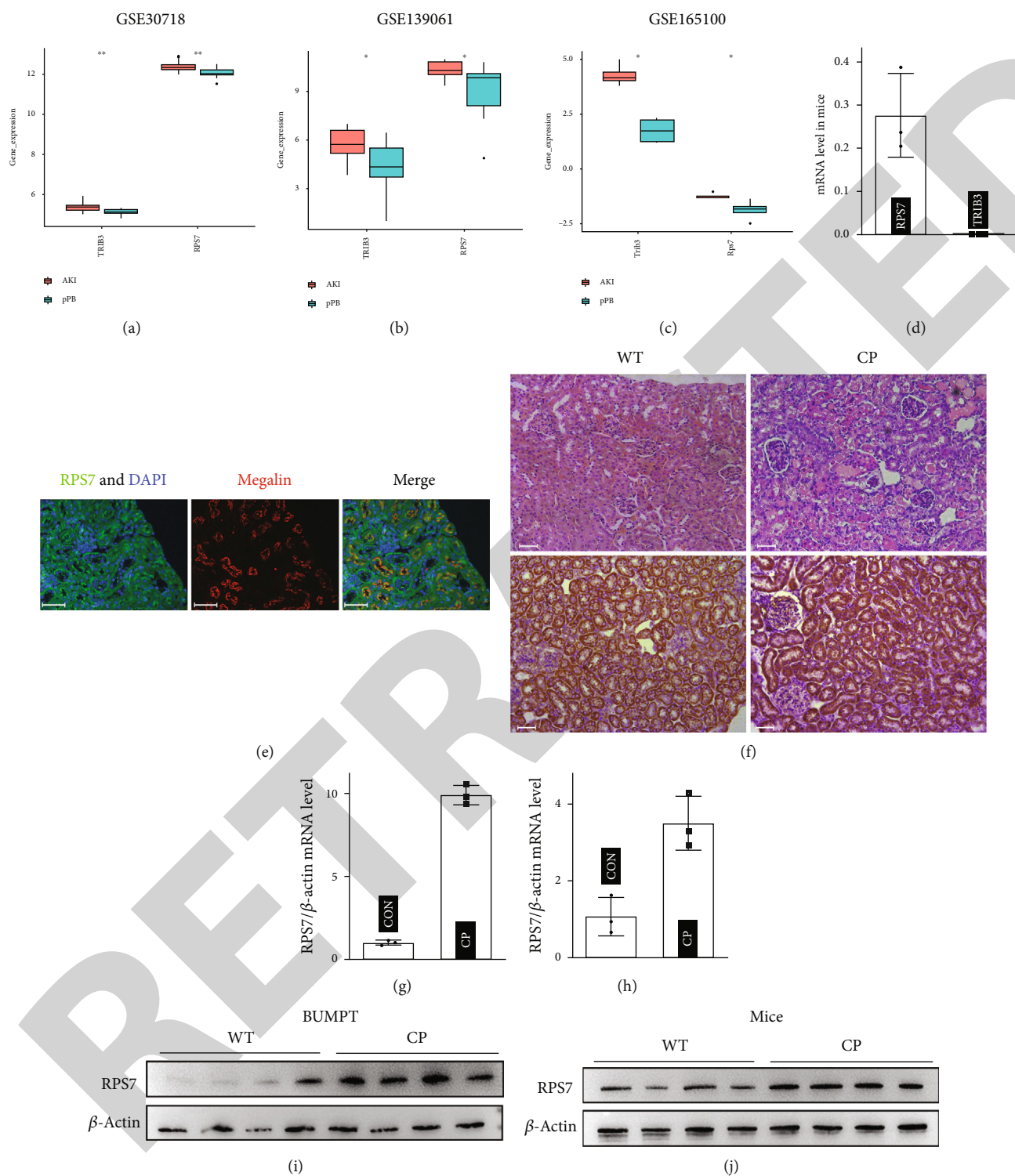


FIGURE 6: The upregulation of RPS7 and TRIB3 in AKI. (a–c) RPS7 and TRIB3 were upregulated in AKI sample in GSE30718, GSE139061, and GSE165100 datasets. (d) The relative repression of RPS7 and TRIB3 in mice kidneys. (e) Immunofluorescence staining of RPS7 and megalin. (f) H&E staining and immunohistochemistry staining (RPS7) of the renal sections. (g–h) qRT-PCR analysis of RPS7 in cisplatin-treated BUMPT cells and kidneys. (i and j) Representative immunoblot analysis of RPS7. CON: control; WT: wide type; CP: cisplatin; scale bars: 100 μm; data are presented as mean ± SD.

biomarkers for AKI to facilitate its diagnosis and treatment in clinical practice. Bioinformatics is an efficient way to screen new biomarkers for various diseases, and their molec-

ular mechanism and potential clinic relevance can also be calculated with certain algorithms. Bioinformatics analysis has been extensively used in the realms of AKI, leading to

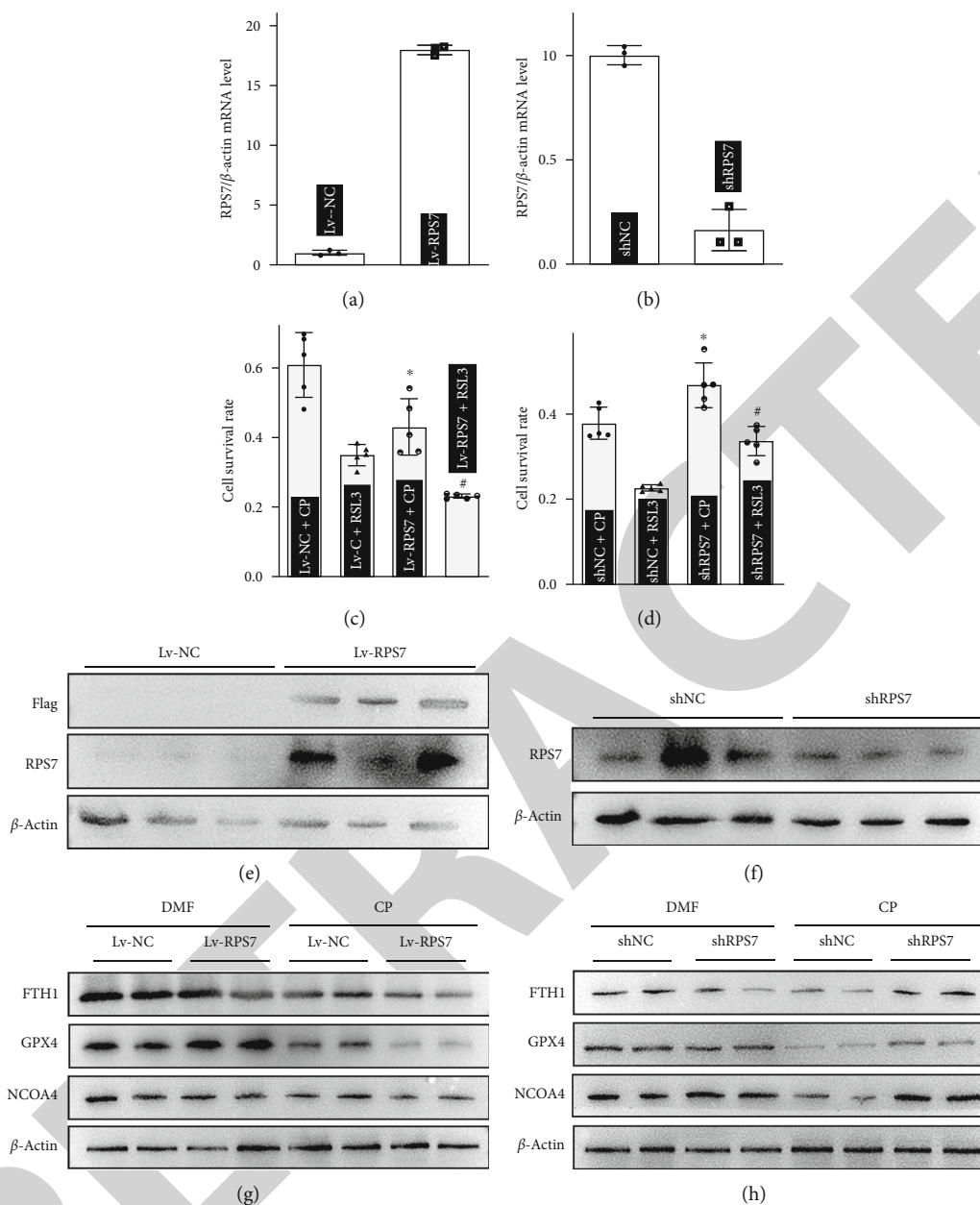


FIGURE 7: RPS7 promotes ferroptosis in cisplatin-treated BUMPT cells. (a and b) qRT-PCR confirmed the intervention of RPS7 gene in BUMPT cells. (c and d) MTT assay showed that RPS7 overexpression accentuated, while its gene disruption attenuated, cisplatin-induced BUMPT cell injuries. (e and f) Immunoblot analysis confirmed the intervention of RPS7 gene in BUMPT cells. (g and h) Immunoblot analysis revealed that RPS7 overexpression accelerated, while its gene disruption decelerated, the depletion of FTH1, GPX4, and NCOA4 in cisplatin-treated BUMPT cells. CP: cisplatin; Lv-NC: empty vector lentivirus for RPS7 overexpression; Lv-RPS7: overexpression of RPS7 by lentivirus; shNC: empty vector lentivirus for RPS7 knockdown; shRPS7: knockdown of RPS7 by lentivirus; data are presented as mean  $\pm$  SD.

the discovery of multiple proteins. Yun et al. used GEO datasets to identify three previously uncovered genes (VMP1, SLPI, and PTX3) in the pathogenesis of sepsis-induced AKI [18], which presented several potential targets for future investigations. In addition, the analysis of human RNA sequencing data of AKI revealed 1160 DEGs, and a novel gene, i.e., STUB1, was identified as the key modulator of cisplatin-induced AKI [19]. Herein, we analyzed two human AKI-related datasets, which led to the determination of 2692

and 2215 DEGs, respectively (Figure 1). In addition, 4568 genes in the turquoise module, selected by CANNA analysis, were used as genes highly associated with AKI (Figure 1). The above-mentioned genes were involved in further bioinformatic investigations to identify novel biomarkers for AKI.

Ferroptosis, a newly recognized type of nonapoptotic cell death, was recently reported to be involved in the pathogenesis of various types of AKI [10]. The process of ferroptosis mainly incorporated three aspects of metabolism: iron metabolism,

lipid metabolism, and amino acid metabolism [9]. The increased free ferrous iron level, generated in the aberrant iron metabolism, catalyzed excessive lipid peroxidation to execute the cells [20]. Noteworthy, the lethal lipid peroxidation can be detoxicated by GPX4 and GSH, a process closely modulated by amino acid metabolism [21]. It was previously demonstrated that therapeutic medication targeting ferroptosis alleviated ischemia-reperfusion injury-, folic acid-, and rhabdomyolysis-induced AKI [22–24], and our previous publication indicated that ferroptosis is operative in cisplatin-induced AKI [11]. Recently, bioinformatics was extensively used in the realms of ferroptotic investigation to recognize its new regulators. The bioinformatics analysis by Liu et al. revealed that the MAPK1-related mRNA-miRNA-lncRNA axis participated in the ferroptotic process in cerebral hemorrhage [25]. Besides, Xu et al. reported using bioinformatics to identify PTGS2 and SQLE as the new ferroptotic genes involved in the immunotherapy of pancreatic adenocarcinoma [26]. In AKI scenarios, previous publications with bioinformatics revealed that miR-3587 and NFE2L2 are involved in the ferroptosis process [27, 28]. In the present study, we acquired 659 ferroptosis-associated genes from the online database, and these genes were overlapped with the DEGs and turquoise module genes, leading to the discovery of four genes related to ferroptosis and AKI (Figure 2). Further investigations revealed that RPS7 and TRIB3 were ferroptosis-associated biomarkers for AKI, and their potential drugs were predicted (Figures 2–4).

RPS7, in its full name small ribosomal protein subunit 7, is an essential part of the small subunit of ribosomes, and it participates in the bioprocess of protein synthesis in normal states [29]. Previous publications revealed that RPS7 is involved in the progression of various malignancies, such as prostate cancer and lung cancer [29, 30], but its role in renal injuries and ferroptosis has not been investigated. TRIB3, in its full name tribbles pseudokinase 3, was reported to play a pivotal role in cellular stress response [31]. The role of TRIB3 has been investigated in the pathogenesis of proteinuria-mediated renal fibrosis and diabetic nephropathy [32, 33]. In this study, our qRT-PCR data revealed that RPS7 was highly expressed in renal tubules while the mRNA level of TRIB3 was much lower (Figure 6). Due to the lack of data on kidneys and its high renal expression, RPS7 was selected for further investigation. Our biochemistry experiments showed that RPS7 was obviously upregulated in cisplatin-induced AKI (Figure 6). In line with the laboratory investigation, the bioinformatics analysis also demonstrated that the upregulated RPS7 may present a potential marker for AKI (Figures 4 and 6). Finally, the modulation of ferroptosis by RPS7 was explored in cisplatin-treated AKI. Within expectation, RPS7 accelerated ferroptosis to promote cisplatin-induced BUMPT cell death (Figure 7). Taken together, these data identified a novel ferroptosis-related marker for AKI and presented a new therapeutic target for cisplatin-related nephropathy; however, its molecular machinery needs further investigation.

## 5. Conclusion

In conclusion, multiple databases were incorporated for bioinformatics analysis in this study, and the results identified RPS7 as a newly recognized marker for AKI. Moreover, we

found that RPS7 participated in the modulation of AKI by accelerating ferroptosis.

## Data Availability

The experimental data used to support the findings of this study are available from the author upon request. Publicly available datasets analyzed in this study can be found in online repositories. GSE30718, GSE139061, and GSE165100 datasets were available in the GEO database (<https://www.ncbi.nlm.nih.gov/geo/>), and ferroptosis genes can be obtained from the FerrDb (<http://www.zhounan.org/ferrdb/current/>) and GeneCards (<https://www.genecards.org/>) databases.

## Ethical Approval

No experiments involving human subjects were performed in this study. All animal experiments in this article were approved by the Animal Research Institute of the Second Xiangya Hospital at Central South University (Approval number: 2022705).

## Conflicts of Interest

The authors declare no conflict of interest.

## Authors' Contributions

Y.W. contributed to the study conception and design. H.Z. performed the experiments. The first draft of the manuscript was written by H.Z., and all authors commented on previous versions of the manuscript. All authors read and approved the final manuscript.

## References

- [1] A. S. Levey and M. T. James, "Acute kidney injury," *Annals of Internal Medicine*, vol. 167, no. 9, pp. ITC66–ITC80, 2017.
- [2] S. Peerapornratana, C. L. Manrique-Caballero, H. Gomez, and J. A. Kellum, "Acute kidney injury from sepsis: current concepts, epidemiology, pathophysiology, prevention and treatment," *Kidney International*, vol. 96, no. 5, pp. 1083–1099, 2019.
- [3] E. A. J. Hoste, J. A. Kellum, N. M. Selby et al., "Global epidemiology and outcomes of acute kidney injury," *Nature Reviews. Nephrology*, vol. 14, no. 10, pp. 607–625, 2018.
- [4] M. E. Thomas, C. Blaine, A. Dawnay et al., "The definition of acute kidney injury and its use in practice," *Kidney International*, vol. 87, no. 1, pp. 62–73, 2015.
- [5] J. Mishra, C. Dent, R. Tarabishi et al., "Neutrophil gelatinase-associated lipocalin (NGAL) as a biomarker for acute renal injury after cardiac surgery," *Lancet*, vol. 365, no. 9466, pp. 1231–1238, 2005.
- [6] J. Herrera and B. Rodriguez-Iturbe, "Stimulation of tubular secretion of creatinine in health and in conditions associated with reduced nephron mass. Evidence for a tubular functional reserve," *Nephrology, Dialysis, Transplantation*, vol. 13, no. 3, pp. 623–629, 1998.
- [7] S. J. Dixon, K. M. Lemberg, M. R. Lamprecht et al., "Ferroptosis: an iron-dependent form of nonapoptotic cell death," *Cell*, vol. 149, no. 5, pp. 1060–1072, 2012.

## Retraction

# Retracted: Compound Shuganjieyu Capsule on CYP450 Enzyme Activity

### BioMed Research International

Received 8 January 2024; Accepted 8 January 2024; Published 9 January 2024

Copyright © 2024 BioMed Research International. This is an open access article distributed under the Creative Commons Attribution License, which permits unrestricted use, distribution, and reproduction in any medium, provided the original work is properly cited.

This article has been retracted by Hindawi following an investigation undertaken by the publisher [1]. This investigation has uncovered evidence of one or more of the following indicators of systematic manipulation of the publication process:

- (1) Discrepancies in scope
- (2) Discrepancies in the description of the research reported
- (3) Discrepancies between the availability of data and the research described
- (4) Inappropriate citations
- (5) Incoherent, meaningless and/or irrelevant content included in the article
- (6) Manipulated or compromised peer review

The presence of these indicators undermines our confidence in the integrity of the article's content and we cannot, therefore, vouch for its reliability. Please note that this notice is intended solely to alert readers that the content of this article is unreliable. We have not investigated whether authors were aware of or involved in the systematic manipulation of the publication process.

Wiley and Hindawi regrets that the usual quality checks did not identify these issues before publication and have since put additional measures in place to safeguard research integrity.

We wish to credit our own Research Integrity and Research Publishing teams and anonymous and named external researchers and research integrity experts for contributing to this investigation.

The corresponding author, as the representative of all authors, has been given the opportunity to register their agreement or disagreement to this retraction. We have kept a record of any response received.

### References

- [1] Y. Tang and Y. Li, "Compound Shuganjieyu Capsule on CYP450 Enzyme Activity," *BioMed Research International*, vol. 2022, Article ID 3228738, 8 pages, 2022.

## Research Article

# Compound Shuganjiayu Capsule on CYP450 Enzyme Activity

Yunqiu Tang<sup>1</sup> and Yunxia Li<sup>2</sup> 

<sup>1</sup>The Third People Hospital of Chengdu, Chengdu, Sichuan Province, 610506, China

<sup>2</sup>School of Pharmacy, Chengdu University of Traditional Chinese Medicine, Chengdu, Sichuan Province, 610506, China

Correspondence should be addressed to Yunxia Li; [lyx028231@163.com](mailto:lyx028231@163.com)

Received 30 August 2022; Revised 17 September 2022; Accepted 19 September 2022; Published 13 October 2022

Academic Editor: Nauman Rahim Khan

Copyright © 2022 Yunqiu Tang and Yunxia Li. This is an open access article distributed under the Creative Commons Attribution License, which permits unrestricted use, distribution, and reproduction in any medium, provided the original work is properly cited.

**Objective.** To evaluate the potential drug-drug interactions of the Shuganjiayu capsule by establishing a Chronic Unpredictable Mild Stress (CUMS) depression model combined with the Cocktail probe substrate method. **Methods.** The whole study was divided into the single-dose and multiple-dose groups. Animals were randomly divided into further subgroups in each group. Following chronic unpredictable mild stress model development, Shuganjiayu capsules were administered to the drug administration group. The single-dose subgroup received the drug for one day, and the multiple-dose subgroup received the drug for three months. Liver microsomes of each group were extracted, and the effects of the Shuganjiayu capsule on the CYP450 enzyme were investigated by liquid chromatography-mass spectrometry (LC-MS) based on the Cocktail probe substrate method. The immunohistochemical method and RT-qPCR were used to detect the activity of CYP450 immunoprotein in rat liver. **Results.** In the single-dose subgroup, there were no statistical differences between the administration and model groups. In the multiple-dose subgroup, the conversion and protein expression rates of CYP1A2 and CYP2C19 were significantly increased in the model group compared with the blank group. In the administration group, the conversion and protein expression rates of CYP1A2 and CYP2C19 were inhibited. **Conclusion.** Long-term administration of the Shuganjiayu capsule could relieve depression-related behaviors in CUMS rats and downregulate the CYP1A2 and CYP2C19 enzyme activities in CUMS rats by inhibiting the expression of CYP1A2 and CYP2C19 protein. Long-term administration of the Shuganjiayu capsule may affect the bioavailability of other drugs metabolized by CYP1A2 and CYP2C19 enzymes, but the clinical guidance's specific significance needs to be clarified further.

## 1. Introduction

Cytochrome P450 (CYP450) is a super large gene family composed of a variety of isoenzymes involved in more than 90% of the body's drug metabolism [1, 2]. CYP1, CYP2, and CYP3 gene families are the leading CYP families involved in the metabolism of most drugs in the body. Cytochrome P450 enzymes are abundant in the liver. CYP1A2, CYP2C9, CYP2C19, CYP2D6, CYP3A4, and CYP3A5 participate in most drug metabolism. The increase or decrease of their activity is likely to lead to drug-drug interaction [3, 4], change the bioavailability of drugs in the body, affect the therapeutic effect of drugs, and even lead to toxic and side effects. Therefore, the research on P450 enzymes plays a vital role in studying drug metabolism. The cocktail probe substrate method refers to various relatively low doses of probe

drugs given simultaneously. The metabolic rate or other metabolic typing indicators of each probe drug in biological samples are measured by ultra-high-performance liquid chromatography-mass spectrometry (LC-MS) (UPLC-MS/MS) to obtain the phenotypic information of multiple metabolic enzymes, which is of great significance for the dose design of those with multiple metabolic pathways [5]. The main components of the Shuganjiayu capsule are *Hypericum perforatum* and *acanthopanax senticosus*. Its functions contain soothing the liver, relieving depression, and calming the mind to improve the symptoms of depression [6]. This study was aimed at investigating the enzyme inhibition or induction capability of Shuganjiayu capsules in animals to elucidate the potential for drug-drug interactions by estimating liver enzyme levels by employing analytical techniques like LCMS and UHPLC-MS/MS.

TABLE 1: The primer sequences.

Gene name	Primer sequence (5'-3')
CYP1A2	F: GTCACCTCAGGGAATGCTGTG R: GTTGACAATCTTCTCCTGAGG
CYP2C9	F: CTGCTGCTGCTGAAACACG R: TTTCATGCAGGGGCTCCG
CYP2C19	F: TGGTCCACGAGGTTTCAGAGATACA R: GGTTGGGAAACTCCTTGCTGTCAT
CYP2D6	F: TGCGAGAGGCACTGGTGA R: CGTGGTCCAAAGCCCCGAC
CYP3A5	F: GGCAAACCTGTCCTGTGAAAGA R: CTGGCGTGAGGAATGGAAAGAGT
CYP3A4	F: GGCAAACCTGTCCTGTGAAAGA R: CTGGCGTGAGGAATGGAAAGAGT
GAPDH	F: TGCTGAGTATGTCGTGGAG R: GTCTTCTGAGTGGCAGTGAT

TABLE 2: Effect of CUMS model on rat body weight ( $n = 6$ ).

Group	Dose (mg/kg)	Weight before modeling (g)	Modeling 56-day body weight (g)
Blank group	—	189.5 ± 6.19	410.67 ± 15.23
Model group	—	190.67 ± 4.84	318.5 ± 8.41**
Administration group	65	187.17 ± 2.99	322.33 ± 12.21**
	130	193.17 ± 6.37	323.33 ± 4.49**
	260	193.33 ± 5.99	321.83 ± 19.72**
	520	189.33 ± 1.21	329.5 ± 8.6**

Compared with the blank group, \*\* means  $P < 0.01$ .

TABLE 3: Effect of CMUS model on sucrose preference test ( $n = 6$ ).

Group	Dose (mg/kg)	Sugar water preference before modeling (%)	Modeling 56-day sugar water preference (%)
Blank group	—	78.14 ± 11.24	81.92 ± 8.43
Model group	—	80.27 ± 8.86	50.28 ± 19.51*
Administration group	65	78.85 ± 9.83	43.87 ± 27.92**
	130	81.46 ± 8.98	56.03 ± 18.36*
	260	76.76 ± 9.96	42.3 ± 21.19**
	520	77.74 ± 9.59	46.55 ± 24.24**

Compared with the blank group, \* means  $P < 0.05$  and \*\* means  $P < 0.01$ .

## 2. Materials and Methods

The following are used in the study: testosterone, paracetamol, phenacetin, and NADPH (Beijing Solarbio Science & Technology Co., Ltd. China); dextran, dextromethorphan, omeprazole, 5-hydroxy omeprazole, tolbutamide, 4-hydroxytolbutamide, and 6 $\beta$ -hydroxytestosterone (Toronto Research Chemicals); BCA protein Kit (Lianke Biotechnology Corporate Limited, No. a81911151); primer (synthesized by Tsingke Biotechnol-

TABLE 4: Effect of CUMS model on forced swim test ( $n = 6$ ).

Group	Dose (mg/kg)	Swimming immobility time (S)
Blank group	—	3.67 ± 1.86
Model group	—	65.33 ± 21.4**
Administration group	65	63.5 ± 31.85**
	130	65.17 ± 29.04**
	260	65.17 ± 21.55**
	520	54.17 ± 10.09**

Compared with the blank group, \*\* means  $P < 0.01$ .

ogy Co., Ltd.); reverse transcription Kit (Tsingke Biotechnology Co., Ltd., No. 20190328); and CYP1A2, cyp2d1, CYP3A4, CYP3A1, CYP2C19, and CYP2C11 antibodies (Abcam Company).

**2.1. Instrument.** The following are used in the study: UPLC-high-resolution time-of-flight mass spectrometer (including quaternary gradient pump autosampler two-stage tube array detector column temperature chamber), ACQUITY (Synaptic G2, Waters Corporation of the United States); Liquid transfer gun (Dragon, KE0003087/KA0056573); Histochemical pen (Gene tech, GT1001); BS 124 S-type analytical balance (Beijing sartorius Instruments Co., Ltd.); Alleger X-12 centrifuge (BECKMAN Coulter, USA); Varioskan flash-3001 microplate reader (Thermo Scientific, USA); and QTOWER real-time fluorescent quantitative PCR instrument (ANALYTIKJENA, Germany).

**2.2. Experimental Grouping.** Healthy male Sprague Dawley rats (weight = 200 ± 10 g) were purchased from Chengdu Gossy Experimental Animals Co. Ltd., China, and were acclimatized for seven days with free access to food and water. The animals were randomly first divided into the single administration and long-term administration groups. The single administration group animals were further divided into the blank control group, model group, and administration group (who were administered doses at rates of 65 mg/kg, 130 mg/kg, 260 mg/kg, and 520 mg/kg). At the same time, the long-term administration group was also subdivided into the blank control group, model group, and administration group (65 mg/kg and 520 mg/kg). The animals in the model and administration groups were allowed to feed freely in a single case and subjected to chronic unpredictable mild stress (CUMS) program to make the model. In contrast, the blank control group was fed in cages without subjecting to CUMS for 56 days. The institutional ethical review board approved the study protocol before starting any experiments on animals.

Following model development in the administration group, the animals were administered Shuganjiyeu capsules solution at dosages of 65 mg/kg, 130 mg/kg, 260 mg/kg, and 520 mg/kg, respectively. The blank and model groups were treated with the same amount of water twice a day for one day and then fasted.



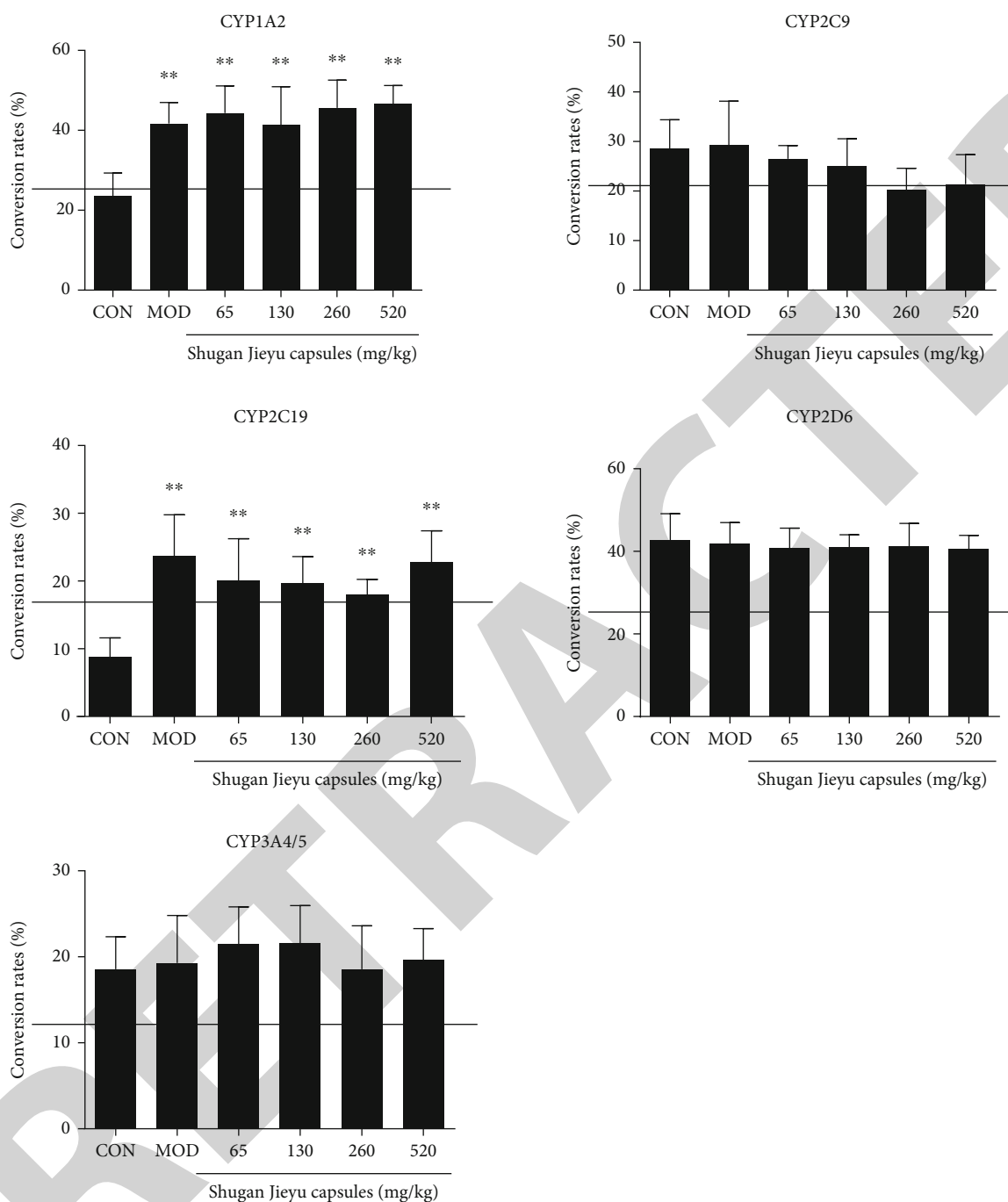


FIGURE 1: The conversion rate of P450 Enzyme in the single-dose subgroup. Compared with the blank group, \*\* means  $P < 0.01$ .

2.3. *Development of CUMS Depression Model.* CUMS program stimulation factors include the following [7]: overnight lighting, fasting, water banning, hot water swimming, and cold water swimming. The above stimulation factors were randomly assigned seven days a week, and two kinds of compound factor stimulation were randomly arranged daily.

The rat depression model was evaluated by measuring the rat body weight [8], rat sugar water preference [9], and rat immobility time [10].

2.4. *Extraction of Liver Microsomes and Determination of Protein Concentration.* The preparation of rat liver microsomes and the determination of protein content were done following the method reported earlier [11].

2.5. *Liver Microsome Incubation.* The total volume of liver microsome incubation system was 200  $\mu\text{L}$ , including 0.8 mg/mL liver microsomes, specific Cocktail probe substrate of each subenzyme (phenacetin 18  $\mu\text{M}$ , tolbutamide

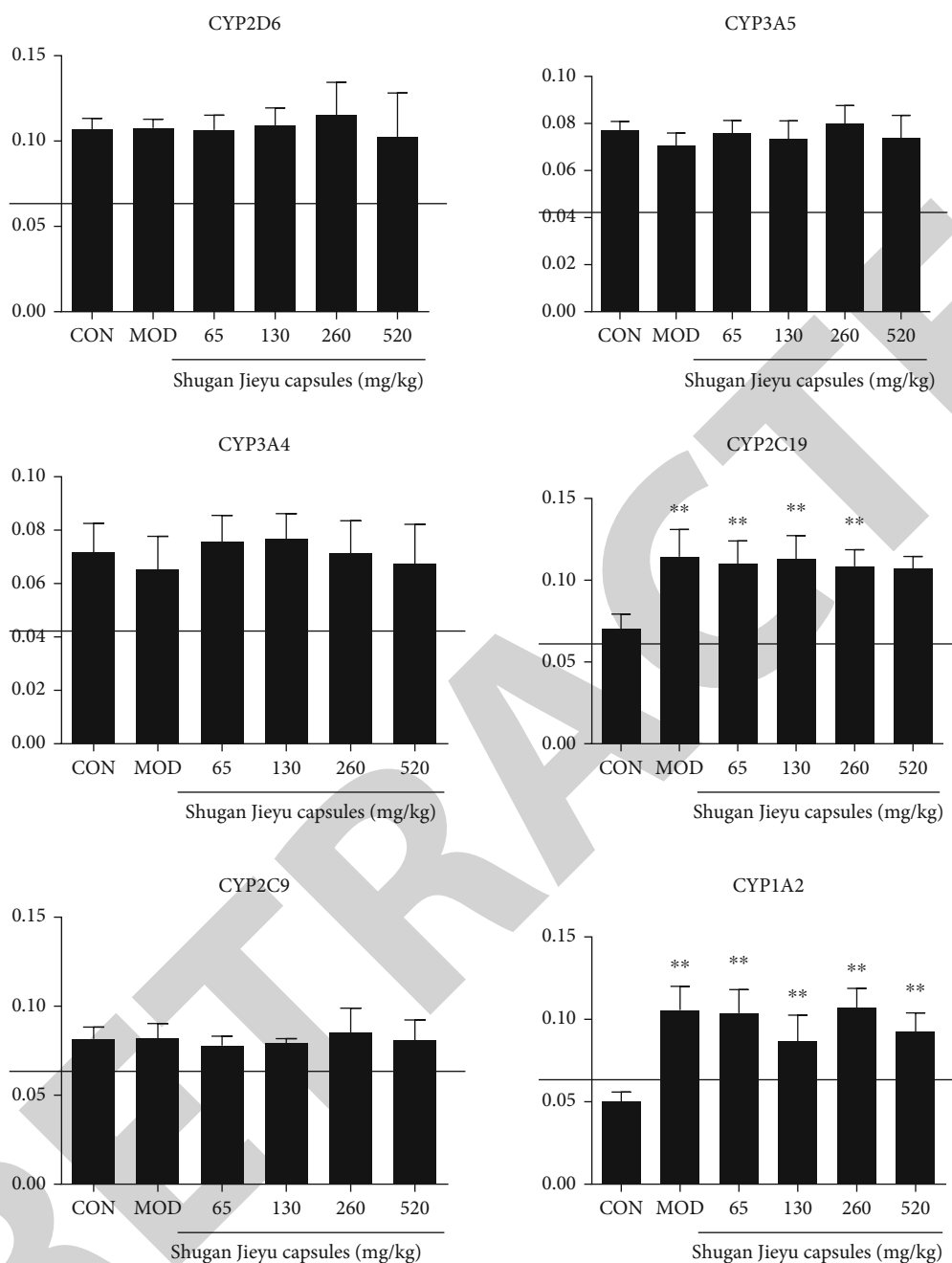


FIGURE 2: Immunohistochemical assay in the single-dose subgroup. Compared with the blank group, \*\* means  $P < 0.01$ .

18  $\mu\text{M}$ , dextromethorphan 20  $\mu\text{M}$ , omeprazole 12  $\mu\text{M}$ , and testosterone 80  $\mu\text{M}$ ), with an added phosphoric acid buffer (0.1 mol/L, pH = 7.4) to make up the system to 180  $\mu\text{L}$ . The system was preincubated for 10 min in a water bath maintained at 37°C, followed by the addition of 20  $\mu\text{L}$  of NADPH. The mixture was again preincubated for 10 min at the same time to start the reaction and further incubated at 37°C in a water bath for 90 min. Following that, a total of 200  $\mu\text{L}$  of an internal standard containing 0.4  $\mu\text{M}$  cold terminator of dexamethasone was added to terminate the reaction, and the mixture was then vortexed at 18000  $\times$  g.

The chromatographic conditions for establishing the metabolite analysis method comprised phase A as an aque-

ous solution containing 0.1% formic acid and phase B comprised acetonitrile solution containing 0.1% formic acid. The mobile phase flow rate was adjusted to 0.2 mL/min. The optimal elution conditions were as follows: 0-2.2 minutes, 20-21% B; 2.2-8.5 minutes, 21-90% B; 8.5-9 minutes, 90-92% B; 9-9.3 minutes, 92% B; 9.3-9.6 minutes, 92-20% B; and 9.6-11.5 minutes, 20% B.

Mass spectrometric conditions for establishing analytical methods for metabolites comprised of positive ion mode for data collection. The mass scanning range was set at 100~1000 m/z, with a drying air flow rate of 9 L/min. The temperature of dry gas was fixed at 350°C, and 150 V was used as fragmentation voltage. Before measuring the sample, the

TABLE 5: Effect of CUMS model on rat body weight ( $n = 6$ ).

Group	Dose (mg/kg)	Weight before modeling (g)	Body weight on 56th day of modeling (g)	Body weight after three months of administration (g)
Blank group	—	212.22 ± 4.57	465.75 ± 13.78	488.17 ± 21.97
Model group	—	214.48 ± 9.53	334.02 ± 20.41**	377.83 ± 22.94**
Administration group	65	212.12 ± 7.62	328.17 ± 27.89**	486.47 ± 24.06##
	520	215.17 ± 6.97	325.2 ± 26.31**	485.67 ± 22.83##

Compared with the blank group, \*\* means  $P < 0.01$ . Compared with the model group, ## means  $P < 0.01$ .

TABLE 6: Effect of CMUS model on sucrose preference test ( $n = 6$ ).

Group	Dose (mg/kg)	Sugar water preference before modeling (%)	Sugar water preference after 56 days of modeling (%)	Sugar water preference after three months of administration (%)
Blank group	—	82.41 ± 7.03	82.56 ± 7.45	84.25 ± 7.47
Model group	—	84.36 ± 6.77	54.91 ± 8.81**	56.97 ± 8.71**
Administration group	65	83.37 ± 9.95	50.48 ± 14.85**	84.6 ± 7.75##
	520	80.43 ± 7.75	53.09 ± 10.43**	84.35 ± 6.4##

Compared with the blank group, \*\* means  $P < 0.01$ . Compared with the model group, ## means  $P < 0.01$ .

TABLE 7: Effect of CUMS model on forced swim test ( $n = 6$ ).

Group	Dose (mg/kg)	56-day swimming immobility time for modeling (S)	Swimming immobility time for three months after administration (S)
Blank group	—	12.67 ± 5.61	9.5 ± 3.83
Model group	—	45 ± 29.4**	45 ± 16.12**
Administration group	65	41.83 ± 17.5**	11.17 ± 4.71##
	520	40.67 ± 17.19**	10.67 ± 4.08##

Compared with the blank group, \*\* means  $P < 0.01$ . Compared with the model group, ## means  $P < 0.01$ .

calibration solution was used to calibrate the mass axis, and the mass accuracy error was adjusted to be less than 10 ppm.

**2.6. Immunohistochemical Detection.** Paraffin sections of the liver tissue were stained with microwave repair antigen, slightly counterstained with hematoxylin, dehydrated, transparent, neutral gum sealing, and examined under a microscope. The micro camera system was used to collect the images of the slices; the average optical density of the collected images was measured by Image-Pro Plus image analysis software.

**2.7. Detection of mRNA Expression by RT-qPCR.** Trizol reagent was used to extract total RNA from tissues as per instructions provided by the manufacturer. Reverse transcription synthesis of cDNA was done with Goldenstar™ DNA Synthesis SuperMix reagent, with GAPDH as an internal reference. The PCR product was amplified with Eva-Green 2X qPCR MasterMix kit after adding the primer of the target gene as given in Table 1.

### 3. Statistical Treatment

SPSS 16.0 statistical software was used. Measurement data were expressed by  $x \pm s$ , and a  $t$ -test was used for comparison between groups. The difference was statistically significant when  $P < 0.05$ .

### 4. Result

#### 4.1. Experimental Results of Single Administration Subgroup

**4.1.1. Establishment of CUMS Depression Model and Behavioral Evaluation after Administration.** There were significant differences in body weight, sugar water preference, and immobility time between the model group, the administration group, and the blank group, indicating that the CUMS model was successful. The results are shown in Tables 2–4.

**4.1.2. Liver Microsome Incubation.** It can be seen from Figure 1 that the conversion rates of CYP1A2 and CYP2C19

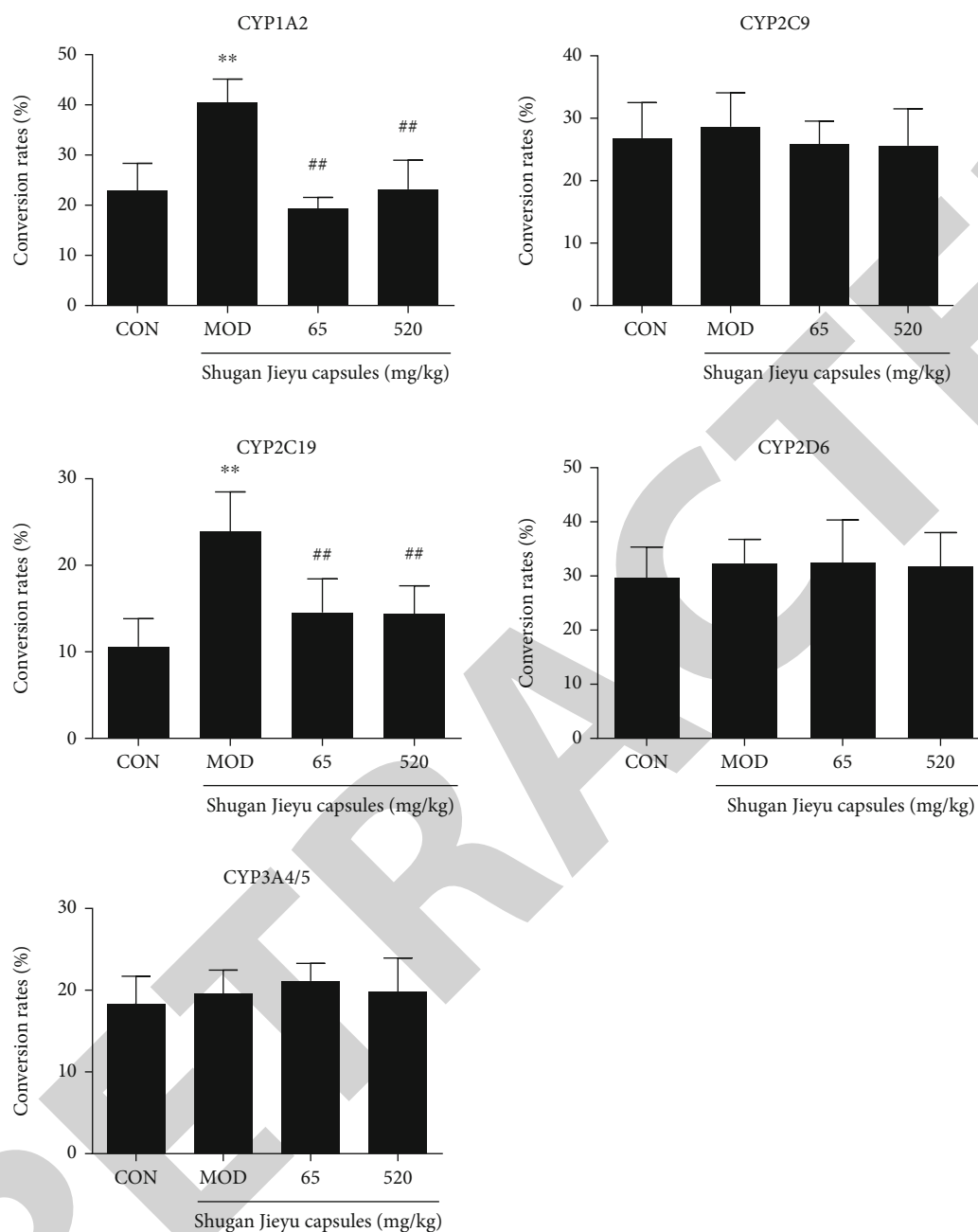


FIGURE 3: The conversion rate of the P450 Enzyme in the multiple-dose subgroup. Compared with the blank group, \*\* means  $P < 0.01$ . Compared with the model group, ## means  $P < 0.01$ .

in the model group and the administration group were significantly higher than those in the blank group. The metabolic conversion rates of other enzymes did not change significantly, indicating that chronic unpredictable stimulation could induce CYP1A2 and CYP2C19 in rats and had no significant effect on CYP2D6, CYP3A4/5, and CYP2C9. A single dose of the Shuganjieyu capsule did not affect the activities of P450 enzymes.

**4.1.3. Immunohistochemical Detection.** It can be seen from Figure 2 that the protein expression of CYP1A2 and CYP2C19 in the model group and the administration group was significantly higher than that in the blank group. The

metabolic conversion rates of other enzymes were not significantly changed, indicating that chronic unpredictable stimulation could promote the protein expression of CYP1A2 and CYP2C19 in rats and had no noticeable effect on CYP2D6, CYP3A4/5, and CYP2C9. A single dose of the Shuganjieyu capsule did not affect the protein expression of P450 enzymes.

## 4.2. Experimental Results of Long-Term Administration Subgroup

**4.2.1. Establishment of CUMS Depression Model and Behavioral Evaluation after Administration.** The results

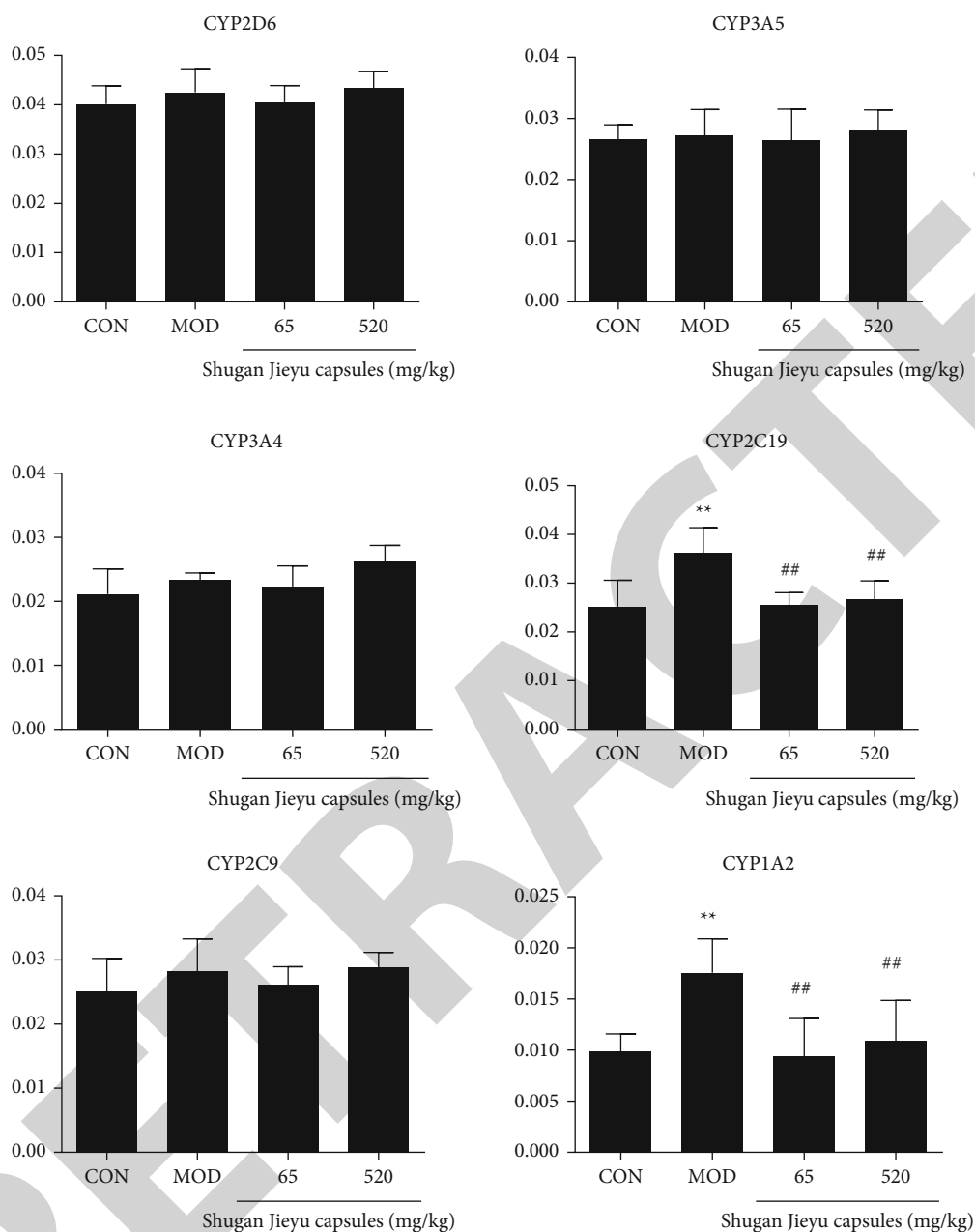


FIGURE 4: Immunohistochemical assay in the multiple-dose subgroup. Compared with the blank group, \*\* means  $P < 0.01$ . Compared with the model group, ## means  $P < 0.01$ .

showed that the body weight and sugar water preference of CUMS rats were significantly lower than those of blank rats, and the immobility time of CUMS rats was significantly higher than that of blank rats. After three months of the administration, the body weight and sugar water preference of rats in the administration group were significantly higher than those in the model group. It shows that the Shuganjieyu capsule can treat the behavioral effects of chronic unpredictable stimuli on rats. (Tables 5–7).

**4.2.2. Liver Microsome Incubation.** It can be seen from Figure 3 that the conversion rates of CYP1A2 and CYP2C19 in the model group were significantly higher than those in

the blank group. The increase could be reversed in the administration group, and the metabolic conversion rates of other enzymes did not change significantly. The results showed that the Shuganjieyu capsule could inhibit the increase of liver CYP1A2 and CYP2C19 activities induced by the CUMS model in rats.

**4.2.3. Immunohistochemical Detection.** It can be seen from Figure 4 that the protein expression of CYP1A2 and CYP2C19 in the model group was significantly higher than that in the blank group, and the increase could be reversed in the Shuganjieyu capsule group, while the expression of other enzymes was not significantly changed. The results

## *Retraction*

# **Retracted: The Connection between High Myopia Patients and MiR-708a or MiR-148 Expression Levels in Aqueous Studies of Visual Acuity**

### **BioMed Research International**

Received 8 January 2024; Accepted 8 January 2024; Published 9 January 2024

Copyright © 2024 BioMed Research International. This is an open access article distributed under the Creative Commons Attribution License, which permits unrestricted use, distribution, and reproduction in any medium, provided the original work is properly cited.

This article has been retracted by Hindawi following an investigation undertaken by the publisher [1]. This investigation has uncovered evidence of one or more of the following indicators of systematic manipulation of the publication process:

- (1) Discrepancies in scope
- (2) Discrepancies in the description of the research reported
- (3) Discrepancies between the availability of data and the research described
- (4) Inappropriate citations
- (5) Incoherent, meaningless and/or irrelevant content included in the article
- (6) Manipulated or compromised peer review

The presence of these indicators undermines our confidence in the integrity of the article's content and we cannot, therefore, vouch for its reliability. Please note that this notice is intended solely to alert readers that the content of this article is unreliable. We have not investigated whether authors were aware of or involved in the systematic manipulation of the publication process.

Wiley and Hindawi regrets that the usual quality checks did not identify these issues before publication and have since put additional measures in place to safeguard research integrity.

We wish to credit our own Research Integrity and Research Publishing teams and anonymous and named external researchers and research integrity experts for contributing to this investigation.

The corresponding author, as the representative of all authors, has been given the opportunity to register their agreement or disagreement to this retraction. We have kept a record of any response received.

### **References**

- [1] J. Shen, H. Lou, Q. Yu, H. Yao, and J. Yuan, "The Connection between High Myopia Patients and MiR-708a or MiR-148 Expression Levels in Aqueous Studies of Visual Acuity," *BioMed Research International*, vol. 2022, Article ID 3363830, 7 pages, 2022.

## Research Article

# The Connection between High Myopia Patients and MiR-708a or MiR-148 Expression Levels in Aqueous Studies of Visual Acuity

Jiang Shen , Hong Lou, Qihua Yu, Hongyan Yao, and Jianshu Yuan

Department of Ophthalmology, Ningbo Eye Hospital, Ningbo, 315040 Zhejiang, China

Correspondence should be addressed to Jiang Shen; [mrogers14@une.edu](mailto:mrogers14@une.edu)

Received 24 July 2022; Revised 13 August 2022; Accepted 20 August 2022; Published 13 October 2022

Academic Editor: Nauman Rahim Khan

Copyright © 2022 Jiang Shen et al. This is an open access article distributed under the Creative Commons Attribution License, which permits unrestricted use, distribution, and reproduction in any medium, provided the original work is properly cited.

Myopia goes far beyond the inconvenience it brings. It is a prevailing and vision-threatening eye disease, especially in Asia. Aberrantly expressed miR-708a and miR-148 are critical for accurate diagnosis, good prognosis, and precise response prediction of myopia. In this paper, we aim to examine the potential contributions of miR-708a, miR-148a, and PAX6 to high myopia (HM). First, aqueous samples were taken from 25 exclusively HM eyes and 25 exclusively cataract eyes. For next-generation sequencing and bioinformatics analysis, RNA from sample 30one was used. Twenty more samples were used for RT-qPCR. 341 miRNAs in total were found in HM eyes; 249 mature miRNAs and 17 new miRNAs showed differential expression. The expression of hsa-miR-127-3p, hsa-let-7i-5p, and hsa-miR-98-5p was identified using RT-qPCR. MiR-708a and miR-148, which may be linked to the development of myopia and serve as possible biomarkers, are notably highly expressed in atrial tissues of HM patients. Our findings may help deepen the understanding of the mechanisms behind the high expression of miR-708a and miR-148 in atrial tissues of patients with HM.

## 1. Introduction

Myopia is the most prevailing causative factor for refractive error (RE) globally. High myopia (HM) is severe, usually accompanied by fundus lesions [1]. Myopia is due to the mismatch between the eyes' axial length (AL) and the energy of its refractive components, resulting in the image focusing ahead the retina and blurring of vision in the distance [2]. As the leading contributor to RE, myopia results in impaired vision and even blindness [3, 4], with over 80% prevalence in young population in China and Singapore [5]. HM is regarded as a RE  $\leq -6.00$  diopters (D), usually along with excessive AL ( $\geq 26$  mm) and other complicating diseases, like retinal detachment, cataract, macular degeneration, and glaucoma, which are also known as pathological myopia [6].

Patients undergoing cataract surgery have many choices of intraocular lens (IOL), which depends on their requirements for spectacle independence and tolerance for latent visual disturbance. Bifocal and trifocal IOLs are superior to extended depth of focus (EDOF) or monofocal

IOLs, since they offer better near vision [7, 8]. Some researchers demonstrated that multifocal IOLs were more prone to visual disturbance than EDOF lenses, but others reported no difference [9, 10]. Previously studied EDOF and multifocal IOLs are related to higher rates of visual disturbance compared to monofocal IOLs [7], however which may be addressed by EDOF lens with monovision correction since IOL effect and monovision offset will produce cumulative effects [11]. Besides, relative to traditional implantable collamer lens (ICL) without central hole, it is more effective in diminishing major postoperative complication, cataract [12, 13], possibly due to the improved aqueous humor (AqH) circulation to the crystalline lens anterior surface [14]. However, as our findings elicited, ICL implantation will cause corneal astigmatism of about 0.5 diopter (D) with-the-rule shift [15]. The upper corneal incision may help to reduce astigmatism clinically, and subsequent vertical ICL fixation is easier to operate than horizontal fixation since ICL rotation is no more needed. However, the efficacy of this novel technique remains unclear [16].

MicroRNAs (miRNAs) are noncoding RNAs consisting of 19 to 22 nucleotides (nt) [17]. It is of importance to understand aberrantly expressed miRNAs in myopia. A previous study assessing the peripheral blood of myopia patients revealed the association between highly expressed miR-328 and the miR-29a rs157907 A/G polymorphism with HM incidence [18]. Understanding the possible intraocular profiling and regulation of miRNAs is imperative since they are tissue/cell-specific [19]. miRNA profiling was only studied in ocular tissues of myopia murine models, and the results were contradictory [20, 21]. In human AqH, compared with circulating blood, miRNA expression was eye-specific [22]. The miRNAs in AqH were thought to involve in eye development and diseases [23]. Paired box protein 6 (PAX6) is crucial for eye and retinal development [24]. It modulates the levels of transcription factors, hormones, cell adhesion molecules, and structural proteins [25] and thus involved in major biological processes, like adhesion, signal transduction, and cell proliferation in physiological and pathological progresses [26, 27].

Therefore, investigating this procedure may offer promising insights into the improvement of HM. We choose 25 exclusively HM eyes and 25 exclusively cataract eyes as aqueous samples and selected miR-708a and miR-148 as the two miRNAs. We used SPSS 21.0 to analyze data and applied the *t*-test for pairwise comparison and one-way ANOVA and Tukey's test for multi-group comparisons. We believe that our research could develop innovative options to improve the management of myopia.

## 2. Materials and Methods

**2.1. Sample Collection.** Patients looking for correction of HM at our institution were recruited, while those with mild to moderate cataracts undergoing ultrasound emulsion surgery served as controls. Each participant provided written informed consent. The study was ratified by ethics committee and followed the Declaration of Helsinki.

Inclusion criteria for HM group included (1)  $\geq 18$  years; (2) AL  $\geq 26$  mm; (3) RE (spherical equivalent)  $> 6.00$  D prior to the operation; (4) without other ocular diseases (except myopia). Inclusion criteria for the cataract group included (1)  $\geq 18$  years; (2) AL between 22 and 24 mm; (3) age-related mild/moderate cataract (e.g., nuclear, cortical, and posterior subcapsular cataracts) diagnosed by dilated pupil examination with slit lamp; without premature, complex and congenital cataract; (4) without any ocular diseases. Participants with serious systemic disease or a history of endophthalmitis surgery or ocular trauma were excluded from both groups. Only one eye was included from each participant. The AL of all participants was determined by an experienced clinician with an IOL Master (Carl Zeiss, Jena, Germany). Next, all subjects were allocated to the group A (HM) and group B (controls) as per the above criteria.

**2.2. Aqueous Samples.** The Aqueous (100-150  $\mu$ L) was first harvested from each included eye under sterile conditions through an anterior chamber puncture and centrifuged

(3,000  $\times$  g, 5 min, 4°C; 12,000  $\times$  g, 20 min, 4°C) immediately to discard cells and cellular debris. To avoid blood contamination, collect Aqueous before performing any conjunctival or intraocular procedures.

The Aqueous harvested from 3 eyes was mixed (300  $\mu$ L Aqueous per sample). Thereby, we got 5 samples from each group. Meanwhile, total RNA was extracted by means of TRIzol reagent (Life Technologies, USA) and then preserved at -80°C.

**2.3. miRNA Sequencing and RT-qPCR.** The miRNA sequencing library was built by each RNA sample with an initial RNA amount (100 ng) and TruSeq RNA Library Preparation Kit (RS-122-2301; Illumina). Following cDNA synthesis, PCR amplification and PAGE were conducted to retrieve PCR products of 0-150 bp (0-22 nt miRNA) and sequencing library quality was determined using the Bioanalyzer. The RNA yield of the sequencing libraries was tested through the ABI StepOnePlus RT-PCR System (Life Technologies, Inc.). Subsequently, sequencing libraries were denatured to single-stranded DNAs and captured into Illumina flow cells, followed by amplification in situ. Sequencing 50 cycles were conducted using the Hieq4000 sequencing platform (Illumina, USA) with Q30 as a quality control. Based on the principal algorithm of miRDeep, differential miRNAs are distinguished from small RNA fragments based on miRNAs location and frequency, loop fragments on miRNA \* and precursor sequences, minimal free energy and stability, 2008 and similarity. 5'ends of recognized mature miRNAs (Friedlander et al.)

The original sequencing data were subsequently eliminated and filtered and normalized to the number of tags per million paired miRNAs. miRNA profiles were verified by arranging the miRNA expression in a descending order and miRDeep2 software (<https://www.mdc-berlin.de/content/mirdeep2-documentation>) was utilized to forecast differential miRNAs, ploidy changes, *p*-values (probability values), and FDRs (*p*-values corrected by the Benjamini-Hochberg method). Differentially expressed miRNAs were distinguished as ploidy change  $\geq 2.0$  and  $p \leq 0.05$ .

After RNA extraction, protein concentration was testified using a NanoDrop 1000 spectrophotometer (Thermo Fisher Scientific, USA) and RNA quality was assessed by a Bioanalyzer (2100, Agilent Technologies), and cDNA was synthesized by the PrimeScript synthesis cDNA kit (Takara, Japan). SYBR Green PCR Master Mix (Takara) was adopted for qPCR to normalize miR-708a/miR-148 expression to U6.

**2.4. Dual-Luciferase Assay and Data Analysis Methods.** Online software TargetScan predicted binding sites of miR-708a/miR-148 and PAX6. PCR amplified the complementary binding sequences of miR-708a, miR-148, and PAX6, respectively, and cloned them into the pmiR-GLO (Promega, USA) to construct PAX6-WT and PAX6-MUT, which were mixed with mimics NC and miR-708a and miR-148mimics, respectively, and transfected into HEK-293T cells after mixing with Lipofectamine™ 2000 liposomes for 48, followed by detecting luciferase activity.



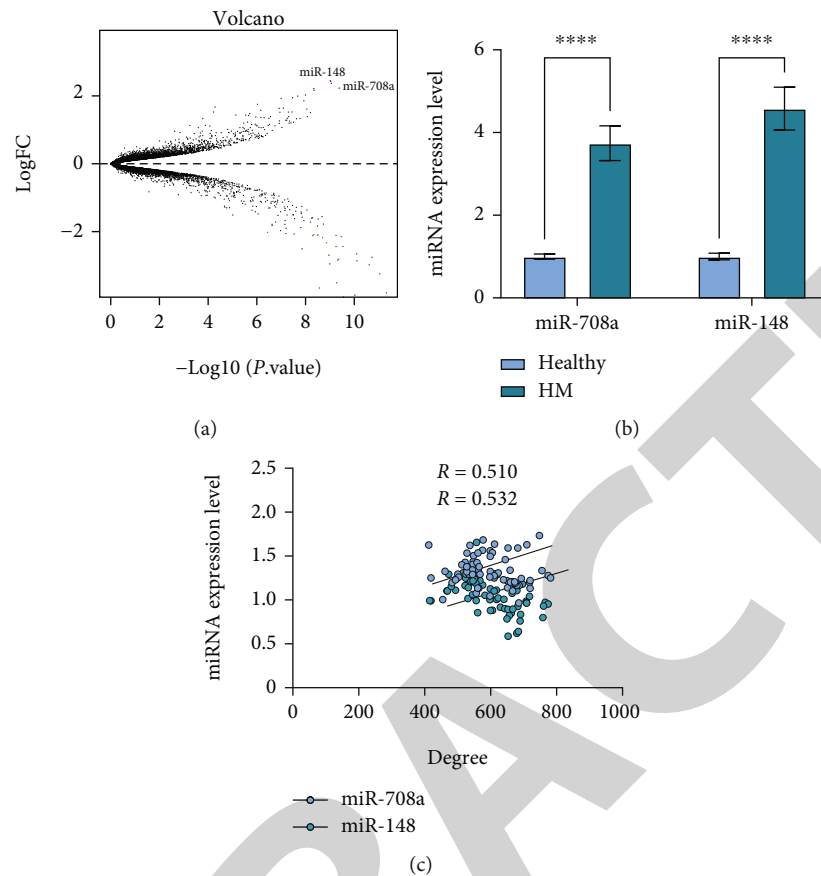


FIGURE 1: High miR-708a/miR-148 expression in the Aqueous of HM patients. Figure 1(a) shows the DE miRNAs in the Aqueous of HM patients analyzed by sequencing. Figure 1(b) shows that qRT-PCR detected the miR-708a and miR-148 expression in HM patients and cataract patients.

SPSS 21.0 (IBM Corp. Armonk, NY, USA) was employed for data analyses. Data were normally distributed as the Kolmogorov-Smirnov test confirmed and depicted as mean  $\pm$  standard deviation. The *t*-test was applied for pairwise comparison and one-way ANOVA and Tukey's test were applied for multi-group comparisons. Fisher's exact test was adopted for counting data; correlation analysis was undertaken by Pearson's test; ROC curves were then plotted to evaluate the effect of serum miR-708a/miR-148. *p*-value was attained from two-sided tests and  $p < 0.05$  indicated statistically significant.

### 3. Experimental Results

**3.1. High miR-708a/miR-148 Expression in Aqueous in HM Patients.** We discovered 341 miRNAs in the Aqueous of HM eyes by sequencing (Figure 1(a)). Based on it, we selected miR-708a and miR-148 as the two miRNAs with the most significant expression differences in sequencing. The miR-708a and miR-148 levels in the Aqueous detected by qPCR were markedly higher in HM patients than cataract patients (Figure 1(b)). Besides, we analyzed the correlation between the myopia of HM patients and miR-708a/miR-148 expression, and we noticed that as miR-708a/miR-148

expression increased, the patients also had notably higher reading (Figure 1(c)).

**3.2. miR-708a/miR-148 Targeted PAX6.** To further clarify the mechanism of action of miR-708a/miR-148, we used TargetScan and RNA Hybrid website to predict and screen miR-708a/miR-148 downstream targets, and we screened to PAX6 (Figure 2(a)). Subsequently, we first verified the target binding relationship between miR-708a and miR-148 and PAX6 using dual luciferase, respectively, and we found reduced luciferase activity in 293T cells delivered with miR-708a and miR-148mimic, and no apparent change in cells with mimic NC or PAX6-MT (Figures 2(b)–2(c)), indicating that miR-708a and miR-148 can have a target binding relationship with the 3'-UTR sequence of PAX6.

**3.3. PAX6 Is Low-Expressed in the Aqueous of HM Patients.** To verify that PAX6 is modulated by miR-708a/miR-148, we first compared the PAX6 levels in HM patients and cataract patients through RT-qPCR and ELISA, which showed lower PAX6 levels in the Aqueous of HM patients (Figures 3(a)–3(b)). Besides, PAX6 was negatively correlated with miR-708a and miR-148 (Figures 3(c)–3(d)), and

Predicted consequential pairing of target region (top) and miRNA (bottom)	Site type	Context <sup>++</sup> score	Context <sup>++</sup> score percentile	Weighted context <sup>++</sup> score	Conserved branch length	P <sub>CT</sub>
5' ...GCAAGAUUCAGUUGGAACAAAU... 3' AGUGCGUCUGGCUUGCUUGUUU	7 mer-A1	-0.15	94	-0.15	7.041	0.35

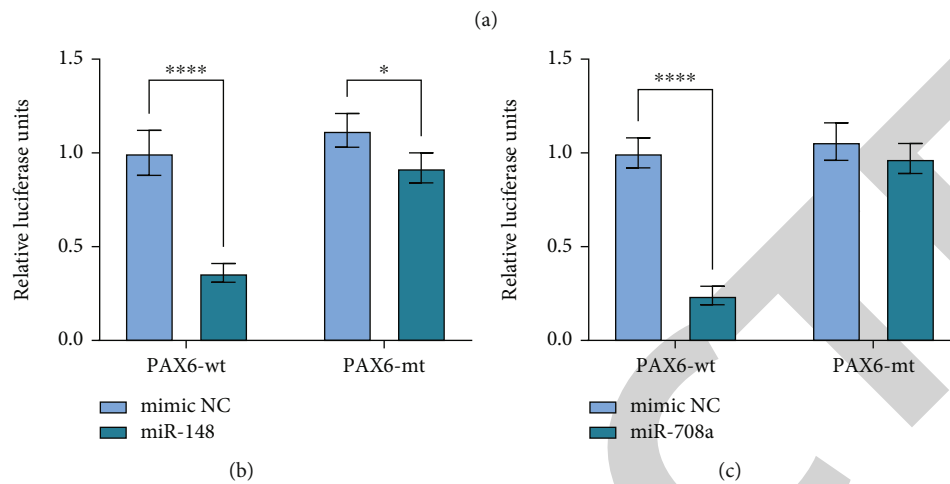


FIGURE 2: miR-708a/miR-148 target PAX6. (a) Bioinformatics analysis of miR-708a or miR-148 targeting mRNAs by TargetScan and RNA hybrid software. (b~c) Determination of binding relationship of miR-708a/miR-148 and PAX6.

positively correlated with the visual acuity level of the patients (Figure 3(e)).

#### 4. Discussion

Without enough intervention, the current prevalence of myopia is supposed to 50% of the world's population by 2050 and become the main reason of irreversible blindness. Though the main symptom blurred vision can be improved through contact lenses, glasses, or refractive surgery, correcting myopia, especially HM, is still in risk of secondary blinding complications, like myopic maculopathy, glaucoma, and retinal detachment, so it needs to be prevented [28]. This is particularly of concern for HM patients [ $> -5$  Dioptres (D)] who have the risk of pathologic myopia and other related eye diseases such as retinal detachment, choroidal neovascularization, glaucoma, and myopic macular degeneration [29, 30]. Pathological myopia is the chief contributor to visual disturbance and blindness in Asian [31].

Tears, vitreous humor, and AqH are main sources of fluids containing extracellular miRNAs in eyes [32, 33]. Several reports have revealed highly expressed miR-29a in AqH of myopia patients and it prevented collagen I synthesis in SF cells, indicating its importance in myopia development [34]. The AqH analysis is very useful to study the molecular mechanism of axial elongation essential for myopia and to understand the role in HM, which will help to develop new therapeutic approaches [35, 36]. As an intraocular fluid, AqH provides nutrition and eliminates metabolic wastes from avascular tissues, which is utilized to determine the link of changed protein levels and prognoses of several eye diseases [37, 38]. Nevertheless, no proteomic study has reported the mechanism

behind HM-induced eye injury. Proteomics could display high-throughput quantitative protein levels, providing theoretical foundation and methods to verify the mechanism [39]. Recent research showed miR-328 was higher in peripheral blood of myopia patients than controls [18]. PAX6 is a key player in eye development and shows low expression in myopia patients [40, 41]. Some studies have provided a comprehensive miRNA profiling of AqH in HM through next-generation sequencing. Regarding aberrant expression of miRNAs in myopia, combined with informatics analyses, it is suggested to confirm these results [42].

Our experiment was completed in three steps. First, we selected miR-708a and miR-148 as the two miRNAs with the most significant expression differences in sequencing. The expression levels of miR-708a and miR-148 detected using qPCR were notably higher in atrial fluid of HM patients than cataract patients, and we found that miR-708a/miR-148 were markedly higher in atrial fluid of HM patients. Then, to clarify the mechanism of miR-708a/miR-148, we used TargetScan and RNA Hybrid website to predict and screen the downstream targets of miR-708a/miR-148. We screened to PAX6, and we confirmed that miR-708a and miR-148 target PAX6 mRNA 3'-UTR sequence. Finally, RT-qPCR and Western blotting examined the level of lncRNA, miRNA, mRNAs, and proteins. Functional experiments measured cell proliferation, apoptosis, and migration. Additionally, the luciferase assay validated the relation of ZFPM2-AS1, miR-511-3p, and PAX6 [43]. With the attention to confirm that PAX6 is modulated by miR-708a/miR-148, we firstly compared PAX6 levels in atrial water from HM patients and cataract patients by RT-qPCR and ELISA, which revealed elevated PAX6 in serum of neonatal retinopathy patients relative to healthy participants. However, this

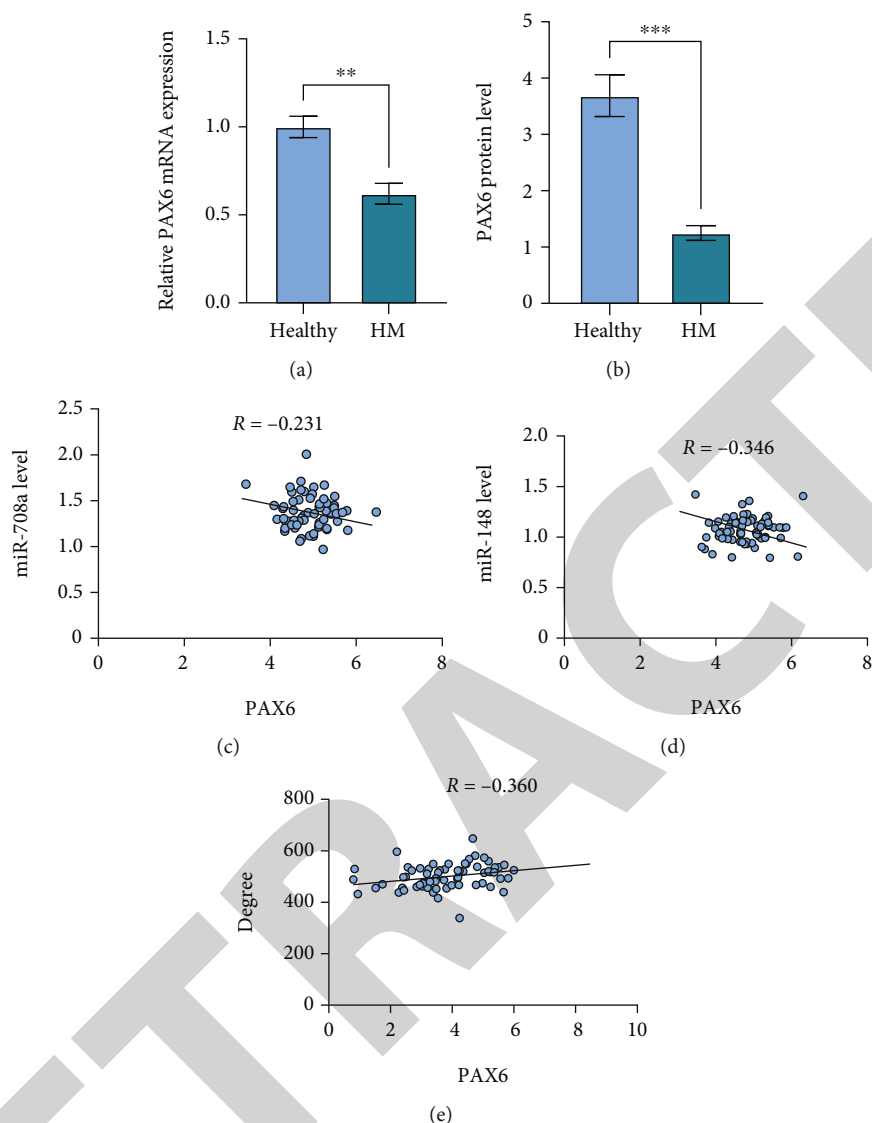


FIGURE 3: PAX6 is upregulated in neonatal retinopathy patients, in comparison with healthy participants. (a~b) qRT-PCR and ELISA to detect PAX6 levels in Aqueous of HM patients and cataract patients. (c~d) Pearson's analysis of miR-708a/miR-148 with PAX6 levels. (e) Pearson's analysis of PAX6 levels with myopia in HM patients.

study may have a positive bias, since the older the age, the greater the choroidal atrophy [44]. Although some therapeutic interventions have improved the HM, its pathogenesis is still unclear.

## 5. Conclusion

In summary, miR-708a and miR-148 are significantly highly expressed in atrial tissues of patients with HM, which may be related to the pathogenesis of myopia and are potential biomarkers. The current study provides a holistic view of miRNA profile in AqH of HM eyes. Those features are possibly related to the pathogenesis of myopia and are underlying biomarkers. Our study will yield good results in safety, predictability, efficacy, and stability.

However, there are some limitations. As a single-site and single-arm study with relatively small sample size, it cannot

be directly compared with other treatment designs. In addition, the lack of multiple clinical trials is one of our limitations. Long-term, careful follow-up of more patients is warranted to confirm our preliminary findings, and it is a target to become our treatment strategy.

## Data Availability

All data are available upon reasonable requests.

## Conflicts of Interest

The authors declared no potential conflicts of interest with respect to the research, authorship, and/or publication of this article.

## References

- [1] F. Zhao, W. Chen, H. Zhou et al., "PDE4B proposed as a high myopia susceptibility gene in Chinese population," *Frontiers in genetics*, vol. 12, article 775797, 2021.
- [2] B. J. Carr and W. K. Stell, *Webvision: The Organization of the Retina and Visual System*, H. Kolb, E. Fernandez, and R. Nelson, Eds., University of Utah Health Sciences Center, 1995.
- [3] B. Cho, J. Shin, and H. J. E. Yu, "Complications of pathologic myopia," *Eye & contact lens*, vol. 42, no. 1, pp. 9–15, 2016.
- [4] D. Flitcroft, M. He, J. B. Jonas et al., "IMI - defining and classifying myopia: a proposed set of standards for clinical and epidemiologic studies," *Investigative ophthalmology & visual science*, vol. 60, no. 3, pp. M20–M30, 2019.
- [5] J. Sun, J. Zhou, P. Zhao et al., "High prevalence of myopia and high myopia in 5060 Chinese university students in Shanghai," *Investigative ophthalmology & visual science*, vol. 53, pp. 7504–7509, 2012.
- [6] M. Zejmo, M. Formińska-Kapuścik, E. Pieczara et al., "Etiopathogenesis and management of high-degree myopia. Part I," *Medical science monitor: international medical journal of experimental and clinical research*, vol. 15, no. 9, pp. RA199–RA202, 2009.
- [7] L. Rodov, O. Reitblat, A. Levy, E. I. Assia, and G. Kleinmann, "Visual outcomes and patient satisfaction for trifocal, extended depth of focus and monofocal intraocular lenses," *Extended Depth of Focus and Monofocal Intraocular Lenses*, vol. 35, no. 7, pp. 434–440, 2019.
- [8] E. Pedrotti, F. Carones, P. Talli et al., "Comparative analysis of objective and subjective outcomes of two different intraocular lenses: trifocal and extended range of vision," *BMJ open ophthalmology*, vol. 5, no. 1, article e000497, 2020.
- [9] G. Monaco, M. Gari, F. Di Censo, A. Poscia, G. Ruggi, and A. Scialdone, "Visual performance after bilateral implantation of 2 new presbyopia-correcting intraocular lenses: trifocal versus extended range of vision," *Journal of Cataract & Refractive Surgery*, vol. 43, pp. 737–747, 2017.
- [10] B. Cochener, G. Boutillier, M. Lamard, and C. Auberger-Zagnoli, "A comparative evaluation of a new generation of diffractive trifocal and extended depth of focus intraocular lenses," *Journal of Refractive Surgery*, vol. 34, pp. 507–514, 2018.
- [11] T. H. Newsom and R. Potvin, "Evaluation of quality of vision and visual outcomes with bilateral implantation of a non-diffractive extended vision intraocular lens with a target of slight myopia in the non-dominant eye," *Clinical Ophthalmology (Auckland, NZ)*, vol. 16, pp. 183–190, 2022.
- [12] S. Kimiya, K. Kazutaka, I. Akihito, and K. Hidenaga, "Long-term comparison of posterior chamber phakic intraocular lens with and without a central hole (hole ICL and conventional ICL) implantation for moderate to high myopia and myopic astigmatism: consort-compliant article," *Medicine (Baltimore)*, vol. 95, no. 14, article e3270, 2016.
- [13] J. F. Alfonso, L. Fernández-Vega-Cueto, B. Alfonso-Bartolozzi, R. Montés-Micó, and L. Fernández-Vega, "Five-year follow-up of correction of myopia: posterior chamber phakic intraocular lens with a central port design," *Journal of refractive surgery*, vol. 35, pp. 169–176, 2019.
- [14] K. Fujisawa, K. Shimizu, S. Uga et al., "Changes in the crystalline lens resulting from insertion of a phakic IOL (ICL) into the porcine eye," *Graefe's Archive for Clinical and Experimental Ophthalmology*, vol. 245, pp. 114–122, 2007.
- [15] K. Kamiya, W. Ando, M. Takahashi, and N. Shoji, "Comparison of magnitude and summated vector mean of surgically induced astigmatism vector according to incision site after phakic intraocular lens implantation," *Eye and Vision*, vol. 8, no. 32, 2021.
- [16] K. Kamiya, W. Ando, H. Hayakawa, S. Gotoda, and N. Shoji, "Vertically fixated posterior chamber phakic intraocular lens implantation through a superior corneal incision," *Ophthalmology and therapy*, vol. 11, no. 2, pp. 701–710, 2022.
- [17] S. Aldridge and J. Hadfield, "Introduction to miRNA profiling technologies and cross-platform comparison," *Next-Generation MicroRNA Expression Profiling Technology*, vol. 32, pp. 19–31, 2012.
- [18] E. Kunceviene, R. Liutkeviciene, B. Budiene, M. Sriubiene, and A. J. G. Smalinskiene, "Independent association of whole blood miR-328 expression and polymorphism at 3'UTR of the PAX6 gene with myopia," *Gene*, vol. 687, pp. 151–155, 2019.
- [19] B. N. Davis and A. Hata, "Regulation of MicroRNA Biogenesis: A miRiad of mechanisms," *Cell Communication and Signaling*, vol. 7, no. 1, pp. 1–22, 2009.
- [20] A. V. Tkatchenko, X. Luo, T. V. Tkatchenko et al., "Large-scale microRNA expression profiling identifies putative retinal miRNA-mRNA signaling pathways underlying form-deprivation myopia in mice," *PLoS One*, vol. 11, no. 9, article e0162541, 2016.
- [21] Y. Tanaka, T. Kurihara, Y. Hagiwara et al., "Ocular-component-specific miRNA expression in a murine model of lens-induced myopia," *International journal of molecular sciences*, vol. 20, no. 15, 2019.
- [22] T. Wecker, M. Neuburger, L. Bryniok et al., "Ab interno trabeculectomy with the Trabectome as a valuable therapeutic option for failed filtering blebs," *Journal of Glaucoma*, vol. 25, no. 9, pp. 758–762, 2016.
- [23] B. Jiang, Y. Huo, Y. Gu, and J. Wang, "The role of microRNAs in myopia. Graefe's Archive for," *Clinical and Experimental Ophthalmology*, vol. 255, no. 1, pp. 7–13, 2017.
- [24] J. W. Park, J. Yang, and R. H. Xu, *PAX6 alternative splicing and corneal development*, vol. 27, no. 6, 2018MARY ANN LIEBERT, INC, 2018.
- [25] T. I. Simpson and D. J. Price, "Pax6; a pleiotropic player in development," *Bioessays*, vol. 24, no. 11, pp. 1041–1051, 2002.
- [26] J. Fang, T. Zhang, Y. Liu et al., "PAX6 downregulates miR-124 expression to promote cell migration during embryonic stem cell differentiation," *Stem cells and development*, vol. 23, no. 19, pp. 2297–2310, 2014.
- [27] X. Zhang, B. F. Li, J. Ding et al., "LncRNA DANCR-miR-758-3p-PAX6 molecular network regulates apoptosis and autophagy of breast cancer cells," *Cancer Cells*, vol. 12, pp. 4073–4084, 2020.
- [28] A. Muralidharan, C. Lança, S. Biswas et al., "Light and myopia: from epidemiological studies to neurobiological mechanisms," *Therapeutic Advances in Ophthalmology*, vol. 13, 2021.
- [29] S. M. Saw, G. Gazzard, E. C. Shih-Yen, and W. H. Chua, "Myopia and associated pathological complications," *Ophthalmic and Physiological Optics*, vol. 25, no. 5, pp. 381–391, 2005.
- [30] M. Ichibe, Yoshizawa, Murakami et al., "Surgical management of retinal detachment associated with myopic macular hole: anatomic and functional status of the macula," *American journal of ophthalmology*, vol. 136, pp. 277–284, 2003.

## Retraction

# Retracted: Development and Optimization of a Prognostic Model Associated with Stemness Genes in Hepatocellular Carcinoma

### BioMed Research International

Received 8 January 2024; Accepted 8 January 2024; Published 9 January 2024

Copyright © 2024 BioMed Research International. This is an open access article distributed under the Creative Commons Attribution License, which permits unrestricted use, distribution, and reproduction in any medium, provided the original work is properly cited.

This article has been retracted by Hindawi following an investigation undertaken by the publisher [1]. This investigation has uncovered evidence of one or more of the following indicators of systematic manipulation of the publication process:

- (1) Discrepancies in scope
- (2) Discrepancies in the description of the research reported
- (3) Discrepancies between the availability of data and the research described
- (4) Inappropriate citations
- (5) Incoherent, meaningless and/or irrelevant content included in the article
- (6) Manipulated or compromised peer review

The presence of these indicators undermines our confidence in the integrity of the article's content and we cannot, therefore, vouch for its reliability. Please note that this notice is intended solely to alert readers that the content of this article is unreliable. We have not investigated whether authors were aware of or involved in the systematic manipulation of the publication process.

Wiley and Hindawi regrets that the usual quality checks did not identify these issues before publication and have since put additional measures in place to safeguard research integrity.

We wish to credit our own Research Integrity and Research Publishing teams and anonymous and named external researchers and research integrity experts for contributing to this investigation.



The corresponding author, as the representative of all authors, has been given the opportunity to register their agreement or disagreement to this retraction. We have kept a record of any response received.

### References

- [1] K. Zhang, K. Xie, X. Huo et al., "Development and Optimization of a Prognostic Model Associated with Stemness Genes in Hepatocellular Carcinoma," *BioMed Research International*, vol. 2022, Article ID 9168441, 28 pages, 2022.

## Research Article

# Development and Optimization of a Prognostic Model Associated with Stemness Genes in Hepatocellular Carcinoma

Kefen Zhang,<sup>1,2</sup> Kaisheng Xie,<sup>2</sup> Xin Huo,<sup>3</sup> Lianlian Liu,<sup>4</sup> Jilin Liu,<sup>4</sup> Chao Zhang ,<sup>4</sup> and Jun Wang <sup>3</sup>

<sup>1</sup>Guangxi University of Science and Technology, Liuzhou 545006, China

<sup>2</sup>Department of Pathology, Second Affiliated Hospital of Guangxi University of Science and Technology, Liuzhou 545006, China

<sup>3</sup>Department of Oncology, Liuzhou People's Hospital Affiliated to Guangxi Medical University, Liuzhou 545006, China

<sup>4</sup>College of Information Science and Engineering, Shandong Agricultural University, Tai'an 271000, China

Correspondence should be addressed to Chao Zhang; [zhangch@sdau.edu.cn](mailto:zhangch@sdau.edu.cn) and Jun Wang; [wangsci@126.com](mailto:wangsci@126.com)

Received 19 August 2022; Accepted 8 September 2022; Published 5 October 2022

Academic Editor: Nauman Rahim Khan

Copyright © 2022 Kefen Zhang et al. This is an open access article distributed under the Creative Commons Attribution License, which permits unrestricted use, distribution, and reproduction in any medium, provided the original work is properly cited.

Hepatocellular carcinoma (HCC) is one of the most lethal cancers worldwide, which is associated with a variety of risk factors. Cancer stem cells are self-renewal cells, which can promote the occurrence and metastasis of tumors and enhance the drug resistance of tumor treatment. This study aimed to develop a stemness score model to assess the prognosis of hepatocellular carcinoma (HCC) patients for the optimization of treatment. The single-cell sequencing data GSE149614 was downloaded from the GEO database. Then, we compared the gene expression of hepatic stem cells and other hepatocytes in tumor samples to screen differentially expressed genes related to stemness. R package “clusterProfiler” was used to explore the potential function of stemness-related genes. We then constructed a prognostic model using LASSO regression analysis based on the TCGA and GSE14520 cohorts. The associations of stemness score with clinical features, drug sensitivity, gene mutation, and tumor immune microenvironment were further explored. R package “rms” was used to construct the nomogram model. A total of 18 stemness-related genes were enrolled to construct the prognosis model. Kaplan-Meier analysis proved the good performance of the stemness score model at predicting overall survival (OS) of HCC patients. The stemness score was closely associated with clinical features, drug sensitivity, and tumor immune microenvironment of HCC. The infiltration level of CD8<sup>+</sup> T cells was lower, and tumor-associated macrophages were higher in patients with high-stemness score, indicating an immunosuppressive microenvironment. Our study established an 18 stemness-related gene model that reliably predicts OS in HCC. The findings may help clarify the biological characteristics and progression of HCC and help the future diagnosis and therapy of HCC.

## 1. Introduction

Tumor heterogeneity is one of the main characteristics of HCC, which makes the progress of treatment slow [1, 2]. At present, there is still a lack of biomarkers and effective prognostic models for diagnosis, prognosis, and prediction of therapeutic efficacy of HCC. This further weakens the possibility of developing personalized treatment. Single-cell genomics is a powerful strategy to depict the complex molecular landscape of

cancer. Recent studies on the relationship between HCC cells and stem cell markers showed that the expression of EPCAM can effectively distinguish between stemness HCC cells and nonstemness HCC cells [3].

Cancer stem cells (CSCs) are self-renewal cells, which can promote the occurrence and metastasis of tumors and enhance the drug resistance of tumor treatment [4]. Transcriptome-based studies in multiple tumors have revealed a significant link between tumor stemness and patient prognosis and tumor

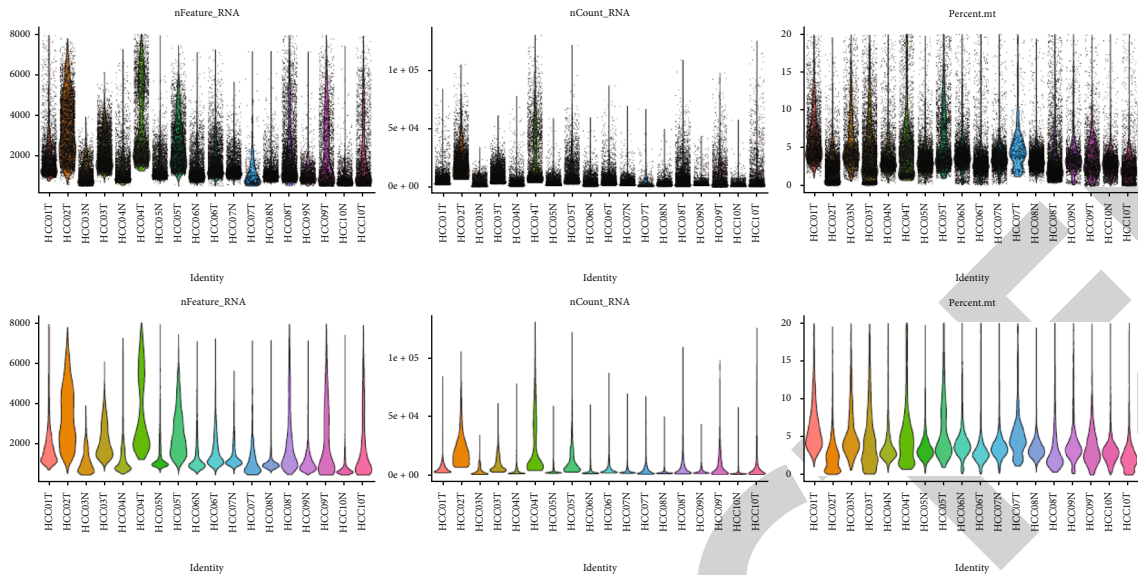


FIGURE 1: The expression distribution of single cell transcriptome.

immune microenvironment [5–7]. Recent studies have confirmed the effect of tumor stemness on immune cells in tumor microenvironment, namely, tumor-associated macrophages (TAMs), myeloid-derived suppressor cell (MDSC), and CD8<sup>+</sup> T cells. In turn, these immune cells also play an important role in maintaining tumor stemness, creating a malignant environment [8]. However, there are few studies on tumor stemness in HCC, especially the relationship between tumor stemness and immune microenvironment. In recent years, the tumor stemness has attracted much attention. The main characteristics of tumor stemness are the strong self-renewal ability and increased tumor heterogeneity [3–4]. Many studies have shown that tumor stemness plays an important role in tumor metastasis, differentiation, and drug resistance [9, 10]. For example, USP22 was reported to promote the stemness of HCC cells by HIF1a pathways [11]. In addition, RALYL could increase HCC stemness via sustaining the mRNA stability of TGF-beta2 [12]. HDAC11, AMD1, and SENP1 were also proved to promote the stemness of HCC cells [13–15]. However, the proven stemness-related genes are far from enough in HCC. Thus, it is necessary and urgent to screen stemness genes and construct the stemness-related prognosis model in HCC.

In our study, we downloaded the single-cell sequencing data GSE149614 to screen stemness genes by comparing the gene expression difference of hepatic stem cells and other hepatocytes. R-package “clusterProfiler” was used to explore the potential function of stemness-related genes. We then constructed a prognostic model using LASSO regression analysis based on the TCGA and GSE14520 cohorts. The associations of stemness score with clinical features, drug sensitivity, gene mutation, and tumor immune microenvironment were further explored. R package “rms” was used to construct nomogram model. Our study defined stemness-related genes and constructed stemness-related prognostic model, which may support new ideas for screening therapeutic targets to inhibit stem characteristics and the development of HCC.

## 2. Materials and Methods

**2.1. Data Collection.** The single-cell sequencing data GSE149614 and RNA array data GSE14520 were downloaded from GEO database (<https://www.ncbi.nlm.nih.gov/gds>). The RNAseq data and clinical information of TCGA were obtained from the UCSC Xena database (<https://xenabrowser.net/datapages/>). In GSE149614, we extracted the data of primary HCC and adjacent tissues for follow-up analysis, including 18 samples (10 cancer tissues, 8 adjacent tissues) and 63101 cells. In GSE14520, after removing the samples with nontumor and incomplete prognostic data, a total of 225 samples were enrolled for subsequent analysis. In TCGA, We selected 362 tumor samples with survival data for follow-up analysis.

**2.2. Identification of Stemness-Related Genes.** Based on the single-cell transcriptome sequencing data of GSE149614, the expression data were quality controlled, standardized, and clustered using the R package “Seurat” (v4.0.5). According to the expression of EPCAM (epithelial cell adhesion molecule) gene, we identified the liver stem cell population and hepatocytes according to the cell annotation information provided by the references [16]. Then, we compared the gene expression of hepatic stem cells and other hepatocytes in tumor samples to screen differential expressed genes related to stemness. Further, we used R-package “clusterProfiler” (v4.0.5) to perform the functional enrichment of stemness-related genes.

**2.3. Construction of Prognosis Model of HCC.** Based on stemness-related genes, LASSO (least absolute shrinkage and selection operator) regression analysis was conducted. The stemness-related genes related to prognosis were screened, and the prognostic risk assessment model was constructed. In order to improve the accuracy of the model, we first filter out the feature factors with high correlation, and the threshold

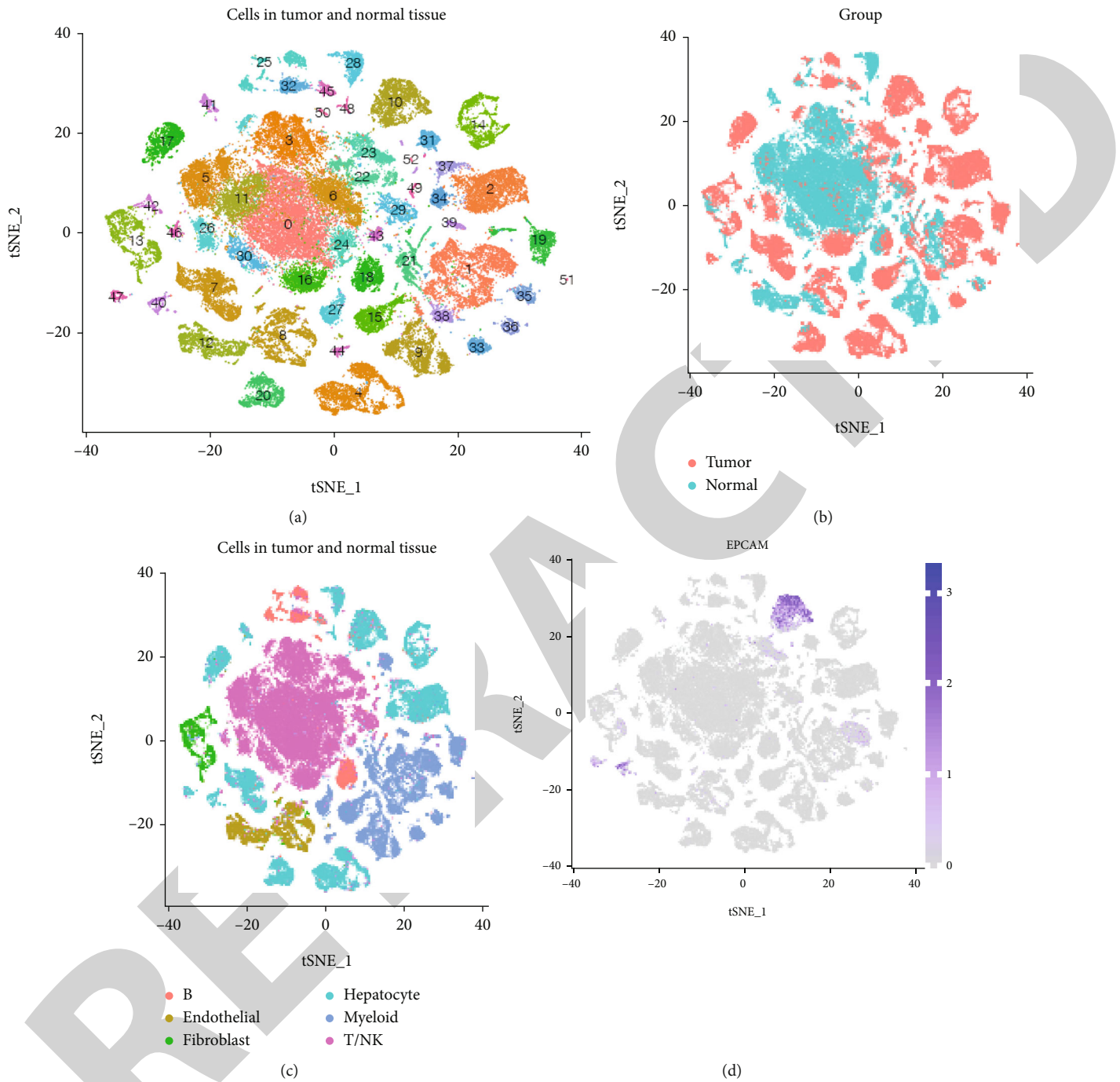


FIGURE 2: Cell clustering of GSE149614. (a) tSNE diagram shows the total clustering. (b) tSNE diagram shows the distribution of tumor cells and normal cells. (c) Cell annotation results. (d) The distribution of EPCAM.

is 0.8. The model construction is based on the R package “glmnet” (v4.1-2), and 10-fold cross-validation is selected. We finally constructed a prognostic risk prediction model containing 18 stemness-related genes. The model is as follows:  

$$\text{Stemness Score} = \text{AKR1B10} * 0.02688 + \text{AKR1C3} * 0.0214 + \text{BSG} * 0.05855 + \text{CD74} * (-0.07195) + \text{CLDN6} * 0.17068 + \text{CYP3A5} * (-0.01822) + \text{GLB1} * 0.005275 + \text{HSP90AA1} * 0.12853 + \text{HSPA6} * 0.002546 + \text{KRT19} * (-0.02418) + \text{MIF} * (-0.02593) + \text{NQO1} * 0.015396 + \text{NUPR}$$

$1 * 0.056 + \text{PDCD6IP} * 0.01709 + \text{PHLDA2} * 0.02894 + \text{PON1} * (-0.06318) + \text{RANBP1} * 0.41467 + \text{SLC2A2} * (-0.02551).$

Furthermore, a nomogram was constructed using the R package “rms.”

**2.4. Statistical Analysis.** Based on the expression profile data of TCGA-LIHC, the immunotherapy efficacy prediction software TIDE (<http://tide.dfci.harvard.edu/>) was used to predict





FIGURE 3: Differentially expressed genes.

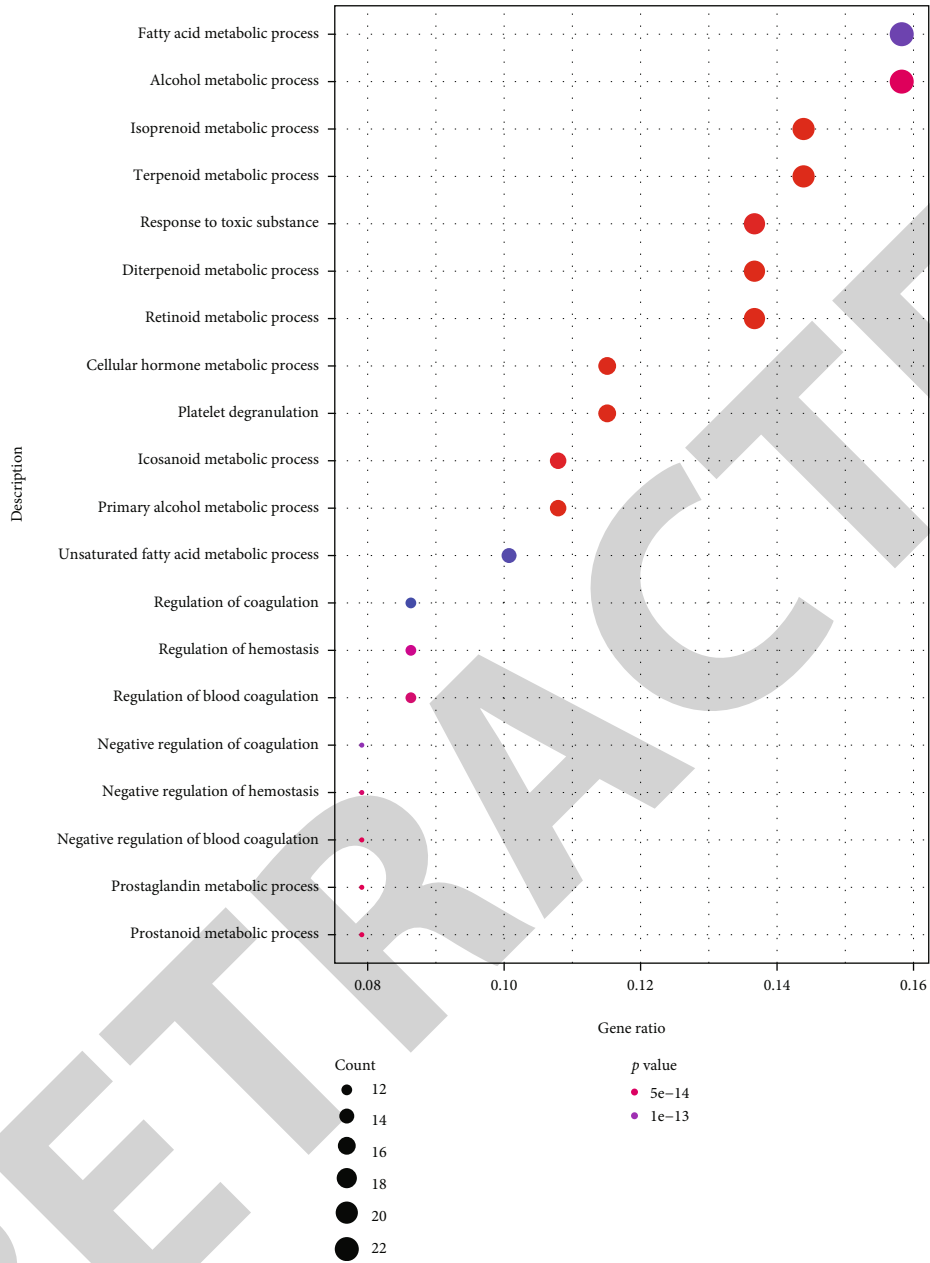
the efficacy score of immunotherapy. The differences of efficacy score between the high- and low-stemness score groups were compared. We also compare the expression of immune checkpoints (PD1, PD-L1, CTLA4) between the high- and low-stemness score groups. The R package “CIBERSROT” was used to calculate the proportion of 22 immune cells. The R package “ESTIMATE” was used to evaluate the stromal, immune, and tumor purity scores using the TCGA-LIHC data. We also calculated the score of HALLMARK pathways using the R package “GSVA.” The HALLMARK pathways were downloaded from the MSigDB database (<http://www.gsea-msigdb.org/gsea/msigdb/collections.jsp>).

Based on the expression data of TCGA-LIHC, the R package “pRRophetic” (v0.5) was used to predict the sensitivity of chemotherapy and targeted therapeutic drugs (half maximal inhibitory concentration: IC50) for HCC patients. The differences of IC50 between the high- and low-stemness score groups were compared. The independent Student’s t-test for continuous data and the  $X^2$  test for categorical data were utilized for pairwise comparisons between groups. The Mann-Whitney  $U$  test was used to compare categorical vari-

ables and nonnormally distributed variables between two groups. The Kruskal-Wallis test was used to compare multiple groups. Correlations between normally distributed variables were assessed with Pearson’s correlation test, while correlations between nonnormally distributed variables were assessed with Spearman’s correlation test. The statistical analyses in this study were performed by using R 4.1.0 software. A two-tailed  $P$  value  $<0.05$  was considered statistically significant.

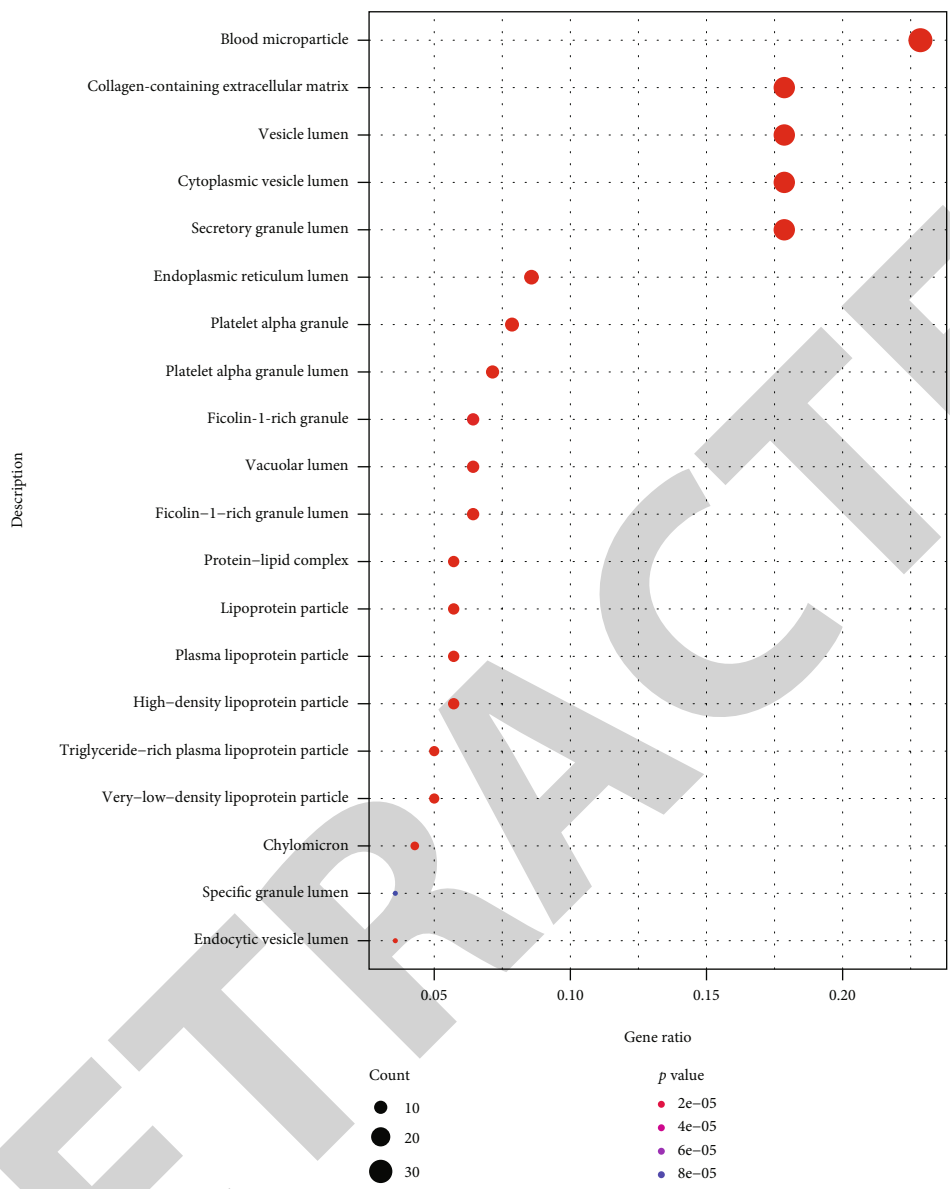
### 3. Results

**3.1. Identification of Stemness-Related Genes.** First, we downloaded the single-cell sequencing data GSE149614 from the GEO database. Figure 1 displays the expression and distribution of genes, cells and mitochondria genes. All the cells were classified into 53 types (Figure 2(a)), in which there were significant differences in the cell community structure between tumor tissues and noncancer tissues. More types of cells and dispersion were observed in tumor tissues (Figure 2(b)). We use the cell annotation information provided by references. Figure 2(c) displays the results of cell



(a)

FIGURE 4: Continued.



(b)  
FIGURE 4: Continued.

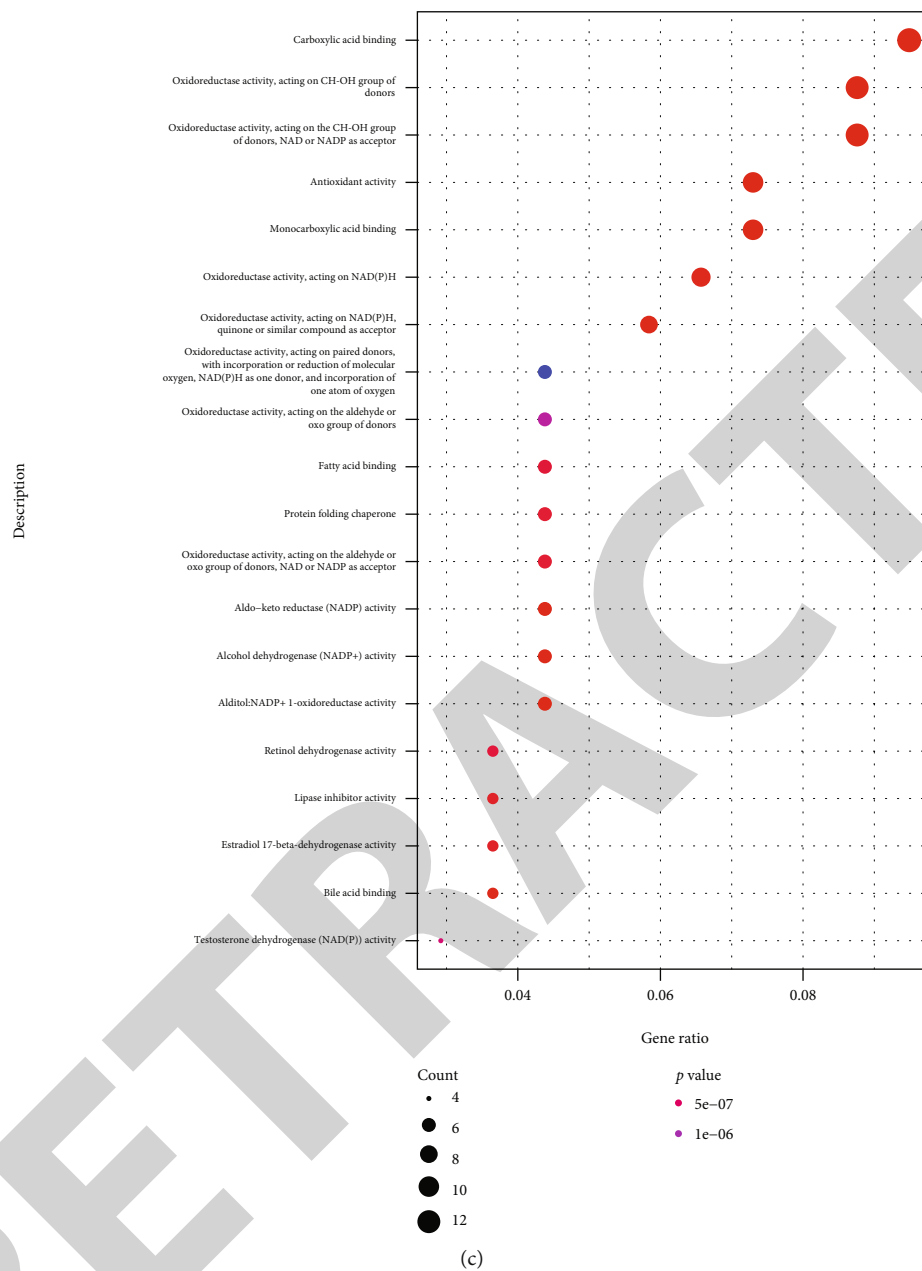


FIGURE 4: Continued.

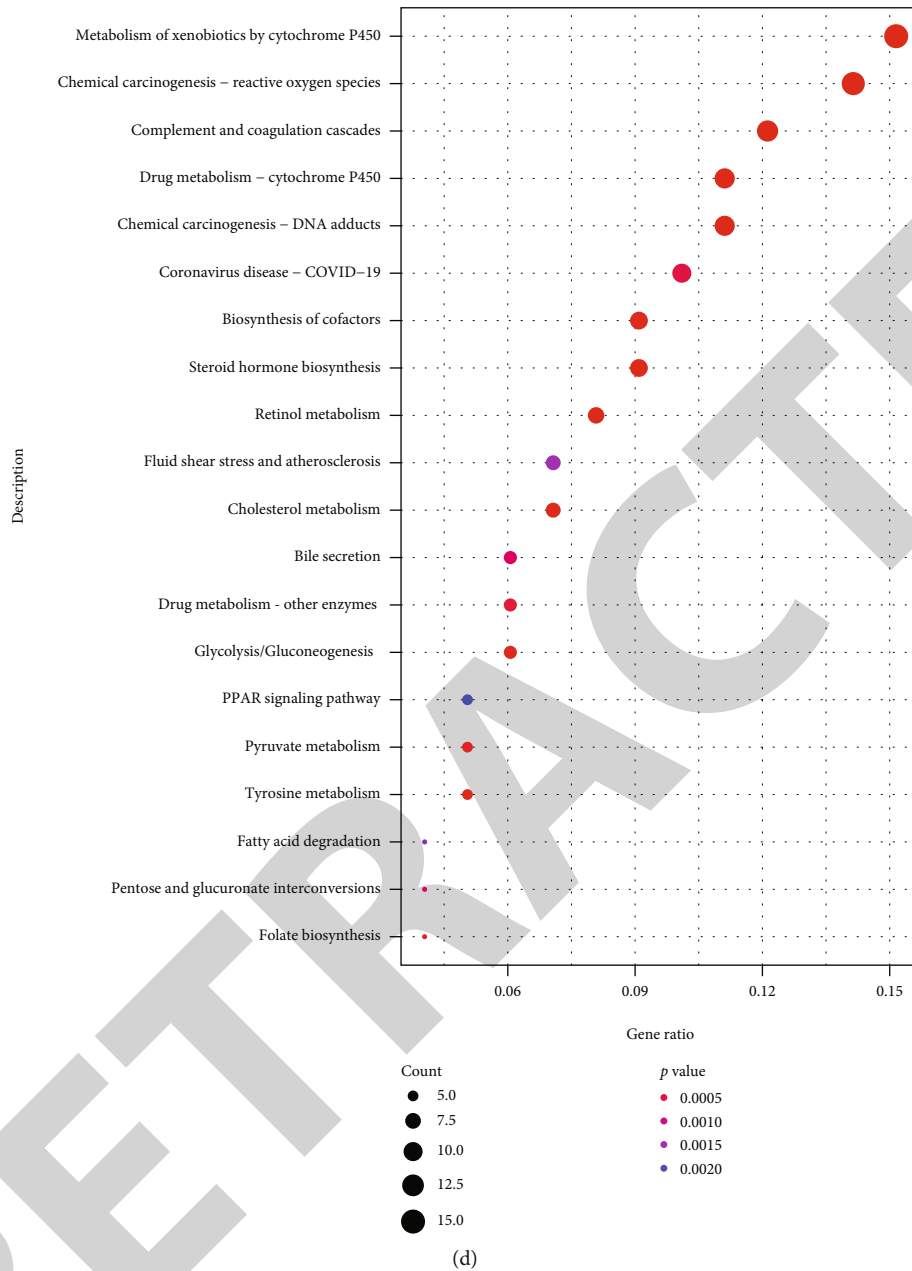


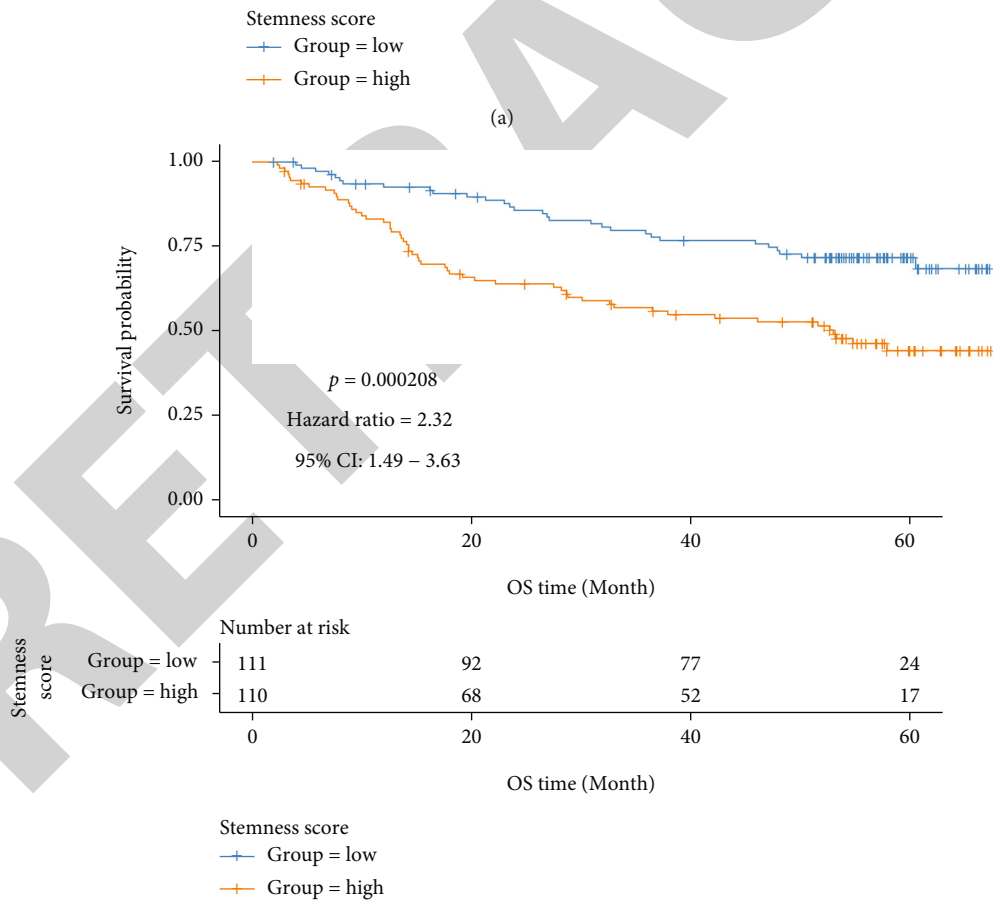
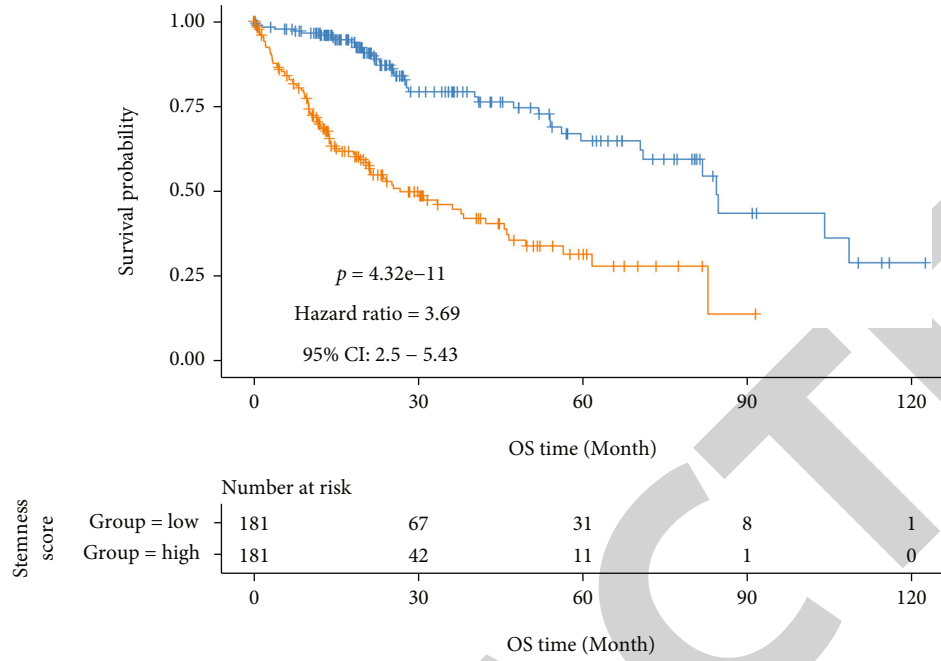
FIGURE 4: Enrichment analysis of stemness-related genes. (a) Top 20 results of GO enrichment analysis in BP terms. (b) Top 20 results of GO enrichment analysis in CC terms. (c) Top 20 results of GO enrichment analysis in MF terms. (d) Top 20 results of KEGG enrichment analysis.

annotation. We found that the noncancerous tissue cells are mainly T/NK cells, myeloid cells, and endothelial cells. Epithelial cell adhesion molecule (EPCAM) is a marker of human liver stem cells (HSC) and progenitor cells, which does not exist in mature hepatocytes. However, EPCAM is also expressed in tumors and damaged liver. In the single-cell transcriptome sequencing data of liver cancer, EPCAM is mainly expressed in tumor cells and concentrated in cluster10 (Figures 2(b) and 2(d)).

Liver cells in tumor tissues are mainly annotated as 9 categories, namely, cluster2, cluster4, cluster7, cluster10, cluster14, cluster17, cluster20, cluster34, and cluster37. We

further screened 145 differential expressed genes, which were considered as stemness-related genes, between cluster10 and other 8 clusters (Figure 3). Heatmap presents differential expressed genes. HSC represents liver stem cells, and HPC represents other hepatocytes.

**3.2. Enrichment Analysis of Stemness-Related Genes.** We also explored the function of 145 stemness-related genes. Results indicated that stemness-related genes were mainly enriched in fatty acid metabolic process and alcohol metabolic process in biological process (BP) (Figure 4(a)), blood microparticle and collagen-containing extracellular matrix in cellular



(b)

FIGURE 5: The survival analysis of stemness gene model. Kaplan-Meier curves of stemness gene model in TCGA-LIHC cohort (a) and GSE14520 cohort (b).

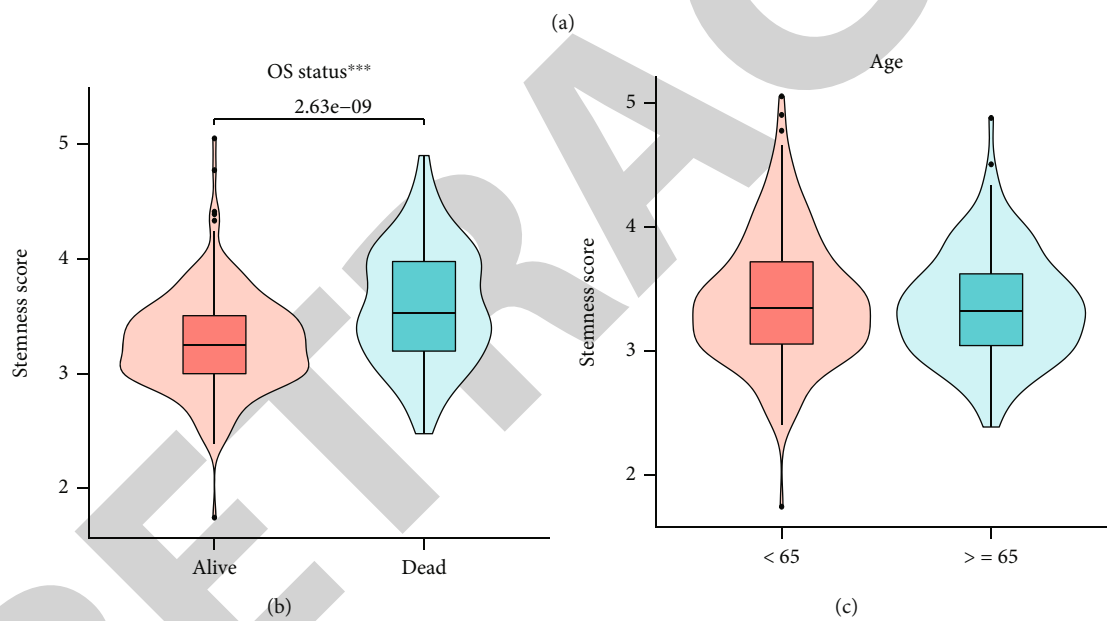
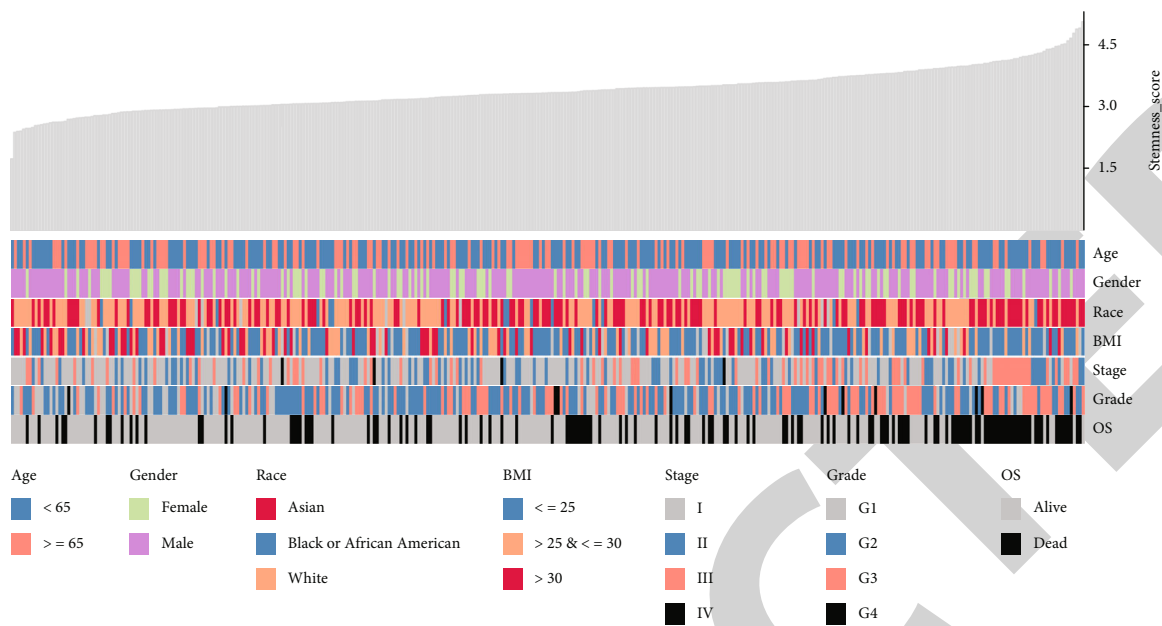


FIGURE 6: Continued.

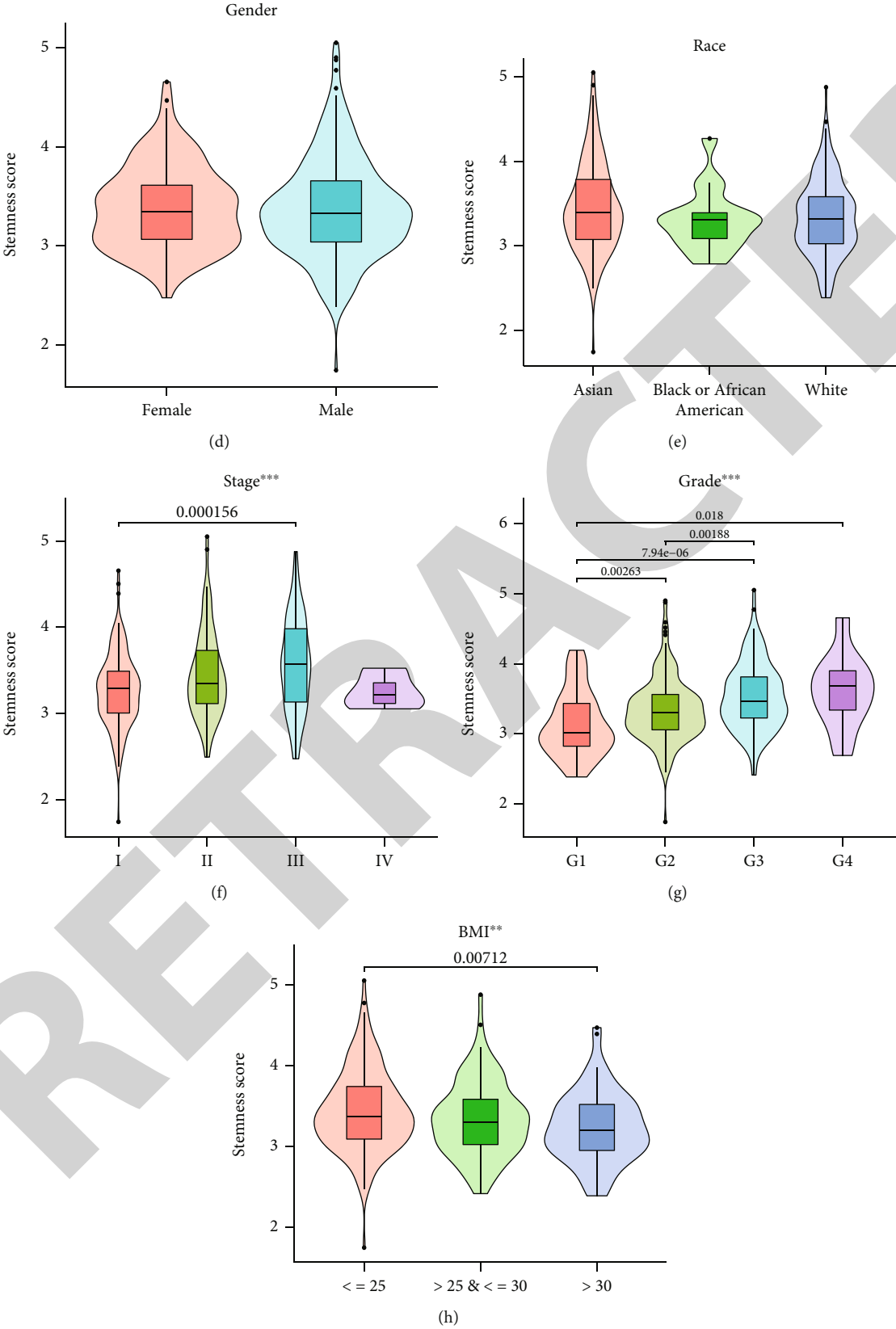


FIGURE 6: Correlation analysis between stemness score and clinical characteristics. (a) Heatmap displays the correlation between stemness score and clinical characteristics. (b-h) The stemness score in indicated groups of various clinical characteristics.



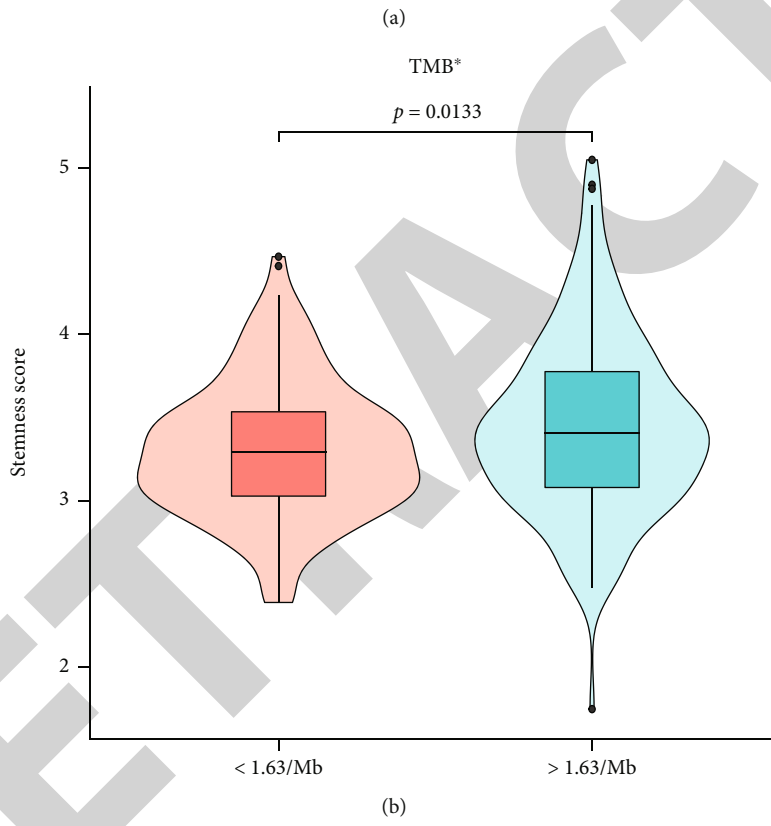
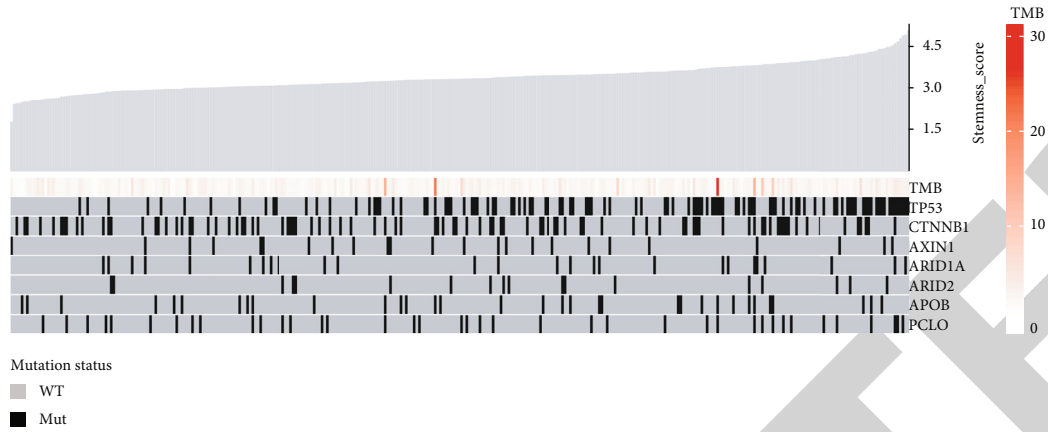
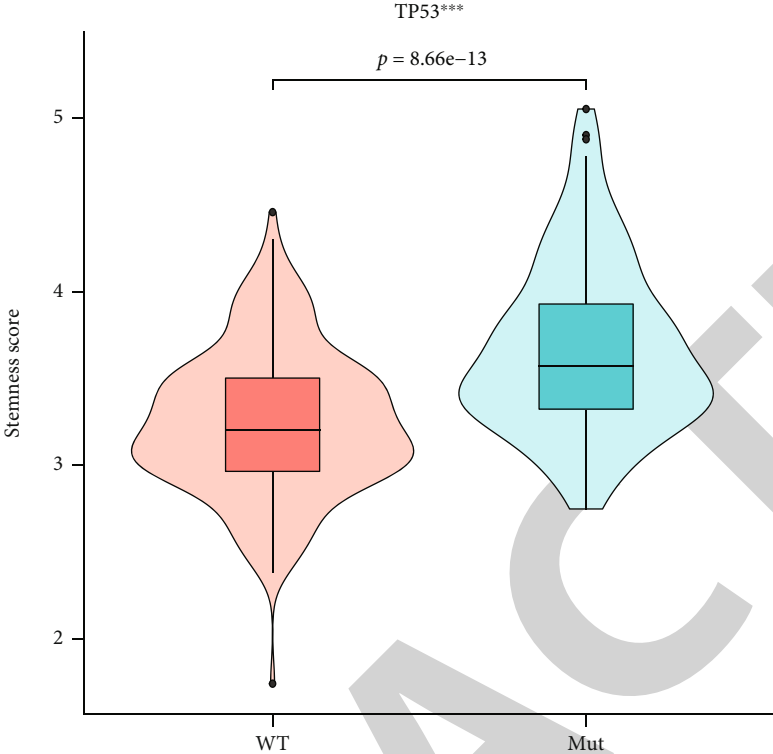
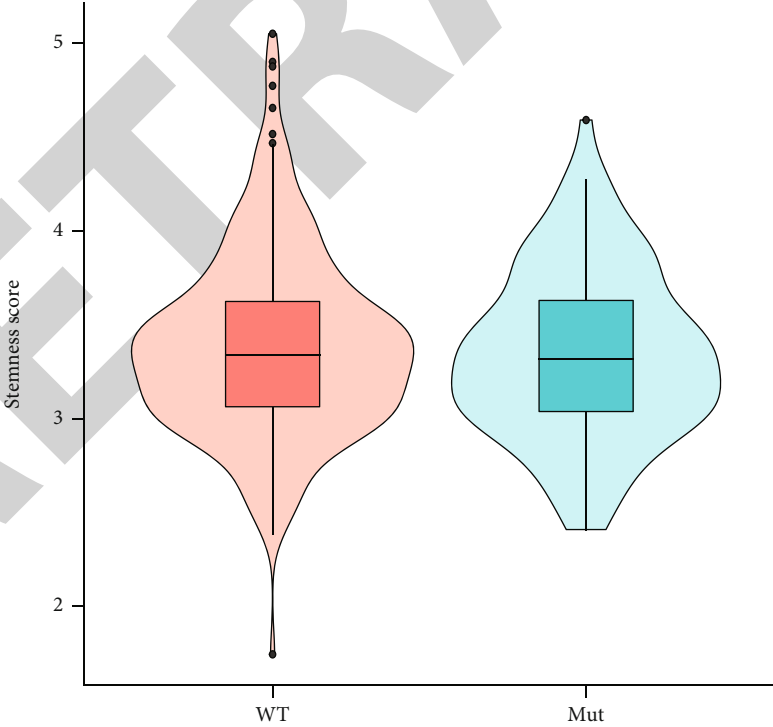


FIGURE 7: Continued.

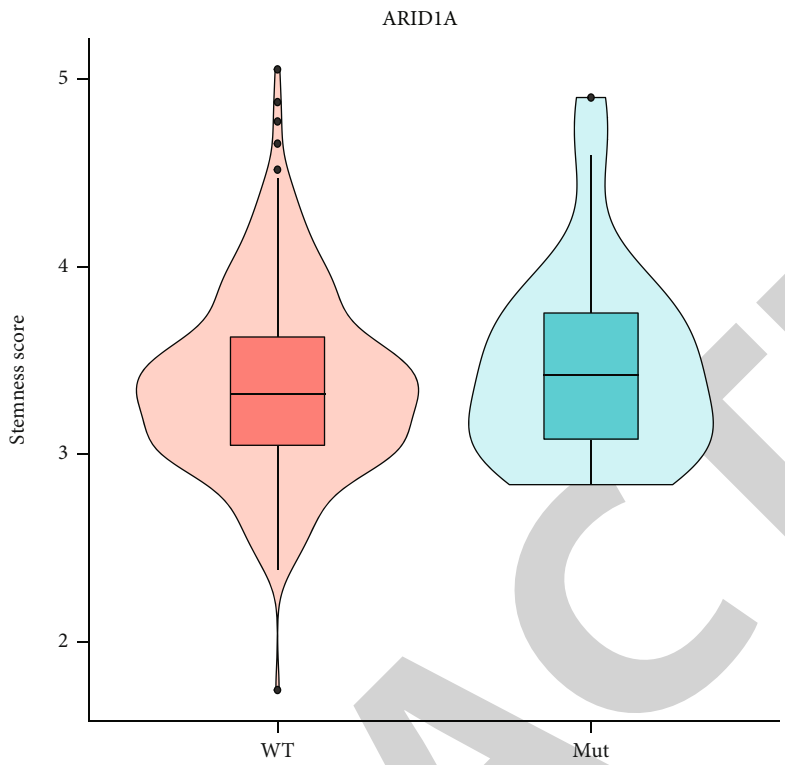


(c)  
CTNNB1

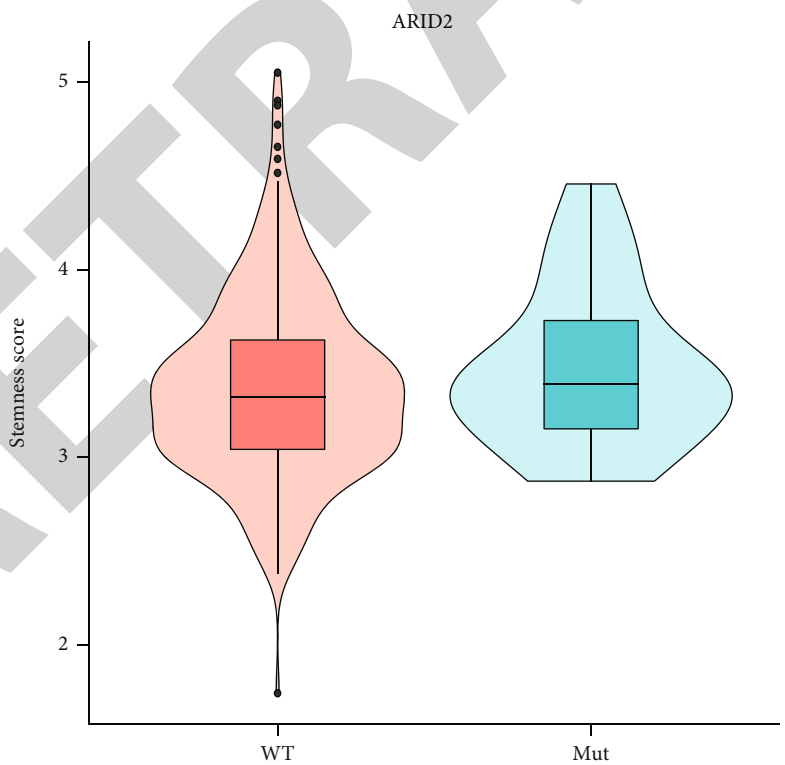


(d)

FIGURE 7: Continued.

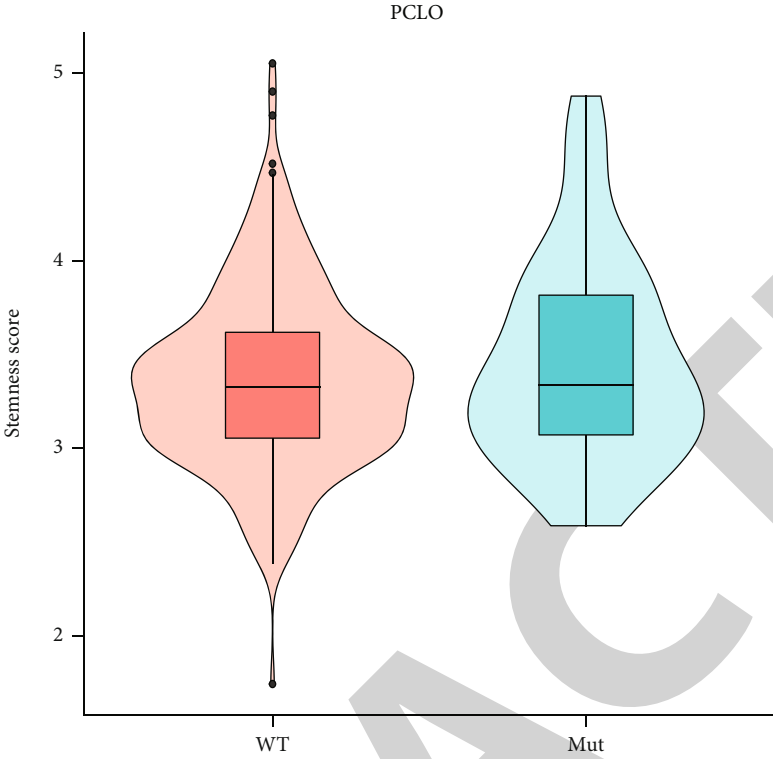


(e)



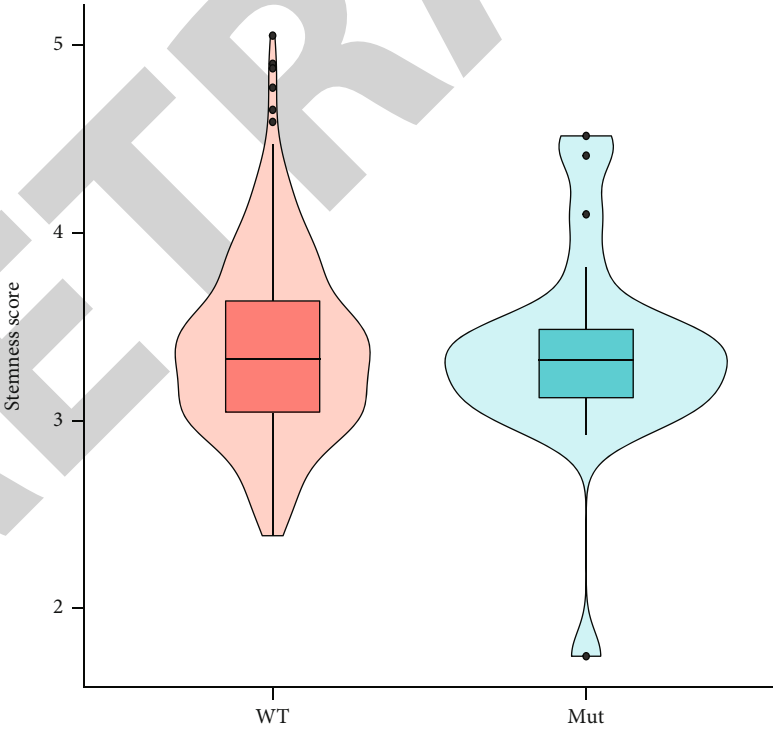
(f)

FIGURE 7: Continued.



(g)

AXIN1



(h)

FIGURE 7: Continued.

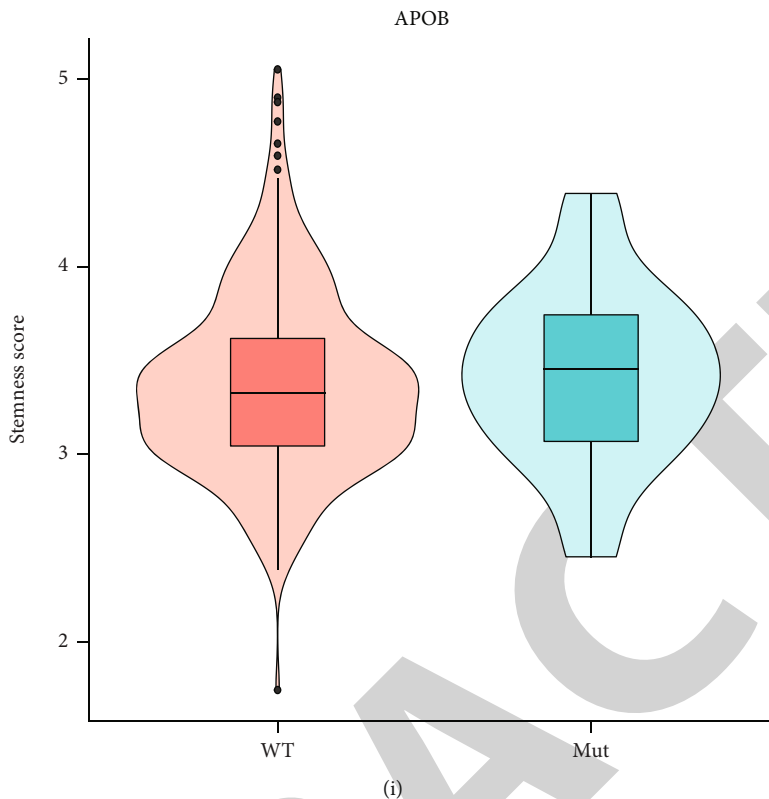


FIGURE 7: Correlation analysis between stemness score and gene mutation. (a) Heatmap displays the correlation between stemness score and gene mutation. (b–i) The stemness score in indicated groups of various gene mutation status.

components (CC) (Figure 4(b)), carboxylic acid binding and oxidoreductase activity, acting on CH-OH group of donors in molecular function (MF) (Figure 4(c)), and metabolism of xenobiotics by cytochrome P450 and chemical carcinogenesis-reactive oxygen species in KEGG (Figure 4(d)).

**3.3. Construction of Prognosis Prediction Model of HCC.** To construct a prognosis prediction model of HCC based on 145 stemness-related genes, we conducted lasso regression analysis using TCGA-LIHC as training cohort and GSE14520 as validation cohort. Finally, 18 stemness-related genes were enrolled to construct the prognosis model. Based on the prognosis model, we calculated the stemness score of each sample and found that patients with high-stemness score have worse survival status in TCGA-LIHC (Figure 5(a)) and GSE14520 cohorts (Figure 5(b)).

**3.4. The Association of Stemness Score with Clinical Characters, Gene Mutation, and Drug Resistance of HCC Patients.** We further explored the association of stemness scores with clinical characters of HCC patients using the TCGA-LIHC cohort (Figure 6(a)). We found that stemness score was significantly correlated with the survival status of patients, and stemness score was higher in the dead patient group (Figure 6(b)). There were no correlation of stemness score with age, gender, and race (Figures 6(c)–6(e)). Stemness score was significantly higher in stage III patients than in stage I patients (Figure 6(f)). In addition, we found that

there was a significant correlation between stemness score and tumor histological grade. The higher the grade, the higher the stemness score (Figure 6(g)). Figure 6(h) shows that stemness score in obese people with BMI greater than 30 is significantly lower than that in normal people with BMI  $\leq 25$ .

We then analyzed the correlation between stemness score and tumor mutation load (Figure 7(a)) and found that stemness score was higher in group with high mutation load (Figure 7(b)). In addition, there was a significant correlation between TP53 mutation status and stemness score in HCC. Stemness score in the mutant group was significantly higher than that in the wild-type group (Figure 7(c)). There was no association of stemness score with mutation of CTNNB1, ARID1A, ARID2, PCLO, AXIN1, and APOB (Figures 7(d) and 7(e)).

Besides, we compared the gene mutation frequency in the high- and low-stemness score group. Results indicated that the mutation frequency of TP53 was the highest in the high-stemness score group, while the mutation frequency of CTNNB1 was the highest in the low-stemness score group (Figures 8(a) and 8(b)). The oncoplot displays the gene mutation frequency in the high- and low-stemness score group.

To explore the relationship between stemness score and tumor drug resistance, we predicted the IC<sub>50</sub> of anti-cancer drugs using the R package “pRRophetic” based on the TCGA-LIHC cohort. We found that there were significant differences in the sensitivity of patients to cisplatin,

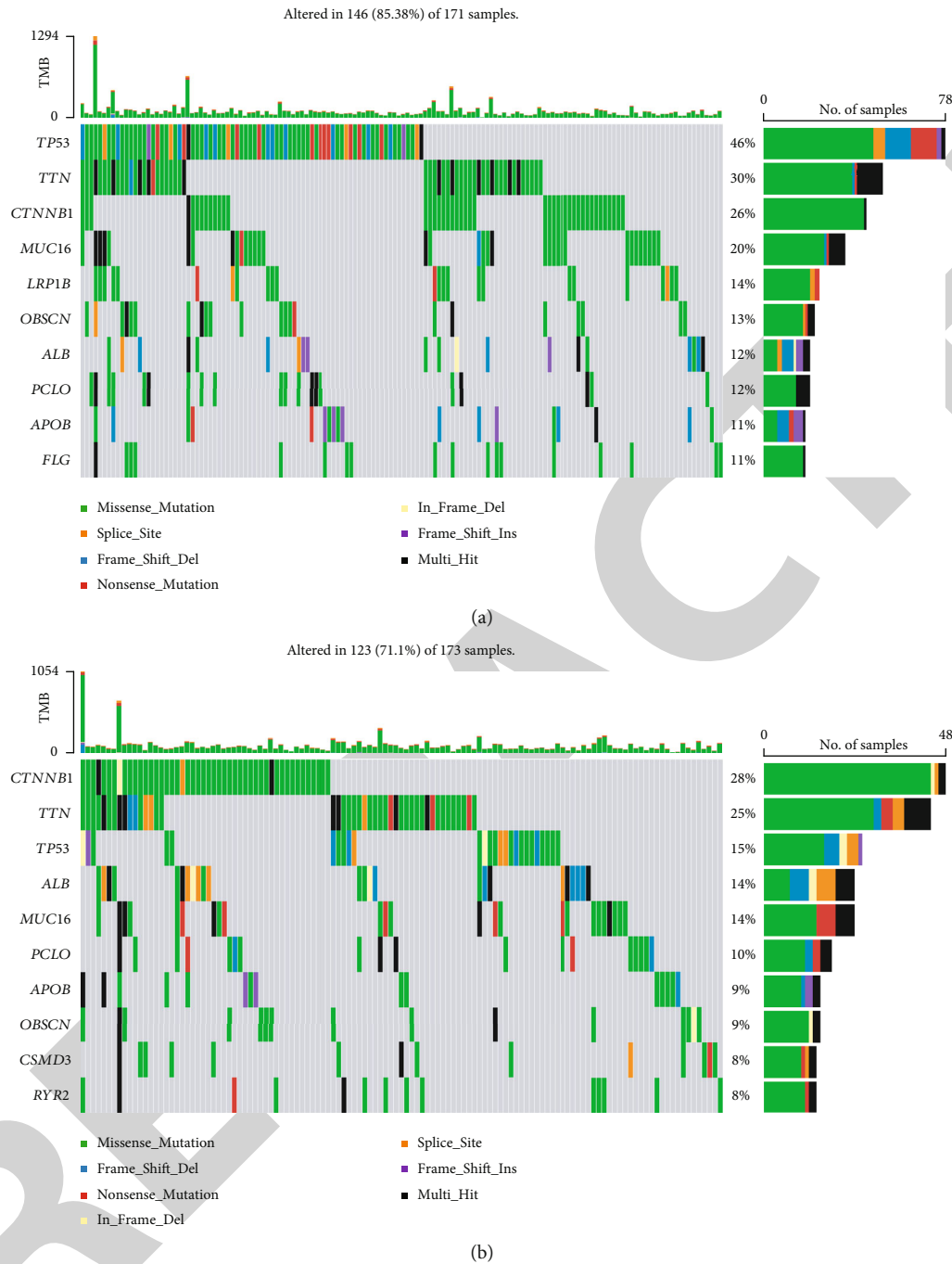


FIGURE 8: Oncoplot of gene mutation.

gemcitabine, and gefitinib, in which the IC50 was lower in the high-stemness score group (Figures 9(a), 9(c), and 9(d)). These results indicated that patients with high-stemness score may be more sensitive to cisplatin, gemcitabine, and gefitinib treatment. In addition, the IC50 value of erlotinib was higher in the high-stemness score group, suggesting that HCC patients with high-stemness score may be more resistant to erlotinib treatment (Figure 9(b)).

3.5. The Association of Stemness Score with Tumor Immune Microenvironment. Since there was no publicly available

immunotherapy dataset of HCC, we used the TIDE database to predict the efficacy score of immunotherapy based on the TCGA-LIHC cohort. We found that the TIDE score was higher in the high-stemness score group, suggesting a poor therapeutic effect of immune checkpoint inhibitors (Figure 10(a)). In addition, CTLA4 and PDCD1 were highly expressed in the high-stemness score group (Figure 10(b)). There was no significant difference of CD274 (Figure 10(c)).

We further explored the association of stemness score with immune cell infiltration. The infiltration level of CD8<sup>+</sup> T cells and monocytes in the high-stemness score

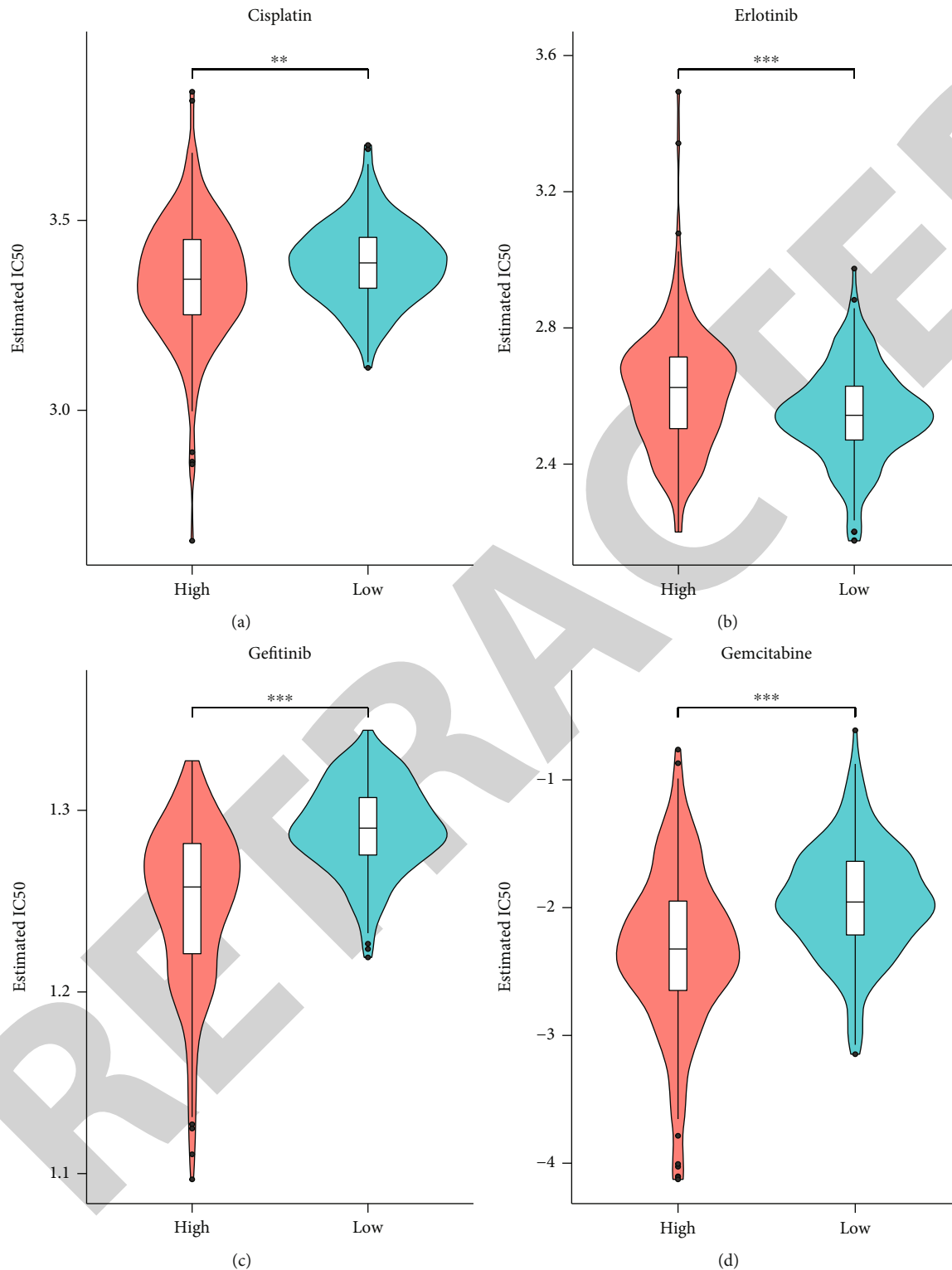
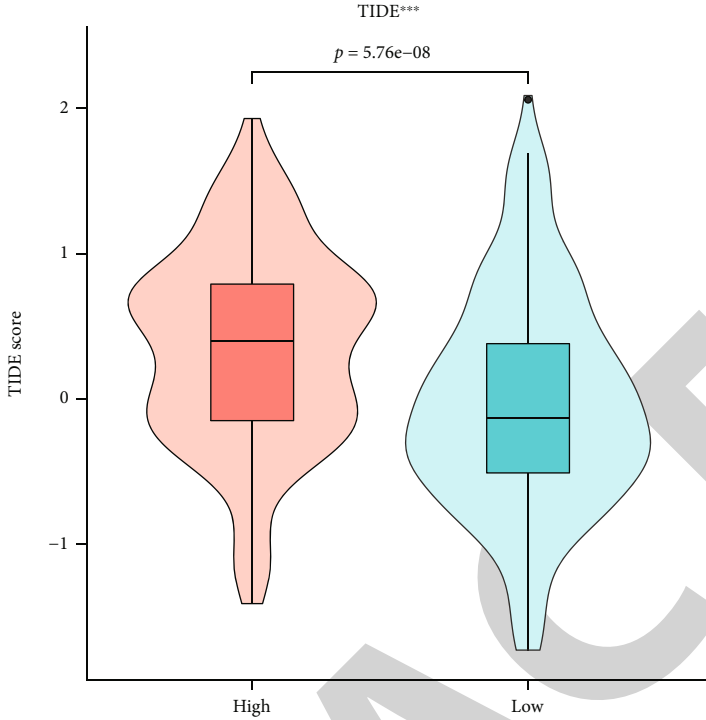


FIGURE 9: The correlation of stemness score with drug sensitivity. (a–d) The IC50 value of indicated drugs in the high- and low-stemness score group \*\* means  $P < 0.01$ , \*\*\* means  $P < 0.001$ .

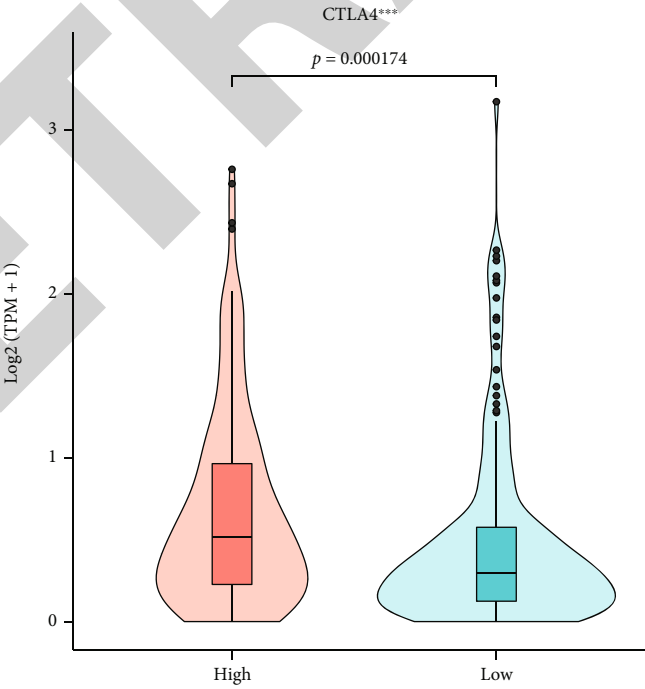
group was significantly lower than that in the low-stemness score group, while the infiltration level of macrophage M0, memory B cells, and eosinophils in the high-stemness score group were significantly higher than that in the low-

stemness score group (Figure 11(a)). Further, the stemness score was positively correlated with macrophage M0 and negatively correlated with CD8<sup>+</sup> T cells (Figure 11(b)). In addition, we observed a slight negative correlation of



Stemness score  
High  
Low

(a)

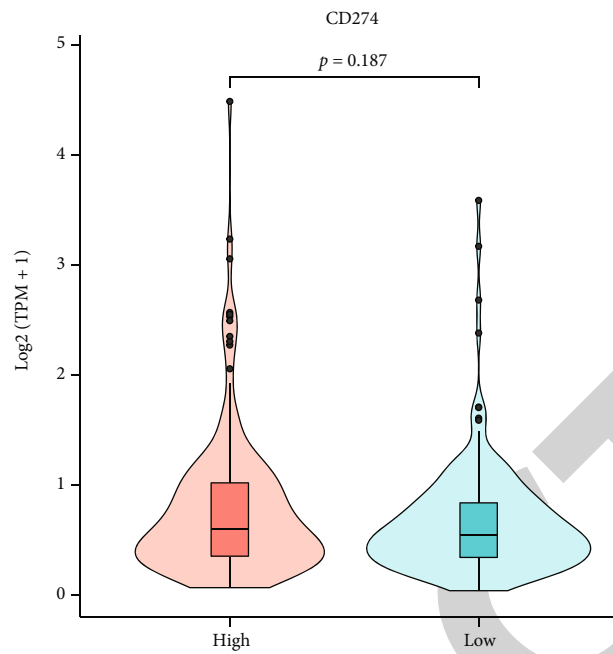


Stemness score  
High  
Low

(b)

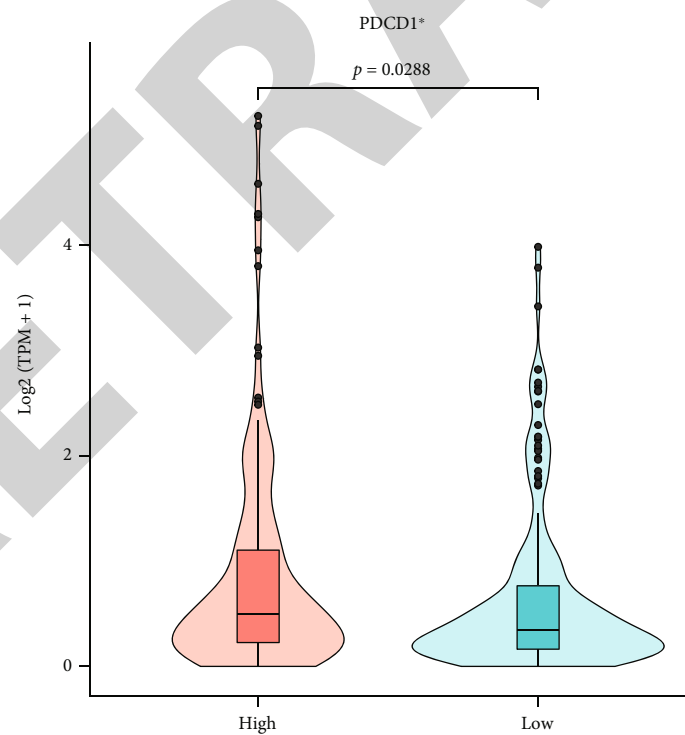
FIGURE 10: Continued.





Stemness score  
High  
Low

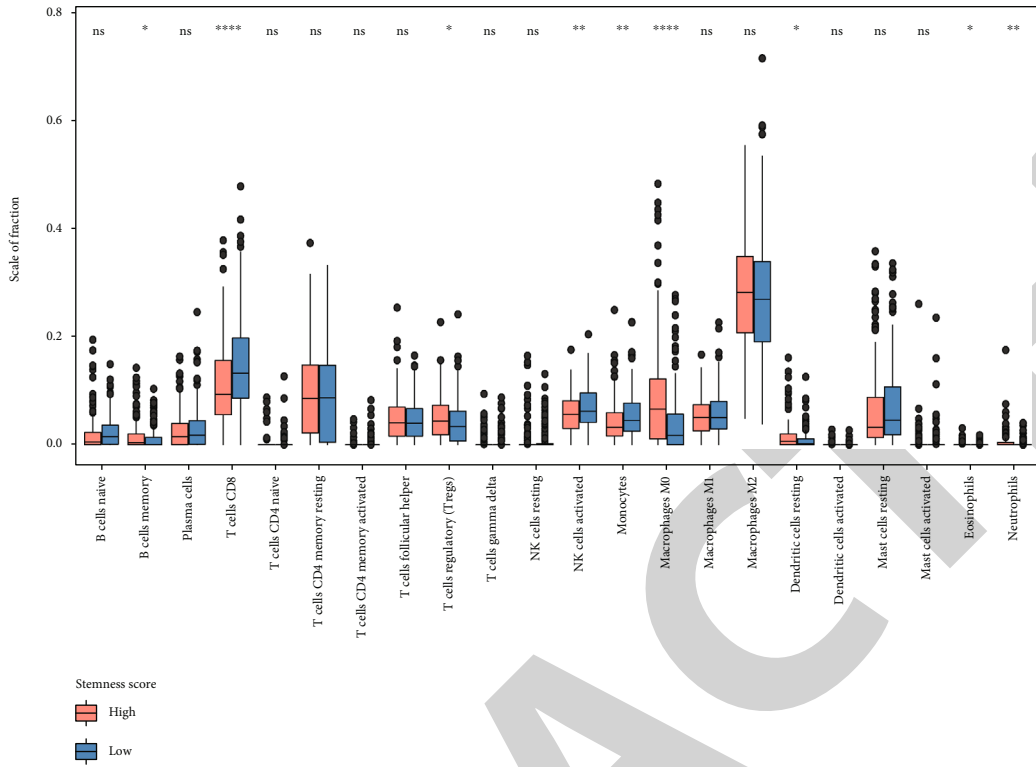
(c)



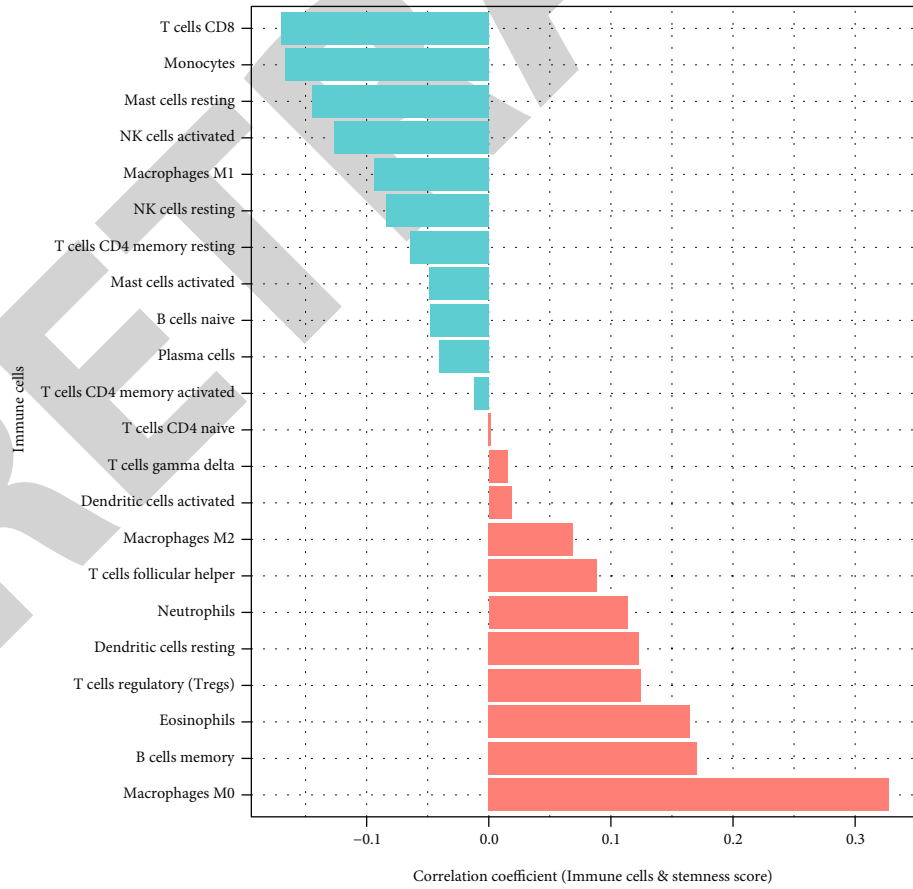
Stemness score  
High  
Low

(d)

FIGURE 10: The association between stemness score and immunotherapy. (a-d) The TIDE score, CTLA4, CD274, and PDCD1 expressions in the high- and low-stemness score group.

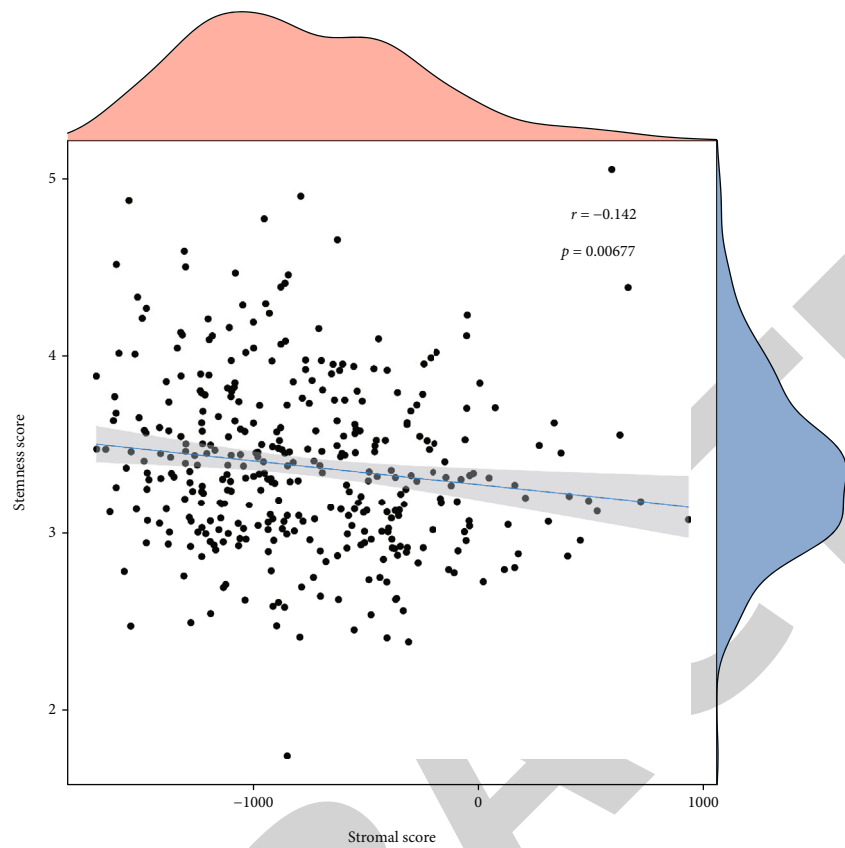


(a)

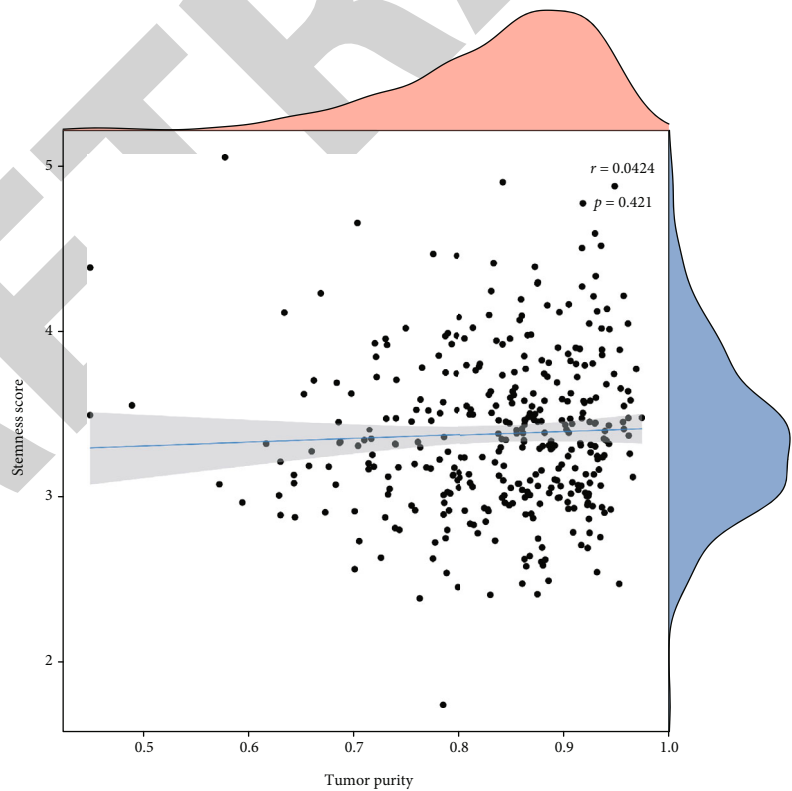


(b)

FIGURE 11: Continued.



(c)



(d)

FIGURE 11: Continued.

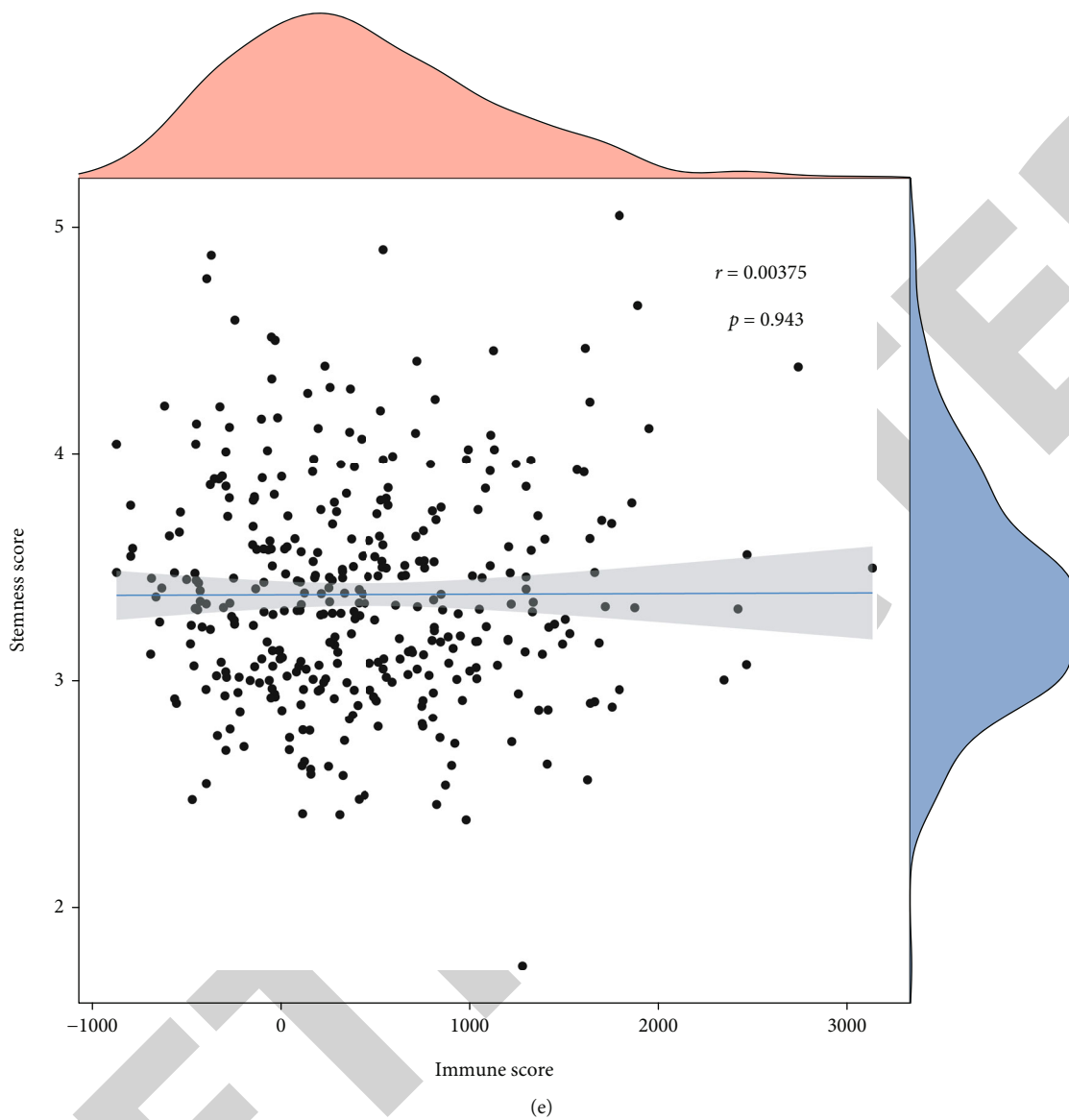


FIGURE 11: Continued.

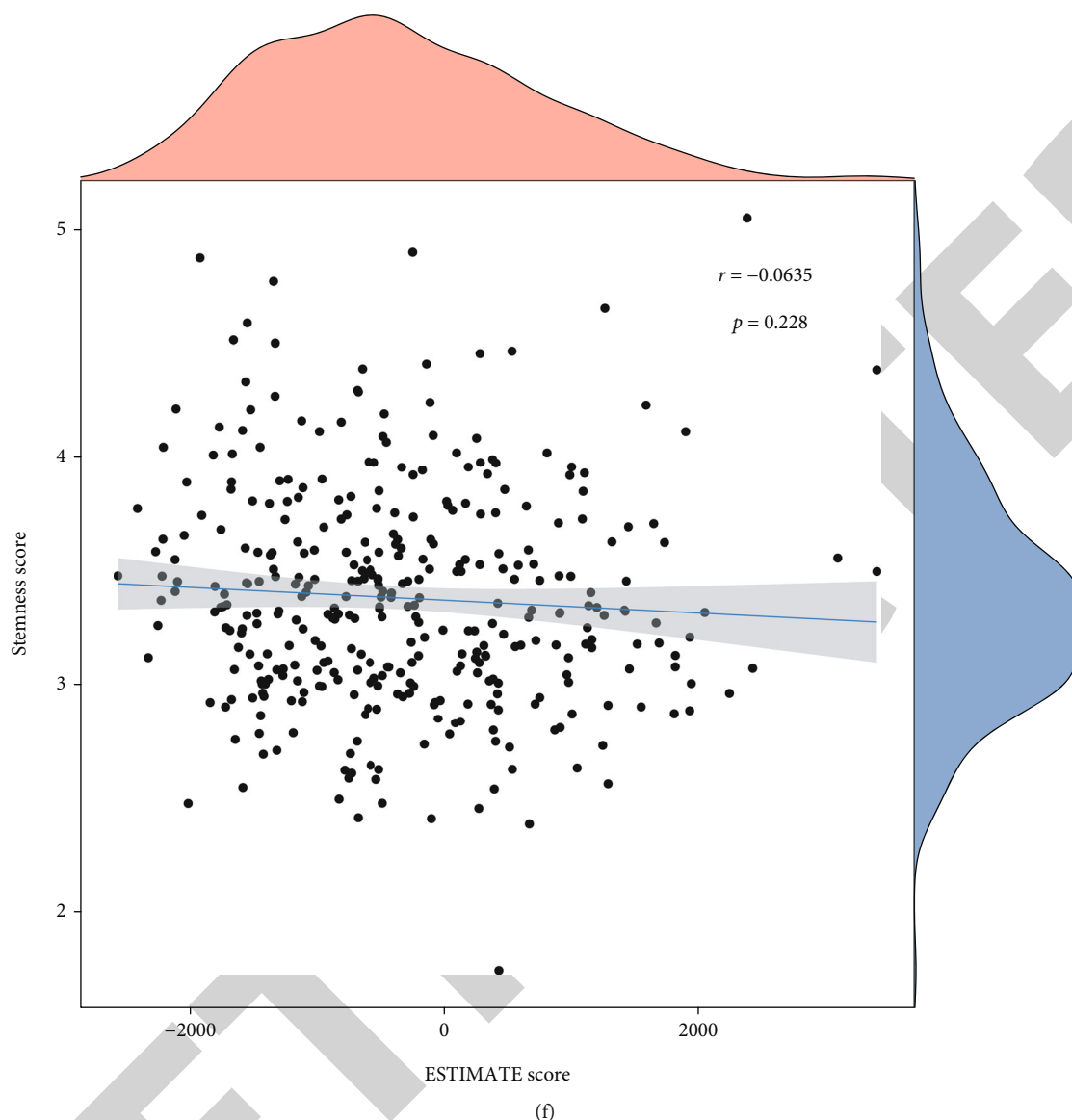


FIGURE 11: The correlation of stemness score with immune cell infiltration. (a) The immune cell infiltration level in the high- and low-stemness score group. (b) The correlation of stemness score with immune cell infiltration level. The correlation between stemness score and stromal score (c), tumor purity (d), immune score (e), and ESTIMATE score (f) 'ns' means  $P < 0.05$ , \* means  $P < 0.05$ , \*\* means  $P < 0.01$ , \*\*\* means  $P < 0.001$ , \*\*\*\* means  $P < 0.0001$ .

stemness score with stromal score (Figure 11(c)) and no significant correlation of stemness score with tumor purity, immune score, and ESTIMATE score (Figures 11(d)–11(f)).

**3.6. The Correlation between Stemness Score and HALLMARK Pathways.** Then, we explored the correlation between stemness score and HALLMARK pathways. We found that the pathways related to cell replication (MITOTIC\_SPINDLE, MYC\_TARGETS\_V1, G2M\_CHECKPOINT, E2F\_TARGETS, DNA\_REPAIR, and MYC\_TARGETS\_V2) were more active in the high-stemness score group, and the pathways related to material/energy metabolism (CHOLESTEROL\_HOMEOSTASIS, COAGULATION, PEROXISOME, FATTY\_ACID\_METABOLISM, XENOBIOTIC\_METABOLISM, BILE\_ACID\_METABOLISM, ADIPOGENESIS, and

OXIDATIVE\_PHOSPHORYLATION) were more active in low-stemness score group (Figure 12). These phenomena suggested that the tumor tissues of the two groups of samples are in significant different status, indicating that our model is of great significance in the risk stratification of tumor prognosis. Heatmap displays the GSVA score of HALLMARK pathways in TCGA cohort.

**3.7. Construction of Nomogram Model of HCC.** Finally, we constructed a nomogram to quantify patient risk based on stemness score and clinical characteristics of HCC patients. ROC curves were used to estimate the predictive ability of the model for prognosis. The nomogram based on TCGA-LIHC showed that the stemness score was a risk factor for the prognosis of HCC. The area under curve (AUC) values

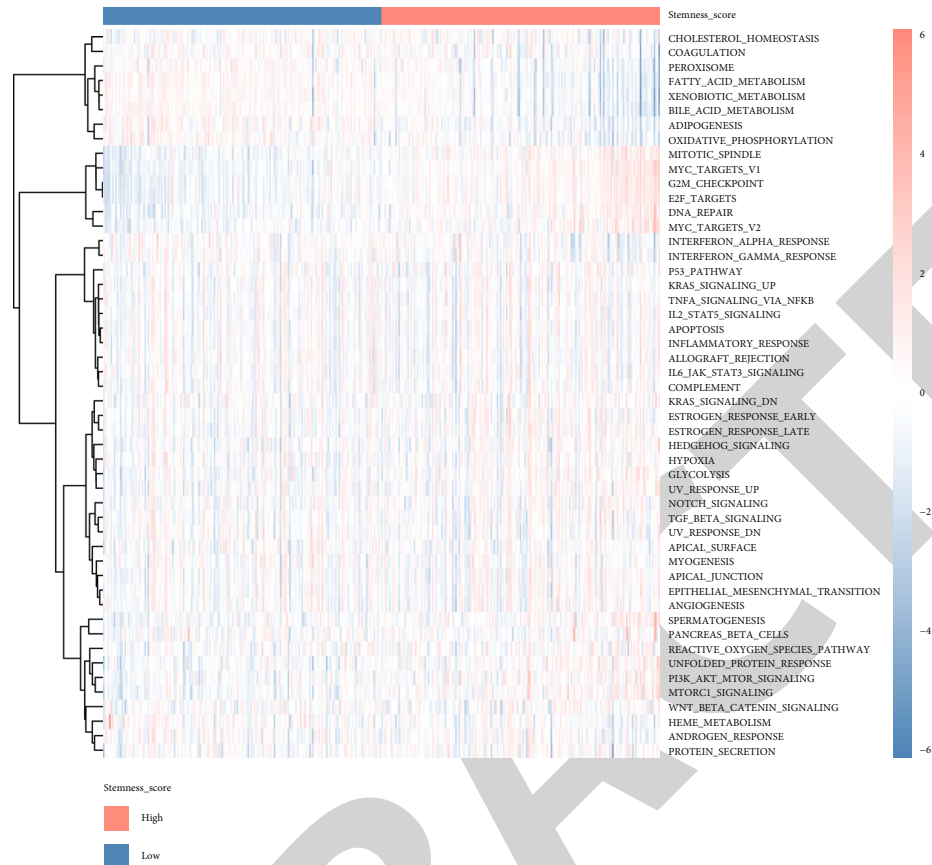


FIGURE 12: GSEA of stemness score.

of 1-, 3-, and 5-year survival were 0.827, 0.74, and 0.724, respectively (Figures 13(a) and 13(b)). In GSE14520, we also proved that the stemness score was a risk factor for the prognosis of HCC. The area under curve (AUC) values of 1-, 3-, and 5-year survival in GSE14520 were 0.682, 0.648, and 0.615, respectively (Figures 13(c) and 13(d)).

#### 4. Discussion

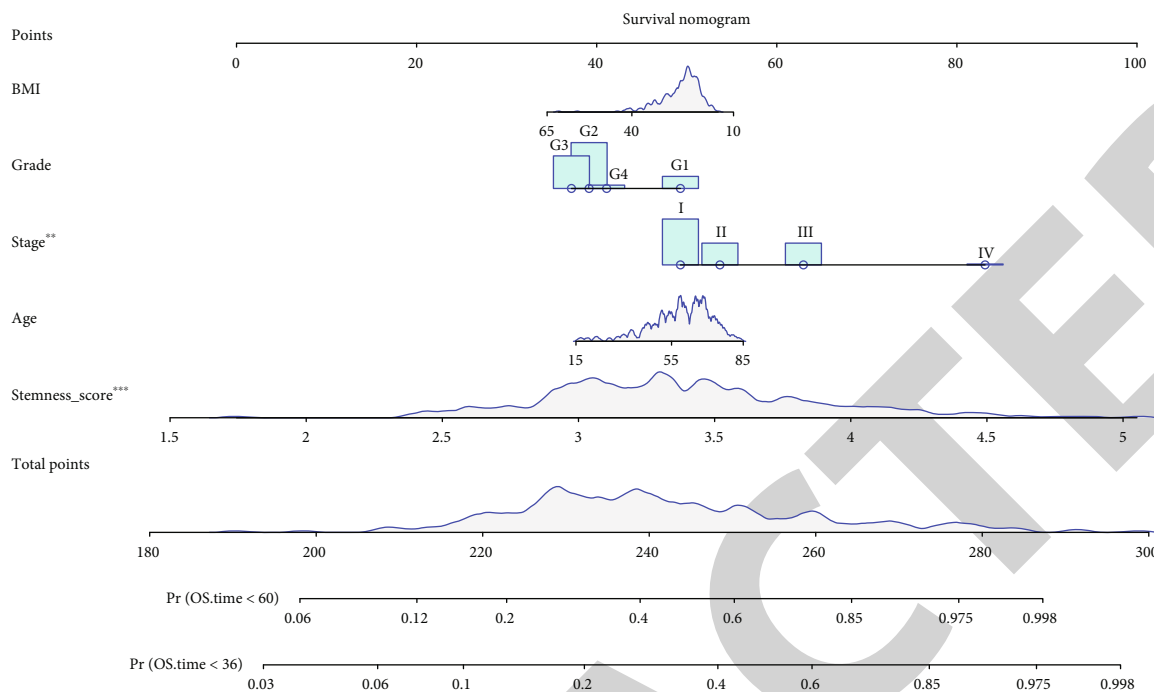
Tumor heterogeneity is one of the main characteristics of HCC, which makes the progress of treatment slow [1, 2]. At present, there is still a lack of biomarkers and effective prognostic models for diagnosis, prognosis, and prediction of therapeutic efficacy of HCC. This further weakens the possibility of developing personalized treatment.

In our work, we firstly downloaded the single-cell sequencing data GSE149614 from GEO database. We found that EPCAM is mainly expressed in tumor cells and concentrated in cluster10. We further screened 145 differential expressed genes, which were considered as stemness-related genes, between stemness HCC cells and nonstemness HCC cells. Enrichment analysis indicated that stemness-related genes were mainly enriched in fatty acid metabolic process and alcohol metabolic process in BP, blood microparticle, and collagen-containing extracellular matrix in CC, carboxylic acid binding and oxidoreductase activity, acting on CH-OH group of donors in MG, and metabolism of xenobiotics by cytochrome P450 and chemical carcinogenesis-reactive oxy-

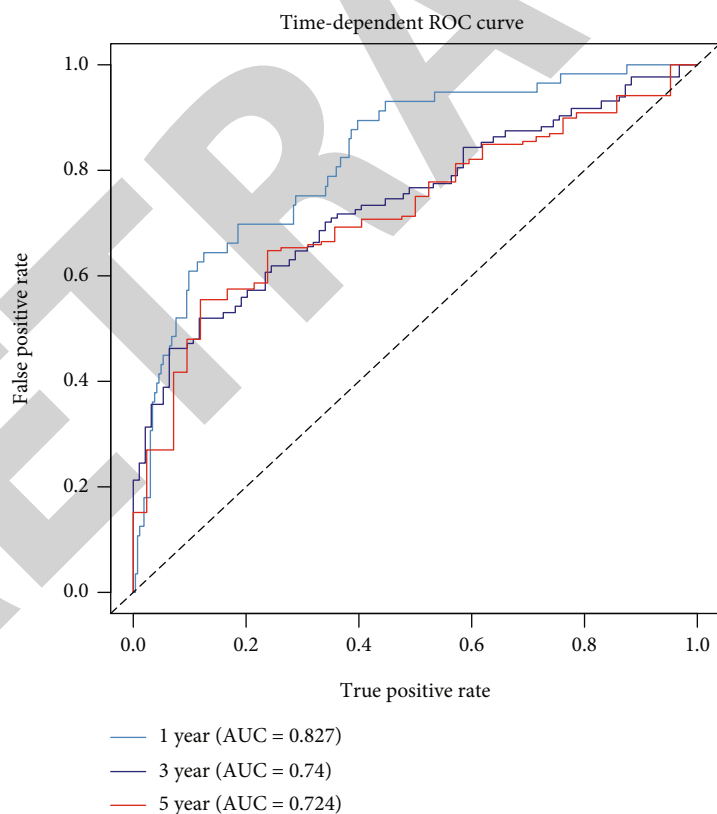
gen species in KEGG. We also conducted LASSO regression analysis using TCGA-LIHC as training cohort and GSE14520 as validation cohort to construct a prognosis prediction model in HCC. Patients with high-stemness score have worse survival status in the TCGA-LIHC and GSE14520 cohorts. We further explored the association of stemness score with clinical characters of HCC patients and found that stemness score was higher in the dead patient group. In addition, the higher the grade of HCC, the higher the stemness score. There was also a significant correlation between TP53 mutation status and stemness score in HCC.

We further explored the association of stemness score with immune cell infiltration. The infiltration level of CD8<sup>+</sup> T cells and monocytes in the high-stemness score group was significantly lower than that in the low-stemness score group, while the infiltration level of macrophage M0, memory B cells, and eosinophils in the high-stemness score group was significantly higher than that in the low-stemness score group. These results suggested that patients with high-stemness score may have immunosuppressive tumor microenvironment.

Finally, we constructed a nomogram to quantify patient risk based on stemness score and clinical characteristics of HCC. The nomogram based on TCGA-LIHC showed that the stemness score was a risk factor for the prognosis of HCC. The area under curve (AUC) values of 1-, 3-, and 5-year survival were 0.827, 0.74, and 0.724, respectively. In GSE14520, we also proved that the stemness score was a risk

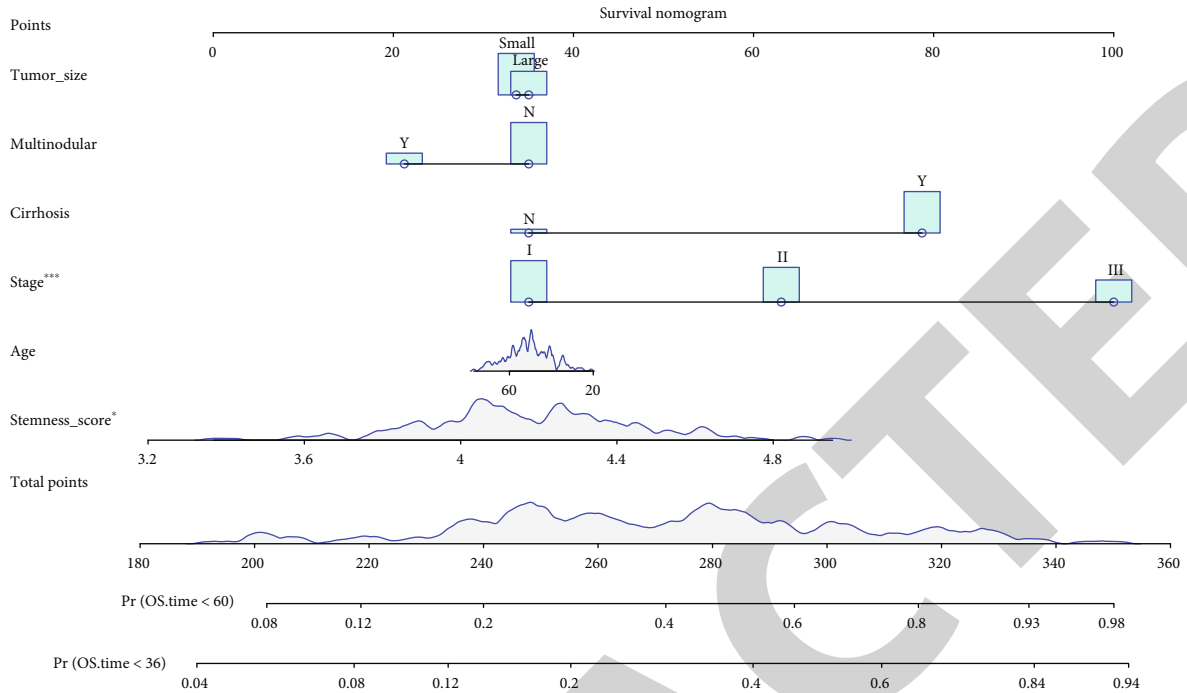


(a)

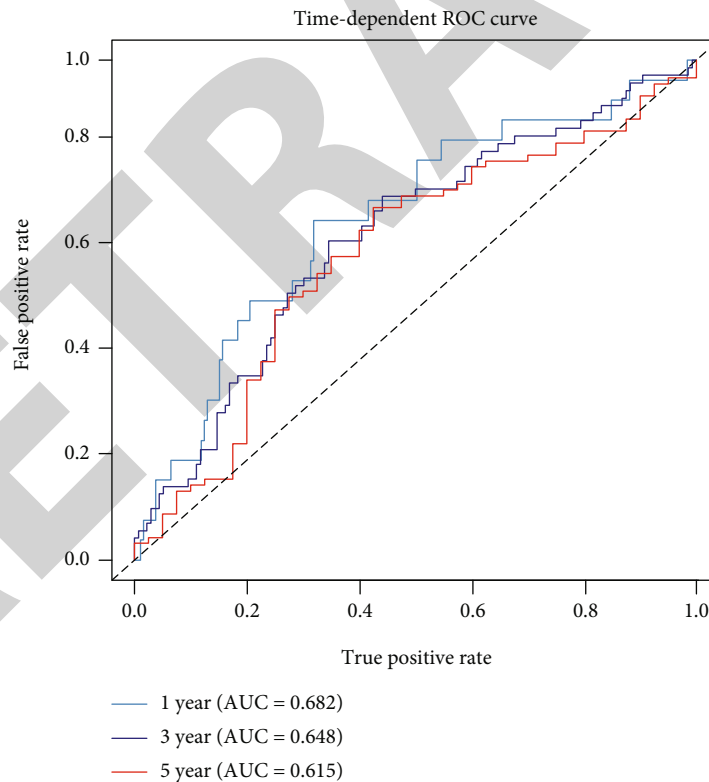


(b)

FIGURE 13: Continued.



(c)



(d)

FIGURE 13: Construction of nomogram model. (a) The nomogram in TCGA-LIHC cohort. (b) The ROC curves in TCGA-LIHC cohort. (c) The nomogram in GSE14520 cohort. (d) The ROC curves in GSE14520 cohort.

factor for the prognosis of HCC. The area under curve (AUC) values of 1-, 3-, and 5-year survival in GSE14520 were 0.682, 0.648, and 0.615, respectively.

In conclusion, our study defined stemness-related genes and constructed stemness-related prognostic model, which may help clarify the biological characteristics and



## *Retraction*

# **Retracted: The Anti-inflammatory Effect of Chitosan Oligosaccharide on Heart Failure in Mice**

### **BioMed Research International**

Received 8 January 2024; Accepted 8 January 2024; Published 9 January 2024

Copyright © 2024 BioMed Research International. This is an open access article distributed under the Creative Commons Attribution License, which permits unrestricted use, distribution, and reproduction in any medium, provided the original work is properly cited.

This article has been retracted by Hindawi, as publisher, following an investigation undertaken by the publisher [1]. This investigation has uncovered evidence of systematic manipulation of the publication and peer-review process. We cannot, therefore, vouch for the reliability or integrity of this article.

Please note that this notice is intended solely to alert readers that the peer-review process of this article has been compromised.

Wiley and Hindawi regret that the usual quality checks did not identify these issues before publication and have since put additional measures in place to safeguard research integrity.

We wish to credit our Research Integrity and Research Publishing teams and anonymous and named external researchers and research integrity experts for contributing to this investigation.


The corresponding author, as the representative of all authors, has been given the opportunity to register their agreement or disagreement to this retraction. We have kept a record of any response received.

### **References**

- [1] Y. Zhang, Y. Wang, Y. Liu, T. Gong, and M. Hou, "The Anti-inflammatory Effect of Chitosan Oligosaccharide on Heart Failure in Mice," *BioMed Research International*, vol. 2022, Article ID 8746530, 9 pages, 2022.

## Research Article

# The Anti-inflammatory Effect of Chitosan Oligosaccharide on Heart Failure in Mice

Yubiao Zhang,<sup>1</sup> Yu Wang,<sup>1</sup> Yunen Liu,<sup>2</sup> Tianxing Gong,<sup>3</sup> and Mingxiao Hou<sup>1,2</sup> 

<sup>1</sup>Department of Food Science, Shenyang Agricultural University, No. 120 Dongling Road, Shenhe District, Shenyang, Liaoning, China 110866

<sup>2</sup>Emergency Medicine Department of General Hospital of Northern Theater Command, Laboratory of Rescue Center of Severe Wound and Trauma PLA, No. 83 Wenhua Road, Shenhe District, Shenyang, Liaoning, China 110016

<sup>3</sup>Sino-Dutch Biomedical and Information Engineering School, Northeastern University, No. 195 Chuangxin Road, Hunnan District, Shenyang, Liaoning, China 110169

Correspondence should be addressed to Mingxiao Hou; [houmingxiao188@163.com](mailto:houmingxiao188@163.com)

Received 12 August 2022; Revised 6 September 2022; Accepted 13 September 2022; Published 5 October 2022

Academic Editor: Nauman Rahim Khan

Copyright © 2022 Yubiao Zhang et al. This is an open access article distributed under the Creative Commons Attribution License, which permits unrestricted use, distribution, and reproduction in any medium, provided the original work is properly cited.

Heart failure is currently one of the leading causes of death worldwide, and the inflammatory factors play an important role in its development. Chitosan oligosaccharide (COS), a low-molecular-weight form of chitosan, has many specific biological activities. In this study, COS effects on heart failure were studied for the first time by performing transverse arch constriction (TAC) surgery in mice, as an animal model of heart failure. Our findings revealed that COS administration (in both 40 mg/kg and 80 mg/kg doses) significantly ameliorated TCA-induced left ventricular (LV) hypertrophy as well as the increase in lung and heart weight in mice, while improving TAC-induced LV dysfunction. Both doses effectively attenuated LV cardiomyocyte hypertrophy, while decreasing heart inflammation after heart failure in mice. In conclusion, our results indicated that the supplementation of COS in normal diet might be an effective way to prevent further myocardial tissue damage in patients suffering from heart failure.

## 1. Introduction

Heart failure is the end-stage manifestation of cardiac dysfunction, indicating that the heart can no longer serve as a pump supporting physiological circulation [1–3]. Heart failure can be caused by ischemic heart disease, myocarditis, cardiomyopathy, and myocardial infarction. Heart failure is becoming a significant global concern. When these cardiovascular diseases occur, the myocardial contractile function will gradually decline; end-stage heart failure will eventually follow after the hemodynamic disorder is intensified [3–5]. In addition, heart disease is recognized as the leading cause of death worldwide. According to the American Heart Association, about 6 million patients are admitted for treatment due to heart failure in the U.S. each year [6, 7].

Chitosan is the only pseudonatural cationic polymer comprised of glucosamine ( $\beta$  (1-4)-linked 2-amino-2-

deoxy-D-glucose) and N-acetylglucosamine (2-acetamido-2-deoxy-D-glucose) and is usually prepared by deacetylation of chitin. Chitin is primarily found in exoskeletons of insects and crustaceans and is the second most abundant naturally occurring polymer after cellulose [7, 8]. Chitosan is formed by the protonation of primary amino groups of glucosamine in the C2 position and is mildly toxic, nonimmunogenic, biodegradable, and soluble in acidic aqueous solutions. As a result, it has been widely studied and is extensively used for biomedical and pharmaceutical applications [9–11].

Chitosan oligosaccharide (COS) is a low-molecular-weight form of chitosan, but it is soluble in neutral pH solutions due to its short chain length. Therefore, it has many beneficial biological functions, including antifungal, antibacterial, antitumor, anti-infection, and immunity enhancing [12, 13]. Furthermore, COS can be easily absorbed through intestinal epithelium and quickly enters systemic circulation.

It is shown that COS can enhance the phagocytic activity of macrophages by a mechanism related to nicotinamide adenine dinucleotide phosphate (NADPH) oxidase, which induces nitric oxide synthase (i-NOS) [14–16]. Several studies have demonstrated protective effects of COS on damaged cardiomyocytes. For example, available evidence is indicated that COS improves the antioxidant capacity of myocardial tissue during vigorous exercise, helps maintain the normal morphological structure of cardiac tissue, and prevents heavy-load exercise-induced myocardial damage [17, 18]. COS can reduce the mortality of LPS-induced sepsis mouse model, inhibit the inflammatory reaction in the whole province, and reduce the TNF in the serum- $\alpha$  and IL-1 content to reduce the damage to the liver, kidney, and lung [13]. However, to the best of our knowledge, the protective effects of COS on heart failure have not been previously investigated.

COS was fed to male mice for two weeks, and heart failure was subsequently induced to evaluate the protective effects of COS on heart failure progression. The expressions of inflammatory-specific genes and proteins were characterized to investigate the mechanisms of protective effects of COS on heart failure.

## 2. Material and Methods

**2.1. Material.** COS (Mn 1,000 Da, >90% deacetylation degree) was prepared by the enzymatic method at the Dalian Institute of Chemical Physics and was kindly provided for this investigation. COS was analyzed by Time-of-Flight Mass Spectrometry (TOF-MS, Agilent, U.S.A.).

**2.2. Animal Model.** The animal study was approved by the animal welfare committee of Shenyang Military Command Hospital (Permit No. 2020-014).

The animal studies conducted as a part of this investigation were approved by the Animal Care and Use Committee of the Northern Theater General Hospital. The study sample included forty 8- to 10-week-old male BALB/c mice obtained from Liaoning Provincial Laboratory Animal Public Service Center. The Laboratory Animal Public Service Center of Liaoning Province provides free food and water for small animals. After one-week acclimation, the animals were randomly divided into four groups ( $n = 10$ ), namely, the sham operation group (control), the group in which the transverse arch constriction (TAC) surgery was performed to induce heart failure and mice were fed normal diet (the TAC group), the two intervention groups, in which the TAC surgery was also performed but mice were fed COS-supplemented (40 mg/kg or 80 mg/kg) diet every day for two weeks prior to surgery, denoted as the TAC-40COS and TAC-80COS groups, respectively.

The purpose of TAC surgery was to induce heart failure. In brief, mice were anesthetized by the intraperitoneal injection of sodium pentobarbital (50 mg/kg, Sigma, U.S.A.), and surgery was performed by an experienced surgeon. Subsequently, the aorta was ligated between the right and left common carotid arteries with a 27-gauge needle and 8-0 sutures. After surgery, mice assigned to the TAC-40COS and TAC-80COS groups were continu-

ously fed with COS-supplemented food for additional four weeks, while those assigned to the control and the TAC group were provided normal diet. At the endpoint (after four weeks postsurgery), mice were euthanized by pentobarbital sodium injection (50 mg/kg).

**2.3. Echocardiographic Assessment.** Prior to euthanization, mice were anesthetized and evaluated for cardiac geometry and function by animal echocardiography (Vevo 770, Fuji-film, Japan). The anterior and posterior wall dimensions of the left ventricle (LV) were determined from three consecutive cycles during one cycle of diastole and systole. Fractional shortening was defined as the ratio of the duration from LV end-diastolic to end-systolic diameters.

**2.4. Tissue and Plasma Collection.** Blood samples were collected in anticoagulating tubes from abdominal arteries and centrifuged at 7500 rpm for 15 min. Only the top layer of plasma was collected and was stored at  $-80^{\circ}\text{C}$  for future use. In addition, cardiac tissues were collected with cryovials and were immediately preserved at  $-80^{\circ}\text{C}$ .

**2.5. Histological Analysis.** Tissues were fixed in 10% formaldehyde solution for more than 72 h and then dehydrated and embedded in paraffin. Slices of  $5\ \mu\text{m}$  thickness were prepared by a microsystem microtome (Leica RM2265, Germany) and were stained with hematoxylin-eosin (H&E, Sigma-Aldrich, U.S.A.) and Masson trichrome (Sigma-Aldrich, U.S.A.). Subsequently, stained slices were observed under light microscope (BX53, Olympus, Japan) to investigate cellular morphology and fibrosis.

**2.6. Biomarker Analysis.** In the present study, malondialdehyde (MDA) and superoxide dismutase (SOD) from serum were evaluated by the enzyme-linked immunosorbent assay (ELISA) method. The ELISA kit was purchased from IBL Company (Germany). In brief, the plasma samples stored at  $-80^{\circ}\text{C}$  were thawed at room temperature, and  $10\ \mu\text{L}$  drops of plasma were transferred to the 96-well plate provided in the ELISA kit. The reagents included in the kit were added into each well according to the manufacturer's instructions. The plate was incubated at  $37^{\circ}\text{C}$  for 10 min away from light and was subsequently read in the microplate reader (CLARIOstar, BMG, Germany) at the wavelength of 450 nm ( $n = 10$  biological replicates).

**2.7. Genetic Analysis.** The genes related to the development of inflammation (IL-1 $\beta$ , IL-6, TNF- $\alpha$ , IL-17, NF- $\kappa\text{B}$ , TGF- $\beta$ , and smad1) were evaluated in this study, and the  $\beta$ -actin gene was used as the housekeeping gene. Using the RNeasy Mini Kit (Qiagen, Texas, U.S.A.), total RNA was isolated from the stored tissue samples and was reversely transcribed to cDNA on the thermal cycler (Bio-Rad, U.S.A.). Subsequently, the cDNA mixtures were amplified via real-time PCR (CFX96, Bio-Rad, U.S.A.) which involved the following steps: initialization at  $95^{\circ}\text{C}$  for 10 min, denaturation at  $95^{\circ}\text{C}$  for 15 s, annealing at  $55^{\circ}\text{C}$ , and extension at  $68^{\circ}\text{C}$ , repeated for 40 cycles. In the data analysis, the fold changes of each gene were calculated by applying the  $2^{-\Delta\Delta\text{Ct}}$  formula, and the relative fold

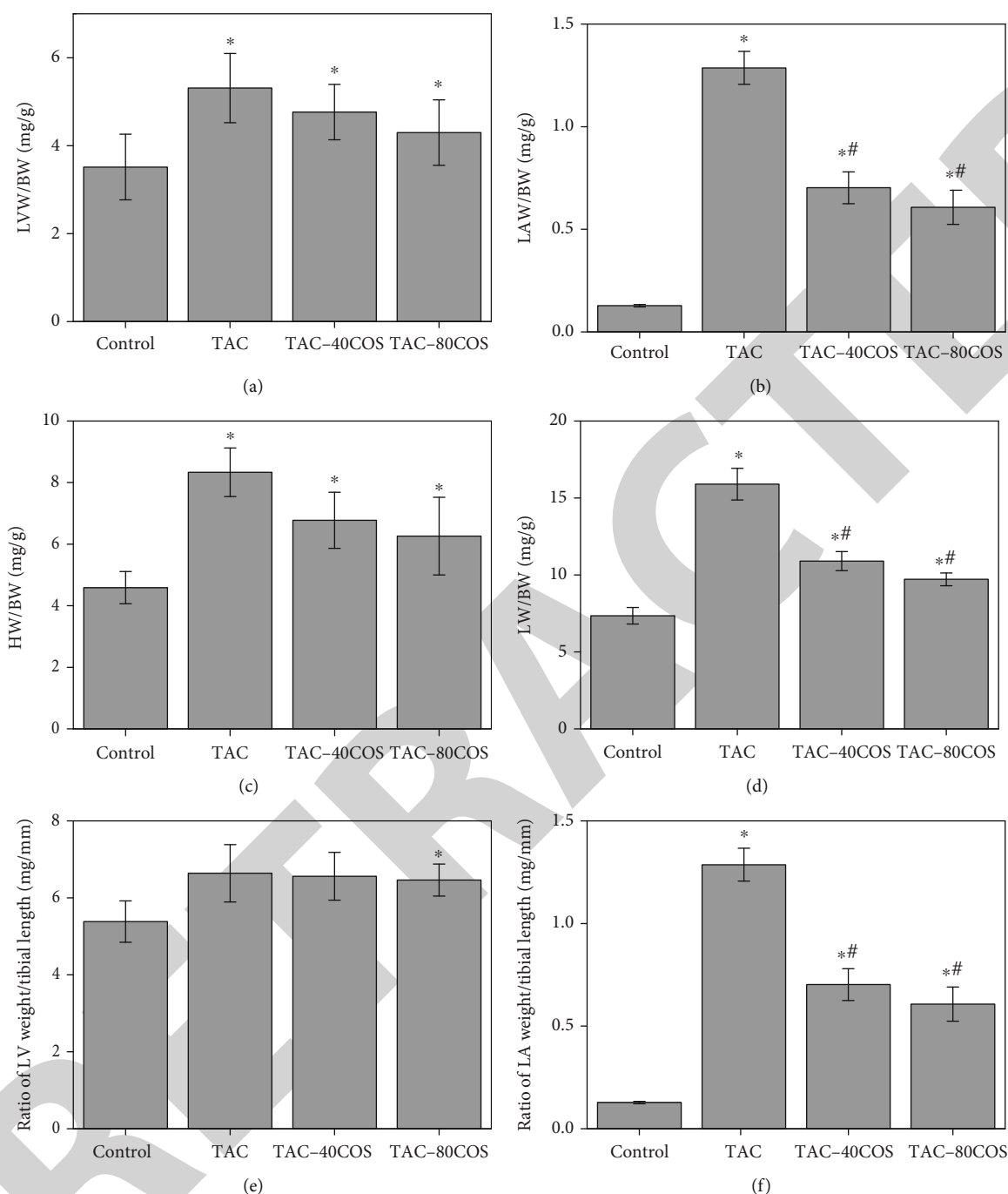


FIGURE 1: COS scavenger attenuates ventricular hypertrophy and pulmonary congestion in response to systolic overload. (a) The ratio of left ventricle (LV) to body weight of mice. (b) The ratio of left atrium (LA) to body weight of mice. (c) The ratio of heart to body weight of mice. (d) The ratio of lung to body weight of mice. (e) The ratio of left ventricle (LV) weight to tibial length. (f) The ratio of left atrium (LA) weight to tibial length. \* $p < 0.05$ , compared to the sham group, and # $p < 0.05$ , compared to TAC group. All values are mean  $\pm$  SEM.

change was calculated as the fold change sample/fold change control ratio based on 10 biological replicates.

**2.8. Western Blot Analysis.** In this study, the Western blot method was adopted to analyze the expressions of proteins related to inflammation. In brief, tissue samples were homogenized (TissueLyser II, Qiagen, U.S.A.), and 160  $\mu$ L of tissue homogenate was separated in the electrophoresis chamber (Mini-PROTEAN, Bio-Rad, U.S.A.) on the SDS-

PAGE gels (Mini-PROTEAN TGX gel, Bio-Rad, U.S.A.). Subsequently, the gels were transferred onto the PVDF membranes (Immun-Blot, Bio-Rad, U.S.A.) in the Western blotting transfer system (Trans-Blot Turbo, Bio-Rad, U.S.A.). The membranes were then incubated with the primary antibodies (rabbit anti-mouse, Abcam, U.S.A.) overnight and were washed with cold PBS to rinse antibody residue before further 4-hour incubation with the secondary antibodies (goat anti-rabbit, Abcam, U.S.A.). Finally, the

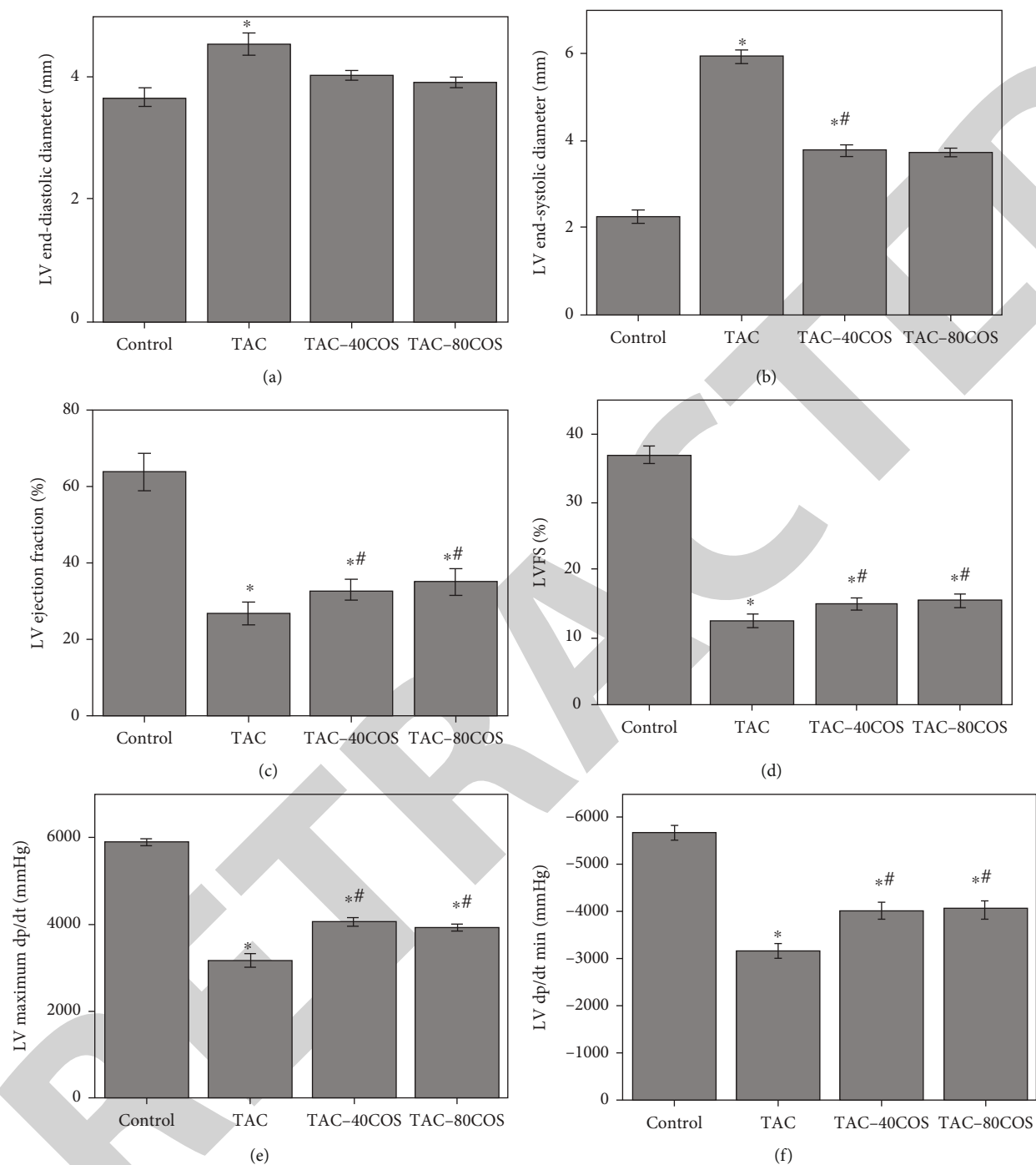


FIGURE 2: Echocardiographic and hemodynamic measurements demonstrating that COS scavenger attenuate TAC-induced left ventricular hypertrophy and dysfunction. (a, b) Summary data from echocardiograms measurements of LV end-diastolic diameter and LV end-systolic diameter. (c, d) Summary data from echocardiogram measurements of LV ejection fraction and LV fraction shortening. (e, f) LV maximum rate of rise of pressure ( $dp/dt_{max}$ ) and LV maximum rate of decline of pressure ( $dp/dt_{min}$ ) from hearts. \* $p < 0.05$ , compared to the sham group, and # $p < 0.05$ , compared to the TAC group. All values are mean  $\pm$  SEM.

antibody-bound membranes were observed in the imaging system (ChemiDoc MP system, Bio-Rad, U.S.A.) to analyze the protein expressions.

**2.9. Statistical Analysis.** The SPSS software (version 19.0, U.S.A.) was used for all statistical analyses, and one-way

ANOVA was performed to determine the significance of between-group differences ( $p < 0.05$ ).

### 3. Results and Discussion

As shown in Figure 1, the weight of left ventricle (Figure 1(a)), left atrium (Figure 1(b)), whole heart

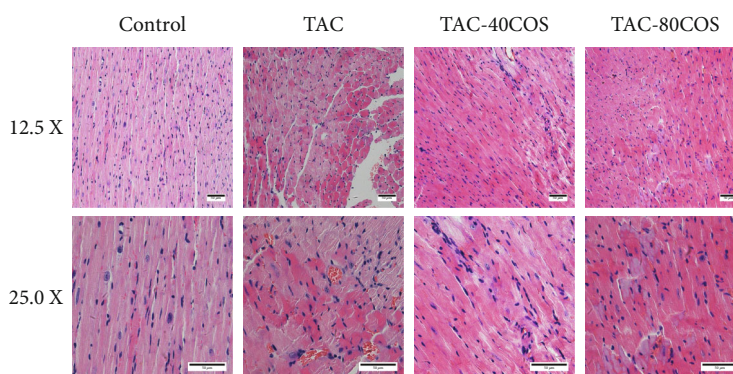


FIGURE 3: HE staining of heart: (a) Sham group; (b) TAC group; (c) TAC+40 mg/kg COS group; (d) TAC+80 mg/kg COS group.

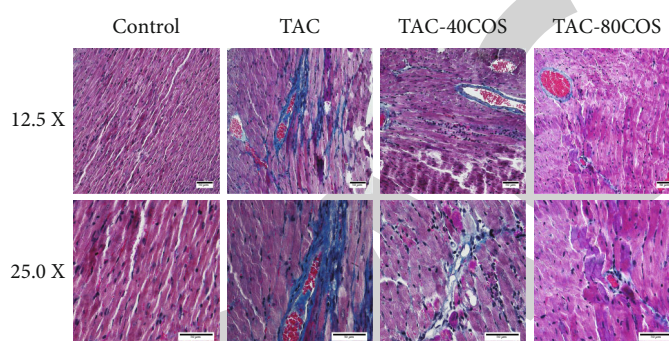


FIGURE 4: COS attenuated TAC heart fibrosis: (a) sham group; (b) TAC group; (c) TAC+40 mg/kg COS group; (d) TAC+80 mg/kg COS group.

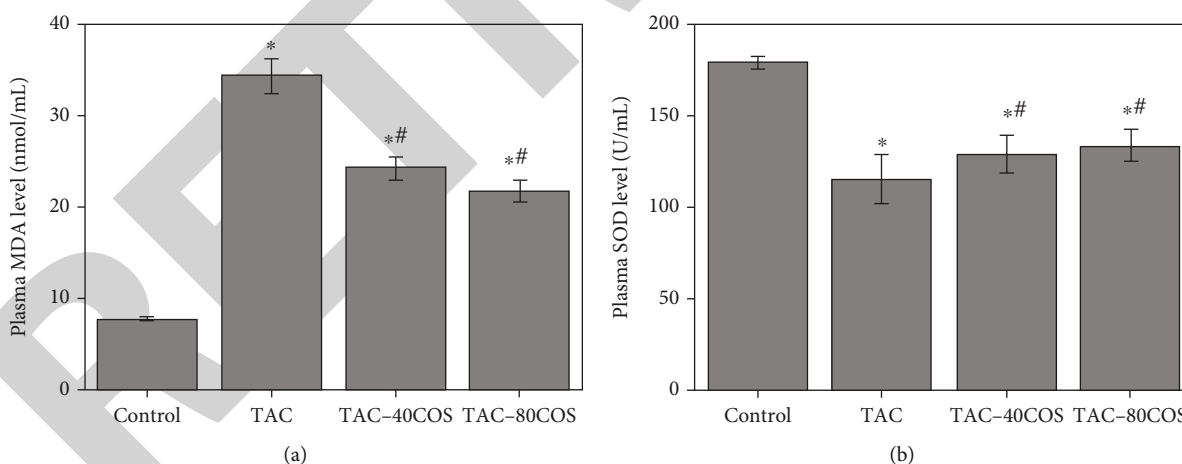


FIGURE 5: Changes of myocardial antioxidant enzymes under cold exposure. (a) The content of MDA in mouse serum. (b) The content of SOD in mouse serum. \* $p < 0.05$ , compared to the sham group, and # $p < 0.05$ , compared to the TAC group. All values are mean  $\pm$  SEM.

(Figure 1(c)), and lung (Figure 1(d)); the ratio of left ventricle (LV) weight to tibial length (Figure 1(e)); and the ratio of left atrium (LA) weight to tibial length (Figure 1(f)) of the TAC surgery significantly increased. Moreover, the mice were fed COS-supplemented diet; hypertrophy of aforementioned tissues was significantly reduced, indicating that COS might have some protective effects against heart failure. Furthermore, as can be seen from Figure 1, the tissue weights

were lower in the TAC-80COS relative to the TAC-40COS group. Although the difference was not statistically significant, these findings suggest that the protective effects of COS might be concentration-dependent. Heart failure leads to elevated inflammatory cytokines, which in turn causes inhibition of myocardial contraction and subsequent hypertrophy and apoptosis of cardiomyocyte [19–21]. These findings are in line with the results reported by Hanna and

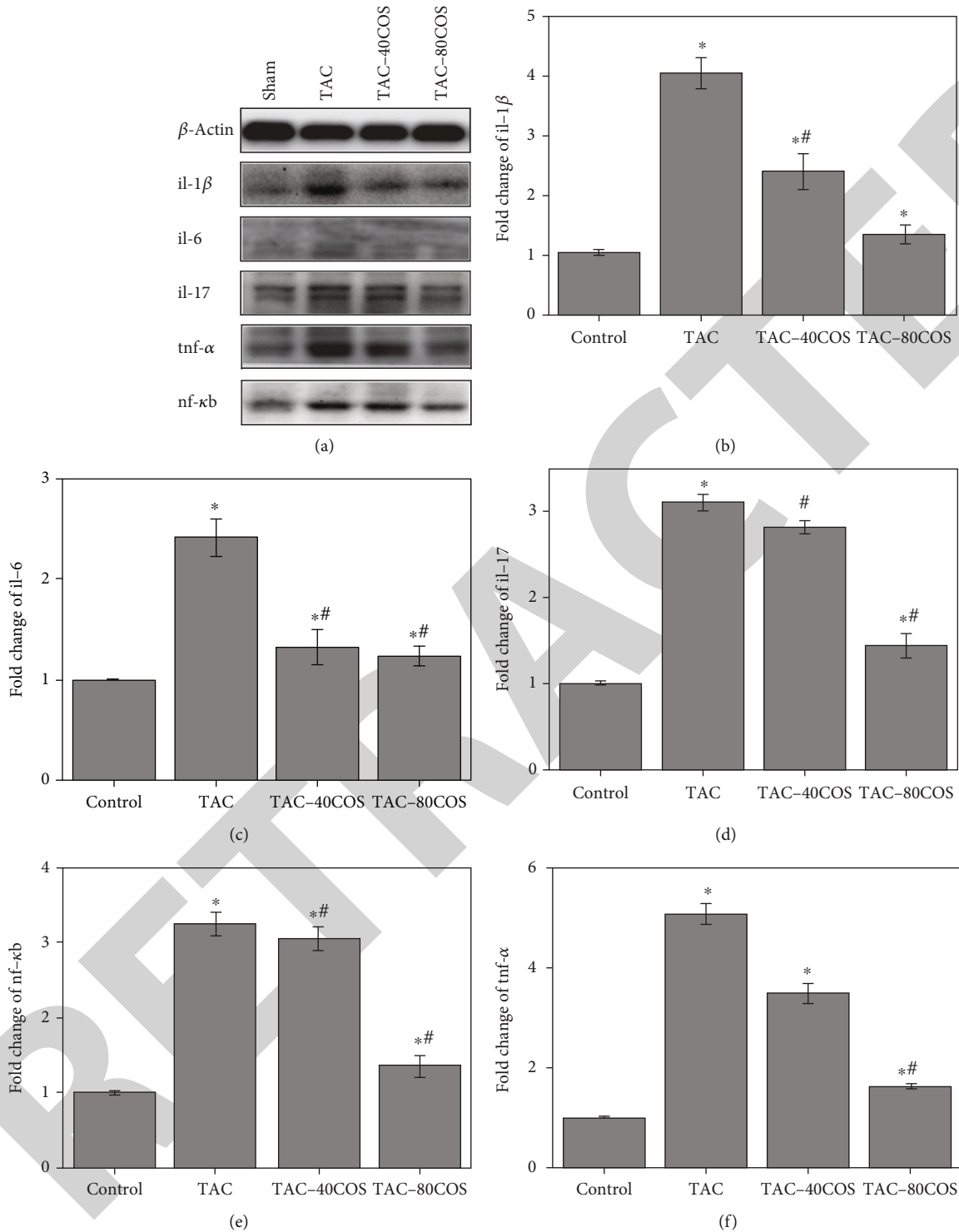


FIGURE 6: Inflammatory proteins and gene in myocardium under TAC. (a) Western blotting images of IL-1 $\beta$ , IL-6, IL-17, TNF- $\alpha$ , and nf- $\kappa$ b in four groups. (b) The gene expression of IL-1 $\beta$ . (c) The gene expression of IL-6. (d) Gene expression of il-17. (e) The gene expression of TNF- $\alpha$ . (f) The gene expression of nf- $\kappa$ b. \* $p$  < 0.05, compared to the sham group, and # $p$  < 0.05, compared to TAC group. All values are mean  $\pm$  SEM.

Frangiannis and Zhou and Qian, who noted that gavage of COS to pollution-affected rats significantly reduced the extent of lung injury in a dose-dependent manner [22, 23]. These effects may be attributed to the ability of COS to counteract the oxidative stress induced by the TAC surgery.

The ultrasound heart function assessments are depicted in Figure 2. As can be seen from Figures 2(a) and 2(b), both the end-diastolic and end-systolic diameters in the left ventricle (LV) increased as a result of heart failure induced by TAC surgery and decreased due to administration of COS.

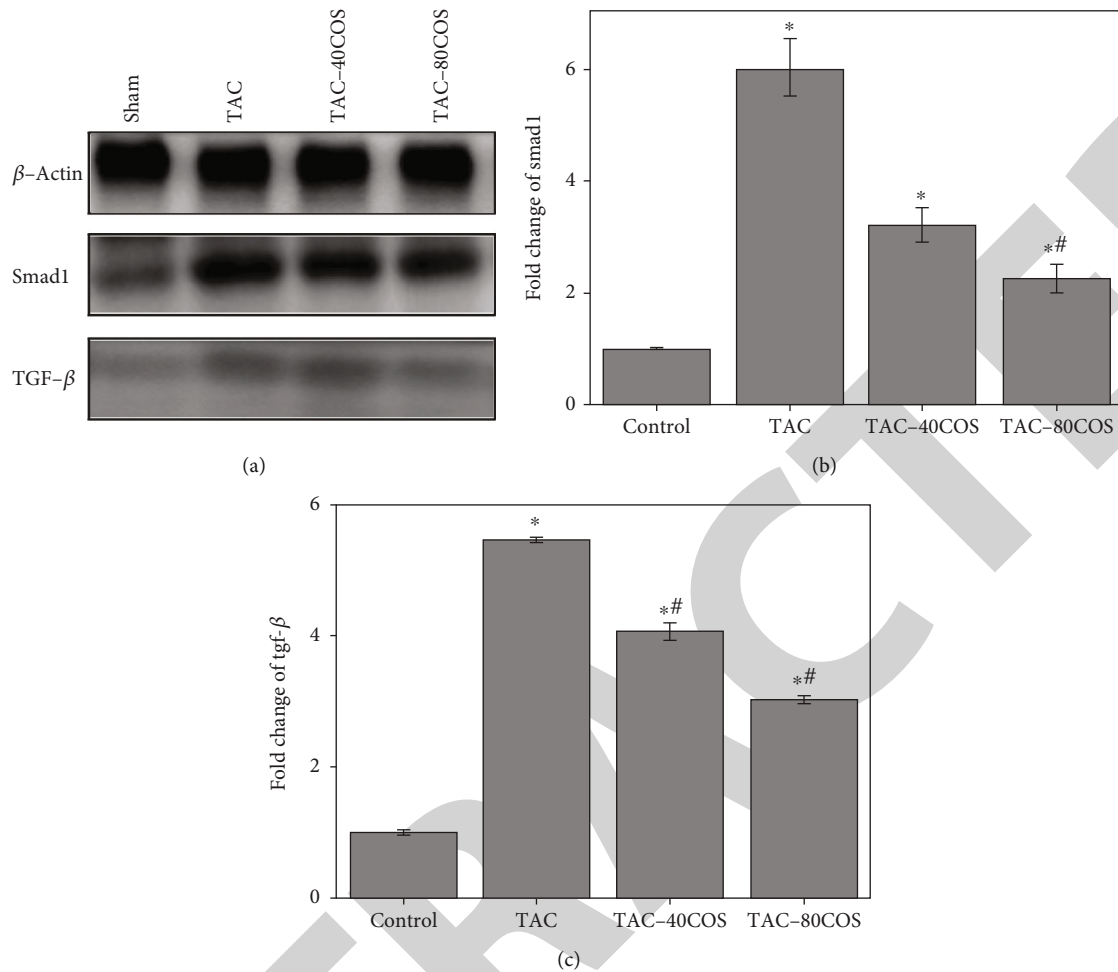


FIGURE 7: Inflammatory proteins and gene in TGF- $\beta$ /smad1 signal pathway. (a) Western blotting images of TGF- $\beta$  and smad1 in four groups. (b) The gene expression of smad1. (c) The gene expression of TGF- $\beta$ . \* $p < 0.05$ , compared to the sham group, and # $p < 0.05$ , compared to the TAC group. All values are mean  $\pm$  SEM.

Moreover, the ejection fraction (LVEF) and the ejection fractional shortening (LVFS) of the left ventricle, depicted in Figures 2(c) and 2(d), respectively, were significantly reduced as a result of heart failure and improved due to COS supplementation. Furthermore, as shown in Figures 2(e) and 2(f), the minimum and the maximum increase and decrease rates in LV were also affected by heart failure and improved due to COS. In this present work, we evaluated the cardiac functions in LV. The changes in these functions strongly indicate that heart failure was successfully induced in mice by the TAC surgery. The results presented in Figures 1 and 2 confirm that COS has effect on cardiac tissue protection from heart failure but warranted further analyses to investigate the protective mechanism of COS in heart failure.

The H&E and Masson staining results are presented in Figures 3 and 4, respectively, to examine the pathological changes of cardiomyocytes. As can be seen in Figure 3(a), the nuclei of cardiomyocytes were purple/blue, and the cytoplasm was gray, confirming that cardiomyocytes were normal in the control group. In the TAC group (Figure 3(b)), hypertrophy was observed, along with cardiomyocytes, accompanied by the infiltrated inflammatory cells. In

Figures 3(c) and 3(d), pertaining to the two groups that were fed COS-supplemented diet, hypertrophy could also be noted along with cardiomyocytes, while the number of inflammatory cells was lower than in the TAC group. Similarly, Figure 4 shows that no fibrosis was present in cardiac tissues in the control group (Figure 4(a)), while serious tissue fibrosis was observed in the TAC group (Figure 4(b)). In addition, six-week COS supplementation significantly reduced myocardial fibrosis (Figures 4(c) and 4(d)). These results strongly indicate that COS could reduce cardiac hypertrophy and the infiltration of inflammatory cells resulting from heart failure.

The MDA and SOD were investigated to evaluate and compare the oxidative stress levels in mice that suffered heart failure (the TAC, TAC-40COS, and TAC-80COS groups). As shown in Figure 5(a), the MDA level in the control group (Figure 5(a)) was significantly lower than in the other three groups. On the other hand, the SOD level (Figure 5(b)) in the control group was significantly higher than in the other three groups. Because both biomarkers are closely related to oxidative stress, the elevation of MDA and reduction in SOD strongly indicate that myocardial tissues were severely affected by heart failure. In addition, these



results are consistent with the findings yielded by the aforementioned analyses, suggesting that COS supplementation plays a protective role against heart failure.

IL-17 is an early T cell-induced inflammatory response initiator, which can amplify the inflammatory response by promoting the release of proinflammatory cytokines. IL-17 plays its biological role through the MAP kinase pathway and nuclear factor  $\kappa$ B (NF- $\kappa$ B) pathway after binding to receptors [24–26]. The inflammation-specific gene and protein expressions are shown in Figures 6 and 7, respectively. Cytokine *nf- $\kappa$ b*, encoded by *nf- $\kappa$ b* gene, is an inflammatory factor and controls the nuclear transcription factor. Cytokine IL-17 induces *nf- $\kappa$ b* activation, which in turn promotes the expressions of IL-1 $\beta$ , IL-6, and TNF- $\alpha$ , thereby accelerating the inflammatory response in heart tissues and leading to cardiomyocyte apoptosis, eventually lead to heart failure. Our results indicate that both genetic and protein expressions of the aforementioned factors significantly increased as a result of TAC surgery but were reduced by COS supplementation ( $p < 0.05$ ). As a signal pathway downstream of MyD88, NF- $\kappa$ B p65 is a key transcription factor in the inflammatory response, NF- $\kappa$ B in resting state with inactive I $\kappa$ B/NF- $\kappa$ B form of complex exists in the cytoplasm. NF- $\kappa$ B can promote gene transcription of cytokines, chemokines, and inflammatory factors and amplify inflammatory signals after activation [27, 28]. TGF- $\beta$  promotes inflammatory response and accelerates heart failure development with the downstream effector of *smad1*. Our analyses indicate that both TGF- $\beta$  and *smad1* expressions were significantly upregulated by the TAC surgery (Figure 7) as compared to the control group ( $p < 0.05$ ) and were reduced by COS supplementation. These gene analysis results are confirmed by Western blot images shown in Figure 7. TGF- $\beta$  makes inflammatory macrophages ineffective and promotes myofibroblast trans-differentiation and matrix synthesis through the Smad protein-dependent pathway. Smad1 also plays a certain role in the process of inflammation [29]. Moreover, the statistically significant differences between the findings obtained for the TAC-40COS and TAC-80COS groups indicate that the role of COS in heart failure prevention is concentration-dependent. Based upon the above analysis, it can be surmised that COS could protect myocardial tissues from heart failure by suppressing the expression of inflammation-specific factors in a concentration-dependent manner.

#### 4. Conclusion

In conclusion, as a part of this investigation, we induced heart failure in mice by performing TAC surgery and supplemented two groups with different doses of COS to assess its protective effects against heart failure. Our results reveal that COS supplementation could significantly suppress the expressions of inflammation-specific factors, such as TNF- $\alpha$ , and can thus protect myocardial tissues from further damage. These findings indicate that COS should be considered as a functional dietary supplement for patients that have suffered cardiac damage in order to prevent further

exacerbation of their condition. Therefore, further studies are needed to comprehensively evaluate COS biosafety in these future applications.

#### Data Availability

The datasets used and/or analyzed during the current study are available from the corresponding author on reasonable request.

#### Conflicts of Interest

The authors declared no potential conflicts of interest with respect to the research, authorship, and/or publication of this article.

#### Acknowledgments

This work was sponsored by the National Natural Science Foundation of China (U1608255) and the Liaoning Natural Science Fund (20180551033).

#### References

- [1] J. Jankowski, J. Floege, D. Fliser, M. Bohm, and N. Marx, “Cardiovascular disease in chronic kidney disease: pathophysiological insights and therapeutic options,” *Circulation*, vol. 143, no. 11, pp. 1157–1172, 2021.
- [2] P. Kasper, H. M. Steffen, and G. Michels, “Zirrhatische kardiomyopathie,” *Deutsche Medizinische Wochenschrift*, vol. 146, no. 16, pp. 1070–1076, 2021.
- [3] W. P. Lafuse, D. J. Wozniak, and M. V. S. Rajaram, “Role of cardiac macrophages on cardiac inflammation, fibrosis and tissue repair,” *Cell*, vol. 10, no. 1, p. 51, 2021.
- [4] A. E. Dikalova, A. Pandey, L. Xiao et al., “Mitochondrial deacetylase Sirt3 reduces vascular dysfunction and hypertension while Sirt3 depletion in essential hypertension is linked to vascular inflammation and oxidative stress,” *Circulation Research*, vol. 126, no. 4, pp. 439–452, 2020.
- [5] A. Groenewegen, F. H. Rutten, A. Mosterd, and A. W. Hoes, “Epidemiology of heart failure,” *European Journal of Heart Failure*, vol. 22, no. 8, pp. 1342–1356, 2020.
- [6] P. A. Glynn, H. Ning, A. Bavishi et al., “Heart failure risk distribution and trends in the United States population, NHANES 1999–2016,” *The American Journal of Medicine*, vol. 134, no. 3, pp. e153–e164, 2021.
- [7] P. A. Heidenreich, B. Bozkurt, D. Aguilar et al., “AHA/ACC/HFSA Guideline for the Management of Heart Failure: A Report of the American College of Cardiology/American Heart Association Joint Committee on Clinical Practice Guidelines,” *Circulation*, vol. 145, no. 18, pp. e895–e1032, 2022.
- [8] S. G. Kou, L. M. Peters, and M. R. Mucalo, “Chitosan: a review of sources and preparation methods,” *International Journal of Biological Macromolecules*, vol. 169, pp. 85–94, 2021.
- [9] J. Ma, L. Zhong, X. Peng, Y. Xu, and R. Sun, “Functional chitosan-based materials for biological applications,” *Current Medicinal Chemistry*, vol. 27, no. 28, pp. 4660–4672, 2020.
- [10] P. Sacco, M. Cok, F. Scognamiglio et al., “Glycosylated-chitosan derivatives: a systematic review,” *Molecules*, vol. 25, no. 7, p. 1534, 2020.

## Retraction

# Retracted: Phytochemical Analysis, Total Phenolic, Flavonoid Contents, and Anticancer Evaluations of Solvent Extracts and Saponins of *H. digitata*

### BioMed Research International

Received 8 January 2024; Accepted 8 January 2024; Published 9 January 2024

Copyright © 2024 BioMed Research International. This is an open access article distributed under the Creative Commons Attribution License, which permits unrestricted use, distribution, and reproduction in any medium, provided the original work is properly cited.

This article has been retracted by Hindawi following an investigation undertaken by the publisher [1]. This investigation has uncovered evidence of one or more of the following indicators of systematic manipulation of the publication process:

- (1) Discrepancies in scope
- (2) Discrepancies in the description of the research reported
- (3) Discrepancies between the availability of data and the research described
- (4) Inappropriate citations
- (5) Incoherent, meaningless and/or irrelevant content included in the article
- (6) Manipulated or compromised peer review

The presence of these indicators undermines our confidence in the integrity of the article's content and we cannot, therefore, vouch for its reliability. Please note that this notice is intended solely to alert readers that the content of this article is unreliable. We have not investigated whether authors were aware of or involved in the systematic manipulation of the publication process.

Wiley and Hindawi regrets that the usual quality checks did not identify these issues before publication and have since put additional measures in place to safeguard research integrity.

We wish to credit our own Research Integrity and Research Publishing teams and anonymous and named

external researchers and research integrity experts for contributing to this investigation.





The corresponding author, as the representative of all authors, has been given the opportunity to register their agreement or disagreement to this retraction. We have kept a record of any response received.

### References

- [1] O. M. Alshehri, S. Alshamrani, M. H. Mahnashi et al., "Phytochemical Analysis, Total Phenolic, Flavonoid Contents, and Anticancer Evaluations of Solvent Extracts and Saponins of *H. digitata*," *BioMed Research International*, vol. 2022, Article ID 9051678, 12 pages, 2022.

## Research Article

# Phytochemical Analysis, Total Phenolic, Flavonoid Contents, and Anticancer Evaluations of Solvent Extracts and Saponins of *H. digitata*

Osama M. Alshehri,<sup>1</sup> Saleh Alshamrani,<sup>1</sup> Mater H. Mahnashi <sup>2</sup>,  
Mohammed Merae Alshahrani,<sup>3</sup> Jalwa Ali Khan,<sup>4</sup> Muhammad Shah,<sup>5</sup>  
Mohammed Ali Alshehri,<sup>6</sup> Rehman Zafar,<sup>7</sup> Muhammad Zahoor <sup>8</sup>,  
Muhammad Saeed Jan <sup>4</sup>, Syed Shams ul Hassan,<sup>9,10</sup> and Abdul Sadiq <sup>11</sup>

<sup>1</sup>Department of Clinical Laboratory Sciences, College of Applied Medical Sciences, Najran University, Najran, Saudi Arabia

<sup>2</sup>Department of Pharmaceutical Chemistry, College of Pharmacy, Najran University, Najran 55461, Saudi Arabia

<sup>3</sup>Department of Clinical Laboratory Sciences, Faculty of Applied Medical Sciences, Najran University, 1988, Najran 61441, Saudi Arabia

<sup>4</sup>Department of Pharmacy, University of Swabi, KP, Pakistan

<sup>5</sup>COMSATS University Islamabad, Abbottabad Campus, Pakistan

<sup>6</sup>Department of Medical Genetics, Collage of Applied Medical Sciences, Najran University, Najran, Saudi Arabia

<sup>7</sup>Riphah Institute of Pharmaceutical Sciences, Riphah International University, Islamabad 44000, Pakistan

<sup>8</sup>Department of Biochemistry, University of Malakand, Chakdara, 18000 Dir (L), KP, Pakistan

<sup>9</sup>Shanghai Key Laboratory for Molecular Engineering of Chiral Drugs, School of Pharmacy, Shanghai Jiao Tong University, Shanghai 200240, China

<sup>10</sup>Department of Natural Product Chemistry, School of Pharmacy, Shanghai Jiao Tong University, Shanghai 200240, China

<sup>11</sup>Department of Pharmacy, University of Malakand, Chakdara, 18000 Dir (L), KP, Pakistan

Correspondence should be addressed to Muhammad Saeed Jan; [saeedjanpharmacist@gmail.com](mailto:saeedjanpharmacist@gmail.com) and Abdul Sadiq; [sadiquom@yahoo.com](mailto:sadiquom@yahoo.com)

Received 23 August 2022; Accepted 22 September 2022; Published 4 October 2022

Academic Editor: Barkat Khan

Copyright © 2022 Osama M. Alshehri et al. This is an open access article distributed under the Creative Commons Attribution License, which permits unrestricted use, distribution, and reproduction in any medium, provided the original work is properly cited.

Cancer is one of the most challenging diseases in the modern era for the researchers and investigators. Extensive research worldwide is underway to find novel therapeutics for prevention and treatment of diseases. The extracted natural sources have shown to be one of the best and effective treatments for cell proliferation and angiogenesis. Different approaches including disc potato model, brine shrimp, and chorioallantoic membrane (CAM) assay were adopted to analyze the anticancer effects. *Habenaria digitata* was also evaluated for MTT activity against NIH/3T3 cell line. The dexamethasone, etoposide, and vincristine sulfate were used as a positive control in these assays. All of the extracts including crude extracts (Hd.Cr), saponin (Hd.Sp), n-hexane (Hd.Hx), chloroform (Hd.Chf), ethyl acetate (Hd.EA), and aqueous fraction (Hd.Aq) were shown excellent results by using various assays. For example, saponin and chloroform have displayed decent antitumor and angiogenic activity by using potato tumor assay. The saponin fraction and chloroform were shown to be the most efficient in potato tumor experiment, demonstrating 87.5 and 93.7% tumor suppression at concentration of 1000  $\mu\text{g/ml}$ , respectively, with  $\text{IC}_{50}$  values of 25.5 and 18.3  $\mu\text{g/ml}$ . Additionally, the two samples, chloroform and saponins, outperformed the rest of the test samples in terms of antiangiogenic activity, with  $\text{IC}_{50}$  28.63  $\mu\text{g/ml}$  and 16.20  $\mu\text{g/ml}$ , respectively. In characterizing all solvent fractions, the chloroform (Hd.Chf) and saponin (Hd.Sp) appeared to display good effectiveness against tumor and angiogenesis but very minimal activity against *A. tumefaciens*. The Hd.Chf and Hd.Sp have been prospective candidates in the isolation of natural products with antineoplastic properties.

## 1. Introduction

Cancer is a challenging disease worldwide because it is a major cause of mortality and morbidity [1]. Due to cancer, death ratio is almost high when compared to other diseases like AIDS, malaria, T.B, pneumonia, and other death causing diseases [2]. Cancer has been ranked as the second largest cause of mortality in developed nations and third major death cause in underdeveloped nations [3]. Every year, over ten million individuals worldwide are diagnosed with cancer, which results in 12.5% of the global total, i.e., 7.1 million deaths approximately. Cancer is characterized by several hallmarks such as avoiding immune destruction, growth suppressors, sustaining proliferation signaling, tumor stimulating inflammation, persuading angiogenesis, instability of genome, metastasis, allowing the immortality replication, dysregulating cellular energetics, and ultimately cell death [4, 5].

Angiogenesis is one of the most important goals for treating various pathological conditions including cancer and other death causing disease. It has a fundamental role in new vascular network formation for supply of oxygen, nutrient, and immune cells also in suppression of waste materials [6]. Angiogenesis is starting from the embryo, where it initiates the primary vascular network as well as a sufficient vasculature for growth and development of organs [7]. Major indicating molecules involved in angiogenesis include angiopoietin 1 and angiopoietin 2 vascular endothelial growth factor (VEGF), basic fibroblast growth factor (BFGF), angiotropin, angiogenin, TNF- $\alpha$ , and TGF- $\beta$ . Freshly discovered angiogenesis inhibitors not only revealed an attractive therapeutic approach against cancer [8].

Potato disc assay is costly, more effective, rapid, and reliable bioassay to provide the source for apparent anticancer and antitumor effectiveness of the tested fractions [9]. In potato disc assay, inhibition of tumor (crown gall) is influenced by *A. tumefaciens* which have the antimutagenic potential and also antitumor property [9]. Neoplastic illness known as crown gall tumor is caused by *A. tumefaciens* in plants [10]. Tumor-inducing plasmids in *A. tumefaciens* include genetic material with information (T-DNA) and can transmit the infection to normal plant cells or damaged areas resulting in autonomous tumor cell [11]. These tumor-inducing plasmids cause plant cells to multiply rapidly without passing through apoptosis, resulting in tumor that grows fast, in the similar manner as human and animal tumors [12].

Likewise, to detect the fundamental cytotoxicity of synthetic and natural drugs, the brine shrimp cytotoxicity activity is a critical technical way before moving to more complicated and advanced research [13]. In terms of phytochemicals, they have definite biological prospects. Like saponins, which are well known for their cytotoxic potential, flavonoids, which are known for their antioxidant potential, and alkaloids, that have been reported by a number of studies and renowned for their antimicrobial activity [14].

The natural anticancer drugs are more effective and less toxic as compared to synthetic anticancer drugs because synthetic anticancer drugs have toxicity issues, are expensive, and have negative side effects; natural products are the

highly promising source of efficient anticancer treatments [15–17]. The herbal medicines are primarily used up to eighty percent of total population for the primary well-being in developing countries. In this perspective, the natural products have been considered rich in phytochemicals such as glycosides, renins, tannins, flavonoids, polyphenol, alkaloids, and terpenoids [18–20]. These active ingredients present in the natural products like plants possess antioxidant, anti-inflammatory, antifungal, antimicrobial, antimycotic, and anticancer properties [21–23].

Genus of the *Habenaria* is related with family Orchidaceae, which consist round about 850 genera and total 35000 species [24]. Orchids were used for different illness like arthritis, stomach problem, syphilis, acidity, jaundice, tumor, boils, piles, inflammations, hepatitis, blood dysentery, malaria, pyrexia, tuberculosis, sexually transmitted diseases, cholera, eczema, wounds, diarrhea, and vermifuge [25]. An attempt to reexplore the medicinal properties of the herbs would aid in management of the diseases like cancer. With the available information, the current study was conducted to assess various anticancer effects of *Habenaria digitata* crude extract and their consequent fractions.

## 2. Material and Methods

**2.1. Collection and Extracts.** *Habenaria digitata* plant was identified and isolated from Lower Dir Lower, Khyber Pakhtunkhwa (KPK), Pakistan, in April mid because the active ingredients are present in increased amount as compared to other months of the year. Afterwards, it was recognized via by Prof. Muhammad Nisar, Chairman of the Department of Botany, University of Malakand Dir (L) KPK, Pakistan. The plant sample was stored and recorded at herbarium having voucher number H.UOM. BG.180. The plant's aerial components (15 kg) were bathed in sterile water and then dried in a totally shaded environment for 14 days. Cut it into little pieces using a mortar and pestle or a grinder once it has dried, and crush it into extremely small particulates (7.5 kg). The small coarse particles were then immersed in 24 L of 80% methanol for around 21 days. After that, the entire material was filtered using the muslin cloth, followed by the Whatman filter paper, and the liquid was collected. The filtrate was then taken to a rotary evaporator (at 40°C) for further extraction [14]. After deliberating 650 g, the final gloomy green color hard methanolic extract of *H. digitata* was obtained.

**2.2. Fractionation.** The methanolic extract was poured into a separating funnel with a vacuum-sealed stopper. After that, the Hd.Cr was combined with 500 ml of n-hexane and a corresponding quantity of water. The separating funnel was shook violently to thoroughly mix all of the materials and then held in place with a stand to separate the water and n-hexane layers. Then, just the hexane layer was separated in both layers. Through 500 ml of n-hexane, the identical operation was done twice. The organic layers were separated three times before being combined and concentrated under reduced pressure in a rotating evaporator at 40°C. Hexane was found to have a concentrated weight of 27.6 gm likewise;

the same method is followed to raise the polarization of the other solvents using the same approach. The next solvent fractions were ethyl acetate, chloroform, and Bt., with weights of 30, 42, and 94 g, respectively. Finally, at a weight of 140 gm, the aqueous stratum was concentrated [26].

**2.3. Quantitative Estimation of Phytochemicals.** The qualitative investigations of plant extract phytochemicals were performed for detection of alkaloids, glycosides, tannins, terpenoids, anthraquinone, saponins, flavonoids, oils, and sterols using the method reported previously [27]. The 0.2 gm of the crude extract was taken and mixed with 2% sulphuric acid. The mixture was hot for a while and then cooled. Afterward, sample filtered and treated with Dragendorff's reagent. The orange red precipitate exhibited presence of alkaloids. For the anthraquinone analysis, the 2 g of crude extract was macerated with the ether. The solution was mixed, and the presence of red, pink, or violet color in aqueous layer formation indicates presence of anthraquinones [28].

For the glycosides test, 1 ml concentrated sulphuric acid and the 5 ml of aqueous extract were mixed with glacial acetic acid (2 ml) having ferric chloride of 1 drop. The brown ring formation was indicated presence of glycosides. For the tannin test, 20 ml distilled water was added to 2 g sample and then heated for 5 min. This solution was filtered and cooled. From this, 1 ml was added to 5 ml water. Then, 2 drops of ferric chloride 10% were added. A bluish-black precipitate showed tannin presence. For terpenoids, identification extract was suspended water (5 ml), heated, and then filtered; after that, 2 ml chloroform was mixed to filtrate, followed by additional 3 ml sulphuric acid. The reddish brown color appearance indicates presence of terpenoids [29].

**2.4. Determination of Total Phenols.** The total phenolic content is determined by the Folin-Ciocalteu reagent [30, 31]. Gallic acid was used to make the calibration curve (a standard phenol). A gallic acid standard solution in 80 percent ethanol (1 mg/ml) was made, from which 20 to 320  $\mu$ l was taken in another test tube and the volume was increased to 1 ml with 80 percent ethanol. Each test tube was then filled with 100  $\mu$ l of Folin-Ciocalteu (1:10) solution, followed by 300  $\mu$ l of 7.5 percent  $\text{Na}_2\text{CO}_3$  solution. This combination was forcefully shaken. The test tubes were allowed to be heated for about 1 minute and then forcefully cooled. The test tubes are heated for about 1 minute, and after heating, cool it vigorously. Optical density (OD) was measured spectrophotometrically at 765 nm after each test tube was diluted to 2 ml with distilled water. OD was obtained after administering crude methanolic and subsequent fractions. Finally, using the OD of the standard phenol with a standard regression curve, the total quantity of phenolic was estimated (referred to gallic acid). The total phenolic content was calculated as  $\mu$ g gallic acid equivalent (GAE) per milliliter of sample.

**2.5. Total Flavonoid Determination.** Total flavonoid (TF) assay was prepared as previously designated with minor

TABLE 1: Total flavonoids and phenolic contents of *H. digitata* crude methanolic extract and their subsequent fractions.

Sample content	Sample total phenolic (mg GAE/g)	Sample total flavonoid (mg RTE/g)
Hd.Cf	178.61 $\pm$ 0.66	132.43 $\pm$ 1.10
Hd.EA	220.44 $\pm$ 0.82	98.44 $\pm$ 1.88
Hd.Cr	98.52 $\pm$ 1.50	72.75 $\pm$ 0.67
Hd.Hx	30.32 $\pm$ 1.70	14.32 $\pm$ 0.52
Hd.Aq	41.43 $\pm$ 0.73	21.50 $\pm$ 0.54

changes [32, 33]. Stock solution of the rutin was prepared in the 80% of ethanol (1 mg/ml). The volume of 1 ml of dilute extract or standard solution of the rutin (20 to 100  $\mu$ g/ml) was placed in the test tube carefully; then, after 5 minutes, 150  $\mu$ l of  $\text{NaNO}_2$  (5%) and 150  $\mu$ l of the  $\text{AlCl}_3$  (10%) were added to it. The mixture was shaken strongly, and after 5 minutes, 1 ml of 1 M solution of NaOH was added to it; then, shake it carefully and after that dilute it to 2 ml by adding distilled water. Then, the absorbance was recorded at 510 nm with respect to the blank. The findings were determined using the rutin calibration curve ( $R^2 = 0.999$ ). The total flavonoid concentration was measured in rutin equivalents (RE) per milliliter of sample.

**2.6. Extraction of Crude Saponins.** This procedure was performed by crushing 20 gm of sample plant with 20% ethanol (100 ml) and allowed to stay in water bath at 55°C for 04 hours. Afterwards, filtration and extraction with 20% ethanol (200 ml) were performed once again. After that, keep it in water bath for few minutes, resulting in volume drop to 40 ml. This sample was poured into funnel and mixed the sample with 20 ml diethyl ether with continuous shaking. The solvent layers including watery and diethyl ether layers would be separated. The n-butanol (60 ml) was added to the aqueous layer, which was then separated using a separating funnel. A 5 percent brine (10 ml) solution was used to wash the n-butanol extract. In a water bath, the final volume was concentrated, then transferred to a beaker. Hd.Sp was dried by placing 1.1 gm of the sample in an oven [32].

**2.7. Study of Phytochemical.** Using the established protocols, a qualitative phytochemical investigation of plant extracts was accepted for the presence of glycosides, anthraquinones, saponins, flavonoids, terpenoids, alkaloids, tannins, and sterol [34, 35]. Plant extracts were hydrolyzed using hydrochloric acid (HCl), followed by neutralization with sodium hydroxide, to identify glycosides (NaOH). The existence of red precipitates was determined by adding a few drops of the solution, Fehling's solution, to the preparation. Dragendorff's reagent was used to identify the phytochemicals or alkaloids. Similarly, samples were exposed to sterol and terpenoids after being treated with petroleum ether and then extracted with chloroform. After treating the chloroform layer with acetic anhydride and strong hydrochloric acid (HCl) in series, the presence of reddish brown terpenoids and the appearance of green to pink sterols were observed.

TABLE 2: Phytochemical ingredients in crude fraction of *H. digitata*.

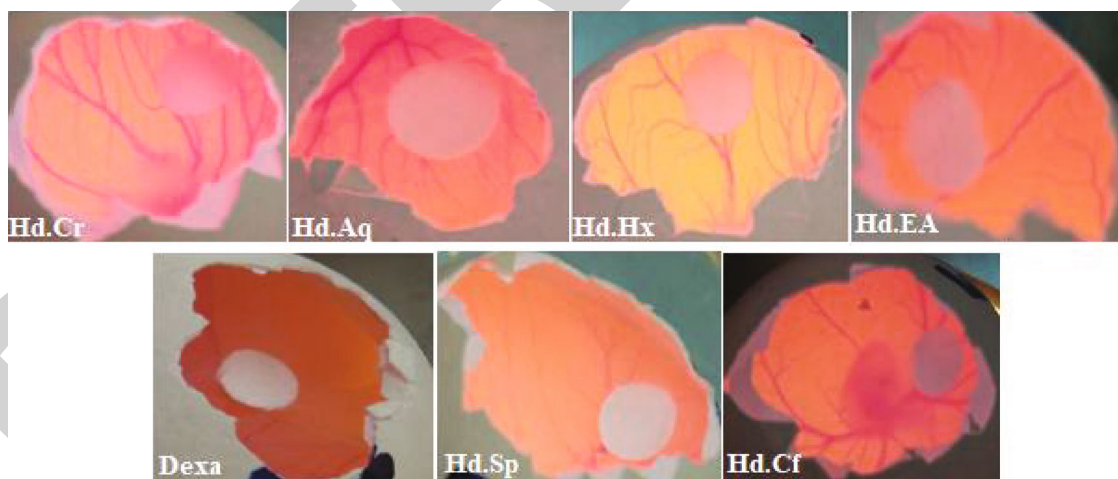
S. no	Phytochemicals	Observations	Results
1.	Alkaloids	Turbidity	+
2.	Glycosides	Red color precipitate formation	+
3.	Tannins	Bluish black color formation	+
4.	Terpenoids	Reddish brown color appearance	+
5.	Anthraquinones	Reddish violet color	+
6.	Flavonoids	Yellow color formation and changed colorless when acid is added	+
7.	Saponins	Frothing bubble formation	+
8.	Oils	Greasy spot formation	+
9.	Sterols	Green to pink color was absent	-

Phytochemicals present = positive sign; phytochemicals absent = negative sign.

TABLE 3: Various samples of antiangiogenic activity of *H. digitata*.

Sample	Percentage angiogenic activity mean $\pm$ SEM ( $n = 5$ )						IC <sub>50</sub> $\mu$ g/ml
	31.25 $\mu$ g/ml	62.5 $\mu$ g/ml	125 $\mu$ g/ml	250 $\mu$ g/ml	500 $\mu$ g/ml	1000 $\mu$ g/ml	
Hd.Cr	29.24 $\pm$ 0.22***	36.30 $\pm$ 1.50***	40.52 $\pm$ 0.60***	45.98 $\pm$ 1.03***	52.37 $\pm$ 0.35***	65.35 $\pm$ 0.86***	460.51
Hd.Hx	21.92 $\pm$ 0.51***	25.34 $\pm$ 1.32***	26.68 $\pm$ 0.91***	32.52 $\pm$ 0.88***	39.85 $\pm$ 1.38***	43.55 $\pm$ 0.44***	1530.44
Hd.Cf	51.01 $\pm$ 1.52***	55.10 $\pm$ 1.80***	61.35 $\pm$ 0.66***	60.95 $\pm$ 1.23***	69.98 $\pm$ 1.66***	78.65 $\pm$ 1.66***	28.63
Hd.EA	44.50 $\pm$ 0.56***	48.52 $\pm$ .088***	52.68 $\pm$ 1.62***	56.05 $\pm$ 0.84***	61.02 $\pm$ 1.13***	69.41 $\pm$ 1.13***	86.73
Hd.Aq	24.02 $\pm$ 0.25***	27.10 $\pm$ 1.17***	28.35 $\pm$ 0.33***	39.35 $\pm$ 0.90***	52.68 $\pm$ 1.47***	61.44 $\pm$ 1.43***	430.80
Hd.Sp	54.64 $\pm$ 0.70***	58.22 $\pm$ 0.72***	59.89 $\pm$ 0.28***	64.20 $\pm$ 1.17**	68.45 $\pm$ 0.99*	76.98 $\pm$ 1.03 <sup>ns</sup>	16.20

Positive control was taken as dexamethasone, with IC<sub>50</sub> data of 11.66  $\mu$ g/ml. Values significantly vary as compared to the standard drug with probability \*  $p < 0.05$ , \*\*  $p < 0.01$ , and \*\*\*  $p < 0.001$  at 90% confidence interval. ns: values not significantly different in contrast to standard drug.

FIGURE 1: Antiangiogenic activity of various extract of the *H. digitata*.

The anthraquinones were identified by mixing the extract in one percent hydrochloric acid (HCl), with benzene, and finally combining with NH<sub>4</sub>OH. The development of violet, crimson, or pink tints indicated the existence of anthraquinones. The presence of saponin phytochemicals was then identified by the creation of bubbles in a beaker when diluted samples were vigorously shaken.

**2.8. Assay of Antiangiogenic Activity.** The antiangiogenic activity of plant extracts and saponins was determined using

the chorioallantoic membrane (CAM) experiment [36]. The fertilised domestic chicken eggs were purchased from a hen merchant in Chakdara, Pakistan, and incubated in a humidified incubator (HYSC Korea (BI-81/150/250) for 4-5 days at 37°C, handling them 3 times per day. After the incubation process was finished, the 7-day old eggs were allowed to be examined under a light to detect and surround the embryo head. The yolk sacs were then separated from the shell membrane by puncturing a small hole in the narrow corner of eggs with an 18 gauge hypodermic needle and aspirating

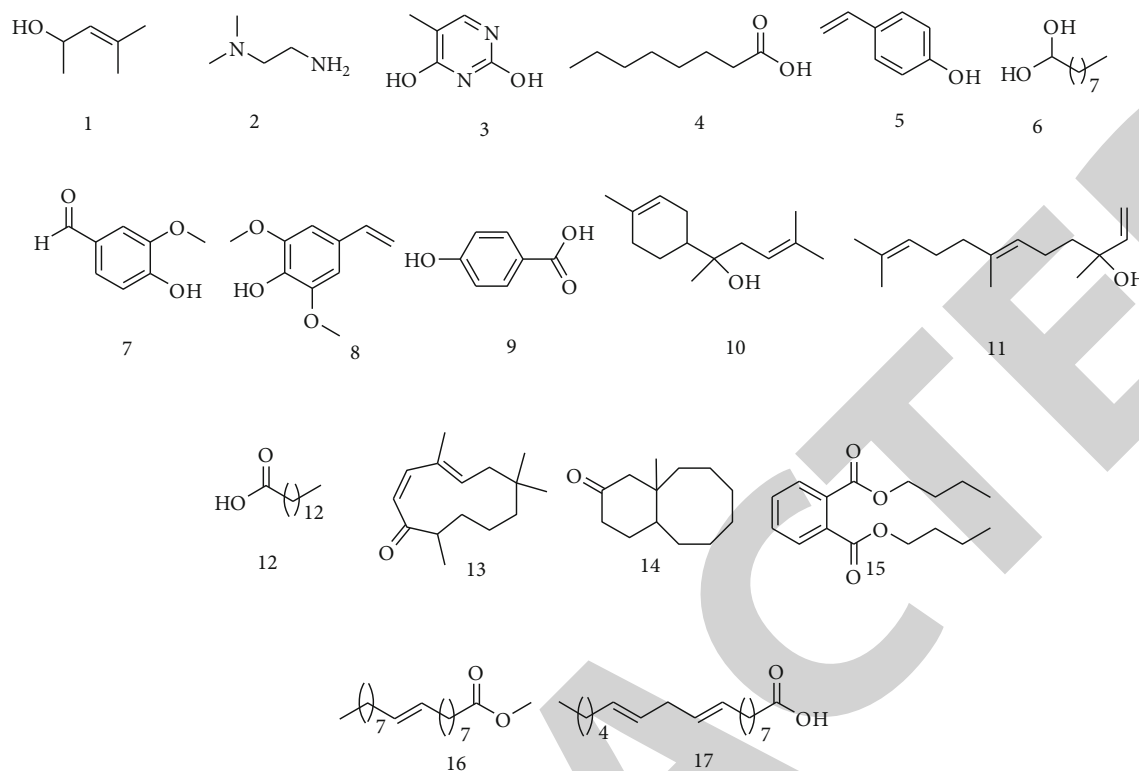


FIGURE 2: Anticancer compounds reported from *H. digitata*.

0.5-1 ml of albumin. The embryo air sac shell was split using forceps, and the membrane around the air sac base was peeled away. A Thermanox cover slip was then carefully put on the membrane of CAM on the eighth day, and it was incubated with 10 different samples at concentration of 31.25-1000  $\mu\text{g/ml}$ . After that, the 33-gauge needle was used to inject acetone with methanol in 1:1 ratio into the

embryo of chorioallantois after 3 days. The vessel number in CAM was counted after it was cut out of eggs. Under a microscope, the vessels were radially converted in direction of the centre and were checked. Each sample dose required at least twenty eggs. The following formula was used to calculate the percent increase and inhibition:

$$\text{Percent Inhibition} = \frac{\text{No. of vessels in CAM treated with normal saline} - \text{No. of Vessels in CAM with Plant Sample}}{\text{No. of vessels in CAM treated with normal saline}} \times 100 \quad (1)$$

## 2.9. Antitumor Bioassay through Potato Disc

### 2.9.1. Plant Extract Preparation of *A. tumefaciens* Mixture.

This bioassay was carried out through McLaughlin and Rogers' standard protocol [36]. A strain B6 tumefaciens with tumor inducing plasmid was cultivated over night at 25°C on soybean casein digest agar (SCDA). Plant extract dilutions in the range from 31.25 to 1000 g/ml were synthesized in DMSO and filtered. The Agrobacterium culture is mixed with the serial dilution of the crude and subsequent fractions of the plant extract to form approximately 1108 colony forming units. The control was prepared in combination with 50 liters of DMSO with 450 liters purified water that was sterile; afterwards, 500 liters of *A. tumefaciens* culture of broth was added.

### 2.9.2. Discs of Potato Preparation.

Potatoes with red skinned were obtained from an active shop near Malakand Chakdara University in Pakistan. The potato discs of a 2 mm height and an 8 mm thickness were prepared with a sterile cork borer. These discs were then surface sterilized for 4 to 5 minutes and a 1 percent  $\text{HgCl}_2$  solution before they were washed with distilled water. Then, for 20 minutes, they were dried aseptically. By using sterile forceps, the discs were placed on 1.5 percent of autoclaved agar medium plates. At the end, 01 of plant extract-bacterium mixture was being injected into the upper shallow of each potato disc. The plates were parafilm sealed and was incubated at 28°C in the dim. Then, potato discs were blemished with Lugol's solution (10 percent KI+5% I<sub>2</sub>), and then, tumors were counted with the help of a separating microscope after 15-

20 days. Vincristine at the rang of 31.25-1000 g/ml was used as a positive control in this assay. The test was done for 3 times, and the record was statistically examined [37].

**2.9.3. Anti-Agrobacterium In Vitro Assay.** Assay of disc diffusion: a qualitative of partial-quantitative disc method was used to observe the plant material effect on development of Agrobacterium and thus on the tumor formation, as described earlier [38]. In the nutshell, test organisms were inoculation on the nutrient agar plates and were prepared aseptically in the laminar flow hood. With sterile forceps, 6 mm diameter sterile paper discs with different amount of the extracts impregnated were deposited on membrane of the Petri dishes that were inoculated. Negative controls used were the blank discs drenched with solvents/DMSO, whereas positive controls used were ceftriaxone discs (Geltis, Shaigan Pharmaceuticals, containing 30g medication). These plates were allowed to incubate for 24 hrs at 37 degrees Celsius, and areas of inhibition surrounding the bores were then measured.

**2.10. Brine Shrimp Cytotoxicity Assay.** Following the standard protocol, the crude extracts and saponins of *H. digitata* were tested for their cytotoxicity against *Artemia salina* (brine shrimp eggs) [39].

**2.10.1. Hatching Procedure.** The hatching of brine shrimp eggs is ideally in the sea salty water. In a narrow rectangular pliable dish measuring 22 × 32 cm, 38 gm of profitable salt mixture was dissolved in a doubled distilled H<sub>2</sub>O to produce an artificial sea water solution. A perforated mechanism was then used to separate the plastic dish into two halves. 50 mg of eggs was scattered in the darkened section much larger and aluminum foil covered; however, the lesser compartmental area was remained wide to normal light for the newborn crosshatched brine shrimp larva. These were then allowed to incubate at 37°C for 2 days. When the larvae hatched after 48 hours, they were lured from the dark side with a lamp and then collected with a Pasteur pipette [10].

**2.11. Cells Viability MTT Assay.** The NIH/3T3 cell line of mouse embryonic fibroblasts was maintained in DMEM media containing 10% FBS and antibiotic (50 units/ml penicillin and 50 units/ml streptomycin) at 37°C in a humid environment containing 5% CO<sub>2</sub>. This test was used to assess cytotoxicity against cultured NIH/3T3 cells [40]. In 200 µl media, NIH/3T3 cells were distributed into 96-well plates at an initial seeding density of 8.0-103 cells/well, then incubated for 24 hours. Later, the culture medium was withdrawn and replaced with a 200 µl media containing successive dilutions of samples (0.0625–1 mg/ml). Positive control cells were cultured with just the medium, and the cells were allowed to proliferate for an additional 24 hours. As a result, each well received 20 µl of MTT solution (5 mg/ml) in PBS. The media containing unreacted color was carefully removed after the cells had been incubated for 4 hours. The purple formazan crystals were then dissolved in 200l of dimethyl sulfoxide (DMSO) each well, and the absorbance was measured at 570 nm in a microplate

TABLE 4: Various samples of antitumor activity of *H. digitata*.

Sample content	Concentration (µg/ml)	Inhibition in average (mean ± SEM)	Inhibition percentage (mean ± SEM)	IC <sub>50</sub> (µg/ml)
Hd.Cr	1000	24.7 ± 0.3	86.4 ± 1.1***	195.7
	500	18.0 ± 0.6	64.3 ± 1.9***	
	250	15.0 ± 1.2	54.4 ± 2.8***	
	125	13.3 ± 0.0	44.6 ± 1.1***	
	62.5	11.0 ± 0.3	39.0 ± 0.0***	
	31.25	10.0 ± 0.6	33.5 ± 1.9***	
Hd.Hex	1000	20.0 ± 0.4	62.3 ± 1.7***	390.2
	500	17.3 ± 0.5	53.4 ± 1.9***	
	250	13.7 ± 1.2	41.2 ± 1.1***	
	125	12.0 ± 0.3	35.7 ± 2.8***	
	62.5	11.5 ± 0.9	33.5 ± 1.1***	
	31.25	09.0 ± 0.6	25.7 ± 0.0***	
Hd.Chf	1000	25.0 ± 1.2	87.5 ± 2.8*	25.5
	500	22.5 ± 0.5	78.8 ± 1.1**	
	250	20.0 ± 0.0	71.7 ± 0.0***	
	125	18.7 ± 0.3	66.5 ± 2.2**	
	62.5	16.2 ± 0.6	59.0 ± 1.7***	
	31.25	14.7 ± 0.6	51.0 ± 1.9***	
Hd.EA	1000	25.0 ± 0.6	81.1 ± 1.7**	60.3
	500	20.5 ± 0.7	66.4 ± 0.2***	
	250	19.0 ± 0.6	61.7 ± 1.9***	
	125	17.6 ± 1.2	54.0 ± 0.2***	
	62.5	16.2 ± 0.0	50.2 ± 2.8***	
	32.25	14.4 ± 0.2	44.4 ± 1.8***	
Hd.Aq	1000	14.0 ± 0.2	46.2 ± 0.4***	1110.7
	500	12.2 ± 0.4	42.0 ± 1.1***	
	250	11.3 ± 0.7	38.8 ± 1.8***	
	125	9.7 ± 0.9	30.0 ± 0.4***	
	62.5	8.2 ± 0.0	28.2 ± 0.8***	
	31.25	5.3 ± 0.5	17.9 ± 0.1***	
Hd.Sp	1000	28.2 ± 0.8	92.7 ± 0.0 <sup>ns</sup>	18.3
	500	25.7 ± 0.1	82.3 ± 1.9*	
	250	23.0 ± 0.0	77.6 ± 1.2*	
	125	19.5 ± 0.3	62.9 ± 1.9**	
	62.5	17.1 ± 0.9	55.2 ± 0.0***	
	31.25	16.8 ± 0.4	53.3 ± 0.5**	

Positive control was taken as vincristine sulfate having IC<sub>50</sub> value < 0.1 µg/ml; \**p* < 0.05, \*\**p* < 0.01, \*\*\**p* < 0.001 Hd.Cr crude methanol extract, Hd.Hex fraction of n-hexane, Hd.Chf fraction of chloroform, Hd.EA fraction of ethyl acetate, Hd.Aq fraction of aqueous layer, Hd.Sp fractions of saponins. ns: nonsignificant.



TABLE 5: Concentration-dependent cytotoxicity of *H. digitata* crude extract and resultant fraction values against *Artemia salina* (brine shrimps) and their LC<sub>50</sub> values.

Samples	Total treated	Concentration dose (mg/ml)	Killed nauplii (n = 3)			Killed mean	Percent cytotoxicity	LC <sub>50</sub> (mg/ml)
			I	II	III			
Hd.Cr	30	1000	18	22	17	19.00 ± 0.58	64.1 ± 1.5	262
		100	14	15	14	14.33 ± 0.56	47.6 ± 1.9	
		10	10	12	14	11.33 ± 0.52	37.4 ± 1.3	
Hd.Hx	30	1000	17	18	19	18.00 ± 0.04	60.2 ± 0.4	630
		100	11	12	10	11.00 ± 0.06	36.7 ± 0.8	
		10	07	08	07	07.33 ± 0.58	24.4 ± 1.9	
Hd.Chf	30	1000	22	24	24	23.31 ± 0.56	77.4 ± 1.7	51
		100	17	19	17	17.66 ± 0.57	58.7 ± 2.2	
		10	12	13	14	13.00 ± 0.20	43.5 ± 0.7	
Hd.EA	30	1000	21	21	19	20.33 ± 0.56	67.6 ± 1.7	481
		100	11	13	11	11.67 ± 0.54	38.7 ± 1.5	
		10	08	09	10	09.01 ± 0.02	30.0 ± 0.4	
Hd.Aq	30	1000	18	19	20	19.00 ± 0.20	63.5 ± 0.2	420
		100	12	13	14	13.00 ± 0.04	43.1 ± 0.4	
		10	08	10	10	09.33 ± 0.56	31.3 ± 1.7	
Hd.Sp	30	1000	29	29	29	29.00 ± 0.20	96.5 ± 0.2	<0.01
		100	22	22	20	21.33 ± 0.56	71.3 ± 1.7	
		10	17	17	18	17.67 ± 0.54	58.7 ± 1.5	

Positive control (etoposide LD<sub>50</sub> 9.8). PPM = part per million; SD = standard deviation; Unbiased =  $s = \sqrt{\sum(x - \bar{x})^2 / n - 1}$ .

spectrophotometer reader. The formula for calculating the inhibition of cell growth is as follows:

$$\text{Cell viability\%} = \frac{\text{Mean of absorbance value of treatment group} - \text{Mean of absorbance value of control}}{\text{Mean of absorbance value of control}} \times 100. \quad (2)$$

**2.12. Statistical Data Analysis.** All the experiment was carried out in three replicates, and values were integrated as mean ± SEM. The two-way ANOVA statistical analysis followed by Bonferroni's post multiple comparison was employed for evaluation of negative control groups along with tested groups. The *p* value beneath 0.05 was measured as significant statistically. IC<sub>50</sub> value was deliberated via linear regression measurement between the percent inhibitions against the tested sample concentration through the Microsoft Office Excel 2010.

### 3. Result and Discussion

**3.1. Total Flavonoid and Phenolic Content.** Total flavonoid and phenolic content results of various divisions of *H. digitata* are tabulated in Table 1. Data specify that chloroform (Hd.Cf), ethyl acetate (Hd.EA), and crude (Hd.Cr) displayed

increased phenolic content, i.e., 178.61 ± 0.66, 220.44 ± 0.82, and 98.52 ± 1.50 mg GAE/g of the dry material correspondingly. However, Hd.Cf, Hd.Cr, and Hd.EA displayed increased flavonoid contents, i.e., 132.43 ± 1.10, 72.75 ± 0.67, and 98.44 ± 1.88 mg RTE/g of the material, respectively. Due to the existence of conjugated dienes and hydroxyl group in structure of these compounds, they gave increased anticancer and antioxidant activity [41]. Flavonoids and phenolic contents in various plant fractions related to the antioxidant and anticancer activity are given below.

**3.2. Phytochemical Investigation.** The results of the preliminary phytochemical analysis of the Hd.Cr are shown in Table 2. The tested sample of Hd.Cr was tested positive for the existence of the alkaloids, glycosides, tannins, terpenoids, anthraquinones, flavonoids, and saponins, as well as oils, but tested negative for sterols.

TABLE 6: Cytotoxicity study results utilizing mouse embryonic fibroblast (NIH/3T3 cell line).

Sample content	Concentration ( $\mu\text{g/ml}$ )	Cell viability percentage	Cytotoxicity percentage	LC <sub>50</sub> ( $\mu\text{g/ml}$ )
Hd.Cr	1000	30.77 $\pm$ 0.52	66.30***	282
	500	41.43 $\pm$ 0.64	58.57***	
	250	53.00 $\pm$ 1.10	47.00***	
	125	61.00 $\pm$ 0.10	39.00***	
	62.5	66.00 $\pm$ 0.00	34.00***	
	31.25	68.10 $\pm$ 0.80	31.90***	
Hd.Hex	1000	21.20 $\pm$ 0.59	78.80***	561
	500	26.00 $\pm$ 1.17	74.00***	
	250	43.50 $\pm$ 0.22	57.00***	
	125	48.00 $\pm$ 0.00	52.00***	
	62.5	56.20 $\pm$ 0.52	43.80***	
	31.25	61.00 $\pm$ 0.50	39.00***	
Hd.Chf	1000	22.00 $\pm$ 0.18	78.00***	142
	500	27.00 $\pm$ 1.17	73.00***	
	250	44.00 $\pm$ 0.46	56.00***	
	125	49.00 $\pm$ 0.00	51.00***	
	62.5	56.00 $\pm$ 0.22	44.00***	
	31.25	60.00 $\pm$ 0.00	40.00***	
Hd.EA	1000	28.16 $\pm$ 1.04	71.84***	158
	500	38.00 $\pm$ 1.17	62.00***	
	250	46.18 $\pm$ 0.18	53.82***	
	125	59.00 $\pm$ 0.00	41.00***	
	62.5	67.44 $\pm$ 0.22	32.56***	
	32.25	73.50 $\pm$ 0.00	26.50***	
Hd.Aq	1000	47.66 $\pm$ 1.22	52.34***	785
	500	51.66 $\pm$ 0.44	48.34***	
	250	59.00 $\pm$ 1.19	41.00***	
	125	70.33 $\pm$ 0.55	29.67***	
	62.5	82.00 $\pm$ 0.00	18.00***	
	31.25	87.00 $\pm$ 0.88	13.00***	
Hd.Sp	1000	28.50 $\pm$ 1.20	71.50***	172
	500	34.66 $\pm$ 1.33	65.34***	
	250	46.00 $\pm$ 0.00	54.00***	
	125	55.22 $\pm$ 1.17	44.78***	
	62.5	67.00 $\pm$ 0.00	33.00***	
	31.25	72.33 $\pm$ 0.44	27.67***	
Negative control	—	100	0	—

Standard drug etoposide as positive control; LD<sub>50</sub> was 5.46  $\mu\text{g/ml}$ . Values were identified as significantly different in comparison to the standard drug; \*\*\*  $p < 0.001$ .

3.3. *Antiangiogenic Assay*. Under normal circumstances, angiogenesis is controlled by a number of intrinsic angiostatic and angiogenic parameters [42]. Angiogenesis inhibitors are overwhelmed by angiogenesis promoters in

aberrant angiogenesis, such as atherosclerosis, cancer, and chronic inflammation [43], resulting in improper cell proliferation and migration. Since the last 15 years, researchers have been trying to identify and characterize novel

antiangiogenic medicines from natural sources such as plants [44]. In this research work, Hd.Chf, Hd.Sp, Hd.EA, and Hd.Cr show maximum antiangiogenesis having  $78.65 \pm 1.66$ ,  $76.98 \pm 1.03$ ,  $69.41 \pm 1.13$ , and  $65.35 \pm 0.86$  percentage inhibition at  $1000 \mu\text{g/ml}$  along with  $\text{IC}_{50}$  value of 28.63, 16.20, 86.73, and  $460.51 \mu\text{g/ml}$ , correspondingly. Standard drug was considered as dexamethasone with  $\text{IC}_{50}$  value of  $11.66 \mu\text{g/ml}$  which was shown in Table 3 and Figure 1. All constituent fractions displayed less significant but concentration dependent activity. Ph.Sp has been observed to have the strongest antiangiogenic effect, with an  $\text{IC}_{50}$  value of  $16.20 \mu\text{g/ml}$ , according to our findings. Likewise, saponins, such as convallamaroside from *Convallaria majalis* and polyphyllin D from *Paris polyphylla*, have been demonstrated to exhibit antiangiogenic properties in all phytochemicals [45, 46]. Similarly, the antiangiogenic potentials of crude extracts from *Viscum album*, *Populus nigra*, *Chryso-balanus icaco*, *Cassia garrettiana*, and *Agaricus blazei* were determined. Antiangiogenic activities of isolated compounds such as torilin from *Torilis japonica*, shikonin from *Lithospermum erythrorhizon*, resveratrol from grapes, deoxydopodophyllo toxin from *Pulsatilla koreana*, genistein from *ginseng*, isoliquiritin from licorice, and epigallocatechin gallate from green tea have been explained in both *in vitro* and *in vivo* study. In the GC-MS evaluation, we reported a total of 65 compounds previously [25] in which 17 were reported as anticancer drug studied from literature (Figure 2).

**3.4. Potato Disc Antitumor Bioassay.** The potato disc antitumor bioassay was carried out for the several samples of *H. digitata* discovered antitumor response in a dose-dependent manner (Table 4). In all the experimental samples, saponins displayed excellent antimalignant activity, i.e.,  $92.7 \pm 0.0$ ,  $82.3 \pm 1.9$ ,  $77.6 \pm 1.2$ ,  $62.9 \pm 1.9$ ,  $55.2 \pm 0.0$ , and  $53.3 \pm 0.5\%$  at different concentrations of 1000 to  $31.25 \mu\text{g/ml}$ , respectively, with  $\text{IC}_{50}$  data of  $18.3 \mu\text{g/ml}$ . Other increased activity was given by fraction of chloroform, i.e.,  $87.5 \pm 2.8$ ,  $78.8 \pm 1.1$ ,  $71.7 \pm 0.0$ ,  $66.5 \pm 2.2$ ,  $59.0 \pm 1.7$ , and  $51.0 \pm 1.9\%$  at 1000- $31.25 \mu\text{g/ml}$  accordingly with the  $\text{IC}_{50}$  value of  $25.5 \mu\text{g/ml}$ . Also, at the concentration of  $1000 \mu\text{g/ml}$ , the Hd.Cr, Hd.Hex, Hd.EA, and Hd.Aq exhibited  $86.4 \pm 1.1$ ,  $62.3 \pm 1.7$ ,  $81.1 \pm 1.7$ , and  $46.2 \pm 0.4\%$  antitumor activity accordingly.

**3.5. Cytotoxicity Assay as Brine Shrimp.** As shown in Table 5, the cytotoxic properties of crude methanolic containing saponins and their resulting fractions of *H. digitata* were evaluated using etoposide as a reference cytotoxic agent ( $\text{LC}_{50}$   $9.8 \text{ mg/ml}$ ). The crude methanolic extract induced  $64.1 \pm 1.5$ ,  $47.6 \pm 1.9$ , and  $37.4 \pm 1.3$  percent cytotoxicity and the standard deviation, respectively, at concentrations of 10-1000 ppm or  $\text{mg/ml}$ , with  $\text{LC}_{50}$  values of  $262.0 \text{ mg/ml}$ . The n-hexane fraction had  $60.2 \pm 0.4$ ,  $36.7 \pm 0.8$ , and  $24.4 \pm 1.9$  effects with an  $\text{LC}_{50}$  value of  $630 \text{ mg/ml}$ , whereas the chloroform fraction had  $77.4 \pm 1.7$ ,  $58.7 \pm 2.2$ , and  $43.5 \pm 0.7$  responses with an  $\text{LC}_{50}$  value of  $51.0 \text{ mg/ml}$ . Ethyl acetate fraction shows  $67.6 \pm 1.7$ ,  $38.7 \pm 1.5$ , and  $30.0 \pm 0.4$  giving the  $\text{LC}_{50}$  value of  $481.0 \text{ mg/ml}$ . Aqueous fraction showed  $63.5 \pm 0.2$ ,  $43.1 \pm 0.4$ , and  $31.3 \pm 1.7$  along with  $420.0 \text{ mg/ml}$

as  $\text{LC}_{50}$ . Saponin fraction presented considerable cytotoxicity of  $96.5 \pm 0.2$ ,  $71.3 \pm 1.7$ , and  $58.7 \pm 1.5$  with the minimum value of  $0.01 \text{ mg/ml}$  as  $\text{LC}_{50}$ .

**3.6. MTT Cell Viability Assay.** The hysterical and aberrant proliferation of cells that characterized cancer is present in over a hundred clinical disorders [47, 48]. Cell adherence, proteolysis, and cell migration have been used to elucidate the link between tumor and tumor-induced angiogenesis. There are strong signs that tumor cells have the potential to assault nearby tissue and induce the production of new capillaries from endothelial cells, resulting in cancer development and dissemination. As a result, the antitumor potential of a particular sample may also correspond to its antiangiogenic potential [49]. Furthermore, the NIH/3T3 cell line was chosen for the viability assay because several cell lines, including the NIH/3T3 mouse embryonic fibroblast, chicken embryo fibroblasts, HeLa cell line, Chinese hamster ovary cells, and others, have been identified as sensitive to leukaemia virus proliferation and sarcoma virus focus formation and transfection that has been analyzed previously using the immunofluorescence parameters [50, 51].

The creation of affordable and broad-spectrum cytotoxic medications is the true problem for researchers because of diverse characteristics of cancer. Anticancer medications and radiation that causes DNA alterations in actively proliferating cells were thought to preferentially kill cancer cells while having only a minor impact on healthy cells. Unfortunately, these drugs are effective against certain forms of cancer but have been linked to harmful effects on normal cells and have also been linked to serious side effects [52]. As a result, it is critical to look for novel anticancer medications that comes from both synthetic and natural sources. Brine shrimp lethality bioassays and antitumor are quick and low-cost tools for determining the cytotoxicity of plant extracts, other isolated chemicals, and synthesized compounds in order to create novel anticancer medications for disease treatment and cure [53]. The percent cytotoxicity of different fractions and saponins in an ascending order is given as Hd.EA > Hd.Sp > Ph.Chf > Hd.Cr > Hd.Hx > Ph.Aq as shown in Table 6.

## 4. Conclusion

The results demonstrate that *H. digitata* possesses a wide range of cytotoxic properties. *In vitro* investigations showed that the samples were ineffective against *A. tumefaciens*, indicating that this is a useful antitumor assay for *H. digitata*. Similarly, research into the separation and purification of new anticancer components might reveal the precise potentials of plants for cancer treatment. Our findings on the fractions and saponins' cytotoxic potentials might provide scientific support for ethnomedicinal usage of this type of plant.

## Data Availability

All data generated or analyzed during this study are included in this published article.

## Ethical Approval

The plant used in the current study is abundantly available and is not endangered species. The plant was collected after permission of related institution (Forest Department Dir Lower, KP, Pakistan), complied with national or international guidelines and legislation. Prof. Muhammad Nisar is the chairman of the Department of Botany, University of Malakand Dir (L) KPK, Pakistan. The plant sample was stored and recorded at herbarium having voucher number H.UOM. BG.180. Our pharmacological studies were evaluated and approved by Departmental of Pharmacy, University of Swabi (DREC-Pharmacy), via reference no DREC/UOS2022-04/01.

## Consent

Consent is not applicable for this submission.

## Conflicts of Interest

All authors declare that they have no competing interests that could appear to be affecting the paper.

## Authors' Contributions

JAK, MZ, and RZ carried out experimental work, data collection and evaluation, literature search, and manuscript preparation under the supervision of MSJ and AS. OMA, SA, MHM, MMA, and MAA refined the manuscript. SSH and MS helped in the final version and drafting of the manuscript. All authors read and approved the final manuscript for publication.

## Acknowledgments

The authors are thankful to the Najran University, Kingdom of Saudi Arabia, and University of Swabi, KP, Pakistan, and for providing lab facility. The authors would like to acknowledge the support of the Deputy for Research and Innovation, Ministry of Education – Kingdom of Saudi Arabia, for this research through a grant (NU/IF/INT/O1/007) under the institutional funding committee (IFC) at Najran University, Kingdom of Saudi Arabia.

## References

- [1] A. T. Khalil, M. Ovais, J. Iqbal et al., "Microbes-mediated synthesis strategies of metal nanoparticles and their potential role in cancer therapeutics," in *Seminars in Cancer Biology*, Elsevier, 2021.
- [2] M. Ovais, M. Z. Hoque, A. T. Khalil, M. Ayaz, and I. Ahmad, "Mechanisms underlying the anticancer applications of bio-synthesized nanoparticles," in *Biogenic Nanoparticles for Cancer Theranostics*, pp. 229–248, Elsevier, 2021.
- [3] C. Patra, I. Ahmad, M. Ayaz, A. T. Khalil, S. Mukherjee, and M. Ovais, Eds., *Biogenic nanoparticles for cancer theranostics*, Elsevier, 2021.
- [4] P. Pisani, F. Bray, and D. M. Parkin, "Estimates of the worldwide prevalence of cancer for 25 sites in the adult population," *International Journal of Cancer*, vol. 97, no. 1, pp. 72–81, 2002.
- [5] M. Ghufuran, A. U. Rehman, M. Shah, M. Ayaz, H. L. Ng, and A. Wadood, "In-silico design of peptide inhibitors of K-Ras target in cancer disease," *Journal of Biomolecular Structure and Dynamics*, vol. 38, no. 18, pp. 5488–5499, 2020.
- [6] S. Ahmad, F. Ullah, M. Ayaz, A. Zeb, F. Ullah, and A. Sadiq, "Antitumor and anti-angiogenic potentials of isolated crude saponins and various fractions of *Rumex hastatus* D. Don," *Biological Research*, vol. 49, no. 1, pp. 18–19, 2016.
- [7] J. Folkman, "Clinical applications of research on angiogenesis," *New England Journal of Medicine*, vol. 333, no. 26, pp. 1757–1763, 1995.
- [8] S. Graver, *Molecular and cellular cross talk between angiogenic, immune and DNA mismatch repair pathways*, Bayerische Julius-Maximilians-Universitaet Wuerzburg (Germany), 2015.
- [9] M. Ayaz, M. Junaid, F. Ullah et al., "Molecularly characterized solvent extracts and saponins from *Polygonum hydropiper* L. show high anti-angiogenic, anti-tumor, brine shrimp, and fibroblast NIH/3T3 cell line cytotoxicity," *Frontiers in Pharmacology*, vol. 7, 2016.
- [10] Z. Kamal, M. Ullah, S. Ahmad et al., "Exvivo antibacterial, phytotoxic and cytotoxic, potential in the crude natural phyto-constituents of *Rumex hastatus* D. Don," *Pakistan Journal of Botany*, vol. 47, Supplement I, pp. 293–299, 2015.
- [11] P. Coker, J. Radecke, C. Guy, and N. D. Camper, "Potato disc tumor induction assay: a multiple mode of drug action assay," *Phytomedicine*, vol. 10, no. 2-3, pp. 133–138, 2003.
- [12] Ľ. Kužma, "Biosynthesis of biological active abietane diterpenoids in transformed root cultures of *Salvia* species," in *Plant Cell and Tissue Differentiation and Secondary Metabolites: Fundamentals and Applications*, pp. 561–584, Springer, 2021.
- [13] K. A. Tawaha, "Cytotoxicity evaluation of Jordanian wild plants using brine shrimp lethality test," *Jordan Journal of Applied Science Natural Sciences*, vol. 8, no. 1, 2006.
- [14] A. Zeb, A. Sadiq, F. Ullah, S. Ahmad, and M. Ayaz, "Phytochemical and toxicological investigations of crude methanolic extracts, subsequent fractions and crude saponins of *Isodon rugosus*," *Biological Research*, vol. 47, no. 1, pp. 1–6, 2014.
- [15] N. H. Nguyen, Q. T. H. Ta, Q. T. Pham et al., "Anticancer activity of novel plant extracts and compounds from *Aedonoma bracteosum* (Bonati) in human lung and liver cancer cells," *Molecules*, vol. 25, no. 12, p. 2912, 2020.
- [16] M. Ovais, A. T. Khalil, M. Ayaz, and I. Ahmad, "Biosynthesized metallic nanoparticles as emerging cancer theranostics agents," in *Nanotheranostics*, pp. 229–244, Springer, 2019.
- [17] M. Ayaz, A. Sadiq, A. Wadood, M. Junaid, F. Ullah, and N. Zaman Khan, "Cytotoxicity and molecular docking studies on phytosterols isolated from *Polygonum hydropiper* L.," *Steroids*, vol. 141, pp. 30–35, 2019.
- [18] M. S. A. Khan and I. Ahmad, "Herbal medicine: current trends and future prospects," in *New Look to Phytomedicine*, pp. 3–13, Elsevier, 2019.
- [19] M. S. Jan, S. Ahmad, F. Hussain et al., "Design, synthesis, *in-vitro*, *in-vivo* and *in-silico* studies of pyrrolidine-2,5-dione derivatives as multitarget anti-inflammatory agents," *European Journal of Medicinal Chemistry*, vol. 186, article 111863, 2020.
- [20] S. M. Shah, F. Ullah, M. Ayaz, A. Wahab, and Z. K. Shinwari, "Phytochemical profiling and pharmacological evaluation of *Ifloga spicata* (forssk.) Sch. Bip. In leishmaniasis, lungs cancer and oxidative stress," *Pakistan Journal of Botany*, vol. 51, no. 6, pp. 2143–2152, 2019.

- [21] K. A. Akinyede, C. N. Cupido, G. D. Hughes, O. O. Oguntibeju, and O. E. Ekpo, "Medicinal properties and in vitro biological activities of selected *Helichrysum* species from South Africa: a review," *Plants*, vol. 10, no. 8, p. 1566, 2021.
- [22] M. H. Mahnashi, Y. S. Alqahtani, B. A. Alyami et al., "GC-MS analysis and various in vitro and in vivo pharmacological potential of *Habenaria plantaginea* Lindl.," *Evidence-based Complementary and Alternative Medicine*, vol. 2022, Article ID 7921408, 13 pages, 2022.
- [23] M. Ayaz, A. Nawaz, S. Ahmad et al., "Underlying anticancer mechanisms and synergistic combinations of phytochemicals with cancer chemotherapeutics: potential benefits and risks," *Journal of Food Quality*, vol. 2022, Article ID 1189034, 15 pages, 2022.
- [24] M. Pedron, C. R. Buzatto, R. B. Singer, J. A. N. Batista, and A. Moser, "Pollination biology of four sympatric species of *Habenaria* (Orchidaceae: Orchidinae) from southern Brazil," *Botanical Journal of the Linnean Society*, vol. 170, no. 2, pp. 141–156, 2012.
- [25] M. H. Mahnashi, B. A. Alyami, Y. S. Alqahtani et al., "Phytochemical profiling of bioactive compounds, anti-inflammatory and analgesic potentials of *Habenaria digitata* Lindl.: Molecular docking based synergistic effect of the identified compounds," *Journal of Ethnopharmacology*, vol. 273, article 113976, 2021.
- [26] A. R. Abubakar and M. Haque, "Preparation of medicinal plants: basic extraction and fractionation procedures for experimental purposes," *Journal of Pharmacy & Bioallied Sciences*, vol. 12, no. 1, pp. 1–10, 2020.
- [27] I. Hussain, R. Ullah, M. Khurram et al., "Phytochemical analysis of selected medicinal plants," *African Journal of Biotechnology*, vol. 10, no. 38, pp. 7487–7492, 2011.
- [28] G. Trease and M. Evans, *Text Book of Pharmacognosy 13th Edition Baille Tindall, London, Toronto, Pgs, Tokyo*, 1989.
- [29] H. O. Edeoga, D. E. Okwu, and B. O. Mbaebie, "Phytochemical constituents of some Nigerian medicinal plants," *African Journal of Biotechnology*, vol. 4, no. 7, pp. 685–688, 2005.
- [30] R. Zafar, H. Ullah, M. Zahoor, and A. Sadiq, "Isolation of bioactive compounds from *Bergenia ciliata* (haw.) Sternb rhizome and their antioxidant and anticholinesterase activities," *BMC Complementary and Alternative Medicine*, vol. 19, no. 1, pp. 1–13, 2019.
- [31] M. Ovais, M. Ayaz, A. T. Khalil et al., "HPLC-DAD finger printing, antioxidant, cholinesterase, and  $\alpha$ -glucosidase inhibitory potentials of a novel plant *Olax nana*," *BMC Complementary and Alternative Medicine*, vol. 18, no. 1, pp. 1–13, 2018.
- [32] M. Ayaz, M. Junaid, J. Ahmed et al., "Phenolic contents, antioxidant and anticholinesterase potentials of crude extract, subsequent fractions and crude saponins from *Polygonum hydropiper* L.," *BMC Complementary and Alternative Medicine*, vol. 14, no. 1, pp. 1–9, 2014.
- [33] T. Zohra, M. Ovais, A. T. Khalil, M. Qasim, M. Ayaz, and Z. K. Shinwari, "Extraction optimization, total phenolic, flavonoid contents, HPLC-DAD analysis and diverse pharmacological evaluations of *Dysphania ambrosioides* (L.) Mosyakin & Clemants," *Natural Product Research*, vol. 33, no. 1, pp. 136–142, 2019.
- [34] I. Ejaz, M. A. Javed, M. S. Jan et al., "Rational design, synthesis, antiproliferative activity against MCF-7, MDA-MB-231 cells, estrogen receptors binding affinity, and computational study of indenopyrimidine-2,5-dione analogs for the treatment of breast cancer," *Bioorganic & Medicinal Chemistry Letters*, vol. 64, article 128668, 2022.
- [35] M. H. Mahnashi, Y. S. Alqahtani, B. A. Alyami et al., "Phytochemical Analysis,  $\alpha$ -Glucosidase and Amylase Inhibitory, and Molecular Docking Studies on *Persicaria hydropiper* L. Leaves Essential Oils," *Evidence-based Complementary and Alternative Medicine*, vol. 2022, Article ID 7924171, 11 pages, 2022.
- [36] M. S. Islam, M. M. Rahman, M. A. Rahman, M. A. Qayum, and M. F. Alam, "In vitro evaluation of *Croton bonplandianum* Baill. as potential antitumor properties using *agrobacterium tumefaciens*," *Journal of Agricultural Technology*, vol. 6, no. 1, pp. 79–86, 2010.
- [37] T. ur Rehman, A. U. Khan, A. Abbas et al., "Investigation of nepetolide as a novel lead compound: antioxidant, antimicrobial, cytotoxic, anticancer, anti-inflammatory, analgesic activities and molecular docking evaluation," *Saudi Pharmaceutical Journal*, vol. 26, no. 3, pp. 422–429, 2018.
- [38] L. Marton, G. J. Wullems, L. Molendijk, and R. A. Schilperoort, "In vitro transformation of cultured cells from *Nicotiana tabacum* by *Agrobacterium tumefaciens*," *Nature*, vol. 277, no. 5692, pp. 129–131, 1979.
- [39] Q. S. Sarah, F. C. Anny, and M. Misbahuddin, "Brine shrimp lethality assay," *Bangladesh Journal of Pharmacology*, vol. 12, no. 2, p. 5, 2017.
- [40] M. B. Tufail, M. A. Javed, M. Ikram et al., "Synthesis, pharmacological evaluation and molecular modelling studies of pregnenolone derivatives as inhibitors of human dihydrofolate reductase," *Steroids*, vol. 168, article 108801, 2021.
- [41] T. Zohra, M. Ovais, A. T. Khalil et al., "Bio-guided profiling and HPLC-DAD finger printing of *Atriplex lasiantha* Boiss.," *BMC Complementary and Alternative Medicine*, vol. 19, no. 1, pp. 1–14, 2019.
- [42] E. Roudier, M. Milkiewicz, O. Birot et al., "Endothelial FoxO1 is an intrinsic regulator of thrombospondin 1 expression that restrains angiogenesis in ischemic muscle," *Angiogenesis*, vol. 16, no. 4, pp. 759–772, 2013.
- [43] M. H. Mahnashi, Y. S. Alqahtani, B. A. Alyami et al., "Cytotoxicity, anti-angiogenic, anti-tumor and molecular docking studies on phytochemicals isolated from *Polygonum hydropiper* L.," *BMC Complementary Medicine and Therapies*, vol. 21, no. 1, pp. 1–14, 2021.
- [44] H. Sonawane, A. Shinde, and J. Jadhav, "Evaluation of anti-angiogenic potential of *Mentha arvensis* Linn. leaf extracts using chorioallantoic membrane assay," *World Journal of Pharmacy Research*, vol. 5, pp. 677–689, 2016.
- [45] Q. Tong, Y. Qing, Y. Wu, X. Hu, L. Jiang, and X. Wu, "Dioscin inhibits colon tumor growth and tumor angiogenesis through regulating VEGFR2 and AKT/MAPK signaling pathways," *Toxicology and Applied Pharmacology*, vol. 281, no. 2, pp. 166–173, 2014.
- [46] S. Man, W. Gao, Y. Zhang, L. Huang, and C. Liu, "Chemical study and medical application of saponins as anti-cancer agents," *Fitoterapia*, vol. 81, no. 7, pp. 703–714, 2010.
- [47] M. Q. Nasar, M. Shah, A. T. Khalil et al., "Ephedra intermedia mediated synthesis of biogenic silver nanoparticles and their antimicrobial, cytotoxic and hemocompatibility evaluations," *Inorganic Chemistry Communications*, vol. 137, article 109252, 2022.
- [48] M. A. Huneif, D. B. Alshehri, K. S. Alshaibari et al., "Design, synthesis and bioevaluation of new vanillin hybrid as

## *Retraction*

# **Retracted: Predicting Mental Health of Best Human Capital for Sustainable Organization through Psychological and Personality Health Issues: Shift from Traditional to Novel Machine Learning-Supervised Technique Approach**

### **BioMed Research International**

Received 8 January 2024; Accepted 8 January 2024; Published 9 January 2024

Copyright © 2024 BioMed Research International. This is an open access article distributed under the Creative Commons Attribution License, which permits unrestricted use, distribution, and reproduction in any medium, provided the original work is properly cited.

This article has been retracted by Hindawi following an investigation undertaken by the publisher [1]. This investigation has uncovered evidence of one or more of the following indicators of systematic manipulation of the publication process:

- (1) Discrepancies in scope
- (2) Discrepancies in the description of the research reported
- (3) Discrepancies between the availability of data and the research described
- (4) Inappropriate citations
- (5) Incoherent, meaningless and/or irrelevant content included in the article
- (6) Manipulated or compromised peer review

The presence of these indicators undermines our confidence in the integrity of the article's content and we cannot, therefore, vouch for its reliability. Please note that this notice is intended solely to alert readers that the content of this article is unreliable. We have not investigated whether authors were aware of or involved in the systematic manipulation of the publication process.

Wiley and Hindawi regrets that the usual quality checks did not identify these issues before publication and have since put additional measures in place to safeguard research integrity.

We wish to credit our own Research Integrity and Research Publishing teams and anonymous and named external researchers and research integrity experts for contributing to this investigation.

The corresponding author, as the representative of all authors, has been given the opportunity to register their agreement or disagreement to this retraction. We have kept a record of any response received.

### **References**

- [1] M. A. Khan, S. Ahmad, M. A. El-Affendi, R. Zaka, S. Mahmood, and M. Jehangir, "Predicting Mental Health of Best Human Capital for Sustainable Organization through Psychological and Personality Health Issues: Shift from Traditional to Novel Machine Learning-Supervised Technique Approach," *BioMed Research International*, vol. 2022, Article ID 5775640, 9 pages, 2022.

## Research Article

# Predicting Mental Health of Best Human Capital for Sustainable Organization through Psychological and Personality Health Issues: Shift from Traditional to Novel Machine Learning-Supervised Technique Approach

Muhammad Anees Khan <sup>1</sup>, Sadique Ahmad <sup>2,3</sup>, Mohammed A. El-Affendi <sup>2</sup>, Rija Zaka,<sup>1</sup> Saima Mahmood,<sup>4</sup> and Muhammad Jehangir<sup>5</sup>

<sup>1</sup>Department of Management Studies, Bahria University, Islamabad, Pakistan

<sup>2</sup>EIAS: Data Science and Blockchain Laboratory, College of Computer and Information Sciences, Prince Sultan University, Riyadh 11586, Saudi Arabia

<sup>3</sup>Department of Computer Science, Bahria University, Karachi Campus, Pakistan

<sup>4</sup>Department of Pharmaceutics, Faculty of Pharmacy, Gomal University, Dera Ismail Khan, Pakistan

<sup>5</sup>Institute of Business and Leadership, Abdul Wali Khan University Mardan, Pakistan

Correspondence should be addressed to Muhammad Anees Khan; manees.buic@bahria.edu.pk

Received 6 July 2022; Revised 26 July 2022; Accepted 28 July 2022; Published 17 September 2022

Academic Editor: Nauman Rahim Khan

Copyright © 2022 Muhammad Anees Khan et al. This is an open access article distributed under the Creative Commons Attribution License, which permits unrestricted use, distribution, and reproduction in any medium, provided the original work is properly cited.

Researchers in the past discussed the psychological issue like stress, anxiety, depression, phobias on various forms, and cognitive issues (e.g., positive thinking) together with personality traits on traditional research methodologies. These psychological issues vary from one human to other human based on different personality traits. In this paper, we discussed both psychological issues together with personality traits for predicting the best human capital that is mentally healthy and strong. In this research, we replace the traditional methods of research used in the past for judging the mental health of the society, with the latest artificial intelligence techniques to predict these components for attaining the best human capital. In the past, researchers have point out major flaws in predicting psychological issue and addressing a right solution to the human resource working in organizations of the world. In order to give solution to these issues, we used five different psychological issues pertinent to human beings for accurate prediction of human resource personality that effect the overall performance of the employee. In this regard, a sample of 500 data has been collected to train and test on computer through python for selecting the best model that will outperform all the other models. We used supervised AI techniques like support vector machine linear, support vector machine radial basis function, decision tree model, logistic regression, and neural networks. Results proved that psychological issue data from employee of different organizations are better means for predicting the overall performance based on personality traits than using either of them alone. Overall, the novel traditional techniques predicted that sustainable organization is always subject to the control of psychological illness and polishing the personality traits of their human capital.

## 1. Introduction

Based on the data of the World Health Organization, one person out of four people is affected by the term called health concerns which affect both his mental and physical performance towards any job. Thus, mental health is such

a type of situation where a person or individual realizes his personal abilities that help in normalizing the stress in general conditions for improving the overall productivity that in one or other way contributing to community and surroundings. The literature on physicians' mental health is expanding day by day. The main reason behind the literature

growth is the general concerns about field-related professionals and especially their mental well-being. On the other hand, the healthcare employees have a lack of focus on their work. As a result, increased efforts have been made around the world to promote physicians' mental health and wellness, dubbed "The Quadruple Aim." "In the past, researchers worked on social, mental, and psychological issues; however, after the era of using statistical techniques, researchers entered into the era of machine learning and artificial intelligence which started in 1990s. It started from using neural networks [1] to using supervised artificial intelligence techniques in 2020 by [2] psychological issue and personality trait indicators [3]. In Pakistan, researchers have predicted psychological and personality trait issues by using traditional statistical techniques, but no work is being done using artificial intelligence techniques.

## 2. Literature Review

Humans are different from each other because personality is a combination of feelings, experience, thoughts, and emotions. It also specifies how one should interact with various individuals in various situations. Some people behave differently in the same situation because their personality is made up of multiple traits. Personality predicts our conduct and has a significant influence on our decision-making abilities. The variance in decision-making sense from person to person is simply due to personality [4]. It is difficult to predict human behavior as it varies from time to time and situation to situation, and personality is not fully exposed and understood. Every individual behavior differs from the other, like their decision because of the different personality they possess. The behavior of investors is the result of their attitudes, personalities, norms values, and other factors such as level of motivation [4]. All these factors become the cause of irrational decision-making. Previously, various studies have been conducted in order to examine the factors that influence individuals' financial and investment decisions. Out of the many factors, personality type is also a factor that influences financial and investment decision. However, financial or investment decisions at the level of individuals need to be generated by the conscious understanding of the individual's level of motivation, personality traits, and other psychological factors. The lack of understanding of these factors may lead to irrational financial and investment decisions. Along with this, the financial advisor also needs to understand the workings of these cognitive factors to reach a critically informed decision. The literature in the relevant field highlights the needs to focus on the proposition that psychological factors play an important role in the decision-making processes. However, different techniques have been used for predicting the personality issues and psychological issues as the following: discriminant analysis is a statistical technique that is used to recognize the relationship between dependent variables and one or more independent variables. The primary difference between regression analysis and multiple discriminant analysis is that in regression analysis, dependent variable is a continuous variable, while discriminant analysis deals with categorical dependent variable [5,

6]. Moreover, using logistic regression differs with linear regression analysis in the use of dependent variable as logistic regression deals in dichotomous dependent variable [7]. In traditional statistical techniques used for predicting psychological issues, logit models also had a prominent place. Hence, the overall discussion about the machine learning is the science and art of programming computers so that they can comprehend patterns in data and develop algorithms for future prediction of data [8]. Patterns in data are identified by software, and an algorithm is developed. After that, algorithm is used for prediction on the basis of previously identified pattern in data. Supervised technique is a subpart of artificial intelligence and is specifically under the category of machine learning. As its name indicates, machine is made to learn under supervision. It means that a computer algorithm is constructed on the basis of training by input data that is being labelled for a specific output. In this way, computer learns the underlying similarities in data and recognizes relationships among the input data that is being used to train the machine. This training data set is a foundation for algorithm development, so this training data set should be well balanced and contains all such readings that are true representative of that data. To test its usefulness, a test data set is fed into that algorithm that results in measuring its accuracy [9].

## 3. Psychological Health Issues

According to several studies, personality has a role in understanding investor behavior. Costa and McCrae provide the big five model of personality, which includes extraversion (extremely chatty, lively), neuroticism (depressed, gloomy), conscientiousness (very organized), openness to experience (very creative), and agreeableness (kind and generous). In the literature, the authors used a questionnaire based on personality which supports the five-factor model [10]. Those who are well organized and highly creative and easily think and understand ideas and information are good in managing personal financial matters and investment decisions. Openness to experience, one of the dimensions of the big five model, contains both creative and thoughtful expressions. Another important dimension of this model also puts the impact on the investment decision, i.e., conscientiousness in which great efforts for expertise and achievements are involved [10].

## 4. Personality Health Traits

We need five traits that will build a personality, which include extraversion, agreeableness, neuroticism, openness to experience, and conscientiousness. Talking about extraversion is a trait that signifies individual variances in a social meeting, confidence, and energy level. Individuals who are highly extraverted relish socializing with others, while expressing themselves in a group situation, they are easily comfortable and frequently show a positive attitude by expressing emotions such as eagerness and excitement [11]. Along with the previous trait, agreeableness is a trait of personality that is based on the concept where variances



in empathy, respectfulness, and acceptance of others are captured by agreeableness. Agreeable persons are highly sensitive towards other's happiness, treat others very well for their personal privileges and preferences, and always think positive about others. Displeasing individuals tend to have less respect for others and social standards of graciousness [11]. Moreover, conscientiousness also signifies variances in organization, productiveness and accountability, command, and structure followed by a highly conscientious person. They work determinedly to achieve their objectives, and they are highly committed while fulfilling their responsibility and compulsion, whereas unconscientious persons are easy to go with the disorder and are less motivated to complete tasks [11]. In addition, it is also observed that Neuroticism is also changes due to intensity of negative emotions. Highly neurotic persons are more inclined to anxiety, sorrow, and mood swings, and they are emotionally unstable [11]. And the last one is openness to experience where variances in intellectual curiosity, artistic sensitivity, and imagination are indicated by openness to experience. Highly open individuals are more creative and enjoy thinking and learning; they are art and beauty conscious and create innovative ideas. Close-minded people tend to have a narrow series of rational and creative interests [11].

## 5. Computational Learning Theory

The purpose of computational learning theory is to comprehend the machine learning algorithm and decide what is learnable. It assists in determining how much data is required for the training of a specific algorithm as well as the required resources for the learning activity. According to the Association for Computational Learning, computational learning theory is "a research subject devoted to investigating the design and analysis of machine learning algorithms. Such algorithms strive to make accurate predictions or representations based on observations." Computational learning theory is an area of theoretical computing that discusses the design of computer programs and their ability to learn, as well as the identification of computing limitations with machines. Computational learning theory aids in posing and answering concerns about the performance of learning algorithms.

## 6. Hypothesis of the Study

*6.1. Predicting Psychological and Personality Health Issues through Neural Networks.* In order to find the psychological issues and personality traits of successful human being for improving the overall performance, a study was conducted in the USA in which they used psychological issues and personality traits as independent variables and performance as the dependent variable. It was found that psychological issues (stress, anxiety, depression, phobias on various forms, and cognitive issues) and personality traits (conscientiousness, openness to experience, and extroverts) are highly skilled, or we can say that they are overconfident in their skills. On the other hand, neuroticism and openness to experience look towards more returns. Openness to experience

and neuroticism were found more in successful investors. A neural network is a series of algorithms that aspires to acknowledge underlying relationships in a data set through a procedure that imitates the way human brain operates. Researchers in the past used neural network technique for psychological issue prediction [12]. In this regard, neural network approach has been introduced to discriminant analysis for predicting human psychological issue that leads to organizational performance. Researchers compared the results with linear classifier, logistic regression, KNN, and ID3 and found it to be an accurate method of measurement. Moreover, according to [13], results of psychological issue model constructed by neural networks outperformed model constructed by multiple discriminant analysis. Keeping the above discussion, the authors will suppose the following hypothesis for testing and contribution.

*Hypothesis 1a.* Predicting psychological issues through neural network algorithm outperforms all the other technique used in this study.

*Hypothesis 1b.* Predicting personality traits through neural network algorithm outperforms all the other technique used in this study.

*6.2. Predicting Psychological Issues and Personality Traits through Decision Tree Model.* The literature is saturated with many findings that discover statistical association among psychiatric difficulties, big 5 personality traits, and risk-taking attitude in preadolescents. Using multiple regression using questionnaires as data, it was discovered that extroverts and openness to experience are strongly associated with risk-taking attitudes, whereas conscientiousness, neuroticism, and agreeableness cannot predict risk-taking attitudes. Thus, this study found that a higher level of extroverts and openness to experience, as well as a lower level of conscientiousness, is associated with a higher level of risk-taking attitude. As discussed in previous lines with a traditional methods, researcher's also used the decision tree model. So here, the decision tree model is a type of arithmetical calculation in which algorithms are build and those algorithms are said to be decision tree models in which inquiries and examinations are done in a calculative manner so that they may aid in holding subsequent tests. [14] used decision tree model for psychological test and organization risk measurement and got 91.2% accuracy result. Similarly, [15] also trains and tests the personality traits and psychological issue data to predict psychological issue indicators using random forest decision tree and obtains 90% average prediction accuracy. Thus, keeping the above discussion as a benchmark, the research develops and assumed the following hypothesis to work on.

*Hypothesis 2a.* Predicting psychological issues through decision tree algorithm outperforms all the other technique used in this study.

*Hypothesis 2b.* Predicting personality traits through decision tree algorithm outperforms all the other technique used in this study.

*6.3. Predicting Psychological Issues and Personality Traits through Genetic Algorithms.* In the past, traditional methodologies produced a large body of literature on the prediction of psychiatric problems and personality traits. For instance, by using multiple regression, it was discovered that personality trait influences financial risk tolerance to some extent. It also pushes an impact on individual investment decisions. So the investment advisors should first study an individual's personality trait and risk tolerance level. Also, the government should take measures to reduce risk tolerance [16]. The most recent research on psychological disorders and personality traits is based on machine learning algorithms such as genetic algorithms, a type of modifying algorithm that uses natural progression strategies to solve generic problems. The genetic algorithms are projected in binary strings. However, this is not the sole form; depending on the issue being deployed, it can also be provided in alternative ways [17]. Furthermore, in the past, researchers presented genetic algorithms for psychological issue prediction and modeling. As a result of the above discussion, the following hypothesis will be trained and evaluated using Python [18].

*Hypothesis 3a.* Predicting psychological issues through genetic algorithms outperforms all the other technique used in this study.

*Hypothesis 3b.* Predicting personality traits through genetic algorithms outperforms all the other technique used in this study.

*6.4. Predicting Psychological Issues and Personality Traits through Support Vector Machines.* On a sample of 300, primary research was conducted to study the influence of personality on socially responsible regression analysis and reliability test. They discovered that agreeableness, neuroticism, and openness to agreeableness control financial decisions in regard to socially responsible investment [19]. Support vector machines are supervised learning models with related learning algorithms that examine data for classification and regression analysis in machine learning. Vladimir Vapnik and his colleagues created it in 1974 at AT&T Bell laboratories. Several researchers conducted psychological problem prediction using support vector machines [20, 21] and discovered that it was suitable for measuring patterns in data. The authors believe the following hypothesis.

*Hypothesis 4a.* Predicting psychological issues through support vector machine algorithm outperforms all the other technique used in this study.

*Hypothesis 4b.* Predicting personality traits through support vector machine algorithm outperforms all the other technique used in this study.

## 7. Research Method of the Study

The Python programming language is exhibiting itself as one of the most admired and used languages for scientific computing. Its advance-level collective nature and its vast spreading capability of comprehending scientific analogies make it a captivating choice for algorithmic development and exploratory data analysis [22]. The types of data required by the researcher and the research design are being followed for the selection of data collection method, i.e., primary data and secondary data, so this study requires the collection of primary data in order to directly obtain information from the people of Pakistan [23]. In this cross-sectional data, we used questionnaires as a data gathering instrument that require less expertise [24], and responses were captured using 5-point Likert scales. The target population is normally associated with the total number of individuals living in a particular country [25]. Therefore, in our study, target population is all literate individuals from nonfinancial companies in Pakistan. So, the following techniques will be used in predication based on algorithms developed through Python. We used the following supervised AI techniques used in model like support vector machine, i.e., radial basic function, logistic regression, decision tree model, and artificial neural network.

*7.1. Performance Evaluation of ML Techniques.* Two well-known performance evaluation metrics are used which are root mean square error (RMSE) and mean absolute error (MAE).

*7.2. Root Mean Square Error.* In equation (1), the RMSE is used for measuring the error rate of the regression models. It is an effective metric to compare the forecasting errors as follows:

$$\text{RMSE} = \sqrt{\sum_{i=1}^n \left( \frac{\hat{y}_i - y_i}{n} \right)^2}, \quad (1)$$

where  $n$  is the number of test samples,  $y_i$  is the true target value of the  $i$ th sample, and  $y_{i\_cap}$  is the forecasted value by the regressor.

*7.3. Mean Absolute Error.* In equation (2), MAE is a performance metric used to evaluate the performance of a regressor. It is calculated as follows:

$$\text{MAE} = \sqrt{\sum_{i=1}^n \left| \frac{y_i - x_i}{n} \right|}, \quad (2)$$

where  $n$  is the number of test samples,  $y_i$  is the true target value of the  $i$ th sample,  $x_i$  is the forecasted value by the regressor, and  $|\cdot|$  represents the absolute value.

## 8. Results and Discussion

Table 1 shows the results of different AI techniques in method column, together with evaluation metrics columns

TABLE 1: Psychological issue model.

Method	Accuracy	Precision	Recall	F1 score	Confusion matrix
Psychological issues - SVM linear	0.911	0.916	0.994	0.917	[29 5 1 27]
Psychological issues - SVM RBF	0.909	0.923	0.911	0.921	[30 4 0 28]
Psychological issues - logistic regression	0.924	0.909	0.907	0.923	[29 5 1 27]
Psychological issues - decision tree	0.823	0.898	0.880	0.890	[30 4 4 24]

Source: own research.

TABLE 2: Psychological issue model and ANN results.

Method	Layers	Neuron	Accuracy	Precision	Recall	F1 score	Confusion matrix
Psychological issues - ANN	1	2	0.886	0.887	0.876	0.871	[26 2 6 28]
Psychological issues - ANN	1	4	0.902	0.855	0.923	0.855	[27 1 4 30]
Psychological issues - ANN	1	8	0.902	0.823	0.923	0.839	[27 1 4 30]
Psychological issues - ANN	1	16	0.274	0.871	0.879	0.887	[27 1 7 27]
Psychological issues - ANN	1	32	0.811	0.887	0.909	0.902	[27 1 5 29]
Psychological issues - ANN	1	64	0.873	0.887	0.909	0.87	[27 1 5 29]
Psychological issues - ANN	1	128	0.938	0.855	0.891	0.889	[26 2 5 29]
Psychological issues - ANN	2	2	0.902	0.887	0.881	0.354	[0 28 0 34]
Psychological issues - ANN	2	4	0.873	0.902	0.909	0.886	[27 1 5 29]
Psychological issues - ANN	2	8	0.854	0.87	0.82	0.879	[27 1 11 23]
Psychological issues - ANN	2	16	0.886	0.853	0.909	0.918	[27 1 5 29]
Psychological issues - ANN	2	32	0.887	0.842	0.888	0.887	[25 3 4 30]
Psychological issues - ANN	2	64	0.903	0.887	0.902	0.853	[25 3 3 31]
Psychological issues - ANN	2	128	0.903	0.879	0.902	0.919	[25 3 3 31]
Psychological issues - ANN	3	2	0.548	0.919	0.873	0.902	[0 28 0 34]
Psychological issues - ANN	3	4	0.905	0.902	0.803	0.902	[26 2 11 23]
Psychological issues - ANN	3	8	0.834	0.902	0.876	0.354	[26 2 6 28]
Psychological issues - ANN	3	16	0.905	0.354	0.941	0.807	[28 0 4 30]
Psychological issues - ANN	3	32	0.907	0.807	0.902	0.874	[25 3 3 31]
Psychological issues - ANN	3	64	0.827	0.874	0.867	0.891	[23 5 3 31]
Psychological issues - ANN	3	128	0.907	0.939	0.852	0.881	[23 5 4 30]
Psychological issues - ANN	4	2	0.887	0.841	0.843	0.909	[25 3 7 27]
Psychological issues - ANN	4	4	0.871	0.886	0.888	0.821	[25 3 4 30]
Psychological issues - ANN	4	8	0.871	0.879	0.879	0.909	[27 1 7 27]
Psychological issues - ANN	4	16	0.919	0.918	0.92	0.888	[26 2 3 31]
Psychological issues - ANN	4	32	0.887	0.887	0.884	0.885	[24 4 3 31]
Psychological issues - ANN	4	64	0.855	0.853	0.855	0.854	[24 4 5 29]
Psychological issues - ANN	4	128	0.887	0.887	0.884	0.885	[24 4 3 31]
Psychological issues - ANN	5	2	0.548	0.274	0.871	0.943	[0 28 0 34]
Psychological issues - ANN	5	4	0.903	0.902	0.905	0.854	[26 2 4 30]
Psychological issues - ANN	5	8	0.911	0.901	0.879	0.807	[25 3 4 30]
Psychological issues - ANN	5	16	0.882	0.872	0.918	0.874	[24 4 5 29]
Psychological issues - ANN	5	32	0.867	0.887	0.887	0.891	[23 5 6 28]
Psychological issues - ANN	5	64	0.882	0.856	0.853	0.881	[24 4 4 30]
Psychological issues - ANN	5	128	0.862	0.923	0.879	0.354	[24 4 3 31]

Source: own research.

used in this study. All the evaluation techniques showed in Table 1 are the source of selecting the best AI technique that will outperform all the other AI technique for predicting the

psychological issues and personality traits for improving the overall performance that will help in attaining the organizational vision and mission. In order to know the performance

TABLE 3: Personality trait-based model.

Method	Accuracy	Precision	Recall	F1 score	Confusion matrix
Personality traits - SVM linear	0.679	0.677	0.675	0.676	[24 10 10 18]
Personality traits - SVM RBF	0.955	0.997	0.987	0.967	[33 1 3 25]
Personality traits - logistic regression	0.611	0.604	0.602	0.601	[22 12 12 16]
Personality traits - decision tree	0.951	0.923	0.921	0.946	[32 2 2 26]

Source: own research.

TABLE 4: Personality trait-based model ANN results.

Method	Layer	Neuron	Accuracy	Precision	Recall	F1 score	Confusion matrix
Personality traits - ANN	1	2	0.681	0.938	0.938	0.821	[24 4 17 17]
Personality traits - ANN	1	4	0.643	0.889	0.659	0.906	[20 8 11 23]
Personality traits - ANN	1	8	0.774	0.938	0.691	0.938	[21 7 8 26]
Personality traits - ANN	1	16	0.756	0.311	0.774	0.952	[21 7 9 25]
Personality traits - ANN	1	32	0.724	0.771	0.809	0.952	[21 7 8 26]
Personality traits - ANN	1	64	0.931	0.782	0.822	0.821	[22 6 0 34]
Personality traits - ANN	1	128	0.923	0.791	0.946	0.906	[24 4 0 34]
Personality traits - ANN	2	2	0.675	0.923	0.946	0.938	[18 10 11 23]
Personality traits - ANN	2	4	0.692	0.954	0.938	0.545	[19 9 10 24]
Personality traits - ANN	2	8	0.764	0.938	0.659	0.766	[22 6 8 26]
Personality traits - ANN	2	16	0.812	0.889	0.811	0.782	[24 4 8 26]
Personality traits - ANN	2	32	0.951	0.947	0.929	0.959	[24 4 0 34]
Personality traits - ANN	2	64	0.842	0.887	0.822	0.967	[26 2 5 29]
Personality traits - ANN	2	128	0.912	0.947	0.899	0.934	[24 4 0 34]
Personality traits - ANN	3	2	0.482	0.226	0.941	0.678	[28 0 34 0]
Personality traits - ANN	3	4	0.774	0.777	0.956	0.707	[19 9 5 29]
Personality traits - ANN	3	8	1	1	1	1	[24 4 10 24]
Personality traits - ANN	3	16	0.743	0.79	0.793	0.707	[23 5 8 26]
Personality traits - ANN	3	32	0.921	0.936	0.911	0.952	[23 5 0 34]
Personality traits - ANN	3	64	0.925	0.952	0.956	0.969	[28 0 3 31]
Personality traits - ANN	3	128	0.732	0.782	0.956	0.638	[28 0 0 34]
Personality traits - ANN	4	2	0.621	0.609	0.609	0.657	[16 12 12 22]
Personality traits - ANN	4	4	0.687	0.684	0.684	0.707	[21 7 13 21]
Personality traits - ANN	4	8	0.832	0.821	0.919	0.821	[23 5 6 28]
Personality traits - ANN	4	16	0.912	0.959	0.902	0.952	[25 3 0 34]
Personality traits - ANN	4	32	0.942	0.905	0.902	0.903	[25 3 0 34]
Personality traits - ANN	4	64	0.953	0.879	0.354	0.903	[28 0 2 32]
Personality traits - ANN	4	128	0.921	0.918	0.807	0.548	[27 1 3 31]
Personality traits - ANN	5	2	0.623	0.887	0.874	0.905	[25 3 21 13]
Personality traits - ANN	5	4	0.721	0.853	0.939	0.834	[19 9 9 25]
Personality traits - ANN	5	8	0.851	0.879	0.942	0.905	[23 5 6 28]
Personality traits - ANN	5	16	0.921	0.882	0.912	0.907	[24 4 2 32]
Personality traits - ANN	5	32	0.952	0.85	0.901	0.827	[28 0 4 30]
Personality traits - ANN	5	64	0.921	0.812	0.892	0.907	[28 0 3 31]
Personality traits - ANN	5	128	0.942	0.896	0.882	0.954	[28 0 3 31]

Source: own research.

of the machine learning techniques, we used the following evaluation metrics that will outperform the best prediction methods. The evaluation metrics include accuracy, precision, recall, F1 score, and confusion matrix.

## 9. Data Analysis and Discussion

9.1. Model 1: Using Psychological Issues. First, psychological issue model is developed based on the five different

TABLE 5: Psychological issue+personality trait-based model results.

Method	Accuracy	Precision	Recall	F1 score	Confusion matrix
Psychological issue+personality trait SVM linear	0.845	0.831	0.842	0.831	[26 8 1 27]
Psychological issue+personality trait SVM RBF	0.978	0.951	0.953	0.959	[33 1 1 27]
Psychological issue+personality trait logistic regression	0.885	0.889	0.842	0.872	[27 7 1 27]
Psychological issue+personality trait decision tree	0.941	0.924	0.945	0.958	[33 1 3 25]

Source: own research.

TABLE 6: Psychological issue+personality trait-based model ANN results.

Method	Layer	Neuron	Accuracy	Precision	Recall	F1 score	Confusion matrix
Psychological issue+personality trait ANN	1	2	0.831	0.951	0.938	0.934	[22 6 6 28]
Psychological issue+personality trait ANN	1	4	0.831	0.714	0.938	0.934	[26 2 7 27]
Psychological issue+personality trait ANN	1	8	0.836	0.887	0.95	0.953	[27 1 4 30]
Psychological issue+personality trait ANN	1	16	0.845	0.919	0.938	0.934	[27 1 2 32]
Psychological issue+personality trait ANN	1	32	0.851	0.951	0.5	0.274	[27 1 3 31]
Psychological issue+personality trait ANN	1	64	0.831	0.967	0.793	0.79	[27 1 1 33]
Psychological issue+personality trait ANN	1	128	0.831	0.951	0.894	0.892	[27 1 2 32]
Psychological issue+personality trait ANN	2	2	0.967	0.951	0.938	0.934	[24 4 15 19]
Psychological issue+personality trait ANN	2	4	0.953	0.807	0.95	0.934	[25 3 4 30]
Psychological issue+personality trait ANN	2	8	0.95	0.951	0.938	0.934	[26 2 3 31]
Psychological issue+personality trait ANN	2	16	0.803	0.95	0.938	0.938	[27 1 2 32]
Psychological issue+personality trait ANN	2	32	0.888	0.967	0.967	0.935	[27 1 1 33]
Psychological issue+personality trait ANN	2	64	0.905	0.95	0.938	0.548	[27 1 2 32]
Psychological issue+personality trait ANN	2	128	0.92	0.953	0.967	0.79	[26 2 1 33]
Psychological issue+personality trait ANN	3	2	0.935	0.811	0.919	0.887	[26 2 11 23]
Psychological issue+personality trait ANN	3	4	0.952	0.886	0.968	0.935	[25 3 4 30]
Psychological issue+personality trait ANN	3	8	0.935	0.902	0.935		[26 2 4 30]
Psychological issue+personality trait ANN	3	16	0.548	0.918	0.952		[26 2 3 31]
Psychological issue+personality trait ANN	3	32	0.79	0.967	0.935		[27 1 1 33]
Psychological issue+personality trait ANN	3	64	0.887	0.934	0.952		[27 1 3 31]
Psychological issue+personality trait ANN	3	128	0.935	0.967	0.936	0.967	[27 1 1 33]
Psychological issue+personality trait ANN	4	2	0.952	0.887	0.891	0.889	[26 2 5 29]
Psychological issue+personality trait ANN	4	4	0.903	0.902	0.902	0.902	[25 3 3 31]
Psychological issue+personality trait ANN	4	8	0.935	0.935	0.935	0.935	[26 2 2 32]
Psychological issue+personality trait ANN	4	16	0.935	0.936	0.951	0.936	[27 1 3 31]
Psychological issue+personality trait ANN	4	32	0.935	0.354	0.95	0.936	[27 1 3 31]
Psychological issue+personality trait ANN	4	64	0.952	0.791	0.967	0.951	[26 2 1 33]
Psychological issue+personality trait ANN	4	128	0.967	0.893	0.95	0.912	[27 1 3 31]
Psychological issue+personality trait ANN	5	2	0.951	0.936	0.953	0.902	[0 28 0 34]
Psychological issue+personality trait ANN	5	4	0.951	0.951	0.811	0.924	[23 5 8 26]
Psychological issue+personality trait ANN	5	8	0.807	0.936	0.886	0.943	[27 1 6 28]
Psychological issue+personality trait ANN	5	16	0.951	0.951	0.902	0.891	[27 1 3 31]
Psychological issue+personality trait ANN	5	32	0.95	0.953	210.9	0.871	[26 2 1 33]
Psychological issue+personality trait ANN	5	64	0.967	0.934	0.938	0.906	[27 1 3 31]
Psychological issue+personality trait ANN	5	128	0.95	0.95	0.953	0.921	[27 1 2 32]

Source: own research.

components like stress, anxiety, depression, phobias on various forms, and cognitive issues. Evaluation metric results of all these techniques are shared in table below.

In Table 1, the prediction percentage for almost all these above performed tests for psychological issue models (like stress, anxiety, depression, phobias on various forms, and

TABLE 7: Final summary.

SVM linear: FR-based model>FR+personality trait-based model>personality trait-based model
SVM RBF: FR+ personality trait-based model>FR-based model>personality trait-based model
Logistic regression: FR-based model>FR+personality trait-based model>personality trait-based model
Decision tree: FR+personality trait-based model>personality trait-based model>FR-based model
ANN: FR+personality trait-based model>FR-based model>personality trait-based model

cognitive issues) exceeds 90% or is near to 90%. It shows that these models predicted psychological issues and all its components like stress, anxiety, depression, phobias on various forms, and cognitive issues with high accuracy and with not much significant errors. Also, Table 2 reflects psychological issues, models, and ANN results.

*9.1.1. Artificial Neural Network and Psychological Issue Model.* The results of evaluation metrics of artificial neural networks are shared below.

*9.2. Model 2: Personality Traits.* Model 2 is built on using neuroticism, conscientiousness, extroversion, agreeableness, and openness to experience. The following are the results of evaluation of personality trait model built using neuroticism, conscientiousness, extroversion, agreeableness, and openness to experience.

In Table 3, the prediction accuracy rates for psychological issue model have quite stark difference in their rates. But logistic regression with least error rates could be considered accurate, and hence, it depicts that personality trait indicators are worst predictors for human being improvement models as they have least accuracy rates. Moreover, Table 4 manifests personality trait-based model results.

*9.2.1. Artificial Neural Network Results.* The following are the results of artificial neural networks of personality trait-based model.

*9.3. Using Both Psychological Issue and Personality Trait Indicators.* The third model is constructed using both psychological issue and personality trait indicators. The results of evaluation metrics of model are shared below.

In Table 5, the results show the highest accurate prediction rate to be 97.8%. It does clearly depict that there is a significant improvement in results by using both psychological issue and personality trait indicator for psychological issue indicator prediction.

*9.3.1. Artificial Neural Network Results.* Table 6 shows the results of artificial neural network technique applied for psychological issue and personality trait indicators as predictors.

## 10. Final Summary

Tables 7 and 8 depict the different models used in the comparison. The above-mentioned results clearly depict that the

TABLE 8: Comparison of techniques used. Source: own research.

Psychological issue-based model: ANN>logistic regression>SVM linear>decision tree>SVM RBF
Personality trait-based model: ANN>SVM RBF>decision tree>SVM linear>logistic regression
Psychological issue-based model+personality trait-based model: ANN>SVM RBF>decision tree>SVM linear>logistic reg

model containing both psychological issue and personality trait indicators performed better than model containing alone the personality trait or psychological issue indicators. Therefore, it can be noted that psychological issues and personality traits are not the best indicators alone.

## 11. Comparison of Technique

Subject to the result tables, it can be concluded the ANN is deemed to have least error rate according to confusion matrix results followed by SVN RBF, decision tree, SVM linear, and logistic regression. Its main reason could be that in different layer of artificial neural networks, different combinations of features were used and improved the efficiency of the model.

## 12. Conclusions

The main aim of this research was to develop the algorithms for prediction of employee health using both psychological health issue and personality health trait indicators. The model developed using the combined data of both psychological issue and personality trait indicators outperformed the model developed using either psychological issue data individual or personality trait indicators for prediction. The model is predicted using five (5) psychological issue indicators and five personality trait indicators. The supervised artificial intelligence techniques used in this study are support vector machine, SVM RBF, logistic regression, decision tree model, and artificial neural networks. The percentage of accuracy of model increased up to 96.4% that makes it an outstanding model for prediction. Using alone psychological issue indicators for prediction displayed dismal results. Our results are in consensus with the study conducted in Taiwan [26], but contrary to research conducted in the USA [2]. Artificial neural networks are deemed to be the best performing technique among other supervised techniques as it has highest accuracy rate and least error rate. This model with positive results would serve as a beacon of light for initiating artificial intelligence in the field of human resource for uplifting the best human capital of Pakistan. To broaden its scope and verify its results, this research can also be conducted on other similar capacity countries to authenticate its results further or identify changes in results in relation to different markets and understanding this variation in relation to them. This study was conducted for predicting psychological issue indicator model; in a similar manner, a model can be constructed for predicting behavior of fraudulent companies using previous data of companies that committed fraud.

## Retraction

# Retracted: The Disparity in the Management of Polycystic Ovary Syndrome between Obstetrician-Gynecologists in Different-Level Hospitals under the Hierarchical Medical System

### BioMed Research International

Received 8 January 2024; Accepted 8 January 2024; Published 9 January 2024

Copyright © 2024 BioMed Research International. This is an open access article distributed under the Creative Commons Attribution License, which permits unrestricted use, distribution, and reproduction in any medium, provided the original work is properly cited.

This article has been retracted by Hindawi following an investigation undertaken by the publisher [1]. This investigation has uncovered evidence of one or more of the following indicators of systematic manipulation of the publication process:

- (1) Discrepancies in scope
- (2) Discrepancies in the description of the research reported
- (3) Discrepancies between the availability of data and the research described
- (4) Inappropriate citations
- (5) Incoherent, meaningless and/or irrelevant content included in the article
- (6) Manipulated or compromised peer review

The presence of these indicators undermines our confidence in the integrity of the article's content and we cannot, therefore, vouch for its reliability. Please note that this notice is intended solely to alert readers that the content of this article is unreliable. We have not investigated whether authors were aware of or involved in the systematic manipulation of the publication process.

Wiley and Hindawi regrets that the usual quality checks did not identify these issues before publication and have since put additional measures in place to safeguard research integrity.

We wish to credit our own Research Integrity and Research Publishing teams and anonymous and named

external researchers and research integrity experts for contributing to this investigation.

The corresponding author, as the representative of all authors, has been given the opportunity to register their agreement or disagreement to this retraction. We have kept a record of any response received.

### References

- [1] Y. Wang, J. Chen, H. Dong et al., "The Disparity in the Management of Polycystic Ovary Syndrome between Obstetrician-Gynecologists in Different-Level Hospitals under the Hierarchical Medical System," *BioMed Research International*, vol. 2022, Article ID 9778678, 12 pages, 2022.

## Research Article

# The Disparity in the Management of Polycystic Ovary Syndrome between Obstetrician-Gynecologists in Different-Level Hospitals under the Hierarchical Medical System

Yue Wang,<sup>1</sup> Jie Chen,<sup>1</sup> Han Dong,<sup>2</sup> Ruilin Ma,<sup>1</sup> Ying Zou,<sup>3</sup> Wei Wang,<sup>4</sup> Qingmei Zheng,<sup>5</sup> Ying Feng,<sup>6</sup> Zhangyun Tan,<sup>7</sup> Xiaoqin Zeng,<sup>8</sup> Yinqing Zhao,<sup>7</sup> Yan Deng,<sup>1</sup> Yanfang Wang,<sup>1</sup> Bei Gu,<sup>9</sup> and Aijun Sun <sup>1,10</sup>

<sup>1</sup>Department of Obstetrics and Gynecology, Peking Union Medical College Hospital, Chinese Academy of Medical Sciences and Peking Union Medical College, Beijing 100730, China

<sup>2</sup>Department of Obstetrics and Gynecology, Women and Children's Hospital of Jinzhou, Jinzhou, 121000 Liaoning, China

<sup>3</sup>Department of Obstetrics and Gynecology, Hunan Provincial Maternal and Child Health Care Hospital, Changsha, 410008 Hunan, China

<sup>4</sup>Department of Reproductive Medicine, The Second Hospital of Hebei Medical University, Shijiazhuang, 050000 Hebei, China

<sup>5</sup>Department of Gynecology, The Affiliated Hospital of Qingdao University, Qingdao, 266500 Shandong, China

<sup>6</sup>Department of Obstetrics and Gynecology, The Second Affiliated Hospital of Nanchang University, Nanchang, 330006 Jiangxi, China

<sup>7</sup>Department of Obstetrics and Gynecology, Xinhui Maternity and Children's Hospital, Nanning, 529100 Guangxi, China

<sup>8</sup>Department of Gynecology, Guangzhou Women and Children's Medical Center, Guangzhou, 510000 Guangdong, China

<sup>9</sup>Department of Obstetrics and Gynecology, Beijing Shijitan Hospital, Capital Medical University, Peking University Ninth School of Clinical Medicine, Beijing 100038, China

<sup>10</sup>Department of Obstetrics and Gynecology, Peking Union Medical College Hospital, Beijing 100010, China

Correspondence should be addressed to Aijun Sun; [saj@pumch.cn](mailto:saj@pumch.cn)

Received 10 June 2022; Accepted 13 July 2022; Published 15 September 2022

Academic Editor: Nauman Rahim Khan

Copyright © 2022 Yue Wang et al. This is an open access article distributed under the Creative Commons Attribution License, which permits unrestricted use, distribution, and reproduction in any medium, provided the original work is properly cited.

**Background.** PCOS is a prevalent endocrine and metabolic disorder in women characterized by abnormal blood glucose, dyslipidemia, and abnormal mental health. To improve patient care, the goal of our study is to find out if there are differences in how PCOS patients are treated at different hospital levels within the hierarchical medical system. **Methods.** Obstetricians and gynecologists from primary, secondary, and tertiary hospitals were the participants in the survey. The responses provided and collected were analyzed using various statistical techniques like the chi-square test, Fisher exact test, and logistic regression with multiple variables. **Results.** The investigation examined 2298 survey replies (13.1% primary hospitals, 52.4% secondary hospitals, and 34.5% tertiary hospitals). As hospital grade increases, more participants inquire about a patient's history of unfavorable pregnancies concerning hormone evaluation; the better the hospital's grade, the greater the number of participants who would undergo AMH and androgen-related tests. The higher the hospital level, the more participants would pick the oral glucose tolerance test (OGTT) to determine insulin resistance, the BMI Asian criteria for defining obesity, and blood lipids. Participants in primary (odds ratio (OR) = 0.383, 95% confidence interval (CI) 0.282-0.520) and secondary (OR = 0.607, 95% confidence interval (CI) 0.481-0.765) hospitals were significantly less likely to select OGTT than those in tertiary hospitals. Comparatively, fewer primary hospitals chose to do lipid profiling than tertiary hospitals (OR 0.689, 95% CI 0.523-0.909). With the increase in hospital level, participants were more knowledgeable about the multiple efficacies and dose alternatives of metformin and selected letrozole and assisted reproduction more frequently. **Conclusion.** Our study uncovered differences in the endocrine evaluation, metabolic screening, and management of PCOS patients across obstetrics and gynecology at various hospital levels. Simultaneously, it underlines the need to improve the hierarchical medical system and close the knowledge gap across hospitals.



## 1. Introduction

Polycystic ovary syndrome (PCOS) is one of the women's most prevalent reproductive endocrine diseases, affecting 9-18% of females [1-3]. Clinically, women with PCOS are widely dispersed across age groups, exhibiting diverse symptoms and prominent genetic traits. Patients with different needs necessitate individualized treatment strategies, posing new difficulties in diagnosing and treating the disease.

PCOS's pathogenesis is complex. Genetic and environmental factors alter the signaling pathway of the hypothalamic-pituitary-ovarian axis, thereby promoting ovarian and adrenal hyperandrogenism. Insulin resistance (IR), adipose tissue accumulation, and lipid toxicity exacerbate PCOS. The dysfunction of oxidative stress also worsens symptoms [4]. Independent of BMI, women with PCOS have a three-fold higher risk of impaired glucose tolerance [5], particularly in Asia and North and South America. There is a strong relationship between obesity and PCOS prevalence [6]. According to a large-scale, high-quality meta-analysis, the risk of obesity in women with PCOS is four times that of women without the condition. White women are more likely to be obese than Asian women [7]. According to Dumesic et al., the prevalence of PCOS increased significantly among women with a BMI greater than 30 kg/m<sup>2</sup> [4]. Hyperandrogenism and obesity have been linked to several psychological disorders [8, 9]. In cross-sectional studies, moderate to severe depression and anxiety symptoms have increased [10]. Several longitudinal studies, meanwhile, have reached similar conclusions [11]. Thus, the syndrome encompasses metabolic, reproductive, and psychological disorders.

PCOS is identified based on three specific factors: oligoovulation, clinical or biochemical androgen excess, and ultrasound assessment of ovarian morphology. Currently, there is no definitive diagnostic model for PCOS. The evidence-based international guidelines [12] endorse the Rotterdam criteria as an exclude-diagnosis. The requirements suggest excluding thyroid diseases, hyperprolactinemia, and atypical congenital adrenal hyperplasia (screening with 17-hydroxyprogesterone) and meeting two of the three diagnostic criteria [13] for the diagnosis of adult women. In Asian women, hyperandrogenism manifests primarily as skin manifestations, such as hirsutism (modified Ferriman-Gallwey (mFG) score), acne, and alopecia [14]. Neither biologically nor clinically is pelvic ultrasound required to diagnose women with menstrual irregularities and hyperandrogenism. The clinical diagnosis is still valid even without a comprehensive ultrasound morphological evaluation. Levels of AMH have been considered as an alternative biomarker for diagnosing polycystic ovary morphology (PCOM), or ultrasound follicle number per ovary (FNPO) counts, as well as an independent marker for PCOS [15]. The total serum AMH level in women with PCOS is two to three times that of women with normal reproductive function, and this level correlates with FNPO ultrasound measurements. Several studies have demonstrated that the median level of AMH in PCOS women is 20-81.6 pmol/L, whereas it ranges from 16.7 to 33.5 pmol/L in normal controls [16, 17]. Lifestyle

modification is the most fundamental treatment that can somewhat alleviate symptoms [18-20]. Oral contraceptives, metformin, and GLP-1 receptor agonist have demonstrated respective advantages in drug therapy [21-23].

The hierarchical medical system classifies hospitals into three levels based on size, scientific research direction, skills, technical prowess, and medical equipment. Several studies [24] demonstrate that primary (community) hospitals play indispensable roles in the early diagnosis, treatment, and long-term management of common diseases such as PCOS. Consequently, the only way to improve diagnosis and treatment technology is to acknowledge the disparity between hospitals of all grades. To promote evidence-based medicine and standardize the diagnosis, treatment, and management of PCOS women, our study seeks to identify disparities in hospital management from various perspectives.

## 2. Methods

*2.1. Study Design, Setting, and Participants.* A countrywide online survey was performed between 1 and 30 September 2020. Physicians who had joined the China Maternal and Child Health Association's online chat groups received an invitation to accept and complete an online questionnaire intended for this purpose, along with instructions and a web link. All individuals were encouraged to participate voluntarily while maintaining their anonymity. Participants' consent to participate in the study was assumed when they completed the survey.

*2.2. Questionnaire Content.* The questionnaires inquired about the demographics, clinical specialties, hospital levels, practice attributes, obesity and IR diagnostic criteria, provider knowledge of obesity, and PCOS evaluation and treatment, as well as weight reduction and treatment procedures for women with PCOS. The questionnaire was piloted with thirty obstetricians and gynecologists, and their feedback was considered; its content was clear and concise.

*2.3. Ethical Approval.* Prior to initiation, the study protocol was approved by the Ethics Committee of Peking Union Medical College Hospital, Chinese Academy of Medical Sciences, China, per protocol number S-K1373.

## 3. Statistical Analysis

SPSS was used to evaluate the collected data (version 23.0, IBM, Armonk, NY, USA). Frequencies and percentages were used to present categorical data. We used the procedures of Ma et al. [25], comparing various groups using Pearson's  $\chi^2$  tests or Fisher's exact tests, depending on the situation. In a multivariable logistic regression analysis, physician gender, specialty, age, hospital grade, the number of PCOS patients seen annually, and the proportion of PCOS women with obesity and insulin resistance (IR) were considered. Statistical significance was defined as a *p* value of less than 0.05.

TABLE 1: General information provided by the study participants.

	Overall (n = 2298)	Primary hospital (n = 301)	Secondary hospital (n = 1204)	Tertiary hospital (n = 793)	p value
Sex					
Female	2256 (98.2)	300 (99.7)	1192 (99.0)	764 (96.3)	<0.001
Male	42 (1.8)	1 (0.3)	12 (1.0)	29 (3.7)	<0.001
Age					
18-35	335 (14.6)	28 (9.3)	120 (10.0)	187 (23.6)	<0.001
36-45	890 (38.7)	124 (41.2)	466 (38.7)	300 (37.8)	NS
>45	1073 (46.7)	149 (49.5)	618 (51.3)	306 (38.6)	<0.001
Specialty					
Ob-Gyn	2117 (92.1)	296 (98.3)	1151 (95.6)	670 (84.5)	<0.001
Repro-Endo	181 (7.9)	5 (1.7)	53 (4.4)	123 (15.5)	<0.001
No. of patients with PCOS treated annually					
<50	1649 (71.8)	269 (89.4)	915 (76.0)	465 (58.6)	<0.001
50-200	511 (22.2)	24 (8.0)	247 (20.5)	240 (30.3)	<0.001
>200	138 (6.0)	8 (2.6)	42 (3.5)	88 (11.1)	<0.001
The chief complaint about clinic attendance in patients with PCOS					
Menstrual disorders	1833 (78.9)	223 (74.1)	957 (79.5)	653 (82.3)	0.009
Infertility	405 (17.6)	67 (22.2)	217 (18.0)	121 (15.4)	<0.001
Obesity/IR	39 (1.7)	5 (1.7)	17 (1.4)	17 (2.1)	0.017
Hirsutism/acne	14 (0.6)	5 (1.7)	8 (0.7)	1 (0.1)	0.013
Others	7 (0.3)	1 (0.3)	5 (0.4)	1 (0.1)	NS
Estimated national prevalence of IR in patients with PCOS (%)					
0-30	1398 (80.8)	211 (70.1)	766 (63.8)	419 (52.8)	<0.001
31-60	754 (32.8)	72 (23.9)	382 (31.8)	300 (37.8)	<0.001
>60	146 (6.4)	18 (6.0)	54 (4.4)	74 (9.4)	<0.001
Estimated national prevalence of obesity in patients with PCOS (%)					
0-30	748 (32.6)	142 (47.2)	387 (32.1)	219 (27.6)	<0.001
30-50	909 (39.5)	87 (26.9)	495 (41.1)	327 (41.2)	<0.001
50-80	522 (22.7)	51 (16.9)	254 (21.2)	217 (27.4)	<0.001
>80	119 (5.2)	21 (7.0)	68 (5.6)	30 (3.8)	NS

Ob-Gyn = obstetrician-gynecologists (specialization outside of reproductive medicine); Repro-Endo = reproductive endocrinologists; PCOS = polycystic ovary syndrome; IR = insulin resistance; NS = not significant.

## 4. Results

A total of 2509 questionnaires were completed and submitted by the participants. Among these, 211 questionnaires completed by nonobstetricians and gynecologists were excluded, resulting in the remaining 2298 questionnaires in the final analysis.

**4.1. General Characteristics of the Participants.** The general information of patients is shown in Table 1, of which 13.1% are from primary hospitals, 52.4% from secondary hospitals, and 34.5% from tertiary hospitals. Among the participants in the survey, 98.2% (2,256) were female, and 1.8% (42) were male. The proportion of male doctors increased as the grade of hospitals increased. More than 80% of participants were over 35 years old, while a total of 181 (7.9%) were reproductive endocrinologists (Repro-Endo), and 2,117 (92.1%) were nonreproductive endocrinologists in obstetrics and gynecology (Ob-Gyn). The

proportion of reproductive endocrinologists in tertiary hospitals increased significantly (15.5%). In tertiary hospitals, the majority of participants admitted 0-50 PCOS patients annually, but over 40% of participants saw more than 50 patients annually. The chief paramount complaints of patients were menstrual disorder (79.8%) and infertility (17.6%). Moreover, a small number of patients were also treated for acne, acanthosis nigricans, abnormal blood glucose, obesity, and other reasons. Regarding understanding PCOS complications, most participants (60.8%) thought about 0-30% of PCOS patients combined with IR. With the grade of the hospital increase, doctors reckoned the proportion of patients combined with IR would be higher ( $p < 0.001$ ), and about half (47.4%) of tertiary hospital doctors believe IR prevalence  $> 30\%$ . Most doctors (72.1%) thought that the probability of PCOS combined with obesity was 0-50%. With the improvement of hospital grades, doctors generally believed that the prevalence of PCOS combined with obesity increased ( $p < 0.001$ ).

TABLE 2: Physicians' approach to patients' management suffering from obesity and PCOS.

	Overall (n = 2298)	Primary hospital (n = 301)	Secondary hospital (n = 1204)	Tertiary hospital (n = 793)	p value
Commonly used diagnostic criterion for IR.					
OGTT-insulin release test	1122 (48.8)	109 (36.2)	570 (47.3)	443 (55.9)	<0.001
Fasting insulin and blood glucose	503 (21.9)	74 (24.6)	280 (23.3)	149 (18.8)	0.029
Fasting and 2 h insulin and blood glucose	285 (12.4)	42 (14.0)	146 (12.1)	97 (12.2)	NS
HOMA-IR	128 (5.6)	15 (5.0)	64 (5.3)	49 (6.2)	NS
Other	260 (11.3)	61 (20.2)	144 (12.0)	55 (6.9)	<0.001
The diagnostic criterion used for obesity					
BMI (WHO criteria)	659 (28.7)	90 (29.9)	347 (28.8)	222 (28.0)	NS
BMI (Chinese criteria)	1355 (59.0)	187 (62.1)	719 (59.7)	449 (56.6)	NS
BMI (Asian criteria)	250 (10.9)	23 (7.6)	115 (9.6)	112 (14.1)	0.001
Measure waistline	31 (1.3)	1 (0.4)	21 (1.7)	9 (1.2)	NS
Other	3 (0.1)	0 (0)	2 (0.2)	1 (0.1)	NS
Family history of diabetes inquiry					
Yes	2188 (95.2)	284 (94.4)	1144 (95.0)	760 (95.8)	NS
Family history of PCOS inquiry					
Yes	2036 (88.6)	261 (86.7)	1069 (88.8)	709 (89.0)	NS
Family history of cardiovascular disease inquiry					
Yes	1518 (66.1)	189 (62.7)	793 (65.9)	536 (67.6)	NS
Family history of unfavorable pregnancy inquiry					
Yes	1889 (82.2)	233 (77.4)	993 (82.5)	663 (83.6)	0.041
Symptoms of anxiety, depression, and other psychological problems inquiry					
Yes	1229 (53.5)	166 (55.1)	630 (52.3)	433 (54.6)	NS

Abbreviations: IR = insulin resistance; OGTT = oral glucose tolerance test; HOMA-IR = homeostasis model assessment-insulin resistance; WHO = World Health Organization; PCOS = polycystic ovary syndrome; BMI = body mass index; NS = not significant.

**4.2. Diagnosis and Evaluation of PCOS Patients.** The international evidence-based guidelines [13] endorse using the Rotterdam criteria for diagnosing PCOS, but a comprehensive evaluation is necessary for newly diagnosed patients, a thorough review, including the history of hormone and metabolic assessment. In the aspect of medical history inquiry (Table 2), different doctors may emphasize PCOS as it is affected by many factors. Almost all participants noticed whether patients had a family history of diabetes (95.2%) and PCOS (88.6%), and 82.7% of participants asked patients whether they had a history of adverse pregnancy and delivery, which was particularly prominent in tertiary hospitals ( $p = 0.041$ ). Most participants also noted a history of thyroid diseases (77.9%), cardiovascular disease, and family history (66.1%). 53.5% of participants would pay attention to patients' mental health, asking whether they have anxiety or depression, and there is no significant statistical difference between different grades of hospitals. Almost all participants (98.7%) underwent six sex hormone tests (Figure 1).

In addition, AMH (57.8%) and other androgen-related indicators such as androstenedione, dehydroepiandrosterone sulfate, and free testosterone (57.2%) were also assessed by some physicians. With the increase in hospital grade, more participants set these hormone levels ( $p < 0.001$ ). The most common metabolic abnormalities associated with PCOS are IR, obesity, and dyslipidemia. The evaluation of metabolic abnormalities is shown in Table 2 and Figure 2.

The gold standard for IR diagnosis is the OGTT test. About half of the participants (48.8%) most often chose OGTT for IR diagnosis, and the number of participants increased successively from the primary, secondary, and tertiary hospitals ( $p < 0.001$ ). In addition, some participants also chose to fast blood glucose and blood insulin (21.9%), 2 hours postprandial blood glucose and blood insulin (12.9%), and HOMA-IR (5.6%) for diagnosis. The evaluation criteria for obesity mainly included BMI and waist circumference. Most participants would choose the BMI China standard (59%) for evaluation, but participants in tertiary hospitals (14.1%) would also adopt BMI Asian standard ( $p = 0.001$ ). Only a minority (1.3%) of participants would choose waist circumference > 80 cm to assess obesity, and there was no significant difference between hospitals.

In univariate analysis, physicians who specialized in reproductive endocrinology had an estimated prevalence of overweight/obesity at 31-80%, and an estimated prevalence of IR >30% was more likely to perform OGTT on PCOS patients. Physicians who specialized in reproductive endocrinology and estimated an IR prevalence of greater than 30 percent were more likely to order lipid profiling for PCOS patients. Participants in primary (odds ratio (OR) 0.383, 95% confidence interval (CI) 0.282-0.520) and secondary (OR 0.607, 95% confidence interval (CI) 0.481-0.764) hospitals were less likely to select OGTT than those in tertiary hospitals. Compared with the tertiary hospital group, fewer

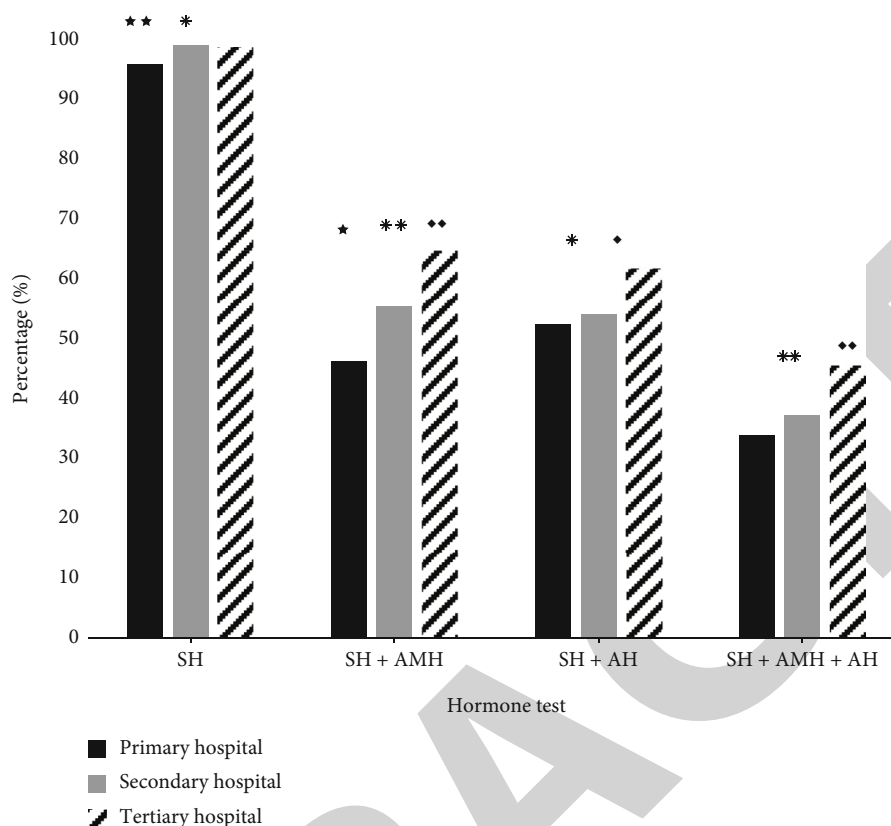


FIGURE 1: Hormonal level estimation for PCOS patients in different grades of hospitals. SH: sex hormone test (including FSH, LH, estradiol, testosterone, PRL, and progesterin); AMH: anti-Müllerian hormone; AH: androgenic hormone test (including androstenedione, dehydroepiandrosterone sulfate, and free testosterone). Primary vs. secondary hospital (\* $p < 0.05$  and \*\* $p < 0.001$ ). Primary vs. tertiary hospital (\* $p < 0.05$  and \*\* $p < 0.001$ ). Secondary vs. tertiary hospital (♦ $p < 0.05$  and ♦♦ $p < 0.05$ ).

primary hospitals chose to perform lipid profiling (OR 0.689, 95% CI 0.523-0.909) (Table 3).

4.3. Treatment and Management of PCOS. PCOS treatment has different needs for women of different ages (Figure 3). Most participants recognize that lifestyle intervention and weight management are the most basic treatment options. Regarding drug therapy, most participants believed that metformin could be used regardless of the patient’s need for fertility. Figure 4 shows the dose selection of metformin. With the increase in hospital grade, physicians would be more active in their choice, preferring 1 g/day or 1.5 g/day. About 1/10 of participants were unclear about the dose selection of metformin, as was 1/5 (22.9%) in the primary hospital group. Most participants (63.8%) of patients without fertility needs believed that oral contraceptives could be used for a long time by regularly checking liver and kidney functions. There was no significant difference among different level hospitals. Some participants agreed to use letrozole, assisted reproductive technology (ART), for patients with fertility needs. The higher the hospital level, the higher the proportion of participants who chose this program. In terms of weight loss, in addition to dietary adjustment, metformin and orlistat were preferred by more physicians with the increase in hospital grade. Some participants in primary hospitals tried traditional Chinese medi-

cine weight loss programs (Figure 5). PCOS is a metabolic disease caused by endocrine disorders under multiple factors, which requires the cooperation and long-term management of hospitals and patients. However, participants also generally reported that patients did not understand the disease well in receiving treatment.

### 5. Discussion

The hierarchical medical system contributes to the hierarchical management of diseases and resolves the problem of individuals’ difficulty in obtaining medical care. Simultaneously, hospitals at all levels carry out their respective responsibilities, thereby enhancing the efficacy of disease diagnosis and treatment, conserving medical resources to some extent, and maximizing the utilization rate of medical resources. Nonetheless, the hierarchical medical system inevitably produces disparities in hospital diagnosis and treatment, particularly for chronic diseases with multiple manifestations and complications, such as PCOS. A lack of reproductive endocrinology specialists, coupled with the fact that primary hospitals treat far fewer patients annually than tertiary hospitals, has led to the current situation in which primary hospital group participants have a limited understanding of diseases. Regarding physician composition, secondary hospitals have the most significant number of

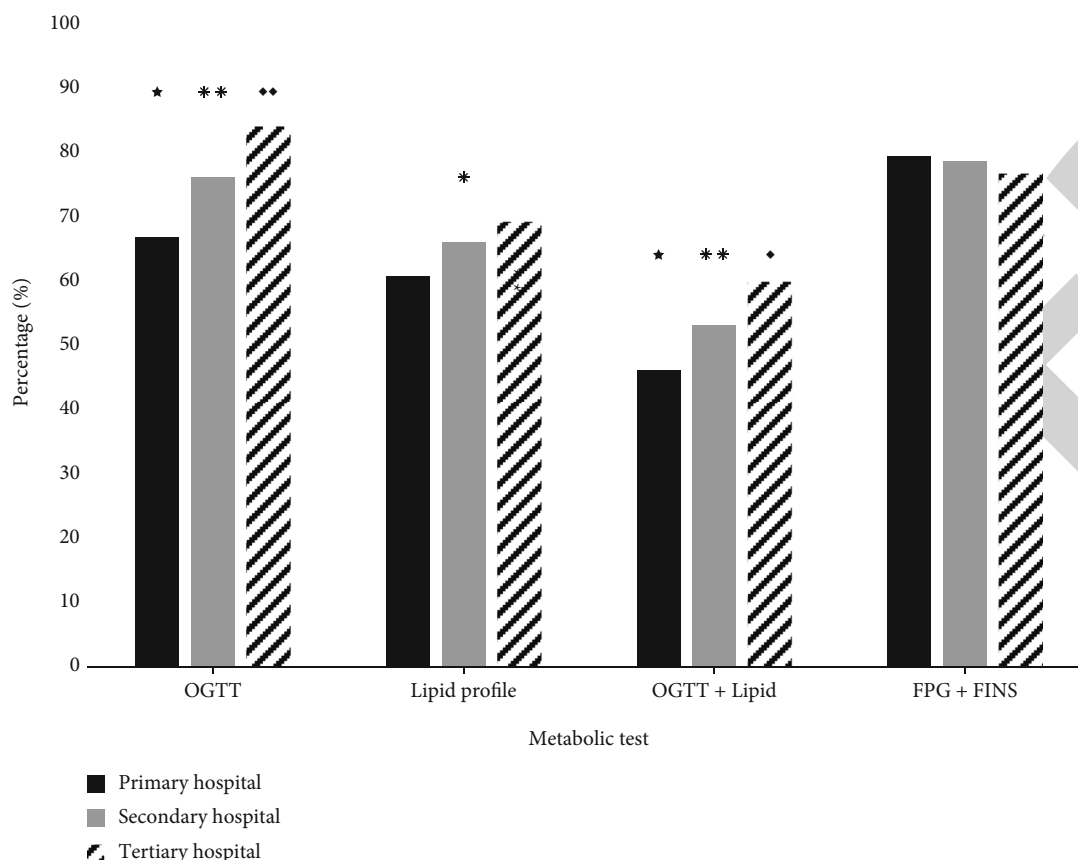


FIGURE 2: Patients with PCOS results of OGTT, FPG, and FINS. Primary vs. secondary hospital ( $*p < 0.05$ ). Primary vs. tertiary hospital ( $*p < 0.05$  and  $**p < 0.001$ ). Secondary vs. tertiary hospital ( $\diamond p < 0.05$  and  $\blacklozenge p < 0.05$ ). OGTT = oral glucose tolerance test; FPG = fasting plasma glucose; FIN = fasting insulin.

participants, which meets the requirements of China's current diagnosis and treatment model. The majority of participants in primary hospitals are female. As hospital conditions improve, the proportion of male obstetricians and gynecologists gradually increases. In terms of age composition, the majority of primary hospital physicians are older. This phenomenon demonstrates that tertiary hospital physicians have shattered the stereotype that "obstetricians and gynecologists are all female physicians" and that an increase in the number of young physicians indicates a greater willingness to update knowledge and engage in lifelong learning. As the hospital level increased, participants generally agreed that PCOS patients had a higher incidence of insulin resistance and obesity, which was helpful in alerting physicians to this aspect of patient assessment. This serves as a reminder to primary care physicians to pay attention to the advancement of research and the updating of their knowledge; tertiary hospitals should also assist primary hospitals in times of difficulty and establish an effective chronic disease cooperative management mechanism.

Almost all participants were concerned about whether or not patients had a family history of diabetes, PCOS, and thyroid-related diseases. However, less than two-thirds of the participants paid attention to a cardiovascular disease history. Insulin resistance is typically involved in the pathogenesis of polycystic ovary syndrome (PCOS), leading to

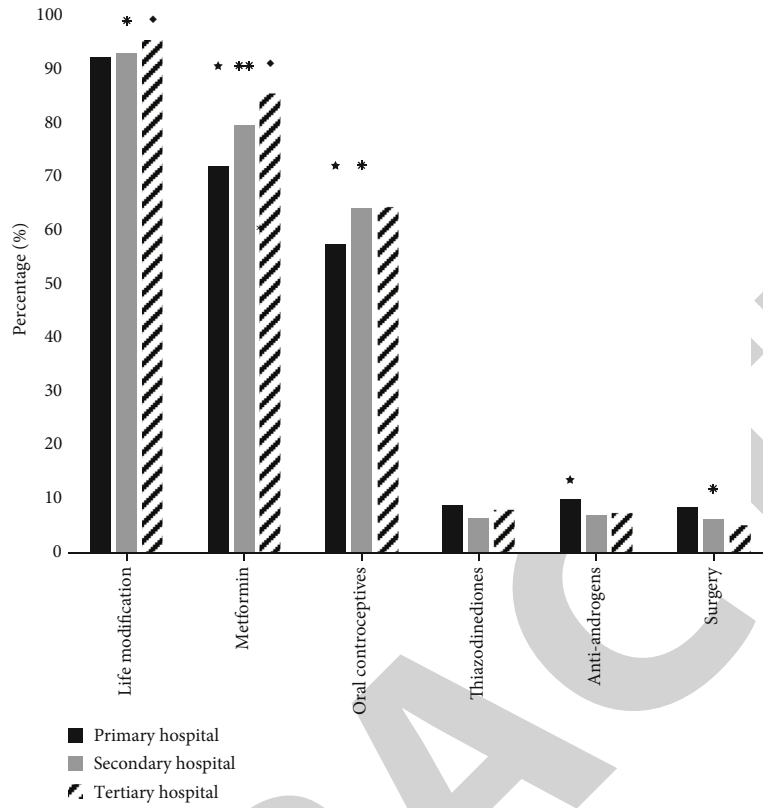
various cardiometabolic abnormalities (such as dyslipidemia, hypertension, glucose intolerance, diabetes, and metabolic syndrome) and thereby increasing the risk of cardiovascular disease in women [26]. Most doctors also inquired about a patient's history of adverse pregnancies, and as hospital grades improved, more participants inquired. The study by Palomba et al. demonstrated that PCOS patients are more likely to experience pregnancy complications, which endanger the mother's and fetus's health. Only fifty percent of participants would inquire about the patients' mental health. Current research indicates that dysfunction of the H-P-O axis may involve a broader range of functional brain regions and lead to psychological and emotional issues [8, 9].

In assessing patients' specific conditions, hospitals of varying acuity also have unique characteristics. Regarding the selection of obesity standards, most physicians use the BMI China standard to define obesity. Some participants in tertiary hospitals will also choose the stricter BMI Asian standard for definition, which can identify high-risk obese individuals earlier than the BMI China standard. Few participants selected a waist circumference greater than 80 cm as the standard for obesity. The waist circumference can effectively detect abdominal obesity in patients, and abdominal obesity in PCOS patients frequently indicates a greater metabolic risk. However, abdominal obesity is not an absolute

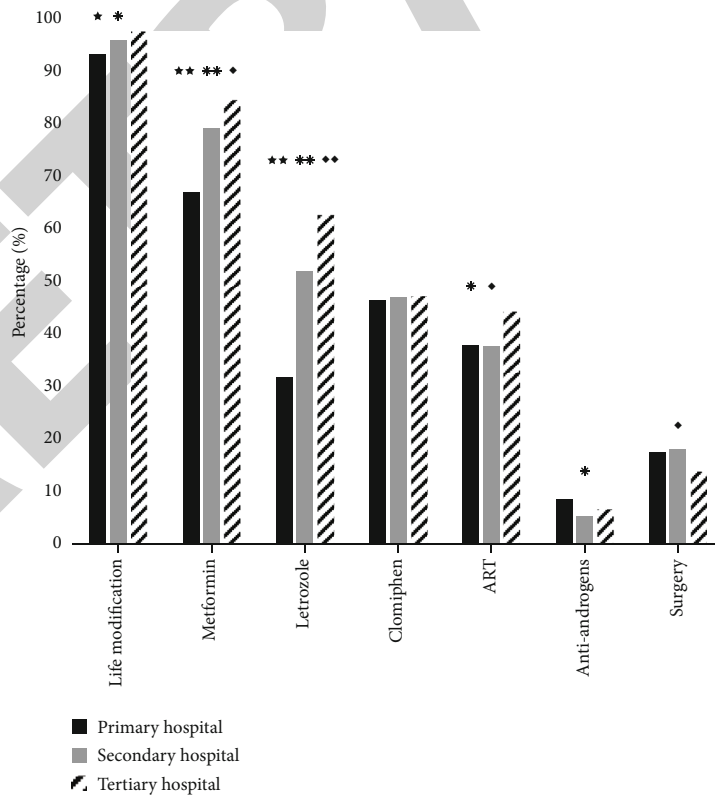
TABLE 3: Multinomial logistic regression analysis results of physician characteristics, OGTT, and lipid profile analysis for PCOS patients.

Variables	Physicians ordering OGTT	Physicians not ordering OGTT	Exp (B)	95% CI	Physicians ordering lipid profiles	Physicians not ordering lipid profiles	Ex (B)	95% CI
<b>Sex</b>								
Female	1750 (98.1)	506 (98.2)	0.943	(0.448, 1.984)	1503 (98.4)	753 (97.8)	1.357	(0.728, 2.529)
Male	33 (1.9)	9 (1.8)	1	1	25 (1.6)	17 (2.2)	1	1
<b>Age</b>								
18-35	273 (15.3)	62 (12.0)	1.437	(1.055, 1.957) <sup>a</sup>	204 (13.4)	131 (17.0)	0.767	(0.595, 0.988) <sup>a</sup>
35-45	701 (39.3)	189 (36.7)	1.210	(0.979, 1.497) <sup>a</sup>	605 (39.6)	285 (37.0)	1.047	0.866, 1.266
≥46	809 (45.4)	264 (51.3)	1	1	719 (47.0)	354 (46.0)	1	1
<b>Hospital grade</b>								
1	201 (11.3)	100 (19.4)	0.383	(0.282, 0.520) <sup>aa</sup>	796 (52.1)	408 (53.0)	0.715	(0.715, 1.105)
2	916 (51.3)	288 (55.9)	0.607	(0.481, 0.764) <sup>aa</sup>	796 (52.1)	408 (53.0)	0.715	(0.715, 1.051)
3	666 (37.4)	127 (24.7)	1	1	549 (35.9)	244 (31.7)	1	1
<b>Specialty</b>								
Repro-Endo	152 (8.5)	29 (5.6)	1.562	(1.037, 2.353) <sup>a</sup>	142 (9.3)	39 (5.1)	1.920	(1.322, 2.768) <sup>aa</sup>
Ob-Gyn	1631 (91.5)	488 (94.4)	1	1	1386 (90.7)	731 (94.9)	1	1
<b>Annual patients with PCOS</b>								
<50	1240 (69.5)	409 (79.4)	0.638	(0.405, 1.005)	1083 (70.9)	566 (73.5)	0.837	(0.574, 1.220)
5-200	429 (24.1)	82 (15.9)	1.101	(0.668, 1.815)	349 (22.8)	162 (21.0)	0.943	(0.624, 1.417)
>200	114 (6.4)	24 (4.7)	1	1	96 (6.3)	42 (5.5)	1	1
<b>The proportion of obesity in PCOS (%)</b>								
0-30	535 (30.0)	213 (41.4)	1.047	(0.684, 1.601)	477 (31.2)	271 (35.2)	0.704	(0.460, 1.077)
31-50	743 (41.7)	166 (32.2)	1.865	(1.215, 2.863) <sup>a</sup>	609 (39.9)	300 (39.0)	0.812	(0.533, 1.237)
51-80	421 (23.6)	101 (19.6)	1.737	(1.107, 2.724) <sup>a</sup>	357 (23.4)	165 (21.4)	0.865	(0.558, 1.342)
>80	84 (4.7)	35 (6.8)	1	1	85 (5.5)	34 (4.4)	1	1
<b>The proportion of IR in PCOS (%)</b>								
0-30	1031 (71.3)	367 (71.3)	0.346	(0.203, 0.589) <sup>aa</sup>	903 (59.1)	485 (64.3)	0.642	(0.437, 0.944) <sup>a</sup>
30-60	622 (34.9)	132 (25.6)	0.580	(0.334, 1.007)	517 (33.8)	237 (30.8)	0.766	(0.514, 1.145)
>60	130 (7.3)	16 (3.1)	1	1	108 (7.1)	38 (4.9)	1	1

Abbreviations: Repro-Endo = reproductive endocrinologists; Ob-Gyn = obstetrician-gynecologists; PCOS = polycystic ovary syndrome; IR = insulin resistance. <sup>a</sup>p < 0.05 and <sup>aa</sup>p < 0.001.



(a) Patients with no fertility demand



(b) Patients with fertility demand

FIGURE 3: Treatment recommendations for women with PCOS. Primary hospital vs. secondary hospital (\* $p < 0.05$  and \*\* $p < 0.001$ ). Primary hospital vs. tertiary hospital (\* $p < 0.05$  and \*\* $p < 0.001$ ). Secondary hospital vs. tertiary hospital (♦ $p < 0.05$  and ♦♦ $p < 0.05$ ).

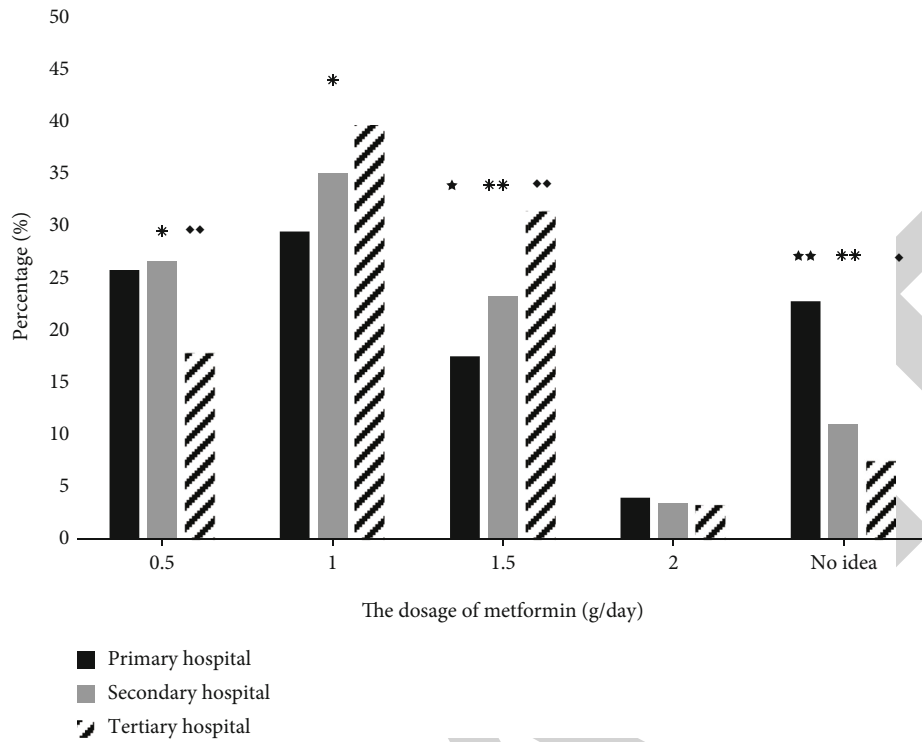


FIGURE 4: Most common dosage of metformin prescribed in women with PCOS.

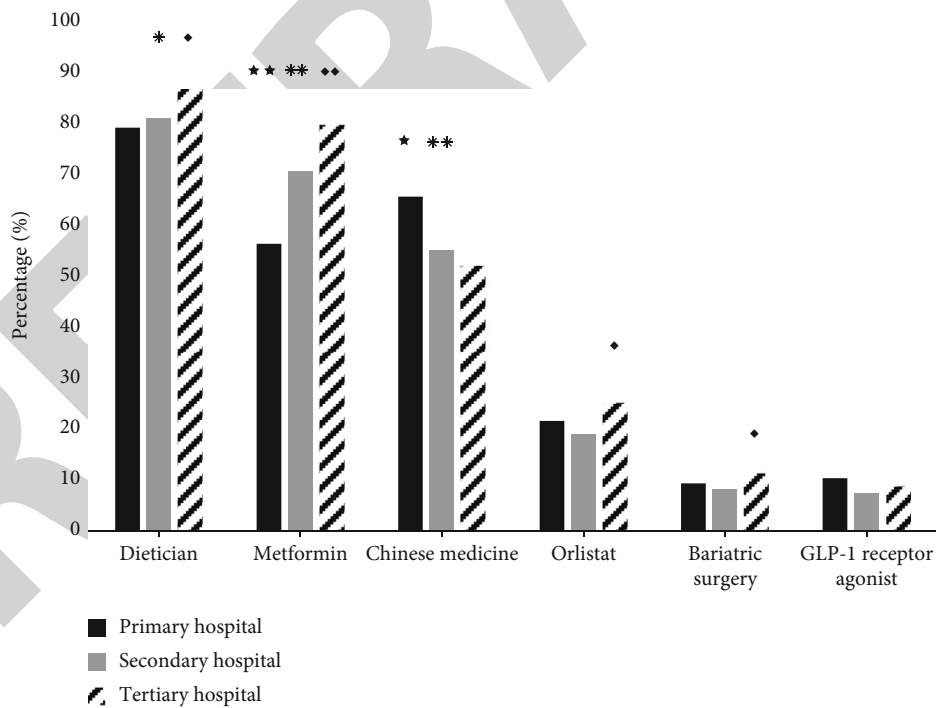


FIGURE 5: The recommended method of weight loss for women with PCOS. GLP-1 receptor agonist, glucagon-like peptide-1 receptor agonist.

measure of obesity; instead, it serves as a supporting factor. At this time, there is no evidence indicating which obesity criteria are more effective at predicting the comorbidities of PCOS patients, and more research is required in this area.

OGTT is the gold standard for evaluating blood glucose and measuring blood glucose.

Nonetheless, in actual clinical practice, the higher the hospital level, the greater the number of participants who



choose OGTT, and the choice of OGTT is also dependent on the time and patient compliance during the administration of this examination. Less than one-third of the participants assessed all patients for IR. Existing studies indicate that IR is independent of obesity, and patients are at particular risk of IR regardless of whether they are overweight or lean [27, 28]. In addition, physicians in tertiary hospitals are more willing to experiment with new blood glucose assessment techniques, such as HOMA-IR. Regarding the assessment of sex hormones, nearly all participants in hospitals at all levels would conduct a six-item evaluation of sex hormones. In addition, more physicians at tertiary hospitals evaluate AMH and other androgens, including androstenedione, dehydroepiandrosterone sulfate, and free testosterone. According to studies, AMH plays an essential role in the early detection of PCOS, and it is independent of BMI and resistant to interference from other factors. The increase of androstenedione (AED), dehydroepiandrosterone sulfate (DHEAS), and free testosterone (T), particularly DHEAS, was observed as a result of abnormalities of androgen precursors in the general population and women with PCOS, according to studies [29]. Increased androgen levels may play a role in preventing cardiovascular disease, but there are currently no conclusive studies on this topic. Several metabolic abnormalities characterize PCOS, and patients with additional needs may require specialized examinations. A comprehensive assessment of the patient's condition is essential for newly diagnosed patients.

Participants in all hospitals were aware that lifestyle modification and weight loss are the most effective treatment strategies. Most participants agreed that timely treatment of PCOS patients with metformin and GLP-1 agonists would help alleviate symptoms. Studies have demonstrated that the benefits of GLP-1 receptor agonists are not limited to the improvement of insulin sensitivity (IR) but also include weight loss and androgen reduction [30]. Although most participants chose metformin, hospital doses varied considerably. Community hospitals were more likely to use a dose of 0.5 g/day, whereas higher-level hospitals were more likely to use a dose of 1.0-1.5 g/day. According to the American Society of Clinical Endocrinology [31], metformin is the first-line treatment for PCOS, with a recommended dosage of 0.85 g/day for patients of normal weight and 1.5-2.5 g/day for those with a higher BMI. Various treatments also depend on whether or not the patient desires to reproduce. After diagnosing infertility, most participants chose oral contraceptives for patients without reproductive needs; if patients have fertility needs, the majority of participants recommended assisted reproductive technology. Additional large-scale clinical trials of alternative treatments and drug combinations are required to improve comorbidities [32, 33].

## 6. Conclusions

This was the most comprehensive survey of PCOS disease management in hospitals of varying grades under the hierarchical medical system. This survey reflects the characteristics and benefits of a hierarchical medical system by comparing the differences in diagnosing and treating PCOS diseases at

various hospital levels. This facilitates identifying potential issues and improving diagnosis and treatment standards within China's tertiary hospital system. Despite this, the survey has limitations. First, participants were distributed unevenly by gender and hospital grade. Second, the age of PCOS patients with IR or obesity was not recorded. Lastly, we did not track specific drug combinations. Consequently, additional research is required to confirm and update our conclusions.

Our findings revealed disparities in the knowledge of metabolic screening for PCOS patients at various hospital levels and differences in assessing and treating participants. Tertiary hospitals have a complete set of diagnosis and treatment standards, so the evaluation is adequate. In contrast, primary hospitals are more open to integrating traditional Chinese and western medicine treatment methods, such as traditional Chinese medicine for weight loss. Secondary hospitals fall between the primary and tertiary hospitals. It also emphasizes the significance of early standardization and comprehensive evaluation of PCOS patients. To narrow the differences in the management of PCOS disease, it is recommended that tertiary hospitals conduct more communication activities in the form of knowledge lectures. Simultaneously, all participants should update their self-knowledge, actively monitor research progress, and improve patient care.

## Data Availability

The datasets used and/or analyzed during the current study are available from the corresponding author on reasonable request.

## Ethical Approval

The Ethics Committee of Peking Union Medical College Hospital, Chinese Academy of Medicine, approved the research (No. S-K1373).

## Consent

Before the online survey, written informed consent was obtained from all participants.

## Conflicts of Interest

The authors declare that they have no competing interests.

## Authors' Contributions

Conceptualization of research topic was carried out by YW and AJS. Questionnaire designing was carried out by JC, HD, RLM, and AJS. Questionnaire refinement, survey completion, and data collection were carried out by WW, QMZ, YF, YZ, HD, ZYT, XQZ, YQZ, YD, YFW, and BG. Data analysis and interpretation were carried out by YW, RLM, WW, YZ, and AJS. Statistical analysis was carried out by YW, YD, and YFW. Manuscript write-up was carried out by YW. Manuscript revision was carried out by AJS, RLM, and YZ. All authors read and approved the final manuscript.

## Acknowledgments

This work was supported by the Capital's Funds for Health Improvement and Research (CFH: 2020-2-40113) and Natural Science Foundation of China (No. 82074143). The authors convey their heartfelt thanks to all participants of the study. Furthermore, we are also thankful to China Maternal and Child Health Association for supporting our survey.

## References

- [1] W. A. March, V. M. Moore, K. J. Willson, D. I. Phillips, R. J. Norman, and M. J. Davies, "The prevalence of polycystic ovary syndrome in a community sample assessed under contrasting diagnostic criteria," *Human Reproduction*, vol. 25, no. 2, pp. 544–551, 2010.
- [2] J. A. Boyle, J. Cunningham, K. O'Dea, T. Dunbar, and R. J. Norman, "Prevalence of polycystic ovary syndrome in a sample of indigenous women in Darwin, Australia," *Medical Journal of Australia*, vol. 196, no. 1, pp. 62–66, 2012.
- [3] B. O. Yildiz, G. Bozdog, Z. Yapici, I. Esinler, and H. Yarali, "Prevalence, phenotype and cardiometabolic risk of polycystic ovary syndrome under different diagnostic criteria," *Human Reproduction*, vol. 27, no. 10, pp. 3067–3073, 2012.
- [4] D. A. Dumesic, D. H. Abbott, S. Sanchita, and G. D. Chazenbalk, "Endocrine-metabolic dysfunction in polycystic ovary syndrome: an evolutionary perspective," *Current Opinion in Endocrine and Metabolic Research*, vol. 12, pp. 41–48, 2020.
- [5] N. S. Kakoly, M. B. Khomami, A. E. Joham et al., "Ethnicity, obesity and the prevalence of impaired glucose tolerance and type 2 diabetes in PCOS: a systematic review and meta-regression," *Human Reproduction Update*, vol. 24, no. 4, pp. 455–467, 2018.
- [6] M. Gibson-Helm, H. Teede, A. Dunaif, and A. Dokras, "Delayed diagnosis and a lack of information associated with dissatisfaction in women with polycystic ovary syndrome," *The Journal of Clinical Endocrinology and Metabolism*, vol. 102, no. 2, pp. 604–612, 2017.
- [7] S. S. Lim, M. J. Davies, R. J. Norman, and L. J. Moran, "Overweight, obesity and central obesity in women with polycystic ovary syndrome: a systematic review and meta-analysis," *Human Reproduction Update*, vol. 18, no. 6, pp. 618–637, 2012.
- [8] C. Coyle and R. E. Campbell, "Pathological pulses in PCOS," *Molecular and Cellular Endocrinology*, vol. 498, p. 110561, 2019.
- [9] Y. Hatanaka, T. Kabuta, and K. Wada, "Disturbance in maternal environment leads to abnormal synaptic instability during neuronal circuitry development," *Frontiers in Neuroscience*, vol. 11, p. 35, 2017.
- [10] L. G. Cooney, I. Lee, M. D. Sammel, and A. Dokras, "High prevalence of moderate and severe depressive and anxiety symptoms in polycystic ovary syndrome: a systematic review and meta-analysis," *Human Reproduction*, vol. 32, no. 5, pp. 1075–1091, 2017.
- [11] J. H. Hung, L. Y. Hu, S. J. Tsai et al., "Risk of psychiatric disorders following polycystic ovary syndrome: a nationwide population-based cohort study," *PLoS One*, vol. 9, no. 5, article e97041, 2014.
- [12] H. J. Teede, M. L. Misso, M. F. Costello et al., "Recommendations from the international evidence-based guideline for the assessment and management of polycystic ovary syndrome," *Human Reproduction*, vol. 33, no. 9, pp. 1602–1618, 2018.
- [13] Rotterdam ESHRE/ASRM-Sponsored PCOS Consensus Workshop Group, "Revised 2003 consensus on diagnostic criteria and long-term health risks related to polycystic ovary syndrome," *Fertility and Sterility*, vol. 81, no. 1, pp. 19–25, 2004.
- [14] M. E. Wierman, "Hyperandrogenic anovulation: differential diagnosis and evaluation," *Endocrinology and Metabolism Clinics of North America*, vol. 50, no. 1, pp. 1–10, 2021.
- [15] L. M. E. Moolhuijsen and J. A. Visser, "Anti-Müllerian hormone and ovarian reserve: update on assessing ovarian function," *The Journal of Clinical Endocrinology and Metabolism*, vol. 105, no. 11, pp. 3361–3373, 2020.
- [16] T. Piltonen, L. Morin-Papunen, R. Koivunen, A. Perheentupa, A. Ruokonen, and J. S. Tapanainen, "Serum anti-Müllerian hormone levels remain high until late reproductive age and decrease during metformin therapy in women with polycystic ovary syndrome," *Human Reproduction*, vol. 20, no. 7, pp. 1820–1826, 2005.
- [17] D. Dewailly, H. Gronier, E. Poncelet et al., "Diagnosis of polycystic ovary syndrome (PCOS): revisiting the threshold values of follicle count on ultrasound and of the serum AMH level for the definition of polycystic ovaries," *Human Reproduction*, vol. 26, no. 11, pp. 3123–3129, 2011.
- [18] G. Jiskoot, A. Dietz de Loos, A. Beerthuis, R. Timman, J. Busschbach, and J. Laven, "Long-term effects of a three-component lifestyle intervention on emotional well-being in women with polycystic ovary syndrome (PCOS): a secondary analysis of a randomized controlled trial," *PLoS One*, vol. 15, no. 6, article e0233876, 2020.
- [19] S. S. Lim, S. K. Hutchison, E. Van Ryswyk, R. J. Norman, H. J. Teede, and L. J. Moran, "Lifestyle changes in women with polycystic ovary syndrome," *Cochrane Database of Systematic Reviews*, vol. 2019, no. 3, article CD007506, 2019.
- [20] H. J. Teede, M. L. Misso, M. F. Costello et al., "Recommendations from the international evidence-based guideline for the assessment and management of polycystic ovary syndrome," *Fertility and Sterility*, vol. 110, no. 3, pp. 364–379, 2018.
- [21] Practice Committee of the American Society for Reproductive Medicine, "Role of metformin for ovulation induction in infertile patients with polycystic ovary syndrome (PCOS): a guideline," *Fertility and Sterility*, vol. 108, no. 3, pp. 426–441, 2017.
- [22] R. A. Al Khalifah, I. D. Florez, B. Dennis, L. Thabane, and E. Bassilious, "Metformin or oral contraceptives for adolescents with polycystic ovarian syndrome: a meta-analysis," *Pediatrics*, vol. 137, no. 5, article e20154089, 2016.
- [23] Y. Han, Y. Li, and B. He, "GLP-1 receptor agonists versus metformin in PCOS: a systematic review and meta-analysis," *Reproductive Biomedicine Online*, vol. 39, no. 2, pp. 332–342, 2019.
- [24] M. Swan, S. Ferguson, A. Chang, E. Larson, and A. Smaldone, "Quality of primary care by advanced practice nurses: a systematic review," *International Journal for Quality in Health Care*, vol. 27, no. 5, pp. 396–404, 2015.
- [25] R. Ma, Y. Zou, W. Wang et al., "Obesity management in polycystic ovary syndrome: disparity in knowledge between obstetrician-gynecologists and reproductive endocrinologists in China," *BMC Endocrine Disorders*, vol. 21, no. 1, p. 182, 2021.

## Research Article

# Novel Curcumin-Encapsulated $\alpha$ -Tocopherol Nanoemulsion System and Its Potential Application for Wound Healing in Diabetic Animals

Muhammad Ali,<sup>1</sup> Nauman Rahim Khan <sup>1,2</sup> Zakia Subhan,<sup>3</sup> Saima Mehmood,<sup>1</sup> Adnan Amin,<sup>4</sup> Imran Rabbani,<sup>2</sup> Fazal-ur -Rehman,<sup>5</sup> Hafiz Muhammad Basit,<sup>6</sup> Haroon Khalid Syed,<sup>7</sup> Ikram Ullah Khan,<sup>7</sup> Muhammad Shuaib Khan,<sup>8</sup> and Sehrish Khattak<sup>9</sup>

<sup>1</sup>Gomal Centre for Skin/Regenerative Medicine and Drug Delivery Research (GCSRDDR), Faculty of Pharmacy, Gomal University, Dera Ismail Khan, 29050 KPK, Pakistan

<sup>2</sup>Department of Pharmacy, Kohat University of Science and Technology, Kohat, 26000 KPK, Pakistan

<sup>3</sup>Kohat Institute of Medical Sciences, Khyber Medical University, Kohat, 26000 KPK, Pakistan

<sup>4</sup>Department of Pharmacognosy/Natural Product Research Lab, Faculty of Pharmacy, Gomal University, Dera Ismail Khan, 29050 KPK, Pakistan

<sup>5</sup>Department of Pharmaceutical Chemistry, Faculty of Pharmacy, Gomal University, Dera Ismail Khan, 29050 KPK, Pakistan

<sup>6</sup>Akhtar Saeed College of Pharmacy, Bahria Golf City, Rawalpindi, Punjab, Pakistan

<sup>7</sup>Department of Pharmaceutics, Faculty of Pharmaceutical Sciences, Government College University, 38000 Faisalabad, Pakistan

<sup>8</sup>Department of Basic Veterinary Sciences, Gomal University, Dera Ismail Khan, 29050 KPK, Pakistan

<sup>9</sup>Department of Microbiology, Kohat University of Science and Technology, Kohat, 26000 KPK, Pakistan

Correspondence should be addressed to Nauman Rahim Khan; [naumanpharma@gmail.com](mailto:naumanpharma@gmail.com)

Received 1 June 2022; Revised 29 August 2022; Accepted 3 September 2022; Published 15 September 2022

Academic Editor: Ahmed AH Abdellatif

Copyright © 2022 Muhammad Ali et al. This is an open access article distributed under the Creative Commons Attribution License, which permits unrestricted use, distribution, and reproduction in any medium, provided the original work is properly cited.

**Objective.** This project was aimed at formulating a novel nanoemulsion system and evaluating it for open incision wound healing in diabetic animals. **Methods.** The nanoemulsions were characterized for droplet size and surface charge, drug content, antioxidant and antimicrobial profiling, and wound healing potential in diabetic animals. The skin samples excised were also analyzed for histology, mechanical strength, and vibrational and thermal analysis. **Results.** The optimized nanoemulsion (CR-NE-II) exhibited droplet size of  $26.76 \pm 0.9$  nm with negative surface charge ( $-10.86 \pm 1.06$  mV), was homogenously dispersed with drug content of  $68.05 \pm 1.2\%$ , released almost  $82.95 \pm 2.2\%$  of the drug within first 2 h of experiment with synergistic antioxidant ( $95 \pm 2.1\%$ ) and synergistic antimicrobial activity against selected bacterial strains in comparison to blank nanoemulsion, and promoted significantly fast percent reepithelization (96.47%). The histological, vibrational, thermal, and strength analysis of selected skin samples depicted a uniform and even distribution of collagen fibers which translated into significant increase in strength of skin samples in comparison to the control group. **Conclusions.** The optimized nanoemulsion system significantly downregulated the oxidative stress, enhanced collagen deposition, and precluded bacterial contamination of wound, thus accelerating the skin tissue regeneration process.

## 1. Introduction

Diabetes is a rapidly progressing health concern associated with adjuvant manifestations including nephropathy, neuropathy, and retinopathy and is also associated with delayed

wound healing, often characterized as a chronic wound with a frustrated and extended healing process [1], where almost 80% of nonhealing diabetic foot ulcers resolve with amputation of the affected body area due to unavailability of satisfactory treatment strategies [2]. Additionally, 80% of

diabetic wounds are prone to more complications due to secondary bacterial infections, which results in significant loss of mobility, functions, and quality of patient's life [3]. The annual cost of diabetic wound treatment is estimated to be 20 billion dollars, which is increasing gradually at an annual growth rate of 4% [4]. Wound healing is a complex and intertwined process consisting of four overlapping phases, including homeostasis, inflammation, proliferation, and remodeling [5]. All four phases further consist of various processes that occur in a systematic and adequate manner [6]. Patients with diabetes typically have impaired wound healing due to vascular dysfunction, high oxidative stress, nerve hypoxia, impaired angiogenesis, defective collagen deposition, and weak immune response [7]. When the integumentary system is compromised, one or more phase of wound healing is likewise impaired. Nonhealing wounds are stagnant in one of these stages, typically the inflammation and proliferation stages [8].

Free radical formation in diabetes by nonenzymatic glycation of proteins, glucose oxidation, and increased lipid peroxidation leads to damage of endogenous antioxidant enzymes and cellular machinery and also increased insulin resistance due to oxidative stress [9]. During the mitochondrial oxidation process, high blood glucose leads to excess glycolysis inside the cells, producing much energy in the mitochondria in the form of ATP, and as a by-product, reactive oxygen species (ROS) are produced. [10], and hence, prolonged exposure to free radicals (ROS) is believed to lead to cellular injury and apoptosis via the destructive oxidation of intracellular proteins, lipids, and nucleic acids [11]. Furthermore, hyperglycemia impairs the normal wound healing process due to prolonged inflammatory phase, and hence persistently, high blood glucose levels attract opportunistic bacteria causing localized bacterial infection and could even lead to septicemia, which further compromises the progress of the inflammatory phase [12].

To date, diabetic wound healing strategies involve the use of oral hypoglycemics and/or injectable insulin to keep blood glycemic conditions in optimal condition and topical and/or oral antimicrobials to prevent bacterial infiltration [13], which not only may lead to an extra financial burden on patients, especially in economically compromised countries, but may also result in reducing patient compliance to multiple drug therapy [14].

Curcumin is the miraculous molecule found in turmeric, which has long been used in spices in Asian countries. Curcumin is reported to possess good antioxidant [15], antimicrobial [16], anti-inflammatory [17], anticancerous [18], antidiabetic [19], anticoagulant [20], antifungal [21], antimutagenic [22], antiviral [23], and wound healing properties [24]. Curcumin has also been widely investigated to promote the skin tissue regeneration process and formulated in the form of gels [25], nanoparticles [26], emulsions [27], nanofibers [28], hydrogel [29], and liposomes [30], where it has been reported to significantly enhance tissue remodeling, tissue granulation, and collagen deposition [31]. Vitamin E is a fat-soluble vitamin and is a mixture of  $\alpha$ -tocopherol and  $\gamma$ -tocotrienol, where the former being the most abundant form and has been utilized for its antioxidant activity

[32] antibacterial activity [33], anti-inflammatory activity [34], and scar management [35] properties. Vitamin E is a potent chain-breaking antioxidant and helps protect the cells from the oxidative damage elicited by free radicals produced inside the cells in response to the metabolic process taking place inside the cell [36].

The delayed wound healing in people with diabetes makes it imperative to develop a treatment strategy with the inherent ability to reduce the oxidative stress by scavenging the free radicals but also inhibit the microbial growth by exerting antimicrobial activity, with efficient local hypoglycemic effect having the ability to improve the neovascularization (angiogenesis) at the wound site. This study proposes to develop a novel curcumin and vitamin E nanoemulsion system to improve the aqueous solubility, stability, and therapeutic efficacy of curcumin, having synergistic antioxidant, antimicrobial, and hypoglycemic effect and efficient wound healing ability in diabetic animals.

## 2. Materials and Methods

**2.1. Materials.** Curcumin 95% purity was purchased from Ceres Biotech Ltd., Zhejiang, China; tween-80 was graciously supplied by BioLabs Islamabad Pakistan. Polyethylene glycol (PEG-400),  $\alpha$ -tocopherol acetate, ethanol, methanol, and acetonitrile (Sigma-Aldrich, USA) were purchased. The selected bacterial strains for antimicrobial assay were graciously provided by the Natural Product Research Laboratory, Faculty of Pharmacy, Gomal University, Pakistan (*Staphylococcus aureus* (ATCC # 33862) and *Pseudomonas aeruginosa* (ATCC # 15442)). All chemicals were used without any further purification.

**2.2. Preparation of Curcumin Nanoemulsions (CR-NE).** The CR-NE was prepared using a high-speed homogenization technique. Briefly, appropriate amount of curcumin was pre-dissolved in PEG-400 under continuous magnetic stirring followed by the addition of tween-80 and thoroughly mixed/dissolved. The mixture was then preceded by the addition of  $\alpha$ -tocopherol in small increments till complete mixing. The water phase preheated at  $45 \pm 2^\circ\text{C}$  was added slowly dropwise to the oil phase under continuous magnetic stirring for one hour, followed by homogenization using a high-speed homogenizer (ULTRA-TURRAX, D7813, Germany) at 10,000 rpm for 2 min. The quantities of different ingredients are varied for optimization [37]. The formulations are given in Table 1.

**2.3. Droplet Size, Surface Charge, and Polydispersity Index.** The particle size, particle size distribution, and surface charge of the samples were determined using dynamic light scattering utilizing the Zetasizer Nano ZS 90 (Malvern Instruments; Worcestershire, UK), equipped with software (version 6.34) and a He-Ne laser preset at a wavelength of 635 nm and static scattering angle of 90 degrees. Briefly, 10  $\mu\text{l}$  of the sample was mixed with 1 ml of deionized water and vortexed for 2 minutes, followed by analysis with a Zetasizer. Each result displayed was measured in triplicate, and the results were averaged [38, 39].

TABLE 1: Curcumin nanoemulsion formulations.

Formulations	Tween-80 (g/g)	PEG-400 (g/g)	Vitamin E (g/g)	Curcumin (g/g)	Water (g/g)
BN-NE	12 g	12 g	3 g	0	73 g
CR-NE-I	12 g	12 g	3 g	0.3 g	72.7 g
CR-NE-II	10 g	14 g	3 g	0.3 g	72.7 g
CR-NE-III	6 g	18 g	3 g	0.3 g	72.7 g

**2.4. Drug Content.** The drug content of nanoemulsions was estimated by adopting the already reported method [40], where 1 ml of nanoemulsion was diluted with 9 ml of absolute ethanol followed by centrifugation (Scilogex, USA) of the mixture at 5000 rpm for 1 min to ensure extraction of curcumin. The samples were filtered through a 0.45  $\mu\text{m}$  nylon membrane syringe filter (Merck Millipore, USA) and analyzed on UHPLC. The curcumin content in the nanoemulsion was measured using high-performance liquid chromatography (Perkin Elmer UHPLC, Shelton, CT, USA) with a column C-18 (Supelco, USA). The analyses were carried out under isocratic conditions, using a mobile phase consisting of acetonitrile and 0.2% acetic acid (80:20 v/v) at a flow rate of 1.0 ml/min. Ten microliters of the sample was injected into the system, and curcumin content was determined using a Flexar FX UV/VIS Detector at a wavelength of 425 nm. The limit of detection, quantification, percent precision, and percent accuracy were calculated accordingly.

**2.5. Antioxidant Assay.** Free radical scavenging activity of optimized nanoemulsion system with and without curcumin was evaluated using 2,2-diphenyl-1-picrylhydrazyl (DPPH) assay using quercetin served as a standard. Compounds with antioxidant activity can reduce the DPPH by donating hydrogen and changing the color from deep violet to light yellow. In this assay, a freshly prepared solution of DPPH (50  $\mu\text{l}$ ; 0.1 mM) was added to 50  $\mu\text{l}$  of the test (varying concentrations), followed by incubation in a dark cabinet. After 30 minutes, the absorbance of the sample was measured at 517 nm. The percent inhibition was calculated as

$$\text{Percent inhibition (\%)} = \frac{1 - \text{sample absorbance}}{\text{standard absorbance}} \times 100. \quad (1)$$

For all tested concentrations, graphs were plotted between percent inhibition versus concentration used [41].

**2.6. Antimicrobial Assay.** The antibacterial activity of the optimized nanoemulsion system with and without curcumin was determined against pathogenic bacteria using minimum inhibitory concentration (MIC) according to the microdilution method described by Shao et al. [42] with slight modifications. First, an aliquot (50  $\mu\text{l}$ ) of two-fold serially diluted nanoemulsion was prepared with distilled water in a 96-microwell plate. Then, the bacteria were inoculated with nutrient broth (50  $\mu\text{l}$ ) in all wells to get the final concentration from 1.5 mg/ml to 0.02 mg/ml and then sealed to avoid the evaporation loss. After 24 h incubation at 37°C, resazurin sodium salt (40  $\mu\text{l}$ ) was added to all wells and subsequently incubated at 37°C for two hours. The color

change was visually observed to evaluate the bacterial growth. MIC was the lowest concentration of curcumin-loaded nanoemulsion, having a full inhibitory effect on the bacterial growth.

**2.7. In Vitro Drug Release.** Franz diffusion cell (Perme Gear, Inc. Model no: 4G-01-00-15-12, diffusion area = 53 cm<sup>2</sup>) was used for the drug release experiment. The receiving compartment of the Franz diffusion cell was filled with 6.4 ml bubble-free phosphate-buffered saline pH 7.4 to mimic wound bed conditions [43] and maintained at 37  $\pm$  0.5°C by continuous flow of thermostatic water through its jackets which was continuously magnetically stirred at 400 rpm. A Tuffryn® membrane (0.2  $\mu\text{m}$  pore size, Sartorius Germany) was affixed as a barrier between Franz diffusion cell's donor and receiving compartment. A total of 1 ml of the optimized nanoemulsion was loaded into the donor compartment. Sample aliquots of 1 ml were withdrawn at regular time intervals of 0, 0.5, 1, 2, 4, 8, 12, 16, 18, 20, and 24 h, where fresh buffer in a volume equal to volume withdrawn was replaced at each sampling interval to maintain sink conditions. The samples withdrawn were filtered through a 0.45  $\mu\text{m}$  membrane filter before analysis on HPLC for drug released estimation. The experiment was conducted in triplicate, and the results were averaged.

Where applicable, the mechanism of drug release was investigated by fitting the drug release data into Weibull function as expressed by

$$F = 1 - \exp(-at^b), \quad (2)$$

where  $F$  is the drug fraction released at time  $t$  and  $a$  and  $b$  are constants.  $b$ , as a shape parameter, is characterized as exponential ( $b = 1$ ), sigmoidal ( $b > 1$ ), or parabolic ( $b < 1$ ).

### 3. Animal Study

**3.1. Diabetes Induction, Wound Infliction, and Wound Contraction Analysis.** Healthy male, Sprague-Dawley rats, aged three months and weighing 200 to 250 g, are acclimatized for seven days in individual housing under 12 h light/dark cycle with deionized water and standard pelletized food given *ad libitum* under ambient conditions. Before diabetes induction, all animals were kept on fasting for 24 h with free access to water, and their fasting blood glucose level was measured using a glucometer (Code-free, SD Biosensor, Korea) followed by diabetes induction by chemical method; viz., a single intraperitoneal injection of streptozotocin (50 mg/kg) freshly prepared in normal saline was used for the purpose [44–46]. All animals were then allowed to be

fed on 5% glucose solution filled into water bottles, and their blood glucose levels were monitored for 72 h. Those animals having fasting blood glucose levels  $\geq 10$  mmol/l were declared diabetic [44]. All diabetic animals were then randomly divided into two groups with  $n = 8$  per group. One group was assigned to the control group and another to the experimental group. All animals were then anaesthetized by a single intramuscular injection of ketamine (100 mg/kg) and xylazine mixture (10 mg/kg), and their dorsal region hairs were carefully shaved using sharp blades. The area for wound infliction was marked, and full-thickness open incision wound was inflicted using surgical scissors. The control group only received standard gauze application, while the experimental group received optimized nanoemulsion application on a daily basis till complete wound closure. All animal experimentation was conducted following the institutional ethics regulations adapting the international guidelines (OECD Environment, Health and Safety). The study protocol was approved by the institutional Ethical Review Board vide reference no. 502/QEC/GU, dated 29/03/2019, Gomal University Pakistan.

The surface morphology of the wound was regularly monitored and recorded. The wounds were photographed with a digital camera (Samsung ST65-China) on days 0, 3, 7, 10, 14, and 21 from a fixed distance to assess the progress of wound closure, while the animals were under anesthesia. The photographs were analyzed by using ImageJ software. Percentage reepithelization that represents the percentage of wound reduction from the wound size at day 0 was calculated using the following relation.

$$\text{Percent reepithelization} = \frac{(\text{wound size at time } 0) - (\text{wound size at time } t)}{\text{wound size at time } 0} \times 100. \quad (3)$$

**3.2. In Vivo Microbial Contamination Test.** For spontaneous microbial assay, Muhammad's procedure was used with slight modification [45]. Briefly, the nutrient agar plates were prepared by dissolving 2.5 g of nutrient agar in 100 ml of distilled water and autoclaved. Then, at days 3, 7, 14, and 21, the microbial growth test was performed by swabbing the wound with a sterile swab and inoculating it on the Petri dishes containing presterilized media and incubated overnight at 37°C in an incubator for 24 h. Following incubation, all Petri dishes were visually inspected for the propensity of microbial colonies formation and compared for the purpose of microbial growth inhibition by the optimized formulation.

**3.3. Skin Histology.** Animals were sacrificed by cervical dislocation, and the newly regenerated skin tissue containing the wound was excised on day 14 and subjected to histological studies. Briefly, the skin tissues were fixed in 10% formalin aqueous solution for three days at room temperature. After that, the skin tissues were trimmed, washed, and dehydrated in ethanol, followed by cleansing using xylene and finally embedded in paraffin wax. About 5  $\mu\text{m}$  thick sections of the skins were sectioned by microtome (HM-340E, Microm Inc. USA) and stained with hematoxylin and eosin

(H&E stain) as well as Masson's trichrome stain [7, 46]. The slides were then photographed using an inverted microscope fitted with a camera (Optika Microscope B-383FL, Italy), and photographs were analyzed for inflammation and collagen deposition.

**3.4. ATR-FTIR.** The dermis layer of the skin extracted from the control group and curcumin nanoemulsion- (CR-NE-II-) treated group were characterized at a resolution of 16  $\text{cm}^{-1}$  over a wavenumber region of 400 to 4000  $\text{cm}^{-1}$  with an acquisition time of 2 min using an attenuated total reflectance-Fourier transform infrared spectroscopy (ATR-FTIR) (UATR TWO, Perkin Elmer, UK). The FTIR spectra of the dermis layer of different animal group skin samples were compared with each other to evaluate the extent of collagen deposition. The dermal amide-I (1640 to 1635  $\text{cm}^{-1}$ ) and amide-II (1557 to 1554  $\text{cm}^{-1}$ ) absorbance bands usually originate from the proteins of the dermal layer, and hence, the absorbance ratio of treated and untreated animal groups was used as a novel tool to estimate the collagen and/or protein deposition in the skin samples. At least triplicates were carried out for each sample, and the results were averaged.

**3.5. Tensiometry.** The excised skin samples were also subjected to tensile strength analysis using a texture analyzer (Testometric M-500, UK). Briefly, skin samples in specific dimensions (35 mm length and 53 mm width) were excised from animals of each group and fixed between the upper and lower jaw of the tensiometer. The test and withdrawal speeds were fixed at 5 and 10 mm/s, respectively. The sample were uniaxially pulled with a 30 kg load. Each sample's maximum stress force, stress peak, stress yield, and young modulus were recorded [47]. Each sample was analyzed in triplicate, and the results were averaged.

**3.6. Thermal Analysis.** Thermal analysis of skin samples was performed on differential scanning calorimetry (DSC) (Perkin Elmer, USA) to estimate changes in transition temperature and enthalpy as a function of different treatments applied. For this purpose, an accurately weighed 3 mg of the skin sample was crimped in a standard aluminium pan and subjected to thermal analysis in the temperature range of 30 to 180°C at a heating rate of 10°C/min under constant purging of nitrogen at 40 ml/min. In addition, the transition temperature ( $\Delta T$ ) and enthalpy ( $\Delta H$ ) of each sample were recorded. Each sample was run three times, and the results were averaged.

## 4. Statistical Analysis

All values are expressed as a mean of three experiments with respective standard deviations. Student's *t*-test and analysis of variance (one-way ANOVA) followed by post hoc analysis by Tukey HSD were used with a level of significance set at  $p < 0.05$ .

## 5. Results and Discussion

**5.1. Droplet Size, Surface Charge, and Polydispersity Analysis.** The droplet's size in nanoemulsion directly depends upon

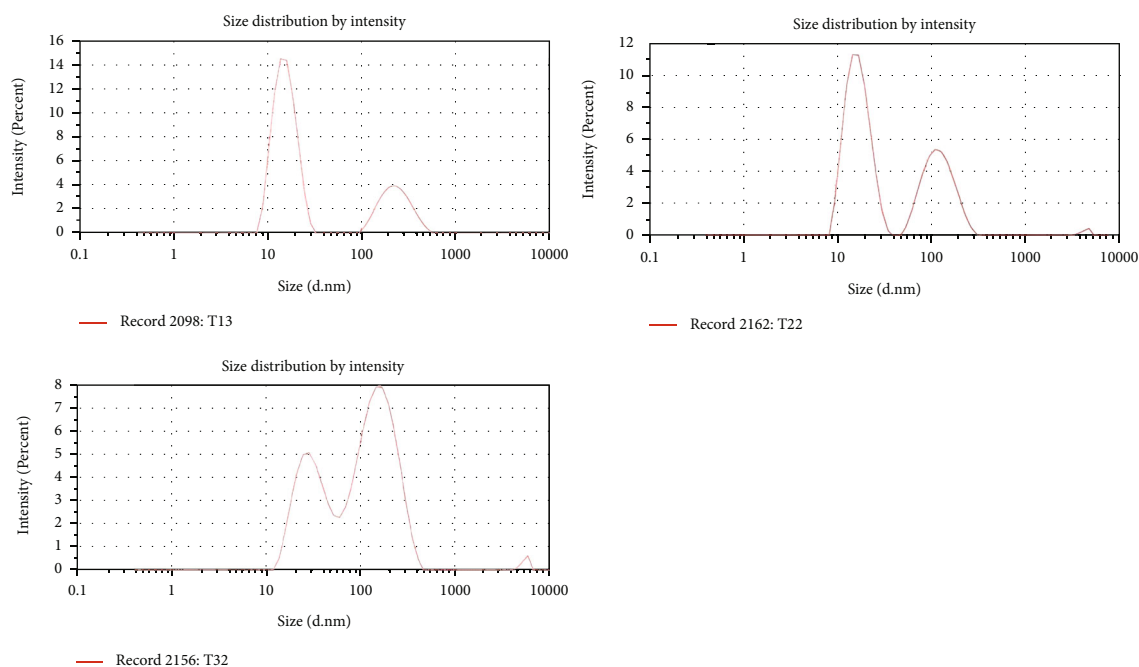


FIGURE 1: Droplet size and polydispersity index of CR-NE-I, CR-NE-II, and CR-NE-III.

TABLE 2: Droplet size, surface charge, and polydispersibility index of CR-NE formulations.

Formulation	Average droplet size (nm)	Polydispersity index (PDI)	Surface charge ( $\zeta$ ) (mv)
CR-NE-I	$19.66 \pm 0.3$	$0.407 \pm 0.02$	$-0.034 \pm 1.85$
CR-NE-II	$26.76 \pm 0.9$	$0.456 \pm 0.04$	$-10.86 \pm 1.06$
CR-NE-III	$63.7 \pm 1.9$	$0.508 \pm 0.002$	$-0.831 \pm 1.43$

the speed of homogenization [48] and the concentration of surfactant [49]. CR-NE had droplet size less than 100 nm due to high shear force applied during homogenization and optimum concentration of surfactant and cosurfactant, which is translated in effectively reducing the interfacial tension between oil and water and also forms a film at the interface between the two immiscible phases to prevent them from recoalescence [50]. In our case, all the formulations showed their droplet size in nanorange Figure 1, which were found to be in the range of 20 to 65 nm, as shown in Table 2. The Pearson correlation analysis depicted that concentration of surfactant (tween-80) is negatively correlated to the size of the droplet ( $R = -0.98$ ,  $p = 0.03$ ) while positively correlated to the surface charge ( $R = 0.11$ ,  $p = 0.45$ ). At the same time, cosurfactant has opposite effect which is positively correlated to the droplet size ( $R = 0.765$ ,  $p = 0.01$ ) but negatively correlated to the surface charge ( $R = -0.97$ ,  $p = 0.15$ ). All the formulations showed a PDI value of less than 1, reflecting uniform size distribution in the formulations [51]. The surface charge of all the formulations was in the range of  $-0.034$  mV to  $-10$  mV, with the latter found for the optimized formulation (CR-NE-II), as shown in Figure 2. The same results is reported by Ahmad et al., who designed a curcumin-loaded nanoemulsion using clove oil as a lipid phase to evaluate its wound repairing and anti-inflammatory

activity. The optimized formulation (Cur-NE) exhibited particle diameter  $93.64 \pm 6.48$  nm and  $PDI = 0.263 \pm 0.021$ , and surface charge was  $-11.67 \pm 0.11$  mV. Nanoemulsions are having a small particle size rendering increased surface area which further leads to enhance the release, transfer, and absorption of drugs. Thus, globular size and size distribution and zeta potential are considered as essential parameters for the formulation stability and efficacy [52]. The Pearson correlation analysis revealed that the surface charge is positively related ( $R = 0.99$ ) to concentration of surfactants and cosurfactants and indirect but weak relationship ( $R = 0.76$ ) to concentration of oil phase in the nanoemulsion system. The results are depicted in Table 2.

**5.2. Drug Content.** The drug content of all formulations is given in Table 3. The estimated drug content of all formulations was in the range of 62 and 68%, respectively, dependent on the concentration of surfactant and cosurfactant added. The high variation in the drug content could be attributed to the photodegradation of the drug during the preparatory stage. Curcumin is a highly photosensitive drug, and its efficient encapsulation reduces its chances of degradation [53]. The optimized formulation, i.e., CR-NE-II, contained the surfactant and cosurfactant in the concentration of 10 g and 14 g, respectively. This combination might have

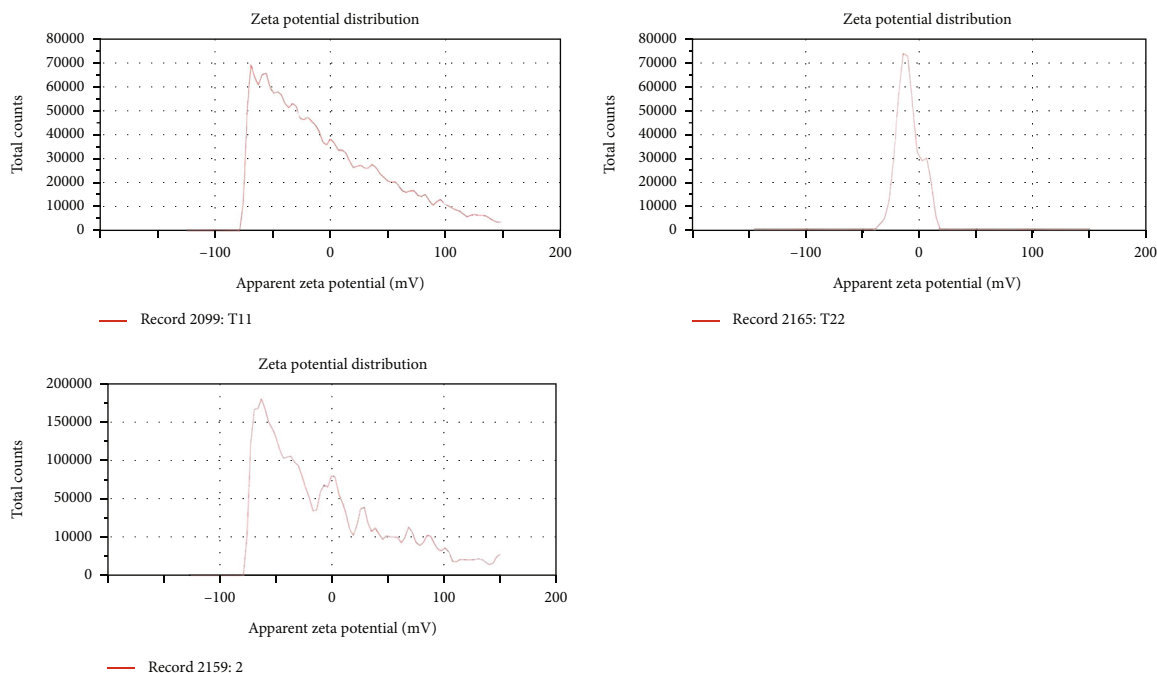


FIGURE 2: Zeta potential of CR-NE-I, CR-NE-II, and CR-NE-III.

TABLE 3: Drug content of curcumin nanoemulsion (CR-NE) formulations.

Formulation	Drug content (%)	Weight percentage
CR-NE-I	$62.85 \pm 1.1$	0.129
CR-NE-II	$68.05 \pm 1.2$	0.204
CR-NE-III	$65.42 \pm 0.9$	0.138

formed a droplet enclosing the maximal drug inside the emulsion droplet with additional protection offered by the surfactant layer, which not only help encapsulate the maximal drug inside the core by maximally solubilizing the drug in the oil phase but also protect the drug from photolytic and chemical degradation [54]. The reason for low drug content in other formulations was unknown and not investigated. The limit of detection, limit of quantification, percent precision, and percent accuracy were calculated and found to be  $0.28 \mu\text{g/ml}$ ,  $0.45 \mu\text{g/ml}$ , 1.52%, and 98%, respectively.

**5.3. Antioxidant Activity.** The antioxidant activity of curcumin-loaded and blank nanoemulsion was investigated through a DPPH assay. The blank nanoemulsion, despite containing  $\alpha$ -tocopherol, showed a weak antioxidant profile compared to curcumin-loaded nanoemulsion, where a synergistic antioxidant activity was observed. The percentage inhibition for blank nanoemulsion was found to be  $50 \pm 4.5\%$  in comparison to CR-NE-II nanoemulsion, where the percentage inhibition was found to be  $95 \pm 2.1\%$  which was found to be significantly high (Student's  $t$ -test,  $p < 0.05$ , Figure 3) at a concentration of  $0.5 \text{ mg/ml}$  where a dose-dependent antioxidant activity was observed. The antioxidant activity of curcumin is attributed to its unique conjugated structure, which shows typical radical-

trapping ability as a chain-breaking antioxidant [55]. Numerous studies reported enhanced antioxidant properties of the curcumin encapsulated in colloidal system such as liposomes [56], polymeric microparticles [57], hydrogel beads [58], nanoparticles [59], and microemulsions [60]. Curcumin containing microemulsion and microemulsion gel was developed with grape seed oil as a lipid phase, where the synergistic antioxidant activity of the optimized microemulsion and gel microemulsions was observed due to the presence of grape seed oil which helped effectively encapsulate and preserve the antioxidant stability of curcumin [61].

The  $\alpha$ -tocopherol is also a potent lipophilic antioxidant and prevents lipid peroxidation by protonation of fatty acid radicals and hence forms stable phenolic free radicals through its chromane ring [57]. Diabetic wounds are flooded by the high production of reactive oxygen species (ROS) [58], which not only prolong the average healing time but also contribute to local tissue necrosis [59]. The synergistic antioxidant of curcumin and  $\alpha$ -tocopherol is thus envisaged to exert a local antioxidant effect upon application to diabetic wounds hence contributing to the rapid skin tissue regeneration process.

**5.4. Antibacterial Activity.** The antibacterial activity of curcumin-loaded and blank nanoemulsion was assessed against selected bacterial strains, i.e., *Staphylococcus aureus* (ATCC # 33862) and *Pseudomonas aeruginosa* (ATCC # 15442). The minimum inhibitory concentrations (MIC) of CR-NE-II nanoemulsion and blank nanoemulsion are depicted in Table 4. The MIC for CR-NE-II was  $93 \mu\text{g/ml}$  against *Staphylococcus aureus* while  $187.5 \mu\text{g/ml}$  against *Pseudomonas aeruginosa*, while the blank nanoemulsion did not exert any antibacterial activity at all. Curcumin is a robust antimicrobial agent that interferes with the bacteria's



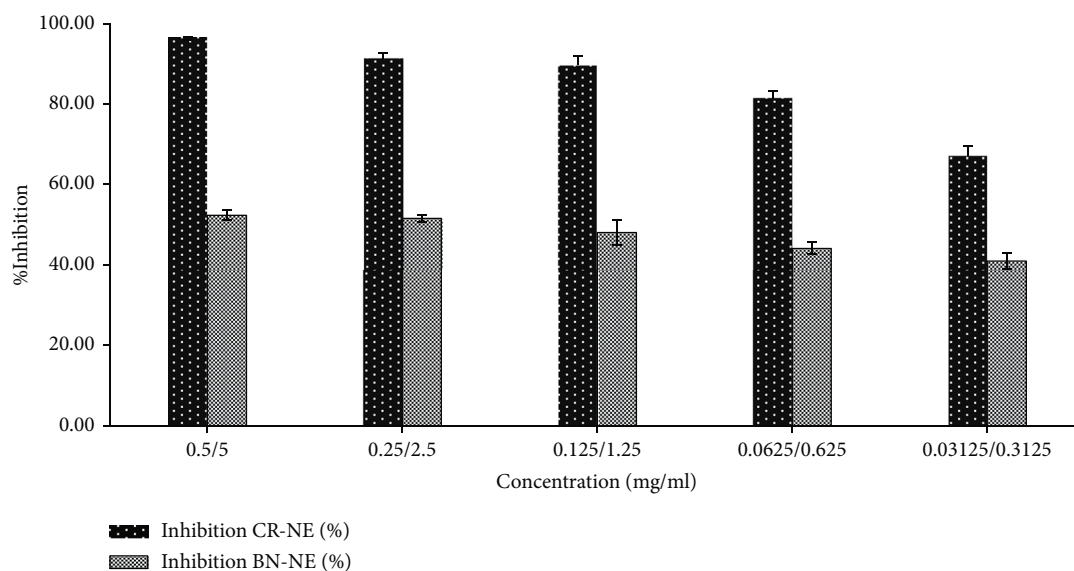


FIGURE 3: Antioxidant activity of nanoemulsion with and without incorporating curcumin.

TABLE 4: MIC of nanoemulsion with and without curcumin against *Pseudomonas aeruginosa* and *Staphylococcus aureus*.

Formulation code	MIC ( $\mu\text{g/ml}$ )	Microbial species
CR-NE-II	187.5	<i>Pseudomonas aeruginosa</i>
CR-NE-II	93	<i>Staphylococcus aureus</i>
BN-NE	Not active (at highest tested 1.5 mg/ml)	Not active against both species

CR-NE = curcumin nanoemulsion, BN-NE = blank nanoemulsion.

cell membrane and exerts a bactericidal activity [60]. The curcumin encapsulated in the oil phase droplet exerted antibacterial activity by its potential to effectively penetrate the bacterial cell wall, resulting in lysis of peptidoglycan layer, translating into a distortion of the bacterial cell and bacterial cell lysis [61].

In a study, curcumin and quercetin were combined in a 3 different ratio in order to test their antimicrobial, antioxidant, and wound healing activities. The results showed the synergism of the quercetin and curcuminoid combination to inhibit the growth of *S. aureus* and *P. aeruginosa*. The selected mixture containing the ratio 3:1 was the optimized formulation in terms of wound healing activity because of its inherent antibacterial, antioxidant, and cell migration-enhancing activities [62]. The exertion of local antimicrobial activity at the wound site by the topical antimicrobial application is considered detrimental to promoting skin tissue regeneration and preventing secondary bacterial infection [63]. Thus, curcumin-loaded  $\alpha$ -tocopherol nanoemulsion is envisaged to exert local antibacterial action and prevent opportunistic bacteria from infiltrating the wound.

**5.5. In Vitro Drug Release.** The *in vitro* drug release from CR-NE-II nanoemulsion using Tuffryn® membrane as a barrier is shown in Figure 4(a). The nanoemulsion released

82.95% of the drug in the first two hours of the experiment and was then maintained till the end of the experiment. Curcumin is a hydrophobic drug, and its solubility in an aqueous medium can be enhanced by formulating it into a nanoemulsion system [62]. The hydrophilicity of curcumin can further be increased if it is formulated into an o/w nanoemulsion where the surfactants and cosurfactants not only help stabilization of nanoemulsion but also enhance the wettability of hydrophobic materials by getting deposited on the surface of the drug particles hence facilitating water penetration into the particle core [64]. Furthermore, the nanodroplet size of the nanoemulsion increases the total surface area where the size range of 10 to 100 nm is stated to be a dynamic microstructure enhancing the better drug solubilization and rapid diffusion into the aqueous medium [65]. The increased surface area results in a higher interfacial area required for the dissolution of hydrophobic drugs formulated into a nanoemulsion system [66, 67]. The *in vitro* drug release data was fitted into Weibull kinetic model, where the  $b$  value obtained was found to be less than 1 ( $b = 0.647$ ,  $r^2 = 0.9866$ , Figure 4(b)), which depicted that there was quick dissolution that resulted in the burst release of the drug from nanoemulsion system. Moreover, a steeper concentration gradient facilitated the process of drug diffusion and release [68].

**5.6. Wound Contraction Analysis.** The photographs of the wound healing period of the control and experimental (CR-NE-II) groups taken on days 0, 3, 7, 10, 14, and 21 are shown in Figure 5(a). The percent wound size significantly and fastly reduces and translated into significantly high percent reepithelization (Figure 5(b)) in the case of the CR-NE-II group in comparison to the control group (Student's  $t$ -test,  $p < 0.05$ ). The percent reepithelization calculated on day 14 was found to be 96.47% in comparison to the control group (60.89%). The time required for complete wound closure and droppage of wound scab in the CR-NE-II group was 18 days,

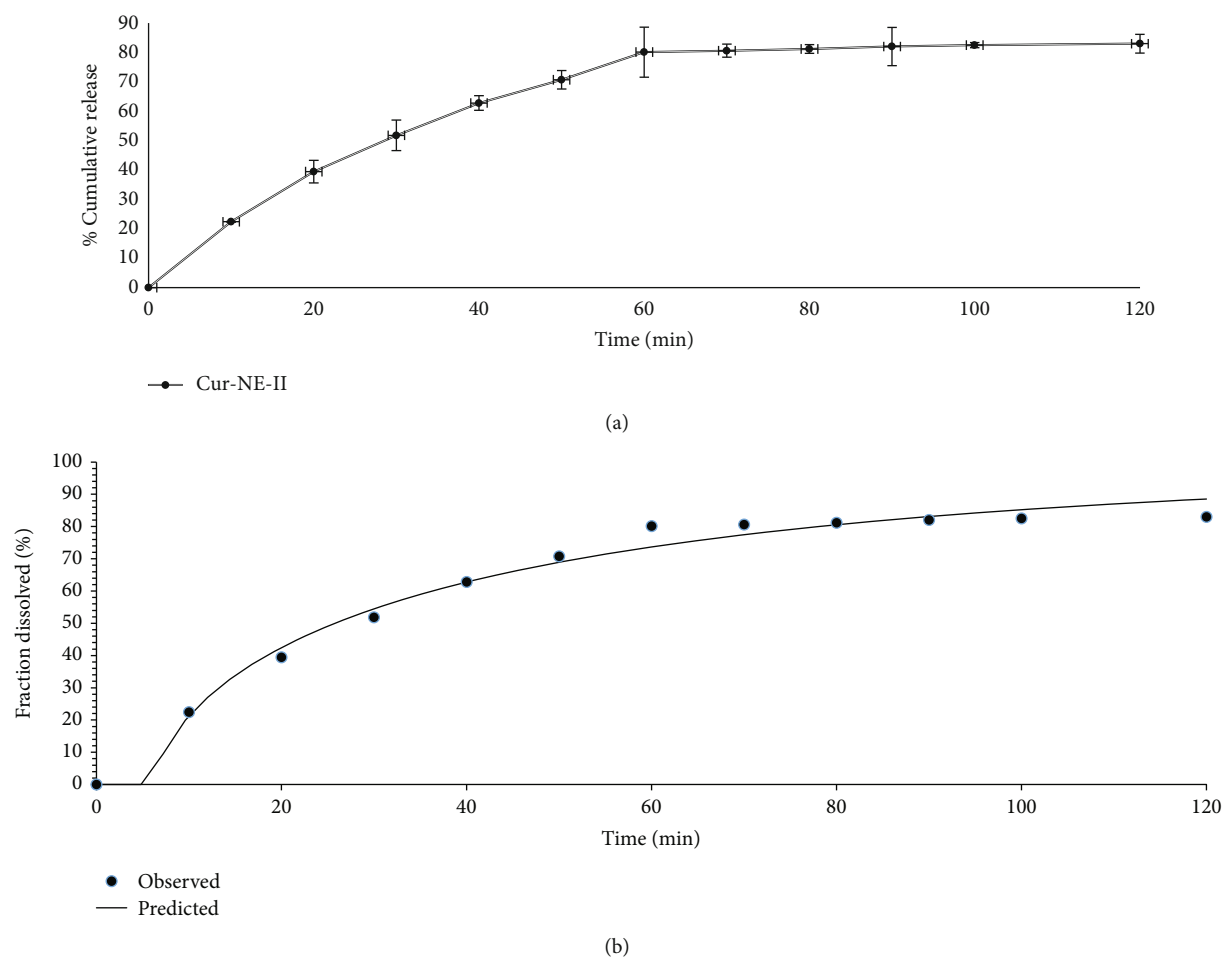


FIGURE 4: (a) *In vitro* release of curcumin. (b) Weibull kinetics model for drug release mechanism.

while the same was found to be 26 days in the control group. The CR-NE-II application onto the wound is envisaged to hasten the skin regeneration by exerting local antioxidant, antimicrobial, and hypoglycemic effects.

These results were also reported in previous studies. A curcumin-loaded self-emulsifying drug delivery system was fabricated for treating wound in diabetic animals. The *in vivo* results depicted that the curcumin-loaded SEDDS group had significantly early wound closure with higher degree of reepithelialization compared with the control and pure curcumin-treated groups [69]. In another study, curcumin nanoparticles and  $\alpha$ -lactalbumin were used in combination for the treatment of diabetic wound infected with resistant microbial species like methicillin-resistant *Staphylococcus aureus* MRSA which significantly proved better topical treatment option for chronic wounds [70]. Furthermore, Bulbake et al. evaluated wound healing properties of curcumin incorporated composite graft of gelatin/PLGA microparticles using diabetic wound model. *In vivo* wound healing studies revealed that composite graft (Gel-Cur-cPMS) shows rapid wound contraction as compared to the Gel-Cur and control groups [71]. On the other hand, the  $\alpha$ -tocopherol is also involved in the wound healing process by remodeling and prevention of hypertrophic scarring [35] and through activation of the expression of CTGF [72]. Thus, curcumin and vitamin

E are envisaged to hasten the skin regeneration process by exerting synergistic antioxidant and anti-inflammatory effects locally in diabetic animal models.

**5.7. *In Vivo* Microbial Contamination Test.** To assess the microbial contamination propensity during the course of the wound healing process, sterile cotton swabs were gently rubbed into the wound and cultured on presterilized nutrient agar plates on day 3, day 7, day 14, and day 21 to assess the antimicrobial effect of CR-NE-II in comparison to the control group (supplementary Figure S1). The control group exhibited a higher number of microbial colonies formation than the CR-NE-II group. The CR-NE-II group also prevented significant microbial infiltration until days 3 and 7, while no microbial growth was seen in the wounds of diabetic animals that received nanoemulsion application. The increased antibacterial activity of CR-NE-II nanoemulsion can be attributed to the better interaction with the bacterial cell wall resulting in increased contact time and enhanced drug transport inside the bacteria [73]. Diabetic wounds are often complicated by secondary bacterial infection [66]. Therefore, the wound healing plate form with the ability to promote skin tissue regeneration but not allowing opportunistic bacteria to infiltrate and grow in the wound bed is detrimental to hastening wound healing in diabetics.

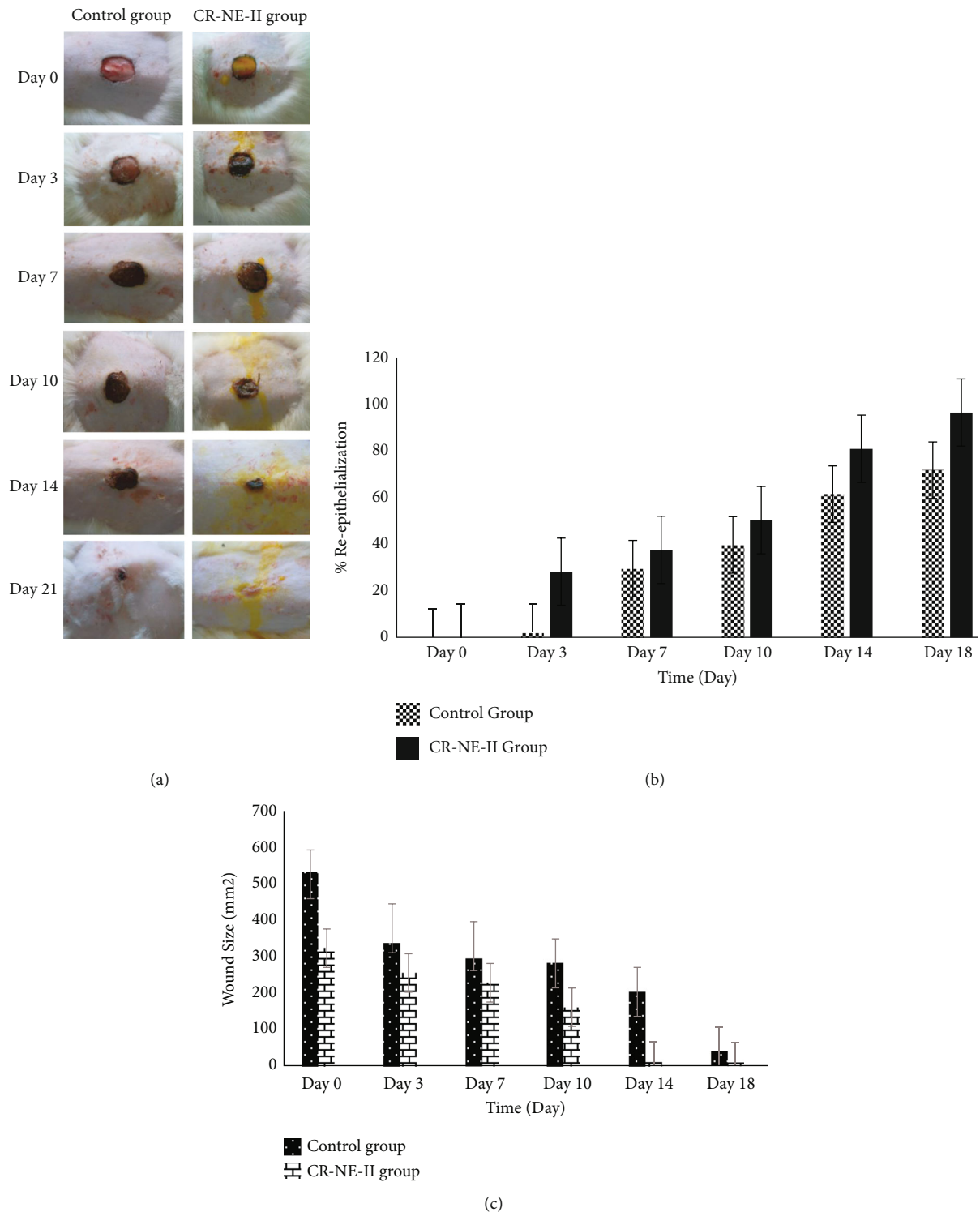


FIGURE 5: (a) Macroscopic wound images of diabetic rats with untreated and CR-NE-II-treated group. (b) Percent reepithelization. (c) Profile of wound size reduction.

**5.8. Skin Histology.** Hematoxylin and eosin staining was performed on day 14 on skin samples excised from various animal groups (Figure 6) to evaluate the structural integrity of the stratum corneum (neopeidermis) inflammatory cell infiltration, blood vessel proliferation, and tissue granulation formation [74]. The control diabetic group sample showed

slow migration of epithelial cells over the dermis layer due to a high concentration of inflammatory cells infiltration leading to dekeratinization (Figure 6(a)).

The CR-NE-II animal group showed complete reepithelization due to rapid migration of epithelial cells from the basement membrane to uppermost layer and hence facilitated

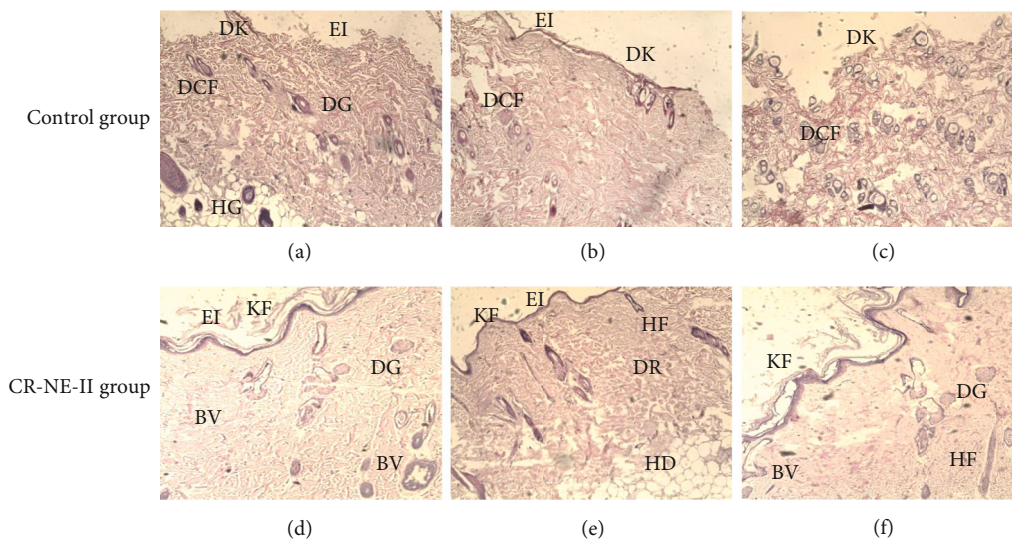


FIGURE 6: Hematoxylin and eosin staining 14-day diabetic wounded tissues of control group and CR-NE-II-treated group. KF: keratin formation; DK: dekeratinization; EI: epidermal integrity; DR: dermis; HD: hypodermis; DCF: degeneration of connective tissue fibers; DG: dermal gland; BV: blood vessels; HF: hair follicles.

the healing process by faster wound closure and rapid scar formation. The epidermis was fully grown, stratified squamous epithelium was shown in different layers of squamous cells, round cells at the bottom, and more flattened cells at the base of the epithelium (Figures 6(d) and 6(d)). The connective tissue fibers were properly arranged with many newly grown connective tissues, as evident in entire dermal tissue in fiber bundles. The dermal glands were fully grown and surrounded by different connective tissue fibers. The attachment of these fibers with the attached base of the dermal gland showed good healing characteristics, as the new fibers formed in the tissue showed proper healing properties (Figure 6(f)). A significant difference was observed in the histological architecture of all skin layers in the nanoemulsion group and control group. The curcumin nanoemulsion formulated with vitamin E exerted significant anti-inflammatory activity in diabetic wound application due to its proangiogenic nature [75]. These progressive changes appeared in the skin epidermal and dermal architecture include keratinization formation and migration of epithelial cells to regenerate stratum corneum, followed by higher reepithelialization. The early and increased migration of fibroblasts and inflammatory cells towards the site of injury in diabetic animals translates into suppression of inflammatory mediators, resulting in the fast generation of lost matrix and its deposition, and reduction in the inflammatory response in later stages helps tissue regain rapid maturation [76].

The collagen fiber deposition results are shown in Figure 7. The histological analysis revealed that the CR-NE-II group (Figures 7(d)–7(f)) resulted in an abundant number of newly formed collagen fibers evenly distributed throughout the skin structure, especially around the dermal gland region and surrounding the hair follicles. Faster and even collagen matrix formation and deposition with smooth, elastic, well-aligned, and dense collagen fibers were observed in the CR-NE-II group, while the control group exhibited

poor collagen deposition (Figures 7(a)–7(c)). Curcumin has been reported to enhance collagen matrix deposition by enhancing fibroblast proliferation and modulating the granulation tissue formation, which facilitates the production of extracellular matrix at the wound site [77]. Similarly, moisture retention on the wound site facilitates rapid regeneration of skin tissue [78]. This was why the CR-NE-II nanoemulsion application resulted in the formation of more evenly distributed collagen fibers throughout the skin microstructure compared to the control animal group.

**5.9. Skin Vibrational Spectroscopic Analysis.** The skin samples excised on day 14 were also subjected to vibrational spectroscopic analysis to elucidate the changes incurred in the skin microstructure through protein propensity during the healing process elicited by various treatments. The results are shown in Figure 8. For the purpose, the dermis layer of the skin was analyzed on ATR-FTIR, and various corresponding bands were recorded with emphasis on absorbance for OH/NH ( $3326$  to  $3295\text{ cm}^{-1}$ ) and amide-I ( $1642$  to  $1638\text{ cm}^{-1}$ ) and amide-II ( $1555.03$  to  $1555.42\text{ cm}^{-1}$ ) which are signature bands originating from peptide linkages of the collagen [79]. The absorbance ratios of these regions in using control skin samples as a standard were used as a novel approach to elucidate protein deposition in the skin sample-treated group. The absorbance ratio of the CR-NE-II-treated group to the control group was found to be  $0.96 \pm 0.01$  for OH/NH region while  $1.46 \pm 0.4$  for amide-I and amide-II, which were significantly high (Student's *t*-test,  $p < 0.05$ ) in comparison to the control group.

Spectral bands in vibrational spectra are molecule specific and provide direct information about the biochemical composition. FTIR peaks are relatively narrow and, in many cases, can be associated with the vibration of a particular chemical bond (or a single functional group) in the molecule [80]. In ATR-FTIR, absorbance is related to the concentration of a

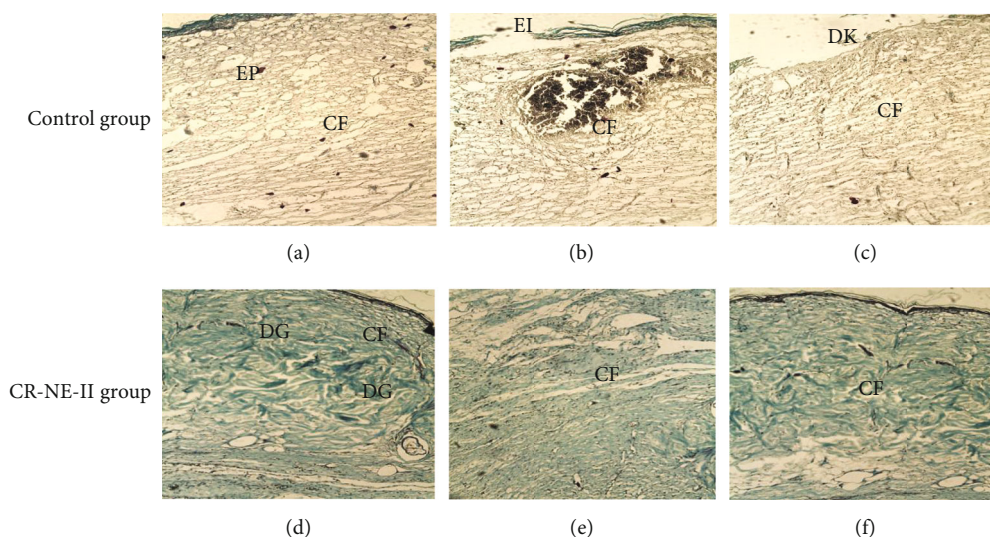


FIGURE 7: Masson trichrome staining of 14-day wounded rat skin of control group and CR-NE-II group. EP: epidermis; SE: subepidermis; DR: dermis; EI: epidermal integrity; DK: dekeratinization; CF: collagen fibers; DG: dermal glands; BV: blood vessels.

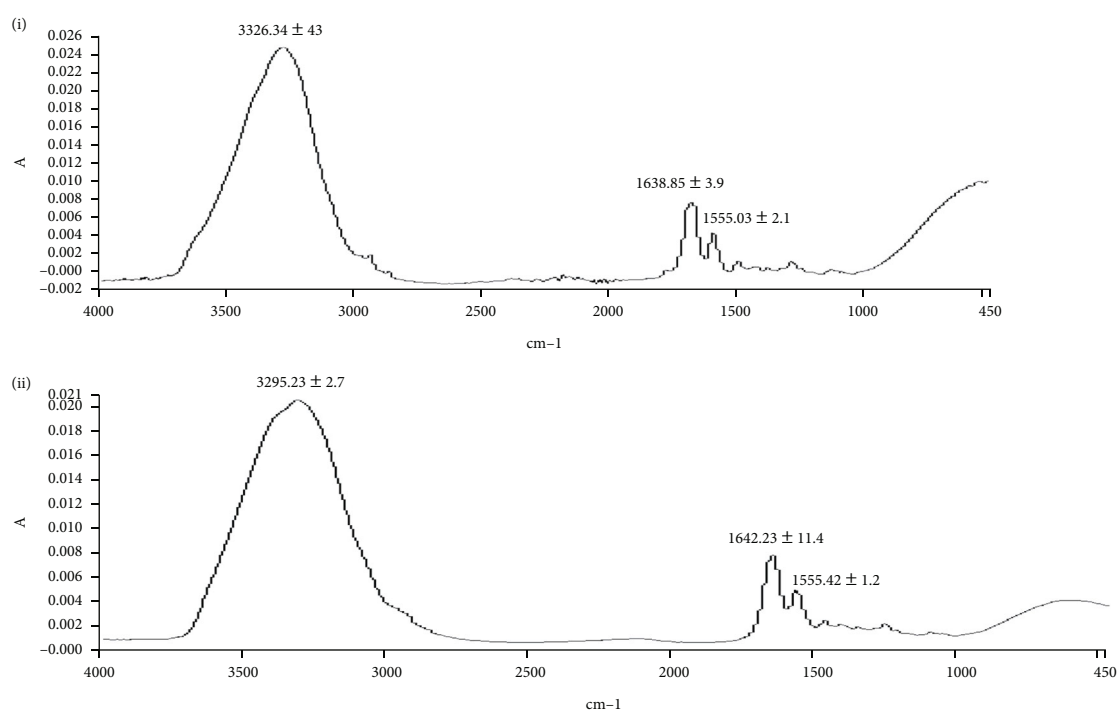


FIGURE 8: ATR-FTIR spectra of dermal layer of the (a) control group and (b) CR-NE-II group.

particular chemical component as stated by Beer-Lambert Law [81]. Therefore, higher absorbance ratio of a particular functional group indicates the higher intensity of that specific region. In this study, the fingerprint region shows a higher absorbance ratio of bands appearing at  $1642\text{ cm}^{-1}$  (amide-I) and  $1555\text{ cm}^{-1}$  (amide-II) in CR-NE-II compared to the control group, which indicates that more collagen protein is deposited at the wound site of curcumin nanoemulsion [82].

**5.10. Tensile Strength.** The skin samples extracted on day 14 of the control wound healing period and CR-NE-II animal group were subjected to stress break analysis, and the results are described in Table 5. The CR-NE-II application resulted in a significant increase in the mechanical strength of the skin containing wound on day 14 (Student's *t*-test,  $p < 0.05$ ) in comparison to the control group. The strength of skin samples is dependent on the quantity of collagen matrix, being the major structural protein in skin, deposited as a function

TABLE 5: Mechanical properties of rat skin samples.

Skin samples	Tensile strength (MPa)	Elongation break (%)	Elastic modulus (MPa)
Control group	$5.428 \pm 2.2$	16.777	1.7143
CR-NE-II group	$10.435 \pm 2.1$	14.714	3.2857

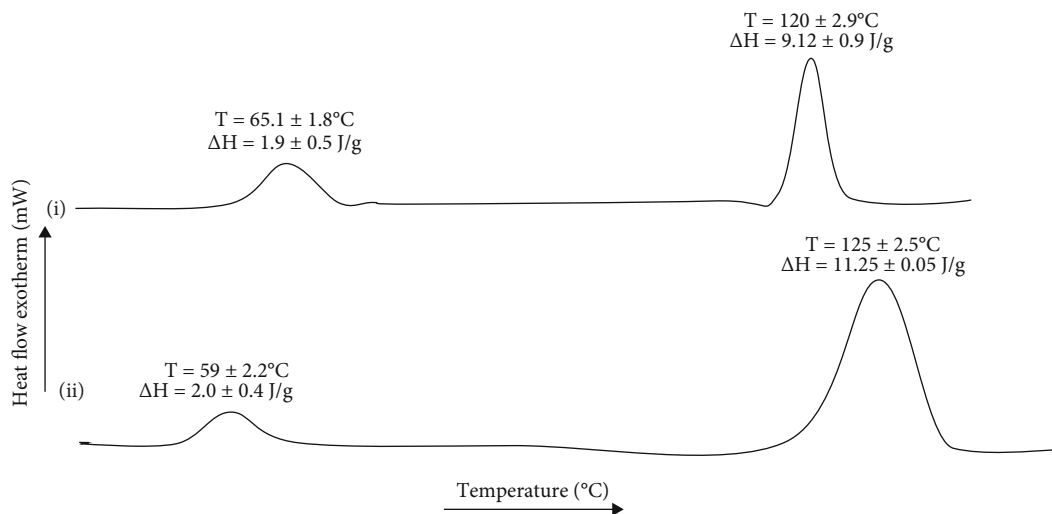


FIGURE 9: DSC thermogram of diabetic rat skin: (a) control group and (b) CR-NE-II group.

of time [83]. The uronic acid and hexosamine are the major matrix molecules which provide a necessary ground substrate for the new extracellular matrix, which are found at higher levels in the initial stages of wound healing while dropping down to normal in subsequent stages [84]. These components translate into the high activity of fibroblasts involved in the generation of substrate for the collagen fibers to be laid down [85]. Curcumin has been reported to increase uronic acid and hexosamine levels until the 8<sup>th</sup> day of the wound healing period [86]. The higher levels of uronic acid at the wound site attract more fibroblasts and thus stimulate collagen synthesis by providing more fluid, which ensures higher cell mobility and early remodeling and helps hasten skin regeneration [84]. Similar results were reported by Basit et al. who developed composite film dressing of sodium alginate and pectin crosslinked with microwave and chitosan-curcumin nanoparticles for burn wound healing purposes. The nanoparticle-film combined application hence translated into a significant rise in the tensile strength as well as percent elongation break in comparison to untreated as well as other experimental animal groups, which is envisaged to be due to synergistic action of curcumin and nanoparticles in ensuring rapid formation of collagen fibers and their uniform deposition at wound site [87]. In the instant case, the animals treated with curcumin nanoemulsion showed higher mechanical strength on day 14, where a 2- to 2.5-fold increase in the tensile strength of the skin samples was observed compared to the control animal group.

**5.11. Skin Thermal Analysis.** The thermal analysis is a widely employed analytical technique for estimation of changes in

the melting temperatures and energy required to induce phase transition of lipidic and proteinous domains in the skin [88]. The thermal analysis results of day 14 skin samples of the control and CR-NE-II-treated groups are shown in Figure 9. The lipidic domains of the skin samples showed melting temperature in the range of 59-65°C with corresponding enthalpies in the range of 1.9 to 2.0 J/g. No significant difference (Student's *t*-test,  $p > 0.05$ ) was observed among the control and CR-NE-II-treated animal groups in their thermal behaviour of lipidic domains, which reflects that skin lipid regeneration was independent of treatment applied [89]. In contrast, the proteinous domains of the skin samples of the CR-NE-II group underwent significant changes (Student's *t*-test,  $p < 0.05$ ) in the melting temperature and the enthalpies of the system compared to the control group. The CR-NE-II-treated group sample showed a significant increase in the melting temperature of up to  $125 \pm 2.5^\circ\text{C}$  in comparison to the control group of  $120 \pm 2.9^\circ\text{C}$ . Curcumin has been reported to hasten skin protein deposition following injury [90]. The increase in transition temperature, as well as enthalpies of the curcumin-treated animal group, reflects more uniform collagen fiber deposition with increased crosslinking [24], which is also evident in a significant increase in the enthalpies of the curcumin-treated animal group samples where a significant increase of up to 11.25 J/g was observed (Student's *t*-test,  $p < 0.05$ ). Enthalpy represents the energy required to induce phase transition [91]. The increased transition temperature and enthalpies with curcumin nanoemulsion treatment are hence envisaged to hasten collagen fiber synthesis and their uniform deposition following injury in diabetic animal models.

## 6. Conclusion

In this project, a novel nanoemulsion-encapsulating curcumin was formulated and evaluated for its wound healing potential in diabetic animals. The optimized formulation (CR-NE-II) showed size in nanorange and was homogeneously dispersed with enough surface charge to ensure stability. The formulation showed a burst drug release pattern, which remained constant throughout the experiment. The novel nanoemulsion system exerted synergistic antioxidant and antibacterial activity. The optimized formulation hastened the skin tissue regeneration with significantly higher percent reepithelization and rapid wound closure in comparison to the untreated animal group, where an increased extent of collagen fiber deposition and reduced inflammatory response with high mechanical strength were observed. The curcumin- $\alpha$ -tocopherol nanoemulsion is hence advocated to be the most suitable formulation for wound healing applications in diabetic animals.

## Data Availability

The data could be accessed and made available by contacting the corresponding author (if required).

## Conflicts of Interest

The authors declare no conflict of interest, and all authors confirm agreement with the final statement.

## Acknowledgments

The authors acknowledged the Kohat University of Science and Technology, Kohat; Gomal University Dikhan; and Higher Education Commission of Pakistan (grant no. 7493) for financial and facility support.

## Supplementary Materials

Figure S1: images of microbial growth at different days of wound healing in the untreated (control) and CR-NE-II-treated groups of diabetic rats. (*Supplementary Materials*)

## References

- [1] D. Mauricio, N. Alonso, and M. Gratacòs, "Chronic diabetes complications: the need to move beyond classical concepts," *Trends in Endocrinology and Metabolism*, vol. 31, no. 4, pp. 287–295, 2020.
- [2] M. Long, M. R. de la Vega, Q. Wen et al., "An essential role of NRF2 in diabetic wound healing," *Diabetes*, vol. 65, no. 3, pp. 780–793, 2016.
- [3] K. Bakker, J. Apelqvist, N. C. Schaper, and on behalf of the International Working Group on the Diabetic Foot Editorial Board, "Practical guidelines on the management and prevention of the diabetic foot 2011," *Diabetes/Metabolism Research and Reviews*, vol. 28, no. 2012, pp. 225–231, 2012.
- [4] C. Mohanty and S. K. Sahoo, "Curcumin and its topical formulations for wound healing applications," *Drug Discovery Today*, vol. 22, no. 10, pp. 1582–1592, 2017.
- [5] E. M. Tottoli, R. Dorati, I. Genta, E. Chiesa, S. Pisani, and B. Conti, "Skin wound healing process and new emerging technologies for skin wound care and regeneration," *Pharmaceutics*, vol. 12, no. 8, p. 735, 2020.
- [6] L. Cañedo-Dorantes and M. Cañedo-Ayala, "Skin acute wound healing: a comprehensive review," *International Journal of Inflammation*, vol. 2019, Article ID 3706315, 15 pages, 2019.
- [7] S. S. Kamar, D. H. Abdel-Kader, and L. A. Rashed, "Beneficial effect of curcumin nanoparticles-hydrogel on excisional skin-wound healing in type-I diabetic rat: histological and immunohistochemical studies," *Annals of Anatomy*, vol. 222, no. 2019, pp. 94–102, 2018.
- [8] T. Aristidis, "Role of Peripheral Neuropathy in the Development of Foot Ulceration and Impaired Wound Healing in," in *Nutritional and Therapeutic Interventions for Diabetes and Metabolic Syndrome*, pp. 93–104, Elsevier Inc., 2018.
- [9] F. A. Matough, S. B. Budin, Z. A. Hamid, N. Alwahaibi, and J. Mohamed, "The role of oxidative stress and antioxidants in diabetic complications," *Sultan Qaboos University Medical Journal*, vol. 12, no. 1, pp. 5–18, 2012.
- [10] A. Ullah, "Diabetes mellitus and oxidative stress—a concise review," *Saudi Pharmaceutical Journal*, vol. 24, no. 5, pp. 547–553, 2016.
- [11] C. Qing, "The molecular biology in wound healing & non-healing wound," *Chinese Journal of Traumatology English Edition*, vol. 20, no. 4, pp. 189–193, 2017.
- [12] M. M. Azevedo, C. Lisboa, L. Cobrado, C. Pina-Vaz, and A. Rodrigues, "Hard-to-heal wounds, biofilm and wound healing: an intricate interrelationship," *The British Journal of Nursing*, vol. 29, no. 5, pp. S6–S13, 2020.
- [13] J. J. Salazar, W. J. Ennis, and T. J. Koh, "Diabetes medications: Impact on inflammation and wound healing," *Journal of Diabetes and Its Complications*, vol. 176, no. 1, pp. 139–148, 2018.
- [14] A. Raghav, Z. A. Khan, R. K. Labala, J. Ahmad, S. Noor, and B. K. Mishra, "Financial burden of diabetic foot ulcers to world: a progressive topic to discuss always," *Therapeutic Advances in Endocrinology and Metabolism*, vol. 9, no. 1, pp. 29–31, 2018.
- [15] X. Chen, L. Zou, J. Niu, W. Liu, S. Peng, and C. Liu, "The stability, sustained release and cellular antioxidant activity of curcumin nanoliposomes," *Molecules*, vol. 20, no. 8, pp. 14293–14311, 2015.
- [16] F. Huang, Y. Gao, Y. Zhang et al., "Silver-decorated polymeric micelles combined with curcumin for enhanced antibacterial activity," *Applied Materials & Interfaces*, vol. 9, no. 20, pp. 16880–16889, 2017.
- [17] F. Maa, F. Liu, L. Ding et al., "Anti-inflammatory effects of curcumin are associated with down regulating microRNA-155 in LPS-treated macrophages and mice," *Pharmaceutical Biology*, vol. 55, no. 1, pp. 1263–1273, 2017.
- [18] K. Pan, H. Chen, S. Joon, and Q. Zhong, "Self-assembled curcumin-soluble soybean polysaccharide nanoparticles: Physicochemical properties and *in vitro* anti-proliferation activity against cancer cells," *Food Chemistry*, vol. 246, pp. 82–89, 2018.
- [19] H. R. Rahimi, "The effect of nano-curcumin on HbA1c, fasting blood glucose, and lipid profile in diabetic subjects: a randomized clinical trial," *Avicenna Journal of Phytomedicine*, vol. 6, no. 5, pp. 567–577, 2016.
- [20] G. Yakub, A. Toncheva, N. Manolova, I. Rashkov, and D. Danchev, "Electrospun polylactide-based materials for curcumin release: photostability, antimicrobial activity, and

- anticoagulant effect,” *Journal of Applied Polymer Science*, vol. 42940, no. 133, pp. 1–11, 2015.
- [21] F. Zhao, H. Dong, Y. Wang et al., “Synthesis and synergistic antifungal effects of monoketone derivatives of curcumin against fluconazole-resistant *Candida* spp.,” *MedChemComm*, vol. 8, no. 5, pp. 1093–1102, 2017.
- [22] K. S. Parvathy, P. S. Negi, and P. Srinivas, “Antioxidant, anti-mutagenic and antibacterial activities of curcumin- $\beta$ -diglucoside,” *Food Chemistry*, vol. 115, no. 1, pp. 265–271, 2009.
- [23] X. X. Yang, C. M. Li, and C. Z. Huang, “Curcumin modified silver nanoparticles for highly efficient inhibition of respiratory syncytial virus infection,” *Nanoscale*, vol. 8, no. 5, pp. 3040–3048, 2016.
- [24] V. V. S. R. Karri, G. Kuppusamy, S. V. Talluri et al., “Curcumin loaded chitosan nanoparticles impregnated into collagen-alginate scaffolds for diabetic wound healing,” *International Journal of Biological Macromolecules*, vol. 93, no. Part B, pp. 1519–1529, 2016.
- [25] W. M. El-Refaie, Y. S. R. Elnaggar, M. A. El-Massik, and O. Y. Abdallah, “Novel curcumin-loaded gel-core hyalurosomes with promising burn-wound healing potential: development, in-vitro appraisal and in-vivo studies,” *International Journal of Pharmaceutics*, vol. 486, no. 1–2, pp. 88–98, 2015.
- [26] A. E. Krausz, B. L. Adler, V. Cabral et al., “Curcumin-encapsulated nanoparticles as innovative antimicrobial and wound healing agent,” *Nanomedicine*, vol. 11, no. 1, pp. 195–206, 2015.
- [27] X. Bao, J. Wu, and G. Ma, “Sprayed Pickering emulsion with high antibacterial activity for wound healing,” *Progress in Natural Science: Materials International*, vol. 30, no. 5, pp. 669–676, 2020.
- [28] N. Fereydouni, M. Darroudi, J. Movaffagh et al., “Curcumin nanofibers for the purpose of wound healing,” *Journal of Cellular Physiology*, vol. 234, no. 5, pp. 5537–5554, 2019.
- [29] L. Pham, L. H. Dang, M. D. Truong et al., “A dual synergistic of curcumin and gelatin on thermal-responsive hydrogel based on chitosan-P123 in wound healing application,” *Biomedicine & Pharmacotherapy*, vol. 117, no. 2019, p. 109183, 2019.
- [30] V. Choudhary, H. Shivakumar, and H. Ojha, “Curcumin-loaded liposomes for wound healing: preparation, optimization, in-vivo skin permeation and bioevaluation,” *Journal of Drug Delivery Science and Technology*, vol. 49, pp. 683–691, 2019.
- [31] M. Tummalapalli, M. Berthet, B. Verrier, B. L. Deopura, M. S. Alam, and B. Gupta, “Composite wound dressings of pectin and gelatin with aloe vera and curcumin as bioactive agents,” *International Journal of Biological Macromolecules*, vol. 82, pp. 104–113, 2016.
- [32] F. Sánchez-Rubio, P. J. Soria-Meneses, A. Jurado-Campos et al., “Nanotechnology in reproduction: vitamin E nanoemulsions for reducing oxidative stress in sperm cells,” *Free Radical Biology & Medicine*, vol. 160, pp. 47–56, 2020.
- [33] N. W. Nawarathne, K. Wijesekera, W. M. D. G. B. Wijayaratne, and M. Napagoda, “Development of novel topical cosmeceutical formulations from *Nigella sativa* L. with antimicrobial activity against acne-causing microorganisms,” *Scientific World Journal*, vol. 2019, article 5985207, 7 pages, 2019.
- [34] J. M. Zingg, “Vitamin E: regulatory role on signal transduction,” *IUBMB Life*, vol. 71, no. 4, pp. 456–478, 2019.
- [35] V. Tanaydin, J. Conings, M. Malyar, R. Van Der Hulst, and B. Van Der Lei, “The role of topical vitamin E in scar management: a systematic review,” *Aesthetic Surgery Journal*, vol. 36, no. 8, pp. 959–965, 2016.
- [36] S. Balasaheb and D. Pal, “Free radicals, natural antioxidants, and their reaction mechanisms,” *Royal Society of Chemistry*, vol. 5, pp. 27986–28006, 2015.
- [37] S. Sood, K. Jain, and K. Gowthamarajan, “Optimization of curcumin nanoemulsion for intranasal delivery using design of experiment and its toxicity assessment,” *Colloids and Surfaces. B, Biointerfaces*, vol. 113, pp. 330–337, 2014.
- [38] F. U. Din, O. Mustapha, D. W. Kim et al., “Novel dual-reverse thermosensitive solid lipid nanoparticle-loaded hydrogel for rectal administration of flurbiprofen with improved bioavailability and reduced initial burst effect,” *European Journal of Pharmaceutics and Biopharmaceutics*, vol. 94, no. 2015, pp. 64–72, 2015.
- [39] K. G. M. Fakhar-ud-Din, “Development and characterisation of levosulpiride-loaded suppositories with improved bioavailability in vivo,” *Pharmaceutical Development and Technology*, vol. 24, no. 1, pp. 63–69, 2019.
- [40] V. Kakkar, I. P. Kaur, A. P. Kaur, K. Saini, and K. K. Singh, “Topical delivery of tetrahydrocurcumin lipid nanoparticles effectively inhibits skin inflammation: in vitro and in vivo study,” *Drug Development and Industrial Pharmacy*, vol. 44, no. 10, pp. 1701–1712, 2018.
- [41] B. Gaba, T. Khan, F. Haider et al., “Vitamin E loaded naringenin nanoemulsion via intranasal delivery for the management of oxidative stress in a 6-OHDA Parkinson’s disease model,” *BioMed Research International*, vol. 2019, Article ID 2382563, 20 pages, 2019.
- [42] Y. Shao, C. Wu, T. Wu et al., “Eugenol-chitosan nanoemulsions by ultrasound-mediated emulsification: formulation, characterization and antimicrobial activity,” *Carbohydrate Polymers*, vol. 193, pp. 144–152, 2018.
- [43] T. Sirkka, J. B. Skiba, and S. P. Apell, “Wound pH depends on actual wound size,” 2016, <https://arxiv.org/abs/1601.06365>.
- [44] A. Ali, “Effective dose of streptozotocin for induction of diabetes mellitus and associated mortality rate in Wistar albino rats,” *Pakistan Journal of Medicine and Dentistry*, vol. 8, no. 4, pp. 50–54, 2019.
- [45] A. A. Muhammad, “Evaluation of wound healing properties of bioactive aqueous fraction from *Moringa oleifera* Lam on experimentally induced diabetic animal model,” *Drug Design, Development and Therapy*, vol. 10, pp. 1715–1730, 2016.
- [46] F. Akbas, “Protective effect of insulin treatment on early renal changes in streptozotocin-induced diabetic rats,” *General Endocrinology*, vol. XIV, no. 2, pp. 169–174, 2018.
- [47] N. Kianvash, A. Bahador, M. Pourhajibagher et al., “Evaluation of propylene glycol nanoliposomes containing curcumin on burn wound model in rat: biocompatibility, wound healing, and anti-bacterial effects,” *Drug Delivery and Translational Research*, vol. 7, no. 5, pp. 654–663, 2017.
- [48] P. S. Lau, N. Bidin, S. Islam et al., “Influence of gold nanoparticles on wound healing treatment in rat model: photobiomodulation therapy,” *Lasers in Surgery and Medicine*, vol. 49, no. 4, pp. 380–386, 2017.
- [49] A. Babakhani, M. Nobakht, H. P. Torodi et al., “Effects of hair follicle stem cells on partial-thickness burn wound healing and tensile strength,” *Iranian Biomedical Journal*, vol. 24, no. 2, pp. 99–109, 2020.
- [50] M. Firoozi, S. Rezapour-Jahani, Z. Shahvegharasl, and N. Anarjan, “Ginger essential oil nanoemulsions: preparation and physicochemical characterization and antibacterial



- activities evaluation,” *Journal of Food Process Engineering*, vol. 43, no. 8, p. 13434, 2020.
- [51] S. Asadinezhad, F. Khodaiyan, M. Salami, H. Hosseini, and B. Ghanbarzadeh, “Effect of different parameters on orange oil nanoemulsion particle size: combination of low energy and high energy methods,” *Journal of Food Measurement and Characterization*, vol. 13, no. 4, pp. 2501–2509, 2019.
- [52] N. Ahmad, R. Ahmad, A. Al-qudaihi, and E. Alaseel, “Preparation of a novel curcumin nanoemulsion by ultrasonication and its comparative effects in wound healing and the treatment of inflammation,” *RSC Advances*, vol. 9, no. 35, pp. 20192–20206, 2019.
- [53] A. Pucek, B. Tokarek, E. Waglewska, and U. Bazylińska, “Recent advances in the structural design of photosensitive agent formulations using ‘soft’ colloidal nanocarriers,” *Pharmaceutics*, vol. 12, no. 6, p. 587, 2020.
- [54] Y. Xiao, X. Chen, L. Yang et al., “Preparation and oral bioavailability study of curcuminoid-loaded microemulsion,” *Journal of Agricultural and Food Chemistry*, vol. 61, no. 15, pp. 3654–3660, 2013.
- [55] T. P. Sari, B. Mann, R. Kumar et al., “Preparation and characterization of nanoemulsion encapsulating curcumin,” *Food Hydrocolloids*, vol. 43, pp. 540–546, 2015.
- [56] W. Liu, N. Pan, Y. Han, D. Li, and J. Chai, “Solubilization, stability and antioxidant activity of curcumin in a novel surfactant-free microemulsion system,” *LWT*, vol. 147, p. 111583, 2021.
- [57] B. Firtın, H. Yenipazar, A. Saygün, and N. Şahin-Yeşilçubuk, “Encapsulation of chia seed oil with curcumin and investigation of release behaviour & antioxidant properties of microcapsules during *in vitro* digestion studies,” *LWT*, vol. 134, p. 109947, 2020.
- [58] H. Wang, X. Gong, X. Guo et al., “Characterization, release, and antioxidant activity of curcumin-loaded sodium alginate/ZnO hydrogel beads,” *International Journal of Biological Macromolecules*, pp. 1–35, 2018.
- [59] G. M. Pontes-Quero, L. Benito-Garzón, J. Pérez Cano, M. R. Aguilar, and B. Vázquez-Lasa, “Amphiphilic polymeric nanoparticles encapsulating curcumin: antioxidant, anti-inflammatory and biocompatibility studies,” *Materials Science and Engineering: C*, vol. 121, article 111793, 2021.
- [60] J. Carpenter, S. George, and V. K. Saharan, “Curcumin encapsulation in multilayer oil-in-water emulsion: synthesis using ultrasonication and studies on stability and antioxidant and release activities,” *Langmuir*, vol. 35, no. 33, pp. 10866–10876, 2019.
- [61] C. Scamoroscenco, M. Teodorescu, S. G. Burlacu et al., “Synergistic antioxidant activity and enhanced stability of curcumin encapsulated in vegetal oil-based microemulsion and gel microemulsions,” *Antioxidants*, vol. 11, no. 5, p. 854, 2022.
- [62] C. Chittasupho, A. Manthaisong, S. Okonogi, S. Tadtong, and W. Samee, “Effects of quercetin and curcumin combination on antibacterial, antioxidant, *in vitro* wound healing and migration of human dermal fibroblast cells,” *International Journal of Molecular Sciences*, vol. 23, no. 1, p. 142, 2022.
- [63] H. Wang, L. Hao, P. Wang, M. Chen, S. Jiang, and S. Jiang, “Release kinetics and antibacterial activity of curcumin loaded zein fibers,” *Food Hydrocolloids*, vol. 63, pp. 437–446, 2017.
- [64] I. Negut, V. Grumezescu, and A. M. Grumezescu, “Treatment strategies for infected wounds,” *Molecules*, vol. 23, no. 9, p. 2392, 2018.
- [65] M. R. Abdulbaqi and N. A. Rajab, “Apixaban ultrafine O/W nano emulsion transdermal drug delivery system: formulation, *in vitro* and *ex vivo* characterization,” *Systematic Reviews in Pharmacy*, vol. 11, no. 2, pp. 82–94, 2020.
- [66] P. K. Barman and T. J. Koh, “Macrophage dysregulation and impaired skin wound healing in diabetes,” *Frontiers in Cell and Development Biology*, vol. 8, no. June, pp. 1–9, 2020.
- [67] R. Iqbal, Z. Mehmood, A. Baig, and N. Khalid, “Formulation and characterization of food grade O/W nanoemulsions encapsulating quercetin and curcumin: insights on enhancing solubility characteristics,” *Food and Bioproducts Processing*, vol. 123, pp. 304–311, 2020.
- [68] M. Mehanny, R. M. Hathout, A. S. Geneidi, and S. Mansour, “Exploring the use of nanocarrier systems to deliver the magical molecule; curcumin and its derivatives,” *Journal of Controlled Release*, vol. 225, pp. 1–30, 2016.
- [69] S. Mahmood, P. Bhattarai, N. R. Khan, Z. Subhan, and G. Razaque, “An investigation for skin tissue regeneration enhancement/augmentation by curcumin-loaded self-emulsifying drug delivery system (SEDDS),” *Polymers*, vol. 14, no. 2904, pp. 1–22, 2022.
- [70] S. Taghavifar, F. Afroughi, and M. S. Keyvan, “Curcumin nanoparticles improved diabetic wounds infected with methicillin-resistant *Staphylococcus aureus* sensitized with HAMLET,” *The International Journal of Lower Extremity Wounds*, vol. 21, no. 2, pp. 141–153, 2020.
- [71] U. Bulbake, S. Jain, N. Kumar, and A. Mittal, “Curcumin loaded biomimetic composite graft for faster regeneration of skin in diabetic wounds,” *Journal of Drug Delivery Science and Technology*, vol. 47, pp. 12–21, 2018.
- [72] R. Hobson, “Vitamin E and wound healing: an evidence-based review,” *International Wound Journal*, vol. 13, no. 3, pp. 331–335, 2016.
- [73] K. Thakur, G. Sharma, B. Singh et al., “Cationic-bilayered nanoemulsion of fusidic acid: an investigation on eradication of methicillin-resistant *Staphylococcus aureus* 33591 infection in burn wound,” *Nanomedicine*, vol. 13, no. 8, pp. 825–847, 2018.
- [74] M. S. Khan, S. M. Ibrahim, A. A. Adamu et al., “Pre-grafting histological studies of skin grafts cryopreserved in  $\alpha$  helix antarctic yeast oriented antifreeze peptide (Afp1m),” *Cryobiology*, vol. 92, pp. 26–33, 2020.
- [75] A. B. Kunnumakara, D. Bordoloi, G. Padmavathi et al., “Curcumin, the golden nutraceutical: multitargeting for multiple chronic diseases,” *British Journal of Pharmacology*, vol. 174, no. 11, pp. 1325–1348, 2017.
- [76] Z. Hussain, H. E. Thu, S. F. Ng, S. Khan, and H. Katas, “Nanoencapsulation, an efficient and promising approach to maximize wound healing efficacy of curcumin: a review of new trends and state-of-the-art,” *Colloids and Surfaces. B, Biointerfaces*, vol. 150, pp. 223–241, 2017.
- [77] Z. Wang, Z. Zhao, N. R. Khan, Z. Hua, J. Huo, and Y. Li, “Microwave assisted chitosan-polyethylene glycol hydrogel membrane synthesis of curcumin for open incision wound healing,” *Die Pharmazie*, vol. 75, no. 4, pp. 118–123, 2020.
- [78] T. G. Sahana and P. D. Rekha, “Biopolymers: applications in wound healing and skin tissue engineering,” *Molecular Biology Reports*, vol. 45, no. 6, pp. 2857–2867, 2018.
- [79] K. Belbachir, R. Noreen, and G. Gouspillou, “Collagen types analysis and differentiation by FTIR spectroscopy,” *Analytical and Bioanalytical Chemistry*, vol. 395, no. 3, pp. 829–837, 2009.

- [80] Z. Movasaghi, S. Rehman, and I. U. Rehman, "Fourier Transform Infrared (FTIR) Spectroscopy of Biological Tissues," *Applied Spectroscopy Reviews*, vol. 43, no. 2, pp. 134–179, 2008.
- [81] F. Palombo, S. G. Cremers, P. D. Weinberg, and S. G. Kazarian, "Application of Fourier transform infrared spectroscopic imaging to the study of effects of age and dietary L-arginine on aortic lesion composition in cholesterol-fed rabbits," *Journal of the Royal Society Interface*, vol. 6, no. 37, pp. 669–680, 2009.
- [82] L. Zhengguang, H. Jie, Z. Yong, C. Jiaojiao, W. Xingqi, and C. Xiaoqin, "Study on the transdermal penetration mechanism of ibuprofen nanoemulsions," *Drug Development and Industrial Pharmacy*, vol. 45, no. 3, pp. 465–473, 2019.
- [83] J. F. Ribeiro, E. H. M. dos Anjos, M. L. S. Mello, and B. de Campos Vidal, "Skin collagen fiber molecular order: a pattern of distributional fiber orientation as assessed by optical anisotropy and image analysis," *PLoS One*, vol. 8, no. 1, pp. 5–7, 2013.
- [84] M. Hu, E. E. Sabelman, Y. Cao, J. Chang, and V. R. Hentz, "Three-dimensional hyaluronic acid grafts promote healing and reduce scar formation in skin incision wounds," *Journal of Biomedical Materials Research Part B: Applied Biomaterials*, vol. 67B, no. 1, pp. 586–592, 2003.
- [85] G. Ramanathan, T. Muthukumar, and U. Tirichurapalli Sivagnanam, "In vivo efficiency of the collagen coated nanofibrous scaffold and their effect on growth factors and pro-inflammatory cytokines in wound healing," *European Journal of Pharmacology*, vol. 814, pp. 45–55, 2017.
- [86] M. Panchatcharam, S. Miriyala, V. S. Gayathri, and L. Suguna, "Curcumin improves wound healing by modulating collagen and decreasing reactive oxygen species," *Molecular and Cellular Biochemistry*, vol. 290, no. 1–2, pp. 87–96, 2006.
- [87] H. M. Basit, M. Ali, M. M. Shah et al., "Microwave enabled physically cross linked sodium alginate and pectin film and their application in combination with modified chitosan-curcumin nanoparticles. A novel strategy for 2nd degree burns wound healing in animals," *Polymers*, vol. 13, no. 16, p. 2716, 2021.
- [88] M. Yang, Y. Gu, D. Yang, X. Tang, and J. Liu, "Development of triptolide - nanoemulsion gels for percutaneous administration: physicochemical, transport, pharmacokinetic and pharmacodynamic characteristics," *Journal of Nanobiotechnology*, vol. 15, no. 1, pp. 1–15, 2017.
- [89] J. Pardeike, K. Schwabe, and R. H. Müller, "Influence of nanostructured lipid carriers (NLC) on the physical properties of the Cutanova Nanorepair Q10 cream and the in vivo skin hydration effect," *International Journal of Pharmaceutics*, vol. 396, no. 1–2, pp. 166–173, 2010.
- [90] A. A. Shefa, T. Sultana, M. K. Park, S. Y. Lee, J. G. Gwon, and B. T. Lee, "Curcumin incorporation into an oxidized cellulose nanofiber-polyvinyl alcohol hydrogel system promotes wound healing," *Materials and Design*, vol. 186, no. 2020, p. 108313, 2020.
- [91] J. Dauvergne, Á. Serrano, E. Palomo, and D. Barrio, "Fast estimation of the enthalpy – temperature function of phase change materials," *Experimental Thermal and Fluid Science*, vol. 122, p. 110317, 2021.

## Retraction

# Retracted: Synthesis and Biomedical Applications of Zirconium Nanoparticles: Advanced Leaps and Bounds in the Recent Past

### BioMed Research International

Received 8 January 2024; Accepted 8 January 2024; Published 9 January 2024

Copyright © 2024 BioMed Research International. This is an open access article distributed under the Creative Commons Attribution License, which permits unrestricted use, distribution, and reproduction in any medium, provided the original work is properly cited.

This article has been retracted by Hindawi following an investigation undertaken by the publisher [1]. This investigation has uncovered evidence of one or more of the following indicators of systematic manipulation of the publication process:

- (1) Discrepancies in scope
- (2) Discrepancies in the description of the research reported
- (3) Discrepancies between the availability of data and the research described
- (4) Inappropriate citations
- (5) Incoherent, meaningless and/or irrelevant content included in the article
- (6) Manipulated or compromised peer review

The presence of these indicators undermines our confidence in the integrity of the article's content and we cannot, therefore, vouch for its reliability. Please note that this notice is intended solely to alert readers that the content of this article is unreliable. We have not investigated whether authors were aware of or involved in the systematic manipulation of the publication process.

Wiley and Hindawi regrets that the usual quality checks did not identify these issues before publication and have since put additional measures in place to safeguard research integrity.

We wish to credit our own Research Integrity and Research Publishing teams and anonymous and named external researchers and research integrity experts for contributing to this investigation.


The corresponding author, as the representative of all authors, has been given the opportunity to register their agreement or disagreement to this retraction. We have kept a record of any response received.

### References

- [1] H. M. Arshad, A. Shahzad, S. Shahid et al., "Synthesis and Biomedical Applications of Zirconium Nanoparticles: Advanced Leaps and Bounds in the Recent Past," *BioMed Research International*, vol. 2022, Article ID 4910777, 9 pages, 2022.

## Review Article

# Synthesis and Biomedical Applications of Zirconium Nanoparticles: Advanced Leaps and Bounds in the Recent Past

Hafiz Muhammad Arshad,<sup>1</sup> Amir Shahzad,<sup>1</sup> Sammia Shahid,<sup>1</sup> Sadaqat Ali,<sup>2</sup> Abdul Rauf,<sup>1</sup> Shahzad Sharif,<sup>3</sup> Muhammad Ehsan Ullah,<sup>4</sup> Muhammad Inam Ullah,<sup>5</sup> Muhammad Ali,<sup>6</sup> and Hafiz Ishfaq Ahmad <sup>7</sup>

<sup>1</sup>Department of Chemistry, School of Science, University of Management and Technology, Lahore, Pakistan

<sup>2</sup>Department of Zoology, Ghazi University, D G Khan, Pakistan

<sup>3</sup>Department of Chemistry, Government College University, Lahore, Pakistan

<sup>4</sup>Department of Physics, School of Science, University of Management and Technology, Lahore, Pakistan

<sup>5</sup>Department of Chemistry, Government College University, Faisalabad, Pakistan

<sup>6</sup>Department of Chemistry, University of Education, Lahore, Sub-Campus, D G Khan, Pakistan

<sup>7</sup>Department of Animal Breeding and Genetics, Faculty of Veterinary and Animal Sciences, The Islamia University of Bahawalpur, Bahawalpur, Pakistan

Correspondence should be addressed to Hafiz Ishfaq Ahmad; hafizishfaq93@gmail.com

Received 29 June 2022; Accepted 20 August 2022; Published 13 September 2022

Academic Editor: Abdul Wahab

Copyright © 2022 Hafiz Muhammad Arshad et al. This is an open access article distributed under the Creative Commons Attribution License, which permits unrestricted use, distribution, and reproduction in any medium, provided the original work is properly cited.

Many synthetic routes manufacture zirconium nanoparticles in metal oxide, nitride, and other combination forms. Coupled with other variables such as concentration, pH, and form of precursor used, the various synthetic methods support synthesizing the zirconium metal oxide nanoparticles with changed features. Various synthetic methods were studied, such as sol-gel, hydrothermal, laser ablation, and precipitation. All have different synthetic routes, different precursors and solvents were used, and the product was characterized by SEM, TEM, photo luminance spectroscopy, UV-absorption spectroscopy, and powder X-ray diffraction. X-ray diffraction determined the crystal structure by identifying the crystal shape, arrangement of atoms, and spacing between them. SEM and TEM studied the particle size and morphology of nanoparticles. UV-visible absorption spectroscopy and PL spectroscopy were used for the determination of optical properties of nanoparticles. Zirconium oxide nanoparticles have many applications in the medical field. The review study primarily focuses on the efficient combination of zirconium dioxide with other additive materials and functionalization techniques used to improve the material's properties, assisting the use of the material in hip arthroplasty and bone tissue applications. The development of sophisticated near-infrared (NIR) absorbing small molecules for useful phototheranostic applications was discussed in this paper.

## 1. Introduction

Nanoparticles have a diameter of 1–100 nm in range. Although nanoparticles have great chemical, mechanical, thermal, magnetic, and electrical capabilities, scientists still encounter difficulties identifying, creating, and analyzing the potential of these nanostructured objects [1]. Different metal oxides of nanoparticles synthesized through joining two metals in the form of oxide give the manufactured product enhanced fea-

tures. The metal oxide nanoparticles differ in various physical properties and chemically and morphological characteristics and are applied in different fields because they have different uses [2]. Nanomaterials deal with the branch of science which studies the particles at a nanoscale level ranging from 10 to 100 nm. The nanoparticles' unique properties depend upon the particles' small size [3]. Zirconium belongs to the class of strong transition metals, their properties resembling titanium due to strong action against corrosion. Mostly, zirconium

metal is obtained from minerals such as zirconium which can be refined with chlorine organic and inorganic compounds and can also be synthesized zirconium metal [4]. Zirconium nanoparticles have been used for different syntheses due to their various assets, such as extraordinary fracture toughness, high tensile strength, and hardness. Naturally, zirconium can exist in five different isotopes form; out of five isotopes,  $^{90}\text{Zr}$  exists abundantly in nature almost (51.45%) [5]. Various synthetic paths have existed to make nanoparticles of metal oxide and mixed metal oxide. Different technical methods have assembled all of these synthetic paths. Zirconium metal complexes have catalytic use [6]. The growing of TWCNs in the size of 2D and 3D graphene layer zirconium nanoparticles (NP) is used as a catalyst. For the formation of good-quality carbon nanotubes (CNTs), using zirconium as a catalyst is the best for such high-purity carbon nanoparticles [7]. Kroll method was good for synthesizing zirconium nanoparticles; when zirconium tetrachloride is treated with magnesium metal, an active metal, then the temperature is maintained at 800–900°C. In this article, we covered the various synthetic methods for creating zirconium nanoparticles [8] in cubic, monoclinic, and mixed phases, including the sol-gel method, the hydrothermal method, the laser ablation method, the wire explosion process, hybrid transparent coating, the chemical polymerization, and the coprecipitation method [9].

## 2. Synthesis of Zirconium Metal Oxide Nanoparticles in Mixed Form

The various synthetic routes applied to manufacture nanoparticles of metal oxide are also in the form of mixed metal oxide. Under a different technological method, every synthetic method has been clustered (Table 1). In unity with the growth of crystals, such as thin film growth [10], thin film growth is classified into two types: one is vapor phase growth (VPG), and second is liquid phase growth (LPG); other growth methods are the formation of solid phase and the hybrid growth of the crystal, which form the nanoparticles with the help of colloidal treating, nanoparticles utilizing rapid growth like template-based growth and thin films growth [11] that have a thickness range from the friction of nanometer to several microns by molecular beam epitaxy [12] and the nanostructure in the form of bulk materials, and also in conflict with the models, a changed practical methodology could be considered [13]. The top-down synthesis approach involves reducing the bulk materials into a nanoscale dimension utilizing a physical approach, but the bottom-up approach is in which the smaller unit is combined to form a bulk unit (Figure 1) [14].

**2.1. Cubic form Zirconium Oxide ( $\text{ZrO}_2$ ) nanoparticles.** The cubic shape of zirconium oxide nanoparticles was manufactured with the reaction of xylene, zirconium oxychloride, and N-cetyl-N, N, N-trimethylammonium bromide taken in different amounts and added to the distilled water of 100 ml and stirred the mixture almost for 2 h [22]. To maintain the pH at 9, sodium hydroxide (0.5 M) solution was added. After that, the white precipitate was obtained, and the mixture was refluxed for 3 h at 85. The reaction mixture

was cool and then stirred strongly for 24 h. The obtained mixture was like a suspension, and the white precipitate was obtained [23], and then, they can be filtered, diluted, and washed with water ( $\text{H}_2\text{O}$ ) and ethanol ( $\text{C}_2\text{H}_5\text{OH}$ ) to separate the xylene and CTAB. The obtained precursor was dried for 17 to 18 h at 100°C. After that, they can be calcinated for 4 h at 500°C [24].

**2.2. Monoclinic and Cubic Phase Nanoparticles.** The mixed monoclinic and cubic phase zirconium oxide nanoparticles were synthesized zirconium oxychloride ( $\text{ZrOCl}_2 \cdot 8\text{H}_2\text{O}$ ), 1-hexanol, and oxalic acid ( $\text{COOH}$ )<sub>2</sub>. Zirconium oxychloride and oxalic acid were taken equal to 1 mol/l, but 1-hexanol ( $\text{C}_6\text{H}_{14}\text{O}$ ) was taken at 2 mol/l [25]. These chemicals were mixed utilizing the pestle and mortar, and the sample was equipped in the form of rheological from the mixture [26]. Then, the mixture was reacted at 98°C for 13 h. It can be washed with ethanol ( $\text{C}_2\text{H}_5\text{OH}$ ) and water and then dried in an oven for 4 h and adjusted to the temperature of 500°C. X-ray powder diffractometers were used to determine the crystallographic features of the sample by using Ge and Cu monochromatized  $\text{K}\alpha$  radiation by using Bragg's relation [26], where  $\lambda = 1.54287 \text{ \AA}$  and  $2\theta$  range of 20–80°.

$$n\lambda = 2d\sin\theta, \quad (1)$$

$$d = \frac{n\lambda}{2 \sin \theta}.$$

The morphologic properties of the crystal are determined by using SEM and TEM. For the determination of optical absorption spectra, spectrometer was used at room temperature. Optical spectra were recorded in 200–800 nm wavelength regions [27]. At room temperature, identification of photoluminescence was achieved by employing a Dilor XY device, which has the capability of being fitted with an additional components monochromator. Electrochemical properties of  $\text{ZrO}_2$  nanoparticles were analyzed by silver-silver and counter electrode with the reference electrode method [4].

**2.3. Ultrafast Laser Ablation.** The metallic form of Zr nanoparticles manufactured by ultrafast laser ablation of a zirconium rod in isopropyl alcohol has been defined in the literature. This process forms a colloidal form of solution of zirconium nanoparticles. In this process, using the femto-second laser pulses for ablation, the proportion dispersal of nanoparticles can be significantly concentrated [28]. For the development of 50 nm metallic zirconium nanoparticles, the setup of plasma-induced cathodic discharge electrolysis under argon (Ar) gas in melted salt was also used. Implants are also made of titanium and zirconium [29]. Zirconium is extremely flammable in powder form and thus has armed uses, such as in manufacturing explosive resources for military capability. The zirconium oxide ( $\text{ZrO}$ ) was then characterized by powder X-ray diffraction [30].

**2.4. Wire Explosion Process.** The zirconium nitride ( $\text{ZrN}$ ) nanoparticles were manufactured by the wire explosion method; in this process, the amount of energy ( $E$ ) accumulated on the wire and the ambient pressure show a

TABLE 1: Different methods for the preparation of zirconium oxide complexes.

Synthesis	Benefits	Drawbacks	Morphology
Coprecipitation method	Preparation is straightforward; minimal equipment is required, and it is commercialized. A representative method for producing heterogeneous catalyst powders with good homogeneity and a relatively low calcination temperature is the usual coprecipitation techniques for producing heterogeneous catalyst powders 50 with good homogeneity and a relatively low calcination temperature coprecipitation technique [15].	One of this method's biggest flaws is the inability to regulate the precipitating particle sizes and subsequent aggregation. Therefore, hybrid approaches that control the size of the particle by deagglomerating the generated nanomaterial should be considered [16]. Under ultrasound irradiation, the precipitated gel undergoes extremely high shear pressures and cavitation heating, creating nanoparticles and high-phase purity in complicated metal oxides. Therefore, agglomeration, poor yield, and finished product purity affect many factors, such as pH values, washing solvents, and dry method.	According to morphological research, the grains are compact and randomly organized, and as the temperature of sintering rises, so does grain size. X-ray photoelectron spectroscopy analysis has been used to investigate the compositional analyses of metal nanoparticles [17]. To explore the surface morphology and particle size fluctuations in metal oxide nanoparticles, the pH value of the solution was changed.
Sol-gel synthesis	The sol-gel method is superior to other methods for creating metal oxide nanoparticles because it is straightforward and inexpensive and uses low temperatures and pressure [18]. Easy to use; high purity; uniform distribution; commercialized, perfect, high purity and time-saving. Newly, alumina membranes with pore sizes of around 3 to 4 nm, thicknesses of 1 to 10 $\mu\text{m}$ , and porosities of about 50% have been created using the sol-gel process.	The relatively substantial shrinkage associated with the gelation process and the drying of gels, the presence of high pore concentrations, and the removal of unwanted residuals such as hydroxyls and organics are some of the key drawbacks of the sol-gel method [19]. It takes a long time to sinter; it has weak sintering characteristic.	The experimental circumstances and processing factors used during the sol-gel synthesis process can have an impact on the materials characteristics. In order to tailor the numerous properties displayed by the produced nanoparticles to the required applications, processing parameters are the operating conditions that must be taken into account throughout the synthesis process of nanoparticles [20]. Effects of variables on the morphology and optical qualities include the pH of the sol, additives (such as capping agents and surfactants), annealing temperature, and calcination.
Hydrothermal method	Metal nanoparticle application in biomedicine and related fields is constantly growing globally. Applications for hydrothermally produced nanoparticles include those in optics, medicine, electronics (including sensors, information, and communication technologies), catalysis, devices (including fuels for energy conversion and storage), and electronics [21].	These techniques produce nanoparticles with less precise size distributions, compositional control, and optoelectronic characteristics. According to Xu et al., hydrothermally created CIS NCs coated in glutathione and exhibiting multiple emission bands in the photoluminescence (PL) spectrum.	At every stage of the process, from the unit cell to the crystallite size to the size and shape of the nanoparticles, the surfactants and dopants have a significant impact [21].

significant character in the size of the shaped particles [31]. The qualitative analysis of the synthesized particles can be analyzed by this method. It is possible to manufacture nitride nanoparticles by giving sufficient energy to the electrode for evaporation and by keeping an effective standard for nitridation [32]. To obtain zirconium, a systematic experimental study was performed. By the explosion of the wire, as well as the blowing up of zirconium nanoparticles while they were being conducted in a nitrogen ( $\text{N}_2$ ) atmosphere, nitride nanoparticles of a much smaller scale were created. The X-ray diffraction (XRD) and designated region electron deflection analysis characterized the synthesized powders [33]. A TEM was used to examine the size and

shape of the constituent part formed by the wire explosion method. Particle bulk dispersal experiments were conducted by following the distribution of log-normal possibility. The connection between the size of nanoparticles, the wire explosion method produced, and the nitrogen ambient pressure was investigated [34].

**2.5. Hybrid Transparent Coating.** The hybrid transparent zirconium nanoparticle filler-based coatings and epoxy resin have improved the scratch conflict of goods polymers without losing their visual properties. The nanocrystalline  $\text{ZrO}_2$  suspensions in the benzyl alcohol have been manufactured using  $\text{ZrCl}_4$  as a precursor through a flexible nonhydrolytic

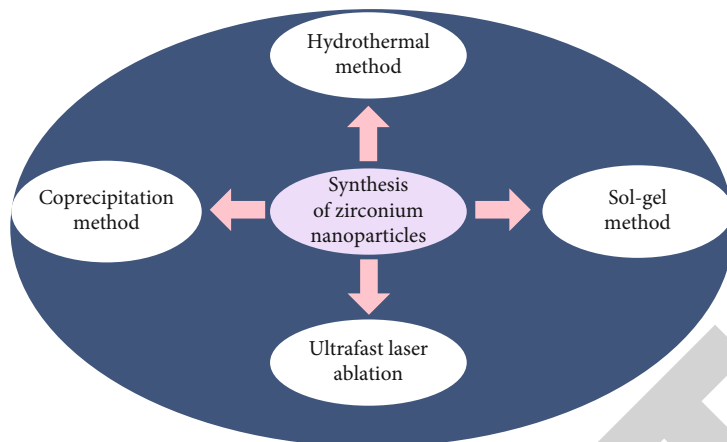


FIGURE 1: Different methods of synthesis of zirconium nanoparticles.

sol-gel process [35]. The  $ZrO_2$  nanoparticles displayed a tetragonal phase-attributable crystalline structure with a normal particle size of 2 nm. A commercial epoxy resin was mixed with  $ZrO_2$  nanoparticles adjoined in tert-butanol. The biological solvent was then vaporized, and the polycarbonate and hybrid composites were deposited [36]. There was a homogeneous adhesion and a marginal effect on the clearness of polymers in the coatings. The improved scratch resistance was achieved by increasing the content of  $ZrO_2$  nanoparticles.

**2.6. Synthesis of Crystalline Zirconium Nanoparticles.** Due to their atom-like size-dependent property, semiconductor particles in the nanometer mass regime have been involved in considerable desirability. Recently, several improved routes have been reported for the amalgamation of such type's nanomaterial [37] with tunable characteristics. Ceramics among the zirconium are an unusual form of transition-metal semiconductor with the functional properties of pathetic acidic and basic goods. Fast combination and categorization of cubic form  $ZrO_2$  nanoparticles with hydrothermal influence over the morphological and crystallinity properties [38]. The temperature is constantly used to produce cubic form  $ZrO_2$  nanoparticles at the lowest rate. In the synthesis process, zirconium isopropoxide, 1 g was taken in the flask made up of Teflon, and then, analytical graded ethanol 6 ml was added. After that, the flask was placed in a desiccator chamber [39]. The  $ZrO_2$  precipitation was obtained lower than the saturated atmospheric condition by introducing a Petri plate with the water at the end of the desiccator. After 12 h, the reaction was immobile, and 25 ml of sodium hydroxide (NaOH) was added. Then, the whole reaction was sealed in the hydrothermal stainless steel for 18 h at  $180^\circ C$ . When the autoclave was done, the solution mixture was cooled at room heat; the mixture solution was continuously washed with 0.1M solution of nitric acid ( $HNO_3$ ) and 1 N hydrochloric acid (HCl) solution [40]. A fibrous and white soft like powder was achieved after drying for almost 3 h under the vacuum. The HREM examined the obtained crystals, which can be synthesized by the hydrothermal method. The image of synthesized zirconium oxide

( $ZrO_2$ ) nanoparticles was taken with the help of TEM by this constituent part mass of nanoparticles from 5 to 6 nm [41].

**2.7. Synthesis of Nanocrystalline by Sol-Gel Method with Organic Precursor.** In manufacturing zirconium nanoparticles, the current research developed the sol-gel process with organic extracts such as glucose and fructose (an example of monosaccharides) as two organic additives [42]. The existence of these organic precursors created some positive effects. The transition phase of the crystal altered from tetragonal to monoclinic, determining the shape and crystallinity bulk of the nanoparticles. Zirconium nanoparticles were synthesized using various techniques, including precipitation, combustion analysis, inert gas condensation, sol-gel, and thermal decomposition. However, the sol-gel method is the most effective for synthesizing nanosize particles, including nanoceramics, nanozirconium, and nanotitanium [43]. The crystalline size, phase, and other characteristics of zirconium nanoparticles depend on the precursor, thermal property, and pH during hydrolysis. By the sol-gel method, zirconium's physical properties, homogeneity, and purity are controllable at low temperatures [44]. Hydrolysis of sucrose in the presence of glucose and fructose yielded cubic phase zirconium nanoparticles; sucrose hydrolyzed into gluconic acid, a chelating form, which then turned into a complex form when combined with metals. The layer form of pectin surrounds this obtained complex, so by this, the process of agglomeration was stopped. Glucose and fructose are comparatively inexpensive [45] and are proposed as organic additives. The additives proposed are also nontoxic, easy to store at room temperature and properly delivered, and polar, so water-soluble. The proposed sol-gel solution is naturally approachable and requires 15-20 h, two major advantages. Organic additives cause particles to take on a spherical shape, reach a reasonably constant size, and reduce the crystalline size in the range of 10–30 nm. Then, the agglomeration of the particles would be stopped because there are efficient agents for capping [46]. Because of this, the size of the particles is reduced, and as a result, the phase transition that occurs at high temperatures where the structural property changes from tetragonal form to monoclinic form is avoided.

Zirconium salt used is zirconium propoxide which is cheaper than others such as zirconium nitrate and zirconium chloride. Initially, n-propanol and n-isopropoxide were mixed in such a way zirconium in the form n-isopropoxide was diluted by using the zirconium precursor, which was 30 wt% [47]. Then, adding ammonia ( $\text{NH}_3$ ) and water, the mixture was diluted with distilled water in the 9–10 pH range. For the hydrolysis, the volume ratio was 1:4 volume zirconium in n-propoxide form and water ( $\text{H}_2\text{O}$ ) was used. The mass ration of 1:1 of glucose to fructose was added in the mixture during vigorous stirring after the homogenization of the solution mixture at continuously stirred at low temperature for several hours [48]. The obtained gel was then polymerized and dried in the oven for 12 h at  $110^\circ\text{C}$  temperature. The temperature ranged from 300 to  $700^\circ\text{C}$ . All the sample mixture was calcinated. The characterization techniques used are XRD, SEM, transmission electron microscope [49], photoluminescence, and infrared for characterizing the synthesized sample.

**2.8. Synthesis of Zirconium Nanoparticles by Coprecipitation Method.** The process of coprecipitation involves using a precipitating medium to precipitate the oxo-hydroxide phase from a salt precursor such as chloride and nitride of metal salt solution in a solvent like water and sodium hydroxide. There is a period of nucleation that is accompanied by a stage of growth of nanoparticles which can be attained at the point of critical species concentration of the solution. The  $\text{ZrO}_2$  nanoparticles have been created with coprecipitation [50]. The  $\text{ZrO}_2$ -CeO was synthesized by two different methods: first one is by sol-gel method, and second one is by coprecipitation method. In the coprecipitation and sol-gel synthesis route of the obtained materials, it was reported that the texture and structural properties depend on the precursor and synthetic routes. The research, classification, and antiseptic features of MgO- $\text{ZrO}_2$  oxide nanoparticles have been examined [51]. The antiseptic analysis was recorded after the experiment to demonstrate that the blended nanoparticles have been used to produce infectious diseases by E. coli. The usefulness of suspension desiccating in preventing powder agglomeration and the development of nanostructure in moderately stabilized zirconium form solid solutions established by coprecipitation were studied [52].

**2.9. Hydrothermal Method.** The hydrothermal process is a solvothermal synthetic route used to formulate multiple nanomaterials. This process involves separating the preliminary material in an acceptable solvent and then subjecting it to temperatures ( $T$ ) and pressures ( $p$ ) that are reasonably high. This creates the conditions that lead to the formation of nanoparticles. Machmudah et al. investigated that hydrothermal synthesizing cesium and zirconium combine oxide and stated that the greater part of the units produced is subject to the temperature provided. Zheng et al. studied that zirconium in the form of mixed oxide organized by constant hydrothermal synthesis method has been investigated utilizing a catalyst in supercritical water [53]. Due to its thinly agglomerated morphology and its potential use as a catalytic agent, it has been stated that the supercritical creation can

clue to zirconium mixed oxides with greater thermal strength and enhanced oxygen storing capacity. Various characterization methods have defined the dimension, crystal configuration, and morphology of the manufactured zirconium metal oxide nanoparticles [54], such as SEM, TEM, and X-ray diffraction (XRD). Researchers used different characterization tools for the characterization of prepared sample materials.

**2.10. Medical Application of Zirconium Nanoparticles.** Due to an increase in accidents and natural disasters that cause flaws in bone structure, the world's population is currently experiencing serious issues. Replacement or repair of bone defects is essential for their proper functioning. This need has spurred the extensive study of orthopedic implants, hip arthroplasty, partial and complete denature removal, radio pacifying agents, bone tissue engineering, and bone cement for biomedical applications (Figure 2) [55].

**2.11. Orthopedic Implants.** Orthopedic implants age more quickly due to crumpling and microcracking, affecting how well the implants wear over time. In the periprosthetic tissues, the particles produced by zirconia wear at contact surfaces cause macrophages to react, which causes the production of proinflammatory cytokines that stimulate osteoclastic bone resorption and osteolysis loosening of orthopedic implants. The reduction in hardness from 18 GPa to 11 GPa ended the material's microcracking. Zirconia's ageing can be stopped by paying attention to fundamental material characteristics, including density, grain size, and uniformity of the phase distribution, which are crucial for maintaining the cohesiveness of the material's particles and observing its mechanical properties [56].

**2.12. Hip Arthroplasty.** Total hip prosthesis wear is a serious clinical issue affecting many patients. Wear experiments are carried out on new biomaterials to lengthen material life in orthopedic implants to learn more about the tribological phenomena involving hip prostheses [21]. Wear debris and corrosion of biomaterial implants have been identified as a significant factor in the failure of medical implants in a recent study on total hip arthroplasty, hip prosthesis, and joint replacement. According to a study, hip replacements are predicted to rise to 5 lac by 2030 [57]. The electrochemical behavior of anodic zirconium dioxide in stimulated bodily fluid was demonstrated by a research reported by Wang and Luo. The experimental findings concluded that the increased performance of zirconia nanotubes in stabilizing zirconium-containing metals led to their application in corrosion resistance for hip arthroplasty [58].

**2.13. Radio Mollifying Agents.** The primary treatment for treating pulpal and periapical disorders is root canal therapy. It should be noted that root canal obturation affects the outcome of treatment. The main method used during the procedure to assess the root canal obturation is X-ray film. So good radiopacity is required for the intended root filling substance. Some metal dioxides, such as bismuth oxide, niobium oxide, and  $\text{ZrO}_2$ , can be suggested as excellent options for the radiopacifiers in cement-base filling material [59].



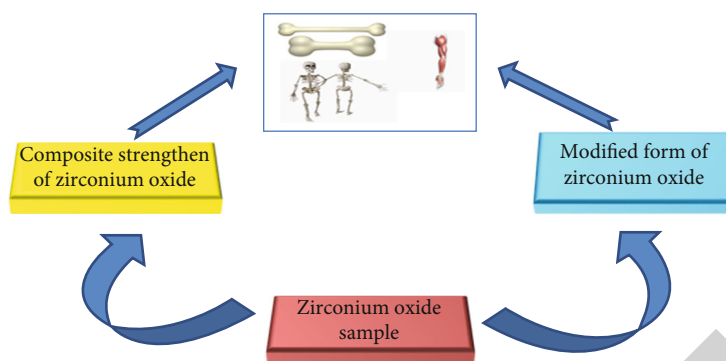


FIGURE 2: Elaborating methodology of zirconium oxide for their biological application. Problem-solving methods for orthopedic implants, bone tissue engineering, and hip prostheses are schematically shown in this figure. They are delivering a suitable response for applying a process for creating a relevant substrate with improved attributes.

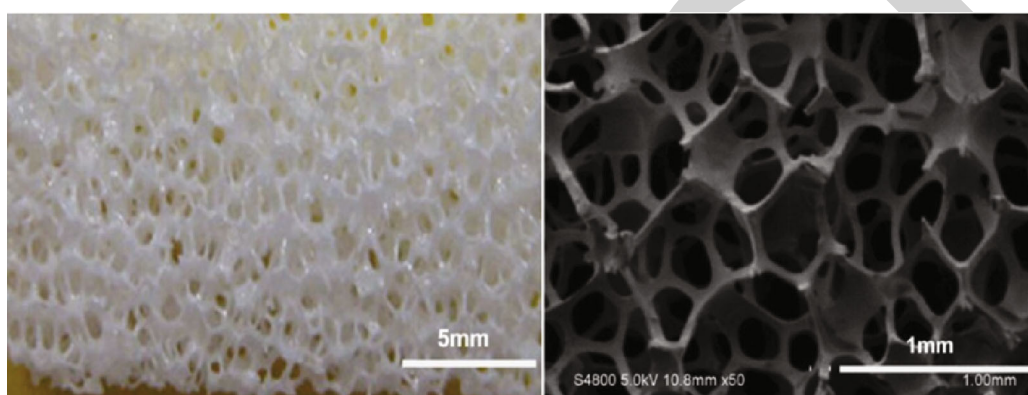


FIGURE 3: SEM image of a sintered  $ZrO_2$  scaffold with interconnectivity. SEM image of a sintered  $ZrO_2$  scaffold with interconnectivity. This explains the functionalization of zirconium dioxide used in applications for bone and tissue [60].

**2.14. Bone Tissue Engineering.** To restore, maintain, or enhance organ function, tissue engineering typically incorporates seed cells, engineering techniques, biomaterial scaffolds, and physical and chemical variables. And the best option for repairing bone abnormalities is known as bone tissue engineering. To satisfy the stressed zone criterion, biomaterial scaffolds must have sufficient mechanical strength [60]. Additionally, in order to enable the development of osteoblasts, vasculature, and new bone, these scaffolds must possess specific osteoinductivity and cytocompatibility qualities as well as the connectivity structure. Through the replication process, researchers have created porous nano- $ZrO_2$  scaffolds (Figure 3) [42].

Various materials are available for the functionalization of zirconium dioxide utilised in bone and tissue applications. The investigation's main goal is to use various functionalization techniques to promote the regeneration of broken bone or tissue, which will substantially impact the usage of ceramic materials in biomedical applications. The modified regenerated bone and tissue's biological and mechanical characteristics have been thoroughly discussed. The entire overview of the resorption process has been provided, taking into account the reactions to the resorbed products in vivo; on the contrary, the bone resorption of implants has been thoroughly examined [61].

**2.15. Bone Resorption.** Wear debris and periprosthetic osteolysis of medical implants have a significant role in loosening prosthetic implants. Zirconium dioxide is typically used to manage debris and inflammatory reactions to wear products. Comparing osteoblast, fibroblast, and macrophage cell proliferation to CoCrMo-alloy, zirconia particles perform better [62]. In osteoarthritis and rheumatoid synovial cells, Liagre et al. investigated the effects of zirconia or aluminum particles on the production of proinflammatory interleukin and the metabolism of arachidonic acid. In this study, Ramaswamy et al. investigated the attachment of human osteoclasts grown in vitro to resorbable bioceramics with various surface properties and chemical compositions to affect osteoclast resorption and the creation of resorption lacunae. Specifically, the researchers were interested in how these factors could affect the resorption of bone. Using a mouse coculture with osteoblast-like cells on bone slices, Sabokbar et al. showed how the addition of zirconium dioxide nanoparticles increased tartrate-resistant acid phosphate (TRAP) expression and bone resorption in the system [63].

### 3. Conclusion

After studying the different literature for synthesizing zirconium nanoparticles, various synthetic routes were identified,

such as hydrothermal, sol-gel, laser ablation, coprecipitation, hybrid transparent coating, and wire explosion process. The materials' various properties such as shapes, size, and other desired features are controlled and regulated by precursor, solvent, and cosolvents used in synthetic routes and temperature. Different characterization tools were used, such as X-ray diffraction, scanning electron microscopy, transmission electron microscopy, and FTIR. The bulk of the synthesized nanoparticles was determined by TEM. The combination of metal oxide has synthesized zirconium and metal nitride. These have various applications in different fields, such as antimicrobial and industrial applications.

## Data Availability

The data will be available to the readers upon request from the first author.

## Conflicts of Interest

The authors declare there is no conflict of interest.

## Acknowledgments

The authors are thankful to Dr. Sohail Nadeem, University of Management and Technology, for providing technical and scientific support in this study.

## References

- [1] M. Mahdavi, M. Ramazani, and Z. Darvishi, "Synthesis and characterization of zirconium carbide nanorods at low temperature," *International Journal of Refractory Metals and Hard Materials*, vol. 56, pp. 59–62, 2016.
- [2] M. N. Tahir, L. Gorgishvili, J. Li et al., "Facile synthesis and characterization of monocrystalline cubic ZrO<sub>2</sub> nanoparticles," *Solid State Sciences*, vol. 9, no. 12, pp. 1105–1109, 2007.
- [3] M. Keshmiri, T. Troczynski, and M. Mohseni, "Oxidation of gas phase trichloroethylene and toluene using composite sol-gel TiO<sub>2</sub> photocatalytic coatings," *Journal of Hazardous Materials*, vol. 128, no. 2-3, pp. 130–137, 2006.
- [4] C. Hu, J. Sun, C. Long, L. Wu, C. Zhou, and X. Zhang, "Synthesis of nano zirconium oxide and its application in dentistry," *Nanotechnology Reviews*, vol. 8, no. 1, pp. 396–404, 2019.
- [5] Z. Dong, Q. Yang, M. Mei et al., "Preparation and characterization of fluoride calcium silicate composites with multi-biofunction for clinical application in dentistry," *Composites Part B: Engineering*, vol. 143, pp. 243–249, 2018.
- [6] D. Morton, S. T. Chen, W. C. Martin, R. A. Levine, and D. Buser, "Consensus statements and recommended clinical procedures regarding optimizing esthetic outcomes in implant dentistry," *The International Journal of Oral & Maxillofacial Implants*, vol. 29, pp. 186–215, 2014.
- [7] R. S. Reddy, M. Kamaraj, U. K. Mudali, S. Chakravarthy, and R. Sarathi, "Generation and characterization of zirconium nitride nanoparticles by wire explosion process," *Ceramics International*, vol. 38, no. 7, pp. 5507–5512, 2012.
- [8] J. Yamazoe, M. Nakagawa, Y. Matono, A. Takeuchi, and K. Ishikawa, "The development of Ti alloys for dental implant with high corrosion resistance and mechanical strength," *Dental Materials Journal*, vol. 26, no. 2, pp. 260–267, 2007.
- [9] M. Hisbergues, S. Vendeville, and P. Vendeville, "Zirconia: established facts and perspectives for a biomaterial in dental implantology," *Journal of Biomedical Materials Research Part B: Applied Biomaterials*, vol. 88B, no. 2, pp. 519–529, 2009.
- [10] V. Sollazzo, A. Palmieri, F. Pezzetti et al., "Genetic effect of zirconium oxide coating on osteoblast-like cells," *Journal of Biomedical Materials Research Part B: Applied Biomaterials*, vol. 84B, no. 2, pp. 550–558, 2008.
- [11] A. Zembic, I. Sailer, R. E. Jung, and C. H. F. Hämmerle, "Randomized-controlled clinical trial of customized zirconia and titanium implant abutments for single-tooth implants in canine and posterior regions: 3-year results," *Clinical Oral Implants Research*, vol. 20, no. 8, pp. 802–808, 2009.
- [12] R. L. Siegel, K. D. Miller, S. A. Fedewa et al., "Colorectal cancer statistics, 2017," *CA: a Cancer Journal for Clinicians*, vol. 67, no. 3, pp. 177–193, 2017.
- [13] R. van Brakel, H. J. Noordmans, J. Frenken, R. de Roode, G. C. de Wit, and M. S. Cune, "The effect of zirconia and titanium implant abutments on light reflection of the supporting soft tissues," *Clinical Oral Implants Research*, vol. 22, no. 10, pp. 1172–1178, 2011.
- [14] G. Theunissen, J. Bouma, A. Winnubst, and A. Burggraaf, "Mechanical properties of ultra-fine grained zirconia ceramics," *Journal of Materials Science*, vol. 27, no. 16, pp. 4429–4438, 1992.
- [15] Y. Sim, J. Yoo, J.-M. Ha, and J. C. Jung, "Oxidative coupling of methane over LaAlO<sub>3</sub> perovskite catalysts prepared by a coprecipitation method: effect of co-precipitation pH value," *Journal of Energy Chemistry*, vol. 35, pp. 1–8, 2019.
- [16] S. Allahyari, M. Haghghi, A. Ebadi, and S. Hosseinzadeh, "Ultrasound assisted co-precipitation of nanostructured CuO-ZnO- Al<sub>2</sub>O<sub>3</sub> over HZSM-5: effect of precursor and irradiation power on nanocatalyst properties and catalytic performance for direct syngas to DME," *Ultrasonics Sonochemistry*, vol. 21, no. 2, pp. 663–673, 2014.
- [17] K. Swaroop and H. Somashekarappa, "Effect of pH values on surface morphology and particle size variation in ZnO nanoparticles synthesised by co-precipitation method," *Research Journal of Recent Sciences*, vol. 2277, p. 2502, 2015.
- [18] L. Habte, N. Shiferaw, D. Mulatu, T. Thenepalli, R. Chilakala, and J. W. Ahn, "Synthesis of nano-calcium oxide from waste eggshell by sol-gel method," *Sustainability*, vol. 11, no. 11, p. 3196, 2019.
- [19] H. Dislich and E. Hussmann, "Amorphous and crystalline dip coatings obtained from organometallic solutions: procedures, chemical processes and products," *Thin Solid Films*, vol. 77, no. 1-3, pp. 129–140, 1981.
- [20] J. E. Lofgreen and G. A. Ozin, "Controlling morphology and porosity to improve performance of molecularly imprinted sol-gel silica," *Chemical Society Reviews*, vol. 43, no. 3, pp. 911–933, 2014.
- [21] S. Affatato, A. Ruggiero, and M. Merola, "Advanced biomaterials in hip joint arthroplasty. A review on polymer and ceramics composites as alternative bearings," *Composites Part B: Engineering*, vol. 83, pp. 276–283, 2015.
- [22] J.-H. Park, S. Park, K. Lee, K.-D. Yun, and H.-P. Lim, "Antagonist wear of three CAD/CAM anatomic contour zirconia ceramics," *The Journal of Prosthetic Dentistry*, vol. 111, no. 1, pp. 20–29, 2014.
- [23] O. Vasylykiv and Y. Sakka, "Synthesis and colloidal processing of zirconia nanopowder," *Journal of the American Ceramic Society*, vol. 84, no. 11, pp. 2489–2494, 2001.

- [24] M. M. Gad, A. Rahoma, A. M. Al-Thobity, and A. S. ArRejaie, "Influence of incorporation of ZrO<sub>2</sub> nanoparticles on the repair strength of polymethyl methacrylate denture bases," *International Journal of Nanomedicine*, vol. 11, pp. 5633–5643, 2016.
- [25] W. Huang, J. Yang, X. Meng et al., "Effect of the organic additions on crystal growth behavior of ZrO<sub>2</sub> nanocrystals prepared via sol-gel process," *Chemical Engineering Journal*, vol. 168, no. 3, pp. 1360–1368, 2011.
- [26] C. I. Ossai and N. Raghavan, "Nanostructure and nanomaterial characterization, growth mechanisms, and applications," *Nanotechnology Reviews*, vol. 7, no. 2, pp. 209–231, 2018.
- [27] C. Duran, J. Yu, K. Sato, Y. Hotta, and K. Watari, "Hydrothermal synthesis of nano ZrO<sub>2</sub> powders," in *Key Engineering Materials*, pp. 195–198, Trans Tech Publ, 2006.
- [28] S. Manjunatha, R. H. Krishna, T. Thomas, B. Panigrahi, and M. Dharmaprakash, "Moss-Burstein effect in stable, cubic ZrO<sub>2</sub>: Eu<sup>+3</sup> nanophosphors derived from rapid microwave-assisted solution-combustion technique," *Materials Research Bulletin*, vol. 98, pp. 139–147, 2018.
- [29] H. Liu and Q. Xue, "Investigation of the crystallization of ZrO<sub>2</sub>(Y<sub>2</sub>O<sub>3</sub> 33 Mol%) nanopowder," *Journal of Materials Research*, vol. 11, no. 4, pp. 917–921, 1996.
- [30] S. Shukla and S. Seal, "Thermodynamic tetragonal phase stability in sol-gel derived nanodomains of pure zirconia," *The Journal of Physical Chemistry B*, vol. 108, no. 11, pp. 3395–3399, 2004.
- [31] M. Yoshimura and S. Sōmiya, "Hydrothermal synthesis of crystallized nano-particles of rare earth-doped zirconia and hafnia," *Materials Chemistry and Physics*, vol. 61, no. 1, pp. 1–8, 1999.
- [32] C. J. Szepesi and J. H. Adair, "High yield hydrothermal synthesis of nano-scale zirconia and YTZP," *Journal of the American Ceramic Society*, vol. 94, no. 12, pp. 4239–4246, 2011.
- [33] J. W. Mclean, "New dental ceramics and esthetics," *Journal of Esthetic and Restorative Dentistry*, vol. 7, no. 4, pp. 141–149, 1995.
- [34] M. Guazzato, M. Albakry, S. P. Ringer, and M. V. Swain, "Strength, fracture toughness and microstructure of a selection of all-ceramic materials. Part II. Zirconia-based dental ceramics," *Dental Materials*, vol. 20, no. 5, pp. 449–456, 2004.
- [35] M. H. M. Daud, Y. H. Zenn, J. Q. Zaman, N. Yahaya, and A. Mughtar, "Evaluation of shear bond strength of a novel nano-zirconia and veneering ceramics," *Ceramics International*, vol. 43, no. 1, pp. 1272–1277, 2017.
- [36] C. Zhou, P. Xie, Y. Chen, Y. Fan, Y. Tan, and X. Zhang, "Synthesis, sintering and characterization of porous nano-structured CaP bioceramics prepared by a two-step sintering method," *Ceramics International*, vol. 41, no. 3, pp. 4696–4705, 2015.
- [37] G. F. Gao, B. Zhao, D. H. Xiang, and Q. H. Kong, "Research on the force characteristics in ultrasonic grinding nano-zirconia ceramics," in *Key Engineering Materials*, pp. 258–262, Trans Tech Publ, 2008.
- [38] W. Q. Yan, T. Nakamura, M. Kobayashi, H. M. Kim, F. Miyaji, and T. Kokubo, "Bonding of chemically treated titanium implants to bone," *Journal of Biomedical Materials Research*, vol. 37, no. 2, pp. 267–275, 1997.
- [39] H. M. Wong, Y. Zhao, V. Tam et al., "In vivo stimulation of bone formation by aluminum and oxygen plasma surface-modified magnesium implants," *Biomaterials*, vol. 34, no. 38, pp. 9863–9876, 2013.
- [40] A. Kirsten, A. Hausmann, M. Weber, J. Fischer, and H. Fischer, "Bioactive and thermally compatible glass coating on zirconia dental implants," *Journal of Dental Research*, vol. 94, no. 2, pp. 297–303, 2015.
- [41] J. Lee, J. H. Sieweke, N. A. Rodriguez et al., "Evaluation of nano-technology-modified zirconia oral implants: a study in rabbits," *Journal of Clinical Periodontology*, vol. 36, no. 7, pp. 610–617, 2009.
- [42] A. Hasan, A. Memic, N. Annabi et al., "Electrospun scaffolds for tissue engineering of vascular grafts," *Acta Biomaterialia*, vol. 10, no. 1, pp. 11–25, 2014.
- [43] M. Okamoto and B. John, "Synthetic biopolymer nanocomposites for tissue engineering scaffolds," *Progress in Polymer Science*, vol. 38, no. 10-11, pp. 1487–1503, 2013.
- [44] S. Gu, B. J. Rasimick, A. S. Deutsch, and B. L. Musikant, "Radiopacity of dental materials using a digital X-ray system," *Dental Materials*, vol. 22, no. 8, pp. 765–770, 2006.
- [45] M. Gad, A. S. ArRejaie, M. S. Abdel-Halim, and A. Rahoma, "The reinforcement effect of nano-zirconia on the transverse strength of repaired acrylic denture base," *International Journal of Dentistry*, vol. 2016, Article ID 7094056, 6 pages, 2016.
- [46] V. Asopa, S. Suresh, M. Khandelwal, V. Sharma, S. S. Asopa, and L. S. Kaira, "A comparative evaluation of properties of zirconia reinforced high impact acrylic resin with that of high impact acrylic resin," *The Saudi Journal for Dental Research*, vol. 6, no. 2, pp. 146–151, 2015.
- [47] M. M. Gad, S. M. Fouda, F. A. Al-Harbi, R. Nöpänkangas, and A. Raustia, "PMMA denture base material enhancement: a review of fiber, filler, and nanofiller addition," *International Journal of Nanomedicine*, vol. 12, pp. 3801–3812, 2017.
- [48] Q. Li, A. D. Deacon, and N. J. Coleman, "The impact of zirconium oxide nanoparticles on the hydration chemistry and biocompatibility of white Portland cement," *Dental Materials Journal*, vol. 32, no. 5, pp. 808–815, 2013.
- [49] H. Daraee, A. Eatemadi, E. Abbasi, S. Fekri Aval, M. Kouhi, and A. Akbarzadeh, "Application of gold nanoparticles in biomedical and drug delivery," *Artificial cells, nanomedicine, and biotechnology*, vol. 44, no. 1, pp. 410–422, 2016.
- [50] B. Gaihre and A. C. Jayasuriya, "Comparative investigation of porous nano-hydroxyapatite/chitosan, nano-zirconia/chitosan and novel nano-calcium zirconate/chitosan composite scaffolds for their potential applications in bone regeneration," *Materials Science and Engineering: C*, vol. 91, pp. 330–339, 2018.
- [51] A. S. Keiteb, E. Saion, A. Zakaria, and N. Soltani, "Structural and optical properties of zirconia nanoparticles by thermal treatment synthesis," *Journal of Nanomaterials*, vol. 2016, Article ID 1913609, 6 pages, 2016.
- [52] R. Espinoza-González, D. E. Diaz-Droguett, J. Avila, C. A. Gonzalez-Fuentes, and V. Fuenzalida, "Hydrothermal growth of zirconia nanobars on zirconium oxide," *Materials Letters*, vol. 65, no. 14, pp. 2121–2123, 2011.
- [53] Y. Zheng, Y. Cheng, Y. Wang et al., "Quasicubic  $\alpha$ -Fe<sub>2</sub>O<sub>3</sub> nanoparticles with excellent catalytic performance," *The Journal of Physical Chemistry B*, vol. 110, no. 7, pp. 3093–3097, 2006.
- [54] T. Chraska, A. H. King, and C. C. Berndt, "On the size-dependent phase transformation in nanoparticulate zirconia," *Materials Science and Engineering: A*, vol. 286, no. 1, pp. 169–178, 2000.

## Retraction

# Retracted: Evaluation of the Antiasthmatic Activity of *Carissa opaca* in Animal Models

### BioMed Research International

Received 8 January 2024; Accepted 8 January 2024; Published 9 January 2024

Copyright © 2024 BioMed Research International. This is an open access article distributed under the Creative Commons Attribution License, which permits unrestricted use, distribution, and reproduction in any medium, provided the original work is properly cited.

This article has been retracted by Hindawi following an investigation undertaken by the publisher [1]. This investigation has uncovered evidence of one or more of the following indicators of systematic manipulation of the publication process:

- (1) Discrepancies in scope
- (2) Discrepancies in the description of the research reported
- (3) Discrepancies between the availability of data and the research described
- (4) Inappropriate citations
- (5) Incoherent, meaningless and/or irrelevant content included in the article
- (6) Manipulated or compromised peer review

The presence of these indicators undermines our confidence in the integrity of the article's content and we cannot, therefore, vouch for its reliability. Please note that this notice is intended solely to alert readers that the content of this article is unreliable. We have not investigated whether authors were aware of or involved in the systematic manipulation of the publication process.

Wiley and Hindawi regrets that the usual quality checks did not identify these issues before publication and have since put additional measures in place to safeguard research integrity.

We wish to credit our own Research Integrity and Research Publishing teams and anonymous and named external researchers and research integrity experts for contributing to this investigation.







The corresponding author, as the representative of all authors, has been given the opportunity to register their agreement or disagreement to this retraction. We have kept a record of any response received.

### References

- [1] M. Ali, U. Salma, I. A. Khan et al., "Evaluation of the Antiasthmatic Activity of *Carissa opaca* in Animal Models," *BioMed Research International*, vol. 2022, Article ID 7011789, 8 pages, 2022.

## Research Article

# Evaluation of the Antiasthmatic Activity of *Carissa opaca* in Animal Models

Muddassar Ali,<sup>1</sup> Umme Salma,<sup>1</sup> Irfan Amir Khan,<sup>1</sup> Taseer Ahmad,<sup>2</sup> Kashif Bashir <sup>1</sup>,  
Taous Khan <sup>1</sup>, Mater H. Mahnashi <sup>3</sup>, Abdulaziz H. Alhasaniah <sup>4</sup>, Ahmed A. Al Awadh,<sup>4</sup>  
Ibrahim A. Almazni,<sup>4</sup> Mohammed M. Alshahrani <sup>4</sup>, and Abdul Jabbar Shah <sup>1</sup>

<sup>1</sup>Cardiovascular Research Group, Department of Pharmacy, COMSATS University Islamabad, Abbottabad Campus, 22060 KPK, Pakistan

<sup>2</sup>Department of Pharmacology, College of Pharmacy, University of Sargodha, University Road, Sargodha, Punjab 40100, Pakistan

<sup>3</sup>Department of Pharmaceutical Chemistry, College of Pharmacy, Najran University, Najran, Saudi Arabia

<sup>4</sup>Department of Clinical Laboratory Sciences, Faculty of Applied Medical Sciences, Najran University, 1988, Najran 61441, Saudi Arabia

Correspondence should be addressed to Abdul Jabbar Shah; jabbarshah@cuiatd.edu.pk

Received 8 July 2022; Accepted 20 August 2022; Published 6 September 2022

Academic Editor: Nauman Rahim Khan

Copyright © 2022 Muddassar Ali et al. This is an open access article distributed under the Creative Commons Attribution License, which permits unrestricted use, distribution, and reproduction in any medium, provided the original work is properly cited.

*Carissa opaca* Stapf ex Haines (*C. opaca*) fruit is used traditionally in the treatment of respiratory illnesses including asthma. However, there is no scientific evidence supporting its antiasthmatic activity. The current study was conducted to evaluate its antiasthmatic effects using *in vivo* and *in vitro* approaches. The methanolic crude extract of *C. opaca* fruit (Co.Cr.) was used and *in vivo* antiasthmatic activity was carried out using ovalbumin- (OVA-) sensitized and OVA-challenged BALB/c mice. In *in vitro* bronchorelaxant activity of crude extract, aqueous and n-hexane fractions of *C. opaca* were carried out on isolated rat tracheal strips. Co.Cr. (200 and 400 mg/kg) attenuated ovalbumin-induced changes in lung histochemistry with % decrease in peribronchial inflammation of  $14.1 \pm 0.21$  and  $65.8 \pm 0.22$  and % decrease in total inflammatory cell count of  $35.7 \pm 2.80$  and  $53.3 \pm 2.30$  in bronchoalveolar lavage fluid. Co.Cr., aqueous, and n-hexane fraction of *C. opaca* attenuated the precontractions induced by high  $K^+$  (80 mM) and carbachol (1  $\mu$ M), respectively. In conclusion, the results showed that *C. opaca* possesses antiasthmatic activity via relaxant effect on bronchial smooth muscle which is mediated through calcium channel blockade and antimuscarinic activity. This study provides scientific evidence of the traditional use of *C. opaca* in the management of allergic asthma.

## 1. Introduction

Asthma mainly involves airway inflammation, hyperresponsiveness, and remodeling with variable expiratory airflow limitation [1]. Asthma is a noncommunicable disease and is among the most common chronic diseases, affecting nearly 334 million people worldwide [2]. In this disease, infiltration of eosinophils into the airways occurs which release several inflammatory mediators. The result is airway inflammation, hypertrophy of airway smooth muscle, goblet cell hyperplasia, and fibrosis [3, 4]. The drugs currently used for asthma have number of side effects when used on long-

term basis. So, there is a growing interest on antiasthmatic potential from natural sources. *C. opaca* belongs to family Apocynaceae [5, 6]. It is locally known as “Garanda.” *C. opaca* is an evergreen thorny shrub with alternate leaves. Ripe fruit is edible and has a sweet-sour taste [6]. *C. opaca* is found in India, Myanmar, Sri Lanka, and Pakistan [7]. The reported pharmacological effects of *C. opaca* are antioxidant [8], hepatoprotective [9], wound healing [10], antimicrobial [6, 11], anticancer [11], cardioprotective [12], enzyme inhibitory [13], vasorelaxant [14], and anti-inflammatory [15]. *C. opaca* leaves and fruit possess a traditional claim in the management of asthma [16, 17].

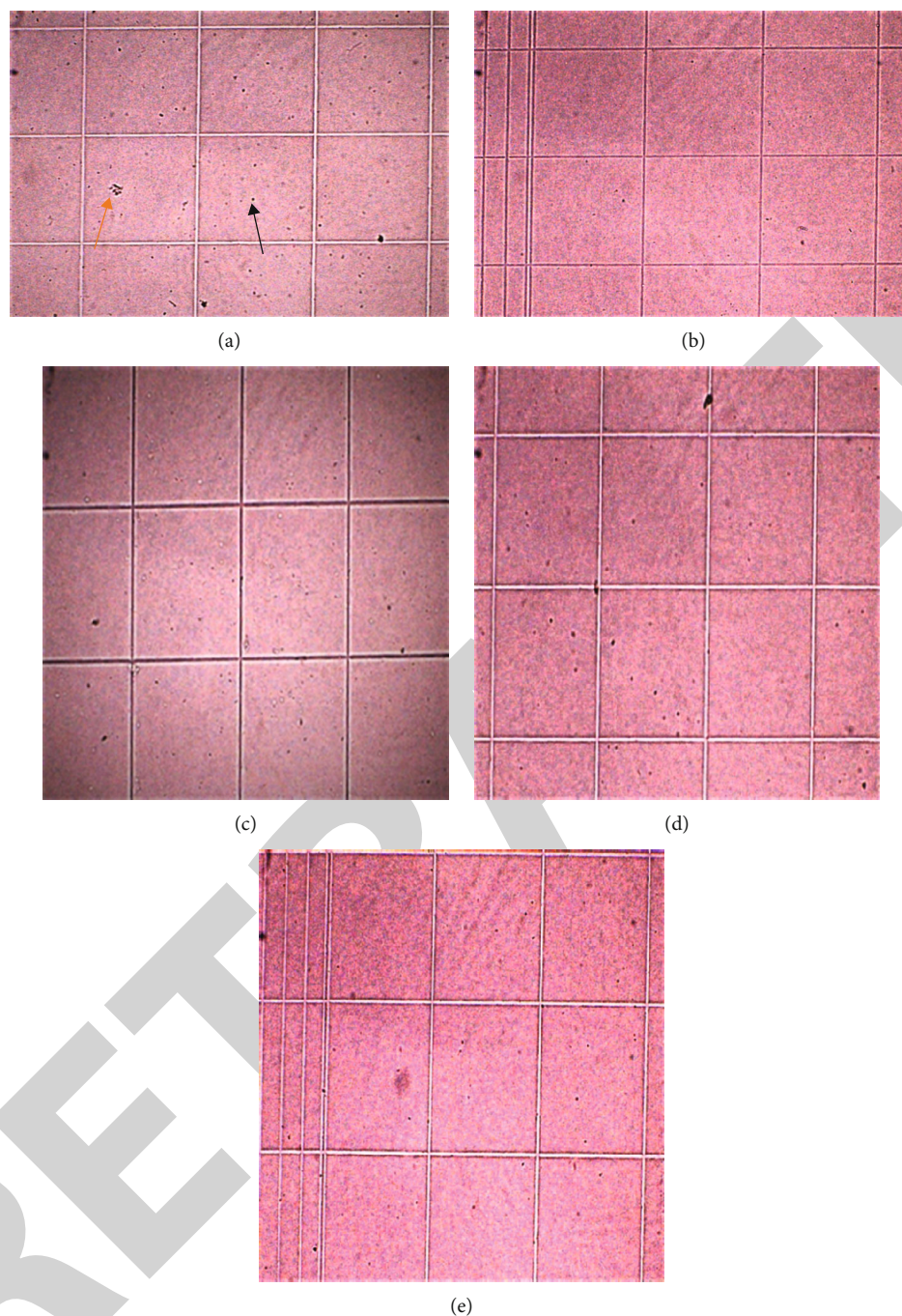


FIGURE 1: Hemacytometer field image (40 $\times$ ) of leukocytes in BALF (dilution factor 10) of OVA-sensitized and OVA-challenged (a) vehicle, (b) dexamethasone (2 mg/kg), (c) *C. opaca* 100 mg/kg, (d) 200 mg/kg, and (e) 400 mg/kg treated BALB/c mice. Arrow points to leukocyte (black) and cluster of leukocytes (orange).

However, to date, there is no scientific evidence of its anti-asthmatic activity. Thus, this study was aimed to explore the *in vivo* and *in vitro* antiasthmatic activities of *C. opaca*.

## 2. Materials and Methods

**2.1. Standard Chemicals.** The chemicals required for the study were ovalbumin (OVA) (Sigma-Aldrich), dexamethasone as sodium succinate (OBS, Pakistan), aluminum

hydroxide (Al(OH)<sub>3</sub>), carbamylcholine chloride (carbachol) (Alfa Aesar, Germany), dimethyl sulfoxide (DMSO) (Sigma-Aldrich), Harris hematoxylin and eosin (DIACHEM, Diagnostic division, Lahore, Pakistan), and ethanol (Sigma-Aldrich).

**2.2. Experimental Animals.** Female BALB/c mice (20-25 g) and Sprague-Dawley (200-250 g) rats were used which were kept in the animal house of the Department of Pharmacy,

CUI, Abbottabad. The standard diet was provided to animals, and temperature was maintained at 20-25°C. Experiments were performed in compliance with the rulings of the Institute of Laboratory Animal Resources, Commission on Life Sciences, National Research Council (NRC, 1996), and approved by the Ethical Committee of Department of Pharmacy, CUI, Abbottabad, in its meeting held on 17-06-2013 video notification EC/PHM/07-2013/CIIT/ATD.

**2.3. Collection, Extraction, and Fractionation of Plant Material.** The ripe *C. opaca* fruit was gathered from Murree in the month of March, 2016. It was made dust-free by washing with distilled water. The fruit was shade dried at 20-25°C and then crushed. The powder thus obtained was subjected to cold maceration with methanol for 21, 7, and 3 days successively with repeated agitation and shaking. The obtained methanolic crude extract underwent filtration by muslin cloth which is followed by Grade 1 Whatman filter paper. The filtrate thus obtained was concentrated using a rotary evaporator at 35°C under reduced pressure. The concentrated methanolic crude extract underwent fractionation by using solvents such as n-hexane, chloroform, and ethyl acetate in terms of increasing polarity.

**2.4. Preliminary Phytochemical Tests.** Preliminary phytochemical tests were performed for detecting the presence of phytochemical constituents like tannins, saponins, phenolic compounds, glycosides, alkaloids, and terpenoids by using the standard procedures [18].

**2.5. Acute Toxicity Study.** BALB/c mice were fasted overnight and divided into 6 groups ( $n = 3 - 5$ ). Group 1 received normal saline (10 mL/kg). Groups 2, 3, 4, 5, and 6 were administered with 500, 1000, 1500, 2000, and 5000 mg/kg, respectively, of crude extract of *C. opaca* (Co.Cr.). After that, mice were assessed for different signs, i.e., behavioral and neurological, for 24 hours [19].

## 2.6. In Vivo Antiasthmatic Activity

**2.6.1. Investigation of the Effect of Co.Cr. in Ovalbumin-Sensitized and Ovalbumin-Challenged BALB/c Mice.** In this protocol, female BALB/c mice (20-25 g) with  $n = 6$  were used and divided into 5 groups. Group 1 was vehicle treated, and group 2 was standard treated, while groups 3, 4, and 5 were treatment groups. All groups received ovalbumin (20 µg, i.p.) and 2 mg aluminum hydroxide (Al(OH)<sub>3</sub>) prepared in 200 µL sterile normal saline on days 1, 7, and 14. From days 15-21, these groups were exposed to 5% ovalbumin in the form of aerosol for 30 min in a chamber. Group 1 was given 200 µL i.p normal saline 30 min before 5% ovalbumin challenge for 7 days. Group 2 received dexamethasone (2 mg/kg, i.p.) 15 minutes before 5% ovalbumin challenge for 7 days. Groups 3, 4, and 5 received Co.Cr. orally in doses of 100, 200, and 400 mg/kg/day, respectively, 30 min before 5% ovalbumin inhalation for 7 days [20].

**2.6.2. Bronchoalveolar Lavage Fluid (BALF) Collection.** After 24 hours of the last ovalbumin challenge, mice were made unconscious by thiopental sodium (100 mg/kg, i.p.). The

TABLE 1: Total leukocyte count in BALF of vehicle, dexamethasone, and different doses of Co.Cr.-treated BALB/c mice.

Group	No. of inflammatory cells/mm <sup>3</sup>
Vehicle treated	15765 ± 573
Dexamethasone 2 mg/kg	6218 ± 385***
Co.Cr. 100 mg/kg	13862 ± 422
Co.Cr. 200 mg/kg	10008 ± 416***
Co.Cr. 400 mg/kg	7154 ± 358***

All values are mean ± SEM ( $n = 6$ ) with \*\*\* $p < 0.001$ .

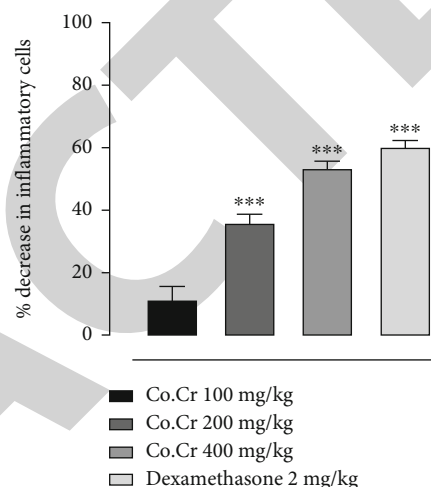


FIGURE 2: Effect of Co.Cr. (100, 200, and 400 mg/kg) and dexamethasone (2 mg/kg) on % decrease in inflammatory cells (leukocytes) in BALF of BALB/c mice model of asthma. All values are mean ± SEM with \*\*\* $p < 0.001$ . One-way ANOVA followed by Dunnett's test.

BALF was collected with ice-cold phosphate buffered saline (PBS) by aspirating PBS three times into the trachea using tracheal catheter, and fluid was collected with syringe and saved in Eppendorf tube (1.5 mL) each time. The BALF thus obtained underwent centrifugation at  $1000 \times g$  at 4°C for 10 min which results in concentration of cells at the bottom of the tube and stored at -80°C [21].

**2.6.3. Total Leukocyte Count in BALF.** For total leukocyte count, 200 µL of PBS in 1.5 mL EP tube was added to BALF and vortexed slightly to form the cell suspension. The resulting fluid was centrifuged at a condition specified before. The concentrated leukocytes were resuspended in 100-200 µL RBC lysis buffer solution and kept on ice for 10 min, which lysed RBCs, and then PBS (1 mL) was added to stop cell lysis. The leukocyte cell suspension was again centrifuged at the same rate and time as before. The BALF leukocyte concentrate thus obtained was resuspended in PBS (400 µL) from which 20 µL is taken using micropipette, and leukocytes were counted using hemocytometer under a microscope [21].

**2.6.4. Lung Histology Study.** After the collection of BALF, the lungs were inflated with 10% formalin via catheter and were

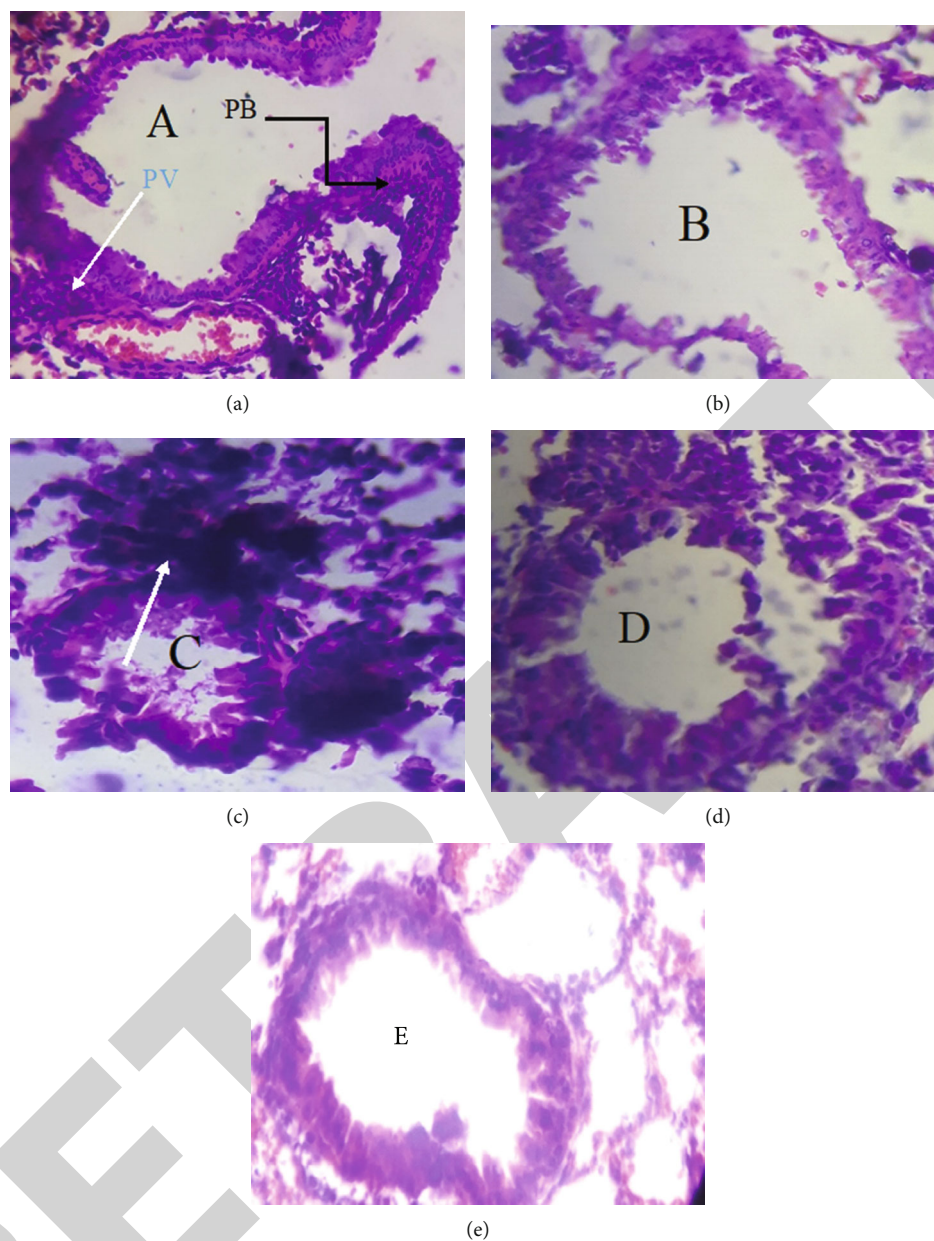


FIGURE 3: Hematoxylin and eosin (H&E) staining of representative lung sections of BALB/c mice (OVA-sensitized and OVA-challenged) of (a) vehicle, (b) dexamethasone (2 mg/kg), (c) Co.Cr. (100 mg/kg), (d) Co.Cr. (200 mg/kg), and (e) Co.Cr. (400 mg/kg) showing the effect of Co.Cr. Arrow marks are as follows: blue: inflammation around vessels and black: inflammation around bronchi.

isolated and fixed in 10% formalin for 24-48 hours followed by paraffin embedding. Thin sections ( $5\ \mu\text{m}$ ) of paraffin embedded lung samples were sliced using microtome and stained with hematoxylin and eosin, and inflammatory cell infiltration was assessed using a microscope [22]. The inflammation grade was given from 0-4, with grade 0 representing no inflammation; grade 1 representing occasional peribronchial thickening with few inflammatory cells; and grades 2 (thin layer), 3 (moderate layer), and 4 (thick layer) of inflammatory cells.

**2.7. In Vitro Bronchodilatory Activity.** Sprague-Dawley (SD) rats (200-250 g) were used for *in vitro* bronchorelaxant activ-

ity and euthanized with the help of cervical dislocation, and then, the trachea was isolated and transferred to a Petri dish containing normal Krebs solution containing carbogen. The trachea was cleaned properly and cut into 2-3 mm wide rings. The rings thus formed were opened by cutting it longitudinally from the opposite side of the smooth muscle, thus forming a strip of trachea with middle portions containing smooth muscles while cartilage on the edges. The prepared tracheal strip was mounted in a tissue bath of 10 mL containing carbogen aerated normal Krebs solution at  $37^\circ\text{C}$  and attached with PowerLab (ML 846, ADInstruments, Australia). A tension of 1 g was applied to each strip of trachea. Sustained contractions of the tracheal smooth



muscle were produced with high  $K^+$  (80 mM) and carbachol (1  $\mu$ M), and bronchorelaxant effects of Co.Cr. and different fractions of *C. opaca* were investigated on tracheal tone [23].

**2.8. Statistical Analysis.** Data was analyzed using one-way and two-way ANOVA with mean  $\pm$  SEM followed by Dunnett's and Bonferroni's post hoc test with significant  $p$  value of  $*p < 0.05$ . Nonlinear regression was applied to construct concentration-response curve (CRC) using GraphPad Prism version 6 (GraphPad, San Diego, USA).

### 3. Results

**3.1. Phytochemical Analysis of *C. opaca*.** Co.Cr. contained phytochemicals like flavonoids, saponins, terpenoids, and glycosides.

**3.2. Acute Toxicity Study.** No behavioral, neurological, and autonomic toxic effects were observed in mice which were given crude extract of *C. opaca* when compared with normal control. The crude extract was found safe up to 5000 mg/kg.

**3.3. Effect of Co.Cr. on Alteration of Total Inflammatory Cells in BALF.** Co.Cr. was evaluated for antiasthmatic activity, and total inflammatory cell count was performed using hemocytometer (Figure 1). Co.Cr. significantly decreases the inflammatory cell infiltration into lung airways (Table 1) with % decrease in inflammatory cell count of  $11.5 \pm 4.00$ ,  $35.7 \pm 2.80$ , and  $53.3 \pm 2.30$  at 100, 200, and 400 mg/kg of Co.Cr. as compared to the vehicle treated group. Dexamethasone produced  $60.3 \pm 1.88\%$  decrease in inflammatory cell count as compared to the vehicle treated group (Figure 2).

**3.3.1. Effect of Co.Cr. on Alteration in Lung Histology of Mice Sensitized and Challenged with OVA.** The histopathology of lung tissues from different groups was performed to reveal the effect of Co.Cr. on lung cytoarchitecture and airway inflammation. It was found that the crude extract preserved the cytoarchitecture (Figure 3) and prevented the airway inflammation with % fall in peribronchial inflammation score of  $6.6 \pm 0.16$ ,  $14.1 \pm 0.21$ , and  $65.8 \pm 0.22$  at 100, 200, and 400 mg/kg of *C. opaca* when compared with the vehicle treated group. Dexamethasone produced 72.5% fall in peribronchial inflammation (Figure 4).

### 3.4. In Vitro Bronchorelaxant Study

**3.4.1. Bronchorelaxant Activity of Co.Cr., Aqueous Fraction of *C. opaca* (Co.Aq.), and *n*-Hexane Fraction of *C. opaca* (Co.*n*-Hex).** The Co.Cr. showed concentration-dependent relaxant effect against high  $K^+$  (80 mM) and carbachol (CCh-) (1  $\mu$ M) induced contraction on rat tracheal strips with  $EC_{50}$  value of 3.01 (1.03-5.01) and 4.31 (3.0-5.62) mg/mL, respectively (Figure 5(a)). Co.Aq. was evaluated *in vitro* for its bronchorelaxant activity which shows bronchorelaxation against both high  $K^+$  (80 mM) and carbachol- (1  $\mu$ M) induced contractions with  $EC_{50}$  value of 6.0 (5.0-7.0) and 4.61 (4.02-5.22) mg/mL, respectively (Figure 5(b)). Co.*n*-hex showed concentration-dependent relaxation of tracheal smooth muscles against both high  $K^+$  and carbachol-

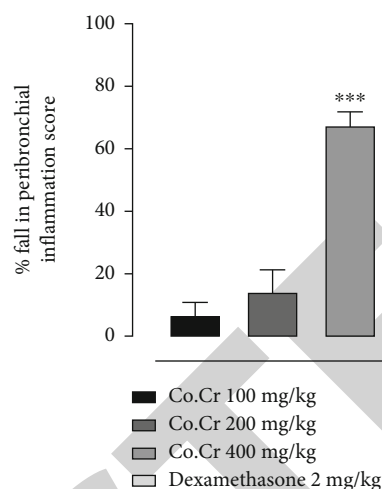


FIGURE 4: Effect of *C. opaca* crude extract (Co.Cr.) (100, 200, and 400 mg/kg) and dexamethasone on % decrease in peribronchial (PB) inflammation compared with the vehicle treated group (data not shown). All values are mean  $\pm$  SEM with \*\*\* $p < 0.001$ . One-way ANOVA followed by Dunnett's test.

induced contraction with  $EC_{50}$  value of 1.07 (0.30-1.84) and 0.08 (0.03-0.13) mg/mL, respectively (Figure 5(c)).

### 4. Discussion

*C. opaca* possesses traditional claim in the management of asthma, but it lacks any scientific evidence for the treatment of asthma. So, the current study was conducted to provide scientific evidence for its traditional use. In this regard, to evaluate *in vivo* the antiasthmatic activity of the crude extract of *C. opaca*, asthma was induced in rodent model using ovalbumin as an inducing agent. It has been well known that ovalbumin produces airway inflammation in animal models, which is comparable to human asthma [24]. Ovalbumin significantly increases the level of IL-4, IL-5, and IL-13 by activating T-cells and eosinophil infiltration into the airways which result in inflammation of airways and hyperresponsiveness, goblet cell metaplasia, and airway remodeling [25]. In this study, allergic asthma was induced in BALB/c mice using ovalbumin. The BALF was taken, and total inflammatory cell count was performed in different groups. The crude extract of *C. opaca* at the doses of 200 and 400 mg/kg significantly ( $p < 0.001$ ) inhibited the infiltration of inflammatory cells in BALF samples in comparison with dexamethasone. In addition, the histopathological study revealed that lung tissues of animals treated with crude extract of *C. opaca* preserved the cytoarchitecture and inhibited airway inflammation more efficiently to 400 mg/kg. The effects of *C. opaca* in inhibiting inflammatory cell infiltration and subsequent airway inflammation were related to dexamethasone. Thus, the *in vivo* antiasthmatic effect of *C. opaca* may be mediated through the inhibition of T-cell activation into TH<sup>2</sup> phenotype and the resulting cytokines such as IL-4, IL-5, and IL-13 [26]. Moreover, *C. opaca* contains flavonoids which have been reported to have anti-inflammatory effects through the inhibition of

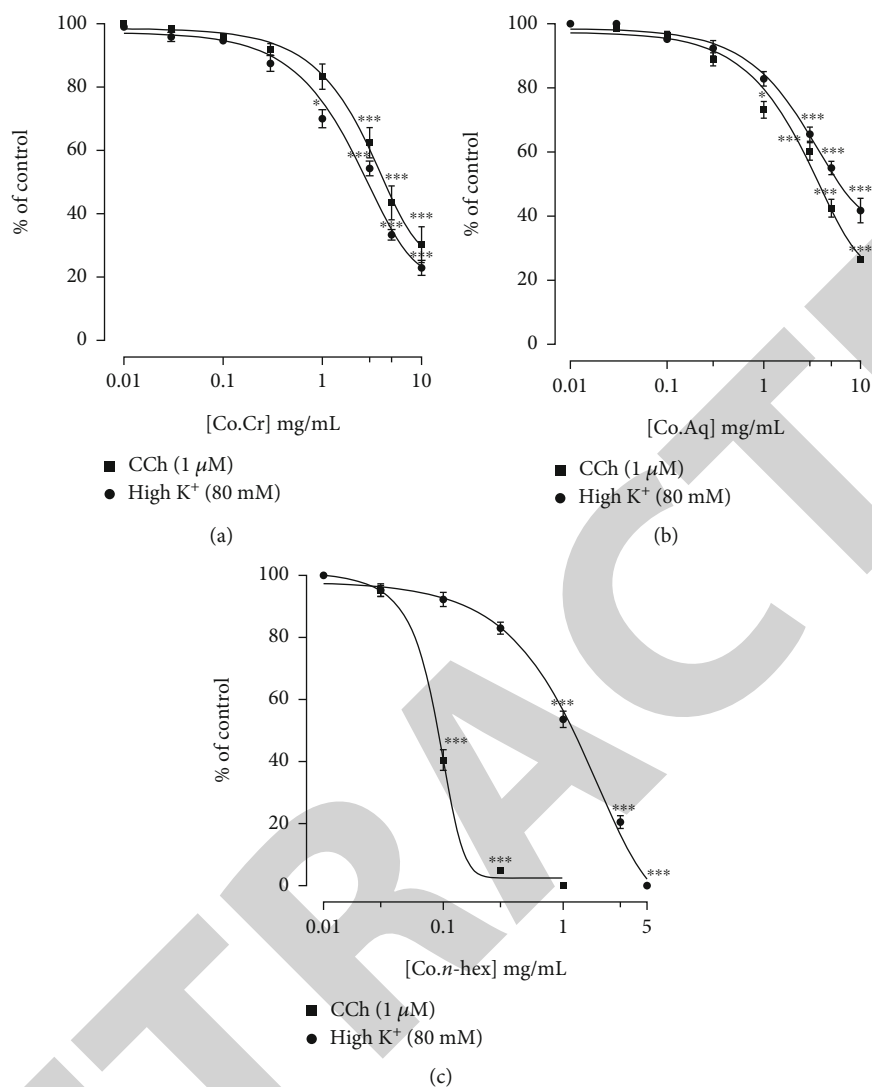


FIGURE 5: Concentration-response curves of Co.Cr. (a), Co.Aq. (b), and Co.n-hex. (c) against contractions induced by carbachol (CCh; 1  $\mu$ M) and high K<sup>+</sup> (80 mM) in isolated rat tracheal strips. All values are mean  $\pm$  SEM with \* $p$  < 0.05 and \*\*\* $p$  < 0.001. Two-way ANOVA followed by Bonferroni's post hoc test.

the production of TH<sup>2</sup> cytokines such as IL-4, IL-5, and IL-13. Moreover, the cytokines influence the level of IgE produced in response to allergen sensitization [27].

Furthermore, airway smooth muscle contributes to the pathophysiology of asthma by regulating the diameter of airways. That is why drugs like albuterol, salmeterol, and ipratropium are used for the treatment of asthma, due to the action on airway smooth muscles [28]. To find out the effect of *C. opaca* on airway smooth muscle, *in vitro* experiments were performed on isolated rat trachea, and response of crude extract and its fractions was studied against high K<sup>+</sup>. Crude extract and its fractions produced concentration-dependent relaxation against high K<sup>+</sup> which initially confirm its bronchodilator effect, mediating through calcium antagonism.

Drugs (like ipratropium) acting as muscarinic (M<sub>3</sub>) receptor antagonist are used in the treatment of asthma and bronchial hyperreactivity disorders. To investigate the cholinergic blocking effect of *C. opaca*, Co.Cr. and its frac-

tions were tested against CCh-induced contraction. Carbachol is a muscarinic (M<sub>3</sub>) receptor agonist which is coupled with Gq protein and in response activates the phospholipase C (PLC) lined IP<sub>3</sub> (inositol 1,4,5-trisphosphate) pathway [29]. So, activation of PLC results in the synthesis of IP<sub>3</sub> which mobilizes the intracellular calcium from endoplasmic reticulum (ER) which binds with calmodulin to form complex which activates myosin light-chain kinase (MLCK) resulting in the phosphorylation of myosin light chains (MLC), thus initiating the process of actin-myosin coupling and contraction. However, this intracellular calcium release is transient and only produces transient contraction. For sustained contraction, there must be sufficient Ca<sup>2+</sup> in the vicinity of the contractile machinery. Diacylglycerol (DAG) is thought to increase Ca<sup>2+</sup> concentration through voltage-gated Ca<sup>2+</sup>-dependent channels (VDCC) by activating protein kinase C (PKC). This results in sustained smooth muscle contraction [30]. This dependency on extracellular Ca<sup>2+</sup> can be evident from the fact that

carbachol produces only transient contraction in  $\text{Ca}^{2+}$ -free solution [31]. Co.Cr. and Co.Aq. were less potent against carbachol-induced contractions (as <80% response was observed at 10 mg/mL), while comparatively potent response was observed with Co.n-hex. With Co.n-hex, 100% relaxation response was observed at 1 mg/mL. This shows the presence of high level of anticholinergic constituents in Co.n-hex.

## 5. Conclusion

The current study revealed that Co.Cr. exhibits *in vivo* antiasthmatic effects possibly mediated through anti-inflammatory response and *in vitro* bronchorelaxant effect through  $\text{Ca}^{2+}$  antagonism and antimuscarinic activity. These findings provide scientific evidence to traditional use of *C. opaca* against asthma. However, additional studies are required to further probe the mechanism of *in vivo* antiasthmatic effect.

## Data Availability

Data is available on request from the corresponding author.

## Conflicts of Interest

The authors have no conflict of interest.

## Acknowledgments

The authors acknowledge the support from the Deanship of Scientific Research, Najran University, Kingdom of Saudi Arabia, for funding this work under the research collaborations funding program grant code number NU/RC/MRC/11/2.

## References

- [1] A. B. Becker and E. M. Abrams, "Asthma guidelines: the global initiative for asthma in relation to national guidelines," *Current Opinion in Allergy and Clinical Immunology*, vol. 17, no. 2, pp. 99–103, 2017.
- [2] T. To, S. Stanojevic, G. Moores et al., "Global asthma prevalence in adults: findings from the cross-sectional world health survey," *BMC Public Health*, vol. 12, no. 1, pp. 1–8, 2012.
- [3] B. N. Lambrecht and H. Hammad, "The airway epithelium in asthma," *Nature Medicine*, vol. 18, no. 5, pp. 684–692, 2012.
- [4] S. S. Athari and S. M. Athari, "The importance of eosinophil, platelet and dendritic cell in asthma," *Asian Pacific Journal of Tropical Disease*, vol. 4, pp. S41–S47, 2014.
- [5] C. P. Khare, *Indian Medicinal Plants: An Illustrated Dictionary*, Springer Science & Business Media, 2008.
- [6] D. Ahmed, A. Waheed, M. A. Chaudhary, S. R. Khan, A. Hannan, and M. Barkaat, "Nutritional and antimicrobial studies on leaves and fruit of *Carissa opaca* Stapf ex Haines," *Asian Journal of Chemistry*, vol. 23, p. 2072, 2011.
- [7] S. Izhar and D. Ahmed, "Carissa opaca: a plant with great potential for future drugs for degenerative and infectious diseases," *Chemistry Select*, vol. 1, pp. 3005–3011, 2016.
- [8] S. Sahreen, M. R. Khan, and R. A. Khan, "Evaluation of antioxidant activities of various solvent extracts of *Carissa opaca* fruits," *Food Chemistry*, vol. 122, no. 4, pp. 1205–1211, 2010.
- [9] S. Sahreen, M. R. Khan, and R. A. Khan, "Hepatoprotective effects of methanol extract of *Carissa opaca* leaves on  $\text{CCl}_4$ -induced damage in rat," *BMC Complementary and Alternative Medicine*, vol. 11, no. 1, p. 48, 2011.
- [10] R. Sanwal and A. K. Chaudhary, "Wound healing and antimicrobial potential of *Carissa spinarum* Linn. in albino mice," *Journal of Ethnopharmacology*, vol. 135, no. 3, pp. 792–796, 2011.
- [11] S. Sahreen, M. R. Khan, R. A. Khan, and N. A. Shah, "Estimation of flavonoids, antimicrobial, antitumor and anticancer activity of *Carissa opaca* fruits," *BMC Complementary and Alternative Medicine*, vol. 13, no. 1, p. 372, 2013.
- [12] S. Sahreen, M. R. Khan, R. A. Khan, and H. M. Alkreaty, "Cardioprotective role of leaves extracts of *Carissa opaca* against  $\text{CCl}_4$ -induced toxicity in rats," *BMC Research Notes*, vol. 7, no. 1, p. 224, 2014.
- [13] R. Saeed and D. Ahmed, "Bioactive compounds from *Carissa opaca* roots and xanthine oxidase and alpha-amylase inhibitory activities of their methanol extract and its fractions in different solvents," *Pharmacognosy Research*, vol. 7, no. 4, p. 295, 2015.
- [14] F. P. Ruphin, R. Baholy, R. Amelie, P. T. Mpiana, V. Mudogo, and K. T. N. Ngbolua, "Ethnobotanical survey and assessment of vasorelaxant activity of some extracts obtained from the leaves of *Carissa spinarum* L. (Apocynaceae) originated from Madagascar on isolated rat thoracic aorta," *Pharmacologia*, vol. 6, no. 3, pp. 88–96, 2015.
- [15] N. R. Beck and K. P. Namdeo, "Evaluation of *in vivo* anti-inflammatory activity of leaves extract of *Carissa spinarum* on formalin induced paw edema in albino rats," *Journal of Pharmaceutical and Biosciences*, vol. 4, no. 1, pp. 36–40, 2016.
- [16] S. Kayani, M. Ahmad, M. Zafar et al., "Ethnobotanical uses of medicinal plants for respiratory disorders among the inhabitants of Gallies–Abbottabad, Northern Pakistan," *Journal of Ethnopharmacology*, vol. 156, pp. 47–60, 2014.
- [17] S. Rashid, M. Ahmad, M. Zafar et al., "Ethnobotanical survey of medicinally important shrubs and trees of Himalayan region of Azad Jammu and Kashmir, Pakistan," *Journal of Ethnopharmacology*, vol. 166, pp. 340–351, 2015.
- [18] P. Tiwari, B. Kumar, M. Kaur, G. Kaur, and H. Kaur, "Phytochemical screening and extraction: a review," *International Pharmaceutical Sciences*, vol. 1, pp. 98–106, 2011.
- [19] P. Lalitha, S. K. Sripathi, and P. Jayanthi, "Acute toxicity study of extracts of *Eichhornia crassipes*," *Asian Journal of Pharmaceutical and Clinical Research*, vol. 5, pp. 59–61, 2012.
- [20] N. K. Singh, D. Garabadu, P. Sharma, S. K. Shrivastava, and P. Mishra, "Antiallergy and antitussive activity of *Clitoria ternatea* L. in experimental animals," *Journal of Ethnopharmacology*, vol. 224, pp. 15–26, 2018.
- [21] F. Sun, G. Xiao, and Z. Qu, "Murine bronchoalveolar lavage," *Bioprotocol*, vol. 7, no. 10, 2017.
- [22] M. Slaoui and L. Fiette, "Histopathology procedures: from tissue sampling to histopathological evaluation," *Methods in Molecular Biology*, vol. 691, pp. 69–82, 2011.
- [23] A. H. Gilani, A. U. Khan, M. Raouf et al., "Gastrointestinal, selective airways and urinary bladder relaxant effects of *Hyoscyamus niger* are mediated through dual blockade of muscarinic receptors and  $\text{Ca}^{2+}$  channels," *Fundamental & Clinical Pharmacology*, vol. 22, no. 1, pp. 87–99, 2008.
- [24] I. Kucharewicz, A. Bodzenta-Łukaszyk, and W. Buczek, "Experimental asthma in rats," *Pharmacological Reports*, vol. 60, no. 6, pp. 783–788, 2008.

## *Retraction*

# **Retracted: Study on the Practice of Enterprise Financial Management System under the Epidemic Norm Based on Artificial Neural Network**

### **BioMed Research International**

Received 8 January 2024; Accepted 8 January 2024; Published 9 January 2024

Copyright © 2024 BioMed Research International. This is an open access article distributed under the Creative Commons Attribution License, which permits unrestricted use, distribution, and reproduction in any medium, provided the original work is properly cited.

This article has been retracted by Hindawi following an investigation undertaken by the publisher [1]. This investigation has uncovered evidence of one or more of the following indicators of systematic manipulation of the publication process:

- (1) Discrepancies in scope
- (2) Discrepancies in the description of the research reported
- (3) Discrepancies between the availability of data and the research described
- (4) Inappropriate citations
- (5) Incoherent, meaningless and/or irrelevant content included in the article
- (6) Manipulated or compromised peer review

The presence of these indicators undermines our confidence in the integrity of the article's content and we cannot, therefore, vouch for its reliability. Please note that this notice is intended solely to alert readers that the content of this article is unreliable. We have not investigated whether authors were aware of or involved in the systematic manipulation of the publication process.

Wiley and Hindawi regrets that the usual quality checks did not identify these issues before publication and have since put additional measures in place to safeguard research integrity.

We wish to credit our own Research Integrity and Research Publishing teams and anonymous and named

external researchers and research integrity experts for contributing to this investigation.

The corresponding author, as the representative of all authors, has been given the opportunity to register their agreement or disagreement to this retraction. We have kept a record of any response received.

### **References**

- [1] K. Ji, "Study on the Practice of Enterprise Financial Management System under the Epidemic Norm Based on Artificial Neural Network," *BioMed Research International*, vol. 2022, Article ID 7728596, 10 pages, 2022.

## Research Article

# Study on the Practice of Enterprise Financial Management System under the Epidemic Norm Based on Artificial Neural Network

Kaiheng Ji 

Edinburgh Business School, Heriot-Watt University, UK

Correspondence should be addressed to Kaiheng Ji; [jasonji@njau.edu.cn](mailto:jasonji@njau.edu.cn)

Received 27 June 2022; Revised 18 July 2022; Accepted 8 August 2022; Published 6 September 2022

Academic Editor: Nauman Rahim Khan

Copyright © 2022 Kaiheng Ji. This is an open access article distributed under the Creative Commons Attribution License, which permits unrestricted use, distribution, and reproduction in any medium, provided the original work is properly cited.

The sudden arrival of the new crown epidemic has had a significant and long-lasting impact on the division's economic environment as well as the production and operation activities of businesses. As far as the financial management is concerned, opportunities and difficulties are faced by enterprises of all types. With reference to the available research data, enterprises have an important contribution to GDP and jobs, but they still face a series of difficulties and challenges in their development in the context of the normalization of the epidemic. By analyzing the impact of the new crown pneumonia epidemic on the financial management work of enterprises, this paper proposes an artificial neural network-based enterprise financial forecasting and early warning method to provide an effective method for enterprise financial management. For the time-series characteristics of enterprise finances, a prediction model based on long- and short-term memory networks is developed which acknowledges the necessity of combining the temporal dimension with the spatial dimension for forecasting. This model incorporates time qualities into the data to the existing forecasting model. It also considers both working and nonworking day data and thoroughly considers the factors influencing corporate finance. Then, using BP neural network for financial risk prediction, nonfinancial index factors should be added to the financial early warning model thus eliminating the limitations of the financial early warning model. At the same time, the accuracy of the prediction can be improved which is more suitable for enterprises to apply in practice. The experimental results demonstrate that the financial prediction model built by multilayer feed forward neural networks and recurrent neural networks based on error back propagation training is inferior to the prediction model built by long- and short-term memory network. Regardless of the degree of fitting or prediction accuracy, the BP neural network model outperforms the conventional model for enterprise financial warning. Under the normalization of the pandemic, the combined use of both can offer an efficient technique for enterprise management.

## 1. Introduction

Globally, the level of epidemic is accelerating the deconstruction of the original world pattern. The global economy is in deep recession, and economic globalization is encountering counter current. The protectionism and unilateralism are in full swing forcing enterprises to seek survival and development in an environment of higher uncertainty.

The new epidemic of 2020 will result in the slowing down of economic growth. In addition to this, the tensions in trade between China and the U.S. contribute those factors which brings difficulties and opportunities for Chinese busi-

ness and enterprise. On the one hand, enterprises are trying to survive dealing with unfavorable circumstances including decreased demand, declining revenue, and limited cash flow, as well as the serious issue of a disruption in the global supply chain and industrial chain. On the other hand, China has been pushed to speed up industrial upgrading due to the outstanding outcomes of epidemic prevention and control and the economic recovery brought about by trade fictions [1]. It further enhances the major strategic deployment at the national level and improves digital technology to bring new dynamic energy and provides a series of important opportunities. It helps enterprises to find opportunities in

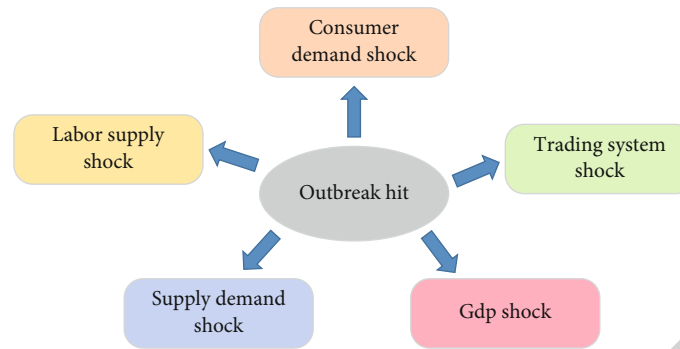


FIGURE 1: Impact of the epidemic on economic activities.

the crisis and seek development in difficulties [2]. Financial management is related to the lifeline of the whole enterprise, especially in the complex and changing economic environment, challenges, and opportunities. It is urgent to innovate and upgrade the enterprise financial management model and build a response strategy for enterprise financial management in the postepidemic era.

As a major public health emergency, the Newcastle pneumonia epidemic will undoubtedly bring significant impacts and challenges to economic development [3]. The impact of the epidemic on economic activities is mainly reflected in the following five aspects as shown in Figure 1.

- (i) Consumer demand shock: the new crown pneumonia epidemic has brought a serious impact on the consumer demand of residents [4]. Unemployment, shopping inconvenience, and wait-and-see mood will cause the consumer demand of residents to drop in the epidemic area
- (ii) Labor supply shock: similarly, a high unemployment rate brought on by an epidemic also aids in its further spread. This results in the increase of economic and social pressure on those who are unemployed
- (iii) Shocks to the supply and demand structure: during the epidemic, the number of illnesses and deaths increases rapidly. People resort to home quarantine to avoid the risk of infection. This results in a sharp decline in labor supply. As a result, some sectors of the economy that are severely affected by the epidemic cease operations. This leads to a more severe crisis in labor supply and consumer demand [5].
- (iv) Impact on regional GDP: sudden epidemics affect the stability of the economic system and impede the growth of regional GDP
- (v) Shocks to the world's commerce and economic systems: the first wave of the epidemic will cause closures and disruptions in national supply chain in areas that serve as the hubs of these networks. This creates production and consumption crises. The second wave will spread infections in more countries which will have the short-term effects of stifling

economic expansion, escalating market fear, and raising financial dangers

Traditional enterprise management places more emphasis on the analysis of enterprise development strategy while ignoring the analysis of enterprise financial management and risk mitigation. This makes it difficult for enterprises to respond quickly when they encounter serious issues [6]. According to numerous real-world examples, financial crises frequently precede enterprise crises. Financial forecasting and early warning models are used to identify hazards and notify managers of various issues so they can find them and address them quickly. These models are built using a variety of information including financial reports, audit reports, and company disclosures.

The high growth and high risk characteristics of enterprises determine that the energy market has a large risk in operation process [7]. Many financial risks do not break out suddenly and can be reflected by financial data in the early stage. The research on financial management of enterprises under the epidemic norm is not ideal even though there are more studies on financial early warning. According to some academics, financial risk has two components: the first is the risk that the company will not be able to pay its debts and obligations; the second is the danger that financial leverage factors would cause variations and fluctuations in share price earnings. One of the symptoms of financial risk is bankruptcy, which occurs automatically when a business becomes insolvent [8]. Many professionals and academics have debated and developed the study on financial forecasting and early warning models. Univariate financial models, multivariate financial models, multivariate logistic regression models, and artificial neural network forecasting models are the models that are frequently utilized in real-world applications. Among them, artificial neural networks have strong fault tolerance and low data requirements and can perfectly handle noisy and incomplete data by breaking through the limitations of traditional statistical methods [9]. Using the characteristics of self-learning, training, and simulation of neural networks, we can adapt to the changing business environment and analyze the financial management of enterprises to determine whether a predicted sample has financial risks.

Based on the above research background, the financial forecasting and early warning models of enterprises began

to receive general attention. In order to address the system and methodological issues in the financial management of enterprises operating under the pandemic norm, this study makes an effort to employ a more rigorous and persuading approach. An enterprise financial forecasting model is built by examining and utilizing LSTM networks to address the financial forecasting issue. Enterprise financial history data are fed into the model repeatedly for training, after which the predicted enterprise financial trend is realized [10].

## 2. Related Works

*2.1. The Impact of the Epidemic on the Financial Management System of Enterprises.* Financial management plays a key role for an enterprise. The basic activities of an enterprise consist of four parts. These five parts are investment, financing, operation, income, and expenditure. This division causes the further division of financial management into four parts. The first is investment management that mainly emphasizes on the capital expenditure of the enterprise. It includes investment to allocate assets for the enterprise which enables the enterprise to obtain higher productivity. The higher productivity then ultimately results into higher efficiency of the enterprise [10]. Secondly, financing management in order to expand business improves the internal management and other needs of enterprises to raise reasonable funds. For better fund raising, it is therefore necessary for enterprises to carry out financing management. Third is working capital management, which mainly manages the working capital and current liabilities of the enterprise [11]. And lastly, through the implementation of income and expenditure management, income and expenditure management can reasonably control and adjust all the economic business transactions and transactions of the whole enterprise. It also reasonably allocates the revenue of the enterprise.

It is a difficult task to integrate the financial information and related data of an enterprise to better serve the management and decision making of an enterprise through scientific and effective implementation of reasonable enterprise capital management [12]. But a major premise needed is to take information technology as the basis, so that enterprise financial data and related information can be integrated with modern information system platform. As a result, enterprises can obtain relevant information and data more systematically and accurately.

The dilemma faced by enterprise finance in the context of the epidemic includes the following four directions:

- (i) Business income of enterprises: the first thing that declined is the impact of shutdown and production suspension. Except a very small number of enterprises such as mask manufacturers, most of the remaining enterprises are stuck in the situation of shutdown and it is difficult to resume work and production
- (ii) Increase in production costs: whether it is due to a sudden public event or the impact caused by the new crown epidemic, the effect on the production

and operation of the enterprise is huge [13]. The instability in the prices of raw material also makes the production cost of enterprises unstable. The production is, therefore, affected from two aspects

- (iii) Difficulty of enterprise capital turnover: different economic situations will have different impacts on the capital turnover of enterprises. Due to the new crown epidemic, the government departments and some related enterprises will put more energy on the prevention and control of the epidemic. Therefore, the debt clearing task of the enterprise cannot be effectively implemented and completed
- (iv) Increased pressure of industrial adjustment: in the new situation of the epidemic, enterprises want to seek development and find a way out. They also seek to adjust their industrial structure and change their development strategy. Enterprises must choose this as a road to adopt [14]

The outbreak of the new crown epidemic has affected the public safety of the society. It has restricted the development of the market economy. The development of the enterprise is also at serious setback. Under the impact of the new crown epidemic, companies need to better coordinate all financial relationships, sound financial budgets and strengthen capital management. It also needs controlled labor costs and raw materials and with open source and cut costs [15].

*2.2. Current Status of Financial Forecasting Model Research.* Through study and business managers' practical knowledge of financial control in day-to-day operations, academics have offered several qualitative methods for enterprise financial forecasting. These methods include the four-stage symptom analysis method [16], the flow chart method, the analytical survey method, and the management scoring method. Despite the relatively late start of the domestic research, a number of excellent research findings have emerged, and deeper investigation and analysis of connected themes have been carried out.

The models used for corporate financial forecasting have evolved from univariate forecasting methods to multivariate forecasting methods. The application of conditional probability models such as logistic models has further improved the performance and prediction accuracy of multivariate models [17]. Artificial neural network models have been used to corporate financial forecasting in recent years in the context of big data technology and machine learning sweeping in the world. This shows better performance and increased predicting accuracy. These models include univariate model, multivariate model, discriminant analysis model, multivariate linear model, and artificial neural network model. Models are given below with detailed description.

- (i) Univariate models: based on this, some researchers continued to investigate the discriminative power of univariate model on financial crises and were the first to construct financial evaluation prediction models using statistical methods. It was concluded

that the three best indicators for predicting the financial condition of a company are the total cash-to-debt ratio, the gearing ratio, and the net profit margin of total assets

- (ii) Multivariate model: the earliest multivariate models were the Z model and the ZETA model. ZETA model was developed from the Z model. The earliest study of corporate finance using multivariate linear discriminant models was the Z model, which applied multiple discriminant variables to corporate finance forecasting models. This model collected data on five financial indicators from 33 failed companies and 33 normal companies of the same size in the manufacturing industry. It constructed a Z model that can be used to predict whether a company is in financial crisis by using a comprehensive weighted average. Based on the Z model, a researcher conducted a more in-depth study and obtained a modified ZETA model [18]
- (iii) Discriminant analysis model: the discriminant analysis is a technique for statistical identification and analysis and is used in financial forecasting. It establishes the discriminant function by using samples with known actual classification and measured observations of each indicator as training samples. The previous Z model and ZETA model are in fact a simple multivariate linear discriminant model. But discriminant analysis is not limited to this, and there are many other methods of discriminant such as maximum likelihood, distance discriminant, canonical discriminant, and Bayes discriminant
- (iv) Multivariate linear model: subsequently, domestic scholars have also adopted logistic model as a method of enterprise financial evaluation. Some researchers have used logistic model to study the financial status of agricultural enterprises after factor analysis of variable indicators and constructed an industry financial evaluation model. Based on this, a researcher used logistic regression to construct a bank financial measurement model with comprehensive monitoring of multiple indicators [19]. Other researchers added financial indicators to the financial forecasting index system and used Z-value model and logistic regression model. By comparing the results of the two financial forecasting models, it was found that the method using logistic regression has a higher accuracy rate than the Z-value model
- (v) Artificial neural network model: in recent years, the artificial neural network model has attracted more attention and has become a newcomer in the enterprise financial forecasting model [20]. Applying the classification method of neural network to the prediction and evaluation, the enterprise finance forms the artificial neural network model of prediction

2.3. *Current Status of Research on Financial Risk Early Warning Model.* Foreign security markets are established

earlier, and scholars there are more mature in financial early warning research than in China. The study of financial risks from several aspects is shown in Figure 2. In China, the study on early warning systems for financial crises is still in the embryonic stage. Despite the large number of literature, the majority of it suffers from several issues. These issues include the use of nonparametric methods. It is also challenging to reflect the complete image of an enterprise's financial state due to the lack of comprehensiveness in financial data.

We must create an integrated framework of "digital technology and traditional management tools" in terms of management tools. Management tools are the means and technologies to conduct financial activities. The use of digital technology by financial activities of enterprises is used as a means to develop ports and analysis systems to connect with business and the outside environment, to establish a new material foundation for information integration and resource allocation of financial activities, and to realize strategies and goals of digital transformation and value sharing. These all are required in order to realize digital transformation and deep integration of business and finance [21]. On the one hand, the traditional management tools such as SWOT can be used to help you understand your business. On the other hand, some other traditional management tools such as comprehensive budgeting, DuPont analysis system, balanced scorecard, job costing, and other management ideas and economic principles are not obsolete and can still play a role in making financial and business decisions to improve the efficiency, analysis, and forecasting ability with the help of digital technology [22]. Therefore, it is necessary to integrate digital technologies with traditional management tools to form a unified framework for their use. As a result, the technical means of financial activities can meet business requirements and become more comprehensive and efficient.

BP neural network method is recognized and widely used by many scholars. The BP neural network algorithm is a nonlinear mapping model which can handle experimental data with high correlation between indicators or incomplete data and produce better prediction results [23]. Compared with traditional statistical methods, BP neural network has its incomparable advantages: (1) in terms of model prediction, the BP neural network model has higher accuracy in predicting financial distress. (2) In terms of sample selection, the BP neural network model does not require the overall sample to obey a particular distribution, thus reducing the difficulty in sample selection and expanding the scope of the research object. (3) The BP neural network model can be set to a smaller size [24]. The BP neural network model can set a small systematic error. The system can find the intrinsic connection between input and output through the learning and training process based on the sample data and make self-correction according to the requirement of systematic error.

In short, it overcomes the limitations of traditional statistical methods to a certain extent and has the ability of fault tolerance and powerful functions of processing information. It is also capable of training of data information so as to predict the future financial situation.



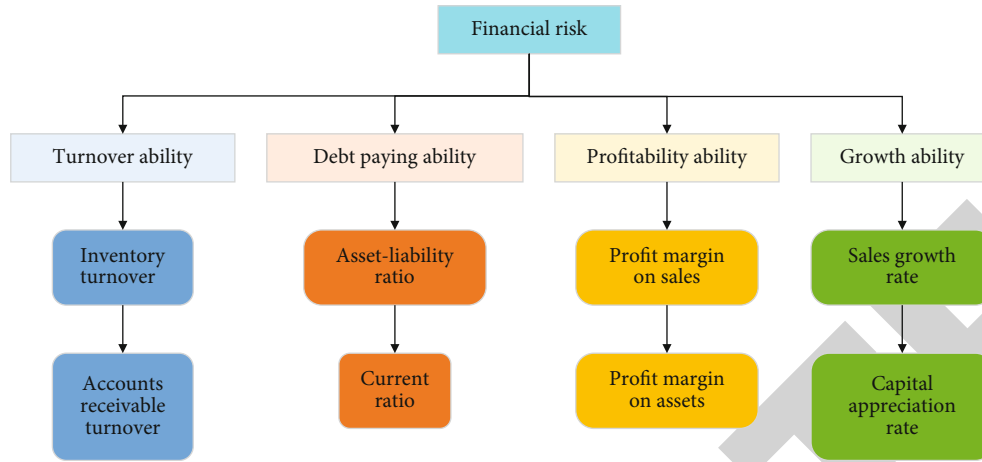


FIGURE 2: Influencing factors of financial risk.

### 3. Algorithm Design

3.1. *LSTM-Based Financial Forecasting Model.* In this section, an LSTM forecasting model is established. The model is established by adding temporal attributes in financial data to the existing forecasting model through the spatiotemporal dependencies between the starting and ending positions in the obtained enterprise financial data. Since the volume of enterprise financial data is influenced by working day and nonworking day factors, it has a strong cyclical pattern. Therefore, by studying and analyzing the data in the previous time period, it is possible to forecast the financial trends in the subsequent period [25]. The construction steps of the financial forecasting model are divided into various points given below.

- (i) Data preprocessing: prior to being smoothed and normalized, the historical financial data are first cleaned and their noise level is decreased. By determining whether the original data is volatile, this method is used to lower its volatility
- (ii) Using spatiotemporal clustering, the original data are categorized, and the data are then divided according to the categorization outcomes
- (iii) Choosing the proper activation function, defining the values of variables like learning rate, and the maximum number of iterations are some examples of ideal neural network parameters
- (iv) Training of the model: until the design criterion of the minimal gradient error calculation function is fully satisfied, the gradient weight function is updated using the minimum gradient error calculation function
- (v) Validate the model effect: financial data are special in that they depend on whether it is a working day as well as the historical time at which they were collected

The framework of the financial forecasting model constructed in this paper is schematically shown in Figure 3.

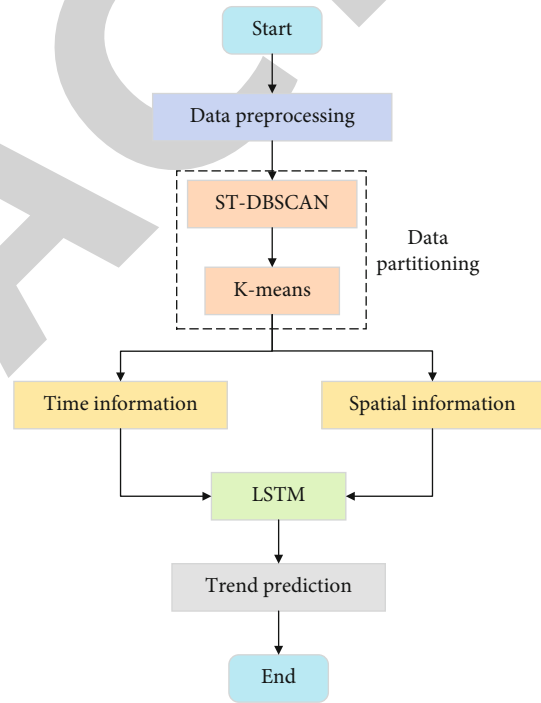


FIGURE 3: Flow chart of prediction model based on LSTM.

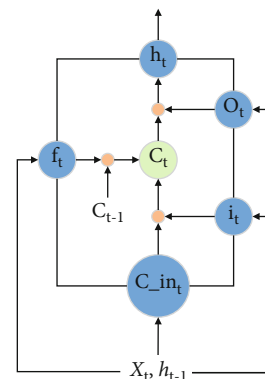


FIGURE 4: LSTM network structure diagram.

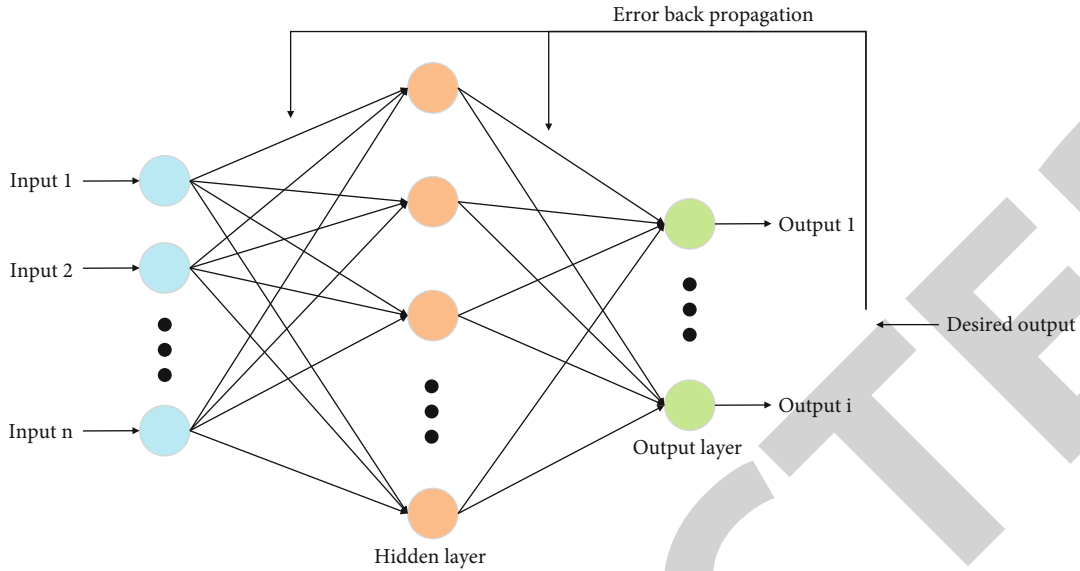


FIGURE 5: Structure of the BP neural network model.

The model first divides the financial data into 12 times series according to one day; then, the original data is divided by a quadratic spatiotemporal clustering algorithm combining ST-DBSCAN and *K*-means. The time series and spatial attributes are input as information into the prediction model of LSTM neural network which can be obtained by analyzing and training a large amount of historical information [26]. As a result, the prediction model based on quadratic spatiotemporal clustering and LSTM neural network is obtained.

A unique type of RNN network called LSTM has distinct forgetting and memory patterns. In the present traditional machine learning analysis methods, it can accurately study and determine the temporal properties of a large amount of data. As a result, it effectively reduces the data gradient explosion and disappearance in the present standard neural network prediction models. Three fully connected layer modules with distinct roles construct the LSTM neural network. These layers are called forgetting gate, input gate, and output gate. The “gate structure,” which is intended to successfully achieve the objective of information control, allows each neuron to transfer information to each other in a selected manner [27]. The training of the models in LSTM neural networks is based on the backpropagation principle, just like in RNN neural networks.

The difference is that when the parameters of the backpropagation process are updated in the network, as shown in Figure 4, the backpropagation direction of the error in the LSTM network has two main directions. One is the backpropagation direction along the point in time in the network and the other direction is the backpropagation of the corresponding error term to the previous layer. According to the corresponding error term, it is to calculate the gradient between the weights [28]. The other direction is to backpropagate the corresponding error terms to the next level and calculate the gradient between the weights according to the corresponding error terms.

Since LSTM is characterized by using historical data to “trace back,” if the historical data is insufficient, the gradient will disappear. Choosing a better activation function and changing the propagation structure are the common solutions to “gradient disappearance.”

The activation function is often used in the training process, and sigmoid is often used as the activation function for deep neural networks. However, problems such as gradient disappearance can easily occur during this function. This problem can cause the weights of the layers to disappear during the training process and can no longer change. Only the data are weighted by the fixed weights causing interference to the training of the neural network [29, 30]. Deep neural networks have similar timing with LSTM. However, to avoid the occurrence of similar gradient disappearance in LSTM networks, this paper uses the ReLU activation function.

The loss function is the mean square error (MSE). It is a loss function representing the error between the actual output and the expected output of a neural network and is calculated as follows:

$$\text{MSE} = \frac{1}{n} \sum_{i=1}^n (y - y')^2, \quad (1)$$

where the sample size is  $n$  and the expected value is  $y$ .

For the stochastic gradient descent algorithm, it is no longer necessary to have all the samples undergo gradient computation during the gradient descent of the network. Parameters are, however, updated based on the results of each execution of the training. The formula for gradient descent is shown as

$$x_{t+1} = x_t - \eta \nabla f(x_t) \quad (2)$$

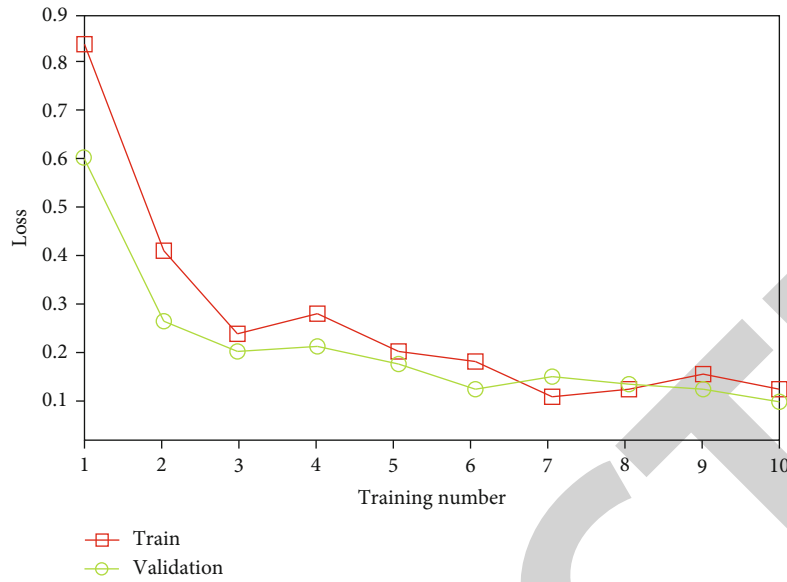


FIGURE 6: LSTM prediction model based on the 10 times training loss curve.

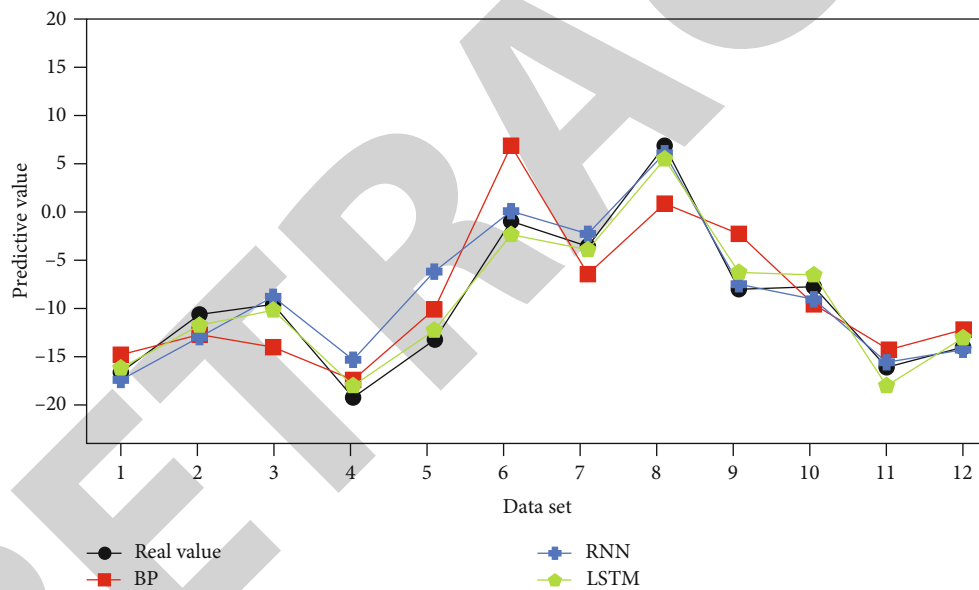


FIGURE 7: Comparison of prediction of three kinds of neural networks.

Neural networks learn faster by using stochastic gradient descent as the optimization function, i.e., faster convergence of the loss function.

3.2. *Financial Risk Early Warning Model Based on BP Neural Network.* The learning process of the model is shown in Figure 5. The learning samples are added in the input layer, and the data are processed in the implicit layer through forward transfer. The values are then passed to the output layer nodes under the joint action of weights, thresholds, and activation functions [31]. In the output layer, the actual value is compared with the expected value. If there is a large error and the expected accuracy is not reached, the model algo-

rithm enters the reverse transfer stage and continuously adjusts to make the output value as close to the expected value as possible.

The number of nodes in the implicit layer of the model is complicated to determine and is generally set by empirical values which is based on the sample size and the number of variables [32]. Therefore, the number of nodes in the implicit layer is set as follows:

$$L = \sqrt{m + n} + a, \tag{3}$$

where  $m$  is the number of input nodes,  $n$  is the number of output nodes, and  $a$  is any constant between 1 and 10.

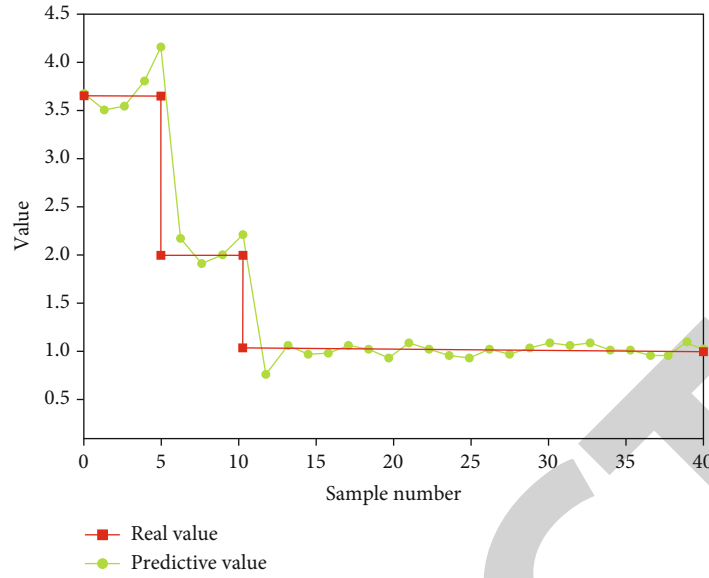


FIGURE 8: Comparison between prediction and actual graph.

TABLE 1: Classification of predictive test results.

Observation value	Predictive value			Percentage correction
	Security	Mild	Severe	
Safety warning interval	31	2	1	95.83%
Mild warning interval	2	23	4	97.66%
Severe warning interval	0	0	7	93.47%
Total percentage	85.21%	76.43%	12.95%	96.35%

TABLE 2: Comparison of financial early warning model results.

Warning interval	Logistic model		BP model	
	Fitting	Predicting	Fitting	Predicting
Safety warning interval	92.34%	91.08%	96.27%	92.42%
Mild warning interval	86.75%	83.82%	91.63%	89.87%
Severe warning interval	90.31%	88.97%	92.49%	90.53%
Total percentage	89.62%	87.53%	90.82%	89.04%

Correction weights using the general error in the implied layer and the input vector in the input layer are as under:

$$\begin{aligned} w_{ij}(N+1) &= w_{ij}(N) + \beta \cdot e_j \cdot x_i, \\ \theta_j(N+1) &= \theta_j(N) + \beta \cdot e_j. \end{aligned} \quad (4)$$

The neural network would not be able to produce the convergence effect if there are more learnings than the set number.

## 4. Experiment

**4.1. Experimental Results of Financial Prediction.** First, the neural network training results are analyzed. The financial prediction model based on the LSTM neural network has a gradually decreasing loss value because the amount of data increases as shown in Figure 6. Although the data volume

is large and the data features are complex, the loss function is not high and can remain stable. The model is trained 10 times, and the loss value of the prediction model gradually stabilizes when the model is trained to a certain degree. The loss value does not decrease with the increase of the number of times the model is trained, so that the gradient of the model in the training process can be effectively avoided to disappear.

Then, the same input information, number of network layers, loss function, and optimization algorithm were used for the prediction models of BP, RNN, and LSTM, respectively. To reduce random errors, each model parameter was carefully tuned separately and tested five times. The final average results are shown in Figure 7. The prediction results obtained using the LSTM neural network match the actual fold (green fold) more closely in the image when compared to the prediction results of the BP (red fold) and RNN (blue fold) network prediction models. This indicates better prediction results.

**4.2. Experimental Results of Financial Risk Early Warning.** The training fit sample is the first 100 data for model training, and the prediction test sample is the last 40 data. The model is validated with the data. If the result is good, the established early warning model is proved to be excellent.

The number of nodes in the implied layer was solved several times according to the above formula. The model was tested in order to find the best fit when the implied layer was 8 according to the error size. The sample training and actual comparison is shown in Figure 8. The fitting result of BP neural network can be considered to be optimal at this time. The fitting result for the enterprise financial warning results reached 97%. The difference between the actual value of 40 data and the target desired output is not significant.

Based on the above verification of the continuous adjustment of the nodes in the implicit layer, it can be concluded that the best accuracy of model fitting was achieved when the number of implicit nodes was set to 8 for the early warning model using the BP neural network. The prediction results for each early warning interval are shown in Table 1. Table 1 shows that the accuracy of model fitting reaches 97.66% and the prediction accuracy is 96.35%. The model results at this time have the highest accuracy and the least training times.

In this paper, three models are applied in practice as financial early warning models for enterprises and the experimental results are shown in Table 2. According to the results of the prediction test, it was found that the prediction effect of the logistic model of financial indexes and the logistic model of comprehensive indexes were in the better interval, 92.34% and 91.08%, respectively. However, the prediction effect of BP neural network was excellent. The integrated logistic model outperformed the logistic model with only financial indicators in terms of fitting and prediction results; however, both the logistic model with only financial indicators and the integrated logistic model with qualitative indicators were not as accurate as the BP neural network.

## 5. Conclusion

The new coronavirus epidemic is a sudden public health event that has caused the world economy to be hit hard. In this situation, the development of enterprises is also facing a huge survival test. In this context, it is important to discuss the financial management of enterprises under the epidemic as their resilience in the face of emergency can effectively reflect their financial management level. In this paper, we propose a system that can automatically predict financial trends and provide early warning of financial risks by combining artificial neural networks with the current difficulties faced by enterprises in the new situation. According to the wide application of machine learning in the field of data mining, this paper constructs a financial prediction model by using the LSTM neural network. By training and learning the enterprise financial data set with different spatial and temporal attributes of data attributes, the future financial trend of the enterprise is finally derived. Then, a BP neural network is combined with the enterprise risk warning model, and the results are obtained by training and learning

the training samples for several times. The experimental results show that the LSTM-based prediction model can effectively predict the enterprise financial trends and has better results than BP and RNN neural networks. The results of risk prediction model based on BP neural network show a satisfactory impact in analysis of enterprise financial early warning. The attempt of study to apply artificial intelligence technology to enterprise financial management can provide some reference for enterprise financial management.

## Data Availability

The datasets used during the current study are available from the corresponding author on reasonable request.

## Conflicts of Interest

The author declares that he has no conflict of interest.

## References

- [1] J. Kim, J. Kim, S. K. Lee, and L. (. R.). Tang, "Effects of epidemic disease outbreaks on financial performance of restaurants: event study method approach," *Journal of Hospitality and Tourism Management*, vol. 43, pp. 32–41, 2020.
- [2] J. H. Marks, "Lessons from corporate influence in the opioid epidemic: toward a norm of separation," *Journal of Bioethical Inquiry*, vol. 17, no. 2, pp. 173–189, 2020.
- [3] R. O. Akingunola, O. A. Adekunle, and O. A. Adedipe, "Corporate governance and bank's performance in Nigeria (post-bank's consolidation)," *European Journal of Business and Social Sciences*, vol. 2, no. 8, pp. 89–111, 2013.
- [4] C. Chen, J. Jiang, Y. Zhou, N. Lv, X. Liang, and S. Wan, "An edge intelligence empowered flooding process prediction using Internet of things in smart city," *Journal of Parallel and Distributed Computing*, vol. 165, pp. 66–78, 2022.
- [5] C. Chaufan and D. Saliba, "The global diabetes epidemic and the nonprofit state corporate complex: equity implications of discourses, research agendas, and policy recommendations of diabetes nonprofit organizations," *Social Science & Medicine*, vol. 223, pp. 77–88, 2019.
- [6] B. Mutizwa, "COVID-19 a global nightmare: revamping the Zimbabwean Health Sector (ZHS) for future epidemic and pandemic management," *Journal of African Problems & Solutions (JAPS)*, vol. 2, no. 1, pp. 59–73, 2020.
- [7] C. R. Boddy, "The corporate psychopaths theory of the global financial crisis," *Journal of Business Ethics*, vol. 102, no. 2, pp. 255–259, 2011.
- [8] H. Xu, "Competition and imitation of corporate social responsibility—take Alibaba and Tencent's CSR behavior under COVID-19 epidemic as an example," *Frontiers in Economics and Management*, vol. 3, no. 2, pp. 633–643, 2022.
- [9] Z. Wong, A. Chen, F. Taghizadeh-Hesary, R. Li, and Q. Kong, "Financing constraints and Firm's productivity under the COVID-19 epidemic shock: evidence of A-shared Chinese companies," *The European Journal of Development Research*, pp. 1–29, 2022.
- [10] M. McMaster, C. Nettleton, C. Tom, B. Xu, C. Cao, and P. Qiao, "Risk management: rethinking fashion supply chain management for multinational corporations in light of the

## Retraction

# Retracted: Effect of Previous Cancer History on Survival of Patients with Different Subtypes of Breast Cancer

### BioMed Research International

Received 8 January 2024; Accepted 8 January 2024; Published 9 January 2024

Copyright © 2024 BioMed Research International. This is an open access article distributed under the Creative Commons Attribution License, which permits unrestricted use, distribution, and reproduction in any medium, provided the original work is properly cited.

This article has been retracted by Hindawi following an investigation undertaken by the publisher [1]. This investigation has uncovered evidence of one or more of the following indicators of systematic manipulation of the publication process:

- (1) Discrepancies in scope
- (2) Discrepancies in the description of the research reported
- (3) Discrepancies between the availability of data and the research described
- (4) Inappropriate citations
- (5) Incoherent, meaningless and/or irrelevant content included in the article
- (6) Manipulated or compromised peer review

The presence of these indicators undermines our confidence in the integrity of the article's content and we cannot, therefore, vouch for its reliability. Please note that this notice is intended solely to alert readers that the content of this article is unreliable. We have not investigated whether authors were aware of or involved in the systematic manipulation of the publication process.

Wiley and Hindawi regrets that the usual quality checks did not identify these issues before publication and have since put additional measures in place to safeguard research integrity.

We wish to credit our own Research Integrity and Research Publishing teams and anonymous and named external researchers and research integrity experts for contributing to this investigation.

The corresponding author, as the representative of all authors, has been given the opportunity to register their agreement or disagreement to this retraction. We have kept a record of any response received.

### References

- [1] W. Lin, Y. Chen, Z. Ji et al., "Effect of Previous Cancer History on Survival of Patients with Different Subtypes of Breast Cancer," *BioMed Research International*, vol. 2022, Article ID 6116658, 15 pages, 2022.

## Research Article

# Effect of Previous Cancer History on Survival of Patients with Different Subtypes of Breast Cancer

Weixun Lin , Yaokun Chen , Zeqi Ji , Lingzhi Chen , Jinyao Wu , Yexi Chen ,  
and Zhiyang Li 

Department of Thyroid, Breast and Hernia Surgery, The Second Affiliated Hospital of Shantou University Medical College, Shantou, 515041 Guangdong, China

Correspondence should be addressed to Yexi Chen; [yxchen3@stu.edu.cn](mailto:yxchen3@stu.edu.cn) and Zhiyang Li; [s\\_zyli4@stu.edu.cn](mailto:s_zyli4@stu.edu.cn)

Received 27 July 2022; Accepted 18 August 2022; Published 2 September 2022

Academic Editor: Nauman Rahim Khan

Copyright © 2022 Weixun Lin et al. This is an open access article distributed under the Creative Commons Attribution License, which permits unrestricted use, distribution, and reproduction in any medium, provided the original work is properly cited.

Patients with a previous cancer history (PCA) are routinely excluded from most clinical trials, which may limit the accuracy and universality of clinical trials. We aimed to explore the association between PCA and survival of patients with different molecular subtypes of breast cancer. Patients diagnosed with breast cancer from the Surveillance, Epidemiology, and End Results (SEER) database between 2010 and 2015 were included in this retrospective cohort study. The primary outcome was overall survival (OS), which was calculated from date of diagnosis to date of death or censor date during this period. The relationship between PCA and OS of patients with different molecular subtypes of breast cancer was analyzed by the Kaplan-Meier curves and multivariate Cox proportional-hazards model. A total of 35,640 primary breast cancer patients were included, and 2,038 (5.72%) patients had a PCA. Female genital system cancer (491 cases, 24.09%) was the largest proportion type of previous cancer, and HER2-positive (24,754 cases, 69.46%) breast cancer was the most common subtype. Patients with previous female genital/endocrine system cancer history and other cancers history were associated with a poorer OS in overall patients, and in patients with triple-negative and HER2-positive subtypes ( $P < 0.05$ ). In patients with Luminal A and Luminal B subtypes, previous other cancers history was related to poor OS ( $P < 0.05$ ), while female genital/endocrine system cancer history may not influence the OS ( $P > 0.05$ ). Subgroup analyses presented that PCA was related to poor OS in patients aged 40-64 years and  $\geq 65$  years ( $P < 0.05$ ), while prognosis in patients aged 18-40 years may not be influenced by PCA ( $P > 0.05$ ). The impact of PCA on the prognosis of breast cancer patients was related to molecular type, patient age, and type of PCA. In clinical trials of breast cancer, the exclusion criteria for PCA patients may be modified according to the above variables.

## 1. Introduction

Breast cancer (BC) has become the leading female malignancy worldwide, and about two-thirds of patients with early non-metastatic BC can be cured [1]. In 2020, 2.26 million women became new BC patients and approximately 684,996 patients died of BC [2]. The number of cancer survivors has been reported on the rise [3], which may lead to a rise in the number of patients with multiple primary cancers [4, 5]. Previous studies have indicated that patients with a previous cancer history (PCA) account for approximately 4% to 14% of all BC patients [6–8].

Patients with PCA are usually listed as exclusion criteria for study populations in the cancer clinical trials [9], which

occur in approximately 77% of BC studies and 80% of lung cancer studies [10, 11]. Only 3%–5% of these patients were enrolled in trials each year [12, 13]. The exclusion of these patients with PCA may limit the accuracy and universality of clinical trials [14, 15]. The Clinical Trial Eligibility Working Group recommended that patients should not be excluded based solely on previous cancer in clinical trials [13, 16]. Several studies found that the impact of PCA on the clinical outcomes of cancer patients may be related to the type of tumor [6, 10, 17, 18]. However, few studies have reported the impact of PCA on the survival of BC patients. Furthermore, previous studies have demonstrated that the molecular type of BC is an important factor influencing the survival of BC patients [19–21]. Only a recent study

showed that PCA was a risk factor for survival in patients with advanced BC [6], but they did not conduct further analyses by molecular type of BC. Exploring the impact of PCA on the prognosis of patients with different molecular types of BC may help improve the accuracy of BC clinical trials.

Therefore, the purpose of this study was to analyze the relationship between PCA and survival of patients with different molecular subtypes of BC. Furthermore, the impact of different types of PCA on the survival of patients was also analyzed.

## 2. Methods

**2.1. Data Source and Populations.** The analysis data of this retrospective cohort study were obtained from the Surveillance, Epidemiology, and End Results (SEER) database (2010 to 2015). The SEER database was established by the National Cancer Institute of the United States (US) to achieve cancer prevention, diagnosis, and treatment by collecting, analyzing, and disseminating cancer-related data. The database covers about 28% of the US population [22], and data include demographic characteristics (e.g., age, sex, and race) and tumor characteristics (e.g., year of diagnosis, primary tumor site, histology, behavior, and stage) were collected. Since the data on the human epidermal growth factor receptor 2 (HER2) molecular type of BC in the SEER database only included after 2010, the data from 2010 to 2015 were utilized for analysis. The International Classification of Diseases for Oncology, 3rd edition (ICD-O-3) codes (C50.0-C50.6, C50.8, and C50.9) were utilized to identify BC patients. Exclusion criteria: (1) age <18 years at diagnosis; (2) previous BC history; (3) patients with incomplete data such as survival data, follow-up data, and molecular types of BC. All data usage in this study was in accordance with the data-use agreements of SEER database. Anonymized patient data from the SEER database were used in this study, and interventions on patients were not involved. Therefore, this study was granted an ethical exemption by the Ethics Committee of The Second Affiliated Hospital of Shantou University Medical College.

**2.2. Data Collection.** Demographic and clinicopathological data were extracted, including age (18-40, 40-65, and  $\geq 65$  years), race (blacks, Hispanics, whites, and others), marital status (married, separated/divorced, single, widowed, and unknown), estrogen receptor (ER) status (negative and positive), pathology grade (I, II, III, IV, and unknown), progesterone receptor (PR) status (negative, positive, and unknown), T stage (T1, T2, T3, T4, unknown), N stage (N1, N2, N3, N4, and unknown), radiation (no or yes), chemotherapy (no or yes), surgery (no or yes), regional nodes positive (no or yes), molecular subtypes (triple negative, HER2 positive, Luminal A, and Luminal B), survival status (alive and dead), and survival months. The primary outcome was overall survival (OS), which was calculated from date of diagnosis to date of death (between 2010 and 2015) or censor date.

The American Joint Committee on Cancer (AJCC) (6th edition) staging system was utilized to determine the T stage and N stage [23]. The classification criteria for molecular

subtypes of BC were based on the criteria in 2011 [24]. PCA was identified by the SEER sequence number, which contained information on all primary reportable tumors in the patient. For example, the sequence number "00" means that the patient has only one primary cancer. If the patient is diagnosed with the second reportable tumor, the sequence number of the first tumor is changed from "00" to "01," the sequence number of the second cancer is "02," and so on.

**2.3. Statistical Analysis.** The Kolmogorov-Smirnov test was utilized to assess the normality of the data. Measurement data were described by mean  $\pm$  standard deviation (SD) or median and interquartile range [M (Q1, Q3)], and the *t*-test or Mann-Whitney *U* rank-sum test was utilized to compare differences between groups. Categorical data were expressed by the numbers and proportions [*n* (%)], and the chi-square test was utilized to compare differences between groups. Univariate analysis was utilized to analyze the differences between patients with and without a PCA. The Kaplan-Meier (K-M) curves and Cox proportional-hazards model were utilized to determine the effect of PCA on survival in patients with different subtypes of BC. Hazard ratio (HR) and 95% confidence interval (CI) were utilized for data measurement. Model 1 was a univariate analysis model; model 2 was an age-adjusted model; model 3 was a multivariate analysis model that adjusted for age, race, marital status, grade, ER (or not), PR (or not), T stage, N stage, chemotherapy, radiation, surgery, and regional nodes positive.

The SAS 9.4 software (SAS Institute Inc., Cary, NC, USA) was utilized to complete the univariate and multivariate analyses, and KM curves were completed by the R 4.20 software (R Foundation for Statistical Computing, Vienna, Austria). *P* < 0.05 was considered to be statistically significant.

## 3. Results

**3.1. Characteristics of Patients.** A total of 44,335 patients with primary BC were extracted from the SEER database (2010 to 2015). Of these patients, 5,741 patients with a previous BC history and 2,954 patients with incomplete BC molecular subtypes data were excluded, 35,640 patients including 2,038 (5.72%) with PCA and 33,602 (94.28%) without were enrolled in this study. Table 1 presents the characteristics of included patients. In terms of BC subtypes, 3,853 (10.81%) patients were triple negative, 24,754 (69.46%) patients were HER2 positive, 2,406 (6.75%) patients were Luminal A, and 4,627 (12.98%) patients were Luminal B. Among the characteristics of patients, more patients were 40-65 years (57.02%), whites (65.36%), married (50.64%), II-III grade (71.88%), ER-positive (81.38%), and PR-positive (70.02%). Among all included patients, 29,387 (82.46%) patients were alive and 6,253 (17.54%) patients died. The median survival time of all patients was 27.00 (11.00, 47.00) months. Among the 2,038 patients with a PCA, female genital system cancer (24.09%), digestive system cancer (20.71%), and respiratory system cancer (11.29%) accounted for a higher proportion of patients (Figure 1).



TABLE 1: Characteristics of all included patients.

Variables	Total (n=35640)	Prior cancer history		Statistics	P
		No (n=33602)	Yes (n=2038)		
Breast subtypes, n (%)				$\chi^2 = 54.815$	<0.001
Triple negative	3853 (10.81)	3658 (10.89)	195 (9.57)		
HER2 positive	24754 (69.46)	23197 (69.03)	1557 (76.40)		
Luminal A	2406 (6.75)	2318 (6.90)	88 (4.32)		
Luminal B	4627 (12.98)	4429 (13.18)	198 (9.72)		
Age, years, n (%)				$\chi^2 = 696.118$	<0.001
18-40	2778 (7.79)	2734 (8.14)	44 (2.16)		
40-65	20322 (57.02)	19590 (58.30)	732 (35.92)		
≥65	12540 (35.19)	11278 (33.56)	1262 (61.92)		
Race, n (%)				$\chi^2 = 136.469$	<0.001
Blacks	4442 (12.46)	4251 (12.65)	191 (9.37)		
Hispanics	4354 (12.22)	4195 (12.48)	159 (7.80)		
Whites	23294 (65.36)	21722 (64.64)	1572 (77.13)		
Others	3550 (9.96)	3434 (10.22)	116 (5.69)		
Marital, n (%)				$\chi^2 = 187.292$	<0.001
Married	18048 (50.64)	17132 (50.99)	916 (44.95)		
Separated/divorced	4038 (11.33)	3812 (11.34)	226 (11.09)		
Single	6023 (16.90)	5766 (17.16)	257 (12.61)		
Widowed	4741 (13.30)	4275 (12.72)	466 (22.87)		
Unknown	2790 (7.83)	2617 (7.79)	173 (8.49)		
Grade, n (%)				$\chi^2 = 45.520$	<0.001
I	5749 (16.13)	5368 (15.98)	381 (18.69)		
II	14079 (39.50)	13250 (39.43)	829 (40.68)		
III	11541 (32.38)	11002 (32.74)	539 (26.45)		
IV	155 (0.43)	150 (0.45)	5 (0.25)		
Unknown	4116 (11.55)	3832 (11.40)	284 (13.94)		
ER, n (%)				$\chi^2 = 26.880$	<0.001
Negative	6636 (18.62)	6345 (18.88)	291 (14.28)		
Positive	29004 (81.38)	27257 (81.12)	1747 (85.72)		
PR, n (%)				$\chi^2 = 3.949$	0.139
Negative	10514 (29.50)	9952 (29.62)	562 (27.58)		
Positive	24955 (70.02)	23490 (69.91)	1465 (71.88)		
Unknown	171 (0.48)	160 (0.48)	11 (0.54)		
T stage, n (%)				$\chi^2 = 80.042$	<0.001
T1	14455 (40.56)	13533 (40.27)	922 (45.24)		
T2	9833 (27.59)	9253 (27.54)	580 (28.46)		
T3	3304 (9.27)	3177 (9.45)	127 (6.23)		
T4	4054 (11.37)	3914 (11.65)	140 (6.87)		
Unknown	3994 (11.21)	3725 (11.09)	269 (13.20)		
N stage, n (%)				$\chi^2 = 94.441$	<0.001
N1	17970 (50.42)	16750 (49.85)	1220 (59.86)		
N2	10705 (30.04)	10231 (30.45)	474 (23.26)		
N3	3011 (8.45)	2879 (8.57)	132 (6.48)		
N4	2370 (6.65)	2268 (6.75)	102 (5.00)		
Unknown	3994 (11.21)	3725 (11.09)	269 (13.20)		
Radiation, n (%)				$\chi^2 = 37.418$	<0.001
No	23356 (65.53)	21893 (65.15)	1463 (71.79)		
Yes	12284 (34.47)	11709 (34.85)	575 (28.21)		

TABLE 1: Continued.

Variables	Total (n=35640)	Prior cancer history		Statistics	P
		No (n=33602)	Yes (n=2038)		
Chemotherapy, n (%)				$\chi^2 = 220.064$	<0.001
No	19145 (53.72)	17726 (52.75)	1419 (69.63)		
Yes	16495 (46.28)	15876 (47.25)	619 (30.37)		
Surgery, n (%)				$\chi^2 = 3.579$	0.059
No	6725 (18.87)	6308 (18.77)	417 (20.46)		
Yes	28915 (81.13)	27294 (81.23)	1621 (79.54)		
Regional nodes positive, n (%)				$\chi^2 = 0.038$	0.845
No	15236 (42.75)	14369 (42.76)	867 (42.54)		
Yes	20404 (57.25)	19233 (57.24)	1171 (57.46)		
Status, n (%)				$\chi^2 = 111.988$	<0.001
Alive	29387 (82.46)	27883 (82.98)	1504 (73.80)		
Dead	6253 (17.54)	5719 (17.02)	534 (26.20)		
Survival months, M (Q <sub>1</sub> , Q <sub>3</sub> )	27.00 (11.00,47.00)	27.00 (11.00,47.00)	25.00 (10.00,43.00)	Z = -3.893	<0.001

Note: HER2: human epidermal growth factor receptor 2; ER: estrogen receptor; PR: progesterone receptor.

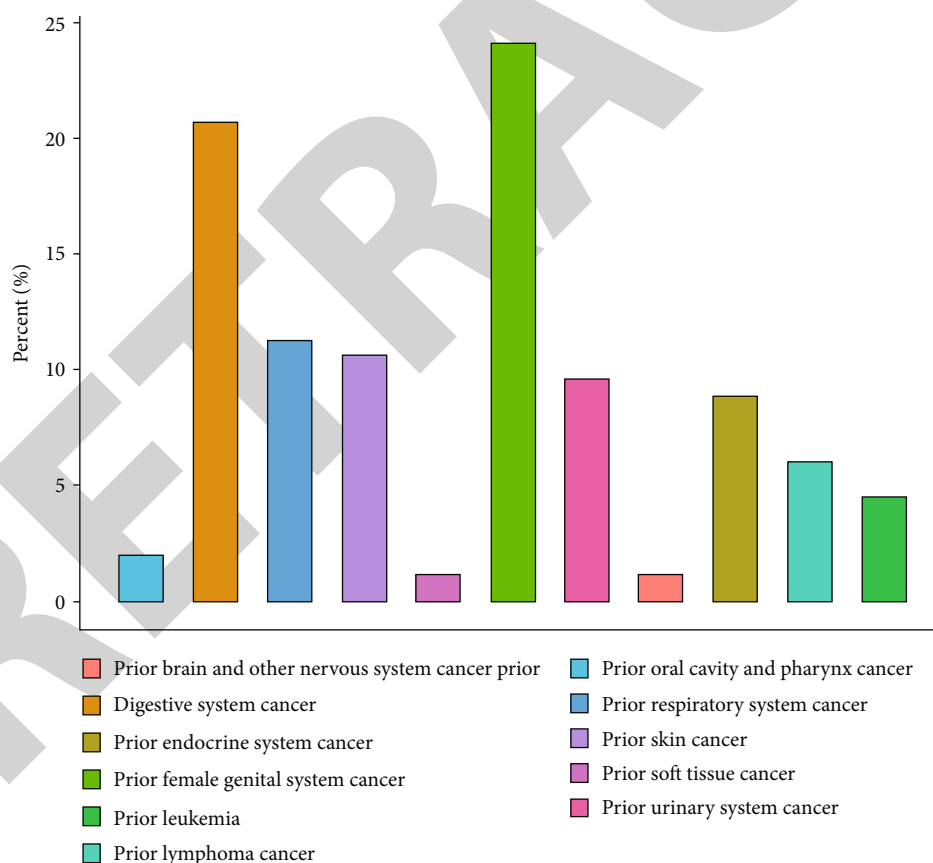


FIGURE 1: Distributions of previous cancer types in patients with breast cancer.

Significant differences were found in breast subtype, age, race, marital status, grade, ER status, T stage, N stage, radiation, chemotherapy, survival status, and survival months among patients with or without PCA (all  $P < 0.001$ ) (Table 1).

**3.2. Relationship between PCA and Survival of Patients with Different BC Subtypes.** To investigate the relationship between different types of PCA and the prognosis of patients with different BC subtypes, the types of PCA were grouped into previous female genital/endocrine system cancer history

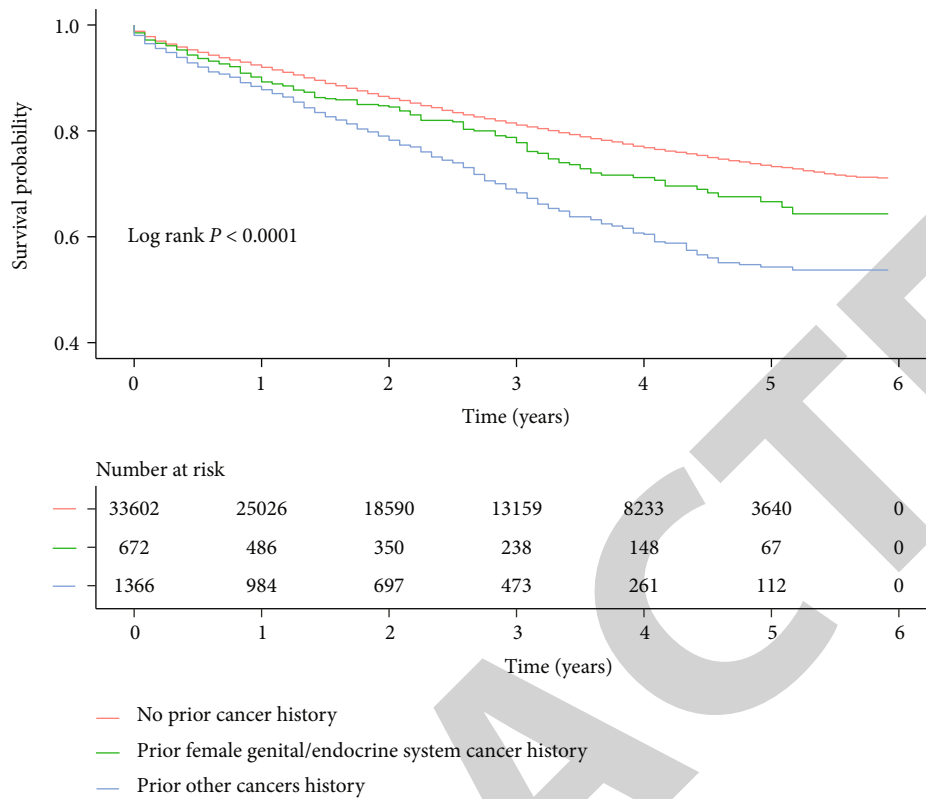


FIGURE 2: The Kaplan-Meier (K-M) curves of the relationship between different types of previous cancer history and the survival of breast cancer patients.

and previous other cancers history. The K-M curves of the relationship between different types of PCA and the prognosis of BC patients are presented in Figure 2. The results indicated that a worse prognosis was found in patients with PCA than those without ( $P < 0.0001$ ). BC patients with a previous female genital/endocrine system cancer history (HR=1.27; 95% CI, 1.08-1.51) and previous other cancers history (HR=1.81; 95% CI, 1.63-1.51) were related to a poor prognosis. After adjusting for all confounders, patients with a previous female genital/endocrine system cancer history (HR=1.38; 95% CI, 1.16-1.63) and previous other cancers history (HR=1.55; 95% CI, 1.40-1.72) were still related to poor OS. In terms of BC subtypes, previous female genital/endocrine system cancer history (HR=1.70; 95% CI, 1.18-2.43) and previous other cancers history (HR=1.49; 95% CI, 1.14-1.96) were related to worse survival in patients with triple-negative subtype. Among HER2-positive subtype patients, patients with previous female genital/endocrine system cancer history (HR=1.32; 95% CI, 1.08-1.64) and previous other cancers history (HR=1.48; 95% CI, 1.31-1.68) were also associated with a poor prognosis. However, previous other cancers history was only related to poor OS in patients with Luminal A (HR=1.64; 95% CI, 1.06-2.55) and Luminal B (HR=2.50; 95% CI, 1.83-3.43) subtypes, while previous female genital/endocrine system cancer history may not influence the prognosis significantly (all  $P > 0.05$ ) (Table 2). The K-M curves of the effect of PCA on the survival of patients with different BC subtypes are demonstrated in Figure 3.

Stratified analyses were conducted according to patient age and race. In terms of age, previous other cancers history was related to poor prognosis in patients aged 40-64 years (HR=2.19; 95% CI, 1.77-2.72) and  $\geq 65$  years (HR=1.39; 95% CI, 1.23-1.57). However, only a previous female genital/endocrine system cancer history (HR=2.50; 95% CI, 1.83-3.43) was a risk factor for OS in patients aged 40-64 years. In addition, the prognosis of patients aged 18-40 years may not be influenced by PCA ( $P > 0.05$ ). Among patients of different races, except for previous female genital/endocrine system cancer may not influence the prognosis of blacks and previous other cancers history may not affect the prognosis of other races ( $P > 0.05$ ), both previous female genital/endocrine system cancer history and previous other cancers history were risk factors for OS of different races ( $P < 0.05$ ) (Table 2). In addition, the K-M curves of PCA for survival in patients with different ages and races were displayed in Figures 4 and 5, respectively.

#### 4. Discussion

The association between PCA and survival of patients with different BC subtypes was analyzed. There were 5.72% of BC patients who had a PCA, and HER2-positive (69.46%) BC was the most common subtype. The results displayed that a PCA was associated with poor OS in BC patients. In terms of BC subtypes, PCA may be related to poor OS in patients with triple-negative and HER2-positive subtypes, while the survival of patients with Luminal A and B subtypes

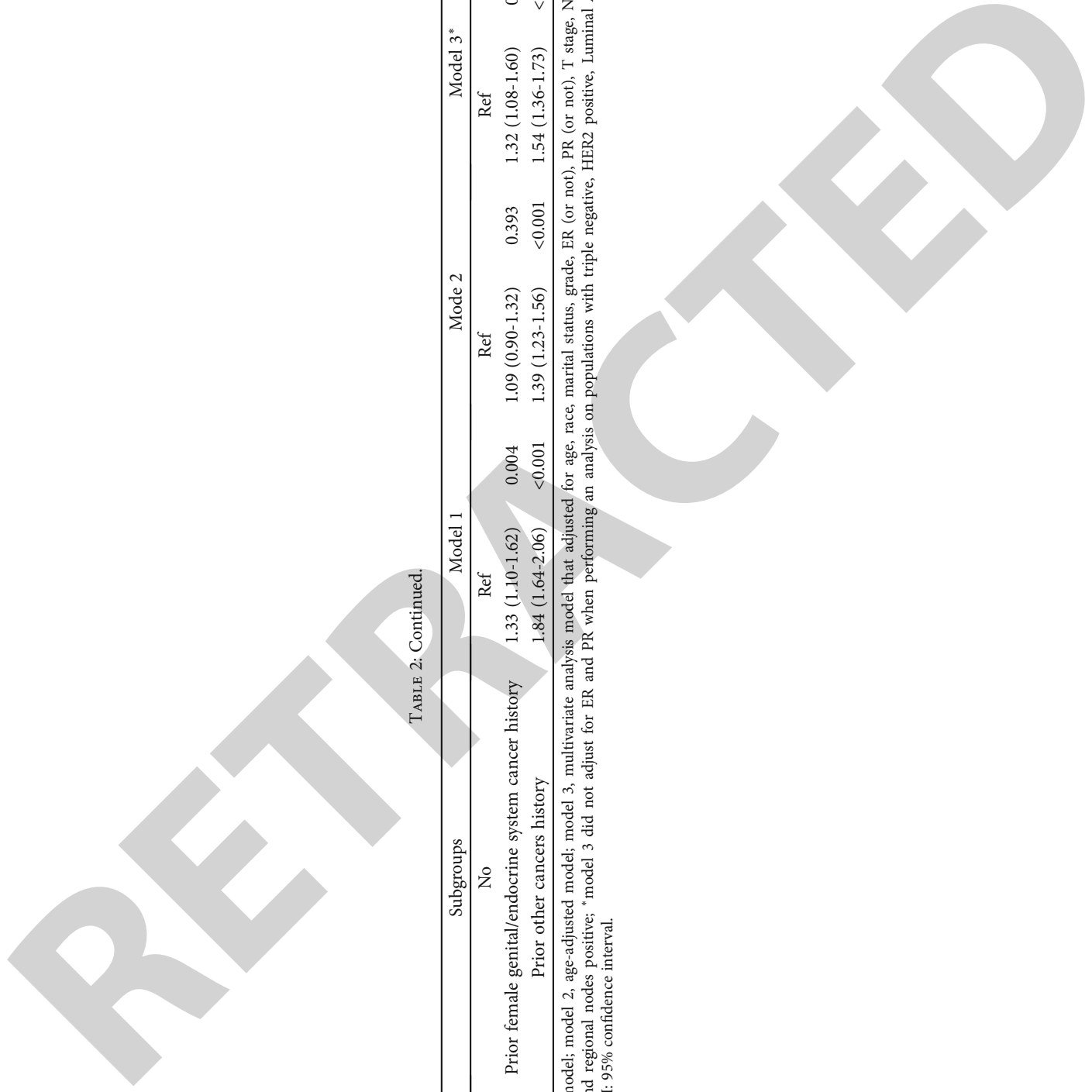
TABLE 2: Impact of prior cancer history on the survival of patients with different breast cancer subtypes.

Populations	Samples	Subgroups	Model 1		Model 2		Model 3*	
			HR (95% CI)	P	HR (95% CI)	P	HR (95% CI)	P
Total	35640		Ref		Ref		Ref	
	33602	No	1.27 (1.08-1.51)	0.005	1.07 (0.91-1.27)	0.412	1.38 (1.16-1.63)	<0.001
	672	Prior female genital/endocrine system cancer history	1.81 (1.63-2.00)	<0.001	1.41 (1.27-1.56)	<0.001	1.55 (1.40-1.72)	<0.001
Triple negative	1366	Prior other cancers history	Ref		Ref		Ref	
	3568	No	1.31 (0.92-1.87)	0.137	1.22 (0.86-1.75)	0.267	1.70 (1.18-2.43)	0.004
	73	Prior female genital/endocrine system cancer history	1.62 (1.25-2.11)	<0.001	1.31 (1.01-1.72)	0.045	1.49 (1.14-1.96)	0.004
HER2 positive	122	Prior other cancers history	Ref		Ref		Ref	
	23197	No	1.35 (1.10-1.66)	0.005	1.10 (0.89-1.36)	0.372	1.32 (1.08-1.64)	0.008
	500	Prior female genital/endocrine system cancer history	1.90 (1.67-2.15)	<0.001	1.45 (1.28-1.65)	<0.001	1.48 (1.31-1.68)	<0.001
Luminal A	1057	Prior other cancers history	Ref		Ref		Ref	
	2318	No	0.81 (0.36-1.81)	0.603	0.65 (0.29-1.45)	0.294	0.88 (0.39-1.99)	0.758
	35	Prior female genital/endocrine system cancer history	2.00 (1.30-3.06)	0.002	1.47 (0.96-2.26)	0.081	1.64 (1.06-2.55)	0.027
Luminal B	53	Prior other cancers history	Ref		Ref		Ref	
	4429	No	1.22 (0.69-2.16)	0.497	1.04 (0.59-1.84)	0.889	1.49 (0.84-2.67)	0.175
	64	Prior female genital/endocrine system cancer history	2.50 (1.85-3.38)	<0.001	1.85 (1.37-2.51)	<0.001	2.50 (1.83-3.43)	<0.001
Age: 18-40 years	134	Prior other cancers history	Ref		—		Ref	
	2734	No	0.91 (0.29-2.84)	0.871	—	—	—	—
	13	Prior female genital/endocrine system cancer history	1.42 (1.08-1.87)	0.012	—	—	2.00 (0.62-6.41)	0.245
Age: 40-44 years	31	Prior other cancers history	Ref		Ref		Ref	
	19590	No	1.66 (1.35-2.05)	<0.001	—	—	—	—
	299	Prior female genital/endocrine system cancer history	1.66 (1.35-2.05)	<0.001	—	—	1.84 (1.40-2.43)	<0.001
Age: ≥65 years	433	Prior other cancers history	Ref		Ref		Ref	
	11278	No	0.95 (0.77-1.17)	0.611	—	—	1.18 (0.95-1.46)	0.132
	360	Prior female genital/endocrine system cancer history	1.35 (1.19-1.51)	<0.001	—	—	1.39 (1.23-1.57)	<0.001
Race: blacks	902	Prior other cancers history	Ref		Ref		Ref	
	4251	No	0.97 (0.56-1.68)	0.919	0.87 (0.50-1.51)	0.624	1.28 (0.74-2.23)	0.381
	54	Prior female genital/endocrine system cancer history	1.45 (1.08-1.94)	0.014	1.25 (0.93-1.68)	0.149	1.41 (1.04-1.92)	0.027
Race: Hispanics	137	Prior other cancers history	Ref		Ref		Ref	
	4195	No	1.38 (0.78-2.45)	0.268	1.25 (0.71-2.22)	0.440	1.91 (1.07-3.41)	0.030
	73	Prior female genital/endocrine system cancer history	2.29 (1.55-3.39)	<0.001	2.02 (1.36-3.00)	<0.001	2.12 (1.41-3.18)	<0.001
Race: others	86	Prior other cancers history	Ref		Ref		Ref	
	3434	No	1.47 (0.79-2.75)	0.229	1.35 (0.72-2.53)	0.347	1.98 (1.04-3.75)	0.037
	55	Prior female genital/endocrine system cancer history	1.71 (0.99-2.97)	0.057	1.41 (0.81-2.45)	0.229	1.55 (0.88-2.72)	0.130
	61	Prior other cancers history						

TABLE 2: Continued.

Populations	Samples	Subgroups	Model 1	Model 2	Model 3*
	21722	No	Ref	Ref	Ref
Race: whites	490	Prior female genital/endocrine system cancer history	1.33 (1.10-1.62)	1.09 (0.90-1.32)	1.32 (1.08-1.60)
	1082	Prior other cancers history	1.84 (1.64-2.06)	1.39 (1.23-1.56)	1.54 (1.36-1.73)

Note: model 1, univariate analysis model; model 2, age-adjusted model; model 3, multivariate analysis model that adjusted for age, race, marital status, grade, ER (or not), PR (or not), T stage, N stage, chemotherapy, radiation, surgery, and regional nodes positive; \*model 3 did not adjust for ER and PR when performing an analysis on populations with triple negative, HER2 positive, Luminal A, and Luminal B; HR: hazard ratio; 95% CI: 95% confidence interval.



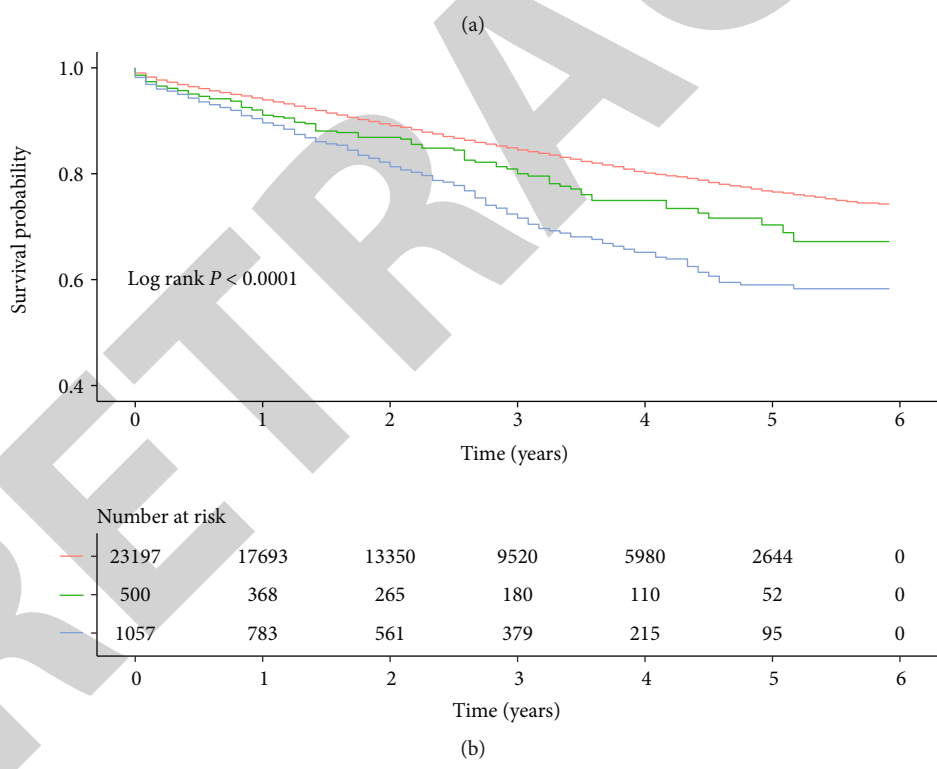
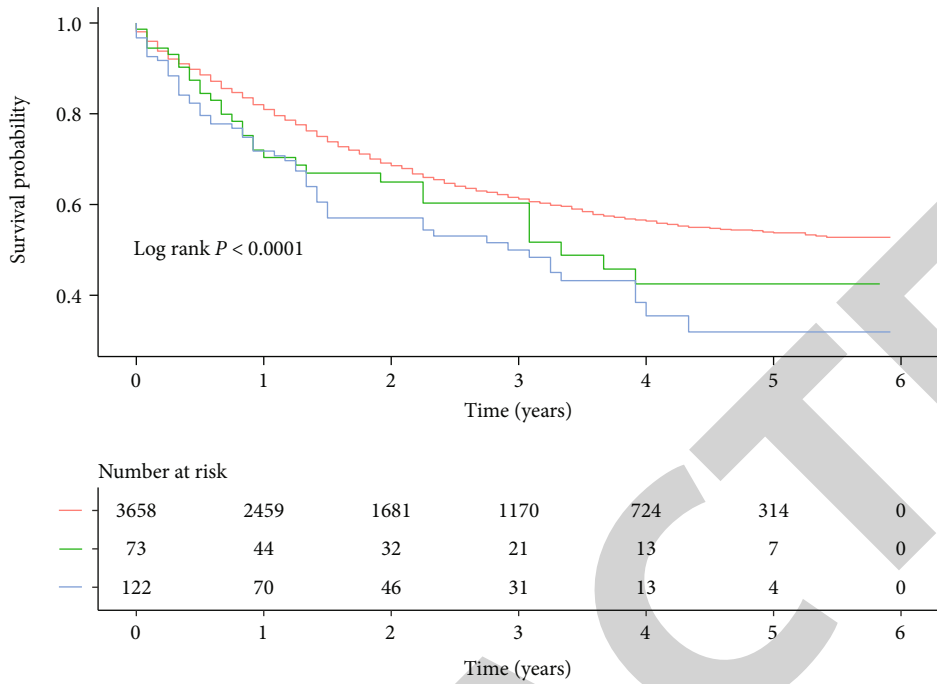


FIGURE 3: Continued.

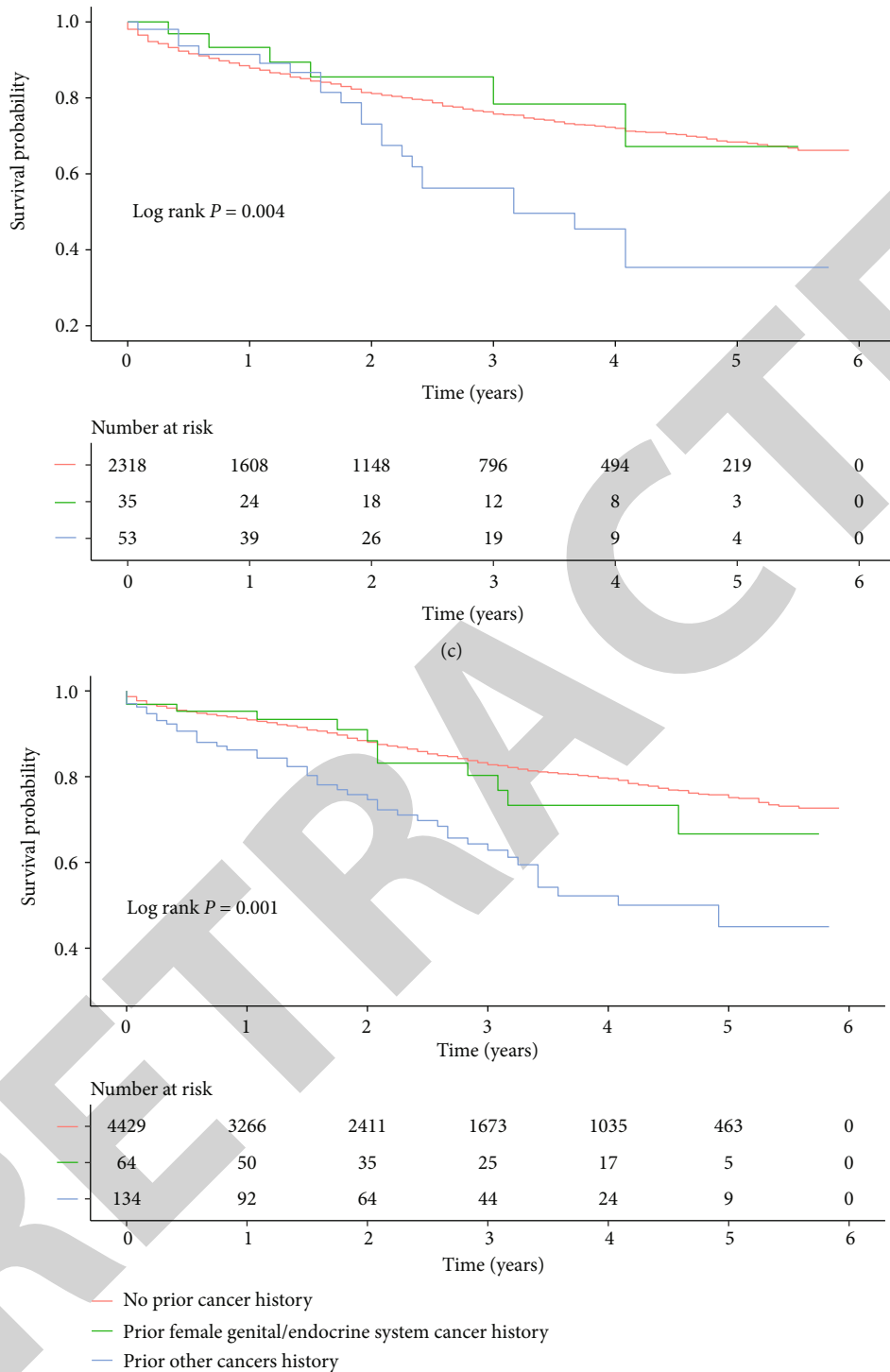


FIGURE 3: The K-M curves of the impact of previous cancer history on the survival of patients with different breast cancer subtypes. (a) Triple-negative subtype; (b) HER-positive subtype; (c) Luminal A subtype; (d) Luminal B subtype.

may not be influenced by previous female genital/endocrine system cancer history. Furthermore, stratified analyses showed that the prognosis of patients aged 18-40 years may not be influenced by PCA, and previous female genital/endocrine system cancer history may also not influence the prognosis of patients aged  $\geq 65$  years.

In clinical practice, patients with PCA are routinely excluded as previous cancers may affect the prognostic outcomes. Previous studies have assessed the relationship between PCA and the prognosis of cancer patients [17, 18, 25, 26]. These studies demonstrated that the relationship between PCA and the prognosis of patients was related to the type of

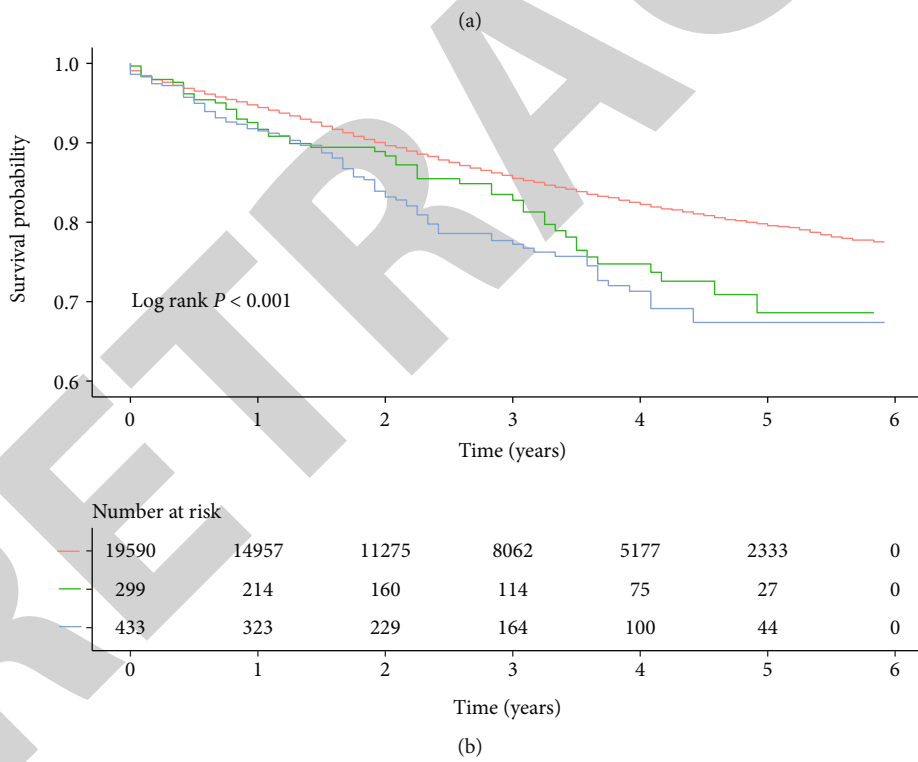
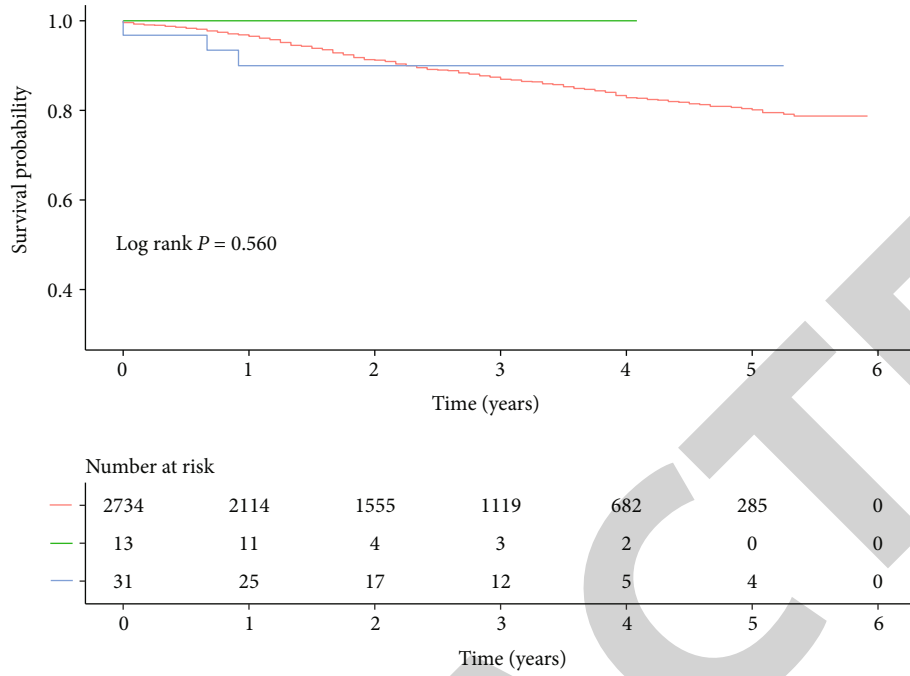


FIGURE 4: Continued.



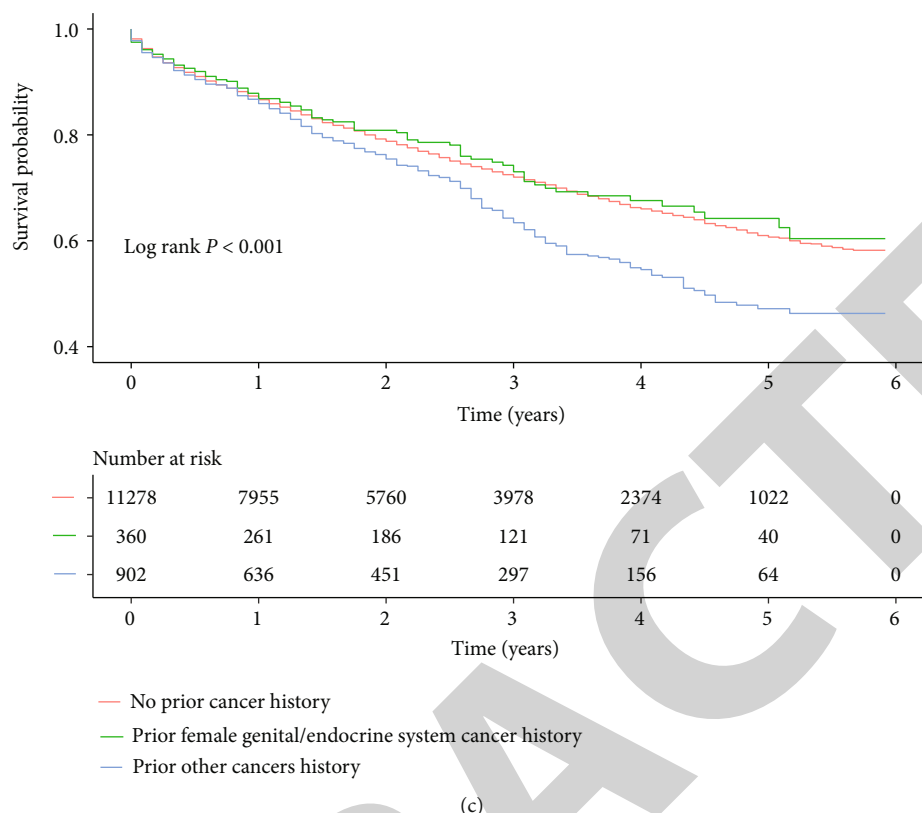


FIGURE 4: The K-M curves of the association between previous cancer history and the survival of patients with different ages. (a) Age 18-40 years; (b) age 40-65 years; (c) age ≥65 years.

cancer. Laccetti et al. found that the prognosis of lung cancer patients may not be affected by PCA, independent of the stage and type of previous cancer [17, 18]. Wen et al. suggested that the clinical prognosis of most gastric cancer patients may be independent of PCA [25]. However, Zhu et al. showed that a PCA was linked to poorer OS in larynx cancer patients [26]. The study conducted by Lin et al. indicated that the poor prognosis in patients with advanced BC was affected by PCA [6], which was similar to our results. The study of Lin et al. was mainly about the impact of the diagnosis time and location of previous cancer on the survival of BC patients, while our study was to assess the influence of PCA on the prognosis of patients with different molecular subtypes. Furthermore, our study analyzed the impact of different types of PCA on the survival of patients.

Our results demonstrated that a PCA was related to poorer OS of patients with triple-negative and HER2-positive subtypes. Ren et al. found that the mortality of patients was linked to BC subtypes, specifically HER2-positive patients had the highest mortality, followed by the triple-negative, Luminal A, and Luminal B subtypes [27]. Furthermore, BC patients with the HER2-positive subtype had the highest number of genetic mutations compared with other subtypes [28]. Our results found that the HER2-positive subtype accounted for the largest proportion in BC patients with PCA. PCA was related to poor prognosis in patients with HER2-positive subtype, and clinicians may need to pay more attention to the treatment and management of these patients. Furthermore, we found

that the survival of patients with Luminal A and Luminal B subtypes may not be influenced by previous female genital/endocrine system cancer history. One possible explanation was that endocrine therapy in BC patients with Luminal A and Luminal B subtypes may reduce the impact of a previous female genital/endocrine system cancer history on the prognosis of patients. Because endocrine therapy has become an essential treatment for patients with ER-positive early BC [29]. Our results also indicated that prior other cancers history was related to poorer survival in patients with Luminal A and Luminal B subtypes. This may be related to many factors, such as the type and treatment methods of previous cancer, and the specific explanation may require further study.

Subgroup analyses presented that the prognosis of BC patients aged 18-40 years may not be influenced by PCA. Age at diagnosis is commonly considered to correlate with prognosis in BC patients [30]. Young age (<40 years) has been identified as an independent risk factor associated with poorer prognosis in BC patients in several studies [31, 32]. However, the association of age with BC mortality is not a simple linear correlation, with women aged 45 to 55 having the lowest risk of dying from BC [33, 34]. In our study, PCA was related to poorer OS in patients aged 40-64 years, whereas OS in patients aged 18-40 years may not be influenced by PCA. This could be potentially explained that young age patients diagnosed with previous cancer were more frequently involved in the healthcare system (e.g., regular follow-up examinations), which led to the early diagnosis of BC. Other possible

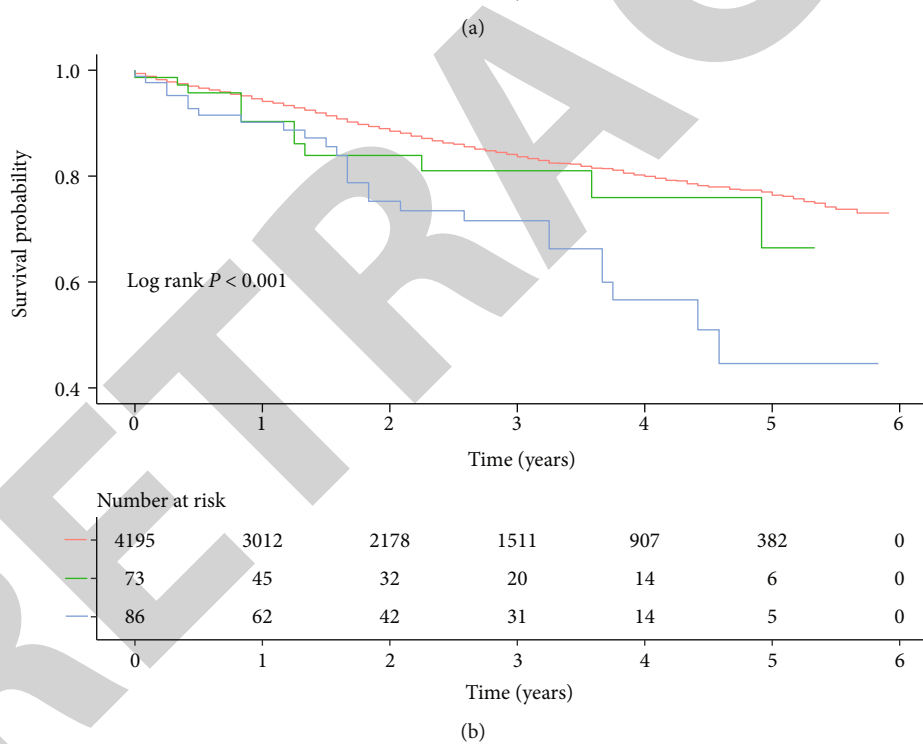
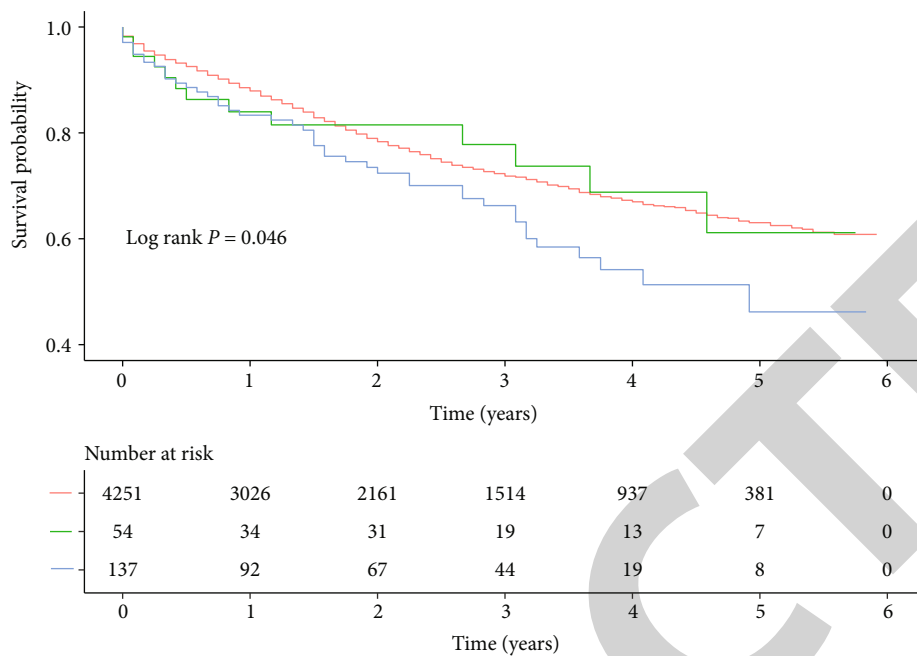
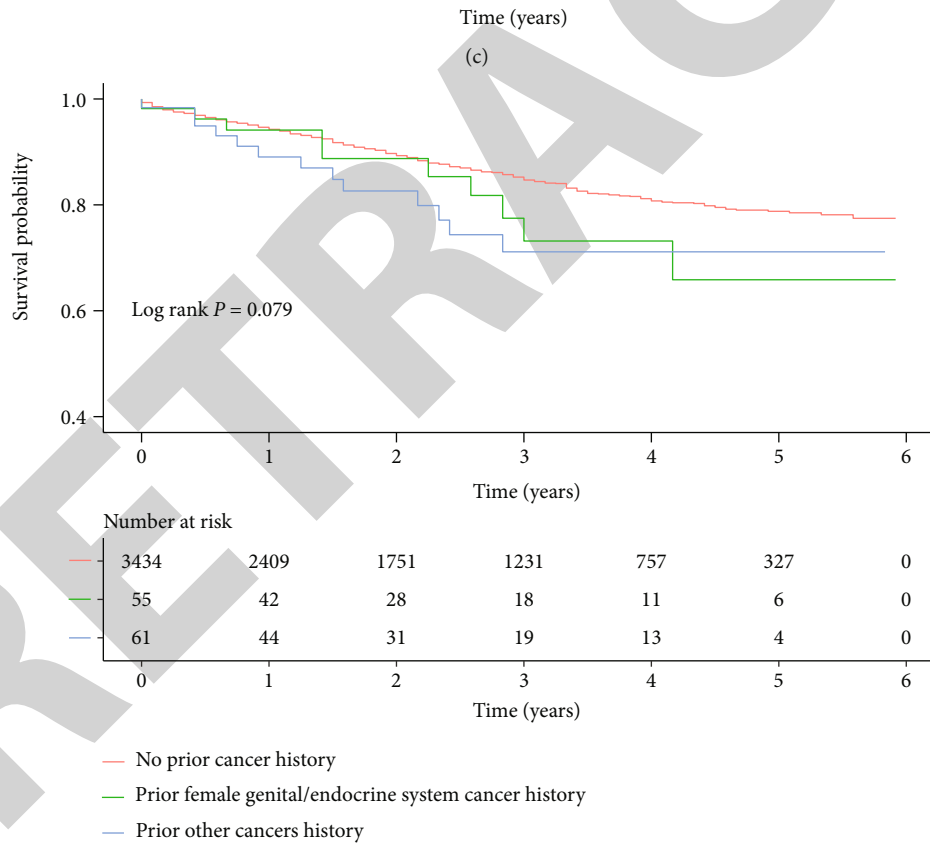
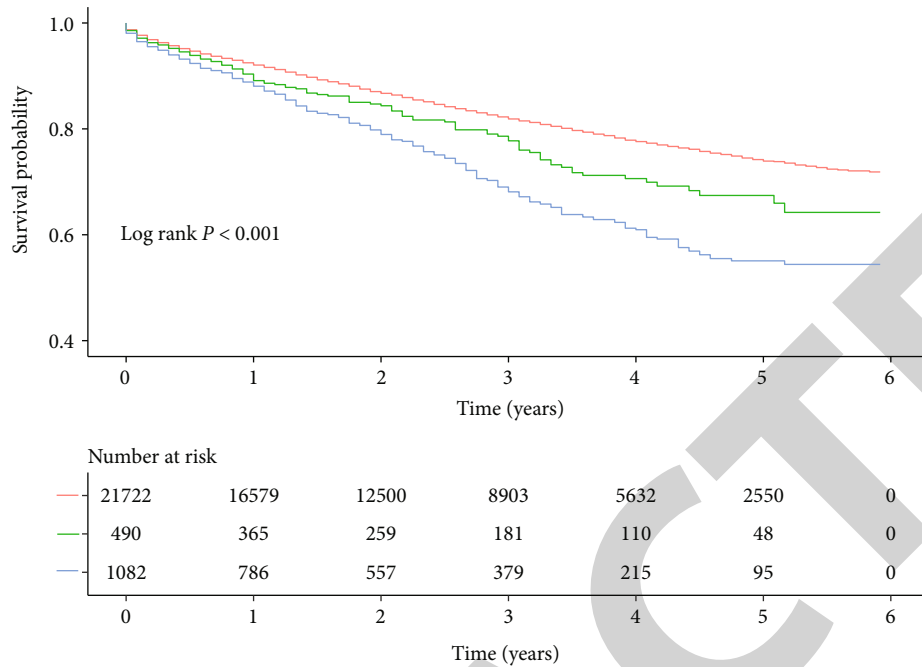


FIGURE 5: Continued.



(d)

FIGURE 5: The K-M curves of the relationship between previous cancer history and the survival of patients with different races. (a) Blacks; (b) Hispanics; (c) whites; (d) others.

explanations included individualized patient biology and treatment responsiveness [18].

This study filled the gap in the relationship between PCA and prognosis of BC patients with different molecular subtypes. However, the study also had some limitations that

should be considered. First, some confounders such as genetic mutations, prior cancer occurred, stage of prior cancer, and type and dose of treatment drugs may affect the survival, but they are not available due to the limitations of the SEER database. Second, compared to the entire SEER

database, the data sample we included in the analysis was small as data on BC molecular subtypes were not complete until after 2010. Third, the sample size of some patients with previous cancer was too small to analyze the relationship between a certain PCA and the survival of BC patients. Fourth, we did not analyze the relationship between PCA and BC-specific survival.

## 5. Conclusion

This study explored the association between PCA and the survival of patients with different molecular subtypes of BC. PCA was associated with poorer survival of patients with triple-negative and HER2-positive subtypes, and the prognosis of patients with Luminal A and Luminal B subtypes may not be influenced by previous female genital/endocrine system cancer history. In BC clinical trials, the exclusion criteria for patients with PCA should be modified according to the BC type, age, and type of PCA rather than directly excluding patients with a history of cancer. Such processing can obtain more accurate clinical trial results.

## Data Availability

The datasets used and/or analyzed during the current study are available from the corresponding author on reasonable request.

## Conflicts of Interest

The authors declare that there is no conflict of interest regarding the publication of this article.

## Authors' Contributions

Weixun Lin, Yaokun Chen, and Zeqi Ji contributed equally to this work and were listed as co-first authors.

## Acknowledgments

This work was supported by the Special Fund Project of Guangdong Science and Technology (No. 210728156901524 and No. 210728156901519), Medical Scientific Research Foundation of Guangdong Province, China (No. A2021432 and No. B2021448), Shantou Medical Science and Technology Planning Project (No. 210521236491457, No. 210625106490696, No. 220518116490772, and No. 220518116490933), and Administration of Traditional Chinese Medicine of Guangdong Province Project (No. 202205092315428030).

## References

- [1] N. Harbeck, F. Penault-Llorca, J. Cortes et al., "Breast cancer," *Nature Reviews Disease Primers*, vol. 5, no. 1, p. 66, 2019.
- [2] H. Sung, J. Ferlay, R. L. Siegel et al., "Global cancer statistics 2020: GLOBOCAN estimates of incidence and mortality worldwide for 36 cancers in 185 countries," *CA: a Cancer Journal for Clinicians*, vol. 71, no. 3, pp. 209–249, 2021.
- [3] A. Jemal, F. Bray, M. M. Center, J. Ferlay, E. Ward, and D. Forman, "Global cancer statistics," *CA: a Cancer Journal for Clinicians*, vol. 61, no. 2, pp. 69–90, 2011.
- [4] M. E. Wood, V. Vogel, A. Ng, L. Foxhall, P. Goodwin, and L. B. Travis, "Second malignant neoplasms: assessment and strategies for risk reduction," *Journal of Clinical Oncology: Official Journal of the American Society of Clinical Oncology*, vol. 30, no. 30, pp. 3734–3745, 2012.
- [5] P. Tanjak, B. Suktipat, N. Vorasan et al., "Risks and cancer associations of metachronous and synchronous multiple primary cancers: a 25-year retrospective study," *BMC Cancer*, vol. 21, no. 1, p. 1045, 2021.
- [6] C. Lin, J. Wu, S. Ding et al., "Impact of prior cancer history on the clinical outcomes in advanced breast cancer: a propensity score-adjusted, population-based study," *Cancer Research and Treatment*, vol. 52, no. 2, pp. 552–562, 2020.
- [7] H. Zhou, Y. Huang, Z. Qiu et al., "Impact of prior cancer history on the overall survival of patients newly diagnosed with cancer: a pan-cancer analysis of the SEER database," *International Journal of Cancer*, vol. 143, no. 7, pp. 1569–1577, 2018.
- [8] C. C. Murphy, D. E. Gerber, and S. L. Pruitt, "Prevalence of prior cancer among persons newly diagnosed with cancer: an initial report from the surveillance, epidemiology, and end results program," *JAMA Oncology*, vol. 4, no. 6, pp. 832–836, 2018.
- [9] S. Jin, R. Pazdur, and R. Sridhara, "Re-evaluating eligibility criteria for oncology clinical trials: analysis of investigational new drug applications in 2015," *Journal of Clinical Oncology: Official Journal of the American Society of Clinical Oncology*, vol. 35, no. 33, pp. 3745–3752, 2017.
- [10] D. E. Gerber, A. L. Laccetti, L. Xuan, E. A. Halm, and S. L. Pruitt, "Impact of prior cancer on eligibility for lung cancer clinical trials," *Journal of the National Cancer Institute*, vol. 106, no. 11, 2014.
- [11] S. L. Pruitt, H. Zhu, D. F. Heitjan et al., "Survival of women diagnosed with breast cancer and who have survived a previous cancer," *Breast Cancer Research and Treatment*, vol. 187, no. 3, pp. 853–865, 2021.
- [12] V. H. Murthy, H. M. Krumholz, and C. P. Gross, "Participation in cancer clinical trials," *Journal of the American Medical Association*, vol. 291, no. 22, pp. 2720–2726, 2004.
- [13] E. S. Kim, S. S. Bruinooge, S. Roberts et al., "Broadening eligibility criteria to make clinical trials more representative: American Society of Clinical Oncology and Friends of Cancer Research Joint Research Statement," *Journal of Clinical Oncology: Official Journal of the American Society of Clinical Oncology*, vol. 35, no. 33, pp. 3737–3744, 2017.
- [14] Y. Q. Wang, J. W. Lv, L. L. Tang et al., "Effect of prior cancer on trial eligibility and treatment outcomes in nasopharyngeal carcinoma: implications for clinical trial accrual," *Oral Oncology*, vol. 90, pp. 23–29, 2019.
- [15] M. Filion, G. Forget, O. Brochu et al., "Eligibility criteria in randomized phase II and III adjuvant and neoadjuvant breast cancer trials: not a significant barrier to enrollment," *Clinical Trials*, vol. 9, pp. 652–659, 2012.
- [16] S. M. Lichtman, R. D. Harvey, M. A. Damiette Smit et al., "Modernizing clinical trial eligibility criteria: recommendations of the American Society of Clinical Oncology-Friends of Cancer Research organ dysfunction, prior or concurrent malignancy, and comorbidities working group," *Journal of Clinical Oncology: Official Journal of the American Society of Clinical Oncology*, vol. 35, no. 33, pp. 3753–3759, 2017.

## *Retraction*

# **Retracted: Polyvinylpyrrolidone K-30-Based Crosslinked Fast Swelling Nanogels: An Impeccable Approach for Drug's Solubility Improvement**

### **BioMed Research International**

Received 8 January 2024; Accepted 8 January 2024; Published 9 January 2024

Copyright © 2024 BioMed Research International. This is an open access article distributed under the Creative Commons Attribution License, which permits unrestricted use, distribution, and reproduction in any medium, provided the original work is properly cited.

This article has been retracted by Hindawi, as publisher, following an investigation undertaken by the publisher [1]. This investigation has uncovered evidence of systematic manipulation of the publication and peer-review process. We cannot, therefore, vouch for the reliability or integrity of this article.

Please note that this notice is intended solely to alert readers that the peer-review process of this article has been compromised.

Wiley and Hindawi regret that the usual quality checks did not identify these issues before publication and have since put additional measures in place to safeguard research integrity.

We wish to credit our Research Integrity and Research Publishing teams and anonymous and named external researchers and research integrity experts for contributing to this investigation.

The corresponding author, as the representative of all authors, has been given the opportunity to register their agreement or disagreement to this retraction. We have kept a record of any response received.

## **References**

- [1] M. U. Minhas, K. U. Khan, M. Sarfraz et al., "Polyvinylpyrrolidone K-30-Based Crosslinked Fast Swelling Nanogels: An Impeccable Approach for Drug's Solubility Improvement," *BioMed Research International*, vol. 2022, Article ID 5883239, 15 pages, 2022.

## Research Article

# Polyvinylpyrrolidone K-30-Based Crosslinked Fast Swelling Nanogels: An Impeccable Approach for Drug's Solubility Improvement

Muhammad Usman Minhas <sup>1</sup>, Kifayat Ullah Khan <sup>2</sup>, Muhammad Sarfraz <sup>3</sup>,  
Syed Faisal Badshah,<sup>4</sup> Abubakar Munir,<sup>5</sup> Kashif Barkat,<sup>4</sup> Abdul Basit <sup>2</sup>, and Mosab Arafat<sup>3</sup>

<sup>1</sup>College of Pharmacy, University of Sargodha, Sargodha City Punjab, Pakistan

<sup>2</sup>Quaid-e-Azam College of Pharmacy, Sahiwal, Punjab, Pakistan

<sup>3</sup>College of Pharmacy, Al Ain University, Al Ain Campus, Al Ain, UAE

<sup>4</sup>Faculty of Pharmacy, University of Lahore, Punjab, Pakistan

<sup>5</sup>Faculty of Pharmacy, Superior University Lahore, Punjab, Pakistan

Correspondence should be addressed to Muhammad Usman Minhas; [us.minhas@hotmail.com](mailto:us.minhas@hotmail.com) and Kifayat Ullah Khan; [kifayat.rph@yahoo.com](mailto:kifayat.rph@yahoo.com)

Received 4 July 2022; Revised 31 July 2022; Accepted 6 August 2022; Published 26 August 2022

Academic Editor: Nauman Rahim Khan

Copyright © 2022 Muhammad Usman Minhas et al. This is an open access article distributed under the Creative Commons Attribution License, which permits unrestricted use, distribution, and reproduction in any medium, provided the original work is properly cited.

Poor solubility is a global issue of copious pharmaceutical industries as large number of drugs in development stage as well as already marketed products are poorly soluble which results in low dissolution and ultimately dosage increase. Current study is aimed at developing a polyvinylpyrrolidone- (PVP-K30-) based nanogel delivery system for solubility enhancement of poorly soluble drug olanzapine (OLP), as solubilization enhancement is the most noteworthy application of nanosystems. Crosslinking polymerization with subsequent condensation technique was used for the synthesis of nanogels, a highly responsive polymeric networks in drug's solubility. Developed nanogels were characterized by percent entrapment efficiency, sol-gel, percent swelling, percent drug loaded content (%DLC), percent porosity, stability, solubility, in vitro dissolution studies, FTIR, XRD, and SEM analysis. Furthermore, cytotoxicity study was conducted on rabbits to check the biocompatibility of the system. Particle size of nanogels was found with  $178.99 \pm 15.32$  nm, and in vitro dissolution study exhibited that drug release properties were considerably enhanced as compared to the marketed formulation OLANZIA. The solubility studies indicated that solubility of OLP was noticeably improved up to 36.7-fold in phosphate buffer of pH 6.8. In vivo cytotoxicity study indicated that prepared PVP-K30-based formulation was biocompatible. On the basis of results obtained, the developed PVP-K30-co-poly (AMPS) nanogel delivery system is expected to be safe, effective, and cost-effective for solubility improvement of poorly soluble drugs.

## 1. Introduction

Poor solubility is a major issue of sundry pharmaceutical industries as about 40% of already marketed drugs and about 75-90% drug candidates in development stage are poorly aqueous soluble [1] calling for exploring effective strategies to improve their solubility and dissolution so as to enhance their efficacies for desirable therapeutic responses [2-4]. These drug products leaves gastrointestinal tract

(G.I.T) before the dissolution and originate inadequate ADME properties leading to reduced clinical effects and dosage escalation [5, 6]. Various strategies have been investigated for solubility enhancement such as polymeric composites [7], polymeric nanoparticles [8], polymeric microneedles [9], polymeric microbeads [10], cocrystals [11], solid lipid nanoparticles (SLNs) [12], micelles [13], hydrogels [14], amorphous solid dispersions [12], liposome [15], nanosuspension [16], nanoemulsion, nanoplex [17],

self-emulsifying drug delivery system (SEDDS), inclusion complexation with cyclodextrins, dendrimers, and nanocapsule [18–20].

Among the aforementioned strategies, due to high swelling ability, high drug loading and entrapment efficiency, stability, reduced particle size, and biocompatibility, nanogels have gained enormous interest in designing the nanocarrier system for solubilization enhancement of poorly soluble drugs [21–24]. Nanogels are solvent swollen nanosized soft polymeric networks that have the ability of absorbing and retaining large amount of water with being dissolved [20, 23, 25]. They are nanoscale hydrogels holding the abilities of hydrogels as well as nanocarriers [20]. They are highly cross-linked networks capable of hosting both hydrophilic and hydrophobic drugs [26, 27]. They are soft nanosized (20–200 nm) and innovative nanocarrier system that could play a dynamic role in addressing various issues faced in pharmaceutical industries related to new chemical entities (NCEs) and marketed products such as inadequate dissolution, poor aqueous solubility, stability, and bioavailability [28–30].

In the current study, olanzapine (OLP) is used as a model drug. It is one of the most appropriate 2<sup>nd</sup> generation atypical antipsychotic drug approved by US FDA as first line therapy for the treatment of psychotic disorders schizophrenia, anxiety, depression, and acute mania with bipolar disorder [31–34]. OLP binds and antagonizes many receptors (serotonin, dopamine, histamine, and alpha-1 adrenergic receptors) [35, 36]. Even though olanzapine (OLP) is a poorly soluble drug (0.0942 mg/mL) which is an impediment to the schizophrenia treatment and leads to poor absorption and unreliable pharmacokinetic profile [37, 38], for this purpose, in the current study, we developed the nanogel drug delivery system to improve the solubility and bioavailability profile of olanzapine.

For polymeric nanocarriers, water loving polymers and monomers offering the most auspicious solution [39]. Hydrophilic polymers/monomers have been widely used for solubility improvement of poorly soluble drugs. Hydrophilic (water loving) polymers shows maximum hydration (90%) as compared to hydrophobic polymers [40]. Previously, our research group has developed poloxamer-407, poly ethylene glycol-4000, and  $\beta$ -cyclodextrin-based nanogels and nanomatrices, respectively [41–43]. Keeping in view, in the current study, polymer polyvinylpyrrolidone (PVP-K30) is investigated for the synthesis of nanogels in which seven (7) different formulations have been developed by changing the ratio of the polymer, monomer, and cross-linker as compared to our previously reported nanogel formulations. PVP-K30 is a water loving nontoxic synthetic polymer with excellent absorbency and biocompatibility [44, 45]. Many researchers reported PVP-K30 in different delivery systems to enhance the solubility of poorly soluble drugs [46, 47].

## 2. Materials and Methods

**2.1. Chemicals.** The active pharmaceutical ingredient (API) of OLP (MW = 312.4 g/mol) was achieved from the Global Pharm. PK. Initiator ammonium persulfate (APS)

(MW = 228.18 g/mol), polymer polyvinylpyrrolidone PVP-K30 (MW = ~ 40000 g/mol), and monomer (AMPS) (MW = 207.24 g/mol) were purchased from Sigma-Aldrich.

## 2.2. Methods

**2.2.1. Synthesis of Polyvinylpyrrolidone- (PVP-K30-) Based Nanogels.** Polyvinylpyrrolidone- (PVP-K30-) based chemically crosslinked nanogels were prepared with some amendments in our previously published polymerization technique [42, 48]. Initially, mixture of polymer polyvinylpyrrolidone and monomer 2-acrylamido-2-methylpropane sulfonic acid (AMPS) was prepared in distilled water using hotplate magnetic stirrer at 300 rpm. The accurately weight amount of crosslinking agent methylene bis-acrylamide (MBA) was solubilized separately in distilled water (20 mL) and ethanol (10 mL) mixture (2:1). After this, weight amount (2 percent with respect to monomer) of reaction initiator APS was added into the PVP/AMPS mixture. Finally, the PVP/AMPS/APS mixture was added into already prepared solution of MBA with continuous stirring (300 rpm) at 50°C, and then the whole mixture was poured into round bottom flask. A round bottom flask was immediately fitted with condenser followed by the reflux-condensation process at 75–85°C. Finally, the prepared gel was sieved and placed in oven for the purpose of drying. The proposed schematic diagram and feed ratio of ingredients used in PVP-K30-based nanogels are shown in Figure 1 and Table 1, respectively.

**2.2.2. Drug Loading of Naive Nanogels.** Developed PVP-K30-based nanogels were loaded with OLP by using the previously reported swelling diffusion method [43]. For drug loading, initially two percent OLP solution (weight/volume) was prepared with methanol and distilled water mixture at the ratio of 4:1. After this, on to the drug solution, specific quantify of developed nanogels was added and sonicated for specific time (30–40 minutes). OLP/nanogel mixture was kept for 24 hours at room temperature for swelling and loading purpose which was then lyophilized (for 4–5 hours) and characterized by various parameters.

## 3. In Vitro Characterization of Nanogels

**3.1. Structural Analysis.** Fourier transform infrared spectroscopy (FTIR) was carried out for structural analysis and to confirm any interactions between drug and ingredients. FTIR (ATR-FTIR, Tensor-27 series, Bruker Co. DEU) was carried out at resolution of 4 cm<sup>-1</sup> for pure drug olanzapine (OLP), polymer polyvinylpyrrolidone (PVP-K30), monomer AMPS, and OLP-loaded nanogels formulation. Scanning range for all samples were kept from 4000 to 600 cm<sup>-1</sup>.

**3.2. Particle Size Analysis.** Particle size of the delivery system is an important factor in solubility and bioavailability enhancement of hydrophobic drugs. For this purpose, a homogenous suspension of prepared optimized nanogels was determined for particle size using particle size analyzer (Malvern instrument, United Kingdom). Prepared nanogel samples were analyzed in ultrapure water filtered with membrane filter having a pore size of 0.22  $\mu$ m [49].

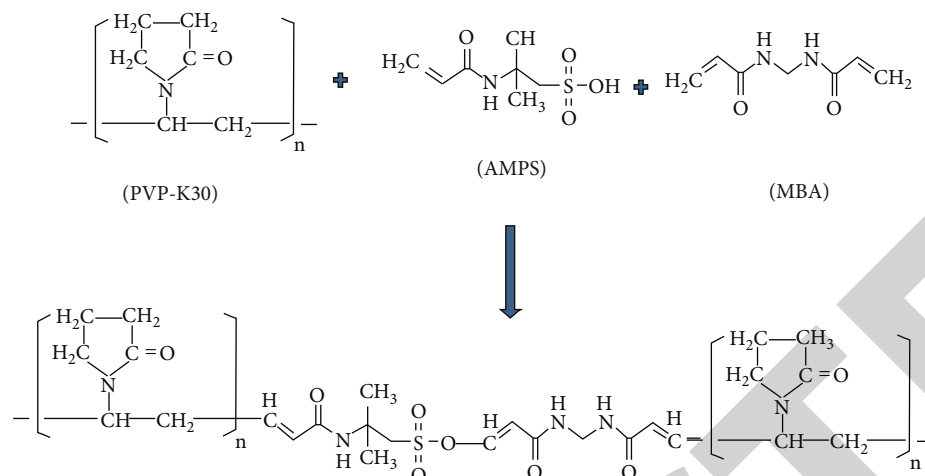


FIGURE 1: Proposed scheme of prepared PVP-K30-based nanogels.

TABLE 1: The ratio of PVP-K30 (g), AMPS (g), methylene bisacrylamide (MBA) (g), and percent drug-loaded content (%DLC) in nanogels.

S/N	Formulation code	PVP-K30	AMPS	MBA	%DLC*
01	PNG-1	01	04	0.5	85.86 ± 1.21
02	PNG-2	02	04	0.5	84.05 ± 2.01
03	PNG-3	03	04	0.5	80.14 ± 2.06
04	PNG-4	03	06	0.5	78.71 ± 1.99
05	PNG-5	03	08	0.5	68.06 ± 2.04
06	PNG-6	03	04	01	90.04 ± 1.78
07	PNG-7	03	04	02	92.89 ± 2.00

\*Values are measured as mean ± SD ( $n = 3$ ).

**3.3. Surface Morphology Using SEM.** Surface morphology of prepared PVP-K30-based formulations was examined by using scanning electron microscope (JSM5910, Japan) with high resolution. For this purpose, PVP-K30-based nanogel samples were spotted on double-adhesive tape attached to gold plated aluminum stub.

**3.4. Powder X-Ray Diffraction Analysis.** Samples of pure drug olanzapine (OLP) and optimized nanogel (loaded & blank) formulations were subjected to X-ray diffraction studies to determine the degree of crystallinity of OLP after loading into the nanogels using X-ray Diffractometer (JDX3522, Japan) as crystallinity is closely related to solubility. PXRD data was recorded in range of 0-60° at 2-theta.

## 4. In Vitro Studies of Prepared Nanogels

**4.1. Swelling Analysis.** Swelling behavior was carried out to analyze the swelling capacity of the prepared nanogels. For this purpose, accurately measured quantity of naive nanogels was placed in unfilled tea bags and then suspended in specified labeled containers of corresponding solutions of pH 6.8 and 1.2 at normal temperature of 37°C ± 0.5. Nanogel samples were taken out at predetermined time intervals, i.e., 02, 05, 10, 15, 20, 30, 40, 50, 60, 90, 120, and 150 minutes

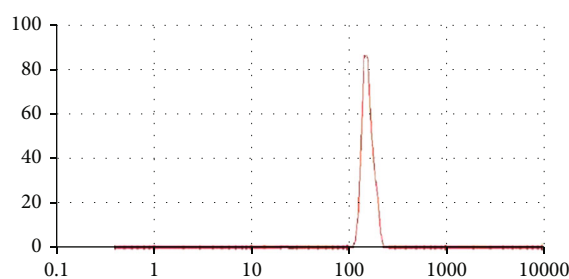


FIGURE 2: Particle size measurement of prepared PVP-K30-based nanogels.

followed by blotted with filter paper. The samples were weighed and returned to their respective containers. Equation (1) was used to calculate swelling index [50].

$$Q \text{ (swelling index)} = \frac{W_2}{W_1}, \quad (1)$$

where  $W_2$  indicates the weight of swollen, and  $W_1$  indicates weight of dried nanogel sample.

**4.2. Sol-Gel Studies.** Sol-gel studies were carried out to analyze the percentage of reactants converted into the product,



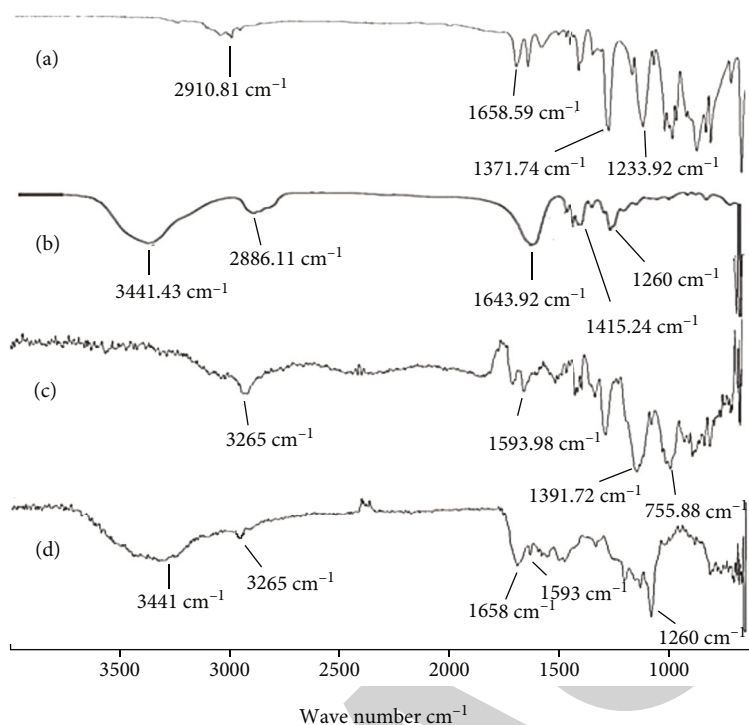


FIGURE 3: FTIR spectra of (a) monomer AMPS, (b) PVP-K30, (c) pure OLP, and (d) OLP-loaded formulation (PNG-7).

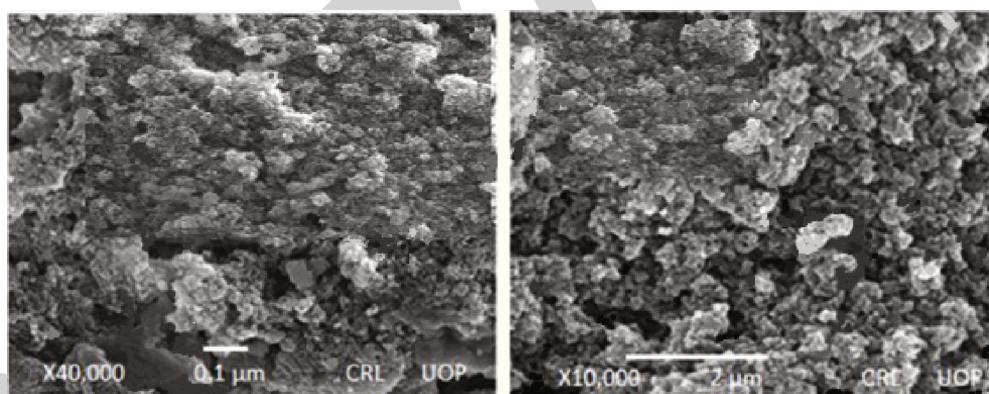


FIGURE 4: SEM micrographs of developed PVP-K30-based formulation (PNG-7) at different resolutions.

i.e., to analyze the % crosslinked as well as uncrosslinked quantity of polymer (PVP-K30) and monomer (AMPS) in the nanogel structure. Sol-gel analysis was done using Soxhlet extraction technique. Accurately measured nanogels, i.e., 500 mg ( $W_1$ ) were taken and subjected to Soxhlet extraction process for approximately 4-5 hours. After extraction process, samples were placed in oven till drying at 40°C and weighed again  $W_2$  in order to measure the % sol-gel fraction by applying Equations (2) and (3).

$$\text{Sol fraction (\%)} = \frac{(W_1 - W_2)}{W_1} \times 100, \quad (2)$$

$$\text{Gel fraction (\%)} = 100 - \text{Sol fraction}. \quad (3)$$

$W_1$  indicates the initial weight (dry) of nanogels, whereas  $W_2$  indicates the weight (dry) after extraction.

**4.3. Entrapment Efficiency and Drug-Loaded Content.** The entrapment efficiency (%) and drug loaded content (%) of PVP-K30-based nanogels were calculated by the absorption and extraction technique [51]. Specific quantity of OLP loaded nanogel formulations (100 mg) was dispersed in the specific solution (50 mL) of phosphate buffer of pH 6.8 followed by stirring at 100 rpm for 1 hour at room temperature. After this, the resultant suspension was filtered through membrane filter having the pore size of 0.45 μm. The resultant solution was then analyzed using UV-spectrophotometer at λ-max 228 nm. %DLC and EE were calculated using

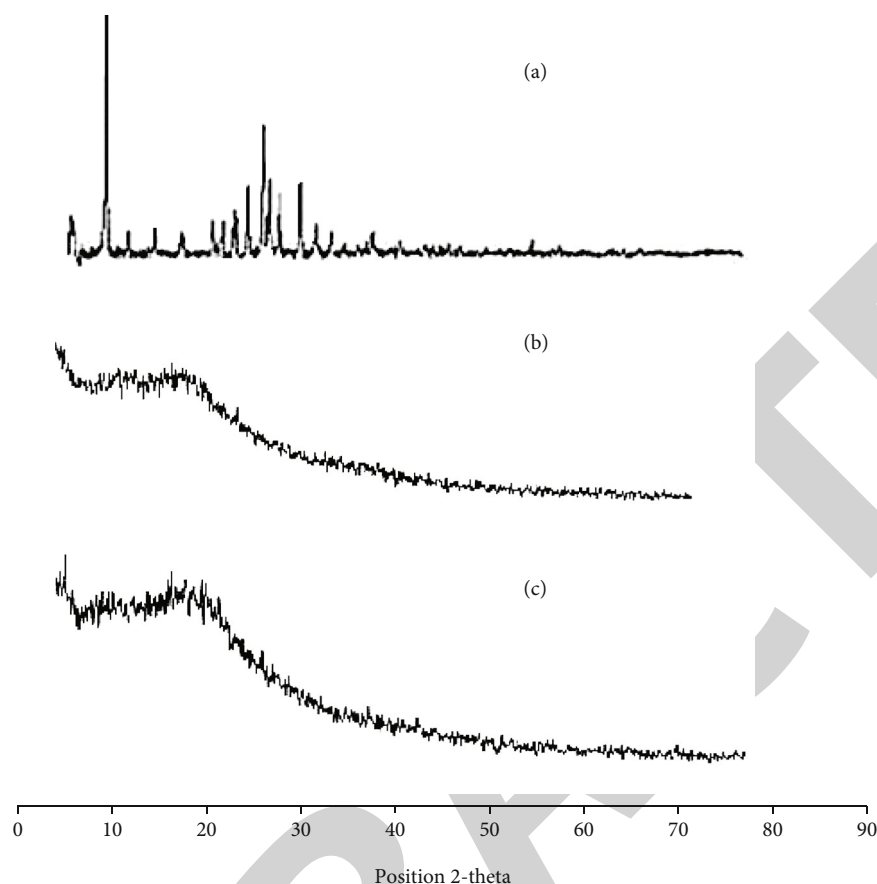


FIGURE 5: PXRD analysis of (a) drug olanzapine (pure), (b) blank nanogels, and (c) OLP-loaded nanogels (PNG-7).

Equations (4) and (5), respectively.

$$\%DLC = \frac{\text{Entrapped drug in formulation}}{\text{Weight of formulation}} \times 100, \quad (4)$$

$$\%EE = \frac{\text{Actual drug contents in formulation}}{\text{Theoretical drug contents in formulation}} \times 100. \quad (5)$$

**4.4. Solubility Studies.** Solubility studies were carried out to analyze the solubility of OLP enhanced by the developed PVP-K30-based nanogels. Solubility of OLP was studied at different pH conditions, i.e., pH 6.8 and pH 1.2 (phosphate buffer solution and HCl solution, respectively) as well as in distilled water. For this purpose, pure drug (OLP) and PVP-K30 nanogel formulations (100 mg) were dispersed in 20 mL of DW, phosphate buffer, and HCl solution separately with continuous stirring at 200 rpm for 24 hours. The solutions were then analyzed using UV-spectrophotometer at  $\lambda$ -max 228 nm [52].

**4.5. Stability and Porosity (%) Evaluation of Nanogels.** ICH guidelines were followed to carry out the stability studies of OLP-loaded PVP-K30 nanogels [53]. For this purpose, formulations were placed in glass vials and kept at  $40 \pm 02^\circ\text{C}$  with  $75 \pm 5\%$  RH in the stability chamber. Various parameters such as any physical changes in the sample, % DLC, FTIR, and

solubility efficiency were analyzed over the specific time period, i.e., six months.

Developed nanogels are highly porous structure which assists in the absorption and drug release from the system. % porosity of PVP-K30-based nanogels were found out using the solvent replacement method. Specific quantity of developed nanogels were weighted and suspended in water and weighted again followed by careful blotting and calculating of weight variation. The percent porosity of formulations was measured using Equation (6).

$$\text{Porosity (\%)} = \frac{(W_h - W_d)}{\rho V} \times 100. \quad (6)$$

$W_h$  represents the weight of saturated nanogels,  $W_d$  represents weight of dried nanogels,  $\rho$  indicates the density of DW, and  $V$  indicates the volume of formulation.

**4.6. In Vitro Drug Release Studies.** Drug release studies of prepared nanogel formulations (PNG1-PNG7) and reference product of olanzapine (OLANZIA) were performed in calibrated 6-station dissolution test apparatus (Curio-Pak.). Samples were placed in 500 mL of phosphate buffer (pH 6.8) and HCl solution (pH 1.2) at 50 rpm ( $37^\circ\text{C} \pm 0.5^\circ\text{C}$ ). Samples were placed in dissolution apparatus using the reported tea bag method. At predefined time intervals, samples were withdrawn (five mL) using a pipette and then diluted with

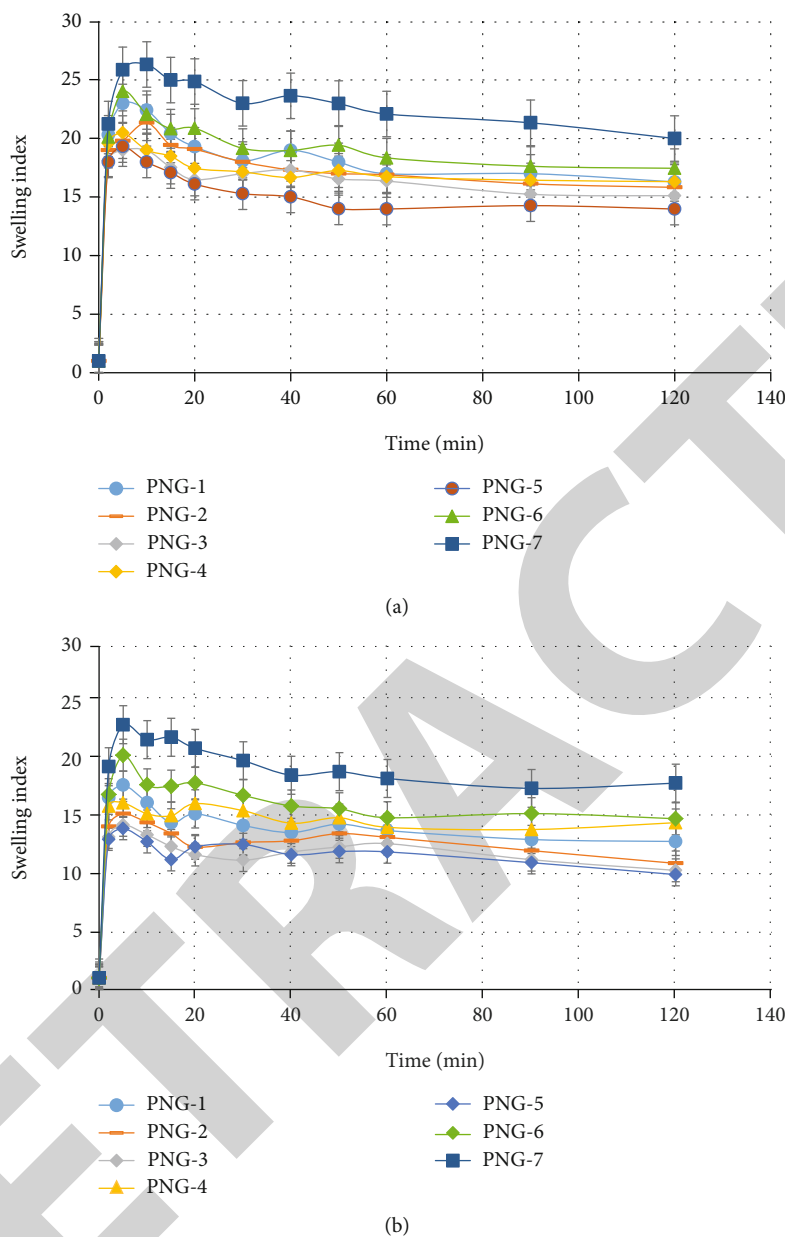


FIGURE 6: (a) Swelling index of developed nanogels (PNG1-PNG7) at phosphate buffer of pH 6.8. (b) Swelling index of developed nanogels (PNG1-PNG7) at HCL buffer of pH 1.2.

equal volume of respective medium to keep the volume constant, and then the amount of drug release was quantified using spectrophotometer at  $\lambda$ -max 228 nm.

**4.7. In Vivo Toxicity Evaluation.** PVP-K30-based developed nanogel formulations are intended to administer orally; for this purpose, compatibility profile of nanogels with the biological environment was analyzed using the rabbit model. Toxicity study was conducted for 14 days in which test animals (rabbits) were randomly divided in to 2 groups, i.e., group C (controlled) and group T (treated) and then kept in cleaned cages. Naive nanogel formulations (5 g/kg) were given orally to group T, and then all animals were observed for water and food consumption, any irritation (ocular/skin), urination, salivation, tremors, general response behavior, diarrhea,

mortality, etc. On the day 15<sup>th</sup>, blood samples were taken followed by slaughtering the animals of both groups for evaluation of blood biochemistry, hematological, liver profile, and weight variation of vital organs [54, 55].

## 5. Results and Discussions

**5.1. Particle Size Analysis.** Large surface area and reduced particle size favor the process of disintegration, dissolution rate, absorption, and ultimately the bioavailability. Solubility of the poorly soluble drugs significantly enhanced when the particle size reduces and vice versa [56]. Nanosystem, i.e., nanogels/nanomatrices/nanosponges/nanoparticles are important and interesting platforms to enhance the solubility, dissolution rate, and bioavailability of poorly soluble drug entities. For

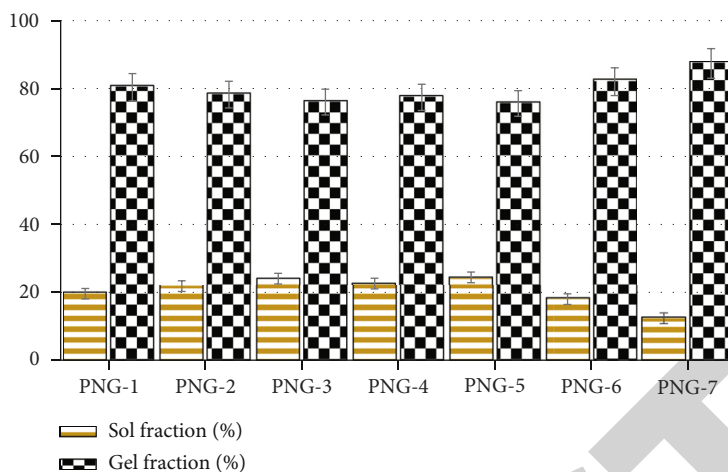


FIGURE 7: Sol-gel analysis of developed nanogel formulations (PNG-1 to PNG-7).

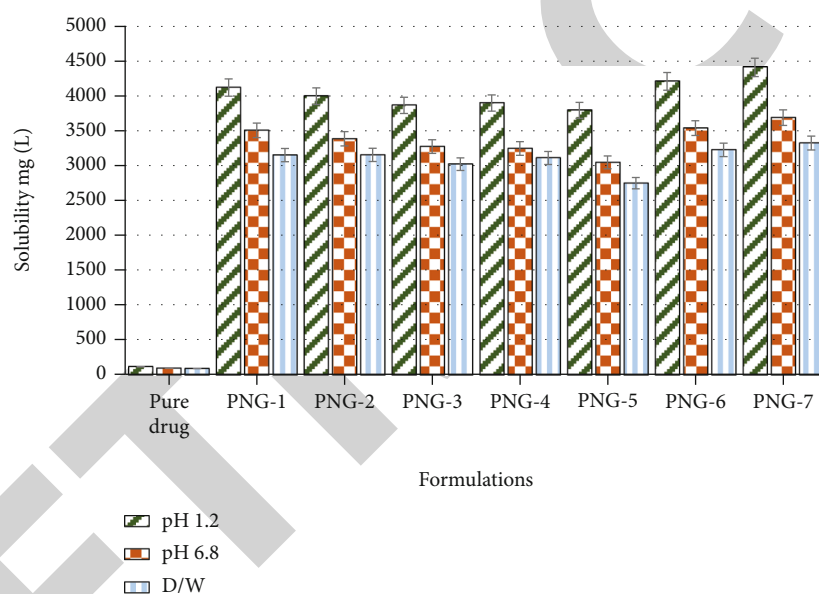


FIGURE 8: Solubility of OLP in prepared nanogels (PNG-1 to PNG-7) and in DW, HCl, and phosphate solutions of pH 6.8 and 1.2, respectively.

particle size analysis, zeta sizer (Nano Zeta Sizer, United Kingdom) was employed. Single peak was observed which indicated that 81% of particle size of PVP-K30-based nanogels were  $178.99 \pm 15.32$  nm as shown in Figure 2. Polydispersity index (PDI) was found 0.51 which indicates that nanogels have very low affinity of forming clusters. Nanotechnology greatly influences the biopharmaceutical performance of the system according to Noyes-Whitney equation, and reduced particle size leads to large surface area which in turn enhances solubility, dissolution rate, and bioavailability [57].

5.2. *Fourier Transform Infrared Spectroscopy (FTIR)*. The FTIR spectra of pure drug olanzapine (OLP), monomer 2-acrylamido-2-methylpropane sulfonic acid (AMPS), polymer polyvinylpyrrolidone (PVP-K30), and OLP loaded formulation (PNG-7) were recorded to confirm

TABLE 2: % porosity of PVP-k30-based nanogels (PNG-1 to PNG-7).

Sr. no.	Formulations	Excipients/reactants	Porosity* (%)
01	PNG-1		$82.054 \pm 1.124$
02	PNG-2	PVP-k30 (polymer)	$78.982 \pm 1.046$
03	PNG-3		$75.846 \pm 1.476$
04	PNG-4		$76.438 \pm 1.354$
05	PNG-5	AMPS (monomer)	$74.854 \pm 0.995$
06	PNG-6		$85.681 \pm 2.001$
07	PNG-7	MBA (crosslinker)	$89.246 \pm 1.763$

\* Values measured as mean  $\pm$  SD ( $n = 3$ ).

TABLE 3: Findings of stability studies of OLP-loaded nanogels.

Sr. no.	Parameters	Fresh reading	After 3 months	After 6 months
1	FTIR analysis	Carried out	Not changed	Not changed
2	%DLC	92.89 ± 2.00	92.001 ± 1.89	91.997 ± 2.013
3	Physical texture	Yellowish appearance	Not changed	Not changed
4	Solubility improvement of OLP by nanogels	Improved up to 36.7-fold	Prominent change not observed	Prominent change not observed

and analyze crosslinking between polymer and monomer as well as check any possible interaction between drug and excipients. FTIR spectra of all reactants have been presented in Figures 3(a)–3(d). The FTIR spectrum of pure AMPS was recorded that showed characteristic band at  $1,658.59\text{ cm}^{-1}$  which was attributed to carbon and oxygen stretching (C=O). Principal peaks at  $1,233.92\text{ cm}^{-1}$  and  $1,371.74\text{ cm}^{-1}$  indicated the symmetrical stretching of sulfur and oxygen group (S=O) that indicated the existence of  $\text{SO}_3\text{H}$  group in AMPS as shown in Figure 3(a). Strong absorption bands at  $1,092.83\text{ cm}^{-1}$  and  $941.96\text{ cm}^{-1}$  were recorded that represent the S-O-C group. Peak at  $2,910.81\text{ cm}^{-1}$  suggested C-H stretching of the  $-\text{CH}_2$  group. FTIR spectrum of polymer PVP-K30 has shown characteristic peak at  $1643.92\text{ cm}^{-1}$  which corresponds to amide C=O bond. Absorption band at  $3441.43\text{ cm}^{-1}$  is attributed to O-H stretching of absorbed water ( $\text{H}_2\text{O}$ ) molecules while absorption peaks at  $2886.11\text{ cm}^{-1}$  and  $1415.24\text{ cm}^{-1}$  attributed to the C-H bonds, and peaks at  $1260\text{ cm}^{-1}$  and  $882\text{ cm}^{-1}$  are allocated to C-N stretching and breathing vibration of the pyrrolidone ring present in the PVP-K30 polymer, respectively, as shown in Figure 3(b) [58]. In the FTIR spectrum of pure drug olanzapine (OLP), characteristic peaks were observed at  $3,265\text{ cm}^{-1}$  which was attributed to the N-H & O-H stretching,  $1,593\text{ cm}^{-1}$  due to C=C,  $2,960\text{ cm}^{-1}$  due to C-H,  $1,391\text{ cm}^{-1}$  due to C=N, and  $755\text{ cm}^{-1}$  due to C-S stretching as shown in Figure 3(c). FTIR band of OLP-loaded nanogels has shown that all the characteristic peaks of drug, polymer polyvinylpyrrolidone (PVP-K30), and AMPS were there with insignificant modifications as shown in Figure 3(d), which indicated the successful crosslinking of reactants and entrapment of drug OLP into the amorphous system of PVP-K30-based nanogels.

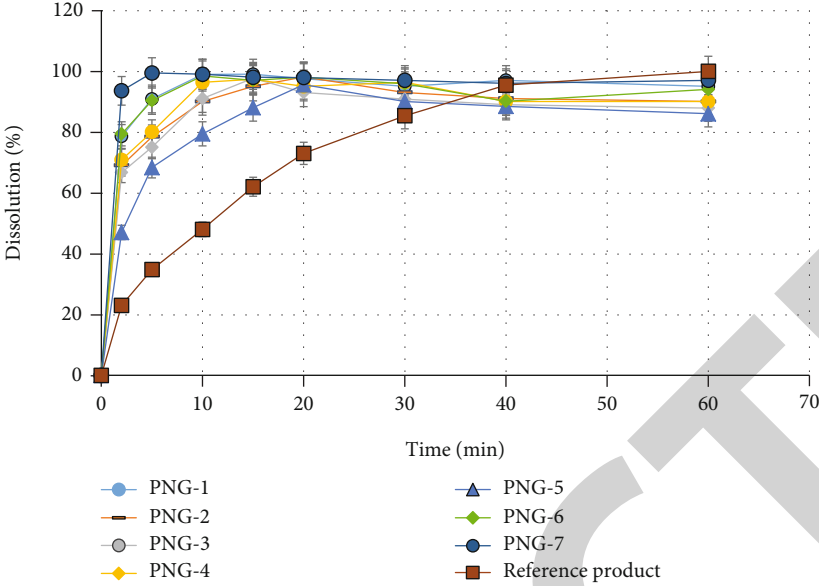
**5.3. Scanning Electron Microscopy (SEM).** In order to examine the surface morphology of the developed PVP-K30-based nanogel formulations, scanning electron microscopy was carried out at different magnifications using scanning electron microscope (JSM-6490A, Tokyo, Japan). SEM images were shown (Figure 4) that developed nanogels were highly porous and spongy. Numerous pores present in PVP-k30-based formulations can be ascribed to the presence of hydrophilic and ionic groups of polymer (PVP-K30) and monomer (AMPS). Upon contact with aqueous media, the porosity favors the nanogels for entrance and release of water and drug, respectively.

**5.4. XRD Analysis.** Figures 5(a)–5(c) present the X-ray diffraction (XRD) patterns of OLP, blank, and OLP-loaded formulation (PNG-7), respectively. The study was conducted

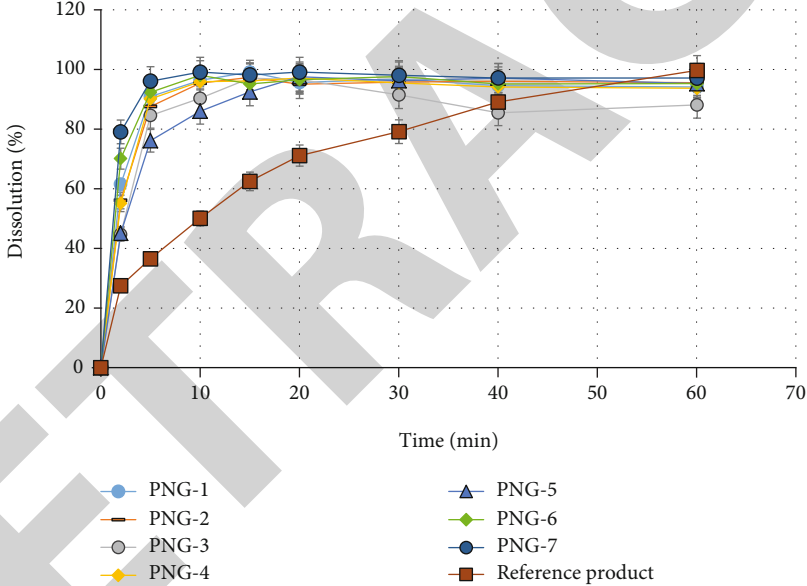
for the purpose to evaluate the degree of crystallinity of pure OLP as well as to find out any possible alterations made in OLP nanocrystals after integrating it into the nanogel amorphous network. It is well known that crystalline drugs have poor aqueous solubility than amorphous form. According to the literature, solubility can be enhanced up to sixteen hundred times due to the amorphous form [59, 60].

The XRD pattern of pure olanzapine (OLP) displayed various characteristics peaks at diffraction angle of 2-theta ( $10\text{--}30^\circ$ ) which pointed of high crystalline nature of OLP as displayed in Figure 5(a). X-ray diffraction spectrum of unloaded PVP-K30 formulation displayed that there was lack of any significant peak which clearly indicated that the crystallinity of OLP by the amorphous nanogels has been effectively masked. In the XRD band of OLP-loaded formulation, the characteristics intense peaks of OLP were there (Figure 5(c)) but with distinct decrease intensity as compared to pure OLP. The broader peaks of OLP with noticeably decrease intensity indicated the successful incorporation of OLP in the amorphous nanogel network which may contributed in the rapid dissolution and solubility enhancement.

**5.5. Swelling Behavior of Nanogels.** Swelling of the system has a huge and direct influence on drug release characteristics; that is why swelling properties of the developed polyvinylpyrrolidone- (PVP-K30-) based nanogel formulations were investigated [61]. Swelling study was carried out in both acid (1.2) and basic (6.8) pH medium to analyze the effect of pH medium as well as polymer PVP-K30, monomer (2-acrylamido 2-methyl propane sulfonic acid), and crosslinking agent MBA concentration on swelling. It was observed from the results that maximum swelling occurred in 2-10 minutes at both pH conditions (1.2 and 6.8), which was ascribed to the highly hydrophilic nature of PVP-K30 and AMPS [62]; moreover, nanogels are small size spongy materials that impart higher swelling abilities which in turn favor the abrupt drug release in aqueous medium [30]. All nanogel formulations have shown excellent swelling results at both higher and lower pH conditions but slightly more at basic pH (6.8) quantitatively as compared to acidic pH (1.2) as shown in Figures 6(a) and 6(b). This was due to the sulfonate anions ( $-\text{SO}_3^-$ ) present in monomer (AMPS) and was protonated into  $-\text{SO}_3\text{H}$ , due to the stout interaction between sulfonate groups resulted additional crosslinking that cause decreased swelling dynamics in acidic medium while in case of higher pH due to the strong electrostatic repulsion between  $-\text{SO}_3^-$  groups as a result of ionization of some sulfonate ions triggered increased swelling dynamics [63, 64].



(a)



(b)

FIGURE 9: Continued.

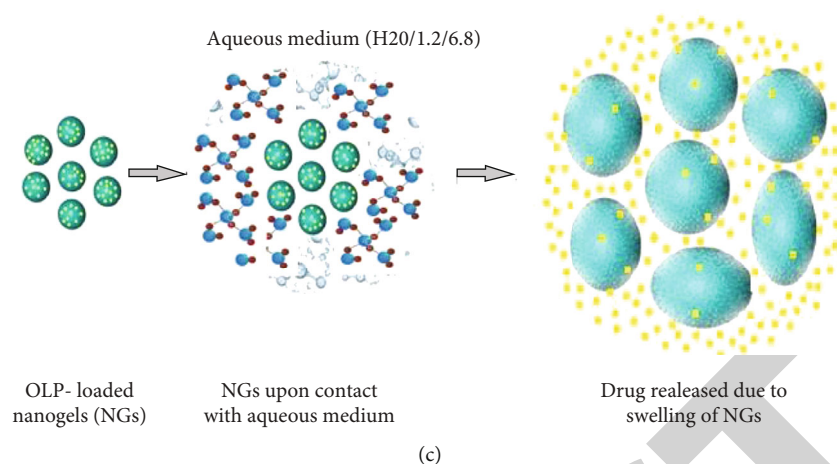


FIGURE 9: (a) Dissolution profile of prepared PVP-K30-based formulations and RP OLANZIA in phosphate buffer of pH 6.8. (b) Dissolution profile of prepared PVP-K30-based formulations (PNG1-PNG7) and RP OLANZIA in HCl solution (pH 1.2). (c) Mechanism illustrating the drug release from the prepared PVP-K30-based formulations.

During swelling experiment, the effect of PVP-K30, AMPS, and crosslinking agent MBA concentration in nanogels was also analyzed. With increase in MBA concentration, swelling index was increased (PNG-6 and PNG-7) due to high crosslinking points in the system. According to Flory's theory, excessive crosslinking causes generation of additional crosslinking points during polymerization process which result in enhanced gelling network and swelling index [65]. The hydrophilic groups (-OH) of polymer (PVP-K30) and monomer (AMPS) and -NH groups introduced by the MBA during radical polymerization are responsible for favorable polymeric network-solvent interaction triggering solvent uptake [66]. Slight decrease was observed in swelling index with increasing mass ratio (Table 1) of polymer/monomer to MBA (PNG1-PNG5) that was due to the availability of less crosslinking points in the solution produced during free radical polymerization which resulted in inadequate gelling structure as shown in Figures 6(a) and 6(b).

**5.6. Sol-Gel Analysis.** Figure 7 has shown the sol-gel analysis of the prepared nanogels (PNG1-PNG7). Sol-gel experiment was conducted in order to find out the uncrosslinked fraction of polymer (PVP-K30) and monomer (AMPS) in the nanogel structure. The results have shown good gelling fraction in all nanogel formulations. Sol fraction is the uncrosslinked components of the gel structure which was removed by extraction process. From sol-gel experiment, it was observed that gel fraction was gradually decreased, and sol fraction increased with increase concentration of polymer polyvinylpyrrolidone (PVP-K30) and monomer AMPS (PNG-1 to PNG-5). Decreased gelling fraction with increase polymer and monomer concentration may be due to excess of free radicals (active sites) produced during polymerization reaction in the system remained uncrosslinked due to less %wt of crosslinking agent (MBA). The ratio of all ingredients is shown in Table 1. Crosslinker is a key factor and directly related to gelling. The result showed that gelling fraction was significantly increased with increase in MBA concentration (PNG-6 and PNG-7) as shown in Figure 7. This may be attrib-

uted to the availability of more crosslinking point in the system, and maximum active site of polymer and monomer was crosslinked to form good gelling network.

**5.7. Solubility Studies.** To determine the solubility of the pure drug OLP by developed PVP-K30-based nanogel formulations (PNG1-PNG7), surplus quantity of pure drug olanzapine (OLP) and nanogel formulations was dispersed in specific amount of DW, HCl, and phosphate solutions of pH 1.2 and 6.8, respectively, by using magnetic hotplate at 300 rpm at 37°C for 24 hrs. UV-spectrophotometer was used to analyze the absorbance both filtered solutions at wavelength of 228 nm. Figure 8 presents the comparison of solubility of pure OLP and OLP-loaded nanogels, in DW, pH 1.2, and pH 6.8 buffer solutions. The solubility of OLP by developed nanogel formulations (PNG-1 to PNG-7) in DW was enhanced up to 33.39, 33.41, 32.01, 32.95, 29.11, 34.19, and 35.21 times, respectively. Similarly, the solubility of OLP by developed nanogel formulations (PNG-1 to PNG-7) in phosphate was improved by 34.51, 33.32, 32.23, 31.94, 29.99, 34.83, and 36.71 times, respectively, while the solubility was enhanced by nanogels in HCl buffer of pH 1.2 up to 33.99, 32.97, 31.88, 32.16, 31.29, 34.73, and 36.39 times, respectively, as compared to the solubility of pure OLP in distilled water, phosphate buffer of pH 6.8, and HCl buffer of pH 1.2.

Substantial enhancement in the solubility of the poorly soluble drug olanzapine may be attributed to the smaller particle size and larger surface area of the PVP-k3-based nanogels, wettability, and solubilizing effect of hydrophilic excipients (polyvinylpyrrolidone-K30 and AMPS) used and amorphous structure of nanogels which also confirmed by XRD analysis. Incorporation of poorly soluble drugs into hydrophilic polymeric matrix leads to enhanced solubility [67].

**5.8. Stability and Porosity (%) Analysis of Nanogels.** Table 2 presents the data of porosity (%) of developed PVP-k30-based nanogels (PNG-1 to PNG-7). It was noted that the number of

pores in the nanogel structure decreased by increasing the concentration of polymer polyvinylpyrrolidone-K30 (PNG-1 to PNG-3) and monomer AMPS (PNG-4 and PNG-5). This was may be due to the high feed content ratio of polymer PVP-K30 in PNG-2 and 3 with respect to the crosslinker MBA, due to which some concentration of polymer molecules remained uncrosslinked due to insufficient crosslinker. The observations did not match with the results of our previously reported studies in which the porosity was increased with the increase in polymer and monomer concentration [43]. In the current study, the feed content ratio of PVP-K30 and AMPS was higher as compared to the previously reported studies which indicated that the feed content ratio of all the ingredients such as polymer, monomer, and crosslinker is a crucial factor that affect the porosity, swelling, and sol-gel fraction as well as drug release. The average number of pores increased with the increasing of the concentration of crosslinking agent MBA (PNG-6 & PNG-7). This may be due to the high crosslinking points in the system due to MBA concentration, i.e., maximum portion of the polymer and monomer was crosslinked, and proper gel structure was formed which results in increased gel fraction as well as porosity as presented in Table 2.

Table 3 shows the data observed during the stability studies. The prescribed study of OLP-loaded PVP-K30-based nanogels over the specified time period, i.e., six months displayed that developed nanogels remained stable. No evident alteration/modification was noticed in physical texture, percent drug-loaded content values, FTIR spectrum, and solubility enhancement efficiency which overall endorsed the stability of the developed PVP-K30-based nanogel formulation.

**5.9. In Vitro Dissolution Studies and Percent Drug-Loaded Content.** To find out the in vitro drug OLP-release profile from polyvinylpyrrolidone- (PVP-K30-) based nanogel carrier system, dissolution study was performed in phosphate and HCl solutions of pH 6.8 and 1.2, respectively. Dissolution experiment was carried out for all prepared nanogel formulations (PNG1-PNG7) as well as for marketed product of olanzapine (OLANZIA) so that to compare the drug release with prepared nanogels. Quick and rapid drug release was observed in 5 to 10 minutes from all prepared nanogel formulations at both pH (1.2 and 6.8) but insignificantly more in 6.8 quantitatively as presented in Figures 9(a) and 9(b). Excellent and rapid drug release was attributed to the hydrophilic and highly amorphous nature of nanogels which favored high swelling and rapid drug release. Moreover, incorporation of a hydrophobic drug entity in a hydrophilic and amorphous polymeric network might result in its enhanced solubility as well as fast dissolution in the aqueous media because when water loving polymer/monomer dissolves, the entrapped drug presents itself as very fine particles for fast dissolution as illustrated in Figure 9(c).

Quantitatively more and rapid OLP release in phosphate buffer was due to the sulfonate anions ( $-\text{SO}_3^-$ ) present in monomer (AMPS) that were protonated into  $-\text{SO}_3\text{H}$ , due to the stout interaction between sulfonate groups resulted more crosslinking which in turn cause decreased swelling ratio in acidic solution (1.2) while in case of basic pH due

TABLE 4: Physical observations examined during toxicity study in both groups.

Parameters observed	Group C	Group T
1. Body weight (kg)		
Prior treatment	01.86 ± 0.14	01.86 ± 0.16
7 <sup>th</sup> day	01.88 ± 0.15	01.87 ± 0.15
14 <sup>th</sup> day	01.89 ± 0.13	01.86 ± 0.14
2. Food consumption (g)		74.01
Prior treatment	71.56 ± 2.12	72.65 ± 2.99
7 <sup>th</sup> day	73.02 ± 2.32	74.34 ± 2.08
14 <sup>th</sup> day	72.87 ± 2.83	74.01 ± 2.56
3. Water consumption (mL)		
Prior treatment	190.04 ± 2.00	188.87 ± 2.79
7 <sup>th</sup> day	191.46 ± 2.85	191.63 ± 2.66
14 <sup>th</sup> day	193.10 ± 2.45	191.09 ± 3.02
4. Dermal toxicity	Not observed	Not observed
5. Ocular toxicity	Not observed	Not observed
6. Mortality rate	No	No

Values are measured as mean ± SD (n = 3).

TABLE 5: Hematological examination of animals of both groups.

Laboratory findings	Group C	Group T
RBC count ( $10^6/\text{mm}^3$ )	05.69 ± 1.02	05.82 ± 1.07
WBC count ( $10^9/\text{L}$ )	06.12 ± 0.45	06.17 ± 0.73
Platelet count ( $10^9/\text{L}$ )	209.11 ± 2.21	204 ± 2.69
Neutrophils (%)	56.62 ± 1.95	53.76 ± 1.53
Monocytes (%)	03.78 ± 0.23	03.84 ± 0.06
Eosinophil (%)	03.33 ± 0.34	03.68 ± 0.29
Hemoglobin (g/dL)	13.13 ± 0.36	13.25 ± 0.44
Lymphocytes (%)	40.25 ± 1.13	41.16 ± 1.00

Values are measured as mean ± SD (n = 3).

TABLE 6: Biochemical examination of liver profile of group C and group T.

Biochemical analysis	Group C	Group T
Cholesterol level ( $\text{mg.dL}^{-1}$ )	62.45 ± 2.56	61.91 ± 2.33
Uric acid level ( $\text{mg.dL}^{-1}$ )	03.67 ± 1.34	03.41 ± 0.94
Bilirubin ( $\text{mg.dL}^{-1}$ )	00.80 ± 0.87	00.90 ± 0.65
Urea (serum) level ( $\text{mg.dL}^{-1}$ )	15.14 ± 2.01	15.88 ± 1.23
Creatinine ( $\text{mg.dL}^{-1}$ )	01.19 ± 0.43	01.05 ± 0.74
Triglycerides level ( $\text{mg.dL}^{-1}$ )	54.07 ± 2.03	53.71 ± 2.73
Alkaline phosphate (IU.L <sup>-1</sup> )	48.89 ± 1.99	52.86 ± 2.01
Aspartate transaminase (IU.L <sup>-1</sup> )	28.08 ± 2.13	27.39 ± 1.90
Alanine aminotransferase (IU.L <sup>-1</sup> )	143.46 ± 2.3	144.78 ± 2.1

Values are measured as mean ± SD (n = 3).



TABLE 7: Effects of administered of PVP-K30 nanogel formulation in the weights (g) of vital organs of test animals.

Animal groups	Heart	Liver	Lung	Kidney	Stomach	Spleen
Group C (control)	5.01 ± 0.43	6.99 ± 2.03	8.95 ± 1.67	13.05 ± 1.44	12.88 ± 1.39	1.85 ± 0.76
Group T (treated)	4.95 ± 0.37	7.21 ± 1.86	9.35 ± 2.00	12.92 ± 2.13	13.08 ± 2.04	1.93 ± 0.82

Values are measured as mean ± SD ( $n = 3$ ).

to the strong electrostatic repulsion between  $-\text{SO}_3^-$  groups as a result of ionization of some sulfonate ions triggered increased swelling ratio and in turn, higher drug release was examined in higher pH 6.8 [61, 63].

Besides the effect of pH on dissolution rate and drug release characteristics, effect of polyvinylpyrrolidone-K30 (polymer), AMPS (monomer), and crosslinking agent concentration was also analyzed. In the first three formulations (PNG1-PNG3), polymer PVP-K30 was gradually increased while kept the concentration of remaining ingredients constant as presented in Table 1. It was observed that drug released was slightly decreased as shown in Figure 9. Similar results were observed in case of AMPS (monomer). This was due to less crosslinking points in the system because the crosslinking agent concentration was remained constant. Similarly, DLC and EE were also decreased with increasing polymer/monomer concentration as shown in Table 1. In formulations PNG-6 and PNG-7, the concentration of MBA was gradually increased while kept the polymer and monomer concentration constant. There was an observed increase in drug release as well as drug-loaded content as shown Figure 9. This was due to the more crosslinking points in the solution, and all active sites of polymer and monomer produced by the initiator were crosslinked to form good gelling structure.

In order to compare the developed PVP-K30-based nanogels, in vitro dissolution study was also carried out for commercially available OLP tablets (OLANZIA) in both pH conditions (6.8 and 1.2). It was observed that in comparison with the prepared nanogels, equal concentration of drug (OLP) was released in 40-60 minutes from the reference product in basic medium (pH 6.8) and 30-40 minutes in acidic medium as displayed in Figures 9(a) and 9(b). This significant difference with the reference product indicates that the solubility and drug release characteristics are significantly enhanced by the developed nanogels.

**5.10. In Vivo Toxicity Evaluation.** As the developed nanogel drug delivery system intended to be administered orally, for this purpose, toxicity study was conducted to analyze the compatibility profile of the system. Toxicity study was performed in accordance with the United Kingdom Animals (Scientific Procedure) act, 1986, and associated guidelines. The procedure followed by the study was reviewed and approved by the Pharmacy Animal Ethics Committee, Department of Pharmaceutics, Faculty of Pharmacy, IUB-Pakistan. During the study, animals were carefully observed physically for water and food consumption, any irritation (ocular/skin), urination, salivation, tremors, general response behavior, body weight, diarrhea, mortality, etc. All the

forementioned physical parameters (Table 4) indicated that there no drastic change was observed.

After the 14<sup>th</sup> day, all animals were slaughtered for the hematological biochemical examination in order to determine the effect of developed nanogels on the biological system. Blood samples from animals were immediately collected in EDTA tubes to avoid blood coagulation. The laboratory findings of hematological/biochemical tests were found normal which confirmed that prepared nanogels were safe and biocompatible as shown in Tables 5 and 6. Previously, similar observations are reported by Minhas et al. [50].

During toxicity study, the effect on weight of vital organs was also evaluated; for this purpose, vital organs of the animals (group C and group T) were carefully removed and immersed in formalin solution. No perceptible change was recorded in organ weights of both groups as presented in Table 7. So, conclusively, toxicity study indicated that the developed nanogels are biocompatible with the biological system.

## 6. Conclusion

To date, 70-90% drugs under development and about 40% marketed drugs are poorly soluble which greatly affect their pharmacokinetic profile. To tackle this common problem, in the current research, PVP-K30-based nanogels have been successfully prepared by free radical polymerization technique. XRD analysis indicated highly amorphous nature of nanogels which was the key factor in solubilization enhancement according to literature solubility that can be enhanced up to 1600 times by applying amorphous form. Solubility studies revealed that olanzapine (OLP) solubility is enhanced 36.7-fold by prepared nanogels. In vitro dissolution studies exhibited significantly higher and rapid release of OLP at both pH conditions (6.8 and 1.2) as compared with OLANZIA (reference product). Cytotoxicity evaluation endorsed the safety of nanogels. Conclusively, it could be mentioned that amorphous, spongy, and porous structure of the developed PVP-K30-based nanogels could made them an excellent choice for the solubility enhancement of poorly soluble drugs.

## Data Availability

The data used to support the findings of this study are included within the article.

## Conflicts of Interest

The authors report no competing interests.

## Authors' Contributions

Muhammad Usman Minhas contributed to the conceptualization, investigation, data curation, writing, methodology, and supervision. Kifayat Ullah Khan contributed to the conceptualization, methodology, and writing-review and editing. Muhammad Sarfraz contributed to the validation, visualization, review, and editing. Syed Faisal Badshah, Kashif Barkat, Abubakar Munir, Abdul Basit and Mosab Arafat contributed to the writing-review and editing.

## Acknowledgments

We acknowledge the Department of Pharmaceutics, Faculty of Pharmacy, the Islamia University of Bahawalpur for providing the research facilities. This research was financially supported by the Higher Education Commission (HEC) of Pakistan in the form of indigenous scholarship. The scholar award number is 518-2MD5-50043811.

## References

- [1] R. Ambrus, P. Szabó-Révész, T. Kiss et al., "Application of a suitable particle engineering technique by pulsed laser ablation in liquid (PLAL) to modify the physicochemical properties of poorly soluble drugs," *Journal of Drug Delivery Science and Technology*, vol. 57, article 101727, 2020.
- [2] S. V. Jermain, C. Brough, and R. O. Williams III, "Amorphous solid dispersions and nanocrystal technologies for poorly water-soluble drug delivery - an update," *International Journal of Pharmaceutics*, vol. 535, no. 1-2, pp. 379–392, 2018.
- [3] Y. Xie and Y. Yao, "Octenylsuccinate hydroxypropyl phytylglycogen, a dendrimer-like biopolymer, solubilizes poorly water-soluble active pharmaceutical ingredients," *Carbohydrate Polymers*, vol. 180, pp. 29–37, 2018.
- [4] N. Bolourchian, M. Nili, S. M. Foroutan, A. Mahboubi, and A. Nokhodchi, "The use of cooling and anti-solvent precipitation technique to tailor dissolution and physicochemical properties of meloxicam for better performance," *Journal of Drug Delivery Science and Technology*, vol. 55, article 101485, 2020.
- [5] M. Sharma, R. Sharma, D. K. Jain, and A. Saraf, "Enhancement of oral bioavailability of poorly water soluble carvedilol by chitosan nanoparticles: optimization and pharmacokinetic study," *International Journal of Biological Macromolecules*, vol. 135, pp. 246–260, 2019.
- [6] B. M. Sanches and E. I. Ferreira, "Is prodrug design an approach to increase water solubility?," *International Journal of Pharmaceutics*, vol. 568, article 118498, 2019.
- [7] A. M. Yousaf, M. Ramzan, Y. Shahzad, T. Mahmood, and M. Jamshaid, "Fabrication and in vitro characterization of fenofibric acid-loaded hyaluronic acid-polyethylene glycol polymeric composites with enhanced drug solubility and dissolution rate," *International Journal of Polymeric Materials and Polymeric Biomaterials*, vol. 68, no. 9, pp. 510–515, 2019.
- [8] N. R. Bali, M. P. Shinde, S. B. Rathod, and P. S. Salve, "Enhanced transdermal permeation of rasagiline mesylate nanoparticles: design, optimization, and effect of binary combinations of solvent systems across biological membrane," *International Journal of Polymeric Materials and Polymeric Biomaterials*, vol. 70, no. 3, pp. 158–173, 2021.
- [9] J. Mao, H. Wang, Y. Xie et al., "Transdermal delivery of rapamycin with poor water-solubility by dissolving polymeric microneedles for anti-angiogenesis," *Journal of Materials Chemistry B*, vol. 8, no. 5, pp. 928–934, 2020.
- [10] K. Ghosal, S. Adak, C. Agatemor, G. Praveen, N. Kalarikkal, and S. Thomas, "Novel interpenetrating polymeric network based microbeads for delivery of poorly water soluble drug," *Journal of Polymer Research*, vol. 27, no. 4, p. 98, 2020.
- [11] A. Naqvi, M. Ahmad, M. U. Minhas, K. U. Khan, F. Batool, and A. Rizwan, "Preparation and evaluation of pharmaceutical co-crystals for solubility enhancement of atorvastatin calcium," *Polymer Bulletin*, vol. 77, no. 12, pp. 6191–6211, 2020.
- [12] D. K. Veni and N. V. Gupta, "Development and evaluation of Eudragit coated environmental sensitive solid lipid nanoparticles using central composite design module for enhancement of oral bioavailability of linagliptin," *International Journal of Polymeric Materials and Polymeric Biomaterials*, vol. 69, no. 7, pp. 407–418, 2020.
- [13] P. D. Maheswari, D. Rambhau, and M. L. Narasu, "Micelles entrapped microparticles technology: a novel approach to resolve dissolution and bioavailability problems of poorly water soluble drugs," *Journal of Microencapsulation*, vol. 37, no. 3, pp. 254–269, 2020.
- [14] B. M. Alam, T. Aouak, N. M. Alandis, and M. M. Alam, "Synthesis, characterization, drug solubility enhancement, and drug release study of poly (methacrylic acid-graft-simvastatin)," *International Journal of Polymeric Materials and Polymeric Biomaterials*, vol. 64, no. 5, pp. 229–241, 2015.
- [15] Y. Bi, B. Lv, L. Li et al., "A liposomal formulation for improving solubility and oral bioavailability of nifedipine," *Molecules*, vol. 25, no. 2, p. 338, 2020.
- [16] A. Alshweiat, I. I. Csóka, F. Tömösi et al., "Nasal delivery of nanosuspension-based mucoadhesive formulation with improved bioavailability of loratadine: preparation, characterization, and in vivo evaluation," *International Journal of Pharmaceutics*, vol. 579, article 119166, 2020.
- [17] B. Dong and K. Hadinoto, "Carboxymethyl cellulose is a superior polyanion to dextran sulfate in stabilizing and enhancing the solubility of amorphous drug-polyelectrolyte nanoparticle complex," *International Journal of Biological Macromolecules*, vol. 139, pp. 500–508, 2019.
- [18] F. Najafi, M. Salami-Kalajahi, H. Roghani-Mamaqani, and A. Kahaie-Khosrowshahi, "A comparative study on solubility improvement of tetracycline and dexamethasone by poly(propylene imine) and polyamidoamine dendrimers: an insight into cytotoxicity and cell proliferation," *Journal of Biomedical Materials Research Part A*, vol. 108, no. 3, pp. 485–495, 2020.
- [19] S. Potharaju, S. K. Mutyam, M. Liu et al., "Improving solubility and oral bioavailability of a novel antimalarial prodrug: comparing spray-dried dispersions with self-emulsifying drug delivery systems," *Pharmaceutical Development and Technology*, vol. 25, no. 5, pp. 625–639, 2020.
- [20] J. Siirilä, S. Hietala, F. S. Ekholm, and H. Tenhu, "Glucose and maltose surface functionalized thermoresponsive poly (N-vinylcaprolactam) nanogels," *Biomacromolecules*, vol. 21, no. 2, pp. 955–965, 2020.
- [21] I. Neamtu, A. G. Rusu, A. Diaconu, L. E. Nita, and A. P. Chiriac, "Basic concepts and recent advances in nanogels as carriers for medical applications," *Drug Delivery*, vol. 24, no. 1, pp. 539–557, 2017.

- [22] H. K. Yadav, N. A. Al Halabi, and G. A. Alsalloum, "Nanogels as novel drug delivery systems-a review," *Journal of Pharmacy and Pharmaceutical Research*, vol. 1, no. 5, pp. 1–8, 2017.
- [23] L. Navarro, L. E. Theune, and M. Calderón, "Effect of cross-linking density on thermoresponsive nanogels: a study on the size control and the kinetics release of biomacromolecules," *European Polymer Journal*, vol. 124, article 109478, 2020.
- [24] K. U. Khan, M. U. Minhas, S. F. Badshah, M. Suhail, A. Ahmad, and S. Ijaz, "Overview of nanoparticulate strategies for solubility enhancement of poorly soluble drugs," *Life Sciences*, vol. 291, article 120301, 2022.
- [25] L. Peltonen, "Practical guidelines for the characterization and quality control of pure drug nanoparticles and nanocrystals in the pharmaceutical industry," *Advanced Drug Delivery Reviews*, vol. 131, pp. 101–115, 2018.
- [26] Y. Zhang, O. C. J. Andrén, R. Nordström et al., "Off-stoichiometric thiol-ene chemistry to dendritic nanogel therapeutics," *Advanced Functional Materials*, vol. 29, no. 18, article 1806693, 2019.
- [27] M. Kaur, K. Sudhakar, and V. Mishra, "Fabrication and biomedical potential of nanogels: an overview," *International Journal of Polymeric Materials and Polymeric Biomaterials*, vol. 68, no. 6, pp. 287–296, 2019.
- [28] A. R. C. Richa, "Synthesis of a novel gellan-pullulan nanogel and its application in adsorption of cationic dye from aqueous medium," *Carbohydrate Polymers*, vol. 227, article 115291, 2020.
- [29] M. Suhail, J. M. Rosenholm, M. U. Minhas et al., "Nanogels as drug-delivery systems: a comprehensive overview," *Therapeutic Delivery*, vol. 10, no. 11, pp. 697–717, 2019.
- [30] S. Jain, R. K. Ancheria, S. Shrivastava, S. L. Soni, and M. Sharma, "An overview of Nanogel–novel drug delivery system," *Asian Journal of Pharmaceutical Research and Development*, vol. 7, no. 2, pp. 47–55, 2019.
- [31] T. Zhuang, W. Zhang, L. Cao et al., "Isolation, identification and characterization of two novel process-related impurities in olanzapine," *Journal of Pharmaceutical and Biomedical Analysis*, vol. 152, pp. 188–196, 2018.
- [32] S. R. S. Rudrangi, V. Trivedi, J. C. Mitchell, S. R. Wicks, and B. D. Alexander, "Preparation of olanzapine and methyl- $\beta$ -cyclodextrin complexes using a single-step, organic solvent-free supercritical fluid process: An approach to enhance the solubility and dissolution properties," *International Journal of Pharmaceutics*, vol. 494, no. 1, pp. 408–416, 2015.
- [33] K. N. Günther, J. Banner, K. Linnet, and S. S. Johansen, "Segmental hair analysis of olanzapine and *N*-desmethyl-olanzapine in postmortem hair from mentally ill patients by LC-MS/MS," *Journal of Pharmaceutical and Biomedical Analysis*, vol. 190, article 113510, 2020.
- [34] N. Jawahar, P. K. Hingarh, R. Arun et al., "Enhanced oral bioavailability of an antipsychotic drug through nanostructured lipid carriers," *International Journal of Biological Macromolecules*, vol. 110, pp. 269–275, 2018.
- [35] N. Anup, S. Thakkar, and M. Misra, "Formulation of olanzapine nanosuspension based orally disintegrating tablets (ODT); comparative evaluation of lyophilization and electro-spraying process as solidification techniques," *Advanced Powder Technology*, vol. 29, no. 8, pp. 1913–1924, 2018.
- [36] D. Riman, J. Rozsypal, V. Halouzka, J. Hrbac, and D. Jirovsky, "The use of micro carbon pencil lead electrode for sensitive HPLC-ED analysis of selected antipsychotic drugs," *Microchemical Journal*, vol. 154, article 104606, 2020.
- [37] M. R. de Freitas, L. A. Rolim, M. F. L. R. Soares, P. J. Rolim-Neto, M. M. Albuquerque, and J. L. Soares-Sobrinho, "Inclusion complex of methyl- $\beta$ -cyclodextrin and olanzapine as potential drug delivery system for schizophrenia," *Carbohydrate Polymers*, vol. 89, no. 4, pp. 1095–1100, 2012.
- [38] N. F. da Costa, A. I. Fernandes, and J. F. Pinto, "Measurement of the amorphous fraction of olanzapine incorporated in a co-amorphous formulation," *International Journal of Pharmaceutics*, vol. 588, article 119716, 2020.
- [39] L. Zhang, Y. Hu, X. Jiang, C. Yang, W. Lu, and Y. H. Yang, "Camptothecin derivative-loaded poly(caprolactone-co-lactide)-b-PEG-b- poly(caprolactone-co-lactide) nanoparticles and their biodistribution in mice," *Journal of Controlled Release*, vol. 96, no. 1, pp. 135–148, 2004.
- [40] S. Shah, N. Rangaraj, K. Laxmikeshav, and S. Sampathi, "Nanogels as drug carriers - Introduction, chemical aspects, release mechanisms and potential applications," *International Journal of Pharmaceutics*, vol. 581, article 119268, 2020.
- [41] K. U. Khan, N. Akhtar, and M. U. Minhas, "Ploxamer-407-co-poly (2-acrylamido-2-methylpropane sulfonic acid) cross-linked nanogels for solubility enhancement of olanzapine: synthesis, characterization, and toxicity evaluation," *AAPS PharmSciTech*, vol. 21, no. 5, p. 141, 2020.
- [42] K. U. Khan, M. U. Minhas, M. Sohail et al., "Synthesis of PEG-4000-co-poly (AMPS) nanogels by cross-linking polymerization as highly responsive networks for enhancement in meloxicam solubility," *Drug Development and Industrial Pharmacy*, vol. 47, no. 3, pp. 465–476, 2021.
- [43] K. U. Khan, M. U. Minhas, S. F. Badshah, M. Sohail, and R. M. Sarfraz, " $\beta$ -cyclodextrin modification by cross-linking polymerization as highly porous nanomatrices for olanzapine solubility improvement; synthesis, characterization and biocompatibility evaluation," *Journal of Drug Delivery Science and Technology*, vol. 67, article 102952, 2022.
- [44] M. Anwar, F. Pervaiz, H. Shoukat et al., "Formulation and evaluation of interpenetrating network of xanthan gum and polyvinylpyrrolidone as a hydrophilic matrix for controlled drug delivery system," *Polymer Bulletin*, vol. 78, pp. 59–80, 2020.
- [45] V. Balamuralidhara, T. M. Pramod Kumar, N. Vishal Gupta, A. Getyala, and H. V. Gangadharappa, "Development of a novel biodegradable superporous hydrogel for gastroretentive application," *International Journal of Polymeric Materials and Polymeric Biomaterials*, vol. 62, no. 10, pp. 524–532, 2013.
- [46] M. Jafar, M. S. Khalid, M. F. E. Aldossari et al., "Formulation of curcumin- $\beta$  cyclodextrin-polyvinylpyrrolidone supramolecular inclusion complex: experimental, molecular docking and preclinical anti-nociceptive assessment," *Drug Development and Industrial Pharmacy*, vol. 46, no. 9, pp. 1524–1534, 2020.
- [47] P. I. Febriyenti, E. Zaini, F. Ismed, and H. Lucida, "Preparation and characterization of quercetin-polyvinylpyrrolidone K-30 spray dried solid dispersion," *Journal of Pharmacy & Pharmacognosy Research*, vol. 8, no. 2, pp. 127–134, 2020.
- [48] S. Asghar, N. Akhtar, M. U. Minhas, and K. U. Khan, "Bi-polymeric spongy matrices through cross-linking polymerization: synthesized and evaluated for solubility enhancement of acyclovir," *AAPS PharmSciTech*, vol. 22, no. 5, p. 181, 2021.
- [49] S. Tanveer, M. Ahmad, M. U. Minhas, A. Ahmad, and K. U. Khan, "Chitosan-PVA-co-poly (2-acrylamido-2-methylpropane sulfonic acid) cross-linked hybrid IPN-nanogels for

## Retraction

# Retracted: Downregulation of miR-221-3p by LncRNA TUG1 Promoting the Healing of Closed Tibial Fractures in Mice

### BioMed Research International

Received 8 January 2024; Accepted 8 January 2024; Published 12 February 2024

Copyright © 2024 BioMed Research International. This is an open access article distributed under the Creative Commons Attribution License, which permits unrestricted use, distribution, and reproduction in any medium, provided the original work is properly cited.

This article has been retracted by Hindawi following an investigation undertaken by the publisher [1]. This investigation has uncovered evidence of one or more of the following indicators of systematic manipulation of the publication process:

- (1) Discrepancies in scope
- (2) Discrepancies in the description of the research reported
- (3) Discrepancies between the availability of data and the research described
- (4) Inappropriate citations
- (5) Incoherent, meaningless and/or irrelevant content included in the article
- (6) Manipulated or compromised peer review

The presence of these indicators undermines our confidence in the integrity of the article's content and we cannot, therefore, vouch for its reliability. Please note that this notice is intended solely to alert readers that the content of this article is unreliable. We have not investigated whether authors were aware of or involved in the systematic manipulation of the publication process.

Wiley and Hindawi regrets that the usual quality checks did not identify these issues before publication and have since put additional measures in place to safeguard research integrity.

We wish to credit our own Research Integrity and Research Publishing teams and anonymous and named external researchers and research integrity experts for contributing to this investigation.

The corresponding author, as the representative of all authors, has been given the opportunity to register their agreement or disagreement to this retraction. We have kept a record of any response received.

### References

- [1] L. Liu and Y. Yuan, "Downregulation of miR-221-3p by LncRNA TUG1 Promoting the Healing of Closed Tibial Fractures in Mice," *BioMed Research International*, vol. 2022, Article ID 1624446, 11 pages, 2022.

## Research Article

# Downregulation of miR-221-3p by LncRNA TUG1 Promoting the Healing of Closed Tibial Fractures in Mice

Laiyou Liu  and Yinpeng Yuan

Department of Orthopedics, The Second Hospital of Shanxi Medical University, Taiyuan, 030001 Shanxi, China

Correspondence should be addressed to Laiyou Liu; [liulaiyou@sydey.org.cn](mailto:liulaiyou@sydey.org.cn)

Received 18 July 2022; Accepted 5 August 2022; Published 26 August 2022

Academic Editor: Nauman Rahim Khan

Copyright © 2022 Laiyou Liu and Yinpeng Yuan. This is an open access article distributed under the Creative Commons Attribution License, which permits unrestricted use, distribution, and reproduction in any medium, provided the original work is properly cited.

**Objective.** To probe into the effect of LncRNA TUG1 on the healing of closed tibial fracture in mice. **Methods.** The closed tibial fracture model of mice was established, selecting the mouse osteoblast line MC3T3-E1, with the cells separated into four groups. The expression levels of TUG1 and miR-221-3p were determined by RT-qPCR analysis, with the targeting relationship between TUG1 and miR-221-3p authenticated by dual luciferase reporter (DLR) assay, detection of cell migration (CM) ability based on Transwell cell migration (TCM) assay, and cell proliferation (CP) acquired by cell counting kit-8 (CCK-8). **Results.** Prediction results of the target gene by bioinformatics software showed that miR-221-3p had binding sites with the 3'-UTR of TUG1, and DLR assay authenticated the targeting relationship between LncRNA TUG1 and miR-221-3p. Downregulation of TUG1 inhibited osteoblast CP and CM and promoted osteoblast cell apoptosis (CA). Cell cycle analysis indicated that miR-221-3p provoked cell cycle arrest in G1 stage of MC3T3-E1 cells. The siLncRNA-NC group had higher anticyclin D1 and D3 levels than the siLncRNA TUG1 group, with a lower CA rate in the former, implying that miR-221-3p overexpression inhibited osteoblast CP and CM and LncRNA TUG1 inhibited CA. Downregulation of miR-221-3p partly reversed the retardation out of downregulating TUG1 on osteoblast CP and CM. Bcl-2 level was higher in the LncRNA TUG1 group compared to the siLncRNA TUG1 and miR-221-3p overexpression groups, with remarkably lower SDF-1 level in the miR-221-3p overexpression group than those in the control, miRNA-NC, and LncRNA TUG1 groups. **Conclusion.** The downregulation of miR-221-3p by LncRNA TUG1 can promote the healing of closed tibial fractures in mice.

## 1. Introduction

Fracture healing is a complex natural recovery process after the occurrence of traumatic fractures with the involvement of multiple molecules and cells among which osteoblast cell proliferation (CP) and cell apoptosis (CA) play a pivotal part in bone healing and remodeling [1]. MicroRNAs (miRNAs), as single-stranded, endogenous, noncoding small RNA molecules, can bind with the 3'-untranslated region (3'-UTR) of target messenger RNAs and affect the differentiation and growth of osteoblasts, chondrocytes, and osteoclasts. According to related studies, LncRNA TUG1, a chromatin-modifying complex located on human chromosome 22q12.2, has a high expression in vascular endothelial cells and regulates the CP and CA of oncocytes, making it a potential tumor biomarker and therapeutic target [2]. Cur-

rently, a lot of research has authenticated that LncRNA TUG1 influences the malignant behavior of tumors by inhibiting miRNAs [3, 4]. For instance, LncRNA TUG1 can adsorb miR-29c-3p, which enhances the malignant behavior of gastric adenocarcinoma [5]. Yao et al. have found that knockout of LncRNA TUG1 can inhibit viability, CM, and differentiation and lead to CA of osteoblasts in patients with maxillary fractures, suggesting that LncRNA TUG1 is also involved in the biological process of osteoblast CP and CA [6].

Inhibitory miRNAs can inhibit osteoblast CP and promote CA by targeting osteogenic genes in vitro [7, 8]. For example, increased miR-221-3p expression during bone healing in diabetic fracture patients can lead to impaired endochondral ossification and reduced bone remodeling [9]. miR-221-3p, a member of miR-221, can regulate the

TABLE 1: qPCR primer sequence (5'→3').

Genes	Sequences
miR-221-3p	Forward primer 5'-ACACTCCAGCTGGGAGCTACATTGTC-3' Reverse primer 5'-CTCAACTGGTGTCGTGGA-3'
TUG1	Forward primer 5'-TCAGTAGCTGCCACCATG-3' Reverse primer 5'-TGCTTGGTGAGTCGTGTCTC-3'
U6	Forward primer 5'-AGAGAAGATTAGCATGGCCCCTG-3' Reverse primer 5'-ATCCAGTGCAGGGTCCGAGG-3'

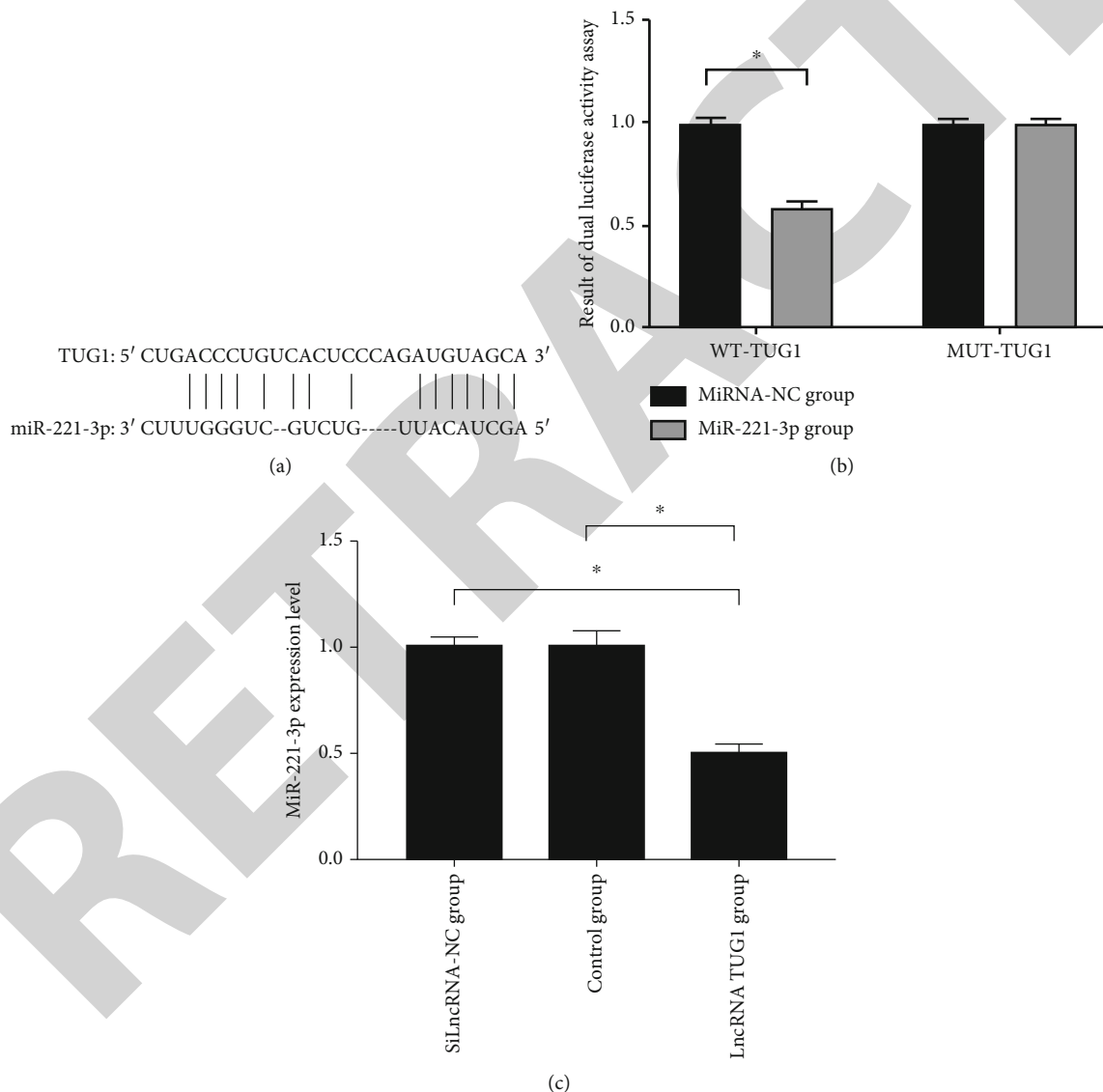


FIGURE 1: (a) Targeting relationship between LncRNA TUG1 and miR-221-3p. (b) TUG1 expression levels acquired by DLR assay. (c) miR-221-3p expression levels acquired by RT-qPCR assay; \* $P < 0.001$ .

CP and differentiation of oncocytes in gastric, thyroid, and hepatic cancers. This miRNA has an approximate mechanism in bone healing in patients with osteoarthritis, and because of its mechanosensitivity, extracellular vesicles in

chondrocytes of osteoarthritis patients can transfer it to osteoblasts so that it acts as an intercellular messenger to reduce the bone formation of osteoblasts in vitro [10]. Although no studies have analyzed the function of miR-

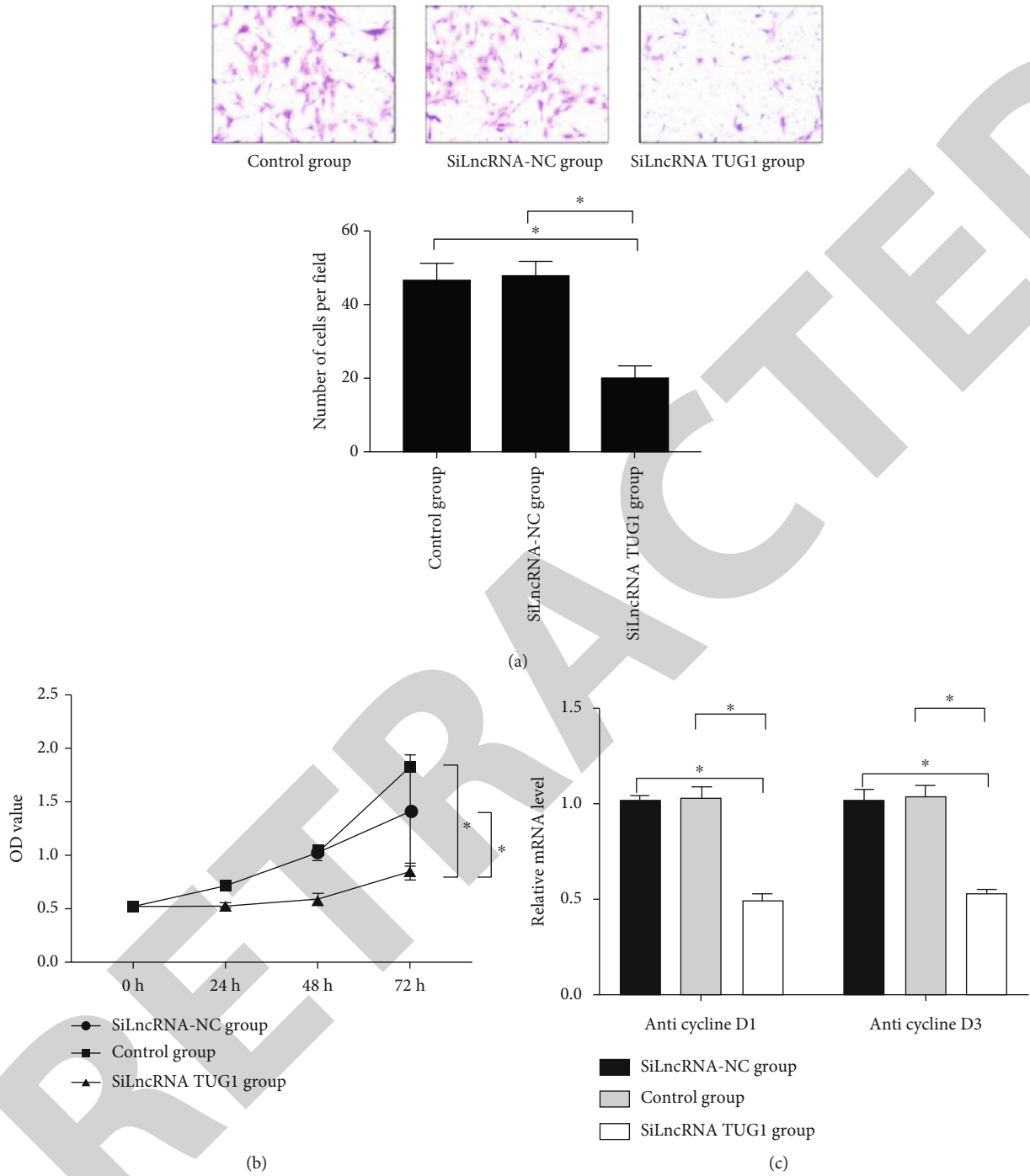


FIGURE 2: Continued.

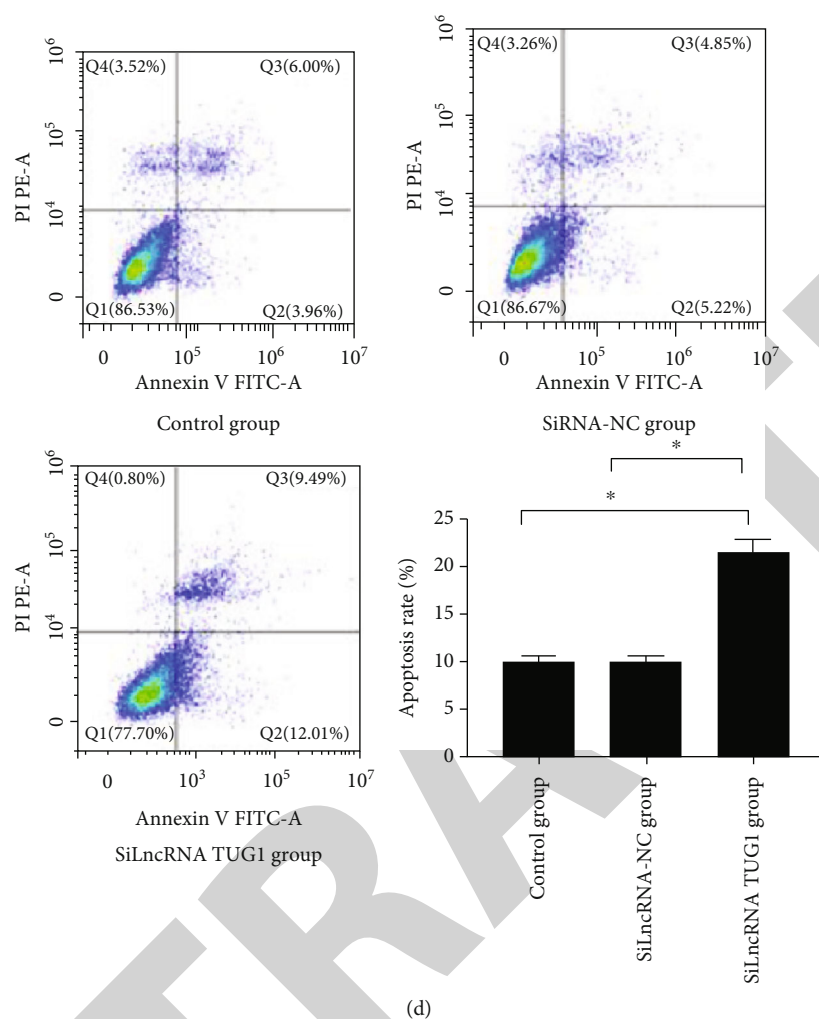


FIGURE 2: (a) CM acquired by TCM assay. (b) CP acquired by CCK-8 assay. (c) Anticyclin D1 and D3 levels based on immunoblot analysis. (d) CA rates acquired by apoptosis assay; \*  $P < 0.001$ .

221-3p on closed tibial fracture patients, the discovery of this miRNA undoubtedly provides information on the pathological process of bone healing in closed tibial fracture patients. Since the targeting relationship with miR-221-3p and ability of adsorbing miRNA and partly reversing its retardation effect, the analysis of long-noncoding RNA (LncRNA) is expected to offer an innovative strategy for treating closed tibial fracture patients. There is still a gap in the research of LncRNA TUG1 and miR-221-3p affecting closed tibial fractures, so this study will explore the molecular mechanism of LncRNA TUG1 promoting osteoblast CP and CM in closed tibial fractures through downregulation of miR-221-3p.

## 2. Materials and Methods

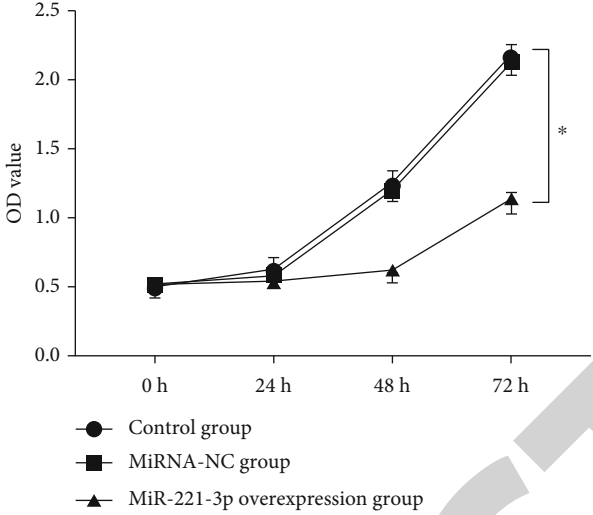
**2.1. Fracture Model of Animal.** SPF 5-6-week-old BALB/c mice ( $n = 60$ ) (Beijing Vital River Laboratory Animal Tech. Co., Ltd.; SCXK (Jing)-2016-0011) were fed in the IVC system of the Animal Experimental Center. The research conformed to the standards of the Animal Care and Use Review Office, and relevant operations were implemented

based on the animal management regulations of SSTC of China. Anesthesia was performed with 3% isoflurane (Lunanbeite Pharma. Co., Ltd., CN). A sterile bench was established for posterolateral incision and blunt dissection of the right tibial fracture model of mice before disinfecting by 0.5% povidone iodine solution (Nanda Pharma. Co., Ltd., Nanjing, CN). The tibia was cut with a diamond disc, with the fracture site fixed with a 0.6 mm intramedullary needle. 30 mice were executed on day 14 after fracture to obtain samples for in-depth analysis, with the remaining mice executed in subsequent experiments.

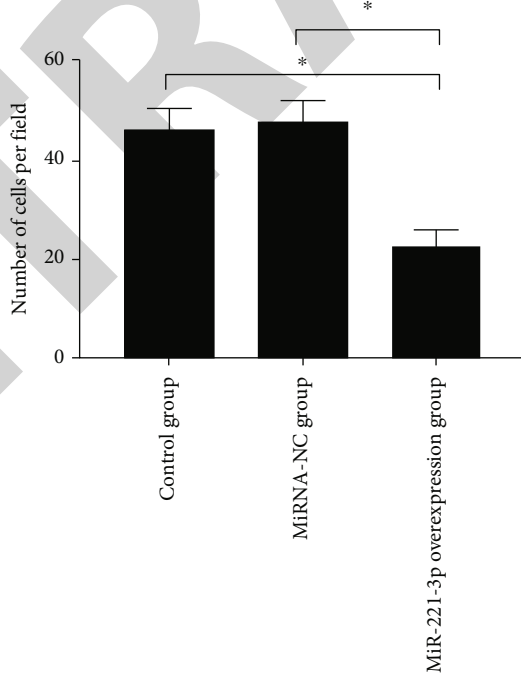
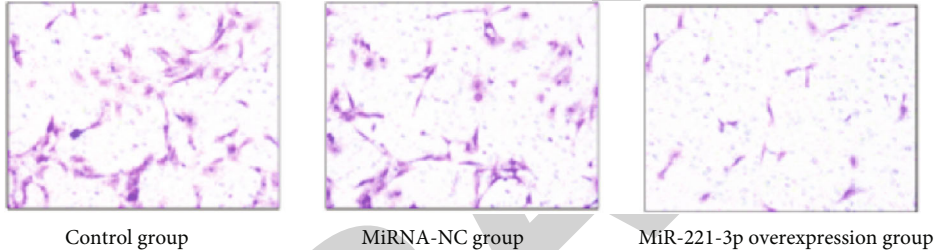
**2.2. Treatment of Mice in Fracture Model.** On days 0, 4, and 7 after surgery, 100  $\mu\text{L}$  of fetal bovine serum (FBS) (Thermo Fisher Sci., SH, CN) was applied to the fracture site of mice in the control group, with 100  $\mu\text{L}$  of 200  $\mu\text{M}$  FBS applied to the siLncRNA TUG1 group, LncRNA TUG1 group, and simiR-221-3p group.

**2.3. Cell Culture and Transfection.** MC3T3-E1, from the cell bank of CAS, was chosen as the murine osteoblastic cell lines. They were cultured in an incubator (37°C, 5% CO<sub>2</sub>)



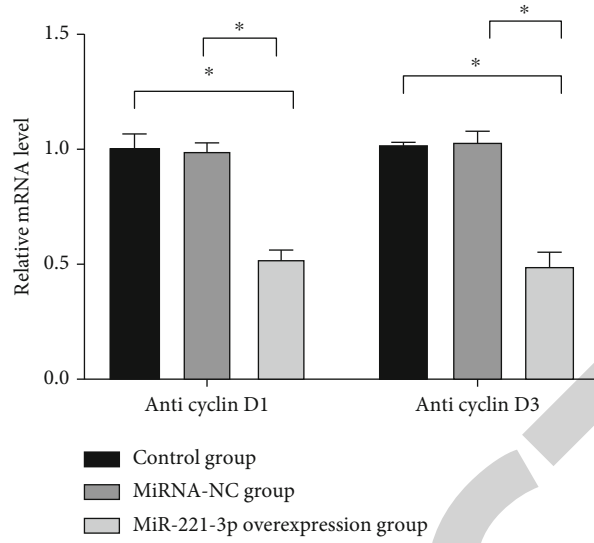


(a)

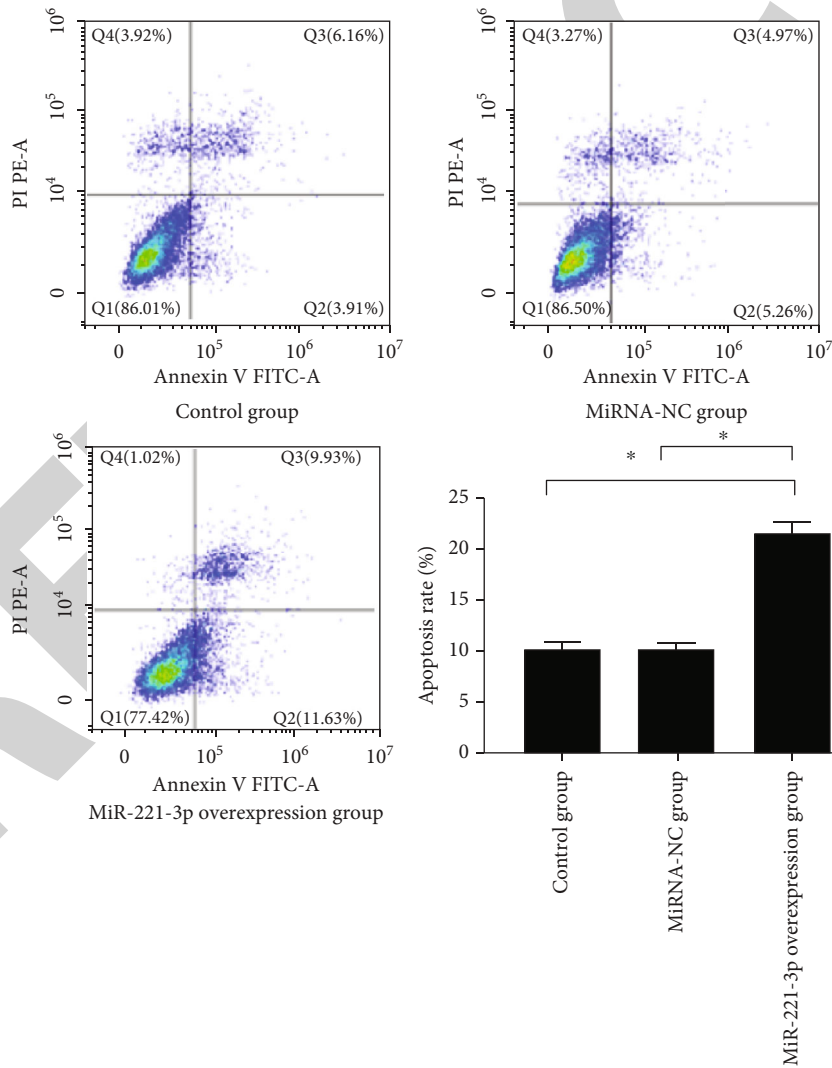


(b)

FIGURE 3: Continued.



(c)



(d)

FIGURE 3: (a) CM acquired by CCK-8 assay. (b) CP acquired by TCM assay. (c) Anticyclin D1 and D3 levels based on immunoblot analysis. (d) CA rates acquired by apoptosis assay; \* $P < 0.001$ .

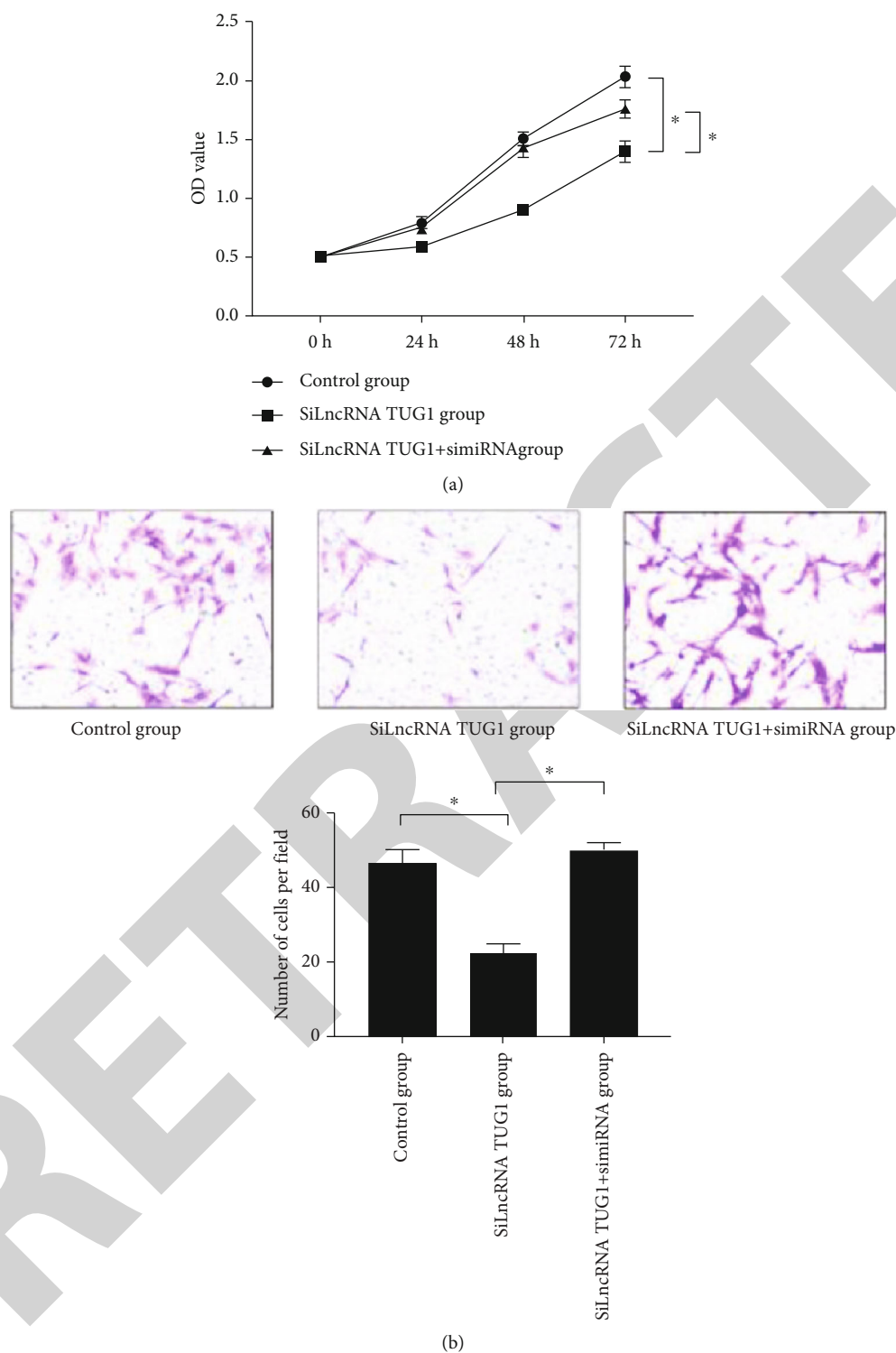


FIGURE 4: (a) CP acquired by CCK-8 assay. (b) CM acquired by TCM assay; \* $P < 0.001$ .

with  $\alpha$ -MEM (Thermo Fisher Sci., SH, CN) (containing 10% FBS (Thermo Fisher Sci., SH, CN) and 1% Pen/Strep (Pfizer, NY, USA)) and dissociated with 0.25% trypsin (Thermo Fisher Sci., SH, CN), with cell passage followed. The logarithmic growth phase cells in good condition were used for

subsequent experiments. LncRNA TUG1-NC, LncRNA TUG1, and simiR-221-3p were synthesized artificially by a gene pharmaceutical company (Sanyuan Gene Pharma. Co., Ltd., Beijing, CN) under the condition of 200  $\mu$ M FBS and transfected into MC3T3 cells with Lipofectamine™

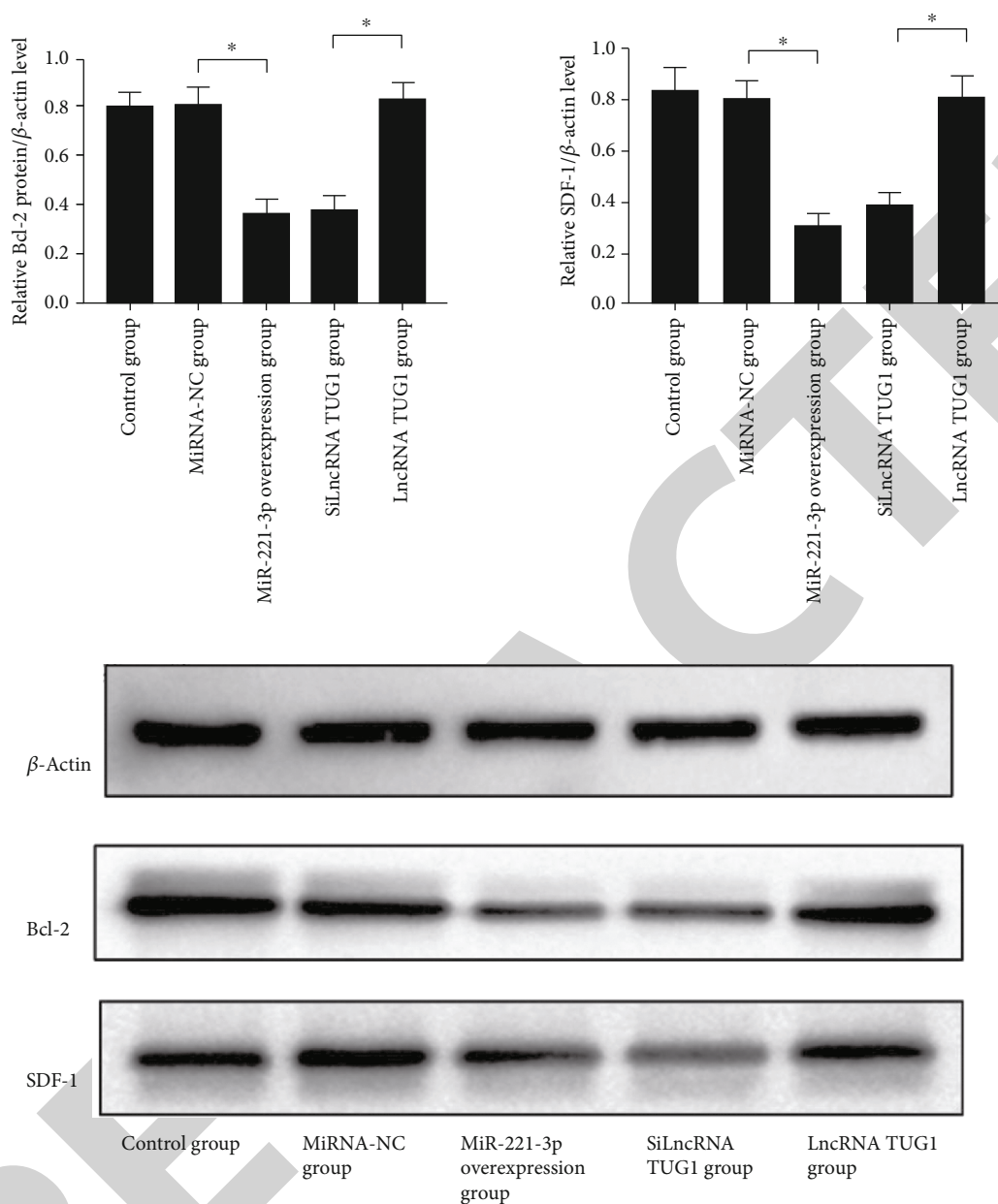


FIGURE 5: Protein expression levels based on immunoblot analysis;  $*P < 0.001$ .

3000 transfection reagent (Invitrogen, CA, USA). All operations were performed strictly based on the instructions, with a 48 h of incubation of the transfected cells for RNA and protein analysis.

**2.4. CCK-8 Assay.** Before 4 h of incubation at 37°C, the cells were planted in 96-well plates ( $1 \times 10^3$  cells/well), supplemented with 10  $\mu$ L of CCK-8 solution. The number of viable cells was detected indirectly by a microplate reader (German Railway Testing Equip. Co., Ltd., Nanjing, CN).

**2.5. Apoptosis Assay.** Before the analysis on cycle status by the cell cycle assay kit (KeyGEN BioTECH, Jiangsu, CN), the cells were planted in 6-well plates ( $1 \times 10^6$  cells/well) with a 48 h transfection. They were separated and fixed in

70% ice-cold ethanol at room temperature of 4°C overnight and then rinsed by PBS and marked by 500  $\mu$ L of reaction solution (RNase/PI = 1/9) for 30 min. Later, the cells were analyzed using ModFit LT of a flow cytometer (FACS Calibur American BD Company, USA), with the CM of MC3T3-E1 cells assessed by Annexin V-FITC/PI apoptosis assay kit (BD Company, USA). Briefly, the treated cells were rinsed with ice-cold PBS and resuspended in 500  $\mu$ L BB, and then, they were processed with 5  $\mu$ L of Annexin V-FITC and 5  $\mu$ L of PI for 15 min in a dark condition and kept at room temperature, with analysis of flow cytometer.

**2.6. TCM Assay.** Resuspend the cells ( $1.5 \times 10^4$  cells/well) in a low-serum (5% FBS) medium, which were planted into the upper chamber of a 24-well Transwell plate (Corning,

Corning, NY, USA) containing an 8  $\mu\text{m}$  pore size filter, with the lower chamber as a complete medium with 10% FBS for compound testing. The cells migrating to the bottom surface were dyed by 0.5% CrV and observed microscopically (Topcon Co., Ltd., Japan) after 12 h, with those on the upper surface of the filter membrane rinsed.

**2.7. Dual Luciferase Reporter (DLR) Assay.** The wild sequence (WT) and mutant sequence (MUT) for the synthesis of TUG1 3'-UTR were designed and amplified, and the amplified fragments were transferred into the miRNA expression vector (Applied Biosystems) of pMIR-reporter<sup>TM</sup> to construct recombinant plasmids capable of expressing luciferase. The constructed recombinant plasmids were transfected into MC3T3-E1 cells together with miR-221-3p mimics and miRNA-NC. After 72 h, the cells were collected, with the procedure performed in strict line with the directions of luciferase reporter gene assay kit. Finally, the ratio of firefly fluorescence to Renilla fluorescence was measured by a chemiluminometer to analyze the binding force between miR-221-3p and TUG1.

**2.8. RT-qPCR Analysis.** The cells were processed with TRIzol reagent (Thermo Fisher Sci., SH, CN), with RNA concentration and purity determined by ultra-micronucleic acid quantitation spectrometer (Thermo Nanodrop 1000). The reverse transcription was implemented based on the directions from the cDNA reverse transcription kit (All-in-One<sup>TM</sup> miRNA First-Strand cDNA Synthesis Kit), with 2  $\mu\text{g}$  RNA taken for reverse transcription into cDNA per sample for RT-qPCR detection. Reaction conditions are as follows: 30 s of pre-denaturation at 95°C, followed by 40 cycles of 95°C for 5 s and 60°C for 30 s. With U6 of each sample as an internal reference, the relative gene expression was calculated and analyzed by the  $2^{-\Delta\Delta C_t}$  method, with the primer sequences detailed as Table 1.

**2.9. Immunoblot Analysis.** Extraction of total cellular protein was achieved by lysing the cells in RIPA buffer and washing them with PBS, with the lysates placed in 10% SDS-PAGE and proteins transferred to PVDF membranes (Millipore, Schwalbach, Germany). The cytomembranes were mainly probed with anticyclin D1 and D3 (1:1000, Yansheng Biochemical Reagent, SH, CN), with protein bands observed by chemiluminescence (Canon, Tokyo, Japan, #LiDE110) before incubation with appropriate secondary antibodies.

**2.10. Statistical Disposal.** The data were processed mainly by SPSS 20.0, with the measurement data represented as mean  $\pm$  std.deviation ( $\bar{x} \pm s$ ). The statistical methods used included one-way ANOVA and *t*-test. The graphs were plotted with GraphPad Prism 6.  $P < 0.05$  indicated a statistically remarkable difference.

### 3. Results

**3.1. Targeting Relationship between LncRNA TUG1 and miR-221-3p.** Target genes were predicted by bioinformatics software such as microRNA.org, TargetScan, and miRBase, with results showing that miR-221-3p had binding sites with

3'-UTR of TUG1 (Figure 1(a)). DLR assay suggested that in contrast to the miRNA-NC group, the miR-221-3p group had a decreased luciferase activity in WT-TUG1 cells, while that in MUT-TUG1 cells was not affected (Figure 1(b)). Further research revealed the decreased miR-221-3p expression of the LncRNA TUG1 group in contrast to the control and siLncRNA-NC groups (Figure 1(c)).

**3.2. Downregulation of TUG1 Inhibited CP and CM and Promoted CA of Osteoblasts.** On the basis of CCK-8 and TCM assays, no remarkable change was found at 24 h in the cell viability of all groups ( $P > 0.05$ ), with remarkably lower cell activity in the siLncRNA TUG1 group than those in the control and siLncRNA-NC group at 48 h and 72 h ( $P < 0.001$ ). It was revealed that compared to siLncRNA-NC, siLncRNA TUG1 significantly inhibited CP and CM (Figures 2(a) and 2(b)). According to cell cycle analysis, anticyclin D1 and D3 levels were higher in the siLncRNA-NC group than in the siLncRNA TUG1 group (Figure 2(c)). Compared to the siLncRNA TUG1 group, the CA rate was lower in the siLncRNA-NC group, whose cells were dyed by Annexin V-FITC and PI (Figure 2(d)).

**3.3. Overexpression of miR-221-3p Inhibited Osteoblast CP and CM.** The results of CCK-8 and TCM assays showed that the miR-221-3p level remarkably increased in MC3T3-E1 cells of the miR-221-3p overexpression group compared to the miRNA-NC group, suggesting the successful construction of miR-221-3p-overexpressing MC3T3-E1 cell line. The viability of MC3T3-E1 cells of the miR-221-3p overexpression group did not change remarkably at 24 h and was remarkably lower than those in the control group and miRNA-NC group at 48 h and 72 h (Figure 3(a)), confirming that overexpression of miR-221-3p inhibited CP, and the CM ability was also lower than those in the control and miRNA-NC groups (Figure 3(b)). Cell cycle analysis also revealed that its anticyclin D1 and D3 levels were remarkably lower than those in the miR-NC and control groups (Figure 3(c)). In addition, Annexin V-FITC and PI staining showed that the miR-221-3p overexpression group had a high CA rate (Figure 3(d)).

**3.4. Downregulation of miR-221-3p Partly Reversed the Retardation out of Downregulating TUG1 on Osteoblast CP and CM.** Compared to the siLncRNA TUG1 group, the cell viability of MC3T3-E1 in the siLncRNA TUG1+simiRNA group did not change remarkably at 24 h and increased remarkably at 48 h and 72 h (Figure 4(a)), with distinctly increased CM number of MC3T3-E1 (Figure 4(b)). The above results authenticated that downregulation of miR-221-3p partly reversed the retardation out of downregulating TUG1 on osteoblast CP and CM.

**3.5. Downregulation of LncRNA TUG1 Inhibited Closed Tibial Fracture Healing in Mice.** Bcl-2, an antiapoptotic signaling protein in the downstream of P53, acts as a pivotal part in regulating CA. Compared to the siLncRNA TUG1 and miR-221-3p overexpression groups, the Bcl-2 level in the LncRNA TUG1 group was higher (Figure 5). SDF-1 was a protein involved in bone regeneration and bone repair.

The SDF-1 level in the miR-221-3p overexpression group was remarkably lower than those in the control, miRNA-NC, and LncRNA TUG1 groups (Figure 5). The above results revealed that miR-221-3p obstructed the healing of closed tibial fractures in mice, and the downregulation of LncRNA TUG1 played the same role.

#### 4. Discussion

LncRNA is a noncoding RNA with a transcript of >200 nt in length, which can perform biological functions as an important class of regulatory molecules in the human genome and coordinate the complex regulatory processes of higher life [11–13]. Recent research has shown that LncRNAs can also act as a competitive endogenous RNA to form double-stranded RNA with complementary miRNA, which can affect the processes of miRNA splicing, processing, and translocation, and participate in the expression of target genes, thus influencing CP, differentiation, and CA [1, 14]. Currently, the academic community has a mature understanding of the regulatory mechanisms of anti-oncogene-related ceRNA, but there is a relative lack of ceRNA studies on fracture healing. With the changing lifestyles of Chinese residents, the incidence of fractures is gradually increasing, as well as the number of patients with closed tibial fractures, including both patients with severe closed tibial fractures due to high-energy damage and elderly patients with osteoporotic closed tibial fractures due to low-energy damage [15–17]. Deepening the research on LncRNA and miRNA can offer important insights into the biological process of bone and bone healing and provide new ideas for treating closed tibial fractures clinically.

At present, some LncRNAs functioning in osteoblast CP, CM, and CA have been demonstrated; for instance, Huang et al. have found that LncRNA H19 can play an important part in osteoblast differentiation through the TGF- $\beta$ 1/Smad3/HDAC signal path [18]. Yu et al. have reported that LncRNA HOXA11-AS can adsorb miR-124-3p to accelerate osteoblast CA. LncRNA TUG1 has been less studied in bone healing, but a study has shown that it can adsorb miR-204-5p, which can upregulate RUNX in aortic valve calcification and accelerate osteoblast differentiation [19]. Another study has shown that LncRNA TUG1 can influence osteoblast CP and differentiation through the Wnt/ $\beta$ -catenin signal path [20]. Based on the above studies showing an increase in LncRNA TUG1 during fracture healing, this study assumes that LncRNA TUG1 plays a promoting role in fracture healing. To this end, the healing tissue models of intact control bone and closed tibial bone in mice with differential expression of LncRNA TUG1 were constructed, with the performance of a DLR assay confirming the targeting relationship between LncRNA TUG1 and miR-221-3p. For purpose of in-deep research on the molecular mechanism of these two in CP, CM, and CA of MC3T3-E1 cells, CCK-8 and TCM assays were carried out. It was found that downregulation of LncRNA TUG1 restricted the CP and CM of MC3T3-E1 cells and supported their CA, while overexpression of miR-221-3p inhibited osteoblast CP and CM, which

was reversed in the miRNA-NC group. In contrast to the miR-221-3p overexpression group, CP rate in the miRNA-NC group remarkably increased after transfection. Flow cytometry revealed that the MC3T3-E1 cell cycle progressed from G0/G1 to S, G2/M in this group, and G1/S transition was hindered by overexpression of miR-221-3p. As for the miR-221-3p overexpression group, the anticyclin D1 and D3 levels were also remarkably reduced, with a higher CA rate corroborated by Annexin V-FITC, confirming that miR-221-3p promoted CA of MC3T3-E1 cells.

Further study revealed that compared with siLncRNA TUG1 and miR-221-3p overexpression groups, the Bcl-2 level in the LncRNA TUG1 group was higher, with remarkably lower SDF-1 level in the miR-221-3p overexpression group than those in the control, miRNA-NC, and LncRNA TUG1 groups. SDF-1, a part of the  $\alpha$  chemokine family, whose specific receptor CXCR4 is expressed on the surface of many cells, and the two can constitute the SDF-1/CXCR4 axis, serving as a key part in tissue injury and bone damage repair [21–23]. Clinical studies have shown that the secretion of SDF-1 in the bone repair site increases, and CXCR4 +-committed stem cells around bone marrow, peripheral circulating blood, and soft tissue of bone trauma migrate to the bone injury site along the gradient of SDF-1 concentration to participate in bone healing [24]. Kawakami et al. have reported that the SDF-1/CXCR4 axis in Tie2-spectrum cells, which includes EPCs, accelerates fracture healing [25], while the study of Arakura et al. showed that SDF-1 levels were remarkably lower during fracture healing in diabetic patients than in the healthy group, suggesting that differential gene expression of SDF-1 is one of the reasons for poor fracture healing in diabetic patients [26]. Moreover, SDF-1 is also closely related to angiogenesis, the high expression of which indicates good blood supply, bringing necessary environmental nutritional support for bone regeneration [27]. Therefore, the low SDF-1 level in the miR-221-3p overexpression group implies that the fracture site is accompanied by tissue ischemia and hypoxia, and endochondral ossification is thus affected. Zheng et al. stated that downregulating miR-221-3p directly targeted the SDF1/CXCR4 signal path and promoted IL-1 $\beta$ -induced cartilage degradation, confirming that cartilage degeneration grade correlates with miR-221-3p level, and that the protection of miR-221-3p against chondrocyte extracellular matrix degradation proceeded through SDF1/CXCR4 signal transduction [28]. Since LncRNA can compete with target gene mRNA to bind miRNA response elements, inhibit miRNA expression, and indirectly increase the expression level of target genes, LncRNA TUG1 can inhibit the retardation effect of miR-221-3p on osteoblast CP and CM; i.e., downregulation of miR-221-3p can partly reverse the retardation out of downregulating TUG1 on the CP and CM of osteoblasts.

In this study, no clinical trial was conducted to probe into the effect of LncRNA TUG1 in closed tibial fracture patients. In summary, the study clarifies the adsorption capacity of LncRNA TUG1 on miR-221-3p and confirms that downregulation of miR-221-3p by LncRNA TUG1 promotes the healing of closed tibial fractures.

## Retraction

# Retracted: Influence of the Physical Inclusion of ZrO<sub>2</sub>/TiO<sub>2</sub> Nanoparticles on Physical, Mechanical, and Morphological Characteristics of PMMA-Based Interim Restorative Material

### BioMed Research International

Received 8 January 2024; Accepted 8 January 2024; Published 9 January 2024

Copyright © 2024 BioMed Research International. This is an open access article distributed under the Creative Commons Attribution License, which permits unrestricted use, distribution, and reproduction in any medium, provided the original work is properly cited.

This article has been retracted by Hindawi following an investigation undertaken by the publisher [1]. This investigation has uncovered evidence of one or more of the following indicators of systematic manipulation of the publication process:

- (1) Discrepancies in scope
- (2) Discrepancies in the description of the research reported
- (3) Discrepancies between the availability of data and the research described
- (4) Inappropriate citations
- (5) Incoherent, meaningless and/or irrelevant content included in the article
- (6) Manipulated or compromised peer review

The presence of these indicators undermines our confidence in the integrity of the article's content and we cannot, therefore, vouch for its reliability. Please note that this notice is intended solely to alert readers that the content of this article is unreliable. We have not investigated whether authors were aware of or involved in the systematic manipulation of the publication process.

Wiley and Hindawi regrets that the usual quality checks did not identify these issues before publication and have since put additional measures in place to safeguard research integrity.

We wish to credit our own Research Integrity and Research Publishing teams and anonymous and named external researchers and research integrity experts for contributing to this investigation.

The corresponding author, as the representative of all authors, has been given the opportunity to register their agreement or disagreement to this retraction. We have kept a record of any response received.

### References

- [1] A. Alrahlah, R. Khan, F. Vohra et al., "Influence of the Physical Inclusion of ZrO<sub>2</sub>/TiO<sub>2</sub> Nanoparticles on Physical, Mechanical, and Morphological Characteristics of PMMA-Based Interim Restorative Material," *BioMed Research International*, vol. 2022, Article ID 1743019, 11 pages, 2022.

## Research Article

# Influence of the Physical Inclusion of $ZrO_2/TiO_2$ Nanoparticles on Physical, Mechanical, and Morphological Characteristics of PMMA-Based Interim Restorative Material

Ali Alrahlah <sup>1,2</sup>, Rawaiz Khan,<sup>1</sup> Fahim Vohra <sup>1,3</sup>, Ibrahim M. Alqahtani,<sup>4</sup> Adel A. Alruhaymi,<sup>5</sup> Sajjad Haider,<sup>6</sup> Abdel-Basit Al-Odayni,<sup>1</sup> Waseem Sharaf Saeed <sup>1</sup>, H. C. Ananda Murthy <sup>7,8</sup> and Leonel S. Bautista<sup>1</sup>

<sup>1</sup>Engineer Abdullah Bugshan Research Chair for Dental and Oral Rehabilitation, College of Dentistry, King Saud University, Riyadh 11545, Saudi Arabia

<sup>2</sup>Restorative Dental Sciences Department, College of Dentistry, King Saud University, Riyadh 11545, Saudi Arabia

<sup>3</sup>Department of Prosthetic Dental Science, College of Dentistry, King Saud University, Riyadh 11545, Saudi Arabia

<sup>4</sup>Public Security Medical Services, Security Patrols Medical Center, Riyadh, Saudi Arabia

<sup>5</sup>Prince Mohammed bin Naif Medical Center, King Fahad Security College, Riyadh, Saudi Arabia

<sup>6</sup>Department of Chemical Engineering, College of Engineering, King Saud University, PO Box 800, Riyadh 11421, Saudi Arabia

<sup>7</sup>Department of Applied Chemistry, School of Applied Natural Science, Adama Science and Technology University, P O Box, 1888 Adama, Ethiopia

<sup>8</sup>Department of Prosthodontics, Saveetha Dental College & Hospital, Saveetha Institute of Medical and technical science (SIMAT), Saveetha University, -600077, Chennai, Tamil Nadu, India

Correspondence should be addressed to Ali Alrahlah; [aalrahlah@ksu.edu.sa](mailto:aalrahlah@ksu.edu.sa) and H. C. Ananda Murthy; [anandkps350@gmail.com](mailto:anandkps350@gmail.com)

Received 21 June 2022; Accepted 28 July 2022; Published 19 August 2022

Academic Editor: Hassan Albarqi

Copyright © 2022 Ali Alrahlah et al. This is an open access article distributed under the Creative Commons Attribution License, which permits unrestricted use, distribution, and reproduction in any medium, provided the original work is properly cited.

Polymethyl methacrylate (PMMA) is often used in restorative dentistry for its easy fabrication, aesthetics, and low cost for interim restorations. However, poor mechanical properties to withstand complex masticatory forces are a concern for clinicians. Therefore, this study aimed to modify a commercially available PMMA-based temporary restorative material by adding  $TiO_2$  and  $ZrO_2$  nanoparticles in different percentages as fillers and to investigate its physio-mechanical properties. Different percentages (0, 0.5, 1.5, and 3.0 wt%) of  $TiO_2$  and  $ZrO_2$  nanoparticles were mixed with the pristine PMMA resin (powder to liquid ratio: 1 : 1) and homogenized using high-speed mixer. The composites obtained were analyzed for their flexural strength (F.S.), elastic modulus (E.M.), Vickers hardness (H.V.), surface roughness Ra, morphology and water contact angle (WCA). The mean average was determined with standard deviation (SD) to analyze the results, and a basic comparison test was conducted. The results inferred that adding a small amount (0.5 wt%) of  $TiO_2$  and  $ZrO_2$  nanoparticles (NPs) could significantly enhance the physio-mechanical and morphological characteristics of PMMA interim restorations. EM and surface hardness increased with increasing filler content, with 3.0 wt.%  $ZrO_2$  exhibiting the highest EM (3851.28 MPa), followed by 3.0 wt.%  $TiO_2$  (3632.34 MPa). The WCA was significantly reduced from  $91.32 \pm 4.21^\circ$  (control) to  $66.30 \pm 4.23^\circ$  for 3.0 wt.%  $ZrO_2$  and  $69.88 \pm 3.55^\circ$  for 3.0 wt.%  $TiO_2$ . Therefore,  $TiO_2$  and  $ZrO_2$  NPs could potentially be used as fillers to improve the performance of PMMA and similar interim restorations.

## 1. Introduction

In restorative dentistry, temporary restorations are generally adopted amid tooth preparation and placement of the final

restoration [1, 2]. Provisional restorations are also beneficial for diagnostic purposes, where the functional, stabilizing, occlusal, and aesthetic parameters are established to determine an optimal therapeutic efficacy before the final



TABLE 1: Material composition of the test groups.

S. no.	Group code	Description
1	Control	Pristine PMMA powder and liquid (1 : 1)
2	0.5-TiO <sub>2</sub>	PMMA powder + liquid (1 : 1) + 0.5 wt.TiO <sub>2</sub>
3	1.5-TiO <sub>2</sub>	PMMA powder + liquid (1 : 1) + 1.5 wt.TiO <sub>2</sub>
4	3.0-TiO <sub>2</sub>	PMMA powder + liquid (1 : 1) + 3.0 wt.TiO <sub>2</sub>
5	0.5-ZrO <sub>2</sub>	PMMA powder + liquid (1 : 1) + 0.5 wt.ZrO <sub>2</sub>
6	1.5-ZrO <sub>2</sub>	PMMA powder + liquid (1 : 1) + 1.5 wt.ZrO <sub>2</sub>
7	3.0-ZrO <sub>2</sub>	PMMA powder + liquid (1 : 1) + 3.0 wt.ZrO <sub>2</sub>

prosthesis is completed [3]. Therefore, provisional restorations have acquired immense importance in restorative dentistry due to very demanding aesthetical outputs and early diagnostic of the performance of final restorations. By adopting the provisional restoration approach, the dentists maintain their patients' confidence by implementing this temporary phase of therapy and foresee critical deficiencies in the ultimate restoration prior to installation [4, 5]. Therefore, provisional restorative materials are usually employed to safeguard the prepared teeth until the final rehabilitation.

Temporary restorations are exposed to masticatory forces and need adequate mechanical strength in order to withstand the recurrent functional stresses of the oral environment. The mechanical properties of intermediate restorations play a vital role in helping practitioners decide on the appropriate material to use in specific clinical conditions such as vertical dimensional changes in full oral rehabilitation, temporomandibular joint disorder, and long-span fixed prostheses [4]. To achieve good mechanical strength in the oral environment, the dental material must be reinforced with such nanofillers that provide adequate mechanical strength to the tooth and are also safe to use. Ceramic nanoparticles such as TiO<sub>2</sub> and ZrO<sub>2</sub> NPs are primarily used for this purpose [6, 7]. TiO<sub>2</sub> NPs are white solids and considered technologically crucial due to their various properties [8, 9] such as ease of synthesis, good tensile strength [10, 11] adequate biocompatibility [12], antibacterial activity [13], and photocatalytic activity [11]. TiO<sub>2</sub> NPs are widely used as catalyst supports in biomedicine, water and air purification [14], pigments [14], cosmetics, solar cells [15], and tissue engineering [16–18]. ZrO<sub>2</sub> was first introduced in 1789 by Martin Heinrich Klaproth. Since then, it has been used as a pigment for ceramics. It occurs in three crystalline forms at different temperatures. The common one is monoclinic (at normal temperature), while the cubic and tetragonal crystalline forms occurs at elevated temperatures. The toughness of ZrO<sub>2</sub> increases with decreasing temperature during phase transformation from tetragonal to monoclinic (a stable phase). This property of ZrO<sub>2</sub> can be used to modify its mechanical properties [18]. Currently, ZrO<sub>2</sub> is frequently utilized in various dental applications such as dental implants, abutments, crown prostheses, and post-implant restorations [19, 20].

PMMA is a popular polymer material in restorative dentistry, particularly for indirect restorations such as dentures,

temporary crowns, and bridges [21–23]. This material is cost-effective, easy to fabricate, and has excellent aesthetical properties. However, its stiffness and fracture toughness are insufficient to withstand the complex masticatory forces [24, 25]. Therefore, the poor mechanical properties limit its clinical application for temporary crowns and fixed bridges for a transitional period [23, 26].

Several efforts have been made to improve the mechanical performance of PMMA interim restorations by adding various filler particles such as fibers [27, 28], NPs [29–33], and nanotubes [34–36]. The inclusion of inorganic nanofillers into PMMA changes the characteristics of the final product based on the size, shape, type, concentration, and filler to matrix interaction [33]. The present study aims to investigate the effect of the physical incorporation of TiO<sub>2</sub> and ZrO<sub>2</sub> NPs on the physical and mechanical properties of the PMMA-based provisional crown material, especially in terms of morphology, hardness, modulus, and hydrophilicity.

## 2. Materials and Methods

**2.1. Materials.** PMMA temporary resin acrylic (Bosworth, Trim Plus; Bosworth Company, USA), TiO<sub>2</sub> (nanopowder, 21 nm, ≥99.5% trace metals basis; Sigma Aldrich, Germany), ZrO<sub>2</sub> nanopowder (<100 nm particle size, Sigma Aldrich, China). The various test groups along with composition are given in Table 1.

**2.2. Mixing of Fillers.** All modified PMMA composites consisted of a liquid-to-powder ratio of 50/50 wt% (1:1 liquid-to-powder resin). TiO<sub>2</sub> and ZrO<sub>2</sub> NPs were added sequentially at 0.5, 1.5 and 3.0 wt% of each filler type, as indicated in Table 1. The required wt.% of filler for each group was dispersed into the powder resin by homogenizing it manually and mixing it by hand with a stainless steel spatula. The powder mixture with the filler was then mechanically mixed three times with an asymmetric double centrifuge at 1500 rpm, with two minutes pause in between.

**2.3. Specimen Fabrication.** A series of pristine (control) and modified PMMA composites (with 0.5, 1.5, and 3.0 wt%-TiO<sub>2</sub>/ZrO<sub>2</sub>) were prepared according to the scheme shown in Figure 1. Sixty bar (2 × 3 × 20 mm) and disc specimens (10 mm × 6 mm) were fabricated in six groups each ( $n = 10$ ) for evaluation of their flexural strength and micro hardness. Silicone molds were developed to prepare the bar and disk specimens. The powder and liquid phases of the PMMA material (Bosworth Trim Plus, USA) were blended in a volume ratio of 1:1 and mixed with the NPs at low speed (1000 rpm for 60 seconds). The silicone molds were brought into contact with a glass slide, and the blended material was poured into them. After removing excess material, a glass slide was placed on the top of the mold until the material was fully polymerized. After complete polymerization, the specimens were stored at 37 °C for 1 hr before removing them from the molds. The specimens were allowed to cool for 30 minutes, removed from the molds, and polished with 600-1000-2400 grit SiC paper for 3 minutes. The specimens

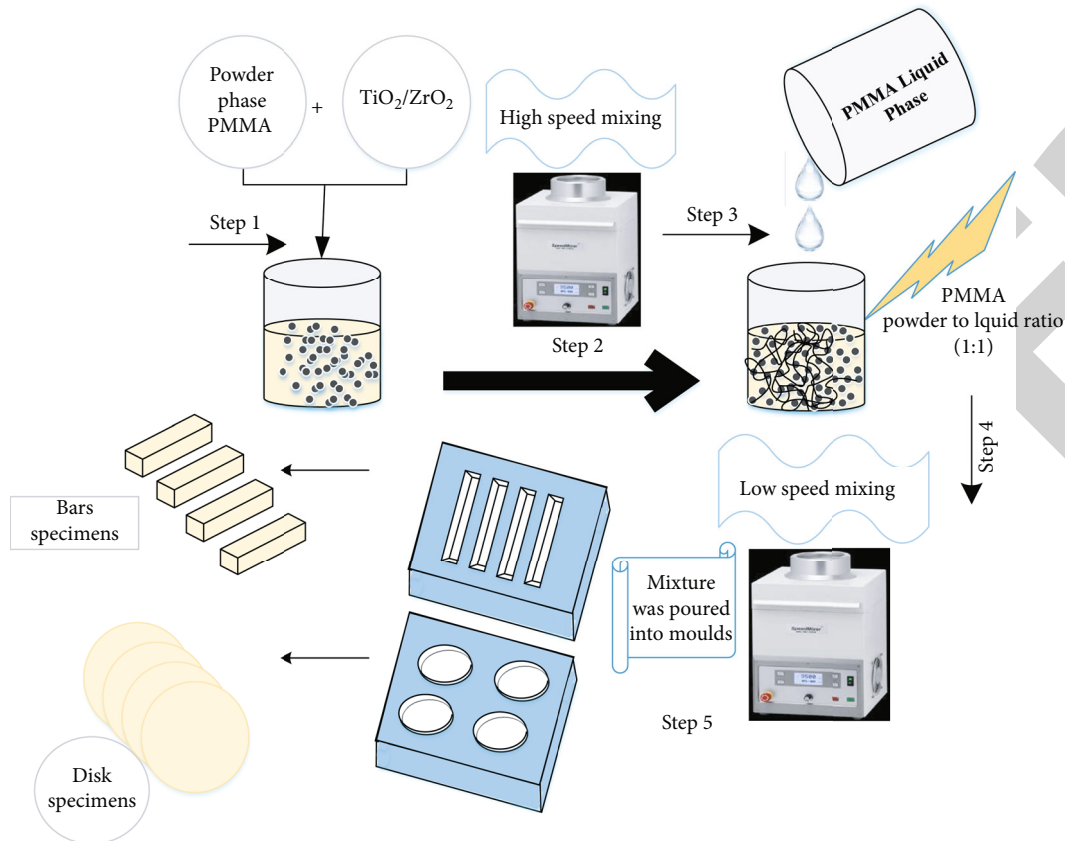


FIGURE 1: Schematic diagram of the preparation of PMMA ( $\text{TiO}_2/\text{ZrO}_2$ ) disk and bar specimens.

were then ultrasonicated with distilled water for 5 minutes to remove impurities and stored at  $37^\circ\text{C}$  for 24 h.

**2.4. Flexural Strength (Three-Point Bending).** For all specimens, a three-point bending test was performed on a universal testing machine (Instron Corp, Model:4202) using a crosshead speed of 0.5 mm/minute and a 100-kg load cell with a 3-point fixture with a span of 15 mm. The bars were oriented to allow high tensile force on the ground surface (bottom) and compression force on the top. The average heights and widths of the parts of the bars and the disc near the fracture point were measured with a micrometer (Model No. CD-4 C.S.; Mitutoyo Corp., Japan). The flexural strength ( $\sigma$ ) and elastic modulus ( $E$ ) are determined as follows:

$$\sigma = 3PL/2WT^2, (\text{MPa}) \quad (1)$$

$$E = FL3/4WT^3d, (\text{MPa}) \quad (2)$$

where  $P$  is the maximum load (N) at fracture,  $L$  is the space amongst the two supports (fixed at 20 mm),  $W$  is the width of the bar (mm), and  $T$  is the height (mm).  $F$  is the applied force (N) and  $d$  is the deflection (mm) due to applied force  $F$ .

**2.5. Microhardness Assessment.** For microhardness testing, a Vickers microhardness indentation was applied to the disc

specimens using a Vickers hardness tester (HMV-2 Shimadzu Corp, Tokyo, Japan). Three indentations were randomly placed on the surface of the specimen. The indentations were 0.5 mm apart and were loaded with 100 g for 15 s dwell period (ASTM C1327-03 standard). The average of the three readings for each specimen was determined as the individual Vickers hardness (V.H.).

**2.6. Surface Roughness and Morphology.** The surface roughness measurement was performed using a 3D non-contact optical microscope contour (GT-K 3D Bruker®). Specimens were measured using a  $5\times$  Michelson magnification objective, a field of view of  $1.0 \times 1.0 \text{ mm}^2$ , a Gaussian regression filter, a scan speed of  $1\times$ , and a threshold of  $4\times$  (vertical scan interferometry). The surface roughness was measured by following the same procedure previously published by our group [37]. In addition, the fractured structure morphology of all the specimens were investigated by scanning electron microscopy (JEOL, JSM-6610 LV, Tokyo, Japan) at 15 kv voltage and resolution from  $100\times$  to  $500\times$ .

**2.7. Contact Angle Measurements.** The water contact angle was measured at room temperature using a standard Ramé-Hart 250 goniometer and DROP image advanced software. The goniometer is equipped with a volume-controlled syringe above the substrate holder, a CCD camera that captures the droplet image, and DROPimage advanced software to process the data. The sessile drop technique

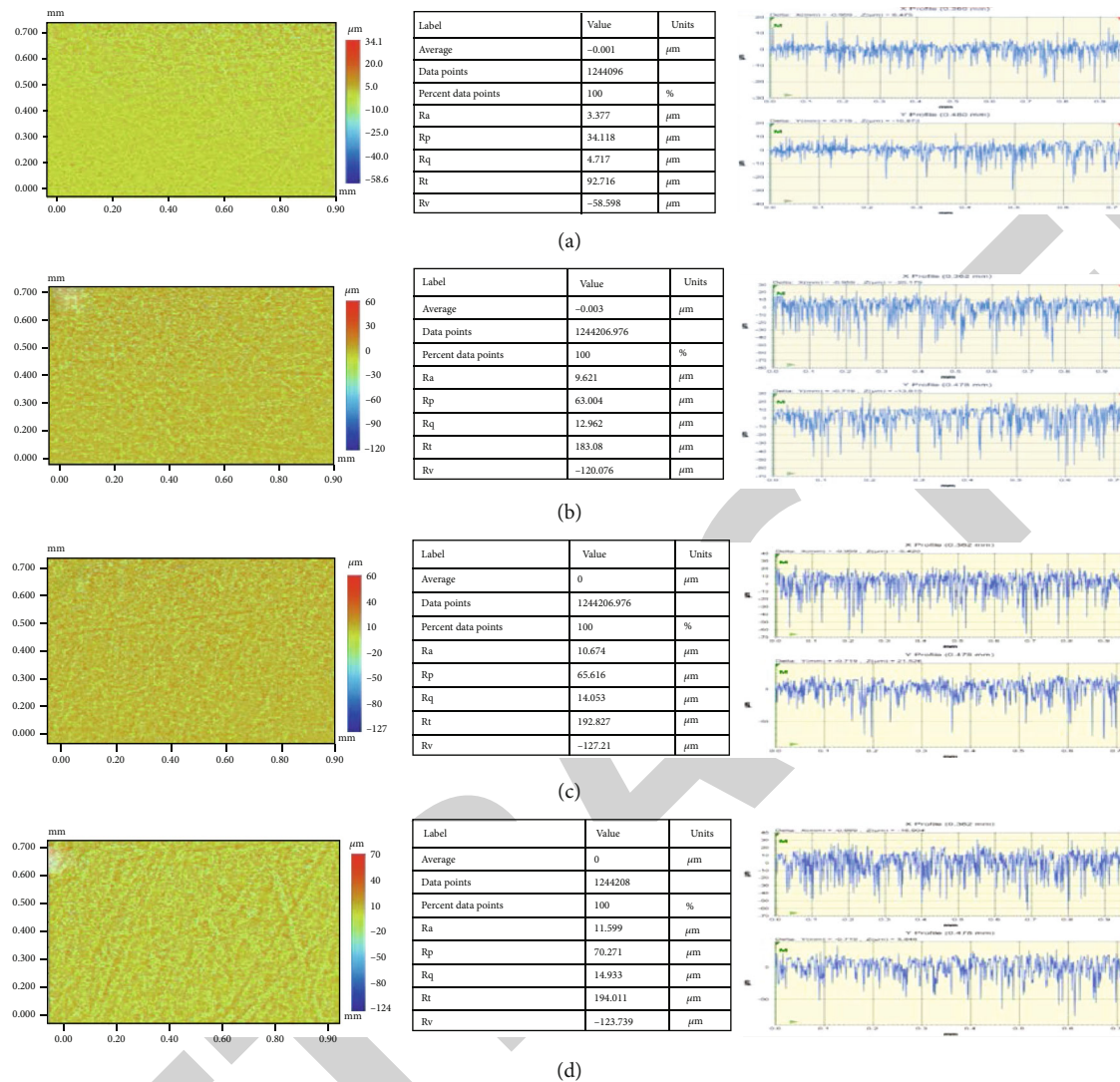


FIGURE 2: Surface roughness and topographic images of  $\text{TiO}_2/\text{Trim}$  composites: (a) pristine PMMA, (b) 0.5- $\text{TiO}_2$ , (c) 1.5- $\text{TiO}_2$ , and (d) 3.0- $\text{TiO}_2$ .

was used, in which a  $5 \mu\text{l}$  drop of water was applied to a substrate, and the contact angle was measured within five seconds.

**2.8. Statistical Analysis.** A univariate two-way ANOVA was performed to analyze significant differences in F.S., EM, WCA, and VH between various test groups at  $p < 0.05$  level of statistical significance.

### 3. Results and Discussion

**3.1. Surface Roughness (Ra).** Figures 2(a)–2(d) show the surface roughness and topographic features of the pristine and  $\text{TiO}_2/\text{PMMA}$  composites. Various mathematical models are used to measure the surface roughness based on the geometric topography. However, researchers mainly use average surface roughness (Ra) and root mean square roughness (Rq) to analyze surface roughness [17, 38–40]. The resulting values of the average surface roughness (Ra) of the control

group and the  $\text{TiO}_2$  NPs reinforced group were recorded as  $3.37 \pm 1.45 \mu\text{m}$ ,  $9.62 \pm 0.84 \mu\text{m}$ ,  $10.67 \pm 1.36 \mu\text{m}$ , and  $11.59 \pm 1.21 \mu\text{m}$  for the control, 0.5- $\text{TiO}_2$ , 1.5- $\text{TiO}_2$ , and 3- $\text{TiO}_2$ , respectively. Also, the root mean square roughness (Rq) was found to be  $4.71 \pm 0.86$ ,  $12.96 \pm 0.69$ ,  $14.05 \pm 1.37$ , and  $14.93 \pm 0.95$  for the control, 0.5- $\text{TiO}_2$ , 1.5- $\text{TiO}_2$ , and 3- $\text{TiO}_2$ , respectively. Figures 3(a)–3(d) show the surface roughness and topographic properties of the control and  $\text{ZrO}_2/\text{Trim}$  composites. The Ra values were  $3.37 \pm$ ,  $8.87 \pm$ ,  $9.38 \pm$ , and  $10.52 \pm$  for the control, 0.5- $\text{ZrO}_2$ , 1.5- $\text{ZrO}_2$ , and 3- $\text{ZrO}_2$ , respectively. Also, the Rq values were  $4.71 \pm 1.04$ ,  $12.18 \pm 1.37$ ,  $12.71 \pm 0.85$ , and  $14.03 \pm 1.54$  for the control, 0.5- $\text{ZrO}_2$ , 1.5- $\text{ZrO}_2$ , and 3- $\text{ZrO}_2$ , respectively. In general, the surface of composites is influenced by many factors such as type and size of filler, shape, dispersion, type of resin matrix, degree of conversion, and bonding efficiency at the filler/matrix interface [41]. The results showed that the Ra of the modified PMMA composites marginally increased by increasing  $\text{TiO}_2$  and  $\text{ZrO}_2$  content. The steady increase

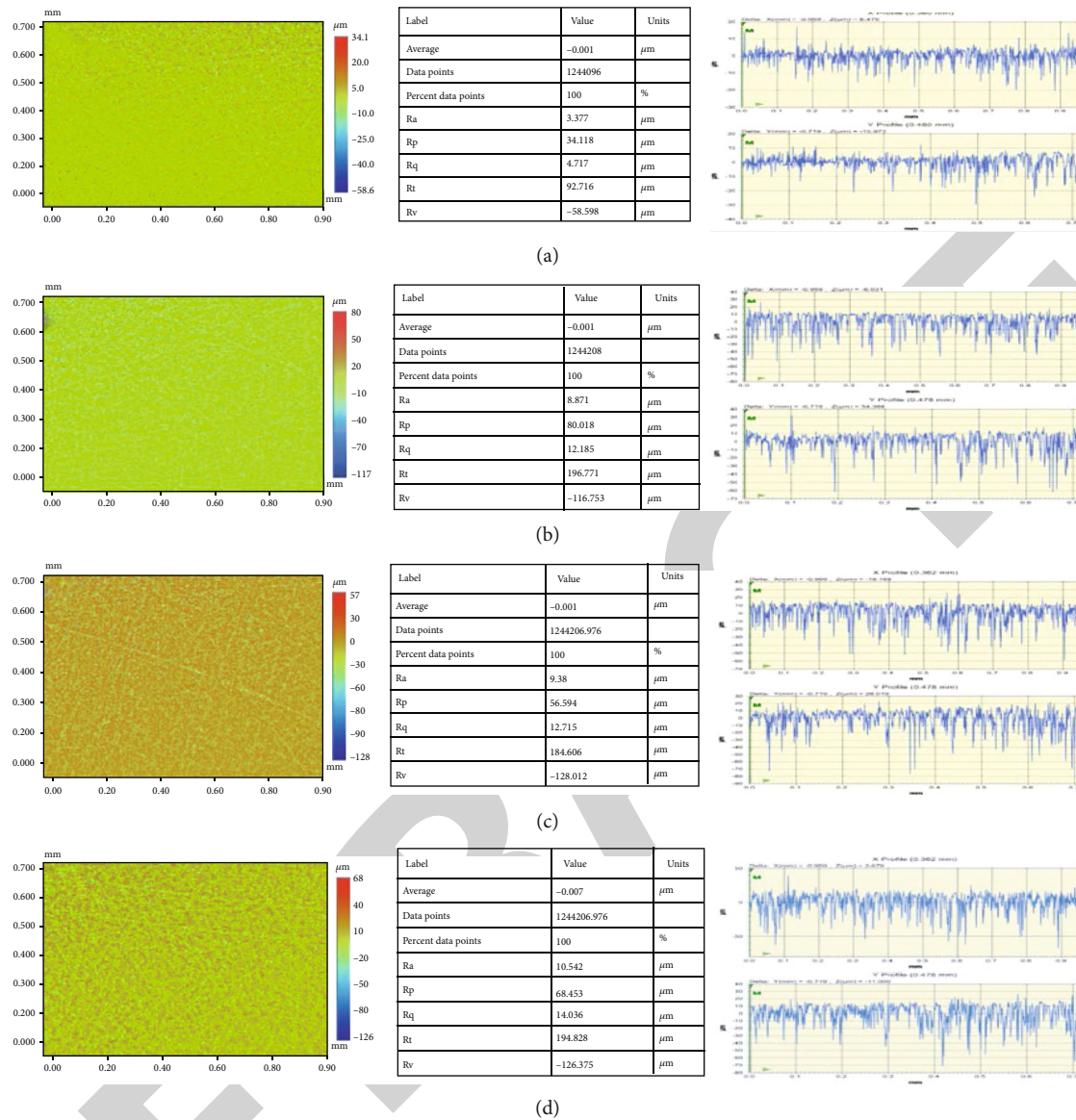


FIGURE 3: Surface roughness and topographic images of ZrO<sub>2</sub>/Trim composites: (a) pristine PMMA, (b) 0.5-ZrO<sub>2</sub>, (c) 1.5-ZrO<sub>2</sub>, and (d) 3.0-ZrO<sub>2</sub>.

in the surface roughness of the modified PMMA nanocomposites due to the incorporation of TiO<sub>2</sub> and ZrO<sub>2</sub> nanofillers could be due to the dispersion of these nanoparticles on the surface, resulting in an uneven surface [37, 42].

**3.2. Flexural Strength and Vickers's Hardness.** It is assumed that differences in filler content, type, size, and dispersion in the polymer matrix will influence the mechanical properties of the composite groups. Figures 4(a)–4(b) summarize the flexural strength (FS) and elastic modulus (EM) of the pristine and the different composite groups reinforced with TiO<sub>2</sub> (0.5-TiO<sub>2</sub>, 1.5-TiO<sub>2</sub>, and 3-TiO<sub>2</sub>) and ZrO<sub>2</sub> (0.5-ZrO<sub>2</sub>, 1.5-ZrO<sub>2</sub>, and 3.0-ZrO<sub>2</sub>). The FS and EM of pristine (control group) were measured to be 87.61 ± 3.21 MPa and 2865.32 ± 98 MPa, respectively. The inclusion of a small amount of TiO<sub>2</sub> and ZrO<sub>2</sub> (0.5 wt%) significantly increased

the FS and EM values of the PMMA pristine interim restorative material. FS and EM values for 0.5-TiO<sub>2</sub> were reported as 107.05 ± 5.11 MPa and 3434.70 ± 101 MPa, respectively. However, further increase in TiO<sub>2</sub> content resulted in much lower FS values of 97.70 ± 4.51 MPa and 94.13 ± 3.98 for 1.5-TiO<sub>2</sub> and 3.0-TiO<sub>2</sub> respectively. Conversely, a gradual increase in EM was observed with increasing TiO<sub>2</sub> filler content, with 3.0-TiO<sub>2</sub> exhibiting the highest EM (3632.34 ± 89 MPa) compared to the other TiO<sub>2</sub>-containing groups. Similarly, 0.5-ZrO<sub>2</sub> resulted in FS and EM values of 111.68 ± 4.35 MPa and 3445.52 ± 79 MPa, respectively. Increasing the ZrO<sub>2</sub> filler content to 3.0wt% resulted in a significant decrease in F.S., but EM was gradually increased with increasing ZrO<sub>2</sub> content (from 3445.52 ± 79 for 0.5-ZrO<sub>2</sub> to 3851.28 ± 112 for 3.0-ZrO<sub>2</sub>). Among the groups reinforced with ZrO<sub>2</sub>, 3.0-ZrO<sub>2</sub> (due to the addition of

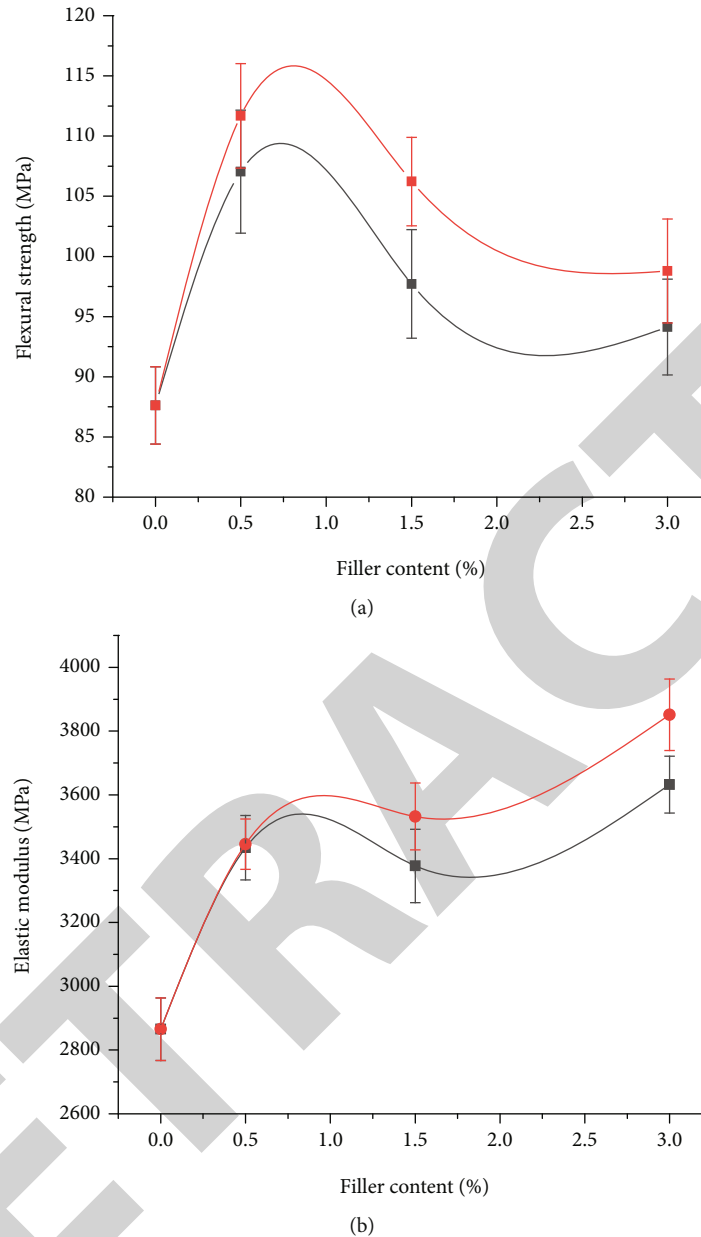


FIGURE 4: Flexural strength (a) and elastic modulus (b) of the pristine and modified PMMA composite groups.

3 wt% nano-ZrO<sub>2</sub>) resulted in the highest EM (3851.28 ± 112).

When comparing the materials of the different test groups, the difference between FS and EM of the control group and the other groups can be explained on the basis of the type, size, and content of the fillers. In general, a good relationship between the mechanical strength and the filler's volume fraction is reported in the literature [43, 44]. Therefore, the composite groups with higher filler content are expected to exhibit higher mechanical strength than those with lower filler content. In the current study, lower FS was observed for 1.5-TiO<sub>2</sub>, 1.5-ZrO<sub>2</sub>, 3.0-TiO<sub>2</sub>, and 3.0-ZrO<sub>2</sub>, possibly due to the higher filler-to-matrix ratio and the presence of weak interaction between the filler and

matrix materials. The increase in EM with increasing filler content could be attributed to increased stiffness [45]. These results are consistent with previous studies in which composites with high filler content exhibited high EM [46–48].

Figure 5 shows the Vickers hardness values for the pristine and composite groups. The pristine trim (control) resulted in a hardness value of 17.2 HV. The addition of TiO<sub>2</sub> nanofiller resulted in a gradual increase in the micro hardness of composite groups from 22.65 HV for 0.5-TiO<sub>2</sub> to 31.73 HV for 3.0-TiO<sub>2</sub>. A similar trend was observed for the composite groups modified with ZrO<sub>2</sub>, with microhardness values ranging from 21.82 HV for 0.5-ZrO<sub>2</sub> to 27.84 HV for 3.0-ZrO<sub>2</sub>. In other words, 3.0-TiO<sub>2</sub> showed the highest hardness values, followed by 3.0-ZrO<sub>2</sub>. The increase in

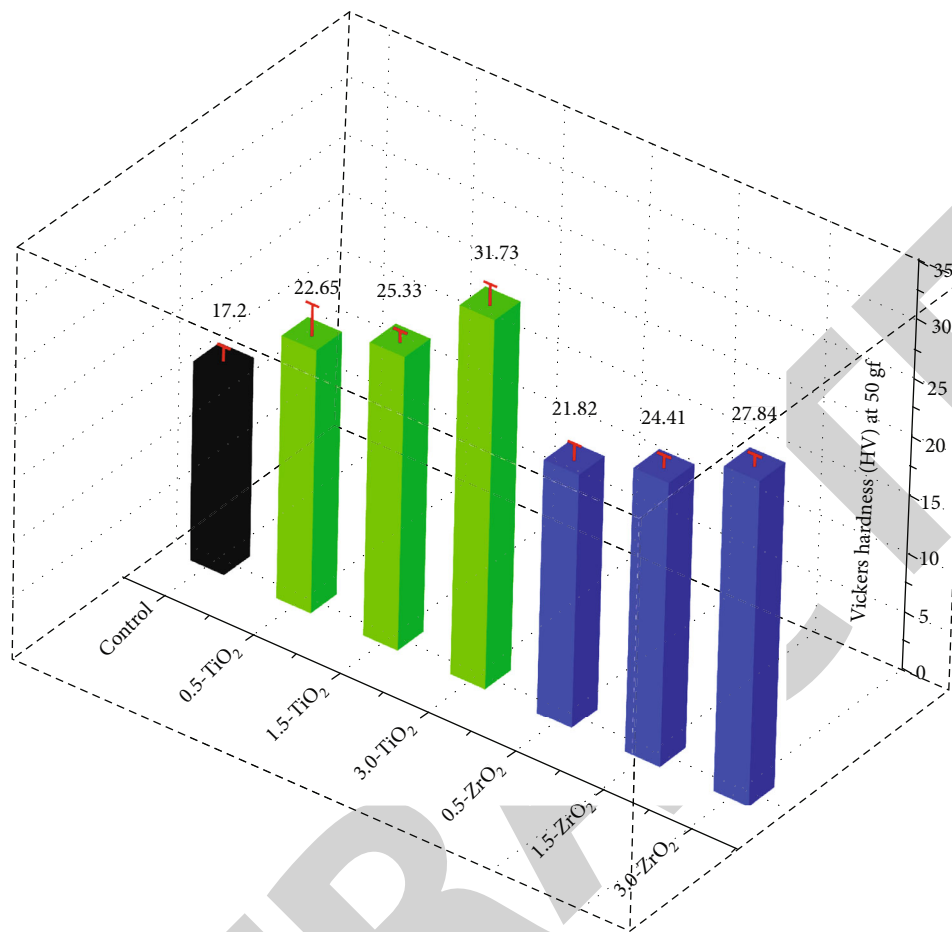


FIGURE 5: Vickers hardness values of the pristine and modified PMMA composite groups.

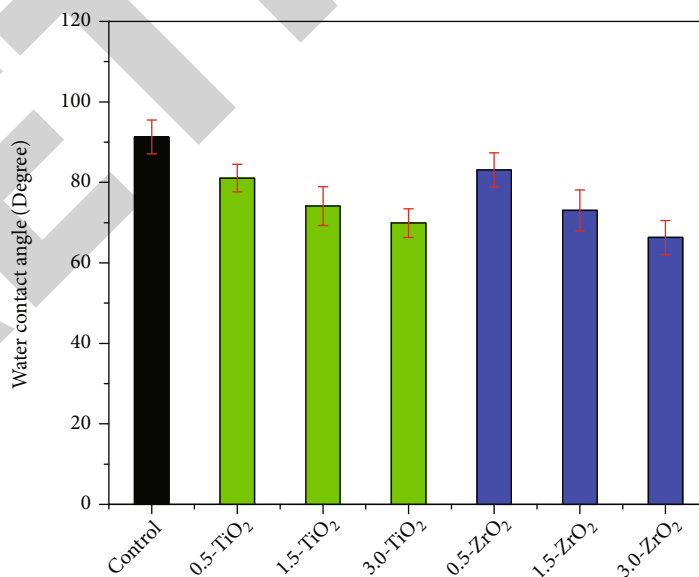


FIGURE 6: Water contact angle of the pristine and modified PMMA composite groups.

microhardness of the modified PMMA nanocomposite groups could be related to the reduction in interparticle spacing As the particle loading in the polymer matrix

increases, leading to an increase in surface resistance to indentation [49]. Shirkavand and Moslehifrad found in their study that the different ratio of PMMA reinforced with TiO<sub>2</sub>

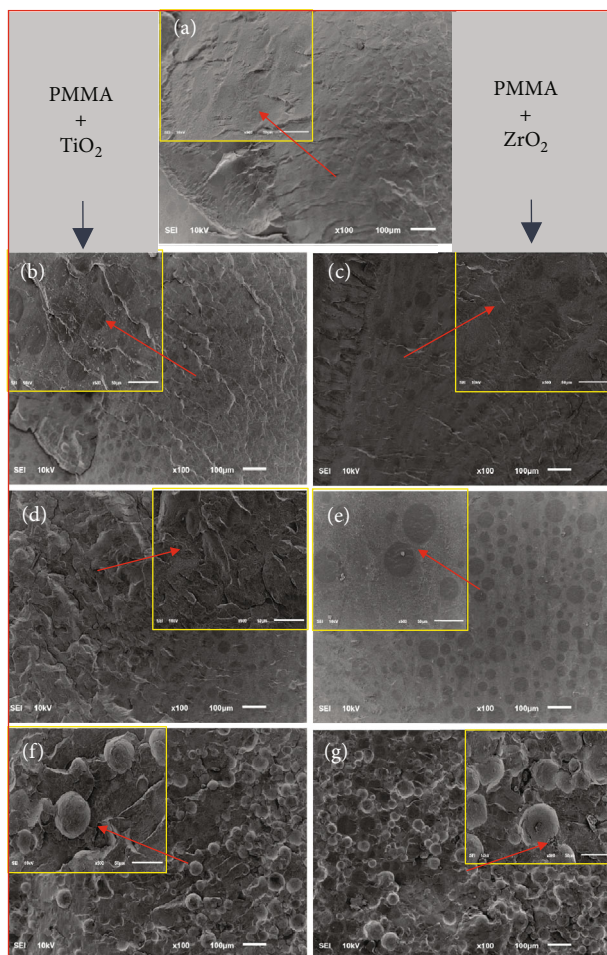


FIGURE 7: Scanning electron microscopy (SEM) images of fractured surface: (a) pristine PMMA, (b) 0.5-TiO<sub>2</sub>, (c) 1.5-TiO<sub>2</sub>, (d) 3.0-TiO<sub>2</sub>, (e) 0.5-ZrO<sub>2</sub>, (f) 1.5-ZrO<sub>2</sub>, and (g) 3.0-ZrO<sub>2</sub>.

increases the mechanical properties at a particular concentration and then decreased with an additional higher amount of TiO<sub>2</sub> [22]. The required mechanical strengths of the composite materials may vary for intended applications. In some cases, high strength and hardness are required in the materials, while in others, flexibility, stiffness, and elasticity are the desired properties [48]. In conclusion, it can be assumed that by controlling the content of the above mentioned particles in PMMA nanocomposite groups, desired mechanical properties can be obtained.

**3.3. Contact Angle.** The contact angle values of all specimens were measured as an indicator of surface wettability and adhesion strength. It was found that increasing the surface roughness improved the wettability and decreased the contact angle value. A relationship exists between polymer surface roughness and liquid contact angles. A change in the surface roughness parameters of any material leads to a change in the contact angles or wettability of the material [50, 51]. Figure 6 shows the contact angle values of the PMMA pristine and nanocomposite specimens. Overall, the pristine specimen gave the highest contact angle

( $91.32 \pm 4.21^\circ$ ). Among the TiO<sub>2</sub> and ZrO<sub>2</sub> composite groups, 0.5-ZrO<sub>2</sub> gave the highest contact angle ( $83.10 \pm 4.25^\circ$ ), followed by 0.5-TiO<sub>2</sub> ( $81.06 \pm 3.41^\circ$ ). Increasing the filler content (TiO<sub>2</sub> and ZrO<sub>2</sub>) in the reinforced composites resulted in a gradual decrease in the contact angle. The lowest contact angle was obtained for 3.0-ZrO<sub>2</sub> ( $66.30 \pm 4.23$ ), followed by 3.0-TiO<sub>2</sub> ( $69.88 \pm 3.55$ ). The decrease in contact angle with increasing filler content could be due to the increased surface roughness, as shown by the surface roughness measurement. It has already been shown that an increase in surface roughness improves the wettability and decreases the contact angle value [52].

Low contact angles indicate that the solid material is hydrophilic and the liquid spreads on the surface. In contrast, higher water contact corresponds to a hydrophobic solid and the liquid does not spread on the surface [53]. A water contact angle greater than  $90^\circ$  or slightly less than  $90^\circ$  corresponds to hydrophobic material, while a water contact angle of  $51.05^\circ \pm 0.84^\circ$  corresponds to a hydrophilic material. Complete wetting of material occurs when the contact angle is  $0^\circ$  [54] [55]. Therefore, based on the above findings, it can be inferred from the current study that the addition of more than 0.5 wt% TiO<sub>2</sub> and ZrO<sub>2</sub> nanofillers transforms the hydrophobic nature of the temporary crown material into a hydrophilic one.

**3.4. SEM Analysis.** Figures 7(a)–7(g) show the fractured cross-sectional microstructure of pristine, TiO<sub>2</sub>, and ZrO<sub>2</sub> nanofilled composites. The analysis of SEM shows that the control group (Figure 7(a)) has a smooth microstructure compared to the nanofilled composites. However, with increasing concentration of the nanofillers TiO<sub>2</sub> (Figures 7(b), 7(d), and 7(f)) and ZrO<sub>2</sub> (Figures 7(c), 7(e), and 7(g)) (0.5 to 3.0 wt%), a rough microstructure with increasing micro cracks is observed. Composites with a lower concentration of nanofillers (0.5-TiO<sub>2</sub> and 0.5-ZrO<sub>2</sub>) exhibited a corrugated fracture surface and showed warped and profound cracks on the surface. Moreover, no deboned nanoparticles were observed on the surface, indicating that the nanoparticles were most likely enclosed by the polymer matrix chains, which indicated a good interaction between filler and polymer [37]. However, with increasing concentration (3.0-TiO<sub>2</sub>, 3.0-ZrO<sub>2</sub>), a ragged microstructure with deeper irregular cracks is obtained together with deboned nanoparticles. The appearance of micro indentations and deep irregular cracks is induced by the pull-out of the resin-coated nanoparticles and indicates significant toughness. These morphological studies confirm the improvement of EM the nanoparticle-filled composites compared to pristine.

## 4. Conclusion

The physical incorporation of a small amount of TiO<sub>2</sub> and ZrO<sub>2</sub> (0.5 wt.%) as fillers into PMMA-based interim restorative material significantly improved the physical, mechanical, and morphological properties. The higher concentration of these fillers resulted in a decrease in FS. However, EM and surface hardness gradually increased with increasing filler

content, with 3.0 wt.% ZrO<sub>2</sub> exhibiting the highest EM (3851.28 MPa), followed by 3.0 wt.% TiO<sub>2</sub> (3632.34 MPa). Moreover, a gradual increase in surface roughness was observed with increasing filler content. In addition, the water contact angle as a measure of wettability was significantly reduced from 91.32 ± 4.21° for the original PMMA to 66.30 ± 4.23° for 3.0 wt.% ZrO<sub>2</sub> and 69.88 ± 3.55° for 3.0 wt.% TiO<sub>2</sub>. Thus, the higher content of TiO<sub>2</sub> and ZrO<sub>2</sub> increases toughness and stiffness on one hand and reduces hydrophobicity and flexibility of the composites on the other hand.

## Data Availability

The data used to support the findings of this study are included within the article.

## Conflicts of Interest

The authors declare no conflict of interest.

## Acknowledgments

The authors are grateful to the Deanship of Scientific Research, King Saud University for the support through the Vice Deanship of Scientific Research Chairs and Engineer Abdullah Bugshan research chair for Dental and Oral Rehabilitation.

## References

- [1] M. Patras, O. Naka, S. Doukoudakis, and A. Pissiotis, "Management of provisional restorations' deficiencies: a literature review," *Journal of Esthetic and Restorative Dentistry*, vol. 24, no. 1, pp. 26–38, 2012.
- [2] M. Solomonov, D. H. Levy, A. Yaya, J. Ben Itzhak, and D. Polak, "Antimicrobial evaluation of polytetrafluoroethylene used as part of temporary restorations: an ex vivo study," *Australian Endodontic Journal*, vol. 48, no. 1, pp. 98–104, 2022.
- [3] D. R. Burns, D. A. Beck, S. K. Nelson, and Committee on Research in Fixed Prosthodontics of the Academy of Fixed Prosthodontics, "A review of selected dental literature on contemporary provisional fixed prosthodontic treatment: report of the committee on research in fixed prosthodontics of the academy of fixed prosthodontics," *The Journal of Prosthetic Dentistry*, vol. 90, no. 5, pp. 474–497, 2003.
- [4] K. K. Kadiyala, M. K. Badisa, G. Anne et al., "Evaluation of flexural strength of thermocycled interim resin materials used in prosthetic rehabilitation-an in-vitro study," *Journal of Clinical and Diagnostic Research: JCDR*, vol. 10, no. 9, p. ZC91, 2016.
- [5] B. Valkov and M. Balcheva, "Temporary filling materials in endodontics—a literature review," *Scripta Scientifica Medicinæ Dentalis*, vol. 8, no. 1, 2022.
- [6] R. Khan, M. R. Azhar, A. Anis, M. A. Alam, M. Boumaza, and S. M. Al-Zahrani, "Facile synthesis of epoxy nanocomposite coatings using inorganic nanoparticles for enhanced thermo-mechanical properties: a comparative study," *Journal of Coatings Technology and Research*, vol. 13, no. 1, pp. 159–169, 2016.
- [7] A. Majid, A. Jabeen, S. U.-D. Khan, and S. Haider, "First principles investigations of vibrational properties of titania and zirconia clusters," *Journal of Nanoparticle Research*, vol. 21, no. 1, pp. 1–15, 2019.
- [8] W. Farooq, S.-D. Khan, S. M. Ali, and M. Aslam, "Effect of gamma rays on nanostructured TiO<sub>2</sub> thin film synthesized with sol gel method," *Journal of Optoelectronics and Advanced Materials*, vol. 18, pp. 712–716, 2016.
- [9] A. Majid, S. Zahid, S. U.-D. Khan, A. Ahmad, and S. Khan, "Photoinjection and carrier recombination kinetics in photoanode based on (TM) FeO<sub>3</sub> adsorbed TiO<sub>2</sub> quantum dots," *Materials Science and Engineering: B*, vol. 273, p. 115423, 2021.
- [10] A. A. Asiri, R. Khan, S. S. Alzahrani et al., "Comparative analysis of the shear bond strength of flowable self-adhering resin-composites adhesive to dentin with a conventional adhesive," *Coatings*, vol. 11, no. 3, p. 273, 2021.
- [11] J. Ahmed, A. Shahzad, A. Farooq, M. Kamran, S. Ud-Din Khan, and S. Ud-Din Khan, "Thermal analysis in swirling flow of titanium dioxide–aluminum oxide water hybrid nanofluid over a rotating cylinder," *Journal of Thermal Analysis and Calorimetry*, vol. 144, no. 6, pp. 2175–2185, 2021.
- [12] S. Naheed, M. Shahid, R. Zahoor et al., "Synthesis and study of morphology and biocompatibility of xanthan gum/titanium dioxide-based polyurethane elastomers," *Polymers*, vol. 13, no. 19, p. 3416, 2021.
- [13] M. A. Raza, F. Anwar, D. Shahwar et al., "Antioxidant and antiacetylcholine esterase potential of aerial parts of *Conocarpus erectus*, *Ficus variegata* and *Ficus maclellandii*," *Pakistan Journal of Pharmaceutical Sciences*, vol. 29, no. 2, pp. 489–495, 2016.
- [14] A. Mahmood, S. U.-D. Khan, and U. A. Rana, "Theoretical designing of novel heterocyclic azo dyes for dye sensitized solar cells," *Journal of Computational Electronics*, vol. 13, no. 4, pp. 1033–1041, 2014.
- [15] Z. Zara, J. Iqbal, S. Iftikhar et al., "Designing dibenzosilole and methyl carbazole based donor materials with favourable photovoltaic parameters for bulk heterojunction organic solar cells," *Computational and Theoretical Chemistry*, vol. 1142, pp. 45–56, 2018.
- [16] F. A. AlAbduljabbar, S. Haider, F. A. Ahmed Ali et al., "TiO<sub>2</sub> nanostructured coated functionally modified and composite electrospun chitosan nanofibers membrane for efficient photocatalytic degradation of organic pollutant in wastewater," *Journal of Materials Research and Technology*, vol. 15, pp. 5197–5212, 2021.
- [17] F. A. AlAbduljabbar, S. Haider, F. A. A. Ali et al., "Efficient photocatalytic degradation of organic pollutant in wastewater by electrospun functionally modified polyacrylonitrile nanofibers membrane anchoring TiO<sub>2</sub> nanostructured," *Membranes*, vol. 11, no. 10, p. 785, 2021.
- [18] R. Raghavan, P. Shajahan, and P. Purushothaman, "Bioceramics: dental implant biomaterials," *The Journal of Prosthetic and Implant Dentistry*, vol. 4, no. 1, 2020.
- [19] S. J. Malode and N. P. Shetti, "18- ZrO<sub>2</sub> in biomedical applications," in *Metal Oxides for Biomedical and Biosensor Applications*, K. Mondal, Ed., pp. 471–501, Elsevier, 2022.
- [20] T. V. Tran, D. T. C. Nguyen, P. S. Kumar, A. T. M. Din, A. A. Jalil, and D.-V. N. Vo, "Green synthesis of ZrO<sub>2</sub> nanoparticles and nanocomposites for biomedical and environmental applications: a review," *Environmental Chemistry Letters*, vol. 20, no. 2, pp. 1309–1331, 2022.



- [21] Affairs, Ada Council on Scientific, "Direct and indirect restorative materials," *The Journal of the American Dental Association*, vol. 134, no. 4, pp. 463–472, 2003.
- [22] S. Shirkavand and E. Moslehifard, "Effect of TiO<sub>2</sub> nanoparticles on tensile strength of dental acrylic resins," *Journal of Dental Research, Dental Clinics, Dental Prospects*, vol. 8, no. 4, pp. 197–203, 2014.
- [23] Z. Y. Duymus, F. Karaalioglu, and F. Suleyman, "Flexural strength of provisional crown and fixed partial denture resins both with and without reinforced fiber," *Journal of Materials Science and Nanotechnology*, vol. 1, no. 3, p. 102, 2014.
- [24] V. Alt, M. Hannig, B. Wöstmann, and M. Balkenhol, "Fracture strength of temporary fixed partial dentures: CAD/CAM versus directly fabricated restorations," *Dental Materials*, vol. 27, no. 4, pp. 339–347, 2011.
- [25] A. Yilmaz and S. Baydas, "Fracture resistance of various temporary crown materials," *The Journal of Contemporary Dental Practice*, vol. 8, no. 1, pp. 44–51, 2007.
- [26] V. Asopa, S. Suresh, M. Khandelwal, V. Sharma, S. S. Asopa, and L. S. Kaira, "A comparative evaluation of properties of zirconia reinforced high impact acrylic resin with that of high impact acrylic resin," *The Saudi Journal for Dental Research*, vol. 6, no. 2, pp. 146–151, 2015.
- [27] M.-C. Chang, C.-C. Hung, W.-C. Chen, S.-C. Tseng, Y.-C. Chen, and J.-C. Wang, "Effects of pontic span and fiber reinforcement on fracture strength of multi-unit provisional fixed partial dentures," *Journal of dental sciences*, vol. 14, no. 3, pp. 309–317, 2019.
- [28] I. J. Ismaeel and H. K. Alalwan, "The effect of the addition of silanated poly propylene fiber to polymethylmethacrylate denture base material on some of its mechanical properties," *Journal of Baghdad College of Dentistry*, vol. 325, no. 2218, pp. 1–17, 2015.
- [29] P. Chaijareenont, H. Takahashi, N. Nishiyama, and M. Arksornnukit, "Effect of different amounts of 3-methacryloxypropyltrimethoxysilane on the flexural properties and wear resistance of alumina reinforced PMMA," *Dental Materials Journal*, vol. 31, no. 4, pp. 623–628, 2012.
- [30] S. Zidan, N. Silikas, J. Haider, A. Alhotan, J. Jahantigh, and J. Yates, "Evaluation of equivalent flexural strength for complete removable dentures made of zirconia-impregnated PMMA nanocomposites," *Materials*, vol. 13, no. 11, p. 2580, 2020.
- [31] I. N. Safi, "Evaluation the effect of nano-fillers (TiO<sub>2</sub>, Al<sub>2</sub>O<sub>3</sub>, SiO<sub>2</sub>) addition on glass transition temperature, E-Modulus and coefficient of thermal expansion of acrylic denture base material," *Journal of Baghdad College of Dentistry*, vol. 325, no. 2212, pp. 1–10, 2014.
- [32] H. A. Alnamel and M. Mudhaffer, "The effect of silicon dioxide nano-fillers reinforcement on some properties of heat cure polymethyl methacrylate denture base material," *Journal of Baghdad College of Dentistry*, vol. 26, no. 1, pp. 32–36, 2014.
- [33] H. A. Rahman, "The effect of addition nano particle ZrO<sub>2</sub> on some properties of autoclave processed heat cure acrylic denture base material," *Journal of Baghdad College Dentistry Research*, vol. 27, no. 1, pp. 32–39, 2015.
- [34] R. Wang, J. Tao, B. Yu, and L. Dai, "Characterization of multiwalled carbon nanotube-polymethyl methacrylate composite resins as denture base materials," *The Journal of Prosthetic Dentistry*, vol. 111, no. 4, pp. 318–326, 2014.
- [35] S. B. Qasim, A. A. Al Kheraif, and R. Ramakrishaniah, "An investigation into the impact and flexural strength of light cure denture resin reinforced with carbon nanotubes," *World Applied Sciences Journal*, vol. 18, no. 6, pp. 808–812, 2012.
- [36] N. Turagam and D. Prasad Mudrakola, "Effect of micro-additions of carbon nanotubes to polymethylmethacrylate on reduction in polymerization shrinkage," *Journal of Prosthodontics: Implant, Esthetic and Reconstructive*, *Dentistry*, vol. 22, no. 2, pp. 105–111, 2013.
- [37] A. Alrahlah, R. Khan, A.-B. Al-Odayni, W. S. Saeed, L. S. Bautista, and F. Vohra, "Evaluation of synergic potential of rGO/SiO<sub>2</sub> as hybrid filler for BisGMA/TEGDMA dental composites," *Polymers*, vol. 12, no. 12, p. 3025, 2020.
- [38] K. Cho, J.-H. Sul, M. H. Stenzel, P. Farrar, and B. G. Prusty, "Experimental cum computational investigation on interfacial and mechanical behavior of short glass fiber reinforced dental composites," *Composites Part B: Engineering*, vol. 200, p. 108294, 2020.
- [39] R. Wu, Q. Zhao, S. Lu, Y. Fu, D. Yu, and W. Zhao, "Inhibitory effect of reduced graphene oxide-silver nanocomposite on progression of artificial enamel caries," *Journal of Applied Oral Science*, vol. 27, 2019.
- [40] M. S. Zafar and N. Ahmed, "The effects of acid etching time on surface mechanical properties of dental hard tissues," *Dental Materials Journal*, vol. 34, no. 3, pp. 315–320, 2015.
- [41] F. C. R. Lins, R. C. Ferreira, R. R. Silveira, C. N. B. Pereira, A. N. Moreira, and C. S. Magalhães, "Surface roughness, microhardness, and microleakage of a silorane-based composite resin after immediate or delayed finishing/polishing," *International Journal of Dentistry*, vol. 2016, Article ID 8346782, 8 pages, 2016.
- [42] S. Ray, A. K. Bhowmick, and S. Bandyopadhyay, "Atomic force microscopy studies on morphology and distribution of surface modified silica and clay fillers in an ethyleneoctene copolymer rubber," *Rubber Chemistry and Technology*, vol. 76, no. 5, pp. 1091–1105, 2003.
- [43] M. Braem, W. Finger, V. Van Doren, P. Lambrechts, and G. Vanherle, "Mechanical properties and filler fraction of dental composites," *Dental Materials*, vol. 5, no. 5, pp. 346–349, 1989.
- [44] K. H. Chung and E. H. Greener, "Correlation between degree of conversion, filler concentration and mechanical properties of posterior composite resins," *Journal of Oral Rehabilitation*, vol. 17, no. 5, pp. 487–494, 1990.
- [45] I. Ozsoy, A. Demirkol, A. Mimaroglu, H. Unal, and Z. Demir, "The influence of micro-and nano-filler content on the mechanical properties of epoxy composites," *Strojnikski Vestnik-Journal of Mechanical Engineering*, vol. 61, no. 11, pp. 601–609, 2015.
- [46] S. Beun, T. Glorieux, J. Devaux, J. Vreven, and G. Leloup, "Characterization of nanofilled compared to universal and microfilled composites," *Dental Materials*, vol. 23, no. 1, pp. 51–59, 2007.
- [47] R. V. Mesquita, D. Axmann, and J. Geis-Gerstorf, "Dynamic visco-elastic properties of dental composite resins," *Dental Materials*, vol. 22, no. 3, pp. 258–267, 2006.
- [48] G. Q. D. M. Monteiro and M. A. J. R. Montes, "Evaluation of linear polymerization shrinkage, flexural strength and modulus of elasticity of dental composites," *Materials Research*, vol. 13, no. 1, pp. 51–55, 2010.

## *Retraction*

# **Retracted: Effect of Dihuang Yinzi on Inflammatory Response in Cerebral Ischemia-Reperfusion Model Rats by Regulating Gut Microbiota**

### **BioMed Research International**

Received 8 January 2024; Accepted 8 January 2024; Published 9 January 2024

Copyright © 2024 BioMed Research International. This is an open access article distributed under the Creative Commons Attribution License, which permits unrestricted use, distribution, and reproduction in any medium, provided the original work is properly cited.

This article has been retracted by Hindawi following an investigation undertaken by the publisher [1]. This investigation has uncovered evidence of one or more of the following indicators of systematic manipulation of the publication process:

- (1) Discrepancies in scope
- (2) Discrepancies in the description of the research reported
- (3) Discrepancies between the availability of data and the research described
- (4) Inappropriate citations
- (5) Incoherent, meaningless and/or irrelevant content included in the article
- (6) Manipulated or compromised peer review

The presence of these indicators undermines our confidence in the integrity of the article's content and we cannot, therefore, vouch for its reliability. Please note that this notice is intended solely to alert readers that the content of this article is unreliable. We have not investigated whether authors were aware of or involved in the systematic manipulation of the publication process.

Wiley and Hindawi regrets that the usual quality checks did not identify these issues before publication and have since put additional measures in place to safeguard research integrity.

We wish to credit our own Research Integrity and Research Publishing teams and anonymous and named external researchers and research integrity experts for contributing to this investigation.

The corresponding author, as the representative of all authors, has been given the opportunity to register their agreement or disagreement to this retraction. We have kept a record of any response received.

### **References**

- [1] X. Wang, L. Ye, W. Sun et al., "Effect of Dihuang Yinzi on Inflammatory Response in Cerebral Ischemia-Reperfusion Model Rats by Regulating Gut Microbiota," *BioMed Research International*, vol. 2022, Article ID 3768880, 9 pages, 2022.

## Research Article

# Effect of Dihuang Yinzi on Inflammatory Response in Cerebral Ischemia-Reperfusion Model Rats by Regulating Gut Microbiota

Xinyu Wang , Lei Ye , Wanru Sun , Liya Li , Chaoyun Wang , Xiaoyan Xu ,  
Zhaohai Pan , and Jianwei Gong 

Binzhou Medical University, Laishan District, Yantai, 264003 Shandong, China

Correspondence should be addressed to Jianwei Gong; [jwgongfzh@163.com](mailto:jwgongfzh@163.com)

Received 27 June 2022; Revised 5 July 2022; Accepted 13 July 2022; Published 17 August 2022

Academic Editor: Nauman Rahim Khan

Copyright © 2022 Xinyu Wang et al. This is an open access article distributed under the Creative Commons Attribution License, which permits unrestricted use, distribution, and reproduction in any medium, provided the original work is properly cited.

Dihuang Yinzi, as a classical Chinese medicine prescription, plays an important role for the treatment of ischemic stroke. Gut microbiota play a functional role for the expression of proinflammatory cytokines and anti-inflammatory cytokines, which further affect central nervous system and change brain function. Our research confirmed that Dihuang Yinzi can exert brain protection by inhibiting inflammatory reaction. Dihuang Yinzi can significantly decrease the contents of interleukin-6 (IL-6), tumor necrosis factor- $\alpha$  (TNF- $\alpha$ ), and interleukin-17 (IL-17) in brain, serum, and colon tissues and increase the contents of transforming growth factor- $\beta$  (TGF- $\beta$ ) and interleukin-10 (IL-10) in cerebral ischemia-reperfusion model rats. The results of 16s rRNA high-throughput sequencing showed that Dihuang Yinzi had a significant effect on microbiome in rats. The firmicutes, bacteroidetes, and proteobacteria were dominant in Dihuang Yinzi group. The content of firmicutes increased with the increase of dosage of Dihuang Yinzi. Especially, the content of actinomycetes in the high-dose group was higher than other groups. At the genus level, the number of bacteroides in the antibiotic groups was significantly higher than that in the other treatment groups. The results suggest that Dihuang Yinzi may play important roles in treatment of ischemic stroke by regulating the gut microbiota and the inflammatory reaction in the colon tissues, serum, and brain of the model rats, to verify the scientific nature of this prescription in relieving brain inflammatory reaction and brain injury by this way and to reveal the brain-gut related mechanism of Dihuang Yinzi in treating ischemic stroke.

## 1. Introduction

Ischemic stroke, the most common type of stroke, occurs when a blood vessel in the neck or brain is blocked [1]. Ischemic stroke is a common disease among middle-aged and elderly people with high incidence, disability, and recurrence rate, which seriously affects the physical and mental health and quality of life of human beings. The reports indicated, in the United States, that more than 795,000 individuals have a stroke each year [2]. The increasing researches suggested that the brain and gastrointestinal tract were involved in complex bidirectional regulation through the neuro-immune-endocrine-gut microbiota [3, 4]. According to the survey of the intensive care unit (ICU) patients, most patients, in the early stage of stroke, are in a state of high stress, which can lead to a strong systemic inflammatory response, leading to intestinal dynamic disorder, imbalance of flora, ischemia, excessive

growth of cytokines, lack of cytokines, and excessive apoptosis of intestinal mucosal epithelial cells, resulting in intestinal mucosal barrier injury. Therefore, we speculate that regulating intestinal function and intestinal microbiota can treat stroke patients to a certain extent [5].

Dihuang Yinzi is based on the theory of traditional Chinese medicine (TCM) and has the function of nourishing kidney yin and nourishing essence [6]. Studies have found that Dihuang Yinzi has good effect in antioxidative damage, inhibiting nerve cell apoptosis and promoting the formation of new blood vessels in the ischemic area of cerebral tissue in the cerebral infarction rats [7]. Gut microbes act on the immune system, make proinflammatory and anti-inflammatory cytokines change, affect the central nervous system, and change brain function. Translational studies manifest that some of the bacteria may have effects on stress responses and cognitive function, shedding new light on manipulating the gut microbiome with

antibiotics to alter brain function [8]. Therefore, we speculated Dihuang Yinzi treats ischemic stroke by improving intestinal microecology and regulating the inflammatory state in vivo.

In this study, we systematically examined the changes of intestinal flora before and after rat modeling and the regulatory effects of each drug on intestinal flora by using microbiome. The mechanism of brain-intestine connection in the treatment of ischemic stroke with Dihuang Yinzi was revealed. It provides the basis for the rational use of Dihuang Yinzi and is also of great significance to improve the evolution of gastrointestinal syndrome in the course of stroke.

## 2. Materials and Method

**2.1. Animals.** 60 healthy male SD rats weighing 250-300 g were purchased from Pengyue. The animal license no. SCXK (lu) was 20190003. 42 rats were divided into 7 groups, including sham operation group; model 1 group; model group; high-, intermediate-, and low-dose groups of Dihuang Yinzi; and antibiotic group (amoxicillin/clavulanic acid) (Figure 1). The rat model of cerebral ischemia-reperfusion was established by clipping the common carotid arteries. Intra-gastric administration was started on the second day after modeling, once a day for 7 consecutive days. The experiments were approved by the Binzhou Medical University Animal Care and Use Committee.

**2.2. Model Building Method.** The rats were anesthetized and fixed on the supine position. The anterior cervical skin was cut open, the bilateral common carotid artery was separated along the left and right trachea, and the bilateral common carotid artery was closed with noninvasive artery clip for 30 min, resulting in acute cerebral ischemia. Loosen the artery clamp after 30 min reperfusion, reoccupy after 30 min noninvasive arterial clip on both sides of common carotid arteries 30 min, and the mold is finished after loosening and stitching. After separation and in the process of bilateral common carotid artery clamping and loosening, gauze soaked in warm saline was used to cover the incision surface to keep the tissue moist. The operation method of sham-operated group was the same as that of the model group, but the common carotid artery on both sides was not clipped.

**2.3. Gene Sequencing.** 16S rRNA sequencing and conducted were performed as previously described [9]. In brief, the QIAamp Fast DNA Stool Mini Kit (Qiagen, California, USA) was selected to extract the bacterial genomic DNA. The 16SrRNA V3-V4 region was used to amplify by using PCR and then sequenced with MiSeq platform.

**2.4. The Levels of Inflammatory Cytokines in Rats Were Detected.** Reagent of IL-6 (batch number: E20191204-30219a), TNF- $\alpha$  (batch number: e20191201-31063a), IL-17 (batch number: e20191202-30201a), TGF- $\beta$  (batch number: e20191206-31072a), and IL-10 (batch number: e20191203-30194a) were purchased from Shanghai Enzyme-Linked Biotechnology Co., Ltd. Blood was collected from the rat heart, centrifuged at 4°C at 3000 r/min for 15 min, and serum was collected and stored at -80°C. The cortical tissue and colon tissue of the rat separately were removed from

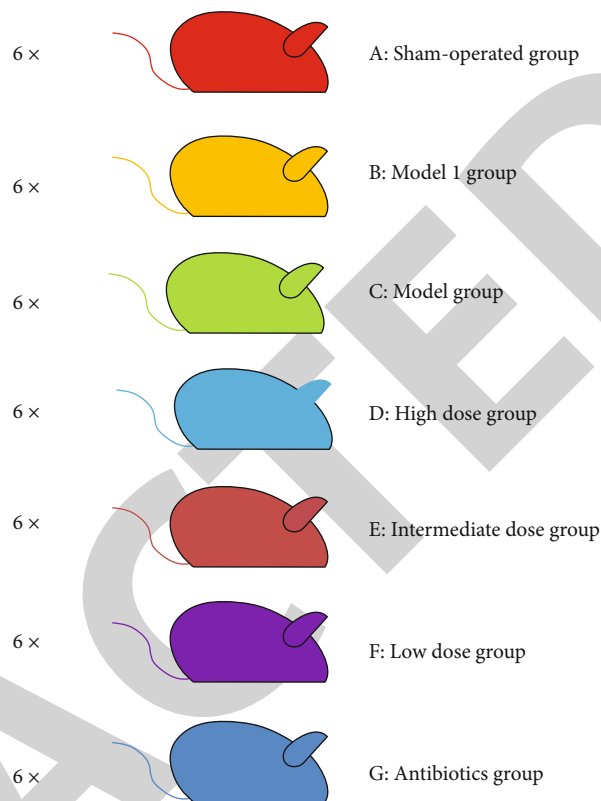


FIGURE 1: An overview of the study design and timeline. One mouse from each cage was treated according to experiment condition ( $N = 42$ , 6 mice per group).

the ice and diluted after homogenization. The contents of proinflammatory factors IL-6, TNF- $\alpha$ , and IL-17 and anti-inflammatory factors TGF- and IL-10 in the cerebral cortex and serum of rats were detected by ELISA.

**2.5. Bioinformatic Analysis.** Quantitative Insights Into Microbial Ecology was used to process the 16S rRNA sequencing data [10]. Sequencing reads was filtered, and feature table was constructed by DADA2 software. Then, vsearch plugin was used to cluster sequences into OTUs at 97% identity [11]. MAFFT [12] was selected to align the sequences, and a phylogenetic tree was generated with FastTree plugin. Q2-diversity was used to conduct alpha and beta diversity analyses. The metagenomes of gut microbiome were processed from 16S rRNA sequences using PICRUSt as described before [13]. The raw sequence data has been submitted to the NCBI Short Read Archive with accession number PRJNA628126.

**2.6. Statistical Analysis.** LEfSe analysis was applied to distinguish taxa or pathways in different group [14]. Fisher's exact test [15] and Kruskal-Wallis test [16] also were adopted to analyze the data. SPSS 23.0 statistical software was used for statistical methods, and  $t$  test was used for measurement data.

## 3. Results

**3.1. Effect of Dihuang Yinzi on the Content of Inflammatory Factors in Cerebral Cortex, Serum, and Colonic Tissues of Rat.**

TABLE 1: Effects of Dihuang Yinzi on levels of proinflammatory factors IL-6, TNF- $\alpha$ , and IL-17 in the cerebral cortex of rats.

Group	IL-6 (pg/g)	TNF- $\alpha$ (pg/g)	IL-17 (pg/g)
Sham-operated group	733.74 $\pm$ 9.26	1837.90 $\pm$ 21.00	93.57 $\pm$ 15.11
Model group	1915.10 $\pm$ 41.80 <sup>##</sup>	3887.68 $\pm$ 61.57 <sup>##</sup>	527.04 $\pm$ 37.52 <sup>##</sup>
Low-dose group	1713.59 $\pm$ 26.52*	3242.96 $\pm$ 43.84**	430.16 $\pm$ 21.67**
Intermediate-dose group	1396.17 $\pm$ 15.95**	2749.47 $\pm$ 29.54**	320.34 $\pm$ 13.35**
High-dose group	1187.95 $\pm$ 26.22**	2347.12 $\pm$ 24.70**	280.35 $\pm$ 11.54**
Antibiotics group	1132.88 $\pm$ 24.75**	2157.77 $\pm$ 28.47**	181.59 $\pm$ 6.13**

<sup>##</sup> $P < 0.01$  compared with sham-operated group; \* $P < 0.05$ , \*\* $P < 0.01$  compared with model group.

TABLE 2: Effect of Dihuangyinzi on the contents of anti-inflammatory factors TGF- $\beta$  and IL-10 in rat cerebral cortex.

Group	TGF- $\beta$ (pg/g)	IL-10 (pg/g)
Sham-operated group	2637.56 $\pm$ 42.76	934.68 $\pm$ 24.68
Model group	646.28 $\pm$ 30.35 <sup>##</sup>	543.32 $\pm$ 39.92 <sup>##</sup>
Low-dose group	1105.80 $\pm$ 24.74**	629.47 $\pm$ 23.56**
Intermediate-dose group	1438.53 $\pm$ 37.76**	677.57 $\pm$ 19.33**
High-dose group	1895.97 $\pm$ 43.35**	769.12 $\pm$ 32.32**
Antibiotics group	2137.29 $\pm$ 32.09**	846.06 $\pm$ 31.02**

<sup>##</sup> $P < 0.01$  compared with sham-operated group; \*\* $P < 0.01$  compared with model group.

TABLE 3: Effects of Dihuang Yinzi on serum levels of proinflammatory factors IL-6, TNF- $\alpha$ , and IL-17 in rats.

Group	IL-6 (pg/ml)	TNF- $\alpha$ (pg/ml)	IL-17 (pg/ml)
Sham-operated group	88.42 $\pm$ 2.22	153.33 $\pm$ 2.38	10.53 $\pm$ 0.64
Model group	221.05 $\pm$ 7.86 <sup>##</sup>	414.32 $\pm$ 10.91 <sup>##</sup>	58.57 $\pm$ 2.47 <sup>##</sup>
Low-dose group	186.60 $\pm$ 4.23**	351.01 $\pm$ 6.40**	46.21 $\pm$ 2.56**
Intermediate-dose group	171.70 $\pm$ 2.53**	300.87 $\pm$ 8.09**	36.55 $\pm$ 1.10**
High-dose group	140.46 $\pm$ 2.85**	262.73 $\pm$ 5.53**	31.71 $\pm$ 1.91**
Antibiotics group	119.64 $\pm$ 4.89**	218.36 $\pm$ 11.66**	19.70 $\pm$ 0.67**

<sup>##</sup> $P < 0.01$  compared with sham-operated group; \*\* $P < 0.01$  compared with model group.

Combined with previous findings, our results indicated that, stroke model group compared with sham group, the contents of IL-6, TNF- $\alpha$ , and IL-17 in cerebral cortex, serum, and colonic tissues were significantly increased ( $P < 0.05$ ), and contents of TGF- $\beta$  and IL-10 obviously were decreased ( $P < 0.05$ ), demonstrating severe inflammatory reaction occurred in rats. Meanwhile, Dihuang Yinzi can significantly reduce content of IL-6, TNF- $\alpha$ , and IL-17 ( $P < 0.05$ ) and increase the contents of TGF- $\beta$  and IL-10 ( $P < 0.05$ ), which is verified that this prescription can control the inflammatory reaction. Dihuang Yinzi can reduce the damage of brain tissue and play a protective role in brain by correcting the imbalance between proinflammatory factors and anti-inflammatory factors in vivo after cerebral ischemia (Table 1–6).

**3.2. Faecal Bacterial Diversity in Rats with Ischemia Apoplexy.**  $\alpha$ -Diversity can effectively detect taxa richness and evenness, and  $\beta$ -diversity compares the similarity or difference in communities between sample.  $\alpha$ -Diversity indices were employed to compare the richness estimators (Chao1 and Ace) and diversity index (Figure 2). We found that the

TABLE 4: Effect of Dihuang Yinzi on serum levels of anti-inflammatory factors TGF- $\beta$  and IL-10 in rats.

Group	TGF- $\beta$ (pg/ml)	IL-10 (pg/ml)
Sham-operated group	282.32 $\pm$ 4.25	93.52 $\pm$ 1.81
Model group	87.48 $\pm$ 2.29 <sup>##</sup>	52.19 $\pm$ 3.22 <sup>##</sup>
Low-dose group	120.34 $\pm$ 2.17**	60.94 $\pm$ 2.69**
Intermediate-dose group	155.97 $\pm$ 7.42**	73.80 $\pm$ 1.22**
High-dose group	194.43 $\pm$ 5.07**	81.13 $\pm$ 3.26**
Antibiotics group	242.30 $\pm$ 7.51**	90.77 $\pm$ 4.30**

<sup>##</sup> $P < 0.01$  compared with sham-operated group; \*\* $P < 0.01$  compared with model group.

gut microbiome of rehmanniae group was markedly more diverse compared to antibiotic group. However, it has no significant changes at the three rehmanniae groups (D, E, and F groups). To further explore the effect of Dihuang Yinzi on microbiomes analysis,  $\beta$ -diversity (PCoA) was adopted to reveal microbiome community structures

TABLE 5: Effects of Dihuang Yinzi decoction on the contents of proinflammatory factors IL-6, TNF- $\alpha$ , and IL-17 in colon tissues of rats.

Group	IL-6 (pg/g)	TNF- $\alpha$ (pg/g)	IL-17 (pg/g)
Sham-operated group	753.36 $\pm$ 33.90	1536.40 $\pm$ 26.25	156.88 $\pm$ 1.87
Model group	1914.23 $\pm$ 23.49 <sup>##</sup>	3317.93 $\pm$ 52.33 <sup>##</sup>	585.88 $\pm$ 13.06 <sup>##</sup>
Low-dose group	1594.68 $\pm$ 27.84 <sup>**</sup>	3203.75 $\pm$ 48.85 <sup>*</sup>	444.11 $\pm$ 15.23 <sup>**</sup>
Intermediate-dose group	1369.23 $\pm$ 38.96 <sup>**</sup>	2759.59 $\pm$ 54.46 <sup>**</sup>	344.76 $\pm$ 9.04 <sup>**</sup>
High-dose group	1233.13 $\pm$ 16.20 <sup>**</sup>	2356.35 $\pm$ 47.34 <sup>**</sup>	324.67 $\pm$ 10.86 <sup>**</sup>
Antibiotics group	847.22 $\pm$ 21.69 <sup>**</sup>	2241.24 $\pm$ 9.13 <sup>**</sup>	247.39 $\pm$ 3.98 <sup>**</sup>

<sup>##</sup> $P < 0.01$  compared with sham-operated group; <sup>\*</sup> $P < 0.05$ , <sup>\*\*</sup> $P < 0.01$  compared with model group.

TABLE 6: Effect of Dihuang Yinzi on contents of anti-inflammatory factors TGF- $\beta$  and IL-10 in colon tissues of rats.

Group	TGF- $\beta$ (pg/g)	IL-10 (pg/g)
Sham-operated group	2800.04 $\pm$ 45.29	910.33 $\pm$ 18.25
Model group	946.28 $\pm$ 27.49 <sup>##</sup>	421.83 $\pm$ 7.30 <sup>##</sup>
Low-dose group	1255.37 $\pm$ 51.88 <sup>**</sup>	571.00 $\pm$ 11.78 <sup>**</sup>
Intermediate-dose group	1494.92 $\pm$ 62.90 <sup>**</sup>	642.28 $\pm$ 15.82 <sup>**</sup>
High-dose group	1828.07 $\pm$ 38.31 <sup>**</sup>	727.52 $\pm$ 6.92 <sup>**</sup>
Antibiotics group	2277.89 $\pm$ 15.58 <sup>**</sup>	772.17 $\pm$ 13.46 <sup>**</sup>

<sup>##</sup> $P < 0.01$  compared with sham-operated group; <sup>\*\*</sup> $P < 0.01$  compared with model group.

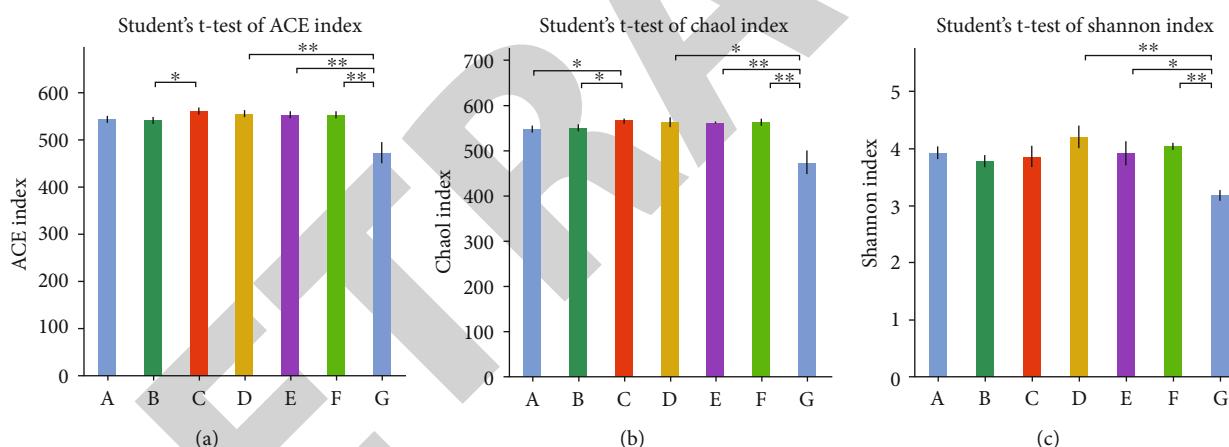


FIGURE 2: Diversity estimation of the 16S rRNA gene. (a) ACE indice; (b) Chao indice; (c) Shannon indice.

similarities (Figure 3), which showed that the microbiota of antibiotic group differed substantially from other individuals. Similar to alpha diversity, it displays the similarity of microbiome community structures in three rehmanniae groups.

**3.3. Bacteria Differentially Abundant in Different Treatment Group.** Community structure were compared, indicating that firmicutes, bacteroidetes, and proteobacteria were the most predominant phyla, and the content of firmicutes keep increasing with improvement of rehmanniae dose (Figure 4(a)). Especially, the content of actinobacteria in the high-dose group was the highest than other groups. At the genus level, bacteroides in the high-dose group was also higher than other treatment groups (Figure 4(b)). In all groups, Lactobacillus in the high-dose group was evidently lower than other groups (Figure 4).

LEfSe analysis was conducted to the faecal microbiota composition among 7 treatment group to identify differentially abundant taxa. Figure 5(a) shows that the taxa differed most between different communities. 43 discriminative features were found by LEfSe analysis (LDA score  $> 4$ ) (Figure 5(b)). 10, 5, and 5 bacteria were significantly more abundant in sham-operated group, model 1 group, and model group, separately. The allobaculum, christensenellaceae, and ruminococcaceae were enriched in the high-dose group. Ruminococcaceae and coprostanoligenes were more abundant in the low-dose group. Ten bacteria including bacteroides, bacteroidaceae, enterobacteriaceae, shigella, and blautia were enriched in antibiotics groups (Figure 5).

**3.4. Microbial Functional Dysbiosis in Samples.** PICRUSt was used to analyze the potential function of the gut microbiota. The results showed that the proportion of digestive system

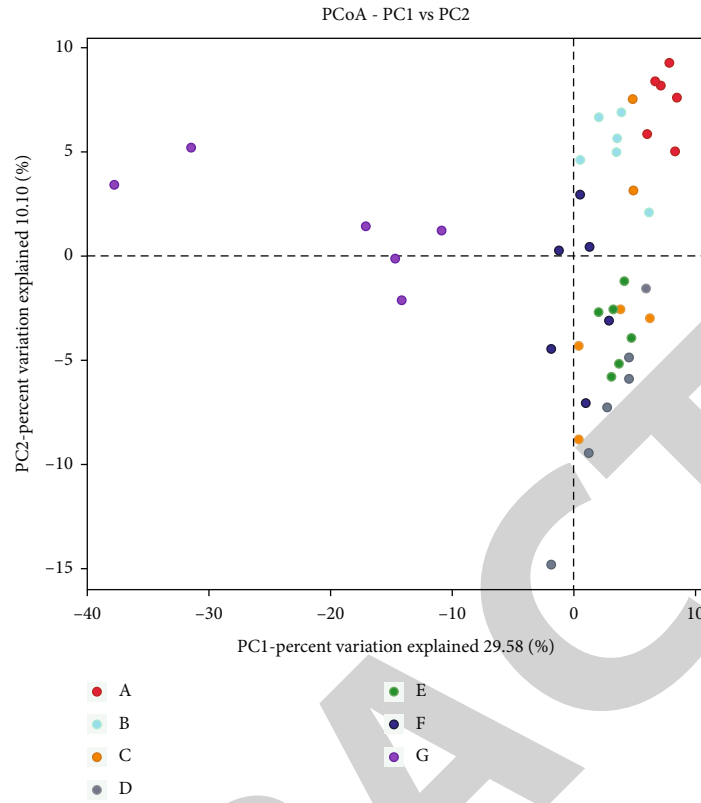


FIGURE 3: PCoA based on unweighted UniFrac matrix showed that the overall faecal microbiota composition was different in different group.

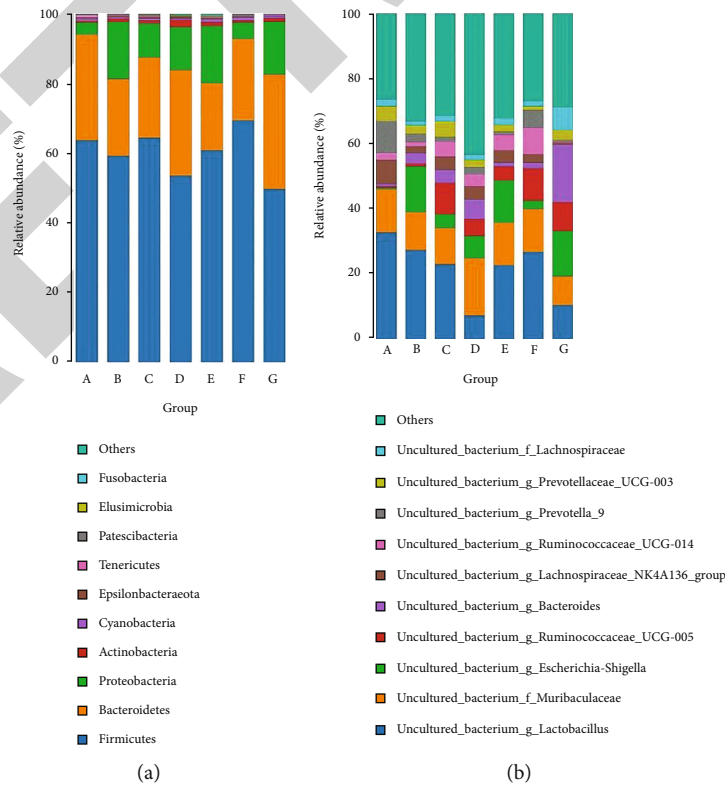


FIGURE 4: Relative abundances of the gut microbiota at phylum level (a) and genus level (b).

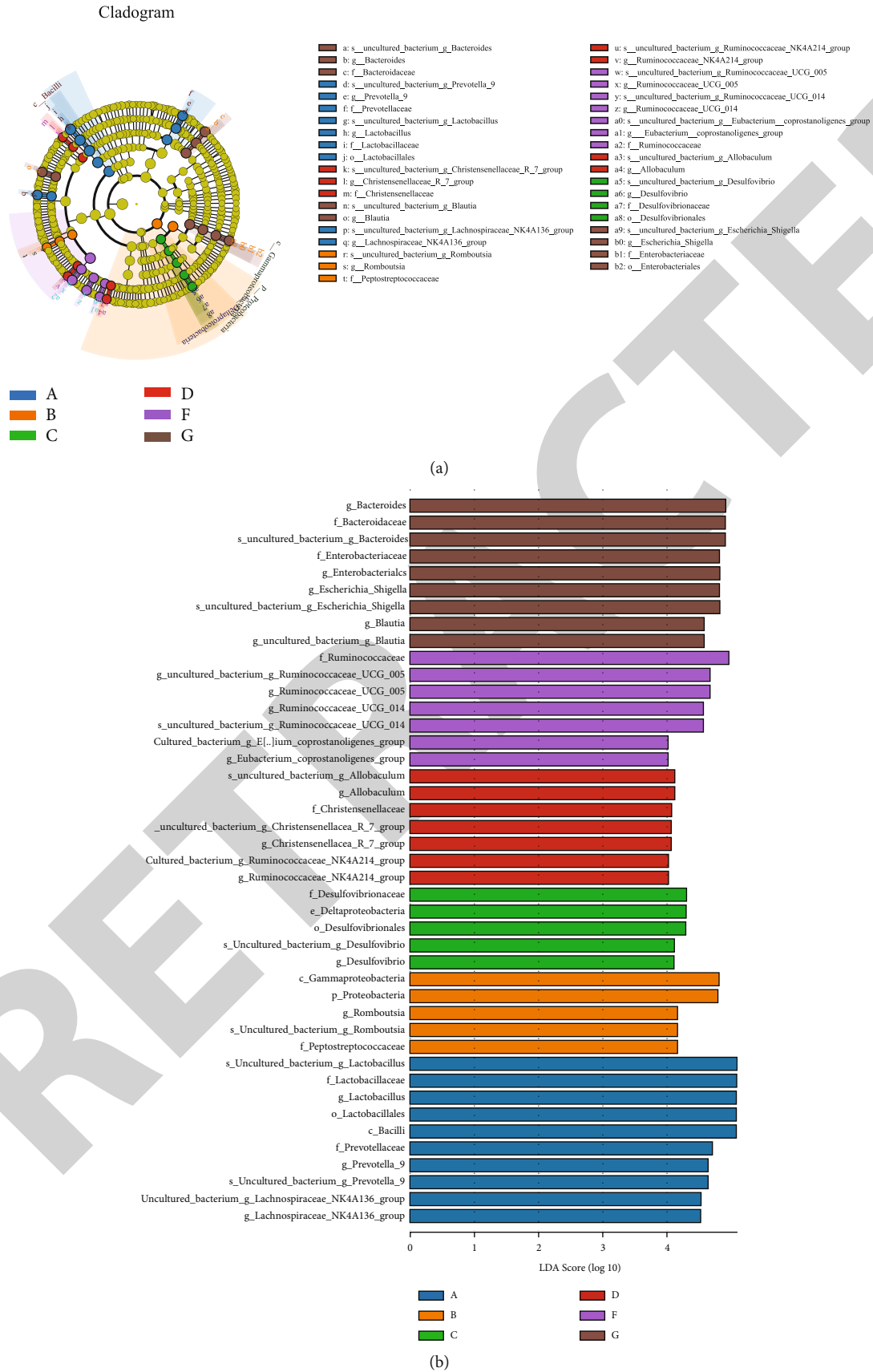


FIGURE 5: Taxonomic differences in 7 group by LefSe and LDA. (a) LefSe results for the bacterial communities. (b) Cladogram using the LDA model results for the bacterial hierarchy.



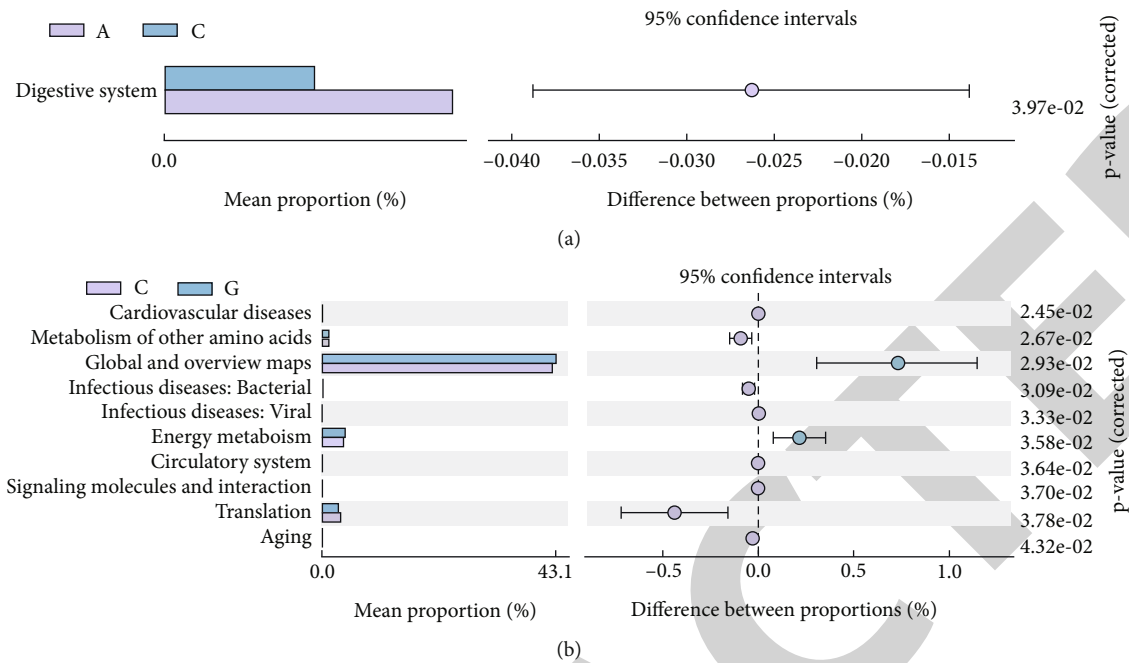


FIGURE 6: Functional analyses of predicted metagenomes. (a) Differentially abundant KEGG pathways across A and C groups. (b) Differentially abundant KEGG pathways across C and G groups.

in the microbiome of the sham group was higher than that of the model group. Energy metabolism was also higher in antibiotics groups. Additionally, global and overview maps was significantly increased in the antibiotics groups (Figure 6).

#### 4. Discussion

Gut microbiota is closely correlated with stroke, and the research has indicated that the microbiota is altered after experimental stroke in young rats [17–19]. Here, Dihuang Yinzi on the gut microbiota has been investigated. The results revealed that Dihuang Yinzi had a protective effect against ischemia apoplexy, decreased the content of proinflammatory factors, and increased the content anti-inflammatory factors. Additionally, Dihuang Yinzi was found to modulate the gut microbiota, enhancing more beneficial microorganisms growth, while suppressing the growth of potential pathogens.

The contents of IL-6, TNF- $\alpha$ , and IL-17 and anti-inflammatory factors TGF- $\beta$  and IL-10 in cerebral, cortex serum, and colon tissue were determined, indicating that Dihuang Yinzi can significantly reduce the levels of IL-6, TNF- $\alpha$ , and IL-17 and improve the contents of TGF- $\beta$  and IL-10. Studies indicated that NK cells, B lymphocytes, and TNF- $\alpha$ , TGF- $\beta$ , CRP, IL-4, IL-6, and IL-10 are altered after stroke [20–22]. Dihuang Yinzi may act as anti-inflammatory protection after stroke in cerebral, cortical serum, and colon tissue, such as TGF- $\beta$  and IL-10, decrease content of proinflammatory factor including IL-6, TNF- $\alpha$ , and IL-17 and may play protective roles on stroke.

Recently, increasing researchers set out to study the effect of gut microbiota on stroke and to explore the reconfiguration of microbial community in experimental models

after stroke of humans and rats. Tascilar et al. found that bacterial translocated to extraintestinal structures in a mouse MCAO [23]. Caso et al. reported bacterial translocation to different body parts in stress before MCAO in the experiment of rats [24]. Winek et al. indicated that several bacteria were abrupt disappearance after stroke after acute brain injury [25]. We discovered that the gut microbiome of model group was markedly more diverse compared to sham-operated group. Compared with model group, the microbiome of the sham group had a higher proportion of the digestive system. After a stroke, the function associated with digestion is reduced, and presumably, microorganisms related with digestion were decreased. Results found that the content of actinobacteria in the high-dose group was higher than other group. Lactobacillus in the high-dose group was evidently lower than other group. Especially, the content of prevotellaceae in Dihuang Yinzi groups was lower than that of the model group. The study by Yamashiro et al. showed that stroke patients had significantly higher rumen Lactobacillus bacteria counts compared with controls [26]. Therefore, we suspect that Dihuang Yinzi inhibits the growth of Lactobacillus.

A high-risk group for stroke had an enrichment of opportunistic pathogens and lactate-producing bacteria, but a decrease in butyrate-producing bacteria, compared with a low-risk group for stroke, one report showed [27], which explain the reason for the increase of allobaculum, christensenellaceae, and ruminococcaceae et al., in Dihuang Yinzi groups. The consumption of a diet containing rehmanniae is conducive to the accumulation of more beneficial microorganisms while inhibiting the growth of potential pathogens [28]. Furthermore, we also analyzed the effect of antibiotics on the intestinal bacteria. Results showed

that antibiotics significantly changed microbiota. Compared with other groups, the species and number of microorganisms were significantly decreased. Researches indicated that antibiotics which altered the gut microbiota reduced neurological impairment and the cerebral infarct volume [29].

In conclusion, our results reveal that Dihuang Yinzi can significantly reduce content of IL-6, TNF- $\alpha$ , and IL-17, improve the content of TGF- $\beta$  and IL-10, and modulate the gut microbiota, promoting a decrease of the ratio of lactobacillus and increasing the relative abundance of allobaculum, christensenellaceae, and ruminococcaceae. Thereby, it provides a new approach against ischemia apoplexy.

### Data Availability

Data to support the findings of this study is available on reasonable request from the corresponding author.

### Ethical Approval

All animal experiments were approved by the Binzhou Medical University Animal Care and Use Committee.

### Conflicts of Interest

Xinyu Wang, Lei Ye, Wanru Sun, Liya Li, Chaoyun Wang, Xiaoyan Xu, Zhaohai Pan, and Jianwei Gong declare that they have no conflicts of interest.

### Authors' Contributions

Jianwei Gong as the corresponding author contributed to the conception of the study; Xinyu Wang and Lei Ye as the co-first authors contributed equally to this study, significantly to analysis and manuscript preparation; Wanru Sun as the third author wrote the manuscript; Liya Li and Chaoyun Wang as the fourth and fifth authors performed the data analyses; Xiaoyan Xu and Zhaohai Pan as the sixth and seventh authors helped perform the analysis with constructive discussions. All authors read and approved the final manuscript. Xinyu Wang and Lei Ye contributed equally to this study.

### Acknowledgments

This study was supported by the Shandong Natural Science Foundation General Project, Yantai Key Research and Development Project (ZR2019MH104), and Yantai Key Research and Development Project (2019XDHZ107).

### References

- [1] D. Mozaffarian, E. J. Benjamin, A. S. Go et al., "Heart disease and stroke statistics-2016 update: a report from the American Heart Association," *Circulation*, vol. 133, no. 4, pp. e38–360, 2016.
- [2] S. A. Randolph, "Ischemic stroke," *Workplace Health & Safety*, vol. 64, no. 9, p. 444, 2016.
- [3] E. A. Mayer, K. Tillisch, and A. Gupta, "Gut/brain axis and the microbiota," *The Journal of Clinical Investigation*, vol. 125, no. 3, pp. 926–938, 2015.
- [4] Y. Tache, M. Larauche, P. Q. Yuan, and M. Million, "Brain and gut CRF signaling: biological actions and role in the gastrointestinal tract," *Current Molecular Pharmacology*, vol. 11, no. 1, pp. 51–71, 2018.
- [5] L. Galland, "The gut microbiome and the brain," *Journal of Medicinal Food*, vol. 17, no. 12, pp. 1261–1272, 2014.
- [6] H. Yuan, M. Yang, X. Han, and X. Ni, "The therapeutic effect of the Chinese herbal medicine, rehmanniae Radix preparata, in attention deficit hyperactivity disorder via reversal of structural abnormalities in the cortex," *Cortex*, vol. 2018, article 3052058, 9 pages, 2018.
- [7] C. Liu, R. Ma, L. Wang et al., "Rehmanniae Radix in osteoporosis: a review of traditional Chinese medicinal uses, phytochemistry, pharmacokinetics and pharmacology," *Journal of Ethnopharmacology*, vol. 198, pp. 351–362, 2017.
- [8] T. G. Dinan and J. F. Cryan, "The microbiome-gut-brain axis in health and disease," *Gastroenterology Clinics of North America*, vol. 46, no. 1, pp. 77–89, 2017.
- [9] R. Tang, Y. Wei, Y. Li et al., "Gut microbial profile is altered in primary biliary cholangitis and partially restored after UDCA therapy," *Gut*, vol. 67, no. 3, pp. 534–541, 2018.
- [10] J. Kuczynski, J. Stombaugh, W. A. Walters, A. González, J. G. Caporaso, and R. Knight, "Using QIIME to analyze 16S rRNA gene sequences from microbial communities," *Current Protocols in Bioinformatics*, vol. 36, 2011.
- [11] J. A. Navas-Molina, J. M. Peralta-Sánchez, A. González et al., "Advancing our understanding of the human microbiome using QIIME," *Methods in Enzymology*, vol. 531, pp. 371–444, 2013.
- [12] T. Nakamura, K. D. Yamada, K. Tomii, and K. Katoh, "Parallelization of MAFFT for large-scale multiple sequence alignments," *Bioinformatics*, vol. 34, no. 14, pp. 2490–2492, 2018.
- [13] M. G. Langille, J. Zaneveld, J. G. Caporaso et al., "Predictive functional profiling of microbial communities using 16S rRNA marker gene sequences," *Nature Biotechnology*, vol. 31, no. 9, pp. 814–821, 2013.
- [14] N. Segata, J. Izard, L. Waldron et al., "Metagenomic biomarker discovery and explanation," *Genome Biology*, vol. 12, no. 6, p. R60, 2011.
- [15] S. Lydersen, M. W. Fagerland, and P. Laake, "Alternativer til Fishers eksakte test," *Tidsskrift for den Norske Lægeforening*, vol. 139, no. 14, 2019.
- [16] C. Fan and D. Zhang, "A note on power and sample size calculations for the Kruskal-Wallis test for ordered categorical data," *Journal of Biopharmaceutical Statistics*, vol. 22, no. 6, pp. 1162–1173, 2012.
- [17] M. S. Szychala, V. R. Venna, M. Jandzinski et al., "Age-related changes in the gut microbiota influence systemic inflammation and stroke outcome," *Annals of Neurology*, vol. 84, no. 1, pp. 23–36, 2018.
- [18] S. Liang, X. Wu, and F. Jin, "Gut-brain psychology: rethinking psychology from the microbiota-gut-brain axis," *Frontiers in Integrative Neuroscience*, vol. 12, p. 33, 2018.
- [19] L. Zhao, Q. Xiong, C. M. Stary et al., "Bidirectional gut-brain-microbiota axis as a potential link between inflammatory bowel disease and ischemic stroke," *Journal of Neuroinflammation*, vol. 15, no. 1, p. 339, 2018.
- [20] A. Hug, A. Dalpke, N. Wiczorek et al., "Infarct volume is a major determiner of post-stroke immune cell function and susceptibility to infection," *Stroke*, vol. 40, no. 10, pp. 3226–3232, 2009.

## Retraction

# Retracted: Metabonomic Study of the Effect of Dingkundan Intervention Comparing with Oral Contraceptives on Primary Dysmenorrhea Using the UPLC-MS Technique

### BioMed Research International

Received 8 January 2024; Accepted 8 January 2024; Published 9 January 2024

Copyright © 2024 BioMed Research International. This is an open access article distributed under the Creative Commons Attribution License, which permits unrestricted use, distribution, and reproduction in any medium, provided the original work is properly cited.

This article has been retracted by Hindawi following an investigation undertaken by the publisher [1]. This investigation has uncovered evidence of one or more of the following indicators of systematic manipulation of the publication process:

- (1) Discrepancies in scope
- (2) Discrepancies in the description of the research reported
- (3) Discrepancies between the availability of data and the research described
- (4) Inappropriate citations
- (5) Incoherent, meaningless and/or irrelevant content included in the article
- (6) Manipulated or compromised peer review

The presence of these indicators undermines our confidence in the integrity of the article's content and we cannot, therefore, vouch for its reliability. Please note that this notice is intended solely to alert readers that the content of this article is unreliable. We have not investigated whether authors were aware of or involved in the systematic manipulation of the publication process.

Wiley and Hindawi regrets that the usual quality checks did not identify these issues before publication and have since put additional measures in place to safeguard research integrity.

We wish to credit our own Research Integrity and Research Publishing teams and anonymous and named external researchers and research integrity experts for contributing to this investigation.


The corresponding author, as the representative of all authors, has been given the opportunity to register their agreement or disagreement to this retraction. We have kept a record of any response received.

### References

- [1] H. Cai, Y. Zhang, X. Ding et al., "Metabonomic Study of the Effect of Dingkundan Intervention Comparing with Oral Contraceptives on Primary Dysmenorrhea Using the UPLC-MS Technique," *BioMed Research International*, vol. 2022, Article ID 6708200, 9 pages, 2022.

## Research Article

# Metabonomic Study of the Effect of Dingkundan Intervention Comparing with Oral Contraceptives on Primary Dysmenorrhea Using the UPLC-MS Technique

Hong Cai,<sup>1</sup> Yijing Zhang,<sup>1</sup> Xiaoxia Ding,<sup>1</sup> Shiyang Zhu,<sup>2</sup> Xuesong Ding,<sup>2</sup> Yan Deng,<sup>2</sup> Xiao Ma,<sup>2</sup> Jingwen Gan,<sup>2</sup> Yanfang Wang,<sup>2</sup> and Aijun Sun <sup>2</sup>

<sup>1</sup>Affiliated Hangzhou First People's Hospital, Zhejiang University School of Medicine, Hangzhou, 310006 Zhejiang, China

<sup>2</sup>National Clinical Research Center for Obstetrics & Gynecologic Diseases, Department of Obstetrics and Gynecology, Peking Union Medical College Hospital, Chinese Academy of Medical Sciences & Peking Union Medical College, Beijing, China

Correspondence should be addressed to Aijun Sun; [saj@pumch.cn](mailto:saj@pumch.cn)

Received 23 June 2022; Revised 8 July 2022; Accepted 12 July 2022; Published 17 August 2022

Academic Editor: Nauman Rahim Khan

Copyright © 2022 Hong Cai et al. This is an open access article distributed under the Creative Commons Attribution License, which permits unrestricted use, distribution, and reproduction in any medium, provided the original work is properly cited.

Primary dysmenorrhea (PD) is a prevalent problem in gynecologic clinics among adolescents and women of reproductive age. Several therapy modalities, including traditional Chinese medicine, are deemed adequate (TCM) and have been in practice for a long time. In China, Dingkundan (DKD), a multicomponent gynecological treatment, has been used to treat PD for centuries. However, the fundamental process remains poorly understood. Comparing plasma samples acquired from DKD-treated and oral contraceptive- (OC-) treated subjects, we performed an integrated plasma metabonomic analysis utilizing the UPLC-MS technology to study the therapeutic mechanisms of DKD in PD patients. Thirty possible biomarkers and metabolic pathways were discovered, primarily steroid hormone production, glycerophospholipid metabolism, and bile secretion. The results suggested that DKD may have therapeutic benefits for PD patients via modulation of various metabolic pathways. This study is envisaged to provide detailed metabolite information regarding the etiology of PD, an assessment of the efficacy of DKD, and a comparison of DKD and OC.

## 1. Introduction

PD (primary dysmenorrhea) is associated with painful uterine contractions incited due to endometrial perforation, starting several days before menstruation and ending for about 48 to 72 hours, where the pain is most prominently felt in the thigh muscles [1]. Primary dysmenorrhea (PD) is a painful uterine contraction caused by endometrial perforation. The pain associated with dysmenorrhea begins several days before the onset of menstruation and lasts between 48 and 72 hours, affecting the thighs and frequently being associated with cramping pain [1]. Dysmenorrhea is one of the most common problems among adolescent and adult ladies. Besides pain, it is accompanied by headache, lethargy, fatigue, hyperhidrosis, and muscle spasms. Dysmenorrhea prevalence has been found to be between 45 and 97% in

the female population [2, 3]. Though the exact mechanism and manifestation of dysmenorrhea are still unknown, it has been suggested that prostaglandin syntheses, preferably E2 and F2, are major players in inducing ischemia and hypoxia, which then translate into uterine contraction and less blood flow to the affected areas [1, 4].

Dysmenorrhea is predominantly treated by the use of various drugs as well as different complementary medicines for a long time [5–7]. NSAIDs and OCs are the most frequently prescribed medicines, which hinder prostaglandins' production and subsequent release, thereby relieving pain. However, long-term use of NSAIDs is associated with various adverse effects, namely, nausea, vomiting, stomach, and duodenal ulcers owing to the nonselective nature of COX enzyme inhibition. In contrast, OC's excessive use may result in anorexia, asthma precipitation, and ace [8, 9].

The OC exerts its action by halting the ovulation stage during the menstrual cycle, reducing endometrial perforation, and enabling endometrial milieu during the early stages of the menstrual cycle, at the time when the prostaglandins are at their lowest level, thereby helping in alleviating the pain. Similarly, other ways of dealing with dysmenorrhea are also reported in the literature like exercising yoga, massaging the affected muscles, use of different supplements like vitamins and minerals, use of acupressure, use of acupuncture [1, 3, 6], and use of different herbal drugs like chamomile, ginger, and fennel [2, 10]. Nevertheless, neither NSAIDs nor natural plants can be the ultimate choice, owing to the former being prone to exacerbate digestive tract problems and the latter not readily available.

Dingkundan (DKD) is one of the most well-known traditional Chinese medicine (TCM) formulae that has demonstrated promising results for over three centuries. TCM is advocated with the advantage of the lesser extent of adverse effects associated with allopathic medicines. However, the mechanism has not been appropriately studied.

This study is aimed at investigating untargeted plasma metabolomic analysis to elucidate the therapeutic mechanism of DKD and compared the metabolomic profiles of DKD with hormonal therapy, one of the first-line management, to explore a better understanding of the difference.

## 2. Methods

**2.1. Study Populations.** A total of seventy-eight patients were recruited in a prospective, double-blind, multicenter, randomized controlled trial designed for primary dysmenorrhea treatment in China from June 2019 to December 2019. All participants enrolled reported a definitive history of primary dysmenorrhea. Patients were separated into two groups: OC treatment (group 1,  $n = 28$ ) and DKD treatment (group 2,  $n = 50$ ) for three months.

Inclusion criteria for this study include nonpregnant women aged between 16 and 35 years, regular menstruation (duration within 3–7 days, cycle within 21–35 days), ability to participate in the 3-month intervention study, and face-to-face follow-up interviews.

Written informed consent was provided to every participant, and the institutional review board approved the study at every medical center.

Patients with a history of secondary dysmenorrhea not limited to endometriosis, adenomyosis, and pelvic inflammatory disease; patients using medications containing female hormones or similar formulae to DKD prior to the study; patients addicted to alcohols and cigars; patients with unstable physical conditions; patients in the first year postpartum or lactating; patients with allergy to any pharmaceutical ingredients contained in OC and DKD; patients with a history or prone to have a thrombotic disease; patients with malignant disease; and patients with uterine endometrial abnormalities were excluded.

**2.2. Plasma Sample Collection and Preparation.** Blood samples were collected in fasting conditions before and after treatment, were subjected to centrifugation to separate

plasma, and were frozen immediately at  $-80^{\circ}\text{C}$ . Before use, all samples were thawed at  $4^{\circ}\text{C}$  in an ice bath, and accurately measured,  $100\ \mu\text{L}$  was taken and added into  $400\ \mu\text{L}$  of methanol: water mixture (4:1  $v/v$ ) to extract the metabolites. All samples were then kept at  $-20^{\circ}\text{C}$  and homogenized using a high-throughput tissue crusher (Wonbio-96c, Shanghai Wanbo Biotechnology Co. Ltd.) at a frequency of 50 Hz for 6 minutes, followed by vortexing for 30 seconds, and subjected to ultrasound treatment at 40 kHz for 30 minutes at  $5^{\circ}\text{C}$ . The samples were then allowed to stand for 30 minutes at  $-20^{\circ}\text{C}$  for protein precipitation, followed by centrifuging all samples at  $13000\ \text{g}$  for 15 minutes at  $4^{\circ}\text{C}$ . The supernatants were carefully separated and collected for subsequent analysis.

**2.3. UPLC-MS Analysis.** All samples were subjected to UPLC-MS analysis using the ExionLC™ AD system (AB Sciex, USA). The column used was ACQUITY UPLC BEH C18 (dimensions  $100\ \text{mm} \times 2.1\ \text{mm}$ ,  $1.7\ \mu\text{m}$ ; Waters Milford, USA). The UPLC was coupled with a quadrupole-time-of-flight mass spectrometer (Triple TOFTM5600+, AB Sciex, USA) and an electrospray ionization (ESI) source operating in both the positive mode and the negative mode. The analysis was performed over a mass range of 50–1000  $m/z$ .

**2.4. Data Interpretation.** Following running each sample on the UPLC-MS system, the data obtained was transported to Progenesis (QI 2.3, Nonlinear Dynamics, Waters, USA) for peak detection and alignment. Different metabolites were detected, and at least 80% in any set of samples was considered retained. The actual mass of each metabolite was used for identification purposes of the mass spectra of metabolites. Furthermore, two different biochemical databases (Human Metabolome <http://www.hmdb.ca/> and METLIN database <https://metlin.scripps.edu/>) were consulted for identifying MS/MS fragment spectra and for distinguishing isotope ratio differences.

## 3. Statistical Analysis

All obtained data were statistically analyzed employing different tests like multivariate analysis (ropls, version 1.6.2) and R package from the Bioconductor on Majorbio Cloud Platform. The panoramic view of metabolites was tested using principal component analysis (PCA), and overall metabolite changes between groups were analyzed using orthogonal partial least square discriminate analysis (OPLS-DA) with variable importance in the projection (VIP). The model parameters, i.e.,  $R^2$  and  $Q^2$ , were calculated to provide information for interpretability and predictability. The  $P$  values were determined using paired Student's  $t$ -test, and the significance level was set to  $P < 0.05$ .

## 4. Results

**4.1. Clinical Characteristics and Outcomes.** Clinical characteristics of participants in this study are listed in Table 1. There was no statistical difference between the DKD and OC groups in parameters including the year of age, procreated ratio, menstruation information, age of menarche, menstrual bleeding duration, and menstrual cycle length.

TABLE 1: Clinical characteristics and treatment results of participants in this study.

	DKD cohort ( <i>n</i> = 50)	COC cohort ( <i>n</i> = 28)	<i>P</i> value
Age (years)	24.63 ± 4.11	26.24 ± 4.49	0.38
Age of menarche (years)	12.79 ± 1.12	12.85 ± 1.23	0.85
Menstrual cycle length (days)	29.50 ± 4.58	30.41 ± 2.94	0.25
Menstrual bleeding duration (days)	6.00 ± 1.12	6.09 ± 1.38	0.39
Procreated rate (%)	6.00	17.86	0.23
VAS before treatment	3.82 ± 1.78	4.56 ± 2.34	0.36
VAS after treatment	2.93 ± 0.27*	1.78 ± 0.28 <sup>#</sup>	<0.01
Pain relief response			
Marked moderate ( <i>n</i> )	29	22	
No relief ( <i>n</i> )	21	6	
Overall effective rate (%)	58.0	78.6	0.06

\*Compared with VAS before treatment,  $P < 0.01$ ; <sup>#</sup>compared with VAS before treatment,  $P < 0.01$ .

Both cohorts collected visual analogue scale (VAS) scores before and after treatment. Results showed distinguish relief in VAS scores after treatment in both groups compared to baseline data ( $P < 0.01$ ). Participants in OC groups reported lower VAS scores after treatment compared to those in DKD groups ( $P < 0.01$ ), but there was no statistical difference in the overall effective rate between DKD and OC groups ( $P = 0.06$ ).

**4.2. OPLS-DA.** Pairwise comparisons between the two groups revealed DKD and OC-related serum metabolites. Partial separation was shown in the OPLS-DA model with  $R^2Y(\text{cum}) = 0.667$  and  $Q^2(\text{cum}) = 0.349$  (Figure 1(a)). The S-plot and VIP value showed the metabolic effect of DKD (Figure 1(b)). A total of 104 specific metabolites were distinguished from two groups. Only metabolic compounds that met the criteria of both projection (VIP) value  $> 2.5$  and  $P$  value  $< 0.05$  were identified as potentially different (Table 2). Most of these differential metabolites were lipids and lipid-like compounds, including elevated levels of glycinoleic acid, taurodeoxycholic acid, bromo fatty acid, dihydroxycholesterol, traumatic acid, etc. and decreased levels of lysophospholipid, lipopolysaccharide, bile acid, cortisol, phosphatidylcholine, etc.

**4.3. Hierarchical Cluster Analysis.** Hierarchical cluster analysis is commonly used for quantitative classification. Data were visualized by an HCA heat map (Figure 2). The result indicated that 78 tested samples (containing 50 DKD and 28 OC samples) could be divided into ten categories based on their chemical composition differences. The heat map showed that the steroid hormone-associated content (tocotrienol, androsterone sulfate, and estrone glucuronide) was at higher levels in DKD than in OC, while the contents of phosphatidylcholine, lysophospholipid, and cortisol were at lower levels accordingly.

**4.4. Pathway Enrichment Analysis.** Detailed impacts of DKD and OC-related alterations in metabolic networks were shown in Figure 3. A pathway impact  $> 0.05$  and log ( $P$ )  $>$

20 were considered the most important. Twenty metabolic pathways were identified, including the steroid hormone biosynthesis, bile secretion, glycerophospholipid metabolism, alpha-linolenic acid metabolism, choline metabolism in cancer, and aldosterone-regulated sodium reabsorption.

Eight metabolites showed to be enriched in KEGG pathway analysis. The serum levels of HMDB0007884 (PC(14:0/20:4(8Z,11Z,14Z,17Z))), HMDB0000564 (PC(16:0/16:0)), and HMDB0000063 (cortisol) were significantly decreased in the DKD group compared with the OC group (all  $P < 0.01$ ), while OC treatment elevated the concentrations of HMDB0000145 (estrone), HMDB0000933 (traumatic acid), HMDB0010318 (pregnanediol-3-glucuronide), HMDB0001032 (dehydroepiandrosterone sulfate), and HMDB0004483 (estrone glucuronide) (Figure 4).

## 5. Discussion

Aiming at investigating the serum metabolic profile of primary dysmenorrhea after DKD treatment, we performed the clinical study using an LC-MS-based metabolomics technique. Furthermore, DKD treatment was compared with oral contraceptives, considered first-line management [10]. The randomized, double-blind trial setting assesses the efficacy of DKD in primary dysmenorrhea. Results showed similar therapeutic outcomes between the two groups that indicated that DKD could be an alternative option for those PD patients who do not want or have contraindications to hormone medicine.

Further analysis revealed partial separation between DKD and OC groups based on metabolic profiling. Most of the differential metabolites were lipids and lipid-like compounds. Several metabolic pathways were involved, including the steroid hormone biosynthesis, bile secretion, glycerophospholipid metabolism, alpha-linolenic acid metabolism, choline metabolism in cancer, and aldosterone-regulated sodium reabsorption. Among these pathways, steroid hormone biosynthesis and bile secretion were impacted most. It is widely accepted that oral contraceptives could manage menstrual pain by suppressing ovulation and endometrial

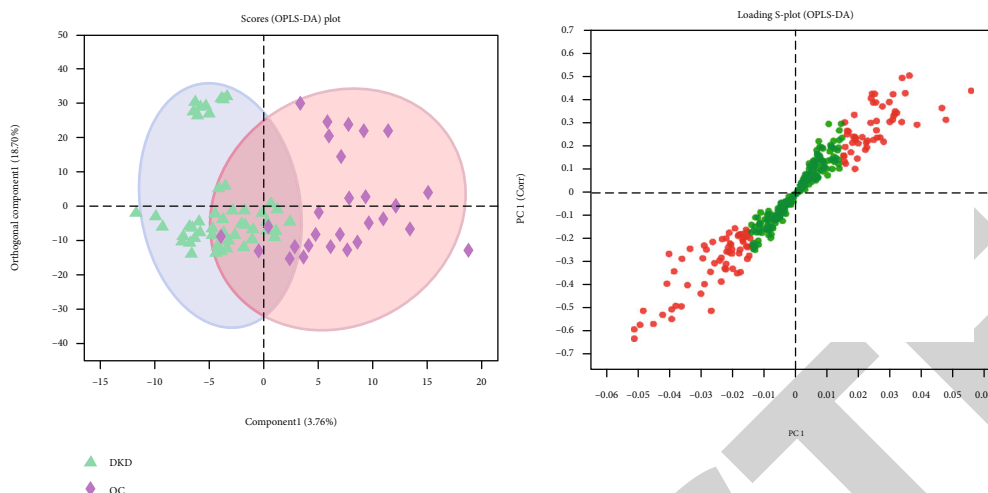


FIGURE 1: Score plot and S-plot for the OPLS-DA model between DKD and OC groups.

TABLE 2: Statistical analysis of differential metabolites from two groups.

Metabolite	VIP_pred_OPLS-DA	FC(DKD vs. OC)	P value
Glycinoeclepin A	4.52	1.24	<0.001
9-Hydroxy-10-O-D-glucuronoside-12Z-octadecenoate	4.10	0.74	0.004
N,N'-Diacetylchitobiose	3.96	1.15	0.008
Tauroursodeoxycholic acid	3.79	0.81	<0.001
12-Bromo-dodecanoic acid	3.52	1.07	<0.001
3'-N'-Acetylfusarochromanone	3.52	1.07	<0.001
(25R)-3Beta,4beta-dihydroxycholest-5-en-26-oate(1-)	3.39	1.12	<0.001
Ferulic acid	3.39	0.84	0.001
N-(1-Deoxy-1-fructosyl)tryptophan	3.33	1.08	0.007
Taurodeoxycholic acid	3.15	0.91	0.004
L-N-(1H-Indol-3-ylacetyl)glutamic acid	3.10	1.06	0.001
1-Phenyl-1,3-eicosanedione	2.92	1.06	<0.001
Fluvoxamino acid	2.90	1.04	0.003
2-Amino-5-phenylpyridine	2.90	1.05	<0.001
Cortisol	2.88	0.95	<0.001
Traumatic acid	2.84	1.10	0.005
LysoPE(0:0/15:0)	2.83	0.88	0.001
Thiomorpholine 3-carboxylate	2.81	1.13	0.020
Taurochenodeoxycholate-7-sulfate	2.79	0.94	0.001
Piperine	2.77	1.15	0.009
4-Cholesten-7alpha,12alpha,24-triol-3-one	2.73	1.05	<0.001
Cytochalasin Ppho	2.72	0.80	0.042
3'-Ketolactose	2.71	1.05	0.005
16-Bromo-9E-hexadecenoic acid	2.71	1.03	0.003
7'-Carboxy-gamma-tocotrienol	2.68	0.94	<0.001
Cis-5-Tetradecenoylcarnitine	2.66	1.11	0.019
15-Octadecene-9,11,13-triynoic acid	2.62	1.05	0.014
Inosine	2.61	0.93	0.041
(±)-Rollipyrrole	2.58	1.06	<0.001
Neomenthol-glucuronide	2.56	1.08	0.012

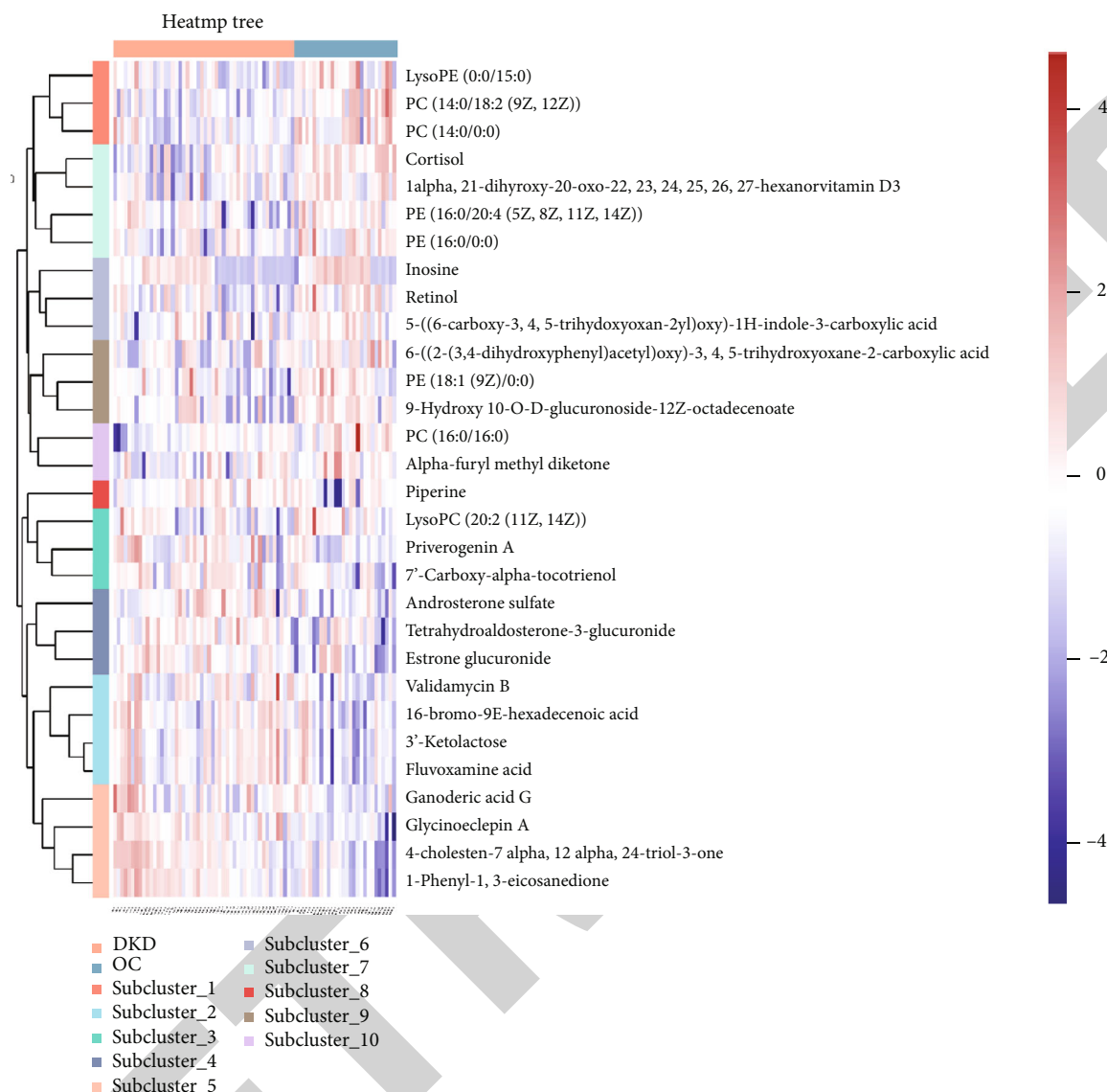


FIGURE 2: Heatmap of hierarchical clustering for the DKD group and OC group. The abscissa represents different experimental sets, the ordinate represents the differential metabolites clustered, and the color represents the relative content of metabolites in the corresponding sample, red for higher and blue for lower contents.

proliferation to block the production of prostaglandins, which also involve alternation of steroid hormone dynamics. At the same time, DKD may contribute to pain relieving through nonsteroid hormone metabolic pathways. KEGG enrichment analysis showed that DKD decreased PC(16:0/16), cortisol, and PC(14:0/20:4(8Z,11Z,14Z,17Z)) in serum levels compared with hormonal therapy, while elevating estrone, estrone glucuronide, traumatic acid, pregnanediol-3-glucuronide, and dehydroepiandrosterone sulfate levels.

PC (16:0/16) is metabolized in PC synthesis and the glycerophospholipid metabolism pathway, and disturbance of the latter is associated with depression. Recent studies revealed that serum levels of PC (16:0/16) were elevated in antenatal depression and showed a positive trending correlation with depression scores [11–13]. Abundant evidence has uncovered psychological risk factors associated with PD, including depression and anxiety, and psychotherapy inter-

ventions are considered effective in PD accordingly [14, 15]. Our results also showed remarkably lower PC(16:0/16) serum levels in DKD profiles, which indicated that regulation of PC-involved metabolic pathways might be employed as an antidepressant method.

Cortisol is regarded as downstream production of the hypothalamic-pituitary-adrenal (HPA) axis and reflects the activation of the central nervous system, which is also the primary pain response system. Patients complaining of chronic pain often present with hypercortisolism, and non-pharmacological therapeutics, cognitive behavioral therapy, and exercise are regarded as promising options in treating centralized pain with serum cortisol level downregulation observed as well [16, 17]. PD is also identified as a central hypersensitivity syndrome characterized by pain hypersensitivity without physical organ injury or a nervous system lesion with both peripheral and central hypersensitivity to



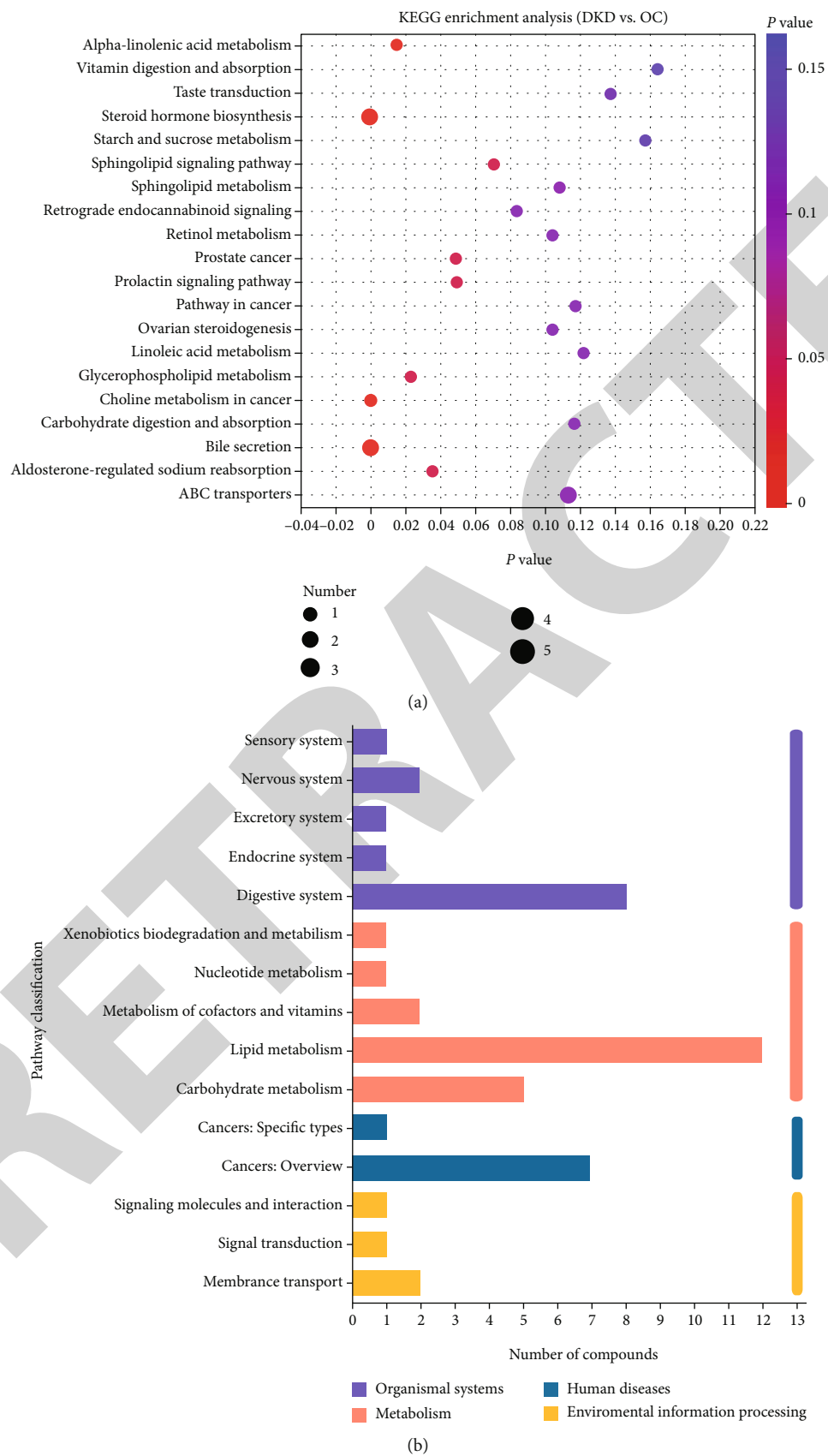


FIGURE 3: KEGG pathway enrichment. (a) KEGG pathway enrichment bubble plot. (b) KEGG pathway classification chart.

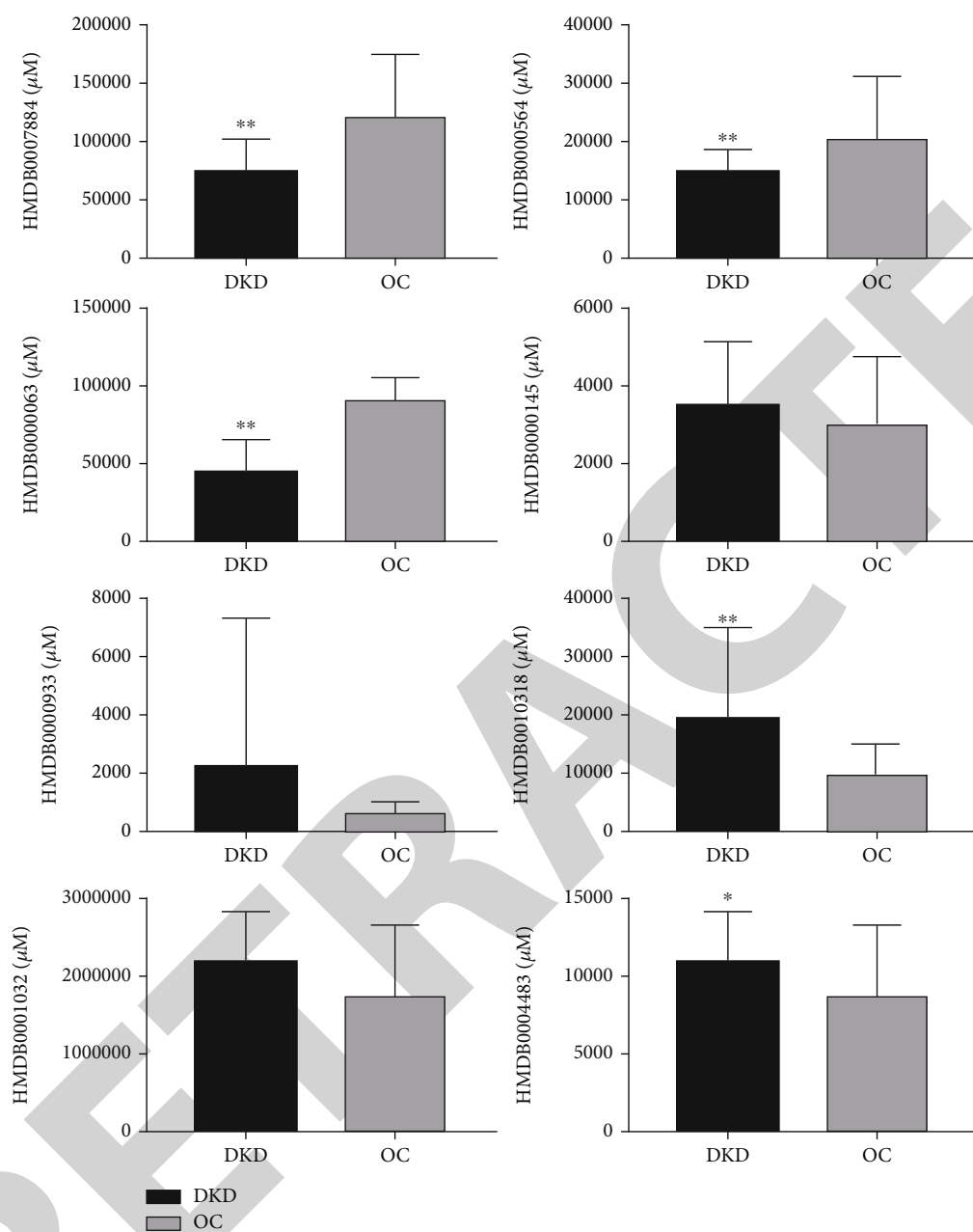


FIGURE 4: Metabolites enriched in the KEGG pathway. Relative expressions of HMDB0007884 (PC(14:0/20:4(8Z,11Z,14Z,17Z))), HMDB000564 (PC(16:0/16)), HMDB000063 (cortisol), HMDB000145 (estrone), HMDB000933 (traumatic acid), HMDB0010318 (pregnanediol-3-glucuronide), HMDB001032 (dehydroepiandrosterone sulfate), and HMDB0004483 (estrone glucuronide) in serum with DKD and OC treatment. \*\* $P < 0.01$ , \* $P < 0.05$ .

pain [18]. Our data revealed significant downregulated cortisol levels in the DKD group compared to OC treatment, hinting that DKD may positively affect pain by improving HPA axis regulation.

Estrone, estrone glucuronide, and pregnanediol-3-glucuronide are hormonal steroids and reflect longer-term levels of E2 and P4 in circulation. Oral contraceptives could suppress the concentrations of the abovementioned metabolites by ovulation suppression.

DKD is one of the most widely used Chinese traditional medicines. It helps alleviate pain, regulate menstrual func-

tion, and nourish ovarian function. The components of DKD include red ginseng, saffron, *cornu-cervi*, *Radix rehmanniae preparata*, *Radix paeoniae alba*, *Angelica sinensis*, *Scutellaria baicalensis*, *Cyperi rhizoma*, *Rhizoma chuanxiong*, motherwort fruit, and *Rhizoma corydalis*. Among these components, red ginseng, *Rhizoma chuanxiong*, saffron, and *Rhizoma corydalis* were the main ingredients for pain relief. Lee et al. suggested that Rb1, the most representative ginsenoside, inhibits inflammatory response and achieves antinociceptive effects by downregulating the activation of L4-L5 spinal cord microglia and astrocytes and

potentially through the estrogen receptor [19]. *Rhizoma chuanxiong* (RCX) is another popular TCM herb that possesses efficacy in alleviating pain. Pharmacological studies have demonstrated bioactivities of RCX, including uterus contraction regulatory activity, antimigraine activity, neuroprotective activity, cardioprotective activity by blocking calcium channels, and antivasular smooth muscle proliferation antioxidant, antiplatelet aggregation, and antithrombosis, and anti-inflammation effects [20]. Saffron has been a folk remedy for pain, cramps, and depressive disorder for a long time. Studies showed that crocin might be the main active component with various pharmacological effects. Clinical studies and animal models have shown that saffron makes an effort on pain relief such as PD, osteoarthritis, and neuropathic pain [21–25]. According to Khan et al., saffron may not act through central mechanisms [26]. Other studies suggested that saffron may retard NF- $\kappa$ B activation through JNK signaling pathway inhibition and repress IL-6 expression and oxidative stress in turn as well [27]. *Rhizoma corydalis* (RC) is another vital compound in ancient China's classical pain relief formula. Recent studies have discovered that RC has a noticeable antinociceptive effect on the central dopaminergic system. A remarkable effect of antidepressant and sedative activity is also reported in patients treated with RC in different diseases [28, 29].

## 6. Conclusion

This work was carried out to investigate the different roles and possible mechanisms of DKD compared to OC for PD by a UPLC-MS-based metabolomics method. We identified 104 compounds in serum with significant metabolic changes. The metabolic pathway analysis showed that the different mechanism was mainly involved in steroid hormone biosynthesis, bile secretion, glycerophospholipid metabolism, alpha-linolenic acid metabolism, choline metabolism in cancer, and aldosterone-regulated sodium reabsorption. Interpretation results showed downregulation of PC activity (16:0/16:0) and cortisol. In contrast, upregulation of the activity of traumatic acid may be responsible for the different effects of DKD compared with OC. Further studies emerged to investigate DKD treatment on PD with more functionally validated metabolite changes. This study also reveals that the LC-MS-based untargeted metabolomics technique may be a promising tool for exploring the mechanism of TCM formulas.

## Data Availability

The datasets during and/or analyzed during the current study are available from the corresponding author upon reasonable request.

## Ethical Approval

This study was performed per the Declaration of Helsinki. Approval was confirmed by the ethics committee of Peking Union Medical College Hospital (March 26, 2019; no. ZS-1913).

## Consent

Every participant has signed a written declaration of informed consent.

## Conflicts of Interest

The authors declare that there are no conflicts of interest.

## Authors' Contributions

H Cai did the data collection and manuscript drafting. YJ Zhang and XX Ding did the sample collection and data interpretation. SY Zhu, Y Deng, and XS Ding did the protocol development and data analysis. X Ma, YF Wang, and JW Gan did the patient recruitment. AJ Sun did the protocol development and manuscript editing.

## Acknowledgments

This study was funded by the National Natural Science Foundation of China (Grant number: 82074143). Dr. Aijun Sun received the research grant.

## References

- [1] Y. Xu, W. Zhao, T. Li et al., "Effects of acupoint-stimulation for the treatment of primary dysmenorrhoea compared with NSAIDs: a systematic review and meta-analysis of 19 RCTs," *BMC Complementary and Alternative Medicine*, vol. 17, no. 1, article 1924, pp. 436–436, 2017.
- [2] K. I. Kim, H. J. Nam, M. Kim, J. Lee, and K. Kim, "Effects of herbal medicine for dysmenorrhea treatment on accompanied acne vulgaris: a study protocol for a randomized controlled trial," *BMC Complementary and Alternative Medicine*, vol. 17, no. 1, article 1813, pp. 318–318, 2017.
- [3] H. Lee, T. Y. Choi, C. S. Myung, and M. S. Lee, "Herbal medicine Shaofu Zhuyu decoction for primary dysmenorrhea: a systematic review protocol," *Systematic reviews*, vol. 5, no. 1, 2016.
- [4] M. Ghafourian, N. A. Band, A. F. Pour, W. Kooti, M. F. Rad, and M. Badiie, "The role of CD16+, CD56+, NK (CD16+/CD56+) and B CD20+ cells in the outcome of pregnancy in women with recurrent spontaneous abortion," *International Journal of Women's Health and Reproduction Sciences*, vol. 3, no. 1, pp. 61–66, 2015.
- [5] M. T. Chao, C. M. Wade, P. D. Abercrombie, and D. Gomolak, "An innovative acupuncture treatment for primary dysmenorrhea: a randomized, crossover pilot study," *Alternative Therapies in Health and Medicine*, vol. 20, no. 1, pp. 49–56, 2014.
- [6] A. Hosseinlou, V. Alinejad, M. Alinejad, and N. Aghakhani, "The effects of fish oil capsules and vitamin B1 tablets on duration and severity of dysmenorrhea in students of high school in Urmia-Iran," *Global Journal of Health Sciences*, vol. 6, pp. 124–129, 2014.
- [7] W. Kooti, E. Mansouri, M. Ghasemiboroon, M. Harizi, D. Ashtary-Larky, and R. Afrisham, "The effects of Hydroalcoholic extract of *Apium graveolens* leaf on the number of sexual cells and testicular structure in rat," *Jundishapur Journal of Natural Pharmaceutical Products*, vol. 9, no. 4, article e17532, 2014.

## Retraction

# Retracted: Meta-Analysis of the Comprehensive Efficacy of Intraocular Lens Implantation in Glaucoma Patients

### BioMed Research International

Received 8 January 2024; Accepted 8 January 2024; Published 9 January 2024

Copyright © 2024 BioMed Research International. This is an open access article distributed under the Creative Commons Attribution License, which permits unrestricted use, distribution, and reproduction in any medium, provided the original work is properly cited.

This article has been retracted by Hindawi following an investigation undertaken by the publisher [1]. This investigation has uncovered evidence of one or more of the following indicators of systematic manipulation of the publication process:

- (1) Discrepancies in scope
- (2) Discrepancies in the description of the research reported
- (3) Discrepancies between the availability of data and the research described
- (4) Inappropriate citations
- (5) Incoherent, meaningless and/or irrelevant content included in the article
- (6) Manipulated or compromised peer review

The presence of these indicators undermines our confidence in the integrity of the article's content and we cannot, therefore, vouch for its reliability. Please note that this notice is intended solely to alert readers that the content of this article is unreliable. We have not investigated whether authors were aware of or involved in the systematic manipulation of the publication process.

Wiley and Hindawi regrets that the usual quality checks did not identify these issues before publication and have since put additional measures in place to safeguard research integrity.

We wish to credit our own Research Integrity and Research Publishing teams and anonymous and named external researchers and research integrity experts for contributing to this investigation.

The corresponding author, as the representative of all authors, has been given the opportunity to register their agreement or disagreement to this retraction. We have kept a record of any response received.

### References

- [1] Q. Zhou, "Meta-Analysis of the Comprehensive Efficacy of Intraocular Lens Implantation in Glaucoma Patients," *BioMed Research International*, vol. 2022, Article ID 5130416, 11 pages, 2022.

## Research Article

# Meta-Analysis of the Comprehensive Efficacy of Intraocular Lens Implantation in Glaucoma Patients

Qingyi Zhou 

Department of Ophthalmology, Zhejiang Provincial People's Hospital, People's Hospital of Hangzhou Medical College, 158 Shangtang Road, Hangzhou, 310014 Zhejiang, China

Correspondence should be addressed to Qingyi Zhou; [zhouqingyi@hmc.edu.cn](mailto:zhouqingyi@hmc.edu.cn)

Received 23 June 2022; Revised 4 July 2022; Accepted 5 July 2022; Published 16 August 2022

Academic Editor: Nauman Rahim Khan

Copyright © 2022 Qingyi Zhou. This is an open access article distributed under the Creative Commons Attribution License, which permits unrestricted use, distribution, and reproduction in any medium, provided the original work is properly cited.

This study is aimed at investigating the efficacy of intraocular lens (IOL) implantation in patients suffering from glaucoma through meta-analysis of the previously published research. For this purpose, different literature databases were searched for identification of clinical studies published between January 2000 and January 2022 on evaluating IOL's efficacy in treating glaucoma. RevMan 5.3 was used to conduct a meta-analysis of the pertinent data. The central anterior chamber depth (ACD), corneal endothelial cell counts, best-corrected visual acuity (BCVA), intraocular pressure (IOP), anti-glaucoma medications (AGM), and axial length (AL) changes were compared, and the incidence of postoperative complications was thoroughly evaluated. The Cochran chi-square test was used to examine the heterogeneity of the evaluation results. According to the inclusion and exclusion criteria, 20 studies included 948 glaucomatous eyes. IOP was significantly lower than before treatment (MD = 8.64, 95% CI: 5.75-11.53;  $Z = 5.86, P < 0.0001$ ), while ACD increased significantly (MD = -1.38, 95% CI: -1.74-1.02;  $Z = 7.49, P < 0.0001$ ). The corneal endothelial cell counts were homogeneous (MD = 225.08, 95% CI: -64.17 to -514.33;  $Z = 1.53, P = 0.20$ ). AGM utilisation decreased (MD = 1.43, 95% CI: 0.752-2.12,  $Z = 4.09, P < 0.0001$ ). AL decreased significantly (MD = 0.31; 95% CI: 0.09-0.54;  $Z = 2.71; P = 0.007$ ). The incidence of complications remained insignificant after IOL treatment (OR = 1.05, 95% CI: 0.42 to 2.60;  $Z = 0.10, P = 0.92; P = 0.92$ ). These findings indicate that IOL treatment can significantly reduce intraocular pressure, glaucoma drug use, and aqueous level (AL) in glaucoma patients while increasing the depth of the central anterior chamber. This study offers a theoretical foundation for selecting glaucoma treatment methods.

## 1. Introduction

Glaucoma is a group of optic neuropathies characterized by structural changes in the optic nerve's characteristic head. In extreme cases, glaucoma can cause visual field loss and even blindness and is considered the second most common cause of blindness after cataracts. Glaucoma patients have increased in recent years due to people's growing reliance on electronic products and are a group of optic neuropathies characterized by structural changes in the optic nerve's characteristic head. The number of glaucoma patients worldwide exceeded 79.6 million in 2020, with more than 11 million suffering from binocular glaucoma. Approximately 10 percent of glaucoma patients are blind, accounting for more than 25 percent of all blindness cases [1]. China has a prevalence of glaucoma of 2.1%, which increases with age, and a

blindness rate of 9.4% [2]. Damage to retinal ganglion cells and axons is the cause of glaucoma, which results in optic disc atrophy and changes to the visual field. Clinical glaucoma mainly includes primary glaucoma, congenital glaucoma, and secondary glaucoma. Primary open-angle glaucoma (POAG) and primary angle-closure glaucoma (PACG) are the two most prevalent types of glaucoma (PACG). Sixty to eighty percent of glaucoma cases involve PACG [3]. Primary angle-closure glaucoma was divided into three stages by the International Society of Geographical and Epidemiologic Ophthalmology: primary angle-closure suspect (PACS), primary angle-closure suspect (PACS), and PACG (ISGEO). Persistent or intermittent intraocular pressure elevations characterize glaucoma. The optic nerve of a patient with excessive intraocular pressure will become gradually atrophic, and the tissues of various eyeball parts and visual function will be severely

damaged and affected, resulting in the gradual narrowing of the patient's field of vision, visual impairment, and eventual loss of visual ability [4]. When POAG and PACG are left untreated, the disease course is typically chronic, with progressive and irreversible visual field loss, which may result in tunnel vision and central vision loss [5]. To reduce the harm caused by glaucoma, early diagnosis, standard treatment, and reasonable evaluation of curative effects are crucial.

The intraocular pressure lowering therapies have demonstrated their effectiveness in various randomized clinical trials [6]. Glaucoma is characterized by recurrence and difficult recovery following surgery. Due to issues with indications, mechanism of action, toxicity and side effects, and duration of drug therapy's efficacy [7], surgery is the most common clinical treatment. Currently, glaucoma filtration, intraocular lens implantation, cataract surgery combined with filtration alone, glaucoma surgery combined with cataract surgery, and glaucoma drainage implants are the most common surgical treatments for glaucoma. Glaucoma filtration is susceptible to complications, including shallow anterior chamber, cataract, malignant glaucoma, endophthalmitis, filter bubble leakage, and suprachoroidal hemorrhage [8]. Cataract surgery combined with filtration is effective, but it can speed up the formation of cataracts and cause functional follicles to vanish or shrink, limiting its clinical application. The combination of glaucoma and cataract surgery can significantly reduce intraocular pressure (IOP). Still, after surgery, the central visual field of patients is impaired, and several complications arise [9]. Intraocular lens implantation (IOL) releases the pupil block. It reopens all or a portion of the aqueous outflow channel for glaucoma, effectively reducing intraocular pressure and enhancing the patient's visual function when the channel is wholly or partially functional. The number of drugs used after IOL implantation is decreased, and some patients who have recovered well no longer require adjuvant drug therapy [10]. Biological ultrasound microscopy revealed that the thickness of the iris, ciliary body, and suspensory ligament did not change significantly after IOL implantation. However, the depth of the anterior chamber increased, indicating that the IOL replaced the eye's hypertrophic lens, and the iris regained its flat shape without contacting the IOL [11]. According to some studies, the IOP control rate was low in patients with glaucoma who were followed for nine months after IOL [12]. In addition, corneal edema, anterior chamber inflammation, posterior capsule rupture, retinal detachment, and other complications are possible following IOL surgery [13], and its safety requires further investigation.

There is still considerable controversy regarding the overall effectiveness of IOL in treating glaucoma. To explore the clinical effect of IOL in the treatment of glaucoma patients and to provide a reference for the treatment of clinical glaucoma patients, a meta-analysis was conducted on the therapeutic effect of IOL in the treatment of glaucoma at the national and international levels.

## 2. Materials and Methods

**2.1. Data Inclusion Methods.** For the study, glaucoma patients were chosen. Study types included randomized con-

trolled trials (RCTs), prospective cohort studies, cross-sectional studies, and case-control studies. IOL surgery was the treatment administered to the participants. The data observations included the author, year, number of patients, number of eyes, duration of follow-up, patient's age, treatment methods, and observation indicators.

**2.2. Literature Inclusion and Exclusion Criteria.** The literature was subjected to prespecified inclusion and exclusion criteria for refinement. The inclusion criteria comprised of (i) articles published between January 2000 and January 2022 on IOL for glaucoma patients; (ii) the subjects which were more than one case of glaucoma patient who received IOL-related treatment; (iii) studies on the evaluation of the therapeutic effect of IOL for glaucoma patients, with detailed records of the therapeutic effect and indicators; (iv) the study types which were randomized controlled study (RCT), prospective cohort study, cross-sectional study, and case-control study; and (v) basic information which was recorded and central anterior chamber depth (ACD), corneal endothelial cell counts, best-corrected visual acuity (BCVA), intraocular pressure (IOP), antiglaucoma medications (AGM), axial length (AL) changes, and postoperative complication rate which were carefully recorded and statistically analyzed.

The exclusion criteria are as follows: (i) individual case reports, literature reviews, expert comments, editorial opinions, news reports, product descriptions, and other publicity literature; (ii) literature without index data; (iii) literature lacking original data; (iv) repeated publications; (v) literature unrelated to the efficacy evaluation of IOL for glaucoma; (vi) literature that did not use IOL for treatment due to various reasons; and (vii) animal test, *in vitro* cell test, and other basic researches.

**2.3. Retrieval Strategy.** The retrieval time range for each online database was between Jan 2000 and Jan 2022. The search terms "intraocular lens (IOL) implantation," "glaucoma," "primary open-angle glaucoma (POAG)," "primary angle-closure glaucoma (PACG)," "treatment," and "surgery" were entered into PubMed, Nature, Web of Science, Spring, and China National Knowledge Infrastructure (CNKI) by combining keywords with "or" and "and" from January 2000 to January 2022; published clinical studies on the efficacy evaluation of IOL in the treatment of glaucoma were searched by entering each keyword separately. The search was conducted without regard to language.

**2.4. Selection of Literature and Evaluation of Quality.** Two reviewers independently examined the quality of selected literature on the basis of the Cochrane Reviewer's handbook system. They extracted the data and excluded literature that did not meet the criteria or was of poor quality. In the event of inconsistent evaluation results, the reviewers involved were eligible to decide whether the literature was to be included or an opinion of a third reviewer was to be sought. All available variable information was extracted and entered into a Microsoft Excel database for the selected study.

The included literature was evaluated using the Cochrane Reviewer's handbook, version 5.1.0, by employing the following preset criteria: (i) correctness and preciseness of the research method, (ii) explanation of random sequence generation, (iii) clear and definitive research results, (iv) selectivity of reported results, (v) blind controlled study of participants and personnel in the article, (vi) results from an evaluation using the blind method, and (vii) data completeness and selective reporting. The included research was assessed according to the standard's seven criteria, with a total score of 7 points, and a score of 4 or higher was considered high-quality.

The literature was reviewed initially based on the title, and missing information was collected by contacting the original author. After a careful reading of the abstract and entire text, the Jadad scale was applied to evaluate the quality of the contained literature. Inclusion in this meta-analysis was restricted to studies with a Jadad score greater than three.

**2.5. Data Extraction.** The included literature was extracted by two literature reviewers, with the literature extraction focusing on the following aspects: (a) basic information such as the title of the article, the first author, the publication year, the publication journal, the type of research, and the start and end dates of the study and (b) observation indicators: central anterior chamber depth (ACD), corneal endothelial cell counts, best-corrected visual acuity (BCVA), intraocular pressure (IOP), anti-glaucoma medications (AGM), axial length (AL), and postoperative complication rate.

### 3. Statistical Analysis

The data of the included literature was arranged using Microsoft excel 16, while Cochrane Reviewer's Handbook and Jadad scale were used to evaluate the quality of the literature. RevMan 5.3 was used for the meta-analysis of the included literature data.

The chi-square test was used for the preliminary heterogeneity test in the heterogeneity analysis, and the significance level was set to  $\alpha = 0.05$  and  $P < 0.05$ . Then,  $I^2$  in RevMan 5.3 was used to evaluate the heterogeneous results quantitatively. When  $I^2$  is less than 25%, heterogeneity in the literature is low. When  $25\% < I^2 < 50\%$ , moderate heterogeneity existed. When  $I^2 > 50\%$ , there was considerable heterogeneity in the literature. Based on this, the fixed-effects model was used for meta-analysis when  $I^2 < 50\%$ . When  $I^2 > 50\%$ , a random-effects model was used for meta-analysis. The measurement data are presented as the mean value (MD) and standard deviation (SD), and point estimates and confidence intervals (CI) for each effect size are provided. In describing dichotomous variables, relative risk (RR), odds ratio (OR), and risk difference were used (RD). RevMan 5.3 was used to generate a funnel plot to analyze publication bias. In the meantime, a forest map was developed, and the Z value and P value were extracted from the results to evaluate the meta-analysis results. The studies with the lowest quality scores were excluded from conducting sensitivity analysis. The inverted funnel plot was dis-

played as a funnel plot to observe publication bias in the literature. When P is less than 0.05, the difference between groups is statistically significant.

## 4. Results

**4.1. Literature Retrieval Process.** After searching PubMed, Nature, Web of Science, Spring, China National Knowledge Infrastructure (CNKI), and Science Direct for "intraocular lens (IOL) implantation," "glaucoma," "primary open-angle glaucoma (POAG)," "primary angle-closure glaucoma (PACG)," "treatment," and "surgery," 1,023 articles were retrieved. Following an initial screening of duplicate literature, 165 relevant studies were included, among which 88 (PubMed), 40 (Web of Science), 20 (Spring), 12 (Nature), and five (Science Direct) articles were extracted. Sixty-seven studies were retrieved after removing those that did not fulfill the inclusion criteria; reviews, brief conference articles, case analyses, and risk factor evaluations were excluded based on the title, abstract, and substance of the literature. The initial screening identified 26 studies that met the inclusion criteria. After a thorough evaluation of the papers included in the study, six studies that we are unable to get original data were eliminated, leaving 20 studies for analysis (Figure 1).

**4.2. Included Literature Basic Information.** A total of 16 of the 20 references eventually included [14–33] provided data on the number of cases in the included studies, while 18 provided data on the proportion of female participants in the included studies. In the literature, 948 eyes with glaucoma treated with IOLs were included. The basic information of the literature included in this study is shown in Table 1.

**4.3. Included Literature Quality Assessment.** The Cochrane Reviewer's Handbook was utilized to assess the quality of the 20 included studies, and an evaluation chart was created to determine the overall quality of the literature. The results are depicted in Figures 2 and 3. Random sequence generation (selection bias), allocation concealment (selection bias), and blinding of participants and personnel (performance bias) were "low risk" in the 20 included studies. In two studies, blinding of outcome assessment (detection bias) was "high risk." Blinding of outcome assessment (detection bias) was "unclear risk" in three studies but "low risk" in others. Incomplete outcome data (attrition bias) posed "uncertain risk" for three studies, "high risk" for one, and "low risk" for the remaining studies. There were four "uncertain risk" articles with selective reporting (reporting bias), two "high risk" articles, and no "low risk" articles. Another bias was classified as "uncertain risk" in three studies and "low risk" in the remaining studies. Therefore, the Cochrane Reviewer's Handbook's literature quality evaluations were above a B.

The Jadad scale was then used to assess the quality of the included literature, which indicated that all included studies had a value of  $>3$ ; hence, sensitivity analysis was unnecessary.

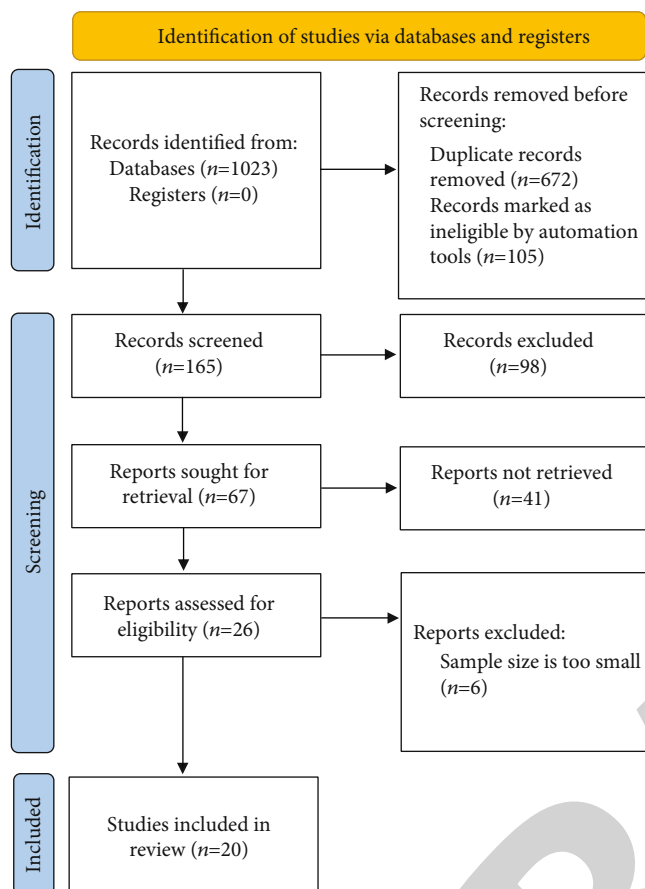


FIGURE 1: Literature retrieval and screening process.

**4.4. Comparison of IOP Values of Glaucoma Patients before and after Treatment.** In the 20 included studies, the IOP values of glaucoma patients before and after IOL treatment were analyzed statistically, and the IOP values of glaucoma patients before and after IOL treatment were meta-analyzed (Figure 4). The IOP values of patients before and after IOL treatment were highly heterogeneous ( $I^2 = 99\%$ ,  $P < 0.0001$ ). Then, a random-effects model was used for analysis, and the IOP value of glaucoma patients after IOL treatment was significantly lower than that before treatment (MD = 8.64, 95% CI: 5.75-11.53;  $Z = 5.90$ ,  $P < 0.0001$ ).

**4.5. Comparison of ACD Values of Glaucoma Patients before and after Treatment.** A meta-analysis was conducted on the ACD values of glaucoma patients before and after IOL treatment, as reported by eight of the 20 studies (Figure 5). There was substantial heterogeneity between ACD values before and after IOL therapy ( $I^2 = 98\%$ ,  $P < 0.0001$ ). The combined effect values were analyzed statistically using the random-effects model. The results demonstrated that the ACD value of glaucoma patients treated with IOLs increased significantly compared to the value before treatment (MD = -1.38, 95% CI: -1.74-1.02;  $Z = 7.4$ ;  $P < 0.0001$ ).

**4.6. Corneal Endothelial Cell Counts before and after Treatment in Glaucoma Patients.** Four of the twenty studies analyzed the changes in corneal endothelial cell counts in

glaucoma patients before and after IOL treatment. The corneal endothelial cell count of glaucoma patients was meta-analyzed before and after treatment (Figure 6). Before and after IOL treatment, there was considerable heterogeneity in corneal endothelial cell counts ( $I^2 = 72\%$ ,  $P = 0.01$ ). For the statistical analysis of the combined effect values, a random-effects model was applied. Comparing corneal endothelial cell counts before and after IOL treatment, there was no significant heterogeneity (MD = 225.08, 95% CI: -64.17 to -514.33;  $Z = 1.53$ ,  $P = 0.13$ ).

**4.7. Comparison of Best-Corrected Visual Acuity (BCVA) before and after Treatment in Glaucoma Patients.** Five of the included studies reported the changes in BCVA values before and after IOL treatment in glaucoma patients. Before and after treatment, the BCVA values of glaucoma patients were subjected to meta-analysis (Figure 7). There was considerable heterogeneity between patients' BCVA values before and after IOL treatment ( $I^2 = 100\%$ ,  $P < 0.0001$ ). The combined effect values were analyzed statistically using the random-effects model. Comparing BCVA values before and after IOL treatment, there was no significant heterogeneity (MD = 0.92, 95% CI: -1.25-3.09;  $Z = 0.83$ ,  $P = 0.41$ ).

**4.8. Comparison of Antiglaucoma Medication (AGM) Usage for Glaucoma Patients before and after Treatment.** Nine studies provided data on AGM use in glaucoma patients before and after IOL treatment. Before and after treatment, a meta-analysis was conducted on AGM use in glaucoma patients (Figure 8). There was substantial heterogeneity between AGM usage before and following IOL treatment ( $I^2 = 96\%$ ,  $P < 0.0001$ ). The combined effect values were analyzed statistically using the random-effects model. After IOL treatment, the use of AGM in patients with glaucoma was significantly reduced compared to before treatment, with considerable heterogeneity (MD = 1.43, 95% CI: 0.75 to 2.12;  $Z = 4.09$ ,  $P < 0.0001$ ).

**4.9. Comparison of Axial Length (AL) Values of Patients with Glaucoma before and after Treatment.** Three of the included studies reported the changes in AL values in glaucoma patients before and following IOL treatment. Changes in AL values of glaucoma patients before and after treatment were investigated using meta-analysis (Figure 9). There was no considerable heterogeneity between AL values before and after IOL treatment ( $I^2 = 42\%$ ,  $P = 0.18$ ). The combined effect values were analyzed using a fixed-effects model. The results demonstrated that the AL value of glaucoma patients treated with IOLs was significantly lower than that before treatment, albeit with considerable heterogeneity (MD = 0.31, 95% CI: 0.09-0.54;  $Z = 2.71$ ,  $P = 0.007$ ).

**4.10. Analysis of the Complication Rate of Glaucoma Patients Treated with IOL.** Five of the included studies statistically analyzed the incidence of complications in glaucoma patients treated with IOLs. A meta-analysis of the incidence of posttreatment complications in glaucoma patients was conducted (Figure 10). The incidence of posttreatment complications were insignificant among the IOL-treated patients



TABLE 1: Included literature basic information.

First author	Year	Case number	Age (years old)	Eye number	Male/female (number of eyes)	Follow-up time (months)
Astle [14]	2009	27	60.7 ± 9.2	37	24/13	48
Chang [15]	2013	10	59.6 ± 10.7	10	6/4	46.3 ± 21.3
Dawczynski [16]	2007	/	66.6 ± 16.8	20	5/15	/
Gazzard [17]	2004	49	67.1 ± 7.6	49	29/20	/
Hata [18]	2008	27	75.8 ± 7.2	27	3/24	9.3 ± 6.3
Hayashi [19]	2001	/	73.6 ± 7.6	150	55/95	12
He [20]	2021	36	70 ± 8.83	36	9/27	6
Kashiwagi [21]	2006	21	76.9 ± 6.2	28	12/16	8
Ki-I [22]	2013	85	66.2 ± 6.9	85	23/62	21.9 ± 11.1
Kubota [23]	2003	15	/	18	11/7	6
Lee [24]	2010	26	68.8 ± 8.8	26	13/13	/
Parihar JKS [25]	2018	26	37.6 ± 10.25	26	14/12	9.6 ± 3.2
Pohjalainen [26]	2000	/	59.6 ± 10.7	38	/	44.4
Poley [27]	2009	/	75.5 ± 8.9	124	/	54 ± 12.8
Rhiu [28]	2012	23	68.57 ± 12.08	23	9/14	/
Su [29]	2011	14	72.63 ± 3.72	16	5/11	/
Tetz [30]	2015	21	76.3 ± 8.4	21	6/15	36
Tow [31]	2001	55	67.9 ± 9.2	57	25/32	22 ± 5.6
Yagev [32]	2019	73	14.3 ± 9.2	124	64/60	/
Zhao [33]	2013	33	69.6 ± 7.7	33	12/21	8.9

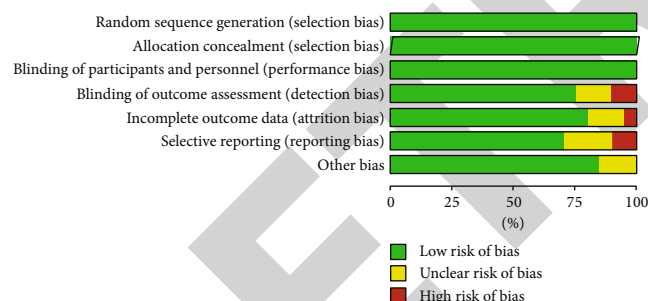


FIGURE 2: Included literature bias assessment.

( $I^2 = 0\%$ ,  $P = 1.00$ ). Similar insignificant results were obtained when the fixed-effects model was applied (OR = 1.05, 95% CI: 0.42 to 2.60;  $Z = 0.10$ ;  $P = 0.92$ ).

**4.11. Analysis of Publication Bias.** The publication bias of the included literature was analyzed using an inverted funnel plot, and the results are presented in Figures 11–15. Notably, the inverted funnel plot of efficacy evaluation indicators and complication incidence of glaucoma patients before and after IOL treatment was symmetric, as were the majority of the included studies. In the funnel plot of IOP value and ACD value evaluation, only a few studies did not fall into the inverted funnel plot. Before and after IOL treatment, the efficacy evaluation indices and complication rate of glaucoma patients were close to the central axis. Based on this information, it was determined that the publication bias of

the included literature used to analyze the comprehensive efficacy evaluation of glaucoma patients after IOL treatment was low and satisfied the requirements.

## 5. Discussion

The leading cause of irreversible blindness is glaucoma. Its pathological basis is the apoptosis and progressive degeneration of retinal ganglion cells and their axons. The incidence of blindness due to glaucoma was 28.6%, significantly higher than the incidence of blindness due to cataracts (14.3%) [34], and more than \$748 million was spent annually on glaucoma-related medical consultations, examinations, and surgeries [35]. China had the highest incidence of glaucoma among middle-aged and older women over the age of 50 years [36]. The peripheral iris obstructed the trabecular mesh, permanent adhesion with the trabecular mesh occurred, and aqueous outflow was obstructed, leading to elevated intraocular pressure and glaucoma. According to the findings of the present study, the incidence of glaucoma is associated with age, gender, race, and geographic location, and its pathogenesis is related to an increase in lens thickness, pupil block caused by the forward position of the lens-iris diaphragm, iris hyperfold, and nonpupillary block. Normal individuals have a central anterior chamber depth of approximately 2.5-3 mm, whereas glaucoma patients have a central anterior chamber depth of about less than 2.4 mm and 1.8 mm on average. When the central anterior chamber depth (ACD) was  $\leq 1.4$  mm, glaucoma incidence gets 100%.

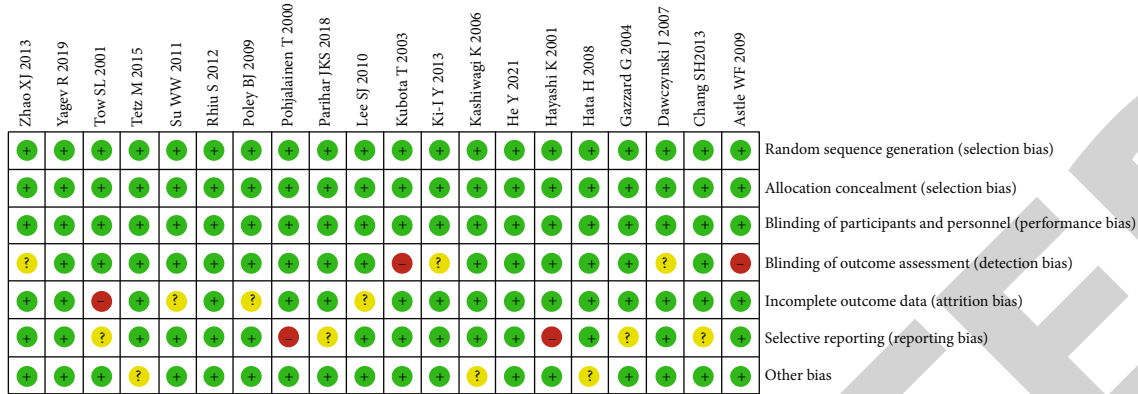


FIGURE 3: Risk evaluation of bias in selected studies.

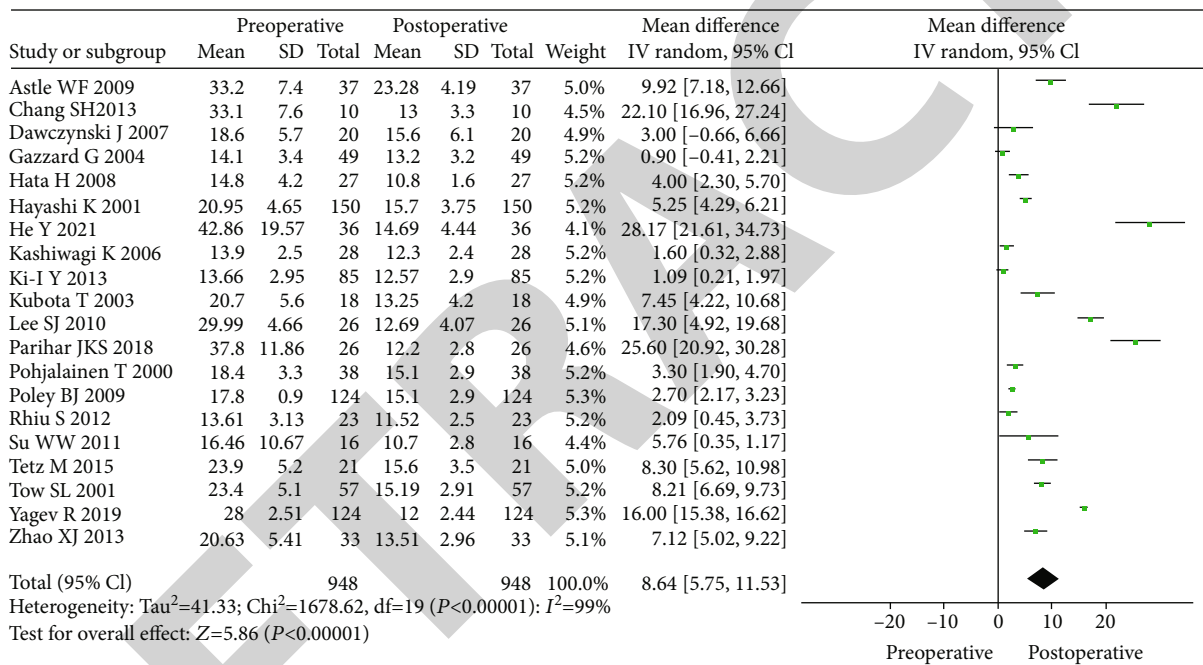


FIGURE 4: Comparison of IOP values in glaucoma patients before and after treatment. CI: confidence interval; SE: standard error.

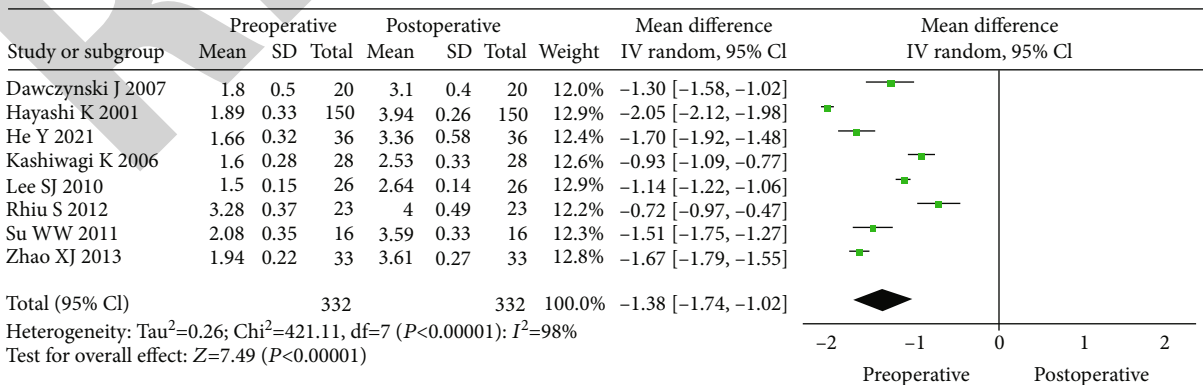


FIGURE 5: Comparison of ACD values of glaucoma patients before and after treatment. CI: confidence interval; SE: standard error.

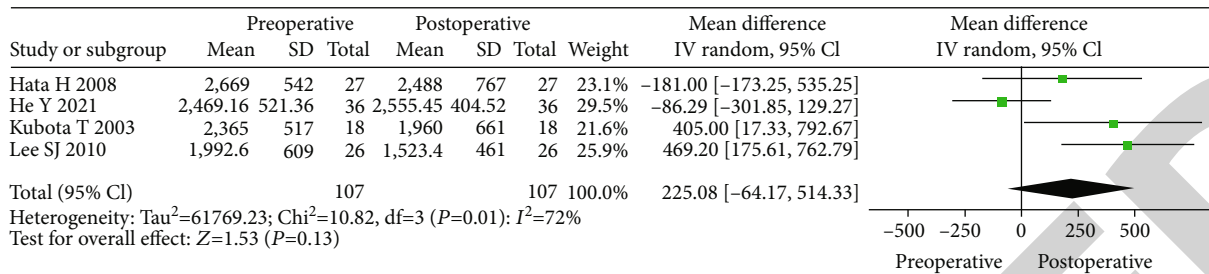


FIGURE 6: Comparison of corneal endothelial cell counts in glaucoma patients before and after treatment. CI: confidence interval; SE: standard error.

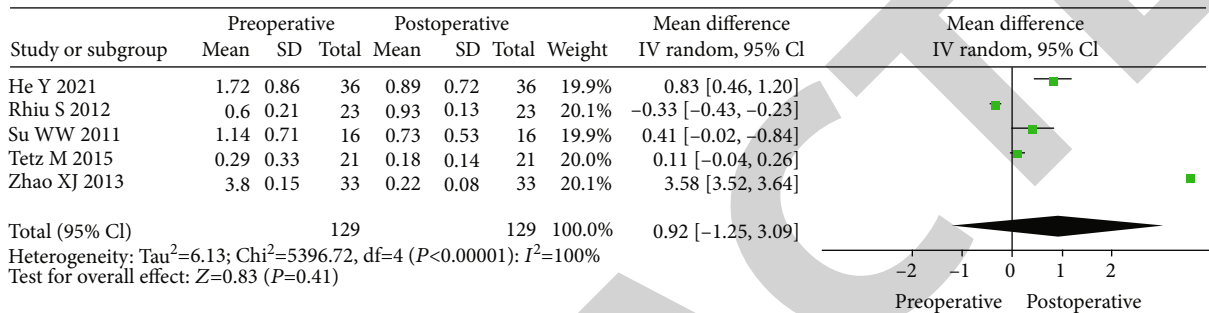


FIGURE 7: Comparison of BCVA values in glaucoma patients before and after treatment. CI: confidence interval; SE: standard error.

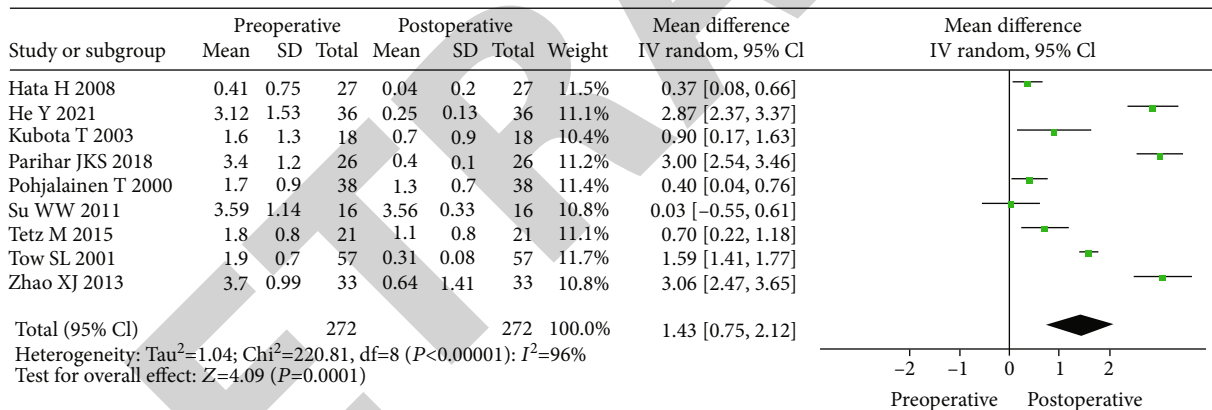


FIGURE 8: Comparison of AGM usage in glaucoma patients before and after treatment. CI: confidence interval; SE: standard error.

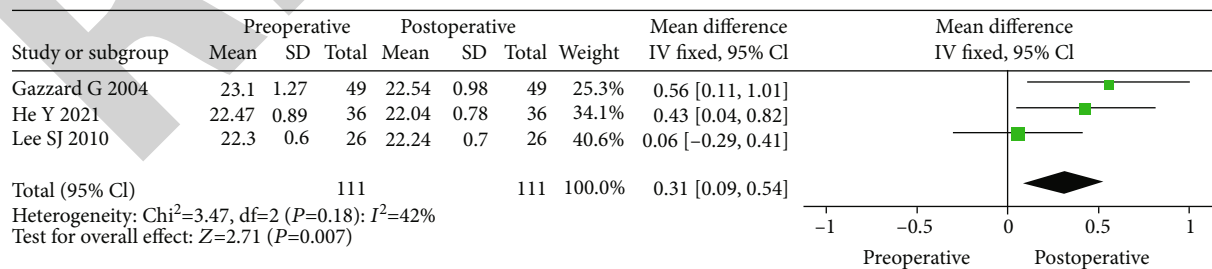


FIGURE 9: Comparison of AL values in glaucoma patients before and after treatment. CI: confidence interval; SE: standard error

The incidence of glaucoma was 77.8% at 1.6 mm [37]. The glaucoma patients included in this study were treated with IOL. The results demonstrated that the ACD value of patients with glaucoma increased significantly after IOL

treatment compared to that before treatment, with a significant difference between the two (MD = -1.38, 95% CI: -1.74-1.02;  $Z = 7.49$ ;  $P < 0.0001$ ). After IOL treatment, the ACD value of glaucoma patients increased significantly.

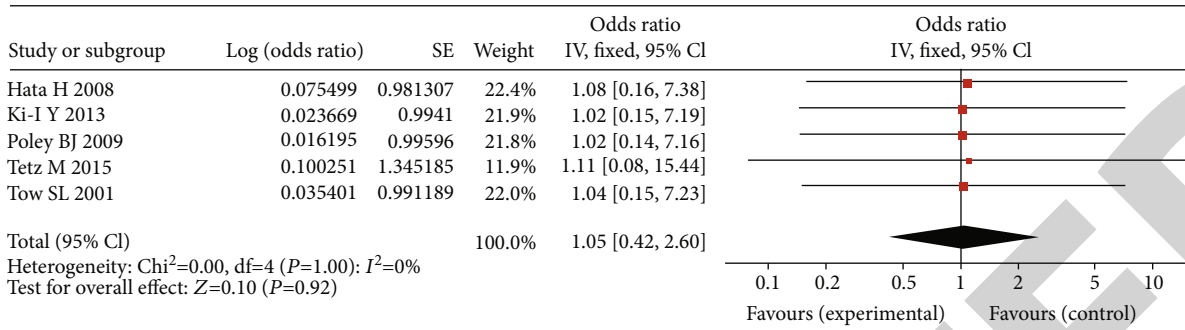


FIGURE 10: Analysis of postoperative complications in glaucoma patients. CI: confidence interval; SE: standard error.

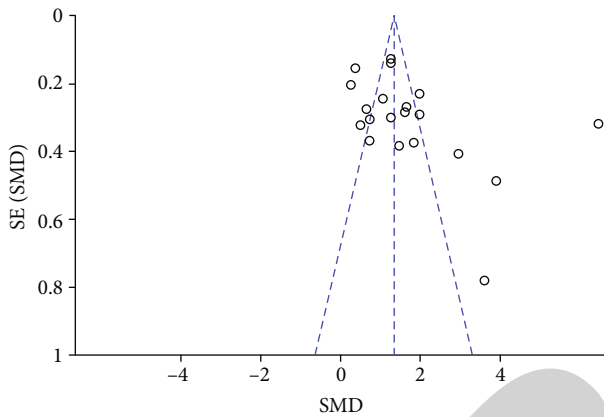


FIGURE 11: Funnel plot of IOP value assessment of glaucoma patients treated with IOL.

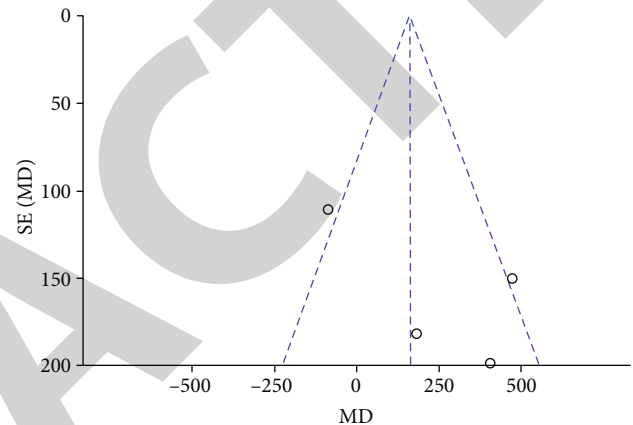


FIGURE 13: Funnel plot of corneal endothelial cell count assessment in glaucoma patients treated with IOL.

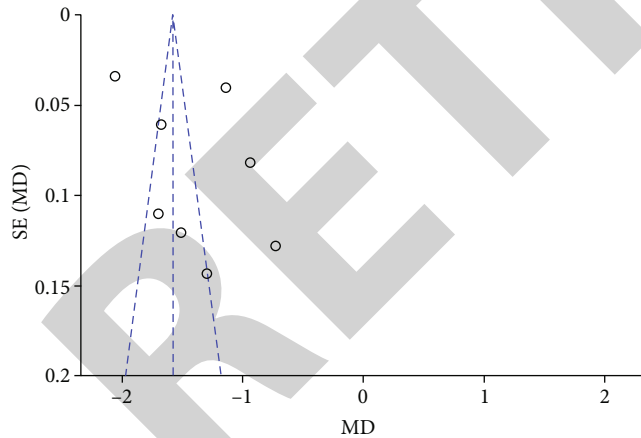


FIGURE 12: Funnel plot for ACD assessment of glaucoma patients treated with IOL.

After replacing an ocular lens with a thickness of less than 1.0 mm with an IOL lens (thickness = 4.0 mm), the central anterior chamber depth (ACD) was deepened, and the atrial angle was increased.

Traditional glaucoma treatments include iris resection and filtration surgery, which are frequently accompanied by accelerated cataract formation, a shallow anterior chamber, purpura marks on filtration vesicles, and inadequate

intraocular pressure control. IOL has the advantages of simple operation, small incision, less tissue damage, rapid visual recovery, short operation time, and fewer complications compared to these other methods. Current findings indicate that IOL implantation can reduce intraocular pressure in patients with glaucoma [38]. This study's meta-analysis revealed that the intraocular pressure (IOP) of patients treated with intraocular lenses (IOLs) decreased significantly compared to that before treatment (MD = 8.64, 95% CI: 5.75-11.53;  $Z = 5.86, P < 0.0001$ ). This supports the conclusion that IOL implantation can significantly lower IOP in glaucoma patients. After replacing the human lens with an IOL, the volume of the eye's contents may decrease, the depth of the central anterior chamber may increase, and the contact plane between the pupil margin and the lens may shift posteriorly. Furthermore, cytokines such as interleukin-1 and prostaglandin released from postoperative aqueous outflow can promote degradation of the extracellular matrix of the trabecular meshwork, increase aqueous outflow, and thus reduce IOP [39].

Corneal endothelial cells play a crucial role in maintaining corneal health and transparency and regulating water and electrolytes inside and outside the cornea. Normal corneal endothelial cells are hexagonal mosaics with approximately 500,000 cells, averaging 2,570 cells/mm<sup>2</sup> [40]. Loss of corneal endothelial cells can be brought on by corneal

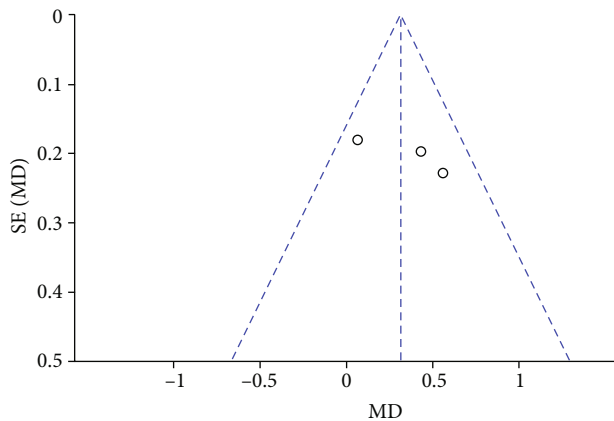


FIGURE 14: Funnel plot of AL evaluation in glaucoma patients treated with IOL. SE: standard error; OR: odds ratio.

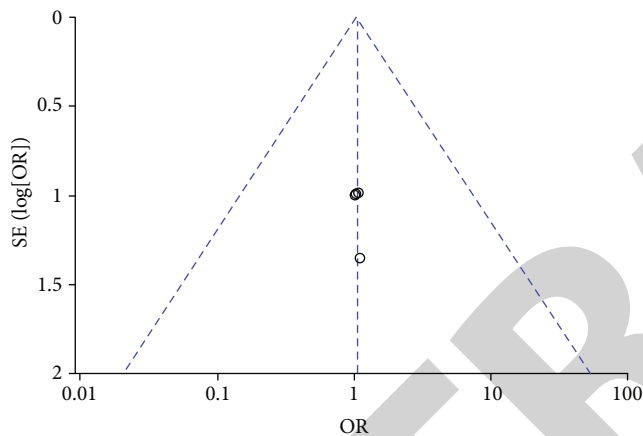


FIGURE 15: Funnel plot for evaluating the complication rate after IOL treatment in glaucoma patients. SE: standard error; OR: odds ratio.

injury and various surgical procedures. Bullae keratopathy occurs when there are 10 to 15% fewer corneal endothelial cells than normal [41]. The results demonstrated that there was no significant heterogeneity in corneal endothelial cell counts after IOL treatment compared to before treatment (MD = 225.08, 95% CI: -64.17 to -514.33;  $Z = 1.53$ ,  $P = 0.13$ ), indicating that the loss of corneal endothelial cells in glaucoma patients was not significant after IOL treatment, thereby decreasing the likelihood of bullae keratopathy.

After surgery, glaucoma patients must continue to take anti-glaucoma medications. Currently, pilocarpine, prostaglandin derivatives, carbonic anhydrase inhibitors, and hypertonic dehydrating agents are the most widely used antiglaucoma medications. Current research indicates that long-term use of antiglaucoma medications induces varying degrees of ocular surface damage, affecting the trabecular meshwork and other structures, resulting in or exacerbating ocular surface diseases. It has been observed that the number of antiglaucoma medications used decreases after IOL implantation [42]. The results demonstrated that the use of AGM in glaucoma patients after IOL treatment was signifi-

cantly reduced compared to before treatment, albeit with considerable heterogeneity (MD = 1.43, 95% CI: 0.75–2.12;  $Z = 4.09$ ,  $P < 0.0001$ ). It showed that patients treated with IOL required less antiglaucoma medication, but this study included few studies and made no comparisons to other surgical procedures. Therefore, the reduction in anti-glaucoma drug dosage for IOL-treated patients must be verified further. The atrial angle of glaucoma patients is significantly opened after IOL treatment, and the outflow pathway of aqueous outflow is reconstructed, thereby reducing the incidence of postoperative complications, as indicated by several domestic studies [43]. There was no significant heterogeneity in complications among glaucoma patients treated with IOL (OR = 1.05, 95% CI: 0.42 to 2.60;  $Z = 0.10$ ,  $P = 0.92$ ), indicating that the incidence of complications was low after IOL treatment.

## 6. Conclusion

In this study, a meta-analysis was conducted to evaluate the overall efficacy of intraocular lenses (IOL) for postglaucoma. The results demonstrated that after IOL treatment, the ACD value increased significantly, the IOP value, the use of anti-glaucoma medications, and the AL value decreased significantly, and the incidence of complications was low. Nonetheless, there are still some flaws in this study. Since most studies are observational, comparing and analyzing the efficacy evaluation indicators with other treatments are impossible. Additional clinical trials will verify the efficacy difference between IOL treatment and other glaucoma treatments. In conclusion, IOL therapy significantly decreased intraocular pressure, glaucoma drug use, and AOA in glaucoma patients while increasing the depth of the central anterior chamber. This work provides a theoretical foundation for the selection of glaucoma treatment methods.

## Data Availability

The datasets used and/or analyzed during the current study are available from the corresponding author on reasonable request.

## Conflicts of Interest

The author declares that there are no conflicts of interest.

## References

- [1] J. M. Kang and A. P. Tanna, "Glaucoma," *The Medical Clinics of North America*, vol. 105, no. 3, pp. 493–510, 2021.
- [2] J. D. Stein, A. P. Khawaja, and J. S. Weizer, "Glaucoma in adults—screening, diagnosis, and management," *Jama*, vol. 325, no. 2, pp. 164–174, 2021.
- [3] C. W. McMonnies, "Historial de glaucoma y factores de riesgo," *Journal of optometry*, vol. 10, no. 2, pp. 71–78, 2017.
- [4] S. He, D. L. Stankowska, D. Z. Ellis, R. R. Krishnamoorthy, and T. Yorio, "Targets of neuroprotection in glaucoma," *Journal of Ocular Pharmacology and Therapeutics*, vol. 34, no. 1–2, pp. 85–106, 2018.

- [5] A. M. Komáromy, D. Bras, D. W. Esson et al., "The future of canine glaucoma therapy," *Veterinary Ophthalmology*, vol. 22, no. 5, pp. 726–740, 2019.
- [6] A. K. Schuster, C. Erb, E. M. Hoffmann, T. Dietlein, and N. Pfeiffer, "The diagnosis and treatment of glaucoma," *Deutsches Arzteblatt international*, vol. 117, no. 13, pp. 225–234, 2020.
- [7] M. Ige and J. Liu, "Herbal medicines in glaucoma treatment," *The Yale Journal of Biology and Medicine*, vol. 93, no. 2, pp. 347–353, 2020.
- [8] A. A. Aref, S. J. Gedde, and D. L. Budenz, "Glaucoma drainage implant surgery," *Developments in Ophthalmology*, vol. 59, pp. 43–52, 2017.
- [9] S. Kwon, S. H. Kim, D. Khang, and J. Y. Lee, "Potential Therapeutic Usage of Nanomedicine for Glaucoma Treatment," *International Journal of Nanomedicine*, vol. 15, pp. 5745–5765, 2020.
- [10] T. Webb, "A review of glaucoma surgical therapy," *Veterinary Ophthalmology*, vol. 24, no. S1, pp. 34–38, 2021.
- [11] D. F. Belov and V. P. Nikolaenko, "Calculation of intraocular lens power after trabeculectomy," *Vestnik Oftalmologii*, vol. 137, no. 6, pp. 61–66, 2021.
- [12] G. S. Negretti, W. O. Chan, and M. Muqit, "Artisan iris-claw intraocular lens implantation in vitrectomised eyes," *Eye (London, England)*, vol. 35, no. 5, pp. 1393–1397, 2021.
- [13] H. M. Rabie, H. Esfandiari, M. H. Rikhtegar, and V. Hekmat, "Management of sulcus-fixated single-piece intraocular lens-induced pigmentary glaucoma with 3-piece IOL exchange," *International Ophthalmology*, vol. 38, no. 1, pp. 145–150, 2018.
- [14] W. F. Astle, O. Alewenah, A. D. Ingram, and A. Paszuk, "Surgical outcomes of primary foldable intraocular lens implantation in children: understanding posterior opacification and the absence of glaucoma," *Journal of Cataract and Refractive Surgery*, vol. 35, no. 7, pp. 1216–1222, 2009.
- [15] S. H. Chang, W. C. Wu, and S. C. Wu, "Late-onset secondary pigmentary glaucoma following foldable intraocular lenses implantation in the ciliary sulcus: a long-term follow-up study," *BMC Ophthalmology*, vol. 13, no. 1, p. 12, 2013.
- [16] J. Dawczynski, E. Koenigsdoerffer, R. Augsten, and J. Strobel, "Anterior segment optical coherence tomography for evaluation of changes in anterior chamber angle and depth after intraocular lens implantation in eyes with glaucoma," *European Journal of Ophthalmology*, vol. 17, no. 3, pp. 363–367, 2007.
- [17] G. Gazzard, P. J. Foster, J. G. Devereux et al., "Effect of cataract extraction and intraocular lens implantation on nerve fibre layer thickness measurements by scanning laser polarimeter (GDx) in glaucoma patients," *Eye (London, England)*, vol. 18, no. 2, pp. 163–168, 2004.
- [18] H. Hata, S. Yamane, S. Hata, and H. Shiota, "Preliminary outcomes of primary phacoemulsification plus intraocular lens implantation for primary angle-closure glaucoma," *The journal of medical investigation: JMI*, vol. 55, no. 3,4, pp. 287–291, 2008.
- [19] K. Hayashi, H. Hayashi, F. Nakao, and F. Hayashi, "Changes in anterior chamber angle width and depth after intraocular lens implantation in eyes with glaucoma," *Ophthalmology*, vol. 107, no. 4, pp. 698–703, 2000.
- [20] Y. He, R. Zhang, C. Zhang et al., "Clinical outcome of phacoemulsification combined with intraocular lens implantation for primary angle closure/glaucoma (PAC/PACG) with cataract," *American Journal of Translational Research*, vol. 13, no. 12, pp. 13498–13507, 2021.
- [21] K. Kashiwagi, F. Kashiwagi, and S. Tsukahara, "Effects of small-incision phacoemulsification and intraocular lens implantation on anterior chamber depth and intraocular pressure," *Journal of Glaucoma*, vol. 15, no. 2, pp. 103–109, 2006.
- [22] Y. Ki-I, T. Yamashita, A. Uemura, and T. Sakamoto, "Long-term intraocular pressure changes after combined phacoemulsification, intraocular lens implantation, and vitrectomy," *Japanese Journal of Ophthalmology*, vol. 57, no. 1, pp. 57–62, 2013.
- [23] T. Kubota, I. Toguri, N. Onizuka, and T. Matsuura, "Phacoemulsification and intraocular lens implantation for angle closure glaucoma after the relief of pupillary block," *International Journal of Ophthalmology*, vol. 217, no. 5, pp. 325–328, 2003.
- [24] S. J. Lee, C. K. Lee, and W. S. Kim, "Long-term therapeutic efficacy of phacoemulsification with intraocular lens implantation in patients with phacomorphic glaucoma," *Journal of Cataract and Refractive Surgery*, vol. 36, no. 5, pp. 783–789, 2010.
- [25] J. Parihar, J. Kaushik, V. K. Jain, H. S. Trehan, A. Mishra, and V. K. Baranwal, "Combined Ahmed valve and phacoemulsification with intraocular lens implantation under infliximab in refractory uveitic glaucoma," *European Journal of Ophthalmology*, vol. 28, no. 3, pp. 294–298, 2018.
- [26] T. Pohjalainen, E. Vesti, R. J. Uusitalo, and L. Laatikainen, "Phacoemulsification and intraocular lens implantation in eyes with open-angle glaucoma," *Acta Ophthalmologica Scandinavica*, vol. 79, no. 3, pp. 313–316, 2001.
- [27] B. J. Poley, R. L. Lindstrom, T. W. Samuelson, and R. Schulze, "Intraocular pressure reduction after phacoemulsification with intraocular lens implantation in glaucomatous and nonglaucomatous eyes: evaluation of a causal relationship between the natural lens and open-angle glaucoma," *Journal of Cataract and Refractive Surgery*, vol. 35, no. 11, pp. 1946–1955, 2009.
- [28] S. Rhiu, E. S. Lee, T. I. Kim, H. S. Lee, and C. Y. Kim, "Power prediction for one-piece and three-piece intraocular lens implantation after cataract surgery in patients with chronic angle-closure glaucoma: a prospective, randomized clinical trial," *Acta Ophthalmologica*, vol. 90, no. 8, pp. e580–e585, 2012.
- [29] W. W. Su, P. Y. Chen, C. H. Hsiao, and H. S. L. Chen, "Primary phacoemulsification and intraocular lens implantation for acute primary angle-closure," *PloS one*, vol. 6, no. 5, article e20056, 2011.
- [30] M. Tetz, N. Koerber, B. J. Shingleton et al., "Phacoemulsification and intraocular lens implantation before, during, or after canaloplasty in eyes with open-angle glaucoma," *Journal of Glaucoma*, vol. 24, no. 3, pp. 187–194, 2015.
- [31] S. L. Tow, T. Aung, F. T. Oen, and S. K. L. Seah, "Combined phacoemulsification, intraocular lens implantation and trabeculectomy for chronic angle closure glaucoma," *International Ophthalmology*, vol. 24, no. 5, pp. 283–289, 2001.
- [32] R. Yagev, N. Khatib, C. Barrett, Y. Lior, T. Lifshitz, and E. Tsumi, "Intraocular lens implantation as an isolated risk factor for secondary glaucoma in pediatric patients," *Canadian journal of ophthalmology. Journal canadien d'ophtalmologie*, vol. 54, no. 5, pp. 621–625, 2019.
- [33] X. J. Zhao, X. X. Yang, Y. P. Fan, B. H. Li, and Q. Li, "Comparison of combined phacoemulsification, intraocular lens implantation, and goniosynechialysis with phacotrabeculectomy in the treatment of primary angle-closure glaucoma and

## Retraction

# Retracted: Glutathione, Cysteine, and D-Penicillamine Role in Exchange of Silver Metal from the Albumin Metal Complex

### BioMed Research International

Received 8 January 2024; Accepted 8 January 2024; Published 9 January 2024

Copyright © 2024 BioMed Research International. This is an open access article distributed under the Creative Commons Attribution License, which permits unrestricted use, distribution, and reproduction in any medium, provided the original work is properly cited.

This article has been retracted by Hindawi following an investigation undertaken by the publisher [1]. This investigation has uncovered evidence of one or more of the following indicators of systematic manipulation of the publication process:

- (1) Discrepancies in scope
- (2) Discrepancies in the description of the research reported
- (3) Discrepancies between the availability of data and the research described
- (4) Inappropriate citations
- (5) Incoherent, meaningless and/or irrelevant content included in the article
- (6) Manipulated or compromised peer review

The presence of these indicators undermines our confidence in the integrity of the article's content and we cannot, therefore, vouch for its reliability. Please note that this notice is intended solely to alert readers that the content of this article is unreliable. We have not investigated whether authors were aware of or involved in the systematic manipulation of the publication process.

Wiley and Hindawi regrets that the usual quality checks did not identify these issues before publication and have since put additional measures in place to safeguard research integrity.

We wish to credit our own Research Integrity and Research Publishing teams and anonymous and named external researchers and research integrity experts for contributing to this investigation.

The corresponding author, as the representative of all authors, has been given the opportunity to register their agreement or disagreement to this retraction. We have kept a record of any response received.

### References

- [1] N. S. Alharthi, H. Khan, F. J. Siyal et al., "Glutathione, Cysteine, and D-Penicillamine Role in Exchange of Silver Metal from the Albumin Metal Complex," *BioMed Research International*, vol. 2022, Article ID 3619308, 10 pages, 2022.

## Research Article

# Glutathione, Cysteine, and D-Penicillamine Role in Exchange of Silver Metal from the Albumin Metal Complex

Nahed S. Alharthi <sup>1</sup>, Haroon Khan <sup>2</sup>, Fahad Jibrán Siyal <sup>3</sup>, Zahid Ali Shaikh <sup>4</sup>,  
Shumaila Parveen Arain <sup>5</sup>, Lienda Bashier Eltayeb <sup>1</sup> and Altaf Ali Mangi <sup>2</sup>

<sup>1</sup>Department of Medical Laboratory Sciences, College of Applied Medical Sciences, Prince Sattam Bin Abdulaziz University, Al-Kharj 11942, Saudi Arabia

<sup>2</sup>Gomal Centre of Pharmaceutical Sciences Faculty of Pharmacy Gomal University D.I. Khan, 29111, Pakistan

<sup>3</sup>Department of Pharmacology, Chandka Medical College, SMBB Medical University Larkana, 77150, Pakistan

<sup>4</sup>Department of Medicine, Chandka Medical College, SMBB Medical University Larkana, 77150, Pakistan

<sup>5</sup>Faculty of Pharmacy University of Sindh Jamshoro, 76060, Pakistan

Correspondence should be addressed to Nahed S. Alharthi; [n.alharthi@psau.edu.sa](mailto:n.alharthi@psau.edu.sa)

Received 8 June 2022; Revised 5 July 2022; Accepted 12 July 2022; Published 8 August 2022

Academic Editor: Nauman Rahim Khan

Copyright © 2022 Nahed S. Alharthi et al. This is an open access article distributed under the Creative Commons Attribution License, which permits unrestricted use, distribution, and reproduction in any medium, provided the original work is properly cited.

The purpose of this study is to investigate the exchange reaction taking place among the bovine serum albumin (BSA), 5,5'-dithiobis-(2-nitrobenzoic acid (ESSE), reduced glutathione, N-acetylcysteine, D-penicillamine (thiolates), and silver metal ( $\text{Ag}^{\text{I}}$ ). For this purpose, stock solutions of BSA and Ellman's reagent were prepared by dissolving 264 mg of BSA in 5 ml of reaction buffer (0.1 M  $\text{KH}_2\text{PO}_4$  at pH 7.8) and 23.8 mg of ESSE in 1.0 ml of reaction buffer which were mixed together. Mixture of BSA- $\text{Ag}^{\text{I}}$  was prepared in a separate procedure by dissolving 0.17 mg of silver nitrate in 1 ml of reaction buffer and then dissolving BSA (200 mg) in the same solution of silver nitrate. Blocking of Cys-34 of BSA with  $\text{Ag}^{\text{I}}$  was confirmed by treating different dilutions of BSA- $\text{Ag}^{\text{I}}$  (500  $\mu\text{M}$ ) solutions with the solutions of ESSE (85  $\mu\text{M}$ ) and  $\text{ES}^-$  (85  $\mu\text{M}$ ) and recording the spectra (300-450) with a UV-visible spectrophotometer. The chromatographed  $\text{Ag}^{\text{I}}$ -modified BSA ((BSA-S) $\text{Ag}^{\text{I}}$ ) samples (typically 500  $\mu\text{M}$ ) were subsequently mixed with thiolates (reduced glutathione, N-acetylcysteine, and D-penicillamine).  $\text{Ag}^{\text{I}}$  and modified BSA (typically 500  $\mu\text{M}$  each) were treated with these low molecular weight thiolates and allowed to react overnight followed by chromatographic separation (Sephadex G25). The redox reactions of  $\text{Ag}^{\text{I}}$ -modified BSA with various low molecular weight thiols revealed a mechanically important phenomenon. In the case of reduced glutathione and N-acetylcysteine, we observed the rapid release of a commensurate amount of Ellman's anion, indicating that an exchange has taken place and low molecular weight thiols (RSH) substituted  $\text{Ag}^{\text{I}}$  species at the Cys-34 of BSA eventually forming disulfide (BSA-SSR) at Cys-34. It can be anticipated from the phase of study involving bovine serum albumin that low molecular weight thiolates (reduced glutathione and N-acetylcysteine) take off  $\text{Ag}^{\text{I}}$  which are attached to proteins elsewhere in the physiological system, making these toxic metals free for toxic action.

## 1. Introduction

Bovine serum albumin is a serum albumin protein derived from cows. It is often used as a protein concentration standard in lab experiments (Peters, [1]). Cow's milk contains around 30–35 g of proteins per litre and includes more than 25 different proteins, but only some of them are known to be

allergenic. BSA is also commonly used to determine the quantity of other proteins, by comparing an unknown quantity of protein to known amounts of BSA. The ALB gene encodes the most abundant protein 5in human blood. Albumin has a high affinity for fatty acids, hematin, and bilirubin and a broad affinity for small negatively charged aromatic compounds [2–4]. It forms covalent adducts with pyridoxyl



phosphate, cysteine, glutathione, and various metals [5]. Heavy metals compromise normal brain development and neurotransmitter function, leading to long-term deficits in learning and social behavior. Albumin, the most abundant protein in mammalian blood plasma, is involved in binding, transport, and delivery of a range of endogenous and exogenous small molecules or ions, such as fatty acids and metal ions [6]. It was used because of its easy availability in my research lab, and second thing, there are numerous advantages of silver metal like its medical uses as wound dressings, creams, and an antibiotic coating on medical devices and strong antioxidant effect [4]. Additionally, because of its abundance, human serum albumin plays a significant role in the pharmacokinetic behaviour of a variety of drugs, including drug half-life in the bloodstream, drug efficacy regulation, drug toxicity decrease, and drug targeting specificity improvement. Serum albumin has strong interactions with anionic and cationic ligands. Since the unbound form is being metabolized and/or excreted from the body, the bound fraction will be released in order to maintain equilibrium. Since albumin is alkalotic, acidic and neutral drugs will primarily bind to albumin. If albumin becomes saturated, then these drugs will bind to lipoprotein (Sadler et al., 1994; [7]), such as metal ions. The redox state of serum albumin's Cys-34 has been proposed to be important for its biological function. In plasma, it is not supported by enzymes (glutaredoxin) and the GSH-regenerating system (hexose monophosphate shunt) [8], and the thiolation/dethiolation process is almost exclusively sustained by albumin. BSA is a serum albumin protein derived from bovine blood by a proprietary heat shock treatment. The plasma used for the process is collected as a byproduct of the meat industry. BSA meets and exceeds the exacting standards demanded by diagnostic, biopharmaceutical, and research customers worldwide. Plasma albumin has a theoretical concentration of 0.6 mM, only one -SH group, and several disulfide bridges. The cysteinyl residue, located in a well-conserved region in position 34 in all mammalian species, has a low pKa (about 5–7) [9–11], because of a salt bridge, with His 39 that stabilizes the thiolate anion. It is well known that albumin -SH is not well exposed, which impedes development of its high potential reactivity related to its low pKa. Indeed, the reaction rate of albumin towards -SH reagents (ESSE) is lower than that of thiol with higher pKa. Compounds such as fatty acids that change albumin conformation, improving Cys-34 exposure, lead to higher reactivity of albumin -SH (Simplicio et al., 1985; [12]). The difference of pKa of thiols involved in protein–thiol-mixed disulfides is an important feature to determine the kind of reaction (substitution or dethiolation) and consequently the end products. The premise is that the slow exchange of species bound to Cys-34 is the basis for a mechanism by which toxic species can become widely distributed around the body. In this study, we have sought to briefly investigate these issues. Since the method for the fractionation of human serum albumin on DEAE-Sephadex A-50, which had been worked out by Janatova [13], appeared to give somewhat better resolution of the albumin components than other published fractionation systems, therefore, this procedure was adopted

for the fractionation of the bovine albumin preparations. The reaction of thiolates with excess Ellman's reagent (ESSE, 5,5'-dithiobis(2-nitrobenzoic acid)) is used for quantitative estimation of thiol by measuring the absorption due to Ellman's thiolate (ES<sup>-</sup>) at  $\lambda$  (412 nm). The reaction of thiolates with 5excess Ellman's reagent is used for quantitative estimation of thiol by measuring the absorption at  $\lambda$  (412 nm) [14–16]. These metal-modified proteins have subsequently been challenged with thiolates (GSH, NAC, and Dpen) in an attempt to remove the metal and regenerate Cys-34. In the second phase of the study, we have metalated albumin with metals (silver nitrate (Ag<sup>1</sup> species)). The disulfide exchange reactions occurring at Cys-34 of BSA with low molecular weight thiolates such as reduced glutathione (GSH), N-acetylcysteine (NAC), and D-penicillamine (Dpen) have been determined; in addition, the reduction of oxidized Cys-34 by these thiolates has also been studied in order to understand the reverse reaction. A reversible reaction is a chemical reaction where the reactants form products that, in turn, react together to give the reactants back. Reversible reactions will reach an equilibrium point where the concentrations of the reactants and products will no longer change. In this research, we have assessed the oxidative modification of and metal binding capacity of Cys-34 with heavy metals to investigate the ease with which it is possible to effect disulfide-thiol exchange at these sites or remove a metal bound at this position.

## 2. Experiment

All reagents were commercially obtained. Ellman's reagent, bovine serum albumin (>98%; agarose gel electrophoresis lyophilised), and Sephadex (G25 coarse) were purchased from Sigma-Aldrich. UV-visible absorption spectra were recorded in a Unicam UV 300 spectrophotometer at room temperature. Thiols were made from haloalkanes by nucleophilic substitution of the halide ion by the sulfhydryl ion (HS<sup>-</sup>), which is an excellent nucleophile.

*2.1. Preparation of Stock Solutions of BSA and Ellman's Reagent.* Different literature reviews, a handbook on pharmaceutical calculations, and some other stuff were followed before proceeding to lab work. BSA 264 mg was dissolved in 5 ml of reaction buffer (0.1 M KH<sub>2</sub>PO<sub>4</sub> at pH 7.8). Dissolution of BSA was achieved by slow vortexing to avoid bubbles. The volume of BSA solution was made 20 ml with reaction buffer to get stock solution (200  $\mu$ M) of BSA. Stock solution of ESSE (60 mM) was prepared by dissolving 23.8 mg of ESSE in 1.0 ml of reaction buffer.

*2.2. Concentration of BSA Standard Solution.* 66.0 mg of BSA was dissolved in 20 ml of reaction buffer for preparation of standard solution (50  $\mu$ M) of commercially purchased BSA (unchromatographed). This standard solution was then serially diluted with reaction buffer to obtain 10  $\mu$ M, 20  $\mu$ M, 30  $\mu$ M, 40  $\mu$ M, and 50  $\mu$ M solutions of unchromatographed BSA. The UV spectra (250–350 nm) of the above five solutions of the BSA standard were recorded taking reaction buffer as a reference. Plotting the absorbance of the solution

at  $\lambda$  (280 nm) gives a straight line ( $R^2 = 0.999$ ). The concentration of protein in solution was calculated using Beers' law at  $\lambda_{\max} = 280$  nm and  $\epsilon = 43,824$  cm<sup>-1</sup> M<sup>-1</sup> (Peters, 1975). The absorbance of these known concentrations of the BSA standard was always used to adjust the working concentration of the column collected (chromatographed) albumin of unknown concentration.

**2.3. Treatment of Ellman's Modified Albumin (BSA-SSE) with Thiolates.** The appearance of the protein in the eluent was identified by testing the liquors with trichloroacetic acid (which precipitates denatured protein) whereupon collection commenced. Periodic sampling identified when the eluent was protein free. The residual Ellman's reagent and anion (identified as a yellow band) were eluted second and were from the column with further aliquots of reaction buffer. To study the reduction of Cys-34, initially, BSA was chemically modified at Cys-34 by Ellman's reagent (ESSE) to give a bovine serum albumin-SE mixed disulfide (BSA-SSE). Solutions of BSA (200 mg, 0.5 ml) and Ellman's reagent (ESSE) (1 mg, 0.5 ml) in reaction buffer (0.1 M KH<sub>2</sub>PO<sub>4</sub>, pH 7.4) were mixed (vol. of the mixture = 1 ml) and allowed to react at room temperature overnight until absorbance at 412 nm was no longer changed. The solution was then carefully applied to a column (10 cm × 2 cm) packed with swollen Sephadex (G25 coarse). The mixture was eluted with reaction buffer. Ellman's assay is a useful tool that can be used to determine the sulfhydryl concentration of unknown solutions. It is done by following Beer's law and the extinction coefficient of TNB.

The BSA-SSE solution collected as above was diluted (1 ml of chromatographed protein solution was diluted to 5 ml) to generate a solution of known concentration (typically, 500  $\mu$ M, approximated from the working range of the known concentration of the BSA standard). The UV spectrophotometric spectrum (200–600 nm) was recorded. This BSA-SSE solution (typically, 500  $\mu$ M) is separately titrated with 100, 200, 300, 400, and 500  $\mu$ M of thiolates (reduced glutathione, N-acetyl cysteine, and D-penicillamine) and each time allowed to react overnight. The spectra were recorded UV spectrophotometrically. The release of Ellman's anion is assessed at  $\lambda_{\max} = 412$  nm ( $\epsilon = 14,150$  cm<sup>-1</sup> M<sup>-1</sup>).

#### 2.4. Blocking of the Cys-34 in BSA

**2.4.1. Blocking the Cys-34 by Ag<sup>I</sup>.** Cysteines are unique among naturally occurring amino acids because of their thiol-containing side chain, which can undergo a variety of different nucleophilic reactions. The one-electron oxidation of a thiol(ate) group generates a thiyl radical, which gives rise to a diverse range of oxidation products, including S-nitrosothiols. Mixture of BSA-Ag<sup>I</sup> was prepared in a separate procedure by dissolving 0.17 mg of silver nitrate in 1 ml of reaction buffer and then dissolving BSA (200 mg) in the same solution of silver nitrate. The mole ratio of BSA with silver nitrate is 3 : 1 (BSA : Ag<sup>I</sup>, 3 : 1). The BSA-Ag<sup>I</sup> mixtures were allowed to react overnight. The BSA-Ag<sup>I</sup> mixtures were carefully applied to a swollen Sephadex (G25 coarse) packed column. The mixtures were collected for metal bound pro-

teins (BSA-Ag<sup>I</sup>) by eluting with reaction buffer. The collected samples were approximated (diluted) with reaction buffer to BSA-Ag<sup>I</sup> (125, 250, 375, and 500  $\mu$ M) solutions by using the absorbance range of known concentrations of BSA standards. Blocking of Cys-34 of BSA with Ag<sup>I</sup> was confirmed by treating different dilutions of BSA-Ag<sup>I</sup> (500  $\mu$ M) solutions with the solutions of ESSE (85  $\mu$ M) and ES<sup>-</sup> (85  $\mu$ M) and recording the spectra (300-450) with a UV-visible spectrophotometer.

**2.4.2. Reaction of Thiolates with Ag<sup>I</sup>-Capped BSA.** The protein samples of BSA-Ag<sup>I</sup> collected through swollen Sephadex (G25 coarse) packed column were mixed with thiolates (reduced glutathione, N-acetylcysteine, and D-penicillamine) in separate procedures. Thiolates were added to BSA-Ag<sup>I</sup> solutions in three equivalents to silver nitrate and allowed to react overnight. In separate procedures, the mixtures of BSA-Ag<sup>I</sup> and solutions with thiolates (reduced glutathione, N-acetylcysteine, and D-penicillamine) were passed again through the clean Sephadex packed column and eluted with reaction buffer. The proteins (identified by testing the liquors with trichloroacetic acid) were eluted first and collected carefully to make sure that there are no free thiolate species in the collected protein samples. Since thiolates might be capable of taking off Ag<sup>I</sup> previously bounded to BSA, rendering Cys-34 in BSA to be regenerated. The collected protein samples collected from the mixtures of BSA-Ag<sup>I</sup> with thiolates (reduced glutathione, N-acetylcysteine, and D-penicillamine) were approximated (diluted) with reaction buffer to BSA-Ag<sup>I</sup>/BSA-S (125, 250, 375, and 500  $\mu$ M) by using the absorbance range of known concentrations of BSA standards. BSA-S<sup>-</sup> was then spectrophotometrically determined for free Cys-34 content by treating the protein dilutions with ESSE (85  $\mu$ M). The release of Ellman's anion is assessed at  $\lambda_{\max} = 412$  nm ( $\epsilon = 14,150$  cm<sup>-1</sup> M<sup>-1</sup>).

### 3. Results and Discussion

The subject of the thiol-disulfide interchange reaction is an important one in biochemistry and has been discussed extensively elsewhere. It has been known since long that glutathione also reacts with other thiol compounds, including proteins, and forms mixed disulfides. The physiological significance of this reaction has, however, been recognized only recently [17]. The subject of the thiol-disulfide interchange reaction is an important one in biochemistry and has been discussed extensively elsewhere. Oxidative stress causes the modification of proteins and impairs their biological functions. Among the amino acids found in albumin, cysteine-34 (Cys-34) is the most susceptible to modification by oxidants. Glutathione, present in the millimolar range in cells, prevents reactive sulfhydryls (Cys-34) of albumin from oxidative modification. It has been known since long that glutathione also reacts with other thiol compounds, including proteins, and forms mixed disulfides. The physiological significance of this reaction has, however, been recognized only recently [17]. Disulfide-reducing reagents are used in biochemistry for a number of purposes, especially in reduction of cysteine groups in albumin and in maintaining essential

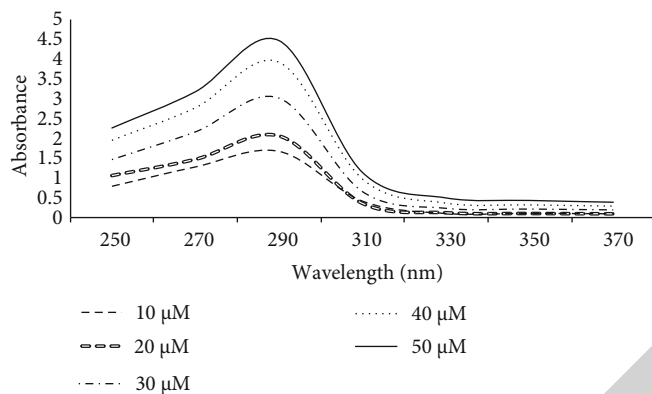


FIGURE 1: UV-vis spectra of 250-350 nm for five dilutions of unchromatographed BSA in reaction buffer.

thiol groups in their reduced state [18]. In this research, we focus on the role of Cys-34 in albumin having a free SH group. A free thiol group in albumin (Cys-34) can be quantitatively determined by different methods, including the use of DTNB (5,5'-dithiobis-(2-nitrobenzoic acid)) ([14]; Jocelyn, 1972; [19]) also termed as Ellman's reagent (ESSE). Ellman's reagent (ESSE) was the earliest reagent widely used for estimating the number of thiol groups. The reaction between ESSE and the thiol group produces an equivalent amount of Ellman's anion ( $ES^-$ ), the absorbance of which can be followed at 412 nm. Reaction rates of ESSE with serum albumins are much slower than those with small thiols of similar pKa; therefore, in the current study, overnight incubations have been provided to the mixtures involving the reaction of ESSE with BSA. Thiol groups are one of the most reactive groups in proteins and can participate in side reactions with reagents used to manipulate other functional groups in a protein and the other solution components.

**3.1. Concentration of BSA Standard Solution.** Five dilutions (10, 20, 30, 40, and 50  $\mu\text{M}$ ) of the unchromatographed BSA sample were prepared and spectrophotometrically investigated for protein concentrations. The UV spectra of BSA were recorded at room temperature (Figure 1). In the wavelength range from 250 to 350 nm, the maximum absorption of BSA was at  $\lambda = 278$  nm. Under the same conditions, the reaction buffer (0.1 M  $\text{KH}_2\text{PO}_4$  at pH 7.4) was used as the blank solution. Concentrations of protein were calculated from the absorbance of the five standard dilutions of unchromatographed BSA at  $\lambda = 278$  using Beers' law at  $\lambda_{\text{max}} = 278$  nm ( $\epsilon = 43,824 \text{ cm}^{-1} \text{ M}^{-1}$ ) (Peter, 1975). Concentrations of protein of the five standard BSA dilutions (10, 20, 30, 40, and 50  $\mu\text{M}$ ) were found to be 9.7, 19.4, 28.8, 38.2, and 44.13  $\mu\text{M}$ , respectively.

The protein concentration is unknown in the experiments which involve collection of free or complexed proteins through the Sephadex packed column, and they are required to be incorporated in this study of thiol disulfide exchange reactions with typically known concentrations. Hence, the absorbance range of the solutions of unchromatographed BSA and the subsequent calculation for protein concentration have been achieved which can be used in this piece of study for the adjustment of and approximating the

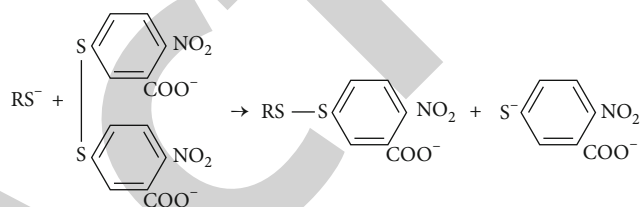


FIGURE 2: Possible pathways for the reactions of BSA-SSE with RSH (J. JANATOVA et al. 1968).

working concentration of chromatographed protein samples of unknown concentration.

**3.2. The Calculation of the Free Thiolate Content of BSA.** The thiolate form of bovine serum albumin (BSA) typically comprises ~30-60% of the protein in the commercially available (unchromatographed) material. This value varies from batch to batch necessitating the calculation of the relative amount of thiolate present on the protein before the study can commence. The thiolate content of BSA is determined by the use of Ellman's reagent (ESSE). The spectrophotometric assay of thiols with Ellman's reagent (ESSE) depends on the cleavage of the disulfide bond of the almost colourless reagent, with the concomitant liberation of the colored anion (Ellman's anion ( $ES^-$ )) (Figure 2).

The pKa of the sulfhydryl group of Ellman's anion is low enough so that the sulfhydryl group is essentially completely dissociated above pH 6.5. The magnitude of the absorbance at 412 nm is thus a measure of the sulfhydryl content of the added thiol.

The thiolate status of the BSA was assessed initially by titrating each of the ten sequentially different dilutions of BSA (50-500  $\mu\text{M}$ ) with Ellman's reagent (85  $\mu\text{M}$ ) (Figure 3).

It is evident from the UV-visible spectra of unchromatographed BSA solutions (50-500  $\mu\text{M}$ ) that the initial four solutions (up to 200  $\mu\text{M}$ ) of unchromatographed BSA exhibited linearity; hence, BSA was assessed subsequently by titrating each of the ten sequentially different dilutions of BSA (20-200  $\mu\text{M}$ ) with Ellman's reagent (85  $\mu\text{M}$ ) (Figure 4).

Since ESSE reacts with thiols to give  $ES^-$ , the amount of  $ES^-$  released in solution represents the amount of thiol at the start of the reaction. Therefore,  $\lambda = 412$  nm ( $\epsilon = 14,150 \text{ cm}^{-1} \text{ M}^{-1}$ )

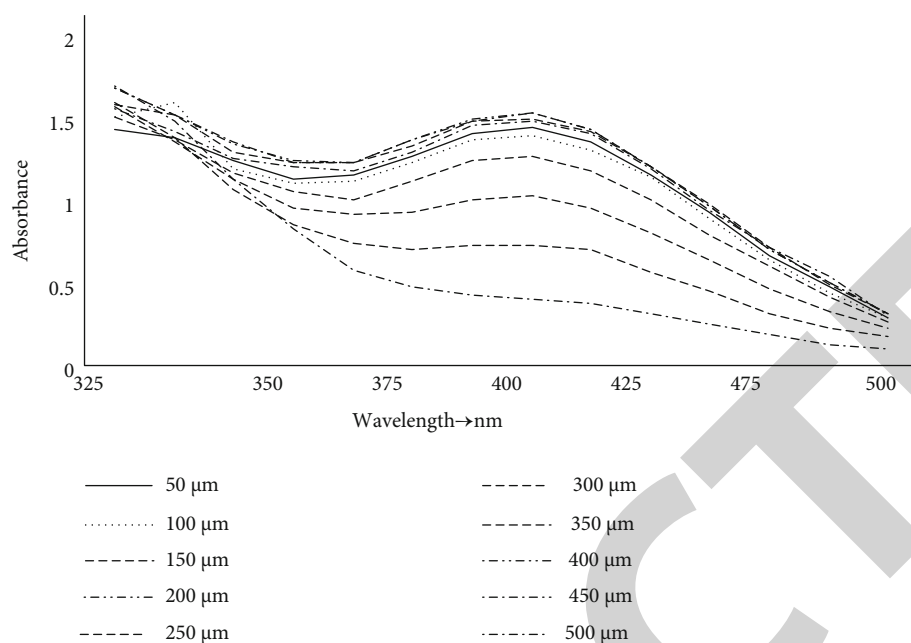


FIGURE 3: UV-visible absorption (325-500 nm) of the titration of Ellman's reagent with unchromatographed BSA (50-500  $\mu\text{M}$ ) in reaction buffer.

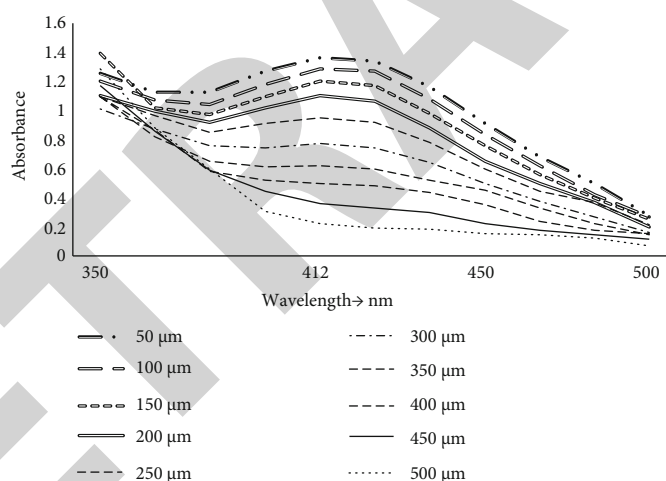
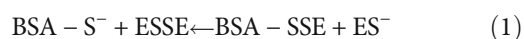


FIGURE 4: UV-visible absorption (325-500 nm) of the titration of Ellman's reagent with unchromatographed BSA (50-200  $\mu\text{M}$ ) in reaction buffer.

was used for calculation of the thiolate content (Cys-34) of commercial BSA (unchromatographed). Rates of Cys-34 reduction were monitored by following the rise in absorbance at 412 nm for the release of  $\text{ES}^-$ . Plotting the amount of Ellman's anion released as the BSA concentration increases allows us to compensate for the natural absorbance of albumin at 412 nm (Figure 5) and hence gain an accurate value for its thiolate status. Using this approach, the BSA used here was found to be 53.9% in the thiolate form.



**3.3. Treatment of BSA-SSE with Thiolates.** Size exclusion chromatography (SEC) is used for separation of proteins (BSA) after reacting BSA with ESSE and subsequently with thiolates

(reduced glutathione, N-acetylcysteine, and D-penicillamine). In size exclusion chromatography (SEC), the larger-sized molecules were essentially eluted first from the column. Size exclusion chromatography (SEC) separates polymer molecules according to their size in dilute solution, but what size to use has been a matter of debate for 35 years. In 1967, Benoit and coworkers found an excellent correlation between elution volume and a dynamically based molecular size, the hydrodynamic volume  $V_H$ , for a wide range of species and large-scale molecular architectures. However, both theory and simulations assume a thermodynamic separation principle. This assumption is based on experimental observations that elution volumes are independent of flow rates. Medium-sized molecules are relatively large compared to the pore size of the solid phase and therefore may find some pores in which they enter

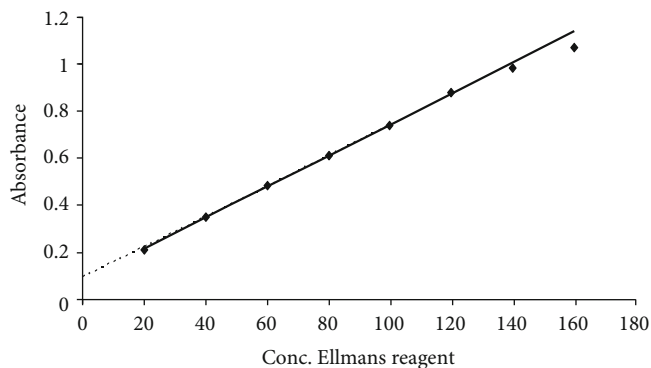


FIGURE 5: The titration of BSA (20-200  $\mu\text{M}$ ) with Ellman's reagent (85  $\mu\text{M}$ ). The expected deviation from linear behaviour at high concentration of unchromatographed commercial BSA (>160  $\mu\text{M}$ ) is evident. An intercept is found which is consistent with residual absorbance by BSA at 412 nm.

and spend some time. Smaller-sized molecules have more pores that are accessible to them and therefore spend more time inside the pores relative to larger-sized molecules. Therefore, smaller molecules are eluted last and larger molecules are eluted first in size exclusion chromatography.

In order to completely access the -SH groups of the Cys-34 of the protein (BSA) by Ellman's reagent, the BSA-SSE mixture was allowed for an overnight reaction. The BSA-SSE mixture was then eluted through the swollen Sephadex (G25 coarse) packed column. The assay method not only releases Ellman's anion but generates a stoichiometric amount of BSA labelled with Ellman's moiety at cysteine-34 (BSA-SSE, equation (1)). By taking advantage of this reaction, it is possible to synthesize significant amounts of BSA which has been capped with Ellman's moiety. Thus, incubate albumin with a small excess of Ellman's reagent overnight (based on the thiolate assay) followed by chromatographic separation (Sephadex G25); we obtained a solution of Ellman's modified BSA in reaction buffer. The solution can be desalted and freeze-dried to give pure and concentrated BSA-SSE in reduced volume. Alternatively, the molar absorptivity of the solution at 280 nm can be used to give a suitable estimate of the protein concentration in the eluent sample. We are interested here in the ability of small thiolate species (glutathione, D-penicillamine, and N-acetylcysteine) to react with Cys-34 in its disulfide form, and as such, we opted to work with the protein solutions.

The chromatographed BSA-SSE sample (typically, 500  $\mu\text{M}$ ) is subsequently mixed with thiolates (reduced glutathione, N-acetylcysteine, and D-penicillamine). BSA-SSE (typically, 500  $\mu\text{M}$ ) is treated with reduced glutathione (100, 200, 300, 400, and 500  $\mu\text{M}$ ) and allowed to react overnight followed by chromatographic separation (Sephadex G25). Reactions of small thiolates with BSA-SSE mixed disulfides were accompanied by rapid massive substitution of  $\text{ES}^-$  (leaving group) by  $\text{RS}^-$  (entering group), marked by an increase in absorption at 412 nm because of free chromophore and an increase in BSA-SSR concentration. The reduction reactions of BSA-SSE with various small thiols revealed a mechanically important phenomenon. We observed the rapid release of a commensurate amount of Ellman's anion (Figure 6) indicat-

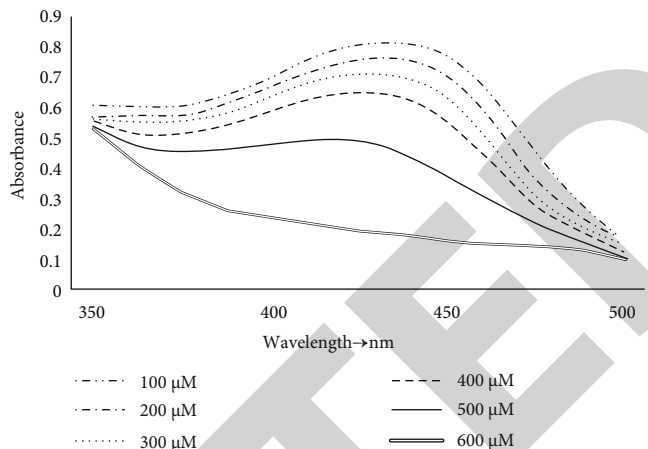


FIGURE 6: The titration of BSA-SSE (conc) with glutathione solutions (100-500  $\mu\text{M}$ ). The formation of Ellman's anion is evident from the appearance of a larger band at 412 nm.

ing that an exchange has taken place leading us to hypothesize the following reaction adjustments, ultimately leading to the release of Ellman's anion ( $\text{ES}^-$ ):



With excess thiols, two pathways for the reduction of BSA-SSE become apparent. When thiols (RSH) attack a disulfide, one sulfur atom in the disulfide bond is the electron acceptor and is incorporated into the new disulfide bond, while the other becomes a thiol. For example, the first step of the reaction can give either  $\text{ES}^-$  and a BSA mixed disulfide adduct (BSA-SSR) or ESSR and the regenerated thiol form of BSA (equations (2) and (3)). The newly formed ESSR can then react further with BSA-SH (equations (4) and (5)). Ellman's anion ( $\text{ES}^-$ ), the only product monitored, is the final product in each case and is reasonably stable due to its low pKa and the existence of several resonance forms.

The chromatographed sample of BSA-SSE (conc., approximately 500  $\mu\text{M}$ ) is treated with N-acetylcysteine (100, 200, 300, 400, and 500  $\mu\text{M}$ ) and allowed to react overnight followed by chromatographic separation (Sephadex G25). We observed the rapid release of a commensurate amount of Ellman's anion (Figure 7) indicating that an exchange has taken place almost in the same fashion as observed with reduced glutathione.

These data, however, indicate that a significant portion of the GSH and NAC can form mixed disulfides with proteins in cells. Both the inhibition of glutathione biosynthesis and recycling would cause oxidative stress and elevated protein-GSH adducts. NAC is generally used to increase intracellular glutathione. Since GSH plays a major role in maintaining intracellular redox state, lowering GSH levels

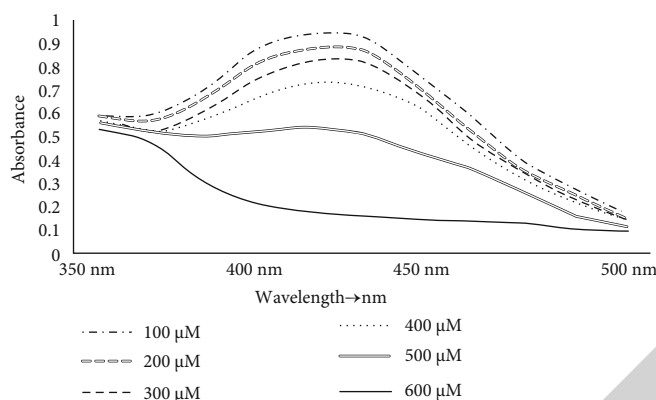


FIGURE 7: The titration of BSA-SSE (conc) with N-acetylcysteine solutions (100-500  $\mu\text{M}$ ). The formation of Ellman's anion is evident from the appearance of a larger band at 412 nm.

causes oxidative stress. Thus, the enhanced protein-GSH adducts might occur during the process of GSH depletion. Further examination would be required to clarify this.

In contrast to reduced glutathione and N-acetylcysteine, the reaction of BSA-SSE (typically, 500  $\mu\text{M}$ ) with D-penicillamine (100, 200, 300, 400, and 500  $\mu\text{M}$ ) produced no Ellman's anion (Figure 8). D-Penicillamine is shown to be not able to substitute  $\text{ES}^-$  in the mixed disulfide (BSA-SSE).

The absorbance peak produced for Ellman's anion ( $\text{ES}^-$ ) is relatively higher if  $\text{ES}^-$  of BSA-SSE is substituted by NAC compared to substitution by GSH. The peak produced for  $\text{ES}^-$  of BSA-SSE by Dpen was lower than peaks of the first two thiols (NAC and GSH).

When BSA-SSE reacted with the thiols, the substitution phase was identified by the release of  $\text{ES}^-$  being dethiolated from BSA-SSE. The difference in BSA-SSE dethiolation made it possible to establish the rank of  $\text{ES}^-$  substitution by NAC > GSH > DPen (Figure 9).

Studies reported elsewhere have shown that D-penicillamine does not exchange with its mixed disulfide of Ellman's reagent to form penicillamine disulfide due to steric problems. This observation suggests that the nature of the protein pocket acts to prevent the release of entities bound at Cys-34. This observation, however, is also an important control for the reactions involving reduced glutathione and N-acetylcysteine. A result similar to that shown in Figures 6 and 7 might be expected from an exchange of thiolate with Ellman's reagent loosely bound (H-bonded or hydrophobically associated) to the protein which remains in solution as a result of poor chromatographic separation. If either of these situations were present, an exchange reaction with D-penicillamine would be expected.

**3.4. Blocking by  $\text{Ag}^{\text{I}}$  Species.** The exchange experiments were carried out to explain protein substitution and dethiolation and more exactly to estimate fate of the metals in thiol disulfide exchange reactions. Metal-modified BSA mixtures were subjected to nucleophilic attack by thiolate anions (as the entering group). The -SH group (Cys-34) of BSA was blocked with  $\text{Ag}^{\text{I}}$  by separately incubating BSA solution with a small excess of silver nitrate overnight, followed by chromatographic separation (Sephadex G25); we obtained a solution of  $\text{Ag}^{\text{I}}$ -

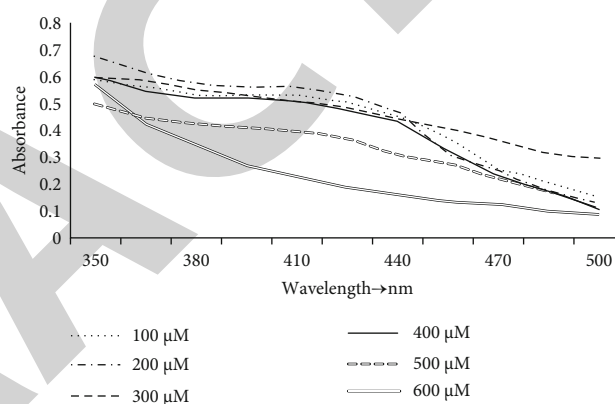


FIGURE 8: The titration of BSA-SSE (conc) with D-penicillamine solutions (100-500  $\mu\text{M}$ ). The reduced formation of Ellman's anion is evident from the appearance of smaller bands at 412 nm.

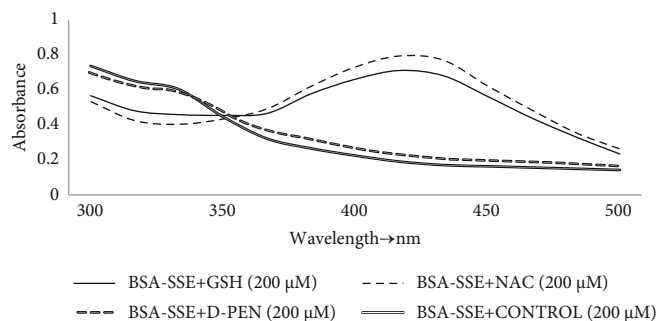


FIGURE 9: Comparison of plots of the addition of a single aliquot (200  $\mu\text{M}$ ) of reduced glutathione, N-acetylcysteine, and D-penicillamine to a BSA-SSE solution (200  $\mu\text{M}$ ).

modified BSA in reaction buffer. The chromatographed  $\text{Ag}^{\text{I}}$ -modified BSA was incubated overnight with the solution of ESSE. ESSE was found to be not able to react with the  $\text{Ag}^{\text{I}}$ -modified -SH groups of Cys-34 in BSA. Treatment with ESSE confirms that -SH groups of Cys-34 in BSA have been

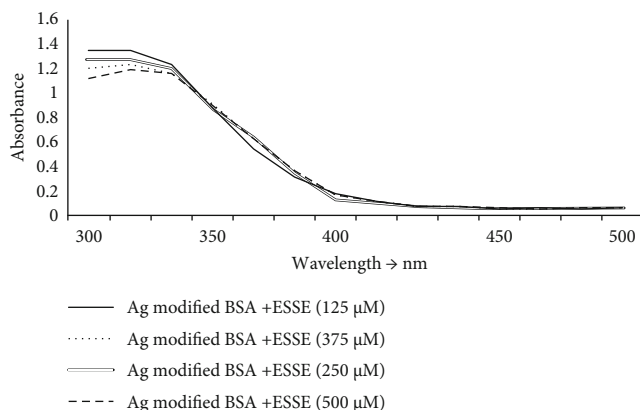
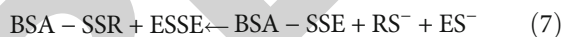


FIGURE 10: UV-visible spectra (250-450 nm) of ESSE reactivity with  $\text{Ag}^{\text{I}}$ -modified BSA (125, 250, 375, and  $500 \mu\text{M}$ ). The spectrum shows no release of  $\text{ES}^-$  at  $\lambda$  (412 nm).

effectively blocked by  $\text{Ag}^{\text{I}}$  as there is no release of  $\text{ES}^-$  in the UV-visible spectrum at 412 nm (Figure 10).

**3.5. Reaction of Thiolates with  $\text{Ag}^{\text{I}}$ -Modified BSA.** The chromatographed  $\text{Ag}^{\text{I}}$ -modified BSA ((BSA-S) $\text{Ag}^{\text{I}}$ ) samples (typically  $500 \mu\text{M}$ ) were subsequently mixed with thiolates (reduced glutathione, N-acetylcysteine, and D-penicillamine).  $\text{Ag}^{\text{I}}$  and modified BSA (typically  $500 \mu\text{M}$  each) were treated with these low molecular weight thiolates and allowed to react overnight followed by chromatographic separation (Sephadex G25). The redox reactions of  $\text{Ag}^{\text{I}}$ -modified BSA with various low molecular weight thiols revealed a mechanically important phenomenon. In the case of reduced glutathione and N-acetylcysteine, we observed the rapid release of a commensurate amount of Ellman's anion (equations (6) and (7)) indicating that an exchange has taken place, and low molecular weight thiols (RSH) substituted  $\text{Ag}^{\text{I}}$  species at the Cys-34 of BSA eventually forming disulfide (BSA-SSR) at Cys-34. The obtained results lead us to elucidate the following reactions:



With excess thiols, an exchange occurs at Cys-34 of BSA previously bound by  $\text{Ag}^{\text{I}}$ . It is apparent that when RSH (GSH (Figure 11) or NAC (Figure 12)) attack  $\text{Ag}^{\text{I}}$ -modified BSA, it binds to Cys-34 of BSA (forming BSA-SSR) and renders  $\text{Ag}^{\text{I}}$  previously bound to Cys-34 of BSA to be free. The subsequent treatment of ESSE with BSA-SSR produces larger bands (release reasonably stable  $\text{ES}^-$ ) in UV spectrophotometric spectra. Reduced Cys-34 was detected in the single-chain peptides, it was the byproduct, and overall the procedure was quite technical and comprehensive to handle.

After an overnight incubation of D-penicillamine with  $\text{Ag}^{\text{I}}$ -modified BSA, the protein samples have been collected through chromatographic separation (Sephadex G25). In contrast to reduced glutathione and N-acetylcysteine, D-penicillamine was not able to take  $\text{Ag}^{\text{I}}$  from the -SH groups of Cys-34 in BSA (Figure 13).

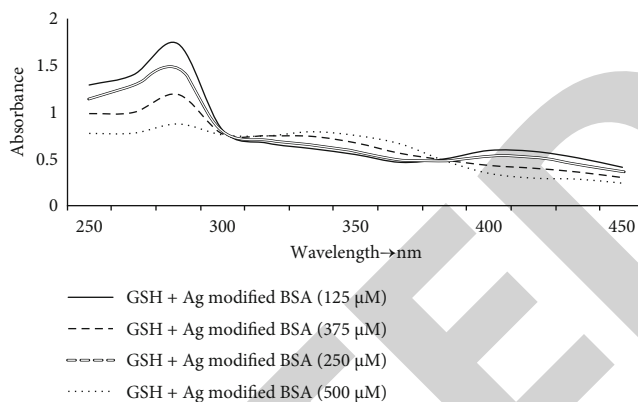


FIGURE 11: UV-visible spectra (250-500 nm) of GSH reactivity with  $\text{Ag}^{\text{I}}$ -modified BSA (125-500  $\mu\text{M}$ ). The spectrum shows sequential increase in  $\text{ES}^-$  at  $\lambda$  (412 nm).

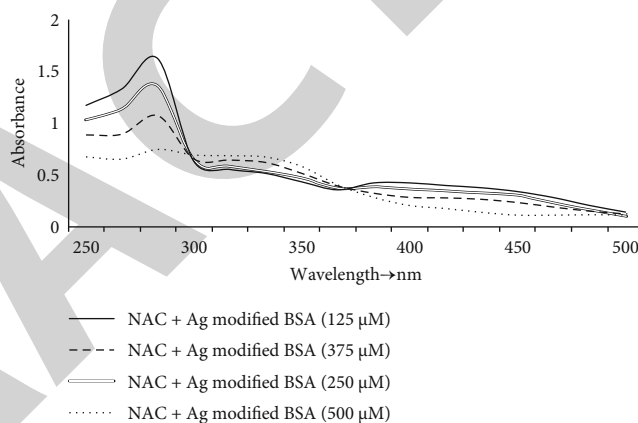


FIGURE 12: UV-visible spectra (250-500 nm) of NAC reactivity with  $\text{Ag}^{\text{I}}$ -modified BSA (125-500  $\mu\text{M}$ ). The spectrum shows sequential increase in  $\text{ES}^-$  at  $\lambda$  (412 nm).

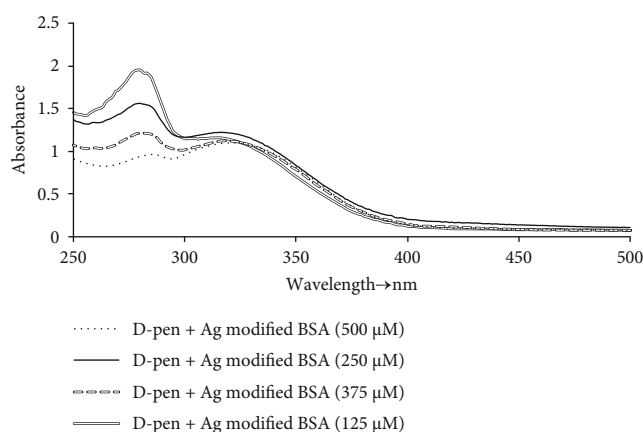


FIGURE 13: UV-visible spectra (250-500 nm) of DPen reactivity with  $\text{Ag}^{\text{I}}$ -modified BSA (125-500  $\mu\text{M}$ ). The spectrum shows no production of  $\text{ES}^-$  at  $\lambda$  (412 nm).

A study was carried out by Mukhtiar et al. (2017) on the role of glutathione, cysteine and D-penicillamine in exchanging palladium and vanadium metals from albumin

metal complex, and that was in good agreement with the current study since it is bound with albumin strongly and cannot be displaced by antioxidant like GSH, cysteine, and D-penicillamine. So exposure of human to these metals may disturb their normal physiology. Another study carried out by Jalilehvand et al. (2009) on the cadmium(II) complex formation with cysteine and penicillamine is in disagreement with the current study that it only reveals differences between cysteine and penicillamine as ligands to the cadmium(II) ion that can explain why cysteine-rich metallothionines are capable of capturing cadmium(II) ions, while penicillamine, clinically useful for treating the toxic effects of mercury(II) and lead(II) exposure, is not efficient against cadmium(II) poisoning.

**3.6. Statistical Analysis.** The chi-square test was performed, and a *p* value of 0.002 showed significant results.

## 4. Conclusion

It can be anticipated from the phase of the study involving bovine serum albumin that low molecular weight thiolates (reduced glutathione and N-acetylcysteine) take off Ag<sup>I</sup> which are attached to proteins elsewhere in the physiological system, making these toxic metals free for toxic action. The low molecular weight thiolates seem to be engaged in regeneration of Ag<sup>I</sup>-bound sulfhydryls of protein across the living systems.

## Data Availability

All datasets generated and analyzed during this study are included in the article.

## Disclosure

This manuscript is taken from a master's thesis given in <http://pr.hec.gov.pk/jspui/handle/123456789/2716>.

## Conflicts of Interest

The authors declare that they have no conflict interests.

## Authors' Contributions

All of the authors listed have represented a tremendous guide and intellectual contribution to the study and have given their permission for it to be published.

## Acknowledgments

This publication was supported by the Deanship of Scientific Research at Prince Sattam Bin Abdul-Aziz University.

## References

- [1] T. Peters, *All About Albumin. Biochemistry, Genetics, and Medical Applications*, Academic Press, San Diego, CA, 1996.
- [2] P. B. Kandagal, S. Ashoka, J. Seetharamappa, S. M. Shaikh, Y. Jadegoud, and O. B. Ijare, "Study of the interaction of an anticancer drug with human and bovine serum albumin: spectroscopic approach," *Journal of Pharmaceutical and Biomedical Analysis*, vol. 41, no. 2, pp. 393–399, 2006.
- [3] A. Mallick, S. C. Bera, S. Maiti, and N. Chattopadhyay, "Fluorometric investigation of interaction of 3-acetyl-4-oxo-6,7-dihydro-12H indolo-[2,3-a] quinolizine with bovine serum albumin," *Biophysical Chemistry*, vol. 112, no. 1, pp. 9–14, 2004.
- [4] S. F. Sun, B. Zhou, H. N. Hou, Y. Liu, and G. Y. Xiang, "Studies on the interaction between oxaprozin-E and bovine serum albumin by spectroscopic methods," *International Journal of Biological Macromolecules*, vol. 39, no. 4-5, pp. 197–200, 2006.
- [5] J. W. Kelly, "The alternative conformations of amyloidogenic proteins and their multi-step assembly pathways," *Current Opinion in Structural Biology*, vol. 8, no. 1, pp. 101–106, 1998.
- [6] P. J. Sadler and J. H. Viles, "<sup>1</sup>H and <sup>113</sup>Cd NMR investigations of Cd<sup>2+</sup> and Zn<sup>2+</sup> binding sites on serum albumin: competition with Ca<sup>2+</sup>, Ni<sup>2+</sup>, Cu<sup>2+</sup>, and Zn<sup>2+</sup>," *Inorganic Chemistry*, vol. 35, no. 15, pp. 4490–4496, 1996.
- [7] R. Artali, G. Bombieri, L. Calabi, and A. Del Pra, "A molecular dynamics study of human serum albumin binding sites," *Il Farmaco*, vol. 60, no. 6-7, pp. 485–495, 2005.
- [8] D. P. Simplicio, S. Frosali, R. Priora et al., "Biochemical and biological aspects of protein thiolation in cells and plasma," *Antioxidants & Redox Signaling*, vol. 7, no. 7-8, pp. 951–963, 2005.
- [9] K. G. Lewis, L. Bercovitch, S. W. Dill, and L. Robinson-Bostom, "Acquired disorders of elastic tissue: part I. Increased elastic tissue and solar elastotic syndromes," *Journal of the American Academy of Dermatology*, vol. 51, no. 1, pp. 1–21, 2004.
- [10] R. Narazaki, M. Hamada, K. Harada, and M. Otagiri, "Covalent binding between buccillamine derivatives and human serum albumin," *Pharmaceutical Research*, vol. 13, no. 9, pp. 1317–1321, 1996.
- [11] E. Nathan and S. E. Pedersen, "Dialysis encephalopathy in a non-dialysed uraemic boy treated with aluminium hydroxide orally," *Acta Paediatrica Scandinavica*, vol. 69, no. 6, pp. 793–796, 1980.
- [12] Y. A. Gryzunov, A. Arroyo, J. L. Vigne et al., "Binding of fatty acids facilitates oxidation of cysteine-34 and converts copper-albumin complexes from antioxidants to prooxidants," *Archives of biochemistry and biophysics*, vol. 413, no. 1, pp. 53–66, 2003.
- [13] J. Janatova, *Ph. D. Thesis, Institute of Organic Chemistry Ary Electrophoretic Analyses, and Dr. Walter Scheider for Perand Biochemistry*, Czechoslovak Academy of Sciences, 1965.
- [14] G. L. Ellman, "Tissue sulfhydryl groups," *Archives of Biochemistry and Biophysics*, vol. 82, no. 1, pp. 70–77, 1959.
- [15] A. F. S. A. Habeeb, "[37] Reaction of protein sulfhydryl groups with Ellman's reagent," in *Methods in enzymology*, vol. 25, pp. 457–464, Academic Press, 1972.
- [16] P. W. Riddles, R. K. Andrews, R. L. Blakeley, and B. Zerner, "Jack bean urease VI. Determination of thiol and disulfide content: reversible inactivation of the enzyme by the blocking of the unique cysteine residue," *Biochimica et Biophysica Acta (BBA)-Protein Structure and Molecular Enzymology*, vol. 743, no. 1, pp. 115–120, 1983.
- [17] P. Klatt and S. Lamas, "Regulation of protein function by S-glutathiolation in response to oxidative and nitrosative stress," *European Journal of Biochemistry*, vol. 267, no. 16, pp. 4928–4944, 2000.



## Research Article

# Physicochemical Characterization of Chitosan-Decorated Finasteride Solid Lipid Nanoparticles for Skin Drug Delivery

Muhammad Sohaib,<sup>1,2</sup> Shefaat Ullah Shah ,<sup>1,2</sup> Kifayat Ullah Shah,<sup>3</sup> Kifayat Ullah Shah,<sup>2,4</sup> Nauman Rahim Khan ,<sup>5</sup> Malik Muhammad Irfan ,<sup>1,2</sup> Zahid Rasul Niazi,<sup>2</sup> Abdulsalam A. Alqahtani,<sup>6</sup> Ali Alasiri,<sup>6</sup> Ismail A. Walbi,<sup>7</sup> and Sajid Mahmood<sup>3</sup>

<sup>1</sup>SRDDR, GCPS, Faculty of Pharmacy, Gomal University, D.I. Khan, Pakistan

<sup>2</sup>Faculty of Pharmacy, Gomal University, D.I. Khan, Pakistan

<sup>3</sup>Department of Pharmacy, Quaid-i-Azam University, Islamabad, Pakistan

<sup>4</sup>PDDDL, GCPS, Faculty of Pharmacy, Gomal University, D.I. Khan, Pakistan

<sup>5</sup>Department of Pharmacy, KUST, Kohat, Pakistan

<sup>6</sup>Department of Pharmaceutics, College of Pharmacy, Najran University, Najran, Saudi Arabia

<sup>7</sup>Department of Clinical Pharmacy, College of Pharmacy, Najran University, Najran, Saudi Arabia

Correspondence should be addressed to Shefaat Ullah Shah; shefaatbu@gmail.com

Received 16 May 2022; Accepted 28 July 2022; Published 6 August 2022

Academic Editor: Andrey Cherstvy

Copyright © 2022 Muhammad Sohaib et al. This is an open access article distributed under the Creative Commons Attribution License, which permits unrestricted use, distribution, and reproduction in any medium, provided the original work is properly cited.

Finasteride is considered the drug of choice for androgenic alopecia and benign prostate hyperplasia. The aim of the study was to formulate nanodrug carriers of finasteride with enhanced retentive properties in the skin. The finasteride was formulated as solid lipid nanoparticles that were decorated with different concentrations of chitosan for improved retentive properties. Solid lipid nanoparticles (SLNs) were synthesized by “high-speed homogenization technique” using stearic acid as a solid lipid while PEG-6000 and Tween-80 were used as surfactants. The SLNs were evaluated for particle size, polydispersity index (PDI), zeta potential, drug entrapment efficiency, and drug release behavior. The mean particle size of SLNs was in the range of 10.10 nm to 144.2 nm. The PDI ranged from 0.244 to 0.412 while zeta potential was in the range of 8.9 mV to 62.6 mV. The drug entrapment efficiency in chitosan undecorated formulations was 48.3% while an increase in drug entrapment was observed in chitosan-decorated formulations (51.1% to 62%). The *in vitro* drug release studies of SLNs showed an extended drug release for 24 hours after 4 hours of initial burst release. The extended drug release was observed in chitosan-coated SLNs in comparison with uncoated nanoparticles. The permeation and retention study revealed higher retention of drug in the skin and low permeation with chitosan-decorated SLNs that ranged from 39.4  $\mu\text{g}/\text{cm}^2$  to 13.2  $\mu\text{g}/\text{cm}^2$ . TEM images depicted spherical shape of SLNs. The stability study confirmed stable formulations in temperature range of 5°C and 40°C for three months. It is concluded from this study that the SLNs of finasteride were successfully formulated and chitosan decoration enhanced the drug retention in the skin layers. Therefore, these formulations could be used in androgenic alopecia and benign prostate hyperplasia to avoid the side effects, drug degradation, and prolonged use of drug with conventional oral therapy.

## 1. Introduction

Finasteride is a competitive inhibitor of 5- $\alpha$ -reductase (type-II), commonly prescribed for the treatment of benign prostate hyperplasia (BPH) and male pattern baldness (androgenic alopecia). Both the disorders occur due to the high level of testosterone conversion into more potent form, i.e.,

dihydrotestosterone, by the action of 5- $\alpha$ -reductase. Dihydrotestosterone cause rapid growth of prostate tissue and destruction of hair follicles [1]. Finasteride competitively blocks the action of 5- $\alpha$ -reductase and hence can be used in the treatment of these diseases. According to BCS, finasteride is classified as class II drug which possesses high permeability and low solubility that directly affects the dissolution

and bioavailability of the drug [2, 3]. The approved daily dose of finasteride in androgenic alopecia is 1 mg/day, and for BPH, it is 5 mg/day. It takes months to achieve the desired drug effects because of low drug solubility which may cause side effects in the form of gynecomastia, mood disturbances, and sexual problems, i.e., decreased libido and erectile and ejaculation disorders [4, 5].

Natural polymers have been extensively used in drug formulations because of their nontoxic, biocompatible, and biodegradable nature. Chitosan is a natural cationic polysaccharide, obtained from alkaline deacetylation of natural chitin which is extensively present in the exoskeletons of fungal cell wall, arthropods, and crustacean shells [6]. Chitosan promotes dermal absorption of drugs by bioadhesion and opening of the intracellular junctions to allow the entry of polar drugs. This effect of chitosan is most likely due to the positive charge of its amino groups, which provides a strong electrostatic interaction with negative charge on the surface of dermal cells and other molecules such as nucleic acids [7].

Topical/transdermal drug delivery is an alternative and effective route of drug administration because it avoids systemically produced side effects, first pass metabolism, and poor patient compliance. Nowadays, many formulations have been developed to produce local therapeutic effects [8, 9]. For maximum drug absorption through skin, various techniques are investigated and developed such as electroporation, iontophoresis, microneedles, ultrasounds, and microwave treatment, and the most recently nanodrug carriers have led to major interest in the transdermal drug delivery system [10].

The nanocarriers such as nanoemulsions, vesicular drug carriers, and lipid nanoparticles have several advantages in pharmaceutical and cosmetic applications over the conventional dosage forms [11]. Among these carriers, SLNs have gained most interest due to the smallest particle size, improved physical stability, low toxicity, low chemical degradation, flexibility in modulated drug release, less side effects, and low production cost [12, 13]. The use of solid lipid also provides an additional advantage of uniform particle size, increased surface area, and drug loading. The lipids used in SLNs are physiological lipids having similar physiological properties to those of the lipids of the skin, and so these lipids enhance cellular interactions resulting in an improved permeability. Due to this reason, SLNs are considered the most suitable drug carrier for topical, dermal, and transdermal drug deliveries [14]. A number of formulation techniques have been designed to prepare SLNs, among them high speed homogenization and microemulsion techniques are most commonly used. In the preparation, molten solid lipid is mixed with the aqueous surfactant solution followed by homogenization at high pressure. The subsequent cooling of the mixture resolidifies the lipid resulting in SLN formation [15]. The size of the SLNs used for skin drug delivery usually ranges from 1 nm to 1000 nm. SLNs increase the skin permeation, drug solubilisation, and retention of drug into the skin layers by fluidizing the stratum corneum [16]. Various researchers have been working on SLNs to enhance the solubility and bioavailability of drugs by delivering nanoparticulate drugs in modified tablets, microspheres, microemulsions, and transdermal patches [17, 18].

The aim of the present work was to improve the bioavailability of finasteride by formulating it as SLNs with enhanced drug retention properties for topical use. Finasteride drug delivery through skin reduces its major systemic side effects due to its oral administration and could improve drug penetration and accumulation in the layer of skin and hair follicles [12, 19, 20].

## 2. Materials and Methods

Finasteride was gifted by Ferozson's Pharmaceutical Laboratories, Pakistan. Stearic acid, chitosan (low molecular weight), PEG-6000, and Tween-80 were purchased from Sigma-Aldrich®, USA. Healthy male Sprague-Dawley rats were purchased from the University of Peshawar, Pakistan. All the chemicals used in the research were of analytical grade and used without any further purification.

*2.1. Preparation of Finasteride SLNs.* SLN formulations were prepared by a high-speed homogenization method [21]. In these formulations, stearic acid was used as a solid lipid, Tween-80 as surfactant, and PEG-6000 as cosurfactant. The formulation was prepared by mixing the aqueous phase containing an emulsifier with the lipid phase containing a known quantity of active drug. The aqueous phase was prepared by adding Tween-80 and PEG-6000 into a known quantity of distilled water with constant stirring on a hot plate magnetic stirrer, and the temperature was maintained at 75°C. The lipid phase was prepared by melting stearic acid at 75°C and mixing of finasteride in it. The aqueous phase was dropwise mixed with the lipid phase at the same temperature of both phases, i.e., 75°C with constant stirring for one hour. The emulsion was then subjected to homogenization for 7 minutes at 10,000 rpm. The final formulation was then immediately cooled at 10°C using an ice bath to obtain SLNs. Chitosan was added to the water phase with different ratios (0.125%, 0.25%, 0.5%, and 1%). Chitosan was solubilized in 1% acetic acid solution and incorporated into the aqueous phase containing surfactants (Table 1).

## 3. Physicochemical Characterization

*3.1. Particle Size, Polydispersity Index, and Zeta Potential.* Particle size has a prime importance in bioavailability and therapeutic index [22]. The samples were evaluated for particle size, polydispersity index (PDI), and zeta potential by photon correlation spectroscopy using Zetasizer (ZS90 Zetasizer; Malvern Instruments Ltd., Worcestershire, UK) at room temperature. For analysis, 5 mg of SLNs was diluted in 5 ml of deionized water and analyzed on Zetasizer. All the experiments were performed in triplicate [23].

*3.2. Entrapment Efficiency.* The drug entrapment efficiency (E.E) was determined to check the concentration of free drug in the dispersion medium [24]. Briefly, 1 ml of dispersion was diluted with 4 ml of distilled water, and the mixture was centrifuged at 15000 rpm for 30 minutes. The supernatant layer was collected and checked for drug contents through HPLC at  $\lambda$  max of 210 nm.

TABLE 1: Formulation composition (finasteride, chitosan, stearic acid, and Tween-80) of SLNs.

F. code	Drug (% w/w)	Stearic acid (% w/w)	PEG-6000 (% w/w)	Tween-80 (% w/w)	Chitosan (% w/w)	Acetic acid (% w/w)	Water (% w/w)
F0	—	1.5	1	2.5	—	—	95.000
F1	0.1	1.5	1	2.5	—	—	94.900
F2	0.1	1.5	1	2.5	0.125	28.108	66.667
F3	0.1	1.5	1	2.5	0.250	41.316	53.334
F4	0.1	1.5	1	2.5	0.500	61.065	33.335
F5	0.1	1.5	1	2.5	1.000	73.900	20.000

TABLE 2: Effect of chitosan coating on particle size, PDI, pH, and viscosity of SLNs.

Formulation code	Particle size (nm)	PDI	Zeta potential (mV)	pH	Viscosity (cp)
F0	10.10 ± 1.046	0.412 ± 0.012	8.9 ± 6.23	5.3 ± 0.652	3.0 ± 0.8
F1	14.68 ± 1.841	0.369 ± 0.043	18.7 ± 8.80	5.5 ± 0.841	3.5 ± 1.1
F2	76.74 ± 2.122	0.297 ± 0.004	23.5 ± 5.59	5.6 ± 0.893	4.5 ± 2.3
F3	109.6 ± 4.363	0.244 ± 0.027	32.1 ± 7.09	5.6 ± 0.789	5.5 ± 2.8
F4	122.4 ± 5.214	0.313 ± 0.016	50.8 ± 8.73	5.5 ± 0.854	23.3 ± 5.6
F5	144.2 ± 6.931	0.291 ± 0.019	62.6 ± 7.98	5.5 ± 0.968	170 ± 18.4

E.E was measured by the following formula:

$$E.E = \left( \frac{W_T - W_F}{W_T} \right) \times 100\%, \quad (1)$$

where E.E is the entrapment efficiency of SLNs,  $W_T$  is the total weight of finasteride added at the time of preparation, and  $W_F$  is the weight unloaded finasteride filtered in the supernatant layer.

**3.3. Infrared Spectroscopy (ATR-FTIR).** All the formulations were subjected to Fourier transform infrared (ATR-FTIR) spectroscopy to check any possible interactions of the formulation components. For this purpose, samples were analyzed as liquid suspension of SLNs and the spectra of ATR-FTIR were taken within the frequency range of 400 to 4000  $\text{cm}^{-1}$  and ambient air as a background, using FTIR spectrophotometer (PerkinElmer Inc., Waltham, MA, USA) while the peaks were determined using Perkin Elmer Spectrum version 6.0.2 software (PerkinElmer, Waltham, MA, USA) [25].

**3.4. In Vitro Drug Release Studies.** The drug release studies were performed on the Franz diffusion cell (PermeGear, USA) with little modification in the already reported method [26]. For this, the receptor compartment was filled with 6 ml of acetate buffer solution pH 5.5 (USP) in simulation of skin, and the donor compartment was loaded with 3 ml of SLN sample. An artificial membrane (polytetrafluoroethylene (PTFE), 0.45  $\mu\text{m}$  pore size; Sartorius AG, Goettingen, Germany) were mounted in between the donor and receptor compartments. The temperature of the receptor compartment was maintained at  $32 \pm 2^\circ\text{C}$ . The buffer solution in the receptor compartment was magnetically stirred at

200 rpm throughout the study [27]. The study was performed for 24 hours, and with the help of a sterilized syringe, 0.5 ml of aliquots was withdrawn from the receptor compartment with the time intervals of 0, 0.5, 1, 2, 4, 8, 12, 16, and 24 hours for further analysis and the same amount of fresh buffer was added to maintain the volume. The samples were then analyzed using HPLC for drug contents.

**3.5. Ex Vivo Drug Permeation Studies.** *Ex vivo* drug permeation studies were performed on healthy male adult Sprague-Dawley rats having weight  $220 \text{ g} \pm 10$  [28]. For this, after the approval of the ethical review committee via notification no. 823/QEC/GU dated 18/06/2019, rats were divided into 5 groups each containing 3 rats ( $n = 3/\text{formulation}$ ). The rats were anesthetized using injections of ketamine and xylazine in the doses of 15 mg and 2 g, respectively, per 220 g of the body weight of rats. The skin was shaved from the back of rats using a sterilized razor. The rats were euthanized by cervical dislocation, and the skin was extracted from the back side, washed with normal saline, and kept in a freezer at  $-40^\circ\text{C}$  till used. The skin was thawed and cut into pieces as per size of the donor compartment of Franz diffusion cell. The receiver chamber was filled with the phosphate buffer solution (pH 7.4). The skin was mounted between the donor and receptor chamber in such a way that its epidermis was in direct contact with the formulation, i.e., facing towards the donor chamber. The temperature of the Franz diffusion cells was maintained at about  $37^\circ\text{C} \pm 2$ , and the formulations were poured into the donor chamber. The samples were drawn after the time intervals of 0, 0.5, 1, 2, 4, 8, 12, 16, and 24 hours. The same amount of fresh buffer was replaced in the receiver chamber every time after the samples were withdrawn, to maintain the constant amount

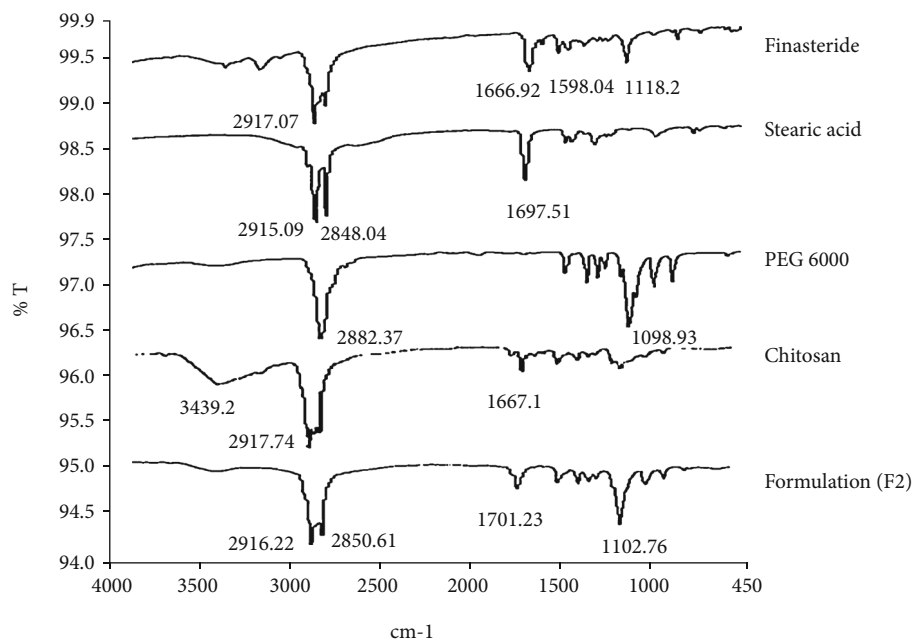


FIGURE 1: FTIR of finasteride: formulation and its components.

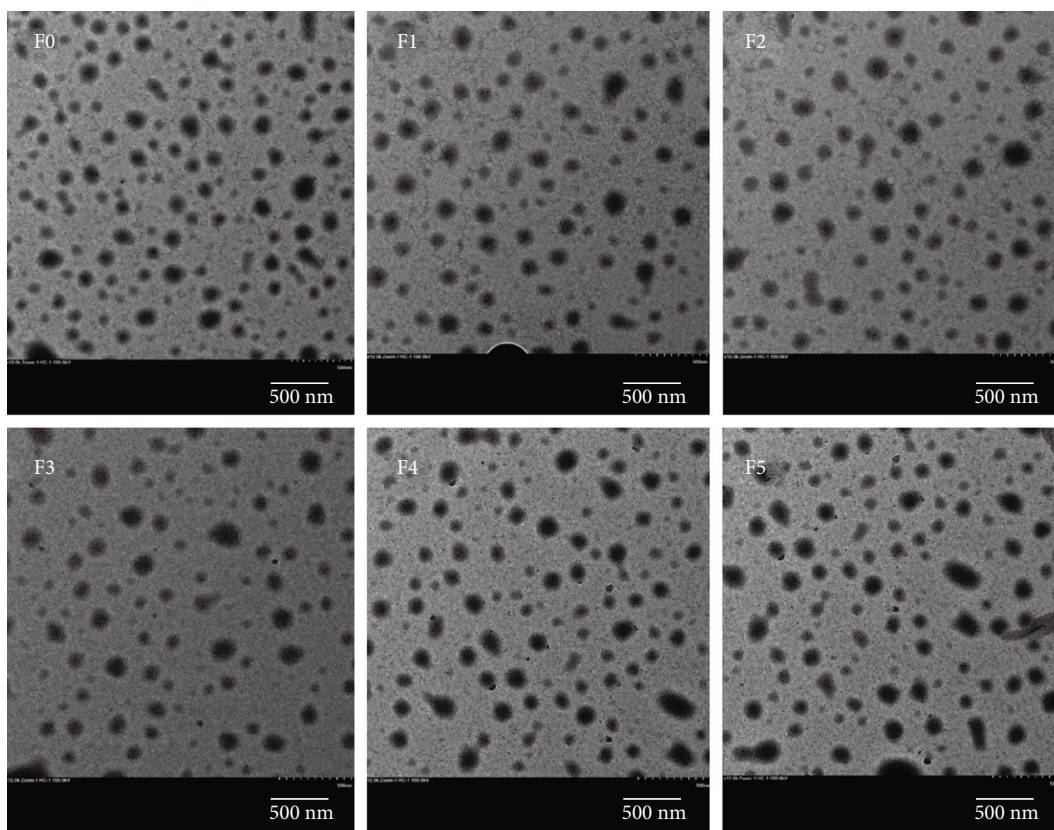


FIGURE 2: Transmission electron microscopy of SLNs.

of buffer solution in the receiving chamber. The samples were then evaluated through HPLC for drug contents. The cumulative amount of drug permeated was then plotted against time.

## 4. Results and Discussion

**4.1. Particle Size Distribution and Zeta Potential.** The particle size distribution and surface charge are determined to

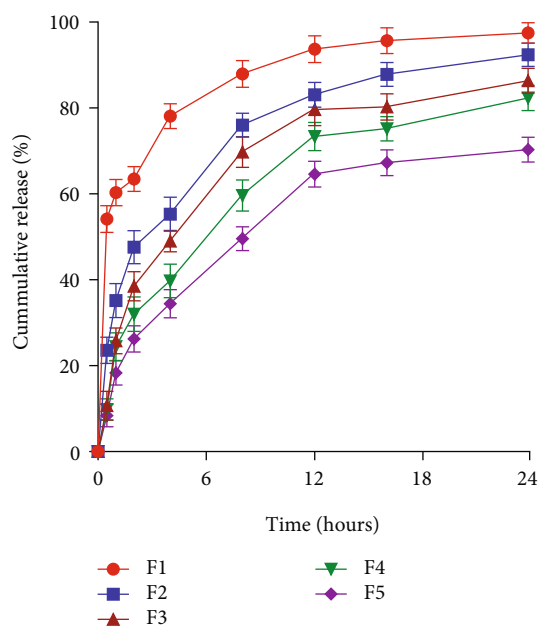


FIGURE 3: *In vitro* drug release profile of SLNs through intact skin.

predict the therapeutic performance and stability [29]. The particle size, PDI, and zeta potential of the freshly prepared SLNs are shown in Table 2. The particle size of blank SNLs (F0) was  $10.10 \pm 1.046$  nm, comparatively smaller than all other formulations. Incorporation of the drug into the formulations increased the particle size (F1) being  $14.68 \pm 1.841$  nm. The smallest particle size of the SLNs might be due to the addition of surfactants in the formulations which reduced the surface tension resulting in the smallest particle size [30]. It was observed that the particle size of the drug-loaded SLNs (F1-F5) was greater than that of the blank (F0) which depicts the successful encapsulation of drug in the solid lipid formulation that increased the particle size [31]. Chitosan coating further increased the particle size and zeta potential in formulations (F2-F5) which was due to the deposition of chitosan layers over the SLNs. Higher concentration of chitosan caused more increase in particle size suggesting the thicker layer formation due to the stronger interaction of stearic acid and positively charged chitosan. The inversion of positive charge may be because of amine group of chitosan [32–34]. No further increase in PDI values was observed which was likely due to the increased repulsive forces among the positively charged surfaces of the SLNs [35, 36]. Increase in zeta potential values was observed with increase in the concentration of chitosan indicating the formation of thicker layer of chitosan over the SLNs which increased the positive surface charge due to the protonated aliphatic amino groups of chitosan which gave it a cationic nature, so addition of chitosan inverts the negative charge to positive and increase in concentration increases the positive charge [37].

**4.2. Entrapment Efficiency.** Drug entrapment efficiency (E.E) and drug association efficiency (DAE) were checked as per previously explained methods with few modifications [24].

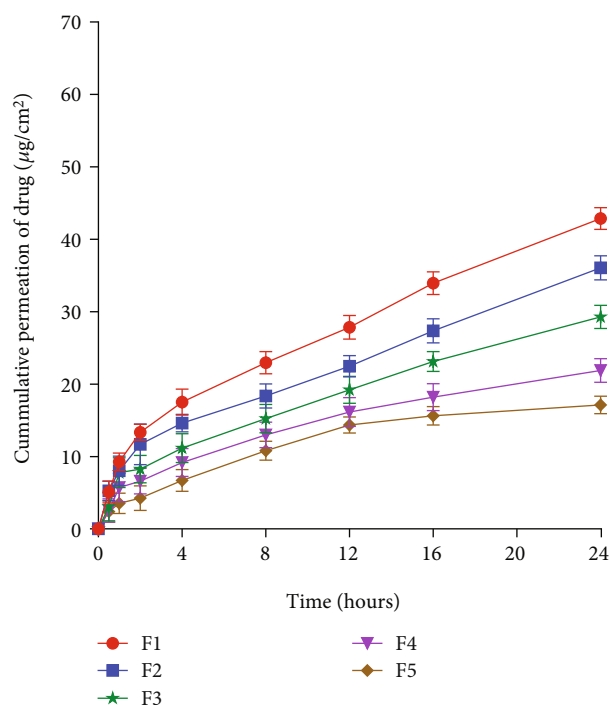


FIGURE 4: Permeation of drug through intact skin from SLNs.

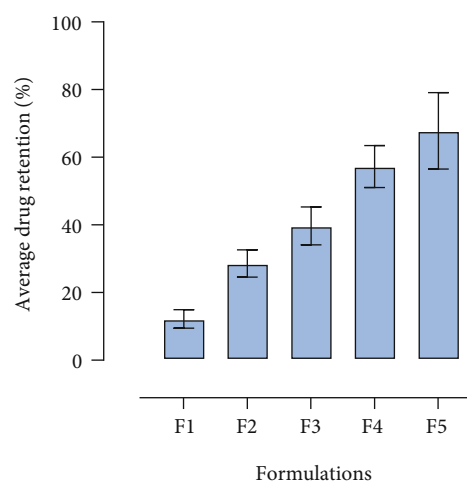


FIGURE 5: Retention of drug from SLNs in the intact skin.

The E.E results showed successful encapsulation of the drug within SLNs for both undecorated ( $48.3\% \pm 1.6$  for F1) and chitosan-decorated formulations ( $51.1\% \pm 2.2$ ,  $54.2\% \pm 2.4$ ,  $57.1\% \pm 2.9$ , and  $62\% \pm 3.3$  for F2-F5). The low percentage of drug entrapment was due to the crystallinity of solid lipid used which was also reported in the previous studies [38]. The selection and amount of lipid affect the E.E; solid lipids have less solubility of drugs than liquid lipids because they possess higher melting points and have crystalline nature at room temperature. Similarly, more amount of lipid encapsulates more drug and vice versa [39, 40]. So finasteride-loaded stearic acid SLNs are having more

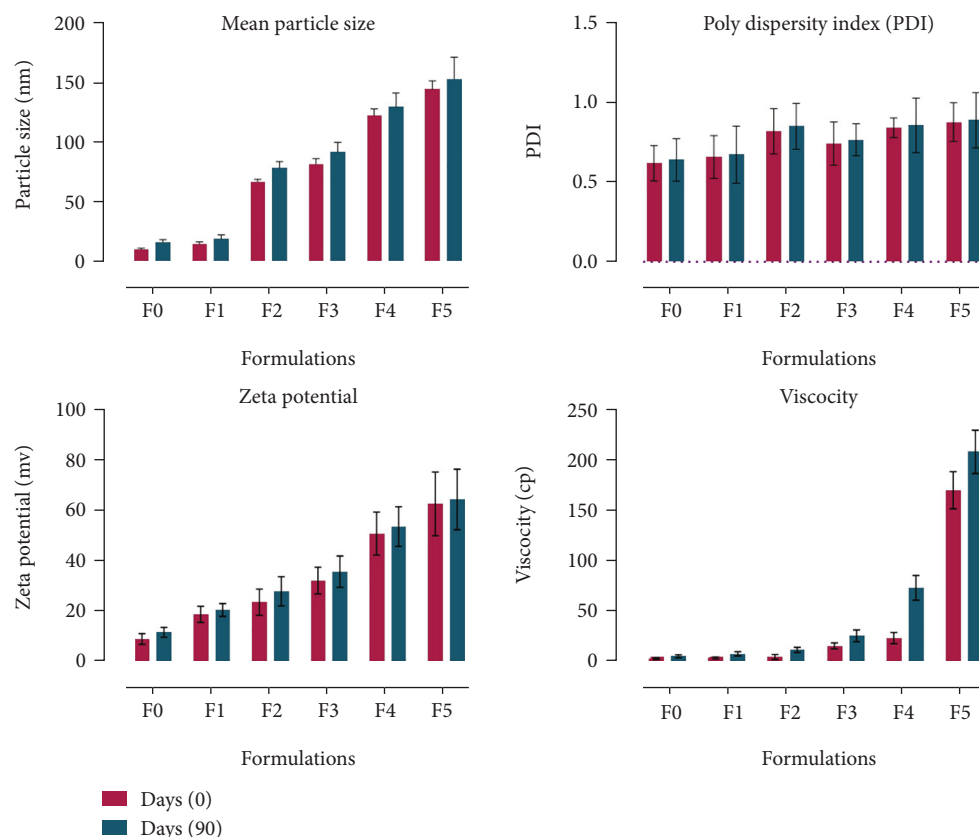


FIGURE 6: Stability studies of SLNs.

capacity of drug loading which makes them safer for use. Similar types of results were also discussed in the previous study where the SLNs of stearic acid showed drug entrapment of 68.38% [41].

**4.3. Fourier Transform Infrared Spectroscopy (FTIR).** The FTIR spectra (Figure 1) show the results of pure drug as well as the components of the formulation and polymer. In the spectra of pure finasteride, absorption bands at  $1600$  to  $1666\text{ cm}^{-1}$  are of amide groups while at  $2917\text{ cm}^{-1}$ , they are of C-H stretch. Other band peaks at  $1390$ - $1400\text{ cm}^{-1}$  are of tertiary butyl group in finasteride.

Mixing of finasteride with other components of the formulation as well as the polymer (chitosan), in physical form and after developed optimized SLN formulation, did not show any interaction, and hence, no interference was observed with the characteristic drug peaks which confirms the compatibility of drug with the additives, as mentioned previously [42, 43]. Stearic acid spectra in Figure 1 show a carbonyl peak at  $1697.51$  while peaks at  $2848.04$  and  $2915.09$  are recognized as  $\text{CH}_2$  symmetric stretch and  $\text{CH}_2$  antisymmetric stretch. The same peaks were also reported by Singh et al. in a study [44]. Chitosan spectra have peaks at  $1667.1\text{ cm}^{-1}$  which shows the amine group and  $2917.74\text{ cm}^{-1}$  which shows C-H stretching and a distinctive wide band at  $3439.2\text{ cm}^{-1}$  which is due to  $\text{OH}/\text{NH}_2$  stretching vibrations [45-47].

**4.4. Transmission Electron Microscopy.** Transmission electron micrographs (Figure 2) also confirmed the monomolecular nanoparticle size of the SLNs in the formulations. The images showed increase in the particle size with the increasing concentration of chitosan while no intraparticle interaction was observed. TEM images demonstrated the nanosize and uniform distribution of the SLNs while the influence of chitosan coating in an increase in the particle size was also observed which was due to the formation of chitosan layers over the particles [48, 49].

**4.5. In Vitro Drug Release Studies.** In *in vitro* drug release study, as explained in Figure 3, all the formulations showed a sustained release pattern except F1 that showed an initial burst release of finasteride due to small particle size and no polymer decoration that can hinder drug release from formulations. The complete drug was released within 12 h. In the case of F2 to F5, the drug release was sustained due to the addition of chitosan, and even after 24 hours, only 60% of the drug was released [50]. Previous studies also showed slow release of drug from chitosan-coated SLNs after 24 hours (60% to 90%) which was supposed to be due to the deposition of particles in the superficial layers of skin and swollen nature of chitosan in hydrophilic environment [23, 51, 52].

The SLNs possess slower polymorphic transition of stearic acid, so the solid lipid in the formulation gives more

stable formulation. The vesicles mostly remain in amorphous form, thereby favouring formation of pores and easy solvation of drug in nanoparticles [53]. Generally, the pressure will cause some detectable changes in hydration because it induces changes in ionization of surface charges due to either electrostriction or changes in charge repulsion, so the particles remain separated from each other for longer period of time which enhances the stability of the formulation. However, the individual stable particles can be penetrated easily by dissolution medium, thereby favouring initial burst release [54]. Chitosan being cationic polymer coats the vesicles of SLNs that control the release of drug from the nanoparticles that follow nonfickian diffusion when determined using the Korsmeyer-Peppas equation. Similarly, regarding membrane-polymer interactions, the amino group of chitosan had been shown to improve the muco-/bioadhesive properties enabling ions to go through so-called ion channels [55].

**4.6. Permeation and Retention Study.** The permeation of drug through intact skin depicted significantly higher permeation for nondecorated SLNs (F1) in comparison to its coated counterparts (F2-F5). This was due to the lipoidal interaction of skin with solid lipid of the formulations. Furthermore, the presence of surfactants further potentiates penetration of drug through the skin. The permeation of 42.7% was achieved for F1 that gradually reduced to 12.8% in the case of F5 (Figure 4). The relatively lower permeation in the case of chitosan-coated formulations could be attributed to larger particle size and high viscosity of the coated SLNs [56]. The findings of permeation study signify the importance of physicochemical properties of SLNs in improved permeation of drug through the skin.

The retention of drug in intact skin from SLNs delivered topically has shown that chitosan-decorated SLNs achieved significantly higher drug retention due to bioadhesive properties of chitosan [57]. The retention of drug increased linearly with increasing concentration of chitosan in SLNs (Figure 5). The cationic nature of chitosan that interacted with the negatively charged skin layers could also be the prominent feature in higher drug retention from formulations (F2-F5) as revealed in the previous studies [58–62].

**4.7. Stability Study.** All the formulations were evaluated for their stability for 3 months at  $05 \pm 2^\circ\text{C}$  and  $40 \pm 2^\circ\text{C}$  [63]. The stability was checked by evaluating the mean particle size, zeta potential, pH, and viscosity [64]. The results have shown no phase separation and no significant change in the pH and zeta potential, but a slight increase in particle size and viscosity was observed which was due to the sedimentation of particles and evaporation of water (Figure 6). On storage, the solid lipid gives more stable formulation because it possesses slower polymorphic transition of hydrocarbons [65].

## 5. Conclusion

The finasteride-loaded chitosan-coated SLNs were successfully prepared by a high-speed homogenization method

from physiologically inert substances. Stearic acid was used as a solid lipid in the formulations. On the basis of obtained results in terms of particle size, PDI, zeta potential, pH, and E.E, developed formulations could be used for application on the skin. The SLNs have shown excellent compatibility and no interaction among the ingredients as revealed by FTIR. *In vitro* release indicated the burst release without chitosan coating while slow sustained release pattern was observed in the case of chitosan-coated SLNs. Higher permeation was observed with chitosan-uncoated SLNs as compared to chitosan-coated SLNs. Moreover, chitosan coating also significantly enhanced the retention of drug within the skin layers. Based on these findings, it was concluded that chitosan-coated SLNs could be used as an alternative to oral drug delivery of finasteride in androgenic alopecia and benign prostate hyperplasia to overcome the harmful side effects and patient compliance.

## Data Availability

The data used to support the findings of this study are included within the article.

## Conflicts of Interest

The authors declare that they have no conflicts of interest.

## References

- [1] D. Rathnayake and R. Sinclair, "Male androgenetic alopecia," *Expert Opinion on Pharmacotherapy*, vol. 11, no. 8, pp. 1295–1304, 2010.
- [2] J. M. Hirshburg, P. A. Kelsey, C. A. Therrien, A. C. Gavino, and J. S. Reichenberg, "Adverse effects and safety of 5-alpha reductase inhibitors (finasteride, dutasteride): a systematic review," *The Journal of Clinical and Aesthetic Dermatology*, vol. 9, no. 7, pp. 56–62, 2016.
- [3] US Food and Drug Administration, "Drug approval package proscar (Finasteride) tablets," 2003, [https://www.accessdata.fda.gov/drugsatfda\\_docs/nda/2003/020180\\_s027\\_ProscarTOC.cfm](https://www.accessdata.fda.gov/drugsatfda_docs/nda/2003/020180_s027_ProscarTOC.cfm).
- [4] N. Carreño-Orellana, C. Moll-Manzur, J. E. Carrasco-Zuber, S. Álvarez-Véliz, D. Berroeta-Mauriziano, and N. Porras-Kusmanic, "Efectos adversos de finasteride: mitos y realidades. Una revisión actualizada," *Revista médica de Chile*, vol. 144, no. 12, pp. 1584–1590, 2016.
- [5] D. Caruso, F. Abbiati, S. Giatti et al., "Patients treated for male pattern hair with finasteride show, after discontinuation of the drug, altered levels of neuroactive steroids in cerebrospinal fluid and plasma," *The Journal of Steroid Biochemistry and Molecular Biology*, vol. 146, pp. 74–79, 2015.
- [6] M. Motiei, S. Kashanian, L. A. Lucia, and M. Khazaei, "Intrinsic parameters for the synthesis and tuned properties of amphiphilic chitosan drug delivery nanocarriers," *Journal of Controlled Release*, vol. 260, pp. 213–225, 2017.
- [7] A. D. Sezer and E. Cevher, "Topical drug delivery using chitosan nano- and microparticles," *Expert Opinion on Drug Delivery*, vol. 9, no. 9, pp. 1129–1146, 2012.
- [8] L. Bartosova and J. Bajgar, "Transdermal drug delivery in vitro using diffusion cells," *Current Medicinal Chemistry*, vol. 19, no. 27, pp. 4671–4677, 2012.

- [9] M. R. Prausnitz and R. Langer, "Transdermal drug delivery," *Nature Biotechnology*, vol. 26, no. 11, pp. 1261–1268, 2008.
- [10] O. Uchechi, J. D. Ogbonna, and A. A. Attama, "Nanoparticles for dermal and transdermal drug delivery," *Application of Nanotechnology in Drug Delivery*, vol. 4, pp. 193–227, 2014.
- [11] L. Montenegro, F. Lai, A. Offerta et al., "From nanoemulsions to nanostructured lipid carriers: a relevant development in dermal delivery of drugs and cosmetics," *Journal of Drug Delivery Science and Technology*, vol. 32, pp. 100–112, 2016.
- [12] O. A. Ahmed and W. Y. Rizq, "Finasteride nano-transfersomal gel formula for management of androgenetic alopecia: ex vivo investigational approach," *Drug Design, Development and Therapy*, vol. 12, pp. 2259–2265, 2018.
- [13] S. M. Badr-Eldin and O. A. Ahmed, "Optimized nano-transfersomal films for enhanced sildenafil citrate transdermal delivery: ex vivo and in vivo evaluation," *Drug Design, Development and Therapy*, vol. 10, p. 1323, 2016.
- [14] M. Liu, J. Wen, and M. Sharma, "Solid lipid nanoparticles for topical drug delivery: mechanisms, dosage form perspectives, and translational status," *Current Pharmaceutical Design*, vol. 26, no. 27, pp. 3203–3217, 2020.
- [15] M. Geszke-Moritz and M. Moritz, "Solid lipid nanoparticles as attractive drug vehicles: composition, properties and therapeutic strategies," *Materials Science and Engineering: C*, vol. 68, pp. 982–994, 2016.
- [16] B. Iqbal, J. Ali, and S. Baboota, "Recent advances and development in epidermal and dermal drug deposition enhancement technology," *International Journal of Dermatology*, vol. 57, no. 6, pp. 646–660, 2018.
- [17] O. A. Ahmed, M. I. Afouna, K. M. El-Say, A. B. Abdel-Naim, A. Khedr, and Z. M. Banjar, "Optimization of self-nanoemulsifying systems for the enhancement of in vivo hypoglycemic efficacy of glimepiride transdermal patches," *Expert Opinion on Drug Delivery*, vol. 11, no. 7, pp. 1005–1013, 2014.
- [18] A. K. Kushwaha, P. R. Vuddanda, P. Karunanidhi, S. K. Singh, and S. Singh, "Development and evaluation of solid lipid nanoparticles of raloxifene hydrochloride for enhanced bioavailability," *BioMed Research International*, vol. 2013, 9 pages, 2013.
- [19] T. Caon, L. C. Porto, A. Granada et al., "Chitosan-decorated polystyrene-b-poly(acrylic acid) polymersomes as novel carriers for topical delivery of finasteride," *European Journal of Pharmaceutical Sciences*, vol. 52, pp. 165–172, 2014.
- [20] M. Caserini, M. Radicioni, C. Leuratti, O. Annoni, and R. Palmieri, "A novel finasteride 0.25% topical solution for androgenetic alopecia: pharmacokinetics and effects on plasma androgen levels in healthy male volunteers," *International Journal of Clinical Pharmacology and Therapeutics*, vol. 52, no. 10, pp. 842–849, 2014.
- [21] A. A. Öztürk, A. B. Gündüz, and O. Ozisik, "Supervised machine learning algorithms for evaluation of solid lipid nanoparticles and particle size," *Combinatorial Chemistry & High Throughput Screening*, vol. 21, no. 9, pp. 693–699, 2018.
- [22] M. Danaei, M. Dehghankhold, S. Ataei et al., "Impact of particle size and polydispersity index on the clinical applications of lipidic nanocarrier systems," *Pharmaceutics*, vol. 10, no. 2, p. 57, 2018.
- [23] H. M. Eid, M. H. Elkomy, S. F. El Menshawe, and H. F. Salem, "Development, optimization, and in vitro/in vivo characterization of enhanced lipid nanoparticles for ocular delivery of ofloxacin: the influence of pegylation and chitosan coating," *AAPS PharmSciTech*, vol. 20, no. 5, pp. 1–14, 2019.
- [24] F. Shi, J.-H. Zhao, Y. Liu, Z. Wang, Y.-T. Zhang, and N.-P. Feng, "Preparation and characterization of solid lipid nanoparticles loaded with frankincense and myrrh oil," *International Journal of Nanomedicine*, vol. 7, pp. 2033–2043, 2012.
- [25] M. S. Qurt, İ. Esentürk, S. B. Tan, M. S. Erdal, A. Araman, and S. Güngör, "Voriconazole and sertaconazole loaded colloidal nano-carriers for enhanced skin deposition and improved topical fungal treatment," *Journal of Drug Delivery Science and Technology*, vol. 48, pp. 215–222, 2018.
- [26] A. Seyfoddin and R. Al-Kassas, "Development of solid lipid nanoparticles and nanostructured lipid carriers for improving ocular delivery of acyclovir," *Drug Development and Industrial Pharmacy*, vol. 39, no. 4, pp. 508–519, 2013.
- [27] A. Froelich, T. Osmalek, A. Snela et al., "Novel microemulsion-based gels for topical delivery of indomethacin: formulation, physicochemical properties and in vitro drug release studies," *Journal of Colloid and Interface Science*, vol. 507, pp. 323–336, 2017.
- [28] H. Kelidari, M. Saeedi, J. Akbari et al., "Formulation optimization and in vitro skin penetration of spironolactone loaded solid lipid nanoparticles," *Colloids and Surfaces B: Biointerfaces*, vol. 128, pp. 473–479, 2015.
- [29] C. S. Kumar, R. Thangam, S. A. Mary, P. R. Kannan, G. Arun, and B. Madhan, "Targeted delivery and apoptosis induction of trans-resveratrol-ferulic acid loaded chitosan coated folic acid conjugate solid lipid nanoparticles in colon cancer cells," *Carbohydrate Polymers*, vol. 231, article 115682, 2020.
- [30] Y. Qin, R. Bao, L. Shang et al., "Effects of particle size and types of porous media on the formation and occurrence of methane hydrate in complex systems," *Energy & Fuels*, vol. 36, no. 1, pp. 655–668, 2022.
- [31] A. A. Öztürk, A. Aygül, and B. Şenel, "Influence of glyceryl behenate, tripalmitin and stearic acid on the properties of clarithromycin incorporated solid lipid nanoparticles (SLNs): formulation, characterization, antibacterial activity and cytotoxicity," *Journal of Drug Delivery Science and Technology*, vol. 54, article 101240, 2019.
- [32] V. Piazzini, L. Cinci, M. D'Ambrosio, C. Luceri, A. R. Bilia, and M. C. Bergonzi, "Solid lipid nanoparticles and chitosan-coated solid lipid nanoparticles as promising tool for silybin delivery: formulation, characterization, and in vitro evaluation," *Current Drug Delivery*, vol. 16, no. 2, pp. 142–152, 2019.
- [33] M. Dawoud, "Chitosan coated solid lipid nanoparticles as promising carriers for docetaxel," *Journal of Drug Delivery Science and Technology*, vol. 62, article 102409, 2021.
- [34] S. Dasineh, M. Akbarian, H. A. Ebrahimi, and G. Behbudi, "Tacrolimus-loaded chitosan-coated nanostructured lipid carriers: preparation, optimization and physicochemical characterization," *Applied Nanoscience*, vol. 11, no. 4, pp. 1169–1181, 2021.
- [35] K. L. Worthington, A. Adamcakova-Dodd, A. Wongrakpanich et al., "Chitosan coating of copper nanoparticles reduces in vitro toxicity and increases inflammation in the lung," *Nanotechnology*, vol. 24, no. 39, article 395101, 2013.



- [36] E.-H. Lee, S.-J. Lim, and M.-K. Lee, "Chitosan-coated liposomes to stabilize and enhance transdermal delivery of indocyanine green for photodynamic therapy of melanoma," *Carbohydrate Polymers*, vol. 224, article 115143, 2019.
- [37] Y. Tan, R. Li, C. Liu et al., "Chitosan reduces vitamin D bioaccessibility in food emulsions by binding to mixed micelles," *Food & Function*, vol. 11, no. 1, pp. 187–199, 2020.
- [38] S. Kumar and J. K. Randhawa, "Solid lipid nanoparticles of stearic acid for the drug delivery of paliperidone," *RSC Advances*, vol. 5, no. 84, pp. 68743–68750, 2015.
- [39] N. Iqbal, C. Vitorino, and K. M. Taylor, "How can lipid nanocarriers improve transdermal delivery of olanzapine?," *Pharmaceutical Development and Technology*, vol. 22, no. 4, pp. 587–596, 2017.
- [40] M. S. Baig, A. Ahad, M. Aslam, S. S. Imam, M. Aqil, and A. Ali, "Application of Box-Behnken design for preparation of levofloxacin-loaded stearic acid solid lipid nanoparticles for ocular delivery: optimization, in vitro release, ocular tolerance, and antibacterial activity," *International Journal of Biological Macromolecules*, vol. 85, pp. 258–270, 2016.
- [41] S. Bhattacharyya and P. Reddy, "Effect of surfactant on azithromycin dihydrate loaded stearic acid solid lipid nanoparticles," *Turkish Journal of Pharmaceutical Sciences*, vol. 16, no. 4, pp. 425–431, 2019.
- [42] F. Pervaiz, M. Saleem, A. Ashames et al., "Development and ex-vivo skin permeation studies of finasteride–poly (lactic acid-co-glycolic acid) and minoxidil–chitosan nanoparticulate systems," *Journal of Bioactive and Compatible Polymers*, vol. 35, no. 2, pp. 77–91, 2020.
- [43] T. A. Ahmed, "Preparation of finasteride capsules-loaded drug nanoparticles: formulation, optimization, in vitro, and pharmacokinetic evaluation," *International Journal of Nanomedicine*, vol. 11, p. 515, 2016.
- [44] A. Singh, G. Yadagiri, S. Parvez et al., "Formulation, characterization and in vitro anti-leishmanial evaluation of amphotericin B loaded solid lipid nanoparticles coated with vitamin B<sub>12</sub>-stearic acid conjugate," *Materials Science and Engineering: C*, vol. 117, article 111279, 2020.
- [45] S. Bashiri, B. Ghanbarzadeh, A. Ayaseh, J. Dehghannya, and A. Ehsani, "Preparation and characterization of chitosan-coated nanostructured lipid carriers (CH-NLC) containing cinnamon essential oil for enriching milk and anti-oxidant activity," *LWT*, vol. 119, article 108836, 2020.
- [46] C. Rodrigues, D. Francieli, M. D. L. Pier et al., "Mechanical, thermal and antimicrobial properties of chitosan-based-nanocomposite with potential applications for food packaging," *Journal of Polymers and the Environment*, vol. 28, no. 4, pp. 1216–1236, 2020.
- [47] N. Ali, A. Khan, M. Bilal, S. Malik, S. Badshah, and H. Iqbal, "Chitosan-based bio-composite modified with thiocarbamate moiety for decontamination of cations from the aqueous media," *Molecules*, vol. 25, no. 1, p. 226, 2020.
- [48] R. Xing, O. Mustapha, T. Ali et al., "Development, characterization, and evaluation of SLN-loaded thermoresponsive hydrogel system of topotecan as biological macromolecule for colorectal delivery," *BioMed Research International*, vol. 2021, 14 pages, 2021.
- [49] S. Sreekumar, F. M. Goycoolea, B. M. Moerschbacher, and G. R. Rivera-Rodriguez, "Parameters influencing the size of chitosan-TPP nano- and microparticles," *Scientific Reports*, vol. 8, no. 1, pp. 1–11, 2018.
- [50] P. K. Gaur, S. Mishra, M. Bajpai, and A. Mishra, "Enhanced oral bioavailability of efavirenz by solid lipid nanoparticles: in vitro drug release and pharmacokinetics studies," *Biomed Research International*, vol. 2014, Article ID 363404, 9 pages, 2014.
- [51] E. B. Souto, R. da Ana, S. B. Souto et al., "In vitro characterization, modelling, and antioxidant properties of polyphenon-60 from green tea in Eudragit S100-2 chitosan microspheres," *Nutrients*, vol. 12, no. 4, p. 967, 2020.
- [52] S. Cometa, M. A. Bonifacio, G. Trapani, S. Di Gioia, L. Dazzi, and E. De Giglio, "In vitro investigations on dopamine loaded solid lipid nanoparticles," *Journal of Pharmaceutical And Biomedical Analysis*, vol. 185, article 113257, 2020.
- [53] A. Gadomski, "Polymorphic phase transitions in systems evolving in a two-dimensional discrete space," *Physical Review E*, vol. 60, no. 2, pp. 1252–1261, 1999.
- [54] A. Gadomski, "Stretched exponential kinetics of the pressure induced hydration of model lipid membranes. A possible scenario," *Journal de Physique II*, vol. 6, no. 11, pp. 1537–1546, 1996.
- [55] A. Gadomski, P. Beldowski, L. Martínez-Balbuena, I. Santamaría-Holek, and Z. Pawlak, "Unravelling a self-healing thermo- and hydrodynamic mechanism of transient pore's late-stage closing in vesicles, and related soft-matter systems, in terms of liaison between surface-tension and bending effects," *Acta Physica Polonica B*, vol. 47, no. 5, p. 1341, 2016.
- [56] Z. M. Adib, S. Ghanbarzadeh, M. Kouhsoltani, A. Y. Khosroshahi, and H. Hamishehkar, "The effect of particle size on the deposition of solid lipid nanoparticles in different skin layers: a histological study," *Advanced Pharmaceutical Bulletin*, vol. 6, no. 1, pp. 31–36, 2016.
- [57] N. K. Ameerduzzafar, N. K. Alruwaili, S. N. A. Bukhari et al., "Improvement of ocular efficacy of levofloxacin by bioadhesive chitosan coated PLGA nanoparticles: Box-Behnken design, in-vitro characterization, antibacterial evaluation and scintigraphy study," *Iranian Journal of Pharmaceutical Research: IJPR*, vol. 19, no. 1, pp. 292–311, 2020.
- [58] E. B. Souto, I. Baldim, W. P. Oliveira et al., "SLN and NLC for topical, dermal, and transdermal drug delivery," *Expert Opinion On Drug Delivery*, vol. 17, no. 3, pp. 357–377, 2020.
- [59] L. A. D. Silva, L. M. Andrade, F. A. P. de Sá et al., "Clobetasol-loaded nanostructured lipid carriers for epidermal targeting," *Journal Of Pharmacy And Pharmacology*, vol. 68, no. 6, pp. 742–750, 2016.
- [60] I. M. Rodríguez-Cruz, V. Merino, M. Merino, O. Díez, A. Nacher, and D. Quintanar-Guerrero, "Polymeric nanospheres as strategy to increase the amount of triclosan retained in the skin: passive diffusion vs. iontophoresis," *Journal of Microencapsulation*, vol. 30, no. 1, pp. 72–80, 2013.
- [61] M. Dorrani, M. Kaul, A. Parhi, E. J. LaVoie, D. S. Pilch, and B. Michniak-Kohn, "TXA497 as a topical antibacterial agent: comparative antistaphylococcal, skin deposition, and skin permeation studies with mupirocin," *International Journal of Pharmaceutics*, vol. 476, no. 1-2, pp. 199–204, 2014.
- [62] S. Ahmad, M. U. Minhas, M. Ahmad, M. Sohail, O. Abdullah, and S. F. Badshah, "Preparation and evaluation of skin wound healing chitosan-based hydrogel membranes," *AAPS PharmSciTech*, vol. 19, no. 7, pp. 3199–3209, 2018.
- [63] U. Ahmad, J. Akhtar, S. P. Singh, A. F. J. Badruddeen, S. Siddiqui, and Wahajuddin, "Silymarin nanoemulsion against human hepatocellular carcinoma: development and

- optimization,” *Artificial cells, nanomedicine, and biotechnology*, vol. 46, no. 2, pp. 231–241, 2018.
- [64] D. P. Gaspar, V. Faria, L. M. Gonçalves, P. Taboada, C. Remuñán-López, and A. J. Almeida, “Rifabutin-loaded solid lipid nanoparticles for inhaled antitubercular therapy: physicochemical and in vitro studies,” *International Journal of Pharmaceutics*, vol. 497, no. 1-2, pp. 199–209, 2016.
- [65] M. A. Kalam, Y. Sultana, A. Ali, M. Aqil, A. K. Mishra, and K. Chuttani, “Preparation, characterization, and evaluation of gatifloxacin loaded solid lipid nanoparticles as colloidal ocular drug delivery system,” *Journal of Drug Targeting*, vol. 18, no. 3, pp. 191–204, 2010.

## Retraction

# Retracted: Antihypertensive Activity in High Salt-Induced Hypertensive Rats and LC-MS/MS-Based Phytochemical Profiling of *Melia azedarach* L. (Meliaceae) Leaves

### BioMed Research International

Received 8 January 2024; Accepted 8 January 2024; Published 9 January 2024

Copyright © 2024 BioMed Research International. This is an open access article distributed under the Creative Commons Attribution License, which permits unrestricted use, distribution, and reproduction in any medium, provided the original work is properly cited.

This article has been retracted by Hindawi following an investigation undertaken by the publisher [1]. This investigation has uncovered evidence of one or more of the following indicators of systematic manipulation of the publication process:

- (1) Discrepancies in scope
- (2) Discrepancies in the description of the research reported
- (3) Discrepancies between the availability of data and the research described
- (4) Inappropriate citations
- (5) Incoherent, meaningless and/or irrelevant content included in the article
- (6) Manipulated or compromised peer review

The presence of these indicators undermines our confidence in the integrity of the article's content and we cannot, therefore, vouch for its reliability. Please note that this notice is intended solely to alert readers that the content of this article is unreliable. We have not investigated whether authors were aware of or involved in the systematic manipulation of the publication process.

Wiley and Hindawi regrets that the usual quality checks did not identify these issues before publication and have since put additional measures in place to safeguard research integrity.

We wish to credit our own Research Integrity and Research Publishing teams and anonymous and named external researchers and research integrity experts for contributing to this investigation.

The corresponding author, as the representative of all authors, has been given the opportunity to register their agreement or disagreement to this retraction. We have kept a record of any response received.

### References

- [1] A. Saeed, K. Bashir, A. J. Shah, R. Qayyum, and T. Khan, "Antihypertensive Activity in High Salt-Induced Hypertensive Rats and LC-MS/MS-Based Phytochemical Profiling of *Melia azedarach* L. (Meliaceae) Leaves," *BioMed Research International*, vol. 2022, Article ID 2791874, 17 pages, 2022.

## Research Article

# Antihypertensive Activity in High Salt-Induced Hypertensive Rats and LC-MS/MS-Based Phytochemical Profiling of *Melia azedarach* L. (Meliaceae) Leaves

Anam Saeed,<sup>1</sup> Kashif Bashir,<sup>1</sup> Abdul Jabbar Shah,<sup>1</sup> Rahila Qayyum,<sup>1,2</sup> and Taous Khan <sup>1</sup>

<sup>1</sup>Department of Pharmacy, COMSATS University Islamabad, Abbottabad Campus, Abbottabad 22060, Pakistan

<sup>2</sup>Gomal Medical College, MTI, Dera Ismail Khan, KPK, Pakistan

Correspondence should be addressed to Taous Khan; [taouskhan@cuiatd.edu.pk](mailto:taouskhan@cuiatd.edu.pk)

Received 24 May 2022; Accepted 22 June 2022; Published 26 July 2022

Academic Editor: Abdul Wahab

Copyright © 2022 Anam Saeed et al. This is an open access article distributed under the Creative Commons Attribution License, which permits unrestricted use, distribution, and reproduction in any medium, provided the original work is properly cited.

*Melia azedarach* L. leaves have been traditionally used but not scientifically evaluated for antihypertensive activity. The focus of the present work was to carry out the detailed phytochemical profiling and antihypertensive potential of methanolic extract and subsequent fractions of this plant. The tandem mass spectrometry-based phytochemical profiling of *M. azedarach* extract (Ma.Cr) and fractions was determined in negative ionization mode while molecular networking was executed using the Global Natural Product Social (GNPS) molecular networking platform. This study resulted in the identification of 29 compounds including flavonoid O-glycosides, simple flavonoids, triterpenoidal saponins, and cardenolides as the major constituents. Ma.Cr at the concentration of 300 mg/kg resulted in a fall in blood pressure (BP), i.e.,  $81.44 \pm 2.1$  mmHg in high salt-induced hypertensive rats *in vivo*, in comparison to normotensive group, i.e.,  $65.36 \pm 1.8$  mmHg at the same dose. A decrease in blood pressure was observed in anaesthetized normotensive and hypertensive rats treated with extract and various fractions of *M. azedarach*. A reasonable activity was observed for all fractions except the aqueous fraction. The highest efficacy was shown by the ethyl acetate fraction, i.e.,  $77.06 \pm 3.77$  mmHg in normotensive and  $88.96 \pm 1.3$  mmHg in hypertensive anaesthetized rats. Ma.Cr and fractions showed comparatively better efficacy towards hypertensive rats as compared to rats with normal blood pressure. Blood pressure-lowering effects did not change upon prior incubation with atropine. *In vitro* testing of Ma.Cr and polarity-based fractions resulted in  $I_1$ -NAME sensitive, endothelium-dependent vasodilator effects on aortic tissues. Pretreatment of aorta preparations with Ma.Cr and its fractions also blocked  $K^+$ -induced precontractions indicating  $Ca^{2+}$  channel blocking activity comparable to verapamil. The extract and polarity-based fractions did not reveal a vasoconstrictor response in spontaneously beating isolated rat aorta. Ma.Cr and fractions when used in atrial preparations resulted in negative inotropic and chronotropic effects. These effects in atrial preparations did not change in the presence of atropine. These effects of extract and fractions explained the antihypertensive potential of *M. azedarach* and thus provided a scientific basis for its ethnopharmacological use in the treatment of hypertension. Among the constituents observed, flavonoids and flavonoid O-glycosides were previously reported for antihypertensive potential.

## 1. Introduction

Hypertension is one of the serious medical conditions that dramatically increases the probability of different health-related issues [1]. It is a noncommunicable global disease with lack of initial symptoms and a high mortality rate and is termed a silent killer. Approximately, 1.13 billion people around the world are suffering from hypertension, including the majority of people from countries with low and middle

income [2]. The overall prevalence of hypertension in Pakistan was 26.34% (25.93%, 26.75%) [3]. Currently, several drugs are used for the treatment of hypertension such as calcium channel blockers,  $\beta$ -blockers, ACE inhibitors, and diuretics [4, 5]. Treatment of hypertension requires a combination of drugs that are acting at various therapeutic sites and thus result in adverse effects. These adverse effects need further management that leads to complications in the treatment of hypertension. Alternatively, herbal drugs that

possess a therapeutically important combination of constituents have various clinical issues [6]; therefore, research is being carried out to find out more effective remedies with lesser side effects.

Natural products obtained from plants have been major contributors to the drug discovery against various diseases. A large population of Asia relies on local remedies for the treatment of different diseases including cardiovascular disorders [7, 8]. Research has confirmed the cardiovascular activity of many plant constituents like allicin from *Allium sativum*, digoxin from *Digitalis purpurea*, curcumin from *Curcuma longa*, and tetrandrine from *Stephania tetrandra* [9, 10].

*M. azedarach* L. (Meliaceae) is one of the plants used by community practitioners for the treatment of hypertension [11]. It is commonly known as Chinaberry or China tree in English and dharek or darek in Urdu [12]. Traditionally, it is used for the management of inflammation, cardiovascular disorders, and leprosy [13, 14] and also as a diuretic, astringent, and wormicidal [15], whereas its oil is used in cramps and rheumatism [16]. It is applied in the Ayurvedic and Unani medicinal system as an analgesic, antioxidative, rodenticidal, and insecticidal and also to treat diabetes, diarrhea, and hypertension [12]. It contains several groups of phytoconstituents like steroids, flavonoids, acids, and terpenoids [12]. The constituents previously reported from this plant include quercetin, kaempferol (flavonoids), campesterol, stigmasterol (phytosterols), phytol (diterpene), heptadecane,  $\beta$ -sitosterol, hexadecanoic acid, tocopherol,  $\beta$ -carotene, 1-eicosanol (triterpene), terpene alcohol and squalene [17],  $\beta$ -D-glucopyranose, daucosterol, liminoid glycoside, melianol, meliacarpin, meliacin, ( $\pm$ ) pinoresinol, and hydroxyl-3-methoxycinnamaldehyde and terpenoids such as azadirachtin-A and azadirachtin-B [18].

*M. azedarach* leaf extracts possess antiviral [19] and antifertility [20] activities, while fruit extract possesses ovicidal [21], larvicidal [22], and antioxidant activity [13, 23]. Its aqueous extract possesses reducing agent potential [24]. It is reported to have antidiabetic potential by inhibiting the effects of the protein tyrosine phosphatase enzyme [25]. Green synthesis of silver nanoparticles of methanolic crude extract of the plant was carried out, which showed antimicrobial, antibacterial, antidiabetic, and wound healing activities [26–28]. Anticancer activity on MCF-7 cell lines was reported on methanolic extract of *M. azedarach* [29]. Studies suggest that phenolics and phytosterols from this plant are important for cosmetics and pharmaceutical applications [30]. Consequently, current studies were undertaken to investigate the antihypertensive potential and vasorelaxant effects of *M. azedarach* and to provide scientific support for the traditional claim of curing hypertension. Furthermore, the constituents in bioactive fractions were dereplicated using LC-MS/MS-based GNPS molecular networking to identify chemical space.

## 2. Methods

**2.1. Chemicals.** Phenylephrine hydrochloride (PE) (S2569), atropine sulfate (CFN90575), acetylcholine chloride (Ach) (CFN90038), norepinephrine (NE) (CFN90047),  $N_{\omega}$ -nitro L-arginine methyl ester hydrochloride ( $l$ -NAME)

(CFN60352), and potassium chloride (104938) were procured from Sigma-Aldrich (US). Injection pentothal sodium was purchased from Abbott Laboratories (Pakistan) whereas injection heparin was purchased from F. Hoffmann-La Roche (Switzerland), respectively.

**2.2. Extraction of Plant Material.** Leaves of *M. azedarach* were collected from Dera Ismail Khan, Khyber Pakhtunkhwa, Pakistan, in the month of July. The leaf specimen was authenticated by Dr. Abdul Nazir, Associate Professor, Department of Environmental Sciences, COMSATS University Islamabad, Abbottabad Campus, Pakistan, and the sample voucher (Ma.L.05/17) was deposited. The leaves were washed, garbled, and dried in shade followed by pulverization to fine particles. The extract was prepared by macerating about 18 kg of the powdered plant material in methanol at ambient temperature, i.e., 23–25°C for 3 weeks, 1 week, and 3 days, respectively, with random stirring [31]. The filtrate was obtained by passing through qualitative grade 1 filter paper (Whatman filter paper). The extract was prepared by concentrating under vacuum using a rotary evaporator. Further polarity-based fractions of the extract were prepared including *n*-hexane (18 g), ethyl acetate (4 g), chloroform (26 g), *n*-butanol (16 g), and aqueous fraction (30 g) using previously reported method [31].

**2.3. LC-MS/MS-Based Phytochemical Analysis.** Phytochemical profiling of the extract and fractions was determined using Orbitrap Velos Pro mass spectrometer (Thermo Fisher Scientific, Germany). The detector used in the chromatographic system was a photodiode array (PDA) detector. The samples were ionized using the ESI technique in negative ionization mode. The solvent system used was prepared using formic acid 0.1% in water (A) and 0.1% formic acid in acetonitrile (B) and was run in the gradient fashion. The gradient elution program was set as the concentration of B for 0.5 min was 5%; for 0.5–6.5 min, B was 5–95%; for 6.5–8.5 min, B was 95%; and for 8.5–10 min, B was 95–5%. The volume of the sample injected was 10  $\mu$ L at the flow rate of 0.5 mL/min. At the *m/z* range of 110–2000, spectra were recorded. The LC-MS/MS data were collected and interpreted with help of the Thermo Xcalibur software. The LC-MS/MS data, which included parameters like retention time, MS-MS fragmentation pattern, *m/z*, dereplication results, and molecular formula. GNPS molecular networking platform was used for phytochemical profiling of the *M. azedarach* extract and fractions. MS convert package from the ProteoWizard software was used to convert all mass spectrometry data into GNPS compatible “.mzXML” format. WinSCP, a recommended FTP client, was used for uploading the files on the GNPS platform. Various features of the spectral data were made visible with the help of Cytoscape 3.8.2. For identification of the majority of metabolites present, MolNetEnhancer tool was used. The outcomes of GNPS analysis were thoroughly compared with the outcome of manual interpretation [32].

## 2.4. Pharmacological Studies

**2.4.1. Experimental Animals and Housing Conditions.** Sprague-Dawley (SD) rats, preferably male, in the weight range

TABLE 1: Phytochemical profile of *M. azedarach* leaf extract and fractions using tandem mass analysis.

Compound No.	Rt	[M-H] <sup>-</sup> m/z	MS2 fragmentation ion [M-H] <sup>-</sup>	Dereplication results	Exact Mass (g/mol)	Molecular Formula
<i>Crude extract of M. azedarach leaves</i>						
1	4.80	395.11	377.72, 374.95, 348.68 (100), 312.58	3,4',5,6,7-pentamethoxyflavone	372.12	C <sub>20</sub> H <sub>20</sub> O <sub>7</sub>
2	5.22	341.10	322.96 (100), 320.64, 300.58	(8,8 dimethyl-2,10-dioxo-9H-pyrano [2,3-f] chromen-9-yl)(Z)-2-methylbut-2-enoate	342.11	C <sub>19</sub> H <sub>18</sub> O <sub>6</sub>
3	5.96	449.22	426.83, 377.78, 232.47, 222.48, 151.831 (100)	Strophanthidine	404.21	C <sub>23</sub> H <sub>32</sub> O <sub>6</sub>
4	4.06	464.38	442.84, 432.77, 414.85, 342.58, 298.31(100)	Isoquercetin	464.09	C <sub>21</sub> H <sub>20</sub> O <sub>12</sub>
5	4.06	623.16	623.80, 605.66, 590.46, 579.43, 563.40 (100), 536.39, 516.33, 492.32, 477.26, 314.61, 299.51	Isorhamnetin 3-O-rutinoside	624.16	C <sub>28</sub> H <sub>32</sub> O <sub>16</sub>
6	4.04	593.15	413.07, 314.64, 284.52, 276.68 (100), 240.36	Kaempferol 3-O-[2''-O (glycopyranoside)]-rhamnopyranoside	594.15	C <sub>27</sub> H <sub>30</sub> O <sub>15</sub>
7	4.1	593.20	475.21, 356.76, 326.65, 284.53 (100), 228.38	Kaempferol 3-O-rutinoside	594.15	C <sub>27</sub> H <sub>30</sub> O <sub>15</sub>
8	4.06	593.15	413.07, 314.64, 284.52, 276.68 (100), 240.36	Kaempferol 7-O-neohesperidoside	594.15	C <sub>27</sub> H <sub>30</sub> O <sub>15</sub>
9	4.10	594.16	284.46 (100), 226.53	Keracyanin	630.13	C <sub>27</sub> H <sub>31</sub> ClO <sub>15</sub>
10	6.24	755.44	593.47, 575.42 (100), 477.07, 431.07, 413.04, 276.58	Quercetin 3-O-[2''-O-(6''-O-p-coumaroyl)-β-D-glucopyranosyl]-α-L-rhamnopyranoside	756.19	C <sub>36</sub> H <sub>36</sub> O <sub>18</sub>
11	8.03	987.52	948.95, 729.61, 654.46, 431.01, 414.80 396.82 (100)	Soyasaponin B	942.51	C <sub>48</sub> H <sub>78</sub> O <sub>18</sub>
12	16.60	675.41	415.100, 397.105 (100)	DGMG 18:3	676.36	C <sub>33</sub> H <sub>56</sub> O <sub>14</sub>
13	3.88	609.15	573.43, 561.42, 518.31, 501.27, 429.07, 300.54 (100), 292.68	Rutin	610.15	C <sub>27</sub> H <sub>30</sub> O <sub>16</sub>
14	4.66	712.40	550.63, 523.60 (100)	Soyacerebroside 1	713.54	C <sub>40</sub> H <sub>75</sub> NO <sub>9</sub>
15	3.75	755.21	709.90, 609.38, 593.46, 575.42 (100), 477.05, 431.07, 413.04, 276.58	Quercetin 3-O-[2''-O-(6'''-O-p-coumaroyl)-β-D-glucopyranosyl]-α-L-rhamnopyranoside	756.19	C <sub>36</sub> H <sub>36</sub> O <sub>18</sub>
<i>n-Hexane fraction of M. azedarach leaves</i>						
4*	4.06	463.09	442.84, 432.77, 414.85, 342.58, 298.31(100)	Isoquercetin	464.09	C <sub>21</sub> H <sub>20</sub> O <sub>12</sub>
8*	4.04	593.15	413.07, 314.64, 284.52, 276.68 (100), 240.36	Kaempferol 7-O-neohesperidoside	594.15	C <sub>27</sub> H <sub>30</sub> O <sub>15</sub>
14*	4.66	712.40	550.63, 523.60 (100)	Soyacerebroside I	713.54	C <sub>40</sub> H <sub>75</sub> NO <sub>9</sub>
16	3.88	609.15	573.43, 561.42, 518.31, 501.27, 429.09, 300.54 (100), 292.68	Quercetin 3-O-neohesperidoside	610.15	C <sub>27</sub> H <sub>30</sub> O <sub>16</sub>
17	6.62	307.19	278.54, 262.57, 260.39, 198.318 (100), 124.00	Fatty acid 18:4	308.19	C <sub>18</sub> H <sub>28</sub> O <sub>4</sub>
18	4.21	559.31	397.044, 380.172, 378.95, 350.967, 160.076, 158.104 (100)	MGMG 18:3	560.0	C <sub>27</sub> H <sub>46</sub> O <sub>9</sub>
19	6.97	721.36	466.39, 401.19, 326.81, 254.53 (100), 240.64	DGMG 18:3	676.797	C <sub>33</sub> H <sub>56</sub> O <sub>14</sub>
20	16.60	675.36	415.100, 397.105 (100)	DGMG 18:3	676.36	C <sub>33</sub> H <sub>56</sub> O <sub>14</sub>

TABLE 1: Continued.

Compound No.	Rt	[M-H] <sup>-</sup> m/z	MS2 fragmentation ion [M-H] <sup>-</sup>	Dereplication results	Exact Mass (g/mol)	Molecular Formula
Chloroform fraction of <i>M. azedarach</i> leaves						
8**	4.04	593.15	413.07, 314.64, 284.52, 276.68 (100), 240.36	Kaempferol-7-neohesperidoside	594.15	C <sub>27</sub> H <sub>30</sub> O <sub>15</sub>
21	1.15	301.04	254.27 (100), 137.923, 136.81, 122.922	Quercetin	302.04	C <sub>15</sub> H <sub>10</sub> O <sub>7</sub>
22	6.13	697.32	515.079, 415.042 (100), 326.824, 278.54, 212.211	Momordicoside	696.40	C <sub>37</sub> H <sub>60</sub> O <sub>12</sub>
23	3.75	755.21	709.90, 609.38, 593.46, 575.42 (100), 477.05, 413.04, 431.07, 276.58	Quercetin 3-O-[2-O-6-z-p-coumaroyl-glucopyranoside]-rhamnopyranoside	756.19	C <sub>36</sub> H <sub>36</sub> O <sub>18</sub>
14**	4.66	712.40	550.63, 523.60 (100)	Soyacerebroside I	713.54	C <sub>40</sub> H <sub>75</sub> NO <sub>9</sub>
9*	4.10	594.16	284.46 (100), 226.53	Keracyanin	630.13	C <sub>27</sub> H <sub>31</sub> ClO <sub>15</sub>
24	4.61	593.19	549.42, 431.22, 366.813, 284.53 (100), 206.206, 168.208	Isosakuranetin-7-O-neohesperidoside	594.19	C <sub>28</sub> H <sub>34</sub> O <sub>14</sub>
Ethyl acetate fraction of <i>M. azedarach</i> leaves						
4**	4.06	463.38	442.84, 432.77, 414.85, 342.58, 298.31(100)	Isoquercetin	464.09	C <sub>21</sub> H <sub>20</sub> O <sub>12</sub>
25	4.04	593.15	413.07, 314.64, 284.52, 276.68 (100), 240.36	Kaempferol 3-O-[2-O-(glucopyranoside)]rhamnopyranoside	594.15	C <sub>27</sub> H <sub>30</sub> O <sub>15</sub>
<i>n</i> -Butanol fraction of <i>M. azedarach</i> leaves						
26	3.84	739.21	559.43, 558.47, 430.97, 326.66, 284.47 (100)	Robinin	740.21	C <sub>33</sub> H <sub>40</sub> O <sub>19</sub>
27	3.81	625.14	462.08, 444.11, 358.90, 315.53 (100), 270.31	Isorhamnetin-3-O-galactoside-6"-rhamnoside	624.16	C <sub>28</sub> H <sub>32</sub> O <sub>16</sub>
28	4.1	593.20	475.21, 356.76, 326.65, 285.44, 276.68 (100), 228.38	Nicotiflorin	594.15	C <sub>27</sub> H <sub>30</sub> O <sub>15</sub>
15*	3.73	755.18	609.387 (100), 489.173, 342.72, 300.56, 298.603, 270.505	Quercetin 3-O-[2"-O-(6"-O-p-coumaroyl)-β-D-glucopyranosyl]-α-L-rhamnopyranoside	756.19	C <sub>36</sub> H <sub>36</sub> O <sub>18</sub>
13*	3.88	609.15	573.43, 561.42, 518.31, 501.27, 429.07, 300.54 (100), 292.68	Rutoside (rutin)	610.15	C <sub>27</sub> H <sub>30</sub> O <sub>16</sub>
29	10.49	574.45	427.168, 349.22, 332.84 (100), 265.761, 246.24, 240.59	Sulfobacin B	575.45	C <sub>32</sub> H <sub>65</sub> NO <sub>5</sub> S
Aqueous fraction of <i>M. azedarach</i> leaves						
23*	3.71	755.18	609.387 (100), 489.173, 342.72, 300.56, 298.603, 270.505	Quercetin 3-O-[2-O-6-z-p-coumaroyl-glucopyranoside]-rhamnopyranoside	756.7	C <sub>36</sub> H <sub>36</sub> O <sub>18</sub>
13**	3.88	609.15	573.43, 561.42, 518.31, 501.27, 429.07, 300.54 (100), 292.68	Rutin	610.5	C <sub>27</sub> H <sub>30</sub> O <sub>16</sub>

of 200-220 g were acquired and kept at the animal house of the university. The temperature was maintained between 23 and 25°C. The protocol was carried out according to the Institute of Laboratory Animal Resources Commission on Life Sciences, National Research Council [33], and endorsed by the Ethical Committee of CUI, Abbottabad Campus, in a meeting called on 7-09-2021 vide approval no. PHM-Eth/CS-M02-060-0721.

**2.4.2. Invasive Blood Pressure Recording.** Both normotensive and hypertensive rats were used for this study, and the protocol as previously described [34] was used with some modifications. SD rats, preferably male, were housed in a

hygienic environment and fed on 8% sodium chloride (NaCl, Scharlau, Spain) in food and water for 8 weeks. Sodium thiopental, 50-90 mg/kg intraperitoneally, was used to induce anaesthesia in rats. Polyethylene tubing (PE-20) was used for cannulation in order to help animal respire spontaneously, whereas polyethylene tubing (PE-50) was used to cannulate right carotid artery, attached to pressure transducer hyphenated to bridge amplifier and PowerLab Data Acquisition System (AD Instruments, Australia). In order to facilitate the injection of standards, Ma.Cr, and fractions, left jugular vein was cannulated. After a stabilization period of 20 min, the animal was injected with 0.1 mL saline

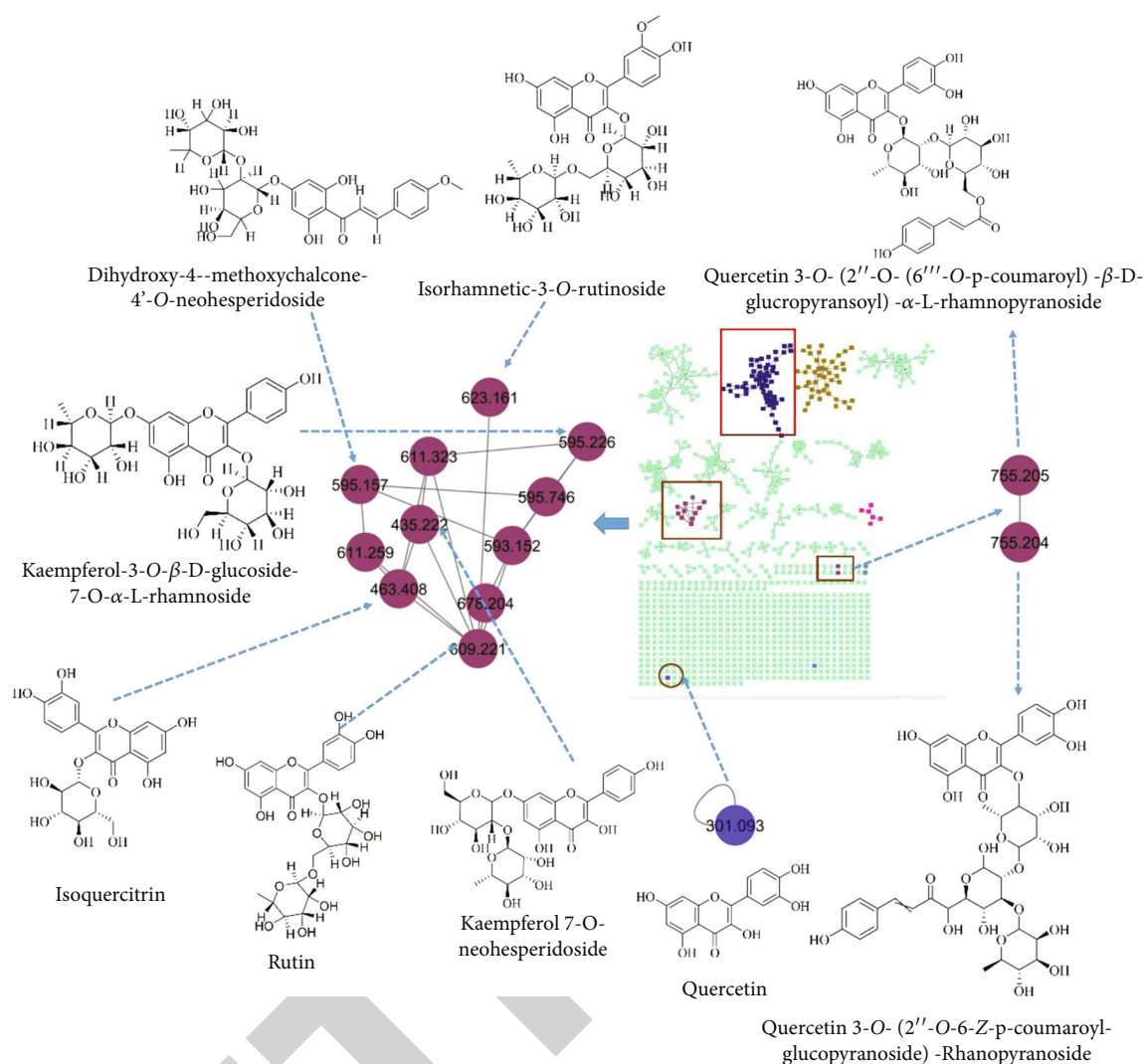


FIGURE 1: Molecular networking analysis of *M. azedarach* leaf extract showing presence of flavonoid O-glycosides using tandem mass data in negative ion mode.

or a test sample. Then, after a waiting period of 10-15 min when the arterial blood pressure was stabilized, standards and test materials were injected intravenously after that a flush of 0.1 mL saline was given. The effects of standards such as Ach ( $1 \mu\text{g}/\text{kg}$ ) and NE ( $1 \mu\text{g}/\text{kg}$ ) were monitored before injecting test material. Hypertensive rats with a BP of 150-190 mmHg were used for the study [35, 36].

**2.4.3. Safety Studies.** Balb-C mice weighing 20-25 g were used in the study for safety tests [37, 38]. These were arranged into four groups ( $n = 5$ ). Increasing doses of plant extract, i.e., 1 g/kg, 3 g/kg, and 5 g/kg, were fed to the animals in 10 mL/kg of saline serving as trial groups. To one group, saline was given (10 mL/kg, p.o.) and was considered as negative control group. During a 24 h test period, the mice were monitored for mortality and toxic symptoms such as anorexia, diarrhea, and lethargy.

## 2.5. In Vitro Experiments

**2.5.1. Vascular Reactivity Studies.** From both normal and hypertensive SD rats, thoracic aortic tissue was carefully

removed and placed in Krebs's solution. It was then prepared by cutting into 3 mm rings and hung in an organ bath in the presence of Krebs's solution and carbogen (5 percent carbon dioxide in oxygen). The organ bath was hyphenated to force transducer and PowerLab Data Acquisition System (AD Instruments, Australia). By changing buffer after every 15 min, the tissue was set to stabilize (60-90 min) at 2 g resting tension. Endothelium was intentionally damaged in a few aortic rings. To check endothelium integrity, after stabilization, contractions were induced with PE ( $1 \mu\text{M}$ ) that were inhibited using Ach ( $1 \mu\text{M}$ ). For 20-30 min, aortic ring preparations were incubated using  $L$ -NAME ( $10 \mu\text{M}$ ). The vasorelaxation produced by the extract and fractions was monitored in the absence as well as in presence of  $L$ -NAME. Responses to the test samples were tested in parallel in denuded tissues and tissues of hypertensive rats [36, 39].

**2.5.2. Isolated Right Atrial Preparations.** SD rats were used to check how the rate and force of contraction were affected by extract and fractions in right atrial preparations [40]. After



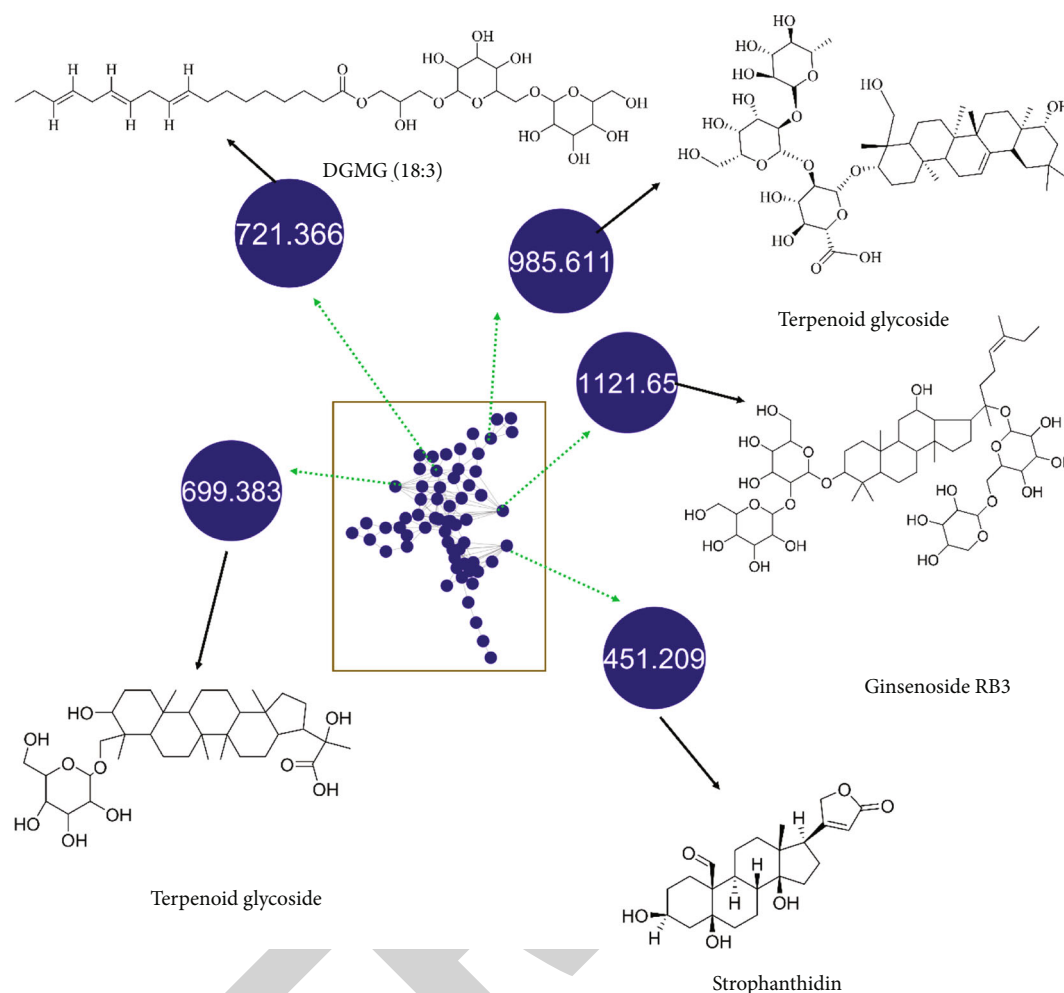


FIGURE 2: GNPS molecular networking outcomes of tandem mass analysis of *M. azedarach* crude extract indicating the presence of terpenoid glycosides.

dissection of the animal, the right atria was taken out and hung in a 10 mL organ bath filled with Krebs's solution at 32°C and in the presence of carbogen connected to a pressure transducer, which was hyphenated with a PowerLab Data Acquisition System. Pacemaker activity of atria caused it to beat freely during the equilibrium period (30 min) at preload of 1 g. Some tissues were incubated with atropine (1  $\mu$ M) to check if muscarinic receptor activation was involved.

**2.6. Statistical Analysis.** The mean standard error ( $\pm$ SEM) was used to express the data from the animal and *in vitro* investigations. The statistical differences between the treatments and the control were assessed using the IBM SPSS software and ANOVA followed by Tukey's test (version 20, SPSS Inc., Chicago, IL). Significance was determined at \* $p < 0.05$ , \*\* $p < 0.01$ , and \*\*\* $p < 0.001$ .

### 3. Results

**3.1. Metabolomic Results and Dereplication.** In the current study, spectroscopic analysis and GNPS molecular networking were used to study the complete phytochemical profile of

the extract and polarity-based fractions of *M. azedarach* leaves. Twenty nine compounds in total were determined in the Ma.Cr and fractions. The major constituents observed belonged to flavonoid *O*-glycoside, triterpenoids, lipids, and saponins. Table 1 enlists the compounds tentatively identified in the Ma.Cr and fractions in negative ion mode showing their retention time, MS/MS fragmentation patterns, and *m/z* values. *n*-Hexane fraction showed the presence of isoquercetin, kaempferol 7-*O*-hexosyl(1-2) deoxyhexoside, soyacerebroside-I, quercetin 3-*O*-neohesperidoside, fatty acid 18:4, monogalactosyl monoglycerol, and digalactosyl monoglycerol. The cluster containing quercetin 3-*O*- $\alpha$ -L-[6'''-*p*-coumaroyl-beta-D-glucopyranosyl-(1->2)-rhamnopyranoside] and quercetin-3-*O*-[2-*O*-6-*z*-*p*-coumaroyl-glucopyranoside]-rhamnopyranoside was observed separately as shown in Figure 1. Triterpenoidal glycosides like cardenolides, momordicoside, and genistin were observed in Ma.Cr, chloroform fraction, and *n*-hexane fraction, respectively, as shown in Figure 2. The observed constituents in chloroform fraction included kaempferol-7-*O*-neohesperidoside, quercetin, quercetin-3-*O*-[2-*O*-6-*z*-*p*-coumaroyl-glucopyranoside]-rhamnopyranoside, soyacerebroside I, keracyanin,

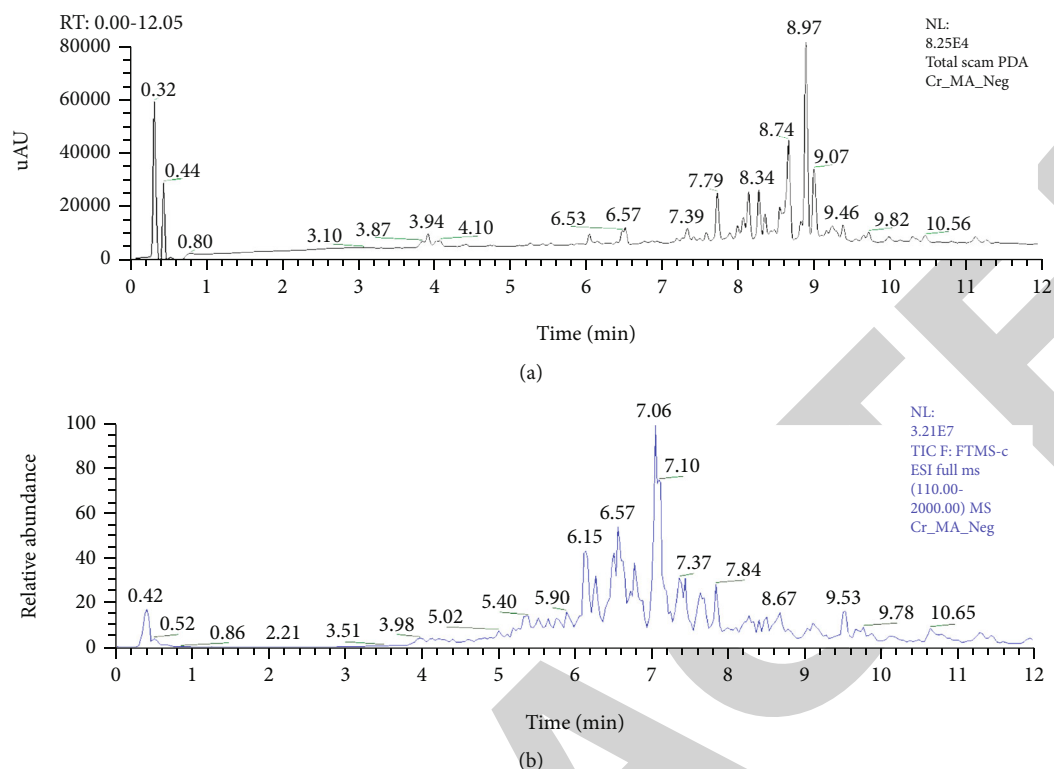


FIGURE 3: UHPLC-PDA-MS/MS analysis of crude extract from *M. azedarach* leaves in negative ion mode. UHPLC-PDA chromatogram of crude extract (a) and total ion chromatogram in negative ion mode (b).

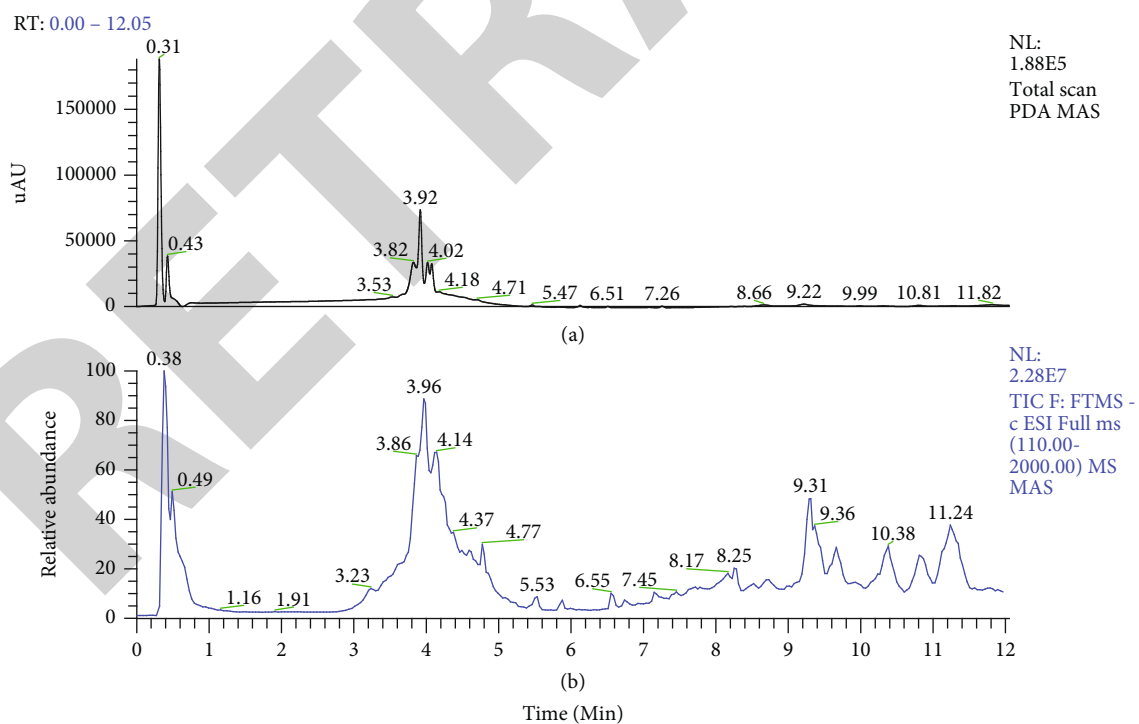


FIGURE 4: UHPLC-PDA-MS/MS analysis of *n*-butanol fraction from *M. azedarach* leaves in negative ion mode. UHPLC-PDA chromatogram of *n*-butanol fraction (a) and total ion chromatogram in negative ion mode (b).

isosakuranetin-7-*O*-neohesperidoside, and momordicoside. Constituents observed in the ethyl acetate fraction consisted of kaempferol 3-*O*-[2-*O*-(glucopyranoside)]-rhamnopyra-

noside, quercetin, and isoquercetin. Furthermore, isoquercitrin, isorhamnetin-3-*O*-galactoside-6''-rhamnoside, kaempferol 3-*O*-robinoside-7-*O*-rhamnoside, 7-*O*-methyl

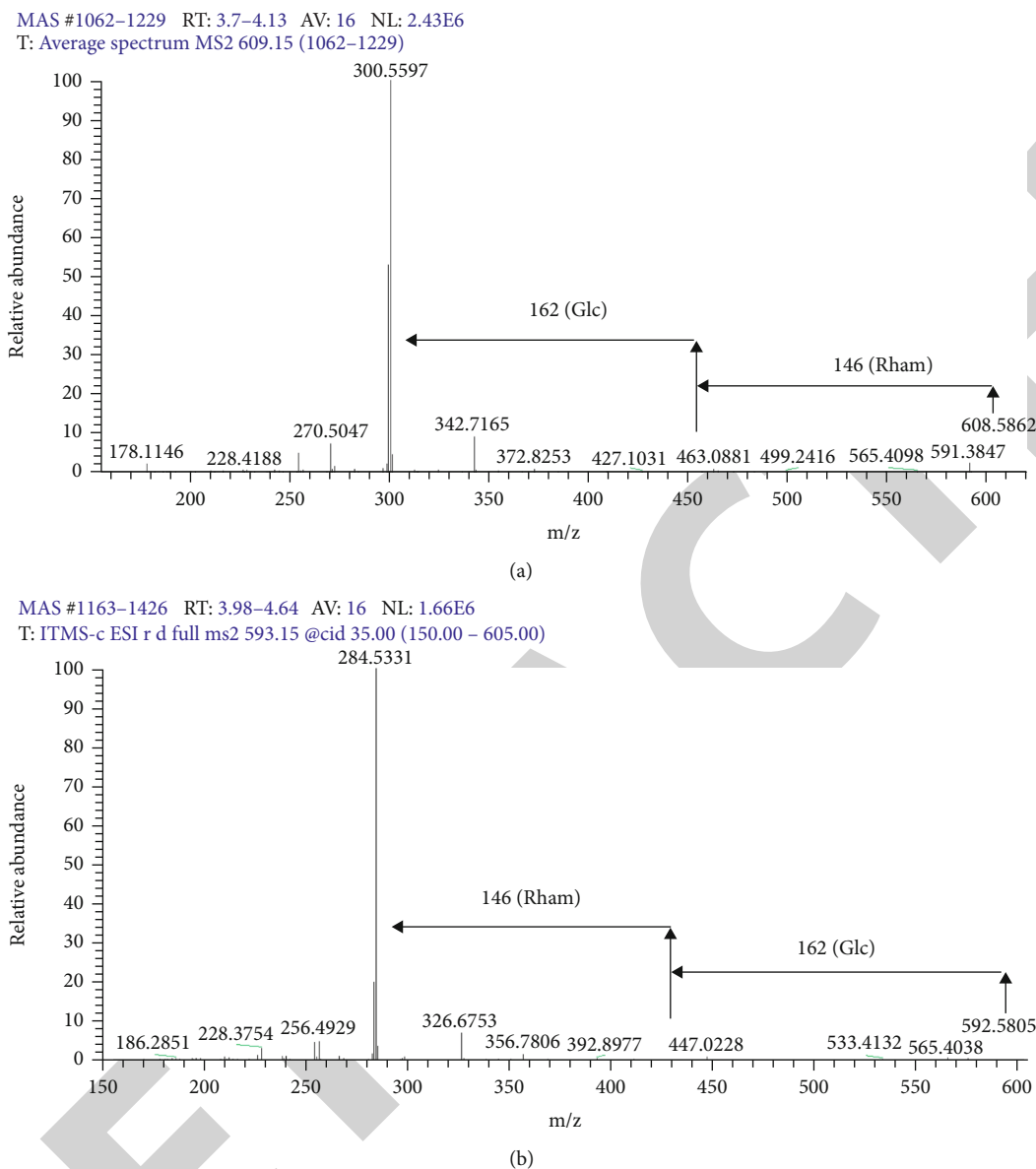


FIGURE 5: MS2 fragmentation pattern of quercetin 3-*O*-neohesperidoside (rutin) *m/z* is 609.15 (MS1) (a) and MS2 fragmentation pattern of kaempferol 7-*O*-neohesperidoside *m/z* is 593.15 (MS1) (b) from *M. azedarach* leaf extract.

genistein, quercetin 3-*O*-[2''-*O*-(6'''-*O*-*p*-coumaroyl)- $\beta$ -D-glucopyranosyl]- $\alpha$ -L-rhamnopyranoside, rutin, sulfobacin B, and nicotiflorin were tentatively detected in *n*-butanol fraction. In aqueous fraction, quercetin 3-*O*-[2-*O*-6-*Z*-*p*-coumaroyl-glucopyranoside]-rhamnopyranoside and quercetin 3-*O*-(2''-*O*-glucopyranoside)-rhamnopyranoside were observed. Flavonoid *O*-glycosides are grouped in one cluster (purple coloured) as shown by molecular networking analysis (Figure 1). The fragmentation of flavonoid *O*-glycosides as seen in a representative UV-chromatogram, total ion chromatogram, and mass spectra is given in Figures 3-5.

### 3.2. Pharmacological Studies

**3.2.1. Safety Studies.** The Ma.Cr in the concentration of 1, 3, and 5 g/kg was determined to be safe in mice, with no evi-

dence of lethality after 24 h of observation along with no behavioral changes, anorexia, diarrhea, or lethargy.

**3.2.2. Antihypertensive Effect.** Standards like NE (1  $\mu$ M) and Ach (1  $\mu$ M) were given before the administration of Ma.Cr and fractions. These drugs induced an increase and a decrease in blood pressure, respectively (Figure 6(a)). Blood pressure in normotensive and high blood pressure animals was  $118 \pm 4.13$  ( $n = 15$ ) and  $160 \pm 3.22$  ( $n = 15$ ), respectively. Ma.Cr was intravenously administered to the normotensive group after anesthetization, which resulted a fall in mean arterial pressure (MAP). At the dose levels of 1, 3, 10, 30, 100, 150, and 300 mg/kg of Ma.Cr, a concentration-dependent lowering of MAP, i.e.,  $2.53 \pm 1.6$ ,  $8.36 \pm 1.3$ ,  $15.43 \pm 2.7$ ,  $26.23 \pm 2.1$ ,  $37.82 \pm 1.2$ ,  $51.85 \pm 1.1$ , and  $65.36 \pm 1.8$  mmHg, was observed, respectively (Figure 6(c)). All

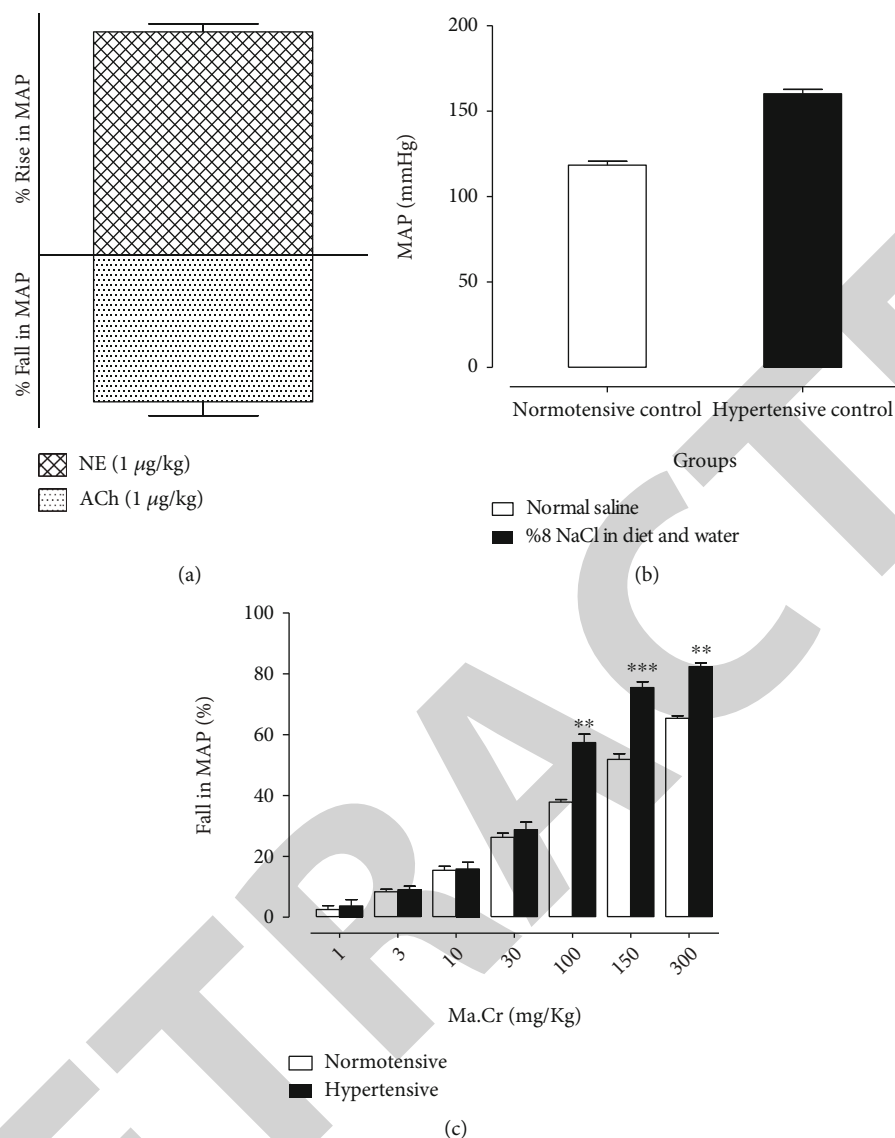


FIGURE 6: The hypertensive and hypotensive effects of norepinephrine (NE) and acetylcholine (ACh), respectively. (a) The blood pressure of normotensive and hypertensive rats. (b) The effect of crude extract of *M. azedarach* (Ma.Cr) (c) on MAP in normotensive and hypertensive rats, under anesthesia ( $n = 6-7$ ); \* $p < 0.05$ , \*\* $p < 0.01$ , and \*\*\* $p < 0.001$ .

fractions tested reduced MAP, with the ethyl acetate fraction at 300 mg/kg dose showing the highest efficacy ( $77.06 \pm 3.77$ ) (Figure 7(a)). When compared to pretreated groups, the percent decrease in all cases was statistically significant ( $p \leq 0.05$ ) at different doses as shown in Figures 7(a)–7(e). Prior incubation of the tissue with atropine ( $1 \mu\text{M}$ ) did not change the effects produced with Ma.Cr and fractions (data not shown).

**3.2.3. Antihypertensive Effect on Hypertensive Rats.** Ma.Cr caused a significant decrease in MAP in hypertensive rats under anaesthesia than in the normotensive groups. By the administration of Ma.Cr, the % decrease in MAP at dose levels of 1, 3, 10, 30, 100, 150, and 300 mg/kg was  $3.51 \pm 2.8$ ,  $8.95 \pm 3.2$ ,  $15.6 \pm 3.5$ ,  $28.49 \pm 4.3$ ,  $57.4 \pm 5$ ,  $73.71 \pm 3.0$ , and  $81.44 \pm 2.1$  mmHg (Figure 6(c)). Ethyl acetate fraction had the highest blood pressure-lowering effect when compared with other fractions. It caused a percent fall in MAP

of  $5.44 \pm 1.6$ ,  $13.66 \pm 1.8$ ,  $24.00 \pm 4.4$ ,  $34.78 \pm 4.8$ ,  $50.77 \pm 5.2$ ,  $77.41 \pm 3.02$ , and  $88.96 \pm 1.3$  mmHg, at respective doses (Figures 7(a)–7(e)). Atropine ( $1 \mu\text{M}$ ) pretreatment did not alter the responses produced by Ma.Cr and fractions (data not shown).

**3.2.4. Nitric Oxide Release-Dependent Effect.** The response of Ma.Cr and fractions was determined using the tissues that induced more than 80% relaxation upon administration of acetylcholine. The contractions were induced with phenylephrine (PE) ( $1 \mu\text{M}$ ) in rings with intact endothelium. The addition of Ma.Cr in the cumulative pattern caused nitric oxide (NO) release-based vasorelaxation showing the  $\text{EC}_{50}$  of 0.70 mg/mL (0.5–1.2).  $\text{L-NAME}$  incubation of intact tissue resulted in an inhibition of the vasorelaxation potential of Ma.Cr, and only 20% relaxation was observed (Figure 8(b)). Ma.Cr did not significantly relax the denuded tissue

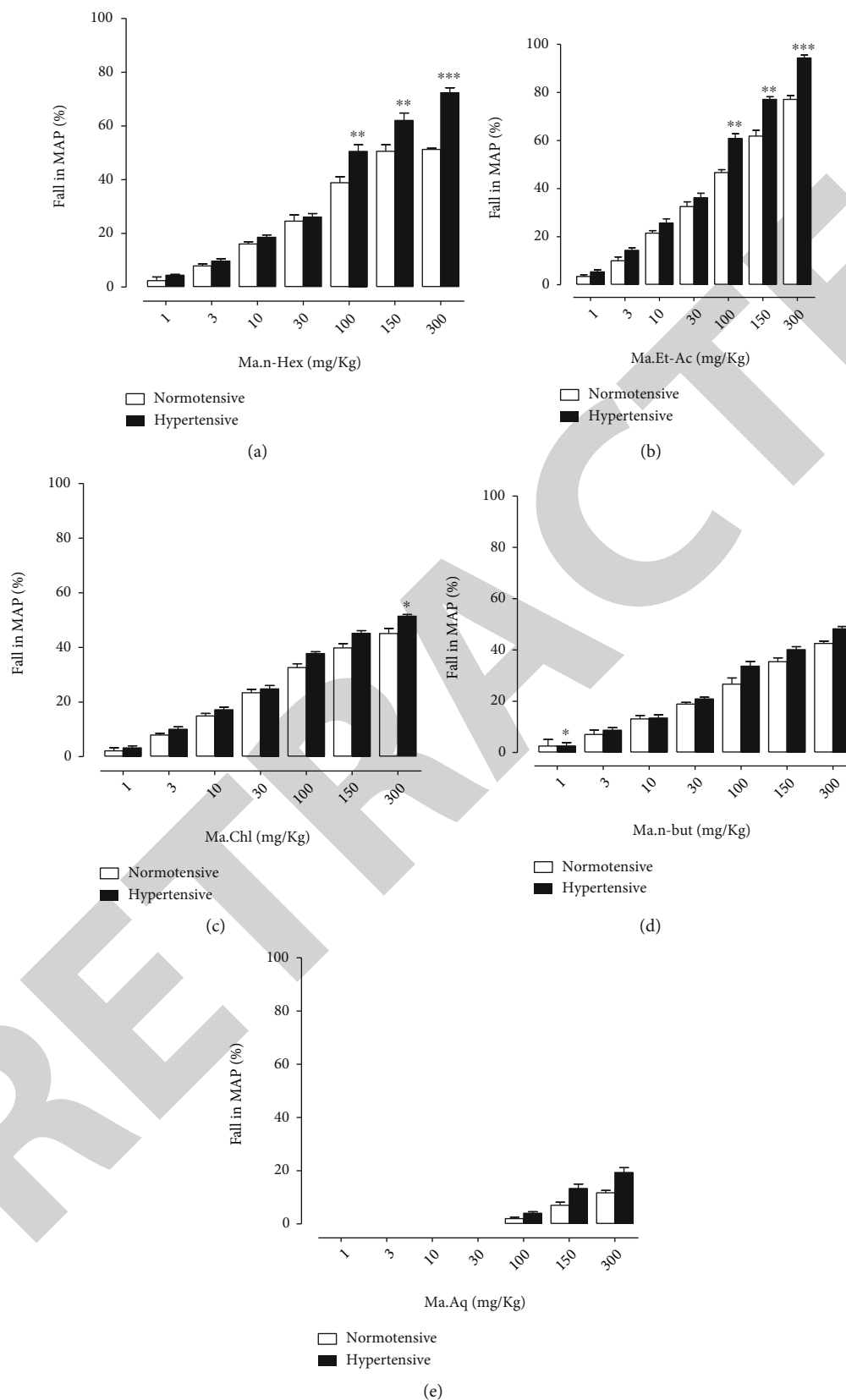


FIGURE 7: Graphs show the effect of ethyl acetate (Ma.EtOAc) (a), *n*-hexane (Ma.*n*-Hex) (b), chloroform (Ma.Chl) (c), *n*-butanol (Ma.*n*-but) (d), and aqueous (Ma.Aq) (e) fractions of *M. azedarach* on mean arterial pressure (MAP) in normotensive and hypertensive rats, under anesthesia. Values shown are mean  $\pm$  SEM ( $n = 6 - 7$ ); \* $p < 0.05$ , \*\* $p < 0.01$ , and \*\*\* $p < 0.001$ .

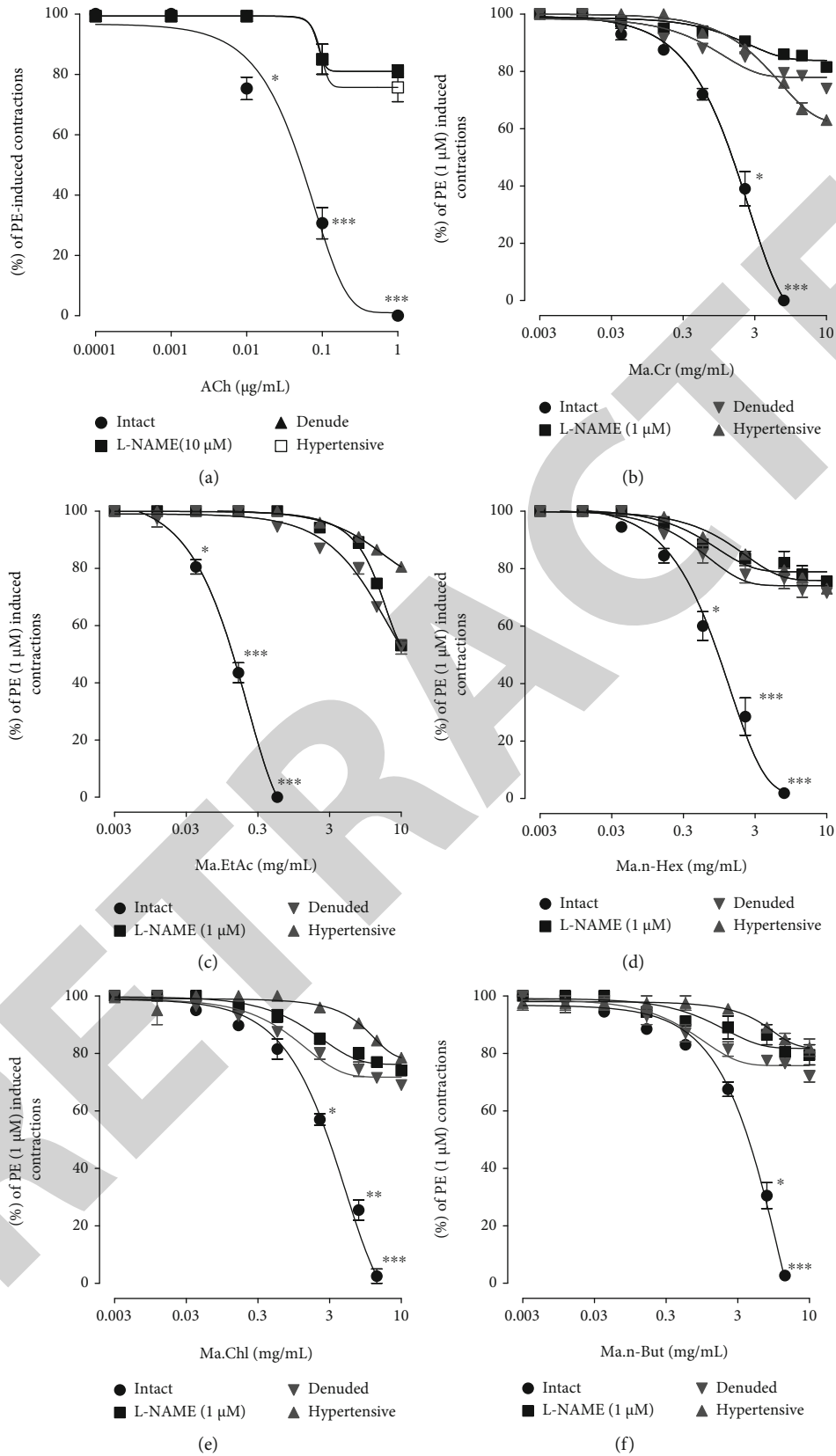


FIGURE 8: Continued.

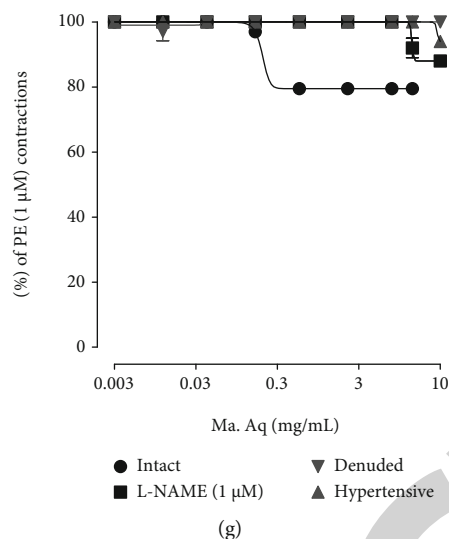


FIGURE 8: Graphs show the response of acetylcholine (a), crude extract of *M. azedarach* (Ma.Cr) (b), its fractions ethyl acetate (Ma.EtOAc) (c), *n*-hexane (Ma.*n*-Hex) (d), chloroform (Ma.Chl) (e), *n*-butanol (Ma.*n*-But) (f), and aqueous (Ma.Aq) (g) on PE-induced contractions in intact (with and without  $L$ -NAME (10  $\mu$ M) pretreatment), denuded aortic rings from normotensive rats and rings from hypertensive rats. Values shown are mean  $\pm$  SEM ( $n = 6-7$ ); \* $p < 0.05$ , \*\* $p < 0.01$ , and \*\*\* $p < 0.001$ .

even at increasing doses. It only induced 26% relaxation at the highest dose. Ma.Cr did not relax the tissue in hypertensive rats' aorta rings precontracted with PE and elicited only 37% relaxation. Similar results were obtained with ethyl acetate fraction on rat aorta. Endothelium-dependent vasorelaxation was elicited in intact tissue with the  $EC_{50}$  value of 0.086 mg/mL (0.05-0.13). The vasorelaxant effect was blocked in intact tissues upon incubation with  $L$ -NAME (10  $\mu$ M), tissues with damaged endothelium and hypertensive groups. Chloroform, *n*-hexane, and *n*-butanol like crude extract also elicited NO release-dependent relaxation (Figures 8(b)–8(g)). The blood pressure-lowering effect produced by Ma.Cr and its fractions was unaffected upon treatment of tissue with atropine (1  $\mu$ M) (data not shown).

High  $K^+$  (80 mM) was utilized to see if the crude extract and fractions have any effect on vascular smooth muscles. Relaxation was caused by the addition of different concentrations of extract and fractions in a cumulative pattern (Figure 9(a)). High efficacy was observed with the ethyl acetate fraction whereas the aqueous fraction has lower activity and caused only partial inhibition. A typical calcium channel blocker, verapamil, was used to induce the endothelium-independent relaxant effect as shown in Figure 9(b).

**3.2.5. Studies on Atrial Tissues.** Rhythmic contractions and relaxations were exhibited by right atria from normotensive animals where the use of acetylcholine in cumulative pattern blocked force (negative inotropic) and rate (negative chronotropic) of contraction, which was also blocked with atropine thus confirming the protocol (Figure 10(a)). The crude extract caused partial inhibition of both rate and force of atrial contractions with the  $EC_{50}$  of 4.18 mg/mL (3.9-8.08) and 5.29 mg/mL (4.71-10.0), respectively. The ethyl acetate fraction completely blocked both rate and force of atrial contractions with the  $EC_{50}$  of 1.38 mg/mL (0.3-1.68) and

0.75 mg/mL (0.55-1.30), respectively (Figure 10(b)). Atropine incubation did not alter either of these responses.

Rate and force of atrial contractions were fully inhibited in the presence of *n*-hexane fraction showing the  $EC_{50}$  of 2.34 mg/mL (1.66-4.0) and 1.95 mg/mL (0.9-2.85), respectively. On the other hand, the chloroform, *n*-butanol, and aqueous fraction did not induce suppression (Figures 10(c)–10(f)). Preincubation with atropine did not alter the responses of these fractions as well.

## 4. Discussion

The methanolic extract of leaves of *M. azedarach* was phytochemically analyzed using LC-MS/MS and GNPS molecular networking. The outcomes of phytochemical profiling showed 29 compounds including simple flavonoids, flavonoid *O*-glycosides, glycolipids, fatty acids, and glycerophosphoinositols, which are varied in terms of structure and fragmentation patterns. Glucose, rhamnose, and pentose were observed, respectively, at 162, 146, and 132 Da as a result of fragmentation of flavonoid-*O*-glycosides [41]. Previously, quercetin, rutin, isoquercetin, kaempferol 7-*O*-neohesperidoside, isorhamnetin 3-*O*-rutinoside, and isosakuranetin 7-*O*-neohesperidoside were reported from *M. azedarach* using LC-MS/MS analysis [42]. One metabolite is representing each node in molecular networking analysis, marked based on its  $m/z$  value. On the basis of similarity in their core chemical structure and fragmentation pattern, different metabolites are grouped accordingly. The ethyl acetate fraction with highest potential as an antihypertensive consisted of the flavonoid *O*-glycosides, i.e., isoquercetin and kaempferol 3-*O*-[2-*O*-(glucopyranoside)] rhamnopyranoside. By the fragmentation of isoquercetin and rutin, quercetin was obtained whereas isorhamnetin-3-*O*-rutinoside and isorhamnetin-3-*O*-glucoside were fragmented to give

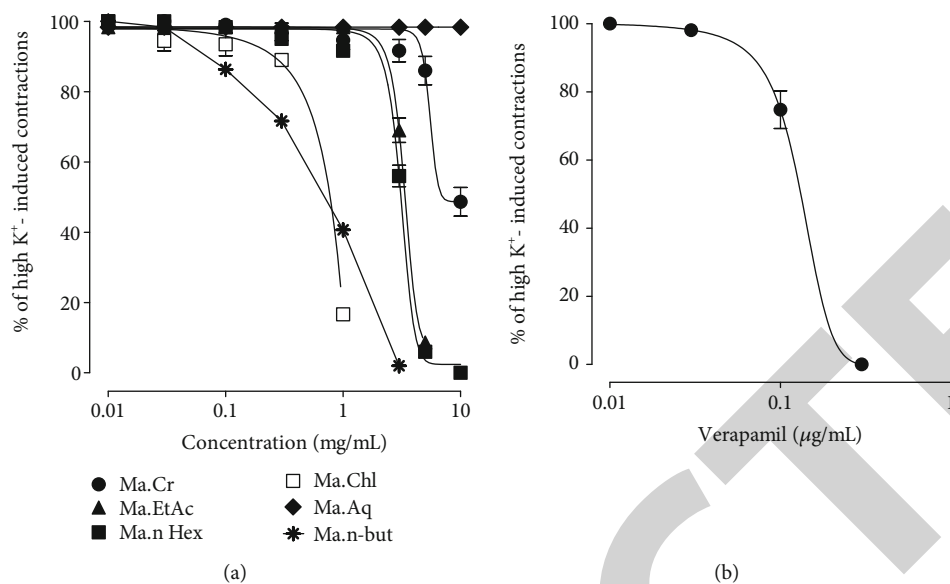


FIGURE 9: Graph shows vasodilator effect of crude extract of *M. azedarach* (Ma.Cr), its fractions ethyl acetate (Ma.EtAc), *n*-Hexane (Ma.nHex), chloroform (Ma.Chl), *n*-butanol (Ma.n-but) and aqueous (Ma.Aq) (a) verapamil (b) on high K<sup>+</sup> (80 mM)-induced contractions in isolated rat aorta rings. Values shown are mean  $\pm$  SEM ( $n = 6-7$ ); \* $p < 0.05$ , \*\* $p < 0.01$ , and \*\*\* $p < 0.001$ .

isorhamnetin. The *n*-hexane fraction contained flavonoid glycosides along with phospholipids and exhibited higher activity after ethyl acetate. The molecular networks of flavonoid *O*-glycosides observed in *M. azedarach* are shown in Figure 1.

Safety studies of the plant were carried out to determine the safety profile for oral use at different doses. It was found that the plant is safe for up to 5 g/kg oral dose. Using an invasive blood pressure approach, Ma.Cr and fractions have a relaxant effect in both normotensive and hypertensive anaesthetized rats, being more potent in hypertensive rats, indicating its antihypertensive potential. The ethyl acetate fraction had a greater relaxant effect when Ma.Cr and fractions were compared. Similarly, in high salt-induced hypertensive rats, the ethyl acetate fraction was found to be more effective. BP is the multiple of cardiac output and peripheral resistance [43, 44]. On the basis of the above-mentioned outputs, this plant was considered for further study *in vitro* to determine the underlying blood pressure-lowering mechanism.

Ma.Cr and ethyl acetate fractions relaxed PE (1  $\mu$ M) induced precontraction in an isolated tissue with an intact endothelium, suggesting the possible involvement of nitric oxide (NO-endothelium-derived relaxing factor) [45]. NO is a powerful vasodilator produced by NO synthase in the endothelium [46] and causes vascular relaxation [47]. Ma.Cr and its fractions did not show a relaxation response to PE (1  $\mu$ M) in high salt-induced hypertensive rat aorta even at higher doses. It has been shown that high dietary salt decreases plasma nitrate and impairs endothelial function [36, 48]. Inhibition of NO synthase or increased superoxide production may be responsible for the unavailability of NO-dependent vascular relaxation [49]. When the tissue was pretreated with L-NAME, an inhibitor of nitric oxide synthase [50, 51], it reduced the vasorelaxant effect caused by

Ma.Cr and fractions similar to denuded tissues. This is an evidence of the involvement of endothelium-based relaxation and NO release.

Ma.Cr and fractions were studied on PE (1  $\mu$ M) and high K<sup>+</sup> (80 mM) based contractions in aortic tissue to determine their effect on voltage-dependent calcium channels (VDCs) [52]. Mechanism of high K<sup>+</sup> (80 mM) induced contractions involves vascular smooth muscle cells and the opening of voltage-dependent L-type Ca<sup>++</sup> channels, as a result of which extracellular Ca<sup>++</sup> enters the cells and produces contractions [36]. The substance that blocks these contractions is recognized as the blocker of Ca<sup>++</sup> influx [53]. When added cumulatively to the precontracted aortic ring, the Ma.Cr and fractions were more potent against PE (1  $\mu$ M) in comparison to high K<sup>+</sup>-induced contractions (80 mM) [54].

The release of calcium from internal stores and also from receptor-operated calcium channels (ROCs) was considered to be blocked by Ma.Cr and its fractions as a result of relaxation of PE (1  $\mu$ M) contractions. Ma.Cr and its fractions were found to be devoid of any contraction upon cumulative addition to the steady-state baseline.

The atrial preparations were studied to determine the involvement of cardiac function in antihypertensive activity. The rate and force of atrial contraction were completely suppressed when atrial preparations were treated with Ma.Cr, ethyl acetate, and *n*-hexane fraction. However, the aqueous, *n*-butanol, and chloroform fractions did not show similar results. Pretreatment of atrial tissues with atropine was carried out to rule out possible involvement of cardiac muscarinic receptor activation in effect of Ma.Cr and fractions. As a result, it was found that rate and force of atrial contraction were not affected by this pretreatment, and thus, muscarinic receptors are not involved [36]. From these results, it can be assumed that decrease in rate and force of atrial contraction may also be related to blockade of calcium



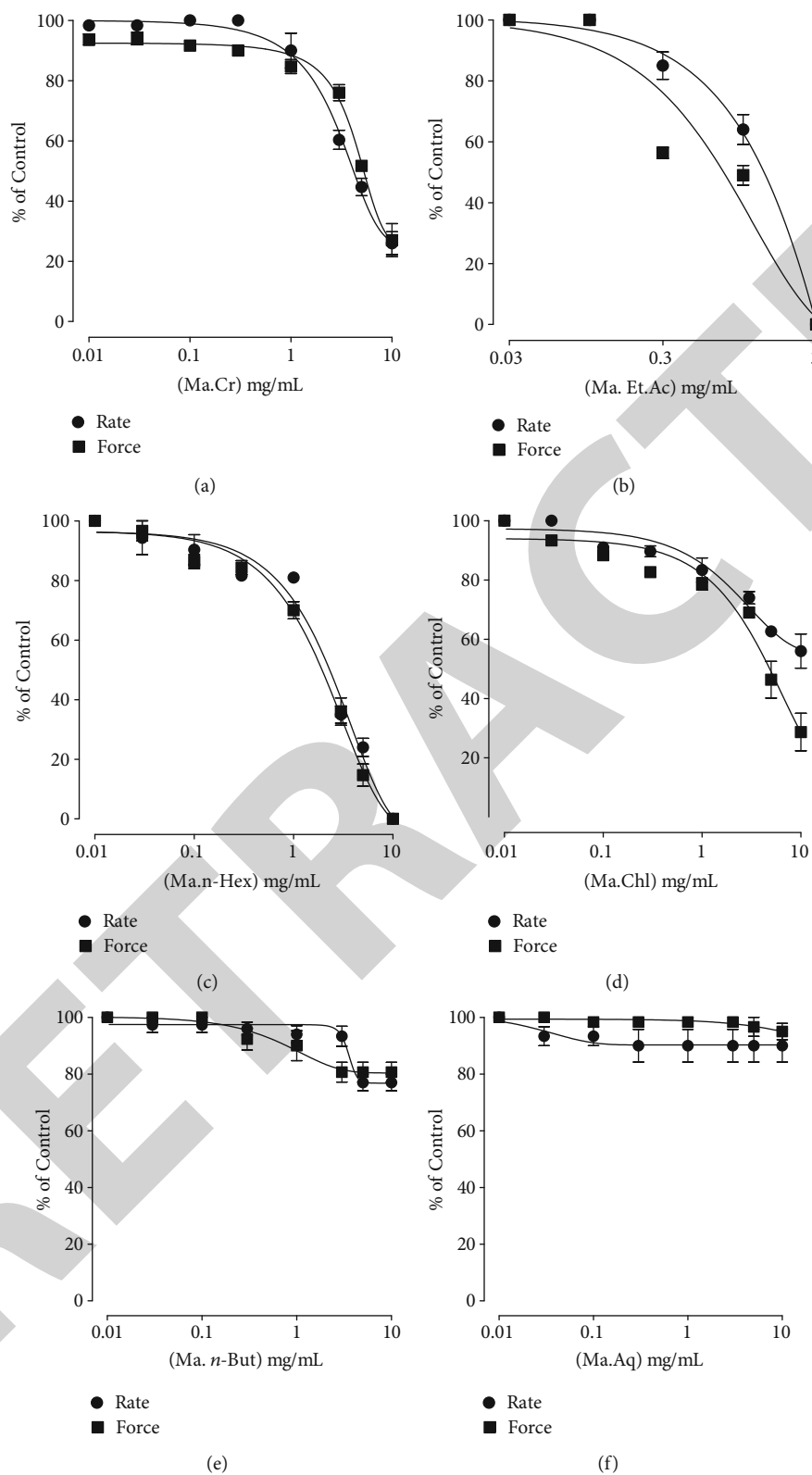


FIGURE 10: Concentration-response curves show the effect of crude extract (Ma.Cr) (a), and fractions, i.e., *n*-hexane (Ma.*n*-hexane) (b), chloroform (Ma.Chl) (c), ethyl acetate (Ma.EtOAc) (d), *n*-butanol (Ma.*n*-but) (e), and aqueous (Ma.Aq) (f) of *M. azedarach* on spontaneously occurring rate and force of contraction in isolated SD rat right atrial preparations. The values shown are mean  $\pm$  SEM ( $n = 5$ ).

transport, i.e., its release from internal stores or influx through VDCs.

The phytochemical profiling demonstrated the richness of the extract and fractions in flavonoid glycosides. Previous studies have shown that flavonoid glycosides contribute to cardiovascular protection [55, 56] and possess anticholinesterase activity [57]. For that reason, the flavonoids present in this plant may be responsible for antihypertensive activity. Similarly, it has been reported that quercetin, kaempferol (flavonoids), campesterol, and stigmasterol (phytosterols) are the key chemical constituents of *M. azedarach* extract [17]. Quercetin, an anticholinesterase [58] and antihypertensive [59] constituent, may be involved in the fall in MAP.

Based on the phenolic profile, we speculate that the antihypertensive activity of *M. azedarach* extract may be partly related to its flavonoid contents. Ma.Cr and its fraction possess vasorelaxation effects through nitric oxide pathways and maybe through calcium channel blocking. Plant-based constituents have vasodilator potential through multiple pathways like NO pathways [60] or through inhibition of calcium release from  $Ca^{++}$  stores [45] in addition to many other mechanisms.

## 5. Conclusion

Detailed phytochemical studies of *M. azedarach* leaves were carried out by highly sensitive LC-MS/MS technique and GNPS molecular networking. Flavonoid O-glycosides, terpenoidal saponins, terpenoidal glycosides, and simple flavonoids were tentatively determined in *M. azedarach* leaves. Flavonoid glycosides were considered to be a major constituent in Ma.Cr and bioactive fractions. Current findings on the cardiovascular activities of *M. azedarach* extract and fractions revealed that it contains phytoconstituents that mediate the relaxant effect via the NO pathway, which could explain its antihypertensive effect. These findings provide a pharmacological foundation for *M. azedarach*'s traditional medical use as an antihypertensive remedy.

## Data Availability

The data will be available on demand.

## Conflicts of Interest

The authors declare that they have no competing interests.

## References

- [1] K. T. Mills, J. D. Bundy, T. N. Kelly et al., "Global disparities of hypertension prevalence and control," *Circulation*, vol. 134, no. 6, pp. 441–450, 2016.
- [2] WHO-World Health Organization, "Fact sheet on hypertension," 2019, <https://www.who.int/news-room/fact-sheets/detail/hypertension>.
- [3] N. Shah, Q. Shah, and A. J. Shah, "The burden and high prevalence of hypertension in Pakistani adolescents: a meta-analysis of the published studies," *Archives of Public Health*, vol. 76, no. 1, pp. 1–10, 2018.
- [4] M. A. Pfeffer and E. D. Frohlich, "Improvements in clinical outcomes with the use of angiotensin-converting enzyme inhibitors: cross-fertilization between clinical and basic investigation," *American Journal of Physiology-Heart and Circulatory Physiology*, vol. 291, no. 5, pp. H2021–H2025, 2006.
- [5] C. Tsioufis and C. Thomopoulos, "Combination drug treatment in hypertension," *Pharmacological Research*, vol. 125, pp. 266–271, 2017.
- [6] X. Rossello, S. J. Pocock, and D. G. Julian, "Long-term use of cardiovascular drugs: challenges for research and for patient care," *Journal of the American College of Cardiology*, vol. 66, no. 11, pp. 1273–1285, 2015.
- [7] D. Praveen, D. Peiris, S. MacMahon et al., "Cardiovascular disease risk and comparison of different strategies for blood pressure management in rural India," *BMC Public Health*, vol. 18, no. 1, pp. 1–11, 2018.
- [8] S. Khiljee, N. U. Rehman, T. Khiljee, R. S. Ahmad, M. Y. Khan, and U. A. Qureshi, "Use of traditional herbal medicines in the treatment of eczema," *Journal of Pakistan Association of Dermatology*, vol. 21, pp. 112–117, 2011.
- [9] N. H. Mashour, G. I. Lin, and W. H. Frishman, "Herbal medicine for the treatment of cardiovascular disease," *Archives of Internal Medicine*, vol. 158, no. 20, pp. 2225–2234, 1998.
- [10] B. Singh, "Medicinal plants and phytomedicines," in *Herbal insecticides, repellents and biomedicines: effectiveness and commercialization*, pp. 127–145, Springer, New Delhi, 2016.
- [11] N. Mukungu, K. Abuga, F. Okalebo, R. Ingwela, and J. Mwangi, "Medicinal plants used for management of malaria among the Luhya community of Kakamega East sub-county, Kenya," *Journal of Ethnopharmacology*, vol. 194, pp. 98–107, 2016.
- [12] D. Sharma and Y. Paul, "Preliminary and pharmacological profile of *Melia azedarach* L.: an overview," *Journal of Applied Pharmaceutical Science*, vol. 3, pp. 133–138, 2013.
- [13] M. F. Ahmed, M. Ibrahim, H. Thayyil, K. Zameeruddin, and M. Ibrahim, "Antioxidative activity of *Melia azedarach* Linn leaf extract," *Iranian Journal of Pharmacology and Therapeutics*, vol. 7, pp. 31–34, 2008.
- [14] M. Ayyanar and S. Ignacimuthu, "Ethnobotanical survey of medicinal plants commonly used by Kani tribals in Tirunelveli hills of Western Ghats, India," *Journal of Ethnopharmacology*, vol. 134, no. 3, pp. 851–864, 2011.
- [15] A. R. Vishnukanta, "*Melia azedarach*: a phytopharmacological review," *Pharmacognosy Reviews*, vol. 2, pp. 173–179, 2008.
- [16] H. Ishaq, "Anxiolytic and antidepressant activity of different methanolic extracts of *Melia azedarach* Linn," *Pakistan Journal of Pharmaceutical Sciences*, vol. 29, no. 5, pp. 1649–1655, 2016.
- [17] A. N. T. A. R. A. Sen and A. M. L. A. Batra, "Chemical composition of methanol extract of the leaves of *Melia azedarach* L.," *Asian Journal of Pharmaceutical and Clinical Research*, vol. 5, pp. 42–45, 2012.
- [18] M. C. Carpinella, C. G. Ferrayoli, and S. M. Palacios, "Antifungal synergistic effect of scopoletin, a hydroxycoumarin isolated from *Melia azedarach* L. fruits," *Journal of Agricultural and Food Chemistry*, vol. 53, no. 8, pp. 2922–2927, 2005.
- [19] L. E. Alché, G. A. Ferek, M. Meo, C. E. Coto, and M. S. Maier, "An antiviral meliacarpin from leaves of *Melia azedarach* L.," *A Journal of Biosciences*, vol. 58, no. 3–4, pp. 215–219, 2003.
- [20] R. Mandal and P. K. Dhaliwal, "Antifertility effect of *Melia azedarach* Linn. (dharek) seed extract in female albino rats," *Indian Journal of Experimental Biology*, vol. 45, no. 10, pp. 853–860, 2007.

- [21] M. C. Carpinella, M. Miranda, W. R. Almiron, C. G. Ferrayoli, F. L. Almeida, and S. M. Palacios, "In vitro pediculicidal and ovicidal activity of an extract and oil from fruits of *Melia azedarach* L.," *Journal of the American Academy of Dermatology*, vol. 56, no. 2, pp. 250–256, 2007.
- [22] C. B. Wandscheer, J. E. Duque, M. A. da Silva et al., "Larvicidal action of ethanolic extracts from fruit endocarps of *Melia azedarach* and *Azadirachta indica* against the dengue mosquito *Aedes aegypti*," *Toxicon*, vol. 44, no. 8, pp. 829–835, 2004.
- [23] N. Gayatri and S. R. Kanta, "In vitro antioxidative activity of *Azadirachta indica* and *Melia azedarach* leaves by DPPH scavenging assay," *Natural Science*, vol. 8, pp. 22–28, 2010.
- [24] S. V. Kumar, D. B. Sanghai, C. M. Rao, and C. S. Shreedhara, "Histological and physiochemical standardization of *Melia azedarach* Linn bark," *Asian Pacific Journal of Tropical Biomedicine*, vol. 2, no. 1, pp. S284–S289, 2012.
- [25] M. F. Khan, A. K. Rawat, B. Pawar, S. Gautam, A. K. Srivastava, and D. S. Negi, "Bioactivity-guided chemical analysis of *Melia azedarach* L. (Meliaceae), displaying antidiabetic activity," *Fitoterapia*, vol. 98, pp. 98–103, 2014.
- [26] S. Shams and S. Pourseyedi, "Green synthesis of silver nanoparticles in *Melia Azedarach* fruit extract and screening its antimicrobial activity," *Scientific Journal of Agriculture*, vol. 38, pp. 55–63, 2015.
- [27] A. Mehmood, G. Murtaza, T. M. Bhatti, and R. Kausar, "Phyto-mediated synthesis of silver nanoparticles from *Melia azedarach* L. leaf extract: characterization and antibacterial activity," *Arabian Journal of Chemistry*, vol. 10, pp. S3048–S3053, 2017.
- [28] G. Chinnasamy, S. Chandrasekharan, and S. Bhatnagar, "Bio-synthesis of silver nanoparticles from *Melia azedarach*: enhancement of antibacterial, wound healing, antidiabetic and antioxidant activities," *International Journal of Nanomedicine*, vol. Volume 14, pp. 9823–9836, 2019.
- [29] T. J. Malar, J. Antonyswamy, P. Vijayaraghavan et al., "In-vitro phytochemical and pharmacological bio-efficacy studies on *Azadirachta indica* A. Juss and *Melia azedarach* Linn for anticancer activity," *Saudi Journal of Biological Sciences*, vol. 27, no. 2, pp. 682–688, 2020.
- [30] S. S. Shrestha, I. Ferrarese, S. Sut et al., "Phytochemical investigations and in vitro bioactivity screening on *Melia azedarach* L. leaves extract from Nepal," *Chemistry & Biodiversity*, vol. 18, no. 5, article e2001070, 2021.
- [31] A. Saeed, F. Wahid, H. M. Rasheed, R. Qayyum, A. J. Shah, and T. Khan, "Effects of *Heliotropium strigosum* and *Trapa bicornis* in hyperactive gut disorders," *Bangladesh Journal of Pharmacology*, vol. 12, no. 2, pp. 190–196, 2017.
- [32] M. Wang, J. J. Carver, V. V. Phelan et al., "Sharing and community curation of mass spectrometry data with global natural products social molecular networking," *Nature Biotechnology*, vol. 34, no. 8, pp. 828–837, 2016.
- [33] National Research Council, *Guide for the Care and Use of Laboratory Animals*, National Academy Press, Washington DC, 8th ed. edition, 2011.
- [34] J. E. Lawler, B. J. Sanders, Y. F. Chen, S. Nagahama, and S. Oparil, "Hypertension produced by a high sodium diet in the borderline hypertensive rat (BHR)," *Clinical and Experimental Hypertension*, vol. 9, no. 11, pp. 1713–1731, 1987.
- [35] A. J. Shah and A. H. Gilani, "Blood pressure-lowering and vascular modulator effects of *Acorus calamus* extract are mediated through multiple pathways," *Journal of Cardiovascular Pharmacology*, vol. 54, no. 1, pp. 38–46, 2009.
- [36] U. Salma, T. Khan, and A. J. Shah, "Antihypertensive effect of the methanolic extract from *Eruca sativa* Mill. (Brassicaceae) in rats: muscarinic receptor-linked vasorelaxant and cardiotonic effects," *Journal of Ethnopharmacology*, vol. 224, pp. 409–420, 2018.
- [37] J. S. Akhila, D. Shyamjith, and M. C. Alwar, "Acute toxicity studies and determination of median lethal dose," *Current Science*, vol. 93, pp. 917–920, 2007.
- [38] S. F. Ansari, A. U. Khan, N. G. Qazi, F. A. Shah, and K. Naeem, "In vivo, proteomic, and in silico investigation of sapodilla for therapeutic potential in gastrointestinal disorders," *BioMed Research International*, vol. 2019, 19 pages, 2019.
- [39] S. S. K. Chan, O. K. C. Angela, and L. J. Robert, "Mechanisms underlying the vasorelaxing effects of butylidenephthalide, an active constituent of *Ligusticum chuanxiong*, in rat isolated aorta," *European Journal of Pharmacology*, vol. 537, no. 1–3, pp. 111–117, 2006.
- [40] N. Yoshihisa, K. Ichihara, R. Yoshida, and Y. Abiko, "Positive inotropic and negative chronotropic effects of (–)-cis-diltiazem in rat isolated atria," *British Journal of Pharmacology*, vol. 105, no. 3, pp. 696–702, 1992.
- [41] W. H. B. Hassan, S. Abdelaziz, and H. M. Al Yousef, "Chemical composition and biological activities of the aqueous fraction of *Parkinsonia aculeata* L. growing in Saudi Arabia," *Arabian Journal of Chemistry*, vol. 12, no. 3, pp. 377–387, 2019.
- [42] Y. M'rabet, N. Rokbeni, S. Cluzet et al., "Profiling of phenolic compounds and antioxidant activity of *Melia azedarach* L. leaves and fruits at two stages of maturity," *Industrial Crops and Products*, vol. 107, pp. 232–243, 2017.
- [43] O. Arunlakshana and H. O. Schild, "Some quantitative uses of drug antagonists," *British Journal of Pharmacology*, vol. 14, no. 1, pp. 48–58, 1959.
- [44] I. Ul Haq, T. Khan, T. Ahmad, and A. J. Shah, "Insight into the cardiovascular mechanisms of blood pressure lowering effect of gitogenin: a steroidal saponin," *Clinical and Experimental Hypertension*, vol. 43, no. 8, pp. 723–729, 2021.
- [45] R. Qayyum, H. M. U. D. Qamar, S. Khan, U. Salma, T. Khan, and A. J. Shah, "Mechanisms underlying the antihypertensive properties of *Urtica dioica*," *Journal of Translational Medicine*, vol. 14, no. 1, pp. 1–13, 2016.
- [46] S. Joen-Rong, "Pharmacological effects of rutaecarpine, an alkaloid isolated from *Evodia rutaecarpa*," *Cardiovascular Drug Reviews*, vol. 17, no. 3, pp. 237–245, 1999.
- [47] E. Martin, K. Davis, and K. Bian, "Cellular signaling with nitric oxide and cyclic guanosine monophosphate," *Seminars in Perinatology*, vol. 24, pp. 2–6, 2000.
- [48] S. Moncada, R. Korb, and S. Bunting, "Prostacyclin is a circulating hormone," *Nature*, vol. 273, no. 5665, pp. 767–768, 1978.
- [49] T. Godfraind, R. Miller, and M. Wibo, "Calcium antagonism and calcium entry blockade," *Pharmacological Reviews*, vol. 3, pp. 321–416, 1986.
- [50] K. Koike, I. Takayanagi, S. Takiguchi, Y. Urita, and N. Miyake, "Ca-blocking action of stereoisomers of CI-951, (+)-CI-951 (NC-1500) and (–)-CI-951 in the isolated muscle preparations," *General Pharmacology*, vol. 23, no. 2, pp. 207–210, 1992.
- [51] S. Kubo, I. Doe, and Y. Nishikawa, "Direct inhibition of endothelial nitric oxide synthase by hydrogen sulfide: contribution to dual modulation of vascular tension," *Toxicology*, vol. 232, no. 1–2, pp. 138–146, 2007.

## *Retraction*

# **Retracted: Synthesis and Evaluation of Finasteride-Loaded HPMC-Based Nanogels for Transdermal Delivery: A Versatile Nanoscopic Platform**

### **BioMed Research International**

Received 8 January 2024; Accepted 8 January 2024; Published 9 January 2024

Copyright © 2024 BioMed Research International. This is an open access article distributed under the Creative Commons Attribution License, which permits unrestricted use, distribution, and reproduction in any medium, provided the original work is properly cited.

This article has been retracted by Hindawi, as publisher, following an investigation undertaken by the publisher [1]. This investigation has uncovered evidence of systematic manipulation of the publication and peer-review process. We cannot, therefore, vouch for the reliability or integrity of this article.

Please note that this notice is intended solely to alert readers that the peer-review process of this article has been compromised.

Wiley and Hindawi regret that the usual quality checks did not identify these issues before publication and have since put additional measures in place to safeguard research integrity.

We wish to credit our Research Integrity and Research Publishing teams and anonymous and named external researchers and research integrity experts for contributing to this investigation.





The corresponding author, as the representative of all authors, has been given the opportunity to register their agreement or disagreement to this retraction. We have kept a record of any response received.

## **References**

- [1] A. Ahmad, M. Ahmad, M. U. Minhas et al., "Synthesis and Evaluation of Finasteride-Loaded HPMC-Based Nanogels for Transdermal Delivery: A Versatile Nanoscopic Platform," *BioMed Research International*, vol. 2022, Article ID 2426960, 22 pages, 2022.

## Research Article

# Synthesis and Evaluation of Finasteride-Loaded HPMC-Based Nanogels for Transdermal Delivery: A Versatile Nanoscopic Platform

Aousaf Ahmad,<sup>1,2</sup> Mahmood Ahmad <sup>1</sup>, Muhammad Usman Minhas <sup>3</sup>,  
Muhammad Sarfraz <sup>4</sup>, Muhammad Sohail,<sup>5</sup> Kifayat Ullah Khan,<sup>2</sup> Sana Tanveer,<sup>1</sup>  
and Shakeel Ijaz <sup>1,2</sup>

<sup>1</sup>Department of Pharmaceutics, Faculty of Pharmacy, The Islamia University of Bahawalpur, 63100 Punjab, Pakistan

<sup>2</sup>Quaid-e-Azam College of Pharmacy, Sahiwal, Punjab, Pakistan

<sup>3</sup>College of Pharmacy, University of Sargodha, University Road Sargodha City, Punjab, Pakistan

<sup>4</sup>College of Pharmacy Al Ain University, Al Ain Campus, Al Ain, UAE

<sup>5</sup>Department of Pharmacy, COMSATS Institute of Information Technology, Abbottabad, 22060 KPK, Pakistan

Correspondence should be addressed to Mahmood Ahmad; [ma786\\_786@yahoo.com](mailto:ma786_786@yahoo.com)  
and Muhammad Usman Minhas; [us.minhas@hotmail.com](mailto:us.minhas@hotmail.com)

Received 19 May 2022; Revised 18 June 2022; Accepted 22 June 2022; Published 19 July 2022

Academic Editor: Nauman Rahim Khan

Copyright © 2022 Aousaf Ahmad et al. This is an open access article distributed under the Creative Commons Attribution License, which permits unrestricted use, distribution, and reproduction in any medium, provided the original work is properly cited.

Herein, we report nanogels comprising diverse feed ratio of polymer hydroxypropyl methylcellulose (HPMC), monomer acrylic acid (AA), and cross-linker methylene bisacrylamide (MBA) fabricated for transdermal delivery of finasteride (FIN). Free radical solution polymerization method with subsequent condensation was employed for the synthesis using ammonium per sulfate (APS) and sodium hydrogen sulfite (SHS) as initiators. Carbopol-940 gel (CG) was formulated as assisting platform to deliver FIN nanogels transdermally. Developed formulations were evaluated by several *in vitro*, *ex vivo*, and *in vivo* parameters such as particle size and charge distribution analysis, Fourier transform infrared spectroscopy (FTIR), thermogravimetric analysis (TGA), differential scanning calorimetry (DSC), scanning electron microscopy (SEM), X-ray diffractogram (XRD), rheological testing, *in vitro* swelling and drug release, and *ex vivo* skin permeation, irritation, and toxicity assessment. The results endorsed the nanogel formation ( $117.3 \pm 29.113$  nm), and the impact of synthesizing method was signified by high yield of nanogels ( $\approx 91\%$ ). Efficient response for *in vitro* swelling and FIN release was revealed at pH 5.5 and 7.4. Skin irritation and toxicity assessment ensured the biocompatibility of prepared nanocomposites. On the basis of the results obtained, it can be concluded that the developed nanogels were stable with excellent drug permeation profile across skin.

## 1. Introduction

Nanogels are basically hydrogels of nanoregime, usually composed of polymeric backbone-based cross-linked network [1, 2]. Bearing the features of hydrogels with added scope of nanoscale particle size, they overcome drawbacks of micro- and macroscale hydrogels [3]. Tuning and optimization of molecular composition, size, and design of nanogels can yield several advantages, i.e., stimuli responsive, easy and efficient drug loading, remarkable permeation

across biological barriers, improved drug release profile, biocompatibility, and physical stability of the system [4, 5]. Due to their wide range of properties, nanogels can encapsulate diverse classes of bioactive materials. Nanogels of polyelectrolyte origin can swiftly capture opposite charged low molecular weight drugs. Drug molecules develop electrostatic interaction and bound in charged network of the system. Mentioned properties help in the formation of a product for biomedical application that aids in improving patient compliance [6, 7].

Benign prostatic hyperplasia (BPH) is a common, progressive androgen-dependent disease in aging men resulting in an enlargement of prostate which in turn can lead to obstruction of urethral lumen and even complete urinary retention [8, 9]. Finasteride (FIN) is a selective 5- $\alpha$ -reductase inhibitor, reduces the conversion rate of testosterone to dihydrotestosterone which is a major cause of BPH, thus reducing the prostate size and improving the urinary symptoms. Persistent reduction in prostate size by FIN therapy can prevent BPH progression and prostate cancer as well [10, 11]. In effective treatment plan of BPH, FIN is continuously prescribed for months by oral route. FIN is also reported for its low oral absorption and bioavailability [12]. As BPH is associated to old age group majorly, long-term therapy of FIN potentially with other drugs also can produce gastric discomfort [13, 14].

Drug delivery by transdermal route provides an alternative way to avoid such complications. By TDDS, higher drug permeation can be achieved due to prolonged contact onto or within layers of skin channels [15]. Hydrogel nanoparticles of biocompatible profile and being of nanoscale can be highly effective in achieving effective treatment by transdermal route [16, 17]. Physicochemical characteristics along with pharmacokinetic and pharmacodynamics profile of drugs are taken as top list factors in designing of drug delivery systems. With emerging novelty and developing efficacious therapy measures, several limitations of conventional systems, i.e., poor pharmacokinetics and toxicity, can be reduced [18]. Ideal candidates for TDDS are characterized by lower molecular weight, optimum lipophilicity, and higher potency. Meeting the said criterion, transdermal route is favorable for molecules having short  $t_{1/2}$ , poor oral absorption, and bioavailability [19].

HPMC is a white, odorless surfactant of nonionic origin. Nanogels are composed of ionic/nonionic network of amphiphilic polymer chains, when dispersed in aqueous media swell to considerable volume and can load efficient amount of drug. Due to its properties, it possesses promising window to be used in biocompatible drug carrier systems [20, 21]. Acrylic acid is a monomer of liquid origin. Due to its physicochemical profile and reactivity, it has tremendous potential to be used in nanogel synthesis. In literature, it has been reported as a constructive part of nanogel design [22, 23].

In the context of the above information, the present study was focused to prepare and characterize HPMC-based nanogels loaded with FIN as a model drug in order to overcome the issues of poor absorption and bioavailability as well as to improve the patient compliance regarding long-term therapy. Manuscript being a bridge of hydrogels and nanoclass systems was aimed at summarizing the output of various *in vitro*, *ex vivo*, and *in vivo* parameters emphasizing nanogels for safe and efficacious transdermal delivery.

## 2. Materials and Methods

**2.1. Materials.** Finasteride was received as kind gift from Linear Pharma, Pakistan. HPMC 15 Cps and acrylic acid

were obtained from Sigma-Aldrich, USA. Ammonium per sulfate (APS), sodium hydrogen sulfite (SHS), sodium hydroxide (NaOH), potassium dihydrogen phosphate ( $\text{KH}_2\text{PO}_4$ ), and methylene bisacrylamide (MBA) were procured by Merck KGaA, Germany. Analytical grade solvents were utilized for the experimental work.

### 2.2. Methods

**2.2.1. Formulation of HPMC-Co-AA Nanogels.** A modified aqueous based free radical polymerization method was adopted for the fabrication of HPMC-co-acrylic acid nanogels [24]. To make HPMC solution, 2/3 of the required distilled water was kept at hot plate magnetic stirrer with temperature maintained at 70°C. The required amount of polymer was added slowly into hot water with continuous stirring at 250 rpm. Temperature was dropped gradually, and the remaining distilled water was added slowly which resulted in the formation of a thick solution. Meanwhile, aqueous solution of APS/SHS was added in AA at 250 rpm, and this mixture was then poured slowly to polymer solution at 700 rpm. Resultant mixture was homogenized by high speed homogenizer for 15 minutes at 11000 rpm with subsequent sonication and purging of nitrogen gas to remove dissolved air. MBA was dissolved in distilled water separately at 50°C. This was added dropwise to the above mixture at 1000 rpm and instantly channelized for gelation to already setup condenser maintained at 85°C. The whole mixture was allowed to condense for 4-5 h. The obtained formulation was subjected for approximately five minutes to the ethanol-water mixture (50:50) to get rid of unreacted constituents. Finally, formulation was sieved and kept in oven for 35-40°C for 48 h to get dried. Various ratios of polymer, monomer, and cross-linker were employed for fabrication of HPMC-based nanogels as shown in Table 1. Figure 1 explains the possible nanogel network structure.

**2.2.2. Drug Loading.** Drug loading in nanogel composites was carried by adapting swelling-diffusion method [25]. 2% (w/v) FIN solution was prepared in a mixture of ethanol-water (50:50). The purpose to use mixture of ethanol and water was to rationalize the solubility of the drug and to promote the swelling of nanogels. Accurately weighed dried nanogels were immersed in calculated volume of drug solution and allowed to stand for 24 h at room temperature. Drug-loaded nanogels were first dried at room temperature and then subjected to lyophilization for freeze drying.

**2.2.3. Preparation of Carbopol-940 Gel.** For the preparation of a gel as a platform to spread hydrogel nanoparticles on skin, 0.6% carbopol-940 solution was prepared by dispersing calculated mass of gelling agent in distilled water at magnetic stirrer for 15-20 minutes while maintaining the rotation speed at 300 rpm. The gel was then made viscous and pH adjusted to 5.5 by using few drops of triethanolamine (TEA).

TABLE 1: Feed ratio scheme of HPMC-based nanogels.

(a)

Sr. no	Formulation code	HPMC (g/100 g)	Acrylic acid (g/100 g)	APS/SHS (g/100 g)	MBA (g/100 g)
SET-I*					
1	NHP-1	0.8	8	0.8/0.8	8
2	NHP-2	1.6	8	0.8/0.8	8
3	NHP-3	2.4	8	0.8/0.8	8
SET-II**					
4	NHP-4	2.4	8	0.8/0.8	8
5	NHP-5	2.4	12	0.8/0.8	8
6	NHP-6	2.4	16	0.8/0.8	8
SET-III***					
7	NHP-7	2.4	8	0.8/0.8	8
8	NHP-8	2.4	8	0.8/0.8	10
9	NHP-9	2.4	8	0.8/0.8	12

(b)

Studied variables	Variables level (g)		
	Low	Medium	High
C-1*	0.8	1.6	2.4
C-2**	8	12	16
C-3***	8	10	12

Abbreviations: C-1\*: HPMC conc.; C-2\*\*: AA conc.; C-3\*\*\*: MBA conc.

**2.2.4. Percent Yield.** The efficiency of method was evaluated by calculating percentage yield of all formulations. Percent yield was measured by the following formula:

$$\text{Percent yield} = \frac{\text{Practical yield}}{\text{Theoretical yield}} \times 100. \quad (1)$$

**2.2.5. FTIR Spectroscopy.** FTIR spectroscopy using Bruker FTIR (Tensor 27 series) was employed for structural analysis and drug-formulation interaction by applying attenuated total reflectance (ATR) technology [26, 27]. Spectra of optimized loaded, unloaded formulation, and their pure components were obtained between scanning range of 400 and 4000  $\text{cm}^{-1}$ , and the recorded data was processed by OPUS Software (Bruker).

**2.2.6. Particle Size and Zeta Potential Analysis.** Particle size and charged distribution of optimized formulation were determined using laser light scattering particle size analyzer (Malvern Zetasizer Nano ZS, UK). 0.1% (w/v) of nanogel dispersion was made with acetone. Homogenous suspension obtained was examined for particle size and zeta potential.

**2.2.7. Thermal Analysis.** Thermal stability was studied by thermogravimetric analysis and differential scanning calorimetry using TA (Q600 Series, USA). Thermogravimetric analyzer was used to determine the rate and extent of weight change relative to temperature. Initially, reference standards

were used to calibrate the weight profile. A known weight (0.5 to 5 mg) of the HPMC, FIN, and prepared formulation was placed in crimped aluminum pans in crucible baskets. The samples were analyzed at a scanning rate of 10°C/min from 0°C to 500°C under inert nitrogen flow rate of 10 ml/min to measure percent weight loss with increasing temperature. Differential scanning calorimetry (DSC) of HPMC, FIN, and developed formulation was used to evaluate melting point with respect to free energy absorbed and released. Sapphire standard was used for the calibration of calorimeter for heat capacity. Indium was used as a standard for cell constant and temperature [28].

**2.2.8. X-Ray Diffraction Analysis.** Optimized formulation along with its constituents was subjected to XRD analysis using X-ray diffractometer (JDX3522, Japan). Tightly packed samples in aluminum cells were exposed to CuK $\alpha$  radiations of wavelength 1.54056 Å. Powder X-ray diffractograms were taken at 2 $\theta$  value up to 60. Operating conditions were 1 sec (count time), 0.050° (step angle), 2.5–30 mA (tube current), and 20–40 kV (tube voltage). The X-ray patterns recorded were then analyzed to study the crystalline/amorphous nature of samples [29, 30].

**2.2.9. Scanning Electron Microscopy.** The surface morphology and shape of nanogels were examined using scanning electron microscopy (JSM5910, Japan). Optimized sample was prepared by sprinkling the formulation on a double-

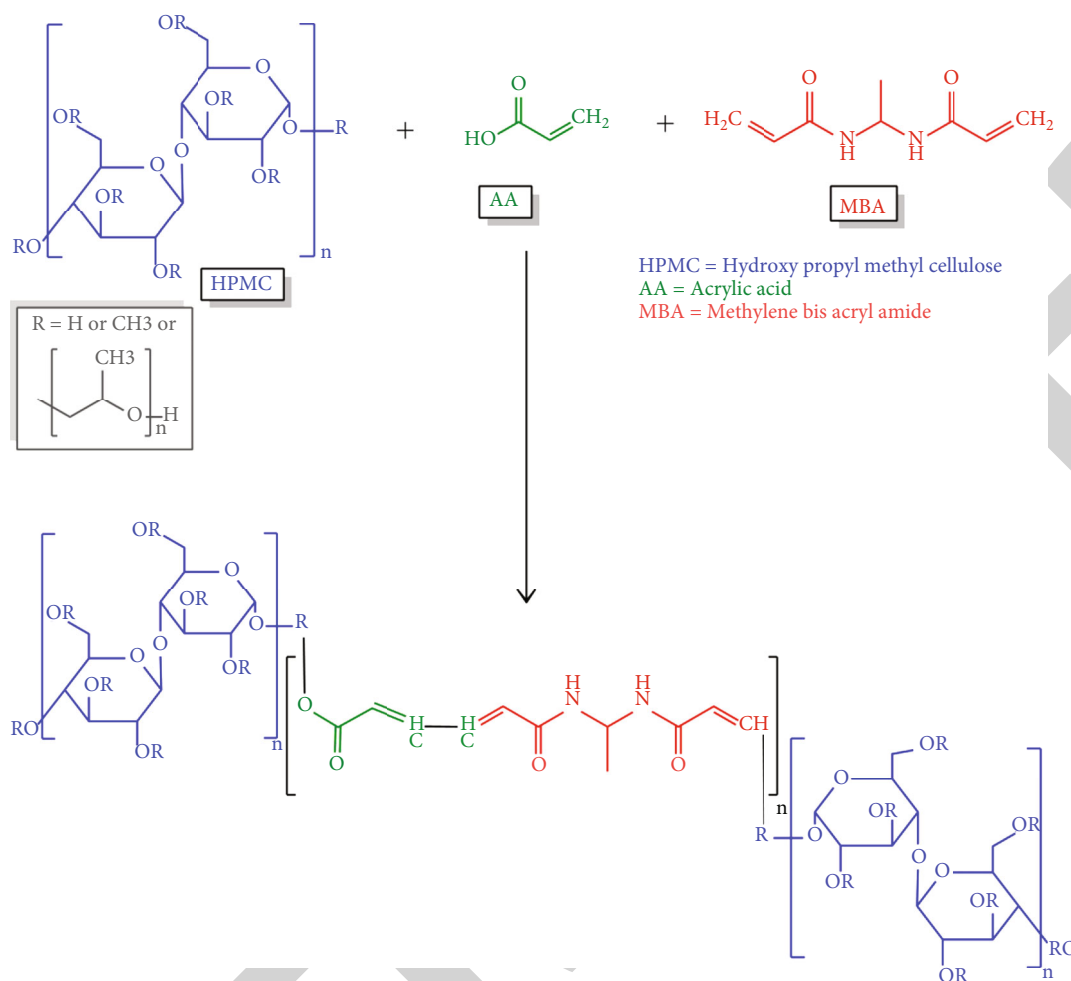


FIGURE 1: Proposed cross-linked structure of HPMC nanogels.

adhesive tape stuck to an aluminum stub. The stub was then coated with gold using a gold sputter module in a high-vacuum evaporator to a thickness of  $\sim 300 \text{ \AA}$  under an argon atmosphere.

**2.2.10. In Vitro Swelling Studies.** Nanogel particles of known weight were placed in dialysis membrane and then immersed in phosphate buffer maintained at pH 5.5 and 7.4. They were allowed to swell; membranes from buffer were removed and weighed again after blotting. The difference in weight was calculated in order to observe the swelling of nanogels. The swelling ratio (SR) was calculated using the following formula [31]:

$$\text{Swelling Ratio} = \frac{W_s}{W_d}, \quad (2)$$

where  $W_s$  represents the weight of swollen state of sample and  $W_d$  is the weight of sample in the dry state.

**2.2.11. Drug Entrapment Efficiency.** The percent drug entrapment efficiency (DEE %) of developed nanogels was calculated by absorption and extraction method. Nanogels were weighed (100 mg) with accuracy and mixed in 50 ml

of acetonitrile. This mixture was kept at magnetic stirrer with rotation speed of 100 rpm for 1 hour at room temperature. Obtained suspension was filtered using  $0.45 \mu\text{m}$  membrane filter. Filtrate was checked by UV spectrophotometric analysis at  $\lambda_{\text{max}} 210 \text{ nm}$ , and following formula was applied for quantitative estimation of entrapment efficiency.

$$\begin{aligned} \text{\%Drug Entrapment Efficiency} \\ = \frac{\text{Actual Drug in Formulation}}{\text{Theoretical Drug in Formulation}} \times 100. \end{aligned} \quad (3)$$

**2.2.12. In Vitro Drug Release Studies.** *In vitro* release studies of FIN from all loaded formulations were evaluated using USP Apparatus-V (paddle over disc method) with tea bag method [32]. Accurately weighed formulations were enclosed in emptied tea bags, and discs were placed in dissolution medium. The medium was composed of buffer maintained at pH 5.5 and 7.4 to simulate with pH of the skin and blood, respectively. For pH 5.5, apparatus was maintained at  $32^\circ\text{C} \pm 0.5^\circ\text{C}$ , while for 7.4 pH, it was maintained at  $37^\circ\text{C} \pm 0.5^\circ\text{C}$  with rotation speed of 50 rpm. Samples were withdrawn up to 120 minutes at



specific intervals of 10, 20, 30, 60, 90, and 120 minutes using a pipette and further diluted, and the amount of drug release was analyzed using UV spectrophotometer at  $\lambda$  max 210 nm.

**2.2.13. Sol-Gel Fraction Analysis.** Nanogels were analyzed for sol and gel fraction using Soxhlet extraction setup where nanogels were kept for 4 hours with water at 80°C. Recollected nanogels were dried in vacuum oven at 45°C till constant mass. The following formulas were applied to calculate the sol and gel fractions.

$$\% \text{Sol Fraction} = \frac{W_0 - wt}{W_0} \times 100, \quad (4)$$

$$\% \text{Gel Fraction} = 100 - \text{Sol Fraction}, \quad (5)$$

where in sol fraction,  $W_0$  is weight of nanogels before extraction and  $wt$  is weight after extraction.

**2.2.14. Porosity Analysis.** Percent porosity (%) of nanogels was measured by fluid displacement method. Initially, pre-weighed oven dried nanogels were immersed in distilled water till saturation, and change in weight was marked. Saturated nanogels were blotted and weight variation was calculated. The following mathematical tool was employed to calculate % porosity.

$$\% \text{Porosity} = \frac{W_s - W_d}{\rho V} \times 100, \quad (6)$$

where  $W_s$  is the weight of saturated nanogels,  $W_d$  is the weight of dried nanogels,  $\rho$  is the distilled water density, and  $V$  is the volume of respective formulation.

**2.2.15. Rheology and Stability of Gel.** Programmable rheometer (Brookfield DV-III ultra) was used to study the viscoelastic behavior of the gel. Data analysis was carried out with Rheocalc V.2.010. Prior to each reading, gel samples were equilibrated. Continuous shear investigation was done with rheometer having CP41 spindle with cone and plate geometry as a measuring system. Shear rate was increased in ascending order as well as in descending order from 0 to 60 D in order to obtain up and down curves. The resultant shear stress was measured accordingly. In order to access the stability of gel formulation, samples were stored at the temperature of 8, 25, 32, and 45°C for three months.

**2.2.16. Ex Vivo Skin Permeation Studies.** *Ex vivo* permeation studies were carried out using excised skin of rabbit. Animals were sacrificed employing an anesthetic agent. Abdominal hair along with fat adhered to dermis was removed by using hair removing cream. Finally, the skin was rinsed with phosphate buffer (pH 7.4). Prepared skin samples were stored in a refrigerator at -20°C and used within 24 hours. *FIN ex vivo* permeation through excised rabbit skin was performed using Franz diffusion cell consisting of two compartments, donor and receptor. The excised skin was mounted between both compartments. Phosphate buffer (pH 7.4) was used as receptor medium. The entire setup was placed

over magnetic stirrer, with temperature maintained at  $37 \pm 0.5^\circ\text{C}$ . After the hydration of excised skin, nanogels were applied on it. A specified volume of medium was collected and replaced with fresh medium. Amount of permeated gel was analyzed using UV spectrophotometer. The sample was collected up to 24 hours at specific intervals of 2, 4, 6, 8, 12, 18, and 24 hours, and then, the amount of drug in permeated samples was calculated. All surgical and experimental procedures had been reviewed and approved by the institute's Pharmacy Research Ethics Committee (PREC).

**2.2.17. Skin Irritation and Toxicity Studies.** Skin irritation and toxicological studies were conducted on albino rabbits for assessment of dermal irritation and toxicological effects. All the procedures were conducted according to the Economic Co-operation and Development (OECD) guidelines and by the approval of institute's Pharmacy Research Ethics Committee (PREC). Rabbits weighing 2–2.5 kg were taken randomly and divided into two groups, i.e., G-1 and G-2, with three rabbits each ( $n = 3$ ). The test animals were caged individually. 24 hours prior to the experiment, dorsal surface of rabbits was shaved properly with depilatory cream. Hair-free surface was marked with an area of approximately  $5 \text{ cm}^2$ . The rabbits were treated as follows:

Test formulation of about 500 mg/kg was applied to the respective area. Observations were made after a period of 24, 48, 72, and 240 hours. On regular basis, animals were physically examined to observe and note any variance in skin appearance, body weight, eating pattern, amount of water and food consumption, sleep habits, salivation, diarrhea, and mortality. Blood of the rabbits was taken for biochemical analysis. Organs, i.e., the kidney, heart, lungs, liver, and spleen, were removed, weighed, and kept in suitable containers with formalin. Slides for histological examination were made. Optical microscope (Nikon E200, Japan) with camera and software (MINISEE) was used to record histopathological images from slides.

Group 1: control group (blank without any test formulation)

Group 2: CG with HPMC-based nanogels

### 3. Result and Discussion

**3.1. Macroscopic Evaluation.** Free radical solution polymerization technique was adopted to formulate HPMC-co-AA hydrogel nanoparticles. Prepared composites appeared white colored and sticky with apparent uniform colloidal output. Figure 2(c) typifies fabricated nanogels with the said characteristics.

**3.2. Particle Size and Zeta Potential.** Fabricated HPMC-based nanocomposites were analyzed for particle size and zeta potential measurement. Figures 2(a) and 2(b) delineate particle size and charge measurements of HPMC nanogels, respectively. Particle diameter turned out to be 117 nm, and PDI was recorded as 0.306. Small polydispersity index (PDI) value indicated that the developed nanogels were homogeneous [33]. Stability and low coagulation tendency

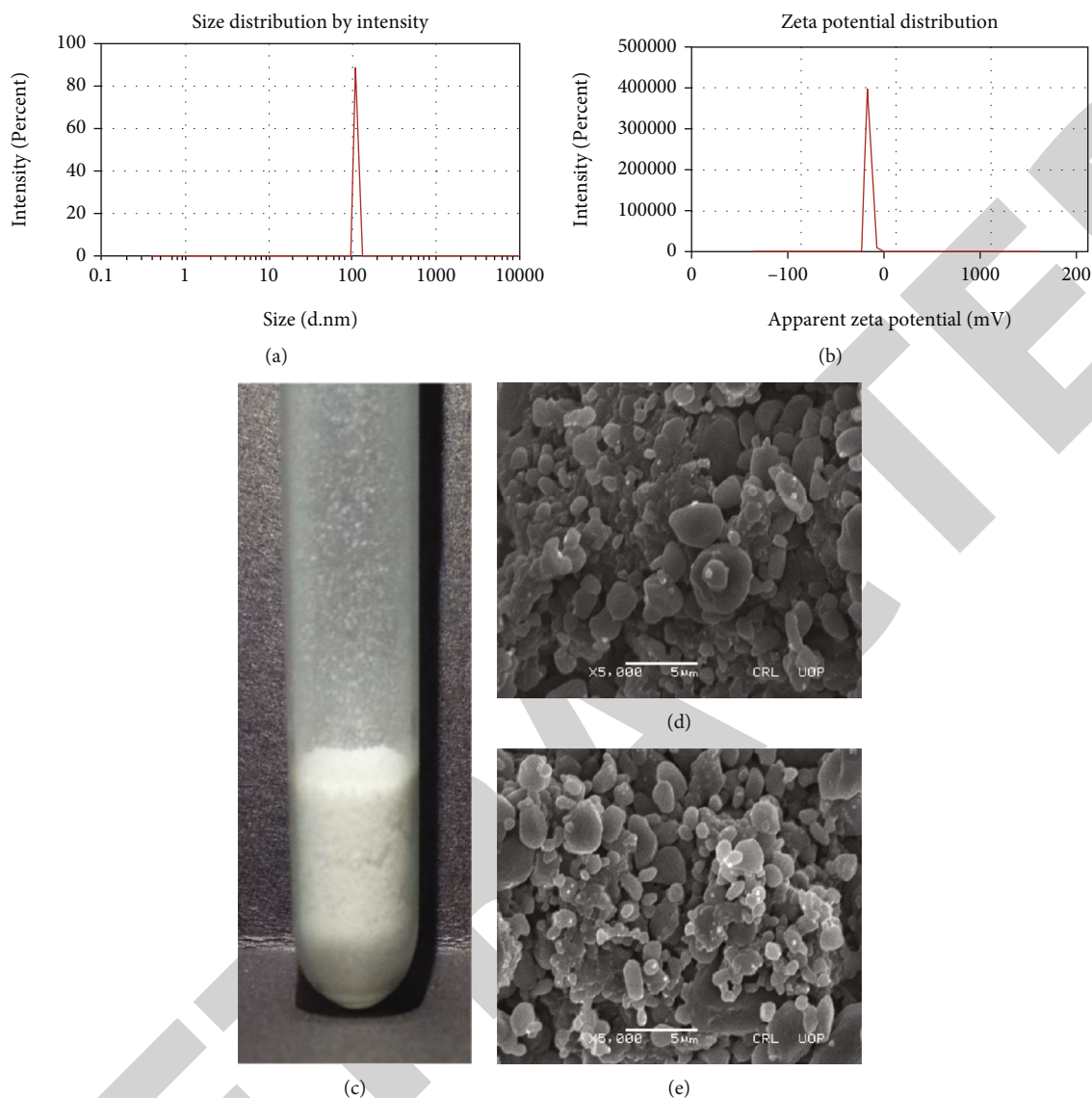


FIGURE 2: (a) Particle size distribution. (b) Zeta potential. (c) Physical state. (d) SEM micrograph of unloaded. (e) FIN-loaded HPMC-co-AA nanogels.

of nanogels by electrostatic repulsiveness is authenticated by low zeta potential value ( $-32$ ). Previously, HPMC-based nanoparticulate systems were reported to have particles size in the range of 38-78 nm [34] and 200 nm [35].

**3.3. Scanning Electron Microscopy.** Surface articulation of formulated cross-linked nanocomposites was evaluated by SEM. Micrographs of analyzed samples are shown in Figures 2(d) and 2(e) for unloaded and FIN-loaded composites, respectively. SEM images portray irregular amorphous texture profile which solidify the stable nanogel formation. Micrograph of FIN-loaded formulation affirms drug trapping in HPMC nanogels.

**3.4. FTIR Analysis.** Developed HPMC-based unloaded and FIN-loaded nanogels along with pure components were analyzed by FTIR in order to identify various functional groups

and colligate any interaction among drug and drug carrier system. FTIR spectra of pure HPMC, AA, MBA, FIN, developed nanogels, and FIN-loaded nanogels are given in Figure 3.

FTIR spectrum of HPMC displayed characteristic  $-OH$  stretching vibrations at  $3483.82\text{ cm}^{-1}$ . Methyl and propyl groups were identified at  $2901.30\text{ cm}^{-1}$ . The spectra showed 6C cyclic ring peak at  $1656.54\text{ cm}^{-1}$ . The peak at  $1374.31\text{ cm}^{-1}$  is associated to C-O-C symmetric bending of methoxy group, and pyranose ring was recognized by a peak at  $1053.18\text{ cm}^{-1}$  [36]. FTIR spectra of AA presented characteristic C=C and C-H peaks at  $2661.74\text{ cm}^{-1}$  and  $2975.73\text{ cm}^{-1}$ , respectively. Intense  $COO^-$  peaks are pointed at  $1410.73$  and  $1616.51\text{ cm}^{-1}$ . The carboxyl dispersion band was recognized at  $1710.57\text{ cm}^{-1}$ . The peak at  $1296.89\text{ cm}^{-1}$  is attributed to C-O stretching vibration [37]. FTIR scan of MBA exhibited stretching N-H vibration at  $3301.58\text{ cm}^{-1}$ ,

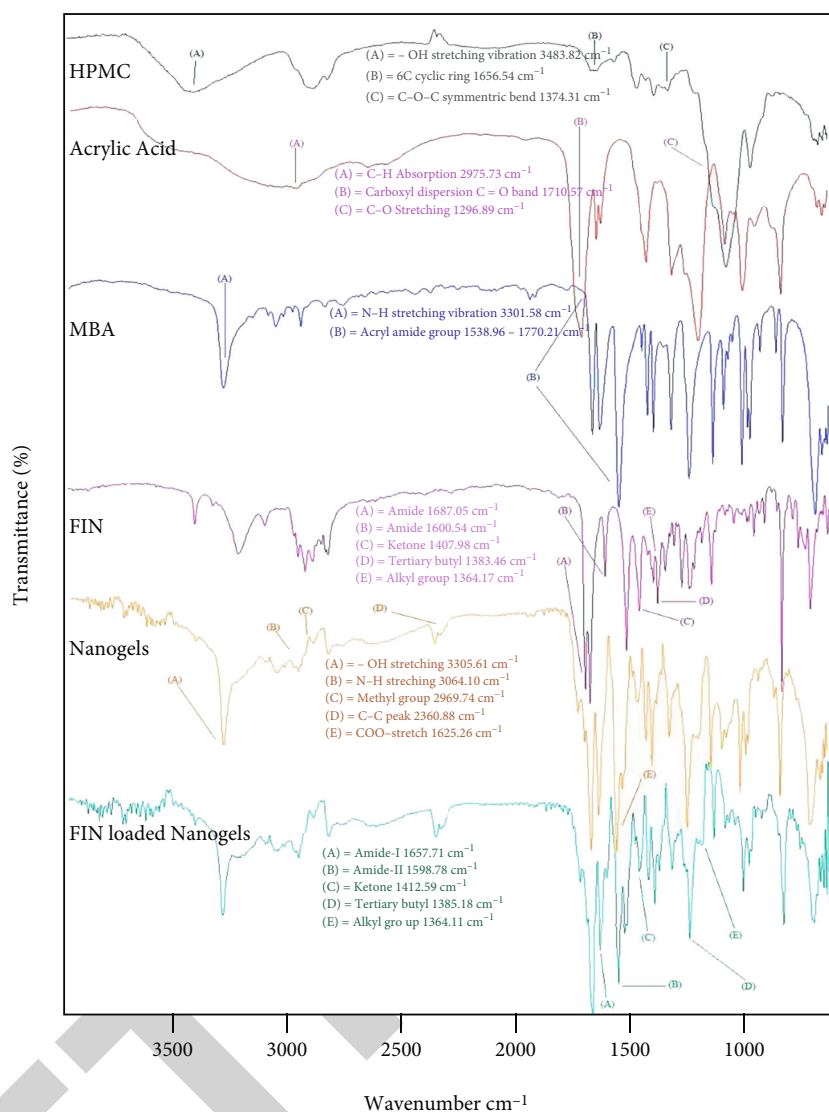


FIGURE 3: FTIR spectrum of HPMC, AA, MBA, FIN, unloaded, and FIN-loaded HPMC-co-AA nanogels.

and stretching frequencies of C=O and N-H groups of acryl amide may be attributed to the peaks in the range of  $1538.96\text{--}1770.21\text{ cm}^{-1}$  [38]. FTIR spectra of FIN expressed alkyl, ketone, and tertiary butyl groups at  $1364.17$ ,  $1407.98$ , and  $1383.46\text{ cm}^{-1}$ , respectively. Peaks for amides I and II were recognized at  $1687.05\text{ cm}^{-1}$  and  $1600.54\text{ cm}^{-1}$ , respectively [39].

Patternize output for shifting of specific peaks in FTIR spectrum of HPMC nanogels confirmed the successful development of cross-linking network among constituents. Peaks for pure constructive components, i.e., -OH stretching vibrations at  $3483.82\text{ cm}^{-1}$ , methyl and propyl groups at  $2901.30\text{ cm}^{-1}$ , C-O-C at  $1374.31\text{ cm}^{-1}$ , carbonyl dispersion at  $1710.57\text{ cm}^{-1}$ , intense  $\text{COO}^-$  stretch band at  $1616.51\text{ cm}^{-1}$ , C-H at  $2975.73\text{ cm}^{-1}$ , C=C at  $2661.74\text{ cm}^{-1}$ , C-O at  $1296.89\text{ cm}^{-1}$ , N-H stretching at  $3301.58\text{ cm}^{-1}$ , and C=O acryl amide frequency at  $1655.78\text{ cm}^{-1}$ , were shifted to  $3305.61$ ,  $2969.74$ ,  $1384.49$ ,  $1716.46$ ,  $1625.26$ ,  $2835.56$ ,

$2360.88$ ,  $3064.10$ , and  $1686.64\text{ cm}^{-1}$ , respectively. This overlapping and shifting of characteristic spectral peaks verified formation of successful cross-linked network. Previous data shows the absence and shifting of components specific peaks in HPMC-based formulation [40]. Presence of drug specific peaks was verified by the FTIR scan of FIN-loaded nanogels. The peaks for amide I, amide II, alkyl, ketone, and butyl groups were indicated at  $1657.71$ ,  $1598.78$ ,  $1364.11$ ,  $1412.59$ , and  $1385.18\text{ cm}^{-1}$ , respectively. Slight shift in peaks of FIN confirmed its successful entanglement in developed nanogels [39].

**3.5. Thermal Analysis.** DSC and TGA of pure constituents and developed nanogels were conducted to inquire the thermal stability and to collect data in context of possible interaction among constituents of the formulation as shown in Figure 4. In DSC scan of pure polymer, endothermic peak starting at  $225^\circ\text{C}$  indicates relaxation of polymeric chain.

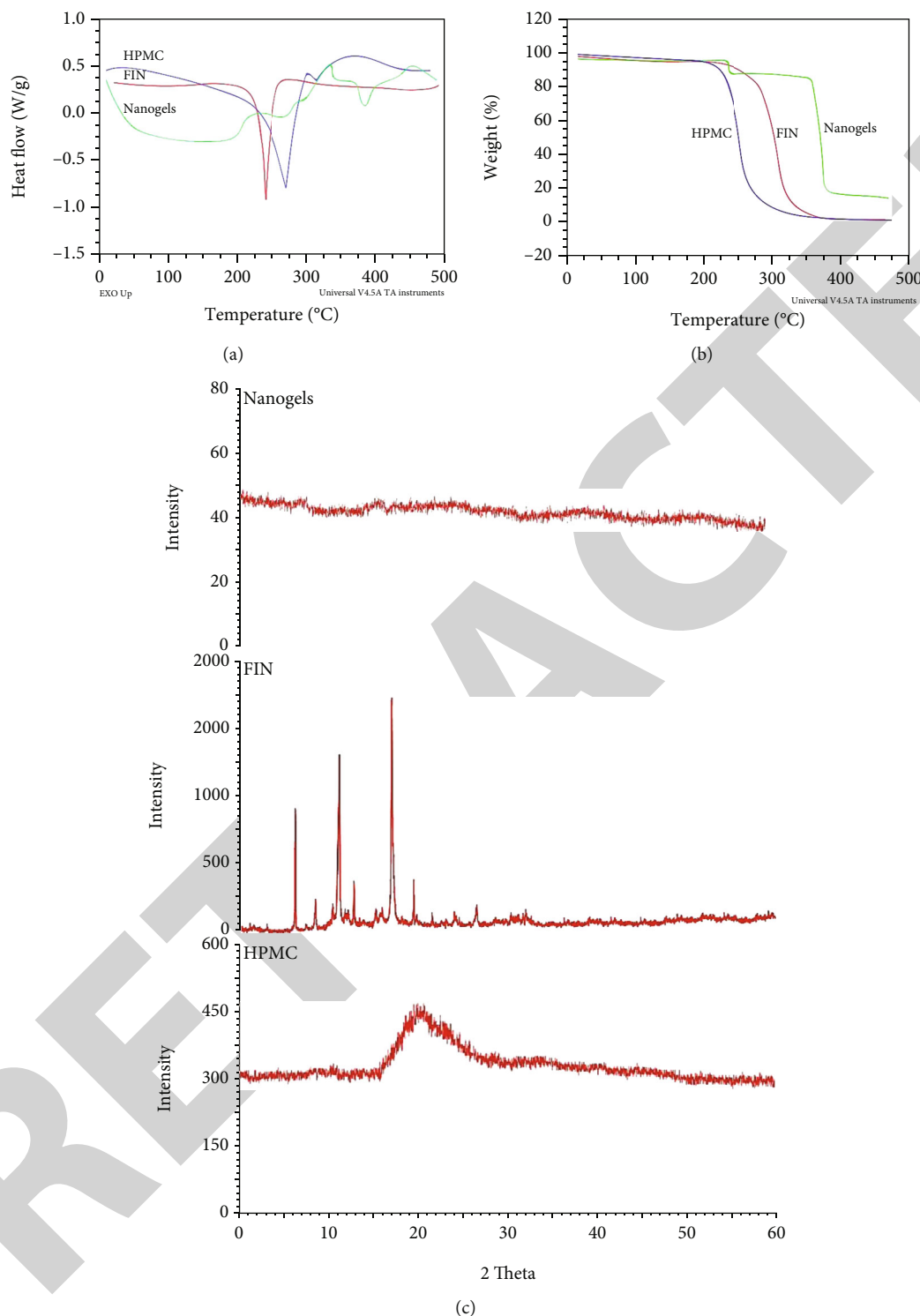


FIGURE 4: The spectra of TGA, DSC, and XRD of polymer HPMC, pure drug FIN, and developed composites.

The phase transition temperature is pointed at 320°C. Combustion of polymer is revealed by slight exothermic peak in the range of 325-400°C [41]. DSC spectra of FIN exhibit sharp and prominent peak at 242°C indicating drug melting point and expressing anhydrous crystalline nature of FIN [42]. DSC scan of nanogels showed stable and packed prod-

uct formation. It was affirmed by the output variation of heat scan of formulated nanogels when compared to pure constituents. Broad endotherm ranging between 30 and 140°C points out the initiation of looseness in polymeric network strands. A broad range of thermal scans also hint the amorphous nature of sample. Evaporation of volatile parts is

indicated by an exothermic peak at 275°C. Another exothermic peak at 335°C expresses the glass transition temperature ( $T_g$ ). The endothermic dip at 380°C indicates the nanogel degradation.

Shifting of thermal peaks and melting temperature ( $T_m$ ) explains a ponderable point that by formation of nanocomposites, the crystalline entities are either converted to or masked by amorphous portion, thus confirming a stable cross-linked system formation. Variation in characteristic endotherm of FIN evidences the successful encapsulation of active ingredient in nanogel network. Previous studies in literature also assert shifting and loss of characteristic endothermic peaks in HPMC-based DDS [43, 44].

TGA scan of HPMC in Figure 4 demonstrates the loss in weight of polymer in three stages. 10% weight loss was noticed in the first stage in the temperature range of 30-210°C. Significance decomposition (80%) of remaining polymer occurred in the range of 211-315°C. The remaining polymeric leftover was degraded in the third stage in the broad temperature range of 325-450°C indicating amorphousness of substance [44, 45]. TGA thermogram of FIN exhibited immediate degradation in the range of 250-300°C which also reveals the crystalline nature of drug [42, 46]. TGA spectra of formulated nanocarrier system portrayed relatively prolonged resistance to thermal decomposition in comparison to those of pure constructive entities. Initial 10% loss of weight occurred from 20 to 225°C indicating the chain relaxation of network. Degradation of major portion of carbon precursor (70%) of nanocomposites is attributed to the detained weight loss in temperature range of 310-390°C. Remaining degradation occurred in temperature higher than 400°C conferring to shrinkage and loss of cross-linking network.

Highly stable nanogel formation is signified by TGA details of composites because of cross-linking network establishment among components when compared to TGA of pure constituents of the formulation. The encapsulation of drug in prepared nanocomposites is also justified by shift in TGA scan when compared to pure FIN. The reason is, when a foreign molecule, i.e., drug moiety, is loaded in the formulated carrier network, its specific thermal characteristics like MP and BP either disappear entirely or make a shift to another temperature range [47]. Enhanced thermal stability of various HPMC-based systems is reported in literature by comparison of thermal scans of constructive entities and developed formulations [48, 49].

**3.6. X-Ray Diffraction Studies.** X-ray diffraction analysis of fabricated nanocomposites and pure components was performed to uncover the information regarding identification of crystalline or amorphous forms of samples. Scans are presented in Figure 4. XRD scan of pure HPMC exhibits characteristic broad peak at  $2\theta$  scale value 20 [50, 51]. XRD spectra of pure FIN confirmed crystalline nature of FIN by demonstration of notable distinct and sharp peaks at  $2\theta$  values of 6, 11, 13, 17, and 19 [12, 52].

Investigation of XRD spectra of developed composites unveils conversion of crystalline form to amorphous entities imprinting the formation of cross-linking network. Success-

ful encapsulation of drug in porous nanogel network was corroborated by absence of specific FIN crystalline spectral peaks. Dissolution of dosage form is also influenced by amorphous or crystalline output. Among the said forms, the former shall produce a relatively fast dissolution rate due to possession of higher internal energy and accreting upsurge molecular motion [53]. Previously, stability of HPMC-based formulations has been reported to be evaluated by XRD [54].

**3.7. Yield, Sol-Gel, and Porosity Analysis.** Percent yield of all prepared nanocomposites came out to be higher than 70%, which insinuates the practical efficiency and impact of method to formulate nanogels. Output of diversity in polymeric, monomeric, and cross-linker content on %yield, sol-gel, and porosity is given in Figure 5. Increase in polymeric concentration in feed ratio of nanogels resulted in higher %yield and gel output. This is attributed to the effect of increased constructive density of developed nanocomposites [55]. Higher %yield and gel were calculated with increase in content of AA. Uplifting the content of constructive entities leads to higher outcome of the said parameters. This could be linked to induction of more free active sites for reaction by availability of activated free radicals for the monomer portion [56]. In the same manner, variation in MBA concentration also influenced the %yield and gel outcome. It is evident from the results that the presence of more cross-linking nodes elevated the cross-link density of fabricated composites that ended up in increased yield and gel content [57].

Results of analysis of porosity of nanocomposites are mentioned in Figure 5 which illustrates that increased HPMC and AA content increased porosity of composites. This is because HPMC and AA grant higher swellability and formation of porous network owing to their hydrophilic nature [58, 59]. In contrast, variation in MBA concentration on %porosity of fabricated nanocomposites unveiled that more stiff and compact cross-linking network was established because of relatively higher net cross-linking density [60].

**3.8. In Vitro Swelling Studies.** The impact of variation in concentration of HPMC, AA, and MBA on *in vitro* swelling at pH 5.5 and 7.4 was appraised to simulate the ambience of skin and blood, respectively. Feed ratio of constituents, cross-linking establishment, and porosity response can mark an influence on *in vitro* swelling phenomenon of designed DDS. The results of swelling response is shown in Figure 5. Measurement of swelling index was comparable at both pH with a higher output of said parameter at pH 7.4. Swelling response of network of nanogels is regulated by the smother and presence of electrically charged entities. Various functional groups are responsible for higher swelling index at alkaline pH (7.4). This is because hydroxyl and carboxylic groups dissociate into ionized form at alkaline pH leading to higher electrostatic repulsion, thus creating more spacious network and ultimately resulting in higher swelling [61]. The effect of variation in HPMC concentration on swelling index narrates that increasing the polymeric

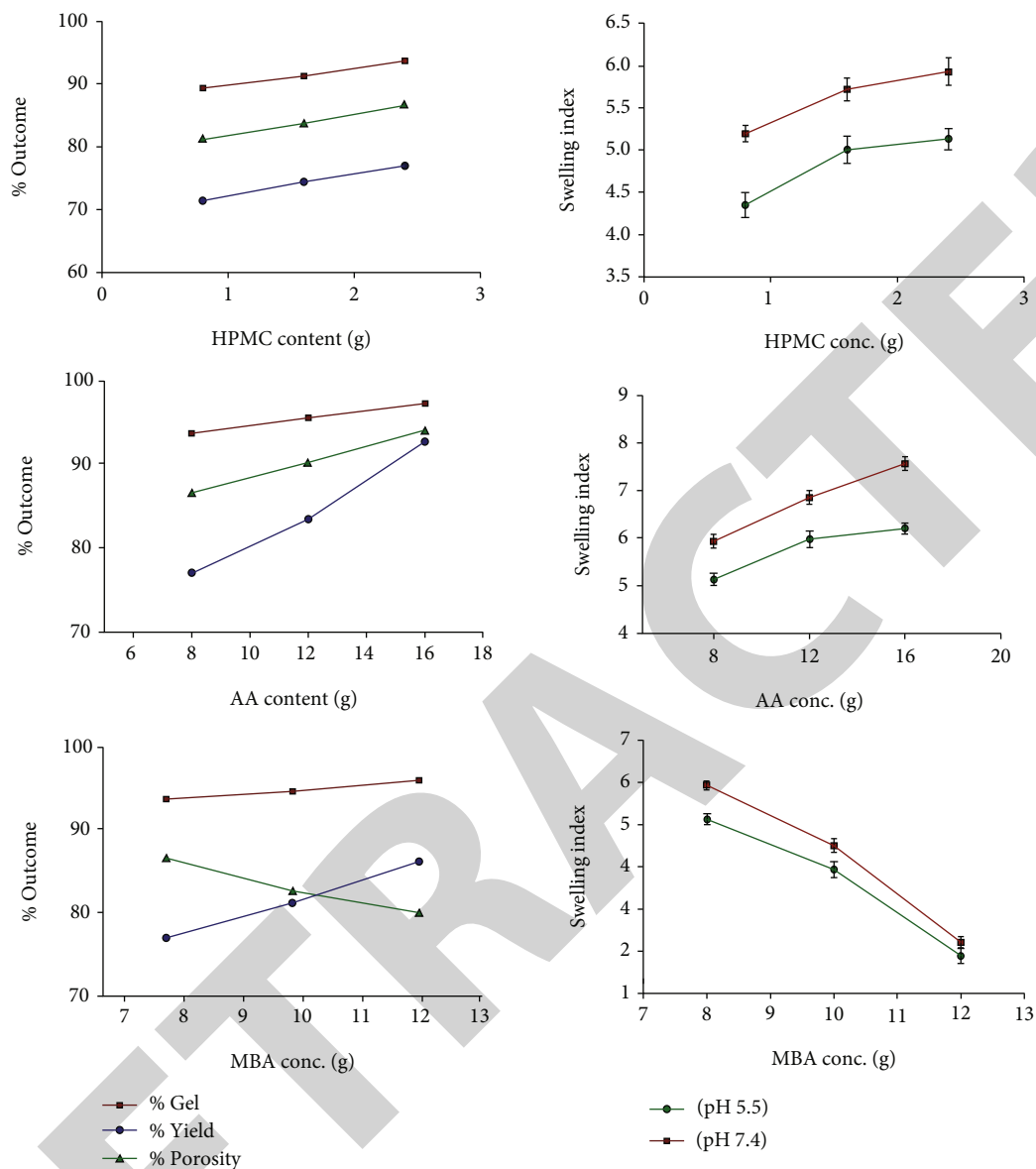
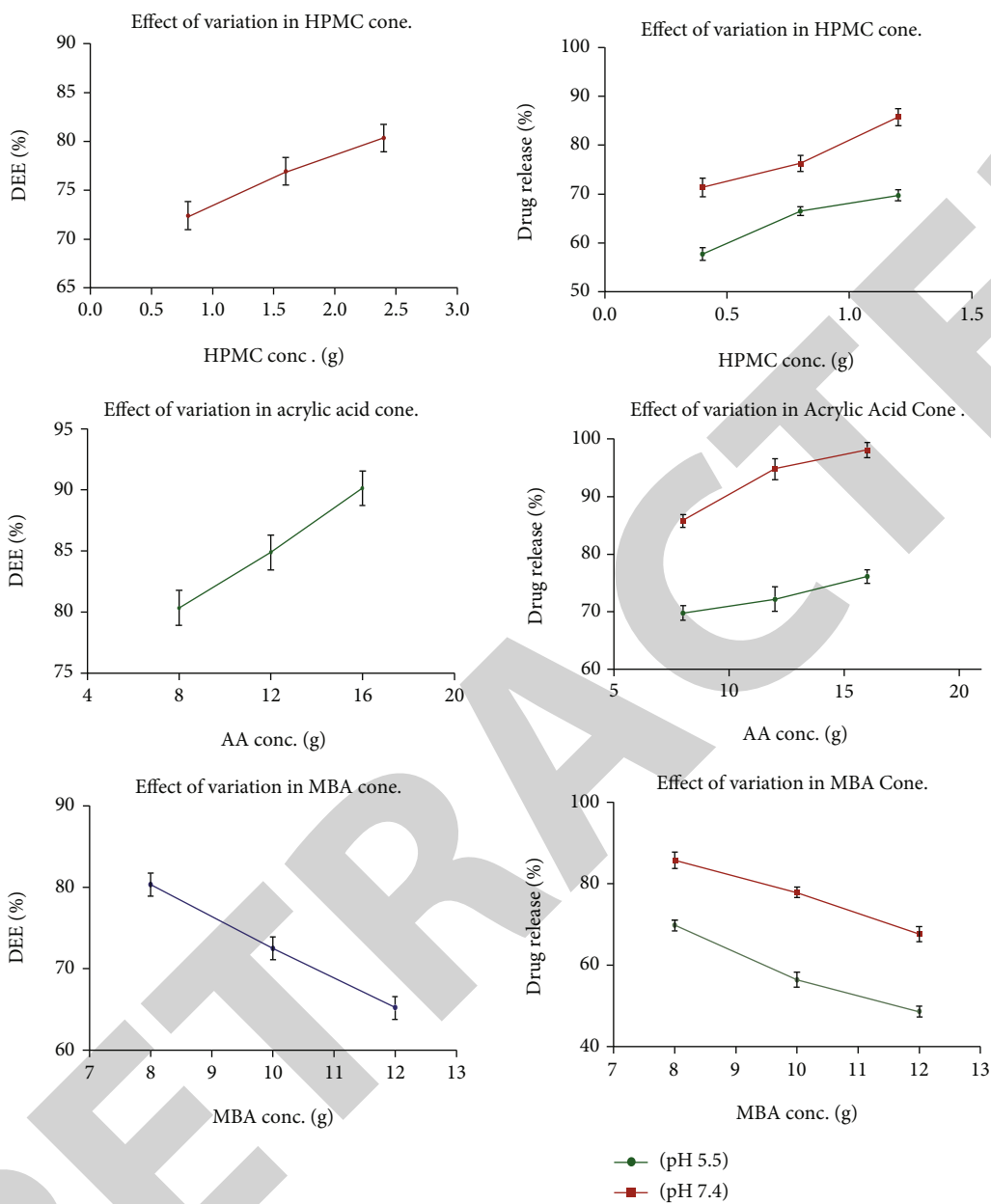


FIGURE 5: Impact of polymer HPMC, monomer AA, and cross-linker MBA variance on percent outcome of gel, yield, porosity, and swelling index.

content increases the swelling index. This is because HPMC possesses great affinity for aqueous media and its formulations can absorb large amount of water in its porous network [58]. The swelling capacity of HPMC-based formulations is directly proportional to its concentration used [62]. An increase in swelling response was observed when AA was increased. This could be comported to relatively higher content of ionized carboxylic groups, subsequently, higher electrostatic repulsion and increased swelling index [63]. The impact of concentration of cross-linking moiety (MBA) on swelling of developed nanogels was evaluated, which showed decreased swelling response with increase in MBA. This could be linked to lower segmental mobility, stiffness, and increased cross-link density of nanogels [64].

3.9. Drug Entrapment Efficiency. Synthesized nanocomposites were evaluated for the capability to encapsulate the drug and effect of varying amount of components was checked; the results are mentioned in Figure 6. The polymers with high molecular weight easily encapsulate low molecular weight drugs [65]. Various mechanisms are reported for drug encapsulation by nanogels but swelling based drug loading stand out among these [66]. The higher the swelling ability and porosity of developed composites, the more drug from solution is captured [67]. The results reveal that increasing HPMC content ended with relatively higher FIN encapsulation efficacy in nanogels. It is due to the fact that as porosity and swelling increased, drug encapsulation efficiency of nanogels also increased [68]. Likewise, increasing



(a)

FIGURE 6: Continued.

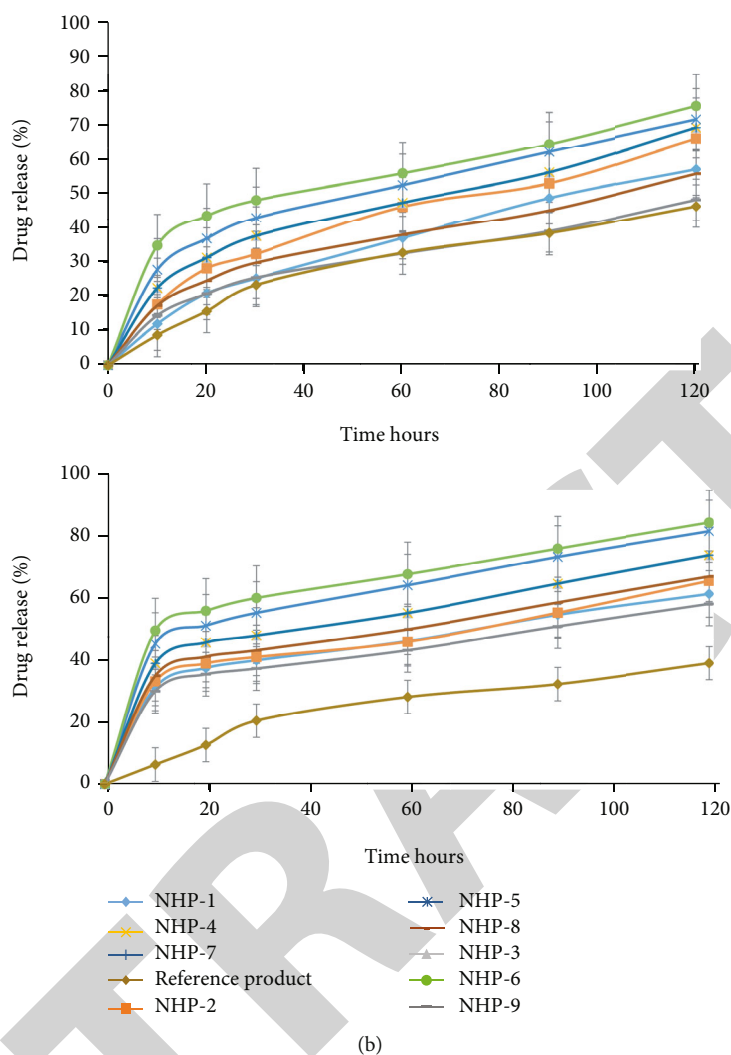


FIGURE 6: (a) Impact of various components on percent drug entrapment efficiency (%DEE) and percent drug release. (b) Percent drug release of developed nanogels and reference product at pH 5.5. (c) Percent drug release of developed nanogels and reference product at pH 7.4.

trend of drug entrapment was observed in case of AA. This output is linked to impact of charged carboxylate ions, higher porosity, and increased swelling capability [69]. Moreover, with an increase amount of MBA, relatively lesser drug was captured in the system because of the formation of relatively compact and denser nanocomposites [70].

**3.10. In Vitro Drug Release Studies.** *In vitro* drug release from synthesized nanocomposites was evaluated, and the results were quantified at pH 5.5 and 7.4 as shown in Figures 6(b) and 6(c), respectively. Variable output of FIN release from nanocomposites was measured against varying content of synthesizing constituents of nanogels as mentioned in Figure 6(a). Swelling, erosion, and diffusion through nanogels play their role in release of active moiety from nanogels. At higher pH, all of the formulations came out with relatively increased drug release outcome correlating to swelling index of nanogels [71].

It is evident from results that *in vitro* FIN release was directly proportional to HPMC content in the nanogel network. This could be linked to the formation of loose networking mesh as a function of water affinitive portion of HPMC [72]. Similarly, effect of increasing AA content on FIN release expressed relatively higher swelling index because of charged carboxylate ions ultimately leads to increased cumulative FIN release profile [73]. On the other hand, FIN release from nanogels was decreased as MBA content increased in the formulation. This output can be attributed to relatively higher cross-link density in developed network which in turn resulted in the production of a closer network mesh that resisted FIN escape from nanogels [64].

**3.11. Ex Vivo Skin Permeation Studies.** Skin permeation evaluation of all developed nanogel formulations was carried by using Franz diffusion cell. Effect of variation in content of HPMC, AA, and MBA was evaluated which showed



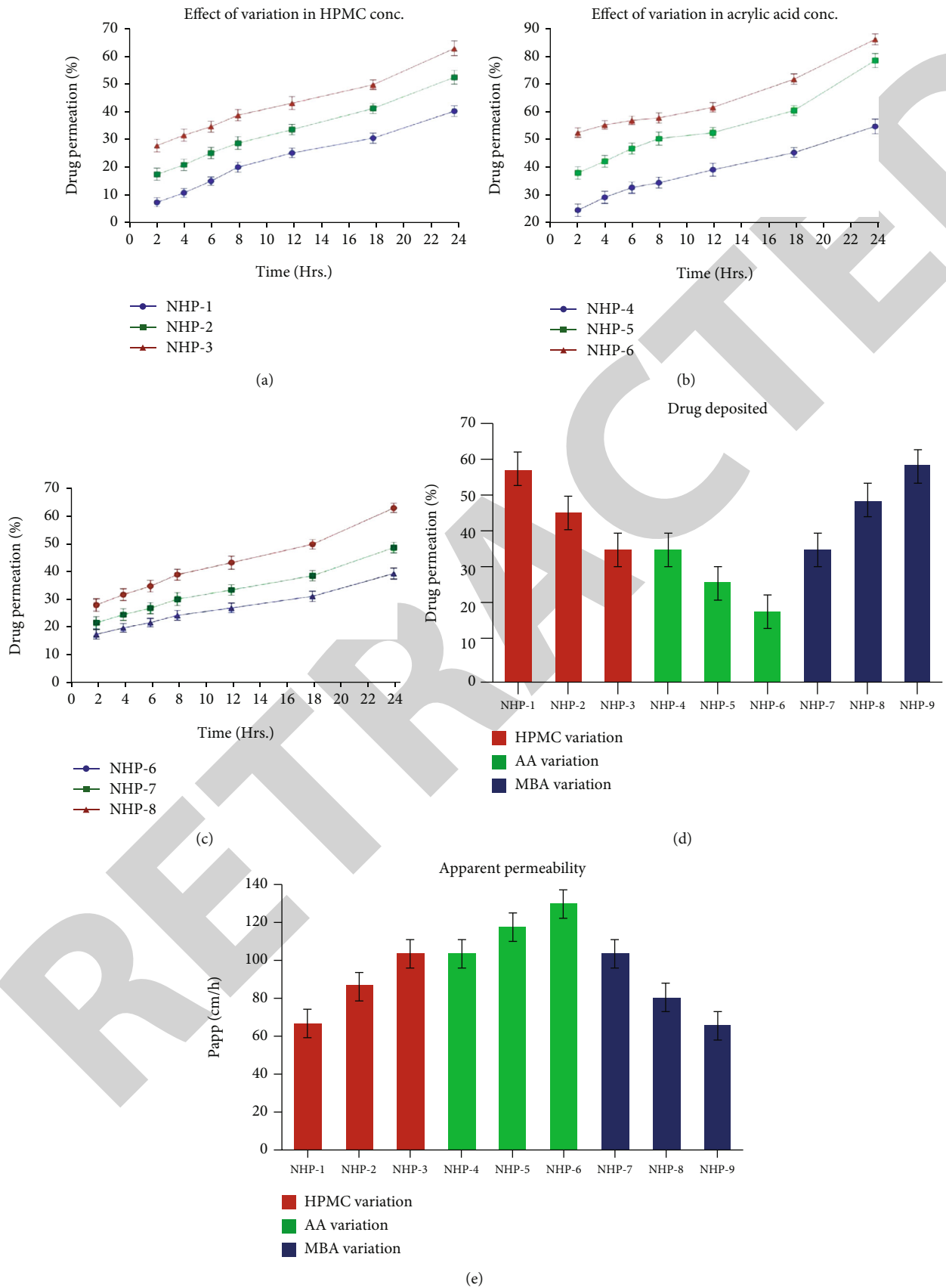


FIGURE 7: Continued.

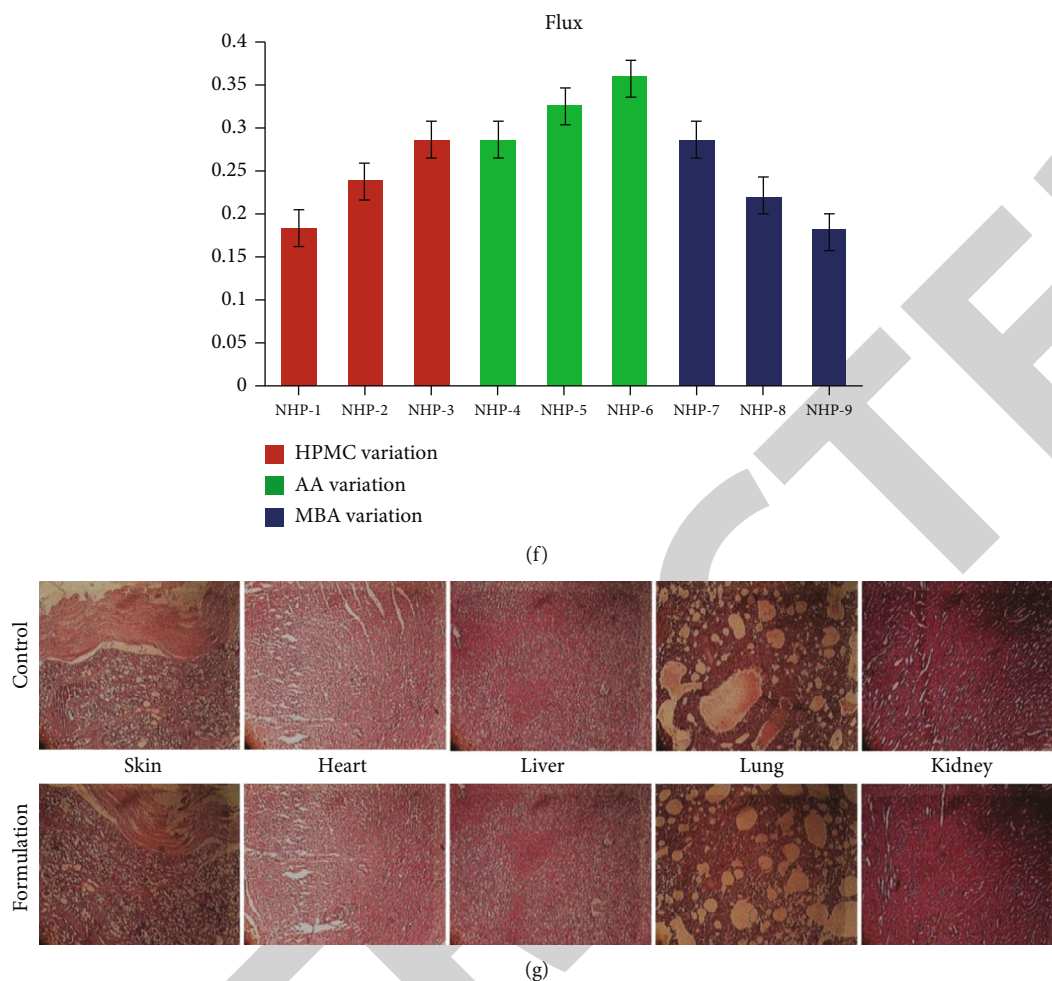


FIGURE 7: Effect of (a) HPMC, (b) AA, (c) MBA on % drug permeation, (d) %drug deposited, (e) apparent permeability, (f) flux, and (g) histological examination of various organs of rabbits.

TABLE 2: Apparent viscosity, flow index, and thixotropy of CG.

Parameter	Time	Temp			
		8°C	25°C	32°C	45°C
Apparent viscosity (dynes/cm <sup>2</sup> )	Fresh		291.59		
	(1) Month	287.15	278.37	281.88	280.9
	(2) Month	285.74	282.07	277.48	272.72
	(3) Month	282.94	281.12	275.29	268.12
Flow index	Fresh		0.63		
	(1) Month	0.62	0.62	0.61	0.61
	(2) Month	0.62	0.6	0.61	0.6
	(3) Month	0.63	0.59	0.59	0.58
Thixotropy (dynes/cm <sup>2</sup> .S)	Fresh		7508		
	(1) Month	7480	7331	7325	7283
	(2) Month	7421	7324	7222	7113
	(3) Month	7352	7283	7170	6970

promising outcome for %FIN permeation, apparent permeability, and flux (Figure 7). HPMC is an important amphiphilic carrier substance that plays an important part in the

penetration of moieties through skin. Amphiphilic substance utilize intercellular channels for infiltration through biological membranes [74]. Carbopol-based composites

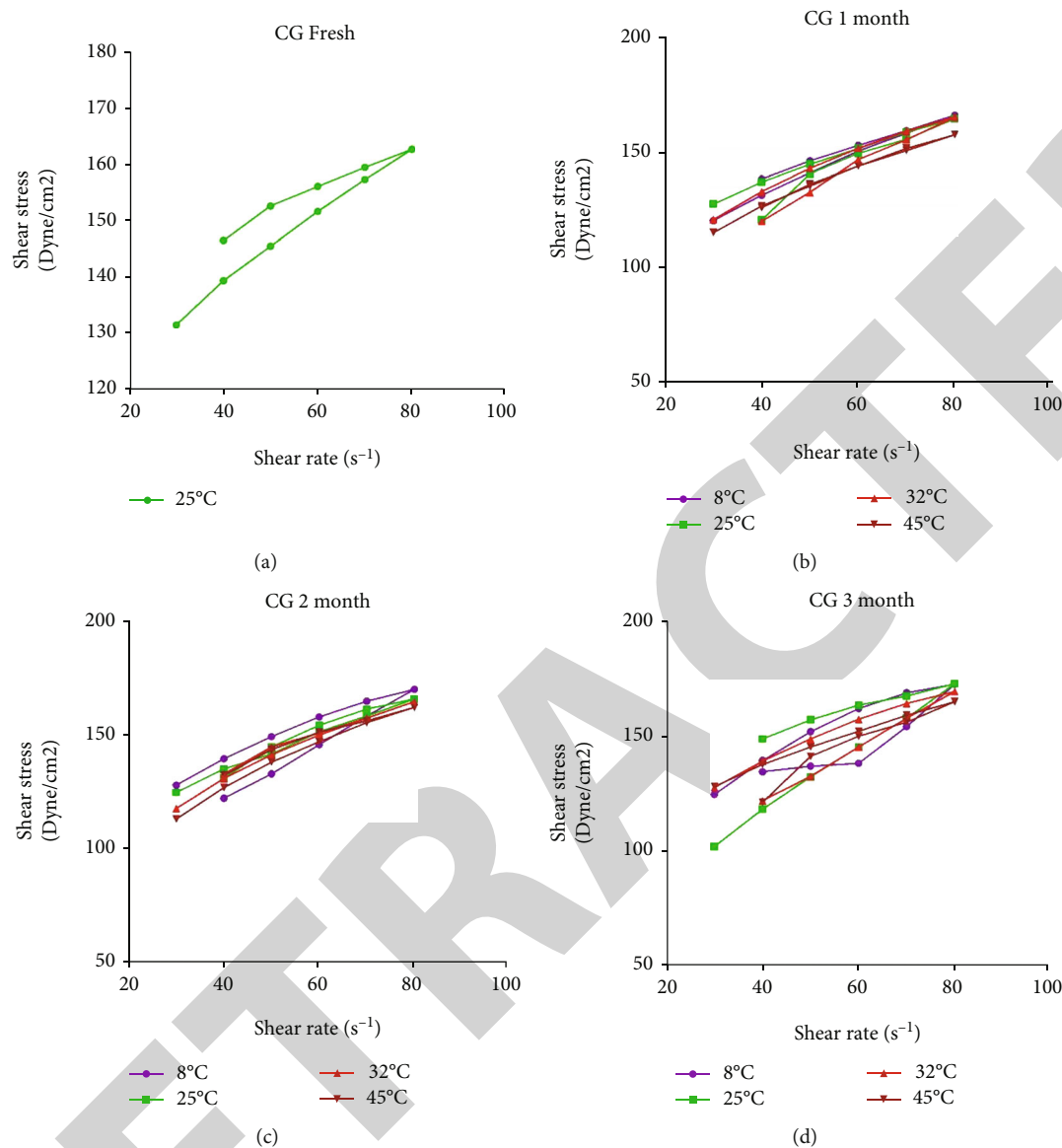


FIGURE 8: Rheograms of carbopol gel (CG) kept at different storage conditions: (a) freshly prepared, (b) after one month, (c) after two months, and (d) after three months.

are reported to have accelerated rate of solute diffusion across biological barriers [75]. The results for effect of variation of HPMC on skin permeation revealed increased permeation pattern with increasing polymeric content. This is because of looseness in mesh of nanogels and amphiphilic nature of polymer [76]. Previously developed HPMC-based drug carrier system has been reported to have increased diffusion across skin with increasing diffusible portion in donor part [77]. Dissociation and repulsion of carboxylic groups of AA at alkaline pH result in the formation of destrangled mesh of network of composites which enhanced permeation of FIN from formulation. Correlation between swelling and penetration of active agent from synthesized formulation is reported in literature by various researchers [78, 79]. Unlike HPMC and AA, the output for FIN penetration across skin was decreased as MBA content

of formulation increased. Obvious reason for this response is increased cross-linking density of nanogels [80].

**3.12. Stability Studies of Carbopol Gel (CG).** Rheological parameters of fresh, 1, 2, and 3 months stored CG were assessed at diverse temperature range, i.e., 8°C, 25°C, 32°C, and 45°C. Measured apparent viscosity, flow index, and thixotropy values are listed in Table 2. Figure 8 also represents rheograms of CG. The results of analysis interpret decreasing pattern in rheological findings with time, but that decrease was apparently very slight and nonsignificant. All the findings authenticate potential stability of developed CG.

It is evident from the results that CG resisted alteration in viscosity considerably as a function of temperature, thus possessing good thermal stability. The cross-linked junctions fend abjection of polymeric strands with increase in

TABLE 3: Results of skin irritation and toxicological studies.

(a)

Irritation test results on rabbits					
Formulation applied		Time of observation			
		24 h	48 h	72 h	240 h
Control	1	—	—	—	—
	2	—	—	—	—
	3	—	—	—	—
HPMC nanogels	1	—	—	—	—
	2	—	—	—	—
	3	—	—	—	—

Irritation scale

Sign	—	+	++	+++	++++
Outcome	None	Very slight	Well defined	Moderate	Eschar formation

(b)

Parameter	Liver, kidney, and lipid profile	
	Control	Nanogels
ALT (SGPT) (U/l)	117 ± 8.26	129 ± 12.17
AST (SGOT) (U/l)	71 ± 4.91	78 ± 4.81
Serum urea (mg/dl)	14.3 ± 0.94	14.8 ± 0.77
Serum creatinine (mg/dl)	0.8 ± 0.11	0.7 ± 0.12
Serum uric acid (mg/dl)	2.9 ± 0.24	3 ± 0.21
Total cholesterol (mg/dl)	58 ± 3.16	63 ± 3.19
Triglycerides (mg/dl)	45 ± 2.49	49 ± 3.08

(c)

Groups	Effect of nanogel administration on organ weights (g) of rabbits ( <i>n</i> = 3)				
	Heart	Liver	Lung	Kidney	Spleen
Control	4.63 ± 0.11	79.42 ± 0.17	9.33 ± 0.26	12.63 ± 0.24	1.03 ± 0.14
Nanogels	4.79 ± 0.11	81.94 ± 0.14	9.53 ± 0.17	13.11 ± 0.23	1.15 ± 0.21

(d)

Parameter	Haematological analysis	
	Control	Nanogels treated
Hb (g/dl)	14.3 ± 0.87	14.4 ± 0.89
pH	7.31 ± 0.04	7.24 ± 0.05
RBCs ( $\times 10^6/\text{mm}^3$ )	6.41 ± 42436	6.44 ± 39974
TLC ( $\times 10^3/\text{mm}^3$ )	9.2 ± 199.64	9.3 ± 232.17
Eosinophil (%)	2.1 ± 0.19	2.2 ± 0.19
Neutrophils (%)	49.2 ± 2.19	51.6 ± 1.86
Monocytes (%)	2.7 ± 0.22	2.9 ± 0.29
Lymphocytes (%)	58.3 ± 2.24	63.5 ± 2.58
PLT ( $\times 10^3/\text{mm}^3$ )	339 ± 5.14	352 ± 5.81
MCV (fl)	64.4 ± 3.28	64.9 ± 2.53
MCH (pg/cell)	19.2 ± 1.11	19.4 ± 1.22
MCHC (g/dl)	30.0 ± 1.73	30.7 ± 1.51

Values expressed as mean ± SD, *n* = 3.

TABLE 4: Clinical observations of toxicity studies.

Parameter observed	Time for observation	Group I (control)			Group III (treated with HPMC nanogels) 500 mg/kg of body weight		
Body weight (kg)	Pretreatment	2.17 ± 0.08			2.19 ± 0.03		
	24 h	2.19 ± 0.12			2.20 ± 0.05		
	48 h	2.18 ± 0.11			2.21 ± 0.03		
	72 h	2.19 ± 0.13			2.22 ± 0.06		
	240 h	2.19 ± 0.17			2.24 ± 0.02		
Food intake (g/day)	Pretreatment	63 ± 10.71			67 ± 7.62		
	24 h	62 ± 13.87			64 ± 9.24		
	48 h	61 ± 8.93			60 ± 5.75		
	72 h	63 ± 11.24			70 ± 7.53		
	240 h	58 ± 9.54			63 ± 9.48		
Water intake (ml/day)	Pretreatment	162 ± 11.72			179 ± 20.74		
	24 h	175 ± 6.89			178 ± 18.45		
	48 h	157 ± 45.34			176 ± 19.67		
	72 h	163 ± 12.82			169 ± 15.09		
	240 h	172 ± 23.09			187 ± 20.42		
Signs of illness	Pretreatment	R1	R2	R3	R1	R2	R3
	24 h	0	0	0	0	0	0
	48 h	0	0	0	0	0	1
	72 h	0	0	0	0	1	0
	240 h	0	0	0	0	0	0
Convulsion	Pretreatment	0	0	0	0	0	0
	24 h	0	0	0	0	0	0
	48 h	0	0	0	0	0	0
	72 h	0	0	0	0	0	0
	240 h	0	0	0	0	0	0
Hyperactivity	Pretreatment	0	0	0	0	0	0
	24 h	0	0	0	0	0	1
	48 h	0	0	2	1	0	0
	72 h	0	0	0	0	1	0
	240 h	0	0	0	0	0	1
Pain response	Pretreatment	1	1	1	1	1	1
	24 h	1	1	1	1	1	1
	48 h	1	0	1	0	1	1
	72 h	1	1	1	1	1	0
	240 h	1	1	1	1	1	1
Scale	Sign Outcome	0	1	2	3		
		Absent	Mild	Moderate	Intense		

temperature, thus justifying the stability of cross-linking web network [81]. This decrease in viscosity is also supported by the previous research [82]. Flow index measurement were recorded below 1, which indicates the pseudoplasticity fea-

ture of developed CG [83]. Rheograms of CG displayed both patterns (ascending and descending) in flow curves. It can be linked to establishment of hysteresis which is also manifested as “thixotropic loop” [84]. Thixotropy is believed to

be one of the desirable characteristics for skin-based DDS. This aids efficient applicability, spreading, and penetrating of the entities dispersed in formulation [85].

**3.13. Skin Irritation Studies.** Optimized HPMC-based nanogels were applied on the skin of shaved albino rabbits in order to evaluate the safety profile. The results of skin irritation analysis are given in Table 3. Satisfying results were observed as no indications of skin irritation were noticed through the course. This can be attributed to biocompatibility of cellulose-based composites [86].

### 3.14. Toxicity Studies

**3.14.1. Clinical Manifestation.** Various parameters, i.e., body weight, water and food intake, signs of illness, hyperactivity, convulsions, and pain response, were noticed during toxicity evaluation of developed nanogels (NHP-6). The results of the abovementioned clinical parameters are given in Table 4 which demonstrated no significant change in the said outcomes with no mortality in both groups under observation. Overall results substantiate the biocompatibility of applied nanogels which could be linked to nontoxic and biocompatible features of HPMC [87, 88].

**3.14.2. Biochemical Investigation.** Safety profile of subjects through toxicity studies can be analyzed by collecting vital data regarding blood and blood-based products. Vital information in the context of pathophysiological status of experimental animals can be gathered through haemopoietic markers [89]. In the present study, blood samples from experimental animals were collected and analyzed in view of toxicity assessment of developed nanogels. Table 3 enlists the results for various biochemical parameters which shows that both groups, i.e., control and nanogels treated, manifested no significant differences between biochemical output values, thus asserting biocompatibility of nanogels [90].

**3.14.3. Weight Variation and Histopathology.** Keeping in view the toxicological studies, autopsy of rabbits of both groups, i.e., control and nanogels treated, was performed to forecast the effect of dabbed formulation on various organs. All experimental work was performed abiding by guidelines of institute's Pharmacy Research Ethics Committee (PREC). Information about the toxic effects of applied formulation can be collected through output of weight variation and histopathological examination [91]. The results of weight measurement of vital organs of rabbits are enlisted in Table 3 which showed no significant weight variation among the animals in groups under examination. The results of histology of vital body organs, i.e., skin, heart, liver, kidney, and lungs are presented in Figure 7(g). The results articulate normal tissue structure with no sign of pathology which hints the biocompatibility of applied nanogels [92].

## 4. Conclusion

On the basis of the current study, it can be concluded that HPMC-based nanogels were prepared for efficient transdermal drug delivery. Characterization (FTIR, SEM, TGA, DSC,

and XRD) confirmed formation of stable composites. In vitro and ex vivo analysis confirmed formation of a stable, effective, and biocompatible drug delivery system. Such transdermal nanogel drug transport structure can be designed to overcome the limitations related to long time oral therapy as well as alternate to invasive drug delivery. Moreover, to avoid the first pass metabolism and promote better outcomes with improved patient compliance. However, in the future, there exists a need to perform *in vivo* studies on human volunteers.

## Data Availability

The data used to support the findings of this study are included within the article.

## Consent

Consent is not necessary.

## Conflicts of Interest

The authors report no conflict of interests.

## Authors' Contributions

Aousaf Ahmad was responsible for the investigation, data curation, and methodology. Mahmood Ahmad and Muhammad Usman Minhas were responsible for the conceptualization, methodology, and supervision and wrote the manuscript. Muhammad Sohail, Kifayat Ullah Khan, Sana Tanveer, and Shakeel Ijaz were responsible for the funding acquisition and wrote, reviewed, and edited the manuscript. Muhammad Sarfraz was responsible for the validation and visualization and reviewed and edited the manuscript.

## Acknowledgments

The authors are pleased to acknowledge the Islamia University of Bahawalpur for providing funds and research facilities for this study.

## Supplementary Materials

Graphical abstract exhibits the preparation technique, characterization, and toxicity evaluation of the developed nanogels. (*Supplementary Materials*)

## References

- [1] K. U. Khan, M. U. Minhas, S. F. Badshah, M. Sohail, A. Ahmad, and S. Ijaz, "Overview of nanoparticulate strategies for solubility enhancement of poorly soluble drugs," *Life Sciences*, vol. 291, article 120301, 2022.
- [2] K. U. Khan, M. U. Minhas, M. Sohail et al., "Synthesis of PEG-4000-co-poly (AMPS) nanogels by cross-linking polymerization as highly responsive networks for enhancement in meloxicam solubility," *Drug Development and Industrial Pharmacy*, vol. 47, no. 3, pp. 465–476, 2021.

- [3] K. U. Khan, N. Akhtar, and M. U. Minhas, "Poloxamer-407-co-poly (2-acrylamido-2-methylpropane sulfonic acid) cross-linked nanogels for solubility enhancement of olanzapine: synthesis, characterization, and toxicity evaluation," *AAPS PharmSciTech*, vol. 21, no. 5, pp. 1–15, 2020.
- [4] A. V. Kabanov and S. V. Vinogradov, "Nanogels as pharmaceutical carriers: finite networks of infinite capabilities," *Angewandte Chemie International Edition*, vol. 48, no. 30, pp. 5418–5429, 2009.
- [5] M. Hamidi, A. Azadi, and P. Rafiei, "Hydrogel nanoparticles in drug delivery," *Advanced Drug Delivery Reviews*, vol. 60, no. 15, pp. 1638–1649, 2008.
- [6] C. Aslan, N. Çelebi, İ. T. Değim, A. Atak, and Ç. Özer, "Development of interleukin-2 loaded chitosan-based nanogels using artificial neural networks and investigating the effects on wound healing in rats," *AAPS PharmSciTech*, vol. 18, no. 4, pp. 1019–1030, 2017.
- [7] S. V. Vinogradov, T. K. Bronich, and A. V. Kabanov, "Nano-sized cationic hydrogels for drug delivery: preparation, properties and interactions with cells," *Advanced Drug Delivery Reviews*, vol. 54, no. 1, pp. 135–147, 2002.
- [8] G. J. Gormley, E. Stoner, R. C. Bruskevitz et al., "The effect of finasteride in men with benign prostatic hyperplasia," *The Journal of Urology*, vol. 167, 2 Part 2, pp. 1102–1107, 2002.
- [9] H. A. Guess, "Benign prostatic hyperplasia: antecedents and natural history," *Epidemiologic Reviews*, vol. 14, no. 1, pp. 131–153, 1992.
- [10] J. D. McConnell, R. Bruskevitz, P. Walsh et al., "The effect of finasteride on the risk of acute urinary retention and the need for surgical treatment among men with benign prostatic hyperplasia," *New England Journal of Medicine*, vol. 338, no. 9, pp. 557–563, 1998.
- [11] J. T. Andersen, J. Curtis Nickel, V. R. Marshall, C. C. Schulman, and P. Boyle, "Finasteride significantly reduces acute urinary retention and need for surgery in patients with symptomatic benign prostatic hyperplasia," *Urology*, vol. 49, no. 6, pp. 839–845, 1997.
- [12] W. Fagir, R. M. Hathout, O. A. Sammour, and A. H. ElShafeey, "Self-microemulsifying systems of finasteride with enhanced oral bioavailability: multivariate statistical evaluation, characterization, spray-drying and in vivo studies in human volunteers," *Nanomedicine*, vol. 10, no. 22, pp. 3373–3389, 2015.
- [13] İ. I. Müderris, F. Bayram, and M. Güven, "A prospective, randomized trial comparing flutamide (250 mg/d) and finasteride (5 mg/d) in the treatment of hirsutism," *Fertility and Sterility*, vol. 73, no. 5, pp. 984–987, 2000.
- [14] A. Rossi, E. Mari, M. Scarnò et al., "Comparative effectiveness and finasteride vs serenoa repens in male androgenetic alopecia: a two-year study," *International Journal of Immunopathology and Pharmacology*, vol. 25, no. 4, pp. 1167–1173, 2012.
- [15] S. Tanveer, M. Ahmad, M. U. Minhas, A. Ahmad, and K. U. Khan, "Chitosan-PVA-co-poly (2-acrylamido-2-methylpropane sulfonic acid) cross-linked hybrid IPN-nanogels for transdermal delivery of ondansetron; synthesis, characterization and toxicological evaluation," *Polymer-Plastics Technology and Materials*, vol. 60, no. 17, pp. 1–22, 2021.
- [16] S. Mangalathillam, N. S. Rejinold, A. Nair, V. K. Lakshmanan, S. V. Nair, and R. Jayakumar, "Curcumin loaded chitin nanogels for skin cancer treatment via the transdermal route," *Nanoscale*, vol. 4, no. 1, pp. 239–250, 2012.
- [17] S. Mavuso, T. Marimuthu, Y. Choonara, P. Kumar, L. du Toit, and V. Pillay, "A review of polymeric colloidal nanogels in transdermal drug delivery," *Current Pharmaceutical Design*, vol. 21, no. 20, pp. 2801–2813, 2015.
- [18] A. J. Sivaram, P. Rajitha, S. Maya, R. Jayakumar, and M. Sabitha, "Nanogels for delivery, imaging and therapy," *Wiley Interdisciplinary Reviews: Nanomedicine and Nanobiotechnology*, vol. 7, no. 4, pp. 509–533, 2015.
- [19] A. Naik, Y. N. Kalia, and R. H. Guy, "Transdermal drug delivery: overcoming the skin's barrier function," *Pharmaceutical Science & Technology Today*, vol. 3, no. 9, pp. 318–326, 2000.
- [20] T. Canal and N. A. Peppas, "Correlation between mesh size and equilibrium degree of swelling of polymeric networks," *Journal of Biomedical Materials Research*, vol. 23, no. 10, pp. 1183–1193, 1989.
- [21] H. J. Chung, D. H. Go, J. W. Bae, I. K. Jung, J. W. Lee, and K. D. Park, "Synthesis and characterization of Pluronic® grafted chitosan copolymer as a novel injectable biomaterial," *Current Applied Physics*, vol. 5, no. 5, pp. 485–488, 2005.
- [22] W. Xiong, W. Wang, Y. Wang et al., "Dual temperature/pH-sensitive drug delivery of poly (N-isopropylacrylamide-co-acrylic acid) nanogels conjugated with doxorubicin for potential application in tumor hyperthermia therapy," *Colloids and Surfaces B: Biointerfaces*, vol. 84, no. 2, pp. 447–453, 2011.
- [23] J. S. Park, H. N. Yang, D. G. Woo, S. Y. Jeon, and K. H. Park, "Poly (N-isopropylacrylamide-co-acrylic acid) nanogels for tracing and delivering genes to human mesenchymal stem cells," *Biomaterials*, vol. 34, no. 34, pp. 8819–8834, 2013.
- [24] Q. Khalid, M. Ahmad, and M. Usman Minhas, "Hydroxypropyl- $\beta$ -cyclodextrin hybrid nanogels as nano-drug delivery carriers to enhance the solubility of dexibuprofen: characterization, in vitro release, and acute oral toxicity studies," *Advances in Polymer Technology*, vol. 37, no. 6, pp. 2171–2185, 2018.
- [25] K. U. Khan, M. U. Minhas, S. F. Badshah, M. Sohail, and R. M. Sarfraz, " $\beta$ -cyclodextrin modification by cross-linking polymerization as highly porous nanomatrices for olanzapine solubility improvement; synthesis, characterization and biocompatibility evaluation," *Journal of Drug Delivery Science and Technology*, vol. 67, article 102952, 2022.
- [26] H. Shah, A. Madni, M. A. Rahim et al., "Fabrication, in vitro and ex vivo evaluation of proliposomes and liposomal derived gel for enhanced solubility and permeability of diacerein," *PLoS One*, vol. 16, no. 10, article e0258141, 2021.
- [27] S. Khan, M. N. Aamir, A. Madni et al., "Lipid poly ( $\epsilon$ -caprolactone) hybrid nanoparticles of 5-fluorouracil for sustained release and enhanced anticancer efficacy," *Life Sciences*, vol. 284, article 119909, 2021.
- [28] S. Asghar, N. Akhtar, M. U. Minhas, and K. U. Khan, "Bi-polymeric spongy matrices through cross-linking polymerization: synthesized and evaluated for solubility enhancement of acyclovir," *AAPS PharmSciTech*, vol. 22, no. 5, pp. 1–16, 2021.
- [29] N. Jan, A. Madni, M. A. Rahim et al., "In vitro anti-leukemic assessment and sustained release behaviour of cytarabine loaded biodegradable polymer based nanoparticles," *Life Sciences*, vol. 267, article 118971, 2021.
- [30] S. Khan, A. Madni, M. A. Rahim et al., "Enhanced in vitro release and permeability of glibenclamide by proliposomes: development, characterization and histopathological evaluation," *Journal of Drug Delivery Science and Technology*, vol. 63, article 102450, 2021.

- [31] M. U. Minhas, O. Abdullah, M. Sohail et al., "Synthesis of novel combinatorial drug delivery system (nCDDS) for co-delivery of 5-fluorouracil and leucovorin calcium for colon targeting and controlled drug release," *Drug Development and Industrial Pharmacy*, pp. 1–14, 2022.
- [32] S. F. Badshah, N. Akhtar, M. U. Minhas et al., "Porous and highly responsive cross-linked  $\beta$ -cyclodextrin based nanomatrices for improvement in drug dissolution and absorption," *Life Sciences*, vol. 267, article 118931, 2021.
- [33] D. Lembo, S. Swaminathan, M. Donalizio et al., "Encapsulation of acyclovir in new carboxylated cyclodextrin-based nanospheres improves the agent's antiviral efficacy," *International Journal of Pharmaceutics*, vol. 443, no. 1-2, pp. 262–272, 2013.
- [34] M. R. De Moura, R. J. Avena-Bustillos, T. H. McHugh, J. M. Krochta, and L. H. Mattoso, "Properties of novel hydroxypropyl methylcellulose films containing chitosan nanoparticles," *Journal of Food Science*, vol. 73, no. 7, pp. N31–N37, 2008.
- [35] Y. Dong, W. K. Ng, S. Shen, S. Kim, and R. B. H. Tan, "Preparation and characterization of spironolactone nanoparticles by antisolvent precipitation," *International Journal of Pharmaceutics*, vol. 375, no. 1-2, pp. 84–88, 2009.
- [36] S. Punitha, R. Uvarani, A. Panneerselvam, and S. Nithyanantham, "Physico-chemical studies on some saccharides in aqueous cellulose solutions at different temperatures - acoustical and FTIR analysis," *Journal of Saudi Chemical Society*, vol. 18, no. 5, pp. 657–665, 2014.
- [37] J. W. Lee, S. Y. Kim, S. S. Kim, Y. M. Lee, K. H. Lee, and S. J. Kim, "Synthesis and characteristics of interpenetrating polymer network hydrogel composed of chitosan and poly (acrylic acid)," *Journal of Applied Polymer Science*, vol. 73, no. 1, pp. 113–120, 1999.
- [38] Y. Fan, M. Zhang, and Y.-Q. Feng, "Poly (acrylamide-vinylpyridine-N, N'-methylene bisacrylamide) monolithic capillary for in-tube solid-phase microextraction coupled to high performance liquid chromatography," *Journal of Chromatography A*, vol. 1099, no. 1-2, pp. 84–91, 2005.
- [39] T. A. Ahmed, "Preparation of finasteride capsules-loaded drug nanoparticles: formulation, optimization, in vitro, and pharmacokinetic evaluation," *International Journal of Nanomedicine*, vol. 11, p. 515, 2016.
- [40] K. P. Dhake, P. J. Tambade, Z. S. Qureshi, R. S. Singhal, and B. M. Bhanage, "HPMC-PVA film immobilized Rhizopus oryzae lipase as a biocatalyst for transesterification reaction," *ACS Catalysis*, vol. 1, no. 4, pp. 316–322, 2011.
- [41] E. Karavas, E. Georgarakis, and D. Bikiaris, "Felodipine nanodispersions as active core for predictable pulsatile chronotherapeutics using PVP/HPMC blends as coating layer," *International Journal of Pharmaceutics*, vol. 313, no. 1-2, pp. 189–197, 2006.
- [42] N. Schultheiss, J. P. Smit, and J. A. Hanko, "Three isostructural solvates of finasteride and their solid-state characterization," *European Journal of Pharmaceutical Sciences*, vol. 38, no. 5, pp. 498–503, 2009.
- [43] D. Kiss, R. Zekó, C. Novák, and Z. Éhen, "Application of DSC and NIRS to study the compatibility of metronidazole with different pharmaceutical excipients," *Journal of Thermal Analysis and Calorimetry*, vol. 84, no. 2, pp. 447–451, 2006.
- [44] M. A. Hussain, M. Badshah, M. S. Iqbal et al., "HPMC-salicylate conjugates as macromolecular prodrugs: design, characterization, and nano-rods formation," *Journal of Polymer Science Part A: Polymer Chemistry*, vol. 47, no. 16, pp. 4202–4208, 2009.
- [45] C. Ding, M. Zhang, and G. Li, "Preparation and characterization of collagen/hydroxypropyl methylcellulose (HPMC) blend film," *Carbohydrate Polymers*, vol. 119, pp. 194–201, 2015.
- [46] A. Othman, J. S. O. Evans, I. R. Evans, R. K. Harris, and P. Hodgkinson, "Structural study of polymorphs and solvates of finasteride," *Journal of Pharmaceutical Sciences*, vol. 96, no. 5, pp. 1380–1397, 2007.
- [47] Z. X. He, Z. H. Wang, H. H. Zhang et al., "Doxycycline and hydroxypropyl- $\beta$ -cyclodextrin complex in poloxamer thermal sensitive hydrogel for ophthalmic delivery," *Acta Pharmaceutica Sinica B*, vol. 1, no. 4, pp. 254–260, 2011.
- [48] R. Das, D. Das, P. Ghosh, S. Dhara, A. B. Panda, and S. Pal, "Development and application of a nanocomposite derived from crosslinked HPMC and Au nanoparticles for colon targeted drug delivery," *RSC Advances*, vol. 5, no. 35, pp. 27481–27490, 2015.
- [49] J. Rotta, E. Minatti, and P. L. M. Barreto, "Determination of structural and mechanical properties, diffractometry, and thermal analysis of chitosan and hydroxypropylmethylcellulose (HPMC) films plasticized with sorbitol," *Food Science and Technology*, vol. 31, no. 2, pp. 450–455, 2011.
- [50] S. V. Dorozhkin, "Is there a chemical interaction between calcium phosphates and hydroxypropylmethylcellulose (HPMC) in organic/inorganic composites?," *Journal of Biomedical Materials Research: An Official Journal of The Society for Biomaterials and The Japanese Society for Biomaterials*, vol. 54, no. 2, pp. 247–255, 2001.
- [51] J. Suksaeree, C. Monton, F. Madaka et al., "Formulation, physicochemical characterization, and in vitro study of chitosan/HPMC blends-based herbal blended patches," *AAPS PharmSciTech*, vol. 16, no. 1, pp. 171–181, 2015.
- [52] F. M. Mady and U. F. Aly, "Experimental, molecular docking investigations and bioavailability study on the inclusion complexes of finasteride and cyclodextrins," *Drug Design, Development and Therapy*, vol. 11, pp. 1681–1692, 2017.
- [53] P. Kumar, C. Mohan, M. Kanamsrinivasan Uma Shankar, and M. Gulati, "Physicochemical characterization and release rate studies of solid dispersions of ketoconazole with pluronic f127 and pvp k-30," *Iranian journal of pharmaceutical research: IJPR*, vol. 10, no. 4, pp. 685–694, 2011.
- [54] M. A. Jyoti, V. V. Thai, Y. K. Min, B. T. Lee, and H. Y. Song, "In vitro bioactivity and biocompatibility of calcium phosphate cements using hydroxy-propyl-methyl-cellulose (HPMC)," *Applied Surface Science*, vol. 257, no. 5, pp. 1533–1539, 2010.
- [55] K.-S. Kim and S.-J. Park, "Effect of porous silica on sustained release behaviors of pH sensitive pluronic F127/poly (acrylic acid) hydrogels containing tulobuterol," *Colloids and Surfaces B: Biointerfaces*, vol. 80, no. 2, pp. 240–246, 2010.
- [56] K. Sohail, I. U. Khan, Y. Shahzad, T. Hussain, and N. M. Ranjha, "pH-sensitive polyvinylpyrrolidone-acrylic acid hydrogels: impact of material parameters on swelling and drug release," *Brazilian Journal of Pharmaceutical Sciences*, vol. 50, no. 1, pp. 173–184, 2014.
- [57] T. Hussain, N. M. Ranjha, and Y. Shahzad, "Swelling and controlled release of tramadol hydrochloride from a pH-sensitive hydrogel," *Designed Monomers and Polymers*, vol. 14, no. 3, pp. 233–249, 2011.
- [58] S. C. Joshi, "Sol-gel behavior of hydroxypropyl methylcellulose (HPMC) in ionic media including drug release," *Materials*, vol. 4, no. 10, pp. 1861–1905, 2011.



- [59] R. Rajera, K. Nagpal, S. K. Singh, and D. N. Mishra, "Niosomes: a controlled and novel drug delivery system," *Biological and Pharmaceutical Bulletin*, vol. 34, no. 7, pp. 945–953, 2011.
- [60] S. Kovačič and M. S. Silverstein, "Superabsorbent, high porosity, PAMPS-based hydrogels through emulsion templating," *Macromolecular Rapid Communications*, vol. 37, no. 22, pp. 1814–1819, 2016.
- [61] H. Hezaveh and I. I. Muhamad, "Controlled drug release via minimization of burst release in pH-response kappa-carrageenan/polyvinyl alcohol hydrogels," *Chemical Engineering Research and Design*, vol. 91, no. 3, pp. 508–519, 2013.
- [62] T. H. Kim, J. S. Ahn, H. K. Choi, Y. J. Choi, and C. S. Cho, "A novel mucoadhesive polymer film composed of carbopol, poloxamer and hydroxypropylmethylcellulose," *Archives of Pharmacol Research*, vol. 30, no. 3, pp. 381–386, 2007.
- [63] C. Zhao, Q. Chen, K. Patel et al., "Synthesis and characterization of pH-sensitive poly (N-2-hydroxyethyl acrylamide)-acrylic acid (poly (HEAA/AA)) nanogels with antifouling protection for controlled release," *Soft Matter*, vol. 8, no. 30, pp. 7848–7857, 2012.
- [64] L.-W. Xia, R. Xie, X. J. Ju, W. Wang, Q. Chen, and L. Y. Chu, "Nano-structured smart hydrogels with rapid response and high elasticity," *Nature Communications*, vol. 4, no. 1, p. 2226, 2013.
- [65] G. Soni and K. S. Yadav, "High encapsulation efficiency of poloxamer-based injectable thermoresponsive hydrogels of etoposide," *Pharmaceutical Development and Technology*, vol. 19, no. 6, pp. 651–661, 2014.
- [66] N. M. Ranjha and U. F. Qureshi, "Preparation and characterization of crosslinked acrylic acid/hydroxypropyl methyl cellulose hydrogels for drug delivery," *International Journal of Pharmacy and Pharmaceutical Sciences*, vol. 6, no. 400, p. 410, 2014.
- [67] S. Yu, X. Zhang, G. Tan et al., "A novel pH-induced thermosensitive hydrogel composed of carboxymethyl chitosan and poloxamer cross-linked by glutaraldehyde for ophthalmic drug delivery," *Carbohydrate Polymers*, vol. 155, pp. 208–217, 2017.
- [68] P. Colombo, "Swelling-controlled release in hydrogel matrices for oral route," *Advanced Drug Delivery Reviews*, vol. 11, no. 1-2, pp. 37–57, 1993.
- [69] M. Changez, K. Burugapalli, V. Koul, and V. Choudhary, "The effect of composition of poly (acrylic acid)-gelatin hydrogel on gentamicin sulphate release: in vitro," *Biomaterials*, vol. 24, no. 4, pp. 527–536, 2003.
- [70] A. Pourjavadi and S. Barzegar, "Smart pectin-based superabsorbent hydrogel as a matrix for ibuprofen as an oral non-steroidal anti-inflammatory drug delivery," *Starch-Stärke*, vol. 61, no. 3-4, pp. 173–187, 2009.
- [71] S. Cafaggi, R. Leardi, B. Parodi, G. Caviglioli, E. Russo, and G. Bignardi, "Preparation and evaluation of a chitosan salt-poloxamer 407 based matrix for buccal drug delivery," *Journal of Controlled Release*, vol. 102, no. 1, pp. 159–169, 2005.
- [72] A. Nochos, D. Douroumis, and N. Bouropoulos, "In vitro release of bovine serum albumin from alginate/HPMC hydrogel beads," *Carbohydrate Polymers*, vol. 74, no. 3, pp. 451–457, 2008.
- [73] M. Paloma, Y. Enobakhare, G. Torrado, and S. Torrado, "Release of amoxicillin from polyionic complexes of chitosan and poly(acrylic acid). study of polymer/polymer and polymer/drug interactions within the network structure," *Biomaterials*, vol. 24, no. 8, pp. 1499–1506, 2003.
- [74] M. Ali, D. Kumar, and H. A. Al-Lohedan, "Salt effect on the cloud point phenomenon of amphiphilic drug-hydroxypropylmethyl cellulose system," *Journal of Chemistry*, vol. 2014, Article ID 293972, 8 pages, 2014.
- [75] O. Pillai and R. Panchagnula, "Transdermal delivery of insulin from poloxamer gel: ex vivo and in vivo skin permeation studies in rat using iontophoresis and chemical enhancers," *Journal of Controlled Release*, vol. 89, no. 1, pp. 127–140, 2003.
- [76] P. P. Shah, P. R. Desai, A. R. Patel, and M. S. Singh, "Skin permeating nanogel for the cutaneous co-delivery of two anti-inflammatory drugs," *Biomaterials*, vol. 33, no. 5, pp. 1607–1617, 2012.
- [77] M. Jug, M. Bećirević-Lačan, A. Kwokal, and B. Cetina-Cizmek, "Influence of cyclodextrin complexation on piroxicam gel formulations," *Acta Pharmaceutica*, vol. 55, no. 3, pp. 223–236, 2005.
- [78] S. Y. Nam and Y. M. Lee, "Pervaporation and properties of chitosan-poly (acrylic acid) complex membranes," *Journal of Membrane Science*, vol. 135, no. 2, pp. 161–171, 1997.
- [79] M. Dorrani, M. Kaul, A. Parhi, E. J. LaVoie, D. S. Pilch, and B. Michniak-Kohn, "TXA497 as a topical antibacterial agent: comparative antistaphylococcal, skin deposition, and skin permeation studies with mupirocin," *International Journal of Pharmaceutics*, vol. 476, no. 1-2, pp. 199–204, 2014.
- [80] T. Cerchiara, B. Luppi, F. Bigucci, I. Orienti, and V. Zecchi, "Physically cross-linked chitosan hydrogels as topical vehicles for hydrophilic drugs," *Journal of Pharmacy and Pharmacology*, vol. 54, no. 11, pp. 1453–1459, 2002.
- [81] M. T. Islam, N. Rodríguez-Hornedo, S. Ciotti, and C. Ackermann, "Rheological characterization of topical carbomer gels neutralized to different pH," *Pharmaceutical Research*, vol. 21, no. 7, pp. 1192–1199, 2004.
- [82] J.-Y. Kim, J. Y. Song, E. J. Lee, and S. K. Park, "Rheological properties and microstructures of carbopol gel network system," *Colloid and Polymer Science*, vol. 281, no. 7, pp. 614–623, 2003.
- [83] L. Gaspar and P. M. Campos, "Rheological behavior and the SPF of sunscreens," *International Journal of Pharmaceutics*, vol. 250, no. 1, pp. 35–44, 2003.
- [84] G. M. Gonçalves and P. M. Campos, "Shelf life and rheology of emulsions containing vitamin C and its derivatives," *Revista de Ciências Farmacêuticas Básica e Aplicada*, vol. 30, no. 2, pp. 217–224, 2009.
- [85] N. M. Corrêa, F. B. Camargo Júnior, R. F. Ignácio, and G. R. Leonardi, "Avaliação do comportamento reológico de diferentes géis hidrofílicos," *Revista Brasileira de Ciências Farmacêuticas*, vol. 41, no. 1, pp. 73–78, 2005.
- [86] A. Sannino, C. Demitri, and M. Madaghiele, "Biodegradable cellulose-based hydrogels: design and applications," *Materials*, vol. 2, no. 2, pp. 353–373, 2009.
- [87] C. Chang and L. Zhang, "Cellulose-based hydrogels: present status and application prospects," *Carbohydrate Polymers*, vol. 84, no. 1, pp. 40–53, 2011.
- [88] D. Klemm, B. Heublein, H. P. Fink, and A. Bohn, "Cellulose: fascinating biopolymer and sustainable raw material," *Angewandte Chemie International Edition*, vol. 44, no. 22, pp. 3358–3393, 2005.

## Retraction

# Retracted: Chemical Composition and Biological Evaluation of *Typha domingensis* Pers. to Ameliorate Health Pathologies: *In Vitro* and *In Silico* Approaches

### BioMed Research International

Received 8 January 2024; Accepted 8 January 2024; Published 9 January 2024

Copyright © 2024 BioMed Research International. This is an open access article distributed under the Creative Commons Attribution License, which permits unrestricted use, distribution, and reproduction in any medium, provided the original work is properly cited.

This article has been retracted by Hindawi following an investigation undertaken by the publisher [1]. This investigation has uncovered evidence of one or more of the following indicators of systematic manipulation of the publication process:

- (1) Discrepancies in scope
- (2) Discrepancies in the description of the research reported
- (3) Discrepancies between the availability of data and the research described
- (4) Inappropriate citations
- (5) Incoherent, meaningless and/or irrelevant content included in the article
- (6) Manipulated or compromised peer review

The presence of these indicators undermines our confidence in the integrity of the article's content and we cannot, therefore, vouch for its reliability. Please note that this notice is intended solely to alert readers that the content of this article is unreliable. We have not investigated whether authors were aware of or involved in the systematic manipulation of the publication process.

Wiley and Hindawi regrets that the usual quality checks did not identify these issues before publication and have since put additional measures in place to safeguard research integrity.

We wish to credit our own Research Integrity and Research Publishing teams and anonymous and named external researchers and research integrity experts for contributing to this investigation.

The corresponding author, as the representative of all authors, has been given the opportunity to register their agreement or disagreement to this retraction. We have kept a record of any response received.

### References

- [1] R. Dilshad, K. U. R. Khan, L. Saeed et al., "Chemical Composition and Biological Evaluation of *Typha domingensis* Pers. to Ameliorate Health Pathologies: *In Vitro* and *In Silico* Approaches," *BioMed Research International*, vol. 2022, Article ID 8010395, 16 pages, 2022.

## Research Article

# Chemical Composition and Biological Evaluation of *Typha domingensis* Pers. to Ameliorate Health Pathologies: *In Vitro* and *In Silico* Approaches

Rizwana Dilshad,<sup>1</sup> Kashif-ur-Rehman Khan <sup>1</sup>, Laiba Saeed,<sup>2</sup> Asmaa E. Sherif <sup>3,4</sup>,  
Saeed Ahmad,<sup>1</sup> Chitchamai Ovatlarnporn,<sup>5</sup> Jawad Nasim,<sup>6</sup> Musaddique Hussain,<sup>7</sup>  
Bilal Ahmad Ghalloo <sup>1</sup>, Abdul Basit,<sup>8</sup> and Imran Mukhtar<sup>9</sup>

<sup>1</sup>Department of Pharmaceutical Chemistry, Faculty of Pharmacy, The Islamia University of Bahawalpur, Bahawalpur 63100, Pakistan

<sup>2</sup>Allama Iqbal Medical College, Lahore, Pakistan

<sup>3</sup>Department of Pharmacognosy, College of Pharmacy, Prince Sattam Bin Abdulaziz University, Alkharj 11942, Saudi Arabia

<sup>4</sup>Department of Pharmacognosy, Faculty of Pharmacy, Mansoura University, Mansoura 35516, Egypt

<sup>5</sup>Department of Pharmaceutical Chemistry, Faculty of Pharmaceutical Sciences, Prince of Songkla University, Hat Yai 90110, Thailand

<sup>6</sup>Division of Bioorganic Chemistry, School of Pharmacy, Saarland University, Saarbruecken, Germany

<sup>7</sup>Department of Pharmacology, Faculty of Pharmacy, The Islamia University of Bahawalpur, Bahawalpur 63100, Pakistan

<sup>8</sup>Quaid-e-Azam College of Pharmacy, Quaid-e-Azam Educational Complex, Sahiwal, Punjab, Pakistan

<sup>9</sup>Sir Sadiq Muhammad Khan Abbasi Post Graduate Medical College, Faculty of Medicine & Allied Health Sciences, The Islamia University of Bahawalpur, Bahawalpur 63100, Pakistan

Correspondence should be addressed to Kashif-ur-Rehman Khan; [kashifur.rahman@iub.edu.pk](mailto:kashifur.rahman@iub.edu.pk)

Received 24 May 2022; Accepted 23 June 2022; Published 14 July 2022

Academic Editor: Hassan Albarqi

Copyright © 2022 Rizwana Dilshad et al. This is an open access article distributed under the Creative Commons Attribution License, which permits unrestricted use, distribution, and reproduction in any medium, provided the original work is properly cited.

Human diseases are becoming more prevalent, necessitating the development of modalities to overcome the challenges of treating various disorders. In the current research, we analyzed the biomedicinal role of *Typha domingensis* which is an important medicinal plant. The species is traditionally used in the treatment of neurological disorders and skin malignancies. The chloroform (CFTD) and *n*-butanol fractions of *T. domingensis* (BFTD) were subjected to chemical profiling through the determination of total polyphenolic contents and GC-MS analysis. The oral toxicity test was applied to investigate the toxicity of the extracts. Antioxidant capacity was analyzed by four *in vitro* methods: DPPH, ABTS, FRAP, and CUPRAC. The pharmacological potential was evaluated through clinically significant enzyme inhibition assays, thrombolytic, and antimicrobial activities. *In silico* molecular docking approach was applied to confirm the role of *T. domingensis* against the enzymes. The polyphenolic quantification revealed that the BFTD was comparatively rich in total phenolic and flavonoid contents (97.14 milligrams gallic acid equivalent (mg GAE/g) and 362.5 milligrams quercetin equivalent per gram of dry extract (mg QE/g DE), respectively), as compared to the CFTD. The GC-MS analysis of the CFTD and BFTD resulted in the tentative identification of 67 and 29 compounds, respectively, with the major components of fatty acids and essential oil. The oral toxicity test revealed the safety and biocompatibility of CFTD and BFTD. Both the fractions showed promising antioxidant activity. Tyrosinase was found as the major enzyme inhibited by BFTD (78.67%) and CFTD (68.09%), whereas the standard kojic acid showed 85.58% inhibition. The inhibition results of acetylcholinesterase and butyrylcholinesterase by BFTD (71.65 and 60.79%, respectively) are higher than CFTD. Both the fractions were found active against various strains of bacteria. Furthermore, the molecular docking studies of the compounds showed a good docking score against all the docked enzymes among which deoxycasaldekaran C was found with the highest binding affinities in comparison to the standard. The current study suggests that *T. domingensis* is nontoxic and can be a potential source of phytoconstituents with promising pharmacological potential.

## 1. Introduction

Nature has endowed humans with a tremendous vast collection of plants and herbs that have been utilized to ameliorate health pathologies [1]. The World Health Organization (WHO) also sees ethnopharmacological considerations as a profitable way to assess medicinal plants as a source of molecules for both conventional and modern medicines. It is estimated that 80% of the worldwide population uses herbal medicine, and in the case of developing countries, the rates may be as high as 95% [2]. Traditional and indigenous medical systems are safer, less expensive, and more easily accessible [3]. Therefore, in the current era, natural therapy is always interested in elucidating the biological potential and chemical composition of plants. As a consequence of these important characteristics, nearly 20,000 species of plants have been used for therapeutical purposes [4]. Although there are several natural and synthetic antibacterials available, on account of the increase in resistance, there is a need of finding new antibacterial agents. Sometimes, there is no antibacterial agent to cure infections caused by these resistant bacterial strains [5].

Phenolic compounds found in medicinal plants are used to treat a variety of human diseases and serve a vital part in healing [6]. Medicinal plants are used to study and analysis of the bioactive phytochemicals that are necessary for the production of new medicines [7]. On utilization of polyphenols, numerous effects likely antibacterial, antioxidants, and anticancer are observed [8]. It is concluded that the beneficial impact of polyphenols is often related to their antioxidant activity [9]. Antioxidants are compounds that can prevent or reduce cell damage initiated by free radicals, produced by the body in response to environmental and other stress. They are also known as “free-radical scavengers.” Antioxidants are obtained from both sources natural and synthetic [10]. Antioxidants are also being investigated as potential therapies for neurodegenerative illnesses such as Alzheimer’s and Parkinson’s disorders. Excessive oxidative damage to cells causes a variety of clinical problems including rheumatoid arthritis, cardiovascular diseases, leukemia, thalassemia, ischemic stroke, hemodialysis, schizophrenia, depression, ulcerogenic, and acquired immunodeficiency diseases, and antioxidants have been linked to improved outcomes in the treatment of these diseases/disorders [11].

*Typha* is a genus of monocotyledonous plants [12]. One genus and 10 to 15 species make up the Typhaceae family [13], and commonly, it is known as cattails, which refers to the genus’ distinctive inflorescence. Cattails are wetland plants found in moist soil, swamps, shallow fresh marshes, and brackish seas around the world [14]. The *Typha domingensis*, a most familiar wetland plant, is found in a variety of wetland ecosystems, including swamps, marshes, and lakeshores. This is spread in tropical and subtropical areas. The plant has a diverse morphology and is found in various countries throughout the world [15]. *Typha* species are unisexual and monoecious plants with air-pollinated blooms that grow in dense spikes.

The female flowers of the *Typha* species are used externally to control bleeding, in addition to wound healing and

burns in Turkish folk medicine [16]. The lower stem has diuretic and astringent properties, and the leaves have analgesic, antioxidant, and diuretic properties [17]. Pollens are stringent, desiccant, diuretic, hemostatic, and vulnerary [13]. It is used for nosebleeds, uterine bleeding, postpartum abdominal discomfort, and abscesses [13]. It is not recommended for pregnant women [18]. The roots have anti-inflammatory, antioxidant, astringent, cytotoxic, and diuretic properties [19]. The spasmolytic, bronchodilator, and vasodilating effect of hydroethanolic extract of *Typha domingensis* was reported earlier [20]. The DPPH and  $\alpha$ -glucosidase inhibition activity of some solvent extracts/fractions of fruits only and the *in vivo* wound healing potential of female flowers of *T. domingensis* have been determined previously [21, 22]. The dichloromethane extract of *T. domingensis* and *T. latifolia* was subjected to the GC-MS for profiling and revealed the presence of alkyl coumarates and ferulates [15]. It is earlier reported that the pollens of *Typha* are largely made up of sterols, terpenoids, flavones, and long-chain hydrocarbons [18]. In the pharmacological study, pollens have been related to several actions, including the induction of cyclic adenosine monophosphate (cAMP), cholesterol-lowering, immunosuppression, and anticoagulation [7]. All the data in the literature revealed the medicinal potential of *T. domingensis*.

The present investigation has been conducted for the screening of bioactive secondary metabolites, antioxidant capacity, *in vitro* biological evaluation, and *in silico* molecular docking of chloroform and *n*-butanol fractions of *T. domingensis* Pers. (Southern cattail). The screening of bioactive compounds was evaluated by qualitative preliminary phytochemical analysis, total polyphenol content determination, and GC-MS investigation. The antioxidant potential was determined by ABTS, FRAP, DPPH, and CUPRAC. The *in vitro* biological potential was analyzed by enzyme inhibition (tyrosinase, acetylcholinesterase, and butyrylcholinesterase), thrombolytic, and antibacterial assays. The major bioactive phytochemicals screened by GC-MS of CFTD and BFTD were further evaluated for molecular docking. All these studies were first time performed for these fractions of the whole parts of *T. domingensis*.

## 2. Materials and Methods

**2.1. Sample Collection and Plant Identification.** The harvest of mature plants was carried out in March 2019 from Multan, Pakistan; the collected plant was identified by the Botany Department, Faculty of Life sciences, the Islamia University of Bahawalpur, and the plant specimen was submitted in the herbarium with reference number 412.

**2.2. Extract Preparation.** The powdered plant material was macerated for 14 days at room temperature in 80% methanol with occasional stirring. Because of its efficiency in extracting phenolics and flavonoids, aqueous methyl alcohol was used as a solvent [23]. To acquire the fine yield, the soaked plant was first filtered through muslin cloth, followed by filtration with Whatman-1 filter paper. A rotary evaporator (Heidolph, Germany) was used to concentrate the filtrate

under reduced pressure and further air-dried. The dried methanolic extract was mixed in deionized water to form a uniform solution for liquid-liquid fractionation by using two solvents: chloroform and *n*-butanol, in the order of increasing polarity. The two fractions chloroform fractions *T. domingensis* (CFTD) and *n*-butanol of *T. domingensis* (BFTD) fractions were obtained. These fractions were also evaporated with the rotary evaporator at 40°C, air-dried, and stored for further analysis [24].

### 2.3. Chemical Composition

**2.3.1. Determination of Total Phenolic Contents (TPC).** For TPC, 25  $\mu$ L fractions or standard (gallic acid) solution was mixed with dilute Folin-Ciocalteu reagent (10  $\mu$ L, 1:9, *v/v*) and shaken vigorously. After 3 minutes, sodium carbonate solution (75  $\mu$ L, 1%) was added, and the absorbance was measured at 760 nm after 2 hours of incubation at 25°C with a BioTek microplate reader. The same procedure was repeated for negative control replacing fraction solution with methanol. Results were exhibited as milligrams of gallic acid equivalent per gram of dry extract (mg GAE/g extract) [25].

**2.3.2. Estimation of Total Flavonoid Contents (TFC).** Aluminum chloride was used to determine the TFC. The solution was made by mixing 0.5 mL of fraction solution (1 mg/mL) or standard (serial dilution of quercetin), 2 mL of distilled H<sub>2</sub>O, and 0.15 mL of 5% NaNO<sub>2</sub> in a test tube. After 5 minutes at room temperature, 0.15 mL of 10% AlCl<sub>3</sub> was added, and the solution was allowed for another 5 minutes. Following that, 1 mL of a 4% NaOH solution was added and diluted in 5 mL of pure water. The resultant solution was vortexed and incubated at room temperature for 15 minutes. A blank was made by mixing the sample solution (0.5 mL) with methanol (1 mL) but without AlCl<sub>3</sub>. Results were exhibited as milligrams of quercetin equivalent per gram of dry extract (mg QE/g extract) [26].

**2.3.3. Gas Chromatography-Mass Spectrometry Analysis (GC-MS).** The CFTD and BFTD were analyzed by GC-MS Agilent (6890 series and Hewlett Packard, 5973 ground sensor). Blown barriers were removed on an HP-5MS column (30 m length  $\times$  250  $\mu$ m diameter  $\times$  0.25 film thickness). GC-MS spectroscopy involves an electron ionization system that uses energy-intensive electricity (70 eV). Injection temperature was set 220 °C, increased to 240°C, and oven temperature was automated from 60°C to 246°C at the rate of 3°C/min Helium gas (99.995%) was used as carrier gas at 1.02 mL/min (at 210°C). The volume of 1.0  $\mu$ L was injected of the reconstituted extract diluted with the appropriate solvent in separation mode at 250°C. The initial temperature was set between 50°C and 150°C, and the rate of rising was 3°C/min. Finally, the temperature was raised to 300°C for 10°C/min and held for 10 minutes. The identification was made using a standard scanning method ranging from 35 to 600 *m/z* (mostly bioactive compounds are low molecular mass compounds ranging from 35 to 600 *m/z*), and the bioactive compounds were tentatively identified by the NIST 2011 library [27].

TABLE 1: Preliminary phytochemical screening of *T. domingensis*.

Sr. no.	Phytochemical	Test	CFTD	BFTD
1	Carbohydrates	Molisch test	+	+
2	Amino acid	Ninhydrin	-	-
3	Protein	Biuret	+	+
4	Tannins and phenols	(a) FeCl <sub>3</sub>	+	+
		(b) Lead acetate	+	+
5	Saponin	Frothing	-	+
		(a) Dragendorff	-	-
6	Alkaloids	(b) Mayers	-	-
		(c) Wagner	-	-
7	Glycosides	Borntrager	-	+
8	Terpenes and steroids	Salkowski	+	+
9	Resins	Acetic acid	+	-

CFTD: chloroform fraction of *T. domingensis*; BFTD: *n*-butanol fraction of *T. domingensis*; +: present; -: not present.

**2.4. Oral Toxicity Test.** The oral toxicity test of CFTD and BFTD was performed according to the guidelines of the Organization for Economic Co-operation and Development (OECD) for the testing of chemicals. Male albino rats were purchased from the Department of Pharmacology, Faculty of Pharmacy, the Islamia University of Bahawalpur, and kept at a controlled room temperature of 22  $\pm$  1°C with a relative humidity of 60-70%. These rats were divided into six groups with six rats in each group. These groups were orally given the doses of CFTD and BFTD with concentrations 0.1, 0.25, 0.5, 1.0, 2.0, and 3.0 g/kg. The experimental animals were observed morbidity after 0.5 h, 1.0 h, and 2 h. The mortality was observed up to 24 h after dose administration. The animals during this period were observed for aggressiveness, convulsions, catalepsy, tail pinch, and spontaneous activity. The physical appearance in terms of skin change, fur, eyes, salivation, and sleep was also monitored [28].

**2.5. Antioxidant Potential.** Antioxidant activity is evaluated by two types of assays. Free radical scavenging activity was estimated by two methods, DPPH and ABTS. Reducing potency was estimated by FRAP and CUPRAC. The sample concentration used in these assays was 1 mg/mL. The outcomes were exhibited as mg of Trolox equivalent/g of the dry extract and calculated by the formula given below [29]:

$$\frac{\text{TE}}{\text{g}} = \frac{C \times V}{M}, \quad (1)$$

where *C* is the concentration of sample, *V* is the volume used for sample extraction, and *M* is the mass of sample used for extraction.

**2.5.1. Free Radical Scavenging (DPPH) Activity.** In this method, 40  $\mu$ L of 0.267 mM DPPH solution was mixed with 10  $\mu$ L of the sample solution and then incubated for 30

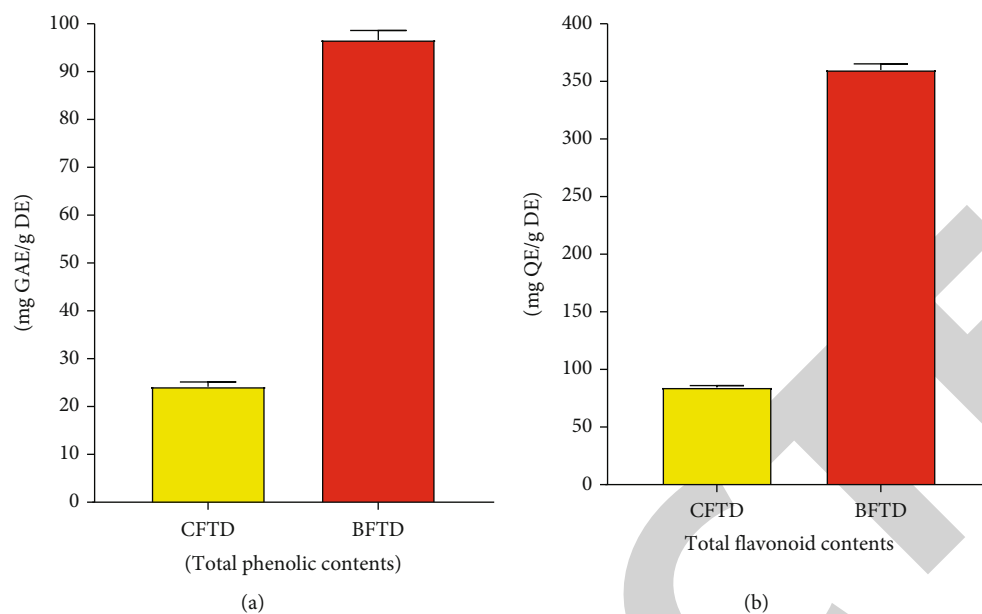


FIGURE 1: Polyphenolic quantification of *T. domingensis*. (a) Total phenolic contents (TPC) and (b) total flavonoid contents (TFC).

minutes, and absorbance was finally noted at 517 nm with a BioTek microplate reader.

**2.5.2. Radical Cation Scavenging (ABTS) Activity.** The generation of ABTS + radical was achieved by reacting a 7 mM ABTS solution with 2.45 mM potassium persulfate. After 30 minutes of incubation, 1 mL of test liquid was combined with 2 mL of ABTS +, and the absorbance was measured at 734 nm with a BioTek microplate reader.

**2.5.3. Cupric Ion Reducing (CUPRAC) Method.** A 0.5 mL sample was mixed with a mixture containing 1 mL of 10 mM  $\text{CuCl}_2$ , 1 mL of 7.5 mM nectarine, and buffer  $\text{NH}_4\text{Ac}$  (1 mL, 1 M, pH7) to accomplish this reaction. The absorbance was measured at 450 nm with a BioTek microplate reader after 30 minutes of incubation.

**2.5.4. Ferric Reducing Antioxidant Power (FRAP) Method.** In this process, 0.1 mL of sample solution was added to a 2 mL substrate in acetate buffer (0.3 M, pH 3.6), 2,4,6-tris(2-pyridyl)-s-triazine (TPTZ) (10 mM) at 40 mM hydrochloric acid, and  $\text{FeCl}_3$  (20 mM) in a ratio (v/v/v) of 10:1:1, and absorbance of resulting mixture was performed at 593 nm with BioTek microplate reader.

## 2.6. Enzyme Inhibition Activities

**2.6.1. Tyrosinase Inhibition Activity of *T. domingensis*.** The volume of 20  $\mu\text{L}$  of 0.1 M potassium phosphate buffer (pH 6.8) and 40  $\mu\text{L}$  fractions or standard (1 mg/mL) was mixed. Fungal tyrosinase enzyme 40  $\mu\text{L}$  (200 units/mL) was mixed into the mixture and incubated for 15 minutes. The substrate L-DOPA 100  $\mu\text{L}$  was added to the incubated solution, and this solution was further incubated for 20 minutes at 37°C. Absorbance was read at 450 nm with a BioTek microplate reader. The same procedure was adopted for neg-

ative control by adding 40  $\mu\text{L}$  of buffer solution instead of fractions [30].

**2.6.2. Acetylcholinesterase (AChE) and Butyrylcholinesterase (BChE) Inhibition Assay.** The reaction mixture consisting of 75  $\mu\text{L}$  sample solution (1 mg/mL), 175  $\mu\text{L}$  3 mM DTNB, and 50  $\mu\text{L}$  enzyme solution (AChE 0.265 U/mL or BChE 0.026 U/mL) in hydrochloric acid buffer was incubated at 25°C for 15 minutes. To the reaction mixture, 50  $\mu\text{L}$  substrates were added (15 mM acetylthiocholine iodide or butyrylthiocholine chloride). After 15 minutes, the absorbance of the final solution was measured at 405 nm. In the same way, a blank solution (without fractions) was made and examined using this method [31].

**2.7. Thrombolytic Activity of *T. domingensis*.** The thrombolytic activity of CFTD and BFTD was performed according to the previously described procedure in the literature [27]. The volume of 0.7 mL blood samples was added to previously weighed Eppendorf tubes. The blood was kept for clotting, and serum was removed after clot formation. 100  $\mu\text{L}$  of fractions (1 mg/mL) or standard was added to these Eppendorf tubes and kept for 30 minutes. The liquid portion of the clot was removed and weighed finally. The difference in weight was calculated, and loss in weight was expressed as percentage lytic activity of fractions or standard. For negative control, water was used instead of fraction solution, and the same procedure was repeated. The results were expressed after subtracting the value of the negative control activity [32].

**2.8. Antibacterial Activity.** *B. subtilis*, *M. luteus*, *S. epidermidis*, *B. pumilus*, *S. aureus* (gram positive), *E. coli*, *B. bronchiseptica*, and *P. aeruginosa* (gram negative) bacterial strains were obtained from the DTL Bahawalpur (Punjab Pakistan).

TABLE 2: Secondary metabolites identified in CFTD by GC-MS.

Peak no.	RT (min)	Identified compounds	Molecular formula	Molecular weight	Area %	Kovats index in the literature
1	3.06	Ethylbenzene	C <sub>8</sub> H <sub>10</sub>	106.16	0.05	865
2	3.14	p-Xylene	C <sub>8</sub> H <sub>10</sub>	106.16	0.41	885
3	3.38	Benzene	C <sub>6</sub> H <sub>6</sub>	78.11	0.19	680
4	6.63	Dodecane	C <sub>12</sub> H <sub>26</sub>	170.33	0.05	1200
5	9.03	Tetradecane	C <sub>14</sub> H <sub>30</sub>	198.39	0.20	1400
6	10.21	Pentadecane	C <sub>15</sub> H <sub>32</sub>	212.41	0.06	1500
7	10.42	Phenol	C <sub>6</sub> H <sub>6</sub> O	94.11	0.40	945
8	10.79	Benzylethyl-m-toluidine	C <sub>16</sub> H <sub>19</sub> N	225.33	0.37	1800
9	11.29	2-Tetradecene	C <sub>14</sub> H <sub>28</sub>	196.37	0.05	1380
10	11.38	Hexadecane	C <sub>16</sub> H <sub>34</sub>	226.41	0.44	1600
11	12.08	2-Methylhexadecane	C <sub>17</sub> H <sub>36</sub>	240.5	0.06	1660
12	12.48	1,3,2-Oxazaborolidine	C <sub>2</sub> H <sub>6</sub> BNO	70.89	0.13	ND
13	13.51	1-Octadecene	C <sub>18</sub> H <sub>36</sub>	252.5	0.11	1785
14	13.59	Octadecane	C <sub>18</sub> H <sub>38</sub>	226.41	0.58	1800
15	13.88	Pentadecanoic acid	C <sub>15</sub> H <sub>30</sub> O <sub>2</sub>	242.4	0.04	1860
16	14.30	Nonadecane	C <sub>19</sub> H <sub>40</sub>	268.5	0.09	1900
17	14.74	Heptadecane	C <sub>17</sub> H <sub>36</sub>	240.5	0.04	1700
18	15.07	Hexadecanoic acid, methyl ester	C <sub>17</sub> H <sub>34</sub> O <sub>2</sub>	270.5	0.50	1619
19	15.57	n-Hexadecanoic acid	C <sub>16</sub> H <sub>32</sub> O <sub>2</sub>	256.42	0.82	1975
20	15.91	Hexadecanoic acid, ethyl ester	C <sub>18</sub> H <sub>36</sub> O <sub>2</sub>	256.4	0.28	1921
21	15.99	Eicosane	C <sub>20</sub> H <sub>42</sub>	282.5	0.59	2000
22	17.10	5-Eicosene	C <sub>20</sub> H <sub>40</sub>	280.5	0.09	2285
23	17.27	8,11-Octadecadienoic acid	C <sub>18</sub> H <sub>32</sub> O <sub>2</sub>	280.4	0.41	2196
24	17.36	9,12,15-Octadecatrienoic acid	C <sub>18</sub> H <sub>30</sub> O <sub>2</sub>	278.43	0.48	2101
25	17.52	Phytol	C <sub>20</sub> H <sub>40</sub> O	296.5	0.15	2105
26	17.67	Octadecanoic acid	C <sub>18</sub> H <sub>36</sub> O <sub>2</sub>	284.5	0.18	2172
27	17.82	9,12-Octadecadienoic acid	C <sub>18</sub> H <sub>32</sub> O <sub>2</sub>	280.4	0.18	2098
28	17.90	Octadec-9-enoic acid	C <sub>18</sub> H <sub>34</sub> O <sub>2</sub>	282.5	0.47	2152
29	18.22	3,5-Difluorobenzaldehyde	C <sub>7</sub> H <sub>4</sub> F <sub>2</sub> O	142.10	0.74	ND
30	18.60	1-Nonadecene	C <sub>19</sub> H <sub>38</sub>	266.5	0.97	1894
31	18.68	Docosane	C <sub>22</sub> H <sub>46</sub>	310.6	0.77	2200
32	18.83	Stigmasta-3,5-dien-7-one	C <sub>29</sub> H <sub>46</sub> O	410.7	0.92	ND
33	19.46	Stigmasta-4,6,22-trien-3.alpha.-ol	C <sub>29</sub> H <sub>46</sub> O	410.7	2.25	ND
34	19.86	Methoxyacetic acid, 2-pentadecyl ester	C <sub>18</sub> H <sub>36</sub> O <sub>3</sub>	300.5	2.30	ND
35	21.44	Cyclotetracosane	C <sub>24</sub> H <sub>48</sub>	336.6	0.25	2899
36	21.53	Tetracosane	C <sub>24</sub> H <sub>50</sub>	338.7	0.79	2661
37	22.91	Benzamide	C <sub>7</sub> H <sub>7</sub> NO	121.14	0.20	1288
38	23.04	1,2-Benzenedicarboxylic acid	C <sub>8</sub> H <sub>6</sub> O <sub>4</sub>	166.13	0.15	1872
39	24.26	5-Acetyl-2-bromopyridine	C <sub>7</sub> H <sub>6</sub> BrNO	200.03	0.37	ND
40	24.32	9-Tricosene	C <sub>23</sub> H <sub>46</sub>	322.6	0.28	2274
41	25.25	1-Chloroheptacosane	C <sub>27</sub> H <sub>55</sub> Cl	415.2	0.42	ND
42	25.49	Pyridine-3-carboxamide	C <sub>6</sub> H <sub>6</sub> N <sub>2</sub> O	122.12	0.29	ND
43	25.75	1-Bromo-11-iodoundecane	C <sub>11</sub> H <sub>22</sub> BrI	361.1	1.12	1668
44	26.11	Tetratriacontane	C <sub>34</sub> H <sub>70</sub>	478.9	0.83	3400
45	26.20	Hexacosane	C <sub>26</sub> H <sub>54</sub>	366.7	0.63	416
46	26.45	Cyclopropane	C <sub>3</sub> H <sub>6</sub>	42.08	0.50	367
47	27.14	9-Methylnonadecane	C <sub>20</sub> H <sub>42</sub>	282.5	0.89	1943
48	27.84	Cholestan-3-one, 4,4-dimethyl-	C <sub>29</sub> H <sub>50</sub> O	414.7	1.67	ND

TABLE 2: Continued.

Peak no.	RT (min)	Identified compounds	Molecular formula	Molecular weight	Area %	Kovats index in the literature
49	27.98	Heneicosane	C <sub>21</sub> H <sub>44</sub>	296.6	1.01	2100
50	28.23	Cyclotriacontane	C <sub>30</sub> H <sub>60</sub>	420.8	0.39	
51	29.24	Cyclohexane	C <sub>6</sub> H <sub>12</sub>	84.16	3.72	670
52	29.82	Triacontane	C <sub>30</sub> H <sub>62</sub>	422.8	0.84	1397
53	30.15	Decyl nitrate	C <sub>10</sub> H <sub>21</sub> NO <sub>3</sub>	203.28	1.45	1319
54	30.76	Hentriacontane	C <sub>31</sub> H <sub>64</sub>	436.8	1.83	3100
55	31.04	Stigmastan-3,5,22-trien	C <sub>29</sub> H <sub>46</sub>	394.7	0.60	2990
56	31.37	Octadecane, 3-ethyl-5-(2-ethylbutyl)-	C <sub>26</sub> H <sub>54</sub>	366.7	0.75	2404
57	34.08	Pregn-4-en-3-one, 17-hydroxy-	C <sub>21</sub> H <sub>32</sub> O <sub>2</sub>	316.5	4.53	ND
58	34.14	Pregn-4-en-3-one	C <sub>21</sub> H <sub>32</sub> O	300.5	2.33	ND
59	35.90	Gamma-sitosterol	C <sub>29</sub> H <sub>52</sub> O <sub>2</sub>	432.7	0.58	3412

R.T.: retention time; ND.: not detected.

TABLE 3: Compounds identified by GC-MS analysis of BFTD.

Peak no.	RT (min)	Identified compounds	Molecular formula	Molecular weight	Area %	Kovats index in the literature
1	2.70	6-Dodecene	C <sub>12</sub> H <sub>24</sub>	168.32	0.21	1187
2	2.76	1-Pentanol	C <sub>5</sub> H <sub>12</sub> O	88.15	1.96	762
3	2.79	Cyclopentane	C <sub>5</sub> H <sub>10</sub>	70.1	0.64	554
4	2.87	Cyclopentanol	C <sub>5</sub> H <sub>10</sub> O	86.13	7.59	790
5	3.07	Ethylbenzene	C <sub>8</sub> H <sub>10</sub>	106.16	1.14	865
6	3.15	p-Xylene	C <sub>8</sub> H <sub>10</sub>	106.16	3.57	885
7	7.62	3H-1,2,4-Triazole-3-thione	C <sub>2</sub> HN <sub>3</sub> S	99.12	0.38	ND
8	9.03	Tetradecane	C <sub>14</sub> H <sub>30</sub>	198.39	0.57	1400
9	10.42	Phenol	C <sub>6</sub> H <sub>6</sub> O	94.11	0.51	945
10	10.52	Tripenyl orthoformate	C <sub>16</sub> H <sub>34</sub> O <sub>3</sub>	274.44	0.17	ND
11	11.37	Hexadecane	C <sub>16</sub> H <sub>34</sub>	226.44	0.62	1600
12	18.65	Nonadecane	C <sub>19</sub> H <sub>40</sub>	268.5	0.35	1900
13	21.50	Heptacosane	C <sub>27</sub> H <sub>56</sub>	380.7	0.27	2700
14	23.68	1,2-Benzenedicarboxylic acid	C <sub>8</sub> H <sub>6</sub> O <sub>4</sub>	166.13	0.77	1871
15	24.35	Eicosane	C <sub>20</sub> H <sub>42</sub>	282.5	0.29	2000
16	25.73	1-Hexacosene	C <sub>26</sub> H <sub>42</sub>	364.7	0.19	2596
17	25.99	3-Eicosene	C <sub>20</sub> H <sub>40</sub>	280.5	0.15	2905
18	27.11	Octadecane	C <sub>18</sub> H <sub>38</sub>	254.5	0.68	1790
19	27.20	Pentadec-7-ene	C <sub>15</sub> H <sub>30</sub>	210.4	0.29	ND
20	28.87	Pyridine-3-carboxamide	C <sub>6</sub> H <sub>6</sub> N <sub>2</sub> O	122.12	3.00	ND
21	29.80	2-(Acetoxymethyl)-3-(methoxycarbonyl)	C <sub>17</sub> H <sub>14</sub> NO <sub>4</sub>	282.29	0.69	2223
22	30.88	Hexadecanoic acid	C <sub>16</sub> H <sub>32</sub> O <sub>2</sub>	256.4	1.49	1964
23	31.38	Tetatriacontane	C <sub>34</sub> H <sub>70</sub>	478.9	14.18	ND
24	32.77	Benzenepropanoic acid	C <sub>9</sub> H <sub>10</sub> O <sub>2</sub>	150.17	6.79	1324
25	33.04	Deoxycasaldehydin C	C <sub>21</sub> H <sub>30</sub> O <sub>3</sub>	330.5	9.02	ND

R.T.: retention time (min); ND.: not detected.

Inoculums were made by combining a few colonies of each bacteria from 24-hour old cultures with a 10 mL sterile nutrient broth medium. The turbidity was set to 0.5 McFarland, which is comparable to 10<sup>8</sup> CFU/mL cell density. In an autoclave, Petri dishes and nutrient agar media were steril-

ized. Agar nutrient was placed into Petri dishes and allowed to solidify in a laminar flow hood. Bacterial cultures were streaked on the agar surface, followed by the development of four 6 mm diameter holes in each Petri dish. Using a micropipette, 60 µL of coamoxiclav (1 mg/mL) and fraction



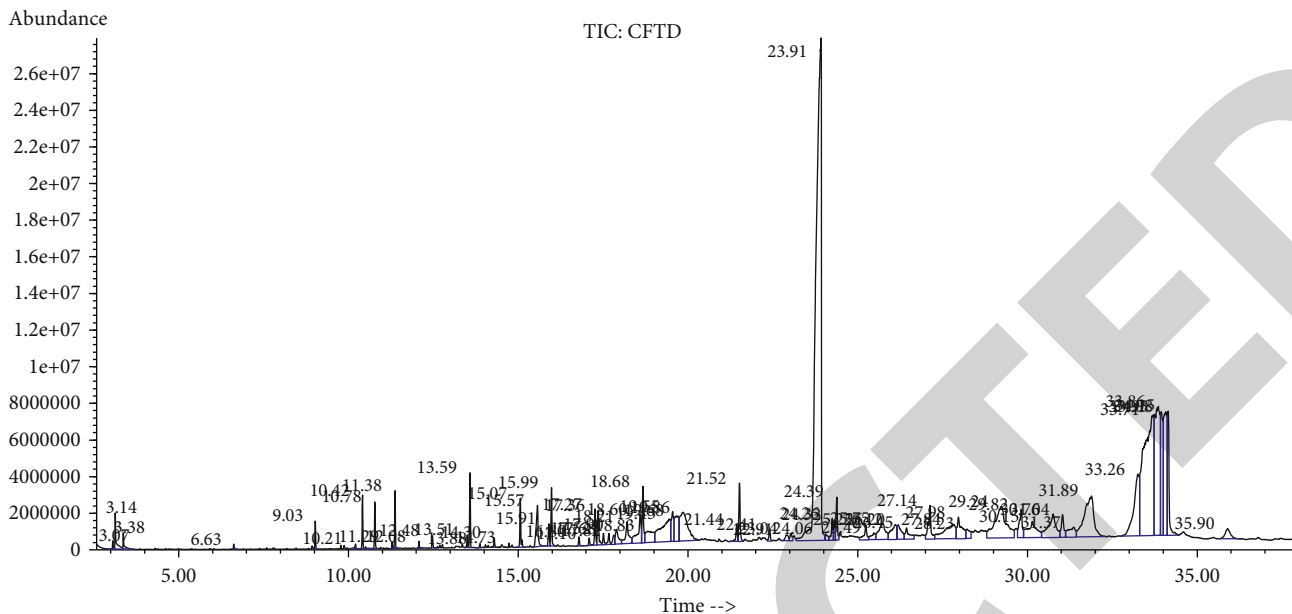


FIGURE 2: GC-MS chromatogram of CFTD.

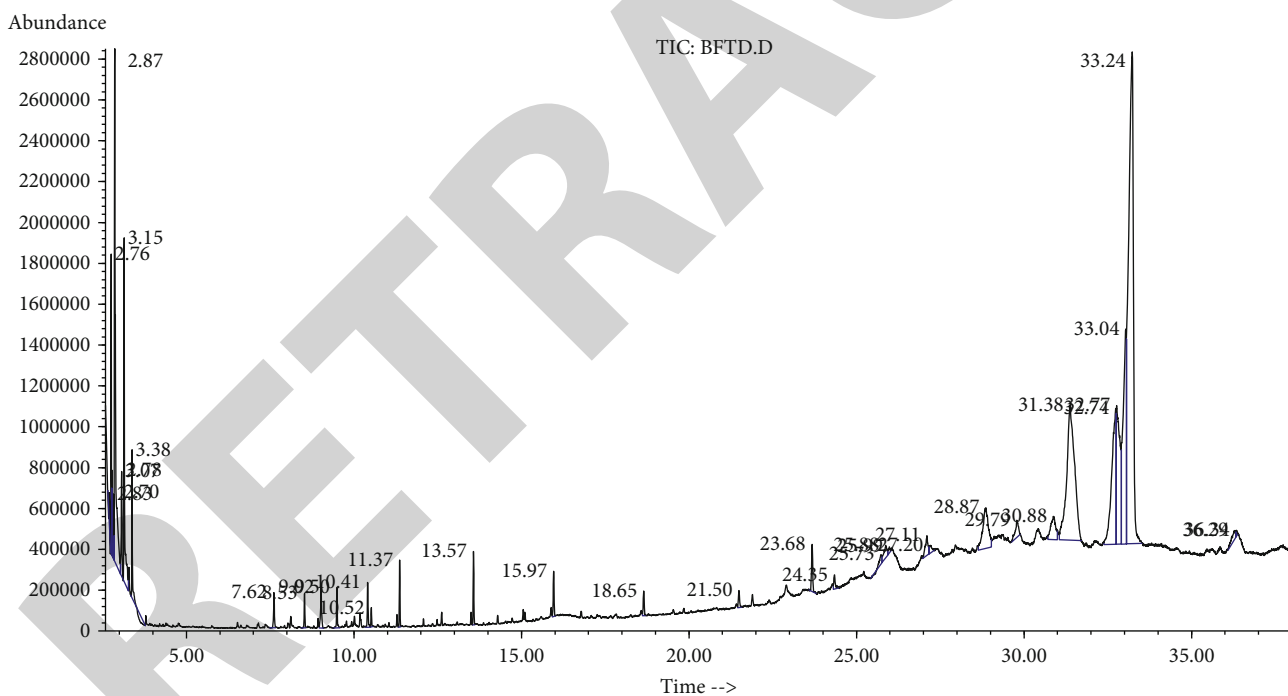


FIGURE 3: GC-MS chromatogram of BFTD.

solutions (40, 20, and 10 mg/mL) were added to wells by using a micropipette. All of these Petri plates were incubated for 18–24 hours at 37°C in an incubator. The zones of inhibition were evaluated after incubation to determine the antibacterial activity. The results were calculated by averaging three experiments [33].

2.9. Molecular Docking Studies. *In silico* molecular docking is a valuable method in the growth of molecular biology and computer-aided drug designing. For molecular docking eval-

uation, different tools may be used, likely AutoDock Vina, Discovery Studio, PyRx, and Open Babel. The molecular docking was performed according to the method given in the literature. The receptor molecule was downloaded from <http://rcsb.org> in pdb format. The preparation of the receptor was performed by Discovery Studio. The structures of ligands were downloaded from the PubChem in SDF format. These prepared receptors and ligands were uploaded in AutoDock Vina which was embedded in PyRx. These drugs provide ligand organization depending on their capacity to

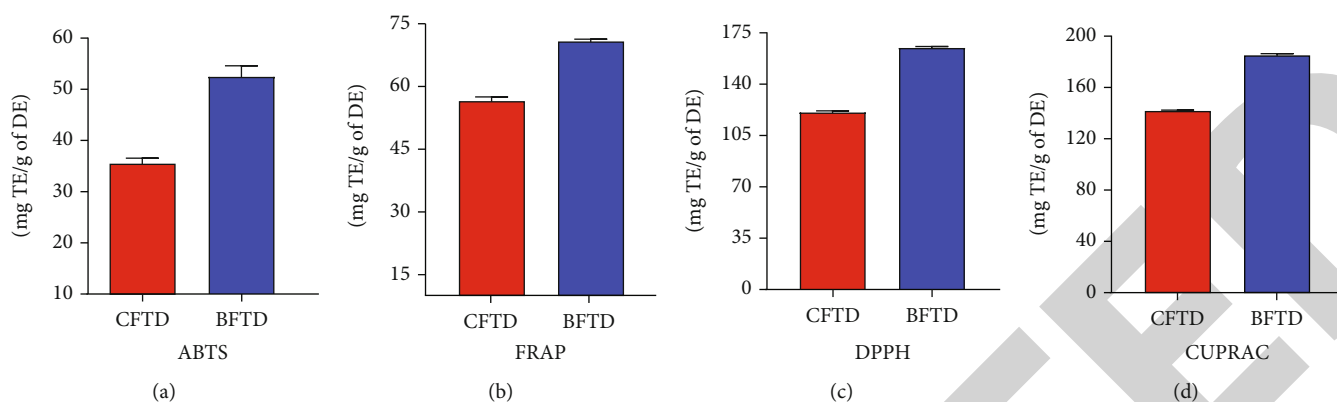


FIGURE 4: Antioxidant potential of *T. domingensis*: (a) ABTS assay; (b) FRAP assay; (c) DPPH assay; (d) CUPRAC assay.

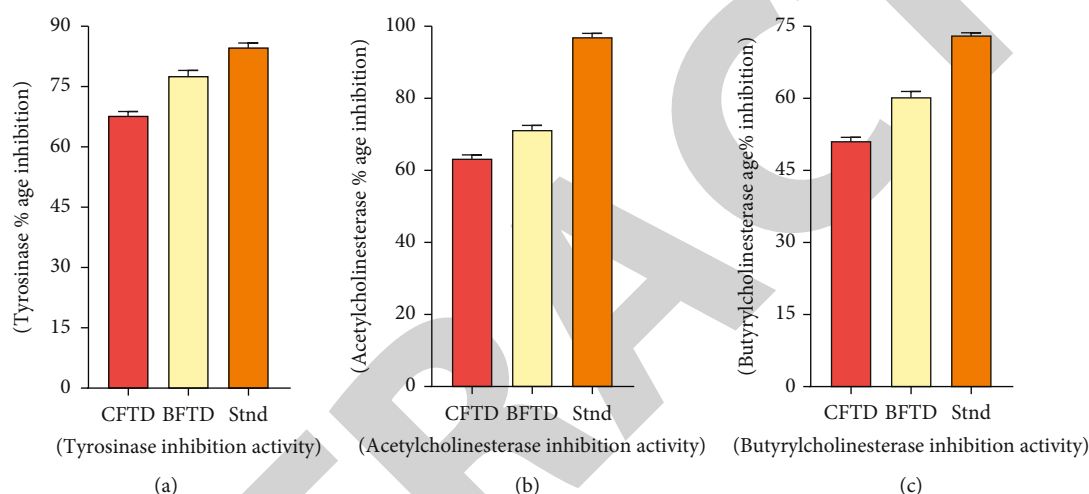


FIGURE 5: *In vitro* enzyme inhibition potential of *T. domingensis*: (a) tyrosinase inhibition activity; (b) acetylcholinesterase inhibition activity; (c) butyrylcholinesterase inhibition activity of CFTD and BFTD.

TABLE 4: The thrombolytic activity of *T. domingensis*.

Fraction	BS 1 (%age lysis)	BS 2 (%age lysis)	BS 3 (%age lysis)	BS 4 (%age lysis)	BS 5 (%age lysis)
CFTD	57.39 ± 0.74	58.30 ± 1.27	58.32 ± 0.76	57.65 ± 0.92	58.67 ± 1.18
BFTD	67.90 ± 0.87	67.74 ± 0.44	68.15 ± 0.55	67.66 ± 1.19	67.06 ± 0.35
Streptokinase (standard)	79.07 ± 1.0	79.15 ± 0.77	79.33 ± 0.57	78.52 ± 1.0	78.66 ± 1.0

CFTD: chloroform fraction; BFTD: *n*-butanol fraction; BS: blood sample.

interact with a certain target tyrosinase, acetylcholinesterase, and butyrylcholinesterase enzymes. The involvement of small molecules of protein in a target entails predefined sampling of the ligand's capacity to fit into a specific target groove to generate an optimal complex shape. This may be accomplished by utilizing the program evaluation function. This provides an alternative approach for detecting target structure, which is the required point for *in silico* drug modeling. Finally, docking was performed with AutoDock Vina. The docked results were visualized with Discovery Studio [34].

**2.10. Statistical Analysis.** Each experiment was conducted in triplicate. All the readings and results were expressed as mean

± standard deviation (STD). One-way ANOVA, followed by *post hoc* Tukey's multiple comparison test, was applied for the analysis of data. The software used was Prism GraphPad 8.1 version.

### 3. Results

#### 3.1. Chemical Composition of *T. domingensis*

**3.1.1. Preliminary Phytochemical Screening.** The qualitative phytochemical screening of CFTD and BFTD was carried out for different chemical constituents. Table 1 reveals the presence of carbohydrates, proteins, saponins, glycosides,

TABLE 5: Antibacterial activity of *T. domingensis*.

Strains	ZI (mm) of coamoxiclav (conc. 1 mg/mL)	Conc. (mg/mL)	ZI of CFTD (mm)	ZI of BFTD (mm)
Gram positive				
<i>Bacillus subtilis</i>	23	10	4	NA
		20	9	7
		40	15	16
<i>Micrococcus luteus</i>	20	10	NA	NA
		20	NA	9
		40	NA	17
<i>Staphylococcus epidermidis</i>	18	10	5	5
		20	11	8
		40	16	15
<i>Bacillus pumilus</i>	21	10	NA	NA
		20	10	NA
		40	19	NA
<i>Staphylococcus aureus</i>	21	10	NA	4
		20	12	9
		40	18	16
Gram negative				
<i>Escherichia coli</i>	24	10	NA	NA
		20	14	8
		40	18	18
<i>Bordetella bronchiseptica</i>	25	10	NA	7
		20	8	11
		40	17	16
<i>Pseudomonas aeruginosa</i>	6	10	NA	NA
		20	NA	NA
		40	13	NA

CFTD: chloroform fraction; BFTD: *n*-butanol fraction; ZI: zone of inhibition.

steroids, terpenes, resins, tannins, and phenols while amino acids and alkaloids were absent.

**3.1.2. Polyphenolic Quantification (TPC and TFC).** The maximum phenolic contents of 97.14 mg GAE/g extract and the maximum flavonoid contents of 362.5 mg QE/g extract were in the BFTD, while in CFTD, total phenolic contents were determined 24.3 mg GAE/g extract and flavonoid contents were 84.71 mg QE/g extract (Figure 1).

**3.1.3. Gas Chromatography-Mass Spectrometry (GC-MS) Analysis.** To obtain more detailed information about phytochemicals, GC-MS screening of the CFTD and BFTD was performed, resulting in the tentative identification of 69 and 27 different metabolites, respectively. The preliminary identification of the metabolites was accomplished with the help of the NIST library database. Tables 2 and 3 provide a list of these tentatively discovered secondary metabolites in the CFTD and BFTD. The GC-MS spectra for the CFTD and BFTD presented in Figures 2 and 3 revealed distinct peaks of tentatively identified phytochemicals. The majority of these component classes comprised a combination of benzenoids, hydrocarbons, fatty acids, organic compounds,

natural product derivatives, lipid-like molecules, alkanes, and phenol, among others. In the both fractions, the major compounds identified include deoxycsaaldekalin C, stigmastan-3,5,22-trien, cyclotetracosane, stigmasta-3,5-dien-7-one, cyclotriacontane, stigmasta-4,6,22-trien-3.alpha.-ol, benzenepropanoic acid, 3H-1,2,4-triazole-3-thione, phytol, p-xylene, tripentyl orthoformate, linolenic acid, phenol, dodecane, and 3,5-difluorobenzaldehyde.

**3.2. Oral Toxicity Test.** In the oral toxicity test, the CFTD and BFTD did not show any sign or symptom of morbidity or mortality for a period of 24 h after the oral dosing of the extracts at concentrations of 0.1–3.0 g/kg body weight. No toxicity-related signs such as convulsions, writhing, behavioral alterations, pain, and ataxia were observed during this period.

**3.3. Antioxidant Potential of *T. domingensis*.** The antioxidant activity for CFTD and BFTD (Figure 4) was determined by ABTS, FRAP, DPPH, and CUPRAC. The antioxidant potential determined by ABTS, FRAP, DPPH, and CUPRAC methods revealed that the BFTD exhibited maximum activity (52.15 + 1.24, 70.58 + 2.12, 163.91 +

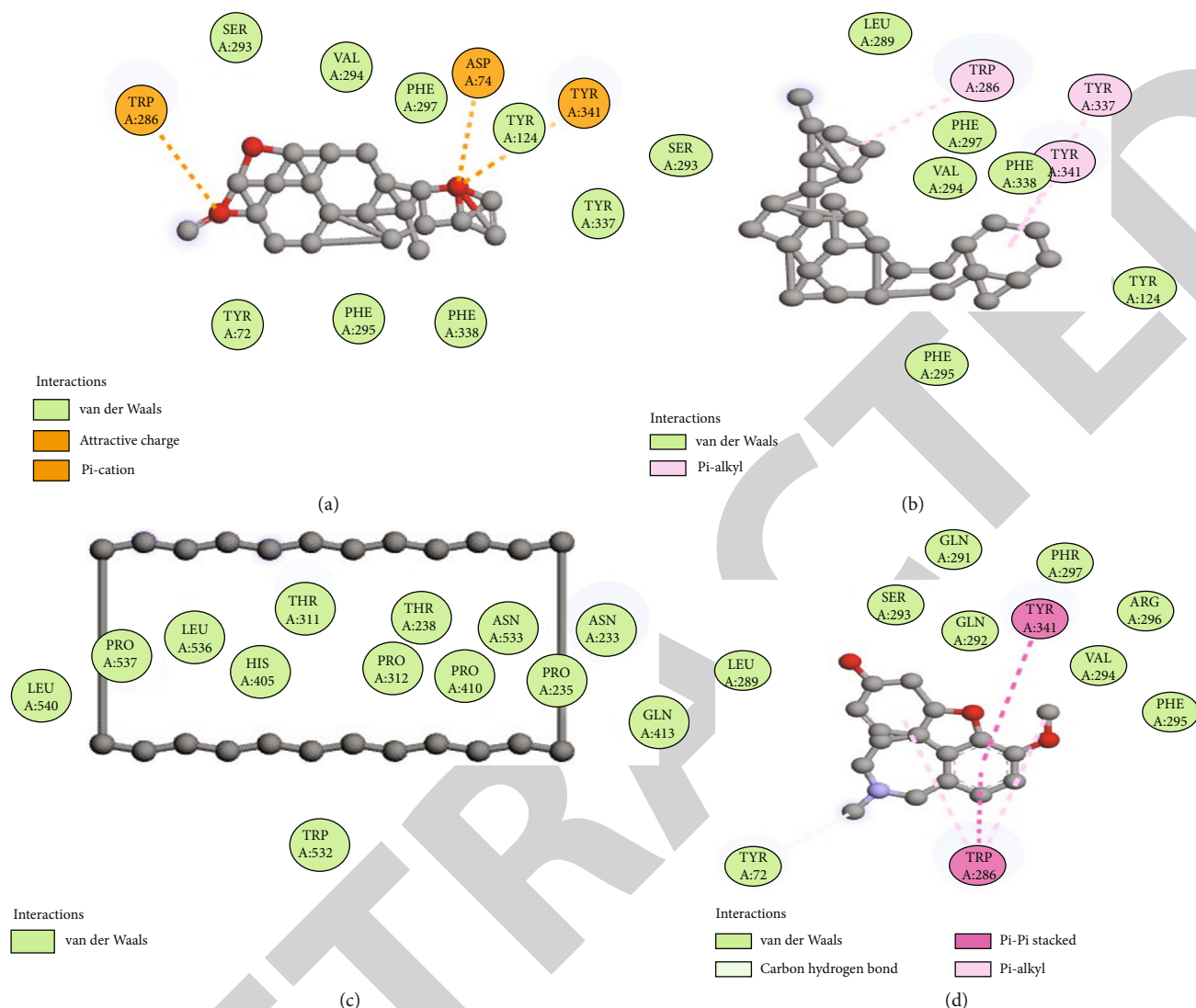


FIGURE 6: Docking of compounds with acetylcholinesterase: (a) interaction of deoxycaesaldehydin C, (b) stigmastan-3,5,22-trien, (c) cyclotetracosane, and (d) galantamine.

10.88, and  $184.05 + 12.7$  mg TE/g DE, respectively), while CFTD has the antioxidant potential of  $35.29 + 0.79$ ,  $55.62 + 1.94$ ,  $119.49 + 5.83$ , and  $140.98 + 6.39$  mg TE/g DE, respectively, with all four methods. The results of antioxidant activities demonstrated that polyphenol content has a direct relationship with antioxidant potential, with the highest phenolic and flavonoid content fractions having a better antioxidant activity.

### 3.4. Enzyme Inhibition Potential of *T. domingensis*

**3.4.1. Tyrosinase Inhibition Activity.** The BFTD has the highest tyrosinase %age inhibition  $78.67 \pm 6.81$  which is very similar to the %age inhibitory activity of kojic acid used as standard ( $85.58 \pm 0.85$ ), and the CFTD revealed  $68.09 \pm 5.79$  %age inhibition (Figure 5).

**3.4.2. Acetylcholinesterase and Butyrylcholinesterase Inhibition Activity (%Age Inhibition).** The BFTD resulted from maxi-

mum acetylcholinesterase and butyrylcholinesterase %age inhibition  $71.65 \pm 4.87$  and  $60.79 \pm 2.78$ , respectively, as compared to %age inhibition of CFTD  $63.47 \pm 3.61$  and  $51.45 \pm 1.14$  (Figure 5).

**3.5. Thrombolytic Activity.** Five samples of blood were taken, and results were observed through thrombolytic activity by the use of streptokinase as a standard. The BFTD showed the highest ( $68.15 \pm 0.55$ ) thrombolytic activity, and the CFTD shows less ( $58.67 \pm 1.18$ ) thrombolytic activity (Table 4).

**3.6. Antibacterial Potential of *T. domingensis*.** By using standard coamoxiclav (amoxicillin-clavulanic acid), a total of eight bacterial strains (*Bacillus subtilis*, *Micrococcus luteus*, *Staphylococcus epidermidis*, *Bacillus pumilus*, *Staphylococcus aureus*, *Escherichia coli*, *Bordetella bronchiseptica*, *Pseudomonas aeruginosa*) were used to check the antibacterial potential of CFTD and BFTD. The CFTD and BFTD at conc. of 40 mg/mL showed the highest zone of inhibition (15 and

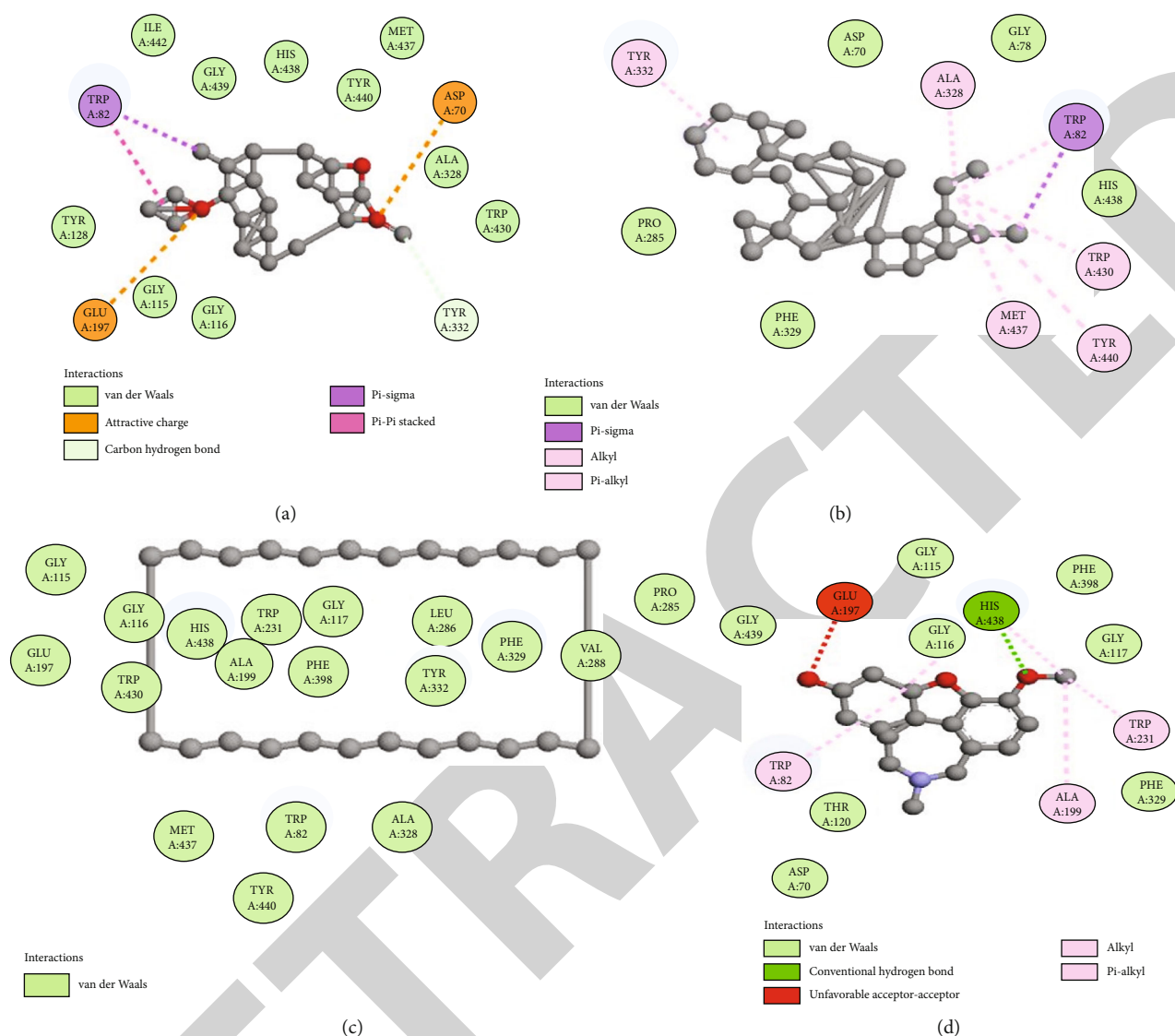


FIGURE 7: Docking of compounds with butyrylcholinesterase enzyme: (a) 2D interaction of deoxycsaaldekarin C, (b) stigmastan-3,5,22-trien, (c) cyclotetrasane, and (d) galantamine.

16 mm) against *Bacillus subtilis*, and the lowest zone of inhibition (4 mm) was shown by CFTD at conc. of 10 mg/mL against. *Micrococcus luteus* showed a maximum sensitivity (17 mm) against BFTD at conc. 40 mg/mL. *Staphylococcus epidermidis* showed maximum sensitivity (15 and 16 mm) against CFTD and BFTD at conc. 40 mg/mL, and the lowest sensitivity (5 mm) showed against both fractions at conc. of 10 mg/mL. *Bacillus pumilus* showed higher sensitivity (18 mm) against CFTD at conc. 40 mg/mL and lowest sensitivity (10 mm) at conc. of 20 mg/mL against same fraction. *Staphylococcus aureus* showed maximum sensitivity (18 and 16 mm) against CFTD and BFTD at conc. of 40 mg/mL, and the lowest sensitivity (4 mm) showed against BFTD at conc. of 10 mg/mL. *Escherichia coli* showed higher sensitivity (18 mm) against both fractions at conc. of 40 mg/mL and the lowest sensitivity (8 mm) against BFTD at conc. of 20 mg/mL. *Bordetella bronchiseptica* showed the highest sensitivity (17 and 16 mm) against CFTD and BFTD and at conc. of 40 mg/mL, and the lowest sensitivity (7 mm) showed against BFTD at conc. of 10 mg/mL. *Pseudomo-*

*nas aeruginosa* showed the highest sensitivity (13 mm) against CFTD at conc. 40 mg/mL (Table 5).

All tested samples were sensitive to *T. domingensis*, the CFTD was the most effective. Overall, from all these results, we can conclude that antibacterial results were dose-dependent.

**3.7. Molecular Docking Study.** The molecular docking of secondary metabolites identified by GC-MS was performed to determine binding affinities and binding interactions. Details of the interacting amino acid residues and binding affinities are displayed (Figures 6–8 and Table 6). The best binding affinity with tyrosinase was revealed by deoxycsaaldekarin C -10.4 kcal/mol while the binding affinity for standard kojic acid was 5.4 kcal/mol.

The best docking scores for acetylcholinesterase and butyrylcholinesterase were revealed as deoxycsaaldekarin C -14.3 and -13.1 kcal/mol, respectively, while the docking scores for standard galantamine were -8.5 and -8.4 kcal/mol, respectively. The results of docking revealed strong

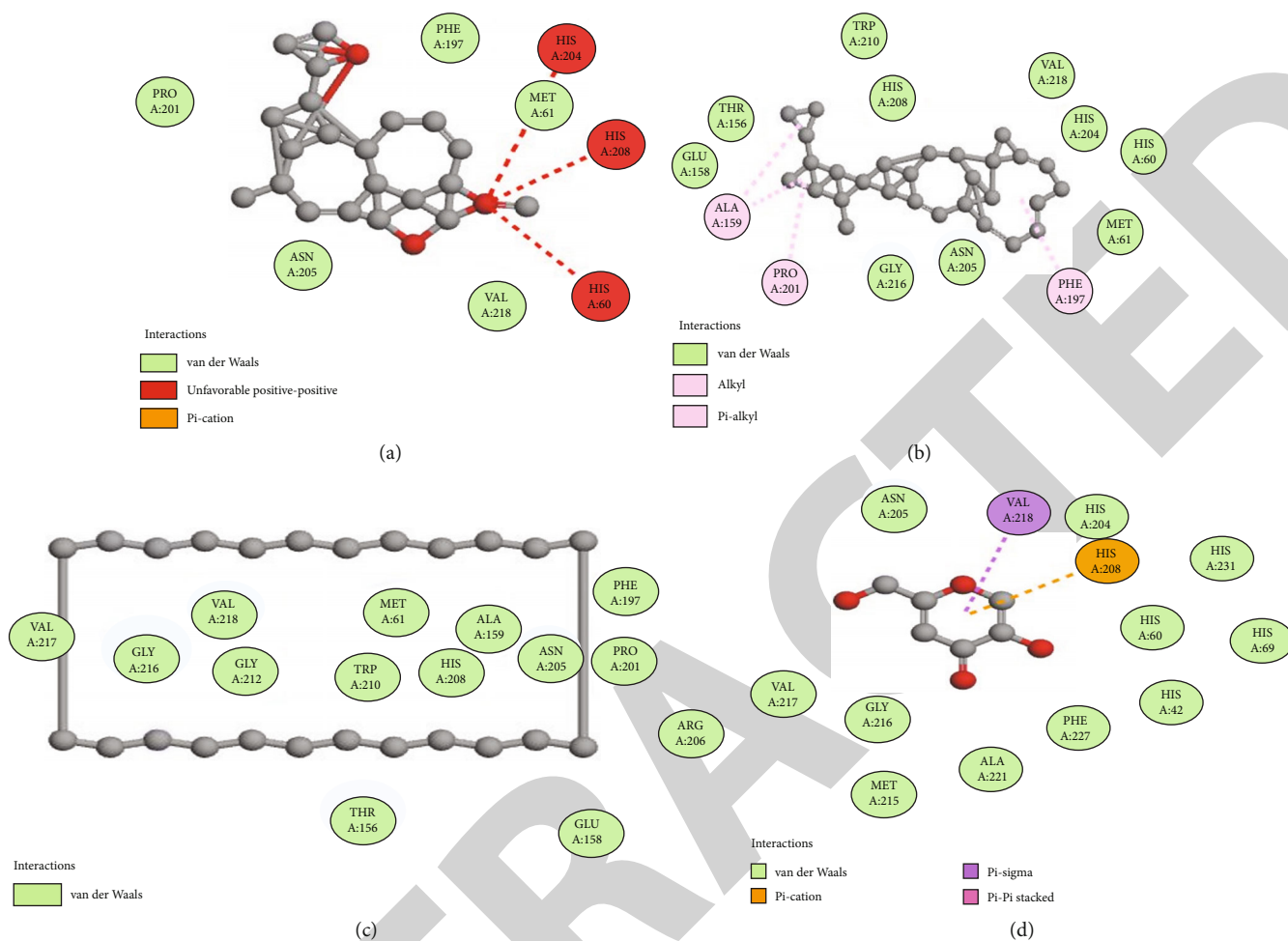


FIGURE 8: Docking of compounds with tyrosinase: (a) 2D interaction of deoxycsaaldekarin C, (b) stigmasteran-3,5,22-trien, (c) cyclotetracosane, and (d) kojic acid with an enzyme.

natural enzyme inhibitors from the GC-MS of CFTD and BFTD.

#### 4. Discussion

The phytochemical screening of *T. domingensis* was carried out on both CFTD and BFTD, which revealed the presence of carbohydrates, proteins, terpenes, and steroids while amino acids and alkaloids were absent (Table 1). Preliminary phytochemical screening of *T. domingensis* rhizome aqueous extracts was determined previously [13]. The selection of appropriate solvents for extraction is the key factor in natural product research. In this study, the chloroform and *n*-butanol solvents were used due to previous evidence of the role of the solvents in extract preparation with a rich quantity of polyphenols [35].

The clinical application of herbal drugs without scientific evidence of their safety profile may lead to serious concerns regarding their toxicity. Therefore, various *in vivo* models are applied to investigate the toxicity of plant extracts [36]. In this study, the toxicity of CFTD and BFTD was investigated using *in vivo* oral toxicity test. The extracts were found safe and biocompatible at 3000 mg/kg in rats. Moreover, the species has also been used as food [37], which rectifies the safety profile of the species revealed in this study. These

results suggest that the edible use of *T. domingensis* is safe and biocompatible.

The health beneficial effects of medicinal plants are due to phenolic compounds. Their utilization can cause a decrease in the risk of diseases such as cancer and cardiovascular diseases. The largest groups of phenolic compounds are flavonoids, and these play numerous roles in plants and the human diet. Flavonoids can be employed for different activities likely antibacterial, antifungal, anti-thrombotic, and anticancer. *Typha elephantina* have anti-thrombotic activity due to its effect on platelet aggregation [38]. The maximum phenolic contents of 97.86 mg GAE/g DE and the maximum flavonoid contents of 362.5 mg QE/g DE were found in the BFTD. While in CFTD, total phenolic contents were determined 24.3 mg GAE/g DE, and flavonoid contents were 84.71 mg QE/g DE extract (Figure 1). The literature review of fruits of *T. domingensis* revealed that these are very rich in polyphenols ( $401.46 \pm 5.77$  mg GAE/g) [39].

Tyrosinase is a copper-containing enzyme found in plant and animal tissues that catalyzes the oxidation of tyrosine to form melanin and other colors [40]. It is found within melanosomes, which are synthesized in human skin melanocytes [41]. Tyrosinase is the enzyme that catalyzes the rate-

TABLE 6: Details of binding affinities and interacting amino acid residues.

Sr. no.	Name of compounds	TYR E (BA)	Interacting amino acid residues	AChE (BA)	Interacting amino acid residues	BChE (BA)	Interacting amino acid residues
1. 2	Stigmastan-3,5,22-trien	-9.8	His60, Met61, Thr156, Glu158, Ala159, Phe197, Pro201, His204, Asn205, His208, Tro210, Gly216, Val218,	-13.9	Tyr124, Trp286, Leu289, Ser293, Val294, Phe295, Phe297, Phe338, Tyr337, Tyr341,	-11.8	Asp70, Gly78, Trp82, Tyr332, Ala328, Phe329, Trp430, Met437, His438, Try440,
2. 6	Cyclotetracosane	-7.5	Met61, Thr156, Glu158, Ala159, Phe197, Pro201, Asn205, Arg206, His208, Trp210, Gly212, Gly216, Val217, Val218	-8.0	Asn233, Pro235, Thr238, Thr311, His405, Pro410, His405, Gln413, Trp532, Asn533, Leu536, Pro537, Leu540	-10.0	Trp82, Gly115, Gly116, Gly117, Glu197, Ala199, Trp231, Pro285, Leu286, Val288, Ala328, Phe329, Tyr332, Phe398, Trp430, Met437, His438, Tyr440
3. 10	Kojic acid	-5.4	His42, His60, His69, Pro201, His204, Asn205, His208, Gly216, Val217, Met215, Val218, Ala221, Phe227				
4. 11	Galantamine			-8.5	Tyr72, Trp286, Leu289, Gln291, Leu292, Ser293, Val294, Phe295, Arg296, Phe297, Tyr341	-8.4	Asp70, Trp82, Gly115, Gly116, Gly117, Thr120, Glu197, Ala199, Trp231, Phe329, Phe398, His438, Gly439

TYR: tyrosinase; AChE: acetylcholinesterase; BChE: butyrylcholinesterase; BA: binding affinity.

limiting step in melanin production, converting tyrosine to DOPA in melanosomes in stages II-IV [42]. The BFTD has the highest tyrosinase inhibition ( $78.67 \pm 6.81\%$ ), which is very similar to the inhibition of kojic acid ( $85.58 \pm 0.85\%$ ) standard, while the CFTD has the lower inhibition ( $68.09 \pm 5.79\%$ ) as displayed in Figure 5. The majority of tyrosinase inhibitors discovered in plants are structurally similar to phenolics, steroids, and alkaloids [43].

Acetylcholinesterase (AChE) is a cholinergic enzyme that degrades or hydrolyzes acetylcholine (ACh), a naturally occurring neurotransmitter, into acetic acid and choline almost instantly [38]. Butyrylcholinesterase, also called pseudocholinesterase or plasma (choline) esterase, is a non-specific cholinesterase enzyme that hydrolyzes a wide range of choline-based esters. Many neurological illnesses, such as senility, ataxia, myasthenia gravis, Parkinson's disease, and Alzheimer's disease, are treated with acetylcholinesterase inhibitors. Therefore, many cholinesterase naturally occurring polyphenols are widely used to treat and ameliorate the risk of a variety of geriatric neurological illnesses, such as macular degeneration and dementia [44]. Antioxidants are also being investigated as potential therapies for neurodegenerative illnesses such as Alzheimer's and amyotrophic lateral sclerosis. According to research, phenolic/flavonoid-rich fractions have potent antiacetylcholinesterase properties [45]. The BFTD expressed maximum acetylcholinesterase and butyrylcholinesterase %age inhibition of  $71.65 \pm 4.87$

and  $60.79 \pm 2.78$ , respectively, by using standard galantamine ( $97.11 \pm 1.26$  and  $72.88 \pm 2.61$ ) as compared to %age inhibition of CFTD ( $63.47 \pm 3.61$  and  $51.45 \pm 1.14$ ) (Figure 5). TPC and TFC were found higher in the BFTD than in the CFTD which confirms maximum inhibition of acetylcholinesterase and butyrylcholinesterase with BFTD. These findings are likely due to the metabolites identified by the GC-MS profile, probably (deoxycaesaldekalin C, stigmastan-3,5,22-trien, cyclotetracosane, stigmasta-4,6,22-trien-3.alpha.-ol, 2-(acetoxymethyl)-3-(methoxycarbonyl), cholestan-3-one, 4,4-dimethyl-, 2,3-diphenyl-5-methoxybenzo-1,4-dioxin, cyclotriacontane, octadecane, 3-ethyl-5-(2-ethyl-butyl)-) with enzymes tyrosinase, acetylcholinesterase, and butyrylcholinesterase, and it could be due to other moieties in these fractions. This shows that *T. domingensis* could be useful in the treatment of neurological diseases.

Thrombolytic medications break blood clots by activating fibrin, which results in the formation of plasmin, a cleaved product. Plasmin is a proteolytic enzyme that may break cross-links between fibrinogen molecules, which are responsible for the structural stability of blood clots [46]. Medicinal plants in a vast area of the world may be a candidate for the development of thrombolytic agents [47]. The thrombolytic activity of CFTD and BFTD is comparable with the thrombolytic activity of streptokinase used as a standard drug. The minor thrombolytic activity of *T. elephantina* has been described [48].

*T. domingensis* used to halt bleeding, as well as burns and wound healing in Turkish traditional medicine [49]. Overall, we may infer that the antibacterial outcomes of CFTD and BFTD against selected strains were dose-dependent. Some compounds identified in the CFTD and BFTD by GC-MS comprise antibacterial activity like ethylbenzene [50], tetradecane [51], benzene [52], pentadecanoic acid [53], heneicosane [54], octadec-9-enoic acid [55], and 3H-1,2,4-triazole-3-thione [56] which confirms the results of antibacterial *T. domingensis*. As the *T. domingensis* has been used traditionally as antiwound activity, it would be a good edition in the pharmaceutical field [57].

Docking is a molecular modeling technique used to estimate how proteins (enzymes) interact with small molecules (binders or ligands) [58]. For the estimation of binding affinities and binding interactions, the *in silico* molecular docking of all compounds identified by GC-MS was performed. Molecular docking gives the most thorough perspective of drug-receptor interaction and has produced a new logical method of drug design in which the structure of the drug is generated based on its fit to the three-dimensional structures of the receptor site. The results of docking revealed that the ligands identified in the GC-MS of these fractions gave better binding affinities than standards used in these assays, and it suggests that these fractions may be very strong inhibitors of enzymes.

*T. domingensis* can be used to treat some common diseases and ailments. For the therapeutic application of this plant, it is important to evaluate its maximum potential in the medical and pharmaceutical sciences. Conclusively, total phytochemical contents, GC-MS analysis, and *in silico* molecular docking evaluation findings confirm our findings of CFTD and BFTD in terms of antioxidant capacity, tyrosinase inhibition activity, antimicrobial assay, and thrombolytic potential.

## 5. Conclusions

The current comparative study was focused on secondary metabolites profiling and *in vitro* biological activities for CFTD and BFTD. The BFTD exhibited the maximum polyphenolic contents (TPC and TFC), antioxidant potential and tyrosinase, acetylcholinesterase, and butyrylcholinesterase inhibition activity. The GC-MS screening of the CFTD and BFTD resulted in the tentative identification of several secondary metabolites. The tyrosinase, acetylcholinesterase, and butyrylcholinesterase inhibition activity of *T. domingensis* was further confirmed by molecular docking studies of GC-MS identified ligands, deoxycasaldekarin C, stigmastan-3,5,22-trien, and cyclotetracosane, with these enzymes. The compounds tentatively identified in the GC-MS analysis of the CFTD and BFTD confirm their preliminary pharmacological efficacy, and the majority of compounds could be extremely beneficial in the pharmaceutical industry for the development of biomedicines. The BFTD revealed the highest thrombolytic activity than the chloroform fraction. CFTD and BFTD revealed very significant and dose-dependent antibacterial against the tested strains. CFTD and BFTD possessed antimicrobial and hemostatic properties as evidenced by

inhibiting the growth of pathogenic bacteria. It has proven that *T. domingensis* can be used in neurological diseases and skin malignancies, and this study provides a rationale for biological activities. The phytochemical and biological potential of this plant highlighted its medicinal value for further isolation of bioactive compounds and preparation of nanoparticles loaded with these fractions, which is currently in progress.

## Data Availability

There is no restriction on data.

## Conflicts of Interest

The authors declare no conflict of interest.

## References

- [1] M.-m. Poo, D. Jiu-lin, N. Y. Ip, Z.-Q. Xiong, B. Xu, and T. Tan, "China Brain Project: basic neuroscience, brain diseases, and brain-inspired computing," *Neuron*, vol. 92, no. 3, pp. 591–596, 2016.
- [2] M. S. Khan and I. Ahmad, "Herbal medicine: current trends and future prospects," in *New Look to Phytomedicine*, pp. 3–13, Elsevier, 2019.
- [3] M. A. Dulebenets, J. Pasha, O. F. Abioye et al., "Exact and heuristic solution algorithms for efficient emergency evacuation in areas with vulnerable populations," *International journal of disaster risk reduction*, vol. 39, 2019.
- [4] A. J. Das, *Biochemical and microbiological characterization of rice beer produced in Assam and therapeutic application of a novel ester synthesized from its components*, Tezpur University, 2017.
- [5] S. Bai-Ngew, T. Chuensun, S. Wangtueai et al., "Antimicrobial activity of a crude peptide extract from lablab bean (*Dolichos lablab*) for semi-dried rice noodles shelf-life," *Quality Assurance and Safety of Crops & Foods*, vol. 13, no. 2, pp. 25–33, 2021.
- [6] A. Wadood, M. Ghufra, S. B. Jamal, M. Naeem, A. Khan, and R. Ghaffar, "Phytochemical analysis of medicinal plants occurring in local area of Mardan," *Biochemistry & Analytical Biochemistry*, vol. 2, no. 4, pp. 1–4, 2013.
- [7] M. Kumar, S. Prakash, N. Kumari et al., "Beneficial role of antioxidant secondary metabolites from medicinal plants in maintaining oral health," *Antioxidants*, vol. 10, no. 7, article 1061, 2021.
- [8] L. Marín, E. M. Miguélez, C. J. Villar, and F. Lombó, "Bioavailability of dietary polyphenols and gut microbiota metabolism: antimicrobial properties," *BioMed research international*, vol. 2015, Article ID 905215, 18 pages, 2015.
- [9] K. Szewczyk, A. Bogucka-Kocka, N. Vorobets, A. Grzywa-Celińska, and S. Granica, "Phenolic composition of the leaves of *Pyrola rotundifolia* L. and their antioxidant and cytotoxic activity," *Molecules*, vol. 25, no. 7, p. 1749, 2020.
- [10] V. Lobo, A. Patil, A. Phatak, and N. Chandra, "Free radicals, antioxidants and functional foods: impact on human health," *Pharmacognosy Reviews*, vol. 4, no. 8, pp. 118–126, 2010.
- [11] M. Gautam, M. Agrawal, M. Gautam, P. Sharma, A. S. Gautam, and S. Gautam, "Role of antioxidants in generalised anxiety disorder and depression," *Indian journal of psychiatry*, vol. 54, no. 3, pp. 244–247, 2012.



- [12] Z. Xu and L. Chang, "Typhaceae," in *Identification and Control of Common Weeds: Volume 3*, pp. 725–731, Springer, 2017.
- [13] M. R. Rao, Y. Saranya, D. Divya, and A. C. Linn, "Preliminary phytochemical analysis of *Typha domingensis* rhizome aqueous extracts," *International Journal of Pharmaceutical Sciences Review and Research*, vol. 37, no. 1, pp. 30–32, 2016.
- [14] R. W. Long and O. Lakela, *Flora of Tropical Florida*, University of Miami Press, 1971.
- [15] D. He, B. R. T. Simoneit, B. Jara, and R. Jaffé, "Gas chromatography mass spectrometry based profiling of alkyl coumarates and ferulates in two species of cattail (*Typha domingensis* P., and *Typha latifolia* L.)," *Phytochemistry Letters*, vol. 13, pp. 91–98, 2015.
- [16] E. Sezik, E. Yeşilada, M. Tabata et al., "Traditional medicine in Turkey VIII. Folk medicine in East Anatolia; Erzurum, Erzincan, Ağrı, Kars, Iğdir provinces," *Economic Botany*, vol. 51, no. 3, pp. 195–211, 1997.
- [17] A. Lopes, M. J. Rodrigues, C. Pereira et al., "Natural products from extreme marine environments: searching for potential industrial uses within extremophile plants," *Industrial Crops and Products*, vol. 94, pp. 299–307, 2016.
- [18] E. J. Al-Kalifawi, Y. J. Al-Azzawi, K. Al-Fartousi, and H. M. Musa, "Physicochemical, phytochemical profiling and biological activities of leaves extract of *Bardy* (*Typha domingensis* Pers.) from Al-Chibayish Marshes in Southern Iraq," in *Arts, humanities and natural sciences conferences*, 2017.
- [19] W. M. Bandaranayake, "Traditional and medicinal uses of mangroves," *Mangroves and Salt Marshes*, vol. 2, no. 3, pp. 133–148, 1998.
- [20] I. Imran, T. Javed, A. Jabeen et al., "Synthesis, characterization and docking studies of amide ligands as anti-leishmanial agents," *Pakistan Journal of Pharmaceutical Sciences*, vol. 33, 1(Supplementary), pp. 385–392, 2020.
- [21] E. K. Akkol, I. Süntar, H. Keles, and E. Yesilada, "The potential role of female flowers inflorescence of *Typha domingensis* Pers. in wound management," *Journal of ethnopharmacology*, vol. 133, no. 3, pp. 1027–1032, 2011.
- [22] T. Chai, M. Mirohsha, H. Ong, and F. Wong, "Antioxidant, iron-chelating and anti-glucosidase activities of *Typha domingensis* Pers (Typhaceae)," *Tropical Journal of Pharmaceutical Research*, vol. 13, no. 1, pp. 67–72, 2014.
- [23] D.-H. Truong, D. H. Nguyen, N. T. A. Ta, A. V. Bui, T. H. Do, and H. C. Nguyen, "Evaluation of the use of different solvents for phytochemical constituents, antioxidants, and in vitro anti-inflammatory activities of *Severinia buxifolia*," *Journal of Food Quality*, vol. 2019, Article ID 8178294, 9 pages, 2019.
- [24] M. Aziz, S. Ahmad, M. N. Iqbal et al., "Phytochemical, pharmacological, and *In-silico* molecular docking studies of *Strobilanthes glutinosus* Nees: An unexplored source of bioactive compounds," *South African Journal of Botany*, vol. 147, pp. 618–627, 2022.
- [25] M. N. Shahzad, S. Ahmad, M. I. Tousif et al., "Profiling of phytochemicals from aerial parts of *Terminalia neotaliala* using LC-ESI-MS<sup>2</sup> and determination of antioxidant and enzyme inhibition activities," *PloS one*, vol. 17, no. 3, article e0266094, 2022.
- [26] P. D. Choudhary and H. A. Pawar, "Recently investigated natural gums and mucilages as pharmaceutical excipients: an overview," *Journal of pharmaceuticals*, vol. 2014, Article ID 204849, 9 pages, 2014.
- [27] B. A. Ghalloo, K.-u.-R. Khan, S. Ahmad et al., "Phytochemical profiling, in vitro biological activities, and in silico molecular docking studies of *Dracaena reflexa*," *Molecules*, vol. 27, no. 3, p. 913, 2022.
- [28] N. U. A. Nawaz, M. Saeed, K. Rauf et al., "Antinociceptive effectiveness of *Tithonia tubaeformis* in a vincristine model of chemotherapy-induced painful neuropathy in mice," *Bio-medicine & Pharmacotherapy*, vol. 103, pp. 1043–1051, 2018.
- [29] F. Tunnisa, D. N. Faridah, A. Afriyanti et al., "Antioxidant and antidiabetic compounds identification in several Indonesian underutilized Zingiberaceae spices using SPME-GC/MS-based volatilomics and *in silico* methods," *Food Chemistry: X*, vol. 14, article 100285, 2022.
- [30] E. Neagu, G. L. Radu, C. Albu, and G. Paun, "Antioxidant activity, acetylcholinesterase and tyrosinase inhibitory potential of *Pulmonaria officinalis* and *Centarium umbellatum* extracts," *Saudi journal of biological sciences*, vol. 25, no. 3, pp. 578–585, 2018.
- [31] E. Bursal, A. Aras, Ö. Kılıç, P. Taslimi, A. C. Gören, and İ. Gülçin, "Phytochemical content, antioxidant activity, and enzyme inhibition effect of *Salvia eriophora* Boiss. & Kotschy against acetylcholinesterase,  $\alpha$ -amylase, butyrylcholinesterase, and  $\alpha$ -glycosidase enzymes," *Journal of food biochemistry*, vol. 43, no. 3, article e12776, 2019.
- [32] M. N. Islam, H. Tasnim, L. Arshad et al., "Stem extract of *Albizia richardiana* exhibits potent antioxidant, cytotoxic, antimicrobial, anti-inflammatory and thrombolytic effects through in vitro approach," *Clinical Phytoscience*, vol. 6, no. 1, pp. 1–9, 2020.
- [33] T. Kebede, E. Gadisa, and A. Tufa, "Antimicrobial activities evaluation and phytochemical screening of some selected medicinal plants: a possible alternative in the treatment of multidrug-resistant microbes," *PLoS One*, vol. 16, no. 3, article e0249253, 2021.
- [34] S. Tabassum, S. Ahmad, K. u. R. Khan et al., "Phytochemical profiling, antioxidant, anti-inflammatory, thrombolytic, hemolytic activity in vitro and in silico potential of *Portulacaria afra*," *Molecules*, vol. 27, no. 8, p. 2377, 2022.
- [35] A. Deghima, N. Righi, N. Rosales-Conrado et al., "Anti-inflammatory activity of ethyl acetate and *n*-butanol extracts from *Ranunculus macrophyllus* Desf. and their phenolic profile," *Journal of Ethnopharmacology*, vol. 265, article 113347, 2021.
- [36] A. Basit, S. Ahmad, A. Naeem, M. Usman, I. Ahmed, and M. N. Shahzad, "Chemical profiling of *Justicia vahlii* Roth. (Acanthaceae) using UPLC-QTOF-MS and GC-MS analysis and evaluation of acute oral toxicity, antineuropathic and antioxidant activities," *Journal of Ethnopharmacology*, vol. 287, article 114942, 2022.
- [37] R. Sorourian, A. E. Khajehrahimi, M. Tadayoni, M. H. Azizi, and M. Hojjati, "Ultrasound-assisted extraction of polysaccharides from *Typha domingensis*: structural characterization and functional properties," *International Journal of Biological Macromolecules*, vol. 160, pp. 758–768, 2020.
- [38] P. K. Mukherjee, V. Kumar, M. Mal, and P. J. Houghton, "Acetylcholinesterase inhibitors from plants," *Phytomedicine*, vol. 14, no. 4, pp. 289–300, 2007.
- [39] T.-T. Chai, M.-J. Chiam, C.-H. Lau et al., "Alpha-glucosidase inhibitory and antioxidant activity of solvent extracts and fractions of *Typha domingensis* (Typhaceae) fruit," *Tropical Journal of Pharmaceutical Research*, vol. 14, no. 11, pp. 1983–1990, 2015.

## Retraction

# Retracted: Ameliorated Stomach Specific Floating Microspheres for Emerging Health Pathologies Using Polymeric Konjac Glucomannan-Based Domperidone

### BioMed Research International

Received 8 January 2024; Accepted 8 January 2024; Published 9 January 2024

Copyright © 2024 BioMed Research International. This is an open access article distributed under the Creative Commons Attribution License, which permits unrestricted use, distribution, and reproduction in any medium, provided the original work is properly cited.

This article has been retracted by Hindawi following an investigation undertaken by the publisher [1]. This investigation has uncovered evidence of one or more of the following indicators of systematic manipulation of the publication process:

- (1) Discrepancies in scope
- (2) Discrepancies in the description of the research reported
- (3) Discrepancies between the availability of data and the research described
- (4) Inappropriate citations
- (5) Incoherent, meaningless and/or irrelevant content included in the article
- (6) Manipulated or compromised peer review

The presence of these indicators undermines our confidence in the integrity of the article's content and we cannot, therefore, vouch for its reliability. Please note that this notice is intended solely to alert readers that the content of this article is unreliable. We have not investigated whether authors were aware of or involved in the systematic manipulation of the publication process.

Wiley and Hindawi regrets that the usual quality checks did not identify these issues before publication and have since put additional measures in place to safeguard research integrity.

We wish to credit our own Research Integrity and Research Publishing teams and anonymous and named external researchers and research integrity experts for contributing to this investigation.





The corresponding author, as the representative of all authors, has been given the opportunity to register their agreement or disagreement to this retraction. We have kept a record of any response received.

### References

- [1] J. M. M. Mohamed, N. Mahajan, M. El-Sherbiny et al., "Ameliorated Stomach Specific Floating Microspheres for Emerging Health Pathologies Using Polymeric Konjac Glucomannan-Based Domperidone," *BioMed Research International*, vol. 2022, Article ID 3670946, 12 pages, 2022.

## Research Article

# Ameliorated Stomach Specific Floating Microspheres for Emerging Health Pathologies Using Polymeric Konjac Glucomannan-Based Domperidone

Jamal Moideen Muthu Mohamed <sup>1</sup>, Nikita Mahajan,<sup>2</sup> Mohamed El-Sherbiny <sup>3,4</sup>,  
Shagufta Khan <sup>2</sup>, Rasha Hamed Al-Serwi,<sup>5</sup> Mohammed A. Attia,<sup>3,6</sup>  
Qamar Alsayed Altriny,<sup>3</sup> and Ahmed H. Arbab <sup>7</sup>

<sup>1</sup>Vaasudhara College of Pharmacy, Sante Circle, Chintamani Road, Hoskote, 562114 Karnataka, India

<sup>2</sup>Institute of Pharmaceutical Education and Research, Borgaon (Meghe), Wardha, Maharashtra 442 001, India

<sup>3</sup>Department of Basic Medical Sciences, College of Medicine, AlMaarefa University, P.O. Box 71666, Riyadh 11597, Saudi Arabia

<sup>4</sup>Department of Anatomy, Faculty of Medicine, Mansoura University, Mansoura, Egypt

<sup>5</sup>Department of Basic Medical Sciences, College of Dentistry, Princess Nourah Bint Abdulrahman University, P.O. Box 84428, Riyadh 11671, Saudi Arabia

<sup>6</sup>Department of Clinical Pharmacology, Faculty of Medicine, Mansoura University, 35516 Mansoura, Egypt

<sup>7</sup>Department of Pharmacognosy, Faculty of Pharmacy, University of Khartoum, Al-Qasr Ave, Khartoum 11111, Sudan

Correspondence should be addressed to Shagufta Khan; shaguftakhan17@rediffmail.com  
and Ahmed H. Arbab; ahmed.arbab@uofk.edu

Received 18 May 2022; Revised 27 June 2022; Accepted 30 June 2022; Published 13 July 2022

Academic Editor: Barkat Khan

Copyright © 2022 Jamal Moideen Muthu Mohamed et al. This is an open access article distributed under the Creative Commons Attribution License, which permits unrestricted use, distribution, and reproduction in any medium, provided the original work is properly cited.

The goal of this study was to use polymeric konjac glucomannan (KGM), Kollidon VA 64 (KVA64), and glutaraldehyde to ameliorate stomach specific floating microspheres (SSFMs) using domperidone (DoN) to increase *in vivo* bioavailability and emerging health pathologies. The SSFM were made using the emulsion cross-linking process, and the polymer was chosen based on its ability to get cross-linked. The thermodynamic parameters were used to determine the  $A_L$  classes of phase solubility curves using ideal complexes produced with KVA64. The optimal interaction constants at 25 and 37°C were found to be 116.14 and 128.05 M<sup>-1</sup>, respectively. The prepared SSFM had an average particle size (PS) of 163.71 ± 2.26 μm and a drug content of 96.66 ± 0.32%. It can be determined from *in vitro* drug release experiments that drug release is good in terms of regulated drug release after 12 h (92.62 ± 2.43%). The SSFMs were approximately sphere-shaped and had smooth surfaces, according to the morphological data. SSFMs were investigated using Fourier transform infrared (FT-IR) spectroscopy, X-ray diffraction (XRD), and differential scanning calorimetry (DSC), and no chemical structural changes were identified. The SSFMs produce a considerable gastric residence time with optimal DoN release and absorption in stomach fluid, and the mean residence time (17.36 ± 1.4 h) and  $t_{1/2}$  (10.47 ± 0.6 h) were considerably longer ( $p < 0.05$ ) than those obtained following i.v. treatment (MRT = 8.42 ± 1.2 h;  $t_{1/2}$  = 9.07 ± 0.7 h). The SSFMs maintained good physical stability for three months when stored at room temperature.

## 1. Introduction

Despite their potential pharmacological action, the bottleneck for the effective introduction of many new drugs is their poor solubility. Aqueous insoluble compounds account

for over 90% of all chemicals in pharmaceutical drug delivery systems. Poor solubility can be a big concern since an active pharmaceutical ingredient (API) cannot reach its molecular target in the body if it remains undissolved in the gastrointestinal tract (GIT) and is therefore removed

[1]. As a result, improving the molecules solubility is a crucial step in ensuring that it survives the pharmaceutical development process. If their bioavailability is restricted by their water solubility, even compounds with a significantly positive impact on their physiological target will not be developed further. Furthermore, poorly water soluble drugs are commonly given at large doses to attain the required plasma drug concentration, resulting in increased adverse reactions and therapy costs, as well as unpredictable pharmacological responses, resulting in poor patient compliance.

Additionally, if the drug is expensive, the manufacturing cost will rise since a huge proportion of API will be used to research and produce the medicinal product. Since a result, solubilization technologies that address this issue are becoming increasingly relevant to the pharmaceutical industry, as they offer up new avenues for developing effective and marketable drug delivery systems from APIs that would otherwise be lost [2]. Solid dispersion, cocrystallization, micronization, nanonization, solid lipid nanoparticles microemulsion, self-microemulsifying and nanoemulsifying drug delivery systems, and liposomes are some of the methods used to improve the dissolution and solubility of poor aqueous soluble drugs [3].

Solid dispersions (SDs) have found more attention over the years for two main reasons: first, they afford a greater enhancement in dissolution or solubility rate associated to crystal habit ensuring effective, and second, they reduce recrystallization/agglomeration of drug molecules due to molecular interactions with the carrier matrices [4]. The SD permits high drug concentrations to be available in the GIT by increasing their apparent solubility and provide several order of improvement in bioavailability of poorly water-soluble drugs. Amorphous carriers like PVP, PEG, cross-povidone (PVP-CL), PVP-VA, and polymethacrylates are widely used to improve solubility. Meloxicam ASD was made by utilizing HPMC and carriers such as polyacrylates and polymethacrylates. SDs of meloxicam exhibited much better dissolution behavior than crystalline meloxicam. It was reported that meloxicam was presented in the amorphous form by SDs which lead to its improved dissolution behavior [5]. Prepared SDs of chlortetracycline hydrochloride using hydrophilic polymers like PVP and copovidone, Authors reported that SDs increased almost ten-fold chlortetracycline hydrochloride solubility, which they attributed to the amorphous characters of the SDs, proposing the event of intermolecular interactions.

While a drug displays not only poor aqueous solubility but also a pH-dependent solubility, it becomes imperative to retain the formulation at the site in the GIT where it shows maximum solubility in order to improve its bioavailability. For the drugs which show greater solubility in the stomach than other parts of the GIT, one of the most significant techniques of achieving stomach retention of such drugs in order to increase their bioavailability is to use a floating drug delivery device.

Entrapment of air (e.g., hollow chambers) or the integration of low-density constituents can produce the inherent low density (e.g., oils or fatty materials or foam powder). A single-unit floating system containing polypropylene foam powder, matrix-forming polymers, drug, and filler was

recently presented. This device exhibited good floating behavior and accurate drug release control. Single-unit dosage formulations, on the other hand, have been associated to problems like sticking together or becoming blocked in the GIT, both of which can be unpleasant [6]. Multiple-unit floating systems, on the other hand, may be appealing since they have been shown to reduce inter- and intrasubject variability in drug absorption as well as the danger of dose spillage.

Numerous multiple-unit floating systems, such as the air compartment multiple-unit system, hollow microspheres (microballoons), microparticles designed for low-density foam powder, and low-density beads, can be widely dispersed throughout the stomach, allowing for a longer and more reliable drug release [7]. Nonetheless, to regulate their qualities, these several unit floating systems are created using tough and demanding approaches with laborious operational settings.

In this study, an attempt was made to develop floating microspheres using a simple, scalable approach that did not require the addition of an effervescent agent, low-density oil, or foam powder, all of which are crucial processing factors. Floating microspheres were prepared using natural polysaccharide konjac glucomannan (KGM) because it is nontoxic, biodegradable, and biocompatible and easily available from the tuber of the *amorphophallus* plant. KGM is made up of 1:6 molar ratio of 4-linked -D- mannose and glucose units. It is a somewhat branched polymer having acetyl groups on the backbone ninth and twentieth positions. The innate polysaccharide KGM was used to make floating microspheres since it is nontoxic, biodegradable, and biocompatible, as well as being readily accessible from the tuber of the *amorphophallus* plant. In the molar ratio of 1:6, KGM is made up of 1, 4-linked  $\beta$ -D-mannose and glucose units. It is a quite branched polymer having acetyl groups on the backbone's ninth and twentieth positions [8]. It has a great feature of quick gelling and high swelling capacity, which is helpful to the floating ability, due to the large number of hydroxyl groups on the saccharide units. However, studies on application of KGM in the preparation of floating microspheres are nonexistent.

In the present investigation, domperidone (DoN) is used as a model drug. The DoN is a peripherally selective dopamine D<sub>2</sub> and D<sub>3</sub> antagonist. By inhibiting dopamine receptors in the gastric antrum and duodenum, it promotes upper gastrointestinal motility to a partial support and lower esophageal sphincter pressure. DoN has poor water solubility, which displays pH dependence with greater solubility in stomach than intestine. Its oral bioavailability is poor (13 to 17%) due to poor aqueous solubility [9]. Therefore, it was attempted to first improve the solubility of DoN by formulating ASD using Kollidon VA 64 and successively formulating floating microspheres loaded with DPASD that can be retained in the stomach.

## 2. Materials

Domperidone (DoN) and Kollidon VA 64 (KVA64) were received as gift samples from FDC Limited, Mumbai, India. Konjac glucomannan (KGM) was purchased from Konjac

TABLE 1: Various composition of prepared SSFMs.

SSFMs	(%w/w)	KGM		Drug % w/w of polymer ratio		Equ. Wt. of SD (mg)
		For 15 mL (mg)		% w/w	wt.in mg	
DF1	1	150		30	45	124.86
DF2	1.5	225		30	67.5	187.29
DF3	2	300		30	90	249.72
DF4	1	150		40	60	166.48
DF5	1.5	225		40	90	249.72
DF6	2	300		40	120	322.96

\*Volume of KGM solution was 15 mL, cotton seed oil was 30 mL, and glutaraldehyde (25% w/v) was 50 mL for all batches.

Food, China. Acetone, Acetonitrile and HPLC grade of methanol were procured from the Loba Chemie Pvt. Ltd., Mumbai, India. Ethanol and isopropyl alcohol were purchased from Thermo Fisher Scientific Pvt. Ltd., Mumbai, India.

**2.1. Phase Solubility Study.** The phase solubility investigation was carried out according to Higuchi and Connors approach [10]. Excess DoN was added to distilled water containing various concentrations of Kollidon VA 64 in 20-mL capped bottles, stirred for 48 h at 25 and  $37 \pm 0.5$  °C on magnetic stirrer, filtered, and spectrophotometrically analyzed at 283 nm using a double-beam spectrophotometer (UV 2401(PC),S.220V Shimadzu Corporation, Japan). According to the following equation, the apparent complexation constant  $K_{1:1}$  of DoN-KVA64 was estimated from the intercept and slope of the straight line of the phase solubility graph.

$$K_{1:1} = \frac{\text{Slope}}{S_0 (1 - \text{Slope})}, \quad (1)$$

where  $S_0$  (intercept) is the solubility of DoN in the absence of complexing agent.

**2.2. Preparation of SD.** Solid dispersion was prepared by the solvent evaporation method [11]. DoN and KVA64 (1:1) were added to 10 mL solvents containing ethanol and acetone (1:1). The mixture was continuously stirred (100 rpm with  $37 \pm 1$  °C), and the solvent was evaporated. The mass was crushed, passed through the sieve no. 40, and stored in desiccators, and physical mixture was also prepared by geometrical mixing of drug and carrier. Drug content of SD was determined by stirring 100 mg SD in 100 mL ethanol for 24 h, and then the mixture was filtered, diluted suitably, and analyzed spectrophotometrically at 208 nm.

**2.3. Saturated Solubility (SS) Study.** The SS of samples (DoN, PM, and SD) was determined in distilled water and pH 1.2 at room temperature (RT). Excess amount of samples was added 20 mL of above stated solution in screw-capped glass vials. Then, the vials were stirred for 48 h at  $25 \pm 0.5$  °C using thermostatically controlled magnetic stirrer (REMI 2) retained at speed of 50 strokes per min [12]. After 48 h, the content in respective vial was withdrawn and filtered using

Whatman filter paper No.42, and the amount of DoN dissolved in different medium was determined spectrophotometrically at 208 nm. Each experiment was carried out in triplicate.

**2.4. Drug Content (DC).** The solid dispersion (50 mg) was dispersed in 50-mL volumetric flask using ethanol and stirred for 24 h at  $25 \pm 0.5$  °C using magnetic stirrer maintained at speed of 50 strokes per min. The material was then filtered via Whatman filter paper no. 42 after 24 h [12]. The absorbance was measured at 284 nm using a twin beam UV visible spectrophotometer after appropriate dilutions were prepared.

**2.5. Dissolution Study.** The dissolution studies on pure DoN, PM, and SD (equivalent to 10 mg of DoN) was supported out by USP paddle apparatus (type II) by 500 mL dissolution medium (distilled water and 0.1 N HCL). Rotation speed was 100 rpm and temperature ( $T$ ) was maintained  $37 \pm 1$  °C [13]. 5 mL sample was removed at regular intervals (30, 60, 90, 120, 150, 180, and 210 min), and aliquot was withdrawn and replaced with equal volume of fresh dissolution medium, filtered, and analyzed, using double-beam UV spectrophotometer at 284 nm.

**2.6. Preparation of Stomach Specific Floating Microspheres (SSFm).** The various concentrations of KGM were allowed to swell overnight in distilled water to get homogeneous solution, and viscosity of each solution was determined. To KGM solutions, SD equivalent to drug 30%w/w of KGM was added and emulsified with cotton seed oil, containing 0.5% w/v span 80 by homogenizing for 3 h at 3000 rpm (Table 1). Glutaraldehyde (aqueous, 25% w/v) comprising 0.5 mL of 1 N HCL was added gently to the emulsion with homogenization for 2 h, and microspheres were collected by centrifugation at 6000-8000 rpm. Thereafter, separated microspheres were washed with isopropyl alcohol to remove the excess oil from surface, and unreacted glutaraldehyde then freeze dried (Lark Innovative Fine Technology, Chennai, India, Model; Penguin Classic Plus;  $-20$  °C and 0.13 bar) for 24 h [14]. DoN content in microspheres was determined by soaking 100 mg crushed microspheres in 100 mL ethanol for 24 h and filtered and then analyzed the filtrate at 208 nm.

The following formulae were used to estimate the drug content and entrapment efficiency (EE):

$$\text{Drug Content} = \frac{\text{Weight of drug in Microspheres}}{\text{weight of Microsphere}}, \quad (2)$$

$$\%EE = \frac{\text{Actual drug content}}{\text{Theoretical drug content}} \times 100.$$

**2.7. Micromeritic Properties.** Particle size (PS) was determined using imaging system (Metzger optical instrument, Sr. No. 666 Mathura, India). Fifty microspheres from each batch were measured, and the average PS was determined.

For bulk density, 1g microspheres were placed in a 10 mL capacity measuring cylinder, and volume was noted. Tapped density was determined by mentioning the volume of the known weight of microspheres after 100 taps. Moreover, micromeritic properties such as Carr's index (% compressibility), Hausner ratio, and angle of repose were evaluated according to the method described by Thapa and Chaudhary [15].

**2.8. Surface Morphology.** For surface morphology, microspheres were layered with platinum and visualized under analytical scanning electron microscope (Model S-3700N, Hitachi, Japan) according to the method described by Muthu et al. [12].

**2.9. Floating Study.** Microspheres (100 mg) were dispersed across the surface of a USP dissolving apparatus type II filled with 300 mL of 0.1 N HCL pH 1.2 for *in vitro* buoyancy testing. A paddle moving at 100 rpm was used to stir the medium for 12 h. Microspheres floating and settling sections were retrieved individually. The microspheres were weighed after drying, and the ratio of the mass of the microspheres that stayed floating to the overall mass of the microspheres was used to compute buoyancy percentage. The following formulas [16] were used to calculate the buoyancy percentage by dividing the mass of the microspheres that remained to float by the overall mass of the microspheres.

$$\%Buoyancy = \frac{W_f}{(W_f + W_s)} \times 100, \quad (3)$$

where  $W_f$  and  $W_s$  are the weights of the floating and settled microspheres.

## 2.10. Solid-State Characterization

**2.10.1. Fourier Transform Infrared (FT-IR) Analysis.** FTIR analysis was performed using an FT-IR spectrophotometer (Model No. 84005 Shimadzu Asia Pacific Pvt. Ltd. Singapore). The powdered samples were pelleted with KBr, and the disc was scanned in the range of 4000-400  $\text{cm}^{-1}$  [17].

**2.10.2. Differential Scanning Calorimetric (DSC) Analysis.** For DSC, 5 mg of samples were enclosed in an aluminum pan and evaluated between 30 and 300°C at a scanning rate of 10°C.min<sup>-1</sup> [17]. During the runs, a nitrogen purge at a

rate of 20 mL.min<sup>-1</sup> was maintained, and indium was used as a benchmark for T and heat flow calibrations (Model DSC 60, Shimadzu Tokyo, Japan).

**2.10.3. Powder X-Ray Diffraction (PXRD) Analysis.** An X-ray diffraction examination was done on a copper anode operating under CuK radiation (1.5406, 45 kV, and 40 mA) (SmartLab, Rigaku Corporation, Tokyo, Japan). Patterns were made on a 2 scale with a step width of 0.05°/s from 2 to 50° at RT [17].

**2.11. In Vitro Drug Release.** Drug release from SSFMs was investigated in 0.1 N HCL at pH 1.2 for 12 h using USP type II apparatus at the stirring speed of 100 rpm. Equivalent weight of SSFMs to 10 mg of DoN was kept in 500 mL of dissolution medium continued at 37 ± 0.5°C. Throughout the dissolution study, 5 mL aliquot was withdrawn at predetermined time intervals and analyzed for percentage dissolved DoN at 283 nm. The aliquots withdrawn were replaced with equal volume of the drug-free medium [13]. Cumulative present drug dissolved was determined at each time interval and plotted against time.

## 2.12. Bioavailability Study in Rats

**2.12.1. Experimental Design.** The study employed male Wistar albino rats weighing 200-250 g. The Institutional Animal Ethical Committee accepted the study (Approval No. IAEC/2018-2019). Animals were kept in polypropylene cages at T of 24 ± 2°F, with a relative humidity (RH) of 40-60% and a 12-hour light-dark cycle. The animals were under fasting for 12 h before dosing and kept fasting throughout the study and allowed to take water.

The study was conducted on 42 rats which were separated into 2 groups (21 rats in each group). Animals of group I received SSFM equivalent to 0.15 to 0.18 mg of DoN at the dose level 0.75 mg/Kg orally [18]. The SSFMs were suspended in 1 mL saline and administered with the help of J tube. Animals of group II received 25  $\mu\text{L}$  DoN dissolved in 0.9% saline with concentration 6 mg/mL intravenously through tail vein, and the dose was equivalent to 0.75 mg/Kg.

Animals were anaesthetized by intraperitoneal injection of 50 mg/kg ketamine, and 0.5 mL blood was withdrawn through the tail vein at the predetermined time intervals in the heparinized tubes [18]. Subsequently plasma was separated, deproteinized by treating with acetonitrile, and centrifuged. 20  $\mu\text{L}$  of supernatant was injected in the reversed phase C18 column (HiQSil C18 HS (250 × 4.6 mm i.d., particle size 5  $\mu\text{m}$ ; KYA Tech Corporation, Japan) and detected by UV detector at 210 nm. The mobile phase contained phosphate buffer pH 7.4, methanol, and acetonitrile (40:30:30) and flowed at 1.5 mL/min, and at each time point, three rats were tested. Standard calibration curve of DoN was prepared with plasma spiked with known amounts of drug with concentration in the range of 2-10  $\mu\text{g/mL}$ .

**2.12.2. Gastroretentive Assessment in Rats.** Microspheres were prepared in the same procedure described previously by adding 50 mg barium sulfate to the 5 mL of glucomannan

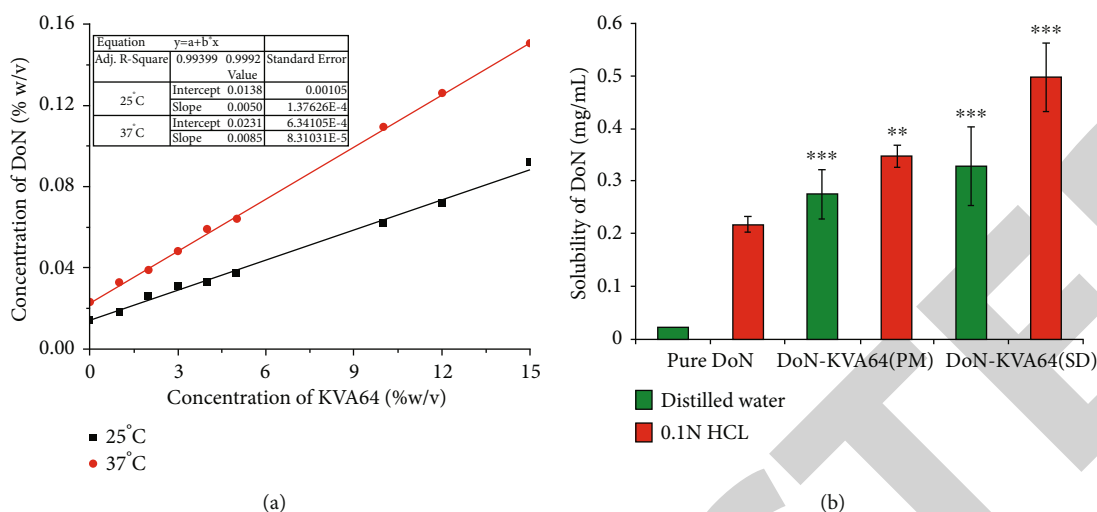


FIGURE 1: (a) Phase solubility diagram of DoN in distilled water at 25 and 37°C in the presence of KVA64 and (b) SS data of pure DoN, PM, and SD (mg/mL). \*\*\*  $p < 0.05$  indicates significant differences between the control group and was assessed using the Student  $t$ -test.

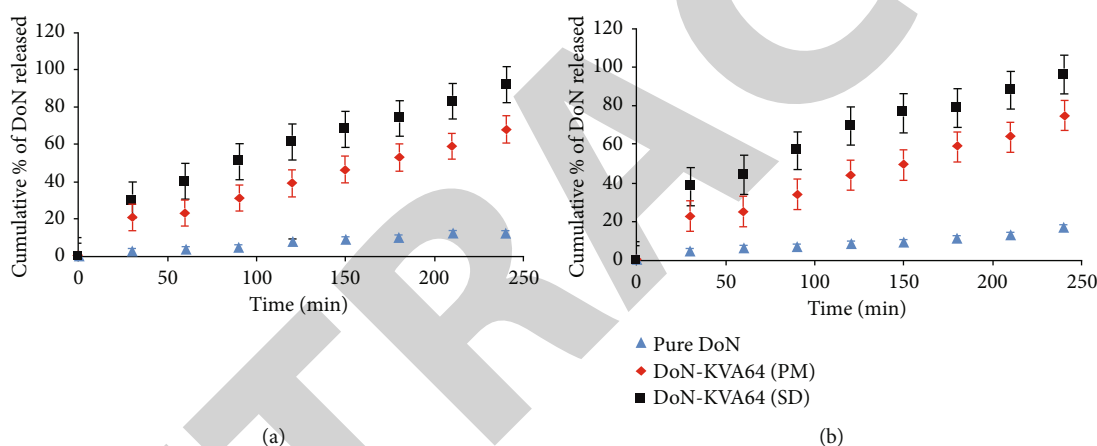


FIGURE 2: Dissolution behavior of DoN-KVA64 PM and SD: (a) 0.1N HCL and (b) distilled water.

solution [19]. Weight of microspheres containing DoN equivalent to 0.75 mg/kg dose was suspended in 1 mL saline and administered per oral route to the rats. X-ray was done, and images were taken at different time points. Three animals were used for the study.

2.13. *Stability Study.* The prepared DoN microspheres (wrapped in aluminum foil) were stored at 40°C and 75 ± 5% RH for six months as part of a stability investigation. The microspheres were visually evaluated every month for physical changes, DC, PS, and *in vitro* drug release [20].

2.14. *Statistical Analysis.* The unpaired (two-tailed)  $t$ -test was used to compare the data of two groups. The significance threshold was chosen at  $p < 0.05$ .

### 3. Result and Discussions

3.1. *Outcome from Phase Solubility Data.* The phase solubility PS curve displayed linear increase in the solubility of DoN with the increase in KVA64 concentration with corresponding T. The KVA64 concentration was varied from

$2.281 \times 10^{-4}$  to  $2.435 \times 10^{-4}$  mM with 25 and 37°C. The stability constant ( $K_{1:1}$ ) was attained from the complex ranked in the order of 25 and 37°C as DoN ( $116.14$  and  $128.05 M^{-1}$ ), which resulted in solubility increase of DoN from 0.171 to 0.433 mM (Figure 1(a)). The equation of the straight line was  $y = 0.0.0050x + 01380$ ,  $R^2 = 0.9992$  and  $y = 0.0.0085x + 0231$ ,  $R^2 = 0.99399$  at 25 and 37°C, respectively. The curve was  $A_L$  type because the slope was less than unity. Mohamed et al. (2021) proven that, this type of curve is obtained when one molecule of DoN complexes with one molecule of the KVA64 as  $K_{1:1}$ . As the phase solubility curve depicted  $A_L$ -type curve, SD was prepared using 1 : 1 ratio of DoN: KVA64 [21].

3.2. *SS.* The SS of pure DoN in distilled water and 0.1 N HCL at 25°C was found to be 0.0225 and 0.218 mg/mL after 48 h, respectively. There was ~12 and ~14 and ~1.5 and ~2.3 fold improvement in SS of DoN from PM and SD in distilled water and 0.1N HCL, respectively (Figure 1(b)). The KVA64 is the amorphous carrier which enhances wettability and dispersibility of drug. The surfactant surface properties increase wetting properties by lowering the surface tension

TABLE 2: Micrometric properties of DoN floating microspheres.

Batches	Micrometric properties					EE (%)
	Bulk density	Tap density	Hausner's ratio	Carr's index	Angle of repose	
DF1	$0.048 \pm 0.02$	$0.059 \pm 0.035$	$1.229 \pm 0.025$	$0.186 \pm 0.035$	$27.47^\circ \pm 0.025$	$88.29 \pm 2.89$
DF2	$0.064 \pm 0.15$	$0.070 \pm 0.02$	$1.093 \pm 0.015$	$0.085 \pm 0.065$	$26.56^\circ \pm 0.064$	$94.93 \pm 2.51$
DF3	$0.119 \pm 0.035$	$0.153 \pm 0.035$	$1.285 \pm 0.019$	$0.222 \pm 0.025$	$31.79^\circ \pm 0.034$	$95.85 \pm 3.55$
DF4	$0.054 \pm 0.025$	$0.080 \pm 0.018$	$1.48 \pm 0.025$	$0.325 \pm 0.055$	$28.81^\circ \pm 0.048$	$91.11 \pm 3.76$
DF5	$0.068 \pm 0.044$	$0.092 \pm 0.063$	$1.35 \pm 0.022$	$0.260 \pm 0.0340$	$39.69^\circ \pm 0.06$	$88.35 \pm 3.34$
DF6	$0.096 \pm 0.06$	$0.137 \pm 0.048$	$1.427 \pm 0.36$	$0.299 \pm 0.048$	$24.70^\circ \pm 0.025$	$92.17 \pm 2.11$

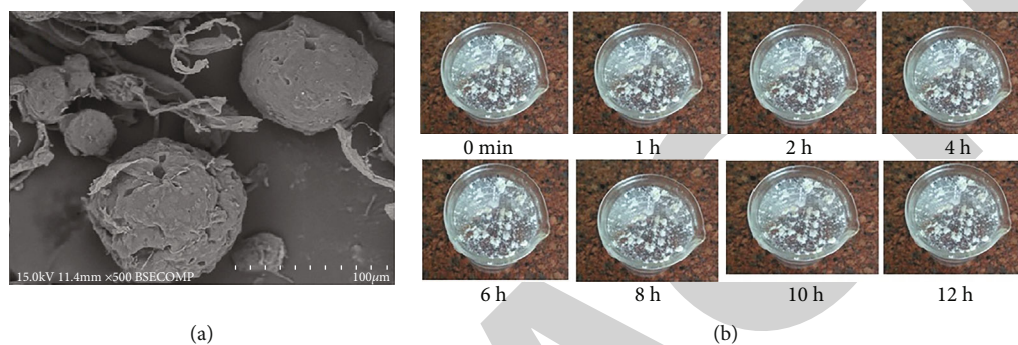


FIGURE 3: (a) Scanning electron micrograph of optimized batch DF2; (b) floating behavior of domperidone floating microsphere (DF2).

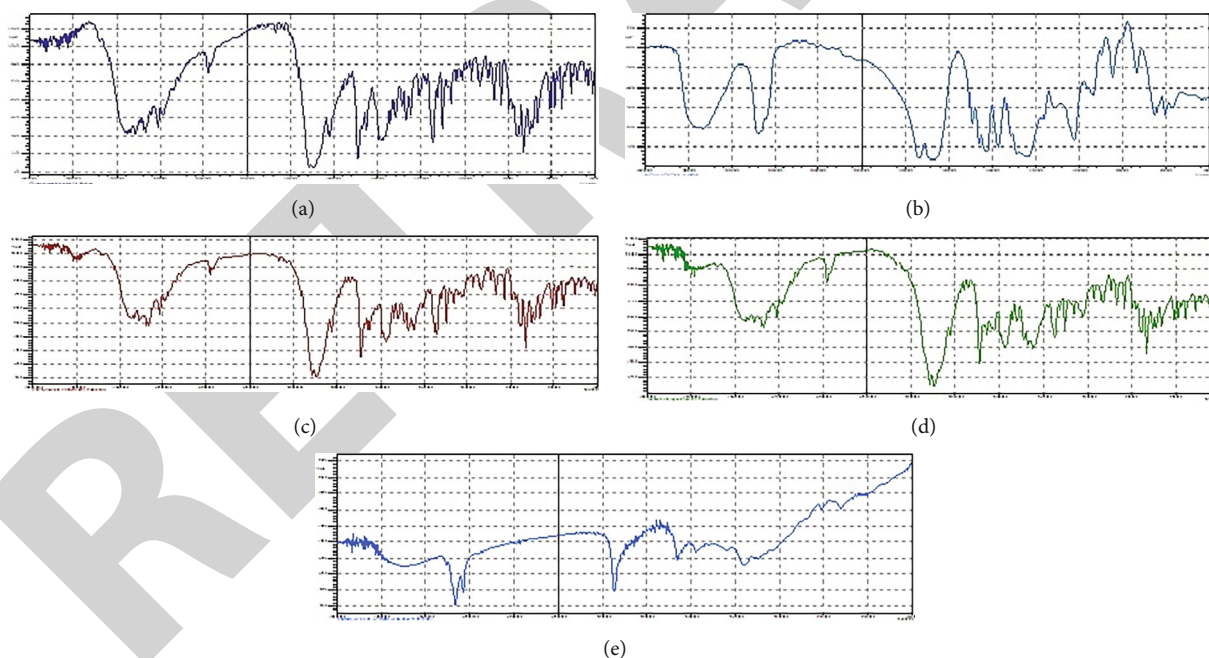


FIGURE 4: FI-IR spectrum of (a) pure DoN, (b) KVA64, (c) DoN-KVA64 (PM), (d) DoN-KVA64 (SD), and (e) SSFM-DF2.

of the vehicle utilized, allowing medication molecules to permeate the aqueous environment [22]. Furthermore, the viscosity of KVA64 may affect the solubility of DoN in aqueous environments.

3.3. DC. The quantity present in the DoN, from prepared SD, ranges from 83.77 to 97.23%, and the material loss with reference to the DoN content was found to be 5.76 to 11.91%

of the material. The moderate material loss was observed with KVA64 because of little cohesive nature and sticky environment in the semisolid state.

3.4. Dissolution of DoN. The free crystalline DoN release was  $12.23 \pm 2.16$  and  $17.12 \pm 1.88\%$  in 4h with distilled water and 0.1N HCL, respectively, while DoN release from PM was  $68.02 \pm 4.09$  and  $75.56 \pm 3.32$  at the end of 4h in water



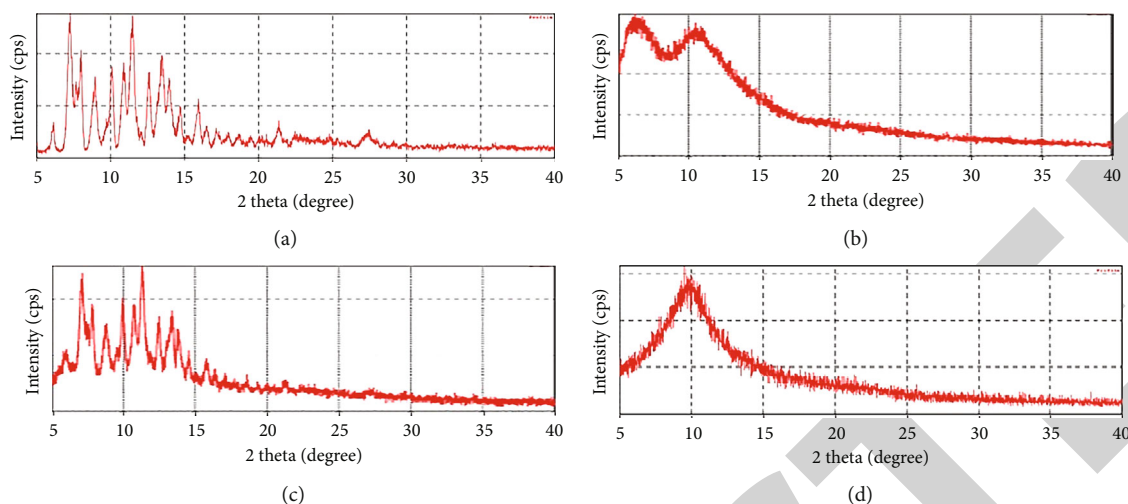


FIGURE 5: XRD pattern of (a) pure DoN, (b) KVA64, (c) DoN-KVA64 (SD), and (d) SSFM-DF2.

and 0.1 N HCL (Figure 2(a)). Figure 2(b) illustrates rapid initial burst release ( $30.26 \pm 2.06$  and  $38.71 \pm 3.18\%$  in 30 min) followed by steady release in both distilled water and 0.1 N HCL from prepared SDs with maximum release of  $92.11 \pm 3.11$  and  $96.11 \pm 4.4\%$  at the end of 4 h. The controlled dissolution is due to molecular dispersion of DoN in SDs. The reason of the molecular dispersion is that greater surface area of DoN was exposed to the medium. The rapid dissolution was due to DoN molecular dispersion in SD because of the molecule dispersion; DoN surface area was exposed to the medium in higher amounts. Rapid dissolution of KVA64 because of its amorphous and hydrophilic nature resulted in the rapid release of DoN which had transformed into amorphous form upon being dispersed in SD; moreover, SD could dissolve rapidly because of their thermodynamic instability [23].

**3.5. EE (%)**. The percent EE of CRL-MC and CRL-NCs, respectively, was  $84.12 \pm 0.33$  and  $83.61 \pm 0.80$  percent (Table 2). CRL lipophilicity ( $\log P = 3.8$ ) can be attributed to these low percent EE values, allowing it to be efficiently integrated into PVP/SDS dual carriers in the prepared formulations. According to Alqahtani et al., a lipophilic drug might enhance EE by employing lipid as an encapsulating carrier [24].

**3.6. Micromeritics**. The mean PS of DoN floating microspheres was in the range of  $16.20 \pm 0.036$  to  $25.19 \pm 0.041$   $\mu\text{m}$ . The PS was found dependent on the concentration of KGM and ratio of KGM to cross-linker (glutaraldehyde). The PS was found to be larger for batches DF3 and DF6 because viscosity of 2% w/v KGM used in their formulation was appreciably high, which could have affected appropriate diffusion of glutaraldehyde in KGM phase for cross-linking. Additionally, amount of cross-linker might perhaps be insufficient for the stated amount of KGM to form dense network. The rank order for particle size was  $\text{DF1} < \text{DF2} < \text{DF3}$ . At low level of KGM, there was better cross-linking as a result of which dense particles with small size were formed.

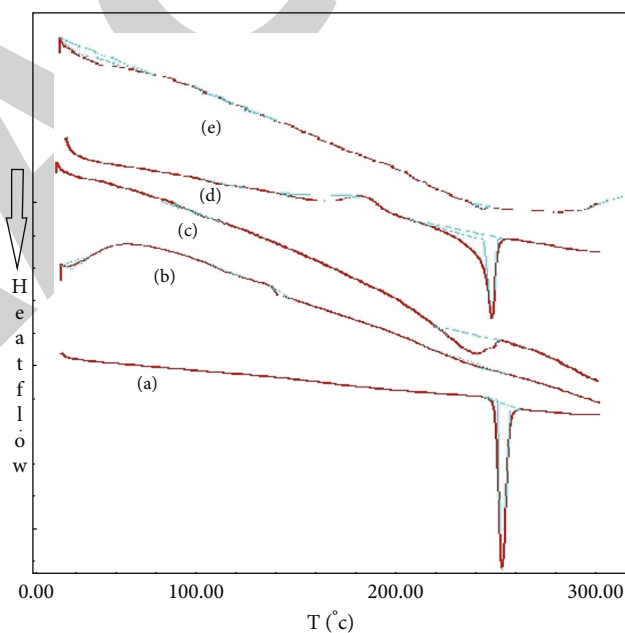


FIGURE 6: DSC thermogram of (a) pure DoN, (b) KVA64, (c) DoN-KVA64 (PM), (d) DoN-KVA64 (SD), and (e) SSFM-DF2.

**3.7. Morphology**. In Figure 3(a), the microspheres were spherical with nearly smooth surface. From the SEM, cross-linked surface was evident. There were few pores on the surface which could be due to diffusion of hydrophilic KVA64 from the microspheres during drug loading and cross-linking process.

**3.8. Buoyancy In Vitro**. The microspheres became buoyant immediately and remained floating for more than 12 h. First, the low density of the microspheres formed from glucomannan held them on the surface. Second, quick and high polymer hydration resulted in a quick volume enlargement of the microspheres, which served to lower the density and

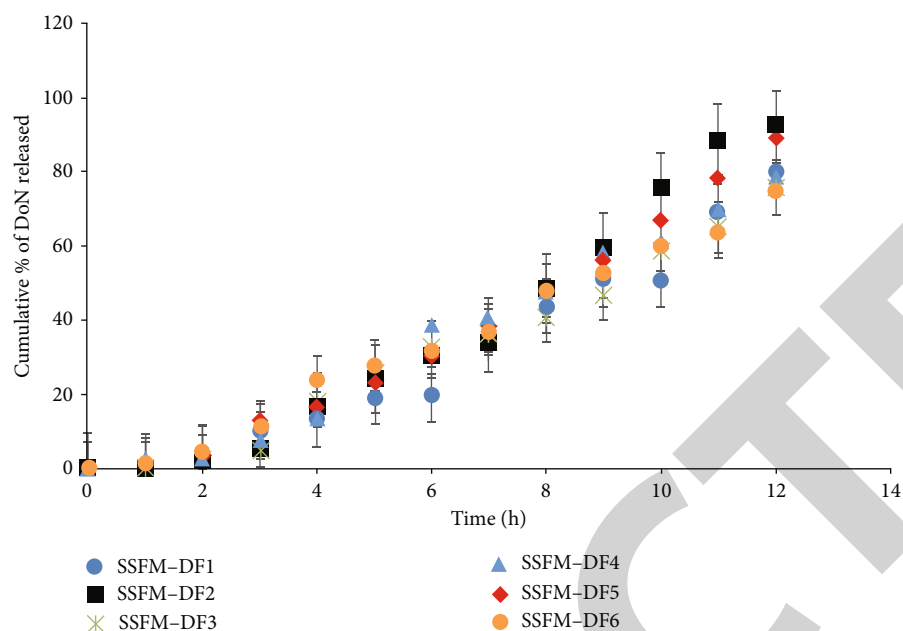


FIGURE 7: *In vitro* DoN released from various SSFMs.

TABLE 3: Treatment of *in vitro* drug release data with different kinetic equations.

Batches	Mathematical model ( $r^2$ )					Release exponents
	Zero order	First order	Hixson-Crowell	Higuchi plot	Korsmeyer-Peppas	
DF1	0.985 ± 0.048	0.928 ± 0.087	0.987 ± 0.089	0.952 ± 0.043	0.895 ± 0.043	1.201 ± 0.192
DF2	0.994 ± 0.056	0.931 ± 0.087	0.991 ± 0.051	0.951 ± 0.047	0.861 ± 0.033	1.567 ± 0.091
DF3	0.992 ± 0.091	0.903 ± 0.076	0.972 ± 0.043	0.973 ± 0.068	0.842 ± 0.081	1.786 ± 0.213
DF4	0.992 ± 0.055	0.913 ± 0.076	0.982 ± 0.054	0.973 ± 0.032	0.881 ± 0.018	1.887 ± 0.134
DF5	0.990 ± 0.061	0.913 ± 0.064	0.992 ± 0.067	0.960 ± 0.078	0.907 ± 0.043	1.524 ± 0.157
DF6	0.996 ± 0.075	0.876 ± 0.092	0.973 ± 0.067	0.983 ± 0.078	0.916 ± 0.032	1.096 ± 0.155

significantly improve the buoyancy of the microspheres [25]. In low pH condition, cross-linked KGM microspheres remained stable and therefore kept floating throughout the 12-h study (Figure 3(b)). The strength of beta chain in glycosidic linkage of glucomannan might have been responsible for stability of microspheres in the low pH condition. Glutaraldehyde synthesis of cross-linked konjac-glucomannan and kappa carrageenan films).

### 3.9. Solid-State Characterization of DPASD by FTIR, DSC, and XRD

**3.9.1. FTIR.** FT-IR spectra of DoN and physical mixture of DoN and Kollidon VA 64 were used to examine likely molecular interactions between DoN and KVA64 in the solid state and to detect the change in characteristics of DoN if any, in ASD. Characteristic IR peaks of DoN were observed at 3122.54, 3024.18, 2923.88, 1716.53, 1670.24, and 1622.02  $\text{cm}^{-1}$  due to NH group, aromatic CH stretching, aliphatic CH group stretching, C=O stretching, NH diffraction, and C-H diffraction (scissoring), respectively (Figure 4). All the characteristic peaks were retained in the

physical mixture of DoN and KVA64. The peaks attributed to DoN were unaltered in the FTIR of SD also, denying any possible chemical interaction between DoN and KVA64 in solid dispersion [26].

FTIR of domperidone shows characteristic peaks at 3122.54  $\text{cm}^{-1}$  due to NH group stretching imide, 3024.18  $\text{cm}^{-1}$  due to aromatic C-H stretching, 2923.88  $\text{cm}^{-1}$  due to aliphatic C-H group stretching, 1716.534 and 1695.31  $\text{cm}^{-1}$  due to C=O stretching, 1670.24 and 1622.02  $\text{cm}^{-1}$  due to NH diffraction, and 1456.16  $\text{cm}^{-1}$  due to C-H diffraction (scissoring).

**3.9.2. XRD.** X-ray diffraction (XRD) analysis of DoN exhibited distinctive diffraction peaks at  $2\theta = 14.49^\circ, 18.36^\circ, 19.5^\circ, 20^\circ, 21^\circ,$  and  $22.8^\circ$  (Figure 5) which confirms crystalline nature of the drug. These characteristics peaks were retained in the physical mixture implicating no change in the crystal behavior of DoN. However, the diffraction pattern for solid dispersion depicted peaks at  $2\theta = 14.55^\circ, 15.02^\circ, 15.64^\circ, 18.45^\circ, 19.74^\circ, 19.98^\circ, 22^\circ,$  and  $22.65^\circ$  which were different from that of DoN demonstrating change in crystal structure. There is no sharp peaks in KVA64 confirming its

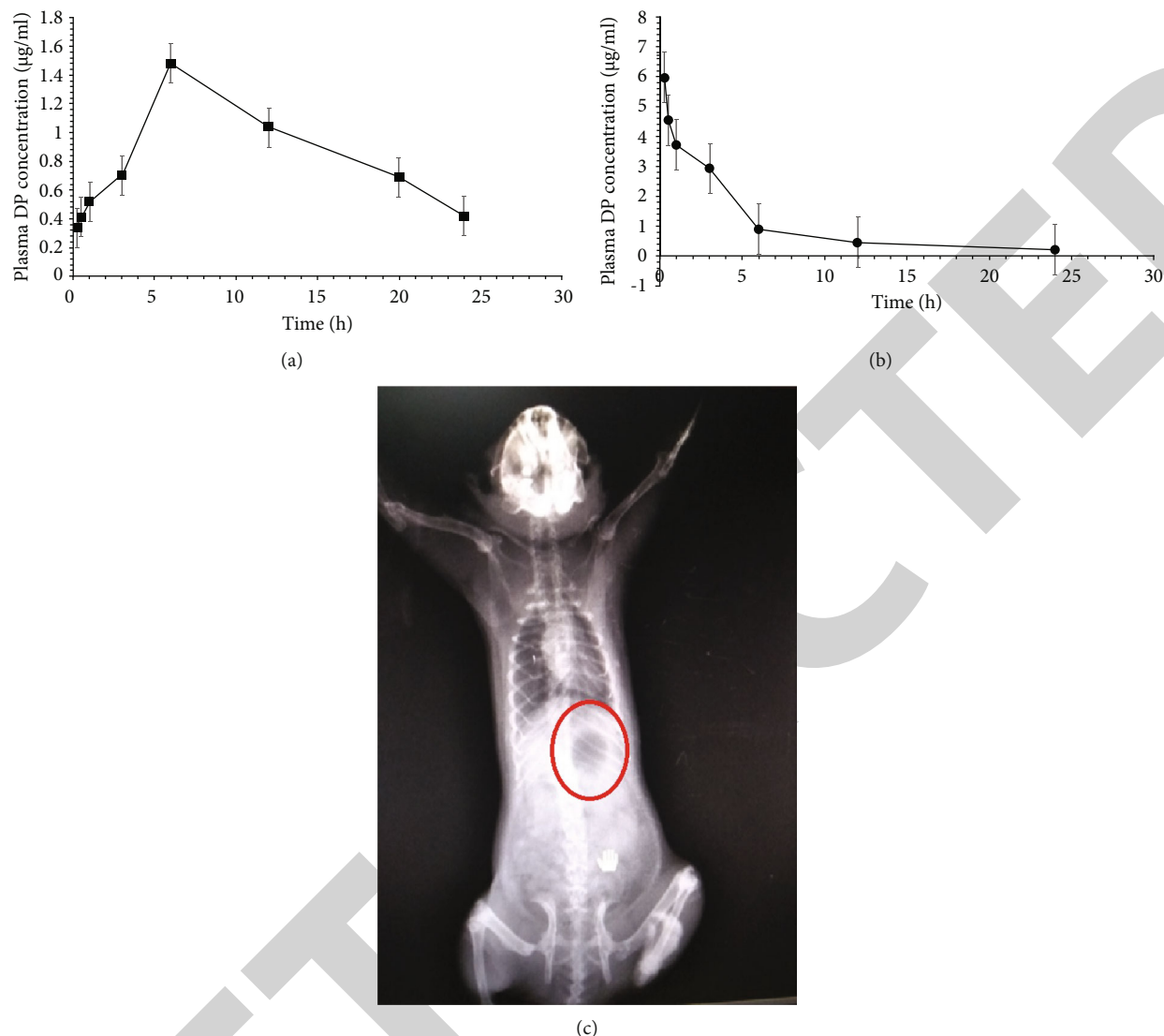


FIGURE 8: Plasma DoN concentration at (a) oral route, (b) intravenous of administration, and (c) 12h after dosage, radiographic X-ray pictures of the formulation in the rat gastrointestinal region.

TABLE 4: Pharmacokinetic parameters of DoN after i.v. and oral floating microspheres administration.

S. no	Parameters	Intravenous	Oral
1	$C_{max}$ ( $\mu\text{g/mL}$ )	$5.99 \pm 0.562^\dagger$	$1.48 \pm 0.54234$
2	$C_0$ ( $\mu\text{g/mL}$ ; extrapolated)	$7.88 \pm 0.527$	—
3	$T_{max}$ (h)	—	6
4	$AUC_{0-24}$ ( $\mu\text{g/mL}\cdot\text{h}$ )	$25.92 \pm 6.481$	$21.55 \pm 4.65$
5	$t^{1/2}$ (h)	$9.07 \pm 0.771$	$10.47 \pm 0.6746$
6	MRT (h)	$8.42 \pm 1.269$	$17.36 \pm 1.4386$

†: nonextrapolated.

amorphous nature (Figure 5(b)). Reduction in intensity of characteristic peaks was observed in physical mixture, which might be because of partial masking of peaks of drug [27]. Change in the position of peaks of the drug and appearance

of the new peaks in the solid dispersion indicates change in the crystalline nature of the drug. Sharp intense peaks of drug was completely missing in microspheres, indicating entrapment of DoN in the microspheres.

3.9.3. DSC. The DSC thermogram of DoN exhibited a characteristic, sharp endothermic peak at  $253.2^\circ\text{C}$  which is associated with the melting point of the drug and indicates the crystalline nature (Figure 6(a)). The peak is slightly broadened in the solid dispersion due to the reduction in crystalline of DoN. The broad endothermic peak at  $244.68^\circ\text{C}$  in the physical mixture of DoN and Kollidon corresponds to the melting of DoN. Broadening of peak and reduction in temperature indicate decrease in crystallinity [28]. Broadened endothermic peak at reduced temperature of  $25^\circ\text{C}$  confirms decrease in crystallinity of DoN. There was a small endothermic peak of the drug in microsphere at reduced T of  $246.63^\circ\text{C}$  indicating decreased crystallinity and encapsulation in the microspheres.

TABLE 5: Various stability parameters of CRL-NCs.

Evaluations	0 month	1 month	3 month	6 month
DC * (%)	96.66 ± 0.32	94.94 ± 1.34	92.15 ± 1.79	89.95 ± 2.66
PS * (μm)	163.71 ± 2.26	167.38 ± 3.98	168.11 ± 4.45	170.88 ± 4.11
EE (%) *	94.93 ± 2.51	91.12 ± 3.23	79.44 ± 2.85	76.54 ± 4.19
<i>In vitro</i> release (after 12 h)*	92.62 ± 2.43	90.21 ± 4.16	87.33 ± 5.32	84.71 ± 5.41

\*Each value expressed as mean, ( $n = 3; \pm$  SD).

**3.10. In Vitro Drug Release.** The cumulative % drug release of all SSFM-DF1 to SSFM-DF6 was in range of  $73.59 \pm 0.41$  to  $92.62 \pm 2.43\%$  in 12 h (Figure 7). Rate of drug release was slower from DF1 as compared to DF2 because the particles were more strongly cross-linked; thus, there was restricted diffusion of drug. Microparticles prepared from high level of KGM (DF3 and DF6) also produced slow dissolution rates. In case of DF3 and DF6, the initial drug release rate was controlled by cross-linking, while with the slumping cross-link strength as the time passed, the viscous gel network due to high level of KGM played predominant role in controlling the drug release rate during later time points.

Formulation DF2 gave maximum drug release ( $92.62 \pm 2.43\%$ ) in 12 h (Table 3). Maximum linearity was observed for zero order ( $R^2 = 0.994$ ), while slope of Korsmeyer-Peppas equation was found 1.567. Slope greater than one indicates super case II that is drug release by diffusion and chain relaxation [29]. Drug release by chain relaxation often happens in cross-linked matrices where cross-linking strength declines with time.

**3.11. In Vivo Bioavailability Testing.** Figures 8(a) and 8(b) show the mean plasma drug concentration time curve of DoN following oral, and i.v. administration of DoN-loaded SSFM, respectively. Table 4 lists the noncompartment pharmacokinetic parameters determined using the software PKSolver. After oral administration of microspheres, the maximal blood concentration was reached at 6 h, and a consistent level of drug was continued for another 12 h. The constant level of DoN was due to prolonged retention of microspheres in the stomach and uniform and prolonged release of the drug in the stomach.

The absolute bioavailability of the DoN from floating microspheres was  $83 \pm 0.579\%$ , which was significantly higher than its reported oral bioavailability of 13 to 17% [30]. The improvement in bioavailability from floating microspheres may be attributed to the improvement in solubility of DoN by solid dispersion and gastroretention of the microspheres in the environment where solubility was good. The mean residence time of drug from microspheres ( $17.36 \pm 1.4$  h) and  $t_{1/2}$  ( $10.47 \pm 0.6$  h) were significantly greater ( $p < 0.05$ ) than obtained after i.v. administration (MRT =  $8.42 \pm 1.2$  h;  $t_{1/2} = 9.07 \pm 0.7$  h).

**3.12. Radiographic Study in Rats.** The floating capability of SSFM was tested in simulated gastric fluid for enhanced stomach residence. KGM: SD (1.5:67.5 percent w/w) was used to make DF2, and DF2 with high *in vitro* buoyancy

was chosen for further testing using the radiological approach. The gastroretentive feature of microspheres is evident in X-ray images collected at 0 and 12 h for the buoyancy investigation (Figure 8(c)), stressing a large gastric residency period for optimal drug release and absorption at stomach fluid due to the porous structure of SSFMs [31].

**3.13. Stability Studies.** The CRL-NCs was maintained for further characterization and stability testing. According to the data in Table 5, the SSFM remained stable for six months at  $45 \pm 0.5^\circ\text{C}$  and 60% RH. Only a minor increase in PS ( $170.88 \pm 4.11 \mu\text{m}$ ) was noticed after six month storage. In another hand, very little impact on DC, % EE, and cumulative *in vitro* DoN release was observed after storage such as  $89.95 \pm 2.66\%$ ,  $76.54 \pm 4.19\%$ ,  $87.34 \pm 3.11\%$ , respectively. This outcome suggests that, when stored at RT, CRL-NCs have a good physical stability [32].

## 4. Conclusion

High degree of improvement in solubility of SD could be achieved for DoN using KVA64 in both distilled water and 0.1 N HCL which was then loaded successfully in floating microsphere containing KGM. It was then prepared by emulsion cross-linking method with the entrapment efficiency as high as  $94.93 \pm 2.51\%$  from the present study, and it was found that glucomannan microspheres had the inherent property to float without the aid of any floating agent. The improvement in *in vivo* bioavailability from SSFM-DF2 might be attributed to the improvement in solubility of DoN by SD and gastroretention of the microspheres where solubility was good. Therefore, KGM can serve as a potential polymeric carrier for formulation of floating microsphere by very simple reproducible and scalable technique as achieved in the present investigation.

## Data Availability

The original contributions presented in the study are included in the article; further inquiries can be directed to the corresponding author.

## Conflicts of Interest

The authors declare that they have no conflicts of interest.

## Acknowledgments

The work was supported by the Researchers Supporting program (MA-006), AlMaarefa University, Riyadh, Saudi Arabia. The work was supported by Princess Nourah Bint Abdulrahman University Researchers Supporting Project number (PNURSP2022R199), Princess Nourah Bint Abdulrahman University, Riyadh, Saudi Arabia.

## References

- [1] K. T. Savjani, A. K. Gajjar, and J. K. Savjani, "Drug solubility: importance and enhancement techniques," *ISRN Pharmacology*, vol. 2012, Article ID 195727, 10 pages, 2012.
- [2] S. Verma, A. Rawat, M. Kaul, and S. Saini, "Solid dispersion: a strategy for solubility enhancement," *Inter JIPBS Pharmacy Tech*, vol. 2, no. 4, pp. 482–494, 2015.
- [3] V. P. Bharti, V. R. Attal, A. V. Munde, A. S. Birajdar, and S. Bais, "Strategies to enhance solubility and dissolution of a poorly water soluble drug," *Journal of Innovations in Pharmaceuticals and Biological Sciences*, vol. 2, no. 4, pp. 482–494, 2015.
- [4] P. Paulsamym, K. Venkatesan, J. M. Muthu Mohamed et al., "Empowerment of primary healthcare providers on the prevention and management of dental or oral health issues among postchemotherapy patients in pandemic," *Journal of Healthcare Engineering*, vol. 2022, Article ID 9087776, 9 pages, 2022.
- [5] H. Suzuki, K. Yakushiji, S. Matsunaga et al., "Amorphous solid dispersion of meloxicam enhanced oral absorption in rats with impaired gastric motility," *Journal of Pharmaceutical Sciences*, vol. 107, no. 1, pp. 446–452, 2018.
- [6] F. S. Razavi, M. Kouchak, F. Feizoleslam, and M. Veysi, "An overview on floating drug delivery systems (FDDS); conventional and new approaches for preparation and *in vitro-in vivo* evaluation," *FABAD Journal of Pharmaceutical Sciences*, vol. 46, no. 3, pp. 345–362, 2021.
- [7] K. Thakar, G. Joshi, and K. K. Sawant, "Bioavailability enhancement of baclofen by gastroretentive floating formulation: statistical optimization, *in vitro* and *in vivo* pharmacokinetic studies," *Drug Development and Industrial Pharmacy*, vol. 39, no. 6, pp. 880–888, 2013.
- [8] J. Apiwongngam, W. Limwikrant, A. Jintapattanakit, and M. Jaturanpinyo, "Enhanced supersaturation of chlortetracycline hydrochloride by amorphous solid dispersion," *Journal of Drug Delivery Science and Technology*, vol. 47, pp. 417–426, 2018.
- [9] T. Charoenying, P. Patrojanasophon, T. Ngawhirunpat, T. Rojanarata, P. Akkaramongkolporn, and P. Opanasopit, "Design and optimization of 3D-printed gastroretentive floating devices by central composite design," *AAPS PharmSciTech*, vol. 22, no. 5, p. 197, 2021.
- [10] T. Higuchi and K. A. Connors, "Phase solubility techniques," *Advances in Analytical Chemistry*, vol. 4, pp. 117–119, 1965.
- [11] M. M. Jamal Moideen, A. Alqahtani, K. Venkatesan et al., "Application of the Box-Behnken design for the production of soluble curcumin: skimmed milk powder inclusion complex for improving the treatment of colorectal cancer," *Food Science & Nutrition*, vol. 8, no. 12, pp. 6643–6659, 2020.
- [12] M. J. Muthu, K. Kavitha, K. S. Chitra, and S. Nandhineeswari, "Soluble curcumin prepared by solid dispersion using four different carriers: phase solubility, molecular modelling and physicochemical characterization," *Tropical Journal of Pharmaceutical Research*, vol. 18, no. 8, pp. 1581–1588, 2019.
- [13] J. M. M. Mohamed, A. Alqahtani, B. A. Khan et al., "Preparation of soluble complex of curcumin for the potential antagonistic effects on human colorectal adenocarcinoma cells," *Pharmaceuticals*, vol. 14, no. 9, p. 939, 2021.
- [14] D. R. Getts, R. L. Terry, M. T. Getts et al., "Therapeutic inflammatory monocyte modulation using immune-modifying microparticles," *Science Translational Medicine*, vol. 6, no. 219, p. 219ra7, 2014.
- [15] C. Thapa and R. Chaudhary, "Formulation and *in-vitro* evaluation of sustained release matrix tablets of domperidone," *Journal of Universal College of Medical Sciences*, vol. 8, pp. 40–45, 2021.
- [16] A. R. Dhole, P. D. Gaikwad, V. H. Bankar, and S. P. Pawar, "A review on floating multiparticulate drug delivery system: a novel approach to gastric retention," *International Journal of Pharmaceutical Sciences Review and Research*, vol. 2, pp. 205–211, 2011.
- [17] J. M. Mohamed, A. Alqahtani, F. Ahmad, V. Krishnaraju, and K. Kalpana, "Pectin co-functionalized dual layered solid lipid nanoparticle made by soluble curcumin for the targeted potential treatment of colorectal cancer," *Carbohydrate Polymers*, vol. 252, p. 117180, 2020.
- [18] U. K. Mandal, B. Chatterjee, and F. G. Senjoti, "Gastro-retentive drug delivery systems and their *in vivo* success: a recent update," *Asian Journal of Pharmaceutical Sciences*, vol. 11, no. 5, pp. 575–584, 2016.
- [19] F. Schneider, M. Koziolok, and W. Weitschies, "*In vitro* and *in vivo* test methods for the evaluation of gastroretentive dosage forms," *Pharmaceutics*, vol. 11, no. 8, p. 416, 2019.
- [20] J. M. M. Mohamed, A. Alqahtani, A. al Fatease et al., "Human hair keratin composite scaffold: characterisation and biocompatibility study on NIH 3T3 fibroblast cells," *Pharmaceuticals*, vol. 14, no. 8, p. 781, 2021.
- [21] J. M. Mohamed, K. Kavitha, K. Ruckmani, and S. Shanmuganathan, "Skimmed milk powder and pectin decorated solid lipid nanoparticle containing soluble curcumin used for the treatment of colorectal cancer," *Journal of Food Process Engineering*, vol. 43, no. 3, pp. 1–15, 2020.
- [22] S. Parvate, P. Dixit, and S. Chattopadhyay, "Superhydrophobic surfaces: insights from theory and experiment," *The Journal of Physical Chemistry B*, vol. 124, no. 8, pp. 1323–1360, 2020.
- [23] A. K. Sav, H. Desai, M. Tarique, and P. Amin, "Solubility and dissolution rate enhancement of curcumin using Kollidon VA64 by solid dispersion technique," *International Journal of Pharm Tech Research*, vol. 4, no. 3, pp. 1055–1064, 2012.
- [24] A. Alqahtani, B. Raut, S. Khan et al., "The unique carboxymethyl fenugreek gum gel loaded itraconazole self-emulsifying nanovesicles for topical onychomycosis treatment," *Polymers*, vol. 14, no. 2, p. 325, 2022.
- [25] A. Y. Kaushik, A. K. Tiwari, and A. Gaur, "Role of excipients and polymeric advancements in preparation of floating drug delivery systems," *International Journal of Pharmaceutical Investigation*, vol. 5, no. 1, pp. 1–12, 2015.
- [26] M. Nagpal, L. Kaur, J. Chander, and P. Sharma, "Dissolution enhancement of domperidone fast disintegrating tablet using modified locust bean gum by solid dispersion technique," *Journal of Pharmaceutical Technology, Research and Management*, vol. 4, no. 1, pp. 1–11, 2016.